

**EXPLORING METAL-ORGANIC FRAMEWORKS
DERIVED NANOMATERIALS FOR ADVANCED
SUPERCAPACITORS**

A THESIS SUBMITTED TO

SHIVAJI UNIVERSITY, KOLHAPUR

FOR THE DEGREE OF

DOCTOR OF PHILOSOPHY

IN

CHEMISTRY

UNDER THE FACULTY OF

SCIENCE AND TECHNOLOGY

BY

Miss. RAKHEE RAGHUNATH BHOSALE

M. Sc.

UNDER THE GUIDANCE OF

PROF. (Dr.) SANJAY S. KOLEKAR

M. Sc., Ph. D.

**ANALYTICAL CHEMISTRY AND MATERIALS SCIENCE LABORATORY,
DEPARTMENT OF CHEMISTRY,
SHIVAJI UNIVERSITY,
KOLHAPUR – 416 004 M.S., INDIA**

JUNE - 2023

DECLARATION

I hereby declare that the thesis entitled, “*EXPLORING METAL-ORGANIC FRAMEWORKS DERIVED NANOMATERIALS FOR ADVANCED SUPERCAPACITORS*”, completed and written by me has not formed earlier on the basis for the award of any degree or similar title of this or any other university or examining body. Further, I declare that I have not violated any of the provisions under the acts of Copyright/Piracy/Cyber/IPR, etc. amended from time to time.

In view of University Grants Commission (Promotion of Academic Integrity and Prevention of Plagiarism in Higher Educational Institutions) Regulations, 2018 dated 31st July 2018, I hereby submit an undertaking that this thesis is my original work and it is free of any plagiarism. Further, this thesis has been duly checked through a Plagiarism detection tool approved by Shivaji University, Kolhapur.

Place: Kolhapur
Date:

Miss. Rakhee Raghunath Bhosale
Research Student
Department of Chemistry,
Shivaji University, Kolhapur

CERTIFICATE

This is to certify that the thesis entitled, “*EXPLORING METAL-ORGANIC FRAMEWORKS DERIVED NANOMATERIALS FOR ADVANCED SUPERCAPACITORS*”, being submitted herewith for the award of **Doctor of Philosophy in Chemistry** under the Faculty of Science and Technology of Shivaji University, Kolhapur is the result of the original research work completed by **Miss. Rakhee Raghunath Bhosale** under my supervision and guidance and to the best of my knowledge and belief, the work embodied in this thesis has not formed earlier on the basis for the award of any degree or similar title of this or any other University or examining body.

In view of university Grants Commission (Promotion of Academic Integrity and Prevention of plagiarism in Higher Educational Institutions) Regulations, 2018 dated 31st July 2018, this is to certify that the work done by the Miss. Rakhee Raghunath Bhosale is plagiarism free.

Place: Kolhapur
Date:

Prof. (Dr.) S. S. Kolekar
Research Guide
Department of Chemistry,
Shivaji University, Kolhapur

Professor and Head
Department of Chemistry,
Shivaji University, Kolhapur

ACKNOWLEDGMENT

First and foremost, I am profoundly indebted to my supervisor, Prof. (Dr.) S. S. Kolekar, Department of Chemistry, Shivaji University, Kolhapur, who gave me an opportunity to join his research group. This thesis could not have been accomplished without his inspiring, enthusiastic guidance, constructive criticism and continuous motivation throughout the course of my research work.

It is a great privilege for me to express my gratitude to Hon'ble, Prof. (Dr.) D. T. Shirke, Vice-Chancellor, Shivaji University, Kolhapur, Hon'ble, Prof. (Dr.) P. S. Patil, Pro Vice-Chancellor, Shivaji University, Kolhapur, Prof. (Dr.) K. D. Sonawane, Head, Department of Chemistry and Prof. (Dr.) G. S. Gokavi, Former Head, Department of Chemistry, Shivaji University, Kolhapur, for the encouragement to achieve excellence at the Department.

It would be great contentment to say thanks to my teachers from the Department of Chemistry for their keen interest and support in my research work. I am also thankful to all the non-teaching staff of the Chemistry Department for their kind help. As well as I would like to thank the technical staff from CFC and staff from USIC, Shivaji University, Kolhapur for their time to time helps.

I am always grateful to my research colleagues and friends Dr. Suryakant Patil, Dr. Pramod Kumbhar, Dattatray Narale, Rachana Ghaware, Omkar Kulkarni, Rohini Sankannavar, Tabbu Shaikh, and Sandip Pise for their kind cooperation, fruitful discussions, affable support and encouragement all through my research efforts. It's my immense pleasure to utter my humble gratitude to Dr. Vithoba Patil, Mr. Vijay Chavan and Prof. Deok-kee Kim.

I would like to extend my thanks to my family especially my brother Ruthivik, my husband Vinod, my sisters Tejaswini and Sneha for their heartfelt support. It's always the happiest feeling to get optimistic support from my family group including in-laws, brother-in-law Vijay, my little niece Swara and every family member, wouldn't be possible to conclude this thesis without the intense support, blessings, unconditional love and affection received from my entire family. I am immensely obliged for the sacrifices put in by my mother Supriya and father Raghunath throughout my life who always stood beside me in all the circumstances.

I am thankful to the Chhatrapati Shahu Maharaj National Research Fellowship, Government of India for their financial support. Finally, I would like to thank all the persons who directly or indirectly gave me support and encouragement throughout my research tenure.

Rakhee



List of Figures

Figure No.	Figure Caption	Page No.
1.1	Different type's energy storage devices	4
1.2	The Ragone plot depicts the energy and power densities of several energy storage devices	5
1.3	Classification of supercapacitors	10
1.4	Charge storage mechanism of supercapacitors, (a) EDLCs, (b) Pseudocapacitors and (c) Hybrid supercapacitors. ³⁶ Reproduced with permission. Copyright © 2021, Royal Society of Chemistry	11
1.5	Properties of MOFs	18
1.6	MOFs as an electrode material for supercapacitor	19
1.7	Schematic of the pristine MOFs for supercapacitor application	20
1.8	Development of the use of various MOFs in the field of supercapacitor application	25
1.9	Diagrammatic representation of plan of thesis	31
2.1	Schematic depiction of reflux condensation assembly	40
2.2	Various sophisticated techniques for the characterization of MOFs and its derived materials	43
2.3	Schematic diagram of X-Ray diffraction techniques	44
2.4	Schematic diagram of FTIR spectrometer	45
2.5	Energy level diagrams showing the states involved in Raman signal	47
2.6	Schematic diagram of Raman spectrometer	48
2.7	Schematic representation of XPS spectrometer	49
2.8	Schematic representation of scanning electron microscope	51
2.9	Schematic diagram showing the possible transition ¹⁴	52
2.10	BET instrument	54
2.11	Schematic representation of transmission electron microscope	55
2.12	Digital photograph of vibrating sample magnetometer	57
2.13	A typical cyclic voltammogram curves of (a) Supercapacitor and (b) Battery. Reproduced with permission. ²⁷ Copyright © 2018, American Chemical Society	59

2.14	A typical galvanostatic charge-discharge curves of (a) Supercapacitor and (b) Battery. Reproduced with permission. ²⁷ Copyright © 2018, American Chemical Society	60
2.15	A Nyquist plot featuring labeled significant regions. Reproduced with permission. ³⁰ Copyright © 2021, Royal Society of Chemistry	61
3.1	Schematic of synthesis of Ni-MOF nanorods via a wet chemical route	70
3.2	XRD pattern of Ni-MOF	72
3.3	FT-IR pattern of Ni-MOF	73
3.4	Raman Spectroscopy of Ni-MOF	73
3.5	SEM images of Ni-MOF	74
3.6	(a) N ₂ adsorption-desorption isotherms, (b) Pore size distribution of Ni-MOF	75
3.7	(a) XPS survey spectrum of Ni-MOF. High-resolution XPS spectra of Ni 2p, (b) C 1s, (c) and O 1s (d) regions	76
3.8	(a) CV profile of Ni-MOF at different scan rates operated from 0 to 0.3 V, (b) GCD profile for Ni-MOF at different current rates (5 to 35 mA cm ⁻²), (c) Nyquist plot of the Ni-MOF, (d) Plot of specific capacitance vs. current densities, (e) Cyclic durability test at a high current of 35 mA cm ⁻² over 3000 GCD cycles with inset of first and last five cycles, (f) Coulombic efficiency as a function of current density	79
3.9	(a) Schematic illustration of hybrid supercapacitor with Ni-MOF as a positive electrode and activated carbon as a negative electrode in KOH aqueous electrolyte, (b) Digital photograph of Ni-MOF//AC HSC device	81
3.10	(a) CV profile of HSC cell at different scan rates operated from 0 to 0.9 V, (b) GCD profile for HSC cell at different current rates (2 to 6 mA cm ⁻²), (c) Nyquist plot of the HSC device, (d) Plot of specific capacitance vs. current densities, (e) Ragone plot of HSC cell, (f) Cyclic durability test at a high current of 6 mA cm ⁻² over 3000 GCD cycles with inset of first and last five cycles	83
3.11	The handmade asymmetric supercapacitor device charged for 15 seconds and glow a red LED for almost 105 seconds (i.e. charging time 15 second discharging time 105 sec)	84

3.12	Radar plot for Ni-MOF based on supercapacitive properties	85
4.1	Schematic illustrations of the synthesis of trimetallic MOFs	94
4.2	XRD patterns of BDC-MOF and BTC-MOF	97
4.3	FTIR spectra of BDC-MOF and BTC-MOF	98
4.4	Raman spectra of BDC-MOF and BTC-MOF	99
4.5	SEM images of (a, b) BTC-MOF and (c, d) BDC-MOF at different magnifications	100
4.6	EDX spectra and elemental mapping of C, O, Co, Ni and Zn elements for (a) BDC-MOF and (b) BTC-MOF	101
4.7	TEM, HR-TEM and SAED pattern of (a) BDC-MOF and (b) BTC-MOF	102
4.8	(a, b) N ₂ adsorption-desorption isotherm and pore size distribution curve BDC-MOF, (c, d) N ₂ adsorption-desorption isotherm and pore size distribution curve BTC-MOF	103
4.9	XPS survey spectra of (a) BDC-MOF and (b) BTC-MOF, high-resolution spectra of C 1s (c, d), O 1s (e, f), Ni 2p (g, h), Co 2p (i, j) and Zn 2p (k, l) of BDC-MOF and BTC-MOF, respectively	104
4.10	(a) Comparative CV curves at 10 mV s ⁻¹ scan rate, (b) Comparative GCD curves at 5 mA cm ⁻² current density, (c) CV curves of BDC-MOF at different scan rates, (d) CV curves of BTC-MOF at different scan rates, (e) GCD curves of BDC-MOF at different current densities, (f) GCD curves of BTC-MOF at different densities	107
4.11	(a) Nyquist plots, (b) Variation of specific capacitance as a function of current density, (c) Ragone plot showing the energy density versus power density	108
4.12	Cycling performance at 25 mA cm ⁻² , and the inset shows the first and last five cycles of BDC-MOF and BTC-MOF	109
4.13	(a) CV, (b) GCD curves of the symmetric device within the various potential windows (0.4 V, 0.6 V, 0.8 V, 1.0 V and 1.2 V), (c) CV curves of the symmetric device at different scan rates, (d) GCD curves of the symmetric device at different current densities	111
4.14	(a) Nyquist plot, (b) Variation of specific capacitance as a function of current density, (c) Ragone plot showing the energy density versus	112

	power density, (d) Cycling performance at 6 mA cm^{-2} , and the inset shows the first and last five cycles of the symmetric device	
4.15	(a) Fabrication schematic of BDC-MOF//2M KOH//BDC-MOF symmetric supercapacitor device, (b) The two handmade symmetric supercapacitor device which glows a red LED	113
4.16	Radar graph for comparative study of BDC-MOF and BTC-MOF based on supercapacitive properties	114
5.1	Schematic diagram of $\text{MnFe}_2\text{-MOF}$ derived manganese ferrite (MnFe_2O_4)	123
5.2	X-ray diffraction patterns of $\text{MnFe}_2\text{-MOF}$ and its derived MnFe_2O_4	126
5.3	FT-IR spectra of $\text{MnFe}_2\text{-MOF}$ and its derived MnFe_2O_4	127
5.4	Raman spectra of $\text{MnFe}_2\text{-MOF}$ and its derived MnFe_2O_4	128
5.5	SEM images at different magnifications of (a, b) $\text{MnFe}_2\text{-MOF}$ and (c, d) its derived MnFe_2O_4	129
5.6	Elemental mapping images of (a) $\text{MnFe}_2\text{-MOF}$ and (b) its derived MnFe_2O_4	130
5.7	TEM, HR-TEM and SAED patterns of (a-d) $\text{MnFe}_2\text{-MOF}$ and (e-h) its derived MnFe_2O_4	131
5.8	Nitrogen adsorption/desorption isotherms of (a) $\text{MnFe}_2\text{-MOF}$ and (b) derived MnFe_2O_4 (the insets show pore size distribution)	132
5.9	Hysteresis curves of $\text{MnFe}_2\text{-MOF}$ and its derived MnFe_2O_4	132
5.10	High-resolution XPS spectra of (a-d) $\text{MnFe}_2\text{-MOF}$ (e-g) its derived MnFe_2O_4	134
5.11	(a) Comparison of cyclic voltammograms of $\text{MnFe}_2\text{-MOF}$ and its derived MnFe_2O_4 electrodes at a potential sweep rate of 100 mV s^{-1} , (b) Comparison of GCD curves of $\text{MnFe}_2\text{-MOF}$ and its derived MnFe_2O_4 electrodes at a current density of 1 mA cm^{-2} , (c) CV curves of $\text{MnFe}_2\text{-MOF}$ in $1 \text{ M Na}_2\text{SO}_4$ at various scan rates, (d) CV curves of derived MnFe_2O_4 in $1 \text{ M Na}_2\text{SO}_4$ at various scan rates, (e) GCD curves of $\text{MnFe}_2\text{-MOF}$ at various current densities, (f) GCD curves of MnFe_2O_4 at various current densities	135
5.12	(a) Comparative rate capability of the $\text{MnFe}_2\text{-MOF}$ and derived MnFe_2O_4 electrodes at 1 to 10 mA cm^{-2} , (b) Ragone plots of the $\text{MnFe}_2\text{-}$	136

	MOF and derived MnFe ₂ O ₄ (c) Nyquist plots of the MnFe ₂ -MOF and derived MnFe ₂ O ₄	
5.13	Cyclic stability (left versus bottom) and Coulombic efficiency (right versus bottom) of (a) MnFe ₂ -MOF and (b) Derived MnFe ₂ O ₄ electrodes for 3000 cycles measured at a current density of 10 mA cm ⁻² , the inset shows the charge-discharge curves of the first and last five cycles	137
5.14	(a) Comparison of cyclic voltammograms of ASC device at a potential sweep rate of 100 mV s ⁻¹ , (b) Comparison of GCD curves of ASC device at a current density of 1 mA cm ⁻² , (c) CV curves of ASC device in 1 M Na ₂ SO ₄ at various scan rates; (d) GCD curves of ASC device at various current densities	138
5.15	(a) Comparative rate capability of the ASC device at 1 to 8 mA cm ⁻² , (b) Ragone plots of the ASC device, (c) Nyquist plots of the ASC device	140
5.16	Cyclic stability (left versus bottom) and Coulombic efficiency (right versus bottom) of ASC device for 3000 cycles measured at a current density of 8 mA cm ⁻² , the inset shows the charge-discharge curves of the first and last five cycles	140
5.17	(a) Schematic illustration of fabricated asymmetric supercapacitor device, (b) Digital photograph of fabricated two handmade asymmetric supercapacitor device connected in series to glow the LEDs	141
5.18	Radar plot for comparative study of MnFe ₂ -MOF and derived MnFe ₂ O ₄ electrodes based on electrochemical properties	142
6.1	Schematic illustration of the synthesis of CoFe ₂ -MOF, its derived CoFe ₂ O ₄ and nanoporous carbon (NPC)	152
6.2	XRD patterns of CoFe ₂ -MOF, CoFe ₂ O ₄ and nanoporous carbon (NPC)	153
6.3	FTIR spectra of CoFe ₂ -MOF, CoFe ₂ O ₄ and nanoporous carbon (NPC)	154
6.4	Raman spectra of CoFe ₂ -MOF, CoFe ₂ O ₄ and nanoporous carbon (NPC)	155
6.5	SEM images at different magnifications of (a, b) CoFe ₂ -MOF (c, d) CoFe ₂ O ₄ (e, f) NPC	157
6.6	Elemental mapping images of (a) CoFe ₂ -MOF and its derived (b) CoFe ₂ O ₄ (c) NPC	158
6.7	TEM, HR-TEM and SAED pattern of the as-prepared CoFe ₂ -MOF (a-d), derived CoFe ₂ O ₄ (e-h) and Nanoporous carbon (i-l)	159

6.8	Nitrogen adsorption-desorption isotherm and BJH pore size distribution plots of (a, d) CoFe ₂ -MOF, (b, e) CoFe ₂ O ₄ and (c, f) NPC	160
6.9	Hysteresis curves of CoFe ₂ -MOF, its derived MnFe ₂ O ₄ and nanoporous carbon	161
6.10	High-resolution XPS spectra of (a-d) CoFe ₂ -MOF (e-g) CoFe ₂ O ₄ (h-j) NPC	162
6.11	CV curves of CoFe ₂ -MOF, CoFe ₂ O ₄ , and NPC within different operating potential windows at a constant scan rate of 100 mV s ⁻¹	163
6.12	The three-electrode electrochemical performances of CoFe ₂ -MOF-derived CoFe ₂ O ₄ and NPC: CV curves at various scan rates of (a) CoFe ₂ -MOF (b) CoFe ₂ O ₄ and (c) NPC, GCD curves at various current densities of (d) CoFe ₂ -MOF (e) CoFe ₂ O ₄ and (f) NPC	164
6.13	(a) Specific capacitance at the different current densities of CoFe ₂ -MOF, CoFe ₂ O ₄ and NPC, (b) Ragone plot of CoFe ₂ -MOF, CoFe ₂ O ₄ and NPC, (c) EIS curves of CoFe ₂ -MOF, CoFe ₂ O ₄ and NPC	165
6.14	Cycle lives measured from galvanostatic charge-discharge of the CoFe ₂ -MOF (at 10 mA cm ⁻² current density), CoFe ₂ O ₄ (at 10 mA cm ⁻² current density) and NPC (at 12 mA cm ⁻² current density) electrodes	166
6.15	Schematic illustration of fabrication of all-in-one hybrid supercapacitor device	168
6.16	Electrochemical tests of the CoFe ₂ O ₄ //NPC hybrid supercapacitor device (HSC). (a) CV curves of the CoFe ₂ O ₄ //NPC HSC device at a scan rate of 100 mV s ⁻¹ within different potential windows, (b) CV curves of CoFe ₂ O ₄ //NPC HSC device at different scan rates, (c) GCD curves of the CoFe ₂ O ₄ //NPC HSC device at 1 mA cm ⁻² with varied potential windows, (d) GCD curves of CoFe ₂ O ₄ //NPC HSC device at various current densities	169
6.17	(a) Rate capability of the CoFe ₂ O ₄ //NPC HSC device according to the GCD curves from 1 to 5 mA cm ⁻² , (b) Ragone plot of the CoFe ₂ O ₄ //NPC HSC device, (c) Nyquist plot of the CoFe ₂ O ₄ //NPC HSC device	170
6.18	Cyclic stability and Coulombic efficiency of CoFe ₂ O ₄ //NPC HSC device for 5000 cycles at the current density of 5 mA cm ⁻² (inset show first and last five GCD cycles of the stability test)	171

6.19	Radar plot for comparative study of CoFe ₂ -MOF, derived CoFe ₂ O ₄ and NPC electrodes based on supercapacitive properties	172
7.1	Schematic illustration of work carried out for thesis	181

List of Tables

Table No.	Table Caption	Page No.
1.1	Relationship between supercapacitors and other energy storage technologies	8
1.2	Properties of transition first series elements	27
2.1	X-ray diffraction methods	45
3.1	Comparison of the specific capacitances of Ni-MOF	77
4.1	Comparison of the specific capacitances of trimetallic MOF with previously reported materials	110
6.1	Textural properties of CoFe ₂ -MOF, its derived CoFe ₂ O ₄ and NPC	160

List of Abbreviations

Abbreviations	Long forms
MOF	Metal-organic framework
EDLC	Electric double-layer capacitor
W kg ⁻¹	Watt per kilogram
Wh kg ⁻¹	Watt hours per kilogram
Q	Charge
V	Voltage
SC	Supercapacitor
PC	Pseudocapacitor
AC	Activated carbon
CNTs	Carbon nanotubes
ESR	Equivalent series resistance
EES	Energy storage systems
1D	One dimensional
2D	Two dimensional
3D	Three dimensional
Csp	Specific capacitance
Es	Energy density
Ps	Power density
F g ⁻¹	Farad per gram
A g ⁻¹	Ampere per gram
mA cm ⁻²	Milliampere per centimeter square
m ² g ⁻¹	Meter square per gram
°C	Degree centigrade
mV s ⁻¹	Millivolt per second
nm	Nanometer
NPC	Nanoporous carbon
BET	Brunauer–Emmett–Teller
ASC	Asymmetric supercapacitor
CV	Cyclic voltammetry
GCD	Galvanostatic charge-discharge
EIS	Electrochemical impedance spectroscopy
LED	Light emitting diode

XRD	X-ray diffraction
FTIR	Fourier transform infrared spectroscopy
XPS	X-ray photoelectron spectroscopy
SEM	Scanning electron microscope
TEM	Transmission electron microscope
GPEs	Gel-polymer electrolytes
EDS	Energy dispersive X-ray spectroscopy
VSM	Vibrating sample magnetometer
Ni-MOF	Nickel-metal organic framework
DMF	N, N-dimethylformamide
PVA	Polyvinyl alcohol
JCPDS	Joint committee on powder diffraction standard
R_s	Series resistance
R_{ct}	Charge transfer resistance
HSC	Hybrid supercapacitor
PVDF	Polyvinylidene fluoride
NMP	N-methyl-2-pyrrolidone
η	Coulombic efficiency
BDC	Terephthalic acid
BTC	Trimesic acid
FWHM	Full-width half maxima
SSC	Symmetric supercapacitor
IUPAC	International union of pure and applied chemistry
SSA	Specific surface area
BJH	Barrett-Joyner-Halenda
MnFe ₂ -MOF	Mn/Fe metal-organic framework
MnFe ₂ O ₄	Manganese ferrite
CoFe ₂ -MOF	Cobalt-iron metal-organic framework
CoFe ₂ O ₄	Cobalt ferrite
PTA	Terephthalic acid

INDEX

Sr. No.	Content	Page No.
1.0	Introduction and Theoretical Background	1 – 37
1.1	Outline	1
1.2	Introduction	2
	1.2.1 The need of supercapacitor	2
	1.2.2 Brief history and current developments in supercapacitor	3
	1.2.3 Types of electrochemical energy storage devices	4
	1.2.3.1 Capacitor	5
	1.2.3.2 Battery	6
	1.2.3.3 Fuel cell	7
	1.2.3.4 Supercapacitor	7
	1.2.4 Types of supercapacitors	9
	1.2.4.1 Electrical double-layer capacitor (EDLC)	10
	1.2.4.2 Pseudocapacitor (PC)	10
	1.2.4.3 Hybrid capacitor	10
	1.2.5 Supercapacitor materials	11
	1.2.5.1 Carbon-based supercapacitor	11
	1.2.5.2 Conducting polymers-based supercapacitor	13
	1.2.5.3 Metal oxides-based supercapacitor	13
	1.2.5.4 MOF-based supercapacitor	14
	1.2.6 Electrical characteristics of the supercapacitor	15
	1.2.6.1 Specific capacitance	15
	1.2.6.2 Specific energy and specific power	15
	1.2.6.3 Operating potential voltage	16
	1.2.6.4 Cyclic stability	16
	1.2.7.5 Electrolyte	16
1.3	General introduction and literature survey of the materials	17
	1.3.1 Introduction to the MOF	17
	1.3.2 Literature survey of MOFs for supercapacitors	18
	1.3.2.1 Pristine MOFs for supercapacitors	19
	1.3.2.2 MOF-derived metal oxides for supercapacitors	21
	1.3.2.3 MOF-derived carbon for supercapacitors	22
	1.3.3 MOFs derived from the first transition series elements serve as electrodes for supercapacitors	25
	1.3.3.1 The properties of transition elements	26
1.4	Purpose of the dissertation	27
1.5	Plan of the work	28
1.6	References	32

2.0	Experimental Details and Characterization Techniques		38-64
2.1	Outline		38
2.2	Introduction		39
2.3	Experimental details		40
	2.3.1	Aqueous chemical method/reflux condensation method	40
	2.3.2	Substrate cleaning	41
	2.3.3	Procedure of the seed slurry and fabrication of working electrodes	42
2.4	Characterization techniques		42
	2.4.1	X-ray diffraction (XRD)	43
	2.4.2	Fourier transform infrared (FTIR) spectroscopy	45
	2.4.3	Fourier transform raman (FT-Raman) spectroscopy	46
	2.4.4	X-ray photoelectron spectroscopy (XPS)	49
	2.4.5	Scanning electron microscope (SEM)	50
	2.4.6	Energy dispersive X-ray (EDS) spectroscopy	52
	2.4.7	Specific surface area analyzer using Brunauer– Emmett– Teller (BET)	53
	2.4.8	Transmission electron microscope (TEM)	55
	2.4.9	Vibrating sample magnetometer (VSM)	56
	2.4.10	Electrochemical studies	57
	2.4.10.1	Cyclic voltammetry (CV)	58
	2.4.10.2	Galvanostatic charge-discharge (GCD)	59
	2.4.10.3	Electrochemical impedance spectroscopy (EIS)	60
	2.4.11	Supercapacitor device fabrication	61
	2.4.11.1	Electrode materials	62
	2.4.11.2	Separator	62
	2.4.11.3	Gel-polymer electrolyte (GPE)	62
2.5	References		63
3.0	Design and Development of Porous Nanorods-Based Nickel-Metal Organic Framework (Ni-MOF) for High-Performance Supercapacitor Application		65-89
3.1	Outline		65
3.2	Introduction		66
3.3	Experimental section		69
	3.3.1	Reagents	69
	3.3.2	Preparation of nickel-based metal-organic framework (Ni-MOF)	68
	3.3.3	Characterization techniques details	70
	3.3.4	Evaluation of electrode materials and electrochemical studies	70
3.4	Results and discussion		71
	3.4.1	X-ray diffraction of Ni-MOF	71
	3.4.2	Fourier transform infrared spectroscopy of Ni-MOF	72

	3.4.3	Raman spectroscopy of Ni-MOF	73
	3.4.4	Scanning electron microscopy of Ni-MOF	74
	3.4.5	Brunauer– Emmett– Teller analysis of Ni-MOF	75
	3.4.6	X-ray photoelectron spectroscopy of Ni-MOF	76
	3.4.7	Electrochemical measurements of Ni-MOF electrode	77
	3.4.8	Electrochemical measurements of hybrid supercapacitor device	81
3.5	Conclusion		85
3.6	References		86
4.0	Construction of Well-Defined Two-Dimensional Architectures of Trimetallic Metal-Organic Frameworks for High-Performance Symmetric Supercapacitors		90-119
4.1	Outline		90
4.2	Introduction		91
4.3	Experimental section		93
	4.3.1	Synthesis of MOFs	93
	4.3.2	Structural and elemental characterization	94
	4.3.3	Electrochemical measurements with a three-electrode assembly	95
	4.3.4	Electrochemical measurements of the symmetric supercapacitor	96
4.4	Results and discussion		96
	4.4.1	X-ray diffraction of trimetallic MOFs	96
	4.4.2	FT-IR spectroscopy of trimetallic MOFs	97
	4.4.3	Raman spectroscopy of trimetallic MOFs	98
	4.4.4	Scanning electron microscopy of trimetallic MOFs	99
	4.4.5	Energy dispersive X-ray analysis of trimetallic MOFs	101
	4.4.6	Transmission electron microscopy of trimetallic MOFs	101
	4.4.7	Brunauer-Emmett-Teller analysis of trimetallic MOFs	102
	4.4.8	X-ray photoelectron spectroscopy of trimetallic MOFs	103
	4.4.9	Electrochemical measurements of trimetallic MOFs	106
	4.4.10	Electrochemical measurements of symmetric supercapacitors device	110
4.5	Conclusion		114
4.6	References		116
5.0	Bimetallic MnFe₂-MOF and Its Derived MnFe₂O₄ Nanostructures for Supercapacitive Applications		120-146
5.1	Outline		120
5.2	Introduction		121
5.3	Experimental Section		123
	5.3.1	Materials	123
	5.3.2	Synthesis of MnFe ₂ -MOF and MnFe ₂ O ₄	124
	5.3.3	Structural and elemental characterization	124

	5.3.4	Electrochemical properties evaluation and preparation of working electrodes	126
5.4	Results and discussion		126
	5.4.1	X-ray diffraction of MnFe ₂ -MOF and MnFe ₂ O ₄	126
	5.4.2	FT-IR spectroscopy of MnFe ₂ -MOF and MnFe ₂ O ₄	127
	5.4.3	Raman spectroscopy of MnFe ₂ -MOF and MnFe ₂ O ₄	127
	5.4.4	Scanning electron microscopy of MnFe ₂ -MOF and MnFe ₂ O ₄	128
	5.4.5	Energy dispersive X-ray analysis of MnFe ₂ -MOF and MnFe ₂ O ₄	129
	5.4.6	Transmission electron microscopy of MnFe ₂ -MOF and MnFe ₂ O ₄	130
	5.4.7	Brunauer-Emmett-Teller analysis of MnFe ₂ -MOF and MnFe ₂ O ₄	131
	5.4.8	Vibrating-sample magnetometer of MnFe ₂ -MOF and MnFe ₂ O ₄	132
	5.4.9	X-ray photoelectron spectroscopy of MnFe ₂ -MOF and MnFe ₂ O ₄	133
	5.4.10	Capacitance characterization of electrode	134
	5.4.11	Capacitance characterization of solid-state asymmetric supercapacitor (ASC) device (MnFe ₂ -MOF//AC)	137
5.5	Conclusion		142
5.6	References		144
6.0	Hybrid Supercapacitor Based on Nanoporous Carbon and CoFe₂O₄ Derived From a Single Bimetallic-Organic Framework: One-for-All Approach		147-175
6.1	Outline		147
6.2	Introduction		148
6.3	Experimental section		149
	6.3.1	Chemicals	149
	6.3.2	Synthesis of CoFe ₂ -MOF and its derived cobalt ferrite and nanoporous carbon	150
	6.3.3	Material characterization	150
	6.3.4	Preparation of working electrodes	151
	6.3.5	Preparation of an all-in-one solid-state hybrid supercapacitor device	151
	6.3.6	Electrochemical measurements	151
6.4	Results and discussion		152
	6.4.1	X-ray diffraction of CoFe ₂ -MOF, CoFe ₂ O ₄ and NPC	153
	6.4.2	FT-IR spectroscopy of CoFe ₂ -MOF, CoFe ₂ O ₄ and NPC	154
	6.4.3	Raman spectroscopy of CoFe ₂ -MOF, CoFe ₂ O ₄ and NPC	155
	6.4.4	Scanning electron microscopy of CoFe ₂ -MOF, CoFe ₂ O ₄ and NPC	156

	6.4.5	Energy dispersive X-ray analysis of CoFe ₂ -MOF, CoFe ₂ O ₄ and NPC	158
	6.4.6	Transmission electron microscopy of CoFe ₂ -MOF, CoFe ₂ O ₄ and NPC	158
	6.4.7	Brunauer-Emmett-Teller analysis of CoFe ₂ -MOF, CoFe ₂ O ₄ and NPC	160
	6.4.8	Vibrating-sample magnetometer of CoFe ₂ -MOF, CoFe ₂ O ₄ and NPC	161
	6.4.9	X-ray photoelectron spectroscopy of CoFe ₂ -MOF, CoFe ₂ O ₄ and NPC	162
	6.4.10	Electrochemical measurements of CoFe ₂ -MOF, CoFe ₂ O ₄ and NPC electrodes	163
	6.4.11	Electrochemical characterization of CoFe ₂ O ₄ //NPC all-in-one hybrid supercapacitor device (CoFe ₂ O ₄ //NPC HSC device)	167
6.5	Conclusion		172
6.6	References		173
7.0	80-Recommendation		176-182
7.1	Outline		176
7.2	Introduction		177
7.3	Conclusion		177
7.4	Summary		180
7.5	Future findings		182

CHAPTER ONE

Introduction and Theoretical Background

1.1 Outline

This chapter provides an overview of energy storage technologies such as supercapacitors and MOF-based supercapacitors, as well as theoretical background of these devices, electrochemical properties and variables affecting their performance. It is also addressed, how metal-organic frameworks are now used in supercapacitor applications. A comprehensive review of the literature has been offered together with suggestions on how to enhance the electrochemical performance of supercapacitors. The numerous methods and procedures for improving the electrochemical characteristics of MOF as a supercapacitor material that are described in the literature are also illustrated. This chapter aims to encourage ongoing innovation to enhance MOF-derived functional materials for supercapacitor application. It also offers some perspectives on current key obstacles and their potential solutions. Finally, a detailed survey of the top five groups on MOF and its derived materials used in supercapacitor applications is provided using the Scopus database.

1.2 Introduction

In the twenty-first century, the quickly growing modern world of technology, transportation, and industrialisation needs massive energy. Due to the limited availability of fossil fuels and their limited global deposition, clean energy sources that include energy storage and conversion are crucial for the sustainable development of human society. A crucial foundation for economic growth is the entry of energy. Industrialization, which is supported by non-renewable resources such as coal, crude oil, and petrol, is the cause of contemporary economic progress. The world is currently dealing with an irreversible environmental problem called global warming, caused by overconsumption of non-renewable resources, which leads to exhaustion. Efforts are being made to produce clean, inexpensive, efficient, and dependable energy sources since they are crucial for socio-economic development in order to address this issue. Renewable energy sources are the only way to meet the need for clean and secure energy sources. But these resources' biggest flaw is that they are sporadic, which makes them unreliable. We need strong and trustworthy energy storage devices to get over this limitation of renewable fuels. In other words, we need to transition from "scanty, sparse and unreliable energy collectors" to "reliable, speedy, superior and sustainable energy storage benefits".¹⁻³

1.2.1 The need of supercapacitor

The growth of technology and human civilization has resulted in increased energy consumption, necessitating expensive energy conversion and storage equipment. Additionally, to lessen the crisis of running out of fossil fuels, combat global warming, and to reduce pollution brought on by the population boom, sustainable and clean energy conversion and storage technologies are needed.⁴ Batteries, capacitors, supercapacitors, and fuel cells are just a few of the energy storage technologies developed to store electrical energy. The benefits and drawbacks of each of these technologies vary. Fuel cells and electrochemical supercapacitors are the two most significant energy storage and conversion innovations. The terms electrochemical double layer capacitor and electrochemical supercapacitor are also used. Initially, the idea of an electrochemical supercapacitor was based on an electrical double layer that was present at the boundary of two plates of an electrolytic capacitor, a condenser that contained an electrolyte solution. First and second generation capacitors are electrostatic and electrolytic capacitors, respectively. The

third generation, known as supercapacitor, has been created as a result of fast material development.^{5,6}

1.2.2 Brief history and current developments in supercapacitor

Supercapacitors have been widely researched during the last few decades. They could offer distinct characteristics such as elevated energy density, high reversibility, quick charge-discharge cycles, and long cycle life stability, all of which are critical parameters for energy storage and conversion. Helmholtz first outlined the notion of a two layer capacitor in 1853. Becker received the construction of a two layer capacitor and its first patent in 1957 from General Electric Corporation Limited (GECL). In that invention, porous carbon material was employed to manufacture electrode material for supercapacitor applications.^{7,8} Standard Oil Company, Cleveland, Ohio (SOHIO) issued a patent on an energy generating and storage system having a porous carbon electrode in 1962. In that instance, the EDLC interface functions like an electrochemical capacitor and has the highest specific capacitance.⁹ Additionally, SOHIO received a patent for a disc-type capacitor in 1970 that used carbon paste solution as its electrolyte.¹⁰ In 1971, NEC obtained a licence from SOHIO on double layer capacitance, and it produced the first double layer capacitor on a commercial scale under the moniker 'supercapacitor'.¹¹ Since then, the supercapacitor has begun to undergo industrialisation, modernization, and the creation of new technologies. This important invention enhanced the process used to make supercapacitors in general. The Panasonic Company, founded in 1978, has since been utilised as a backup source for memory applications. As a result, the supercapacitor is sometimes known as a gold capacitor. The Pinnacle Research Institute (PRI), under the name PRI Ultracapacitors, created the first metal oxide-based material for high power density EDLC in 1982. Later, Conway et al. created a RuO₂ electrode material for supercapacitors that had reduced internal resistance and a maximum specific capacitance and that demonstrated the substantial advances made in the 1970s and 1980s.^{12,13} Hybrid cars were first mentioned by the US Energy Department in 1992, with a major contribution coming from Maxwell's use of ultracapacitors.

Many industries around the world have reported supercapacitor production. Industries including Panasonic, AVX, NEC, Epcos, Cooper, and ELNA, among others, have created several versions of EDLC and its components in America and Japan. Additionally, using integrated circuits, Maxwell and Evans created and produced voltage balanced circuits. By offering several types of electric double layer

capacitors, ESMA created hybrid electric vehicles in Russia and improved power quality applications. Due to supercapacitors' special characteristics and numerous applications listed below, their commercialization and use have dramatically increased in recent years. In the sphere of transportation, supercapacitors are utilised as an electric backup source in autos, electric vehicles, hybrid electric vehicles, regenerative braking systems, startup applications, and energy conversion systems. Supercapacitors are also used as a power backup source in consumer devices including microcomputers, keyboards, clocks, telecoms, toys, digital cameras, and uninterruptible power supply. Supercapacitors are employed in robotics and factory automation in industrial applications. Additionally, supercapacitors have applications in the production of energy from renewable sources, including wind and solar energy systems.¹⁴⁻¹⁹

1.2.3 Types of electrochemical energy storage devices

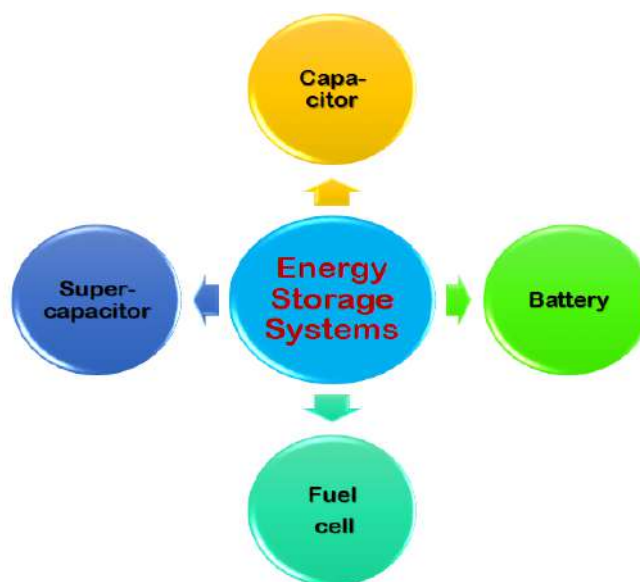


Figure 1.1: Different type's energy storage devices

Energy storage alternatives come in a variety of forms, and new ones are appearing as the technology becomes increasingly important to the development of the global energy systems of the future. The figure 1.1 represents the different types of energy storage devices. The development of future wearable and bio-integrated electronics depends on a programmable electrochemical energy storage system. Electrochemical energy storage systems convert electrical energy into chemical energy or vice versa, allowing heterogeneous chemical processes to occur using charge transfer to or from electrodes (i.e. cathodic or anodic). Reversible electrochemical processes are used in electrochemical energy storage systems to

convert and store electrical energy through the simultaneous movement of electrons and ions. The electrochemical thermodynamics and kinetics are the most crucial aspects that should be considered in order to sustain adequate electrochemical performance under severe circumstances.^{20,21}

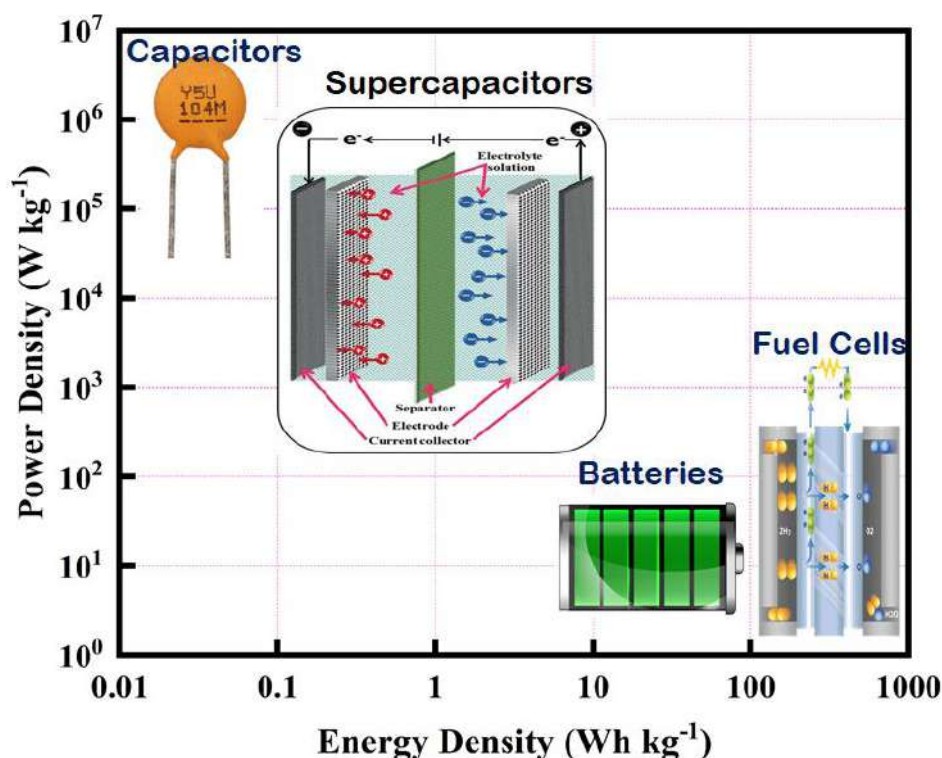


Figure 1.2: The Ragone plot depicts the energy and power densities of several energy storage devices

As illustrated in figure 1.2, the Ragone plot is the diagram that explains the comparative research of the performance of various energy storage systems. The power density is shown in this graph along the Y axis, measured in Watt per kilogram (W kg⁻¹), while the energy density is shown along the X axis, measured in Watt hours per kilogram (Wh kg⁻¹). In order to show how much energy is available in the devices as well as how rapidly the energy can be provided or stored, a Ragone plot is frequently employed. The four most significant electrochemical energy storage devices are capacitors, battery, fuel cell and supercapacitors, as seen in a Ragone plot.²²

1.2.3.1 Capacitor

A capacitor is a device that holds electrical charge. As illustrated in Figure 1.2, a capacitor consists of two conducting plates that are spaced apart by a modest distance and have a dielectric substance filled in the space between them. Different

types of dielectric materials exist, including titanate, mica, air, oiled papers, glass, and porcelain. The capacitor charges when a potential difference between outside sources is placed across its two plates. Positive charge gradually accrue on one plate while charging, while negative charges gradually build up on the other plate. When the external voltage difference is eliminated, the positive and negative charges both moved in the direction of the corresponding electrodes.²³

As a result, capacitors are used to separate the electrical charges. The following is a definition of capacitance:

$$C = \frac{Q}{V} \dots\dots\dots (1.1)$$

The following equation is used to calculate how much charge is present in the capacitor.

$$C = \epsilon \frac{A}{d} \dots\dots\dots (1.2)$$

Where C, ϵ , A and d denotes the capacitance, dielectric constant of medium, area and thickness of the dielectric media, respectively.

1.2.3.2 Battery

A battery is a device made up of different electrochemical cells that use chemical reduction-oxidation processes to transform stored chemical energy to electrical energy. Because of its small weight, high energy density, and capacity to be recharged, batteries are frequently utilised as a power source for a variety of gadgets in modern life, including laptops, hybrids, and electric automobiles. Two current collectors, an anode, a separator, an electrolyte, and a cathode make up a battery. When a battery is discharging, a flow of electrons from one side to the other is created when the anode discharges lithium ions to the cathode. In contrast, as the battery is being charged, the cathode releases lithium ions, which the anode then collects.²⁴

Batteries are divided into two categories based on the charging process:

(i) **Primary Battery:** Primary batteries are also called as non-rechargeable disposable batteries. When primary cells are completely depleted, they cannot be recharged, and the battery is said to be a single-cycle battery. They have a chemical within that is consumed through time and use, and after it is completely emptied, it must be disposed-off. Alkaline batteries, Aluminum-Air batteries, dry cells are types of primary batteries.

(ii) **Secondary Battery:** Multicycle batteries are the ones used in these batteries. These batteries have a long lifespan and may be recharged several times.

These batteries are typically used in electric vehicles (EVs), phones, cars, portable electronics, and a variety of other applications. Li-ion battery, Li-polymer battery, and Lead acid battery are types of secondary batteries.²⁵

1.2.3.3 Fuel cell

In 1838, the first fuel cell was invented by William Grove. NASA's space programmes saw the first commercial application of fuel cells. Fuel cell is electrochemical machinery that extracts electricity from fuel without accumulating it first. Similar to other electrochemical devices, fuel cells use reactants that are supplied from outside sources as they are consumed. Through a chemical process with oxygen or another oxidising agent, the fuel cells turn the chemical energy of the fuel into electrical energy. One of the fuels most frequently utilised in fuel cells is hydrogen. The process through which fuel is converted into energy is electrochemical. This energy production method uses electrochemistry, which is a simple, efficient, and clean process. The primary classification of these fuel cells is depending on the fuel utilised. Fuel cells are still in the research and development stage and are looking for a useful application that can break into the energy industry while remaining competitive with batteries and supercapacitors.^{26,27}

1.2.3.4 Supercapacitor

A supercapacitor (SC), also known as an ultracapacitor, is an electrochemical capacitor with a large capacity and capacitance values that are significantly greater than those of conventional capacitors. Supercapacitors operate similar to traditional capacitors. The increased charge can be held by the many pores inside the electrodes' high surface area, but supercapacitors are able to store more energy since the charge separation happens over a relatively short distance, i.e. among the electrolyte and an electrode. An electrolyte, a separator, and two electrodes are the basic components of a supercapacitor. Electrodes possess high surface area. Water-based combination of positive and negative ions is known as an electrolyte. The membrane, or separator, that separates these two electrodes permits the movement of charged ions. A cylindrical container is formed by rolling or folding the separator. It might be aqueous, organic, or solid state. Ion adsorption or quick surface redox reactions are two ways that supercapacitors store energy. Owing to this power features, supercapacitors are employed in hybrid electric cars to improve the power distribution and storage capabilities of batteries and fuel cells, supplying the necessary power for quick acceleration. This is because of their distinctive qualities, which include

environmental friendliness, short charging times, increased power densities, and increased durability.^{28,29} In summary, supercapacitors are gaining popularity because they include ion motions to and from electrode surfaces, resulting in fast storage. Furthermore, supercapacitors are low-maintenance materials with a long life cycle.

The following list includes several supercapacitor characteristics:

- ❖ Supercapacitors are known for their extended cycling times and high cycle efficiencies, which are regarded as some of their most crucial characteristics.
- ❖ Supercapacitors have a lower potential for contamination because no heavy metals are employed in their production.
- ❖ Supercapacitors have the ability to have a longer service life of roughly 10 to 15 years.
- ❖ Capacitance in supercapacitors can range from 1mF to more than 10 kF.
- ❖ Supercapacitors may charge or discharge between a few seconds to a few milliseconds.
- ❖ The energy density of supercapacitors can reach 10 Wh kg⁻¹.
- ❖ Supercapacitors are chosen over batteries and traditional capacitors because they have larger capacitance with small voltage restrictions.

Table 1.1: Relationship between supercapacitors and other energy storage technologies

Variables	Capacitors	Battery	Fuel cell	Supercapacitor
Electrode materials	Tantalum, Aluminum, Silver plates i.e. Conductive plates	Metal oxide materials, carbon materials	Gold coated carbon / Platinum / metal base	Conducting polymer, metal oxides, carbon materials, sulphides, nitrides
Storage mechanism	Electrode polarization caused by an applied electric field	Chemical energy is converted into electrical energy	Chemical energy is converted into electrical energy	An applied electric field causes the formation of an electric-double layer and a redox reaction

Principle	Polarization	Faradaic reactions in the bulk of the electrode	Oxidation and reduction	Faradaic/ Non-Faradaic
Electrolyte	Dielectric materials is used in place of electrolytes.	Acids, salt (NaCl, ClO ⁴⁻ , PF ⁶⁻ , BF ⁴⁻) + solvent (water, PLC, EC)	Sulphonated polymers, KOH, H ₃ PO ₄	Aqueous, organic, polymer electrolytes and Ionic liquids
Potential window	6 to 800	1.25 to 4.2	0.6	1 to 4
Energy density	<0.1	8 to 600	300 to 3000	1 to 10
Power density	0.25 to 10000	0.005 to 0.4	0.001 to 0.1	10 to 120
Life span	>100000 cycles	150 to 1500 cycles	1500 to 1000 h	50000 + h, unlimited cycles
Efficiency	>95%	70 to 85%	Up to 60%	90 to 95%

1.2.4 Types of supercapacitors

Supercapacitors are also known as ultracapacitors, power capacitors, gold capacitors, and super condensers. These are divided into three groups based on their charge storage mechanism as shown in figure 1.3 and 1.4.

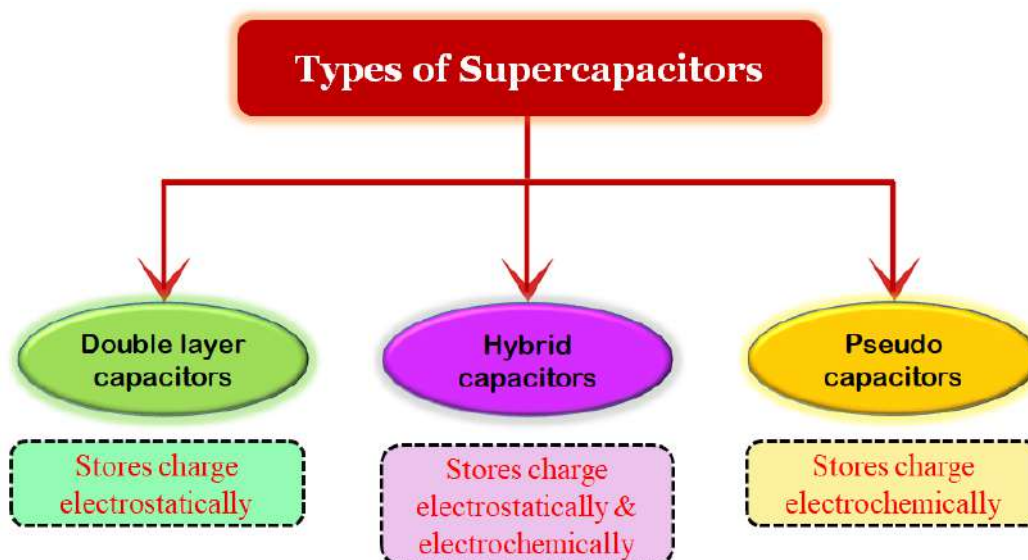


Figure 1.3: Classification of supercapacitors

1.2.4.1 Electrical double-layer capacitor (EDLC)

This type of capacitor operates on the charge storage mechanism, whereby a charge is really held on the electrode surface without resulting in any irreversible chemical processes by forming an electrical double layer. Carbon-based electrodes are often employed in supercapacitors that are detached by a dielectric material that functions as an insulator and has electrical characteristics that impact the supercapacitor's performance. In EDLC, charges are held electrostatically. As soon as a voltage is employed across the terminals, an electric field is produced at each electrolyte and that causes the electrolyte to become polarized. Ions then diffuse to the porous electrodes with opposing charges via the dielectric as a consequence. At every electrode, an electric double layer is created in this fashion. As a result, the space between the electrodes is compressed and each electrode's surface area increases.^{30,31}

1.2.4.2 Pseudocapacitor (PC)

Pseudo-capacitors are also referred to as faradaic supercapacitors. Pseudo-capacitors employ electrodes constructed of redox-active substances like metal oxides and conducting polymers. These electrodes use reversible faradaic reaction processes to store charge close to the electrode or at the electrode surface, where charges are transported across the metal-electrolyte junction. Capacitance or charge storage in pseudo-capacitors arises from charge transfer among the electrode and electrolyte.^{32,33}

1.2.4.3 Hybrid capacitors

Hybrid capacitors are created by combining techniques from pseudo-capacitors and double layer capacitors. The mechanics of both EDLCs and

pseudocapacitors have been included into these capacitors. Electrodes with varied properties depending on chemical as well as electrical principles make up hybrid capacitors. Because of this, one electrode displays electrostatic capacitance, while the other offers electrochemical capacitance. Hybrid supercapacitors are made up of two electrodes with distinct properties, and those are further classified as composite, symmetric, asymmetric, and battery type capacitors. Comparing the hybrid capacitors to individual EDLC and pseudocapacitors reveals improved power and energy densities. This promotes the use of them as energy storage devices rather than alternative storage technologies.^{34,35}

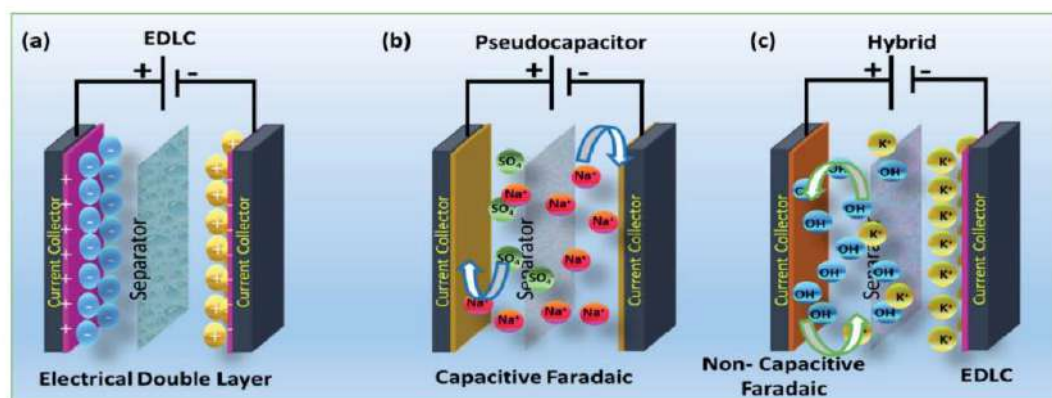


Figure 1.4: Charge storage mechanism of supercapacitors, (a) EDLCs, (b) pseudocapacitors and (c) hybrid supercapacitors.³⁶ Reproduced with permission. Copyright © 2021, Royal Society of Chemistry

1.2.5 Supercapacitor materials

A crucial factor that can affect a supercapacitor's electrochemical performance is the electrode material. They need to be very conductive, superbly temperature stable, chemically stable, possess a high specific surface area, be reasonably priced, and be environmentally benign. To create a high-performance supercapacitor, selecting an efficient and effective electrode material is crucial. The next sections highlight a few of the materials that have been used for energy storage devices, such as carbon based materials, conducting polymers, metal oxides, and metal-organic frameworks.³⁷

1.2.5.1 Carbon-based supercapacitor

Carbon materials have been discovered to be relevant materials for supercapacitor electrodes on account of they are ample in nature, inexpensive, environmental safe, high electrical conductivity, simple scalable processing,

adjustable pore size, good chemical stability, large specific surface area, and stable performance over a broad temperature range. The physical characteristic of carbon-based substances appears akin to that of a semiconductor, possessing a lower charge density of charge carriers (either electrons or holes), which renders them valuable electrode materials. In EDLC, electrode materials used are mostly carbon-based materials, and the storage mechanism they provide is an electrochemical double layer created at the electrode/electrolyte interface. As a result, capacitance is mostly determined by the surface area available to electrolyte ions. Specific surface area, pore size distribution, pore shape and structure, electrical conductivity and surface functionality are all important aspects that determine electrochemical performance.³⁸

Depending on the output need, a variety of carbon materials, including activated carbon, graphene, carbon nanotubes, and carbon aerogel, are employed as supercapacitor electrodes. Activated carbon is a common choice for electrode materials as it possesses a large surface area, porous structure, and excellent conductivity. Historically, AC was derived from fossil fuels such as petroleum coke and coal, however, due to the limited availability of these resources, scientists have been compelled to explore alternative, eco-friendly sources of carbon. Currently, numerous investigators are concentrating on producing supercapacitor electrodes using economical and environmentally friendly sources of carbon such as biomass residue. The carbon that is obtained from the precursor of biomass has exceptional qualities such as large surface area, customizable structure, diverse range of pore sizes, and great conductivity. Despite having limited surface area, CNTs have a network of mesopores that facilitate even charge distribution and enhance the utilization of surface area to a greater extent than activated carbon electrodes. Carbon aerogels are highly porous carbon materials that possess a three-dimensional hierarchical structure and are commonly utilized in various sustainable energy-based applications. It consists of a consistent mesh of carbon nanoparticles possessing a mesoporous configuration. Its chemical bonding ability with the existing collector eliminates the need for any external adhesive. The carbon aerogel's impressive power density and low ESR make it an appealing choice as a lightweight electrode material for supercapacitors. Graphene is a different variation of carbon that consists of a singular layer of graphite wherein the atoms are arranged in a sp^2 hybridized form. This displays remarkable characteristics such as significant flexibility in structure, a favorable relationship between surface area and volume, a broad range of potential

operating conditions, and excellent electrical conductivity. The utilization of graphene as an electrode encounters certain drawbacks, such as a decrease in specific capacitance caused by the restacking of graphene sheets through van der Waals interaction.³⁹⁻⁴³

1.2.5.2 Conducting polymers-based supercapacitor

A group of scientists consisting of Alan G. Heeger, Aann G. MacDiarmid, and Hideki Shirakawa developed conducting polymers in the 19th century. These polymers are made up of a chain of linked monomers and possess exceptional electrical conductivity. In the year 2000, those three researchers achieved the honor of receiving the Nobel Prize in Chemistry.⁴⁴ The significance of conducting polymers lies in their ability to serve as a replacement for metallic substrates and semiconductors, as well as their advantageous properties such as supreme flexibility, excellent conductivity, and highly-redox behavior, allowing them to be utilized as functional materials. The most notable conductive polymers include polypyrrole, polyaniline, polythiophene and poly(3,4-ethylenedioxythiophene). These polymers exhibit significant electrical conductivity under typical conditions. The capacity for these polymers to alternate smoothly between redox states and exhibit strong ion-exchange characteristics is made possible through their synthesis using both aqueous and organic media.⁴⁵⁻⁴⁷ The electrochemical capability of a supercapacitor is negatively impacted by the swelling and shrinking of conducting polymer electrodes that occurs during the charge-discharge process, leading to mechanical breakage. In order to reduce this problem, conducting polymers are utilized to create composites with carbon or metal oxide based substances to enhance the cyclic stability and general electrochemical functioning.

1.2.5.3 Metal oxides-based supercapacitor

In the past few years, there has been an increasing focus on the advancement of supercapacitors based on metal oxides due to their superior energy density compared to carbon materials and greater stability compared to electrode materials made from polymers. The metal oxide electrode materials facilitate energy storage through rapid and reversible faradic reactions occurring at the interface between the electrolyte and electrode. A range of transition metal oxides including NiO, MnO₂, RuO₂, Co₂O₃, IrO₂, SnO₂, and Fe₂O₃ have been investigated as potential supercapacitor electrodes. Out of all the options available, RuO₂ stands out with various benefits including an extensive potential range, exceptional specific

capacitance, conductive metallic characteristics, and an incredibly efficient reversible oxidation-reduction process. RuO₂ is prohibitively costly to manufacture and poses a hazard to human health. Researchers are currently investigating the possible use of MnO₂ in supercapacitors as a substitute for RuO₂. This is due to the fact that MnO₂ is significantly more affordable to produce, widely accessible, and lacks toxic properties.⁴⁸ Transition metal oxide-derived electroactive materials are highly intriguing for their unique blend of electrical, mechanical, structural, and electrochemical characteristics. Their abundance, environment-friendly nature, and rich redox chemistry enable them to possess prominent specific capacitance and energy density. Additionally, their rapid and reversible charge-discharge processes at a relatively low-cost make them the most favorable materials for the development of next-generation supercapacitors.⁴⁹

1.2.5.4 MOF-based supercapacitor

Over the last few decades, there has been an impressive discovery and development of Metal-organic frameworks (MOFs), which was initially conceptualized by Yaghi and Li in 1995.⁵⁰ MOFs are a recently developed class of porous materials that consist of crystalline structures constructed from metal ions or clusters, combined with organic linkers. Transition metals, alkaline earth metals, and lanthanides are commonly employed as metal equivalents. On the other hand, organic linkers commonly consist of molecules that possess donor atoms such as oxygen (O-) or nitrogen (N-) like polyamines, pyridyl, carboxylates, etc. Introducing side chain ligands can enhance the material's capabilities, enabling the potential for a highly customizable molecular system. By carefully selecting the metal ions and organic linkers used in synthesizing MOFs, researchers are able to achieve the desired level of tunability in terms of network dimensionality (1D, 2D, or 3D) and unique topologically diverse open network structures. MOFs possess several benefits over traditional porous materials including a varied scaffold structure, modifiable pore size, notable surface area, and a profusion of active sites. Due to their exceptional characteristics, MOFs are widely utilized in the realm of energy storage systems (EES).⁵¹⁻⁵³ MOFs can be utilized in two primary ways for supercapacitor electrodes. The first approach involves using MOFs as a framework to create various porous materials, such as metal oxide, metal sulfides, and metal phosphides, and their composites, through pyrolytic processing or ion exchange.⁵⁴⁻⁵⁶ The second approach involves directly using MOFs as supercapacitor electrode materials.^{57,58}

1.2.6 Electrical characteristics of the supercapacitor

1.2.6.1 Specific capacitance

Specific capacitance is important property of a supercapacitor. Capacitance is the term used to describe a circuit's capacity for holding and maintaining electrical energy in the form of a charge. The specific capacitance refers to the measure of capacitance in relation to the active material's mass. The nature of the electrode materials utilized plays a critical role in determining the specific capacitance of a supercapacitor. Employing a porous material for constructing supercapacitors amplifies the specific capacitance owing to the considerable increase in surface area. The supercapacitor's high mass causes a reduction in specific capacitance. As a result, the inverse relationship between specific capacitance and mass is observed. At higher current densities, the primary reason for reduced capacitance values is the notable impact of the Ohmic drop, along with slow electrochemical kinetics.

The specific capacitance of the supercapacitor is calculated by using formula,

$$C_{sp} = \frac{I \times t}{m \times V} \dots\dots\dots (1.3)$$

Where C_{sp} , I , t , m and V denotes specific capacitance, current density, discharge time, mass of the supercapacitor and working potential window of the device, respectively.

1.2.6.2 Specific energy and specific power

The specific energy of supercapacitors is the maximum amount of energy that may be held in a given mass. The measurement is determined gravimetrically and expressed as watt-hours per kilogram. Even though supercapacitors have lower energy density compared to batteries, they possess a superior specific power density than batteries. The capability of a device to rapidly provide the energy it has stored to the load is referred to as specific power. Supercapacitors exhibit a considerably higher specific power than batteries, approximately tenfold. This kind of technology is utilized in situations that require the rapid release of energy stored in a device.

Equation 1.4 and 1.5 represents the formula used to determine the specific energy and specific power by analyzing the charge-discharge curve.

$$E_s = \frac{0.5 \times C_{sp} \times \Delta V^2}{3.6} \dots\dots\dots (1.4)$$

$$P_s = \frac{E_s \times 3600}{\Delta t} \dots\dots\dots (1.5)$$

Where E_s and P_s denotes specific energy in Wh kg^{-1} and specific power in W kg^{-1} , respectively.

1.2.6.3 Operating potential voltage

Super capacitors are devices that operate at comparatively lower voltages. To ensure safe usage of the device, it is necessary to maintain the voltage within the designated range. The rated voltage is commonly referred to as the level of safety. The rated voltage incorporates a safety buffer range as well as the voltage point at which the electrolyte breaks down. When the voltage applied surpasses its rated level, the solvent molecules fail to uphold a proper distance between the electrical charges, leading to their breakdown into hydrogen gas or the initiation of a short circuit. The operating voltage is significantly influenced by the type of electrolyte utilized. When working with aqueous electrolytes, it is necessary to apply a rated voltage within the 2.0 - 2.2 V range. However, when utilizing organic solvents, the required voltage range is between 2.5 to 2.7 V. On the other hand, employing ionic electrolytes can result in an operating voltage surpassing 3.5 V. By maintaining a voltage level lower than the rated voltage of the supercapacitor, it is possible to prolong the cycles of charging and discharging. Nevertheless, in situations where elevated voltages are necessary, an arrangement of electrochemical cells must be linked in a series configuration.

1.2.6.4 Cyclic stability

The endurance of supercapacitors depends on the cyclic stability of its electrodes, which is a significant indicator of performance. The ability of supercapacitors to maintain their capacitance under standardized testing conditions after a specific working period or number of charging-discharging cycles is referred to as cyclic stability of electrode materials or devices. Supercapacitors possess an infinite lifespan in terms of cycles, whereas batteries are limited to a cycle range of 500-1200. Supercapacitors are highly valuable in situations that demand repeated storage and conversion of energy owing to their exceptional cyclic stability. Parameters like operating potential window, type of electrode material, current density/ scan rate and electrolyte used strongly influence the cyclic stability of supercapacitor.⁵⁹

1.2.6.5 Electrolyte

Electrolytes are essential and significant components in supercapacitors. Due to their physical and chemical properties, they play a vital role in electrochemical

performances, such as specific capacity, energy density, power density, rate performance, cycling stability, and safety.^{60,61} The necessities for an ideal electrolyte are broad potential window, high ionic conductivity, extended operating temperature range, high chemical and electrochemical stability, large chemical and electrochemical inertness to supercapacitor constituents (e.g., electrodes, current collectors, and packaging), convenience with electrode materials, low volatility and flammability, eco-friendliness, and inexpensiveness. In all honesty, it is challenging for an electrolyte to fulfill all of these necessities; also, each possesses its advantages and limitations. The selection of electrolytes is vital to safe and high-performance supercapacitors. Concerning electrochemical supercapacitor electrolytes, various electrolytes used in the supercapacitors that have been studied are aqueous electrolytes, organic electrolytes, ionic liquid electrolytes, redox-active electrolytes, and solid-state or quasi solid-state electrolytes.⁶²⁻⁶⁵

1.3 General introduction and literature survey of the materials

1.3.1 Introduction to the MOF

In 1995, a new category of porous materials with remarkable properties known as metal-organic frameworks (MOFs) was introduced by Yaghi. These materials are notable for their enduring porosity and extensive surface area, thanks to the robust bonds formed between metallic ions and electrically charged organic ligands.⁶⁶ MOFs offer several advantages over conventional porous materials, such as the ability to achieve crystal engineering and create crystal structures that are deliberately designed and considered highly desirable. Additionally, the synthetic potential of MOFs coupled with their ability to integrate various chemical functionalities enables the creation of MOFs featuring lightweight organic linkages, which exhibit high specific surface area and exceptional porosity that are beyond the realm of conventional materials like zeolites and porous carbon. Because of their enormous surface area and redox-active metal ions (Figure 1.5), MOFs have recently received a lot of attention as electrode materials for SCs.^{67,68}



Figure 1.5: Properties of MOFs

1.3.2 Literature survey of MOFs for supercapacitors

MOFs can be employed in supercapacitors in three different ways:

- 1) Pristine MOFs can be utilized to house electrolyte ions on their internal surfaces for the purpose of accumulating electric charges through physical adsorption, in order to leverage the reversible redox reactions of the metal centers.
- 2) MOFs are utilized to produce metal oxides and maintain the movement of electrons through charge transfer from the electrode to the electrolyte.
- 3) One method for enhancing capacitance involves using MOFs to create porous carbon materials with improved electrical conductivity.

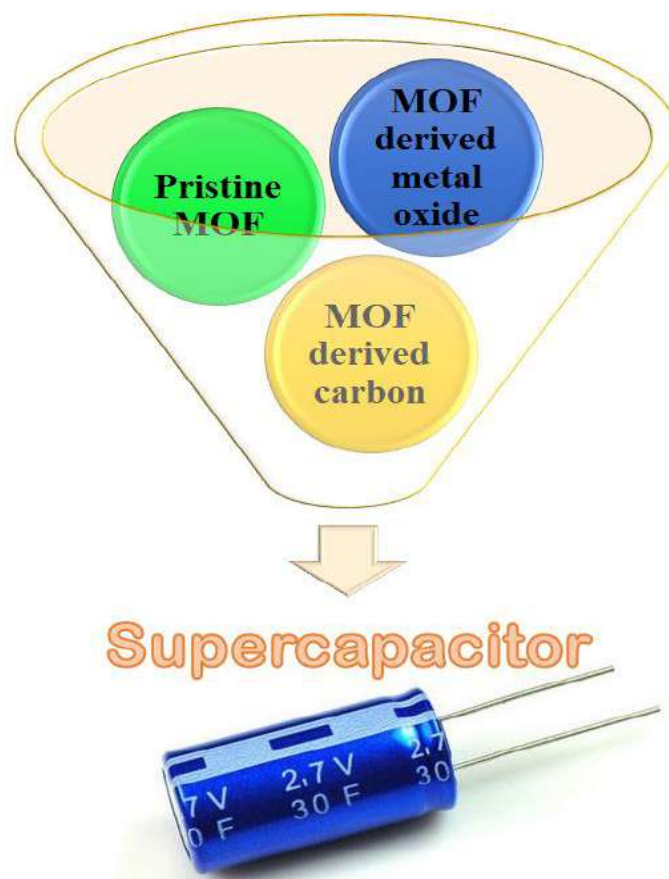


Figure 1.6: MOFs as an electrode material for supercapacitor

1.3.2.1 Pristine MOFs for supercapacitors

Building block patterns of the pristine MOFs can be realized by wise choice and transformation of metal ions and organic linkers. The pristine MOF has physical and chemical properties, such as versatile compositions, high surface area, tunable pores, uniform dispersion, and defined active centres.^{69,70} Pure MOFs store energy through the physisorption of electrolyte ions on their internal surfaces at the metal centres.⁷¹ The important parameters that influence the electrochemical performance are the structure of MOF, which includes chemical structure, and the geometries of the organic ligands.⁷² Due to their longer charge/discharge cyclabilities, larger specific capacitances, and faster ion diffusion, pristine MOFs are used for electrode preparation. To date, more than 40 types of pristine MOFs have been fabricated using many different metals, such as Cu, Cr, Co, Ni, Fe, Mn, Zr, Zn, In, Al, Cd, and Mg in mixture with organic ligands like BTC, BDC, and imidazole.^{73,74}

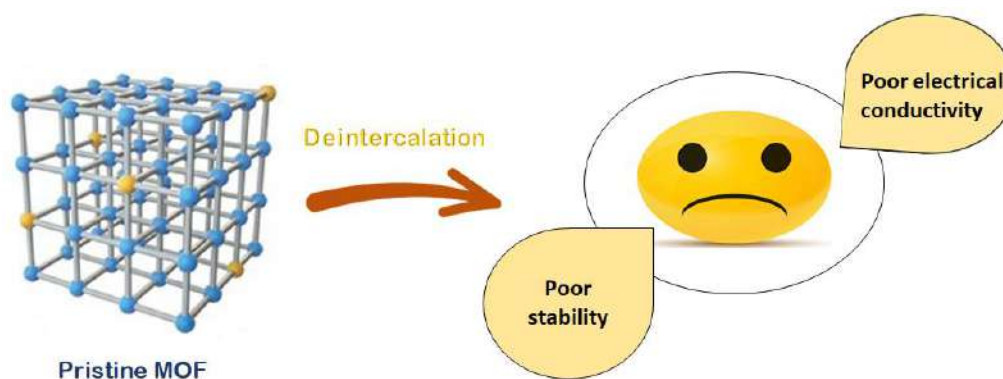


Figure 1.7: Schematic of the pristine MOFs for supercapacitor application

Yang et al. synthesized a layered gear-like Ni-TDA $[(\text{Ni}_3(\text{OH})_2(\text{C}_2\text{H}_6\text{O}_4\text{S})_2, \text{Ni-MOF}]$ material that was found to be a promising electrode material for the flexible all-solid-state asymmetric supercapacitor, and with high specific capacitance of 1518.8 F g^{-1} at a current density of 1 A g^{-1} . The capacitance retention of over 95.5 % can be maintained even after 10000 cycles at current density of 20 A g^{-1} , which shows excellent cycling stability at higher current densities.⁷⁵ Yan et al. prepared a novel accordion-like Ni-MOF superstructure $[(\text{Ni}_3(\text{OH})_2(\text{C}_8\text{H}_4\text{O}_4)_2(\text{H}_2\text{O})_4)] \cdot 2\text{H}_2\text{O}$ to fabricate a flexible supercapacitor. It shows specific capacitances of 988 and 823 F g^{-1} at a current densities of 1.4 and 7.0 A g^{-1} respectively, while sustaining excellent cycling stability (capacitance retention of 96.5 % after 5000 cycles at current density of 1.4 A g^{-1}). Additionally, by using Ni-MOF and activated carbon, a high performance flexible solid-state asymmetric supercapacitor was constructed with a specific capacitance of 230 mF cm^{-2} at current densities of 1.0 mA cm^{-2} , which shows little capacitance change after more than 5000 charge-discharge cycles, with only 7.2 % decay at a current density of 5.0 mA cm^{-2} .⁷⁶ Krishnamurthy et al. used a solvothermal method to report Mn-MOF $(\text{Mn}[\text{Tpa}][\text{Mi}][\text{DMF}])$ employing terephthalic acid and methyl imidazole ligands. It shows specific capacitance up to 4000 F g^{-1} . Also, it has an energy density and power density of 500 Wh kg^{-1} and 0.125 W kg^{-1} , respectively. The surface area of this material is outstanding, i.e. $2352 \text{ m}^2 \text{ g}^{-1}$ and pore volume of $0.00569 \text{ cc g}^{-1}$; Mn-MOF electrode possesses a high charge-discharge Coulombic efficiency, low polarization, and high specific capacitance, along with good cycling stability.⁷⁷ Zhu et al. synthesized a 3D hierarchically structured Co-MOF supported on nickel foam (Co-MOF/NF), which shows better capacitive properties with good rate performance in 2 M KOH. Further, they constructed an asymmetric supercapacitor device by using Co-MOF/NF as a

positive electrode and activated carbon as a negative electrode; it shows a high energy density of 1.7 mWh cm^{-2} at a power density of 4.0 mW cm^{-2} , with capacitance retention of almost 69.70 % after 2000 cycles.⁷⁸

1.3.2.2 MOF-derived metal oxides for supercapacitors

The poor structural stability and electrical conductivity of the pristine MOFs have hampered their practical utilization as electrodes in supercapacitor applications. Transforming the pristine MOFs into metal oxides is a significant way of enhancing their structural and electrochemical stability, including electrical conductivity. The MOF-derived metal oxide show unique structural features, such as porous morphology, robust structure, high electrical conductivity, and high redox behaviour. Therefore, metal oxides derived from MOFs are preferred for the construction of electrode materials. MOF-derived metal oxides electrode materials store energy through charge transfer between electrolyte-ions and the electrodes. Metal oxides are mostly made via the general procedure of calcination. MOFs are heated to a temperature of a few hundred degrees in an inert furnace.⁷⁹ Throughout the annealing procedure, metal sites are oxidized to the isonomous metal oxides, and organic ligands are transmuted into carbon dioxide and water vapour, which frame ample pores. MOF-derived metal oxides sustain their primitive morphology, showing huge pores and associated gaps.^{80,81}

Lan et al. prepared a porous flower-like MnNi_2O_4 using bimetallic Mn/Ni–MOF as a precursor that exhibits astounding electrochemical behaviour with the most significant specific capacitance of 2848 F g^{-1} at 1 A g^{-1} with good stability of 93.25 % capacitance retention after 5000 cycles at 10 A g^{-1} . Further, they constructed an asymmetric supercapacitor using MnNi_2O_4 positive electrode and active carbon as the negative electrode, which shows a large energy density of 142.8 Wh kg^{-1} at a high-power density of 800 W kg^{-1} .⁸² Xiao et al. synthesized an ultrathin Co_3O_4 nanosheet using Co-based MOF by hydrolysis followed by calcination procedure, which exhibits outstanding supercapacitor performance due to the abundant meso- and macro-pores. In addition, they fabricated an asymmetric supercapacitor using Co_3O_4 nanosheets as a positive electrode and activated carbon as a negative electrode, which shows a high energy density of 32.8 Wh kg^{-1} at the power density of 752 W kg^{-1} and retains 98.1 % of its initial capacitance after 6000 charge/discharge cycles at the current density of 2 A g^{-1} with long-term cycling stability.⁸³ Wu and co-workers synthesized hollow core in double-shell NiO nanospheres by the calcination of Ni-based MOF; as they are

calcined at different temperatures, they show distinct surface areas and electrical conductivities, which play an important role in the redox reaction that takes place at the surface of the active materials. Material calcined at 400 °C shows a specific capacitance of 473 F g⁻¹ at the current density of 0.5 A g⁻¹, which shows good cycling stability, even after 3000 cycles. Additionally, they constructed an asymmetric supercapacitor with high energy storage capacity and outstanding cycling performance.⁸⁴ Li et al. fabricated hierarchical double-shelled NiO/ZnO hollow spheres by annealing a bimetallic organic framework in air and used it as an electrode material for high-performance supercapacitor applications. It shows a specific capacitance of 497 F g⁻¹ at a current density of 1.3 A g⁻¹ with outstanding cycling stability, even after 2000 cycles.⁸⁵ Xu et al. investigated a scheme to set up unique Co₃O₄/ZnO nano heterostructures through the thermal conversion of center-shell ZIF-eight@ZIF-67, displaying superior pseudocapacitive behaviour. It shows a high specific capacitance of 415 F g⁻¹ at 0.5 A g⁻¹ with enhanced rate capability (93.2 % retention at 10 A g⁻¹), compared to Co₃O₄ and ZnO derived from single MOFs precursor. Further, they fabricated an asymmetric supercapacitor by using Co₃O₄/ZnO heterostructure as a positive electrode, and active carbon as a negative electrode. The electrochemical performance determined in an aqueous electrolyte, i.e., 6 M KOH in expanded 1.4 V working voltage, shows an energy density of 43.2 Wh kg⁻¹ at a power density of 1401 W kg⁻¹.⁸⁶ The nanoporous NiO, NiCo₂O₄, and Co₃O₄ were prepared using the hydrothermal method and an annealing process that exhibits a large surface area and porous nature. As compared with monometallic oxides, the mixed metal oxides, i.e., NiCo₂O₄, shows high specific capacitance of 684 F g⁻¹ at 0.5 A g⁻¹ current density, and outstanding cycling stability with the specific capacitance retention of 86 % after 3000 cycles at the current density of 10 A g⁻¹, performance of which makes it a promising material for energy storage and conversion devices.⁸⁷

1.3.2.3 MOF-derived carbon for supercapacitors

MOF-derived nanoporous carbon (NPC) material is obtained by the calcination of MOF at high temperatures or the pyrolysis of MOF followed by acid treatment or base activation. NPCs maintain the structure and morphology of MOF, which enables the conducting properties of carbon. Many nanoporous carbon (NPC) materials have been widely examined for supercapacitor applications, due to their outstanding chemical and mechanical stability, large specific surface area, good electrical conductivity, and adjustable pore structure.⁸⁸⁻⁹⁰ To increase the capacitance

of carbon material, heteroatom doping (e.g., B, S, N, P) is a new strategy to elevate the surface wettability and contribute reversible pseudo-capacitor behaviour to a material. The addition of metals can supply extra benefits in the carbon array, which encourages the applications of carbon materials as electrode materials. Incorporating specific metals like Co, Ni, and Fe can amazingly ameliorate the crystallinity and electrical conductivity of carbon, owing to their catalytic graphitization of the amorphous carbon. Hence, heteroatom doping or metal-modified carbons are promising materials for supercapacitor application and have attracted much interest.^{91–94} Nowadays, the performance of supercapacitors is mainly influenced by electrode materials. Among different electrode materials, carbon is the most broadly used material for supercapacitors due to its multiple advantages: wide source, large specific surface area, environmental warmth, and good electrical conductivity. Large specific surface area and suitable pore size are the chief techniques to achieve high capacitance of carbon materials; carbon materials mainly store energy by constructing an electric double-layer across the separated charges of electrolyte ions on the surface.⁹⁵

Due to its easy synthesis, controllable morphology, and high nitrogen content, ZIF-8 is a common precursor for synthesizing many porous carbon materials for supercapacitors. Tang et al. put nanoporous hybrid carbon materials containing nitrogen-doped carbon (NC) as the cores and highly graphitic carbon (GC) as the shells using core-shell structured ZIF-8@ZIF-67 crystals. This novel NC@GC material holds a high surface area (up to $1276 \text{ m}^2 \text{ g}^{-1}$) and high N content (10.6 wt. %) derived from core ZIF-8, and a better graphitic structure derived from shell ZIF-67. It shows an eminent specific capacitance of 270 F g^{-1} at a current density of 2 A g^{-1} .⁹⁶ Liu et al. investigated a new strategy to design a flexible hierarchical porous carbon film (HPCF) for binder-free and high-performance energy storage devices consisting of MOF-derived porous carbon polyhedra and carbon nanotubes (CNTs). They prepared HPCF (1, 2, 3, 4, and 5) by the calcination at different temperatures of 400, 500, 600, 800, and 900°C respectively, from which HPCF₄ gives the largest BET ($620.1 \text{ m}^2 \text{ g}^{-1}$), and shows the highly porous structure, excellent flexibility, with highest electrical conductivity (1320 S m^{-1}). HPCF₄ offers excellent rate capability larger than 60 % retention from (2 to 100) A g^{-1} with high electrical conductivity and successful ion transport networks, compared with the other flexible carbon electrodes. In addition, they fabricated an aqueous symmetrical supercapacitor that shows an

energy density of 9.1 Wh kg^{-1} with a power density of 3500 W kg^{-1} .⁹⁷ Duan and his co-workers discovered three types of activated porous carbon (APC) by the annealing and thermolysis of Cu-MOF with different morphologies, varying its reaction temperatures at 0, 25, and 60°C . APC-25 reveals cabbage-like morphology out of those APCs with the largest specific surface area, i.e. $1880.4 \text{ m}^2 \text{ g}^{-1}$ and $0.81 \text{ cm}^3 \text{ g}^{-1}$ pore volume; it also exhibits the highest specific capacitance of 196 F g^{-1} at 0.5 A g^{-1} current density. Additionally, they fabricated an asymmetric supercapacitor (ASC) device using APC-25, giving an incredible 11.8 Wh kg^{-1} energy density at a power density of 350 W kg^{-1} with outstanding cycling stability. Noticeably, using six ASCs, five light-emitting diodes are lighted, which confirms that APC-25 might be used in energy storage devices.⁹⁸ Wang et al. demonstrated a fruitful route to increase the conductivity performance of N-doped MOFs-based hierarchical carbon (NPC) to defeat the insulating problems of MOFs by electrochemically twisting together MOF crystals with a conductive polymer. They prepared a new N-doped MOFs-based hierarchical carbon (NPC) by electrospinning method, followed by pyrolysis to get nanofibers; it shows superior energy storage capacity to that of the earlier recorded MOF-derived carbon materials with innovative 1D hollow structures. NPCF exhibits 332 F g^{-1} specific capacitance at 1 A g^{-1} current density and excellent cycling stability with a specific capacitance retention of 98.9 % after 5000 cycles at 1 A g^{-1} current density.⁹⁹

Chen and colleagues investigated a fruitful method for manufacturing hollow particle-based nitrogen-doped carbon nanofibers (HPCNFs-N) by an easy carbonization treatment of an electrospun ZIF-8/PAN composite precursor. HPCNFs-N material significantly increases the electrochemical property as an electrode material for supercapacitors with incredible specific capacitance at different current densities, high energy/power density, and long cycling stability of over 10000 cycles.¹⁰⁰ Hao et al. synthesized nitrogen-doped porous carbon polyhedra (N-PCMPs) by directly carbonizing ZIF-11 polyhedra stimulated by fused KOH to enhance the surface area and pore volume. Activated N-PCMPs (N-PCMPs-A) show 307 F g^{-1} specific capacitance at 1.0 A g^{-1} current density, which is incredibly higher than that of N-PCMPs, i.e. 165 F g^{-1} ; even further, the specific capacitance of N-PCMPs-A retains 198 F g^{-1} at a regular high amount of current density, i.e. 10 A g^{-1} , which compared to N-PCMPs, is significant. N-PCMPs show incredible cycling stability

with a specific capacitance retention of 90 %, even after 4000 cycles at the current density of 10 A g^{-1} .¹⁰¹

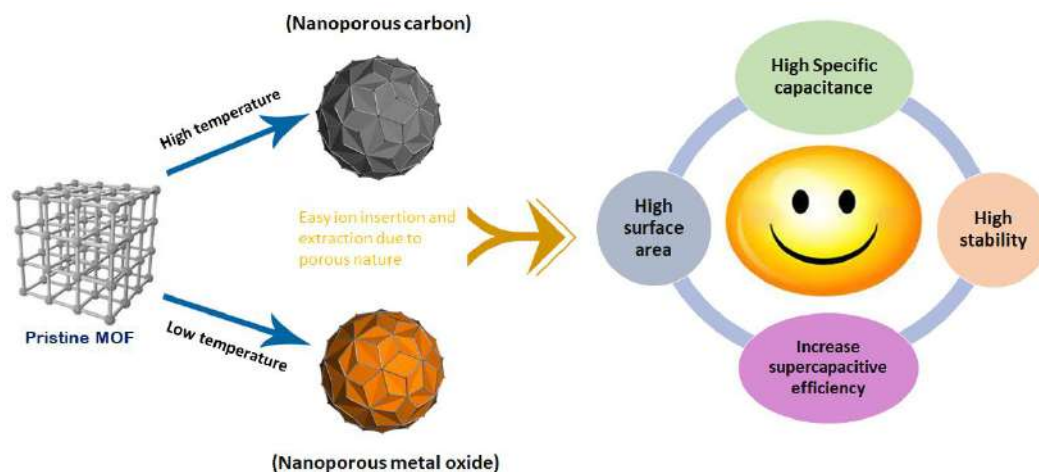


Figure 1.8: Development of the use of various MOFs in the field of supercapacitor application

1.3.3 MOFs derived from the first transition series elements serve as electrodes for supercapacitors

Metal-organic compounds derived from the first transition elements have emerged as prime contenders for top-notch active materials in supercapacitor, thanks to their advantageous characteristics, as outlined below.¹⁰²

- ❖ Metal-organic compounds belonging to the first transition metal series come with several benefits, including simplified synthesis, affordable pricing, regulated structure, and a vast range of structural variations. Additionally, the metals that belong to the initial series of transition metals are abundant on the earth, economical, and non-harmful.
- ❖ The high valence states of transition elements facilitate redox reactions and effective electron transfer, which enable the pseudocapacitive mechanism to operate efficiently.
- ❖ Transition metals can create porous structures by coordinating tetrahedrally or octahedrally and by using multidentate ligands. This process is often utilized in the creation of porous structures within metal coordination polymers, particularly in metal-organic frameworks (MOFs). The EDLC mechanism gains an advantage from this as it allows for an increased number of channels that facilitate the transportation of ions during the procedures of charging and discharging.

- ❖ In contrast to the other transition elements, the first transition elements exhibit lower molecular weights, leading to increased values of specific gravimetric capacitance.

1.3.3.1 The properties of transition elements

Transition elements, or sometimes referred to as transition metals, are a group of elements possessing d orbitals that are only partially occupied. According to the International Union of Pure and Applied Chemistry, transition elements can be classified as elements with a partially filled d subshell of electrons or elements that possess the capacity to generate stable cations using an incompletely filled d orbital.

The general characteristics of the transition elements are as described below:

- ❖ The presence of these components results in the creation of coloured compounds and ions. The color of this can be attributed to the d-d electron transition.
- ❖ These elements have the capability to bind with a vast range of ligands. As a result, transition elements can generate a diverse range of stable compound structures.
- ❖ The elevated boiling and melting points of transition elements can be attributed to the involvement of delocalized d electrons within metallic bonding.
- ❖ The possible oxidation states of transition elements have a relatively small energy difference. Hence, the elements in the transition group demonstrate various states of oxidation.
- ❖ These elements have the ability to form several paramagnetic compounds owing to the unpaired electrons present in the d orbital.
- ❖ These elements exhibit a high charge-to-radius ratio.
- ❖ The ability of transition elements to conduct electricity proficiently is attributed to their metallic bonding, which involves the delocalized d electrons.
- ❖ Transition elements possess a hard nature and display greater densities in contrast to other elements.

The five elements from transition first series elements namely Manganese (Mn), Iron (Fe), Cobalt (Co), Nickel (Ni) and Zinc (Zn) are more potential. The table below outlines the distinct characteristics of these elements.

Table 1.2: Properties of transition first series elements

Property	Manganese	Iron	Cobalt	Nickel	Zinc
Electron configuration	[Ar]3d ⁵ 4s ²	[Ar]3d ⁶ 4s ²	[Ar]3d ⁷ 4s ²	[Ar]3d ⁸ 4s ²	[Ar]3d ¹⁰ 4s ²
Melting point (°C)	1246	1538	1495	1455	419.5
Boiling point (°C)	2061	2862	2927	2730	907
Density (g/cm ³)	7.21–7.44	7.87	8.9	8.9	7.133
Electro negativity	1.55	1.83	1.88	1.91	1.65
Covalent radius (Å)	1.39	1.32	1.26	1.24	1.22
Ionic radius (Å)	0.80	0.69	0.70	0.72	0.74

1.4 Purpose of the dissertation

Energy holds significant significance in several facets of human existence. As long as the population continues to grow and people aspire to live a better lifestyle, the demand for energy will persistently increase. To satisfy the rising global energy needs, it is imperative that the energy sources of the future are not only efficient and reliable but also cleaner and adaptable. Energy is found in diverse forms that are not readily accessible, thus various energy storage devices are designed to transform the difficult-to-use energy into more convenient forms. Batteries and capacitors are the typical energy storage mechanisms that are commonly accessible. The usage of batteries is limited due to their low energy delivery rate, making them unsuitable for applications that require fast energy delivery. Capacitors are capable of delivering power rapidly, but their ability to store energy is significantly restricted. The gadget exhibiting dual features is known as the supercapacitor. Supercapacitors possess the prospective advantages of elevated energy and power density, prolonged lifespan, and accelerated charge and discharge rates, contributing to their enhanced efficiency. The electrode material is a crucial factor in the charge storing process of a supercapacitor device. Extensive research has been conducted on numerous electrode materials for supercapacitors, however, there are still certain obstacles that need to be overcome.

To conquer these obstacles, the metal-organic frameworks are used as an electrode materials in supercapacitors due to its exceptional chemical and structural characteristics. MOFs can serve as both a precursor and a template to create a diverse range of functional materials for supercapacitor.

The objective of the current research is to create a supercapacitor device that is sustainable, economical, and effective. This supercapacitor device should have a high specific capacitance and energy and power density, as well as an exceptional cycle life. With this aim, the MOFs are used as electrode materials due to their customizable pore structures, vast surface areas, and versatile structures. After a thorough investigation of prior research, it is discovered that MOF exhibits favorable electrochemical characteristics, its potential for commercialization is hindered by limited charge rate ability and low stability. Various approaches have been put in place up until now to address these downsides, which have been specifically discussed earlier. Upon thorough analysis of the methods employed thus far, we have observed that scientists have utilized combinations of MOF with various functional components to overcome its limitations. Despite their excellent electrochemical charge storage capacity, they exhibit low electrical conductivity and cyclic stability. Consequently, in order to enhance both the rate capability and durability, it is necessary to alter the substance through thermal processing so that it displays favorable features such as effective electrical conductivity, efficient capacity for holding electrochemical charge, and consistent long-term performance. With regards to all of these factors, the objective of this dissertation is to enhance the MOF's ability to store charges, its rate of capability, and its stability by constructing a highly conductive derived material by heat treatment of MOF that demonstrate pseudocapacitive charge storage capability. The synergic effect of high surface area of MOF and its derived materials will greatly enhance the specific capacitance and energy density of supercapacitor electrode. This electrode further used for fabrication of symmetric, asymmetric and hybrid supercapacitors devices.

1.5 Plan of the work

The following strategies are employed in this thesis to address the issues highlighted in the preceding section.

Chapter 1 covers the topic of energy storage mechanisms, including battery, capacitors, and the advancement of supercapacitor technology. The operations and

categories of supercapacitor gadgets have also been deliberated. Following this, issues related to the earlier literature are outlined, along with the rationale for conducting the current research and the significance of the findings.

In Chapter 2, the methods employed for producing MOFs are detailed alongside the techniques utilized to analyze their structural attributes. Additionally, it encompasses the process of crafting working electrodes and supercapacitor gadgets. In conclusion, the electrochemical properties of the working electrodes and devices produced through fabrication are thoroughly examined using an electrochemical workstation.

In the Chapter 3, a straightforward and inexpensive reflux method is employed to synthesize and characterize pure Ni-MOF. In order to provide a detailed analysis of the structural components, characterization methods were utilized. The electrochemical features of Ni-MOF were investigated by means of various methods such as CV, GCD, and EIS in an aqueous electrolyte of 2 M KOH. Additionally, a hybrid supercapacitor device was constructed to evaluate the capacity of Ni-MOF.

Chapter 4 focuses on creating new trimetallic MOFs with the intention of developing superb electrode materials for supercapacitors. To thoroughly examine the structural elements, an array of characterization techniques were employed. Research was conducted to investigate how the structural and electrochemical characteristics of MOF are impacted by tricarboxylic and dicarboxylic ligands. We have successfully manufactured a symmetrical device with a solid-state symmetric supercapacitor which glows a red LED light. This remarkable achievement showcases the vast potential of our device.

Chapter 5 outlines the procedure for creating a new bimetallic MOF and its resulting oxide through a straightforward heat treatment method. Sophisticated techniques were employed to comprehensively examine the structural components. The electrochemical properties of bimetallic MOF and its corresponding oxides are explored through multiple techniques including CV, GCD, and EIS in a 1 M neutral Na₂SO₄ electrolyte. We have effectively produced a solid-state asymmetrical supercapacitor device that illuminates a cluster of red LED lights. The immense capabilities of our device are clearly demonstrated by this impressive accomplishment.

Chapter 6 explores the synthesis and characterization of a bimetallic MOF, its oxide derivative, and nanoporous carbon. The purpose of this investigation is to create

exceptional electrode materials for supercapacitors. Advanced methods were utilized to thoroughly analyze the structural constituents. Several techniques including CV, GCD, and EIS were utilized to investigate the electrochemical characteristics of bimetallic MOF, its corresponding oxide, and nanoporous carbon in a 2 M KOH electrolyte. A single all-in one device called the solid-state asymmetrical supercapacitor has been successfully constructed, that utilizes the electrodes made from derived materials i.e. nanoporous carbon and oxide which shows remarkable electrochemical performance.

In Chapter 7, the key findings from this thesis are summarized and suggestions are provided for potential future endeavors that could build upon the outcomes of this research.

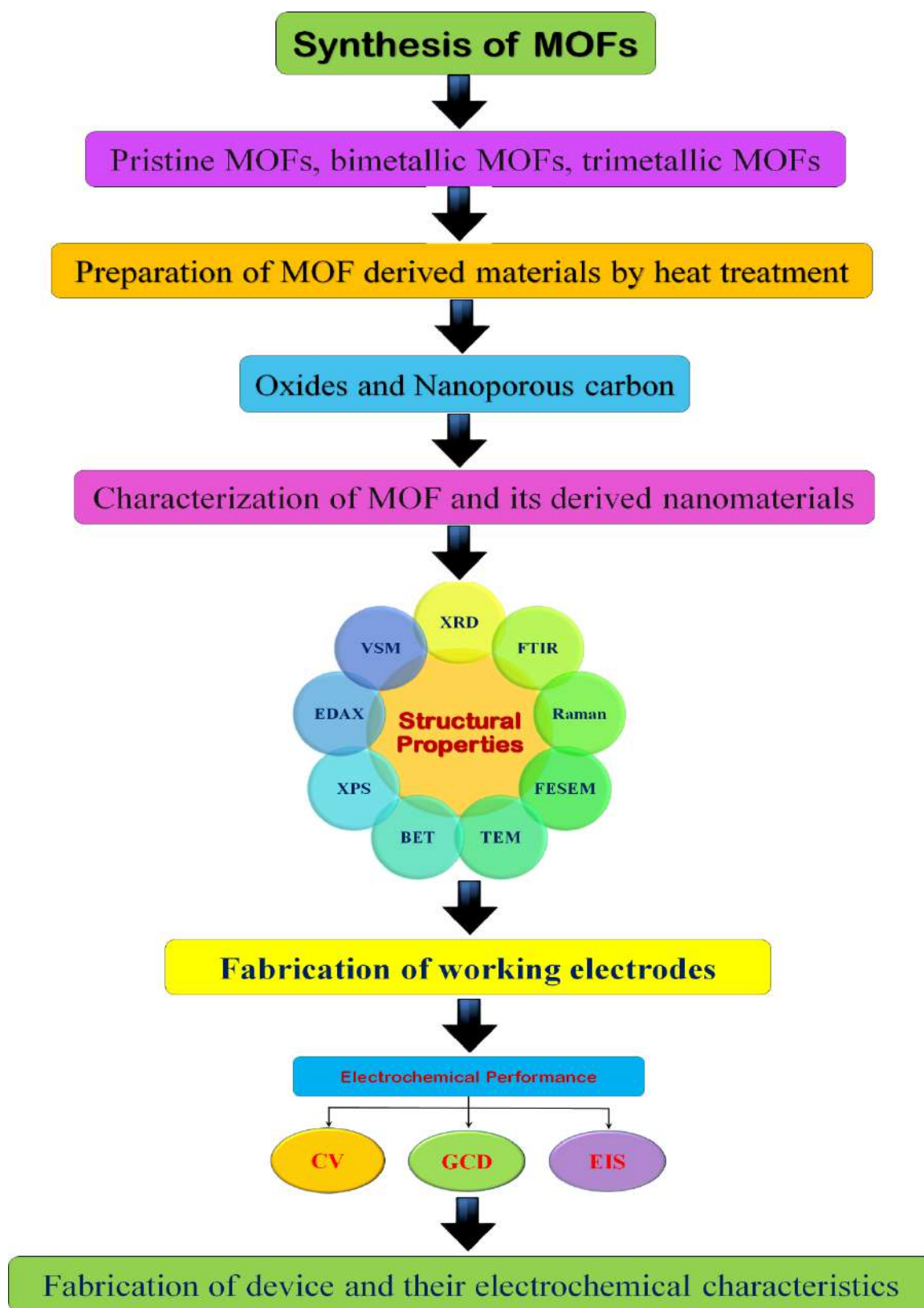


Figure 1.9: Diagrammatic representation of plan of thesis

1.6 References

- 1 L. Zhang and X. S. Zhao, *Chem. Soc. Rev.*, 2009, **38**, 2520–2531.
- 2 P. J. Hall and E. J. Bain, *Energy Policy*, 2008, **36**, 4352–4355.
- 3 J. Murray and D. King, *Nature*, 2012, **481**, 433–435.
- 4 M. Winter and R. J. Brodd, *Chem. Rev.*, 2004, **104**, 4245–4269.
- 5 J. R. Miller and P. Simon, *Science*, 2008, **321**, 651–652.
- 6 A. Burk, *J. Power Sources*, 2000, **91**, 37–50.
- 7 H. Kelly-Holmes, *Advert. as Multiling. Commun.*, 2016, **45**, 1–206.
- 8 H. I. Becker, *US Pat.*, 1957, 2800616-2800624.
- 9 R. A. Rightmire, *US Pat.*, 1966, 3288641-3288650.
- 10 D. L. Boos and G. Heights, *US Pat.*, 1970, 3536963-3536969.
- 11 M. Endo, T. Takeda, Y. J. Kim, K. Koshiba and K. Ishii, *Carbon Sci.*, 2001, **1**, 117–128.
- 12 B. E. Conway, *Proc. Int. Power Sources Symp.*, 1991, 319–327.
- 13 B. E. Conway, *Electrochem. Encycl.*, 2003, 1–8.
- 14 A. Schneuwly and R. Gallay, *Pcim*, 2000, 1–10.
- 15 G. Wang, L. Zhang and J. Zhang, *Chem. Soc. Rev.*, 2012, **41**, 797–828.
- 16 P. Sharma and T. S. Bhatti, *Energy Convers. Manag.*, 2010, **51**, 2901–2912.
- 17 J. P. Zheng, *J. Electrochem. Soc.*, 2005, **152**, A1864-A1869.
- 18 C. Z. Yuan, B. Gao and X. G. Zhang, *J. Power Sources*, 2007, **173**, 606–612.
- 19 J. R. Miller, *Electrochim. Acta*, 2006, **52**, 1703–1708.
- 20 S. P. S. Badwal, S. S. Giddey, C. Munnings, A. I. Bhatt and A. F. Hollenkamp, *Front. Chem.*, 2014, **2**, 1–28.
- 21 J. Maier, *Angew. Chemie - Int. Ed.*, 2013, **52**, 4998–5026.
- 22 T. Brousse, D. Bélanger, K. Chiba, M. Egashira, F. Favier, J. Long, J. R. Miller, M. Morita, K. Naoi, P. Simon and W. Sugimoto, *Springer Handbooks*, 2017, 495–561.
- 23 A. Nishino, *J. Power Sources*, 1996, **60**, 137–147.
- 24 T. Jin, G. Singer, K. Liang and Y. Yang, *Mater. Today*, 2022, **62**, 151–167.
- 25 D. Linden and T. B. Reddy, *Handbook of batteries*, 1995, **3**, 1-50.
- 26 S. S. Siwal, Q. Zhang, N. Devi and V. K. Thakur, *Polymers*, 2020, **12**, 1–31.
- 27 I. Staffell, D. Scamman, A. Velazquez Abad, P. Balcombe, P. E. Dodds, P. Ekins, N. Shah and K. R. Ward, *Energy Environ. Sci.*, 2019, **12**, 463–491.

- 28 P. S. Joshi and D. S. Sutrave, *J. Inf. Comput. Sci.*, 2019, **9**, 609-625.
- 29 S. I. Kim, S. W. Kim, K. Jung, J. B. Kim and J. H. Jang, *Nano Energy*, 2016, **24**, 17–24.
- 30 H. Ji, X. Zhao, Z. Qiao, J. Jung, Y. Zhu, Y. Lu, L. L. Zhang, A. H. MacDonald and R. S. Ruoff, *Nat. Commun.*, 2014, **5**, 1–7.
- 31 X. You, M. Misra, S. Gregori and A. K. Mohanty, *ACS Sustain. Chem. Eng.*, 2018, **6**, 318–324.
- 32 S. Fleischmann, J. B. Mitchell, R. Wang, C. Zhan, D. E. Jiang, V. Presser and V. Augustyn, *Chem. Rev.*, 2020, **120**, 6738–6782.
- 33 N. R. Chodankar, H. D. Pham, A. K. Nanjundan, J. F. S. Fernando, K. Jayaramulu, D. Golberg, Y. K. Han and D. P. Dubal, *Small*, 2020, **16**, 1–35.
- 34 A. Borenstein, O. Hanna, R. Attias, S. Luski, T. Brousse and D. Aurbach, *J. Mater. Chem. A*, 2017, **5**, 12653–12672.
- 35 A. Vlad, N. Singh, J. Rolland, S. Melinte, P. M. Ajayan and J. F. Gohy, *Sci. Rep.*, 2014, **4**, 1–7.
- 36 N. Swain, B. Saravanakumar, M. Kundu, L. Schmidt-Mende and A. Ramadoss, *J. Mater. Chem. A*, 2021, **9**, 25286–25324.
- 37 Z. S. Iro, C. Subramani and S. S. Dash, *Int. J. Electrochem. Sci.*, 2016, **11**, 10628–10643.
- 38 H. Jiang, P. S. Lee and C. Li, *Energy Environ. Sci.*, 2013, **6**, 41–53.
- 39 R. Singh, S. Sansare and S. Shidhaye, *Biomed. Appl. Nanoparticles*, 2019, 319–339.
- 40 Y. Zhai, Y. Dou, D. Zhao, P. F. Fulvio, R. T. Mayes and S. Dai, *Adv. Mater.*, 2011, **23**, 4828–4850.
- 41 L. Deng, R. J. Young, I. A. Kinloch, A. M. Abdelkader, S. M. Holmes, D. A. De Haro-Del Rio and S. J. Eichhorn, *ACS Appl. Mater. Interfaces*, 2013, **5**, 9983–9990.
- 42 S. Sundriyal, V. Shrivastav, H. D. Pham, S. Mishra, A. Deep and D. P. Dubal, *Resour. Conserv. Recycl.*, 2021, **169**, 105548-105555.
- 43 P. Forouzandeh, V. Kumaravel and S. C. Pillai, *Catalysts*, 2020, **10**, 1–73.
- 44 H. Shirakawa, E. J. Louis, A. G. MacDiarmid, C. K. Chiang and A. J. Heeger, *J. Chem. Soc. Chem. Commun.*, 1977, 578–580.
- 45 Q. Meng, K. Cai, Y. Chen and L. Chen, *Nano Energy*, 2017, **36**, 268–285.
- 46 I. Shown, A. Ganguly, L. C. Chen and K. H. Chen, *Energy Sci. Eng.*, 2015, **3**,

- 2–26.
- 47 G. A. Snook, P. Kao and A. S. Best, *J. Power Sources*, 2011, **196**, 1–12.
- 48 J. Liu, J. Bao, X. Zhang, Y. Gao, Y. Zhang, L. Liu and Z. Cao, *RSC Adv.*, 2022, **12**, 35556–35578.
- 49 A. Kumar, H. K. Rathore, D. Sarkar and A. Shukla, *Electrochem. Sci. Adv.*, 2021, **2**, e2100187-e2100229.
- 50 O. M. Yaghi and H. Li, *J. Am. Chem. Soc.*, 1995, **117**, 10401–10402.
- 51 H. Gao, H. Shen, H. Wu, H. Jing, Y. Sun, B. Liu, Z. Chen, J. Song, L. Lu, Z. Wu and Q. Hao, *Energy and Fuels*, 2021, **35**, 12884–12901.
- 52 F. Boorboor Ajdari, E. Kowsari, M. Niknam Shahrak, A. Ehsani, Z. Kiaei, H. Torkzaban, M. Ershadi, S. Kholghi Eshkalak, V. Haddadi-Asl, A. Chinnappan and S. Ramakrishna, *Coord. Chem. Rev.*, 2022, **422**, 213441-213448.
- 53 Y. Zhao, J. Liu, M. Horn, N. Motta, M. Hu and Y. Li, *Sci. China Mater.*, 2018, **61**, 159–184.
- 54 J. Y. Long, Z. S. Yan, Y. Gong and J. H. Lin, *Appl. Surf. Sci.*, 2018, **448**, 50–63.
- 55 R. R. Salunkhe, Y. V. Kaneti and Y. Yamauchi, *ACS Nano*, 2017, **11**, 5293–5308.
- 56 Z. Lv, Q. Zhong and Y. Bu, *Appl. Surf. Sci.*, 2018, **439**, 413–419.
- 57 Y. Wang, Y. Liu, H. Wang, W. Liu, Y. Li, J. Zhang, H. Hou and J. Yang, *ACS Appl. Energy Mater.*, 2019, **2**, 2063–2071.
- 58 F. Bigdeli, C. T. Lollar, A. Morsali and H. C. Zhou, *Angew. Chemie - Int. Ed.*, 2020, **59**, 4652–4669.
- 59 Q. Wu, T. He, Y. Zhang, J. Zhang, Z. Wang, Y. Liu, L. Zhao, Y. Wu and F. Ran, *J. Mater. Chem. A*, 2021, **9**, 24094–24147.
- 60 L. Xia, L. Yu, D. Hu and G. Z. Chen, *Mater. Chem. Front.*, 2017, **1**, 584–618.
- 61 D. Aurbach, Y. Talyosef, B. Markovsky, E. Markevich, E. Zinigrad, L. Asraf, J. S. Gnanaraj and H. J. Kim, *Electrochim. Acta*, 2004, **50**, 247–254.
- 62 K. Tönurist, T. Thomberg, A. Jänes, I. Kink and E. Lust, *Electrochem. commun.*, 2012, **22**, 77–80.
- 63 S. Paul, K. S. Choi, D. J. Lee, P. Sudhagar and Y. S. Kang, *Electrochim. Acta*, 2012, **78**, 649–655.
- 64 B. H. Wee and J. D. Hong, *Langmuir*, 2014, **30**, 5267–5275.
- 65 B. Pal, S. Yang, S. Ramesh, V. Thangadurai and R. Jose, *Nanoscale Adv.*,

- 2019, **1**, 3807–3835.
- 66 X. Zhang, Z. Chen, X. Liu, S. L. Hanna, X. Wang, R. Taheri-Ledari, A. Maleki, P. Li and O. K. Farha, *Chem. Soc. Rev.*, 2020, **49**, 7406–7427.
- 67 W. Li, X. Zhao, Q. Bi, Q. Ma, L. Han and K. Tao, *Dalt. Trans.*, 2021, **50**, 11701–11710.
- 68 R. Vinodh, R. S. Babu, R. Atchudan, H. J. Kim, M. Yi, L. M. Samyn and A. L. F. de Barros, *Catalysts*, 2022, **12**, 375–391.
- 69 J. Yu, X. Gao, Z. Cui, Y. Jiao, Q. Zhang, H. Dong, L. Yu and L. Dong, *Energy Technol.*, 2019, **7**, 1900018–1900039.
- 70 T. Qiu, Z. Liang, W. Guo, H. Tabassum, S. Gao and R. Zou, *ACS Energy Lett.*, 2020, **5**, 520–532.
- 71 D. Sheberla, J. C. Bachman, J. S. Elias, C. J. Sun, Y. Shao-Horn and M. Dincă, *Nat. Mater.*, 2017, **16**, 220–224.
- 72 N. Sahiner, S. Demirci and M. Yildiz, *J. Electron. Mater.*, 2017, **46**, 790–801.
- 73 F. Wang, S. Xiao, Y. Hou, C. Hu, L. Liu and Y. Wu, *RSC Adv.*, 2013, **3**, 13059–13084.
- 74 Y. Tan, W. Zhang, Y. Gao, J. Wu and B. Tang, *RSC Adv.*, 2015, **5**, 17601–17605.
- 75 C. Yang, X. Li, L. Yu, X. Liu, J. Yang and M. Wei, *Chem. Commun.*, 2020, **56**, 1803–1806.
- 76 Y. Yan, P. Gu, S. Zheng, M. Zheng, H. Pang and H. Xue, *J. Mater. Chem. A*, 2016, **4**, 19078–19085.
- 77 B. M. Omkaramurthy, G. Krishnamurthy and S. Foro, *Mater. Res. Express*, 2019, **6**, 125544–125557.
- 78 G. Zhu, H. Wen, M. Ma, W. Wang, L. Yang, L. Wang, X. Shi, X. Cheng, X. Sun and Y. Yao, *Chem. Commun.*, 2018, **54**, 10499–10502.
- 79 Y. Li, Y. Xu, W. Yang, W. Shen, H. Xue and H. Pang, *Small*, 2018, **14**, 1–24.
- 80 J. Li, D. Yan, S. Hou, T. Lu, Y. Yao and L. Pan, *Chem. Eng. J.*, 2018, **354**, 172–181.
- 81 Z. Zhang, Y. Huang and S. Bai, *Mater. Sci. Forum*, 2017, **890**, 68–73.
- 82 M. Lan, X. Wang, R. Zhao, M. Dong, L. Fang and L. Wang, *J. Alloys Compd.*, 2020, **821**, 153546–153554.
- 83 Z. Xiao, L. Fan, B. Xu, S. Zhang, W. Kang, Z. Kang, H. Lin, X. Liu, S. Zhang and D. Sun, *ACS Appl. Mater. Interfaces*, 2017, **9**, 41827–41836.

- 84 M. K. Wu, C. Chen, J. J. Zhou, F. Y. Yi, K. Tao and L. Han, *J. Alloys Compd.*, 2018, **734**, 1–8.
- 85 G. C. Li, P. F. Liu, R. Liu, M. Liu, K. Tao, S. R. Zhu, M. K. Wu, F. Y. Yi and L. Han, *Dalt. Trans.*, 2016, **45**, 13311–13316.
- 86 J. Xu, S. Liu and Y. Liu, *RSC Adv.*, 2016, **6**, 52137–52142.
- 87 L. T. Gong, M. Xu, R. P. Ma, Y. P. Han, H. B. Xu and G. Shi, *Sci. China Technol. Sci.*, 2020, **63**, 1470–1477.
- 88 Z. Lei, D. Bai and X. S. Zhao, *Microporous Mesoporous Mater.*, 2012, **147**, 86–93.
- 89 M. Zhong, E. K. Kim, J. P. McGann, S. E. Chun, J. F. Whitacre, M. Jaroniec, K. Matyjaszewski and T. Kowalewski, *J. Am. Chem. Soc.*, 2012, **134**, 14846–14857.
- 90 H. Zhu, J. Yin, X. Wang, H. Wang and X. Yang, *Adv. Funct. Mater.*, 2013, **23**, 1305–1312.
- 91 T. A. Centeno, A. B. Fuertes and F. Stoeckli, *Electrochim. Acta*, 2009, **52**, 3207–3215.
- 92 T. Wang, J. Tang, X. Fan, J. Zhou, H. Xue, H. Guo and J. He, *Nanoscale*, 2014, **6**, 5359–5371.
- 93 R. R. Salunkhe, Y. Kamachi, N. L. Torad, S. M. Hwang, Z. Sun, S. X. Dou, J. H. Kim and Y. Yamauchi, *J. Mater. Chem. A*, 2014, 19848–19854.
- 94 Z. Chen, Y. Qin, D. Weng, Q. Xiao, Y. Peng, X. Wang, H. Li, F. Wei and Y. Lu, *Adv. Funct. Mater.*, 2009, **19**, 3420–3426.
- 95 J. Ren, Y. Huang, H. Zhu, B. Zhang, H. Zhu, S. Shen, G. Tan, F. Wu, H. He, S. Lan, X. Xia and Q. Liu, *Carbon Energy*, 2020, **2**, 176–202.
- 96 J. Tang, R. R. Salunkhe, J. Liu, N. L. Torad, M. Imura, S. Furukawa and Y. Yamauchi, *J. Am. Chem. Soc.*, 2015, **137**, 1572–1580.
- 97 Y. Liu, G. Li, Y. Guo, Y. Ying and X. Peng, *ACS Appl. Mater. Interfaces*, 2017, **9**, 14043–14050.
- 98 H. H. Duan, C. H. Bai, J. Y. Li, Y. Yang, B. L. Yang, X. F. Gou, M. L. Yue and Z. X. Li, *Inorg. Chem.*, 2019, **58**, 2856–2864.
- 99 C. Wang, C. Liu, J. Li, X. Sun, J. Shen and W. Han, *ChemComm*, 2017, **1**, 1751–1754.
- 100 L. F. Chen, Y. Lu, L. Yu and X. W. Lou, *Energy Environ. Sci.*, 2017, **10**, 1777–1783.

- 101 F. Hao, L. Li, X. Zhang and J. Chen, *Mater. Res. Bull.*, 2015, **66**, 88–95.
102 B. Chen, L. Xu, Z. Xie and W. Y. Wong, *EcoMat*, 2021, **3**, e12106-e12160.

CHAPTER TWO

Experimental Details and Characterization Techniques

2.1 Outline

This chapter provides a thorough explanation of the experimental and characterization techniques. The theoretical background, along with characterization techniques and the synthesis method, has been briefly discussed. The article thoroughly examines various physicochemical analyses that can be employed to verify the properties of materials utilized in the testing and production of supercapacitors. An explanation of the electrode's fabrication and the experimental setup of this technique is provided. This chapter provides an in-depth account of the various physical characterization techniques used to analyze the pristine MOFs, MOF-derived metal oxides and nanoporous carbon samples that have been developed as part of this study. These techniques include X-ray diffraction, Fourier transform infrared spectroscopy, Raman spectroscopy, X-ray photoelectron spectroscopy, Field emission scanning electron microscopy, Energy dispersive X-ray analysis, Brunauer–Emmett–Teller analysis, Transmission electron microscopy and Vibrating sample magnetometer. This chapter provides a comprehensive discussion of the electrochemical performance of the materials, which was evaluated using an electrochemical workstation.

2.2 Introduction

This thesis aims to enhance the efficiency of supercapacitors by proposing novel approaches. The introductory chapter provides a description of the background. The current study involves the synthesis of MOF materials to serve as electrodes and electrolytes in order to assemble a supercapacitor. This chapter outlines the experimental method employed for the synthesis of the MOF and its derived materials. Afterwards, the characterization methods implemented are explained in detail. First, the electrode and electrolyte materials are prepared and characterized and then, supercapacitors are fabricated and characterized. The electrode materials that were taken into consideration were pristine MOF, bimetallic MOFs, trimetallic MOFs, ferrites and nanoporous carbon. Pristine MOF, bimetallic and trimetallic MOFs were synthesized using a wet chemical method i.e. Reflux condensation method. Also, the ferrites and nanoporous carbon are prepared by using MOFs as a precursors via simple pyrolysis process. The methods of preparation are elaborated in details.

The physical properties of the synthesized materials are investigated through a variety of techniques such as X-ray diffraction (XRD), Fourier transform infrared spectroscopy (FTIR), Raman spectroscopy, X-Ray Photoelectron Spectroscopy (XPS) Technique, Scanning electron microscope (SEM), Energy dispersive X-ray (EDAX) spectroscopy, Specific surface area analyzer using Brunauer– Emmett– Teller (BET) Technique and Transmission electron microscope (TEM). This chapter includes a comprehensive explanation of these methods. Adequate electrolyte solutions were created through the dispersion of the corresponding salt in an appropriate solvent. Appropriate aqueous electrolytes were prepared by dissolving the relevant salt in water. To prepare gel-polymer electrolytes (GPEs), the polyvinyl alcohol polymer was utilized to encapsulate the aqueous electrolyte. The efficiency of constructed supercapacitor cells were assessed using a two-electrode assembly. The characterization techniques employed for the evaluation of electrochemical performance are cyclic voltammetry (CV), galvanostatic charge-discharge (GCD) and electrochemical impedance spectroscopy (EIS). The succeeding section also covers the discussion of these methods of characterization.

2.3 Experimental details

2.3.1 Aqueous chemical method/reflux condensation method

The reflux technique is a cost-effective and facile wet chemical method to produce nanomaterials. The reflux technique involves gradually growing crystals by controlling precipitation through the hydrolysis and condensation reactions of metal ions or their complexes in a solution. Reflux is a process by which the vapors are condensed and the resulting condensate is reintroduced back into the system it came from. It has applications both in industrial settings and laboratory setups for the purpose of distillation. In chemistry, it is employed to provide sustained energy to reactions. The reflux setup, as depicted in figure 2.1, comprises various components that include a round bottom flask (reaction bath), a condenser (cooling mode), and a temperature controller unit with an integrated stirring and heating mechanism. The precursor solution was stirred with a magnetic bar in a round-bottomed flask to produce a uniform solution. By utilizing a temperature controller, a stable and uninterrupted amount of thermal energy was supplied to the flask to carry out the reaction. The reaction can proceed for any desired duration because the reactant solvent cannot evaporate from the system, thanks to the process of condensation.¹



Figure 2.1: Schematic depiction of reflux condensation assembly

The reflux technique offers numerous benefits when compared to other synthesis methods. Following are several benefits that are highlighted:

- ❖ The reaction may be sustained over a prolonged duration without the need for further solvent addition or concern regarding the drying of the reaction vessel owing to the fact that the condenser readily captures the vapors.
- ❖ The primary benefit of utilizing this method is the upsurge in output, as all the reactants are fully employed in the reaction.
- ❖ By adjusting reaction time, temperature, pH of solution, and other reaction parameters, the characteristics of nanomaterial can be readily optimized.
- ❖ This approach can be readily implemented for industrial purposes as it does not necessitate a vacuum or top-notch targets at any point.

2.3.2 Substrate cleaning

To evaluate the electrochemical performance of the material, it should be deposited on the conductive substrate to form an electrode. The fabrication of an electrode involves the use of a substrate, and achieving high-quality and consistent results is heavily dependent on thoroughly cleaning the substrate. This process is crucial for ensuring that the electrode displays strong adhesion and a uniform, smooth surface. The approach utilized for cleaning will vary based on the type of surface, the level of cleanliness desired, and the type of pollutants that need to be eliminated. Some of the usual impurities that can be found are oil droplets, dust particles that are carried in the air, absorbed water, as well as grease. The act of cleansing involves the detachment of impurities from the base materials while keeping the materials unharmed. Numerous techniques exist for providing energy to break those bonds, including ion bombardment, thermal means, and scraping. The prescribed technique employed to clean the stainless steel mesh substrates was as follows.

- ❖ In the initial stage of substrate cleaning, the stainless steel mesh was first thoroughly rinsed with regular water.
- ❖ Then, the stainless steel mesh was subjected to treat with laboratory-grade cleaning agent for 15 minutes and subsequently rinsed with ordinary water.
- ❖ An ample amount of distilled water was poured into the beaker to facilitate the immersion of the stainless steel mesh, which were subsequently sonicate it in the distilled water for 15 minutes.
- ❖ Lastly, the stainless steel mesh substrates were rinsed with acetone to remove the impurities.

- ❖ The cleaned stainless steel mesh were dried at 70°C and further used as a substrate for fabrication of electrode.

2.3.3 Procedure of the seed slurry and fabrication of working electrodes

To fabricate the electrode, a seed slurry was prepared by mixing the active material, binder, and acetylene black in an appropriate proportion. To prepare seed slurry, 80 wt% of MOFs and its derived materials were used as active materials, 10 wt% of polyvinylidene pyrrolidone as a binder, and 10 wt% of acetylene black as a conducting material were grinded in N-Methyl-2-Pyrrolidone as a solvent. Then it was grinded to prepare a smooth and homogeneous seed slurry. Finally, it is ready to be used for the construction of the working electrode.

For the construction of working electrodes, stainless steel mesh was used as a substrate. The earlier prepared seed slurry was pasted on a stainless steel mesh of area 1 cm² to prepare the working electrode. Finally, the pasted stainless steel mesh was dried in an oven at 70°C for few hours, and it is now ready to be used as a working electrode to evaluate the electrochemical performance.

2.4 Characterization techniques

In present time, nanoscience and nanotechnology have emerged as the most effective answers to various technological challenges owing to their collaboration with materials science. It is imperative to utilize diverse conventional methods of characterization in order to examine the physical and chemical attributes of these materials. The newly created materials possess a set of distinctive characteristics, which include their structural, morphological, optical, electrical, and surface properties. As a consequence, the materials science field has witnessed the development of numerous innovative methods.² This section encompasses various physical and chemical methods along with their operating principles (Figure 2.2).

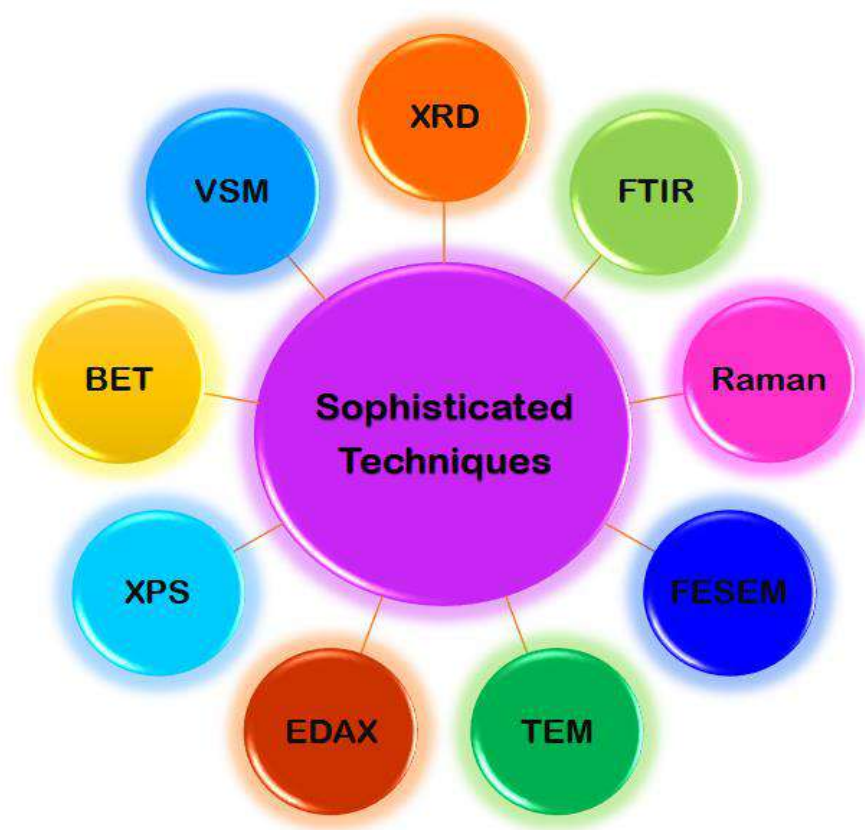


Figure 2.2: Various sophisticated techniques for the characterization of MOFs and its derived materials

2.4.1 X-ray diffraction (XRD)

Principle

Using a monochromatic X-ray beam to irradiate the target material, the non-invasive XRD technique measures the scattering angles and intensities of the diffracted beam. At angles when Bragg's law ($2d\sin\theta = n\lambda$) is satisfied, the maximum intensity of the diffracted beam is observed.^{3,4}

Construction and working of XRD

The XRD is made up of three parts

1. X-ray tube
2. Sample holder
3. X-ray detector

Figure 2.3 displays the schematic of XRD machines. A monochromatic X-ray beam is produced by the X-ray tube, which is essentially a Cathode Ray Tube (CRT). The CRT tube is constructed up of

- ❖ Evacuated glass tube: makes it possible for the molecules to hit the target without touching.

- ❖ Heated filament (Cathode): This substance typically has low ionization energy.
- ❖ Target (Anode): Usually, this is a substance having a high melting point, like Mo or W.
- ❖ Cooling system: In order to stop the anode from melting.
- ❖ High voltage source: The thermionic electrons are accelerated using a high voltage of 20–60 kV.

The produced monochromatic X-ray beam is collimated and directed at the target substance. Typically, a monochromatic beam of 1.54 \AA is produced using a Cu filter with a Ni filter. Diffraction occurs when the monochromatic beam comes into contact with the sample. The sample serves as a scattering center for the incident X-rays, while the detector collects the diffracted photons. For the angles that comply with Bragg's law, an intensity peak is created. The sample is scanned from 10 to 90° s, and the diffraction pattern is obtained. By comparing the data with the databases of the Joint Committee on Powder Diffraction or the American Standard for Testing of Materials (ASTM), one can identify the material from the sample by looking at this pattern.

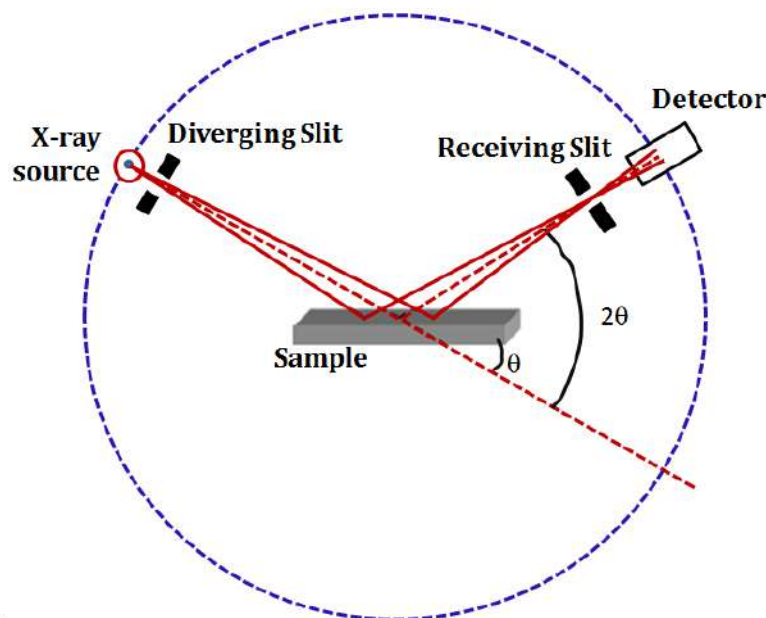


Figure 2.3: Schematic diagram of X-Ray diffraction techniques

[<http://pd.chem.ucl.ac.uk/pdnn/inst1/optics1.htm>]

We can identify the phase, ascertain the crystal structure, assess the quality of the thin film, and calculate a number of parameters, including residual stress/strain, crystal size, crystallographic roughness, flaws, etc. from the XRD pattern.

Bragg's condition in crystals can be fulfilled in one of two ways: continually changing or all over the experiment. Three distinct diffraction methods are produced by varying these parameters. These are listed in table 2.1, which is provided below.

Table 2.1: X-ray diffraction methods

Sr. No.	Method	λ	θ
1	Rotating crystal Method	Fixed	Variable (in part)
2	Powder Method	Fixed	Variable
3	Laue Method	Variable	Fixed

According to the Bragg's law, for certain d values, constructive interference of diffracted X-rays should occur at specific θ (i.e., Bragg's angle), and for other angles, destructive interference should occur, resulting in the least intensity of the diffracted beam. Subsequently, if the diffracting crystal's size is tiny, there won't be any more completely destructive interference at $\theta \pm d\theta$, which causes the peak to broaden in proportion to crystallite size and is used to determine crystallite size.

2.4.2 Fourier transform infrared (FTIR) spectroscopy

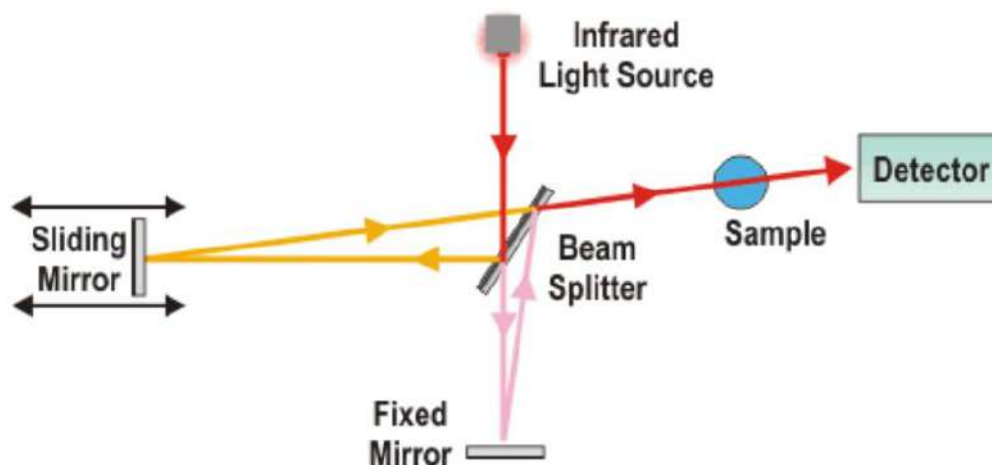


Figure 2.4: Schematic diagram of FTIR spectrometer

(<https://www.tribonet.org/wiki/fourier-transform-infrared-spectroscopy/>)

The FTIR technique plays a significant role in revealing details about the molecular structure or chemical bonds present in materials. The FTIR generates results based on frequency. The illustration depicted in figure 2.4 displays the schematic layout of the FTIR spectrometer. When a sample is exposed to IR radiation, a portion of the radiation is absorbed by the sample while the rest passes through it. When the sample is detected, a signal is obtained that essentially serves as its unique identifier, reflecting its particular fingerprint or structure.

The unique spectral signatures vary among various chemicals. The absorption is directly related to the specific bonds within the molecule. The wave numbers that are usually measured in the FTIR spectrum are within the frequency range of 400-6000 cm^{-1} . Initially, the IR source is evaluated for its emission spectrum, after which the emission spectrum of the IR source is measured along with the sample. The absorption spectrum of samples can be accurately determined by observing the ratio between the sample spectrum and the background spectrum. The absorption spectrum that arises from the natural vibration of the bond is produced as a result. The frequencies detected imply the existence of diverse functional groups and chemical bonds within the specimen. Due to the distinctive vibrational frequencies in the infrared range, FTIR is highly beneficial in determining organic molecular groups and compounds, which encompass a variety of functional groups, cross-links, and side chains.^{5,6}

The process of identifying functional groups occurs in the following manner.

- (1) Source: A black-body source generates and emits infrared radiation. The level of energy delivered to the specimen is regulated by the aperture, which enables the beam to pass through.
- (2) Interferometer: The phenomenon known as "Spectral encoding" takes place at the moment the beam goes into the interferometer. Afterwards, the signal from the interferogram is released through the interferometer.
- (3) Sample: The sample compartment serves as the entry point for the beam, which interacts with the sample's surface based on the specific analysis being conducted, either by passing through or bouncing off it. The sample absorbs distinct frequencies of energy that are indicative of its unique characteristics.
- (4) Detector: After navigating through the system, the beam ultimately arrives at the detector for its ultimate evaluation. The utilized sensors are uniquely engineered to gauge the distinctive interferogram signal generated.
- (5) Computer: By using computer hardware and software, the digitized signal is processed. The ultimate infrared spectrum is displayed to the user for analysis and additional alterations.

2.4.3 Fourier transform Raman (FT-Raman) spectroscopy

Raman spectroscopy is one of the spectroscopic methods used to examine rotational, vibrational, and specific additional modes in a system among the various spectroscopic techniques. Sir C. V. Raman discovered in 1928 that some of the light

that is deflected by a transparent medium changes in wavelength. This phenomenon is known as Raman scattering and this results from the Raman Effect. It depends on Raman scattering, also known as inelastic scattering of monochromatic light, which typically comes from a laser and may be in the visible, near-infrared, or near-ultraviolet spectrum. In Raman spectroscopy, laser radiations engage with the system's molecular vibrations generating phonons or other excitations. It causes the energy of the laser photons to change, either upward or downward. It provides details on the system's vibrational modes. There are possibilities with rotational and vibrational spectroscopes. With the aid of stimulating radiations energy, the type of transition that takes place will be identified.⁷

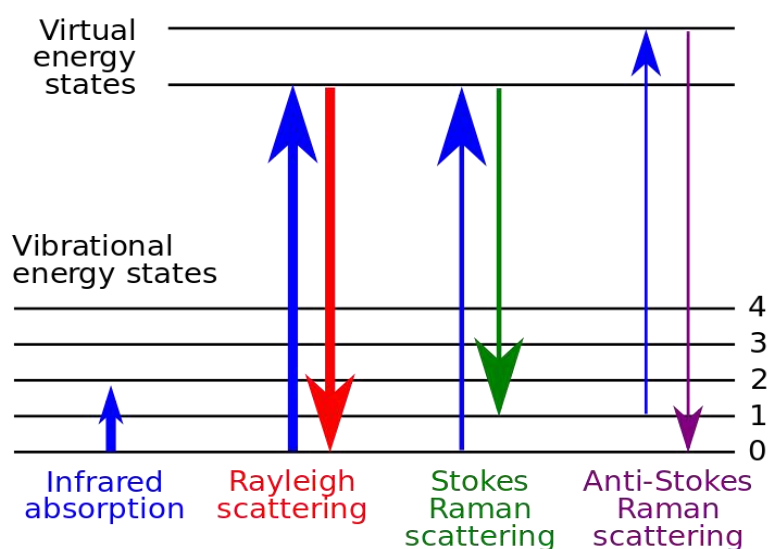


Figure 2.5: Energy level diagrams showing the states involved in Raman signal

[https://en.wikipedia.org/wiki/Raman_spectroscopy]

In Raman spectroscopy, a sample is lit with a laser beam, and the light that is scattered from that area is then captured with a lens spectrometer and provided through a monochromator. Due to elastic Rayleigh scattering, wavelengths that are nearer the laser line are filtered out, and the remaining collected light is scattered onto a detector. Separating weakly elastically scattered light from slightly more intense Rayleigh scattered laser light is the main challenge in Raman spectroscopy. The reason for this is because spontaneous Raman scattering is usually relatively feeble. To obtain a high level of laser rejection, spectroscopic Raman spectrometers used holographic gratings and numerous dispersion stages. The preferred detector for dispersive Raman setups in the past was a photomultiplier.

Principle

A molecule experiences the Raman Effect when light strikes it and interacts with its electron cloud and bonds. A photon excites the molecule in the case of the spontaneous Raman Effect, moving it from its ground state to a simulated energy level. The molecule, which is in an excited state, relaxes during which it produces a photon and returns to a rotational or vibrational state. The frequency of the emitted photon shifts away from the excitation wavelength due to the energy difference between the original state and the new state. The Raman Effect is a phenomena of light scattering as opposed to absorption, which occurs when a molecule is excited to a distinct energy level, as in fluorescence. The states involved in the Raman signal are depicted in figure 2.5 energy level diagram.

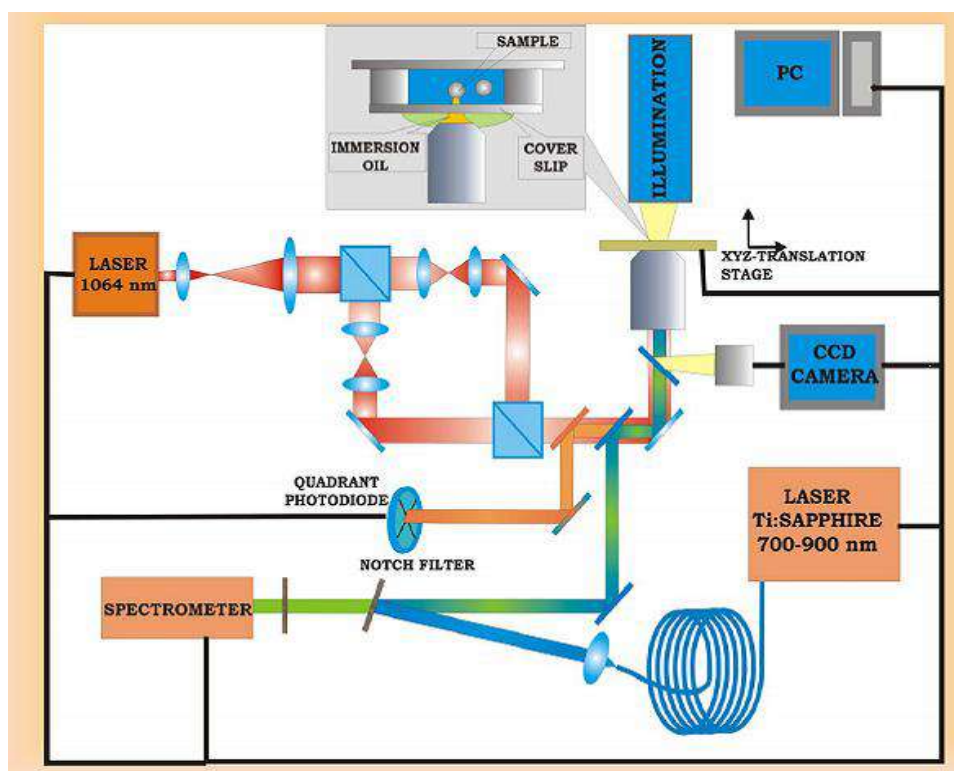


Figure 2.6: Schematic diagram of Raman spectrometer

If a molecule's long-term vibrational state is more energetic than its original condition, then the transmitted photon's frequency shifts towards a lower frequency, and the ideal state of the systems overall energy of molecules is maintained. Stokes shift describes this change in frequency. The same is true when a molecule's ultimate vibrational state is less energetic than its beginning state, the emitted photon's frequency shifts in favour of higher frequency. Anti-Stokes shift is the term used to

describe this change in frequency. Raman scattering is a manifestation of inelastic scattering due to the energy transfer that occurs when molecules and photons interact.

A schematic diagram of a Raman spectrometer is shown in figure 2.6. There are typically five main parts within the Raman system:

1. Excitation source (Laser)
2. Sample illumination system and light collection optics
3. Wavelength selector (Filter or Spectrophotometer)
4. Detector (Photodiode array, CCD or PMT)
5. Computer Interfacing software

2.4.4 X-ray photoelectron spectroscopy (XPS)

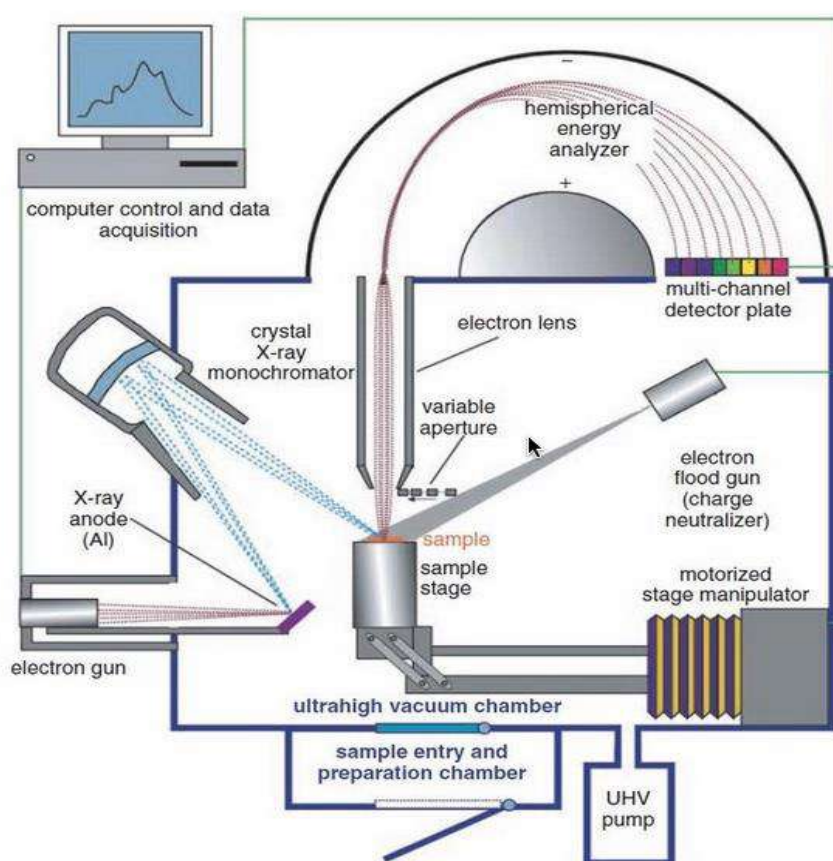


Figure 2.7: Schematic representation of XPS spectrometer

[https://serc.carleton.edu/msu_nanotech/methods/xps.html]

One of the most accurate methods for determining the chemical environment and composition of the specimen surface is X-ray photoelectron spectroscopy (XPS). It is based on the fundamental idea of the photoelectron effect, according to which an incident photon with enough energy ($E = h\nu$) causes the emission of an electron from an atom on the surface of the specimen (10–15 nm away).^{8,9}

Principle:

Monochromatic low energy (1.5 keV) X-rays incident on the surface of the specimen cause photoelectrons to be produced. These photoelectrons have energy that is specific to a given atomic state and can reveal important details about the chemical environment of specimen's.

The following are the components of typical XPS equipment:

1. A source of monochromatic low energy X-rays
2. Ultra-high vacuum chamber
3. An electron energy analyzer (concentric hemispherical analyzer)

In XPS, a monochromatic X-rays photons of sufficient (~ 1.5 keV) known energy are produced from X-ray source, are impinged on the specimen surface placed on a specimen stage. In order to allow an interference-free study of photo emitted electrons, the specimen stage is enclosed in an ultra-high vacuum chamber. As seen in figure 2.7, these X-ray photons interact with the specimen's atoms and cause their core level electrons to emit. The photoelectrons that are released will definitely have kinetic energies lower than these energies, leading to an extremely short electronic mean-free path. The signal is only created from the core level electrons expelled from the atoms present in the few atomic layers at the surface since the electron produced much deeper in the specimen's bulk will be absorbed in the specimen itself.

2.4.5 Scanning electron microscope (SEM)

An image that shows the morphological and topological details of the specimen in a scanning electron microscope is produced by the collection and non-destructive processing of secondary and backscattered electrons that are produced during the scattering of a high mono-energetic and focused electron beam accelerated (30kV) onto the surface of the specimen under vacuum.

In SEM, the specimen surface is incident with a mono-energetic beam that has been well targeted. When this mono-energetic electron beam interacts with the specimen, secondary electrons and backscattered electrons form, and these electrons are primarily utilised for generating the specimen image. The atomic number of the host atoms impacts the amount of backscattered electrons. The valence electrons of the constituent atoms emit secondary electrons, which are then developed. Only secondary electrons generated and released from specimen surfaces are detected because their energy is quite low, whereas secondary electrons generated in the bulk of the specimen are destroyed. In spite of their high sensitivity to the specimen's

surface, these secondary electrons generate the brightness and contrast needed for images. The electrons that are elastically dispersed backward from their host atoms are known as backscattered electrons. These electrons are more energetic than secondary electrons and are affected by the specimen's composition.^{10,11}

Construction in brief

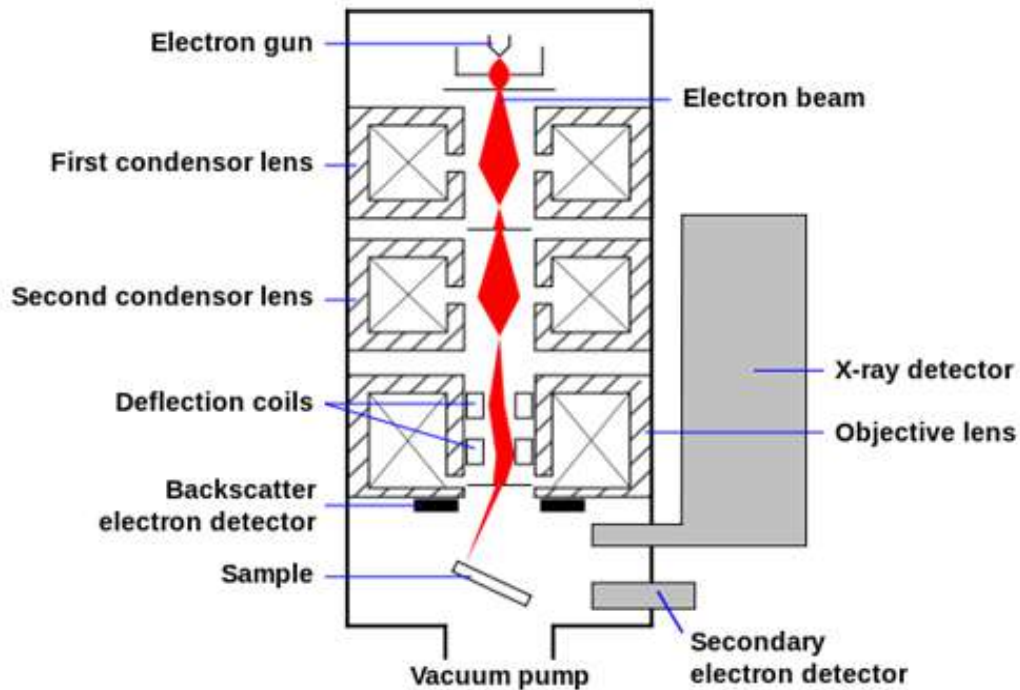


Figure 2.8: Schematic representation of scanning electron microscope

[http://en.wikipedia.org/wiki/Scanning_electron_microscope]

In a typical SEM, an electron gun is largely needed to provide an electron probe beam that gives light in an optical microscope. A series of magnetic electron lenses and deflection coils combine to form an electron beam that scans the surface of a specimen put on a specimen stage in an electron optical system. High vacuum is required to maintain an undistorted electron beam, in the path of which is positioned a specimen stage that allows the research specimen to be readily oriented in the proper direction for a detailed analysis. The specimen surface is hit by an electron beam, which generates a variety of signals, including secondary and backscattered electrons, which must be collected out. In order to collect the appropriate electrons and other signals, such as X-rays, for energy dispersive analysis of the X-rays from the specimen, a group of detectors is used.

An image display unit that offers the necessary view of specimen morphology further processes and displays the signal generated by this set of detectors. The figure

2.8 depicts the schematic representation of SEM and its key elements. So an electron gun, electron lenses, a sample stage, a vacuum chamber, detectors for the appropriate signals, a data output device, cooling system, and power supply make up a typical SEM machine.

2.4.6 Energy dispersive X-ray (EDS) spectroscopy

The elements present in the material are quantitatively examined using energy dispersive X-ray analysis (EDS). With the help of the EDS technique, the elements with atomic numbers 4 (Be) to 92 (U) can be identified; this is one of the best benefits over other techniques to detect a wide range of elements.^{12,13}

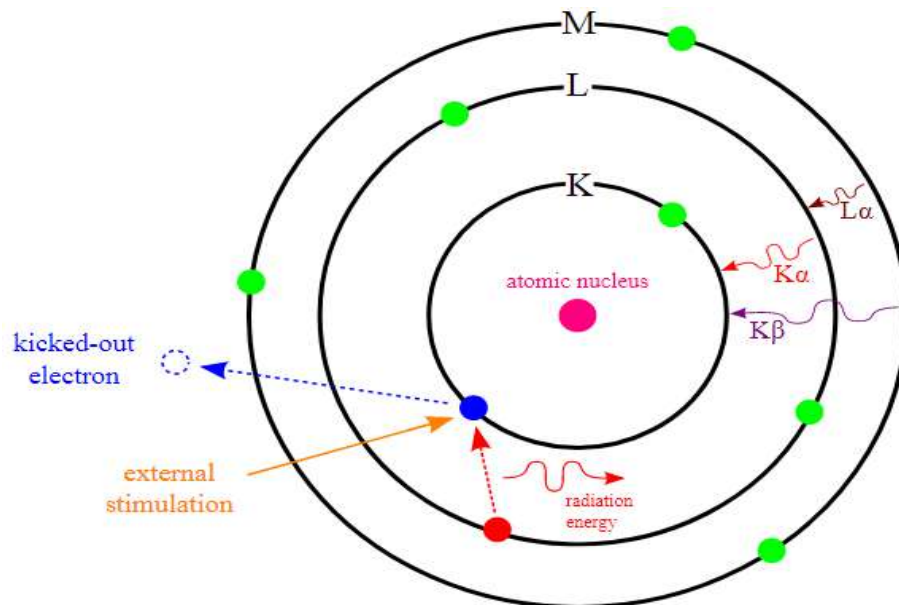


Figure 2.9: Schematic diagram showing the possible transition¹⁴

Principle of EDS

Using the EDS analytical method, the chemical characterization of materials and quantitative evaluation of components are explored. In EDS, an electron ray with enough energy can hit the samples top layer, causing inner shell electrons to change and eject from an atomic orbit. Then, with the same amount of time, an electron from the top energy shell falls to take its place. As upper energy shell electrons continuously go down, they give up some of their energy to get into the low energy shell. The transition shown in figure 2.9 is one that is likely to occur and release energy on the order of an X-ray wavelength. This energy is then counted, gathered, and converted to atomic or weight percentages. With only a few spectral peaks, the various elements often generate characteristic X-rays at different energies that overlap.

Working of EDS

In EDS, precise electron beam energy that is focused on the sample is employed for material analysis. Energy is lost when an electron beam interacts with a material in a number of ways (e.g. X-ray emission). In particular, inelastic collisions in the incident electron beam can cause the electron to be ejected from the material. As a result, an atom produces an electron vacancy that creates a hole. It follows that this causes the atom to lose energy and to automatically rearrange its electron shells. The atom's distinctive property is the generation of free X-rays. Using the X-ray detector, EDS calculates the big amount of released X-ray energy. A solid-state lithium-drifted silicon detector is typically utilized. When the emitted X-ray hits the detector, it produces a pulse with that energy. This pulse alters a voltage pulse within the charge-sensitive amplifier. Then, a different channel analyzer has created a range of voltage-related pulses. The measurement of voltage to all incident X-rays is determined by energy and sent to the computer for data analysis. The X-ray energy against counts was used to determine the percentage of the elements in the sample. The precision of the EDS is based on the several variables that are connected to the sample. Less than 5 atomic number elements (such as Be, H, and He) cannot be detected by an EDS detector. Another is that high voltage in the EDS can alter the position of the peak in the spectrum. Additionally, the peaks of certain elements, such as Mn K_{β} and Fe K_{α} have not yet split as well. Furthermore, the sample's inherent characteristics affect how precisely the EDS spectrum is generated. As a result, the EDS is the most effective method to determine the proportion of elements in the sample with atomic numbers greater than 6.

2.4.7 Specific surface area analyzer using Brunauer– Emmett– Teller (BET)

Principle

A low-temperature nitrogen gas adsorption on a solid surface of a material is used in Brunauer-Teller-Emmett (BET) surface area study. It is a crucial technique since it provides details about the materials' surface area and porosity. The BET theory is an important analytical tool for determining a material's specific surface area, pore size, and pore volume. It also explains the physical adsorption of gas molecules on solid surfaces.^{15–17}

With the following hypotheses, Stephen Brunauer, Paul Hugh Emmett, and Edward Teller expanded Langmuir theory, a theory for monolayer molecule adsorption, to multilayer adsorption.

- i) Physically, gas molecules adhere to a solid in an unlimited number of layers.
- ii) Every adsorption layer is independent of one another.
- iii) Each layer can be analysed using the Langmuir theory.

Working

As impurities like water and oil may impact the actual surface area of a given material, sample preparation is crucial before analysis in BET surface area measurement. As a result, solid surfaces must be free of these contaminants before conducting gas sorption tests. Most frequently, a sample is placed in a glass cell and heated under vacuum or a flowing gas to remove such impurities this process is known as surface cleaning (degassing).

By using an external bath, the prepared sample is heated to an accurate temperature. Then, tiny volumes of gas (a Nobel gas like N_2) are gradually allowed into the sample zone that has been evacuated. A thin layer that covers the whole surface of the solid (adsorbent) is stated to be formed when N_2 gas molecules adhere to the solid's surface and are considered to have been adsorbed. The volume of gas adsorbed onto the surface of a powdered or porous substance can be calculated as its surface area. The entire surface that the gas can reach, whether it is exterior or internal, is included in the surface area analysed.



Figure 2.10: BET instrument

In general, only Van der Waals forces cause solids to absorb weakly bonded gases. The solid must be properly frozen to the gas's boiling point in order for enough gas to be absorbed for surface area measurement. Most frequently, liquid nitrogen (77.35 K) is used to cool down the solid while nitrogen gas serves as the adsorbate.

Adsorption doesn't stop until the concentration of N₂ in the gas phase and the amount of N₂ adsorbed are in equilibrium.

2.4.8 Transmission electron microscope (TEM)

When an ultrathin specimen (less than 200 nm) is exposed to a high-energetic beam of accelerated electrons at a voltage of about 300 kV, a variety of interactions result obtained; that causes the transmission of direct or distributed electrons through the specimen. Depending on the mode of operation, these transmitted electrons are focused through a set of electromagnetic lenses to create an image, a diffraction pattern, or another nano-analytical spectrum.^{18,19}

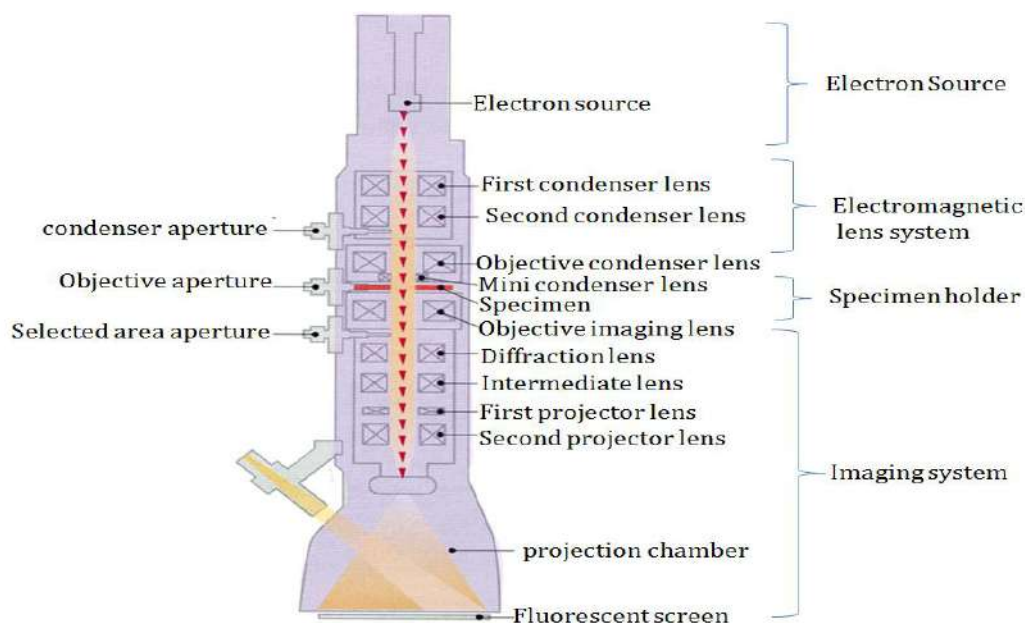


Figure 2.11: Schematic representation of transmission electron microscope

[<http://micron.ucr.edu/public/manuals/Tem-intro.pdf>]

The fundamental structure of a TEM is similar to that of an optical microscope, however with a TEM, an electron beam with high energy is employed in place of light, and electromagnetic lenses are used in place of glass lenses. Figure 2.11 depicts a common TEM setup design. We can see from the picture that a TEM can be easily broken down into four primary components. The specimen holder, imaging system, electromagnetic lens system, and electron source or gun.

Electron Gun: It offers a potent, powerful, and highly energetic electron beam. Depending on the phenomenon employed for electron ejection, there are three primary categories of electron guns.

Thermionic emission (TE) electron gun: When the cathode filament is heated to a high temperature and propelled towards the anode with a certain acceleration voltage (up to 30 kV), electrons are released.

Field emission (FE) electron gun: When high resolution imaging is necessary, this electron gun is utilized. The field emission happens when a strong field is applied to a metal tip that is very small (less than 100 nm) and electrons are released as a result of the tunneling phenomena. In contrast to the thermionic electron gun's 10–20 mm diameter, the electron beam created here functions as an electron source with a diameter of 5–10 nm.

Shottkey-emission (SE) electron gun: With an additional applied electric field on the heated metal surface, it is comparable to the TE gun. Compared to a FE gun, this electron gun creates a beam with a bit less stability but a higher current. It can be viewed as combining more of the benefits and less of the drawbacks of both TE and FE guns.

Electromagnet lens system: An essential element of an electron microscope is the magnetic lens system. It is used to channel post-interaction electrons for picture generation as well as to focus an electron beam on the subject. Condenser lenses, objective lenses, and projector lenses are the three basic types of electromagnet lens systems. A group of lenses known as condenser lenses is in charge of controlling the spot size of the primary electron beam convergence. An image is created by the objective lens, which gathers transmitted electrons from the specimen, and is then magnified and projected by a group of intermediate and projector lenses.

Specimen holder: The specimen is held by the sample holder, which is a platform with a mechanical arm and a feature for regulating the specimen's position.

Imaging system: A set of electromagnetic lenses and the display device are also included in it. Here, the electromagnetic lenses serve two purposes specifically. The image is magnified and projected on a phosphorescent screen or a detector that shows the image on a monitor by one method of focusing the electrons sent through the specimen, while the image is shown on the monitor by another method.

2.4.9 Vibrating sample magnetometer (VSM)

The materials magnetic characteristics are measured using a vibrating sample magnetometer (VSM). The material was magnetized after being placed in a constant magnetic field, using a piezoelectric material, physical sinusoidal vibration of the sample was applied. In a typical setup, a lock-in amplifier that uses the piezoelectric

signal as the reference signal calculates the induced voltage. It is possible to obtain the materials hysteresis curve by estimating the field of an outside electromagnet. The foundation of VSM is Faraday's law of induction, which states that an electric field is produced when a magnetic field changes. This measured electric field can reveal information about the formation of the magnetic field. If the sample is magnetized, the alignment of the magnetic domains in the field leads the sample to become magnetized. The magnetization increases as the constant field size increases.²⁰⁻²³ The digital photograph of vibrating sample magnetometer as shown in figure 2.12.



Figure 2.12: Digital photograph of vibrating sample magnetometer
(<https://qdusa.com/products/ppms.html>)

2.4.10 Electrochemical studies

Sophisticated electrochemical analysis methods are employed in order to methodically investigate how the working electrode stores charges and their kinetics. This thesis employs both two-electrode and three-electrode configurations for electrochemical experimentation. The three-electrode step-up was used to investigate the electrochemical responses and capacity for storing charges in an electrode system. Additionally, the two-electrode setup is employed to assess the practical potential of a constructed supercapacitor device.

In order to gain insights into how an electrode behaves electrochemically, a variety of characterization tests are performed, including cyclic voltammetry, galvanostatic charge-discharge, and electrochemical impedance spectroscopy.

2.4.10.1 Cyclic voltammetry (CV)

Cyclic voltammetry refers to a variety of potentiodynamic electrochemical techniques. Cyclic voltammetry is a well-regarded electrochemical method that is employed to investigate the oxidation and reduction mechanism of manufactured materials. To scrutinize the capacitive characteristics of the electrodes, CV assessments are carried out with variable scan rates, while keeping the voltage range steady. Three electrode assembly was used to study the single electrode system. The CV graph is depicted by placing voltage along the x-axis and current along the y-axis, as shown in figure 2.13. The CV would appear as a rectangle in the case of an ideal capacitor. The CV curves of EDLC based materials show a rectangular in shape. Simultaneously, the electrode with a battery-type or pseudocapacitor material displays peaks indicative of redox processes in cyclic voltammetry graphs. In CV measurements, the applied voltage is studied in relation to the cell current. During a CV experiment, the electrode's potential is swept linearly from the beginning to the end and then back to the starting point. The peak current is observed at the voltage of maximum potential after the electrochemical species present on the electrodes surface have been exhausted. The amount of Faradic current reflects the speed of electron transfer between the electrode and redox molecule.²⁴⁻²⁶

The conclusions derived from CV curves:

- ❖ The use of a CV curves can effectively examine redox reactions and various chemical reactions that involve the transfer of electrons.
- ❖ The working electrodes charge storage capacity can be determined using CV curves.
- ❖ It is possible to distinguish between supercapacitor and battery electrodes based on the configuration of their CV curves. In the case of a supercapacitor electrode, a rectangular curve is observed in the CV, whereas batteries typically exhibit strong redox peaks that are reflective of the material being used.
- ❖ The charge storage kinetics of electrodes can be comprehensively analyzed by thoroughly examining the CV curves.

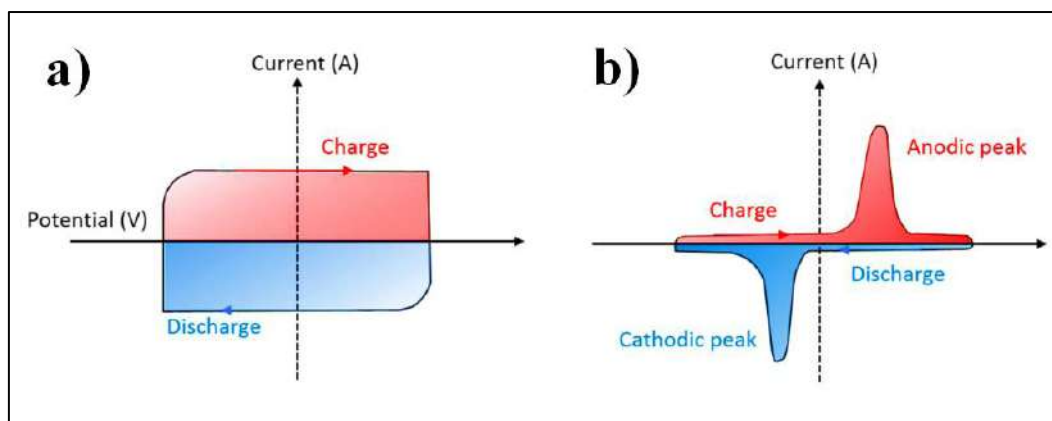


Figure 2.13: A typical cyclic voltammogram curves of a) supercapacitor and b) battery. Reproduced with permission.²⁷ Copyright © 2018, American Chemical Society

2.4.10.2 Galvanostatic charge-discharge (GCD)

Galvanostatic charge-discharge evaluation are utilised to assess a materials ability to store charge. The process involves charging and discharging the supercapacitor at a constant applied current within a defined range of two voltages, as depicted in figure 2.14. Ideally, the GCD curve would exhibit a linear pattern, characterized by alternating positive and negative gradients. Non-linearities may arise as a result of the swift decline in voltage during the transition from charging to discharging. Furthermore, it can be observed that authentic supercapacitors tend to discharge themselves when they are fully charged and left without any external load being connected.

The electrodes specific capacitance (computed in F g^{-1}) can be obtained from the GCD curve using the equation:

$$C_{\text{sp}} = \frac{I \times \Delta t}{m \times \Delta V} \dots\dots\dots (2.1)$$

Where C is the specific capacity (F g^{-1}), I is the current density (A), Δt is the discharging time (s), m is the mass (g) of the active electrode materials, and ΔV is the potential window of the discharge process (V). The GCD tests hold significant value in assessing capacitance. The potential range for pseudocapacitors remains in a fixed state. However, in the scenario of EDLC, the scope of plausible windows is not limited since the capacity for storing charge is not reliant on potential.

The GCD curve was used to calculate the specific energy and specific power for a two-electrode cell setup, using the given formulas.²⁸

$$E = \frac{0.5 \times C_{\text{sp}} \times \Delta V^2}{3.6} \dots\dots\dots (2.2)$$

$$P = \frac{E \times 3600}{\Delta t} \dots\dots\dots (2.3)$$

Where E and P are the specific energy (Wh kg⁻¹) and specific power (W kg⁻¹), respectively, ΔV is the discharging voltage (V), and Δt is the discharging time in seconds.

The effective use of the supercapacitor in practical applications is dependent on its ability to maintain capacitance over a long period, known as cyclic stability. This capability is achieved through the deployment of GCD. The cell consistently performs charging and discharging cycles without interruption. The assessment of performance differences or similarities is conducted by measuring the difference in capacitance before and after cycling. Typically, EDLCs exhibit greater durability compared to pseudocapacitors, which have a limited cycle life due to factors like redox reactions, electrode material swelling and shrinking caused by charge/discharge cycle.²⁹

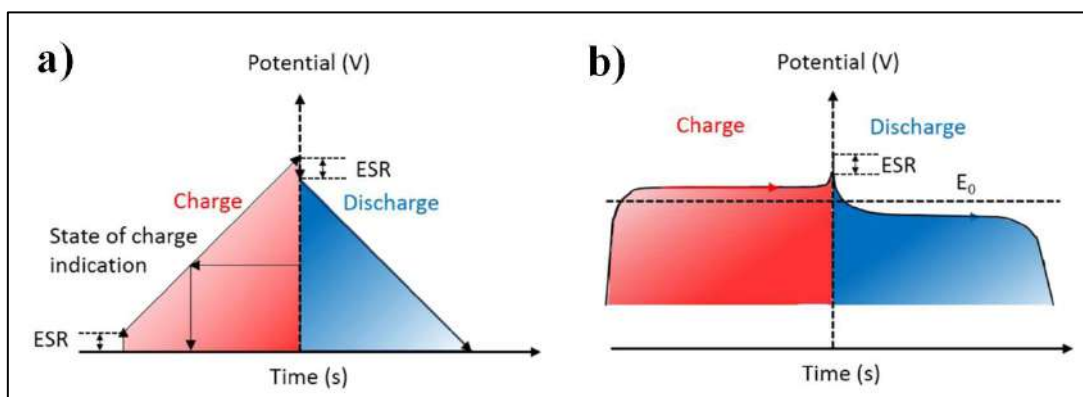


Figure 2.14: A typical galvanostatic charge–discharge curves of a) supercapacitor and b) battery. Reproduced with permission.²⁷ Copyright © 2018, American Chemical Society

2.4.10.3 Electrochemical impedance spectroscopy (EIS)

The EIS examinations assess the electrodes resistance at a constant voltage throughout different frequencies. In this evaluation, a consistent voltage is overlaid with a low-amplitude sinusoidal voltage. The Nyquist plot is a useful tool for analyzing the signal produced by the EIS technique. The Nyquist plot depicts the relationship between the real impedance (Z') and imaginary impedance (Z'') in graphical form. The Nyquist plot is divided into three distinct parts as shown in figure 2.15.

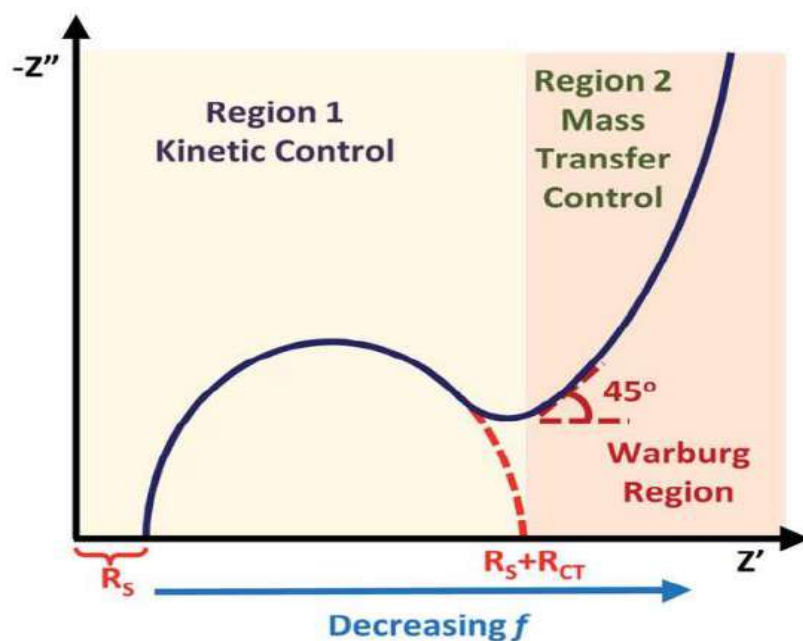


Figure 2.15: A Nyquist plot featuring labeled significant regions. Reproduced with permission.³⁰ Copyright © 2021, Royal Society of Chemistry

- (1) The high-frequency interceptions imply the resistance of the solution.
- (2) In the range of high to medium frequencies, a semicircle can be observed that signifies the presence of charge transfer resistance at the interface of the electrode and electrolyte.
- (3) In the low-frequency region, the presence of a Warburg resistance is signaled by vertical line or a straight line angled around 45° degrees to the real axis.

2.4.11 Supercapacitor device fabrication

The supercapacitor device is constructed to understand the real practical ability of the electrode materials. Supercapacitor device generally consist of electrodes, electrolyte and a separator. Depending on the electrode material used to fabricate supercapacitor device, the supercapacitors are again divided into subtypes are symmetric, asymmetric and hybrid supercapacitor device.

Based on the electrolyte used, the supercapacitor device is of two types, i.e. aqueous or liquid state supercapacitor device and solid-state-supercapacitor device. The advantages of the solid-state supercapacitor device as compared to the liquid-based supercapacitors device are numerous, such as increased flexibility, hassle-free production, improved safety features and ability to operate in a broader temperature range. Solid-state supercapacitors possess distinctive electrochemical features such as exceptional stability, elevated power output, flexible structure, and moderate energy density, implying their immense potential for various prospective applications.

Flexibly constructed solid-state supercapacitors can serve as a source for powering electronic gadgets and various energy storage or conversion tools including lithium-ion batteries, fuel cells and so on.³¹

2.4.11.1 Electrode materials

Superior performance of supercapacitors can be attained by creating appropriate electrodes utilizing inexpensive and environmentally friendly techniques. Through these techniques, it becomes possible to produce materials that have a morphology and porosity that align with predetermined specifications. A thorough comprehension of the process of storing charges, routes for ion transportation, and locations of electrochemically responsive areas is necessary. A variety of electrode materials are utilized in the application of supercapacitors. These encompass electrode materials comprised of carbon based materials, polymers that conduct electricity, as well as oxides derived from transition metals and rare earth elements.

2.4.11.2 Separator

The separator plays a crucial role in the operation of a supercapacitor device. These materials have the ability to facilitate the transportation of charges while preventing the physical and electrical connection between two electrodes due to their ion-permeability. Typically, nonwoven fabric or polymer-coated paper is used as separators in SCs that employ aqueous electrolytes. Typically, these insulators are saturated in the electrolytic solution for a set amount of time prior to their utilization in the apparatus.

2.4.11.3 Gel-polymer electrolyte (GPE)

Gel-polymer electrolyte are a type of electrolyte that involves the confinement of liquid electrolytes in a polymer matrix. Gel-polymer electrolytes have a reduced amount of available water when compared to liquid electrolytes. This attribute results in lower levels of water oxidation processes. As a result, gel-polymer electrolytes can widen the range of voltages that can be used, which was previously a limitation in supercapacitors based on liquid electrolytes. As a result, polyvinyl alcohol served as a matrix for KOH/Na₂SO₄ as the liquid electrolyte. Polyvinyl alcohol ability to hold water and promote effective ion conduction pathways was due to its -OH/SO₄ groups.³²

2.5 References

- 1 S. K. Aditha, A. D. Kurdekar, L. A. A. Chunduri, S. Patnaik and V. Kamiseti, *MethodsX*, 2016, **3**, 35–42.
- 2 S. Mourdikoudis, R. M. Pallares and N. T. K. Thanh, *Nanoscale*, 2018, **10**, 12871–12934.
- 3 C. F. Holder and R. E. Schaak, *ACS Nano*, 2019, **13**, 7359–7365.
- 4 A. A. Bunaciu, E. gabriela Udriștioiu and H. Y. Aboul-Enein, *Crit. Rev. Anal. Chem.*, 2015, **45**, 289–299.
- 5 M. Dendisová, A. Jenišťová, A. Parchaňská-Kokaislová, P. Matějka, V. Prokopec and M. Švecová, *Anal. Chim. Acta*, 2018, **1031**, 1–14.
- 6 J. L. R. Arrondo, A. Muga, J. Castresana and F. M. Goñi, *Prog. Biophys. Mol. Biol.*, 1993, **59**, 23–56.
- 7 B. Chase, *Mikrochim. Acta*, 1987, **93**, 81–91.
- 8 F. A. Stevie and C. L. Donley, *J. Vac. Sci. Technol. A*, 2020, **38**, 063204-063225.
- 9 E. Korin, N. Froumin and S. Cohen, *ACS Biomater. Sci. Eng.*, 2017, **3**, 882–889.
- 10 M. Pluskal, L. Oskwarek, R. Rak and A. Czerwinski, *2007 IEEE Instrumentation & Measurement Technology Conference IMTC 2007*, 2007, 1-4.
- 11 A. Mohammed and A. Abdullah, *Proc. 2018 Int. Conf. Hydraul. Pneum. - HERVEX*, 2019, 77–85.
- 12 H. Schwenke, J. Knoth, *Nucl. Instrum. Methods Phys. Res.*, 1982, **193**, 239–243.
- 13 W. C. Campbell, *Analyst*, 1979, **104**, 177-195.
- 14 Z. M. Zhang, C. J. Fu and Q. Z. Zhu, *Advances in Heat Transfer*, 2003, **37**, 179–296.
- 15 F. Ambroz, T. J. Macdonald, V. Martis and I. P. Parkin, *Small*, 2018, **2**, 1800173-1800190.
- 16 R. Bardestani, G. S. Patience and S. Kaliaguine, *Can. J. Chem. Eng.*, 2019, **97**, 2781–2791.
- 17 D. N. P. R. Jayakantha, N. Gunawardhana, H. M. N. Bandara, E. Comini, N. M. Gunawardana and S. M. M. L. Karunarathne, *Instrum. Sci. Technol.*, 2021,

- 50, 47–56.
- 18 M. Malatesta, *Int. J. Mol. Sci.*, 2021, **22**, 12789-12806.
- 19 L. E. Franken, K. Grünewald, E. J. Boekema and M. C. A. Stuart, *Small*, 2020, **16**, 1906198-1906213.
- 20 E. E. Bragg and M. S. Seehra, *J. Phys. E.*, 1977, **10**, 216-223.
- 21 B. R. Sankhi and E. Turgut, *J. Magn. Magn. Mater.*, 2020, **502**, 166560-166567.
- 22 J. P. Phillips, S. Yazdani, W. Highland and R. Cheng, *Magnetochemistry*, 2022, **8**, 1–7.
- 23 J. A. Gerber, W. L. Burmester and D. J. Sellmyer, *Rev. Sci. Instrum.*, 1982, **53**, 691–693.
- 24 G. A. Mabbott, *J. Chem. Educ.*, 1983, **60**, 697–702.
- 25 P. T. Kissinger and W. R. Heineman, *J. Chem. Educ.*, 1983, **60**, 702–706.
- 26 N. Elgrishi, K. J. Rountree, B. D. McCarthy, E. S. Rountree, T. T. Eisenhart and J. L. Dempsey, *J. Chem. Educ.*, 2018, **95**, 197–206.
- 27 Y. Shao, M. F. El-Kady, J. Sun, Y. Li, Q. Zhang, M. Zhu, H. Wang, B. Dunn and R. B. Kaner, *Chem. Rev.*, 2018, **118**, 9233–9280.
- 28 R. Bhosale, S. Bhosale, P. Kumbhar, D. Narale, R. Ghaware, C. Jambhale and S. Kolekar, *New J. Chem.*, 2023, **47**, 6749–6758.
- 29 Q. Wu, T. He, Y. Zhang, J. Zhang, Z. Wang, Y. Liu, L. Zhao, Y. Wu and F. Ran, *J. Mater. Chem. A*, 2021, **9**, 24094–24147.
- 30 N. O. Laschuk, E. B. Easton and O. V Zenkina, *RSC Adv.*, 2021, **11**, 27925–27936.
- 31 X. Lu, M. Yu, G. Wang, Y. Tong and Y. Li, *Energy Environ. Sci.*, 2014, **7**, 2160–2181.
- 32 A. Barua and A. Paul, *Energy Fuels*, 2021, **35**, 10262–10273.

CHAPTER THREE

Design and Development of Porous Nanorods-Based Nickel-Metal Organic Framework (Ni-MOF) for High-Performance Supercapacitor Application

3.1 Outline

Metal-organic frameworks have received increasing attention as promising electrode materials in supercapacitors. In this study, we synthesized a nickel-metal-organic framework (Ni-MOF) by a simple and low-cost reflux condensation technique using non-hazardous trimesic acid as an organic ligand. The structures and morphologies of the Ni-MOF material were characterized by X-ray diffraction, Fourier-transform infrared spectroscopy, and scanning electron microscopy techniques. The prepared Ni-MOF was found to have a rod-like morphology and these morphologies can provide beneficial paths for electrolyte ion penetration, obtaining an enlarged contact area between the active material and electrolyte. The Ni-MOF had a considerable specific surface area of $398.4 \text{ m}^2 \text{ g}^{-1}$. Further, its highly porous structure offered excellent supercapacitor performance. The charge-storage mechanism of the electrodes was investigated by cyclic voltammetry, charge-discharge cycling, and electrochemical impedance spectroscopy using 2 M KOH as an electrolyte in a three-electrode assembly. The specific capacitance of the Ni-MOF was found to be 1956.3 F g^{-1} at a current density of 5 mA cm^{-2} by GCD studies and it retained 81.13% of its initial capacitance even after 3000 GCD cycles at a 35 mA cm^{-2} current density. An as-fabricated Ni-MOF//activated carbon hybrid supercapacitor (HSC) exhibited a specific energy of 98.15 Wh kg^{-1} at a specific power of $1253.47 \text{ W kg}^{-1}$ and excellent capacity retention of 99.29% over 3000 cycles. The results of this study imply a great potential of the Ni-MOF for application in efficient and sustainable energy-storage devices.

3.2 Introduction

In the 21st century, the production of energy from different sources has tremendously increased, and its transformation is also increasing day by day in different ways with the ever-increasing demands from industry, buildings, utilities, and transportation.¹ The increasing demand for energy and fuel due to the ever-increasing world population has become one of the important worries for all the global prime economies. Today there is an urgent need for environmentally friendly renewable energy resources to solve the problems related to the dwindling reserves of fossil fuels.^{2,3} In this regard, energy-conversion and -storage technologies have acquired significant attention to support the future use of renewable energy sources. Many researchers from around the globe are devoted to developing sustainable energy sources, like wind, solar, hydropower, and tidal energy, to address the shortage of fossil fuels and to reduce carbon emissions and global warming. Hence, from various points of view, electrochemical energy-storage devices (EESDs), like rechargeable batteries, supercapacitors, fuel cells, and hybrid devices, have an important part to play in strategies to produce various amounts of energy and power density to meet the demands from different application scenarios.⁴⁻⁶

Supercapacitors (SCs), also known as electrochemical capacitors, offer the advantages of batteries as well as conventional capacitors, and have consequently become extraordinary energy-storage devices for large power output applications. Supercapacitors.^{7,8} SCs generally offer a fast charging-discharging process (1–10 s), large power density (500–10 000 W kg⁻¹), high cyclic stability (4500 000 h), and easy operation. However, current SCs have a low energy density (1–10 W h kg⁻¹), which remains a prime challenge in the development of SC technologies. To conquer the drawback of their low energy density, there is a need for the development of high-performance electrode materials for SCs.^{9,10} Due to their profitable features, such as high power density, excellent cyclic stability, exceptional rate capability, and eco-friendliness, SCs have become key components in many fields, such as aerospace, electronic communications, and electric transport, and thus have attracted increasing attention, but still, there is a need for further advancements in SCs to meet the excessive energy demand of modern society.¹¹ A supercapacitor is like a battery, which means it stores and releases electricity, but instead of storing energy in the form of chemicals, supercapacitors store electricity in a static state, making them

better at rapidly charging and discharging energy. Supercapacitors can be mainly divided into two types based on the charge-storage mechanism. The first type is electric double-layer supercapacitors (EDLCs). In EDLCs, the capacitance is obtained from the electrostatic charge assembled at the electrode/electrolyte interface; hence, it is completely dependent on the surface area of the electrode materials that is available to electrolyte ions. The other type is pseudocapacitors, in which the capacitance comes from the reversible redox reactions between the electrolyte and electroactive species on the surface of the electrodes under the applied potential.¹²⁻¹⁴ The electrochemical performance of a supercapacitor device depends on numerous parameters, like choosing its constituents, the synthesis route used for the electrode materials, the potential window of the electrodes, the choice of electrolytes, and the type of current collectors, binders, and separators.^{15,16}

Metal-organic frameworks (MOFs) are attractive materials to fulfil the requirement for next-generation energy-storage technologies because of their extraordinary properties, such as high porosity, many accessible active sites, high surface area, extraordinary stability, vast structural and chemical tunability, tailorable pore size, and pre-and post-synthesis structural modifiability. Also, MOFs are a unique type of nanoporous materials formed by coordinated metal nodes and organic linkers. MOF-based materials have been utilized in many applications, including energy storage and conversion, catalysis, gas separation, drug delivery, hydrogen storage, gas adsorption, and purification.¹⁷⁻²⁰ Concurrently, due to the strong coordination capability of transition metals (TMs), TMs are often used as the metal centres of MOFs, and they also offer the advantages of possessing variable valences and good electrochemical properties, which means they can work as pseudocapacitive redox centres.²¹ MOFs can be feasibly included in a supercapacitor by two strategies: by directly utilizing the MOF as an electrode material for supercapacitors or by utilizing MOF-derived materials, like nanoporous carbon, oxides, sulfides, ferrites, which can be evolved and then utilized as electrode materials, such as the Ni, Co, Zn, Cu, and Fe-based MOFs, which have been reported previously to possess good supercapacitive performance.²²⁻³¹ However, the current, MOFs show poor electrical conductivity; therefore, scientists have taken efforts to increase the electrical conductivity through different strategies, such as through developing composite MOFs with different conductive materials, like metal oxides,³² metals,³³ conductive polymers,³⁴ carbon nanotubes,³⁵ graphene.³⁶ Wang et al. proposed a surfactant-free

and solvent-assisted solvothermal method to synthesize microflower Ni-MOF, which exhibited a high specific capacitance of 1093 F g^{-1} at 1 A g^{-1} with good rate capability, which were attributed to the fast ion transport and low electrical resistance emerging from its microflower-like structure and the specific capacitance resulting from the incorporation of nickel hydroxide species.³⁷ Wu et al. investigated nanosheet-stacked flower-like Ni-MOF via a solvothermal method using anionic surfactants. The usage of the static sealing effect among the negatively charged anionic surfactant head groups and metal ions suppressed the growth of crystals on the crystal surface. Their study revealed that the electrochemical performance of Ni-MOF with the surfactant was superior to that of Ni-MOF without the surfactant, whereby it possessed a specific capacitance of 1030 F g^{-1} at a current density of 1 A g^{-1} with a capacitance retention of 50% after even 3000 cycles. Further, they assembled an asymmetric supercapacitor by using Ni-MOF as a positive electrode and activated carbon as a negative electrode.³⁸ Gao et al. reported the cuboid Ni-MOF by a simple one-step hydrothermal method, which showed a loosely stacked layer-cuboid structure with plentiful mesopores, which were useful for the charge transfer and ion transport for supercapacitors. It also exhibited an exceptional specific capacitance of 804 F g^{-1} at a current density of 1 A g^{-1} , with a retention of 302 F g^{-1} after 5000 cycles. Additionally, they fabricated an asymmetric supercapacitor using Ni-MOF and activated carbon as the positive and negative electrodes, respectively.³⁹ Zhang et al. prepared Ni-MOF using a mixed-ligand approach, using trimesic acid as a modulator to partially replace the terephthalic acid. Replacing the terephthalic acid with trimesic acid influenced the formation of an albizia flower-like spheres@nanosheets structure, which helped the adsorption of OH^- ions on the surface. Also, the electrochemical performance was increased due to the synergistic effect of the surface property and its unique structure. It exhibited an excellent specific capacitance of 920 F g^{-1} at a current density of 1 A g^{-1} . In addition, they constructed an asymmetric supercapacitor with the help of Ni-MOF as a positive electrode and activated carbon as a negative electrode, which showed a high energy density of 42.4 W h kg^{-1} at a power density of 0.8 kW kg^{-1} .⁴⁰

In the present work, we used an unprecedented simple and scalable method, i.e. a reflux condensation method, to prepare a nanorod-like nickel-based metal-organic framework (Ni-MOF), in a controlled high temperature. The as-synthesized Ni-MOF revealed a one-dimensional (1D) nanorod-like morphology with a high

specific surface area $398.4 \text{ m}^2 \text{ g}^{-1}$ and highly nanoporous structure, which could produce more electrochemical sites, which increased the consumption of the electroactive material. In addition, for the fabrication of the electrode we used a stainless steel mesh substrate, which has not been reported to date, which is easily available and low cost compared to other reported substrates. Because of the abundant active sites and extremely porous nature of the material, the penetration of electrolyte ions into the material was increased, resulting in an enhancement of the specific capacitance of the material. Also, we constructed a handmade asymmetric supercapacitor device, which could get a red LED to glow for almost 105 s after charging for only 15 s.

3.3 Experimental section

3.3.1 Reagents

Nickel nitrate hexahydrate, N, N-dimethylformamide (DMF), and potassium hydroxide (KOH) were purchased from Loba Chemie (India). Benzene-1, 3, 5-tricarboxylic acid (H3BTC), carbon black, polyvinylidene difluoride (PVDF), N-methyl-2-pyrrolidone (NMP) were purchased from Sigma Aldrich (USA). All the reagents were of analytical grade and used as received without any further purification.

3.3.2 Preparation of nickel-based metal-organic framework (Ni-MOF)

Ni-MOF was synthesized by the method reported elsewhere⁴¹ with slight modification. The reflux method was used for the synthesis of Ni-MOF, which also helped to lower the reaction time of Ni-MOF compared to that reported in the literature. First, 0.15 M of H3BTC was dissolved in 10 mL of DMF with continuous stirring at room temperature; this mixture was denoted as H3BTC solution. Then, the H3BTC solution was transferred to a 50 mL round-bottom flask and heated up to 100°C using an oil bath with constant stirring. Thereafter, 0.3 M aqueous nickel nitrate (20 mL) solution was added drop by drop into the H3BTC solution. The reaction mixture was stirred for 24 h at 100°C. After cooling, the resulting precipitate was washed with alcohol several times and finally, a pale-green coloured precipitate was obtained and then dried at 80°C for 12 h. Figure 3.1 shows a schematic of the preparation of the Ni-MOF.

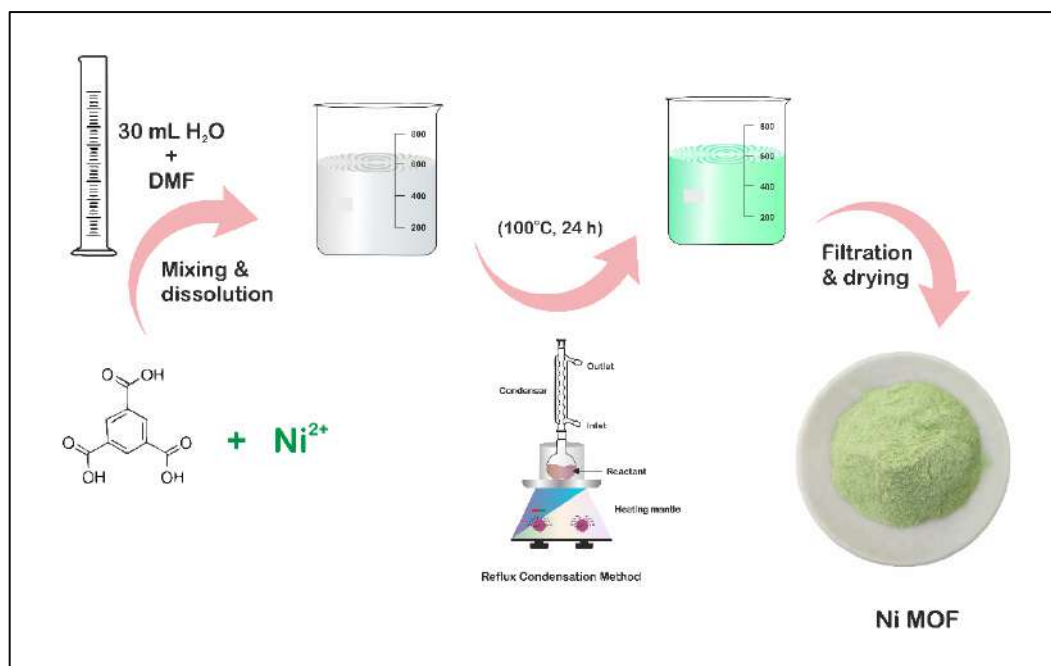


Figure 3.1: Schematic of synthesis of Ni-MOF nanorods via a wet chemical route

3.3.3 Characterization techniques details

The phase and crystallinity of the Ni-MOF sample was investigated by using an X-ray diffractometer (XRD) (Bruker D8 Phaser X-ray diffractometer with Cu K α radiation ($\lambda = 1.541 \text{ \AA}$)). The functional groups and types of bonding were confirmed by Fourier transform infrared (FT-IR) spectroscopy (Bruker Alpha-100508 spectrometer) and the microstructure and surface topography of the Ni-MOF sample was studied by using scanning electron microscopy (JEOL-JSM 6360, Japan). The Raman spectrometer (LabRAM HR Evolution Confocal Raman Microscope, France) was used for point group analysis. The chemical composition and elemental valence states of as-prepared Ni-MOF was evaluated by X-ray photoelectron spectroscopy (JPS 9030, JEOL ASIA PTE LTD.). In addition, N₂ isotherms and pore size distribution data were collected from a surface area and pore volume analyzer (NOVA1000e Quantachrome, USA).

3.3.4 Evaluation of electrode materials and electrochemical studies

All the electrochemical experiments were performed on a CHI608 electrochemical analyzer using a conventional three-electrode system in 2 M KOH electrolyte at room temperature, with graphite employed as the counter electrode, saturated Ag/ AgCl as the reference electrode, and Ni-MOF loaded stainless steel mesh as the working electrode. The working electrode was prepared by making a slurry of 80 wt% Ni-MOF (active material), 10 wt% polyvinylidene fluoride (PVDF),

and 10 wt% carbon black (Super P) in NMP solvent. This slurry was coated on the stainless steel mesh (1 cm × 1 cm), followed by vacuum drying at 80°C for 12 h.

The electrochemical tests included cyclic voltammetry (CV), galvanostatic charging–discharging (GCD) profiles, and electrochemical impedance spectroscopy (EIS) measurements. A solid-state hybrid supercapacitor (Ni-MOF//AC) was fabricated using Ni-MOF as the positive electrode and activated carbon as the negative electrode. As a separator, cellulose filter paper was used as a sandwich between two electrodes, with the separator and PVA-KOH gel loaded between the two electrodes and assembled on opposite sides. The device was kept at room temperature overnight for natural drying. The PVA-KOH gel electrolyte was prepared according to a literature report.⁴² In a typical procedure, 1 g of polyvinyl alcohol (PVA) was dissolved in 20 mL distilled water keeping the temperature of the bath solution at 80°C for 30 min. The aqueous KOH solution was then added dropwise to the PVA solution and heated at 80°C for 30 min to give a viscous gel electrolyte.

The specific capacitance was calculated according to the equation (3.1),

$$C = \frac{I \Delta t}{m \Delta V} \dots\dots\dots (3.1)$$

where, C is the specific capacity (F g⁻¹), I is the current density (A), Δt is the discharging time (s), m is the mass (g) of the active electrode materials and ΔV is the potential window of the discharge process(V).

Using equations (3.2) and (3.3), the specific energy and specific power of the hybrid supercapacitor were calculated, respectively.⁴³

$$E = \frac{0.5 \times C \times \Delta V^2}{3.6} \dots\dots\dots (3.2)$$

$$P = \frac{E \times 3600}{\Delta t} \dots\dots\dots (3.3)$$

Where E and P are the specific energy (Wh kg⁻¹) and specific power (W kg⁻¹), respectively. ΔV is the discharging voltage (V) and Δt is the discharging time in seconds.

3.4 Results and discussion

3.4.1 X-ray diffraction of Ni-MOF

The phase purity and crystallinity of the Ni-MOF sample were investigated by the XRD technique. The obtained XRD pattern of prepared Ni-MOF together with the data of JCPDS card no. 00-028-1734 are shown in figure 3.2. The prepared Ni-MOF data were in close agreement with the given JCPDS card,⁴⁴⁻⁴⁶ revealing that the Ni-

MOF had a polycrystalline nature. Some of the major peaks obtained were in good agreement with the corresponding angles as reported earlier for Ni-MOF. Furthermore, using Debye–Scherrer’s formula [equation (3.4)], the crystallite size was calculated for the major characteristic peak of Ni-MOF,

$$D = \frac{0.9\lambda}{\beta \cos\theta} \dots\dots\dots (3.4)$$

Where D is the average crystallite size, λ is the wavelength of the X-rays, β is the full-width half maxima and θ is Bragg’s diffraction angle. The average crystallite size derived from the (110) plane is 6.89 nm.

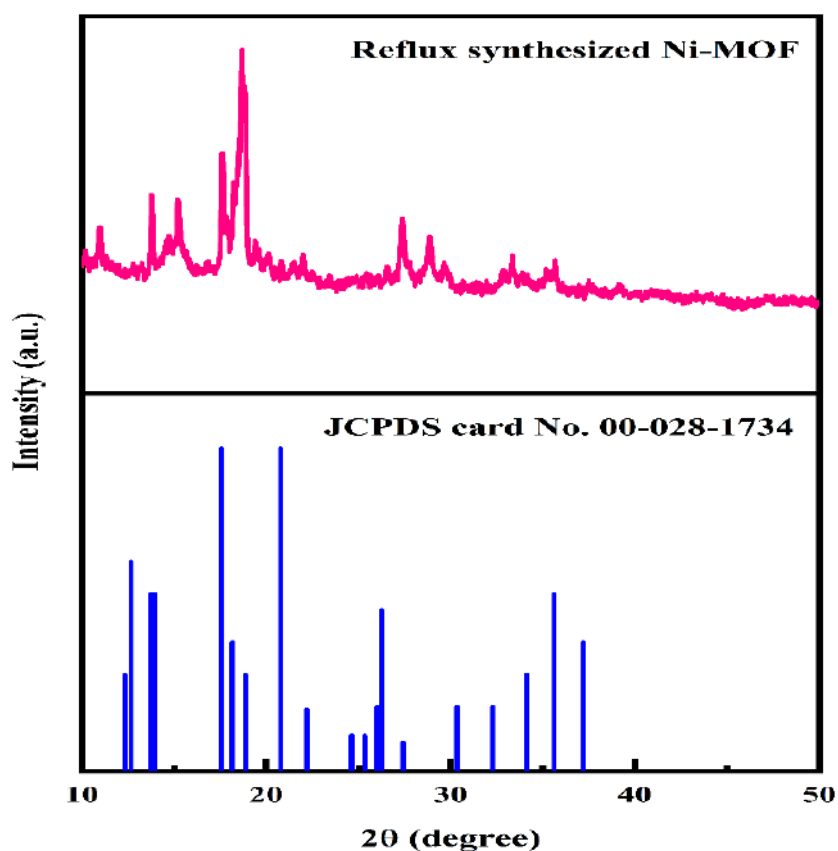


Figure 3.2: XRD pattern of Ni-MOF

3.4.2 FT-IR spectroscopy of Ni-MOF

Investigation of the chemical structure and functional groups of Ni-MOF was carried out by FT-IR. The FT-IR spectrum of the Ni-MOF sample is shown in figure 3.3. In the spectrum, the strong absorption peak at 1349 cm^{-1} was assigned to the C–H stretching vibrations, while the peaks at 3081 and 3399 cm^{-1} could be indexed to the O–H stretching vibrations of water molecules, showing that water molecules existed within the Ni-MOF structure. Additionally, the peaks observed at 1506 and 1608 cm^{-1} were attributed to the symmetric and asymmetric vibrations of carboxyl groups (–

COO⁻), related to the BTC linkers.^{47,48} Another intense peak was observed at 715 cm⁻¹, confirming the presence of the Ni-O bond.

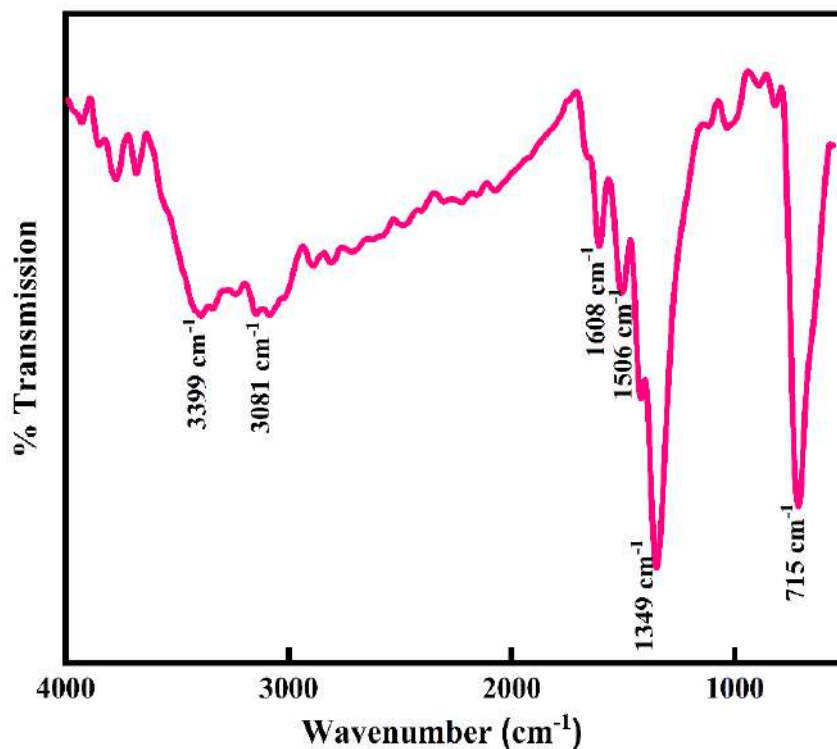


Figure 3.3: FT-IR pattern of Ni-MOF

3.4.3 Raman spectroscopy of Ni-MOF

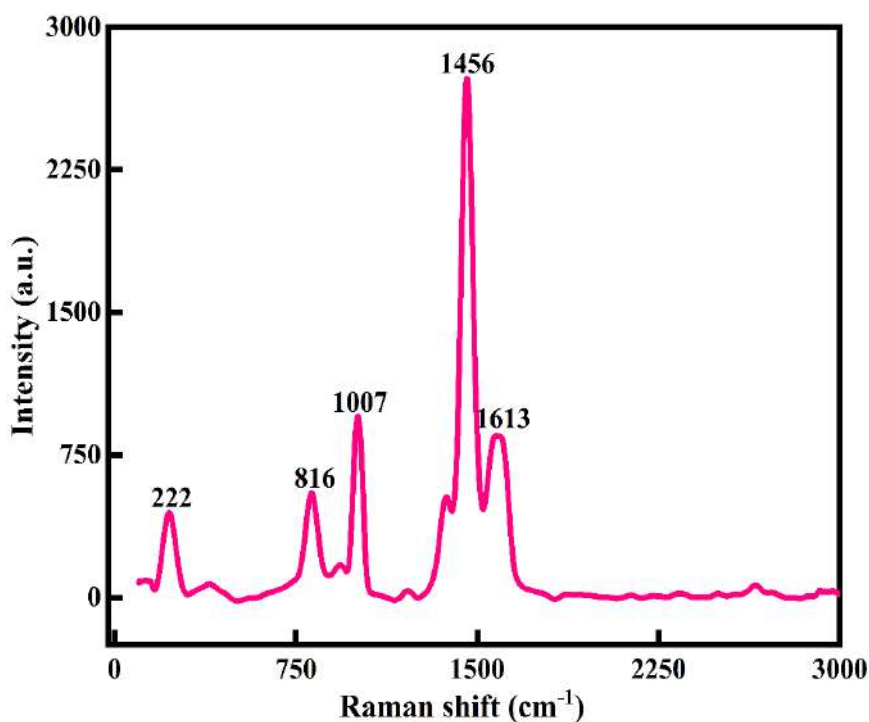


Figure 3.4: Raman Spectroscopy of Ni-MOF

Raman spectroscopy was used to confirm the crystallography of the prepared Ni-MOF samples. Also, the inelastic scattering of the Ni-MOF samples was confirmed by Raman spectroscopy. The Raman spectrum of the Ni-MOF and the specified peaks of the prepared sample are shown in figure 3.4. The peaks of Ni-MOF at 816 and 1007 cm^{-1} could be associated to the plane deformation of the C-H in the aromatic ring and C-O stretching of the trimesic ligand, respectively. Also, D and G bands were observed at 1456 and 1613 cm^{-1} due to the in-plane vibration mode of the benzene ring.⁴⁹ The peak at 222 cm^{-1} could be attributed to H-O-H. All these peaks revealed the crystallography and structure of the Ni-MOF sample.

3.4.4 Scanning electron microscopy of Ni-MOF

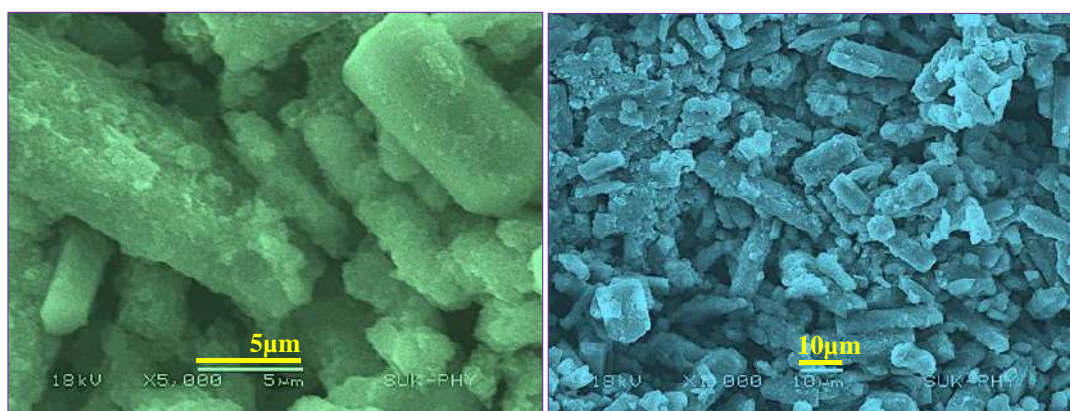


Figure 3.5: SEM images of Ni-MOF

The surface morphology of the Ni-MOF was investigated by SEM, and the SEM images of Ni-MOF with different magnifications are shown in figure 3.5. The SEM images showed a nanorod-like morphology and porous nature of the Ni-MOF, which was responsible for the increased surface area of the Ni-MOF and also for the increase in the specific capacitance. The average length of the nanorods was about 19.09 nm. The different lengths and diameters of the nanorods indicated an increase in the aspect ratio of the nanorods. Also, the porous nanorods were interconnected to each other, which provides more active sites for the transportation of the charging kinetics and decreases the diffusion length of the electrolyte, which is helpful for improvement of the energy storage and high rate capability. Again, a birds-eye view of the SEM images showed that the small and large sized nanorods overlapped with each other and between these two nanorods there were some voids, which in turn would support the enhanced adsorption of electrolyte ions, which would help to increase the specific capacitance of the Ni-MOF. The porous and 1D morphology was

favourable for ion diffusion and hence contributed to an increase in the specific capacitance of the Ni-MOF.

3.4.5 Brunauer-Emmett-Teller analysis of Ni-MOF

The surface area and porosity of the Ni-MOF were obtained by using the BET technique and measuring nitrogen adsorption-desorption isotherm of the samples at 77 K. Here, the prepared sample was degassed at 150°C under a nitrogen atmosphere for 4 h before the measurements. The surface area and pore-size distribution of the sample were calculated by the Brunauer-Emmett-Teller (BET) equation and NLDFT method. The BET measurement results are presented in figure 3.6(a). The calculated surface area of the Ni-MOF sample was found to be 398.4 m² g⁻¹. Based on the literature, it has been observed that the larger the pore radius, then the higher porosity a sample will show in nature. Also, the pore-size distribution for Ni-MOF was estimated using the NLDFT method to establish the correct distribution of pores in the material, as shown in figure 3.6 (b).^{50,51} The half pore width measured by DFT was 1.585 nm, with a micropore volume of 0.831 cc g⁻¹, confirming the extremely mesoporous nature and hierarchical pore-size distribution. According to the literature, Ni-MOF shows a type II isotherm with plenty of mesopores in the material.⁵² This massive amount of mesopores in the structure boosts the permeation of electrolyte ions into the electrode, hence increasing the specific capacitance of the material. Such a high specific surface area and mesoporous structure could produce more electrochemical reaction sites, which increases the consumption of the electroactive material.

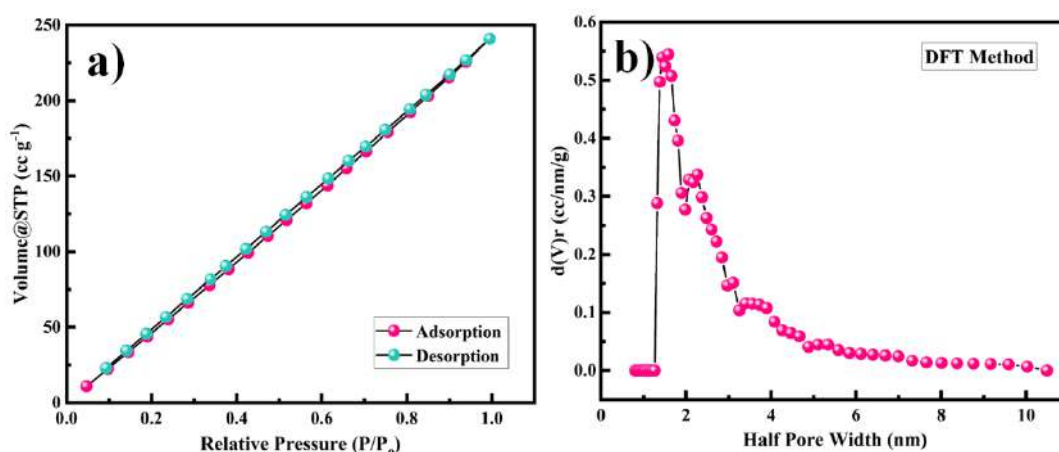


Figure 3.6: (a) N₂ adsorption–desorption isotherms, (b) Pore size distribution of Ni-MOF

3.4.6 X-ray photoelectron spectroscopy of Ni-MOF

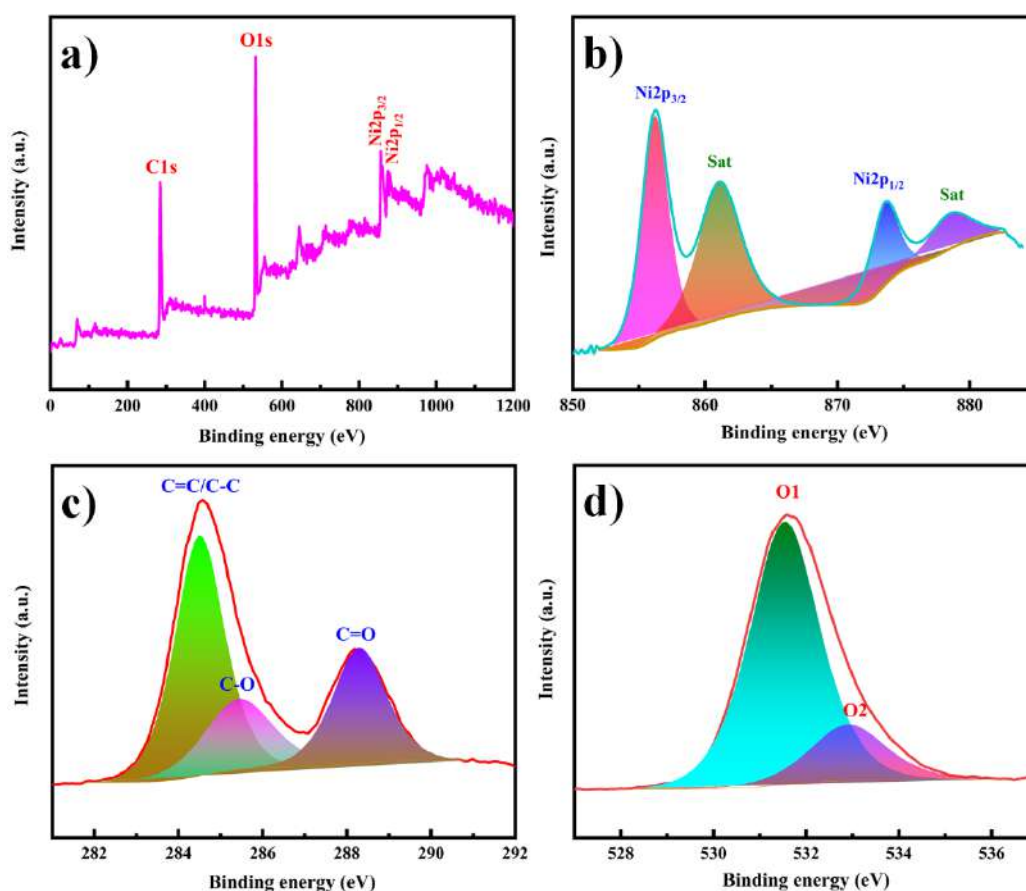


Figure 3.7: (a) XPS survey spectrum of Ni-MOF. High-resolution XPS spectra of Ni 2p, (b) C 1s, (c) and O 1s (d) regions

XPS was used to examine the surface elemental composition and valence states of Ni-MOF. The presence of Ni, C, and O elements was confirmed by the survey spectrum in figure 3.7 (a). Ni 2p_{1/2} and 2p_{3/2} displayed two significant peaks at 873.6 and 856.2 eV, respectively, with two satellite peaks at 878.7 and 861.0 eV, implying the presence of Ni in a divalent state [Figure 3.7(b)]. The peak at 284.5 eV in the C 1s area [Figure 3.7(c)] is a typical outcome for specimens charging using C 1s as the reference. The peak at 288.2 eV was associated with the O=C–OH, whereas the peak at 285.4 eV was associated with the aryl carbon from the benzene ring. The spectrum of O 1s (Figure 3.7(d)) could be separated into two peaks. Carbonyl displayed a peak at 531.5 eV, and the –OH group from the adsorbed H₂O molecules had a peak at 532.8 eV.^{53,54}

3.4.7 Electrochemical measurements of Ni-MOF electrode

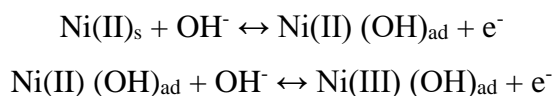
The electrochemical performance of the as-prepared Ni-MOF electrode was evaluated by using the three-electrode system in 2 M KOH electrolyte and the results are presented in figure 3.8. As shown in figure 3.8(a), cyclic voltammetry (CV) was carried out in the potential range from 0 to 0.3 V at scan rates from 10 to 100 mV s⁻¹. It could be observed that the area under the CV curve of the Ni-MOF electrode was higher and the redox current density also increased, leading to a greater capacitive behaviour compared to the literature (Table 3.1).

Table 3.1: Comparison of the specific capacitances of Ni-MOF

Electrode material	Substrate used	Electrolyte	Current density	Specific capacitance	Ref.
Ni-MOF	Nickel foam	3 M KOH	5 A g ⁻¹	1224.6 F g ⁻¹	58
Ni-MOF	Nickel foam	3 M KOH	5 A g ⁻¹	612.25 F g ⁻¹	59
Ni-MOF	Nickel foam	6 M KOH	5 A g ⁻¹	430 C g ⁻¹	60
Ni-MOF	Nickel foam	3 M KOH	5 A g ⁻¹	95 F g ⁻¹	61
Ni-MOF	Platinum plate	2 M KOH	5 mA cm ⁻²	47 F g ⁻¹	62
Ni-MOF	Stainless steel mesh	2 M KOH	5 mA cm⁻²	1956.3 F g⁻¹	This work

All the CV curves revealed well-defined redox pairs, which specified the change in the oxidation states of the Ni²⁺/Ni³⁺, redox reactions, and intercalation–deintercalation of the K⁺ ion in the porous structure during the electrochemical reactions, due to the pseudocapacitive behaviour of the prepared Ni-MOF.^{55,56} This could be due to a shift in the valence states of nickel ions, specifying that the pseudocapacitance was mostly driven by surface oxidation generated by the reduction reaction. Additionally, the diffusion of OH⁻ ions also contributed to the redox reaction, and the diffusion might be because of the impurity ions in the aqueous electrolyte. The redox peaks of Ni-MOF in aqueous electrolytes were caused by the

reversible redox between $\text{Ni}^{2+}/\text{Ni}^{3+}$, and the reaction can be explained by the possible charge-discharge mechanism of Ni-MOF as follows,



With increasing the scanning speed, the curve area and peak current rose, demonstrating a good capacitive behaviour and charge-storage capabilities. The equivalent and similar CV curves obtained at different scan rates showed a shift in the redox peaks and specified the pseudocapacitive behaviour of the material, as shown in figure 3.8(a). The area under the CV curve increased with the increase in the scan rate, whereas the specific capacitance decreased as the scan rate increased. This is due to the fact that at slower scan rates, electrolyte ions are completely diffused within the electrode material. As a result, the complete active surface of the electrode material can be used to store charge. At higher scan rates, however, diffusion restricts the movement of electrolyte ions, and only the outer active surface is employed for charge storage.⁵⁷ The outstanding performance of the Ni-MOF electrode could be assigned to the good crystallinity and porous nanorod-like structure, which could successfully boost the intercalation/deintercalation of OH^- ions within the Ni-MOF electrode. One of the important tools for assessing the electrochemical properties of an electrode is the charge-discharge measurement. Figure 3.8(b) presents the charge-discharge curves of the Ni-MOF electrode in aqueous 2 M KOH electrolyte. The charging and discharging times were directly in tune with the charge-storage capacity of the active material. The impact of different current densities (5-35 mA cm^{-2}) on the charge-discharge curve was also studied. The natures of the curves were identical to each other, which supported the pseudocapacitive properties of the Ni-MOF nanorods. The specific capacitance of the Ni-MOF was calculated using the discharging curve and equation (3.1). The maximum specific capacitance of 1956.3 F g^{-1} at the 5 mA cm^{-2} current density was obtained. This specific capacitance value is higher than those reported earlier (Table 3.1). Due to the plentiful active sites and highly porous nature, the penetration of electrolyte ions into the material increased, which supported the enhancement of the specific capacitance of the material.

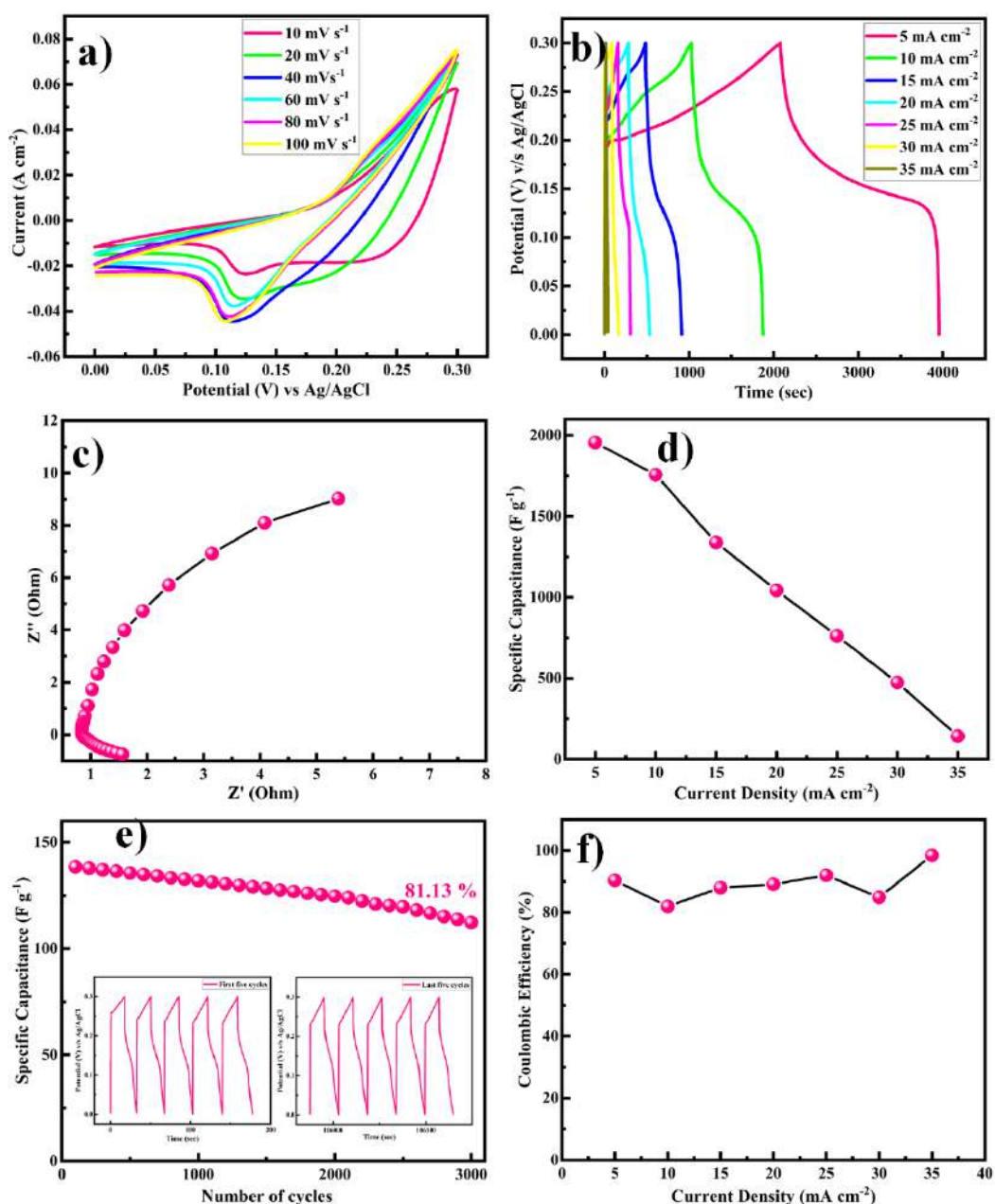


Figure 3.8: (a) CV profile of Ni-MOF at different scan rates operated from 0 to 0.3 V, (b) GCD profile for Ni-MOF at different current rates (5 to 35 mA cm⁻²), (c) Nyquist plot of the Ni-MOF, (d) Plot of specific capacitance vs. current densities, (e) Cyclic durability test at a high current of 35 mA cm⁻² over 3000 GCD cycles with inset of first and last five cycles, (f) Coulombic efficiency as a function of current density

One of the important factors for supercapacitor electrodes is the electrical resistance, which can be determined from electrochemical impedance spectroscopy (EIS) measurements. EIS tests were thus carried out to investigate the electroconductibility and reaction kinetics of the Ni-MOF electrode, as shown in

figure 3.8(c). The electrode's charge-transfer resistance (R_{ct}) could be obtained from the diameter of a semicircle in the high-frequency area. It was demonstrated that the Ni-MOF had a small diameter and thus a smaller charge-transfer resistance, while the slope of the lines in the low-frequency area represents the ion-diffusion resistance. The Nyquist plot had a high slope, which showed that the as-prepared Ni-MOF was beneficial to ion transport and electrolyte diffusion because of its typical structure, which meant it possessed a high specific surface area and could support rich ion transportation. The straight line in the low-frequency region was due to Warburg resistance. Based on the preceding results, it can be concluded that the Ni-MOF had a higher conductivity. Hence, the smaller charge-transfer resistance (0.5Ω) confirmed that the prepared Ni-MOF porous nanorods had highly pseudocapacitive properties. The specific capacitance decreased from 1756.3, 1338.4, 1043.8, 761.5, 473.8, and 142.2 F g^{-1} with the increase in the current density to 10, 15, 20, 25, 30, and 35 mA cm^{-2} , respectively, as shown in figure 3.8(d). The specific capacitance decreased as the current density increased because at higher current density the electrolyte ions participate in the bulk surface for the electrochemical reaction, and due to this there is a restriction in the ion transport, so the value of the specific capacitance decreases, and considering the low current density, the electrolyte ions have enough time to move across the inner pores of the electrode material, resulting in a higher specific capacitance value. The Ni-MOF showed a longer discharging time, which clearly indicated that the porous nanorods structure of the Ni-MOF possessed more surface active sites for the efficient charge-discharge process and increased the energy-storage ability of the Ni-MOF electrode. The cyclic stability of the electrode was explored by galvanostatic charge-discharge (GCD) persistence tests at 35 mA cm^{-2} current density for 3000 cycles, as shown in figure 3.8(e). It could be seen that the specific capacitance was retained at over 81.13% after 3000 cycles for the Ni-MOF electrode, which suggested its good electrochemical reversibility during the charge-discharge process.

The Coulombic efficiency ($\eta\%$), another important parameter to examine the interfacial stability of Ni-MOF electrode as a function of charge-discharge cycles, is shown in figure 3.8(f). Equation (3.5) was used to calculate the Coulombic efficiency for the Ni-MOF electrode at different current densities.⁶³

$$\eta (\%) = \frac{t_d}{t_c} \times 100 \dots \dots \dots (3.5)$$

where t_d and t_c are the discharging and charging times in seconds, respectively.

The Coulombic efficiencies of the Ni-MOF electrode were 90.37%, 81.92%, 87.98%, 89.11%, 92.00%, 84.88%, and 98.45% at different current densities of 5, 10, 15, 20, 25, 30, and 35 mA cm⁻², respectively. The Coulombic efficiency of the Ni-MOF electrode rose and the specific capacitance decreased with the increase in current density, which might be assigned to the electrodes inner active sites, which were not capable of supporting the redox reactions at high current density. A promising electrochemical stability and excellent reversibility of Ni-MOF electrodes were observed for up to the 3000 GCD cycles. The Ni-MOF samples showed that the orchestrating effects of the 1D morphology, surface area, and porosity led to their excellent application potential in terms of specific capacitance, energy density, power density, and cyclic stability.

3.4.8 Electrochemical measurements of hybrid supercapacitor device

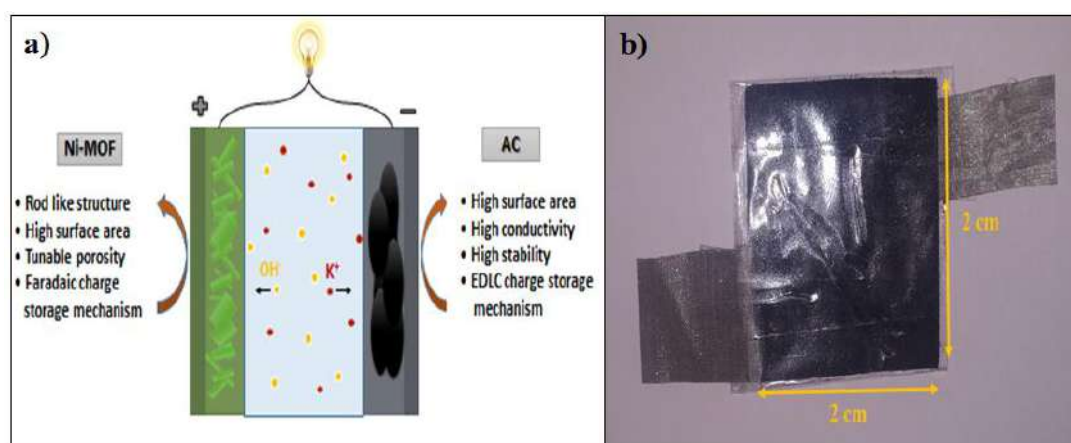


Figure 3.9: (a) Schematic illustration of hybrid supercapacitor with Ni-MOF as a positive electrode and activated carbon as a negative electrode in KOH aqueous electrolyte, (b) Digital photograph of Ni-MOF//AC HSC device

To understand the practical ability of the Ni-MOF electrode in functional devices, a hybrid supercapacitor device was assembled using the as-prepared Ni-MOF as a positive electrode and activated carbon as the negative electrode, as shown in figure 3.9. Both electrodes were prepared by the slurry coating method. In short, the slurry was prepared by mixing the active material (Ni-MOF or AC) (80 mg), polyvinylidene fluoride (10 mg), and carbon black (10 mg) in 0.5 mL of methyl-2-pyrrolidone (NMP) solvent. Then, the required volume of the slurry was dispersed onto a stainless steel mesh with an area of 2 cm × 2 cm and dried at 60°C overnight. Primarily, the side borders of the electrodes were formed as non-conducting through

insertion of a band to avoid electrical contact. The PVA-KOH gel was pasted on one side of the electrodes and created one side of the electrical contact. Later, both electrodes were patched together like a sandwich, with the gel-pasted sides facing each other. The fabricated device was kept under 1 ton pressure for 12 h, to acquire a good connection within the electrodes and gel electrolyte and also to remove the air gap. Afterwards, the device was used for assessment of the electrochemical performance. Hybrid supercapacitor devices have advantages, like high energy density, high specific capacitance, long cycle stability, and large potential window, over symmetric supercapacitors. The performance of the assembled hybrid device was studied using CV, GCD, and EIS measurements.

Primarily, CV tests were performed to understand the electrochemical performance of the Ni-MOF//AC hybrid supercapacitor (HSC) at different scan rates, as shown in figure 3.10(a). The Ni-MOF//AC hybrid SC exhibited a symmetric rectangular CV curve and a large area enclosed under the CV curve at up to 0-0.9 V. With the increase in scan rate from 10 to 100 mV s⁻¹, the increase in area under the CV curves revealed the excellent reversibility of the Ni-MOF. Additionally, GCD curves were obtained at different current densities from the hybrid device, indicating the ideal capacitive behaviour of the device, as shown in figure 3.10(b). The Nyquist plots of the Ni-MOF//AC HSC device are shown in figure 3.10(c), indicating that the fabricated device had an R_{ct} value of 0.36 Ω. According to the EIS studies, the fabricated Ni-MOF//AC HSC device had good electrical conductivity with a low ionic resistance. However, the specific capacitance decreased from 195.76, 94.79, 60.0, 42.70, and 31.67 F g⁻¹ with the increase in the current density from 2, 3, 4, 5, and 6 mA cm⁻², respectively, as shown in figure 3.10(d). The Ragone plot of the as-constructed HSC, expressing the relationship between the energy density (E) and power density (P), was obtained based on the galvanostatic charge-discharge curves [Figure 3.10(e)].

The cyclic stability of the assembled hybrid supercapacitor device was investigated systematically. The device showed 99.29% capacitance retention over 3000 cycles, indicating its excellent cyclic stability. The specific capacitance was constant over 2500 cycles and later it slightly decreased. The insets of figure 3.10(f) show the first and last five charge-discharge cycles of the device in 2 M KOH electrolyte. The Coulombic efficiencies of the asymmetric supercapacitor device were 84.15%, 65.00%, 68.57%, 74.54%, and 80.00% at various current densities of 2, 3, 4,

5, and 6 mA cm⁻², respectively [equation (3.5)]. The device's energy density and power density were calculated using equation (3.2) and (3.3). The HSC device exhibited a maximum energy density of 79.5 Wh kg⁻¹ at a higher power density of 1015.3 W kg⁻¹, which was comparable to or even higher than recent literature values (Table 3.1) for hybrid supercapacitors.

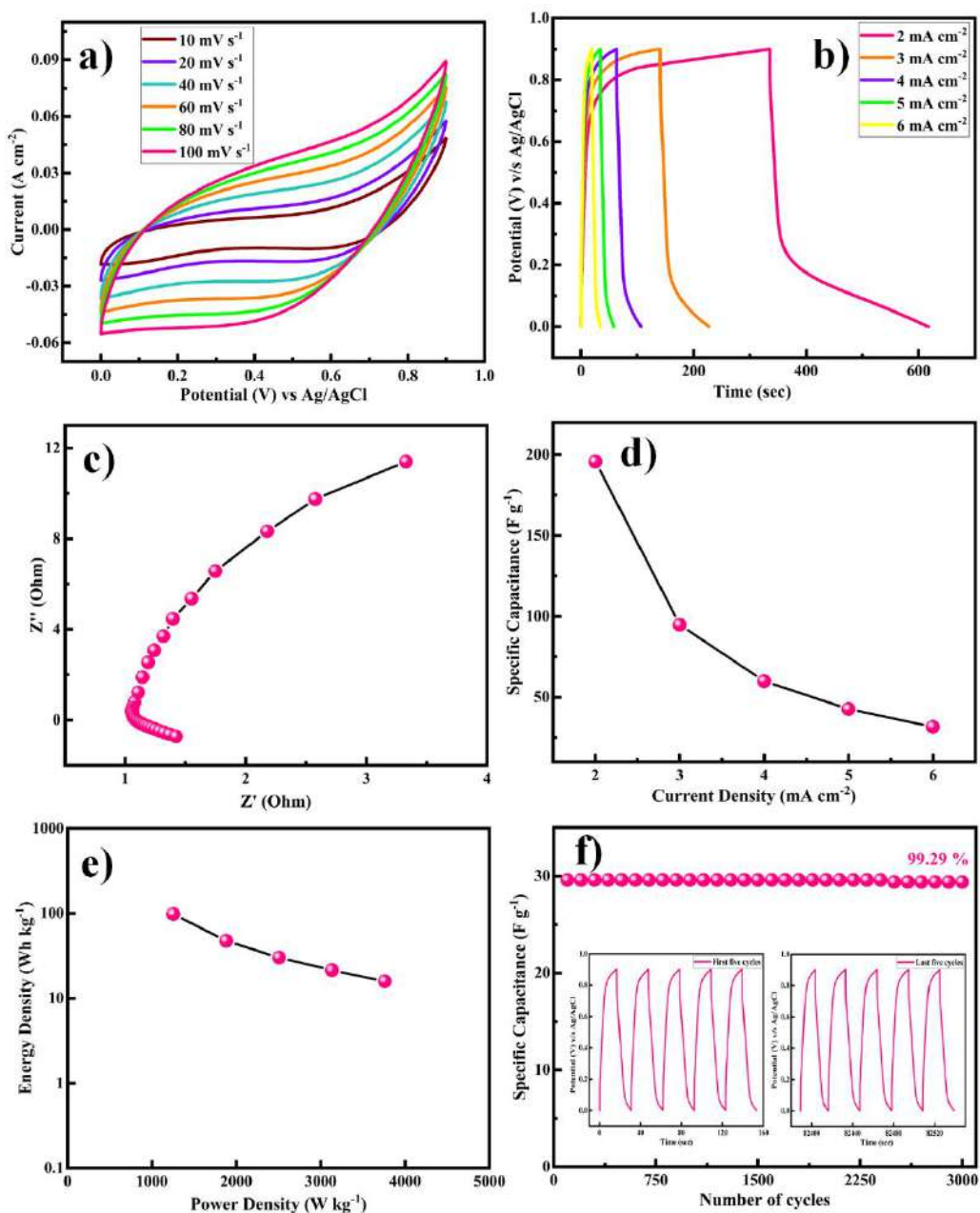


Figure 3.10: (a) CV profile of HSC cell at different scan rates operated from 0 to 0.9 V, (b) GCD profile for HSC cell at different current rates (2 to 6 mA cm⁻²), (c) Nyquist plot of the HSC device, (d) Plot of specific capacitance vs. current densities, (e) Ragone plot of HSC cell, (f) Cyclic durability test at a high current of 6 mA cm⁻² over 3000 GCD cycles with inset of first and last five cycles

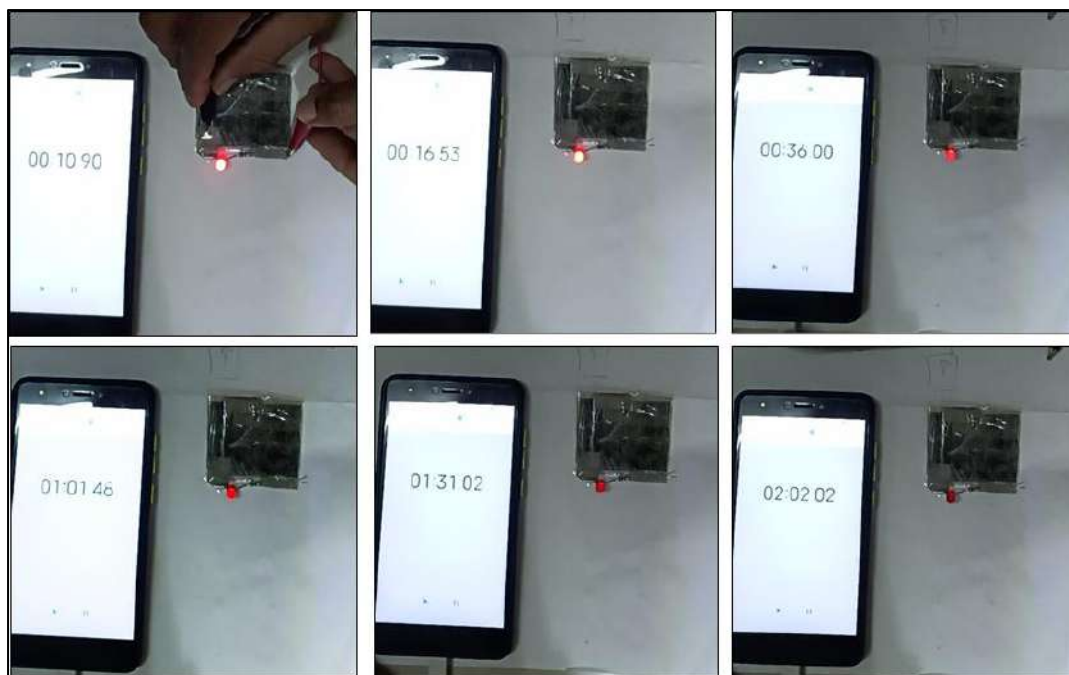


Figure 3.11: The handmade asymmetric supercapacitor device charged for 15 seconds and glow a red LED for almost 105 seconds (i.e. charging time 15 second discharging time 105 sec)

The fabricated device could light a red-light-emitting diode (LED) for over 105 s when charged for 15 s due to the device's high energy density and maximum operational potential of 0.9 V, as shown in figure 3.11. It can be seen that the dazzling light was obvious at first, and then the brightness change is shown over time. After 105 s, we can see that the red light was still faintly glowing, confirming that the Ni-MOF//AC HSC device had an amazing ability to store charge. The good performance could be attributed to Ni-MOF's rod-like structure and pore-size distribution. The study discovered that the encouraging results may pave the way for the development of new electrode materials for supercapacitors and other energy-storage devices.

The study of the electrochemical parameters at different current densities of the chemically synthesized Ni-MOF is concluded in the radar graph shown in figure 3.12. The different apexes reveal the various parameters, such as specific capacitance, energy density, power density, and Coulombic efficiency, of the Ni-MOF. As seen in figure 3.12, this report contains the script for the Ni-MOF-based supercapacitor. These results indicate that the Ni-MOF has much better electrochemical performance than that of other reported MOFs due to its high specific capacitance, high energy density, large power density, and good Coulombic efficiency.

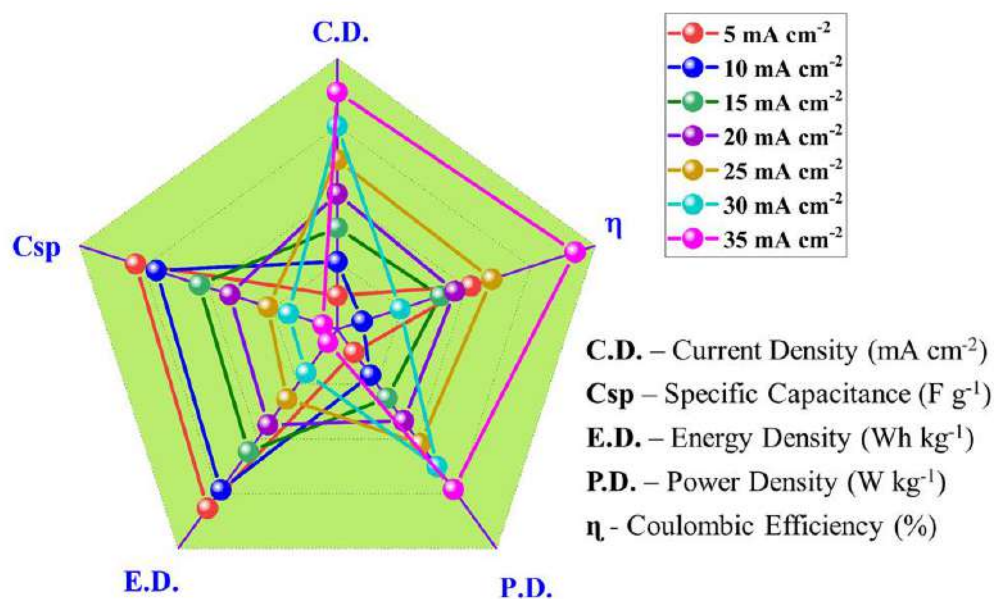


Figure 3.12: Radar plot for Ni-MOF based on supercapacitive properties

3.5 Conclusion

In summary, we successfully prepared Ni-MOF by using the reflux condensation technique. The structural properties and electrochemical performance of the Ni-MOF were studied systematically using various advanced tools. The porous and nanorod-like morphology, as confirmed by SEM analysis, provided both faster and more electroactive sites. An as-prepared Ni-MOF sample exhibited a high surface area of $398.4 \text{ m}^2 \text{ g}^{-1}$. Furthermore, In a three-electrode system with 2 M KOH aqueous electrolyte, the synthesized Ni-MOF porous nanorods showed a high specific capacitance of 1956.3 F g^{-1} at a current density of 5 mA cm^{-2} , and more stability for 3000 cycles with 81.13% retention. When assessed as a positive electrode for a flexible hybrid supercapacitor (HSC) device in combination with activated carbon as a negative electrode, the HSC cell exhibited a superhigh electrochemical behaviour. The device also exhibited a high charge-storage capacity of 195.76 F g^{-1} at a current density of 2 mA cm^{-2} , super-specific energy (98.15 Wh kg^{-1}), and excellent power density ($1253.47 \text{ W kg}^{-1}$), including long-term stability of 3000 cycles with 99.29% capacity retention. The extraordinary energy-storage properties of the Ni-MOF electrode are attributed to its nanorod-like structure and higher surface area. This study provides a new platform for supercapacitors and other energy-storage devices.

3.6 References

- 1 S. Koochi-Fayegh and M. A. Rosen, *J. Energy Storage*, 2020, **27**, 101047-101070.
- 2 M. B. Askari, P. Salarizadeh, M. Seifi, M. H. Ramezan zadeh and A. Di Bartolomeo, *J. Alloys Compd.*, 2021, **860**, 158497-158508.
- 3 X. Zhao, K. Tao and L. Han, *Nanoscale*, 2022, **14**, 2155–2166.
- 4 Y. Tang, W. Guo and R. Zou, *Coord. Chem. Rev.*, 2022, **451**, 214242-214268.
- 5 Poonam, K. Sharma, A. Arora and S. K. Tripathi, *J. Energy Storage*, 2019, **21**, 801–825.
- 6 S. Sanati, Z. Rezvani and B. Habibi, *New J. Chem.*, 2018, **42**, 18426–18436.
- 7 S. De, C. K. Maity, S. Sahoo and G. C. Nayak, *ACS Appl. Energy Mater.*, 2021, **4**, 3712–3723.
- 8 H. M. Nguyet, L. T. T. Tam, D. T. Tung, N. T. Yen, H. T. Dung, N. T. Dung, H. Phan N, L. A. Tuan, P. N. Minh and L. T. Lu, *New J. Chem.*, 2022, **46**, 13996–14003.
- 9 Y. Shao, M. F. El-Kady, J. Sun, Y. Li, Q. Zhang, M. Zhu, H. Wang, B. Dunn and R. B. Kaner, *Chem. Rev.*, 2018, **118**, 9233–9280.
- 10 R. Liu, A. Zhou, X. Zhang, J. Mu, H. Che, Y. Wang, T. T. Wang, Z. Zhang and Z. Kou, *Chem. Eng. J.*, 2021, **412**, 128611-128633.
- 11 A. Mohanty, D. P. Jaihindh, Y. P. Fu, S. P. Senanayak, L. S. Mende and A. Ramadoss, *J. Power Sources*, 2021, **488**, 229444-229467.
- 12 S. Kumar, G. Saeed, L. Zhu, K. N. Hui, N. H. Kim and J. H. Lee, *Chem. Eng. J.*, 2021, **403**, 126352-126370.
- 13 L. Li, J. Meng, M. Zhang, T. Liu and C. Zhang, *Chem. Commun.*, 2022, **58**, 185–207.
- 14 X. Chu, F. Meng, T. Deng and W. Zhang, *Nanoscale*, 2021, **13**, 5570–5593.
- 15 P. Forouzandeh, P. Ganguly, R. Dahiya and S. C. Pillai, *J. Power Sources*, 2022, **519**, 230744-230771.
- 16 C. V. V. Muralee Gopi, R. Vinodh, S. Sambasivam, I. M. Obaidat and H. J. Kim, *J. Energy Storage*, 2020, **27**, 101035-101060.
- 17 S. Sanati, R. Abazari, A. Morsali, A. M. Kirillov, P. C. Junk and J. Wang, *Inorg. Chem.*, 2019, **58**, 16100–16111.
- 18 A. E. Baumann, D. A. Burns, B. Liu and V. S. Thoi, *Commun. Chem.*, 2019, **2**,

- 1–14.
- 19 W. Li, X. Zhao, Q. Bi, Q. Ma, L. Han and K. Tao, *Dalt. Trans.*, 2021, **50**, 11701–11710.
- 20 H. M. Ma, J. W. Yi, S. Li, C. Jiang, J. H. Wei, Y. P. Wu, J. Zhao and D. S. Li, *Inorg. Chem.*, 2019, **58**, 9543–9547.
- 21 Y. Liang, W. Yao, J. Duan, M. Chu, S. Sun and X. Li, *J. Energy Storage*, 2021, **33**, 1–11.
- 22 L. Zheng, J. Song, X. Ye, Y. Wang, X. Shi and H. Zheng, *Nanoscale*, 2020, **12**, 13811–13821.
- 23 S. Zhou, S. Wang, S. Zhou, H. Xu, J. Zhao, J. Wang and Y. Li, *Nanoscale*, 2020, **12**, 8934–8941.
- 24 P. Du, Y. Dong, C. Liu, W. Wei, D. Liu and P. Liu, *J. Colloid Interface Sci.*, 2018, **518**, 57–68.
- 25 C. Yang, X. Li, L. Yu, X. Liu, J. Yang and M. Wei, *Chem. Commun.*, 2020, **56**, 1803–1806.
- 26 U. A. Khan, N. Iqbal, T. Noor, R. Ahmad, A. Ahmad, J. Gao, Z. Amjad and A. Wahab, *J. Energy Storage*, 2021, **41**, 102999-103009.
- 27 S. Wang, S. Wang, X. Guo, Z. Wang, F. Mao, L. Su, H. Wu, K. Wang and Q. Zhang, *Inorg. Chem. Front.*, 2021, **8**, 4878–4886.
- 28 N. Wu, H. Wu, J. Zhang, Y. Zhang, D. Cao, L. Bai and T. Hu, *J. Alloys Compd.*, 2021, **856**, 157466-157506.
- 29 N. Liu, X. Liu and J. Pan, *J. Colloid Interface Sci.*, 2022, **606**, 1364–1373.
- 30 D. Y. Lee, S. J. Yoon, N. K. Shrestha, S. H. Lee, H. Ahn and S. H. Han, *Microporous Mesoporous Mater.*, 2012, **153**, 163–165.
- 31 G. Zhu, H. Wen, M. Ma, W. Wang, L. Yang, L. Wang, X. Shi, X. Cheng, X. Sun and Y. Yao, *Chem. Commun.*, 2018, **54**, 10499–10502.
- 32 S. Xiong, S. Jiang, J. Wang, H. Lin, M. Lin, S. Weng, S. Liu, Y. Jiao, Y. Xu and J. Chen, *Electrochim. Acta*, 2020, **340**, 135956-135967.
- 33 Q. Li, H. Guo, R. Xue, M. Wang, M. Xu, W. Yang, J. Zhang and W. Yang, *Int. J. Hydrogen Energy*, 2020, **45**, 20820–20831.
- 34 L. Wang, X. Feng, L. Ren, Q. Piao, J. Zhong, Y. Wang, H. Li, Y. Chen and B. Wang, *J. Am. Chem. Soc.*, 2015, **137**, 4920–4923.
- 35 X. Wang, N. Yang, Q. Li, F. He, Y. Yang, B. Wu, J. Chu, A. Zhou and S. Xiong, *J. Solid State Chem.*, 2019, **277**, 575–586.

- 36 M. Azadfalsh, A. Sedghi and H. Hosseini, *J. Electron. Mater.*, 2019, **48**, 7011–7024.
- 37 C. H. Wang, D. W. Zhang, S. Liu, Y. Yamauchi, F. B. Zhang and Y. V. Kaneti, *Chem. Commun.*, 2022, **58**, 1009–1012.
- 38 Y. Wu, X. Ding, Y. Luo, F. Xu, L. Sun, J. H. Lao, X. Qin, C. Dan, Y. Wang, Q. Yin, T. Wang, K. Zhang, B. Li, H. Zhang and Y. Zou, *Int. J. Electrochem. Sci.*, 2021, **16**, 1–11.
- 39 S. Gao, Y. Sui, F. Wei, J. Qi, Q. Meng and Y. He, *J. Mater. Sci.*, 2018, **53**, 6807–6818.
- 40 X. Zhang, N. Qu, S. Yang, Q. Fan, D. Lei, A. Liu and X. Chen, *J. Colloid Interface Sci.*, 2020, **575**, 347–355.
- 41 V. Veeramani, B. M. Matsagar, Y. Yamauchi, A. Y. Badjah, M. Naushad, M. Habila, S. Wabaidur, Z. A. Alothman, Z. L. Wang and K. C. W. Wu, *J. Taiwan Inst. Chem. Eng.*, 2019, **96**, 634–638.
- 42 R. Velmurugan, J. Premkumar, R. Pitchai, M. Ulaganathan and B. Subramanian, *ACS Sustain. Chem. Eng.*, 2019, **7**, 13115–13126.
- 43 S. B. Bandgar, M. M. Vadiyar, Y. C. Ling, J. Y. Chang, S. H. Han, A. V. Ghule and S. S. Kolekar, *ACS Appl. Energy Mater.*, 2018, **1**, 638–648.
- 44 S. Gao, Y. Sui, F. Wei, J. Qi, Q. Meng and Y. He, *J. Mater. Sci. Mater. Electron.*, 2018, **29**, 2477–2483.
- 45 F. Israr, D. Chun, Y. Kim and D. K. Kim, *Ultrason. Sonochem.*, 2016, **31**, 93–101.
- 46 F. Israr, D. K. Kim, Y. Kim and W. Chun, *Quim. Nova*, 2016, **39**, 669–675
- 47 X. Zhang, N. Qu, S. Yang, D. Lei, A. Liu and Q. Zhou, *Mater. Chem. Front.*, 2021, **5**, 482–491.
- 48 X. Liu, D. Xu, Q. Wang and L. Zhang, *Small*, 2018, **14**, 1–12.
- 49 Q. Liu, L. Xie, X. Shi, G. Du, A. M. Asiri, Y. Luo and X. Sun, *Inorg. Chem. Front.*, 2018, **5**, 1570–1574.
- 50 M. Thommes, K. Kaneko, A. V. Neimark, J. P. Olivier, F. Rodriguez-Reinoso, J. Rouquerol and K. S. W. Sing, *Pure Appl. Chem.*, 2015, **87**, 1051–1069.
- 51 R. Bardestani, G. S. Patience and S. Kaliaguine, *Can. J. Chem. Eng.*, 2019, **97**, 2781–2791.
- 52 M. Khalifaoui, S. Knani, M. A. Hachicha and A. Ben Lamine, *J. Colloid Interface Sci.*, 2003, **263**, 350–356.

- 53 G. Li, Y. Qi, H. Lin, N. Lu, J. Chen, J. Wang, Q. Han and F. Liu, *J. Memb. Sci.*, 2021, **635**, 1–9.
- 54 Q. Bi, Q. Ma, K. Tao and L. Han, *Dalt. Trans.*, 2021, **50**, 8179–8188.
- 55 J. Yang, P. Xiong, C. Zheng, H. Qiu and M. Wei, *J. Mater. Chem. A*, 2014, **2**, 16640–16644.
- 56 X. G. Han, P. F. Wang, Y. H. Zhang, H. Y. Liu, J. J. Tang, G. Yang and F. N. Shi, *Inorganica Chim. Acta*, 2022, **536**, 120916-120927.
- 57 S. S. Shah, E. Cevik, M. A. Aziz, T. F. Qahtan, A. Bozkurt and Z. H. Yamani, *Synth. Met.*, 2021, **277**, 116765-116780.
- 58 C. Zhang, Q. Zhang, K. Zhang, Z. Xiao, Y. Yang and L. Wang, *RSC Adv.*, 2018, **8**, 17747–17753.
- 59 Y. Li, Y. Xu, Y. Liu and H. Pang, *Small*, 2019, **15**, 1–8.
- 60 J. W. Wang, Y. X. Ma, X. Y. Kang, H. J. Yang, B. L. Liu, S. S. Li, X. D. Zhang and F. Ran, *J. Solid State Chem.*, 2022, **309**, 122994-123012.
- 61 S. Wang, J. Wang, M. Zeng, J. Yang, N. Hu, Y. Su, Z. Zhou, H. Pang and Z. Yang, *J. Energy Storage*, 2021, **38**, 102528-102537.
- 62 C. Feng, C. P. Lv, Z. Q. Li, H. Zhao and H. H. Huang, *J. Solid State Chem.*, 2018, **265**, 244–247.
- 63 K. T. Kubra, A. Javaid, R. Sharif, G. Ali, F. Iqbal, A. Salman, F. Shaheen, A. Butt and F. J. Iftikhar, *J. Mater. Sci. Mater. Electron.*, 2020, **31**, 12455–12466.

CHAPTER FOUR

Construction of Well-Defined Two-Dimensional Architectures of Trimetallic Metal-Organic Frameworks for High-Performance Symmetric Supercapacitors

4.1 Outline

The high surface-to-volume ratio and extraordinarily large-surface area of two-dimensional (2D) metal-organic framework (MOF) architectures have drawn particular interest for use in supercapacitors. To achieve an excellent electrode material for supercapacitors, well-defined 2D nanostructures of novel trimetallic MOFs were developed for supercapacitor applications. Multivariate MOFs (terephthalate and trimesate MOF) with distinctive nanobrick and nanoplate-like structures were successfully synthesized using a straightforward one-step reflux condensation method by combining Ni, Co, and Zn metal species in equimolar ratios with two different ligands. Furthermore, the effects of the tricarboxylic and dicarboxylic ligands on cyclic voltammetry, charge-discharge cycling, and electrochemical impedance spectroscopy were studied. The derived terephthalate and trimesate MOFs are supported with stainless-steel mesh and provide a suitable electrolyte environment for rapid faradaic reactions with an elevated specific capacity, excellent rate capability, and exceptional cycling stability. It shows a specific capacitance of 582.8 F g^{-1} , a good energy density of $40.47 \text{ W h kg}^{-1}$, and a power density of 687.5 W kg^{-1} at 5 mA cm^{-2} with an excellent cyclic stability of 92.44% for 3000 charge-discharge cycles. A symmetric BDC-MOF//BDC-MOF supercapacitor device shows a specific capacitance of 95.22 F g^{-1} with low capacitance decay, high energy, and power densities which is used for electronic applications. These brand-new trimetallic MOFs display outstanding electrochemical performance and provide a novel strategy for systematically developing high-efficiency energy storage systems.

4.2 Introduction

Over the past few decades, the need to develop clean and sustainable energy has become extremely urgent due to the increasing requirement for clean energy and solving serious environmental problems.¹ Nowadays, much research is focused on current renewable energy storage devices in order to minimize pollution and raise worries about future energy problems.^{2,3} Under some environmental circumstances, it is challenging to produce power from sustainable energy sources (biomass, hydro, solar, wind, etc.), which causes an imbalance between the supply and demand of energy. In order to balance and equalize energy needs, energy storage devices must be integrated with energy production, which is crucial for a renewable energy supply.^{4,5} Because of their excellent energy capability and clean electrical systems, electrochemical energy storage equipment have gained widespread interest. One energy storage device that stands out above most of the others is the supercapacitor, which shows the utmost characteristics like high energy density, fast charging/discharging process, and excellent cycle stability, and also they are feasibly used in many fields.⁶⁻⁸ The energy storage mechanism is non-identical for every class because of the different materials used within the components.⁹ It is broadly confessed that the features of electrode materials like structure, morphology, electronic conductivity, electrochemical activity, and chemical and mechanical stability all put up to their electrochemical performance.^{10,11} Transition metals have fascinated ample interest for many energy storage devices due to their good physical and chemical characteristics, high conductivity, improved redox activity, and long cycle stability.¹² The supercapacitor's performance is also affected by the electrolyte utilized. Electrolytes are important and necessary components of supercapacitors. Due to their physical and chemical characteristics, they have a significant impact on the electrochemical performances of specific capacity, energy density, power density, rate capability, cycle stability, and safety. In comparison to aqueous electrolytes, the solid-state electrolyte is a crucial element that might significantly affect the capacitance retention and stability of supercapacitors. Liquid electrolytes possess some limitations like leakage problems, and it shows low electrochemical performance. Gel polymer electrolytes (GPEs) are the most commonly used solid-state electrolytes in solid-state supercapacitors due to their relatively high ionic conductivity, improved interfacial contacts between electrodes and GPE, broad operating potential range, higher ion

transfer number, and improved stability.^{13,14} Metal-organic frameworks (MOFs) have emerged as attractive prospects in a variety of sectors in recent years due to structural and electrical properties such as high porosity, excellent specific surface area (SSA), high stability, and adjustable arrangement of active sites. Owing to the structural and electronic features of MOFs, they are employed in supercapacitors. MOFs show pseudocapacitive nature because of the oxidative-reductive behavior of positively charged metal ions inside MOFs which create channels for electrons as well as show electric double layer capacitor (EDLC) behavior due to the organic linker structure which promotes charge transfer inside the framework which leads to the EDLC behavior.^{15,16} MOFs are formed at the micro/nanosize using central metal nodes and organic linkers, resulting in one-dimensional (1D), two-dimensional (2D) structures, and three-dimensional superstructures.^{17,18} In the exploration of advanced materials with enhanced characteristics over standard MOFs, the tendency is to encourage synergistic effects succeeding from the existence of two or more metals in multimetallic MOFs.¹⁹ In comparison to monometallic MOFs, the multimetallic MOFs have many advantages including strong chemical reactivity, improved electronic charge transfer, a variety of morphologies, high selectivity and sensitivity, virtue, strain in the lattice, different geometric impacts, and chemical change.²⁰⁻²⁴ Due to the excellent properties of MOFs, the electrochemical performance of supercapacitors is enhanced by their ability to store a huge quantity of charge and by encouraging the dissemination of electrolyte ions. As a result, MOFs have received a lot of interest when it comes to the use of supercapacitor electrode materials.²⁵ The limitations of the monometallic MOFs have been overcome by multimetallic MOFs which have advantages like the synergic effect which enhance the redox reactions and electrical conductivity. Also, the presence of various metal centers enhances the electroactive sites for ion transfer and helps the interaction with electrolyte in the course of the electrochemical reactions. The advancement of an perfect and beneficial electrode material composed of non-noble metals with remarkable steadiness and nature depicts the key challenge in these areas.²⁶⁻²⁸ As an outcome, a considerable study has been performed to reduce the obstacles caused by MOF's low conductivity and structural configuration. The direct application of MOF-based materials for effective supercapacitors remains difficult, despite the significant advances made in manufacturing MOF-based materials for energy storage applications.²⁹ Nagaraju et al. put together binder-free Ni-Co-Mn-based MOFs via a polarity-induced solution-

phased technique. Dual-layered Ni-Co-Mn-based MOFs with versatile features demonstrated the highest capacity of $1311.4 \text{ Ah cm}^{-2}$ at a 5 mA cm^{-2} current density with high capacitance retention of about 86.1% after applying 4000 cycles in the aqueous alkaline electrolyte. Additionally, they have created a pouch-type supercapattery with a bilayered Ni-Co-Mn-based MOF/Ni foam as an anode and nitrogen-oxygen-enriched activated carbon/Ni foam as a cathode. This device exhibits good cycling durability due to the high capacity of the supercapattery retained at 90.1% and the good Faradaic efficiency of 98.6%. Furthermore, they created a pouch-type supercapattery using bilayered Ni-Co-Mn-based MOF/Ni foam as an anode and nitrogen-oxygen enriched activated carbon/Ni foam as a cathode, resulting in a supercapattery with a high capacity retention of 90.1% and an exceptional Faradaic efficiency of 98.6%, illustrating the device's great cycling longevity.³⁰ Andikaey et al. prepared a new nanocomposite mesoporous ordered silica SBA-15/ MWCNTs embellished with a trimetallic organic framework (NiCoCu-BTC) using a facile, cost-effective one-step solvothermal technique. The synthesized nanocomposite exhibited outstanding electrochemical performance having a remarkable 868 C g^{-1} (2067 F g^{-1}) specific capacity at a 1 A g^{-1} current density with great cycling durability. Additionally, they have fabricated an asymmetric supercapacitor device with a high energy density 52.4 W h kg^{-1} at a power density of 1124 W kg^{-1} with high capacitance retention of about 87.2% after applying 5000 cycles.³¹

In view of this, we present the synthesis of trimetallic MOFs for high-performance symmetric supercapacitors by applying two different organic linkers, i.e., trimesic acid and terephthalic acid. To the finest of our information, this is the primary report in which a comparative study of two MOFs is carried out only by changing the organic linker, and they are used as dynamic anode materials for supercapacitors. The physico-chemical properties of both the trimetallic MOFs were thoroughly investigated by using different characterization techniques. In addition, a symmetric supercapacitor shows a high energy density and great chemical steadiness in a 2 M KOH electrolyte.

4.3 Experimental section

4.3.1 Synthesis of MOFs

All chemicals used to synthesize trimetallic MOFs were obtained from Loba Chemie (India) and were used without further purification. The trimetallic Ni-Co-Zn-

BDC MOFs (BDC-MOF) were prepared using a single-step reflux condensation method. In a typical synthesis, 0.415 g of terephthalic acid (BDC), 0.363 g of nickel nitrate hexahydrate, 0.363 g of cobalt nitrate hexahydrate, and 0.371 g zinc nitrate hexahydrate were dissolved step by step in 30 mL of N, N-dimethylformamide with continuous stirring at ambient temperature.

After which, the reaction mixture was transferred to a 50 mL round-bottom flask. The reaction mixture was kept at 120 °C for 12 h to produce the BDC-MOF sample and then cooled at ambient temperature. The final precipitate was carefully washed a few times with alcohol. Finally, the purple-colored product was air-dried for 12 h at 80 °C. A similar procedure was adopted for the synthesis of trimetallic Ni-Co-Zn-BTC MOF (BTC-MOF), except that terephthalic acid was replaced with trimesic acid. A schematic illustration for the synthesis of trimetallic MOFs by the reflux condensation method is shown in Figure 4.1.

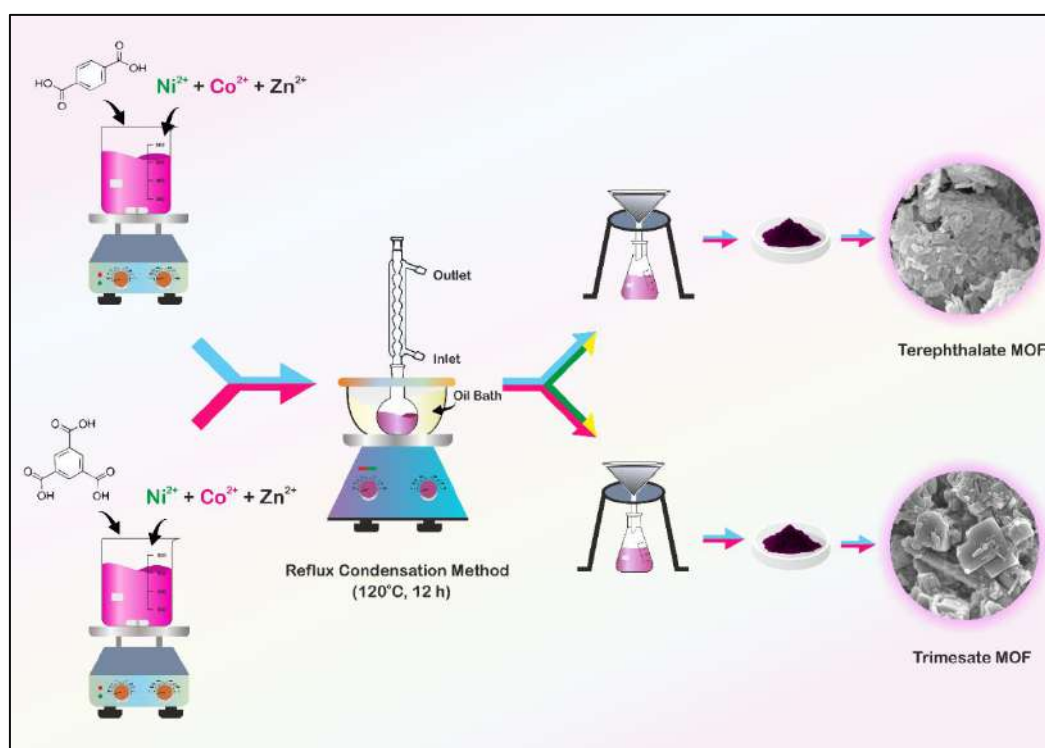


Figure 4.1: Schematic illustrations of the synthesis of trimetallic MOFs

4.3.2 Structural and elemental characterization

The crystal structure and phase purity of the synthesized trimetallic MOFs were confirmed by the X-ray diffraction (XRD) technique [Bruker D8 Phaser X-ray diffractometer with Cu K α radiation ($\lambda = 1.541 \text{ \AA}$)]. The types of bonding and functional groups were analyzed by Fourier transform infrared (FT-IR) spectroscopy (PerkinElmer 1760X spectrophotometer). The Raman spectrometer (LabRAM HR

Evolution Confocal Raman Microscope, France) was used for point group analysis. The morphology of the as-prepared materials was investigated by scanning electron microscopy (SEM) (JEOL-JSM 6360, Japan). The elemental composition of the trimetallic MOFs was examined using an energy-dispersive X-ray analysis (EDAX) spectrometer [Oxford Instrumentations inbuilt with field emission (FE-SEM)]. The elemental oxidation state and chemical composition of the as-prepared materials were investigated by X-ray photoelectron spectroscopy (XPS) with a K-alpha (Thermo VG, UK) spectrometer and a monochromatic Al X-ray source (AlK α line: 1486.6 eV, 3 mA, and 12 kV). The surface area and pore size were determined by Brunauer-Emmett-Teller (BET) (NOVA1000e Quantachrome, USA).

4.3.3 Electrochemical measurements with a three-electrode assembly

Electrochemical measurements were performed on a CHI608 electrochemical analyzer (CH Instruments Inc, Austin, USA). A standard three-electrode assembly in a 2 M KOH electrolyte was used to explore the electrochemical characteristics of a constructed electrode. A saturated Ag/AgCl was used as a reference electrode, graphite as the counter electrode, and trimetallic MOF-loaded stainless-steel mesh as the working electrode. The working electrode was fabricated by making a paste of 80 wt % of active materials (BDC-MOF and BTC-MOF), 10 wt % of carbon black (Super P) as a conducting material, and 10 wt % of polyvinylidene fluoride (PVDF) as a binder in the N-methyl-2-pyrrolidone (NMP) solvent. This paste was applied to a stainless-steel mesh measuring with size about 1 cm² and then air-dried for 12 h at 80 °C. With the help of electrochemical workstation, cyclic voltammetry (CV), galvanostatic charge-discharge (GCD), and electrochemical impedance spectroscopy (EIS) studies were carried out. In the frequency range of 1 Hz to 100 kHz, the EIS test was conducted. According to equation (4.1), specific capacitance of the prepared samples was determined.

$$C = \frac{I \times \Delta t}{\Delta V \times m} \dots\dots\dots (4.1)$$

Where “C” stands for the specific capacitance measured in F g⁻¹, “I” stands for the current measured in mA, “ Δt ” stands for the discharging time measured in seconds, “ ΔV ” stands for the potential window measured in volt, and “m” stands for the mass of the active electrode material measured in mg.

4.3.4 Electrochemical measurements of the symmetric supercapacitor

A solid-state symmetric supercapacitor (SSC) device was constructed by stainless-steel mesh substrates with size about 2 cm coated with the BDC-MOF, and a thick layer of polyvinyl alcohol (PVA)-KOH was sandwiched in between them. The device was allowed to naturally dry out overnight at ambient temperature. As per literature report, the PVA-KOH gel electrolyte was prepared.³² Using a conventional method, 1 g of PVA was dissolved in 20 mL of distilled water while the bath solution temperature was held at 80 °C for 30 min. To create the viscous gel electrolyte, the PVA solution was combined with the aqueous KOH solution dropwise and heated once more at 80 °C for 30 min.

Using equation (4.2-4.4), the specific capacitance, energy density, and power density of the symmetric supercapacitor were computed, respectively.^{33,34}

$$C_s = \frac{I \times \Delta t}{\Delta V \times M} \dots\dots\dots (4.2)$$

$$E = \frac{0.5 \times C \times \Delta V^2}{3.6} \dots\dots\dots (4.3)$$

$$P = \frac{E \times 3600}{\Delta t} \dots\dots\dots (4.4)$$

where “Cs” stands for the specific capacitance measured in F g⁻¹, “E” stands for the specific energy measured in Wh kg⁻¹, “P” stands for the specific power measured in W kg⁻¹, and “M” stands for the total mass of the two electrodes measured in mg.

4.4 Results and discussion

4.4.1 X-ray diffraction of trimetallic MOFs

The crystallographic structure and crystallite size of the trimetallic BDC-MOF and BTC-MOF were found by using the XRD pattern, and the results are presented in Figure 4.2. For the BDC-MOF, the peak located at an angle 10.0° is indexed to the (011) plane of Ni (PDF no. 10-0735), the diffraction peak at 8.7° is attributed to the (100) plane of Co (PDF no. 19-1523), and the diffraction peak at 16.6° is attributed to the (002) plane of Zn (PDF no. 01-0037). While for the BTC-MOF, the peak located at 10.6° is indexed to the (011) plane of Ni (PDF no. 10-0735), the diffraction peak at 8.7° is attributed to the (100) plane of Co (PDF no. 13-0733), and the diffraction peak at 17.5° is attributed to the (311) plane of Zn (PDF no. 01-0037), respectively, indicating that these MOFs have the similar structure.^{35,36} Furthermore, the crystallite size was determined using Debye-Scherrer’s formula, as shown in equation (4.5).³⁷

$$D = \frac{0.9\lambda}{\beta \cos\theta} \dots\dots\dots (4.5)$$

Where “D” stands for the average crystallite size, “λ” stands for the wavelength of the X-rays, “β” stands for the full-width half-maxima (fwhm), and “θ” stands for Bragg’s diffraction angle. According to the XRD spectra, the trimetallic BDC-MOF and BTC-MOF derived from the (011) plane have average crystallite sizes of 3.55 and 5.97 nm, respectively.

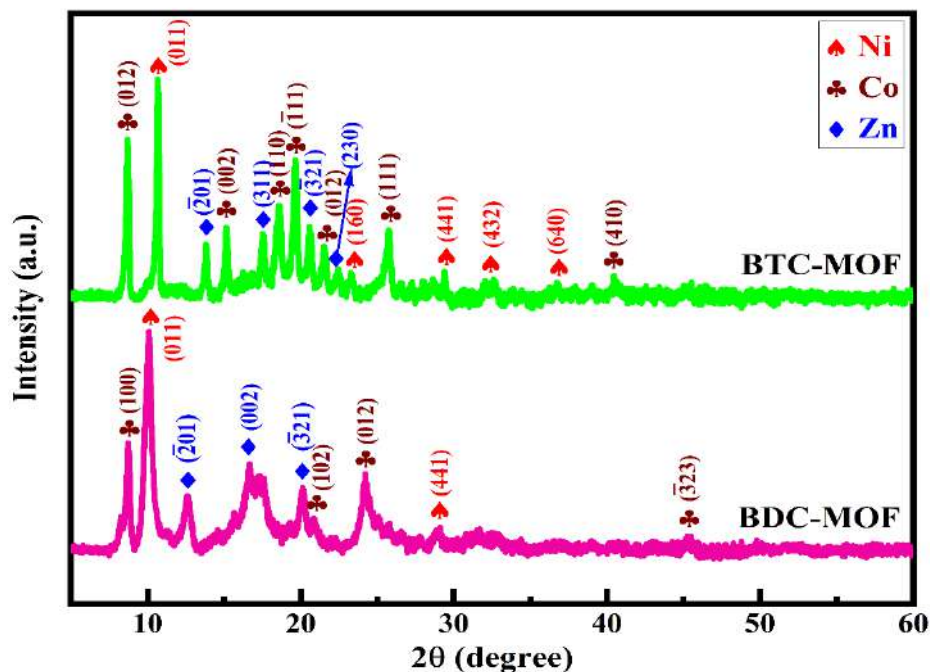


Figure 4.2: XRD patterns of BDC-MOF and BTC-MOF

4.4.2 FT-IR spectroscopy of trimetallic MOFs

The identification of the functional group of the BDC-MOF and BTC-MOF was obtained by using the FT-IR spectra. Trimetallic MOF FT-IR spectra are shown in Figure 4.3. The bands at 3351 and 3310 cm^{-1} were caused by moisture induced O-H stretching vibrations in BDC-MOF and BTC-MOF, respectively. Aromatic C=C in plane vibrations are assigned to the bands at 1647 and 1609 cm^{-1} . The asymmetric stretching vibration of the coordinated (-COO-) group displays the peak at 1436 cm^{-1} , while the symmetric stretching vibrations show the peak at 1361 cm^{-1} . In BDC-MOF, the sp^2 carbon stretching vibration peaks of C=O due to the carboxylic group are displayed at 1677 cm^{-1} , and the peak at 1575 cm^{-1} represents the aromatic C=C in-plane vibrations. The C-H bending vibrations of CH_3 and CH_2 are represented by the prominent adsorption peaks at 1373 and 1287 cm^{-1} , respectively. The in-plane and out-of-plane C-H bending modes are allocated to several bands in the ranges of 1200-

1000 and 1000-700 cm^{-1} , respectively. Multiple bands in the range of 700-400 cm^{-1} are assigned to the metal-oxygen bands.^{38,39}

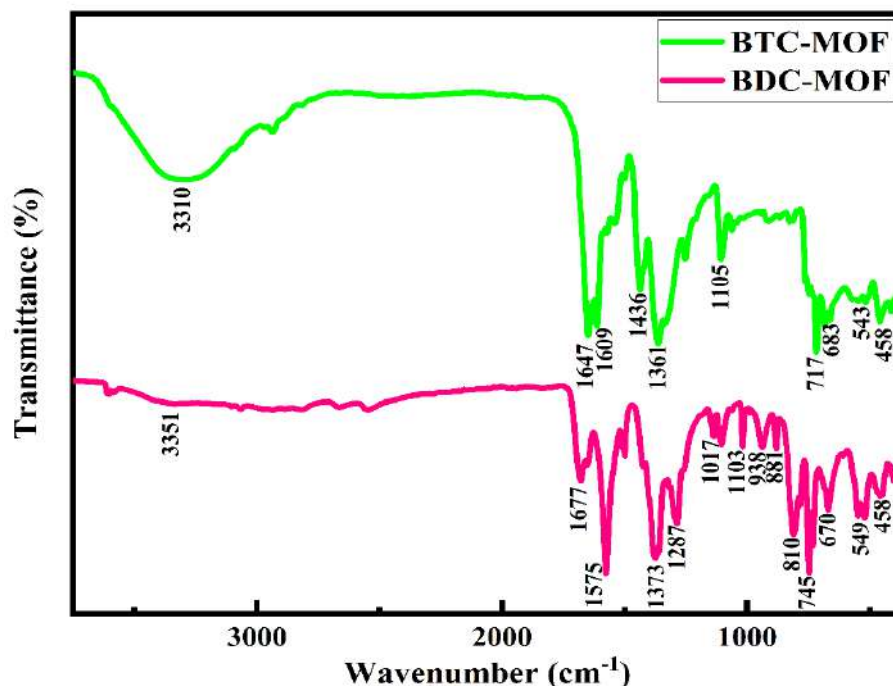


Figure 4.3: FTIR spectra of BDC-MOF and BTC-MOF

The bond vibration of trimetallic MOFs was confirmed by Raman spectroscopy, as seen in Figure 4.4. The peaks of trimetallic MOFs correlate to different bands, confirming the existence of the BDC and BTC moieties in the material. The Raman spectra of BDC-MOF and BTC-MOF displayed a $\nu(\text{C}=\text{C})$ modes of the benzene ring observed at 1133 and 999 cm^{-1} , respectively, and the observed peaks at the low-frequency region of 500-850 cm^{-1} correspond to benzene ring C-H bending modes and the presence of metal-oxygen bond vibration, respectively.^{40,41} In BDC-MOF, the vibrational modes of $\nu_{\text{as}}(\text{COO}^-)$ and $\nu_{\text{s}}(\text{COO}^-)$ were noticed as doublets at 1608 and 1427 cm^{-1} in BDC-MOF, and the vibrational modes of $\nu_{\text{as}}(\text{COO}^-)$ and $\nu_{\text{s}}(\text{COO}^-)$ were noticed as doublets at 1595 and 1453 cm^{-1} in BTC-MOF, respectively, and these findings point to the synthesis of trimetallic MOFs, which was previously supported by FT-IR data.^{42,43}

4.4.3 Raman spectroscopy of trimetallic MOFs

Raman spectroscopy was used to confirm the bond vibration of trimetallic MOFs, which is given in Figure 4.4. The trimetallic MOFs peaks corresponds to various bands which confirms the presence of the BDC and BTC moiety in the material. The Raman spectra of BDC-MOF and BTC-MOF exhibited a $\nu(\text{C}=\text{C})$ modes

of the benzene ring was observed at 1133 cm^{-1} and 999 cm^{-1} , respectively and the observed peaks at the low-frequency region of 500 to 850 cm^{-1} were assigned to benzene ring C-H bending modes and the presence of metal-oxygen bond vibration.^{35,36} In BDC-MOF, the vibrational modes of $\nu_{\text{as}}(\text{COO}^-)$ and $\nu_{\text{s}}(\text{COO}^-)$ were observed as doublets at 1608 and 1427 cm^{-1} in BDC-MOF and the vibrational modes of $\nu_{\text{as}}(\text{COO}^-)$ and $\nu_{\text{s}}(\text{COO}^-)$ were observed as doublets at 1595 and 1453 cm^{-1} in BTC-MOF, respectively and these results indicate the formation of BDC and BTC based trimetallic MOF which was earlier boosted by FT-IR results.^{37,38}

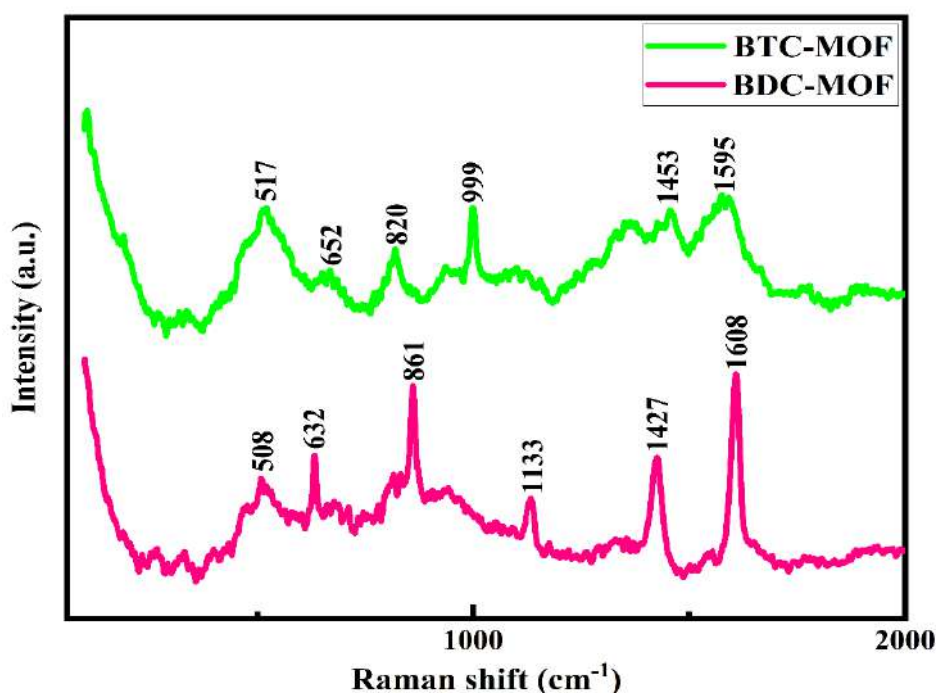


Figure 4.4: Raman spectra of BDC-MOF and BTC-MOF

4.4.4 Scanning electron microscopy of trimetallic MOFs

SEM was used to study the surface morphology of BTC-MOF and BDC-MOF. The influence of the trimesic and terephthalic ligands on the formation of surface morphology for MOF was examined. Figure 4.5 reveals the surface morphological images of BTC-MOF and BDC-MOF with different magnifications. From Figure 4.5(a, b), it has been observed that the small nanoparticles start to construct the nanobrick-like morphology of BTC-MOF, and nanobricks were observed all over area of the sample which are randomly distributed in the sample. The width of the nanobricks was observed from 200 to 300 nm in size. It was noticed that nanobricks are interconnected to each other, and also the edges of the nanobricks are mingling with one another; hence, the nanobricks are found to be cut in small

pieces, which are responsible for the irregular shapes of nanobricks formed in the BTC-MOF sample. Additionally, some of the spacing between two nanobricks is seen in the BTC-MOF sample, which is helpful for adsorbing the electrolyte and boosts the material-specific capacitance. It is seen that the variation of ligands in MOF samples has a great impact on the characteristic morphology of MOF samples. Here, it is observed that with change in the ligands, there was a change in the surface morphology of MOF samples.

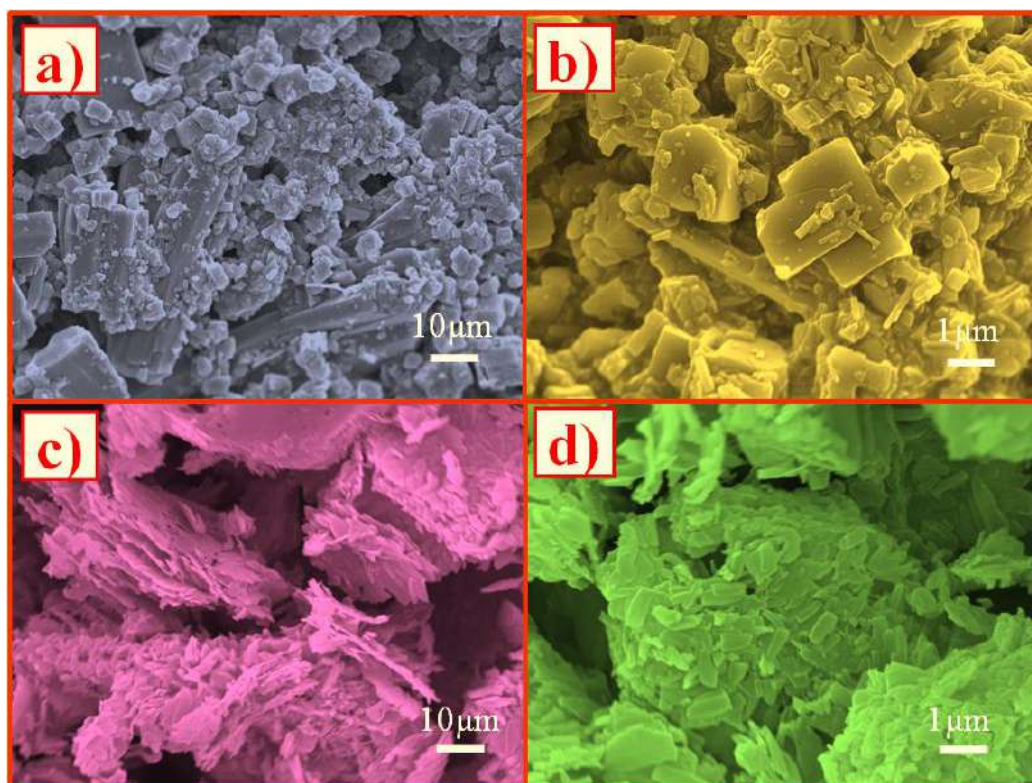


Figure 4.5: SEM images of (a, b) BTC-MOF and (c, d) BDC-MOF at different magnifications

The sample BDC-MOF demonstrated the nanoplate-like morphology with irregular arrangement of the nanoplates occurring throughout the sample. Some of the nanoplates were formed together, leading to big porous bricks which are shown in Figure 4.5(c, d). The thickness of the nanoplates was observed in the nanometer range, and a bunch of the nanoplates formed the brick-like morphology, hence increasing the surface area of the sample. The bunch of nanoplates provides a larger SSA for the adsorption of the electrolyte increasing the specific capacitance of the sample. The surface area of BDC-MOF is the greater of the two samples examined in the BET investigation. Also, SEM outcomes are in good agreement with BET

analysis. Hence, among these two samples, BDC-MOF executes a good electrochemical performance.

4.4.5 Energy dispersive X-ray analysis of trimetallic MOFs

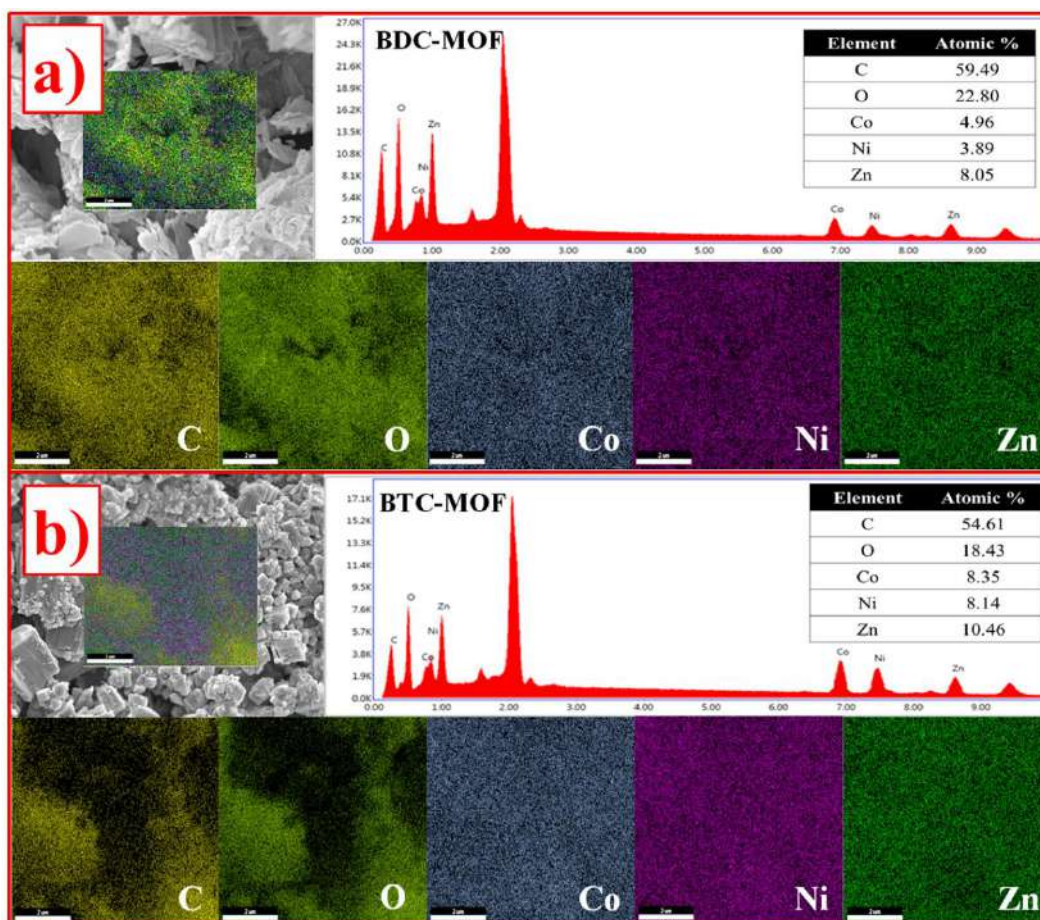


Figure 4.6: EDX spectra and elemental mapping of C, O, Co, Ni and Zn elements for (a) BDC-MOF and (b) BTC-MOF

The EDAX of both the trimetallic MOFs is presented in Figure 4.6. Figure 4.6 demonstrates that the elements Ni, Co, Zn, C, and O are distributed evenly throughout the sample, which confirms the presence of three metal ions in the MOFs as well as maintained the stoichiometry of the samples; hence, it proved that the trimetallic MOFs were obtained. The SSA and pore diameter of the MOF samples were obtained by using BET analysis.

4.4.6 Transmission electron microscopy analysis of trimetallic MOFs

Transmission electron microscopy (TEM) examination was performed to have a better understanding of the structure of the as-prepared nanomaterials. Figure 4.7(a) depicts a typical TEM image of BDC-MOF with a 2D nanoplate-like shape with many voids. Furthermore, the high-resolution TEM (HRTEM) image of BDC-MOF (Figure 4.7b) confirms an amorphous nature due to the lack of apparent lattice fringes

and no indication of crystallinity, representing that the particles were amorphous. The selected area electron diffraction (SAED) pattern (Figure 4.7c) consistently exposed only diffuse rings, confirming the amorphous nature of the as-synthesized BDC-MOF particles. Figure 4.7(d) shows a typical TEM image of a 2D nanobrick-like morphology of BTC-MOF. The HRTEM image of BTC-MOF (Figure 4.7e) disseminated that the particles were amorphous due to the lack of visible lattice fringes and no evidence of crystallinity, suggesting that the particles were amorphous. The SAED pattern (Figure 4.7f) consistently displayed only diffuse rings, confirming the amorphous nature of the BTC-MOF particles as synthesized.

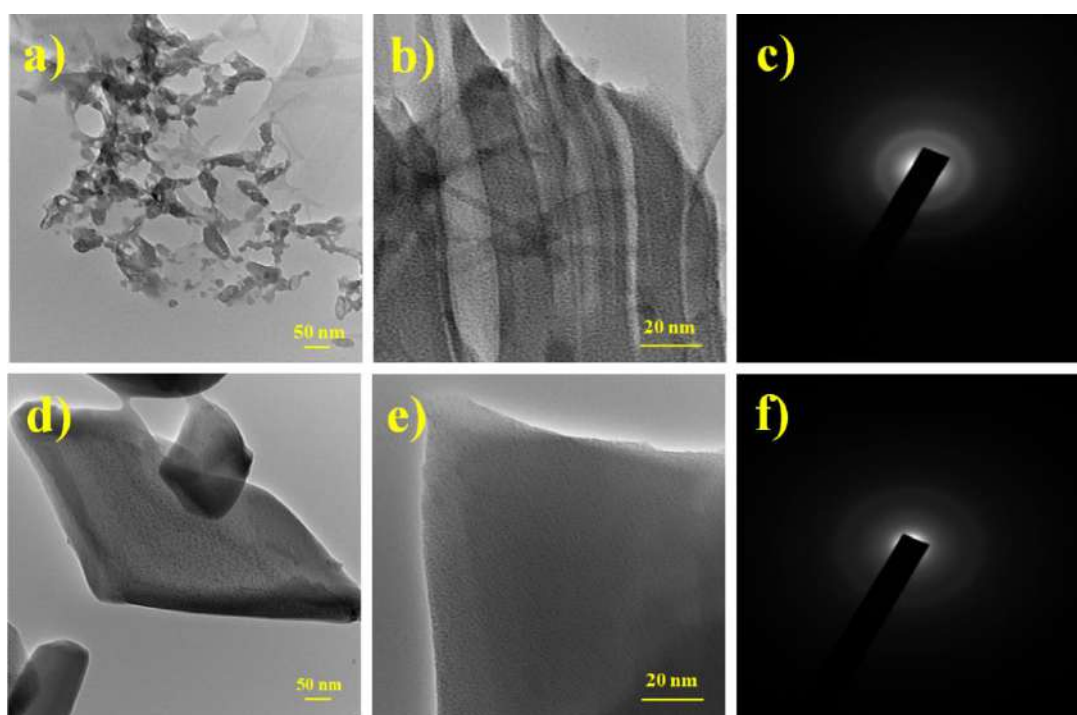


Figure 4.7: TEM, HR-TEM and SAED pattern of (a-c) BDC-MOF and (d-f) BTC-MOF

4.4.7 Brunauer-Emmett-Teller analysis of trimetallic MOFs

N₂ adsorption/desorption measurements confirmed the porous structure of the obtained MOFs, and the corresponding isotherms are shown in Figure 4.8. Before adsorption measurements, MOF samples were outgassed at 100 °C for 4 h. BDC-MOF and BTC-MOF had SSA of 267.85 and 216.93 m² g⁻¹, respectively. The average pore size of BDC-MOF and BTC-MOF was found to be 16 and 31 nm simultaneously, which is obtained from the BJH curve. According to the IUPAC classifications, the BDC-MOF and BTC-MOF isotherms are types IV and II, respectively,⁴⁴ clearly indicating that the BDC-MOF have a larger SSA than the

BTC-MOF. The SSA and average pore radius values agree well with the crystallite size determined by XRD and the specific capacitance determined by electrochemical performance study.

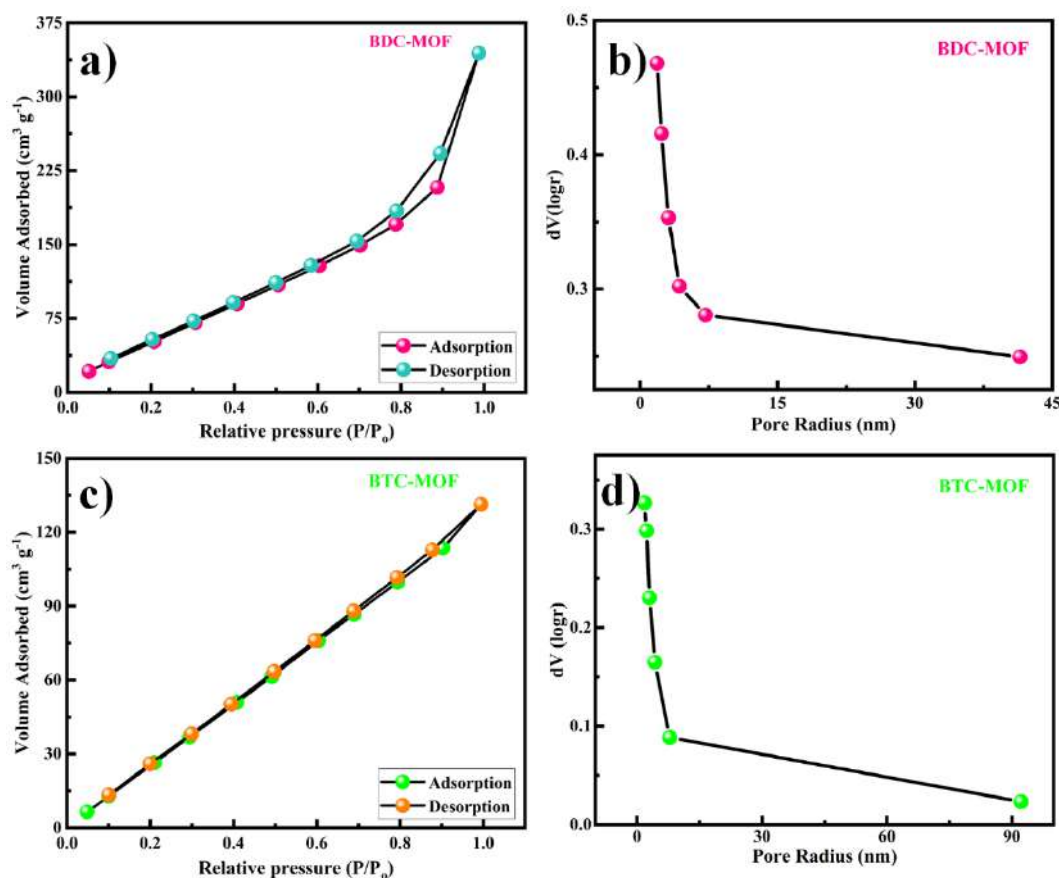


Figure 4.8: (a, b) N₂ adsorption-desorption isotherm and pore size distribution curve BDC-MOF, (c, d) N₂ adsorption-desorption isotherm and pore size distribution curve BTC-MOF

4.4.8 X-ray photoelectron spectroscopy of trimetallic MOFs

The chemical composition and oxidation states of trimetallic MOFs were obtained by using XPS and explored the charge-transfer mechanisms in the valence state of the Ni, Zn, and Co ions of trimetallic MOFs along with the synergetic effect of its species. Figure 4.9(a, b) shows the survey spectra of both trimetallic MOFs. The core level spectra of C 1s, Ni 2p, Co 2p, O 1s, and Zn 2p of both the trimetallic MOFs are depicted in Figure 4.9(c-i). As seen in Figure 4.9(a, b), the existence of trimetallic MOFs was attributed by the XPS full survey scan spectrum, which contained the signals of the elements Ni, Co, O, C, and Zn. Figure 4.9(c, d) reveals the C 1s spectra of both the MOFs. It consists of distinct peaks caused by benzene rings from the BDC and BTC ligands with binding energy 284.7 and 284.8 eV, respectively.

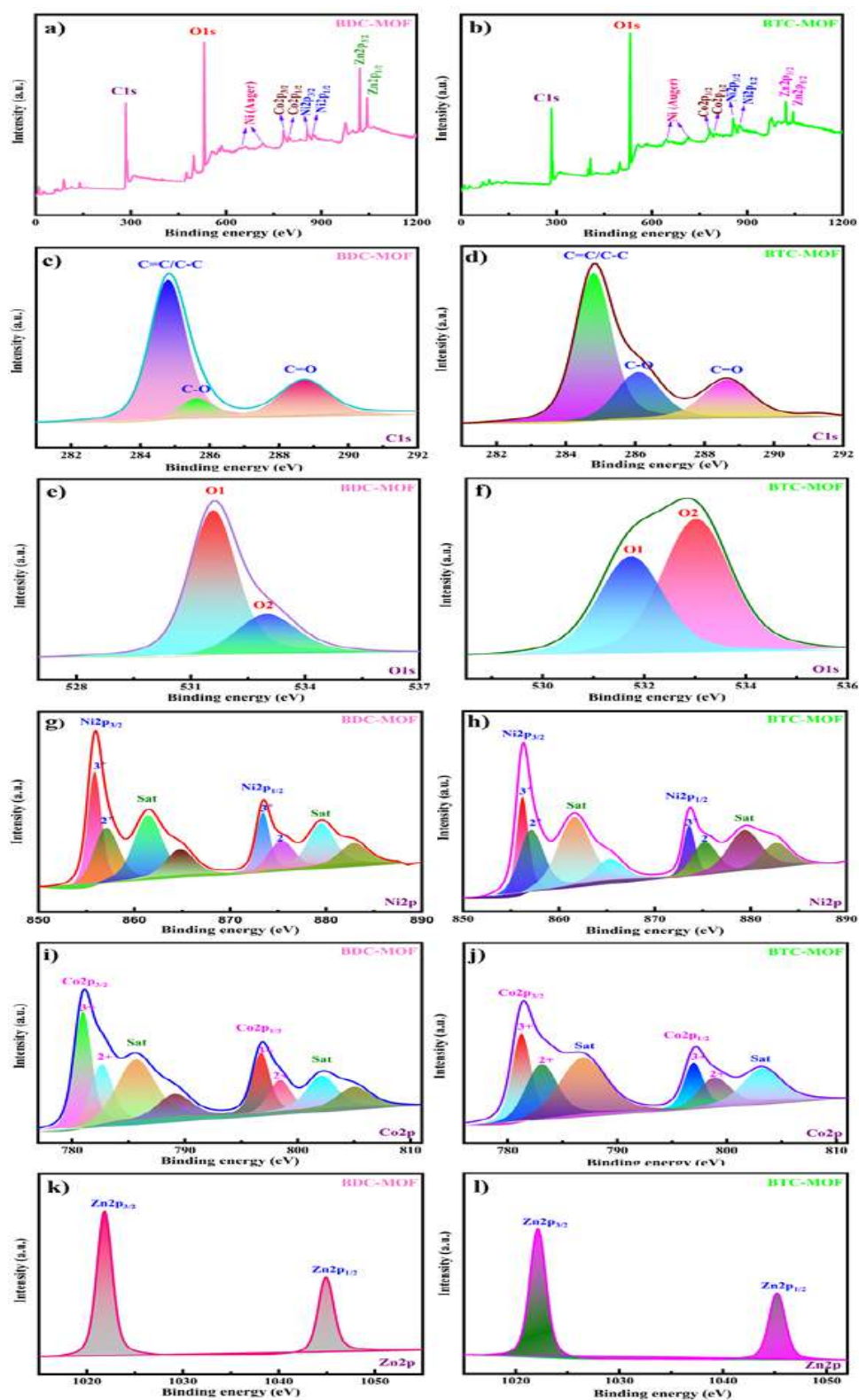


Figure 4.9: XPS survey spectra of BDC-MOF (a) and BTC-MOF (b), high-resolution spectra of C 1s (c, d), O 1s (e, f), Ni 2p (g, h), Co 2p (i, j), and Zn 2p (k, l) of BDC-MOF and BTC-MOF, respectively

Then, carboxylate rings from the (-C=O) groups of the organic ligand with binding energy 288.7 and 288.6 eV, respectively, of both the MOFs and the species -C-O with a binding energy of 285.5 and 286.0 eV are shown.

Furthermore, the O 1s spectra of BDC and BTC MOF are presented in Figure 4.9(e, f), which includes two oxygen peaks denoted as O1 and O2. The first fitted peak at a 531.5 and 531.6 eV binding energy is related to the presence of metal-oxygen bond, i.e., oxygen atoms on the Ni, Co, and Zn-O bonds of both the MOFs, and the second fitted peak at 532.9 eV binding energy is associated with the carboxylate moiety of the organic ligand of MOF samples.⁴⁵ The Ni 2p emission spectrum shows two distinct nickel species, Ni²⁺ and Ni³⁺. The Ni 2p spectra were deconvoluted into two spin-orbit doublets (Ni 2p_{1/2} and Ni 2p_{3/2}) and two satellite peaks using the Gaussian fitting method, as shown in Figure 4.9(g, h). The peak fitted at binding energies of 855.9 and 873.4 eV are ascribed to Ni 2p_{3/2} and Ni 2p_{1/2} for BDC-MOF. Similarly, the binding energies of Ni 2p_{3/2} and Ni 2p_{1/2} for BTC-MOF are 856.2 and 873.6 eV, respectively, as illustrated in Figure 4.9(h). The spin-orbital energy of the Ni peaks in two MOF slightly differs. First, the binding energy difference between these two peaks is determined to be 17.5 eV for BDC-MOF, and the binding energy peak of the “Ni” element was shifted at lower binding energy, i.e., 17.4 eV may be due to the acidic behavior for BTC MOF.

The satellite peaks, as shown in Figure 4.9(i, j), indicate two types of Co species, comprising Co²⁺ and Co³⁺ for two spin-orbit doublets (Co 2p_{1/2} and Co 2p_{3/2}), which were observed as a result of fitting the Co 2p emission spectra of both the MOFs. The fitted peaks with binding energy of 781.0 and 796.8 eV indicate the Co 2p_{3/2} and Co 2p_{1/2}, respectively, for the BDC-MOF sample. The Co peak spin-orbital energies in two MOFs varied slightly from one another. For BDC-MOF, the binding energy difference between these two peaks spin-orbital coupling is found to be 15.8 eV, and the “Co” element’s binding energy peak was relocated to a lower binding energy for BTC MOF, i.e., 15.7 eV. Again the peaks at 781.4 and 797.1 eV are associated to the Co 2p_{3/2} and Co 2p_{1/2} for the BTC-MOF sample. The other satellite peaks of Co elements for both the MOFs samples are also observed in Figure 4.9(i, j).⁴⁶⁻⁴⁸ The peaks at binding energy 1021.8 and 1022.0 eV are assigned to the energy level Zn 2p_{3/2} in BDC-MOF and BTC-MOF, respectively. Similarly, the peaks at 1044.8 and 1045.1 eV are observed for Zn 2p_{1/2} for BDC-MOF and BTC-MOF,

respectively. The detailed deconvolution peaks of Zn 2p_{3/2} and Zn 2p_{1/2} are observed in Figure 4.9(k, l). The differences between the spin-orbital energy of both the MOF samples are nearly equal, confirming that prepared samples are well matched with the literature value of XPS.⁴⁹⁻⁵¹ The calculated binding energy difference among these two peaks spin-orbital coupling is 23 eV, which is in good accordance with the literature value. Moreover, the difference between the spin-orbital energy of the BTC-MOF sample is slightly changed which may be due to the more acidic nature of the BTC-MOF sample.

4.4.9 Electrochemical measurements of trimetallic MOFs

The electrochemical characteristics of the MOF samples were assessed to determine their suitability for usage as active materials in supercapacitors. CV measurements of the as-synthesized MOF hybrid structures with various organic ligands (trimesic acid and terephthalic acid) were performed in a 2 M KOH electrolyte in a potential sweep window of 0-0.5 V, as shown in Figure 4.10. The CV curves of trimetallic MOFs reveal that the integral areas change throughout the operating potential range at 0-0.5 V, indicating that the charge storage mechanism is both pseudocapacitive and electric double layer type. The capacitance is mostly due to the charge stored at the electrode-electrolyte interface. The region beneath the CV curve of BDC-MOF is larger than that of BTC-MOF, as shown in Figure 4.10(a).

In the potential range of 0-0.5 V, the GCD profiles (Figure 4.10b) were examined at a current density of 5 mA cm⁻². As predicted, compared to the BTC-MOF electrode, the BDC-MOF electrode displayed a significantly longer charge/ discharge time and increased specific capacitance. A comparison of the CV curves of both trimetallic MOFs, i.e., BDC-MOF and BTC-MOF (Figure 4.10c, d) at a different scan rate was performed in the potential range of 0-0.5 V. As the scan rate decreases, the area under the CV curve decreases; hence, specific capacitance increases. This occurs due to the complete diffusion of electrolyte ions into the electrode material at slower scan rates. Hence, a charge on the whole active surface of the electrode material may be stored. Only the superficial active surface is used for charge storage at a higher scan rate because diffusion limits the passage of electrolyte ions.⁵² The area under the curve grows from 0 to 0.5 V with a broad range of scan rates from 10 to 100 mV s⁻¹, indicating rapid rates of ionic and electronic transport at the electrode/electrolyte interfaces. The GCD characteristics of BDC-MOF and BTC-MOF electrodes were

investigated at current densities ranging from 5 to 25 mA cm⁻² in 2 M KOH electrolyte across a potential range of 0-0.5 V (Figure 4.10e, f).

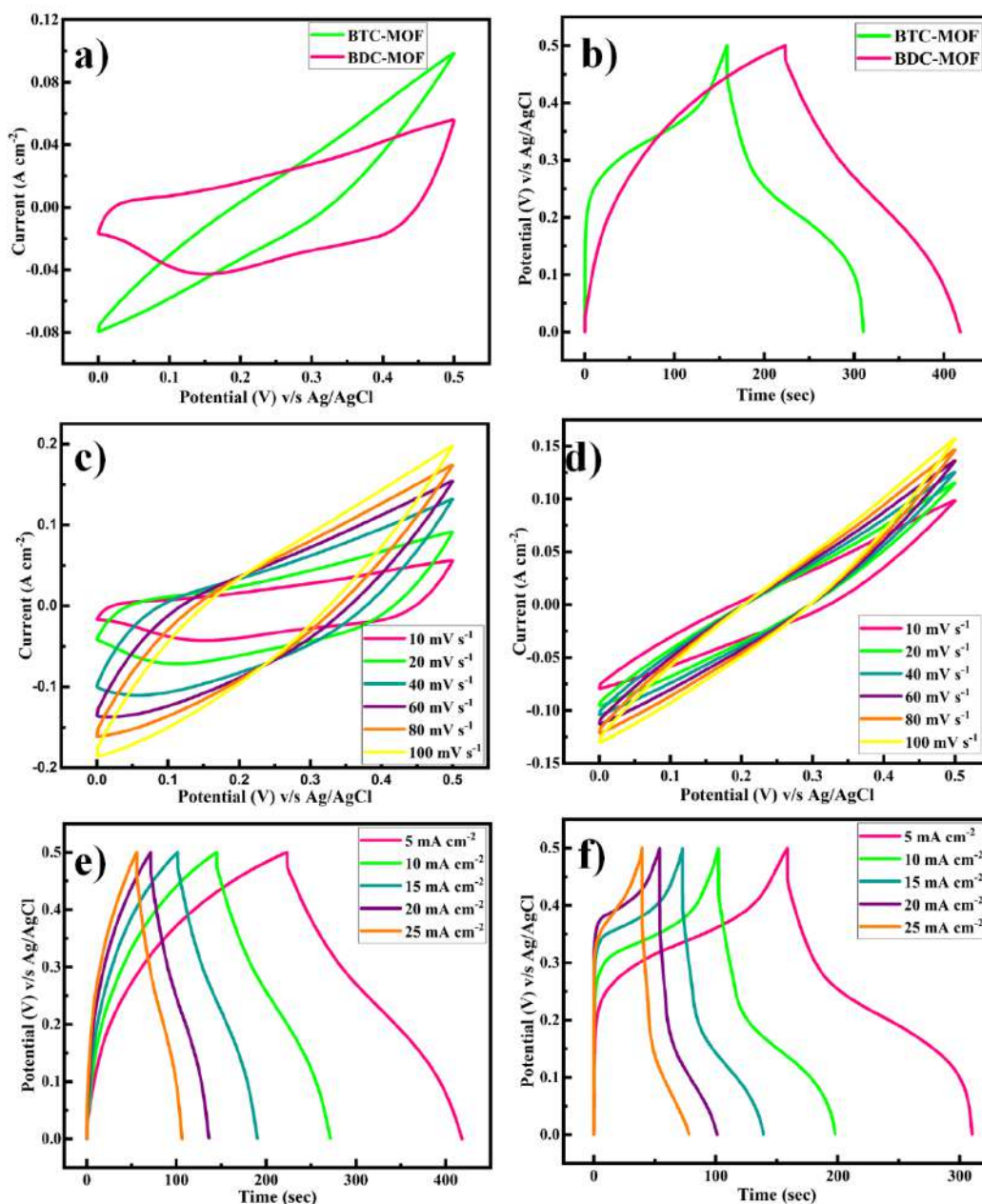


Figure 4.10: (a) Comparative CV curves at 10 mV s⁻¹ scan rate, (b) Comparative GCD curves at 5 mA cm⁻² current density, (c) CV curves of BDC-MOF at different scan rates, (d) CV curves of BTC-MOF at different scan rates, (e) GCD curves of BDC-MOF at different current densities, (f) GCD curves of BTC-MOF at different densities

EIS measurements were performed to determine the internal resistive characteristics as well as the capacitive behavior of the MOF electrode. The Nyquist plots of MOFs in 2 M KOH electrolyte are shown in Figure 4.11(a). A straight line

detected in the lower-frequency portion of the Nyquist plot was due to the migration of electrolyte ions from the bulk solution to the electrode surface. The charge-transfer activity at the electrode/ electrolyte interface is responsible for the presence of a semicircle in the high-frequency zone, and the semicircle diameter shows the charge-transfer resistance (Rct). The charge-transfer resistance of BDC-MOF and BTC-MOF is 0.19 and 0.46 Ω , respectively. BDC-MOF (0.19 Ω) has a lower charge-transfer resistance than BTC-MOF (0.46 Ω). These Rct values show that both electrodes have high electrical conductivities, which are connected to the presence of carbon in their composition, which increases the conductivity of the manufactured electrode. In practice, the carbon in the electrode structure reduces the resistance to charge transfer and improves the connectivity between the active sites for electron transfer.⁵³

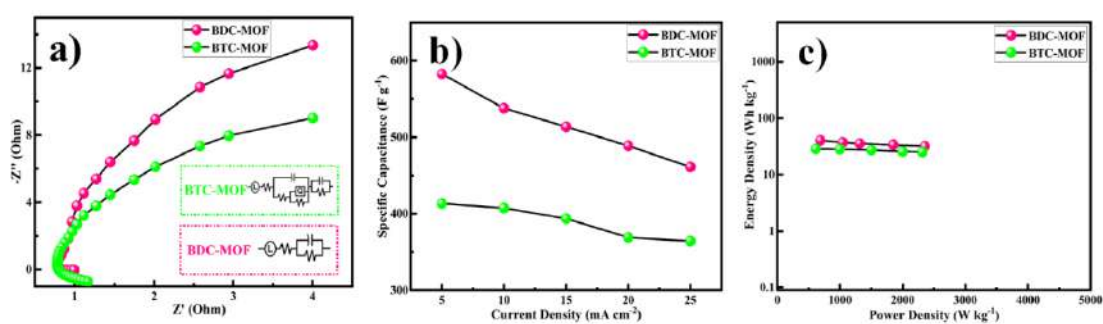


Figure 4.11: (a) Nyquist plots, (b) Variation of specific capacitance as a function of current density, (c) Ragone plot showing the energy density versus power density

Figure 4.11(b) depicts the change of specific capacitance as a function of current density, and Figure 4.11(c) depicts the Ragone plot of energy density vs power density for both trimetallic MOFs. The specific capacitance of the BDC-MOF electrode is 582.8 F g⁻¹ at 5 mA cm⁻² current density, which is more than the specific capacitance of the BTC-MOF electrode, which has 413.4 F g⁻¹ at 5 mA cm⁻² current density, according to the GCD curves. The examined BDC-MOF and BTC-MOF electrodes exhibit a longer charge and discharge time with lowering currents, resulting in greater specific capacitance values, implying that as current increases, the specific capacitance falls in typical behavior. Trimesic acid and terephthalic acid have pKa values of 3.14 and 4.82, respectively. Trimesic acid has a low pKa value, which makes it act as a strong acid since it has a high acidity.⁵⁴ Due to the high acidity, the BTC-MOF electrode gets etched, which degrades the deposition of the film that clogs the pores and prevents the electrolyte from entering the electrode material, increasing resistance and lowering specific capacitance. The cluster of nanoplates that comprise

the porous brick-like morphology of BDC-MOF operate as an “ion-buffering reservoir”, enhancing charge-discharge and shortening the diffusion length for ions to enter the electrode. The charging/discharging curves are also affected by the trimesic and terephthalic ligands; the nature of the curves differs for BDC-MOF and BTC-MOF.

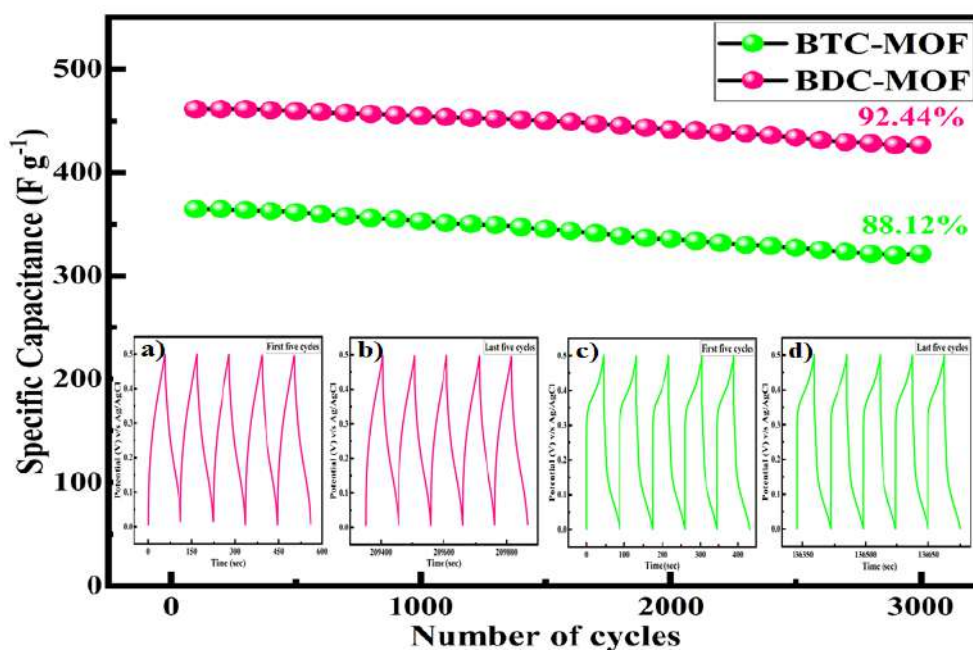


Figure 4.12: Cycling performance at 25 mA cm⁻², and the inset shows the first and last five cycles of BDC-MOF and BTC-MOF

To examine the cyclic stability of the MOF electrodes, the specific capacitance as a function of cycle number was measured at a prolonged current density of 25 mA cm⁻². The BDC-MOF electrode demonstrated good cycling stability after 3000 continuous cycles, with about 92.44% retention of the original capacitance (Figure 4.12). This exceptional long-cycle lifespan was greater than that of the BTC-MOF, which has 88.12% retention even after 3000 GDC cycles at a current density of 25 mA cm⁻², as shown in Figure 4.12. On 1D stainless-steel mesh substrate with substantially poorer electrical conductivity, BDC-MOF demonstrated a remarkable specific capacity of 528.8 F g⁻¹. At all the current densities, the specific capacity of BDC-MOF was relatively high, and a reversible capacity of 461.2 F g⁻¹ can be sustained at an extremely high current density of 25 mA cm⁻², with 86.14% capacity retention compared to the capacity at 5 mA cm⁻², showing a high rate capability. The increase in the cycle number causes a drop in specific capacitance due to the partial leaching of the active electrode material during faradic operations.⁵⁵ The remarkable

energy storage efficiency can be attributed to the combined impact of a group of nanoplates forming the porous bricks, such as morphology, and the huge SSA of the extremely porous material. The electrochemical performance of a few different MOFs that have been previously characterized is compared to that of the synthesized trimetallic MOF in Table 4.1.

Table 4.1: Comparison of the specific capacitances of trimetallic MOFs with previously reported materials

Sr. No.	Material	Electrolyte	Substrate	Specific Capacitance	Current Density	Stability	Ref.
1	NiCoMn-MOF	3M KOH	Nickel foam	907.4 C g ⁻¹	1 A g ⁻¹	64.7%	⁵⁶
2	ZnNi-MOF	3M KOH	Nickel foam	466.5 F g ⁻¹	0.5 A g ⁻¹	44.0%	⁵⁷
3	NiCo-MOF	1M KOH	Nickel foam	1107.3 F g ⁻¹	1 A g ⁻¹	70.1%	⁵⁸
4	Ni/Co-MOF	6M KOH	Nickel foam	982.5 F g ⁻¹	0.5 A g ⁻¹	84.0%	⁵⁹
5	NiCoZn-MOF	2M KOH	Stainless steel mesh	582.8 F g ⁻¹	5 mA cm ⁻²	92.44%	This work

4.4.10 Electrochemical measurements of symmetric supercapacitors device

A SSC device was assembled with BDC-MOF for both electrodes and PVA/KOH gel both as the separator and electrolyte to further evaluate the practical application of the BDC-MOF. The slurry coating method was used to prepare both electrodes. In short, the slurry was made by combining 80 mg of active material (BDC-MOF), 10 mg of PVDF, and 10 mg of carbon black in 0.5 mL of the NMP solvent. The appropriate volume of slurry was then dispersed onto a 2 × 2 cm flexible stainless-steel mesh and air-dried overnight at 60 °C. To avoid electrical contact, the electrode borders were first made non-conducting using a band. The PVA-KOH gel was applied to one side of the electrode, resulting in one point of electrical contact. Both electrodes were eventually patched together in the shape of a sandwich, with gel-pasted sides facing each other. For 12 h, the device was subjected to 1-ton pressure to establish a strong connection between the electrodes and gel electrolyte and to eliminate the air gap. Following that, the device was utilized to evaluate electrochemical performance. CV, GCD, and EIS measurements were performed to

examine the performance of the assembled SSC device. The assembled SSC device CV curves displayed ideal rectangular shapes within an operating voltage window 0.4-1.2 V, demonstrating excellent capacitive behavior. Figure 4.13(a, b) displays CV and GCD profiles of the SSC device within various potential windows and exhibits excellent linear slopes and triangular shapes, which suggest ideal capacitive behavior in line with the CV curves.

In practice, the SSC device's potential window can reach 1.2 V without causing significant changes in the CV and GCD curves, signifying outstanding electrochemical stability. Figure 4.13(c) depicts the SSC device's CV curves at various scan rates. The CV curves remained consistent when the scan rate was raised from 10 mV s^{-1} to 100 mV s^{-1} ; however, the closed regions grew, confirming the symmetric device's high rate capacity. Furthermore, the GCD curves of the SSC device at various current densities are shown in Figure 4.13(d), and the nearly symmetric charge/discharge curves indicate excellent rate capability.

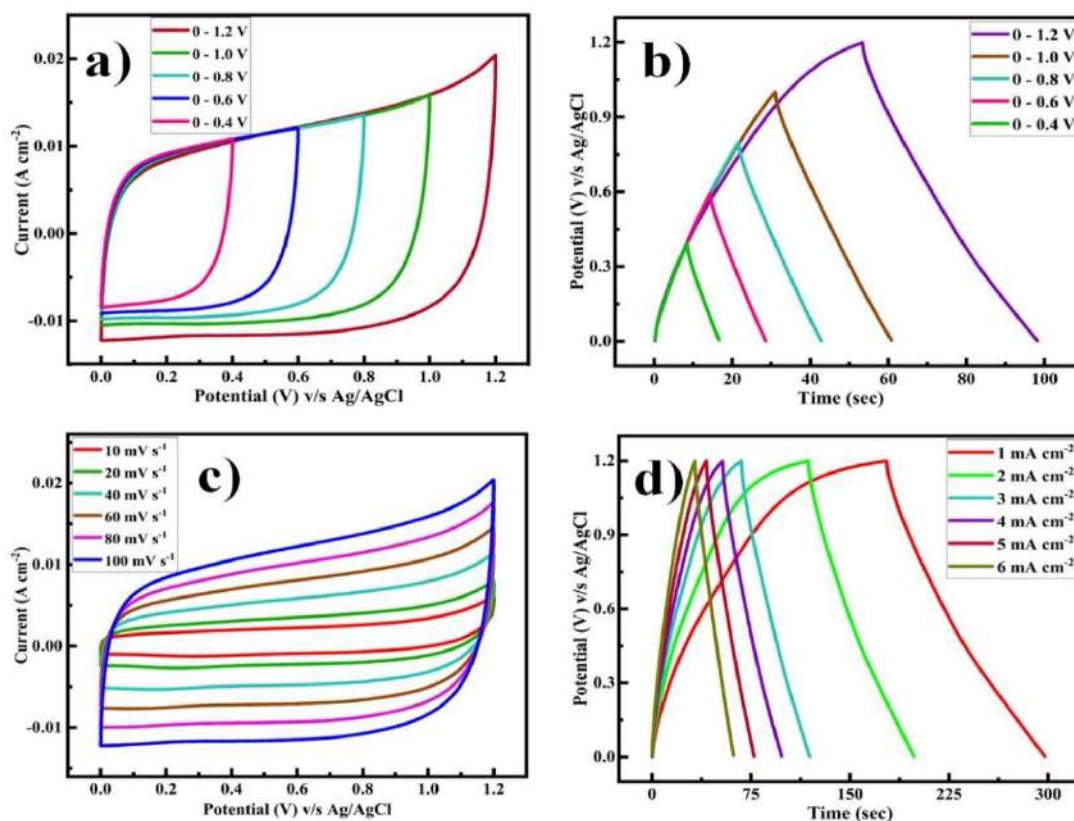


Figure 4.13: (a) CV, (b) GCD curves of the symmetric device within the various potential windows (0.4, 0.6, 0.8, 1.0, and 1.2 V), (c) CV curves of the symmetric device at different scan rates, (d) GCD curves of the symmetric device at different current densities

The EIS studies show that the fabricated SSC device has good electrical conductivity with low ionic resistance and a charge-transfer resistance of 0.4Ω , as depicted in Figure 4.14(a). As a result, the small semicircle diameter reveals low charge-transfer resistance and excellent conductivity. The specific capacities calculated from the discharge curves at current densities of 1, 2, 3, 4, 5, and 6 mA cm^{-2} were 94.92, 93.56, 91.83, 90.67, 89.44, and 87.74 F g^{-1} , respectively (Figure 4.14b). Figure 4.14(c) depicts the Ragone plot of the SSC device, and also the SSC device delivers a high energy density of $47.59 \text{ W h kg}^{-1}$ at a power density of $1367.42 \text{ W kg}^{-1}$. Additionally, at a current density of 6 mA cm^{-2} , the SSC device exhibits outstanding cycling performance, with 99.26% capacitance retention even after 3000 cycles (Figure 4.14d).

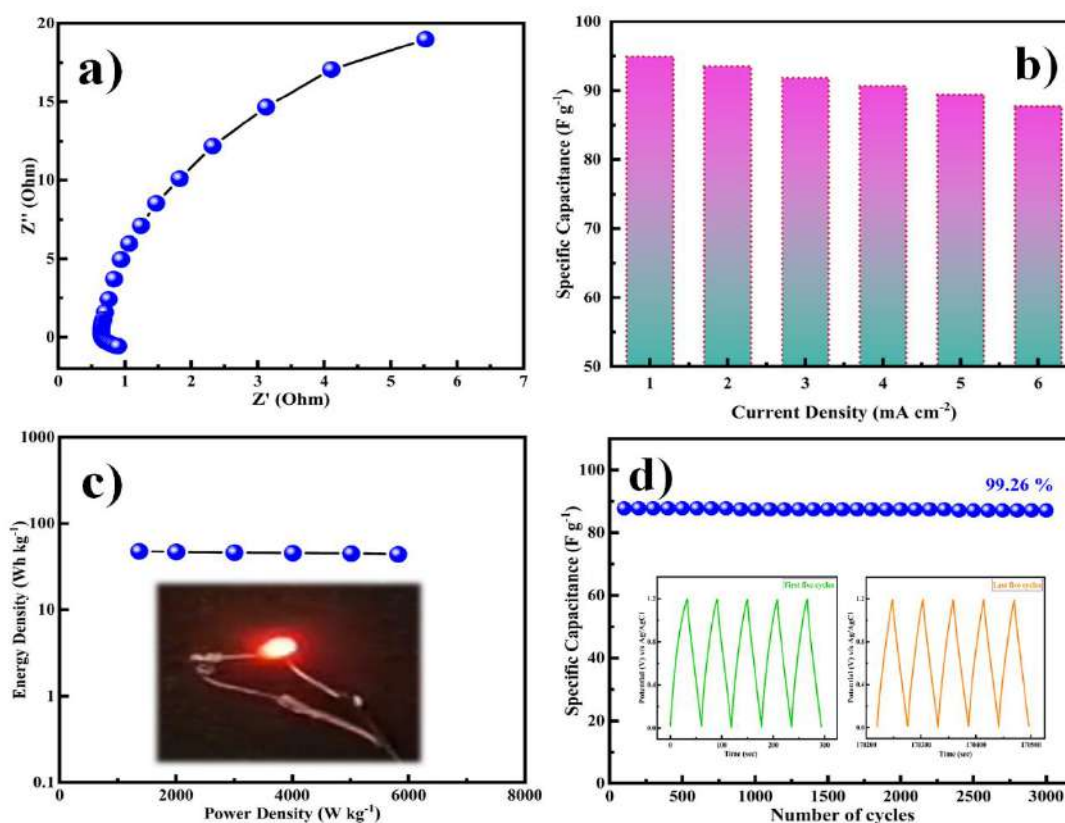


Figure 4.14: (a) Nyquist plot, (b) Variation of specific capacitance as a function of current density, (c) Ragone plot showing the energy density versus power density, (d) Cycling performance at 6 mA cm^{-2} , and the inset shows the first and last five cycles of the symmetric device

Power density and energy density are critical parameters for assessing the supercapacitor electrochemical performance. The BDC-MOF architecture exceptional electrochemical performance is due to its distinct hierarchical structure. Good

electrochemical activity is ensured by the uniform distribution of the brick-like morphology of the nanoplates, and the electrolyte's hierarchical structure offers a high SSA that can make sufficient contact with the electrolyte and enhance ion transport. Finally, the distinct hierarchical structure of the BDC-MOF architecture reduces volume expansion during the cycle process, improving structural integrity and enhancing cycle stability.

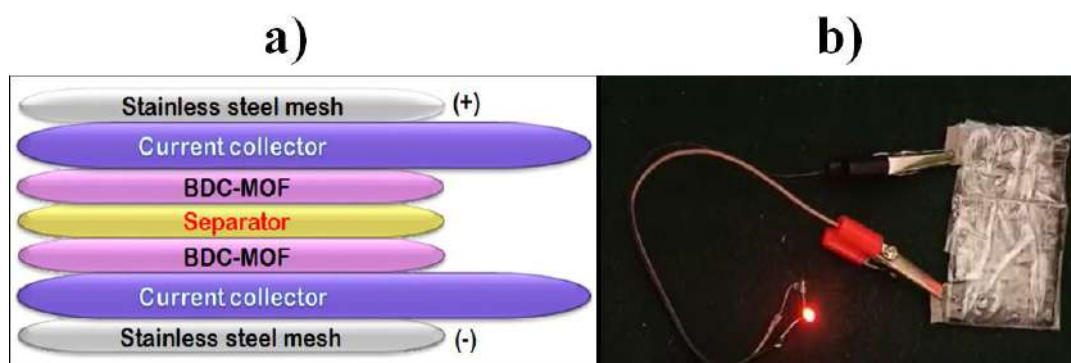


Figure 4.15: (a) Fabrication schematic of BDC-MOF//2M KOH//BDC-MOF symmetric supercapacitor device, (b) Two handmade symmetric supercapacitor device which glows a red LED

The lighting red light-emitting diode (LED) shows that how our SSC device can be used in real applications by connecting two of them in series (where each device is of size 2×2 cm). Figure 15a shows the schematic presentation of the SSC device, and Figure 4.15(b) displays the device's digital image. The LED was glowing brilliantly for about a minute after the device had been charged for just 2 s, demonstrating the astonishing application of our solid-state SSC devices (Supporting Information). The developed capacitor is suitable for use in real-world energy storage and transfer applications because the discharge time is longer than the charging time.

The electrochemical behavior of chemically produced trimetallic MOFs was compared using a radar graph, as shown in Figure 4.16. Each vertex indicates the properties of the different trimetallic MOFs, such as crystallite size, specific capacitance, energy density, power density, stability, charge-transfer resistance, SSA, and average pore radius. The electrochemical performance of trimetallic MOFs is represented by the integral area under the curve. According to Figure 4.16, the integral area of BDC-MOF is greater than that of BTC-MOF. It has been established that the BDC-MOF small crystallite size, large SSA, and low charge-transfer

resistance come up with increased specific capacitance, energy density, power density, and cycle stability.

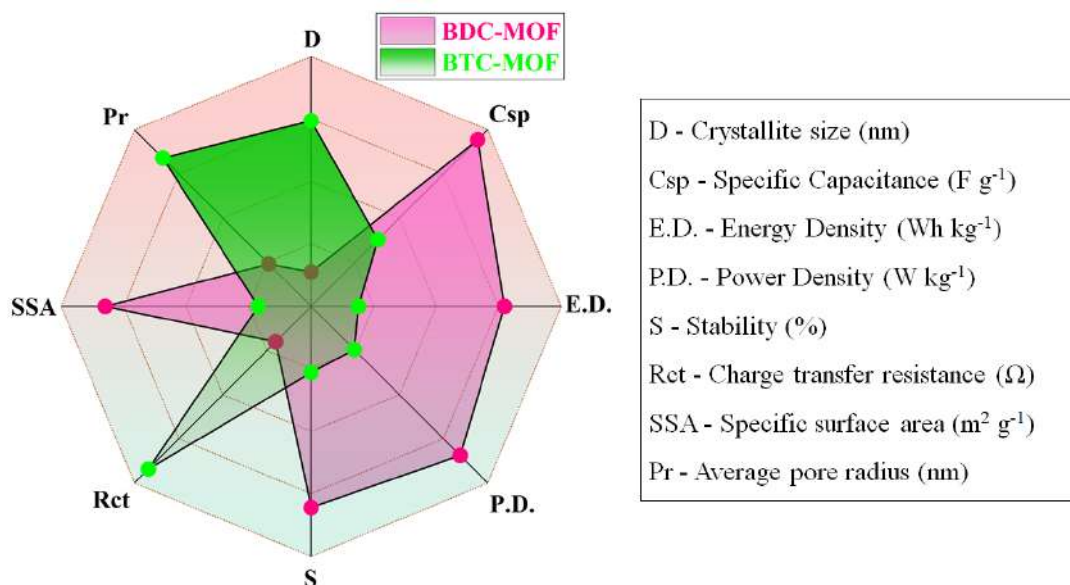


Figure 4.16: Radar graph for comparative study of BDC-MOF and BTC-MOF based on supercapacitive properties

4.5 Conclusion

In outline, a novel 2D architecture of trimetallic MOFs (BDC-MOF and BTC-MOF) as supercapacitor electrode materials was successfully prepared by the reflux condensation method which is simple, low cost, and environmentally friendly. The effects of different ligands of MOFs on the structural, surface, and electrochemical performance of MOF samples have been studied systematically. Due to their nanoplate-like structures with good mechanical and electrical contact, rich redox reactions, low crystallinity, good tuneability, high conductivity and transport rate for both electrolyte ions and electrons, and lower acidity, BDC-MOFs exhibit improved electrochemical performance. The BDC-MOFs show higher capacitance due to the synergistic effect, also they exhibit pseudocapacitive behavior due to the redox activity of metal cations inside MOFs, which offers a channel for electrons, as well as EDLC behavior due to the organic linker structure, which facilitates charge transfer within the framework. The BDC-MOF electrode material achieves a good SSA of 265.87 m² g⁻¹, specific capacity of 582.8 F g⁻¹ at a current density of 5 mA cm⁻², and exceptional cycling stability with 92.44% retention after 3000 cycles at 25 mA cm⁻² due to its porous nature and adequate SSA. The SSC device BDC-MOF//BDC-MOF was built with the BDC-MOF as both electrodes have a high energy density of 47.59

W h kg⁻¹ at a power density of 1367.42 W kg⁻¹ and exceptional cycling stability with 99.26% capacitance retention over 3000 cycles. This novel 2D trimetallic MOF electrode synthesis technique throws light on prospective high-performance MOF-based electrode materials, with the generated BDC-MOF serving as a promising electrode material for better energy storage devices. It is necessary to further enhance the MOF thermal, mechanical, and chemical stability. Since most MOFs decompose and have their skeletons collapse in water, acid, or base, their widespread use in energy storage applications has been severely hampered. Sensible selection of organic ligands and metal secondary building blocks can overcome this issue. The inherent fragility and finite processability of MOFs may also be overcome by using novel methods, such as pressing and phase change treatment operations, without changing their original properties.

4.6 References

- 1 C. Wei, L. Tan, Y. Zhang, Z. Wang, B. Xi, S. Xiong and J. Feng, *EnergyChem.*, 2022, **4**, 100089-100120.
- 2 A. Ray, A. Roy, S. Saha, M. Ghosh, S. Roy Chowdhury, T. Maiyalagan, S. K. Bhattacharya and S. Das, *Langmuir*, 2019, **35**, 8257–8267.
- 3 N. Swain, B. Saravanakumar, M. Kundu, L. Schmidt-Mende and A. Ramadoss, *J. Mater. Chem. A*, 2021, **9**, 25286-25324.
- 4 P. K. Katkar, S. J. Marje, V. G. Parale, C. D. Lokhande, J. L. Gunjekar, H. H. Park and U. M. Patil, *Langmuir*, 2021, **37**, 5260–5274.
- 5 R. Mehek, N. Iqbal, T. Noor, M. Z. B. Amjad, G. Ali, K. Vignarooban and M. A. Khan, *RSC Adv.*, 2021, **11**, 29247–29266.
- 6 X. Zhao, Q. Bi, C. Yang, K. Tao and L. Han, *Dalt. Trans.*, 2021, **50**, 15260–15266.
- 7 D. P. Chatterjee and A. K. Nandi, *J. Mater. Chem. A*, 2021, **9**, 15880–15918.
- 8 Y. A. Sun, L. T. Chen, S. Y. Hsu, C. C. Hu and D. H. Tsai, *Langmuir*, 2019, **35**, 14203–14212.
- 9 G. A. Tafete, M. K. Abera and G. Thothadri, *J. Energy Storage*, 2022, **48**, 103938-103953.
- 10 W. Song, X. Teng, Y. Liu, J. Wang, Y. Niu, X. He, C. Zhang and Z. Chen, *Nanoscale*, 2019, **11**, 6401–6409.
- 11 Y. Bai, C. Liu, T. Chen, W. Li, S. Zheng, Y. Pi, Y. Luo and H. Pang, *Angew. Chemie - Int. Ed.*, 2021, **60**, 25318–25322.
- 12 J. Acharya, G. P. Ojha, B. Pant and M. Park, *J. Mater. Chem. A*, 2021, **9**, 23977–23993.
- 13 X. Cheng, J. Pan, Y. Zhao, M. Liao and H. Peng, *Adv. Energy Mater.*, 2018, **8**, 1702184–2170220.
- 14 X. Lu, M. Yu, G. Wang, Y. Tong and Y. Li, *Energy Environ. Sci.*, 2014, **7**, 2160–2181.
- 15 X. Yin, H. Li, R. Yuan and J. Lu, *J. Colloid Interface Sci.*, 2021, **586**, 219–232.
- 16 M. U. Tahir, H. Arshad, H. Zhang, Z. Hou, J. Wang, C. Yang and X. Su, *J. Colloid Interface Sci.*, 2020, **579**, 195–204.
- 17 W. Li, X. Guo, P. Geng, M. Du, Q. Jing, X. Chen, G. Zhang, H. Li, Q. Xu, P. Braunstein and H. Pang, *Adv. Mater.*, 2021, **33**, 1–9.

- 18 S. Zheng, Q. Li, H. Xue, H. Pang and Q. Xu, *Natl. Sci. Rev.*, 2020, **7**, 305–314.
- 19 Y. Jiao, J. Pei, D. Chen, C. Yan, Y. Hu, Q. Zhang and G. Chen, *J. Mater. Chem. A*, 2017, **5**, 1094–1102.
- 20 S. Akhter, N. K. Mohd Zain, M. Shalauddin, V. K. Singh, I. I. Misnon, R. K. Sharma, S. Das, W. J. Basirun, M. R. Johan and R. Jose, *Sensors Actuators, A Phys.*, 2021, **325**, 112711-112722.
- 21 K. D. Modibane, *Curr. Opin. Electrochem.*, 2022, **36**, 101112–101121.
- 22 C. Kang, L. Ma, Y. Chen, L. Fu, Q. Hu, C. Zhou and Q. Liu, *Chem. Eng. J.*, 2022, **427**, 131003-131103.
- 23 D. Taherinia, H. Hatami and F. Mirzaee Valadi, *J. Electroanal. Chem.*, 2022, **922**, 116720-116729.
- 24 X. G. Han, P. F. Wang, Y. H. Zhang, H. Y. Liu, J. J. Tang, G. Yang and F. N. Shi, *Inorganica Chim. Acta*, 2022, **536**, 120916-120927.
- 25 B. Zhang, S. Song, W. Li, L. Zheng and X. Ma, *Ionics*, 2021, **27**, 3553–3566.
- 26 X. Luo, R. Abazari, M. Tahir, W. K. Fan, A. Kumar, T. Kalhorizadeh, A. M. Kirillov, A. R. Amani-Ghadim, J. Chen and Y. Zhou, *Coord. Chem. Rev.*, 2022, **461**, 214505-214529
- 27 H. Wang, J. Li, K. Li, Y. Lin, J. Chen, L. Gao, V. Nicolosi, X. Xiao and J. M. Lee, *Chem. Soc. Rev.*, 2021, **50**, 1354–1390.
- 28 R. Rajak, R. Kumar, S. N. Ansari, M. Saraf and S. M. Mobin, *Dalt. Trans.*, 2020, **49**, 11792–11818.
- 29 Y. Seo, P. A. Shinde, S. Park and S. Chan Jun, *Electrochim. Acta*, 2020, **335**, 135327–135336.
- 30 G. Nagaraju, S. C. Sekhar, B. Ramulu, S. K. Hussain, D. Narsimulu and J. S. Yu, *Nano-Micro Lett.*, 2021, **13**, 1–18.
- 31 Z. Andikaey, A. A. Ensafi, B. Rezaei, S. S. Malek and J. S. Hu, *New J. Chem.*, 2021, **45**, 18090–18101.
- 32 R. Bhosale, S. Bhosale, P. Kumbhar, D. Narale, R. Ghaware, C. Jambhale and S. Kolekar, *New J. Chem.*, 2023, **47**, 6749–6758.
- 33 S. Liu, S. C. Lee, U. Patil, I. Shackery, S. Kang, K. Zhang, J. H. Park, K. Y. Chung and S. Chan Jun, *J. Mater. Chem. A*, 2017, **5**, 1043–1049.
- 34 H. Vijeth, S. P. Ashokkumar, L. Yesappa, M. Niranjana, M. Vandana and H. Devendrappa, *RSC Adv.*, 2018, **8**, 31414–31426.
- 35 S. Gopi, S. Perumal, E. M. Al Olayan, O. D. AlAmri, A. S. Aloufi, M.

- Kathiresan and K. Yun, *Chemosphere*, 2021, **267**, 129243–129254.
- 36 Y. Li, M. Lu, Y. Wu, H. Xu, J. Gao and J. Yao, *Adv. Mater. Interfaces*, 2019, **6**, 1900290–1900298.
- 37 M. M. Vadiyar, S. S. Kolekar, N. G. Deshpande, J. Y. Chang, A. A. Kashale and A. V. Ghule, *Ionics*, 2017, **23**, 741–749.
- 38 N. K. Gupta, S. Kim, J. Bae and K. S. Kim, *RSC Adv.*, 2021, **11**, 4890–4900.
- 39 S.-M. You, W. M. A. El Rouby, L. Assaud, R.-A. Doong and P. Millet, *Hydrogen*, 2021, **2**, 58–75.
- 40 H. Li, J. Qin, Y. Zhang, S. Xu, J. Du and J. Tang, *RSC Adv.*, 2018, **8**, 39352–39361.
- 41 Q. Zha, M. Li, Z. Liu and Y. Ni, *ACS Sustain. Chem. Eng.*, 2020, **8**, 12025–12035.
- 42 V. H. Nguyen, T. D. Nguyen and T. Van Nguyen, *Top. Catal.*, 2020, **63**, 1109–1120.
- 43 R. Kaur, M. Chhibber, P. Mahata and S. K. Mittal, *ChemistrySelect*, 2018, **3**, 3417–3425.
- 44 K. S. W. Sing, D. H. Everett, R. A. W. Haul, L. Moscou, R. A. Pierotti, J. Rouquerol, T. Siemieniewska, (Recommendations 1984). *Pure Appl. Chem.* 1985, **57**, 603–619.
- 45 N. K. Mohd Zain, C. Karupppiah, I. I. Misnon, S. Das, K. Ikechukwu Ozoemena, C. C. Yang and R. Jose, *Electroanalysis*, 2020, **32**, 3180–3188.
- 46 L. G. Beka, X. Bu, X. Li, X. Wang, C. Han and W. Liu, *RSC Adv.*, 2019, **9**, 36123–36135.
- 47 H. Shu, T. Lai, J. Ren, X. Cui, X. Tian, Z. Yang, X. Xiao and Y. Wang, *Nanotechnology*, 2022, **33**, 135502–135517.
- 48 P. Thangasamy, S. Shanmuganathan and V. Subramanian, *Nanoscale Adv.*, 2020, **2**, 2073–2079.
- 49 Y. Wu, X. Song, S. Xu, Y. Chen, O. Oderinde, L. Gao, R. Wei and G. Xiao, *Dalt. Trans.*, 2020, **49**, 312–321.
- 50 J. Lin, C. Zeng, X. Lin, R. C. K. Reddy, J. Niu, J. Liu and Y. Cai, *ACS Sustain. Chem. Eng.*, 2019, **7**, 15660–15670.
- 51 Y. ping Wei, Y. wen Zhang, J. S. Chen, C. jie Mao and B. K. Jin, *Microchim. Acta*, 2020, **187**, 1–9.
- 52 M. R. Manikandan, K. P. Cai, Y. D. Hu, C. L. Li, J. T. Zhang, Y. P. Zheng, Y.

- F. Liang, H. R. Song, M. Y. Shang, X. N. Shi, J. X. Zhang, S. Q. Yin, S. Y. Shang and X. W. Wang, *Appl. Phys. A Mater. Sci. Process.*, 2021, **127**, 421–431.
- 53 W. W. Song, B. Wang, C. N. Li, S. M. Wang and Z. B. Han, *J. Mater. Chem. A*, 2022, **10**, 3710–3721.
- 54 G. Mouchaham, S. Wang and C. Serre, *Metal-Org. Frameworks: Applications in Separations and Catalysis*, 2018, 1–28.
- 55 M. Suksomboon, P. Srimuk, A. Krittayavathananon, S. Luanwuthi and M. Sawangphruk, *RSC Adv.*, 2014, **4**, 56876–56882.
- 56 M. Ashourdan, A. Semnani, F. Hasanpour, S. E. Moosavifard, *J. Electroanal. Chem.* 2021, **895**, 115452-115463.
- 57 Y. Zhu, Z. Tao, C. Cai, Y. Tan, A. Wang, Y. Yang, *Inorg. Chem. Commun.* 2022, **139**, 109391-109400.
- 58 X. Zhang, J. Wang, X. Ji, Y. Sui, F. Wei, J. Qi, Q. Meng, Y. Ren, Y. He, D. Zhuang, *J. Mater. Sci. Mater. Electron.* 2020, **31**, 16260–16268.
- 59 X. Kang, J. Wang, Y. Ma, X. Shi, X. Chen, H. Tian, F. Ran, *J. Solid State Chem.* 2022, **310**, 123056-123067.

CHAPTER FIVE

Bimetallic MnFe₂-MOF and Its Derived MnFe₂O₄ Nanostructures for Supercapacitive Applications

5.1 Outline

At present, supercapacitor (SC) based on metal-organic frameworks (MOFs) has gained a lot of attention in energy storage and conversion application because of their fascinating properties such as low densities, variable chemical functions, high surface area, and porosity. The chapter covers the synthesis of bimetallic MOF and MOF-derived ferrites via chemically wet route and heat treatment process respectively. This prepared electrode material was utilised to construct the asymmetric supercapacitor devices. The MnFe₂-MOF electrode exhibits outstanding electrochemical properties over the derived MnFe₂O₄ along with high reversibility, fast kinetics, low charge transfer resistance (2.9 Ω), the excellent specific capacitance of 1226 F g⁻¹ at a current density of 1 A g⁻¹ with a superb cyclic stability of approximately 95.68 % of the initial capacitance even after 3000 subsequent charge-discharge cycles. Additionally, to confirm the practical viability of MnFe₂-MOF as an anode and activated carbon as a cathode, an asymmetric device was fabricated. The fabricated asymmetric device demonstrates an excellent specific capacitance of 91.87 F g⁻¹ at a 1 mA cm⁻² current density with a specific energy of 32.67 Wh kg⁻¹ and a high specific power of 1000 W kg⁻¹. Simultaneously, the fabricated ASC device unveil exceptional cyclic stability (98.52 %) and coulombic efficiency (96.75 %) of at a higher current density of 8 mA cm⁻² even after 3000 charge-discharge cycles. These perceptible results based on MOF-derived ferrite nanostructure can make it significant electrode material for supercapacitor application in today's technological applications.

5.2 Introduction

Energy storage technologies are being developed rapidly to fulfil global demand owing to the exhaustion of fossil fuels and associated environmental problems. To meet the long-term development demands of our civilization, the use of inexhaustible energies like solar, tidal, and wind in energy infrastructure has increased dramatically. Nevertheless, because sustainable energies are intermittent, the electricity produced from them cannot be straight away connected to the power system.¹⁻³ Hence, the construction of reliable and effective electrical energy storage (EES) systems is urgently required. Innovative energy storage systems and next-generation energy storage and conversion technologies have successfully been developed through study and exploration. The SC (electrochemical capacitor), a new kind of energy storage component in the middle of rechargeable batteries and conventional capacitors. It is utilized extensively in the fields of electronic appliances, defence, automobiles, communication technologies etc. due to its benefits of quick charge and discharge, enduring lifespan, high power potential, strong rate performance, energy savings, and environmental protection.⁴⁻⁷ Supercapacitors are still limited in their utility in many real-world scenarios because of their poor energy density. By utilizing porous materials in supercapacitors, it has been attempted to boost energy density by enhancing specific capacitance and extending the operating potential window of electrode materials.^{8,9}

Metal-organic frameworks are crystalline porous materials with attractive features like enormous surface area, well-defined crystalline structure, low density and effortlessly tunable structure and highly organized pores/channels. Metal-ligand coordination, metal cluster copolymerization, and interactions between hydrogen bonds have all been used as a scheme for assembling these frameworks. Several similar frameworks have been discovered to display favourable zeolitic characteristics like stability and microporosity.^{10,11} MOFs have been regarded as useful predecessors or sacrificial templates to produce unique porous nanomaterials with attractive features because of their varied topologies.^{12,13} Ferrites are appealing materials owing to their remarkable magnetic, electrical, and optical characteristics, also their capacity to show many redox states and electrochemical stability.

Throughout transition metal oxide derived from MOFs, iron-based MOF-derived transition metal oxides have superior electrical conductivity and much lower

charge activation energies. It has mixed valencies Fe²⁺ and Fe³⁺ which contribute to enhancing electrical conductivity.¹⁴⁻¹⁷ Patil et al. synthesized NiFe₂O₄ derived from NiFe₂ MOF using a solvothermal method followed by a heating process i.e. annealing. They have observed different morphologies like grains, mesh-like structures and threads at 550 °C (NFO550), 500 °C (NFO 500) and 460 °C (NFO460), respectively; hence morphology has been greatly influenced by the annealing temperatures. The NiFe₂O₄ electrode annealed at 500 °C (NFO500) temperature shows sharp-edged rhombus nanoplates with an interwoven mesh-like structure with mesoporous nature of the surface area of 38.17 m² g⁻¹. The NFO500 electrode derived from MOF shows the highest specific capacitance as compared to NFO460 and NFO550 electrodes. The NFO500 electrode reveals 833 F g⁻¹ specific capacitance at 0.25 A g⁻¹ current density with an outstanding capacitance retention of 74 % even after 3000 charge-discharge cycles at 3 A g⁻¹ current density. The mesh-like architecture that allows the migration of OH⁻ ions within the electrode and the small recombination resistance among the electrode and electrolyte contact are responsible for the good electrochemical performance of MOF-derived NFO500 in comparison to NFO460 and NFO550 electrodes. This research has the doors to modifying the morphologies of nanostructures produced from MOF for supercapacitor applications.¹⁸ Safari et al. synthesized Fe₂Co-MOF derived cobalt ferrite (CoFe₂O₄) nanostructured using a simple ultrasonic-assisted solvothermal method followed by calcination. During thermal treatment at 450 °C in air, the spindle shape of Fe₂Co-MOF converts into the yolk-shell morphology of CoFe₂O₄. The specific capacitance of Fe₂Co-MOF and CoFe₂O₄ electrodes are 489.9 and 192.6 F g⁻¹ at 1 A g⁻¹ current density, respectively, owing to a decrease in active sites on the CoFe₂O₄ electrode and low metal oxide conductivity. The cyclic stability of Fe₂Co-MOF and CoFe₂O₄ electrodes was investigated at 10 A g⁻¹ current density for 3000 cycles. The retention rates for Fe₂Co-MOF and CoFe₂O₄ electrodes were 92 % and 90 %, respectively. Further, they have fabricated an asymmetric supercapacitor device using Fe₂Co-MOF and activated carbon electrodes as anode and cathode respectively, which demonstrated that constructed electrodes are well-suited for energy storage applications.¹⁹

There are numerous reports for the synthesis of iron based bimetallic MOFs by using simple one-pot solvothermal reaction for exotics applications. However, to the best of our knowledge the synthesis of MnFe₂-MOF via reflux condensation method for energy storage application has not been reported so far. Inspired of this, the porous

magnetic MnFe₂O₄ has been successfully synthesized using a MnFe₂-MOF as a self-sacrificing template as well as predecessor. The synthesis comprises merely a simple reflux condensation to form MnFe₂-MOF, subsequent thermal annealing in air. Furthermore, the synthesized MnFe₂-MOF was employed as an electrode material for electrochemical experiments. MnFe₂-MOF showed a greater specific capacitance value than the rest of the sample. Furthermore, the fabricated asymmetric device shows an excellent specific capacitance of 91.87 F g⁻¹ at a 1 mA cm⁻² current density with a maximum specific energy of 32.67 Wh kg⁻¹ and a high specific power of 1000 W kg⁻¹.

5.3 Experimental section

5.3.1 Materials

Ferrous chloride tetrahydrate (FeCl₂·4H₂O) was purchased from Merck, USA. Terephthalic acid, N-Methyl-2-pyrrolidone (NMP) and polyvinylidene fluoride (PVDF) were purchased from Sigma-Aldrich, USA. Manganese chloride tetrahydrate (MnCl₂·4H₂O) and Acetylene black were obtained from, Loba Chemie, India and Alfa Aesar, USA respectively. All reagents were used without any further purification.

5.3.2 Synthesis of MnFe₂-MOF and MnFe₂O₄

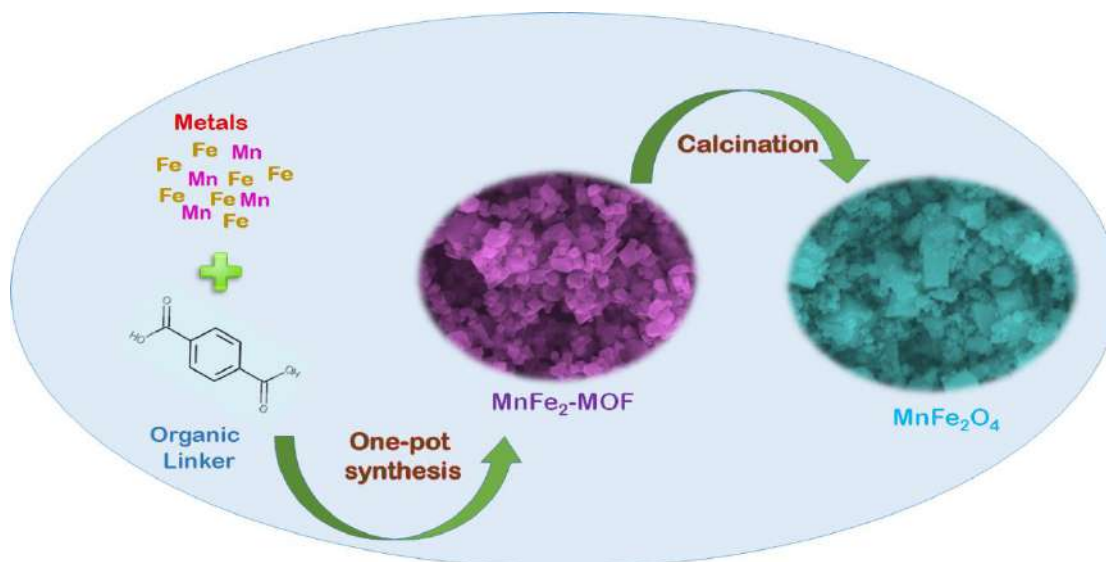


Figure 5.1: Schematic diagram of MnFe₂-MOF derived manganese ferrite (MnFe₂O₄)

The Mn/Fe metal-organic framework (MnFe₂-MOF) was synthesized by using a typical procedure. 0.1 M manganese chloride tetrahydrate and 0.2 M ferrous chloride tetrahydrate were dissolved in 25 ml N, N-dimethylformamide (DMF), and stirred well. 0.2 M terephthalic acid was then dissolved in 25 ml N, N-dimethylformamide (DMF) and add to it above metal salt solution. Then, after stirring

the solution for 10 min it was transferred to a round bottom flask maintained at 120 °C for 12 h. The subsequent brown-colored precipitate was collected by a DMF washing and drying process at 70 °C overnight and was referred as MnFe₂-MOF. The MOF-derived manganese ferrite (MnFe₂O₄) was prepared by thermal heating i.e. annealing of MnFe₂-MOF at 500 °C for 2 h in air and cooled at ambient temperature. Figure 5.1 shows the schematic presentation of synthesis of MnFe₂-MOF and its derived MnFe₂O₄.

5.3.3 Structural and elemental characterization

Crystal structure and phase purity of MnFe₂-MOF and derived MnFe₂O₄ were investigated by Bruker D8 Phaser X-ray diffractometer with Cu K α radiation ($\lambda=0.1541$ nm). The Perkin Elmer 1760X spectrophotometer was used to record Fourier Transform Infrared spectra between 400 and 4000 cm⁻¹. Raman spectra of MnFe₂-MOF and derived MnFe₂O₄ samples were studied by Renishaw in via Raman spectrometer by using a He-Ne (633 nm) laser excitation source. The surface morphology and elemental confirmation of the prepared samples were obtained from scanning electron microscopy and Energy dispersive X-ray Analysis spectrometer (EDAX, Oxford Instrumentations inbuilt with FE-SEM). Also, the surface morphology with d-spacing of the MnFe₂-MOF and derived MnFe₂O₄ samples were found by using transmission electron microscopy (TEM) analysis from Hitachi/HF-3300 TEM (300 kV). The oxidation states of the metals in the MnFe₂-MOF and derived MnFe₂O₄ was investigated using X-ray photoelectron spectroscopy (XPS) with a Thermo Fisher Scientific SIGMA PROBE. The porosity of the materials was investigated on NOVA1000e Quantachrome (BET), USA. The magnetic behavior of the MnFe₂-MOF and derived MnFe₂O₄ samples were investigated by using Vibrating-sample magnetometer (VSM) from superconducting quantum interference device (SQUID) vibrating sample magnetometry (VSM) (Quantum Design, USA).

5.3.4 Electrochemical properties evaluation and preparation of working electrodes

All electrochemical measurements were carried out on an electrochemical workstation (CHI 608E, CH instrument co., LTD, USA) for parameters like cyclic voltammograms (CV), galvanostatic charge-discharge (GCD), and electrochemical impedance spectra (EIS) at ambient temperature in 1 M Na₂SO₄ as a neutral electrolyte. The working electrodes were made by using a composition of 80:10:10 weight % of active material (MnFe₂-MOF and MnFe₂O₄), acetylene black and

polyvinylidene fluoride in N-Methyl-2-pyrrolidone as a solvent respectively to prepare a homogeneous paste. The obtained homogenous paste was coated on an unprecedented substrate stainless steel mesh area of 1 x 1 cm² and dried in an oven at 70 °C for 10 hours and used as the current collector. A three-electrode setup was employed to evaluate the electrochemical properties of the prepared electrodes by using an active material loaded stainless steel mesh, graphite, and a saturated Ag/AgCl as the working electrode, counter electrode, and reference electrode, respectively. CV curves were measured at different scan rates ranging from 10 to 100 mV s⁻¹ and GCD curves were measured at various current densities ranging from 1 to 10 mA cm⁻² in the operating potential window of 0 to 0.5 V.^{20,21}

For solid-state supercapacitor device fabrication, a solid gel electrolyte was prepared, 20 ml of distilled water was used to dissolve 1 g of polyvinyl alcohol (PVA) while maintaining bath solution at 80°C for 30 minutes. The sticky gel electrolyte was prepared by adding the aqueous Na₂SO₄ solution dropwise to the above PVA solution and heated it at 80 °C for 30 minutes.²² A solid-state asymmetric supercapacitor device (MnFe₂-MOF//AC) was constructed by using MnFe₂-MOF and AC electrode as anode and cathode respectively, a filter paper and PVA-Na₂SO₄ gel was employed as a separator and it was assembled between the two electrodes. The electrodes effective area for the devices were 2 x 2 cm². CV was measured at different scan rates and GCD was measured at different current densities of asymmetric supercapacitor device in potential range of 0 - 1.6 V. Cyclic stability measurement was performed in the 0 - 1.6 V range for the asymmetric supercapacitor device.

The specific capacity, specific energy density and specific power density were determined from charge-discharge cycles of the fabricated asymmetric supercapacitor devices using equations 5.1 to 5.3,²³⁻²⁵

$$C_s = \frac{I \times \Delta t}{m \times \Delta V} \dots\dots\dots (5.1)$$

$$E = \frac{C_s \times (\Delta V)^2}{7.2} \dots\dots\dots (5.2)$$

$$P = \frac{E \times 3600}{\Delta t} \dots\dots\dots (5.3)$$

Where, ‘C_s’ is the specific capacity measured in F g⁻¹, ‘E’ is the specific energy density measured in Wh kg⁻¹, ‘P’ is the specific power density measured in W kg⁻¹, ‘I’ is the discharge current measured in ampere, ‘Δt’ is the discharge time

measured in seconds, ‘m’ is the mass of the electrode material measured in grams, ‘ΔV’ is the potential window measured in volt in the process.

5.4 Results and discussion

5.4.1 X-ray diffraction of MnFe₂-MOF and MnFe₂O₄

X-ray diffraction was used to investigate the structural analysis and crystallite size of the MnFe₂-MOF and its derived manganese ferrite, as depicted in figure 5.2. The peaks were observed at 9.32°, 9.86°, 17.8°, 25.46° and 33.42° for MnFe₂-MOF are in good agreement with the earlier reported MnFe₂-MOF.²⁶ MnFe₂O₄ pattern observed peaks at 30.34°, 35.5°, 42.88°, 53.98° and 62.32° are assigned to the crystal planes of (220), (311), (400) and (440) respectively. The XRD pattern of derived MnFe₂O₄ shows cubic phase which is well matched with the literature value (JCPDS card No. 10-0319).²⁷ There are no additional peaks that suggests the purity of the prepared samples. According to the Debye-Scherrer’s equation, the average crystallite size were 7.8 and 15.6 nm of MnFe₂-MOF and its derived MnFe₂O₄, respectively.²⁸

$$D = \frac{0.9\lambda}{\beta \cos \theta} \dots\dots\dots (5.4)$$

Where, D stands for crystalline size, λ stands for the wavelength of X-rays emitted from the target, θ stands for the Bragg diffraction angle of the diffraction peaks, and β stands for the full width at half maximum (FWHM) of the diffraction peak. The smallest crystallite size was observed for MnFe₂-MOF sample as compared to the derived sample, which is helpful for the charge transportation in application part.

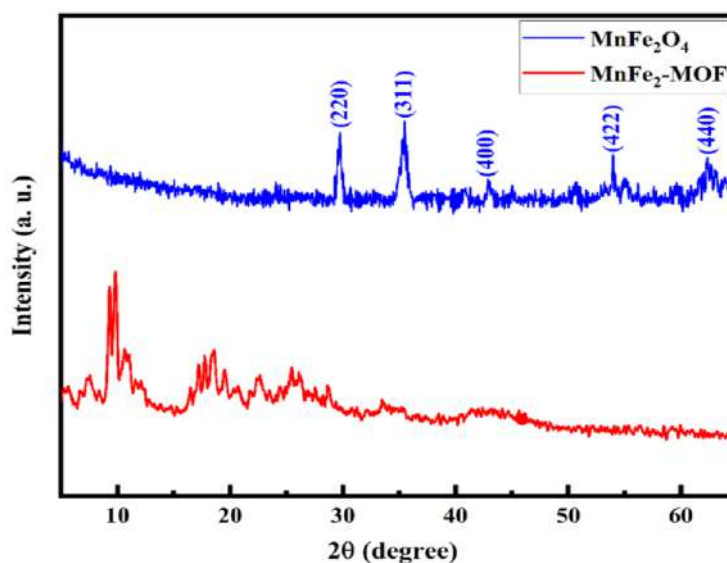


Figure 5.2: X-ray diffraction patterns of MnFe₂-MOF and its derived MnFe₂O₄

5.4.2 FT-IR spectroscopy of MnFe₂-MOF and MnFe₂O₄

To investigate the functional groups and molecular structure of the MnFe₂-MOF and its derivate MnFe₂O₄, Fourier transform infrared spectroscopy (FT-IR) was used. The FT-IR spectra of MnFe₂-MOF and its derived MnFe₂O₄ as shown in figure 5.3. In FT-IR spectra the absorption peaks at 1599 and 1379 cm⁻¹ in MnFe₂-MOF is attributed to the symmetric and asymmetric vibrations of the carboxylate group of ligand and the absorption band at 748 cm⁻¹ is assigned for C-H vibration of the benzene ring. Furthermore, the absorption peak appear at 534 cm⁻¹ in the MnFe₂-MOF spectrum indicate the oscillation of the metal-oxygen bonds.²⁹ In MnFe₂O₄ spectra, the peaks in the range of 400-600 cm⁻¹ are due to the Mn-O and Fe-O bonds of spinel form oxide.³⁰

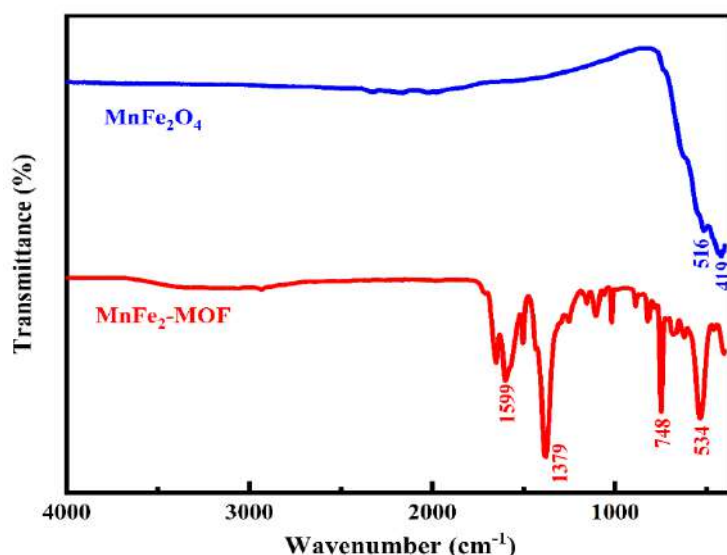


Figure 5.3: FT-IR spectra of MnFe₂-MOF and its derived MnFe₂O₄

5.4.3 Raman spectroscopy of MnFe₂-MOF and MnFe₂O₄

Raman spectroscopy study was used to explore the structural irregularities of MnFe₂-MOF and its derived MnFe₂O₄ at ambient temperature which is shown in figure 5.4. Raman spectra of MnFe₂-MOF shows a measurable peak at 1609 cm⁻¹ is assigned to the C=O stretching of carboxylate group, considering that the peaks at 1430 and 1140 cm⁻¹ are assigned to in-plane vibration modes of benzene ring and a small peak at 862 cm⁻¹ corresponds to the out-of-plane deformation of C-H bond.^{31,32} Raman spectra of MnFe₂O₄ shows four distinct peaks at 200-700 cm⁻¹ range as shown in figure 5.4. The noticeable four peaks in the spectrum at 217, 280, 391 and 595 cm⁻¹ are assigned to the stretching vibrational modes of MnFe₂O₄. And the peaks at 391 and 595 cm⁻¹ appear from E_g and T_{2g} vibrational modes, respectively.^{33,34}

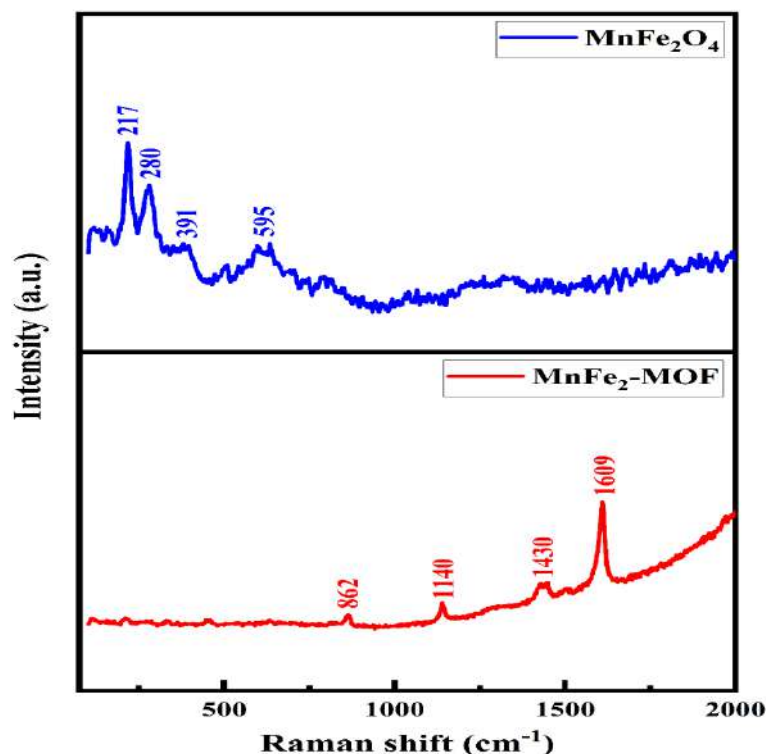


Figure 5.4: Raman spectra of MnFe₂-MOF and its derived MnFe₂O₄

5.4.4 Scanning electron microscopy of MnFe₂-MOF and MnFe₂O₄

The surface morphologies of the MnFe₂-MOF and its derived MnFe₂O₄ were characterized by SEM techniques and depicted in figure 5.5. It is observed that the cubic and bricks like morphology were obtained from MnFe₂-MOF and MnFe₂O₄, respectively as shown in figure 5.5(a-d). The lower and higher magnification of MnFe₂-MOF reveals that the size of the cube was irregular in shape but uniformity of the cubes was observed throughout the sample. Moreover, the surface of the cube became rougher and more porous in nature as shown in figure 5.5(a-b). The average length of the cube was measured to be approximately 200-300 nm in size. Also, more interestingly the voids are formed between the big cubes and small cubes. This voids and cube like morphology support in ion transfer and store more ions which were helpful for improving the electrochemical performance. Similarly, the SEM images of MnFe₂-MOF derived MnFe₂O₄ are as shown in figure 5.5(c-d) wherein, it was observed that there is a bricks like morphology with some nanoparticles. Also, it was observed that bricks were irregular in shape as well as the cracks of the bricks converted into small pieces have adverse effect on the redox reaction. These bricks were compacted to each other and some of the space was covered by nanoparticles hence there were no voids for adsorption of electrolyte, resulting in the decrease in the

active surface area for redox reaction. Overall, it could be concluded that the MnFe₂-MOF is most favourable for improving the electrochemical performance of MnFe₂-MOF based supercapacitor electrode than MOF derived MnFe₂O₄ electrode.

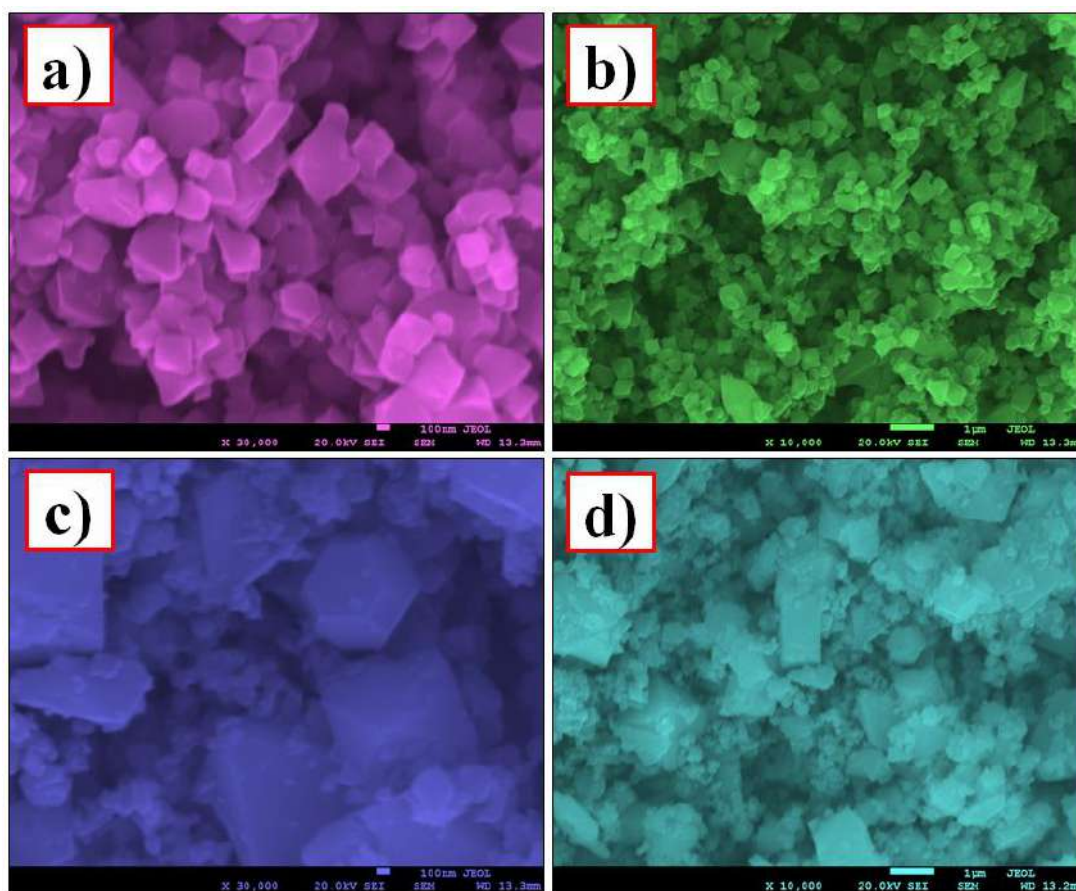


Figure 5.5: SEM images at different magnifications of (a, b) MnFe₂-MOF and (c, d) its derived MnFe₂O₄

5.4.5 Energy dispersive X-ray analysis of MnFe₂-MOF and MnFe₂O₄

The chemical composition and color mapping of MnFe₂-MOF and its derived MnFe₂O₄ were employed by using the EDX spectroscopy. The EDX spectrum and color mapping of both the samples are depicted in figure 5.6(a, b). From this spectrum, the elements like Mn, Fe, C, O and Mn, Fe, O were detected in the in MnFe₂-MOF and its derived MnFe₂O₄ respectively. The atomic percentage of the corresponding elements is well distributed in resulting material. Hence, it was confirmed that our prepared samples were in the pure form and would be beneficial for energy storage applications.

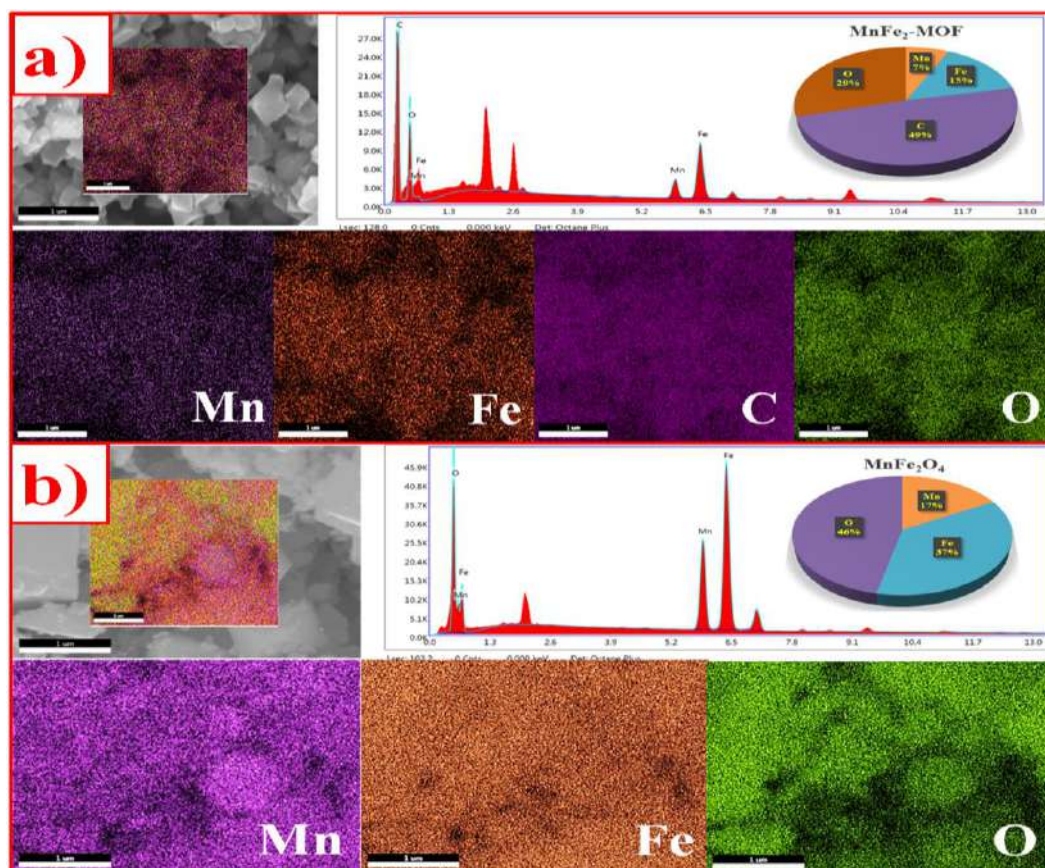


Figure 5.6: Elemental mapping images of (a) $MnFe_2-MOF$ and (b) its derived $MnFe_2O_4$

5.4.6 Transmission electron microscopy of $MnFe_2-MOF$ and $MnFe_2O_4$

The morphological and structural characteristics of $MnFe_2-MOF$ and its derived $MnFe_2O_4$ were investigated using TEM, HRTEM, and selected area electron diffraction (SAED). The TEM image in figure 5.7(a) indicates that the amorphous $MnFe_2-MOF$ s have a cubical shape with varying sizes, and the HRTEM images (Figure 5.7b, c) likewise demonstrates an amorphous nature due to the absence of apparent lattice fringes. Furthermore, a high-resolution TEM image revealed no indication of crystallinity, indicating that the particles were amorphous. The SAED pattern, as shown in figure 5.7(d), revealed only diffuse rings, implying that the as-synthesized $MnFe_2-MOF$ material is amorphous.³⁵ The TEM images of derived $MnFe_2O_4$ reveals the bricks like morphology with plenty of nanoparticles in it as shown in figure 5.7(e and f). The lattice fringe spacing in the accompanying HRTEM image as depicted in figure 5.7(g) is about 0.226 nm, which is consistent with the (311) plane of cubic $MnFe_2O_4$. The spinel cubic structure of $MnFe_2O_4$ is visible in the SAED pattern (Figure 5.7h), which is compatible with the XRD analysis and the

emergence of (220), (311), (400), (422) and (440) planes of material, indicating the formation of MnFe₂O₄.³⁶

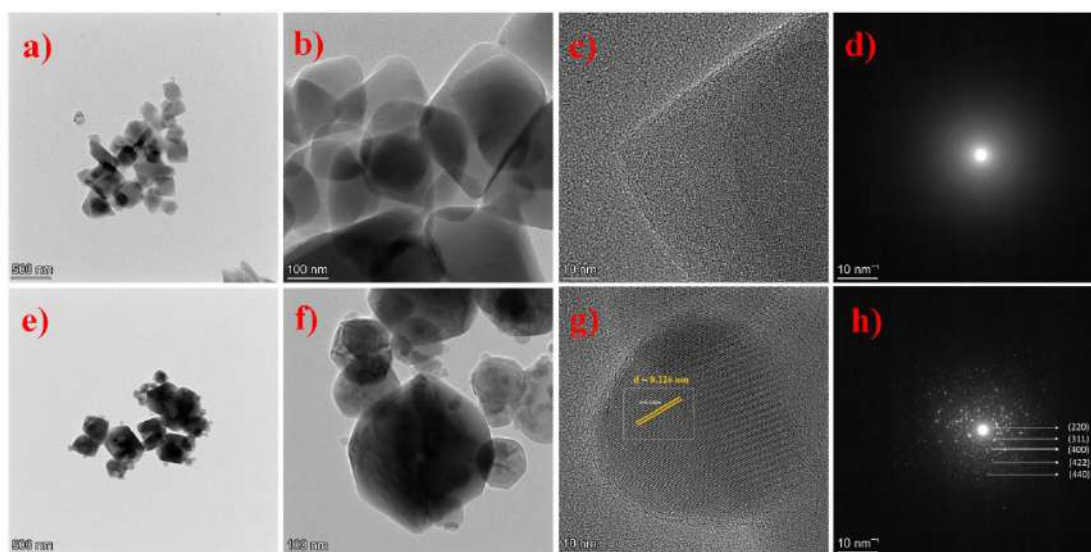


Figure 5.7: TEM, HR-TEM and SAED patterns of (a-d) MnFe₂-MOF and (e-h) its derived MnFe₂O₄

5.4.7 Brunauer-Emmett-Teller analysis of MnFe₂-MOF and MnFe₂O₄

The surface area is a crucial factor for effecting the storage capabilities of electrode materials because of its direct impact on the accessibility of reaction sites. Brunauer-Emmett-Teller analysis was used to study the surface area and porosity of the MnFe₂-MOF and its derived MnFe₂O₄. The N₂ adsorption/desorption isotherms and BJH pore size distribution curves of MnFe₂-MOF and its derived MnFe₂O₄ are depicted in figure 5.8. Figure 5.8(a, b) shows a typical type IV isotherm with hysteresis loop in a relative pressure (P/P₀) between 0.5 to 0.9 confirming the mesopores in the materials. The specific surface area of MnFe₂-MOF and its derived MnFe₂O₄ was determined to be 303 m² g⁻¹ and 263 m² g⁻¹, respectively. The results of the Barrett-Joyner-Halenda study showed a pore size distribution of MnFe₂-MOF and its derived MnFe₂O₄ at 16 nm and 24 nm, respectively. The MnFe₂-MOF with cubic morphology has the largest specific surface area compared to MnFe₂O₄, resulting in adsorption of electrolytes in the sites of the sample hence improved electrochemical properties. The average pore widths of MnFe₂-MOF and its derived MnFe₂O₄ were of mesopores nature that improves ion diffusion of materials and leads to better electrochemical performance.^{37,38}

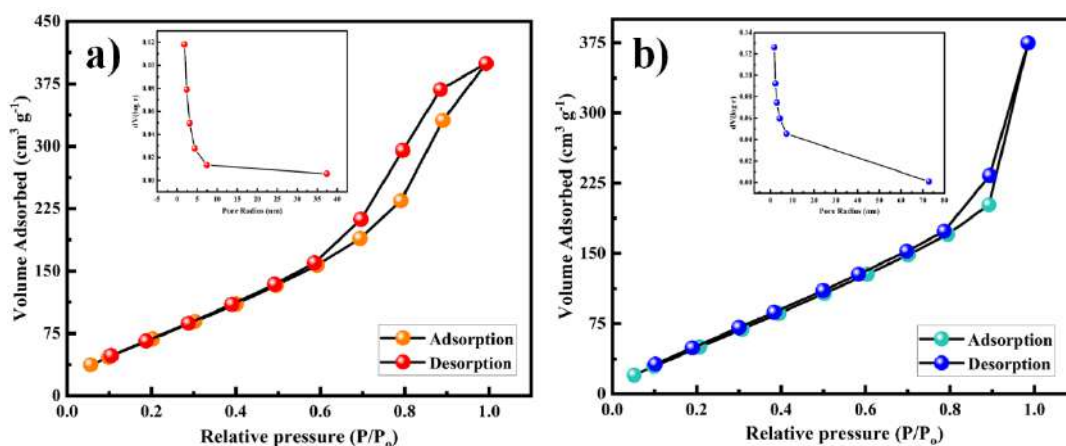


Figure 5.8: Nitrogen adsorption/desorption isotherms of (a) MnFe₂-MOF, (b) derived MnFe₂O₄ (the insets show pore size distribution)

5.4.8 Vibrating-sample magnetometer of MnFe₂-MOF and MnFe₂O₄

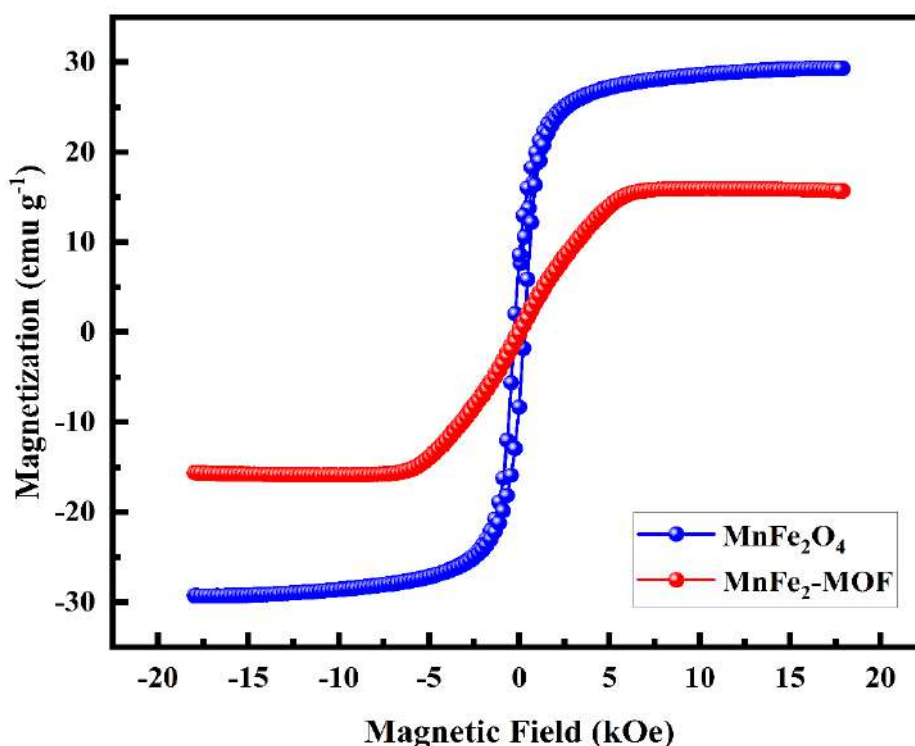


Figure 5.9: Hysteresis curves of MnFe₂-MOF and its derived MnFe₂O₄

The magnetization of the developed materials was measured using vibrating sample magnetometer (VSM) as a function of magnetic field. The samples MnFe₂O₄ and MnFe₂-MOF were subjected to extensive magnetic studies to examine the effect of functionalization on magnetic nanoparticles behaviour. Figure 5.9 displays the magnetization curves of the MnFe₂O₄ and MnFe₂-MOF at RT. Due to the non-saturating magnetization even at higher fields, the saturation magnetization (M_s) value was determined by fitting the M against 1/H curves. MnFe₂O₄ and MnFe₂-MOF

have Ms values of 29.324 and 15.917 emu g⁻¹, respectively. Thus, the Ms values plays vital role in supercapacitor application. The power density, energy density, and cyclic stability can be increased by the magnetic behavior of the nanomaterials. The charge/discharge behaviour of the materials is influenced by the magnetic field effect on electric diffusion and the shape of the EDLC charge transfer resistance.³⁹ The specific surface area, porosity, and the magnetic behavior of the MnFe₂-MOF sample would be beneficial for supercapacitor application.

5.4.9 X-ray photoelectron spectroscopy of MnFe₂-MOF and MnFe₂O₄

X-ray photoelectron spectroscopy investigate the chemical compositions of both the MnFe₂-MOF and its derived MnFe₂O₄, as shown in figure 5.10. The extensive XPS spectrum of the MnFe₂-MOF and its derived MnFe₂O₄ material suggests the presence of Mn, Fe, C, and O elements, which supports the results obtained through the elemental mapping. Figure 5.10(a) depicts the deconvoluted Mn 2p peaks of MnFe₂-MOF. The orbital separation energy between the peaks is significant 12 eV, which is consistent with the energies of Mn 2p_{3/2} and Mn 2p_{1/2}. The notable Mn 2p_{3/2} peaks found at 641.4 eV and the Mn 2p_{1/2} peaks at 653.1 eV are attributed to the Mn 2p binding state. Figure 5.10(b) depicts the deconvoluted XPS spectrum of Fe 2p of MnFe₂-MOF, which is ascribed to Fe³⁺ (711.6 and 725.2 eV) and accompanying shakeup satellites (715.3 and 728.6 eV). As shown in figure 5.10(c), the C 1s spectra of MnFe₂-MOF has three peaks at 284.5, 285.3, and 288.3 eV, which were assigned to C=C, C-C, and C=O bonds, respectively. The high-resolution spectra of MnFe₂-MOF O1s was deconvoluted into two peaks at 531.5 and 533.4 eV, which were ascribed to metal-oxygen and carboxylate bonding, respectively, in figure 5.10(d).^{40,41}

In figure 5.10(e), which depicts the high-resolution Mn 2p spectra of MnFe₂O₄, the peaks with centres at 641.4 and 653.2 are identified as Mn 2p_{3/2} and Mn 2p_{1/2} of Mn(II), respectively. The presence of the Mn²⁺ oxidation state in the MnFe₂O₄ is further supported by the two satellite peaks at 643.9 and 655.7 eV. The Fe 2p spectrum of MnFe₂O₄ is shown in figure 5.10(f), and it has two characteristic peaks of Fe 2p_{3/2} and Fe 2p_{1/2} at 710.4 and 724.7 eV, respectively. This indicates that the chemical state of Fe in the MnFe₂O₄ is +3. The O1s high-resolution spectra of MnFe₂O₄, as shown in figure 5.10(g) revealed three oxygen peaks at 529.5, 531.9, and 533.5 eV, respectively. The first peak, at 529.5 eV, was identified as a normal M-O bond, but the second peak, at 531.9 eV, may be attributed to various defect sites such

as hydroxyls or carboxyls. The third peak, centered at 533.5 eV, might be due to the physically either chemically absorbed water.^{42,43}

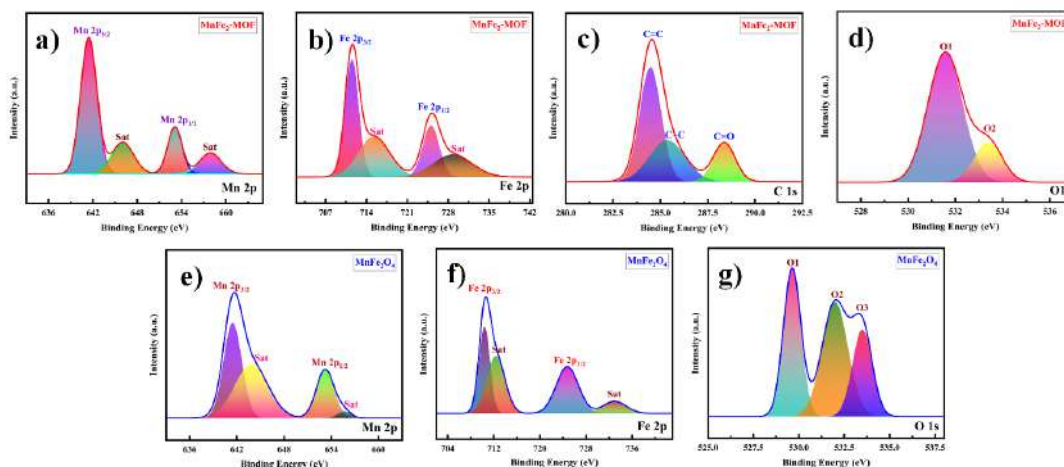


Figure 5.10: High-resolution XPS spectra of (a-d) MnFe₂-MOF, (e-g) its derived MnFe₂O₄

5.4.10 Capacitance characterization of electrode

The electrochemical measurements of prepared electrode materials were performed in a 1 M Na₂SO₄ neutral electrolyte in three-electrode assembly using standard Ag/AgCl as a reference electrode, graphite as a counter electrode and fabricated MnFe₂-MOF / MnFe₂O₄ as a working electrode. Figure 5.11(a) illustrates the comparative CV curves at a scan rate of 100 mV s⁻¹ and figure 5.11(b) depicts the comparative GCD curves at a 1 mA cm⁻² current density of the MnFe₂-MOF and MnFe₂O₄, in a potential window of 0 - 0.5 V. The cyclic voltammograms of MnFe₂-MOF and MnFe₂O₄ have an approximately semi-rectangular shape, indicating that the main electric double layer capacitance behaviour is present, as well as some pseudocapacitive character. Figure 5.11(c, d) show CV curves of MnFe₂-MOF and MnFe₂O₄ at different scan rates, i.e. 10 - 100 mV s⁻¹, which are almost symmetric, demonstrating the electrochemical reaction's excellent reversibility. Also, the semi-rectangular shape has demonstrated great kinetic capabilities because it has not distorted at higher scan rates. The area under the CV curves increases with scan rate, while specific capacitance falls because electrolyte ions completely penetrate the electrode materials at decreasing scan rates. As a result, charge storage may be used across the whole electrode material's surface. At higher scan speeds, however, only the outer active surface is used for charge storage because diffusion restricts the flow of electrolyte ions.⁴⁴ And it is clear from the CV curves that MnFe₂-MOF has a higher current than MnFe₂O₄.

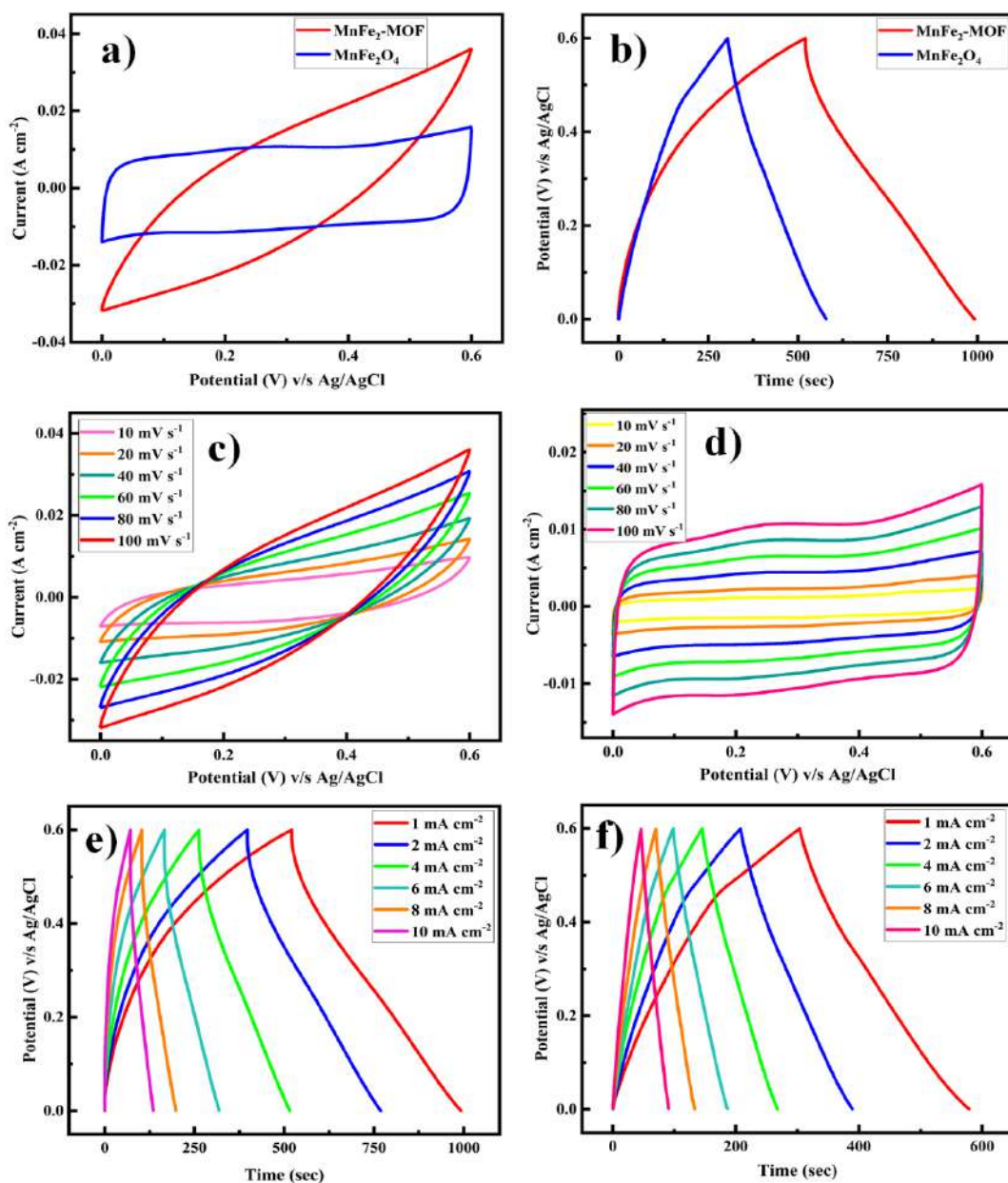


Figure 5.11: (a) Comparison of cyclic voltammograms of MnFe₂-MOF and its derived MnFe₂O₄ electrodes at a potential sweep rate of 100 mV s⁻¹, (b) Comparison of GCD curves of MnFe₂-MOF and its derived MnFe₂O₄ electrodes at a current density of 1 mA cm⁻², (c) CV curves of MnFe₂-MOF in 1 M Na₂SO₄ at various scan rates, (d) CV curves of derived MnFe₂O₄ in 1 M Na₂SO₄ at various scan rates, (e) GCD curves of MnFe₂-MOF at various current densities, (f) GCD curves of MnFe₂O₄ at various current densities

To examine the charge/discharge behaviour of various electrodes, galvanostatic charge/discharge (GCD) tests were performed at different current densities, as shown in figure 5.11(e, f). For MnFe₂-MOF and MnFe₂O₄, the GCD curves have triangular shapes, which are consistent with CV data indicating the

creation of an electric double layer. Equation (5.1) was used to determine the electrode materials specific capacitance using galvanostatic charge-discharge (GCD) curves. The specific capacitances determined from GCD curves (Figure 5.11 e) for MnFe₂-MOF is 1226, 1191, 1158, 1097, 1004 and 876 F g⁻¹ at 1, 2, 4, 6, 8 and 10 mA cm⁻², respectively. And also the specific capacitances evaluated from GCD curves (Figure 5.11f) for derived MnFe₂O₄ is 865, 802, 763, 710, 649 and 590 F g⁻¹ at 1, 2, 4, 6, 8 and 10 mA cm⁻², respectively. Rate capability MnFe₂-MOF and derived MnFe₂O₄ electrodes at 1 to 10 mA cm⁻² were shown in figure 5.12(a). For all determined current densities, the MnFe₂-MOF has the higher specific capacitance than the MnFe₂O₄. The Ragone plot are received from charge-discharge curves of the MnFe₂-MOF and derived MnFe₂O₄ at different power densities were depicted in figure 5.12(b). The energy and power densities of MnFe₂-MOF and its derived MnFe₂O₄ were calculated using equations (5.2 and 5.3). The Ragone plot indicates that as power density increases, energy density decreases.

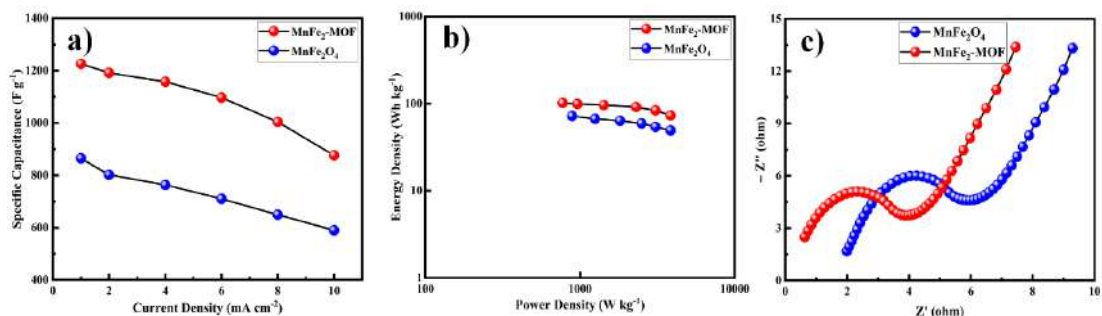


Figure 5.12: (a) Comparative rate capability of the MnFe₂-MOF and derived MnFe₂O₄ electrodes at 1 to 10 mA cm⁻², (b) Ragone plots of the MnFe₂-MOF and derived MnFe₂O₄, (c) Nyquist plots of the MnFe₂-MOF and derived MnFe₂O₄

Electrochemical impedance spectroscopy (EIS) were used to assess the charge-transfer behaviour of electrodes in order to better understand capacitive characteristics. The EIS spectrum is divided into two parts: the semicircle part in the high-frequency region, which is related to the charge transfer resistance (R_{ct}) at the electrode surface/electrolyte interface, and the sloped line part in the low-frequency region, which is associated to the ion diffusion behaviour of the electrolyte inside the electrode material. The Nyquist plots of MnFe₂-MOF and derived MnFe₂O₄ were shown in figure 5.12(c). Significantly, the MnFe₂-MOF electrode (2.9 ohm) show a

lower charge transfer resistance (Rct) than the derived MnFe₂O₄ electrode (3.75 ohm), confirming the fast electron transport kinetics and high conductivity.

Cyclic stability is crucial factor for the virtual application of supercapacitors and Coulombic efficiency is important factor to inspect the interfacial stability of MnFe₂-MOF and derived MnFe₂O₄ electrodes as a function of GCD cycles, as depicted in figure 5.13(a and b). The cyclic stability of MnFe₂-MOF and derived MnFe₂O₄ electrodes were performed using charge-discharge cycles at 10 mA cm⁻² for 3000 cycles within a potential window of 0 to 0.6 V. After 3000 successive GCD cycles, the MnFe₂-MOF and MnFe₂O₄ electrodes still retained 95.68 % and 94.50 % of their original capacitance, respectively. The inset shows first five and last five charge-discharge cycles. Coulombic efficiency of MnFe₂-MOF and derived MnFe₂O₄ electrodes were determined using equation (5.5) at several GCD cycles. The MnFe₂-MOF and derived MnFe₂O₄ electrodes shows excellent Coulombic efficiency of 99.10 % and 97.93 %, respectively.⁴⁵

$$\eta = \frac{t_d}{t_c} \times 100 \dots \dots \dots (5.5)$$

Where, η stands for the Coulombic efficiency measured in %, t_d stands for the discharging time and t_c stands for the charging time measured in seconds.

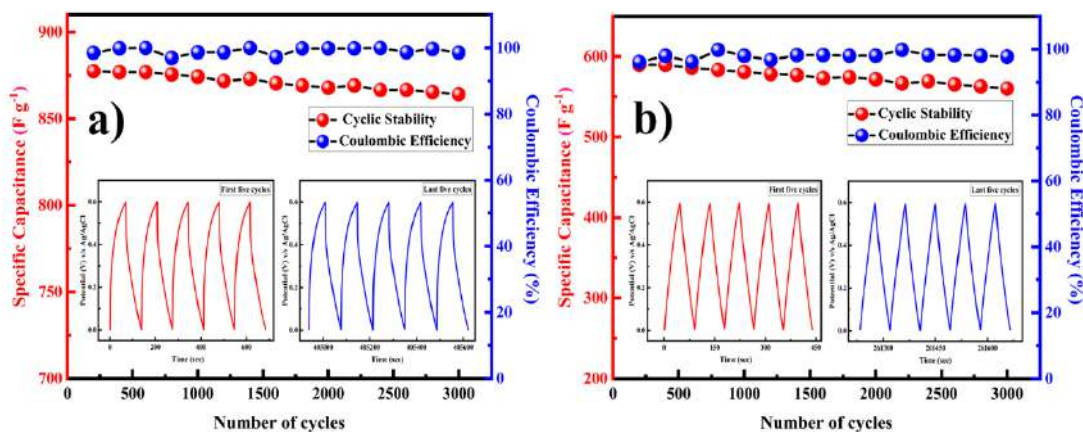


Figure 5.13: Cyclic stability (left versus bottom) and Coulombic efficiency (right versus bottom) of (a) MnFe₂-MOF and (b) derived MnFe₂O₄ electrodes for 3000 cycles measured at a current density of 10 mA cm⁻², the inset shows the charge-discharge curves of the first and last five cycles

5.4.11 Capacitance characterization of solid-state asymmetric supercapacitor (ASC) device (MnFe₂-MOF//AC)

It is familiar that one of the elements affecting the rise in supercapacitor energy density is the wide potential window. The potential window for an asymmetric

cell with an aqueous electrolyte is restricted to the range between 0 - 1 V due to water electrolysis. Using ionic liquids or organic electrolytes can result in a voltage window 3 - 4 times wider than using aqueous electrolytes, but several factors such as cost, toxicity, and flammability make their use less desirable. Therefore, the construction of asymmetric supercapacitor is proposed to overcome the challenges of water splitting in aqueous electrolytes. This arrangement ordinarily comprised of a positive electrode served as the energy source and a negative electrode served as the power source. As a result, boosting the cell's operating voltage improves energy density and specific capacitance in asymmetric supercapacitor devices.

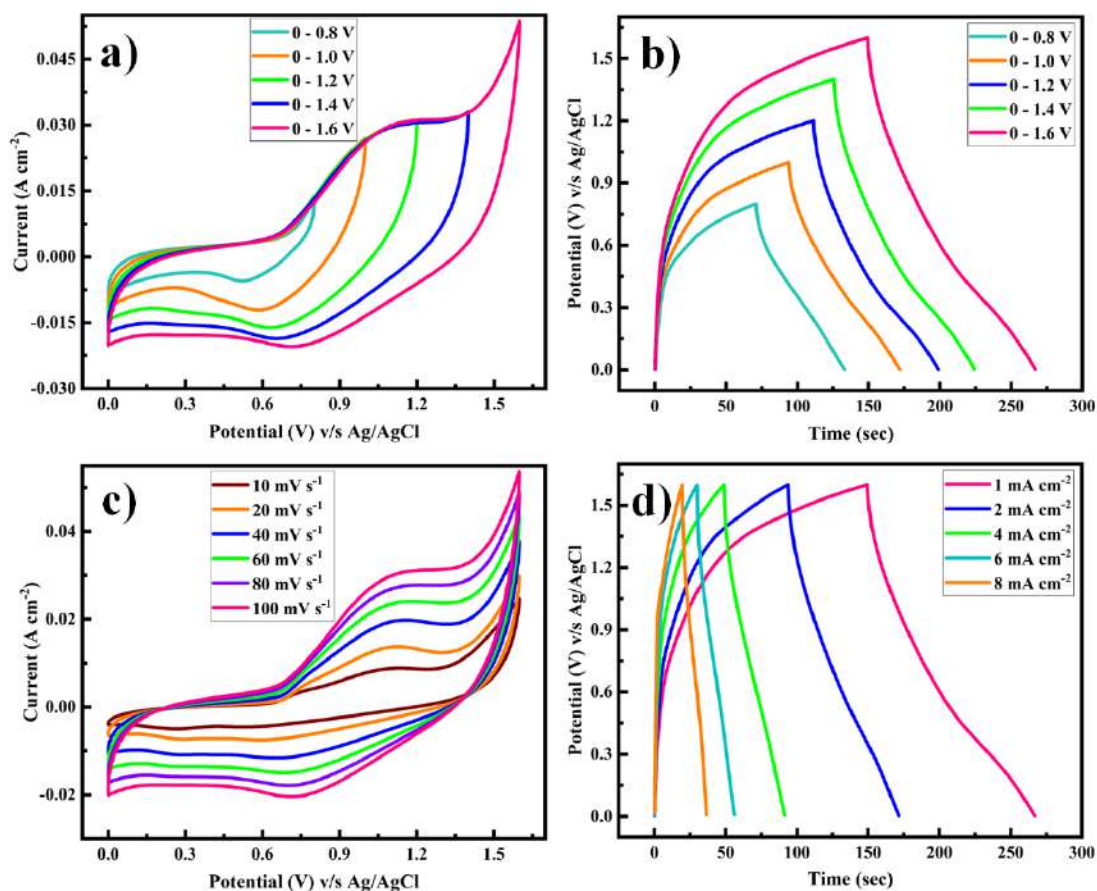


Figure 5.14: (a) Comparison of cyclic voltammograms of ASC device at a potential sweep rate of 100 mV s⁻¹, (b) Comparison of GCD curves of ASC device at a current density of 1 mA cm⁻², (c) CV curves of ASC device in 1 M Na₂SO₄ at various scan rates, (d) GCD curves of ASC device at various current densities

In this study, a solid-state asymmetric supercapacitor is put together utilizing MnFe₂-MOF and activated carbon (AC) electrodes as the anode and cathode in order to further evaluate the capacitive performance of the electrodes as obtained in a whole cell setup. This study utilized a gel electrolyte comprising a polyvinyl alcohol (PVA)-

Na₂SO₄ combination. This solid-state device provides a number of benefits over liquid-based supercapacitors, including flexibility, ease of production, a wide operating temperature range, and better safety. MnFe₂-MOF and AC were used as electrodes (2 x 2 cm²) in a solid-state asymmetric supercapacitor device sandwiched by a PVA-Na₂SO₄ gel electrolyte. Figure 5.14(a and b) depicts the comparative CV and GCD curves of the MnFe₂-MOF//AC device, which varied from 0 to 1.6 V due to the restrictions imposed by oxygen evolution at voltages greater than 1.6 V. As a result, the potential range of 1.6 V in the 1 M Na₂SO₄ electrolyte was chosen for all electrochemical measurements of the fabricated device. The CV curves of the MnFe₂-MOF//AC device are shown in figure 5.14(c) at various scan rates varying from 10 to 100 mV s⁻¹. Both electric double-layer capacitance from AC and pseudocapacitance from MnFe₂-MOF for charge storage validate this. As the scan rate increases, so does the area under the CV curves, and therefore the current. The GCD curves for the MnFe₂-MOF//AC device at various current densities, varying from 1 to 8 mA cm⁻², are shown in figure 5.14(d). The CV curves agree with the unconventional triangular shapes found using GCD curves. The specific capacitances of the MnFe₂-MOF//AC device evaluated from the charge-discharge cycles are depicted in figure 5.15(a). The as-constructed MnFe₂-MOF//AC device delivers specific capacitance from 91.87, 84.16, 76.25, 73.12 and 68.75 F g⁻¹ at 1, 2, 4, 6 and 8 mA cm⁻² current density, respectively. As current density increases the carbon-based electrode's ion exchange rate exceeds that of a pseudo capacitive electrode, resulting in unbalanced charges between the two electrodes of a MnFe₂-MOF//AC device and also the Faradaic process will be constrained at the electrodes' outer surfaces due to the restriction of the diffusion effect. As a result, as current density increases, the specific capacitances of the MnFe₂-MOF//AC device steadily decrease.

The Ragone plot of the assembled MnFe₂-MOF//AC device are exhibited in figure 5.15(b). As the results showed, the MnFe₂-MOF//AC device delivers a maximum energy density of 32.67 Wh kg⁻¹ with a power density of 1000 W kg⁻¹. The internal resistance and charge transfer resistance of the MnFe₂-MOF//AC device was examined using the EIS technique. Figure 5.15(c) shows the Nyquist plot of the MnFe₂-MOF//AC device which reveals low charge transfer resistance of 0.5 Ω with a 0.9 Ω internal resistance which demonstrates the best capacitor performance of the MnFe₂-MOF//AC device, small contact resistance, small diffusion resistance, and

quick electron transfer kinetics. A tiny semicircle denotes increased electrolyte ion buildup and redox reactions on the electrode surface.

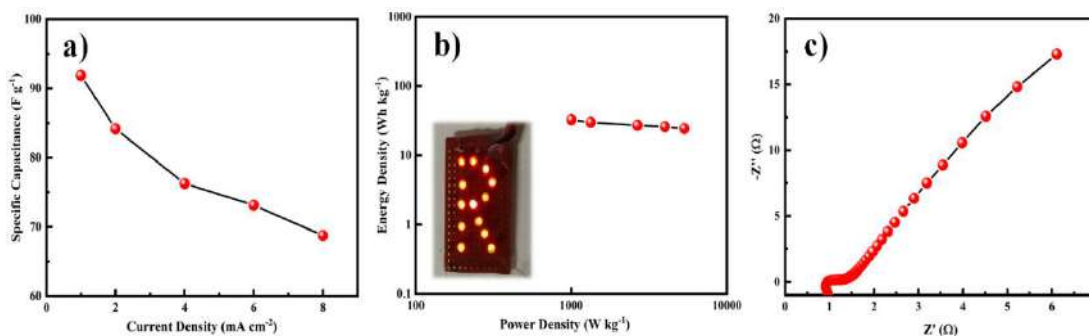


Figure 5.15: (a) Comparative rate capability of the ASC device at 1 to 8 mA cm⁻², (b) Ragone plots of the ASC device, (c) Nyquist plots of the ASC device

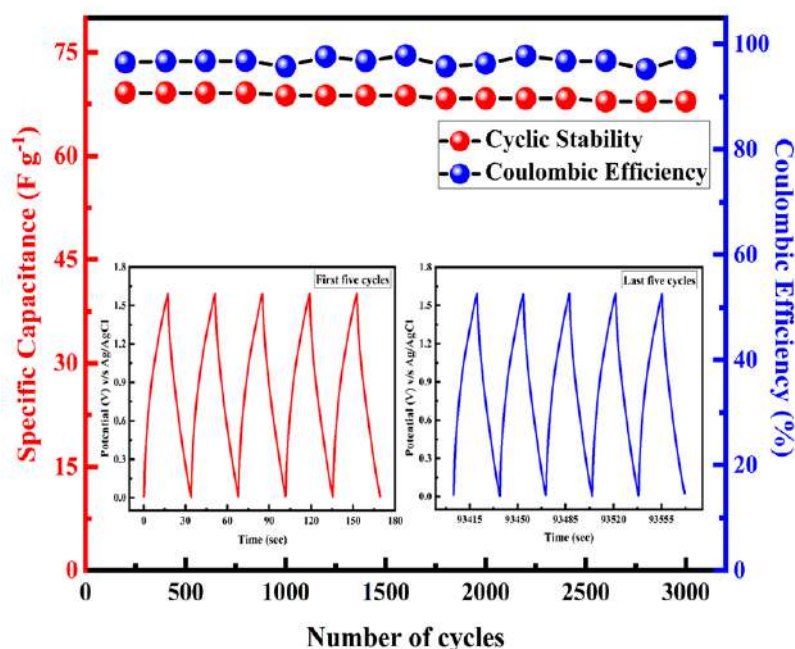


Figure 5.16: Cyclic stability (left versus bottom) and Coulombic efficiency (right versus bottom) of ASC device for 3000 cycles measured at a current density of 8 mA cm⁻², the inset shows the charge-discharge curves of the first and last five cycles

Figure 5.16 shows the cyclic stability and Coulombic efficiency which was investigated at a prolonged current density of 8 mA cm⁻² for 3000 GCD cycles. After repeating the 3000 charge-discharge cycles, the device shows high Coulombic efficiency of 96.75 % and the capacitance retention of the MnFe₂-MOF//AC fabricated asymmetric supercapacitor device achieved nearly 98.52 %, and no discernible degradation is seen, indicating that the MnFe₂-MOF exhibits outstanding stability as an electrode material for supercapacitor application. Its exceptional cycle stability is related to PVA as a binder and the polymer electrolyte's capacity to

safeguard the structure of MOF-based electrodes. Additionally, this type of all-solid-state supercapacitor device has a straightforward assembly procedure and eliminates the possibility of electrolyte leakage that is in liquid electrolyte capacitors.

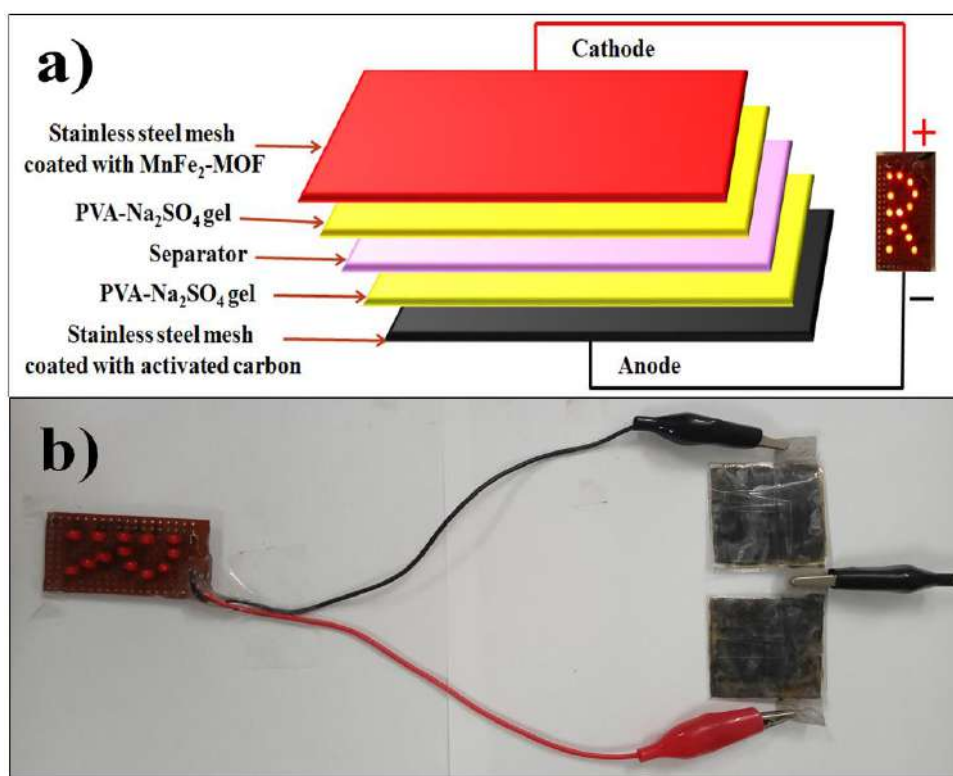


Figure 5.17: (a) Schematic illustration of fabricated asymmetric supercapacitor device, (b) Digital photograph of fabricated two handmade asymmetric supercapacitor device connected in series to glow the LEDs

The lighting red LEDs demonstrate how we may utilize our asymmetric supercapacitor device in real applications by connecting two such devices in series (each device is 2 cm X 2 cm in size). Figure 5.17(a) shows the schematic illustration of a fabricated asymmetric supercapacitor device and figure 5.17(b) displays the digital photograph of fabricated devices arranged in series to glow the red LEDs. After only fifteen seconds of charging, the LED shone brightly for almost seven minutes, illustrating the incredible utility of our solid-state asymmetric supercapacitor devices (see Supporting Information video). Our designed supercapacitor's longer discharge time than charging time makes it appropriate for use in practical energy storage and conversion applications.

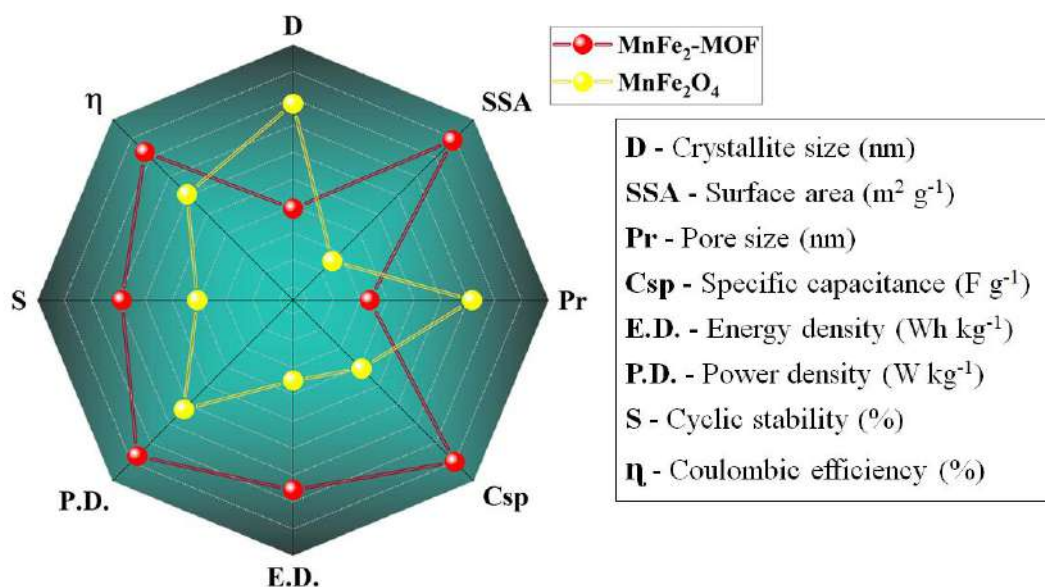


Figure 5.18: Radar plot for comparative study of MnFe₂-MOF and derived MnFe₂O₄ electrodes based on electrochemical properties

As shown in figure 5.18, a radar graph was used for the comparative investigation of the electrochemical properties of chemically synthesized MnFe₂-MOF and derived MnFe₂O₄. Each apex displays parameters such as crystallite size, specific surface area, pore size, specific capacitance, energy density, power density, cyclic stability and coulombic efficiency of the MnFe₂-MOF and derived MnFe₂O₄. The solid area under the curve indicates the electrochemical properties of the electrodes. Figure 5.18 shows that the integral area of MOF is significantly greater than that of ferrite. It has been observed that small crystallite size and large specific surface area contributed to excellent specific capacitance, energy density, power density, and cyclic stability.

5.5 Conclusion

A novel MnFe₂-MOF and its derived MnFe₂O₄ was synthesized for the first time using a simple reflux condensation technique followed by annealing process. XRD, FT-IR, Raman, SEM, EDX, TEM, VSM, BET, and XPS measurements were used to characterize the as-prepared. MnFe₂-MOF and its derived MnFe₂O₄. The electrochemical tests of MnFe₂-MOF and its derived MnFe₂O₄ in 1 M Na₂SO₄ neutral electrolyte exhibit a high specific capacitance of 1226 and 865 F g⁻¹ at 1 mA cm⁻² current density with excellent capacitance retention of 95.68 % and 94.50 % over 3000 cycles, respectively. The practical application of the prepared electrode was examined by fabricating a solid-state asymmetric supercapacitor device working at

1.6 V operating potential window using the electrodes as MnFe₂-MOF as anode and activated carbon as the cathode, and PVA-Na₂SO₄ gel as the gel-polymer electrolyte. The assembled asymmetric supercapacitor device illustrates a remarkable energy density of 32.67 Wh kg⁻¹ at a power density of 1000 W kg⁻¹ with an outstanding cyclic stability of 98.52 % even after 3000 GCD cycles. In conclusion, the electrochemical supercapacitor performance of MnFe₂-MOF//AC asymmetric cell can be utilized as potential application towards the electrochemical energy storage prospect effectively.

5.6 References

- 1 J. Zhou, S. Zhang, Y. N. Zhou, W. Tang, J. Yang, C. Peng and Z. Guo, *Electrochem. Energy Rev.*, 2021, **4**, 219-248.
- 2 Y. Jiang and J. Liu, *Energy Environ. Mater.*, 2019, **2**, 30-37.
- 3 J. Hao, H. Liu, S. Han and J. Lian, *ACS Appl. Nano Mater.*, 2021, **4**, 1330–1339.
- 4 X. Zhang, A. Chen, M. Zhong, Z. Zhang, X. Zhang, Z. Zhou and X. H. Bu, *Electrochem. Energy Rev.*, 2019, **2**, 29-104.
- 5 W. Li, X. Zhao, Q. Bi, Q. Ma, L. Han and K. Tao, *Dalt. Trans.*, 2021, **50**, 11701–11710.
- 6 H. Gao, H. Shen, H. Wu, H. Jing, Y. Sun, B. Liu, Z. Chen, J. Song, L. Lu, Z. Wu and Q. Hao, *Energy and Fuels*, 2021, **35**, 12884–12901.
- 7 S. Zallouz, B. Réty, L. Vidal, J. M. Le Meins and C. Matei Ghimbeu, *ACS Appl. Nano Mater.*, 2021, **4**, 5022–5037.
- 8 Y. Li, X. Han, T. Yi, Y. He and X. Li, *J. Energy Chem.*, 2019, 54–78.
- 9 D. P. Chatterjee and A. K. Nandi, *J. Mater. Chem. A*, 2021, **9**, 15880–15918.
- 10 X. Gao, Y. Dong, S. Li, J. Zhou, L. Wang and B. Wang, *Electrochem. Energy Rev.*, **2020**, **3**, 81-126.
- 11 O. M. Yaghi, H. Li, *J. Am. Chem. Soc.*, 1995, **117**, 10401–10402.
- 12 F. Zou, X. Hu, Z. Li, L. Qie, C. Hu, R. Zeng, Y. Jiang and Y. Huang, *Adv. Mater.*, 2014, **26**, 6622–6628.
- 13 G. Wang, Z. Yan, N. Wang, M. Xiang and Z. Xu, *ACS Appl. Nano Mater.*, 2021, **4**, 9034–9043.
- 14 and G. L. Shouheng Sun, Hao Zeng, David B. Robinson, Simone Raoux, Philip M. Rice, Shan X. Wang, *J. Am. Chem. Soc.*, 2004, **126**, 273–279.
- 15 B. Bhujun, M. T. T. Tan and A. S. Shanmugam, *Results Phys.*, 2017, **7**, 345–353.
- 16 C. D. Lokhande, D. P. Dubal and O. S. Joo, *Curr. Appl. Phys.*, 2011, **11**, 255–270.
- 17 L. Sun, C. H. Hendon, S. S. Park, Y. Tulchinsky, R. Wan, F. Wang, A. Walsh and M. Dincă, *Chem. Sci.*, 2017, **8**, 4450–4457.
- 18 P. D. Patil, S. R. Shingte, V. C. Karade, J. H. Kim, T. D. Dongale, S. H. Mujawar, A. M. Patil and P. B. Patil, *J. Energy Storage*, 2021, **40**, 102821-

- 102832.
- 19 M. Safari and J. Mazloom, *J. Solid State Electrochem.*, 2021, **25**, 2189–2200.
- 20 Y. Liu, G. Li, Y. Guo, Y. Ying and X. Peng, *ACS Appl. Mater. Interfaces*, 2017, **9**, 14043–14050.
- 21 P. Tang, L. Han and L. Zhang, *ACS Appl. Mater. Interfaces*, 2014, **6**, 10506–10515.
- 22 R. Velmurugan, J. Premkumar, R. Pitchai, M. Ulaganathan and B. Subramanian, *ACS Sustain. Chem. Eng.*, 2019, **7**, 13115–13126.
- 23 R. Barik, A. Raulo, S. Jha, B. Nandan and P. P. Ingole, *ACS Appl. Energy Mater.*, 2020, **3**, 11002–11014.
- 24 C. Yu, Y. Wang, J. Cui, D. Yu, X. Zhang, X. Shu, J. Zhang, Y. Zhang, R. Vajtai, P. M. Ajayan and Y. Wu, *J. Mater. Chem. A*, 2018, **6**, 8396–8404.
- 25 J. Yuan, D. Yao, L. Jiang, Y. Tao, J. Che, G. He and H. Chen, *ACS Appl. Energy Mater.*, 2020, **3**, 1794–1803.
- 26 P. Janjani, U. Bhardwaj, R. Gupta and H. Singh Kushwaha, *Anal. Chim. Acta*, 2022, **1202**, 339676-339687.
- 27 H. Qin, Y. Yang, W. Shi and Y. She, *Environ. Sci. Pollut. Res.*, 2021, **28**, 26558–26570.
- 28 S. J. S. Qazi, A. R. Rennie, J. K. Cockcroft and M. Vickers, *J. Colloid Interface Sci.*, 2009, **338**, 105–110.
- 29 T. T. K. Ngan, T. B. Thuy, L. van Tan and T. T. Nguyen, *Bull. Chem. React. Eng. Catal.*, 2021, **16**, 916–924.
- 30 F. Siadatnasab, S. Farhadi, A. A. Hoseini and M. Sillanpää, *New J. Chem.*, 2020, **44**, 16234–16245.
- 31 M. Fiaz, M. Kashif, M. Fatima, S. R. Batool, M. A. Asghar, M. Shakeel and M. Athar, *Catal. Letters*, 2020, **150**, 2648–2659.
- 32 R. A. Rather and Z. N. Siddiqui, *Appl. Organomet. Chem.*, 2019, **33**, 1–14.
- 33 A. Manohar, C. Krishnamoorthi, C. Pavithra and N. Thota, *J. Supercond. Nov. Magn.*, 2021, **34**, 251–259.
- 34 B. Bashir, W. Shaheen, M. Asghar, M. F. Warsi, M. A. Khan, S. Haider, I. Shakir and M. Shahid, *J. Alloys Compd.*, 2017, **695**, 881–887.
- 35 N. Saha, A. Sarkar, A. B. Ghosh, A. K. Dutta, G. R. Bhadu, P. Paul and B. Adhikary, *RSC Adv.*, 2015, **5**, 88848–88856.
- 36 M. Hazarika, P. Chinnamuthu and J. P. Borah, *J. Mater. Sci. Mater. Electron.*,

- 2018, **29**, 12231–12240.
- 37 B. Ameri, S. S. H. Davarani, R. Roshani, H. R. Moazami and A. Tadjarodi, *J. Alloys Compd.*, 2017, **695**, 114–123.
- 38 R. Roshani and A. Tadjarodi, *J. Mater. Sci. Mater. Electron.*, 2020, **31**, 23025–23036.
- 39 R. Sikkema and I. Zhitomirsky, *Appl. Phys. Rev.*, *Appl. Phys. Rev.*, 2023, **10**, 021307-021324.
- 40 K. Yuan, T. Song, D. Wang, Y. Zou, J. Li, X. Zhang, Z. Tang and W. Hu, *Nanoscale*, 2018, **10**, 1591–1597.
- 41 J. Zhou, Z. Han, X. Wang, H. Gai, Z. Chen, T. Guo, X. Hou, L. Xu, X. Hu, M. Huang, S. V. Levchenko and H. Jiang, *Adv. Funct. Mater.*, 2021, **31**, 1–13.
- 42 M. Hua, L. Xu, F. Cui, J. Lian, Y. Huang, J. Bao, J. Qiu, Y. Xu, H. Xu, Y. Zhao and H. Li, *J. Mater. Sci.*, 2018, **53**, 7621–7636.
- 43 R. Gupta, R. Tomar, S. Chakraverty and D. Sharma, *RSC Adv.*, 2021, **11**, 16942–16954.
- 44 S. S. Shah, E. Cevik, M. A. Aziz, T. F. Qahtan, A. Bozkurt and Z. H. Yamani, *Synth. Met.*, 2021, **277**, 116765-116780.
- 45 R. Bhosale, S. Bhosale, P. Kumbhar, D. Narale, R. Ghaware, C. Jambhale, S. Kolekar, *New J. Chem.*, 2023, **47**, 6749–6758.

**CHAPTER
SIX**

Hybrid Supercapacitor Based on Nanoporous Carbon and CoFe₂O₄ Derived From a Single Bimetallic-Organic Framework: One-for-All Approach

6.1 Outline

The rational design of nanomaterials derived from metal-organic framework has received a lot of interest due to their high potential for energy storage and conversion applications because of their high conductivity, strong redox activity and large specific surface area. In this study, a “One-for-All” approach was used to synthesize positive and negative electrodes from a single bimetallic CoFe₂-MOF to fabricate a hybrid supercapacitor device. Hierarchical bimetallic CoFe₂-MOF architectures were synthesized by a straightforward scalable solution method. The Cobalt ferrite was prepared by annealing the bimetallic CoFe₂-MOF in air and the nanoporous carbon was achieved by heating the CoFe₂-MOF in an inert atmosphere. The CoFe₂-MOF derived nanoporous carbon exhibits a high specific capacitance of 1271 F g⁻¹ at 2 mA cm⁻² current density with an excellent cycle stability of 96.87 % even after 5000 cycles owing to its huge surface area of 614 m² g⁻¹ and plenty of mesopores in it. The as-prepared cobalt ferrite and nanoporous carbon derived from CoFe₂-MOF were employed to construct the All-in-One hybrid supercapacitor (HSC) device using PVA-KOH as a gel-polymer electrolyte. At 1 mA cm⁻² current density, the manufactured All-in-One HSC device shows a high specific capacitance of 112.1 F g⁻¹, an energy density of 56.2 Wh kg⁻¹, and a power density of 1091.5 W kg⁻¹. It demonstrated high cyclic stability of 97.91 % of its original capacitance over 5000 subsequent GCD cycles with a coulombic efficiency of 98.54 %. This discovery might significantly progress research towards the creation of MOF-derived electrode materials for a bright future in energy storage and conversion.

6.2 Introduction

The global demand for clean energy storage and delivery is pushing technological developments to their limits, as pollution and the energy crisis become more and more serious.^{1,2} Owing to the widespread concern over the rapidly increasing need for energy in the future, energy storage technologies are now in demand.³ Due to the intermittent nature of these emerging energy sources, it is critical to priorities fulfilling the rapid growth demands of energy storage and conversion devices.⁴ At present, supercapacitors, fuel cells and batteries are being considered as energy storage and conversion technologies. Supercapacitors have gained attention as renewable energy storage systems due to their comparatively good efficiency in storing the energy produced by these sources; however, the high demand for devices with smaller size, lighter weight, higher level of flexibility, energy density, and power density, excellent life cycle, and lower cost presents a challenge for these energy storage systems.⁵⁻⁷ Electrochemical double-layer capacitors (EDLCs), hybrid capacitors, and pseudocapacitors are the different types of supercapacitors that can be categorized based on their electrode configurations. Supercapacitor's ability to perform better is largely dependent on the materials they are made of, including the electrodes and electrolytes.^{8,9} Researchers worldwide have shown great interest in studying advanced materials with good textural and electrochemical properties, such as high porosity, excellent conductivity, and an abundance of redox-active sites, to further improve the performance of these electrodes.¹⁰ The advantages of batteries and supercapacitors might be combined in a hybrid device called an asymmetric supercapacitor (ASC), which could be used to power electric vehicles and other future multifunctional electrics. Therefore, recent advances in supercapacitor research have focused on the creation of such asymmetric supercapacitors.¹¹⁻¹³

Metal-organic frameworks (MOFs), often referred to as porous coordination polymers (PCPs), are created when metal ions and organic linkers self-assemble. MOFs have drawn a lot of attention in the fields of energy storage due to their distinctive advantages, including their highly devisable structures, well-dispersed metal components, super-large surface area and governable porosity.^{14,15} MOF-based materials have been broadly investigated within the field of electrochemical energy storage and conversion in recent years. However, many classic MOFs have restricted uses because of their poor electrical conductivity and stability. Thermal treatment is a

useful way to improve conductivity by partially carbonising the skeleton, but it can cause channel collapse and structural changes in MOFs. MOF-derived nanomaterials with exceptional stability not only serve as a vital supporting structure for a variety of electrode materials, but also increase specific surface area, enrich the active centers, and promote electrochemical reactions.¹⁶⁻¹⁹ A more fascinating advantage of utilizing MOFs as predecessor for the electrode materials in supercapacitors is the ability to create both the cathode (NPC) and anode (metal oxides) from a sole MOF by using the "One-for-All" approach.²⁰ Kang et al. have synthesized metal-organic frameworks (MOFs) derived from hollow rod-like NiCoMn ternary metal sulfides via the etching/ion-exchange reaction and additional sulfurization technique. The material has a rich redox reaction, great synergy, and exceptional electrical conductivity because of the multi-metal and sulphide composition. The as-prepared NiCoMn-S electrode shows an excellent specific capacitance of 2098.2 F g⁻¹ at 1 A g⁻¹ current density. Further, they have fabricated a NiCoMn-S//AC asymmetric supercapacitor device which exhibits an outstanding specific capacitance of 124.5 F g⁻¹ at 1 A g⁻¹ current density with a cycling stability of 73.6 % over 6000 cycles.²¹ Tang et al. successfully synthesized Ni/ZnO nano-sponges from bimetallic Ni/Zn-MOF via optimal heat treatment at 600°C. Ni/ZnO electrode exhibits a high specific capacitance of 807 F g⁻¹ at 1 A g⁻¹ current density and retains 86 % of its initial capacitance after 5000 charge/discharge cycles at the 10 A g⁻¹ current density with long-term cycling stability. Furthermore, they have manufactured an asymmetric supercapacitor (Ni/ZnO-600//AC) that exhibits remarkable cycling stability of 89 % over subsequent 5000 GCD cycles at a high current density of 5 A g⁻¹.²²

In this chapter, we have used the "One-for-all" approach to synthesize nanoporous carbon (NPC) and cobalt ferrite (CoFe₂O₄) from a single bimetallic cobalt-iron metal-organic framework (CoFe₂-MOF). As-prepared NPC and ferrite derived from bimetallic MOF were employed as cathode and anode in the construction of a hybrid supercapacitor (HSC) with 2 M KOH as the aqueous alkaline electrolyte. Capacitive performance was investigated using a three-electrode setup.

6.3 Experimental section

6.3.1 Chemicals

Cobalt nitrate hexahydrate (Co(NO₃)₂.6H₂O; 98%) and N, N-dimethylformamide (DMF; 99.8 %) were purchased from Loba Chemie India.

Terephthalic acid (PTA, 98 %), ferric chloride hexahydrate ($\text{FeCl}_3 \cdot 6\text{H}_2\text{O}$) and N-methyl-2-pyrrolidone (NMP) were purchased from Sigma Aldrich (USA). All chemicals were of analytical grade and were utilized without further purification.

6.3.2 Synthesis of $\text{CoFe}_2\text{-MOF}$ and its derived cobalt ferrite and nanoporous carbon

For the synthesis of $\text{CoFe}_2\text{-MOF}$, reflux condensation method was used in which terephthalic acid (0.15 M) was dissolved in DMF (20 ml). Cobalt nitrate hexahydrate (0.05 M) and ferric chloride hexahydrate (0.1 M) were dissolved in DMF (20 ml) to form a solution. Then, both these solutions were mixed and stirred for 10 min to obtain a homogeneous solution and NaOH solution was added dropwise to the above solution till precipitation. Finally, the precipitate was transferred to a round bottom flask and kept at 100 °C for 12 h. Next, the brown-colored suspension was filtered and the final powder was dried at 60 °C for 12 h to obtain $\text{CoFe}_2\text{-MOF}$.

Cobalt ferrite and nanoporous carbon both were prepared from the as-prepared $\text{CoFe}_2\text{-MOF}$. To get MOF-derived cobalt ferrite, the $\text{CoFe}_2\text{-MOF}$ was annealed at 500°C for 3 h at a heating rate of 5 °C min^{-1} in air; the resulting sample was designated as cobalt ferrite (CoFe_2O_4). For the synthesis of nanoporous carbon, the $\text{CoFe}_2\text{-MOF}$ was heated at 800 °C for 3 hrs at a ramping rate of 5 °C min^{-1} in a nitrogen environment, then cooled to room temperature.

6.3.3 Material characterization

Crystal structure and phase purity of $\text{CoFe}_2\text{-MOF}$ and derived nanoporous carbon were analysed on a Bruker D8 Phaser X-ray diffractometer with Cu $K\alpha$ radiation ($\lambda = 0.1541$ nm). The Perkin Elmer 1760X spectrophotometer was used to record Fourier Transform Infrared spectra between 400 and 4000 cm^{-1} . Raman spectra of $\text{CoFe}_2\text{-MOF}$ and derived nanoporous carbon samples were analyzed by Renishaw in via Raman spectrometer by using a He-Ne (633 nm) laser excitation source. The surface morphology and elemental confirmation of the prepared samples were obtained from scanning electron microscopy and Energy dispersive X-ray Analysis spectrometer (EDAX, Oxford Instrumentations inbuilt with FE-SEM). Also, the surface morphology with d-spacing of the $\text{CoFe}_2\text{-MOF}$ and derived nanoporous carbon samples were found by using transmission electron microscopy (TEM) analysis from Hitachi/HF-3300 TEM (300 kV). The elemental content of the $\text{CoFe}_2\text{-MOF}$ and derived nanoporous carbon samples was investigated using X-ray photoelectron spectroscopy (XPS) with a Thermo Fisher Scientific SIGMA PROBE.

The porosity of the material was investigated on NOVA1000e Quantachrome (BET), USA. The magnetic behavior of the CoFe₂-MOF and derived nanoporous carbon samples were investigated by using Vibrating-sample magnetometer (VSM) from superconducting quantum interference device (SQUID) vibrating sample magnetometry (VSM) (Quantum Design).

6.3.4 Preparation of working electrodes

Stainless steel mesh was employed as a current collector to fabricate working electrodes. Prior to the fabrication of the electrodes, the substrate, stainless steel mesh, was cleaned using an ultrasonic cleaning process with soap solution, deionized water, and acetone for 20 minutes each. To fabricate the working electrodes, stainless steel mesh was then coated with a homogenous slurry and dried at 70°C. The slurry contained CoFe₂-MOF/ CoFe₂O₄/ nanoporous carbon, polyvinylidene fluoride, and acetylene black in an 80:10:10 weight ratio in N, N-dimethyl formamide. Each electrode had a surface area of 1 cm × 1 cm.

6.3.5 Preparation of an all-in-one solid-state hybrid supercapacitor device

Gel electrolyte was prepared prior to the device's construction by combining 1 g of polyvinyl alcohol (PVA, 99 %, M. W. = 1700-1800, Loba Chemie Pvt. Ltd., India) powder with 20 ml of deionized water at 80 °C for 20 min. The aforementioned solution was then mixed with 10 ml of 2 M potassium hydroxide (KOH), dropwise, and agitated for an additional 2 hours at room temperature to produce a translucent gel electrolyte (PVA-KOH).²³ The constructed all-in-one hybrid supercapacitor device was then built in a sandwich type with two distinct working electrodes (CoFe₂O₄ and nanoporous carbon as a anode and cathode, respectively) coated with PVA-KOH gel electrolyte, joined together with gel sided face to each other, and left at room temperature overnight for natural drying.

6.3.6 Electrochemical measurements

Electrochemical performance of the CoFe₂-MOF, CoFe₂O₄ and NPC electrodes were tested on a CHI608 electrochemical analyzer at room temperature in an aqueous 2 M KOH electrolyte. The electrochemical properties of electrodes were assessed using cyclic voltammetry (CV), galvanostatic charge–discharge (GCD), and electrochemical impedance spectroscopy (EIS) using three electrode assembly in an aqueous 2 M KOH electrolyte. The fabricated CoFe₂-MOF, CoFe₂O₄ and NPC electrodes were employed as a working electrodes, saturated Ag/AgCl was employed as reference electrode and graphite is employed as a counter electrode. The frequency

range used for the electrochemical impedance spectroscopy (EIS) experiments was 1 Hz to 100 kHz.

Using the equation (6.1), the specific capacitance of the CoFe₂-MOF, CoFe₂O₄ and NPC electrode was estimated using a charge-discharge cycle.

$$C_{sp} = \frac{I\Delta t}{m\Delta V} \dots\dots\dots (6.1)$$

Where C_{sp} denotes specific capacitance measured in F g⁻¹, I denotes the specified current measured in ampere, Δt denotes the discharge time measured in seconds, m denotes the mass of the materials measured in grams, and ΔV denotes the potential window of the discharging process measured in volt.

The specific energy and power of the all-in-one hybrid supercapacitor device was determined by using equations (6.2-6.3),²⁴

$$E_s = \frac{0.5 \times C_{sp} \times \Delta V^2}{3.6} \dots\dots\dots (6.2)$$

$$P_s = \frac{E_s \times 3600}{\Delta t} \dots\dots\dots (6.3)$$

Where E_s denotes the specific energy measured in Wh kg⁻¹ and P_s denotes the specific power measured in W kg⁻¹.

6.4 Results and discussion

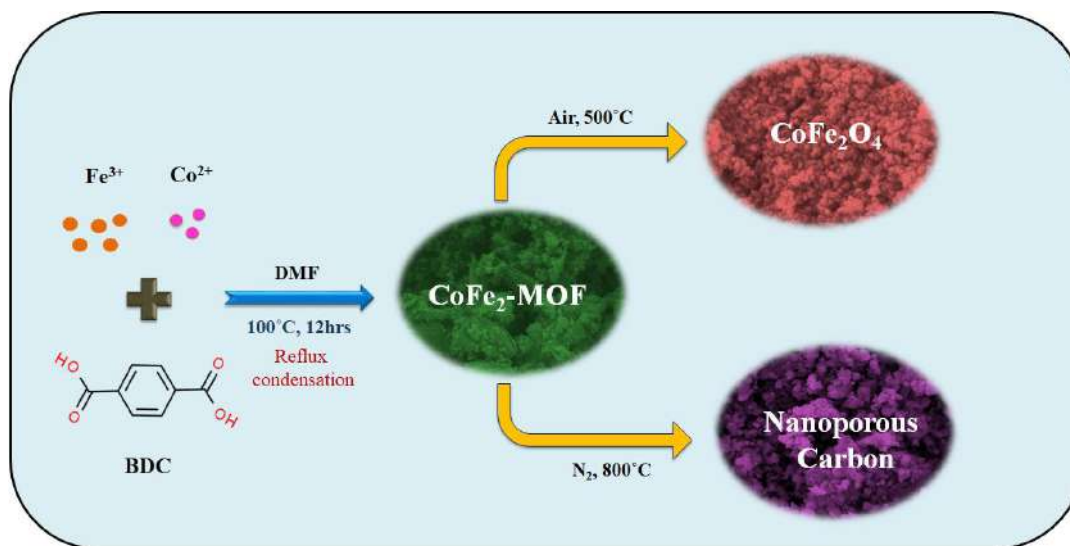


Figure 6.1: Schematic illustration of the synthesis of CoFe₂-MOF, its derived CoFe₂O₄ and nanoporous carbon (NPC)

Figure 6.1 depicts a schematic overview of the experimental procedures employed in this investigation to the synthesis of CoFe₂-MOF derived CoFe₂O₄ and nanoporous carbon using the "One-for-All" approach. Two basic steps were involved in the synthesis process. In the first step, the bimetallic CoFe₂-MOF array precursor

was initially prepared through the complexation reaction of Co^{2+} , Fe^{3+} , and terephthalic acid. Second, following the first step, the synthesized bimetallic $\text{CoFe}_2\text{-MOF}$ were used as a precursor to synthesize both CoFe_2O_4 and NPC by directly pyrolyzing them at 500°C in air atmosphere and 800°C in nitrogen atmosphere, respectively.

6.4.1 X-ray diffraction of $\text{CoFe}_2\text{-MOF}$, CoFe_2O_4 and NPC

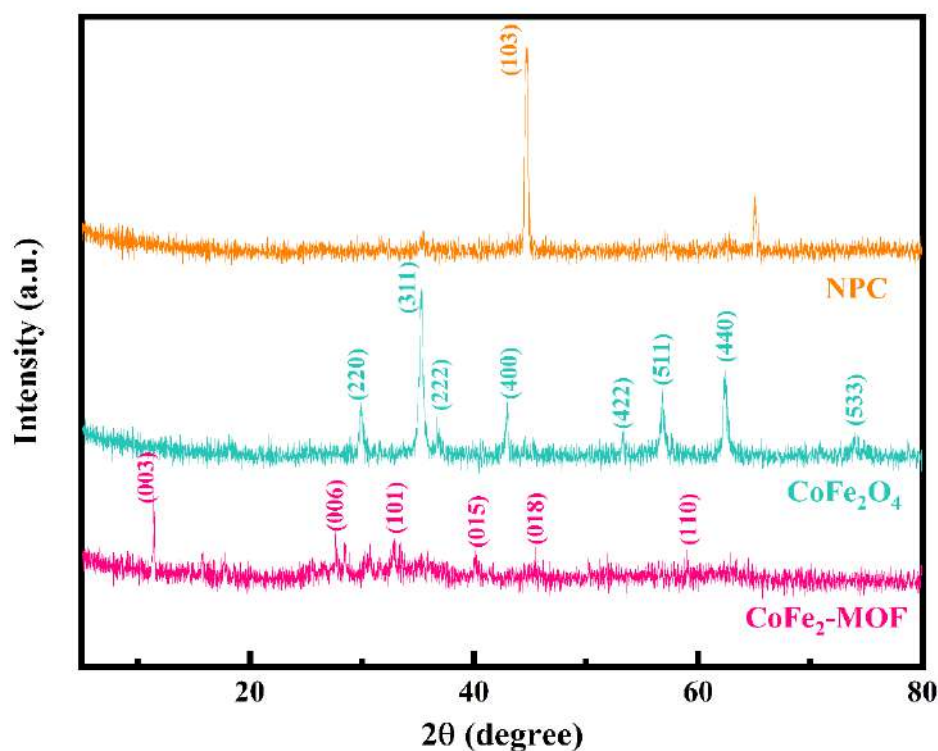


Figure 6.2: XRD patterns of $\text{CoFe}_2\text{-MOF}$, CoFe_2O_4 and NPC

The structural, morphological and compositional features of the as-synthesized hierarchical MOF and their derived materials were identified using a various characterization techniques. The $\text{CoFe}_2\text{-MOF}$ has been successfully synthesized, as indicated by the fact that the diffraction peaks closely match with those of the earlier reports.^{25,26} The XRD pattern of $\text{CoFe}_2\text{-MOF}$ exhibits major diffraction peaks at 2θ values of 11° , 26° , 33° , 39° , 46° , and 59° corresponding to (003), (006), (101), (015), (018) and (110) planes with a rhombohedral phase (JCPDS card No. 00-050-0235). To confirm the crystalline structure and phase of the $\text{CoFe}_2\text{-MOF}$ annealed at 500°C under air atmosphere was also examined by XRD technique. In the XRD pattern of CoFe_2O_4 , the diffraction peaks are located at 30° , 35° , 37° , 43° , 53° , 56° , 62° and 73° and can be ascribed to the (220), (311), (222), (400), (422), (511), (440) and (533) planes of the CoFe_2O_4 with a cubic phase (JCPDS card No. 01-077-0426). When the

bimetallic MOF was carbonized at 800°C it produces nanoporous carbon, the XRD pattern of NPC shows the presence of one intense peak rooting from the (103) plane at 2θ of 44° with a cubic phase which is well matched with the JCPDS card no. 01-075-0410.

6.4.2 FT-IR spectroscopy of CoFe₂-MOF, CoFe₂O₄ and NPC

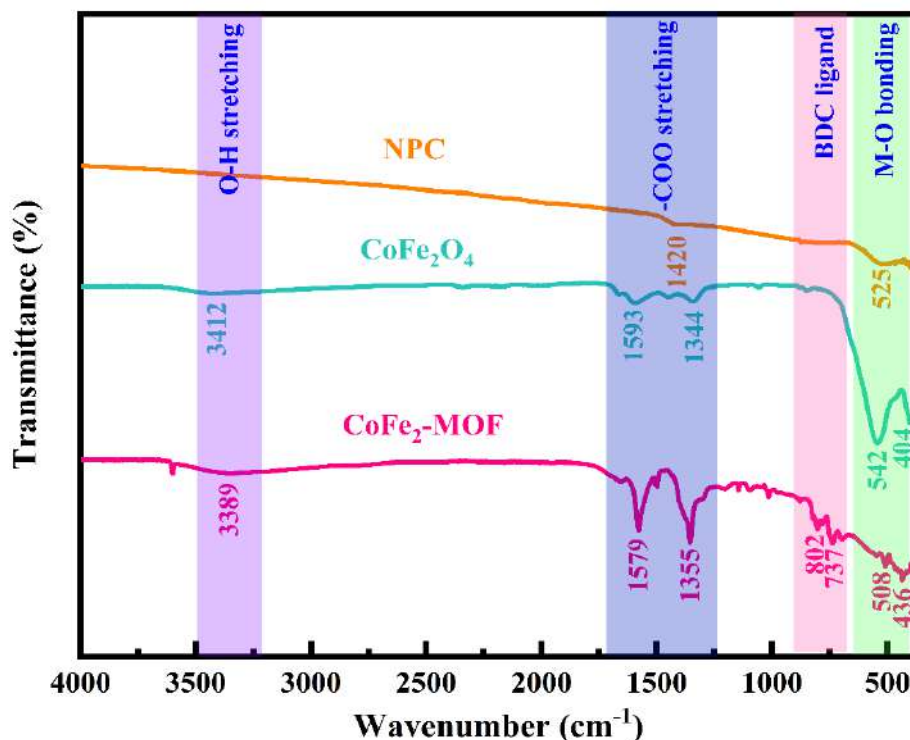


Figure 6.3: FTIR spectra of CoFe₂-MOF, CoFe₂O₄ and NPC

To investigate the presence of functional groups, the FTIR analysis of the CoFe₂-MOF and its MOF-derived CoFe₂O₄ and NPC was performed, depicted in figure 6.3. The absorption band at 3389 and 3412 cm⁻¹ in CoFe₂-MOF and CoFe₂O₄ spectra is responsible to stretching vibrations of the water molecules adsorbed from solvent. In the CoFe₂-MOF spectra, the absorption bands at 1355 and 1579 cm⁻¹ are assigned to the symmetric and asymmetric stretching modes of -COO groups, respectively.²⁷ The division of these symmetric and asymmetric modes suggests that carboxylate group of terephthalic acid (bidentate ligand) is coordinated to nickel with a formation of polymer structure. Additionally, the absorption bands at 737 and 802 cm⁻¹ in the CoFe₂-MOF spectra are attributed to the terephthalic ligand.²⁸ In the CoFe₂-MOF derived CoFe₂O₄ spectra, the weak absorption bands at 1593 and 1344 cm⁻¹, also in derived NPC spectra a weak band at 1420 cm⁻¹ are attributed to the asymmetric and symmetric stretching modes of -COO groups, respectively.^{29,30} The

bands ascribed to terephthalic acid are disappearing in CoFe_2O_4 and NPC due to the decomposition of organic ligand with increasing annealing temperature. The bands observed in the range $400\text{-}600\text{ cm}^{-1}$ in all the spectra are assigned to the metal-oxygen bonding.³¹

6.4.3 Raman spectroscopy of $\text{CoFe}_2\text{-MOF}$, CoFe_2O_4 and NPC

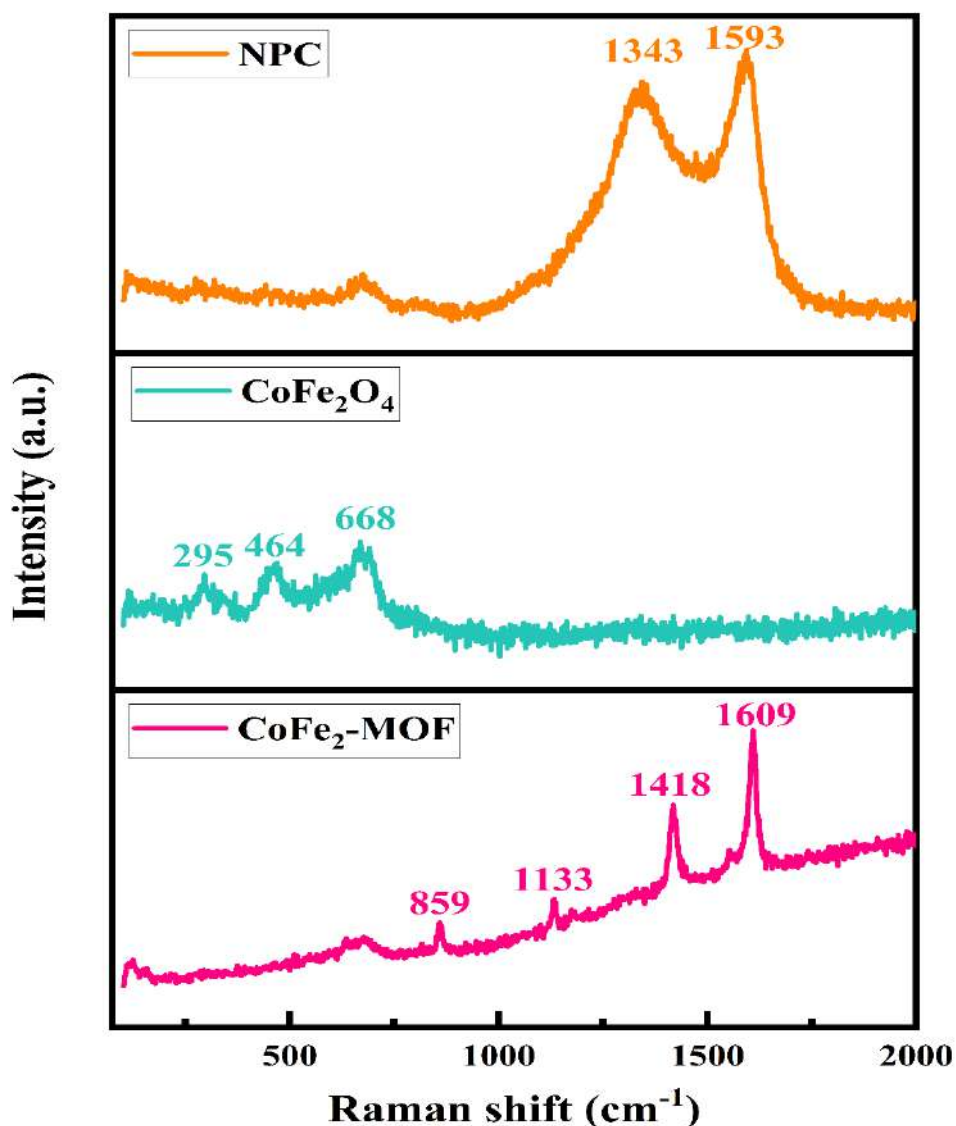


Figure 6.4: Raman spectra of $\text{CoFe}_2\text{-MOF}$, CoFe_2O_4 and NPC

Raman spectroscopy was utilized to explore the structure of $\text{CoFe}_2\text{-MOF}$ and changes in crystal structure as a result of heat treatment of $\text{CoFe}_2\text{-MOF}$. Raman spectra of $\text{CoFe}_2\text{-MOF}$ and $\text{CoFe}_2\text{-MOF}$ derived CoFe_2O_4 and NPC are presented in figure 6.4. In Raman spectra of $\text{CoFe}_2\text{-MOF}$, the bands observed at 1609 and 1418 cm^{-1} are due to the carboxylate group and they are assigned to the asymmetric and symmetric vibration modes. The band at 1133 cm^{-1} was attributed to the vibration of

C-C bond between the benzene ring and the carboxylate group, also the plane of C-H bonding deformation is ascribed to the band at 859 cm^{-1} . As shown in Raman spectra of CoFe₂-MOF, which included a BDC linker, and no Raman signals corresponding to cobalt oxides, iron oxides, or other contaminants were detected.³² According to figure 6.4, the Raman spectra of CoFe₂O₄ exhibit three different peaks in the 200-700 cm^{-1} region. The stretching vibrational modes of CoFe₂O₄ were attributed to the three spectral peaks at 295, 464, and 668 cm^{-1} .³³ Furthermore, the E_g and T_{2g} vibrational modes are responsible for the peaks at 464 and 668 cm^{-1} , respectively. Furthermore, the Raman spectra of NPC shows the peaks at 1343 and 1593 cm^{-1} , which reflect the D and G bands from the A_{1g} and E_{2g} symmetries for nano-structures graphitic carbon, also indicate that the nanoporous carbon calcined under nitrogen atmosphere contains graphitic carbon. Moreover, the D band presence can be linked to the disorder predominantly brought on by the presence of metals, as seen in the XRD and XPS results.^{34,35}

6.4.4 Scanning electron microscopy of CoFe₂-MOF, CoFe₂O₄ and NPC

Surface morphological study of bimetallic CoFe₂-MOF derived CoFe₂O₄ and NPC with lower and higher magnifications is as presented in Figure 5. The uniformly distributed rock shaped morphology of CoFe₂-MOF has been observed and presented in the figure 6.5 (a, b). Additionally, as meticulous observation it is seen that, the tiny granules with few nanometer in size are anchored all over side of the rock hence, the interconnected rocks are noticed in the material it will help to charge transportation in supercapacitor application. In between these two rocks some gaps also present, which is connected to tiny granules therefore has no any chance to interfere of electrolyte and working electrode. This gap increases the surface area of the sample which is useful at application level. The sizes of the rocks are in few micrometers but interconnected tiny granules are few nanometers in size throughout the sample. After modifying the experimental condition, the bimetallic CoFe₂-MOF gets converted into cobalt ferrite and nanoporous carbon at calcination temperature of 500 °C in air atmosphere and 800 °C temperature in nitrogen atmosphere respectively for 3 hr. The intersected layer structure with smooth surface of nanograin like morphology of CoFe₂O₄ has been seen in the figure 6.5 (c, d). The CoFe₂O₄ exhibited the interconnected grain like morphology with average size in few nanometers.

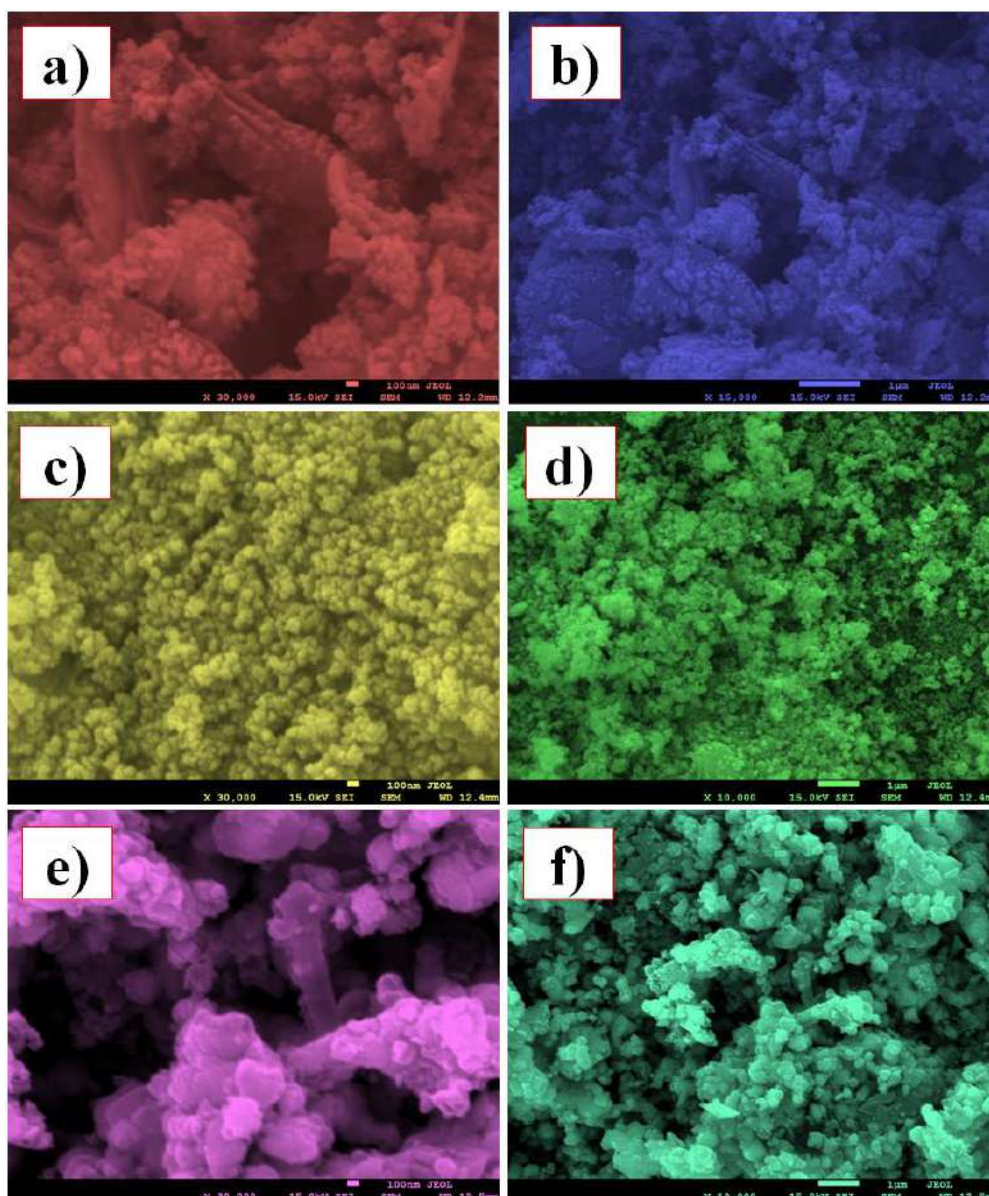


Figure 6.5: SEM images at different magnifications of (a, b) CoFe₂-MOF (c, d) CoFe₂O₄ (e, f) NPC

The CoFe₂O₄ morphology is totally different than bimetallic CoFe₂-MOF may be due to the calcination temperature plays major role in the morphological formation. After calcination in air, rock converted into the grain with porous nature of the sample and creates some pores on the surface of the grain which is discussed under the BET analysis. Then, moving towards calcination at 800 °C in nitrogen atmosphere, the bimetallic CoFe₂-MOF sample gets converted into nanoporous carbon. The small nanobricks like morphology with plenty of pores and the irregular arrangement with different shape and size of the nanobricks are observed (Figure 6.5 (e, f)). More interestingly, the numerous porous bricks are cross connected to each other creating the space in between these nanobricks, which could enhance the surface area of the

sample and it will be more beneficial for the ion-electrolyte transport hence improving electrochemical performance. Out of these three samples, NPC is most favorable sample for enhancing the electrochemical performance of supercapacitor electrode.

6.4.5 Energy dispersive X-ray analysis of CoFe₂-MOF, CoFe₂O₄ and NPC

Figure 6.6 (a-c) depicts the typical EDX spectrum and color mapping of bimetallic CoFe₂-MOF derived CoFe₂O₄ and NPC samples. In reality of Co, Fe, O, C and N peaks in EDX specify the samples contain the cobalt, iron, oxygen, carbon and nitrogen, as anticipated. The atomic percentage of all the samples are uniformly distributed all over the samples and it is in well agreement with the stoichiometry of all the samples. The inset of the figure reveals the pie diagram of all the elements in the corresponding samples. More interestingly, after calcination of the bimetallic CoFe₂-MOF in air, the percentage of the oxygen is rich in consent sample. Similarly, bimetallic CoFe₂-MOF calcination in nitrogen atmosphere shows increase in the percentage of the carbon in the corresponding sample. Also, the figure 6.6 (a-c) shows colour mapping of different elements like Co, Fe, O, C and N in all samples. Hence, it is confirmed that our prepared samples are in the pure form and will be beneficial for energy storage application.

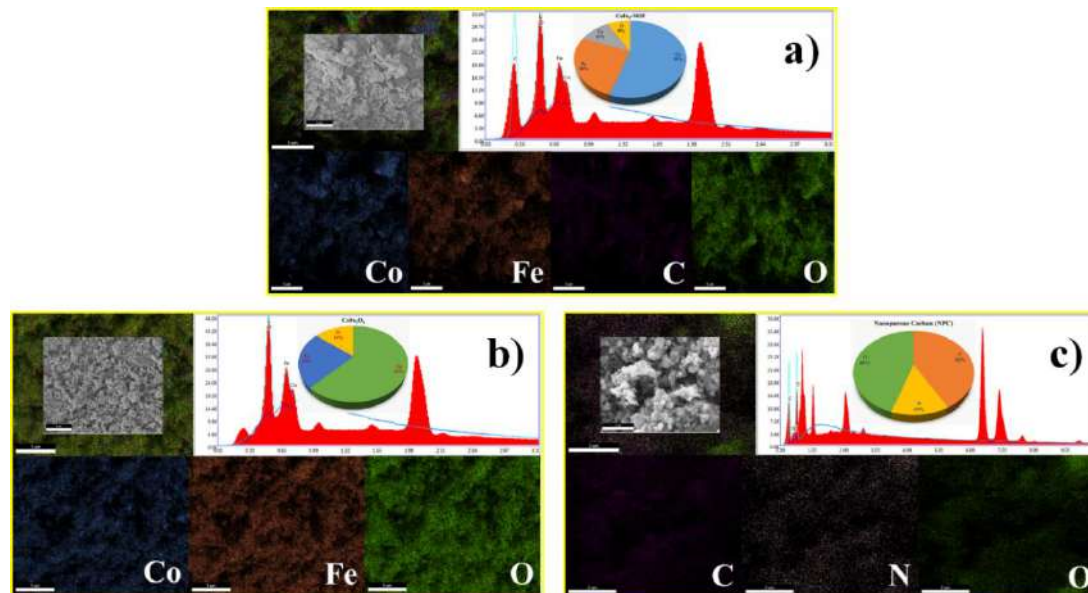


Figure 6.6: Elemental mapping images of (a) CoFe₂-MOF (b) CoFe₂O₄ (c) NPC

6.4.6 Transmission electron microscopy of CoFe₂-MOF, CoFe₂O₄ and NPC

TEM, HRTEM, and SAED analysis were carried out to gain a thorough understanding of the structure of CoFe₂-MOF and its generated CoFe₂O₄ and NPC. Figure 6.7(a and b) shows TEM images of CoFe₂-MOF with a rock-like shape, which

corresponds to the FESEM findings. The lattice fringe spacing in the following HRTEM image as shown in figure 6.7(c) is about 0.205 nm, which is compatible with the (003) plane of CoFe₂-MOF. The SAED pattern indicates the polycrystalline nature of CoFe₂-MOF as shown in figure 6.7(d) and that is consistent with the XRD findings, suggesting the development of CoFe₂-MOF.^{36,37} The TEM images of CoFe₂O₄ exhibit grain-like microstructures, as seen in figure 6.7(e and f), which are compatible with the FESEM pictures. The lattice spacing of 0.307 nm from the HRTEM image in figure 6.7(g) corresponds to the (311) plane of CoFe₂O₄. Furthermore, the SAED picture in figure 6.7(h) shows that CoFe₂O₄ is polycrystalline.^{38,39} The TEM images of NPC indicate nanobricks-like structures, as seen in figures 6.7(i and j) that are compatible with the FESEM images. The lattice spacing of 0.225 nm from the HRTEM image in figure 6.7(k) corresponds to the (103) plane of NPC. The SAED pattern, as shown in figure 6.7(l), reveals the polycrystalline nature of NPC and is compatible with the XRD findings, implying the creation of NPC.⁴⁰

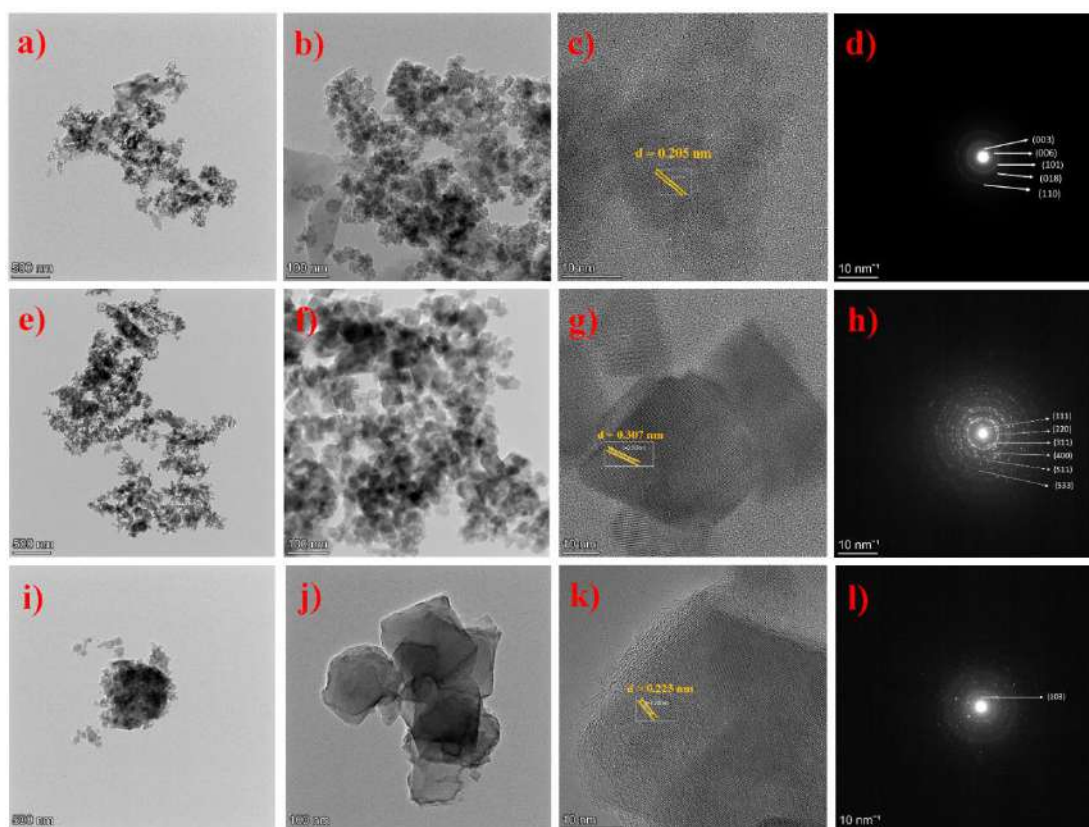


Figure 6.7: TEM, HR-TEM and SAED pattern of the as-prepared CoFe₂-MOF (a-d), CoFe₂O₄ (e-h) and NPC (i-l)

6.4.7 Brunauer-Emmett-Teller analysis of CoFe₂-MOF, CoFe₂O₄ and NPC

The specific surface area and porosity of NPC and CoFe₂O₄ derived from CoFe₂-MOF were characterised using nitrogen adsorption/desorption studies at 77 K and BJH pore size distributions analyses, as shown in figure 6.8(a-c). The fact that all of the samples exhibit a type-IV hysteresis loop at relative pressures between 0.4 and 0.9 indicates that the samples are mesoporous in nature. While CoFe₂-MOF (406 m² g⁻¹) and CoFe₂O₄ (289 m² g⁻¹) have lower specific surface areas than the NPC (614 m² g⁻¹), which is depicted in table 6.1. Furthermore, BJH pore size analysis of NPC reveals a 1.78 nm pore size with a maximal number of mesopores. CoFe₂-MOF and CoFe₂O₄ have pore radius of 1.80 and 1.84 nm, respectively, as illustrated in figure 6.8(d-f). NPC has a higher surface area than CoFe₂-MOF and CoFe₂O₄ according to BET surface area measurement.

Table 6.1: Textural properties of CoFe₂-MOF, its derived CoFe₂O₄ and NPC.

Samples	Surface area (m ² g ⁻¹)	Pore radius (nm)
CoFe ₂ -MOF	406	1.80
CoFe ₂ O ₄	289	1.84
NPC	614	1.78

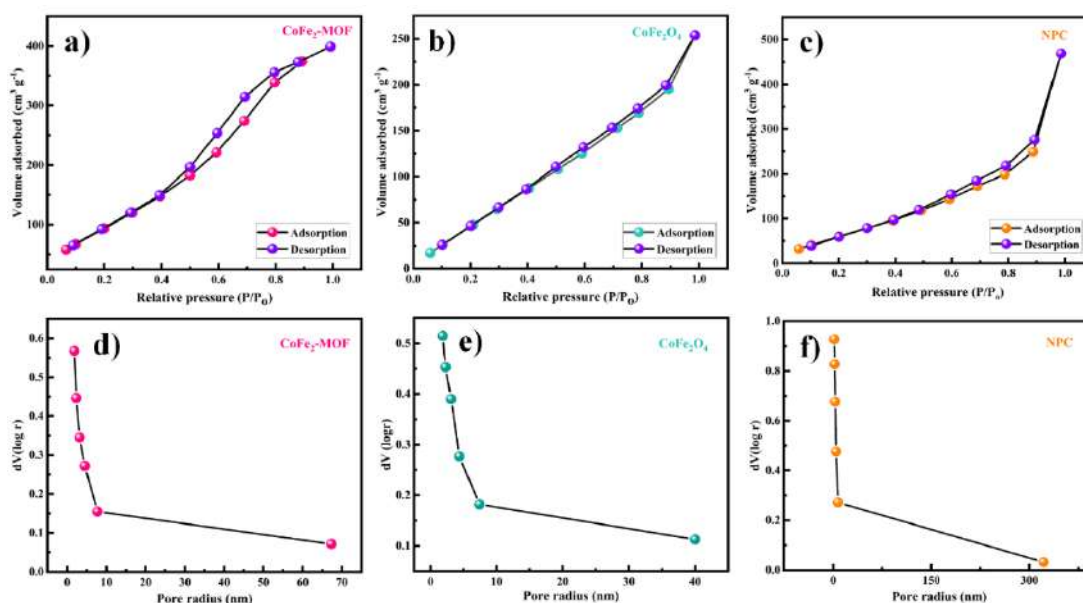


Figure 6.8: Nitrogen adsorption-desorption isotherm and BJH pore size distribution plots of (a, d) CoFe₂-MOF, (b, e) CoFe₂O₄ and (c, f) NPC

6.4.8 Vibrating sample magnetometer of CoFe₂-MOF, CoFe₂O₄ and NPC

The VSM measurements were performed to measure the magnetization of the prepared materials as a function of magnetic field. In-depth magnetic measurements were made on CoFe₂O₄, CoFe₂-MOF and CoFe-MOF derived nanoporous carbon in order to analyze the impact of functionalization on MNPs magnetic behavior. Figure 6.9 displays the magnetization curves of the NPC and CoFe₂O₄ derived from CoFe₂-MOF at ambient temperature. The saturation magnetization (M_s) value, calculated by fitting the M vs. $1/H$ curves due to the non-saturating magnetization even at higher fields. The M_s values of CoFe₂-MOF, CoFe₂O₄, and CoFe-MOF derived NPC are 2.12, 51.07, and 110.95 emu g⁻¹, respectively. Thus, the M_s value of NPC is much higher than the CoFe₂-MOF, CoFe₂O₄, samples.

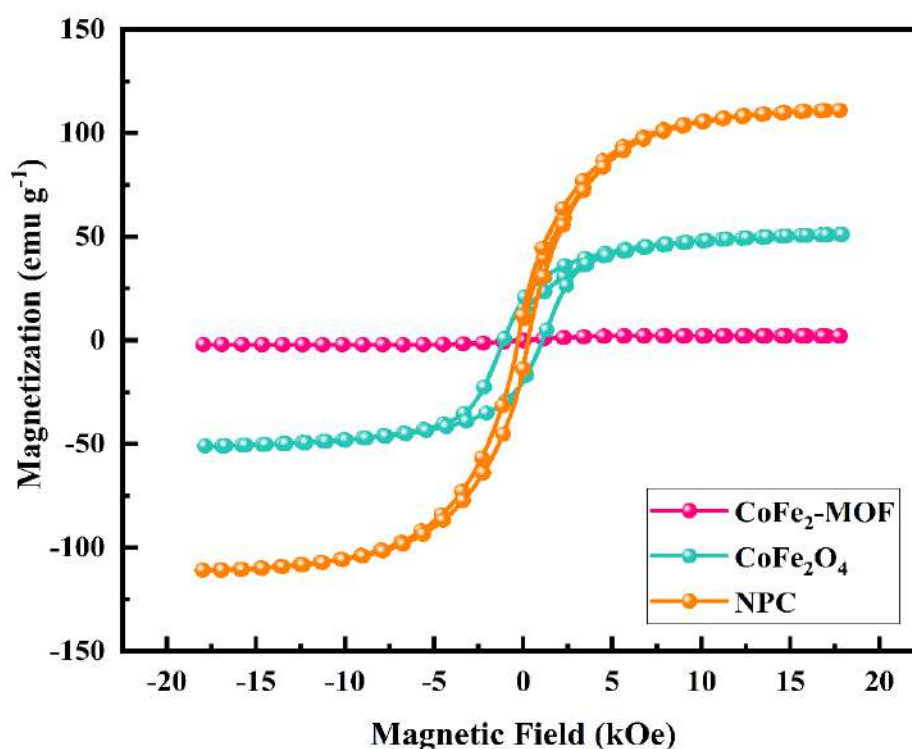


Figure 6.9: Hysteresis curves of CoFe₂-MOF, CoFe₂O₄ and NPC

Still, the relation between M_s and SC is not yet highly explored. The magnetic and electric coupling of the materials provides a new insightful way for magnetoelectric phenomenon. However, the magnetic field can enhance the power density, energy density, and improves cyclic stability. Further, Rebecca Sikkema et al. stated that higher the magneto capacitance and magnetoelectric phenomenon, the effect of magnetic field on electric diffusion, structure of EDLC charge transfer resistance influences the charge/discharge behavior of the materials.⁴¹ Hence, NPC

will be more beneficial for many technological applications especially for supercapacitor because of its surface area, pore size and higher M_s value. We believe that the obtained high M_s values and high capacitance value of the material will pave the way for the novel physio-chemical phenomena in the field of magnetoelectric supercapacitor.

6.4.9 X-ray photoelectron spectroscopy of CoFe₂-MOF, CoFe₂O₄ and NPC

The X-ray photoelectron spectroscopy analysis was utilized to examine the chemical makeup and electronic configuration of CoFe₂-MOF, CoFe₂O₄, and nanoporous carbon. The figure 6.10 shows the XPS spectrums of CoFe₂-MOF, CoFe₂O₄, and nanoporous carbon revealing the presence of Co, Fe, C, N and O components in the materials.

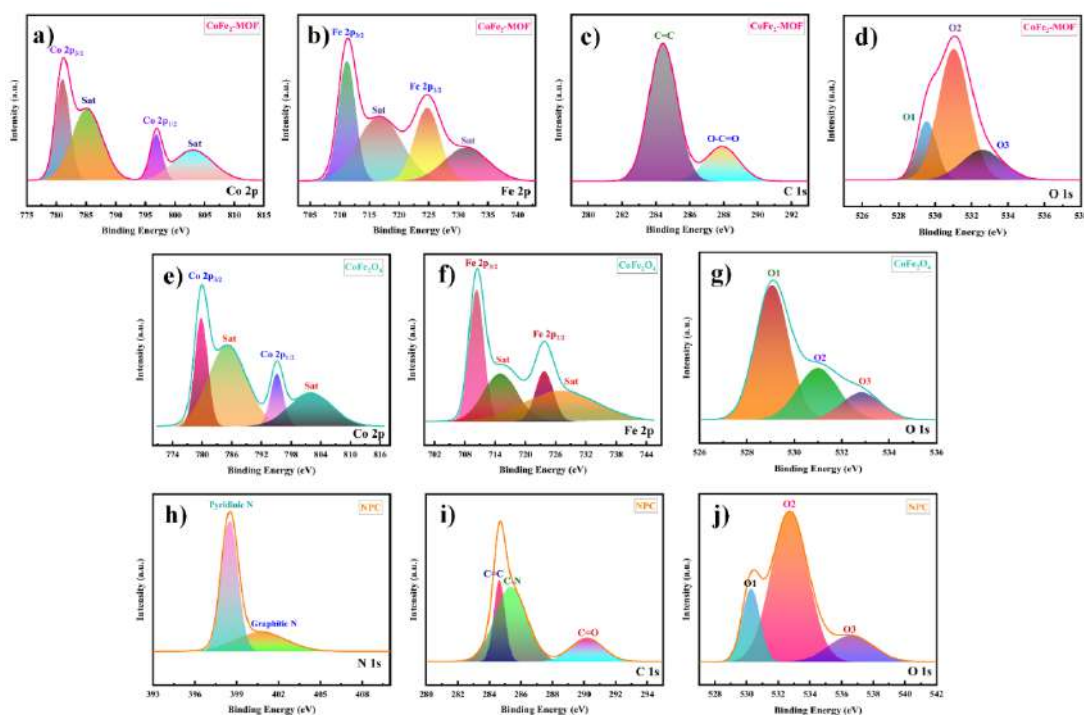


Figure 6.10: High-resolution XPS spectra of (a-d) CoFe₂-MOF (e-g) CoFe₂O₄ (h-j) NPC

The high-resolution XPS spectrum of Co 2p show peaks at 781.0 and 796.8 eV in CoFe₂-MOF, also the peaks at 779.8 and 795.1 eV in CoFe₂O₄ are assigned to Co 2p_{3/2} and Co 2p_{1/2} of Co(II) as depicted in figure 6.10(a, e). Moreover, the existence of two satellite peaks situated at 785.1 and 802.8 eV in CoFe₂-MOF and peaks at 785.0 and 801.7 eV in CoFe₂O₄ substantiates the occurrence of Co²⁺ oxidation state in the materials. In CoFe₂-MOF, the Fe2p spectrum exhibits peaks at 711.2 and 724.7 eV, while in CoFe₂O₄, the peaks are at 710.3 and 723.8 eV, indicates

the +3 oxidation state of Fe in both samples as shown in figure 6.10(b, f). At high magnification, the figure 6.10(c) shows the spectra of C1s reveal a dual peak structure with binding energies of 284.4 and 287.9 eV, which correspond to the C=C and O-C=O bonds found in CoFe₂-MOF. Additionally, three peaks can be observed at binding energies of 284.6, 285.3, and 290.1 eV, which provide confirmation of the existence of C=C, C-N, and C=O bonds in nanoporous carbon as shown in figure 6.10(i). Figure 6.10(d, g, j) displays the deconvoluted O1s spectra for CoFe₂-MOF, CoFe₂O₄, and nanoporous carbon. The presence of three peaks for each material indicates the existence of M-O, C-O, and C=O bonds in them.^{42,43} The N1s spectra of nanoporous carbon material were analyzed and two separate peaks were identified. These peaks corresponded to the binding energies of pyridinic-N at 398.4 eV and graphitic-N at 400.7 eV, as shown in the figure 6.10(h).⁴⁴

6.4.10 Electrochemical measurements of CoFe₂-MOF, CoFe₂O₄ and NPC electrodes

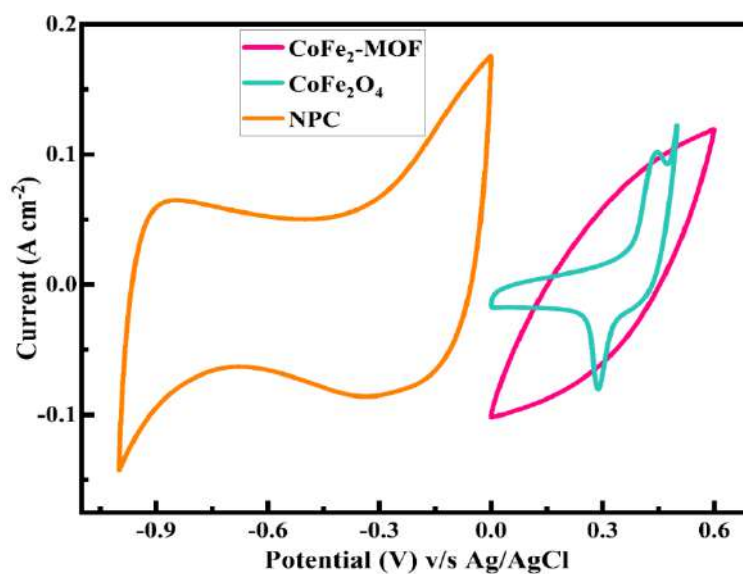


Figure 6.11: CV curves of CoFe₂-MOF, CoFe₂O₄, and NPC within different operating potential windows at a constant scan rate of 100 mV s⁻¹

The intriguing structural and morphological characteristics of CoFe₂-MOF, CoFe₂O₄ and NPC materials compel us to investigate their electrochemical properties. Electrochemical performance of the fabricated CoFe₂-MOF, CoFe₂O₄ and NPC electrodes were investigated using a 2 M KOH as aqueous electrolyte in a three-electrode system utilizing saturated Ag/AgCl employed as a reference electrode, graphite employed as a counter electrode and fabricated electrodes employed as a working electrode. The CV curves for CoFe₂-MOF, CoFe₂O₄ and NPC electrodes at a

scan rate of 100 mV s^{-1} are shown in figure 6.11. It is revealed that $\text{CoFe}_2\text{-MOF}$, CoFe_2O_4 and NPC electrodes operate in various potential range. Figure 6.12(a-c) represents the CV profiles of $\text{CoFe}_2\text{-MOF}$, CoFe_2O_4 and NPC electrodes at scan rates from 10 to 100 mV s^{-1} . The CV curves of $\text{CoFe}_2\text{-MOF}$ electrodes are semirectangular in form and may be characterised by the presence of double-layer capacitance as well as pseudocapacitive behaviour, as illustrated in figure 6.12(a). The CV curves of the CoFe_2O_4 electrode show distinct redox peaks, indicating that the unique capacitance properties are mostly caused by faradic redox reactions, as illustrated in figure 6.12(b). Furthermore, the CV profiles of NPC are rectangular in shape, indicating EDLC behaviour with good capacitive performance and quick current responses, as shown in figure 6.12(c). From the aforementioned CV results, it can be deduced that as scan rate decreases, the area under the CV curve also decreases, which leads to a decrease in current. This is because electric charges may find it challenging to occupy all of the available sites at the electrode-electrolyte interface assignable to their slow rate of migration and erratic orientation in the electrolyte.^{45,46} This behaviour also demonstrates that the NPC electrode facilitates fast ion diffusion via the pores at high rates, as compared to $\text{CoFe}_2\text{-MOF}$ and CoFe_2O_4 . The area under the CV curve of the NPC is bigger than that of the $\text{CoFe}_2\text{-MOF}$ and CoFe_2O_4 , showing improved EDLC behaviour.

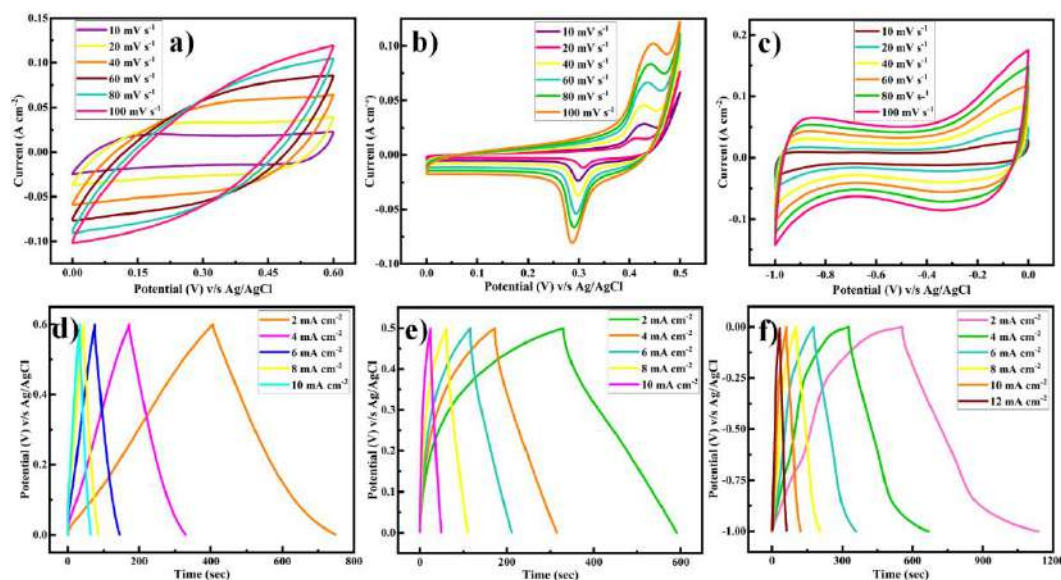


Figure 6.12: The three-electrode electrochemical performances of $\text{CoFe}_2\text{-MOF}$ -derived CoFe_2O_4 and NPC: CV curves at various scan rates of (a) $\text{CoFe}_2\text{-MOF}$, (b) CoFe_2O_4 , (c) NPC, GCD curves at various current densities of (d) $\text{CoFe}_2\text{-MOF}$, (e) CoFe_2O_4 , (f) NPC

Galvanostatic charge-discharge (GCD) testing with varied current densities is used to further examine the capacity and rate capabilities of CoFe₂-MOF, CoFe₂O₄, and NPC electrodes as shown in figure 6.12(d-f). Every GCD curve has a pair of charge-discharge plateaus. The charge-discharge curve shows remarkable symmetry, signifying excellent reversibility. The specific capacitance of the CoFe₂-MOF, CoFe₂O₄, and NPC electrodes is determined depending on GCD curves and equation (6.1), and outcomes are depicted in figure 6.13(a). The GCD outcomes strongly imply that the NPC electrode provided the maximum specific capacitance at different current densities and excellent electrochemical performance. The NPC electrode had a greater specific capacitance of 1271 F g⁻¹ at 2 mA cm⁻² than the CoFe₂-MOF (1038 F g⁻¹ at 2 mA cm⁻²) and CoFe₂O₄ (973 F g⁻¹ at 2 mA cm⁻²) electrodes. The specific capacitances of NPC were 1271, 1170, 992, 749, 553, and 331 F g⁻¹, corresponding to 2, 4, 6, 8, 10, and 12 mA cm⁻² current density, demonstrating the superior rate capability, which is significantly greater than that of CoFe₂-MOF (1038, 961, 670, 567 and 469 F g⁻¹, corresponding to 2, 4, 6, 8 and 10 mA cm⁻² current density) and CoFe₂O₄ (973, 906, 776, 628 and 437 F g⁻¹ corresponding to 2, 4, 6, 8 and 10 mA cm⁻² current density) electrodes. Figure 6.13(a) indicates the rate capability of CoFe₂-MOF, CoFe₂O₄ and NPC electrode, illustrating that when the current density increases, specific capacitance falls slightly. According to the preceding data, specific capacitance reduces as current density increases and vice versa. This is due to the fact that at higher current densities, the electrolyte ions participate in the bulk surface for the electrochemical reaction due to ion transport restrictions, so capacitance values decrease, whereas at low current densities, the electrolyte ions have enough time to move across the interior pores of the electrode material, so capacitance values increase.

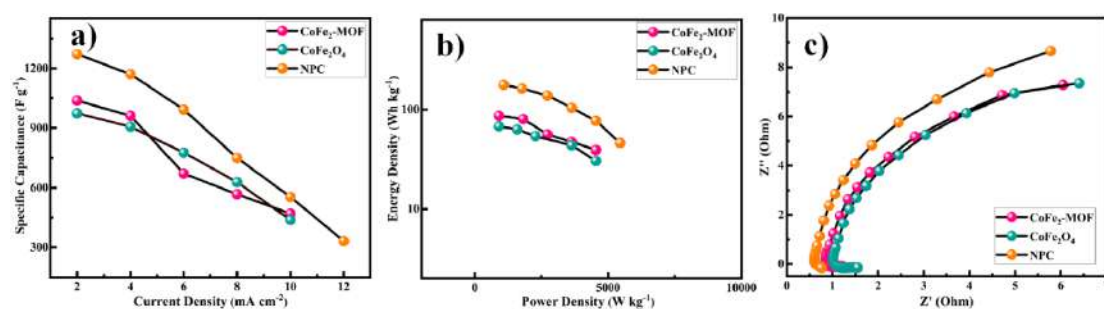


Figure 6.13: (a) Specific capacitance at the different current densities of CoFe₂-MOF, CoFe₂O₄ and NPC, (b) Ragone plot of CoFe₂-MOF, CoFe₂O₄ and NPC, (c) EIS curves of CoFe₂-MOF, CoFe₂O₄ and NPC

The two most important metrics for evaluating the performance of supercapacitor devices are energy density and power density, which were computed and depicted in the Ragone plot as shown in figure 6.13(b). The NPC reaches a maximum energy density of 176 Wh kg^{-1} at a power density of 1090 W kg^{-1} as compared to the $\text{CoFe}_2\text{-MOF}$ (86 Wh kg^{-1} at 909 W kg^{-1}) and CoFe_2O_4 (67 Wh kg^{-1} at 900 W kg^{-1}), respectively. EIS was used to examine the internal resistance of electrodes and the ion/electron transport kinetics at the electrode-electrolyte connection.⁴⁷ The EIS spectra for $\text{CoFe}_2\text{-MOF}$, CoFe_2O_4 and NPC electrodes were measured in the frequency range 1 Hz to 100 kHz and are displayed as Nyquist plots in figure 6.13(c). From EIS spectra, the semicircle in the high-frequency region was utilized to calculate the charge transfer resistance (R_{ct}) at the electrode-electrolyte contact. It is obvious that the semicircle of the NPC electrode was smaller than of the $\text{CoFe}_2\text{-MOF}$ and CoFe_2O_4 electrodes, indicating a quicker charge transfer that permitted the quick redox reactions. The charge transfer resistance of the $\text{CoFe}_2\text{-MOF}$, CoFe_2O_4 , and NPC electrodes were evaluated to be 0.34, 0.46 and 0.15Ω , respectively. Therefore, the improved electrochemical characteristics of the NPC electrode may be effectively explained by the combined benefits of ion diffusion kinetics and rapid electron transport.

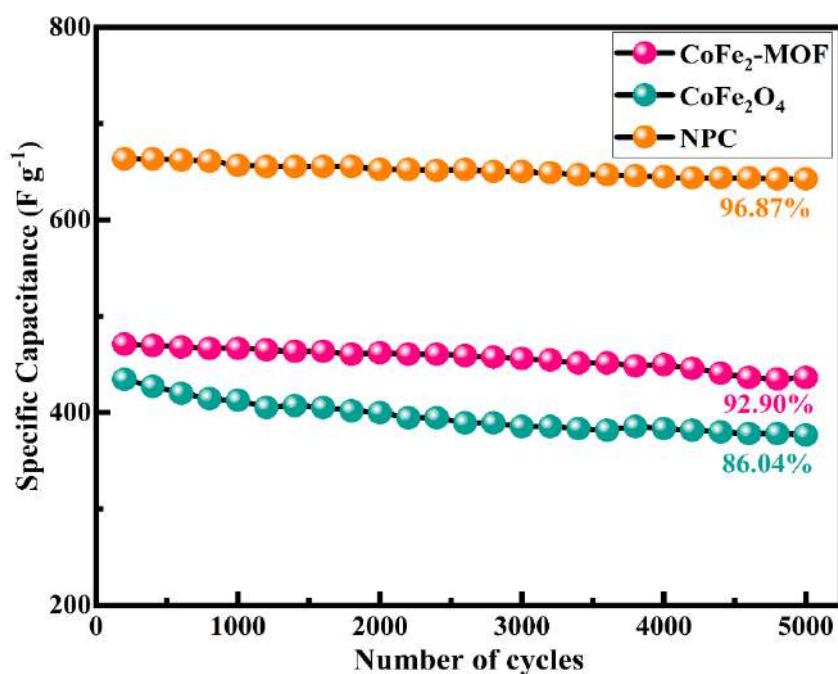


Figure 6.14: Cycle lives measured from galvanostatic charge-discharge of the $\text{CoFe}_2\text{-MOF}$ (at 10 mA cm^{-2} current density), CoFe_2O_4 (at 10 mA cm^{-2} current density) and NPC (at 12 mA cm^{-2} current density) electrodes

The cyclic stability of energy storage devices is crucial for their practical use. Figure 6.14 depicts the long-term cyclic stability evaluations of CoFe₂-MOF, CoFe₂O₄ and NPC electrodes performed at 10, 10, and 12 mA cm⁻² current density for 5000 charge-discharge cycles. Compared to CoFe₂-MOF and CoFe₂O₄ electrodes, the NPC electrode retained an ultrahigh cycling life with 96.87 % of the original capacitance as the current density grew six-fold up to 12 mA cm⁻² even after 5000 cycles. The MOF and ferrite electrode shows 92.90 and 86.04 % cyclic stability at five-fold increased current density of 10 mA cm⁻², respectively. The enormous surface area of NPCs, which can offer more active sites inside the pores for quick electrochemical reactions and enhance the transport of ions or electrons at the electrolyte/electrode contact, is a contributing factor in their superior electrochemical performance. The existence of mesopores in the NPC material can provide a rapid diffusion channel for electrolyte infusion as well as ion or electron transport.

6.4.11 Electrochemical characterization of CoFe₂O₄/NPC all-in-one hybrid supercapacitor device (CoFe₂O₄/NPC HSC device)

To further examine the feasibility of the CoFe₂-MOF, CoFe₂O₄, and NPC electrode materials for practical use, ‘all-in-one’ a hybrid supercapacitor device was built utilizing the synthesized CoFe₂O₄ electrode as an anode, NPC electrode as a cathode and PVA-KOH as a gel -polymer electrolyte (denoted as CoFe₂O₄/NPC). Liquid electrolytes used in supercapacitors poses a concern due to its susceptible to evaporation and leakage problem, which restricts their long-term usage. Gel-polymer electrolyte are made of liquid electrolytes that have been numbed in a polymer matrix, which solves the leakage issue. Gel-polymer electrolyte contain significantly less free water than liquid electrolytes, they can decrease water oxidation processes, therefore expands the operating voltage window, which have long been a barrier in liquid electrolyte-based supercapacitors. As a result, the KOH liquid electrolyte was embedded in a matrix of poly vinyl alcohol, on account of its OH⁻ groups, can retain water and provide excellent ion-conducting routes.^{48,49} Motivated by the electrode's excellent capacitive performance, its possibilities in real-world applications were built by fabricating a solid-state hybrid supercapacitor device, as illustrated in figure 6.15. CV, GCD, and EIS measurements were used to evaluate the capacitive performance of the fabricated all-in-one hybrid supercapacitor device. In the charge-discharge process, K⁺ and OH⁻ ions move in opposite directions, towards the negative and positive electrodes. On the negative electrode, EDLC behaviour is caused by the

adsorption and desorption of K^+ ions, whereas on the positive electrode, pseudocapacitive behaviour is caused by reversible fast surface redox processes involving OH^- ions. The operating potential range of the cathode and anode in a three-electrode assembly allows for adjustment of the hybrid supercapacitor's cell voltage. The $CoFe_2O_4//NPC$ HSC device displays strong rectangular-shaped CV curves with redox peaks at the cell voltage of 1.4 V, demonstrating the synergistic effect of EDLC and pseudocapacitance.



Figure 6.15: Schematic illustration of fabrication of all-in-one hybrid supercapacitor device

Figure 6.16(a) depicts the CV curves of a hybrid supercapacitor with a potential voltage of 0.6 - 1.4 V; moreover, there was no substantial change in the CV curves, suggesting that the voltage to be reached was achievable. Figure 6.16(b) displays the CV curves of the $CoFe_2O_4//NPC$ HSC device at different scan rate ranging from 10 to 100 $mV s^{-1}$. This is supported by both the pseudocapacitance from the $CoFe_2O_4$ and the electric double-layer capacitance from the NPC for the charge storage process. Similarly, GCD curves of $CoFe_2O_4//NPC$ HSC device at a fixed current density of 1 $mA cm^{-2}$ from potential range of 0.8 to 1.4 V demonstrated that there is no evident hydrogen or oxygen evolution behaviour and that the cell has excellent electrochemical reversibility, as shown in figure 6.16(c). As a result, a complete analysis of the $CoFe_2O_4//NPC$ HSC device is carried out in the voltage range of 0 - 1.4 V. The GCD curves of the $CoFe_2O_4//NPC$ HSC device at various current densities ranging from 1 to 5 $mA cm^{-2}$ are shown in figure 6.16(d). The triangular forms produced by GCD curves are consistent with CV curves. Figure 6.17(a) depicts the specific capacitances of the $CoFe_2O_4//NPC$ HSC device calculated

from the GCD curves using equation (6.1). The assembled $\text{CoFe}_2\text{O}_4/\text{NPC}$ HSC device achieved high specific capacitance from 112.1 F g^{-1} at 1 mA cm^{-2} to 85.1 F g^{-1} at 5 mA cm^{-2} current density. Additionally, even after raising the current density by five times, the initial specific capacitance retains, as is seen in figure 6.17(a). This outcome attests to its excellent electrochemical performance. Energy density and power density are used to assess the efficiency of supercapacitors.

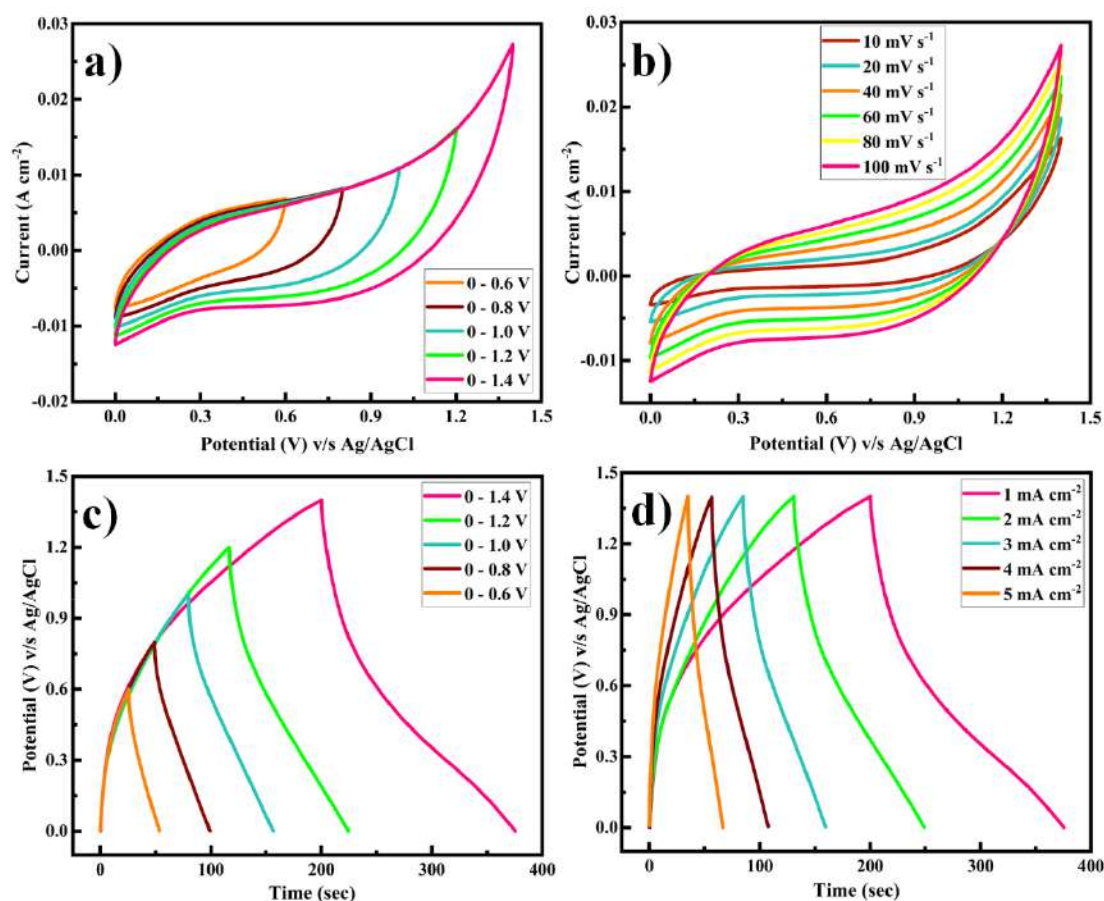


Figure 6.16: Electrochemical tests of the $\text{CoFe}_2\text{O}_4/\text{NPC}$ hybrid supercapacitor device (HSC), (a) CV curves of the $\text{CoFe}_2\text{O}_4/\text{NPC}$ HSC device at a scan rate of 100 mV s^{-1} within different potential windows, (b) CV curves of $\text{CoFe}_2\text{O}_4/\text{NPC}$ HSC device at different scan rates, (c) GCD curves of the $\text{CoFe}_2\text{O}_4/\text{NPC}$ HSC device at 1 mA cm^{-2} with varied potential windows, (d) GCD curves of $\text{CoFe}_2\text{O}_4/\text{NPC}$ HSC device at various current densities

The Ragone plot of the constructed $\text{CoFe}_2\text{O}_4/\text{NPC}$ HSC device at 1.4 V clearly shows that the device has extended energy and power densities. The figure 6.17(b) clearly shows that the manufactured $\text{CoFe}_2\text{O}_4/\text{NPC}$ HSC may deliver a high energy density without compromising much power density. The constructed $\text{CoFe}_2\text{O}_4/\text{NPC}$ HSC device showed an outstanding energy density of 56.2 Wh kg^{-1}

and a power density of 1091.5 W kg^{-1} at 1 mA cm^{-2} current density. Even at a high current density of 5 mA cm^{-2} , the fabricated $\text{CoFe}_2\text{O}_4/\text{NPC}$ HSC device provided an energy density of 42.6 Wh kg^{-1} and a power density of 4297.6 W kg^{-1} . To determine the charge transfer kinetics of the $\text{CoFe}_2\text{O}_4/\text{NPC}$ HSC device, EIS measurements were performed within the frequency range of 1 Hz to 100 kHz as shown in figure 6.17(c). The real axis intercept of the EIS Nyquist plot could be used to calculate the series resistance of the electrode (R_s), which included the inherent resistance of the constructed device. The charge transfer resistance (R_{ct}) at the interface between electrode and electrolyte was estimated using a semicircle in the high-frequency region. The R_s and R_{ct} of the $\text{CoFe}_2\text{O}_4/\text{NPC}$ HSC device were found to be 1.25 and 5.14Ω , respectively.

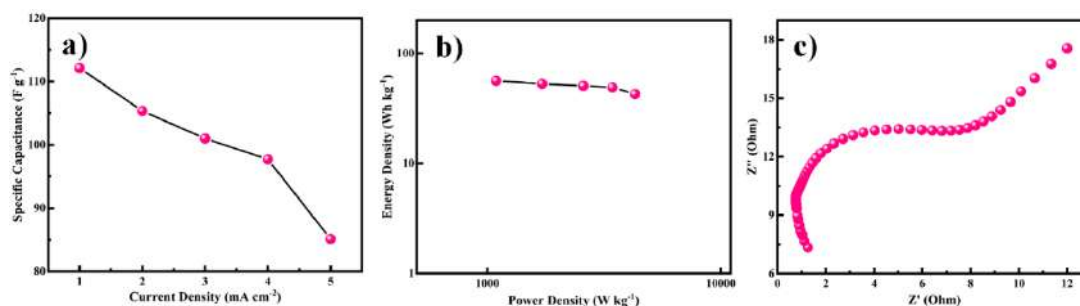


Figure 6.17: (a) Rate capability of the $\text{CoFe}_2\text{O}_4/\text{NPC}$ HSC device according to the GCD curves from 1 to 5 mA cm^{-2} , (b) Ragone plot of the $\text{CoFe}_2\text{O}_4/\text{NPC}$ HSC device, (c) Nyquist plot of the $\text{CoFe}_2\text{O}_4/\text{NPC}$ HSC device

Furthermore, the cycle life and Coulombic efficiency of the $\text{CoFe}_2\text{O}_4/\text{NPC}$ HSC device at 6 mA cm^{-2} current density for 5000 cycles are investigated and depicted in figure 6.18. During cycling, the coulombic efficiency stays about 98.54%, indicating good reversibility. After 5000 cycles, the specific capacitance as a function of cycle number exhibits outstanding electrochemical stability of 97.91%. Additionally, inset of figure 6.18 displays the first five and last five cycles. Even after 5000 GCD cycles, the nature of GCD curve remained almost unchanged, further demonstrating the exceptional cyclic stability. The $\text{CoFe}_2\text{O}_4/\text{NPC}$ HSC device's extended cycle life is due to its high specific area and hierarchical structure, which promotes OH^- diffusion and provides ample room for buffering stresses throughout the charge and discharge process. These findings revealed that the HSCs device constructed with the CoFe_2O_4 and NPC produced from the single $\text{CoFe}_2\text{-MOF}$ predecessor had intriguing potentials in the realm of applicable energy storage devices.

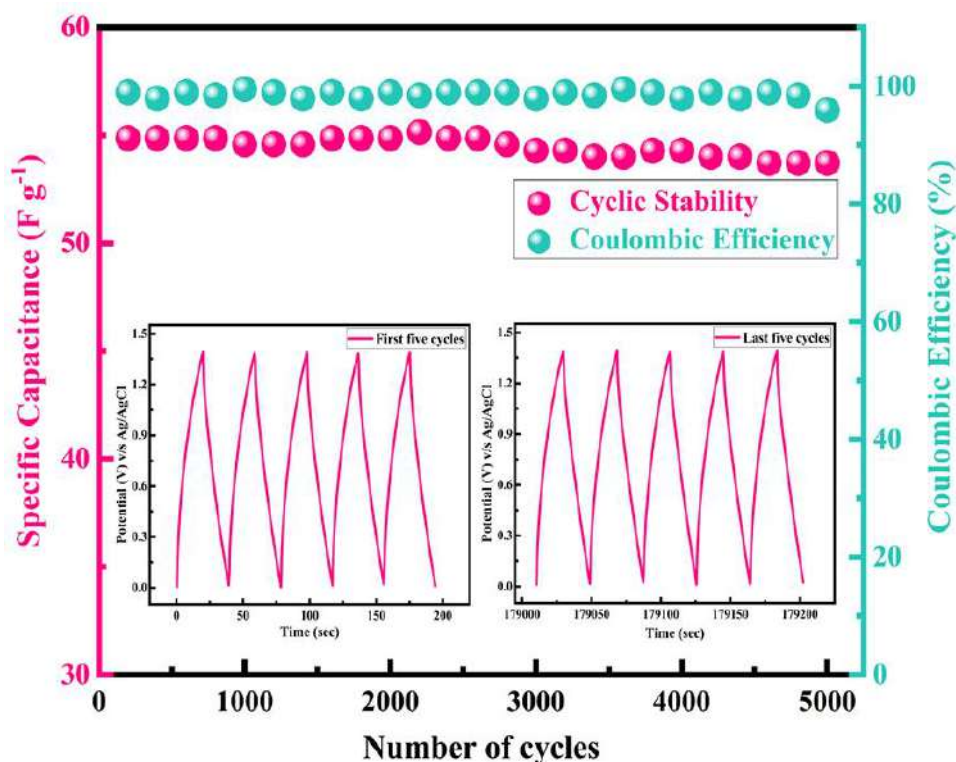


Figure 6.18: Cyclic stability and Coulombic efficiency of CoFe₂O₄//NPC HSC device for 5000 cycles at the current density of 5 mA cm⁻² (inset show first and last five GCD cycles of the stability test)

From above fabricated devices, two were linked in series to investigate their potential uses based on the constructed HSC device's exceptional electrochemical performance. The LED glowed brilliantly for approximately eight minutes after only fifteen seconds of charging, demonstrating the extraordinary usefulness of our all-in-one gadgets (Supporting Information video). A LED powered by the tandem devices, implies the promising application perspective of the constructed all-in-one CoFe₂O₄//NPC HSC device as a developing energy storage and conversion systems.

As illustrated in figure 6.19, a radar graph was plotted to compare the electrochemical characteristics of chemically synthesized bimetallic CoFe₂-MOF, its derived CoFe₂O₄ and NPC. Each vertex exhibits characteristics such as specific surface area, pore radius, specific capacitance, energy density, power density, charge transfer resistance and cyclic stability of the CoFe₂-MOF, its derived CoFe₂O₄ and NPC. The electrodes' electrochemical characteristics are indicated by the filled region beneath the curve. The integral area of NPC is much bigger than that of CoFe₂-MOF and CoFe₂O₄, as seen in figure 6.19. It has been noted that minute crystallite size and

great specific surface area contributed to outstanding specific capacitance, energy density, power density, and cyclic stability.

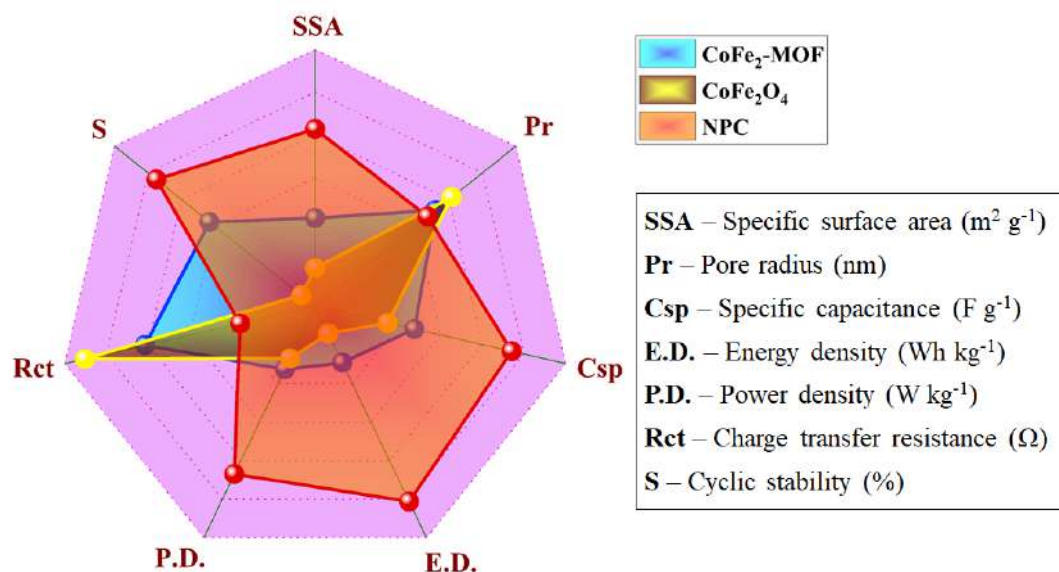


Figure 6.19: Radar plot for comparative study of CoFe₂-MOF, CoFe₂O₄ and NPC electrodes based on supercapacitive properties

6.5 Conclusion

In conclusion, a straightforward "One-for-All" approach is used to produce both anode and cathode for HSC device from a single bimetallic MOF, with CoFe₂O₄ and NPC deriving from CoFe₂-MOF as the sole precursor. To prepare CoFe₂O₄ and NPC, the conversion procedure was improved. By annealing CoFe₂-MOF at 500 °C in air and 800 °C in an inert environment, CoFe₂O₄ and NPC materials with greater phase purity are produced. The derived nanoporous carbon has good electrochemical characteristics, a large specific surface area, and very hierarchically porous structures because of its special structure. The constructed all-in-one CoFe₂O₄//NPC HSC device exhibits an excellent specific capacitance with energy density of 56.2 Wh kg⁻¹ and power density of 1091.5 W kg⁻¹ at 2 mA cm⁻² current density. Additionally, it shows outstanding cyclic stability of 97.91 % over 5000 GCD cycles. This research presents a revolutionary 'One-for-All' concept, which opens up a new potential for next-generation supercapacitors with excellent safety, cheap cost, a wide voltage window, and prolonged cycle stability.

6.6 References

- 1 A. E. Baumann, D. A. Burns, B. Liu and V. S. Thoi, *Commun. Chem.*, 2019, **2**, 1–14.
- 2 S. Lai, J. Zhu, W. Zhang, J. Jiang and X. Li, *Energy and Fuels*, 2021, **35**, 3407–3416.
- 3 N. Swain, B. Saravanakumar, M. Kundu, L. Schmidt-Mende and A. Ramadoss, *J. Mater. Chem. A*, 2021, **9**, 25286–25324.
- 4 C. Y. Zhu, Y. W. Ye, X. Guo and F. Cheng, *New Carbon Mater.*, 2022, **37**, 59–92.
- 5 T. M. Gür, *Energy Environ. Sci.*, 2018, **11**, 2696–2767.
- 6 L. Li, Z. Wu, S. Yuan, X. B. Zhang, *Energy Environ. Sci.*, 2014, **7**, 2101–2122.
- 7 K. Allado, M. Liu, A. Jayapalan, D. Arvapalli, K. Nowlin, J. Wei, *Energy and Fuels*, 2021, **35**, 8396–8405.
- 8 S. Verma, S. Arya, V. Gupta, S. Mahajan, H. Furukawa, A. Khosla, *J. Mater. Res. Technol.*, 2022, **11**, 564–599.
- 9 B. Pal, S. Yang, S. Ramesh, V. Thangadurai, R. Jose, *Nanoscale Adv.*, 2019, **1**, 3807–3835.
- 10 K. O. Otun, M. S. Xaba, S. Zong, X. Liu, D. Hildebrandt, S. M. El-Bahy, Z. M. El-Bahy, *Colloids Surfaces A Physicochem. Eng. Asp.*, 2022, **634**, 128019–128030.
- 11 M. J. Deng, T. H. Chou, L. H. Yeh, J. M. Chen, K. T. Lu, *J. Mater. Chem. A*, 2018, **6**, 20686–20694.
- 12 C. Guo, Y. Zhang, T. Zeng, D. Huang, Q. Wan, N. Yang, *Carbon*, 2020, **157**, 298–307.
- 13 W. Ma, H. Nan, Z. Gu, B. Geng, X. Zhang, *J. Mater. Chem. A*, 2015, **3**, 5442–5448.
- 14 Q. Jing, W. Li, J. Wang, X. Chen, H. Pang, *Inorg. Chem. Front.*, 2021, **8**, 4222–4229.
- 15 D. Chen, L. Wei, J. Li, Q. Wu, *J. Energy Storage*, 2020, **30**, 101525–101537.
- 16 W. Hu, M. Zheng, B. Xu, Y. Wei, W. Zhu, Q. Li, H. Pang, *J. Mater. Chem. A*, 2021, **9**, 3880–3917.
- 17 H. Duan, Z. Zhao, J. Lu, W. Hu, Y. Zhang, S. Li, M. Zhang, R. Zhu, H. Pang, *ACS Appl. Mater. Interfaces*, 2021, **13**, 33083–33090.

- 18 W. Liu, F. Zhu, B. Ge, L. Sun, Y. Liu, W. Shi, *Chem. Eng. J.*, 2022, **427**, 130788-130797.
- 19 R. Zhu, J. Ding, J. Yang, H. Pang, Q. Xu, Q. Xu, D. Zhang, P. Braunstein, *ACS Appl. Mater. Interfaces*, 2020, **12**, 25037–25041.
- 20 C. Qu, Z. Liang, Y. Jiao, B. Zhao, B. Zhu, D. Dang, S. Dai, Y. Chen, R. Zou, M. Liu, *Small*, 2018, **14**, 1–8.
- 21 C. Kang, L. Ma, Y. Chen, L. Fu, Q. Hu, C. Zhou, Q. Liu, *Chem. Eng. J.*, 2022, **427**, 131003-131013.
- 22 A. Tang, C. Wan, X. Hu, X. Ju, *Nano Res.*, 2021, **14**, 4063–4072.
- 23 R. Velmurugan, J. Premkumar, R. Pitchai, M. Ulaganathan, B. Subramanian, *ACS Sustain. Chem. Eng.*, 2019, **7**, 13115–13126.
- 24 R. Bhosale, S. Bhosale, P. Kumbhar, D. Narale, R. Ghaware, C. Jambhale, S. Kolekar, *New J. Chem.*, 2023, **47**, 6749–6758.
- 25 M. Safari, J. Mazloom, *J. Solid State Electrochem.*, 2021, **25**, 2189–2200.
- 26 T. Zhang, J. Du, P. Xi, C. Xu, *ACS Appl. Mater. Interfaces*, 2017, **9**, 362–370.
- 27 T. K. N. Tran, C. P. K. Phan, T. C. Q. Ngo, N. B. Hoang, L. D. Truong, T. K. O. Nguyen, *Processes*, 2022, **10**, 1–14.
- 28 P. D. Patil, S. R. Shingte, V. C. Karade, J. H. Kim, T. D. Dongale, S. H. Mujawar, A. M. Patil, P. B. Patil, *J. Energy Storage*, 2021, **40**, 102821-102832.
- 29 T. Prabhakaran, R. V. Mangalaraja, J. C. Denardin, K. Varaprasad, *J. Mater. Sci. Mater. Electron.*, 2018, **29**, 11774–11782.
- 30 G. R. Patta, V. R. Kumar, B. V. Ragavaiah, N. A. Veeraiah, *Appl. Phys. A Mater. Sci. Process.*, 2020, **126**, 1–11.
- 31 E. K. Nyutu, W. C. Conner, S. M. Auerbach, C. H. Chen, S. L. Suib, *J. Phys. Chem. C*, 2008, **112**, 1407–1414.
- 32 V. H. Nguyen, T. D. Nguyen, L. G. Bach, T. Hoang, Q. T. P. Bui, L. D. Tran, C. V. Nguyen, D. V. N. Vo, S. T. Do, *Catalysts*, 2018, **8**, 487-507.
- 33 P. B. Kharat, S. B. Somvanshi, J. S. Kounsalye, S. S. Deshmukh, P. P. Khirade, K. M. Jadhav, *AIP Conf. Proc.*, 2018, 1–5.
- 34 A. K. Ipadeola, R. Barik, S. C. Ray, K. I. Ozoemena, *Electrocatalysis*, 2019, **10**, 366–380.
- 35 K. Kim, K. J. Lopez, H. J. Sun, J. C. An, G. Park, J. Shim, *J. Appl. Electrochem.*, 2018, **48**, 1231–1241.
- 36 M. G. Radhika, B. Gopalakrishna, K. Chaitra, L. K. G. Bhatta, K. Venkatesh,

- M. K. Sudha Kamath, N. Kathyayini, *Mater. Res. Express*, 2020, **7**, 054003-054017.
- 37 R. Jia, C. Zhao, Z. Huang, X. Liu, D. Wang, Z. Hui, X. Xu, *Ionics*, 2020, **26**, 6309–6318.
- 38 P. Sivagurunathan, S. R. Gibin, *J. Mater. Sci. Mater. Electron.*, 2016, **27**, 8891–8898.
- 39 G. P. Ratkovski, K. T. O. Do Nascimento, G. C. Pedro, D. R. Ratkovski, F. D. S. Gorza, R. J. Da Silva, B. G. Maciel, L. C. Mojica-Sánchez, C. P. De Melo, *Langmuir*, 2020, **36**, 2920–2929.
- 40 M. Sevilla, C. Salinas Martínez-De Lecea, T. Valdés-Solís, E. Morallón, A. B. Fuertes, *Phys. Chem. Chem. Phys.*, 2008, **10**, 1433–1442.
- 41 R. Sikkema, I. Zhitomirsky, *Appl. Phys. Rev.*, 2023, **10**, 021307-021324.
- 42 K. Liu, Y. Chen, X. Dong, Y. Hu, H. Huang, *Electrochim. Acta*, 2023, **456**, 142441-142450.
- 43 P. Sayadi, S. Zeinali, S. Momeni, S. F. NamiAna, M. Tohidi, *J. Electron. Mater.*, 2023, **52**, 3877–3891.
- 44 R. R. Salunkhe, J. Tang, Y. Kamachi, T. Nakato, J. H. Kim, Y. A. Yamauchi, *ACS Nano*, 2015, **9**, 6288-6296.
- 45 D. P. Dubal, R. Holze, *Energy*, 2013, **51**, 407–412.
- 46 S. S. Shah, E. Cevik, M. A. Aziz, T. F. Qahtan, A. Bozkurt, Z. H. Yamani, *Synth. Met.*, 2021, **277**, 116765-116780.
- 47 P. L. Taberna, P. Simon, J. F. Fauvarque, *J. Electrochem. Soc.*, 2003, **150**, A292-A300.
- 48 A. Barua, A. Paul, *Energy Fuels*, 2021, **35**, 10262–10273.
- 49 S. Alipoori, S. Mazinani, S. H. Aboutalebi, F. Sharif, *J. Energy Storage*, 2020, **27**, 101072-101095.

List of Publications

1	R. Bhosale , S. Bhosale, P. Kumbhar, D. Narale, R. Ghaware, C. Jambhale and S. Kolekar, Design and development of a porous nanorod-based nickel-metal-organic framework (Ni-MOF) for high-performance supercapacitor application, <i>New Journal of Chemistry</i> , 2023, 47, 6749.
2	R. Bhosale , S. Bhosale, M. Vadiyar, C. Jambhale, K. -W. Nam, S. Kolekar, Recent Progress on Functional Metal-organic Framework for Supercapacitive Energy Storage Systems, <i>Energy Technology</i> , 2023, 2300147.
3	R. Bhosale , S. Bhosale, D. Narale, C. Jambhale, S. Kolekar, Construction of well-defined two-dimensional architectures of trimetallic metal-organic frameworks for high-performance symmetric supercapacitors, <i>Langmuir</i> , 2023, 39, 34, 12075.
4	R. Bhosale , S. Bhosale, R. Sankannavar, V. Chavan, C. Jambhale, H. Kim, S. Kolekar, Bimetallic MnFe ₂ -MOF and Its Derived MnFe ₂ O ₄ Nanostructures for Supercapacitive Applications, <i>ACS Applied Nano Materials (Revision submitted)</i> .
5	R. Bhosale , S. Bhosale, V. Chavan, C. Jambhale, D. -k Kim, S. Kolekar, Hybrid supercapacitor based on nanoporous carbon and CoFe ₂ O ₄ derived from a single bimetallic-organic framework: One-for-All Approach, <i>ACS Applied Nano Materials (Revision submitted)</i> .
6	P. Kumbhar, D. Narale, R. Bhosale , C. Jambhale, J. -H. Kim, S. Kolekar, Synthesis of tea waste/Fe ₃ O ₄ magnetic composite (TWMC) for efficient adsorption of crystal violet dye: Isotherm, kinetic and thermodynamic studies, <i>Journal of Environmental Chemical Engineering</i> , 2022, 10, 107893.
7	D. Narale, P. Kumbhar, R. Bhosale , R. Ghaware, K. Patil, J. H. Kim, S. Kolekar, Rational design of binder free NiFe ₂ O ₄ @CoFe ₂ O ₄ core-shell nanoflake arrays synthesized by chemical bath deposition for supercapacitor application, <i>Journal of Energy Storage</i> , 2023, 66, 107477.
8	S. Bhosale, R. Bhosale , K. Jagadhane, A. Gore, G. Kolekar, S. Kolekar, P. Anbhule, J. Recent trends in synthetic Top-down approach for Mesoporous Carbon: A seminal review, <i>Journal of Materials Nanoscience</i> , 2023, 10, 601.
9	S. Bhosale, R. Bhosale , S. Shinde, A. Moyo, R. Dhavale, S. Kolekar, P. Anbhule, Biomass nanoarchitectonics with Annona reticulate flowers for mesoporous

carbon impregnated on CeO₂ nanogranular electrode for energy storage application, *Inorganic Chemistry Communications*, 2023, 154, 110949.

- 10 R. Ghaware, P. Sanadi, D. Narale, **R. Bhosale**, K. Patil, J. Kim, S. Kolekar, Effect of Small Change in Reaction Conditions on the Size of Monoclinic BiVO₄ Nanoparticles and their Photocatalytic Abilities, *ChemistrySelect*, 2023, 8, e202301320.

International/National Conferences Presentation

1	Got 3 rd prize for Poster Presentation at the International Conference on “Sustainable Development in Chemistry and Scientific Application” organized by the Department of Chemistry, Sadguru Gadage Maharaj College, Karad on 16 th -17 th December 2021.
2	National Conference on ‘Impact of Chemistry and Biology to the Society and Industry’ organized by the Department of Industrial Chemistry, Kuvempu University, Shivamogga, Karnataka, 20 th - 21 st May 2022.
3	National Seminar on ‘Advances in Chemistry and Material Science’ organized by Prof. Dr. N. D. Patil Mahavidyalaya, Malkapur, 28 th May 2022.
4	Two-day “International Conference on Functional Material and Nanotechnology (ICFMN-2K22)” organized by the Department of Physics, Nehru Institute of Technology, Coimbatore in collaboration with Indian Association for Crystal Growth on 20 & 21 July 2022.
5	9 th Interdisciplinary Symposium on Materials Chemistry, ISMC–2022 organized by Society for Materials Chemistry, Mumbai & Chemistry Division, BARC on 7 to 10 th December 2022.
6	Two-day National Conference on “Advances in Analytical Techniques for Materials and Biomedical Applications” organized by the Rani Channamma University, Belagavi, Karnataka, India on 15 -16 December 2022.
7	International Conference on "Emerging Trends in Basic and Applied Sciences (ETBAS-2023)" organized by Karmaveer Hire Arts, Science, Commerce and Education College, Gargoti, on 17 January 2023.
8	International Conference on Frontier Areas of Science and Technology (ICFAST-2023) organized jointly by Shivaji University, Kolhapur (SUK) & Indian JSPS Alumni Association (IJAA) on 8 & 9 September 2023.

Participated in Workshop


1	Two Day Workshop & hands-on training on Vector Network Analyzer (VNA) organized by SAIF (CFC), Shivaji University, Kolhapur under the STRIDE (Scheme for Trans-disciplinary Research for India's Developing Economy) program on 22-23 Feb 2021.
2	One Day National Level Workshop on "How To Write Review Article?" organized by the Department of Chemistry, Balwant College, Vita on Thursday, 1st July 2021.
3	Workshop and hands-on training on BIO-ATOMIC FORCE MICROSCOPY (BIO-AFM) organized by SAIF (CFC) Shivaji University Kolhapur, 4-5 th January 2022.
4	Workshop 'IP Awareness/Training program under National Intellectual Property Awareness Mission' organized by Intellectual Property Office India, 04 March 2022.

PAPER



Cite this: *New J. Chem.*, 2023, 47, 6749

Design and development of a porous nanorod-based nickel-metal–organic framework (Ni-MOF) for high-performance supercapacitor application

Rakhee Bhosale,  Sneha Bhosale, Pramod Kumbhar, Dattatray Narale, Rachana Ghaware, Chitra Jambhale  and Sanjay Kolekar *

Metal–organic frameworks have received increasing attention as promising electrode materials in supercapacitors. In this study, we synthesized a nickel-metal–organic framework (Ni-MOF) by a simple and low-cost reflux condensation technique using non-hazardous trimesic acid as an organic ligand. The structures and morphologies of the Ni-MOF material were characterized by X-ray diffraction, Fourier-transform infrared spectroscopy, and scanning electron microscopy techniques. The prepared Ni-MOF was found to have a rod-like morphology and these morphologies can provide beneficial paths for electrolyte ion penetration, obtaining an enlarged contact area between the active material and electrolyte. The Ni-MOF had a considerable specific surface area of $398.4 \text{ m}^2 \text{ g}^{-1}$. Further, its highly porous structure offered excellent supercapacitor performance. The charge-storage mechanism of the electrodes was investigated by cyclic voltammetry, charge–discharge cycling, and electrochemical impedance spectroscopy using 2 M KOH as an electrolyte in a three-electrode assembly. The specific capacitance of the Ni-MOF was found to be 1956.3 F g^{-1} at a current density of 5 mA cm^{-2} by GCD studies and it retained 81.13% of its initial capacitance even after 3000 GCD cycles at a 35 mA cm^{-2} current density. An as-fabricated Ni-MOF//activated carbon hybrid supercapacitor (HSC) exhibited a specific energy of $98.15 \text{ W h kg}^{-1}$ at a specific power of $1253.47 \text{ W kg}^{-1}$ and excellent capacity retention of 99.29% over 3000 cycles. The results of this study imply a great potential of the Ni-MOF for application in efficient and sustainable energy-storage devices.

Received 30th January 2023,
Accepted 5th March 2023

DOI: 10.1039/d3nj00456b

rsc.li/njc

Introduction

In the 21st century, the production of energy from different sources has tremendously increased, and its transformation is also increasing day by day in different ways with the ever-increasing demands from industry, buildings, utilities, and transportation.¹ The increasing demand for energy and fuel due to the ever-increasing world population has become one of the important worries for all the global prime economies. Today there is an urgent need for environmentally friendly renewable energy resources to solve the problems related to the dwindling reserves of fossil fuels.^{2,3} In this regard, energy-conversion and -storage technologies have acquired significant attention to support the future use of renewable energy sources. Many researchers from around the globe are devoted to developing sustainable energy sources, like wind, solar, hydropower, and tidal energy, to address the shortage of fossil fuels and to

reduce carbon emissions and global warming. Hence, from various points of view, electrochemical energy-storage devices (EESDs), like rechargeable batteries, supercapacitors, fuel cells, and hybrid devices, have an important part to play in strategies to produce various amounts of energy and power density to meet the demands from different application scenarios.^{4–6}

Supercapacitors (SCs), also known as electrochemical capacitors, offer the advantages of batteries as well as conventional capacitors, and have consequently become extraordinary energy-storage devices for large power output applications.^{7,8} SCs generally offer a fast charging–discharging process (1–10 s), large power density ($500\text{--}10\,000 \text{ W kg}^{-1}$), high cycling stability ($> 500\,000 \text{ h}$), and easy operation. However, current SCs have a low energy density ($1\text{--}10 \text{ W h kg}^{-1}$), which remains a prime challenge in the development of SC technologies. To conquer the drawback of their low energy density, there is a need for the development of high-performance electrode materials for SCs.^{9,10} Due to their profitable features, such as high power density, excellent cycling stability, exceptional rate capability, and eco-friendliness, SCs have become key components in many fields, such as aerospace, electronic communications, and electric

Analytical Chemistry and Materials Science Research Laboratory, Department of Chemistry, Shivaji University, Kolhapur 416 004, India.
E-mail: sskolekar@gmail.com

transport, and thus have attracted increasing attention, but still, there is a need for further advancements in SCs to meet the excessive energy demand of modern society.¹¹ A supercapacitor is like a battery, which means it stores and releases electricity, but instead of storing energy in the form of chemicals, supercapacitors store electricity in a static state, making them better at rapidly charging and discharging energy. Supercapacitors can be mainly divided into two types based on the charge-storage mechanism. The first type is electric double-layer supercapacitors (EDLCs). In EDLCs, the capacitance is obtained from the electrostatic charge assembled at the electrode/electrolyte interface; hence, it is completely dependent on the surface area of the electrode materials that is available to electrolyte ions. The other type is pseudocapacitors, in which the capacitance comes from the reversible redox reactions between the electrolyte and electroactive species on the surface of the electrodes under the applied potential.^{12–14} The electrochemical performance of a supercapacitor device depends on numerous parameters, like choosing its constituents, the synthesis route used for the electrode materials, the potential window of the electrodes, the choice of electrolytes, and the type of current collectors, binders, and separators.^{15,16}

Metal–organic frameworks (MOFs) are attractive materials to fulfil the requirement for next-generation energy-storage technologies because of their extraordinary properties, such as high porosity, many accessible active sites, high surface area, extraordinary stability, vast structural and chemical tunability, tailorable pore size, and pre- and post-synthesis structural modifiability. Also, MOFs are a unique type of nanoporous materials formed by coordinated metal nodes and organic linkers. MOF-based materials have been utilized in many applications, including energy storage and conversion, catalysis, gas separation, drug delivery, hydrogen storage, gas adsorption, and purification.^{17–20} Concurrently, due to the strong coordination capability of transition metals (TMs), TMs are often used as the metal centres of MOFs, and they also offer the advantages of possessing variable valences and good electrochemical properties, which means they can work as pseudocapacitive redox centres.²¹ MOFs can be feasibly included in a supercapacitor by two strategies: by directly utilizing the MOF as an electrode material for supercapacitors or by utilizing MOF-derived materials, like nanoporous carbon, oxides, sulfides, ferrites, which can be evolved and then utilized as electrode materials, such as the Ni, Co, Zn, Cu, and Fe-based MOFs, which have been reported previously to possess good supercapacitive performance.^{22–31} However, the current, MOFs show poor electrical conductivity; therefore, scientists have taken efforts to increase the electrical conductivity through different strategies, such as through developing composite MOFs with different conductive materials, like metal oxides,³² metals,³³ conductive polymers,³⁴ carbon nanotubes,³⁵ and graphene.³⁶ Wang *et al.* proposed a surfactant-free and solvent-assisted solvothermal method to synthesize microflower Ni-MOF, which exhibited a high specific capacitance of 1093 F g⁻¹ at 1 A g⁻¹ with good rate capability, which were attributed to the fast ion transport and low electrical resistance emerging from its microflower-like structure and the specific capacitance resulting from the incorporation of nickel hydroxide species.³⁷ Wu *et al.* investigated nanosheet-

stacked flower-like Ni-MOF *via* a solvothermal method using anionic surfactants. The usage of the static sealing effect among the negatively charged anionic surfactant head groups and metal ions suppressed the growth of crystals on the crystal surface. Their study revealed that the electrochemical performance of Ni-MOF with the surfactant was superior to that of Ni-MOF without the surfactant, whereby it possessed a specific capacitance of 1030 F g⁻¹ at a current density of 1 A g⁻¹ with a capacitance retention of 50% after even 3000 cycles. Further, they assembled an asymmetric supercapacitor by using Ni-MOF as a positive electrode and activated carbon as a negative electrode.³⁸ Gao *et al.* reported the cuboid Ni-MOF by a simple one-step hydrothermal method, which showed a loosely stacked layer-cuboid structure with plentiful mesopores, which were useful for the charge transfer and ion transport for supercapacitors. It also exhibited an exceptional specific capacitance of 804 F g⁻¹ at a current density of 1 A g⁻¹, with a retention of 302 F g⁻¹ after 5000 cycles. Additionally, they fabricated an asymmetric supercapacitor using Ni-MOF and activated carbon as the positive and negative electrodes, respectively.³⁹ Zhang *et al.* prepared Ni-MOF using a mixed-ligand approach, using trimesic acid as a modulator to partially replace the terephthalic acid. Replacing the terephthalic acid with trimesic acid influenced the formation of an albizia flower-like spheres@nanosheets structure, which helped the adsorption of OH⁻ ions on the surface. Also, the electrochemical performance was increased due to the synergistic effect of the surface property and its unique structure. It exhibited an excellent specific capacitance of 920 F g⁻¹ at a current density of 1 A g⁻¹. In addition, they constructed an asymmetric supercapacitor with the help of Ni-MOF as a positive electrode and activated carbon as a negative electrode, which showed a high energy density of 42.4 W h kg⁻¹ at a power density of 0.8 kW kg⁻¹.⁴⁰

In the present work, we used an unprecedented simple and scalable method, *i.e.* a reflux condensation method, to prepare a nanorod-like nickel-based metal–organic framework (Ni-MOF), in a controlled high temperature. The as-synthesized Ni-MOF revealed a one-dimensional (1D) nanorod-like morphology with a high specific surface area 398.4 m² g⁻¹ and highly nanoporous structure, which could produce more electrochemical sites, which increased the consumption of the electroactive material. In addition, for the fabrication of the electrode we used a stainless steel mesh substrate, which has not been reported to date, which is easily available and low cost compared to other reported substrates. Because of the abundant active sites and extremely porous nature of the material, the penetration of electrolyte ions into the material was increased, resulting in an enhancement of the specific capacitance of the material. Also, we constructed a hand-made asymmetric supercapacitor device, which could get a red LED to glow for almost 105 s after charging for only 15 s.

Experimental section

Reagents

Nickel nitrate hexahydrate, *N,N*-dimethylformamide (DMF), and potassium hydroxide (KOH) were purchased from Loba

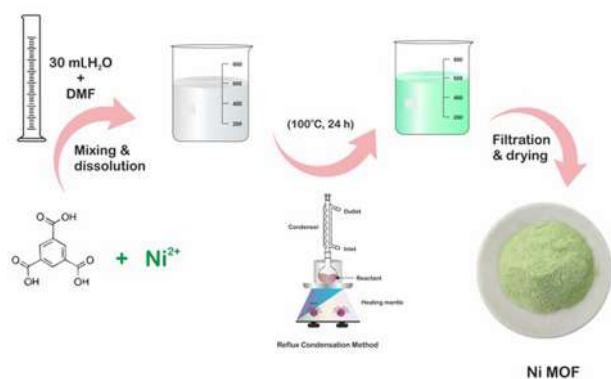


Fig. 1 Schematic of the synthesis of Ni-MOF nanorods via a wet chemical route.

Chemie (India). Benzene-1,3,5-tricarboxylic acid (H3BTC), carbon black, polyvinylidene difluoride (PVDF), and *N*-methyl-2-pyrrolidone (NMP) were purchased from Sigma Aldrich (USA). All the reagents were of analytical grade and used as received without any further purification.

Preparation of nickel-based metal–organic framework (Ni-MOF)

Ni-MOF was synthesized by a method reported elsewhere⁴¹ with slight modification. The reflux method was used for the synthesis of Ni-MOF, which also helped to lower the reaction time of Ni-MOF compared to that reported in the literature. First, 0.15 M of H3BTC was dissolved in 10 mL of DMF with continuous stirring at room temperature; this mixture was denoted as H3BTC solution. Then, the H3BTC solution was transferred to a 50 mL round-bottom flask and heated up to 100 °C using an oil bath with constant stirring. Thereafter, 0.3 M aqueous nickel nitrate (20 mL) solution was added drop by drop into the H3BTC solution. The reaction mixture was stirred for 24 h at 100 °C. After cooling, the resulting precipitate was washed with alcohol several times and finally, a pale-green coloured precipitate was obtained and then dried at 80 °C for 12 h. Fig. 1 shows a schematic of the preparation of the Ni-MOF.

Material characterization

The phase and crystallinity of the Ni-MOF sample were investigated by X-ray diffractometry (XRD) (Bruker D8 Phaser X-ray diffractometer) with Cu K α radiation ($\lambda = 1.541 \text{ \AA}$). The functional groups and types of bonding were confirmed by Fourier-transform infrared (FT-IR) spectroscopy (Bruker Alpha-100508 spectrometer) and the microstructure and surface topography of the Ni-MOF sample were studied by scanning electron microscopy (SEM, JEOL-JSM 6360, Japan). Raman spectroscopy (Lab RAM HR Evolution Confocal Raman Microscope, France) was used for the point group analysis. The chemical composition and elemental valence states of the as-prepared Ni-MOF were evaluated by X-ray photoelectron spectroscopy (XPS, JPS 9030, JEOL ASIA PTE LTD.). In addition, N₂ isotherms and

pore-size distribution data were collected using a surface area and pore volume analyzer (NOVA1000e Quantachrome, USA).

Evaluation of the electrode materials and electrochemical studies

All the electrochemical experiments were performed on a CHI608 electrochemical analyzer using a conventional three-electrode system in 2 M KOH electrolyte at room temperature, with graphite employed as the counter electrode, saturated Ag/AgCl as the reference electrode, and Ni-MOF loaded stainless steel mesh as the working electrode. The working electrode was prepared by making a slurry of 80 wt% Ni-MOF (active material), 10 wt% polyvinylidene fluoride (PVDF), and 10 wt% carbon black (Super P) in NMP solvent. This slurry was coated on the stainless steel mesh (1 cm \times 1 cm), followed by vacuum drying at 80 °C for 12 h.

The electrochemical tests included cyclic voltammetry (CV), galvanostatic charging–discharging (GCD) profiles, and electrochemical impedance spectroscopy (EIS) measurements. A solid-state hybrid supercapacitor (Ni-MOF//AC) was fabricated using Ni-MOF as the positive electrode and activated carbon as the negative electrode. As a separator, cellulose filter paper was used as a sandwich between two electrodes, with the separator and PVA-KOH gel loaded between the two electrodes and assembled on opposite sides. The device was kept at room temperature overnight for natural drying. The PVA-KOH gel electrolyte was prepared according to a literature report.⁴² In a typical procedure, 1 g of polyvinyl alcohol (PVA) was dissolved in 20 mL distilled water keeping the temperature of the bath solution at 80 °C for 30 min. The aqueous KOH solution was then added dropwise to the PVA solution and heated at 80 °C for 30 min to give a viscous gel electrolyte.

The specific capacitance was calculated according to eqn (1),

$$C = \frac{I\Delta t}{m\Delta V} \quad (1)$$

where C is the specific capacity (F g^{-1}), I is the current density (A), Δt is the discharging time (s), m is the mass (g) of the active electrode materials, and ΔV is the potential window of the discharge process (V).

Using eqn (2) and (3), the specific energy and specific power of the hybrid supercapacitor were calculated, respectively,⁴³

$$E = \frac{0.5 \times C \times \Delta V^2}{3.6} \quad (2)$$

$$P = \frac{E \times 3600}{\Delta t} \quad (3)$$

where E and P are the specific energy (W h kg^{-1}) and specific power (W kg^{-1}), respectively, ΔV is the discharging voltage (V), and Δt is the discharging time in seconds.

Results and discussion

The phase purity and crystallinity of the Ni-MOF sample were investigated by XRD. The obtained XRD pattern of the prepared

Ni-MOF together with the data of JCPDS card no. 00-028-1734 are shown in Fig. 2(a). The prepared Ni-MOF data were in close agreement with the given JCPDS card,^{44–46} revealing that the Ni-MOF had a polycrystalline nature. Some of the major peaks obtained were in good agreement with the corresponding angles as reported earlier for Ni-MOF. Furthermore, using Debye-Scherrer's formula (eqn (4)), the crystallite size was calculated for the major characteristic peak of Ni-MOF,

$$D = \frac{0.9\lambda}{\beta \cos \theta} \quad (4)$$

where D is the average crystallite size, λ is the wavelength of the X-rays, β is the full-width at half maxima, and θ is Bragg's diffraction angle. The average crystallite size derived from the (110) plane was 6.89 nm.

Investigation of the chemical structure and functional groups of Ni-MOF was carried out by FT-IR. The FT-IR spectrum of the Ni-MOF sample is shown in Fig. 2(b). In the spectrum, the strong absorption peak at 1349 cm^{-1} was assigned to the C-H stretching vibrations, while the peaks at 3081 and 3399 cm^{-1} could be indexed to the O-H stretching vibrations of water molecules, showing that water molecules existed within the Ni-MOF structure. Additionally, the peaks observed at 1506 and 1608 cm^{-1} were attributed to the symmetric and asymmetric vibrations of carboxyl groups ($-\text{COO}^-$), related to the BTC linkers.^{47,48} Another intense peak was observed at 715 cm^{-1} , confirming the presence of the Ni-O bond.

Raman spectroscopy was used to confirm the crystallography of the prepared Ni-MOF samples. Also, the inelastic scattering of the Ni-MOF samples was confirmed by Raman spectroscopy. The Raman spectrum of the Ni-MOF and the specified peaks of the prepared sample are shown in Fig. 3. The peaks of Ni-MOF at 816 and 1007 cm^{-1} could be associated to the plane deformation of the C-H in the aromatic ring and C-O stretching of the trimesic ligand, respectively. Also, D and G bands were observed at 1456 and 1613 cm^{-1} due to the in-plane vibration mode of the benzene ring.⁴⁹ The peak at 222 cm^{-1} could be attributed to H-O-H. All these peaks revealed the crystallography and structure of the Ni-MOF sample.

The surface morphology of the Ni-MOF was investigated by SEM, and the SEM images of Ni-MOF with different magnifications are shown in Fig. 4. The SEM images showed a

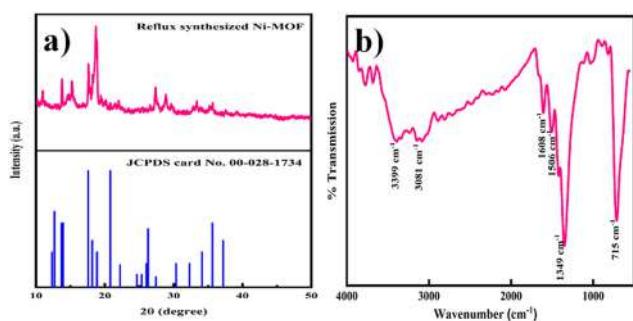


Fig. 2 (a) XRD pattern of Ni-MOF and JCPDS card. (b) FTIR spectra of Ni-MOF.

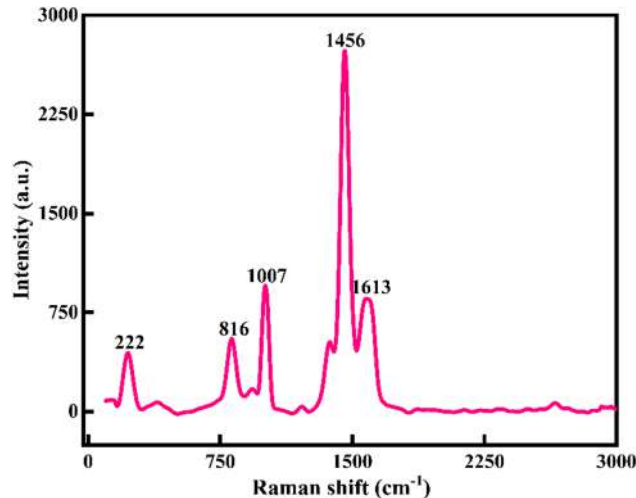


Fig. 3 Raman spectrum of Ni-MOF.

nanorod-like morphology and porous nature of the Ni-MOF, which was responsible for the increased surface area of the Ni-MOF and also for the increase in the specific capacitance. The average length of the nanorods was about 19.09 nm.

The different lengths and diameters of the nanorods indicated an increase in the aspect ratio of the nanorods. Also, the porous nanorods were interconnected to each other, which provides more active sites for the transportation of the charging kinetics and decreases the diffusion length of the electrolyte, which is helpful for improvement of the energy storage and high rate capability. Again, a birds-eye view of the SEM images showed that the small and large sized nanorods overlapped with each other and between these two nanorods there were some voids, which in turn would support the enhanced adsorption of electrolyte ions, which would help to increase the specific capacitance of the Ni-MOF. The porous and 1D morphology was favourable for ion diffusion and hence contributed to an increase in the specific capacitance of the Ni-MOF.

The surface area and porosity of the Ni-MOF were obtained by using the BET technique and measuring nitrogen adsorption-desorption isotherm of the samples at 77 K. Here, the prepared sample was degassed at $150 \text{ }^\circ\text{C}$ under a nitrogen atmosphere for 4 h before the measurements. The surface area and pore-size distribution of the sample were calculated by the Brunauer-Emmett-Teller (BET) equation and NLDFT method. The BET measurement results are presented in Fig. 5. The

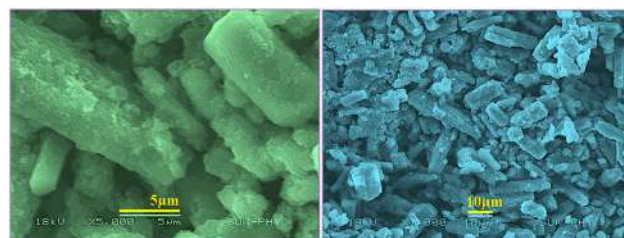


Fig. 4 SEM images of Ni-MOF.

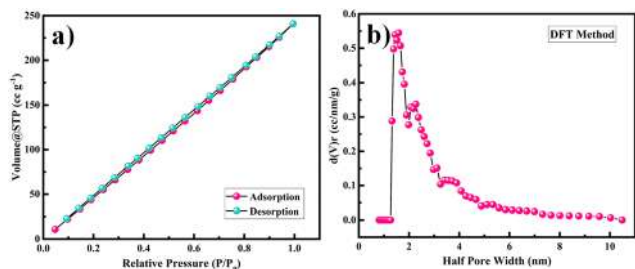


Fig. 5 (a) N_2 adsorption–desorption isotherms and (b) pore-size distribution of Ni-MOF.

calculated surface area of the Ni-MOF sample was found to be $398.4 \text{ m}^2 \text{ g}^{-1}$. Based on the literature, it has been observed that the larger the pore radius, then the higher porosity a sample will show in nature. Also, the pore-size distribution for Ni-MOF was estimated using the NLDFT method to establish the correct distribution of pores in the material, as shown in Fig. 5(c).^{50,51} The half pore width measured by DFT was 1.585 nm, with a micropore volume of 0.831 cc g^{-1} , confirming the extremely mesoporous nature and hierarchical pore-size distribution. According to the literature, Ni-MOF shows a type II isotherm with plenty of mesopores in the material.⁵² This massive amount of mesopores in the structure boosts the permeation of electrolyte ions into the electrode, hence increasing the specific capacitance of the material. Such a high specific surface area and mesoporous structure could produce more electrochemical reaction sites, which increases the consumption of the electroactive material.

XPS was used to examine the surface elemental composition and valence states of Ni-MOF. The presence of Ni, C, and O elements was confirmed by the survey spectrum in Fig. 6(a). Ni $2p_{1/2}$ and $2p_{3/2}$ displayed two significant peaks at 873.6 and 856.2 eV, respectively, with two satellite peaks at 878.7 and 861.0 eV, implying the presence of Ni in a divalent state (Fig. 6(b)). The peak at 284.5 eV in the C 1s area (Fig. 6(c)) is a typical outcome for specimens charging using C 1s as the reference. The peak at 288.2 eV was associated with the O=C–OH, whereas the peak at 285.4 eV was associated with the aryl carbon from the benzene ring. The spectrum of O 1s (Fig. 6(d)) could be separated into two peaks. Carbonyl displayed a peak at 531.5 eV, and the –OH group from the adsorbed H_2O molecules had a peak at 532.8 eV.^{53,54}

The electrochemical performance of the as-prepared Ni-MOF electrode was evaluated by using the three-electrode system in 2 M KOH electrolyte and the results are presented in Fig. 7. As shown in Fig. 7(a), cyclic voltammetry (CV) was carried out in the potential range from 0 to 0.3 V at scan rates from 10 to 100 mV s^{-1} . It could be observed that the area under the CV curve of the Ni-MOF electrode was higher and the redox current density also increased, leading to a greater capacitive behaviour compared to the literature (Table 1). All the CV curves revealed well-defined redox pairs, which specified the change in the oxidation states of the Ni^{2+}/Ni^{3+} , redox reactions, and intercalation–deintercalation of the K^+ ion in the porous

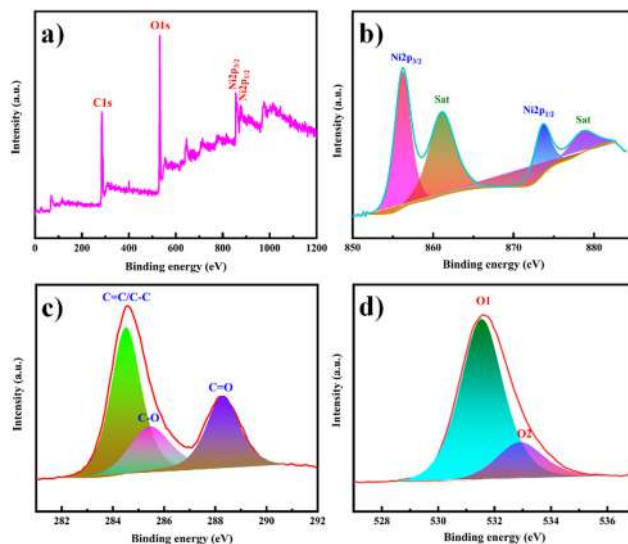


Fig. 6 (a) XPS survey spectrum of Ni-MOF. High-resolution XPS spectra in the (b) Ni 2p, (c) C 1s and (d) O 1s regions.

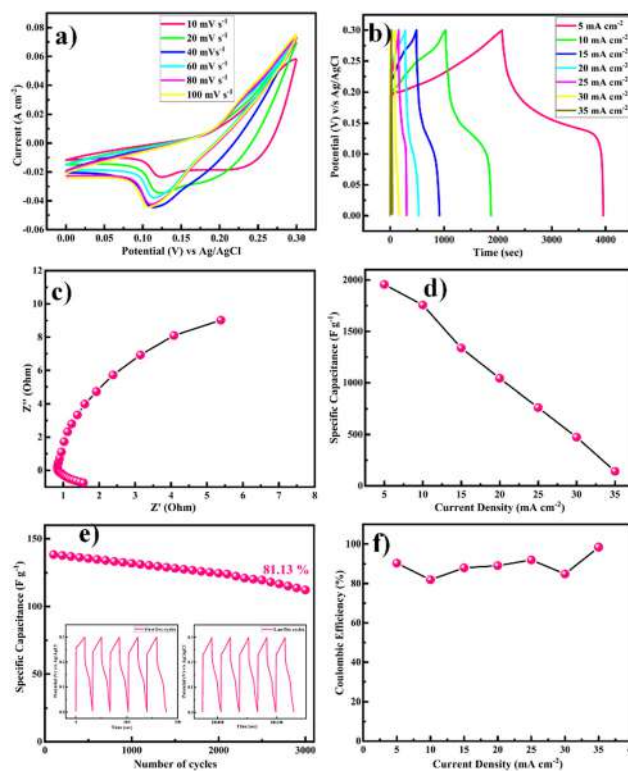


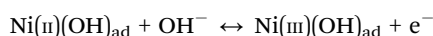
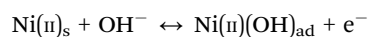
Fig. 7 (a) CV profile of Ni-MOF at different scan rates operated from 0 to 0.3 V. (b) GCD profiles for Ni-MOF at different current rates (5–35 mA cm^{-2}). (c) Nyquist plot of the Ni-MOF. (d) Plot of the specific capacitance vs. current density. (e) Cyclic durability test at a high current of 35 mA cm^{-2} over 3000 GCD cycles; insets show the first and last five cycles. (f) Coulombic efficiency as a function of the current density.

structure during the electrochemical reactions, due to the pseudocapacitive behaviour of the prepared Ni-MOF.^{55,56} This

Table 1 Comparison of the specific capacitances of Ni-MOF in different studies

Electrode material	Substrate used	Electrolyte	Current density	Specific capacitance	Ref.
Ni-MOF	Nickel foam	3 M KOH	5 A g ⁻¹	1224.6 F g ⁻¹	58
Ni-MOF	Nickel foam	3 M KOH	5 A g ⁻¹	612.25 F g ⁻¹	59
Ni-MOF	Nickel foam	6 M KOH	5 A g ⁻¹	430 C g ⁻¹	60
Ni-MOF	Nickel foam	3 M KOH	5 A g ⁻¹	95 F g ⁻¹	61
Ni-MOF	Platinum plate	2 M KOH	5 mA cm ⁻²	47 F g ⁻¹	62
Ni-MOF	Stainless steel mesh	2 M KOH	5 mA cm ⁻²	1956.3 F g ⁻¹	This work

could be due to a shift in the valence states of nickel ions, specifying that the pseudocapacitance was mostly driven by surface oxidation generated by the reduction reaction. Additionally, the diffusion of OH⁻ ions also contributed to the redox reaction, and the diffusion might be because of the impurity ions in the aqueous electrolyte. The redox peaks of Ni-MOF in aqueous electrolytes were caused by the reversible redox between Ni²⁺/Ni³⁺, and the reaction can be explained by the possible charge-discharge mechanism of Ni-MOF as follows,



With increasing the scanning speed, the curve area and peak current rose, demonstrating a good capacitive behaviour and charge-storage capabilities.

The equivalent and similar CV curves obtained at different scan rates showed a shift in the redox peaks and specified the pseudocapacitive behaviour of the material, as shown in Fig. 7(a). The area under the CV curve increased with the increase in the scan rate, whereas the specific capacitance decreased as the scan rate increased. This is due to the fact that at slower scan rates, electrolyte ions are completely diffused within the electrode material. As a result, the complete active surface of the electrode material can be used to store charge. At higher scan rates, however, diffusion restricts the movement of electrolyte ions, and only the outer active surface is employed for charge storage.⁵⁷ The outstanding performance of the Ni-MOF electrode could be assigned to the good crystallinity and porous nanorod-like structure, which could successfully boost the intercalation/deintercalation of OH⁻ ions within the Ni-MOF electrode. One of the important tools for assessing the electrochemical properties of an electrode is the charge-discharge measurement. Fig. 7(b) presents the charge-discharge curves of the Ni-MOF electrode in aqueous 2 M KOH electrolyte. The charging and discharging times were directly in tune with the charge-storage capacity of the active material. The impact of different current densities (5–35 mA cm⁻²) on the charge-discharge curve was also studied. The natures of the curves were identical to each other, which supported the pseudocapacitive properties of the Ni-MOF nanorods. The specific capacitance of the Ni-MOF was calculated using the discharging curve and eqn (1).

A maximum specific capacitance of 1956.3 F g⁻¹ at a 5 mA cm⁻² current density was obtained. This specific

capacitance value is higher than those reported earlier (Table 1). Due to the plentiful active sites and highly porous nature, the penetration of electrolyte ions into the material increased, which supported the enhancement of the specific capacitance of the material. One of the important factors for supercapacitor electrodes is the electrical resistance, which can be determined from electrochemical impedance spectroscopy (EIS) measurements. EIS tests were thus carried out to investigate the electroconductibility and reaction kinetics of the Ni-MOF electrode, as shown in Fig. 7(c). The electrode's charge-transfer resistance (R_{ct}) could be obtained from the diameter of a semicircle in the high-frequency area. It was demonstrated that the Ni-MOF had a small diameter and thus a smaller charge-transfer resistance, while the slope of the lines in the low-frequency area represents the ion-diffusion resistance. The Nyquist plot had a high slope, which showed that the as-prepared Ni-MOF was beneficial to ion transport and electrolyte diffusion because of its typical structure, which meant it possessed a high specific surface area and could support rich ion transportation. The straight line in the low-frequency region was due to Warburg resistance. Based on the preceding results, it can be concluded that the Ni-MOF had a higher conductivity. Hence, the smaller charge-transfer resistance (0.5 Ω) confirmed that the prepared Ni-MOF porous nanorods had highly pseudocapacitive properties. The specific capacitance decreased from 1756.3, 1338.4, 1043.8, 761.5, 473.8, and 142.2 F g⁻¹ with the increase in the current density to 10, 15, 20, 25, 30, and 35 mA cm⁻², respectively, as shown in Fig. 7(d). The specific capacitance decreased as the current density increased because at higher current density the electrolyte ions participate in the bulk surface for the electrochemical reaction, and due to this there is a restriction in the ion transport, so the value of the specific capacitance decreases, and considering the low current density, the electrolyte ions have enough time to move across the inner pores of the electrode material, resulting in a higher specific capacitance value. The Ni-MOF showed a longer discharging time, which clearly indicated that the porous nanorods structure of the Ni-MOF possessed more surface active sites for the efficient charge-discharge process and increased the energy-storage ability of the Ni-MOF electrode. The cyclic stability of the electrode was explored by galvanostatic charge-discharge (GCD) persistence tests at 35 mA cm⁻² current density for 3000 cycles, as shown in Fig. 7(e). It could be seen that the specific capacitance was retained at over 81.13% after 3000 cycles for the Ni-MOF electrode, which suggested its good electrochemical reversibility during the charge-discharge process.

The Coulombic efficiency (η %), another important parameter to examine the interfacial stability of Ni-MOF electrode as a function of charge–discharge cycles, is shown in Fig. 7(f). Eqn (5) was used to calculate the Coulombic efficiency for the Ni-MOF electrode at different current densities,⁶³

$$\eta(\%) = \frac{t_d}{t_c} \times 100 \quad (5)$$

where t_d and t_c are the discharging and charging times in seconds, respectively.

The Coulombic efficiencies of the Ni-MOF electrode were 90.37%, 81.92%, 87.98%, 89.11%, 92.00%, 84.88%, and 98.45% at different current densities of 5, 10, 15, 20, 25, 30, and 35 mA cm⁻², respectively. The Coulombic efficiency of the Ni-MOF electrode rose and the specific capacitance decreased with the increase in current density, which might be assigned to the electrodes inner active sites, which were not capable of supporting the redox reactions at high current density.

A promising electrochemical stability and excellent reversibility of Ni-MOF electrodes were observed for up to the 3000 GCD cycles. The Ni-MOF samples showed that the orchestrating effects of the 1D morphology, surface area, and porosity led to their excellent application potential in terms of specific capacitance, energy density, power density, and cyclic stability.

To understand the practical ability of the Ni-MOF electrode in functional devices, a hybrid supercapacitor device was assembled using the as-prepared Ni-MOF as a positive electrode and activated carbon as the negative electrode, as shown in Fig. 8. Both electrodes were prepared by the slurry coating method. In short, the slurry was prepared by mixing the active material (Ni-MOF or AC) (80 mg), polyvinylidene fluoride (10 mg), and carbon black (10 mg) in 0.5 mL of methyl-2-pyrrolidone (NMP) solvent. Then, the required volume of the slurry was dispersed onto a stainless steel mesh with an area of 2 cm × 2 cm and dried at 60 °C overnight. Primarily, the side borders of the electrodes were formed as non-conducting through insertion of a band to avoid electrical contact. The PVA-KOH gel was pasted on one side of the electrodes and created one side of the electrical contact. Later, both electrodes were patched together like a sandwich, with the gel-pasted sides facing each other. The fabricated device was kept under 1 ton pressure for 12 h, to acquire a good connection within the

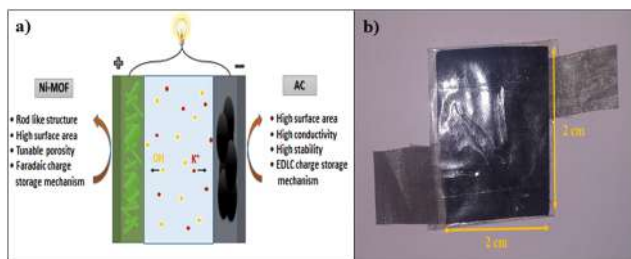


Fig. 8 (a) Schematic illustration of a hybrid supercapacitor with Ni-MOF as a positive electrode and activated carbon as a negative electrode in KOH aqueous electrolyte. (b) Digital photograph of the Ni-MOF//AC HSC device.

electrodes and gel electrolyte and also to remove the air gap. Afterwards, the device was used for assessment of the electrochemical performance. Hybrid supercapacitor devices have advantages, like high energy density, high specific capacitance, long cycle stability, and large potential window, over symmetric supercapacitors. The performance of the assembled hybrid device was studied using CV, GCD, and EIS measurements.

Primarily, CV tests were performed to understand the electrochemical performance of the Ni-MOF//AC hybrid supercapacitor (HSC) at different scan rates, as shown in Fig. 9(a). The Ni-MOF//AC hybrid SC exhibited a symmetric rectangular CV curve and a large area enclosed under the CV curve at up to 0–0.9 V. With the increase in scan rate from 10 to 100 mV s⁻¹, the increase in area under the CV curves revealed the excellent reversibility of the Ni-MOF. Additionally, GCD curves were obtained at different current densities from the hybrid device, indicating the ideal capacitive behaviour of the device, as shown in Fig. 8(b). The Nyquist plots of the Ni-MOF//AC HSC device are shown in Fig. 9(c), indicating that the fabricated device had an R_{ct} value of 0.36 Ω. According to the EIS studies, the fabricated Ni-MOF//AC HSC device had good electrical conductivity with a low ionic resistance. However, the specific capacitance decreased from 195.76, 94.79, 60.0, 42.70, and 31.67 F g⁻¹ with the increase in the current density from 2, 3,

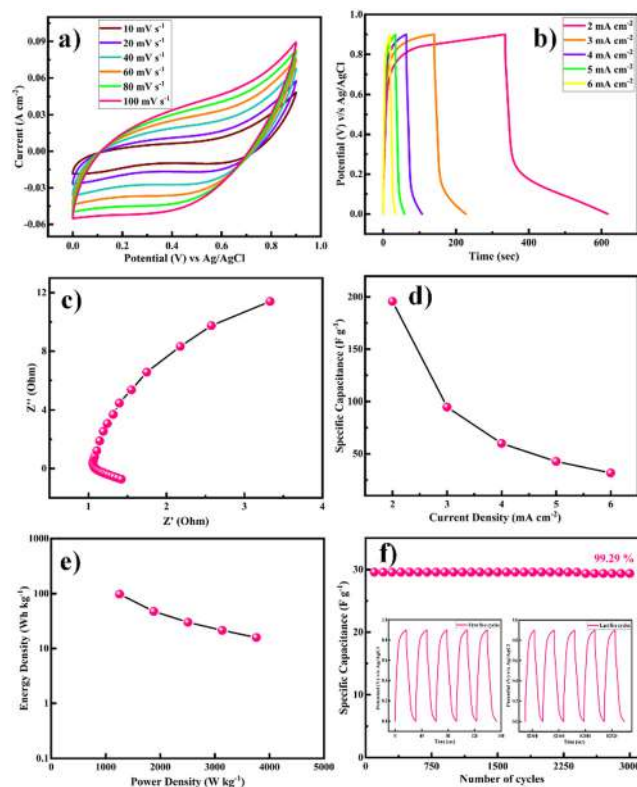


Fig. 9 (a) CV profile of HSC cell at different scan rates operated from 0 to 0.9 V. (b) GCD profiles for the HSC cell at different current rates (2–6 mA cm⁻²). (c) Nyquist plot of the HSC device. (d) Plot of the specific capacitance vs. current density. (e) Ragone plot for the HSC cell. (f) Cyclic durability test at a high current of 6 mA cm⁻² over 3000 GCD cycles; insets show the first and last five cycles.

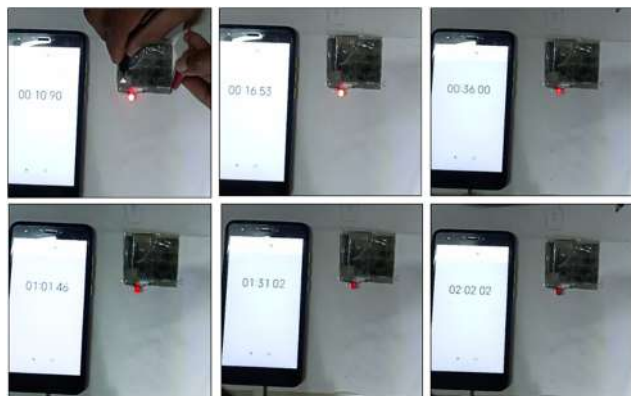


Fig. 10 The handmade asymmetric supercapacitor device was charged for 15 s and caused a red LED to glow for almost 105 s (i.e. charging time 15 s and discharging time 105 s).

4, 5, and 6 mA cm⁻², respectively, as shown in Fig. 9(d). The Ragone plot of the as-constructed HSC, expressing the relationship between the energy density (E) and power density (P), was obtained based on the galvanostatic charge–discharge curves (Fig. 9(e)). The cycling stability of the assembled hybrid supercapacitor device was investigated systematically. The device showed 99.29% capacitance retention over 3000 cycles, indicating its excellent cycle stability. The specific capacitance was constant over 2500 cycles and later it slightly decreased. The insets of Fig. 9(f) show the first and last five charge–discharge cycles of the device in 2 M KOH electrolyte. The Coulombic efficiencies of the asymmetric supercapacitor device were 84.15%, 65.00%, 68.57%, 74.54%, and 80.00% at various current densities of 2, 3, 4, 5, and 6 mA cm⁻², respectively (eqn (5)).

The device's energy density and power density were calculated using eqn (2) and (3). The HSC device exhibited a maximum energy density of 79.5 W h kg⁻¹ at a higher power density of 1015.3 W kg⁻¹, which was comparable to or even higher than recent literature values (Table 1) for hybrid supercapacitors.

The fabricated device could light a red-light-emitting diode (LED) for over 105 s when charged for 15 s due to the device's high energy density and maximum operational potential of 0.9 V, as shown in Fig. 10. It can be seen that the dazzling light was obvious at first, and then the brightness change is shown over time. After 105 s, we can see that the red light was still faintly glowing, confirming that the Ni-MOF//AC HSC device had an amazing ability to store charge. The good performance could be attributed to Ni-MOF's rod-like structure and pore-size distribution. The study discovered that the encouraging results may pave the way for the development of new electrode materials for supercapacitors and other energy-storage devices.

The study of the electrochemical parameters at different current densities of the chemically synthesized Ni-MOF is concluded in the radar graph shown in Fig. 11. The different apexes reveal the various parameters, such as specific capacitance, energy density, power density, and Coulombic efficiency, of the Ni-MOF. As seen in Fig. 11, this report contains the script

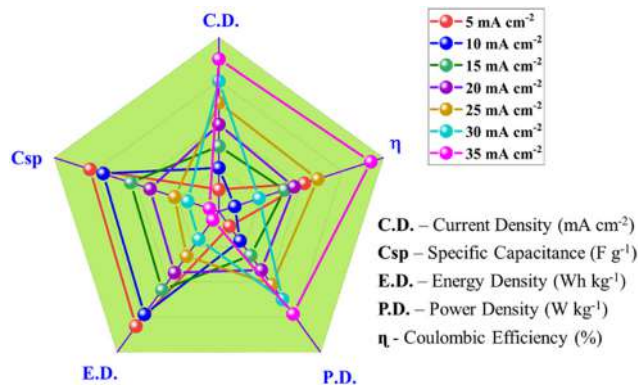


Fig. 11 Radar plot for Ni-MOF based on its supercapacitive properties.

for the Ni-MOF-based supercapacitor. These results indicate that the Ni-MOF has much better electrochemical performance than that of other reported MOFs due to its high specific capacitance, high energy density, large power density, and good Coulombic efficiency.

Conclusions

In summary, we successfully prepared Ni-MOF by using the reflux condensation technique. The structural properties and electrochemical performance of the Ni-MOF were studied systematically using various advanced tools. The porous and nanorod-like morphology, as confirmed by SEM analysis, provided both faster and more electroactive sites. An as-prepared Ni-MOF sample exhibited a high surface area of 398.4 m² g⁻¹. Furthermore, in a three-electrode system with 2 M KOH aqueous electrolyte, the synthesized Ni-MOF porous nanorods showed a high specific capacitance of 1956.3 F g⁻¹ at a current density of 5 mA cm⁻², and more stability for 3000 cycles with 81.13% retention. When assessed as a positive electrode for a flexible hybrid supercapacitor (HSC) device in combination with activated carbon as a negative electrode, the HSC cell exhibited a superhigh electrochemical behaviour. The device also exhibited a high charge-storage capacity of 195.76 F g⁻¹ at a current density of 2 mA cm⁻², super-specific energy (98.15 W h kg⁻¹), and excellent power density (1253.47 W kg⁻¹), including long-term stability of 3000 cycles with 99.29% capacity retention. The extraordinary energy-storage properties of the Ni-MOF electrode are attributed to its nanorod-like structure and higher surface area. This study provides a new platform for supercapacitors and other energy-storage devices.

Author contributions

Rakhee Bhosale: formal analysis, investigation, methodology and writing original draft; Sneha Bhosale: data curation; Pramod Kumbhar: visualisation; dattatray Narale: validation and methodology; Rachana Ghaware: discussions and review; Chitra Jambhale: editing of the draft; Sanjay Kolekar: conceptualization, supervision and funding acquisition.

Conflicts of interest

There are no conflicts to declare.

Acknowledgements

The authors are thankful to UGC-SAP, DST-FIST and DST-PURSE for the financial support and instrument facilities at the Department of Chemistry, Shivaji University, Kolhapur. Author Rakhee Bhosale is thankful to SARTHIL, Government of Maharashtra, India for the 'Chhatrapati Shahu Maharaj National Research Fellowship-2021'.

References

- 1 S. Koohi-Fayegh and M. A. Rosen, *J. Energy Storage*, 2020, **27**, 101047.
- 2 M. B. Askari, P. Salarizadeh, M. Seifi, M. H. Ramezan zadeh and A. Di Bartolomeoss, *J. Alloys Compd.*, 2021, **860**, 158497.
- 3 X. Zhao, K. Tao and L. Han, *Nanoscale*, 2022, **14**, 2155–2166.
- 4 Y. Tang, W. Guo and R. Zou, *Coord. Chem. Rev.*, 2022, **451**, 214242.
- 5 Poonam, K. Sharma, A. Arora and S. K. Tripathi, *J. Energy Storage*, 2019, **21**, 801–825.
- 6 S. Sanati, Z. Rezvani and B. Habibi, *New J. Chem.*, 2018, **42**, 18426–18436.
- 7 S. De, C. K. Maity, S. Sahoo and G. C. Nayak, *ACS Appl. Energy Mater.*, 2021, **4**, 3712–3723.
- 8 H. M. Nguyet, L. T. T. Tam, D. T. Tung, N. T. Yen, H. T. Dung, N. T. Dung, H. Phan N, L. A. Tuan, P. N. Minh and L. T. Lu, *New J. Chem.*, 2022, **46**, 13996–14003.
- 9 Y. Shao, M. F. El-Kady, J. Sun, Y. Li, Q. Zhang, M. Zhu, H. Wang, B. Dunn and R. B. Kaner, *Chem. Rev.*, 2018, **118**, 9233–9280.
- 10 R. Liu, A. Zhou, X. Zhang, J. Mu, H. Che, Y. Wang, T. T. Wang, Z. Zhang and Z. Kou, *Chem. Eng. J.*, 2021, **412**, 128611.
- 11 A. Mohanty, D. P. Jaihindh, Y. P. Fu, S. P. Senanayak, L. S. Mende and A. Ramadoss, *J. Power Sources*, 2021, **488**, 229444.
- 12 S. Kumar, G. Saeed, L. Zhu, K. N. Hui, N. H. Kim and J. H. Lee, *Chem. Eng. J.*, 2021, **403**, 126352.
- 13 L. Li, J. Meng, M. Zhang, T. Liu and C. Zhang, *Chem. Commun.*, 2022, **58**, 185–207.
- 14 X. Chu, F. Meng, T. Deng and W. Zhang, *Nanoscale*, 2021, **13**, 5570–5593.
- 15 P. Forouzandeh, P. Ganguly, R. Dahiya and S. C. Pillai, *J. Power Sources*, 2022, **519**, 230744.
- 16 C. V. V. Muralee Gopi, R. Vinodh, S. Sambasivam, I. M. Obaidat and H. J. Kim, *J. Energy Storage*, 2020, **27**, 101035.
- 17 S. Sanati, R. Abazari, A. Morsali, A. M. Kirillov, P. C. Junk and J. Wang, *Inorg. Chem.*, 2019, **58**, 16100–16111.
- 18 A. E. Baumann, D. A. Burns, B. Liu and V. S. Thoi, *Commun. Chem.*, 2019, **2**, 1–14.
- 19 W. Li, X. Zhao, Q. Bi, Q. Ma, L. Han and K. Tao, *Dalton Trans.*, 2021, **50**, 11701–11710.
- 20 H. M. Ma, J. W. Yi, S. Li, C. Jiang, J. H. Wei, Y. P. Wu, J. Zhao and D. S. Li, *Inorg. Chem.*, 2019, **58**, 9543–9547.
- 21 Y. Liang, W. Yao, J. Duan, M. Chu, S. Sun and X. Li, *J. Energy Storage*, 2021, **33**, 1–11.
- 22 L. Zheng, J. Song, X. Ye, Y. Wang, X. Shi and H. Zheng, *Nanoscale*, 2020, **12**, 13811–13821.
- 23 S. Zhou, S. Wang, S. Zhou, H. Xu, J. Zhao, J. Wang and Y. Li, *Nanoscale*, 2020, **12**, 8934–8941.
- 24 P. Du, Y. Dong, C. Liu, W. Wei, D. Liu and P. Liu, *J. Colloid Interface Sci.*, 2018, **518**, 57–68.
- 25 C. Yang, X. Li, L. Yu, X. Liu, J. Yang and M. Wei, *Chem. Commun.*, 2020, **56**, 1803–1806.
- 26 U. A. Khan, N. Iqbal, T. Noor, R. Ahmad, A. Ahmad, J. Gao, Z. Amjad and A. Wahab, *J. Energy Storage*, 2021, **41**, 102999.
- 27 S. Wang, S. Wang, X. Guo, Z. Wang, F. Mao, L. Su, H. Wu, K. Wang and Q. Zhang, *Inorg. Chem. Front.*, 2021, **8**, 4878–4886.
- 28 N. Wu, H. Wu, J. Zhang, Y. Zhang, D. Cao, L. Bai and T. Hu, *J. Alloys Compd.*, 2021, **856**, 157466.
- 29 N. Liu, X. Liu and J. Pan, *J. Colloid Interface Sci.*, 2022, **606**, 1364–1373.
- 30 D. Y. Lee, S. J. Yoon, N. K. Shrestha, S. H. Lee, H. Ahn and S. H. Han, *Microporous Mesoporous Mater.*, 2012, **153**, 163–165.
- 31 G. Zhu, H. Wen, M. Ma, W. Wang, L. Yang, L. Wang, X. Shi, X. Cheng, X. Sun and Y. Yao, *Chem. Commun.*, 2018, **54**, 10499–10502.
- 32 S. Xiong, S. Jiang, J. Wang, H. Lin, M. Lin, S. Weng, S. Liu, Y. Jiao, Y. Xu and J. Chen, *Electrochim. Acta*, 2020, **340**, 135956.
- 33 Q. Li, H. Guo, R. Xue, M. Wang, M. Xu, W. Yang, J. Zhang and W. Yang, *Int. J. Hydrogen Energy*, 2020, **45**, 20820–20831.
- 34 L. Wang, X. Feng, L. Ren, Q. Piao, J. Zhong, Y. Wang, H. Li, Y. Chen and B. Wang, *J. Am. Chem. Soc.*, 2015, **137**, 4920–4923.
- 35 X. Wang, N. Yang, Q. Li, F. He, Y. Yang, B. Wu, J. Chu, A. Zhou and S. Xiong, *J. Solid State Chem.*, 2019, **277**, 575–586.
- 36 M. Azadfalsh, A. Sedghi and H. Hosseini, *J. Electron. Mater.*, 2019, **48**, 7011–7024.
- 37 C. H. Wang, D. W. Zhang, S. Liu, Y. Yamauchi, F. B. Zhang and Y. V. Kaneti, *Chem. Commun.*, 2022, **58**, 1009–1012.
- 38 Y. Wu, X. Ding, Y. Luo, F. Xu, L. Sun, J. H. Lao, X. Qin, C. Dan, Y. Wang, Q. Yin, T. Wang, K. Zhang, B. Li, H. Zhang and Y. Zou, *Int. J. Electrochem. Sci.*, 2021, **16**, 1–11.
- 39 S. Gao, Y. Sui, F. Wei, J. Qi, Q. Meng and Y. He, *J. Mater. Sci.*, 2018, **53**, 6807–6818.
- 40 X. Zhang, N. Qu, S. Yang, Q. Fan, D. Lei, A. Liu and X. Chen, *J. Colloid Interface Sci.*, 2020, **575**, 347–355.
- 41 V. Veeramani, B. M. Matsagar, Y. Yamauchi, A. Y. Badjah, M. Naushad, M. Habila, S. Wabaidur, Z. A. Allothman, Z. L. Wang and K. C. W. Wu, *J. Taiwan Inst. Chem. Eng.*, 2019, **96**, 634–638.
- 42 R. Velmurugan, J. Premkumar, R. Pitchai, M. Ulaganathan and B. Subramanian, *ACS Sustainable Chem. Eng.*, 2019, **7**, 13115–13126.
- 43 S. B. Bandgar, M. M. Vadiyar, Y. C. Ling, J. Y. Chang, S. H. Han, A. V. Ghule and S. S. Kolekar, *ACS Appl. Energy Mater.*, 2018, **1**, 638–648.

- 44 S. Gao, Y. Sui, F. Wei, J. Qi, Q. Meng and Y. He, *J. Mater. Sci.: Mater. Electron.*, 2018, **29**, 2477–2483.
- 45 F. Israr, D. Chun, Y. Kim and D. K. Kim, *Ultrason. Sonochem.*, 2016, **31**, 93–101.
- 46 F. Israr, D. K. Kim, Y. Kim and W. Chun, *Quim. Nova*, 2016, **39**, 669–675.
- 47 X. Zhang, N. Qu, S. Yang, D. Lei, A. Liu and Q. Zhou, *Mater. Chem. Front.*, 2021, **5**, 482–491.
- 48 X. Liu, D. Xu, Q. Wang and L. Zhang, *Small*, 2018, **14**, 1–12.
- 49 Q. Liu, L. Xie, X. Shi, G. Du, A. M. Asiri, Y. Luo and X. Sun, *Inorg. Chem. Front.*, 2018, **5**, 1570–1574.
- 50 M. Thommes, K. Kaneko, A. V. Neimark, J. P. Olivier, F. Rodriguez-Reinoso, J. Rouquerol and K. S. W. Sing, *Pure Appl. Chem.*, 2015, **87**, 1051–1069.
- 51 R. Bardestani, G. S. Patience and S. Kaliaguine, *Can. J. Chem. Eng.*, 2019, **97**, 2781–2791.
- 52 M. Khalfaoui, S. Knani, M. A. Hachicha and A. Ben Lamine, *J. Colloid Interface Sci.*, 2003, **263**, 350–356.
- 53 G. Li, Y. Qi, H. Lin, N. Lu, J. Chen, J. Wang, Q. Han and F. Liu, *J. Membr. Sci.*, 2021, **635**, 1–9.
- 54 Q. Bi, Q. Ma, K. Tao and L. Han, *Dalton Trans.*, 2021, **50**, 8179–8188.
- 55 J. Yang, P. Xiong, C. Zheng, H. Qiu and M. Wei, *J. Mater. Chem. A*, 2014, **2**, 16640–16644.
- 56 X. G. Han, P. F. Wang, Y. H. Zhang, H. Y. Liu, J. J. Tang, G. Yang and F. N. Shi, *Inorg. Chim. Acta*, 2022, **536**, 120916.
- 57 S. S. Shah, E. Cevik, M. A. Aziz, T. F. Qahtan, A. Bozkurt and Z. H. Yamani, *Synth. Met.*, 2021, **277**, 116765.
- 58 C. Zhang, Q. Zhang, K. Zhang, Z. Xiao, Y. Yang and L. Wang, *RSC Adv.*, 2018, **8**, 17747–17753.
- 59 Y. Li, Y. Xu, Y. Liu and H. Pang, *Small*, 2019, **15**, 1–8.
- 60 J. W. Wang, Y. X. Ma, X. Y. Kang, H. J. Yang, B. L. Liu, S. S. Li, X. D. Zhang and F. Ran, *J. Solid State Chem.*, 2022, **309**, 122994.
- 61 S. Wang, J. Wang, M. Zeng, J. Yang, N. Hu, Y. Su, Z. Zhou, H. Pang and Z. Yang, *J. Energy Storage*, 2021, **38**, 102528.
- 62 C. Feng, C. P. Lv, Z. Q. Li, H. Zhao and H. H. Huang, *J. Solid State Chem.*, 2018, **265**, 244–247.
- 63 K. T. Kubra, A. Javaid, R. Sharif, G. Ali, F. Iqbal, A. Salman, F. Shaheen, A. Butt and F. J. Iftikhar, *J. Mater. Sci.: Mater. Electron.*, 2020, **31**, 12455–12466.

Recent Progress on Functional Metal–Organic Frameworks for Supercapacitive Energy Storage Systems

Rakhee Bhosale, Sneha Bhosale, Madagonda Vadiyar, Chitra Jambhale, Kyung-Wan Nam,* and Sanjay Kolekar*

As porous coordination organic polymers, both metal–organic frameworks (MOFs) and their derived materials and MOF-based composites offer unique organic or inorganic chemistries that display superior features of high specific surface area, accessible active sites, robust structural and chemical diversity, tailorable pore size, exceptional porosity, and pre- and postsynthesis structural tunability. Therefore, MOF-based materials are attractive for energy storage applications, specifically for supercapacitor devices. This review presents recent progress in designing and utilizing pristine MOFs, MOF-derived nanomaterials, and MOF-based composite materials for supercapacitors. Most importantly, herein, recent highlights and classifications of electrolytes and their vital role in the structure–property correlation between the structures of MOF-based materials and suitable electrolyte choices for ideal supercapacitor devices are discussed. Finally, together with a discussion of the progress and outcomes of MOF electrodes, the obstacles and prospects for future MOF-related research and applications are discussed. To help this intriguing topic continue to advance, this review offers useful insights into the logical design of MOF-based electrode materials.

to the isolated large-scale power plant facilities that presently supply most electrical energy.^[4,5] Likewise, we need better energy storage systems to efficiently use these energy sources, for example, transportation systems and pulsed electronic devices.^[6] Unfortunately, we can currently store only about 1% of the energy produced worldwide, primarily based on hydroelectric energy (98%) storage.^[7] To address these issues, there is a great demand for clean, environment-friendly, sustainable, and high-efficiency energy storage technologies.^[8–11]

The Ragone plot is a tool for comparing the performance of various energy storage technologies. In this plot, the values of the energy densities (Wh kg^{-1}) are plotted against the power densities (W kg^{-1}) of the energy storage devices. Energy storage devices like batteries, conventional capacitors, and supercapacitors (SCs) are located in the Ragone plot, as shown in **Figure 1**.

SCs offer a workable middle ground between capacitors and batteries.^[12,13] Among various electrochemical energy storage devices, batteries and SCs are the most favorable due to their high energy and power density, fast charging/discharging, and long cycle life.^[14,15] Of particular interest, SCs are the best-suited energy storage devices that can be coupled with intermittent renewable systems due to their unmaintainable long lifespan, fast charging and discharging times, and high power density.^[16–18] Based on the charge storage mechanism, the SC is classified as a non-Faradaic electric double-layer capacitor (EDLC), a pseudocapacitor, and hybrid capacitor. EDLC involves physical adsorption and desorption of ions at the electrolyte/electrode interface, while a pseudocapacitor stores charge via facile reversible surface redox reactions.^[19,20] The electrode materials for SCs must possess beneficial characteristics, like high electrochemical activity, large specific surface area, adjustable pore size distribution, and good electrical conductivity and hybrid capacitors depending on both types of mechanisms.^[21]


EDLCs exhibit a high power density and strong cycle stability but a low specific capacitance. Although pseudocapacitors show large specific capacitance, they possess low power density and cyclic stability. Thus, both faradaic and non-Faradaic methods may be used to store charge in order to achieve high power densities and alleviate the disadvantages of low cyclability in both pseudocapacitors and EDLCs, where the right electrode pairings can boost cell voltage and specific capacitance. Because of this,

1. Introduction

With the ever-increasing global energy requirements, the unsustainable burning of fossil fuels, and the limitations of renewable energy resources, securing energy sources for the future is one of the most critical tasks.^[1–3] Undoubtedly, a favorite choice is utilizing renewable clean energies, such as solar, wind, biomass, and tidal energy. Recently, different types of solar cells, such as silicon, biohybrid, dye-sensitized, perovskites, and thin-film cells, have been developed to efficiently convert this renewable energy into electricity. However, these renewable resources are all inherently intermittent and mostly dispersed compared

R. Bhosale, S. Bhosale, C. Jambhale, S. Kolekar
Analytical Chemistry and Materials Science Research Laboratory
Department of Chemistry
Shivaji University
Kolhapur 416004, Maharashtra, India
E-mail: ssk_chem@unishivaji.ac.in

M. Vadiyar, K.-W. Nam
Department of Energy and Materials Engineering
Dongguk University
Seoul 04620, Republic of Korea
E-mail: knam@dongguk.edu

 The ORCID identification number(s) for the author(s) of this article can be found under <https://doi.org/10.1002/ente.202300147>.

DOI: 10.1002/ente.202300147

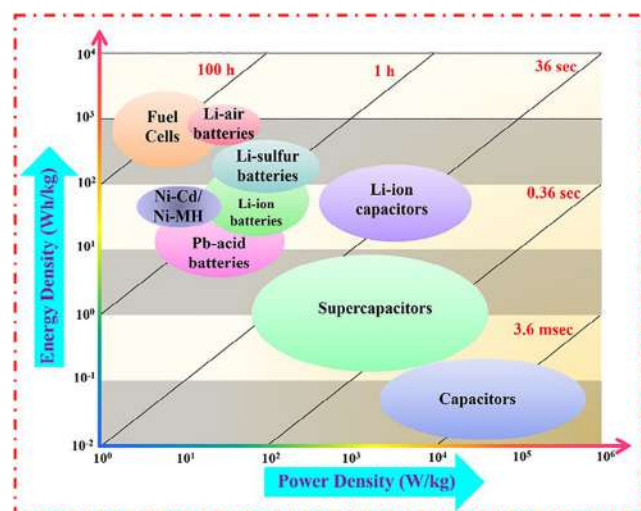


Figure 1. Ragone plot showing the specific power versus specific energy of different EES devices. Reproduced with permission.^[12] Copyright 2023, Elsevier.

these hybrid SCs can retain stability, have longer cycle life, and have greater energy and power densities.^[22–24]

Owing to their definite structure and the large specific surface area, metal–organic frameworks (MOFs) materials have attracted significant attention in multifunctional applications. MOFs are porous materials prepared using metal ions or clusters (secondary building units, or SBUs) and organic ligands.^[25,26] The pristine MOFs, MOF composites, and MOF derivatives have attracted increasing interest in electrochemical energy storage and conversion (EESC) applications thanks to their outstanding chemical stability and electrochemical performance.^[27,28] The field of MOFs has become one of the most rapidly growing areas in chemistry due to their structural and functional tunability. Their high porosity and systematic porous structure have resulted in MOFs being considered as good electrode materials for SCs.^[29,30] With the high-speed development of pristine MOFs, MOF composites, MOF-derived materials, and many EESC technologies, a small but all-inclusive review that “summarizes” the most recent growth and discovery may prove to be useful for their future developments in several high-efficiency EESC systems.

Due to their remarkable features, MOFs offer a lot of advantages over both inorganic and organic materials, and they have a lot of promise for use in metal-ion hybrid capacitors (MIHCs).

MIHCs are seen to be a viable option for bridging the gap between metal-ion batteries and SCs. MIHCs use distinct mechanisms for the cathode and anode to produce high power and energy densities at the same time. The benefits of MIBs and SCs are combined in MIHCs, which provide high energy and extended cycle life without compromising high power.^[31] Several MIHCs have been produced, including lithium-ion hybrid capacitors (LIHCs),^[32] sodium-ion hybrid capacitors (SIHCs),^[33] potassium-ion hybrid capacitors (PIHCs),^[34] zinc-ion hybrid capacitors (ZIHCs),^[35] and other forms of multivalent MIHCs. MIHCs have a battery-type anode and a capacitor-type cathode, which have two different charge storage processes, resulting in a mismatch in the capacity and kinetics of the anode and cathode, making it challenging to attain MIHCs’ overall high performance.^[36] Some of the MOFs as electrode materials for MIHCs are summarized in **Table 1**.

In this minireview, we provide a current study survey of the electrochemical performance of pristine MOFs, MOF composites, and MOF derivatives. We first briefly introduce the synthetic strategies for MOF composites and MOF-derived materials based on their composition, structure, and performance growth. Then, we focus on the recent advances in engineering MOF-derived functional materials as advanced electrodes for SC applications. Specifically, we discuss the following: 1) MOFs and their derived materials; 2) MOF composites with different materials; 3) different electrolytes for the electrochemical performance of a derived electrode for SC application; and 4) MOF application in an energy storage device, that is, a SC. Finally, this minireview concludes with some of our perceptions of the recent significant hurdles and their prospective solutions, hoping to stimulate continuous innovation to advance MOF-derived functional materials for SC application.

2. MOFs and Their Derived Materials

MOFs and their derived materials are influenced by the porous types of MOFs and their interesting elements, together with different kinds of organic linkers and metal-containing units. MOFs have been significantly investigated as attractive precursors to synthesize various nanomaterials, varying from carbon-based materials to metal-based materials (e.g., oxides, hydroxides, carbides, chalcogenides, and phosphides) with well-ordered porous structures.^[37] MOFs and their derived materials have also been broadly provided for energy storage applications, due to their

Table 1. MOFs as electrode materials for MIHCs.

Sr. No.	MOF materials	Composition	Applications	Current density [A g ⁻¹]	Energy density [Wh kg ⁻¹]	Power density [W kg ⁻¹]	Cyclic stability [Cycles]	References
1	Zr-MOF	Zr-MOF//AC	LIHC	2	122.5	12 500	1000	[195]
2	Co ₃ (HHTP) ₂	Co ₃ (HHTP) ₂ //AC spheres	LIHC	1	64	10 000	1000	[196]
3	UiO-66@PVDF-HFP	TiO ₂ //AC	SIHC	1	182	5280	10 000	[197]
4	Glass fiber@ZIF-7	Li ₂ TiSiO ₅ //AC	LIHC	2	238.56	14 295	4000	[198]
5	Ni-HAB	Ni-HAB//Na ₃ V ₂ O ₂ (PO ₄) ₂ F//AC	SIHC	1	127	17 309	5000	[199]
6	Carbon cloth@ZIF-8	Zn/carbon cloth@ZIF-8//carbon	ZIHC	1	107.4	16 200	10 000	[200]
7	Black phosphorus@ZIF-8	Black phosphorus@ZIF-8//AC	PIHC	1	93	9380	6500	[201]

unique organic–inorganic hybrid nature, well-defined porosity, high surface area, tunable chemical composition, and facile adjustability. Modifying MOFs into several MOF-derived nanostructures by thermal or chemical treatment can also lead to unique properties over the pristine MOFs.^[38,39]

2.1. The Pristine MOFs

Building block patterns of the pristine MOFs can be realized by wise choice and transformation of metal ions and organic linkers. The pristine MOF has physical and chemical properties, such as versatile compositions, high surface area, tunable pores, uniform dispersion, and defined active centers.^[40,41] Pure MOFs store energy through the physisorption of electrolyte ions on their internal surfaces at the metal centers.^[42] The important parameters that influence the electrochemical performance are the structure of MOF, which includes chemical structure and the geometries of the organic ligands.^[43] Due to their longer charge/discharge cyclabilities, larger specific capacitances, and faster ion diffusion, pristine MOFs are used for electrode preparation. To date, more than 40 types of pristine MOFs have been fabricated using different metals, such as Cu, Cr, Co, Ni, Fe, Mn, Zr, Zn, In, Al, Cd, and Mg in mixture with organic ligands like BTC, BDC, and imidazole.^[44–46]

Yang et al. synthesized a layered gear-like Ni–TDA [(Ni₃(OH)₂(C₂H₆O₄S)₂, Ni–MOF] material that was found to be a promising electrode material for the flexible all-solid-state asymmetric SC (ASC), with high specific capacitance of 1518.8 F g⁻¹ at a current density of 1 A g⁻¹. The capacitance retention of over 95.5% can be maintained even after 10 000 cycles at current density of 20 A g⁻¹, which shows excellent cycling stability at higher current densities.^[47] Yan et al. prepared a novel accordion-like Ni–MOF superstructure [(Ni₃(OH)₂(C₈H₄O₄)₂(H₂O)₄·2H₂O) to fabricate a flexible SC. It shows specific capacitances of 988 and 823 F g⁻¹ at a current density of 1.4 and 7.0 A g⁻¹ respectively, while sustaining excellent cycling stability (capacitance retention of 96.5% after 5000 cycles at current density of 1.4 A g⁻¹). Additionally, using Ni–MOF and activated carbon (AC), a high-performance flexible solid-state ASC was constructed with a specific capacitance of 230 mF cm⁻² at current density of 1.0 mA cm⁻², which shows little capacitance change after more than 5000 charge–discharge cycles, with only 7.2% decay at a current density of 5.0 mA cm⁻².^[48] Krishnamurthy et al. used a solvothermal method to report Mn–MOF (Mn[Tpa][Mi][DMF]) using terephthalic acid and methyl imidazole ligands. It shows specific capacitance up to 4000 F g⁻¹. Also, it has an energy density and power density of 500 Wh kg⁻¹ and 0.125 W kg⁻¹, respectively. The surface area of this material is outstanding, that is, 2352 m² g⁻¹ and pore volume of 0.00569 cc g⁻¹; Mn–MOF electrode possesses high-charge–discharge Coulombic efficiency, low polarization, and high specific capacitance, along with good cycling stability.^[49] Zhu et al. synthesized a 3D hierarchically structured Co–MOF supported on nickel foam (Co–MOF/NF), which shows better capacitive properties with good rate performance in 2 M KOH. Further, they constructed an ASC device using Co–MOF/NF as a positive electrode and AC as a negative electrode; it shows a high energy density of 1.7 mWh·cm⁻² at a

power density of 4.0 mW·cm⁻², with capacitance retention of almost 69.70% after 2000 cycles (**Figure 2**).^[50]

Wang and co-workers successfully synthesized an ultrathin NiCo–MOF nanosheet via facile ultrasonication at room temperature (RT), which is used as a promising electrode material for SC applications. It shows a high specific capacitance of 1202.1 F g⁻¹ at 1 A g⁻¹; furthermore, an ASC was fabricated using NiCo–MOF and AC, which shows a high energy density of 49.4 Wh kg⁻¹ at a power density of 562.5 W kg⁻¹ and 76.3% capacitance retention after 5000 cycles (**Figure 3**).^[51]

In short, the MOFs have metal ions and ligands, which give them a lot of redox sites for electrochemical processes. Therefore, the electrochemical performance of MOFs and the materials generated from them is greatly influenced by the pores, architectures, and crystal shapes. Using pristine MOFs as electrode materials is directly fraught with difficulties, which limits their usefulness. Even though most MOFs have weak conductivity, it can be improved by creating conjugate systems and 3D network topologies, allowing for the direct use of well-designed pristine MOFs as electrode materials for SCs.

2.2. MOF-Derived Metal Oxides

The poor structural stability and electrical conductivity of the pristine MOFs have hampered their practical utilization as electrodes in SC applications. Transforming the pristine MOFs into metal oxides is a significant way of enhancing their structural and electrochemical stability, including electrical conductivity. The MOF-derived metal oxide shows unique structural features, such as porous morphology, robust structure, high electrical conductivity, and high redox behavior. Therefore, metal oxides derived from MOFs are preferred for the construction of electrode materials. MOF-derived metal oxide electrode materials store energy through charge transfer between electrolyte–ions and the electrodes. Metal oxides are mostly made via the general procedure of calcination. MOFs are heated to a temperature of a few hundred degrees in an inert atmosphere furnace.^[52,53] Throughout the annealing procedure, metal sites are oxidized to the isonomous metal oxides, and organic ligands are transmuted into carbon dioxide and water vapor, which frame ample pores. MOF-derived metal oxides sustain their primitive morphology, showing huge pores and associated gaps.^[54,55]

Lan et al. prepared a porous flower-like MnNi₂O₄ using bimetallic Mn/Ni–MOF as a precursor that exhibits astounding electrochemical behavior with the most significant specific capacitance of 2848 F g⁻¹ at 1 A g⁻¹ with good stability of 93.25% capacitance retention after 5000 cycles at 10 A g⁻¹ (**Figure 4**). Further, they constructed an ASC using MnNi₂O₄ positive electrode and active carbon as the negative electrode, which shows a large energy density of 142.8 Wh kg⁻¹ at a high power density of 800 W kg⁻¹.^[56]

Xiao et al. synthesized an ultrathin Co₃O₄ nanosheet using Co-based MOF by hydrolysis followed by calcination procedure, which exhibits outstanding SC performance due to the abundant meso- and macropores. In addition, they fabricated an ASC using Co₃O₄ nanosheets as a positive electrode and AC as a negative electrode, which shows a high energy density of 32.8 Wh kg⁻¹ at the power density of 752 W kg⁻¹ and retains 98.1% of its initial

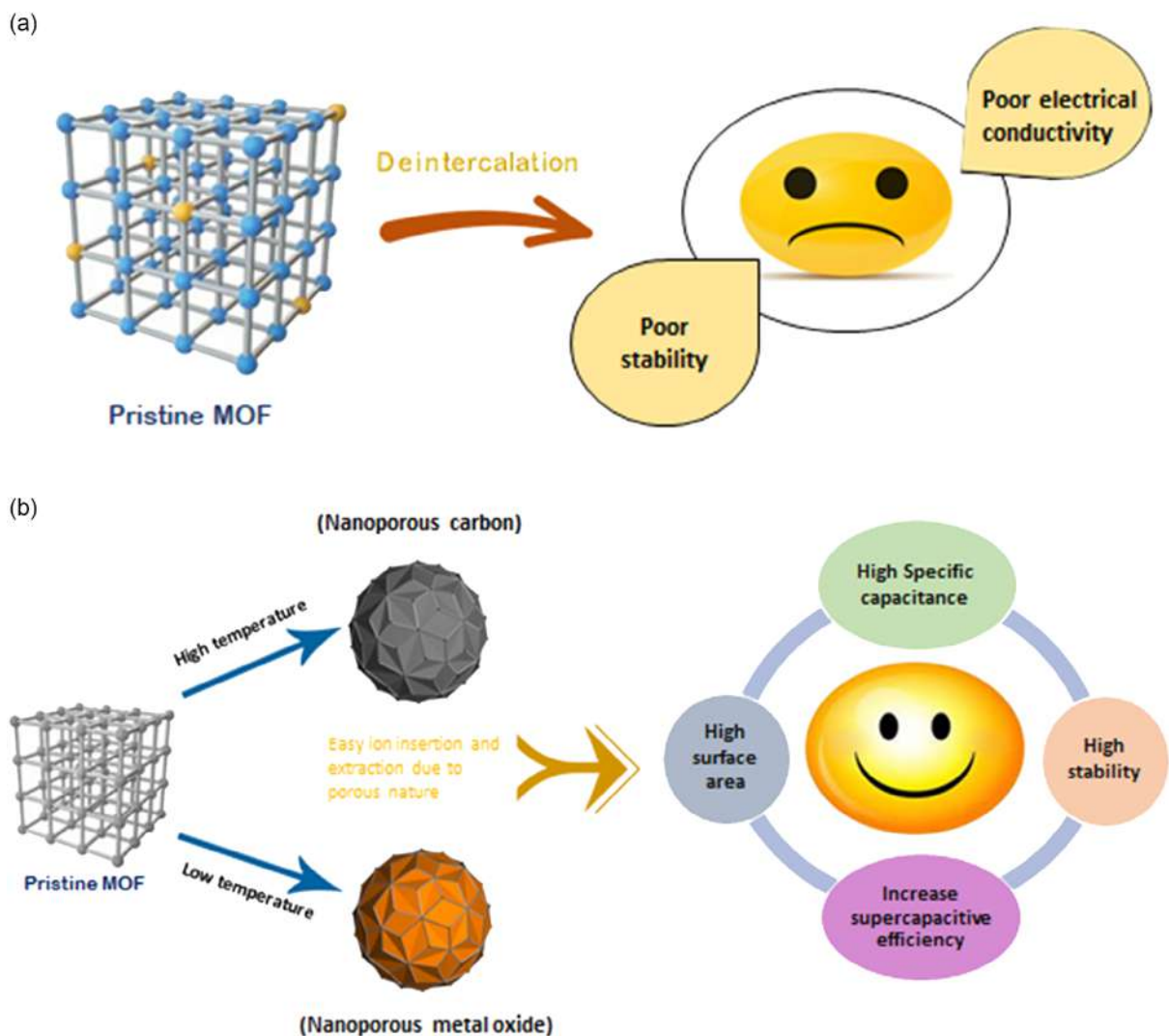


Figure 2. a) Schematic of the pristine MOFs for SC application. b) Development of the use of various MOFs in the field of SC application.

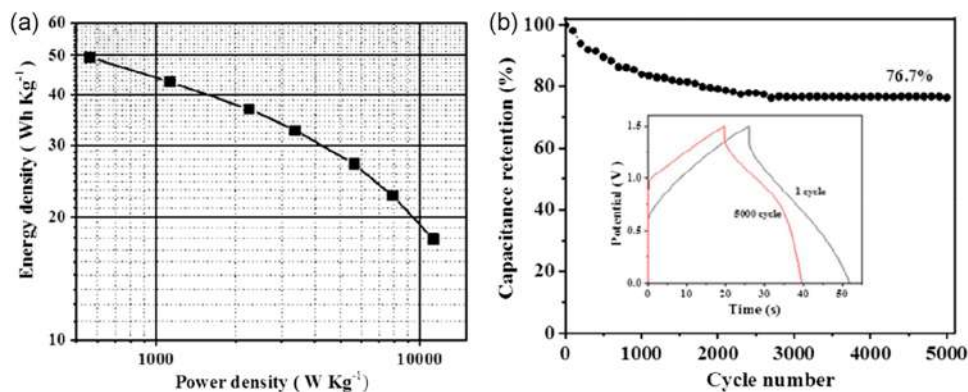


Figure 3. a) Ragone plot of the ASC device and b) the cycling stability at 5 A g⁻¹ over 5000 cycles. Reproduced with permission.^[51] Copyright 2019, American Chemical Society.

capacitance after 6000 charge/discharge cycles at the current density of 2 A g⁻¹ with long-term cycling stability.^[57] Wu and co-workers synthesized hollow core in double-shell NiO

nanospheres by the calcination of Ni-based MOF; as they are calcined at different temperatures, they show distinct surface areas and electrical conductivities, which play an important role in the

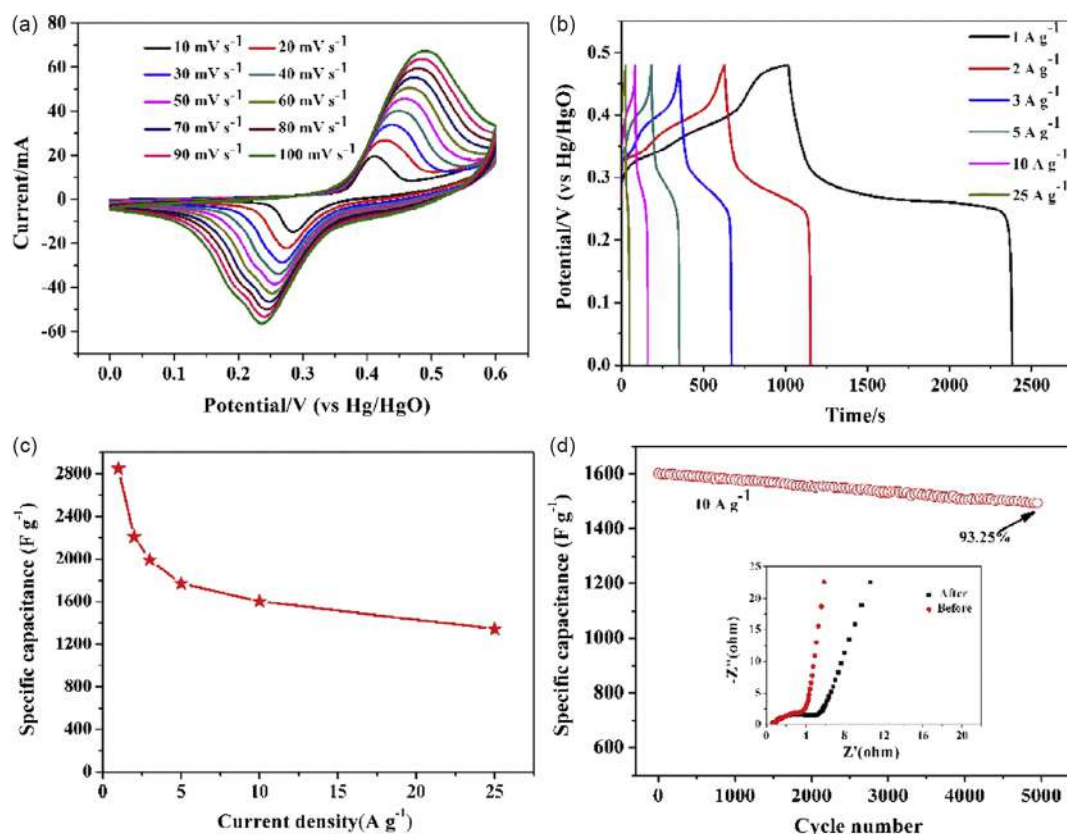


Figure 4. a) Cyclic voltammetry (CV) curves at different scan rates from 10 to 100 mV s^{-1} , and b) charge/discharge curves of the MnNi_2O_4 electrode at various current densities from 1 to 25 A g^{-1} . c) Specific capacitance of the MnNi_2O_4 electrode. d) Cycling stability of the MnNi_2O_4 electrode at a current density of 10 A g^{-1} ; the inset presents Nyquist plots of the MnNi_2O_4 electrode before and after cycling. Reproduced with permission.^[56] Copyright 2019, Elsevier.

redox reaction that takes place at the surface of the active materials. Material calcined at 400 °C shows a specific capacitance of 473 F g^{-1} at the current density of 0.5 A g^{-1} , which shows good cycling stability, even after 3000 cycles. Additionally, they constructed an ASC with high-energy storage capacity and outstanding cycling performance.^[58] Li et al. fabricated hierarchical double-shelled NiO/ZnO hollow spheres by annealing a bimetallic organic framework in air and used it as an electrode material for high-performance SC applications. It shows a specific capacitance of 497 F g^{-1} at a current density of 1.3 A g^{-1} with outstanding cycling stability, even after 2000 cycles.^[59] Xu et al. investigated a scheme to set up unique $\text{Co}_3\text{O}_4/\text{ZnO}$ nano heterostructures through the thermal conversion of center-shell $\text{ZIF-8}@\text{ZIF-67}$, displaying superior pseudocapacitive behavior. It shows a high specific capacitance of 415 F g^{-1} at 0.5 A g^{-1} with enhanced rate capability (93.2% retention at 10 A g^{-1}), compared to Co_3O_4 and ZnO derived from single MOF precursor.

Further, they fabricated an ASC using $\text{Co}_3\text{O}_4/\text{ZnO}$ heterostructure as a positive electrode and active carbon as a negative electrode. The electrochemical performance determined in an aqueous electrolyte (AE), that is, 6 M KOH in expanded 1.4 V working voltage, shows an energy density of 43.2 Wh kg^{-1} at a power density of 1401 W kg^{-1} .^[60] The nanoporous NiO , NiCo_2O_4 , and Co_3O_4 were prepared using the hydrothermal

method and an annealing process that exhibits a large surface area and porous nature. As compared with monometallic oxides, the mixed metal oxides, that is, NiCo_2O_4 , show high specific capacitance of 684 F g^{-1} at 0.5 A g^{-1} current density and outstanding cycling stability with the specific capacitance retention of 86% after 3000 cycles at the current density of 10 A g^{-1} , whose performance makes it a promising material for energy storage and conversion devices.^[61]

2.3. MOF-Derived Nanoporous Carbon Materials

MOF-derived nanoporous carbons (NPC) material is obtained by the calcination of MOF at high temperatures or the pyrolysis of MOF followed by acid treatment or base activation. NPCs maintain the structure and morphology of MOF, which enables the conducting properties of carbon. Many NPCs materials have been widely examined for SC applications, due to their outstanding chemical and mechanical stability, large specific surface area, good electrical conductivity, and adjustable pore structure.^[62–64] To increase the capacitance of carbon material, heteroatom doping (e.g., B, S, N, P) is a new strategy to elevate the surface wettability and contribute reversible pseudocapacitor behavior to a material. The addition of metals can supply extra benefits in the carbon array, which encourages the applications of carbon

materials as electrode materials. Incorporating specific metals like Co, Ni, and Fe can amazingly ameliorate the crystallinity and electrical conductivity of carbon, owing to their catalytic graphitization of the amorphous carbon. Hence, heteroatom doping or metal-modified carbons are promising materials for SC applications and has attracted much interest.^[65–68] Nowadays, the performance of SCs is mainly influenced by electrode materials. Among different electrode materials, carbon is the most broadly used material for SCs due to its multiple advantages: wide source, large specific surface area, environmental warmth, and good electrical conductivity. Large specific surface area and suitable pore size are the chief techniques to achieve high capacitance of carbon materials; carbon materials mainly store energy by constructing an electric double layer across the separated charges of electrolyte ions on the surface.^[69]

Due to its easy synthesis, controllable morphology, and high nitrogen content, ZIF-8 is a common precursor for synthesizing many porous carbon materials for SCs. Tang et al. put nanoporous hybrid carbon materials containing nitrogen-doped carbon (NC) as the cores and highly graphitic carbon (GC) as the shell using core-shell-structured ZIF-8@ZIF-67 crystals. This novel NC@GC material holds a high surface area (up to $1276 \text{ m}^2 \text{ g}^{-1}$) and high N content (10.6 wt%) derived from core ZIF-8 and a better graphitic structure derived from shell ZIF-67. It shows an eminent specific capacitance of 270 F g^{-1} at a current density

of 2 A g^{-1} (Figure 5).^[70] Liu et al. investigated a new strategy to design a flexible hierarchical porous carbon film (HPCF) for binder-free and high-performance energy storage devices consisting of MOF-derived porous carbon polyhedra and carbon nanotubes (CNTs). They prepared HPCF (1, 2, -3, -4, and -5) by the calcination at different temperatures of 400, 500, 600, 800, and $900 \text{ }^\circ\text{C}$ respectively, from which HPCF₄ gives the largest Brunauer–Emmett–Teller ($620.1 \text{ m}^2 \text{ g}^{-1}$) and shows the highly porous structure, excellent flexibility, with highest electrical conductivity (1320 S m^{-1}). HPCF₄ offers excellent rate capability larger than 60% retention from 2 to 100 A g^{-1} with high electrical conductivity and successful ion transport networks, compared with the other flexible carbon electrodes. In addition, they fabricated an aqueous symmetrical SC that shows an energy density of 9.1 Wh kg^{-1} with a power density of 3500 W kg^{-1} .^[71] Duan and co-workers discovered three types of activated porous carbon (APC) by the annealing and thermolysis of Cu–MOF with different morphologies, varying the reaction temperatures at 0, 25, and $60 \text{ }^\circ\text{C}$. APC-25 reveals cabbage-like morphology, out of those APCs with the largest specific surface area, that is, $1880.4 \text{ m}^2 \text{ g}^{-1}$ and $0.81 \text{ cm}^3 \text{ g}^{-1}$ pore volume; it also exhibits the highest specific capacitance of 196 F g^{-1} at 0.5 A g^{-1} current density. Additionally, they fabricated an ASC device using APC-25, giving an incredible 11.8 Wh kg^{-1} energy density at a power density of 350 W kg^{-1} with outstanding cycling stability.

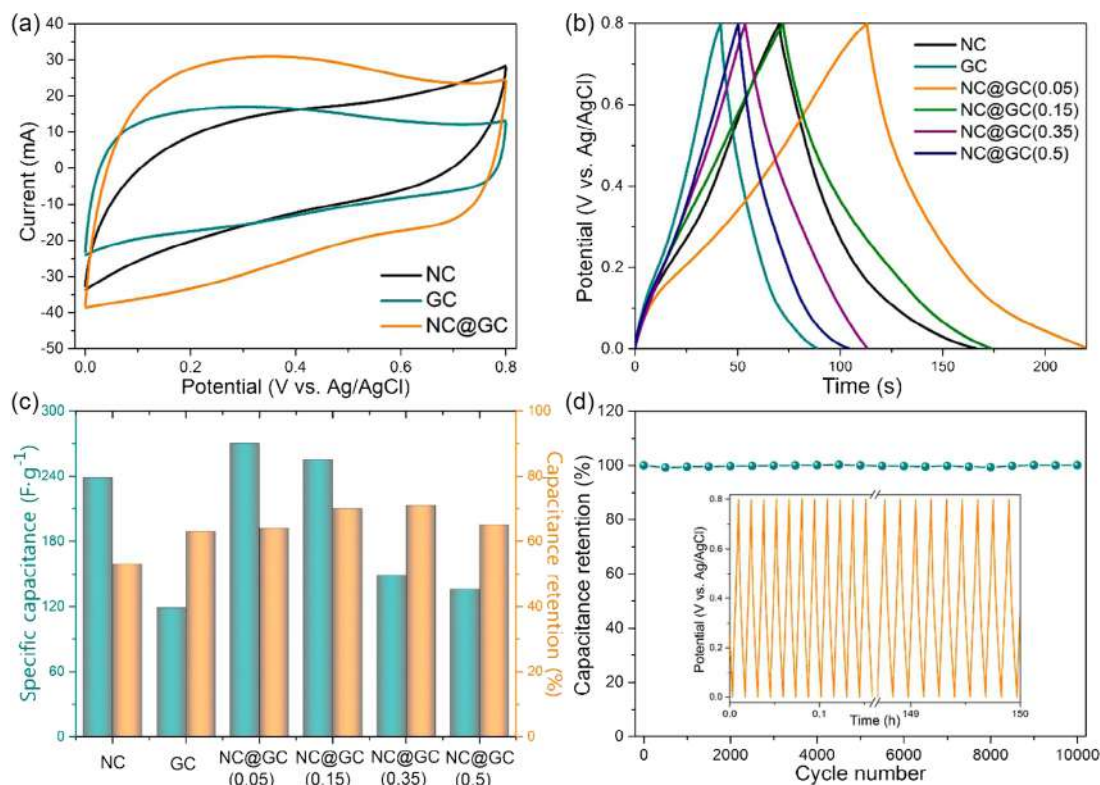


Figure 5. a) CV at a potential scan rate of 200 mV s^{-1} for NC, GC, and NC@GC (0.15). b) Charge–discharge curves of NC, GC, NC@GC (0.05), NC@GC (0.15), NC@GC (0.35), and NC@GC (0.5) electrodes at a current density of 2 A g^{-1} . c) The specific capacitance values obtained at a current density of 2 A g^{-1} and the capacitance retention ratios at a higher current density of 10 A g^{-1} for NC, GC, NC@GC (0.05), NC@GC (0.15), NC@GC (0.35), and NC@GC (0.5) electrodes, respectively. d) Cyclic stability of NC@GC (0.15) at a charge–discharge current density of 5 A g^{-1} for 10 000 cycles. Inset shows the galvanostatic charge–discharge curves. All measurements were conducted in $1.0 \text{ M H}_2\text{SO}_4$ using a three-electrode system. Reproduced with permission.^[70] Copyright 2015, American Chemical Society.

Noticeably, using six ASCs, five light-emitting diodes (LED) were lighted, which confirms that APC-25 might be used in energy storage devices.^[72] Wang et al. demonstrated a fruitful route to increase the conductivity performance of N-doped MOFs-based hierarchical carbon (NPC) to defeat the insulating problems of MOFs by electrochemically twisting together MOF crystals with a conductive polymer. They prepared a new N-doped MOFs-based hierarchical carbon (NPC) by electrospinning method, followed by pyrolysis to get nanofibers; it shows superior energy storage capacity to that of the earlier recorded MOF-derived carbon materials with innovative 1D hollow structures. NPCF exhibits 332 F g^{-1} specific capacitance at 1 A g^{-1} current density and excellent cycling stability with a specific capacitance retention of 98.9% after 5000 cycles at 1 A g^{-1} current density.^[73]

Chen and colleagues investigated a fruitful method for manufacturing hollow particle-based nitrogen-doped carbon nanofibers (HPCNFs-N) by an easy carbonization treatment of an electrospun ZIF-8/PAN composite precursor. HPCNFs-N material significantly increases the electrochemical property as an electrode material for SCs with incredible specific capacitance at different current densities, high energy/power density, and long cycling stability of over 10 000 cycles.^[74] Hao et al. synthesized nitrogen-doped porous carbon polyhedra (N-PCMPs) by directly carbonizing ZIF-11 polyhedra stimulated by fused KOH to enhance the surface area and pore volume. Activated N-PCMPs (N-PCMPs-A) show 307 F g^{-1} specific capacitance at 1.0 A g^{-1} current density, which is incredibly higher than that of N-PCMPs, that is, 165 F g^{-1} ; even further, the specific capacitance of N-PCMPs-A retains 198 F g^{-1} at a regular high amount of current density, that is, 10 A g^{-1} , which compared to N-PCMPs, is significant. N-PCMPs show incredible cycling stability with a specific capacitance retention of 90%, even after 4000 cycles at the current density of 10 A g^{-1} .^[75]

In this part, we provided a brief summary of material design techniques to illustrate the wide range of potential applications from the chemical makeup and physical characteristics of MOF-derived materials. The development of a variety of fascinating functional materials with desirable composition, tuning morphologies, structures, and characteristics can be facilitated by the use of MOFs as potential precursors or sacrificial templates. As a result of numerous benefits, such as high surface area, ordered porosity, adaptable topological morphology, and various chemical composition of MOFs, as well as improvements in material synthesis and characterization techniques, functional materials derived from MOFs have demonstrated great potential for creating advanced electrodes for clean, secure, and long-lasting energy storage systems.

3. MOF Composites with Different Materials

MOFs are novel spongy coordination polymers that exhibit remarkable properties, like organized porous structure, a large surface area, an adjustable structure, a high electrochemical response, and chemical tunability and hence have been broadly studied for energy conversion and storage applications. These nanostructures are profitably used as electrode materials in energy storage devices like SCs, due to their enhancement of charge transfer within the MOF structure and the redox nature

of their metal ions.^[76–78] While the research of MOF as an electrode material for SC applications is still in the primary phase, the field is becoming larger at a rapid rate. Some works have been published for energy storage devices, such as Ni-MOF, Fe-MOF, Co-MOF, and Co-Zn MOF as electrode materials for SCs. However, from an overall point of view, most MOFs still suffer from poor stability, narrow micropores, poor electrical conductivity, low use of active sites, and hindered ion entrance, which mostly limit the practical applications of many of the MOFs for SC applications.^[79–83] One strategy to overcome these problems is to upgrade MOFs by designing composites. MOF composites are prepared using MOFs and different functional materials, like metal oxides/hydroxides, quantum dots, reduced graphene oxide, metal sulfides, conducting polymers (CP), etc., to minimize the disadvantages of an individual building block.

To construct MOF composites, the direct reaction of MOFs with functional materials is a logical strategy and makes them candidates for energy storage applications.^[84] The composites can be synthesized in two ways: first, in a one-step procedure, where the different functional materials participate in the reaction during MOFs preparation. The second way is the composite of MOFs with different functional materials that can be executed after the preparation of MOFs. Single materials tend to run across certain obstacles and limitations; hence, materials with various advantageous features are incorporated. A synergistic effect within two compounded materials can be applied to boost the advantages of single materials or orderly reduce their limitations. Due to this, the composite formation logical strategy permits the construction of hybrid electrodes for SC applications. Hybrid electrodes can sustain the EDLC and pseudocapacitive feature compared to single materials. This hybrid plan helps develop a high value of specific capacitance, long cycle life, high energy density, and power density. We have reviewed the research work to explore MOF composites with proper materials given later in subgroups. Those hybrid materials have been certified to be beneficial to fabricate unique electrodes for highly advanced SCs.^[85] The production of a hybrid MOF with different functional materials to engender MOF composites exhibits immense advantages, due to their synergistic effect.

3.1. MOF@metal Oxides/Hydroxides

Owing to their size, crystallinity, controllable shape, and functionality, metal oxide nanomaterials are extensively used in energy storage applications.^[86–88] Metal oxide nanomaterials are measured as perfect pseudocapacitive electrode materials due to their high theoretical specific capacitance, inexpensiveness, and significant reversibility. However, they have increased surface energies and are prone to aggregation, moving toward pseudocapacitive performance.^[89,90] Furthermore, metal oxides as an electrode material for energy storage devices are widely limited, due to low surface area.^[91] Hence, a low-cost procedure is needed to enhance the specific surface areas of metal oxides, which is essential to obtain significant pseudocapacitive activity.

One of the plans of action is to combine the merits of both metal oxides and MOFs by mixing metal oxides with MOFs possessing large surface area, in which a single building block preserves its character while contributing remarkable features to

the entire process.^[92,93] Xiong and co-workers reported a new reverse thinking strategy to prepare a well-arranged porous metal oxide@MOF composite, that is, NiO@Ni-MOF/NF, by a two-step hydrothermal method. The hydrothermal method was selected due to the rapidity of its synthesis technique and also its effortlessness. To begin with, nickel foam (NF) was used as a unique self-sacrificing template and precursor for the preparation of nickel oxides (NiO), followed by the addition of the organic ligand (H₃BTC) to transform into Ni-MOF. Finally, the metal oxide@MOF composite was fruitfully prepared under the fine-tuned conditions, exhibiting 1853 C cm⁻² specific capacitance at 1 mA cm⁻² current density (**Figure 6**).

Furthermore, they assembled ASC devices using NiO@Ni-MOF/NF as a positive electrode and CNT as a negative electrode. This HSC device exhibits 144 F g⁻¹ specific capacitance at 1 A g⁻¹ current density with a high energy density of 39.2 Wh kg⁻¹ at a power density of 700 W kg⁻¹ and 94% capacitance retention after 3000 cycles (**Figure 7**). This synthetic technique takes a significant direction and provides a well-organized approach to obtaining other well-arranged metal oxide@MOFs composite materials.^[94]

Zheng et al. designed and reported highly alkaline stable cobalt oxide nanocubes on Co-MOF sheet composite (Co₃O₄@Co-MOF) by a facile and controllable one-pot hydrothermal method. The Co₃O₄@Co-MOF composite exhibits 1020 F g⁻¹ specific capacitance at 0.5 A g⁻¹ current density and enormous cycling stability with only 3.3% decay after 5000 cycles at 5 A g⁻¹ current density. Furthermore, they fabricated the Co₃O₄@Co-MOF//AC solid-state flexible device with maximum

energy density, revealing that solid-state flexible devices can be used in movable, portable, and lightweight electronic applications.^[95] Zhang et al. established that an effortless one-step chemical method gives rise to the self-transformation process to form the composite by combining metal oxides into the MOF systems using MOF-manganese hexacyanoferrate hydrate (MHCF) nanocubes as a starting material. The composite MnO_x-MHCF exhibits a remarkable threefold increase in capacitance compared to the pristine MOFs, revealing that MnO_x-MHCF composite material shows excellent promise for flexible energy storage. Furthermore, a flexible solid state-hybrid-SC (SSHHC) device was constructed using MnO_x-MHCF and AC as two electrodes, which exhibited an areal capacitance of 175 mF cm⁻² at 0.5 mA cm⁻² current density. Also, the device exhibits capacitance retention of 94.5% after 10 000 cycles at 5.0 mA·cm⁻² current density, with excellent long-term cycling stability.^[96]

3.2. MOF@CPs

While metal-organic frameworks are used as promising electrode materials in SCs due to their remarkable features, such as high surface area, tunable pore size, highly porous framework, open metal sites, and controllable functional linkers, some MOFs possess low conductivity.^[97] Unfortunately, due to low conductivity, the MOFs have limitations in utilization in SCs. An efficient strategy to enhance the conductivity of MOFs is the mixing of conductive polymers (CPs), like polyethylene dioxythiophene (PEDOT), polyaniline (PANI), and polypyrrole (PPy),

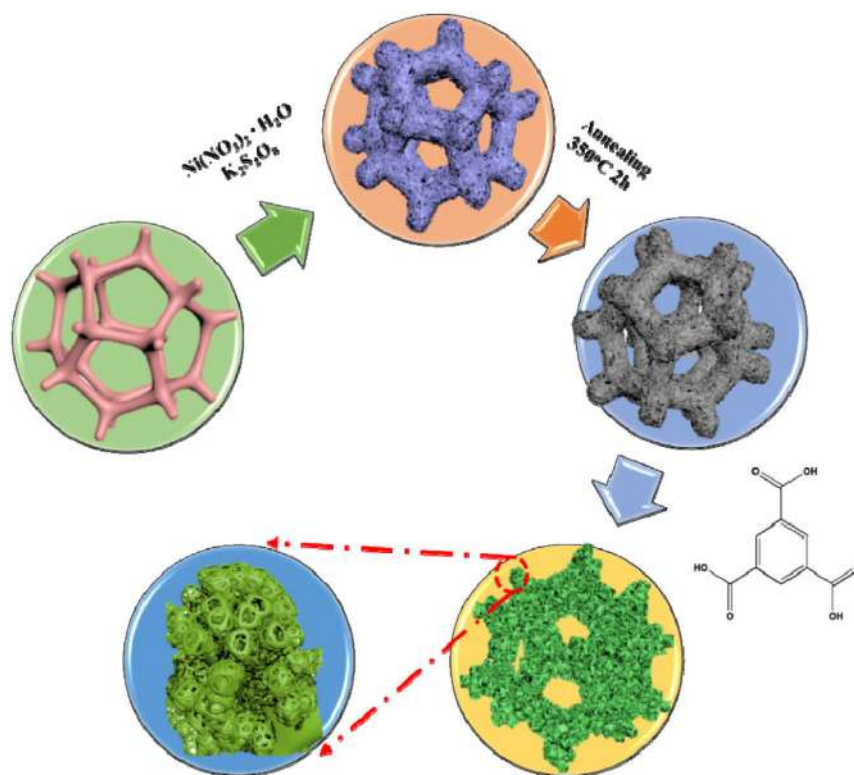


Figure 6. Schematic of the fabrication of NiO@Ni-MOF on Ni foam. Reproduced with permission.^[94] Copyright 2020, Elsevier.

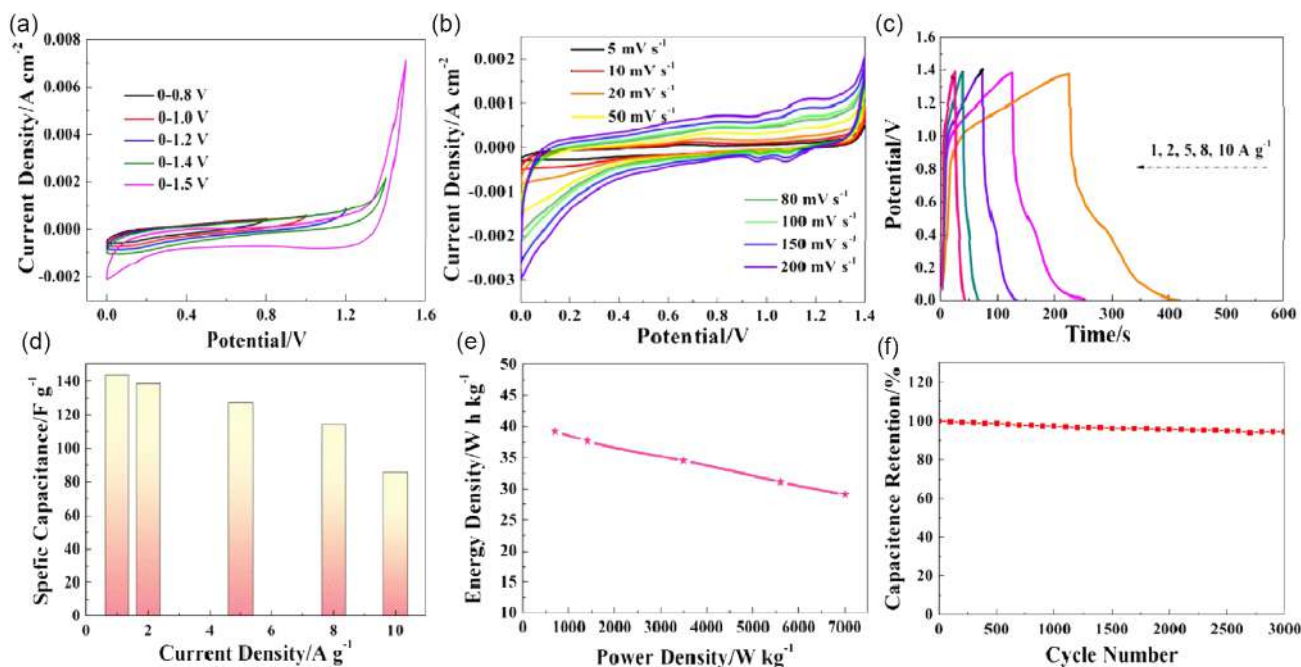


Figure 7. The electrochemical performance of NiO@Ni-MOF-12//CNT hybrid SC: a) CV curves at various voltage windows at the scan rate of 50 mV s^{-1} ; b) CV curves at various scan rates ranging from 5 to 200 mV s^{-1} in the voltage window of 0 – 1.4 V ; c) Galvanostatic charge/discharge (GCD) curves at different current densities ranging from 1 to 10 A g^{-1} in the voltage window 0 – 1.4 V . d) Histogram of the specific capacitance at different current densities. e) Ragone plot (energy density vs power density). f) Cycling performance up to 3000 cycles at the current density of 10 A g^{-1} . Reproduced with permission.^[94] Copyright 2020, Elsevier.

which adds up to a conducting route for MOFs. Owing to their low cost, effortless preparation, large theoretical specific capacitance, and excellent conductivity, CPs-based electrode materials are widely used in SCs.^[98–100]

Zhang et al. constructed PPy@UIO-66@CT fabric electrodes for flexible SCs by depositing polypyrrole (PPy) nanotubes and Zr-based MOF (UiO-66) particles on cotton fabrics. Primarily, UIO-66 was developed in situ on the surface of cotton fabric via a facile solvothermal method; later, PPy nanotubes were placed on the surface of UIO-66@CT, utilizing a reactive template, that is, FeCl_3 -MO complex. Due to its outstanding aqueous, acid, and thermal stability, UIO-66 was used along with PPy nanotubes to provide conductive connectors for UIO-66 particles because of its better conductivity. PPy@UIO-66@CT fabric electrodes possess high conductivity with better specific capacitance of 565 F g^{-1} at 0.8 mA cm^{-2} current density in a two-electrode system. Also, fabric electrodes exhibit admirable stability with capacitance retention of 90% after 500 charge/discharge cycles and upstanding rate capability.^[100] Qi et al. reported a strategy to design and construct a MOF/CP hybrid, that is, UiO-66/polypyrrole hybrid, for a high-performance all-solid-state fabric fiber SC via a one-pot electrodeposition method in the presence of dopamine. The manufactured UiO-66/PPY hybrid fabric fiber has high-performance capacitive properties, broad working temperatures, good mechanical flexibility, and long-term cycling stability; these properties show great potential for the fibrous energy storage device. It exhibits a specific capacitance of 10 mF cm^{-1} (206 mF cm^{-2}), a power density of $132 \mu\text{W cm}^{-1}$ ($2102 \mu\text{W cm}^{-2}$), and an energy density of $0.8 \mu\text{Wh cm}^{-1}$

($12.8 \mu\text{Wh cm}^{-2}$) with outstanding mechanical flexibility over a broad range of working temperatures.

Moreover, the fabricated fiber device was applied under a straight variety of bending angles and frizzy conditions to estimate its practical, flexible property.^[101] Wang et al. summarized a novel approach to attain high-performance SCs to overcome the insulating difficulty of MOFs by the electrochemically blending of MOF crystals with a conductive polymer. They fabricated the PANI-ZIF-67-CC electrode by depositing ZIF-67 on carbon cloth and then electrochemically blended PANI with it (Figure 8). PANI-ZIF-67-CC electrodes possess a high areal capacitance of 2146 mF cm^{-2} at 10 mV s^{-1} , compared to other reported SCs based on carbon nanoparticles (CNPs), CNTs, reduced graphene oxide, conductive polymers, and metal oxides. In addition, they fabricated a flexible solid-state SC device with an outstanding areal capacitance of 35 mF cm^{-2} and power density of 0.833 W cm^{-3} at 0.05 mA cm^{-2} current density; also, it exhibits capacitance retention of 80% after 2000 cycles at 0.05 mA cm^{-2} current density with excellent cycling stability.^[102] Ehsani et al. reported an RT electrochemically synthesized novel nanocomposite material, that is, poly ortho aminophenol/Cu-bipy-BTC composite for electrochemical redox capacitors possessing remarkable benefits, like simple method, high surface area, and stability in AE. Here, poly ortho aminophenol (POAP) is used as a polymer to enhance the more active sites for the Faradaic reaction and increase the specific capacitance of Cu-bipy-BTC.^[103] Srinivasan and co-workers prepared Co-MOF/PANI composite from cobalt nitrate, 1,3,5-benzene tricarboxylic acid, and aniline by the in situ chemical oxidative polymerization process. Here, PANI

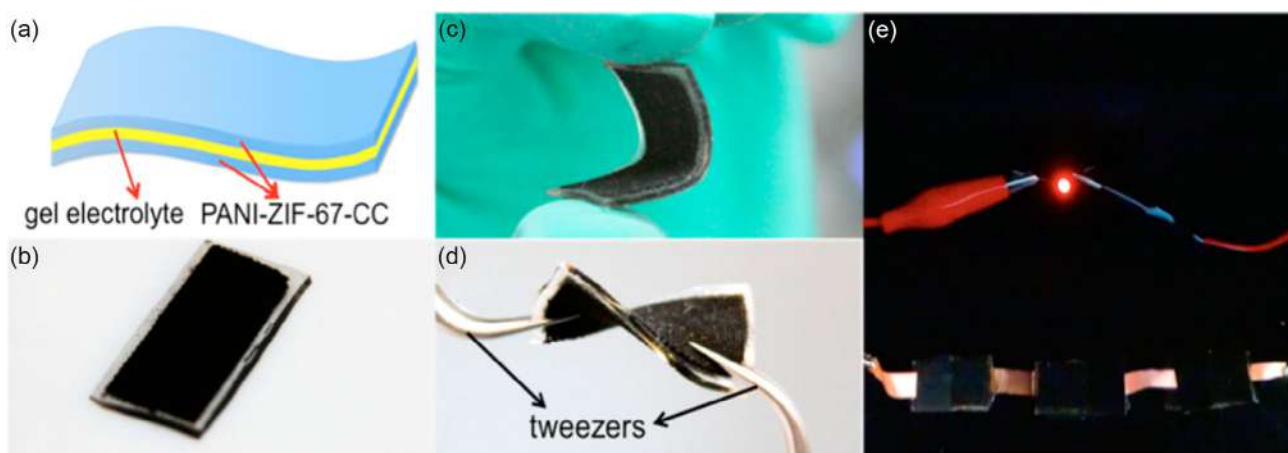


Figure 8. a) Schematic of the PANI-ZIF-67-CC flexible solid-state SC device. b–d) Optical photographs of the fabricated flexible solid-state SC device under b) normal, c) bent, and d) twisted state. e) Photograph of a red LED powered by the three SCs connected in series. Reproduced with permission.^[102] Copyright 2015, American Chemical Society.

is used as a polymer, because it is the cheapest and the most thermally stable intrinsic conductive polymer; it supplies high specific capacitance owing to its unique proton/dedoping technique. Co-MOF/PANI composite shows 504 F g^{-1} specific capacitance at 1 A g^{-1} current density and good cycling stability with the specific capacitance retention of 90% after 5000 cycles at 2 A g^{-1} current density, which reveals that Co-MOF/PANI composite can be utilized as electrode material in energy storage devices.^[104]

3.3. MOF@MOF

Like single MOF, the MOF-on-MOF hybrid is a promising material for energy storage devices. MOF-on-MOF scheme can enhance the composition, like organic linkers and metal ions, and the structural varieties of MOF, like pore, surface properties, and roles.^[105] Many MOF-on-MOF hybrids are established by different strategies, like surfactant-assisted growth, ligand exchange, nucleation kinetic-guided growth, epitaxial growth, and heteroepitaxial growth, with several building designs containing core-satellite, hollow multishell, core-shell, yolk-shell, asymmetric structure, and film on film.^[106,107] The combination of more than two MOFs possessing diverse structures and building blocks by the MOF-on-MOF development method is an exciting strategy for manufacturing hybrid MOFs bearing complex, novel features and ably designed from their composite components and structures. Some MOF-on-MOF composites show excellent features, enhanced conductivity, and better electrochemical performance due to the dual MOFs, while the limitations of single MOFs can be neutralized by making hybrid MOFs.^[108–111]

Deng et al. introduced a new MOF-on-MOF strategy to increase 2D MOFs conductivity and electrochemical performance. They prepared integrated two-layered MOFs, that is, Ni-MOF-24// $\text{Cu}_3(\text{HITP})_2$ (Ni//Cu MOF) array by Ni-MOF-24 as an active unit and $\text{Cu}_3(\text{HITP})_2$ (HITP = 2,3,6,7,10,11-hexamino-triphenylene) used as a conducting MOF to activate near-Ni-MOF-24, which exhibits

a triple high capacitance of 1424 F g^{-1} at a current density 2 A cm^{-2} and outstanding rate capability, in comparison with the pristine Ni-MOF. In addition, they fabricated a hybrid SC that shows a high energy density of 57 Wh kg^{-1} and an extreme power density of $48\,000 \text{ W kg}^{-1}$. The conductive $\text{Cu}_3(\text{HITP})_2$ MOF both extends the intrinsic conductivity for electron transfer and is uniformly scattered in the structure to motivate near Ni^{2+} species in a redox reaction, which increases the specific capacitance, energy density, power density, and rate capability of the hybrid MOF (Figure 9).^[112]

Hu et al. successfully synthesized core-shell ZIF-67@amorphous ZIF material via a facile solvothermal method, which shows a high specific capacitance of 1176.8 F g^{-1} at low current density of 1 A g^{-1} with excellent capacitance retention of 98% after 1000 cycles. Synthesized core-shell ZIF-67@amorphous-based electrodes are promising materials for energy storage devices, revealing a larger specific capacitance and outstanding cycling stability, compared to the individual ZIF-67 and amorphous ZIF. Furthermore, they fabricated an ASC device using ZIF-67@amorphous ZIF as a positive electrode, and AC as a negative electrode. The ASC device exhibits 65.9 F g^{-1} specific capacitance at 0.5 A g^{-1} current density with energy density of 23.4 Wh kg^{-1} at power density of 0.48 W kg^{-1} and 100% capacitance retention after 2000 cycles at 10 A g^{-1} .^[113] Zhang and colleagues prepared core-shell ZIF-L(Zn)@ZIF-67 nanoleaves in an aqueous medium at RT, used as anion templates for hierarchically meso/microporous hybrid carbon materials having graphitic carbon as the shells and amorphous carbon as the cores with nitrogen doping. Their strategy was to synthesize various core-shell designs of ZIFs, and further, they provided a new approach to the preparation of unique core-shell N-C@GC/CNTs with higher capacitance and outstanding stability. The achieved N-C@GC/CNTs materials are used to fabricate SCs from the optimized N-C@GC/CNTs to show the eminent capacitance of 252.1 F g^{-1} with 91.2% capacitance retention after 10 000 cycles, owing to their high nitrogen content, hierarchical pore structure, and better electrical conductivity, arising from the graphitic structure and CNTs.^[114]

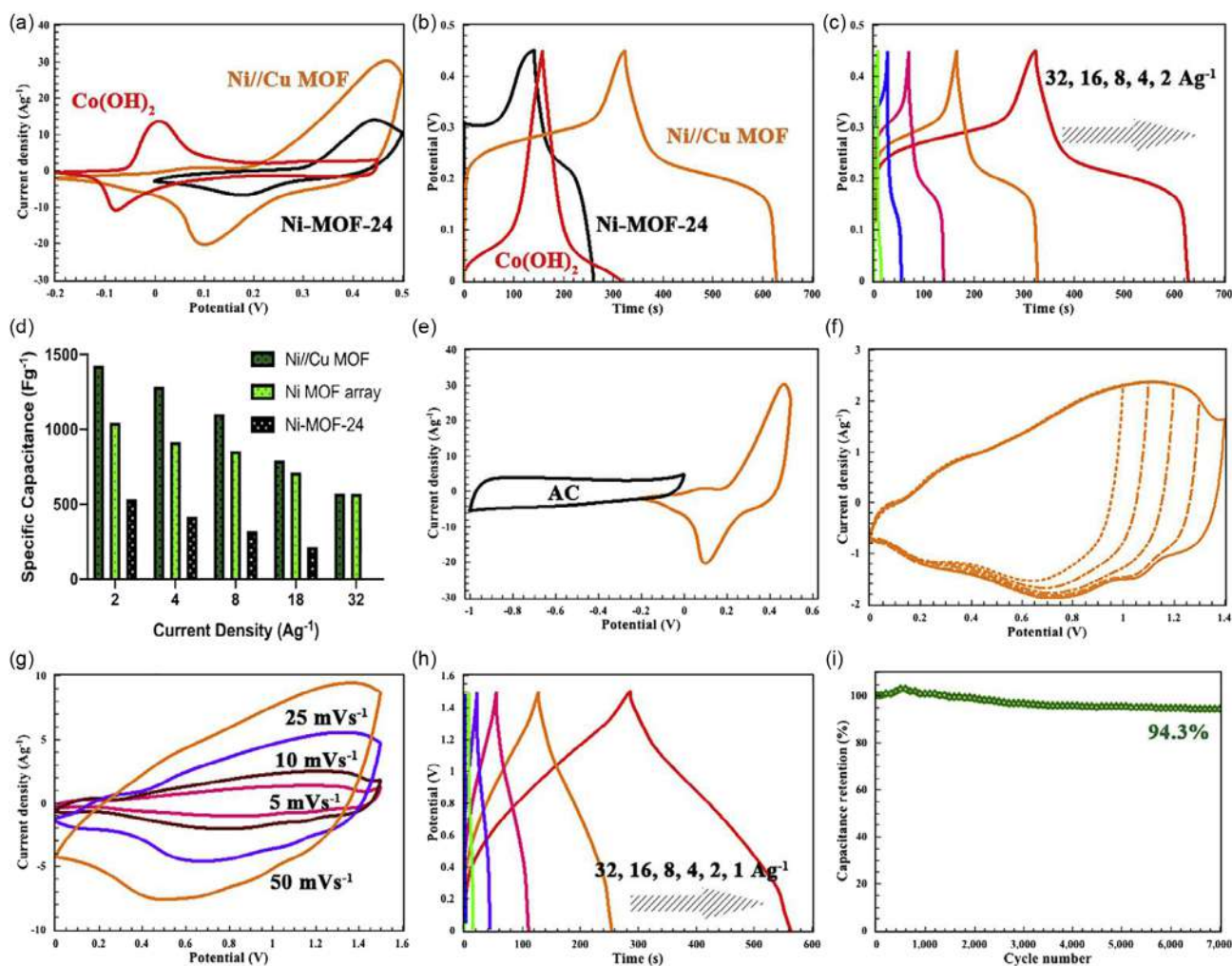


Figure 9. Electrochemical evaluation of Ni//Cu MOF and the corresponding hybrid SC. a) The CV curve of Ni//Cu MOF, Ni-MOF-24, and Co(OH)₂ was collected at 10 mV s⁻¹. b) Galvanostatic profiles of Ni//Cu MOF, Ni-MOF-24, and Co(OH)₂ at the current density of 2 A g⁻¹, and the capacitance can reach 1472, 533, and 688 F g⁻¹, respectively. c) Galvanostatic profiles of Ni//Cu MOF at various current densities. d) The capacitance comparison of Ni//Cu MOF, Ni MOF array, and powder Ni-MOF-24 at all current densities. e) CV curves of Ni//Cu MOF and AC at the scan rate of 10 mV s⁻¹. f) CV curves of hybrid SC with different potential windows. g) CV curves at different scan rates, ranging from 5 to 50 mV s⁻¹. h) Galvanostatic profiles were collected at various current densities. i) The stability test of the capacitor. After 7000 cycles, the capacitance holds 94.3% retention of its initial capacitance. Reproduced with permission.^[112] Copyright 2020, Elsevier.

3.4. MOF@CNT Nanocomposites

Owing to their low conductivity and minor stability, MOFs have limitations in electrochemical energy storage applications. Thus, it is a feasible scheme to incorporate conductive and stable materials with MOFs to design composites.^[115,116] CNT are a superb functional material for MOF composites and are 1D carbon materials with graphene layer structure. CNTs show electrical conductivity, unique pore structure, good thermal/mechanical stabilities, and excellent flexibility.^[117,118] On that account, the MOF@CNTs composites can fulfil the needs of an efficient electrode material for SC applications. However, MOFs@CNT hybrid composites possess large specific area and excellent pore size distribution because of MOFs and better electrical conductivity through highly conducting CNTs.^[119,120]

Zhang et al. introduced a unique necklace-like zeolitic imidazole framework@multiwalled CNTs (ZIF-8@MWCNTs) via a rapid and low-cost electrodeposition method; in addition to carbonization and acid treatment, it gives porous carbon material (C-ZIF-8@MWCNTs) that sustains the necklace-like design with a large surface area of 1063.2 m² g⁻¹. It exhibits large specific capacitance of 259.2 F g⁻¹ at 0.5 A g⁻¹ current density with capacitance retention of 92%, even after 5000 cycles at 15 A g⁻¹ current density. (Figure 10).^[121]

Wang and co-workers constructed flower-string-like NiCo-MOF/MWCNT composites material by a facile solvothermal process where MWCNT is enfolded with 2D NiCo-MOF nanosheets. The optimized NiCo-MOF/MWCNT composite exhibited specific capacitance of 1010 F g⁻¹ at current density of 0.5 A g⁻¹ with good rate capability and excellent cycling stability.

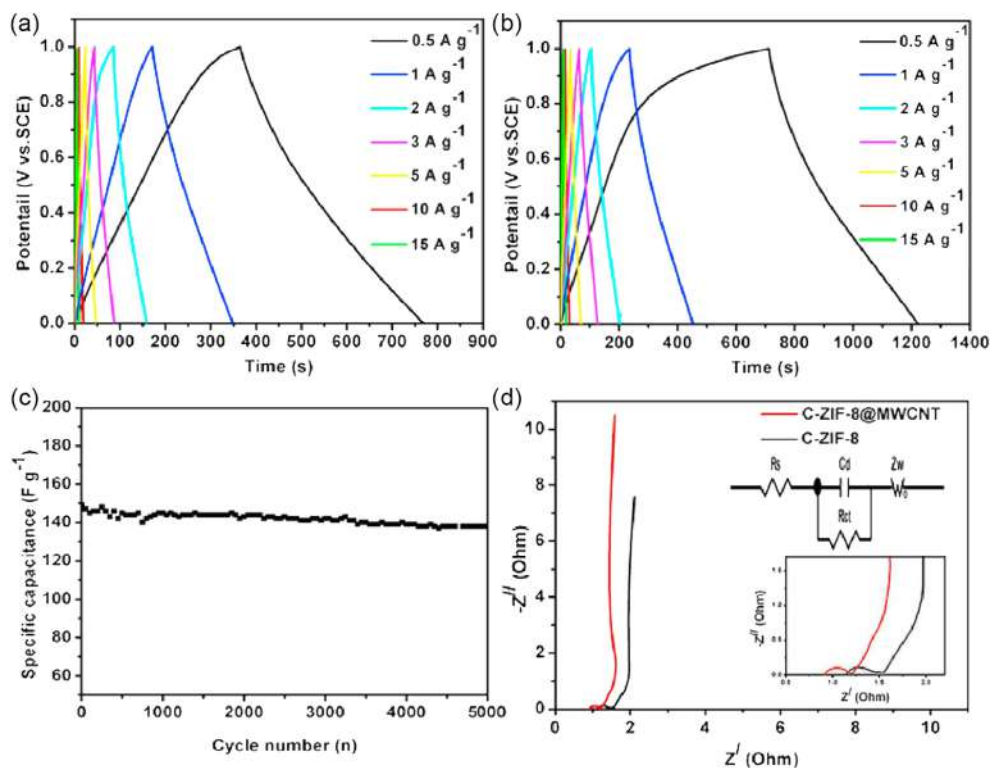


Figure 10. GCD curves at various current densities for a) C-ZIF-8, b) C-ZIF-8@MWCNTs, c) cyclic stability at 15 A g^{-1} for C-ZIF-8@MWCNTs, and d) EIS results for C-ZIF-8 and C-ZIF-8@MWCNTs (magnified Nyquist plots of C-ZIF-8 and C-ZIF-8@MWCNTs). Reproduced with permission.^[121] Copyright 2020, Elsevier.

Using NiCo-MOF/MWCNT composite as an electrode material, they assembled an ASC that reveals large energy density at high power density, outstanding rate capability, great cycling stability, and reversibility.^[122] Wen et al. prepared nickel metal-organic frameworks/CNTs (Ni-MOF/CNTs) composites via a simple solvothermal method, which exhibits outstanding electrochemical performance (i.e., 1765 F g^{-1} specific capacitance at 0.5 A g^{-1} current density) because of the synergistic effects of the Ni-MOF specific design and high conductivity from CNTs. Further, they assembled an ASC utilizing Ni-MOF/CNTs as a positive electrode and reduced graphene oxides/graphitic carbon nitride (rGO/g- C_3N_4) as a negative electrode, which reveals excellent energy density of 36.6 Wh kg^{-1} at power density of 480 W kg^{-1} with capacitance retention of 95%, even after 5000 cycles. Hence, it is a most promising material for future high-energy storage devices.^[123] Wang et al. proposed a simple one-step solvothermal approach to construct core-shell-structured flower-like composite MWCNTs@Ni(TA) by incorporating MWCNTs into Ni(TA), by which the surface area and the electroactivity of the composite were immensely enhanced. This reveals a specific capacitance of 115 mAh g^{-1} at 2 A g^{-1} current density and excellent cycling stability with capacitance retention of 81.6%, even after 5000 cycles at 10 A g^{-1} current density.^[124]

3.5. MOF@Graphene Nanocomposites

Individual MOFs exhibit restricted performance owing to their intrinsic weaker features, like electrical conductivity, electroactivity, and stability. Hence, multielement systems combine

MOFs with different materials, such as graphene, carbon black, and CNT. From these, graphene or reduced graphene oxide has emerged as a unique conducting additive for energy storage applications, due to its large electrical conductivity and exceptional mechanical strength arising from its 2D carbon structure.^[125,126]

Azadfalsh et al. prepared novel hierarchical flower-like copper metal-organic frameworks/graphene composite by a facile and low-cost one-step solvothermal method. The composite shows excellent electrochemical performance due to the synergistic effects of Cu-MOF design and the large conductivity of graphene. It shows a high specific capacitance of 482 F g^{-1} at a scan rate of 10 mV s^{-1} and exhibits outstanding cycling stability with specific capacitance retention of 93.8%, even after 1000 cycles at 0.3 A g^{-1} current density in 6 M KOH . Additionally, they demonstrated an ASC that reveals a high energy density of 34.5 Wh kg^{-1} and power density of 1350 W kg^{-1} at 0.5 A g^{-1} current density. Electrochemical investigation revealed that the Cu-MOF/G nanocomposite is a promising electrode for high-performance energy storage materials.^[127] Sundriyal et al. prepared Ni-doped ZIF-67/rGO composite by an easy one-pot stirring procedure, which possesses high porosity, high surface area, and enhanced electrical conductivity. To achieve beneficial redox activity and electrical conductivity, the doping percentage of Ni is 33%, and the 20% of reduced graphene oxide (wt%) in the composite material is optimized, which delivers high specific capacitance of 304 F g^{-1} at a current density of 1 A g^{-1} in $1 \text{ M H}_2\text{SO}_4$.

Furthermore, they prepared a solid-state symmetric SC that exhibits high energy density of 21.5 Wh kg^{-1} at 1 kW kg^{-1} power density with capacitance retention of 87%, even after 4500 cycles.^[128] Hong et al. synthesized Ni-Co-MOF/GO composite by directly developing dual metal centers metal-organic framework on graphene oxide sheets using a one-pot solvothermal method, by optimizing the quantity of graphene oxide 3D chestnut-shaped nanostructures that were obtained. Ni-Co-MOF/GO-2 (quantity of graphene oxide, 0.2 g) yields a maximum specific capacitance of 447.2 F g^{-1} at 1 A g^{-1} current density with excellent cycling stability of 99.6%, even after 300 cycles. The synthesized Ni-Co-MOF/GO composite is a beneficial material for high-performance SC electrode materials due to its novel mechanical strength, large surface area, controllable porous structure, good charge transfer route, and a stable interface between the electrolyte and electrodes.^[129] Sundriyal et al. prepared a highly porous ZIF-67/rGO composite by an easy stirring, acid-free, and environment-friendly process, which shows a large specific surface area (e.g., $947 \text{ m}^2 \text{ g}^{-1}$) and excellent electrochemical performance in the presence of redox additive electrolytes (RAEs). ZIF-67/rGO composite delivers a high specific capacitance of 1453 F g^{-1} at the current density of 4.5 A g^{-1} with outstanding cycling stability of 90.5%, even after 1000 cycles; the use of RAE is to increase the electrochemical performance. In addition, they fabricated a symmetric SC that possesses an energy density of 25.5 Wh kg^{-1} at a power density of 2.7 kW kg^{-1} with a capacitance retention of 88.8%, even after 1000 cycles.^[130]

3.6. MOF@Metal

Metal-doped MOFs are a unique strategy to increase the electrochemical performance of the individual MOFs, as they can supply the benefits of the doping metal material, such as better conductivity, good redox centers, and structural stability. Utilizing this concept, Li et al. constructed Mo-doped Ni-MOF nanosheets (M-NMN) via a one-pot hydrothermal method, from which M-NMN-1 composite (Ni: Mo = 1:1) shows excellent performance, compared to the different quantity of materials. M-NMN-1 electrode yields high specific capacity of 802 C g^{-1} at current density of 1 A g^{-1} with capacitance retention of 96%, even after 20 000 cycles. The metal Mo doping enlarged the potential window and enhanced the conductivity and stability of materials. Also, they constructed a battery-SC hybrid device (M-NMN-1//AC) that reveals outstanding energy density of 59 Wh kg^{-1} at power density of 802 W kg^{-1} with excellent capacitance retention of 93%, even after 20 000 cycles.^[131] For the first time, Yang et al. designed Zn-doped Ni-MOFs composite material with a flower-like microsphere; it exhibits charge transfer resistances that express a faster electron transfer rate. It shows high specific capacitances of 1620 and 854 F g^{-1} at current density of 0.25 and 10 A g^{-1} , respectively, with capacitance retention of 91%, even after 3000 cycles. Zn-doped Ni-MOFs composite material is used as electrode material for SCs due to its layered design with extended interlayer gap, high specific capacitance, high rate capability, outstanding cycling stability, and flower-like microsphere morphology.^[79] Zheng and colleagues constructed an Mn-doped ultrathin Ni-MOF nanosheet array on nickel foam ($\text{Mn}_{0.1}\text{-Ni-MOF/NF}$) from manganese nickel layered double

hydroxide (MnNi-LDH/NF) by a solvothermal method. The $\text{Mn}_{0.1}\text{-Ni-MOF/NF}$ reveals ultrahigh areal capacity of 6.48 and 4.72 C cm^{-2} (C: (1178 and 858) C g^{-1}) at current densities of 2 and 20 mA cm^{-2} , respectively, with capacitance retention of 80.6%, even after 5000 cycles in 6 M KOH. Furthermore, they assembled an ASC device ($\text{Mn}_{0.1}\text{-Ni-MOF/NF//AC}$) that delivers high energy density of 39.6 Wh kg^{-1} at a power density of 143.8 W kg^{-1} with capacitance retention of 83.6%, even after 5000 cycles. Hence, $\text{Mn}_{0.1}\text{-Ni-MOF/NF}$ contributes to a highly stable and capacitive SC positive electrode.^[132] Wang et al. designed a nickel-functionalized copper MOF (Ni@Cu-MOF) via a facile volatilization process, followed by a post-modification synthesis method at RT. This shows higher specific capacitance of 526 F g^{-1} at current density of 1 A g^{-1} , compared to the monometallic Cu-MOF, that is, 126 F g^{-1} , and also exhibits good cycling stability with specific capacitance retention of 80% after 1200 cycles. Also, they fabricated an ASC device (Ni@Cu-MOF //AC) that yielded a specific capacitance value of 48.7 F g^{-1} at current density of 1 A g^{-1} with high energy density of 17.3 Wh kg^{-1} at power density of 798.5 W kg^{-1} . Therefore, the outcomes reveal that bimetallic MOFs are favorable candidates for SCs.^[133]

3.7. MOF@QD

Quantum dots are 0D semiconductor nanocrystals of (2–10) nm in size. Due to their novel tunable and size-dependent electronic features, quantum dots have been utilized in many applications. Xue et al. extended their implementation by using them with MOF as a functional material to form MOF@QD composite.^[134] MOF@QD composite can be prepared by one-pot synthesis, the double solvent method, and the solvothermal method by directly incorporating presynthesized QDs in MOFs.

Gao and co-workers prepared SnO_2 quantum dots@ZIF-8 using a facile in situ epoxide precipitation approach; this shows good pseudocapacitive performance due to its synergistic effect of ZIF-8 and SnO_2 quantum dots. Due to the porous structure of ZIF-8, it easily incorporates SnO_2 quantum dots to accelerate the usage of active material, leading to high specific capacitance. It exhibits the highest specific capacitance of 931 F g^{-1} at scan rate of 5 mV s^{-1} , which is much higher than that of SnO_2 quantum dots and ZIF-8, with outstanding cycling stability over 500 cycles. The synthesized SnO_2 quantum dots@ZIF-8 composite material shows good electrochemical performance in 6 M KOH; hence, it is used as electrode material in SC devices (Figure 11).^[135]

Li et al. synthesized SnO_x quantum dots@Zr-MOFs (UIO-66) composites by a unique technique that blends the dehydration of inorganic group in metal-organic frameworks with water-free sol-gel chemistry, followed by a pyrolysis method to yield SnO_x quantum dots@Zr-MOFs (UIO-66) composites with remarkable properties, like high thermal stability (upto 773 K), a highly porous structure, and excellent electrochemical stability of UIO-66. After 100 cycles, it still shows a specific capacity of 994 mAh g^{-1} at current density of 50 mA g^{-1} . This approach is appropriate, low cost, and time-saving, with increased specific capacity, outstanding rate capability, and excellent cycling stability, leading to a promising anode material in LIBs.^[136] Yu et al. manufactured C@GQD composite via a successful in situ self-assembly method by blending MOF (ZIF-8) and graphene

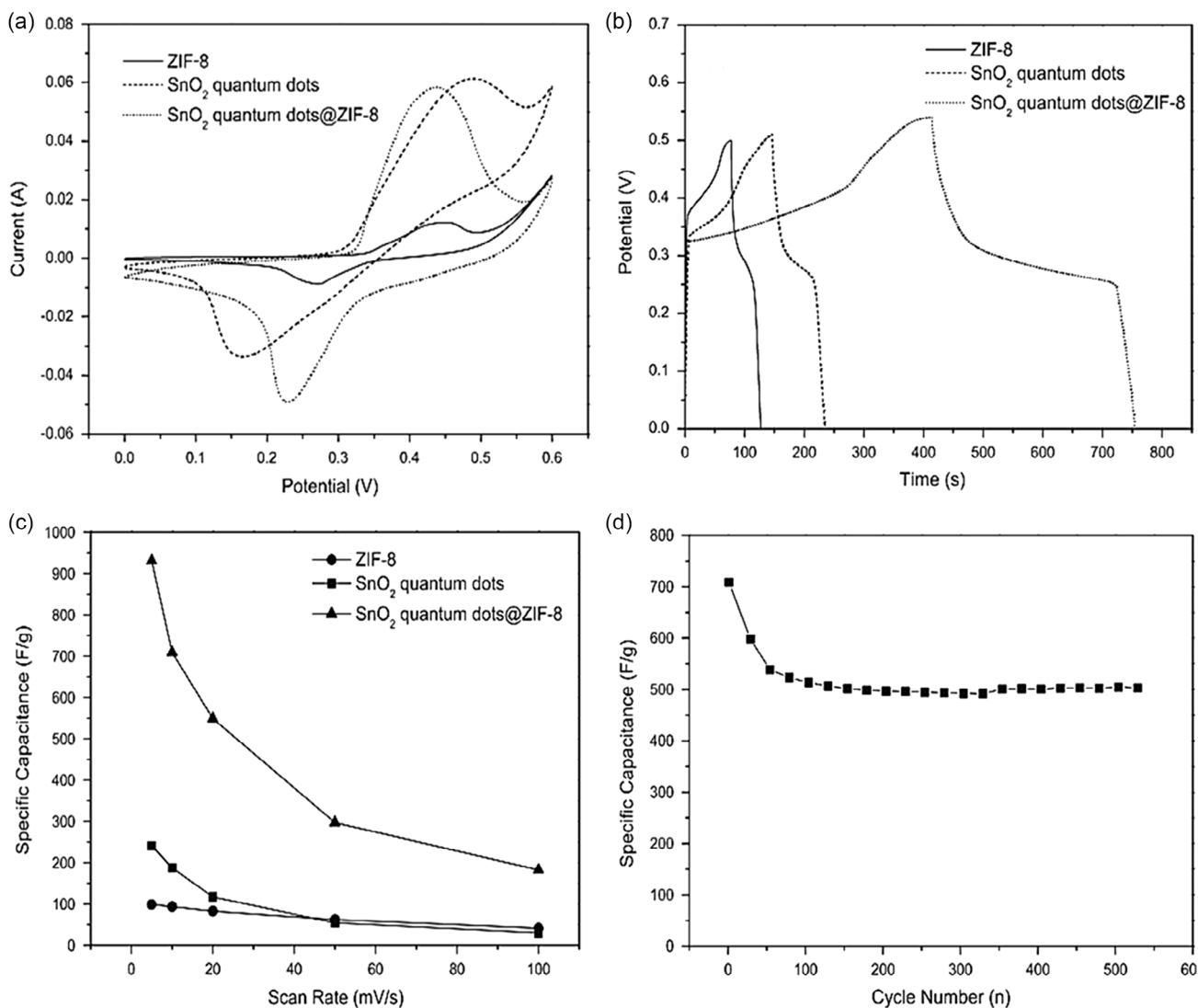


Figure 11. a) CV curves of different samples at a scan rate of 5 mV s⁻¹. b) CP curves of different samples at a current density of 5 mA cm⁻². c) The specific capacitance as a function of the scan rate of different samples. d) Cycling performance of SnO₂ quantum dots@ZIF-8 at scan rate of 10 mV s⁻¹. Reproduced with permission.^[135] Copyright 2014, Elsevier.

quantum dots, followed by high-temperature calcination and etching to obtain a novel class of porous carbonaceous material. The C@GQD composite possesses many micro- and mesopores with high specific surface area of 668 m² g⁻¹. In addition, it is used as a SC electrode material to show outstanding double-layer capacitance and specific capacitance retention of 130 F g⁻¹ at current density of 2 A g⁻¹ with long-term cycling stability, even after 10 000 cycles.^[137]

Concisely, pristine MOFs have been restricted by their weak electrical conductivity and small micropores. As a result, there are synergistic effects and unique potentialities that cannot be realized by separate pieces. The advantages of MOFs and other kinds of functional materials may be successfully integrated in MOF composites, and the production of MOF-based composites will become easy. In order to counteract the drawbacks of individual components, MOF composites, in which MOFs are mixed

with a range of functional materials, have been developed. MOF composite materials may be employed directly as outstanding materials for development of energy storage devices.

4. Designing Electrolyte Selection by Metal–Organic Frameworks and Their Composites for SC Application

An electrolyte is an ionic conductor, although an electronic insulator; it is either a solid or, more frequently, a liquid that generally works with a sponge-like layer or gel in electrochemical energy storage devices. Electrolytes are essential and significant components in SCs. Due to their physical and chemical properties, they play a vital role in electrochemical performances, such as specific capacity, energy density, power density, rate performance,

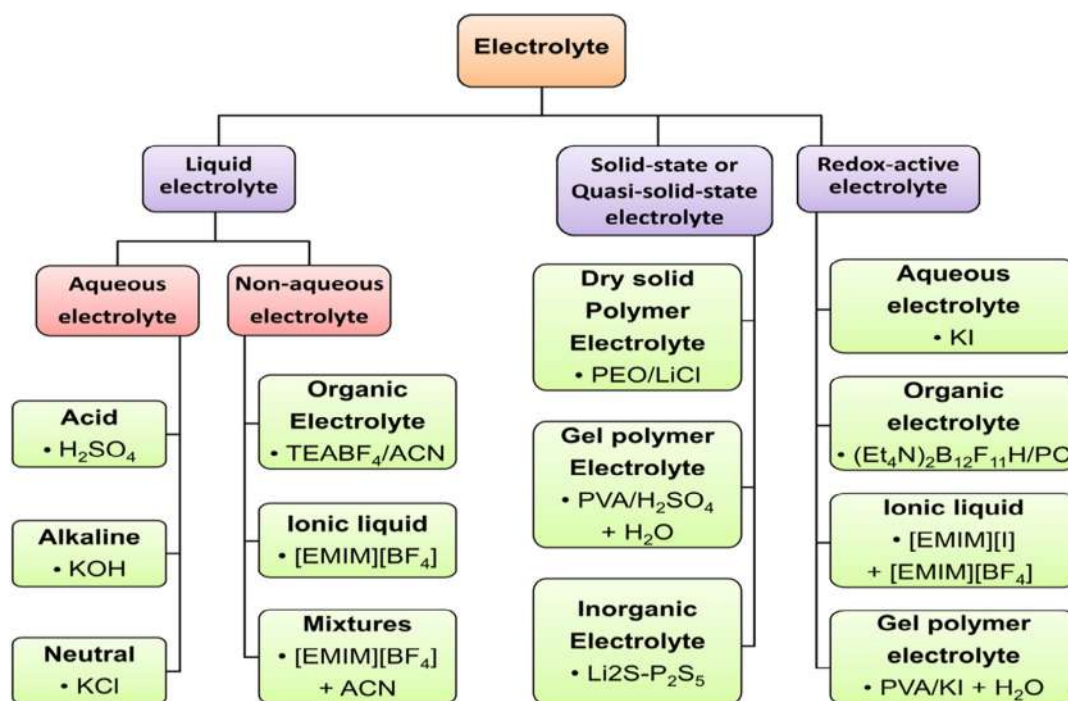


Figure 12. Classification of electrolytes used in SCs.

cycling stability, and safety.^[138,139] The necessities for an ideal electrolyte are broad potential window, high ionic conductivity, extended operating temperature range, high chemical and electrochemical stability, large chemical and electrochemical inertness to SC constituents (e.g., electrodes, current collectors, and packaging), convenience with electrode materials, low volatility and flammability, ecofriendliness, and inexpensiveness. In all honesty, it is challenging for an electrolyte to fulfill all of these necessities; also, each possesses its advantages and limitations.^[140–143]

The selection of electrolytes is vital to safe and high-performance SCs.^[144] Concerning electrochemical SC electrolytes, various electrolytes used in the SCs that have been studied are AEs, organic electrolytes (OEs), ionic liquid electrolytes (ILEs), redox-active electrolytes (RAEs), and solid-state or quasi-solid-state electrolytes.^[145,146] Ionic conductivity and mobility, dielectric constant, thermal stability, electrochemical stability, and dispersion interaction are the principal components to estimate the performance of electrolytes. The thermal stability of SCs is based on the electrolyte's interaction with an electrode and the thermal stability of the electrolyte itself. Hence, the thermal stability of an electrolyte is resolved mainly by its proportions, like salt, solvent, and additive.^[143] The safety and lifecycle of SCs depend on electrochemical stability, and electrochemical stability is based on the elements of the electrolyte and the affinity of the electrolyte to the electrode material. Equivalent series resistance (ESR) is the sum of different resistances containing intrinsic resistance of the electrode material and electrolyte, mass transfer resistance of the particle, and junction resistance between the electrode material and the current collector. ESR is a vital variable for calculating the power density of SCs; as

the ESR value increases, the power density decreases (**Figure 12**).^[147,148]

4.1. AEs

Because of their low cost, and simple handling in the laboratory compared to other electrolytes, AEs have been broadly applied in research and development. AEs acquire higher ionic concentrations, low resistance, smaller ionic radius, higher capacitance, and higher conductivity than ionic and OEs, which are advantageous for lowering the same series resistance and producing greater power density SCs.^[126] Altogether, AEs can be subdivided into acid, alkaline, and neutral AEs, in which H₂SO₄, KOH, and Na₂SO₄ are examples, they are the most used electrolytes.^[147,149]

The choosing criteria for AEs mainly consider the particle size of material, hydrated cations and anions, and the mobility of ions, which influence ionic conductivity and specific capacity. Survey shows that those neutral electrolytes have a wider range of potential windows than acid and alkaline electrolytes.^[150,151] Regarding MOFs and their composite materials, AEs are widely used, such as H₂SO₄, KCl, KOH, LiOH, NaOH, and Na₂SO₄. Some examples of analogous SCs were earlier reviewed in the previous parts. Below we go over a few selected examples.^[152] Metal oxide@MOF composite (Co₃O₄@Co-MOF)-based electrode was investigated in the presence of 3 M KOH. Synthesized composite material exhibits extraordinary alkaline stability, which sustains its original structure in 3 M KOH for a minimum of 15 days; it shows high cycling stability after 5000 cycles, with only 3.3% decay at 5 A g⁻¹ current density.^[95] Neutral AEs, such as KCl, Na₂SO₄, and LiCl, are primarily used in different concentrations. Due to the broad potential window with less

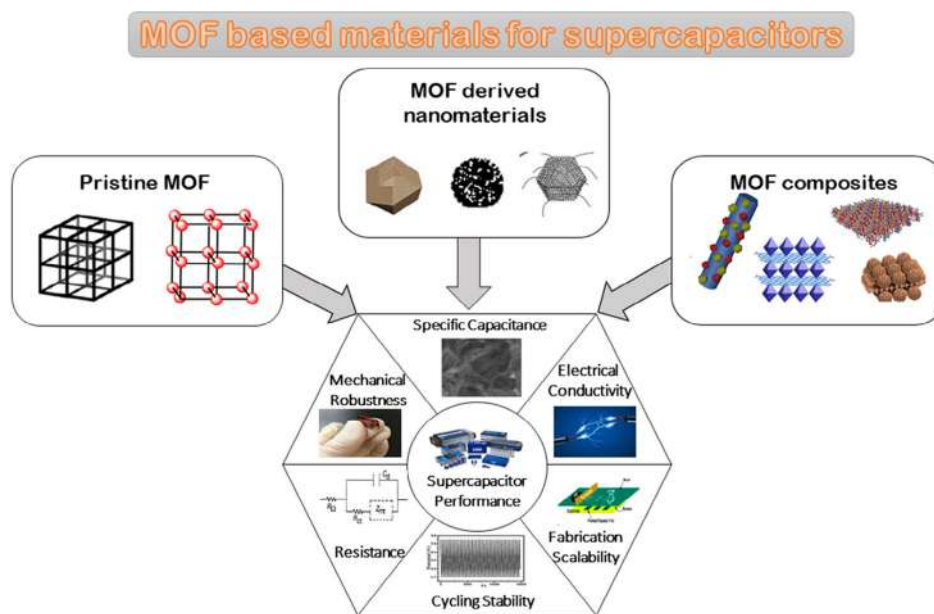


Figure 13. Schematic of MOF-based materials as electrode materials for SCs. Pristine MOF icon reproduced with permission.^[190] Copyright 2020, MDPI. MOF-derived nanomaterials icon reproduced with permission.^[191] Copyright 2017, Wiley. MOF composites icon reproduced with permission.^[191] Copyright 2017, Wiley and reproduced with permission.^[192] Copyright 2018, Wiley. Supercapacitor performance icon reproduced with permission.^[193] Copyright 2017, Royal Society of Chemistry and reproduced with permission.^[194] Copyright 2019, De Gruyter.

corrosive character, neutral AEs are safely used. Wang et al. proposed the application of 3 M KCl during their investigations of an electrode made of a ZIF-67/PANI composite that exhibits a specific capacitance of 371 F g^{-1} at a scan rate of 10 mV s^{-1} .^[102] H_2SO_4 is the most frequently used acid electrolyte for aqueous-based electrochemical SCs in MOF-based electrodes out of several acidic electrolytes, mainly because of its outstanding ionic conductivity.^[79,127] H_2SO_4 electrolytes show lower ESR value than neutral electrolytes, giving high specific capacitance and high conductivity. Bao et al. proposed the application of 1 M H_2SO_4 through their investigations of an rGO/Zn-MOF@PANI electrode, which reveals specific capacitance of 371.91 F g^{-1} at current density of 0.1 A g^{-1} .^[153]

To summarize, several factors of AEs significantly affect the electrochemical performance of SCs, like salt concentration, types of cationic and anionic species, hydrated ion size, specific conductance, and conductivity. Among AEs, neutral AEs are widely used because of their low cost, low corrosive action, and ecofriendliness, leading to a wide potential window, high specific capacity, and energy density. However, more development in the electrochemical performance of SCs with AEs is still required to enhance the energy density and cycling stability of SCs.

4.2. Organic Electrolytes (OEs)

OEs of acetonitrile, propylene carbonate (PC), diethylene carbonate, quaternary ammonium salts like tetraethyl ammonium tetrafluoroborate (TEABF_4), tetrahydrofuran (THF), and lithium hexafluoro phosphate (LiPF_6) are used in SCs to overcome the limitation of the confined potential window examined of AEs. OEs generally include conducting salts dissolved in organic

solvents for SC devices. Tetraethyl ammonium tetrafluoroborate (TEABF_4) is the most frequently used conducting salt for electrolytes in SCs.^[154] In addition to TEABF_4 , different salts have been evolved to enhance many properties of electrolytes, like solubility, conductivity, stability, and temperature performance. Several types of OEs have extraordinary applications in economic SCs, and also, they can supply a wide potential window with enhanced energy and power densities.

The potential window is an important property of the OE, which determines the electrochemical performance of SCs, like cell voltage, energy, and power densities. The potential window of the OEs depends on many aspects, like solvent, conducting salts like cation and anion, and impurities, such as a trace amount of water.^[155] Salunkhe et al. synthesized a high-performance SC made up of NPC material derived from ZIF-8; they investigated the electrochemical performance in OEs, that is, 2 M $\text{NEt}_4\text{BF}_4/\text{PC}$. The system shows a broad operating potential window of 2.4 V, revealing a specific capacitance of 20.6 F g^{-1} with very high surface area of $1873 \text{ m}^2 \text{ g}^{-1}$.^[156] Ghosh's group reported new materials, that is, lanthanide MOFs (MOF-Ce, MOF-Pr, and MOF-Nd), and investigated their electrochemical behavior in 1 M TEABF_4 in acetonitrile as an electrolyte within a potential window of 0.0–0.8 V for SC application. Among the three MOFs, MOF-Ce shows a maximum specific capacitance of 572 F g^{-1} at current density of 1 A g^{-1} with capacitance retention of 81%, even after 5000 cycles.^[157] Choi et al. reported a series of graphene-doped nMOFs and investigated the electrochemical performance in an OE, that is, 1 M $(\text{C}_2\text{H}_5)_4\text{NBF}_4$ in acetonitrile. This delivers high capacitance of 726 F g^{-1} at current density of 6.95 mA g^{-1} .^[158]

OEs have low conductivity, which leads to a higher ESR value that restricts the power density. Another limitation of OEs is the

higher resistivity than AEs, because of their large molecules, which need a large pore size in the electrodes. Compared to AEs, OEs are costly, and precautions should be taken because of their flammability, volatility, and toxicity, showing smaller specific capacity and lower ionic conductivity. In addition, OEs need intricate purification, and manufacturing procedures are restricted to controlled conditions to remove unused impurities (e.g., water), which show high-performance degradation and self-discharge problems.^[147]

4.3. Solid-State Electrolytes (SEs)

SEs offer more benefits than other electrolytes, such as simple packaging and fabrication processes, good ionic conducting media, and freedom from liquid leakage. The SEs are used as the ionic conducting media and a separator between electrodes. SEs progressed for energy storage devices like SCs depending on polymer electrolytes. The polymer-based SEs are further divided into three subtypes: the solid polymer electrolyte (SPEs, also named dry polymer electrolytes), the gel polymer electrolyte (GPE, due to the presence of liquid media, it is also called quasi-SE), and the polyelectrolyte.^[159,160]

Due to their advantages, like simple packaging and manufacturing process, good electrochemical stability, freedom from liquid leakage, and corrosion problem, SPEs and GPEs have mainly been used in electrolytes other than liquid electrolytes. However, SPEs have limitations in flexible devices, due to their low conductivity and poor elastic or flexible properties.^[161] SPEs are made up of dissolving the salt of alkali metals of type MX (M = Na, Li, Ag, Cu, etc. and X = F, Cl, I, and Br) in polymers like polyethylene oxide and polypropylene oxide.^[162] GPEs include conducting salt dissolved in solvent or composed of polymer (e.g., PEO, PEG, PVA, etc.) with AE (e.g., KOH, H₂SO₄, or K₂SO₄).^[163] Due to its properties, like higher ionic conductivity, high porosity, and outstanding mechanical properties through the freeze-thawing process, PVA has been widely used for hydrogel polymer electrolytes.^[164] In practical applications of energy storage devices, such as EDLCs, GPEs have received immense attention compared to other liquid electrolytes, due to disadvantages, like poor safety, liquid leakage, and strict geometry. However, compared to other liquid electrolytes, EDLCs investigated using GPEs possess lower specific capacity, low ionic mobility, and a poor electrode/electrolyte interface contact.^[165,166]

Currently, MOFs have revealed potential for the construction of high-performance SEs due to their porous crystalline inorganic-organic materials, which have grown into an exciting research area. MOFs provide great scope for manipulating the physicochemical and electrochemical features of SEs and supply perfect platforms to investigate the underlying mechanisms of ion conduction and the structure-property techniques.^[167] Wang et al. constructed flexible solid-state micro-SCs (MSCs) using induced graphene as flexible electrode materials and the multilayer film of ZIF-67 and PANI as substrates. The performance of a multilayer-modified LIG-PANI-ZIF-67 electrode in combination with PVA/H₂SO₄, which functioned as a polymer gel electrolyte, was investigated. The fabricated device shows specific capacitance of 719.2 mF cm⁻² at current density of 0.5 mA cm⁻² with capacitance retention of 87.6%, even after 6000 cycles.^[168] Similarly, Shao et al. used PVA/H₂SO₄ gel electrolyte in a SC

whose electrode was fabricated from a PANI/UiO-66 composite material. The device yielded specific capacitance of 647 F g⁻¹ at current density of 1 A g⁻¹ with capacitance retention of 91% after 5000 cycles.^[169]

Overall, among all these three types, GPEs have the highest ionic conductivity, due to the liquid phase. Because of their high ionic conductivity, GPEs are recently commanding SE-based SC devices, and due to this, the use of SPEs is restricted. However, owing to the presence of water and comparatively low mechanical strength, GPEs suffer from a narrow operative temperature range.

4.4. Ionic Liquid Electrolytes (ILEs)

Ionic liquids are unique new types of solvents and materials with special properties and have attracted immense attention in energy storage devices like SCs.^[170] They comprise bulky organic cations and inorganic or charged localized anions with beneficial properties like negligible volatility, low flammability, wide liquid temperature range, high ionized condition, and broad potential windows, compared to aqueous and OEs.^[171,172] Due to their advantageous properties, ionic liquids are safe alternatives to recent OEs. Hence, ionic liquids are an excellent substitute for conventional electrolytes for SCs and have attracted significant attention.^[173] Aprotic pyrrolidinium and imidazolium-based quaternary ammonium salts are commonly used ionic liquids as potential electrolytes for SC application.^[172]

Recently, ionic liquids have been used as solvents for MOF synthesis (ionothermal synthesis), providing multiple reaction conditions, due to their designable and tunable features. As compared to solvothermal synthesis, ionothermal synthesis for MOFs has many advantages. The ionic liquid both acts as a solvent and acts as a structure-directing agent. Additionally, an ionic liquid used as a solvent for MOF synthesis has attractive properties, like simultaneously dissolving organic and inorganic starting materials, greatly low volatility, and high thermal and chemical stability.^[174]

The design of MOF-based SCs using ILEs has not been sufficiently studied to date. Zhang et al. skilfully encapsulated ILs into polyoxometalate-based MOFs (POMOFs), to fabricate a series of conductivity-improved POMs-ILs@MOFs. Exclusively, the PMo₁₀V₂-ILs@MIL-100 achieved a noticeable capacity of 1248 mAh g⁻¹, even after 100 cycles. In addition, the charge capacity of PMo₁₀V₂-ILs@MIL-100 reduces slightly at 1032.8, 929.2, 774.7, 633.6, 503.8, and 347.5 mAh g⁻¹ with increased current density at 0.1, 0.2, 0.5, 1, 2, and 3 A g⁻¹ respectively.^[175] Similarly, Fujie et al. developed ionic liquid-based lithium electrolytes that are infused in the micropores of ZIF-8, a Zn-based MOF, to produce ionic conductors.^[176] Nowadays, high-performance energy storage devices are in need; SCs using ionic liquid-based electrolytes are slowly competing with other energy storage devices.

4.5. Redox-Active Electrolytes (RAEs)

A novel strategy has been developed to enhance the capacitance of SCs by influencing the pseudo capacitive supplement from the RAEs. RAEs are special electrolytes to which redox-active

materials have been added. This can significantly enhance the electrochemical performance of SCs for two reasons: first, the electrolyte additive is a vital part of the redox reactions of the SCs, and second, the electron transfer that occurs between the electrode material and the redox material in the electrolyte is due to the redox reactions in the electrolyte, which are conductive.^[177] The RAEs are made up of the addition of concentration of redox-active materials, like hydroquinone and halide ions, and $K_3[Fe(CN)_6]$ in commonly used AEs, like H_2SO_4 , Na_2SO_4 , and KOH. The RAEs encourage faster kinetics of redox reactions at the electrode surface, due to the presence of the redox-active materials.^[165,178]

Akinwolemiwa et al. reported the use of a redox additive (1 M Na_2SO_4 and 0.2 M $K_3[Fe(CN)_6]$) in conjunction with two of the same electrodes made up of a composite of ZIF-67/rGO.^[178] Ultrahigh specific capacitance of $326 F g^{-1}$ at current density of $3 A g^{-1}$ was achieved, and high energy density of $25.5 Wh kg^{-1}$ at power density of $2.7 kW kg^{-1}$.^[130] Similarly, Sundriyal et al. used 0.2 M $K_3[Fe(CN)_6]$ in 1 M Na_2SO_4 as a redox-active additive electrolyte in an SC whose electrode was assembled from an Mn-MOF. The device revealed high specific capacitance of $1590 F g^{-1}$ at current density of $3 A g^{-1}$ with capacitance retention of 82%, even after 3000 cycles.^[179] A RAE provides a wider potential window in SC applications than does AE. Likewise, several redox-active species or materials have still not been used as redox additives in electrolytes for SC applications.

As the data presented in this section shows, different electrolytes are being utilized to improve SCs; choosing a suitable electrolyte depends upon the needed performance and practical applications of electrochemical SCs by controlling the factors, like the ionic conductivity, ion mobility, operating voltage window, operating temperature range, and electrochemical and thermal stabilities of the electrolytes.^[180]

5. Performance Appraisal of MOF-Derived Electrodes in SCs

With increasing global and environmental concerns, plentiful work has been done to advance alternative energy technologies. In recent years, a widening interest in affordable, efficient, renewable, sustainable, and environment-friendly energy storage devices has been highly recognized. A SC is a renewable electrochemical energy storage device with high energy and power density, fast charge and recharge capability, and rate efficiency, due to its exceptional reaction mechanism.^[181,182] The evolution of MOF-based materials used as SCs in new, leading energy storage devices has attracted rapidly evolving importance, due to their adjustable pore size, controllable microporous structure, and large surface area. MOF materials are used for supercapacitive applications in three different ways, as the prepared MOFs material are used directly as an energetic electrode material for SCs.^[47–51] MOFs are used as a template to synthesize metal oxides.^[56–61] and porous carbon compounds^[70–75] for SCs. Finally, MOFs are hybridized using different functional materials to form MOF composites for SCs (Figure 13).^[183]

Table 2 summarizes several parameters of MOFs and their derived nanostructured electrodes, such as electrical density, energy density, specific capacitance, and life cycle, to compare

their electrochemical performance. However, the direct application of pristine MOFs as electrodes may not provide good electrical conductivity. The migration of electrons and ions is easy with high specific surface area and uniform pore size distribution of MOFs. If such MOFs are combined with AEs (e.g., H_2SO_4 and KOH), they could attain high specific capacitance of about (200–2800) $F g^{-1}$. Unlike the pristine MOFs, their derived structures (metal oxides and NPC) show remarkable electrical conductivity, while high specific surfaces can also be maintained.^[184] MOFs like Mn/Ni-MOFs, UPC-9, MOF-74, ZIF-8, and ZIF-67 are successfully converted into functional metal oxides, while NPC electrodes of AEs looks to be a more preferable choice than other kinds of electrolytes.

Similarly, Table 3 shows that MOFs may be conjugated with CPs, metal oxides/hydroxides, CNTs, graphene oxide (GO), and quantum dots (QD) for SC applications.^[185] In such a way, the resultant composites provide large surface areas, high chemical and thermal stabilities, notable specific capacitance, energy densities, and cyclic stability.^[186,187] MOFs (e.g., UIO-66, ZIF-67, Co-MOF, and Zn-MOF) have been interlinked with CPs (e.g., CT, PPy, PANI, and POAP), to integrate their discrete pseudocapacitive properties. As a result, MOF@CPs composite provides rapid kinetics between oxidation and reduction to give specific capacitances of about 200–550 $F g^{-1}$. Nevertheless, cyclic stability was sometimes inadequate, due to their participation in the Faradaic reactions.^[188] Hence, further research is required to optimize the specific capacitance and cyclic stability of the MOF@CP-based SCs. Likewise, MOFs and their derivatives (e.g., Ni-MOF, Co-MOF, and MHCF, ZIF-67) are also used to fabricate metal MOF@metal oxide/hydroxides, MOF@MOF, and MOF@metal electrodes, working on the principle of Faradaic reactions.^[119] Since these composites possess different porous morphologies in contrast with CPs and exhibit larger specific surface areas, they show pseudocapacitive charge transport and deliver specific capacitances of as high as 1500 $F g^{-1}$ with adequate cyclic stability. The SC electrode made from MOF@CP, MOFs@metal oxide/hydroxide, MOF@MOF, and MOF@metal governs the pseudocapacitive behavior. However, these composites suffer from issues, such as low energy and power densities with relatively short cycle lives. MOFs have been interlinked with various nanomaterials that permit the enlargement of electrode materials of the EDLC.^[189] In particular, MOFs can be nanocomposites with CNTs (SWCNTs and MWCNTs), graphene oxide, and quantum dots to achieve high specific capacitance and good energy density. Nanocomposites of MOFs containing CNT, graphene oxide, or quantum dots are usually determined by non-Faradaic reaction mechanisms; hence, they equally improve the whole stability and cycle life of the respective SC, compared to the composite of MOF with CP or metal oxide/hydroxides. So, when MOFs were combined with CNTs, most MOFs (e.g., ZIF-8, NiCo-MOF, and Ni(TA)) showed pseudocapacitive and EDLC properties; as a result, it was used to make electrodes with upgraded specific capacitances (e.g., of 200–2000 $F g^{-1}$). Generally, H_2SO_4 or KOH was preferably used as electrolyte.

Furthermore, MOF@GO and MOF@QD composites are superior materials in the research field of SCs. MOF@graphene and MOF@QD with large specific surface areas, uniform pore size distribution, and high electrical conductivities can drive

Table 2. MOF and their modified nanostructures as electrodes for SC.

Sr. No.	Electrode material	Specific surface area [$\text{m}^2 \text{g}^{-1}$]	Substrate used	Electrolyte	Scan rate/ Current density	Specific capacitance [F g^{-1}]	Cyclic stability [%]	Number of cycles	References
The Pristine MOFs									
1	Ni-MOF	–	–	2 M KOH	1 A·g ⁻¹	1518.8	95.5	10 000	[47]
2	Ni-MOF	117.42	Nickel foam	3 M KOH	1.4 A·g ⁻¹	988.0	96.5	5000	[48]
3	Mn-MOF	1.2352	Nickel mesh	3 M KOH	10 mV·s ⁻¹	270.0	–	–	[49]
4	Co-MOF	–	Nickel foam	2 M KOH	2 A·g ⁻¹	13.6	79.4	1000	[50]
5	NiCo-MOF	54.6	Nickel foam	2 M KOH	1 A·g ⁻¹	1202.1	89.5	5000	[51]
6	Co-MOF	2900	ITO coated glass	1 M LiOH	0.6 A·g ⁻¹	206.76	98.5	1000	[202]
7	Ni ₃ (HITP) ₂ MOF	–	Nickel foam	0.5 M Na ₂ SO ₄	0.1 mA·cm ⁻²	279.1	97	6500	[203]
8	Mn-BDC	202	Nickel foam	2 M KOH	1 A·g ⁻¹	567.5 mAh·g ⁻¹	92.3	5000	[204]
9	Ni-MOF	40.36	Carbon cloth	3 M KOH	1 A·g ⁻¹	1057	70	2500	[205]
MOF derived metal oxides									
1	Mn/Ni-MOFs derived porous MnNi ₂ O ₄	50.80	Nickel foam	6 M KOH	1 A·g ⁻¹	2848	93.25	5000	[56]
2	UPC-9 derived Co ₃ O ₄ nanosheets	101.7	Nickel foam	6 M KOH	1 A·g ⁻¹	1121	98.2	6.000	[57]
3	Ni-MOF derived NiO nanospheres	66.8	Nickel foam	3 M KOH	0.5 A·g ⁻¹	473	94	3000	[58]
4	Ni-Zn MOF derived NiO/ZnO hollow spheres	36.4	Nickel foam	3 M KOH	1.3 A·g ⁻¹	497	117.1	2000	[59]
5	ZIF8@ZIF-67 derived Co ₃ O ₄ /ZnO	–	Nickel foam	6 M KOH	0.5 A·g ⁻¹	415	93.2	1000	[60]
6	MOF-74 derived NiO, NiCo ₂ O ₄ , Co ₃ O ₄	59.6	Nickel foam	1 M KOH	0.5 A·g ⁻¹	684	89.0	3000	[61]
7	Ni-MOF derived NiO nanosheets	118.2	–	–	1 A·g ⁻¹	527.1	80.2	500	[206]
8	Co/Ni-MOF derived NiCo ₂ O ₄ nanoparticles	178.3	Nickel foam	6 M KOH	5 A·g ⁻¹	1315	90.7	10 000	[207]
9	Ce-BTC derived CeO ₂	77	Nickel foam	3 M KOH + 0.1 M K ₄ Fe(CN) ₆	0.2 A·g ⁻¹	502	–	5000	[208]
10	ZIF-67 derived hollow Co ₃ O ₄	128	Nickel foam	3 M KOH	1.25 A·g ⁻¹	1100	95.1	6000	[209]
MOF derived NPC									
1	ZIF-8@ZIF-67 derived NPC	1276	Graphite	1 M H ₂ SO ₄	2 A·g ⁻¹	270	64	10 000	[70]
2	HKUST-1 derived HPCF	620.1	–	6 M KOH	2 A·g ⁻¹	194.8	95	10 000	[71]
3	Cu-MOF derived APCs	1880.4	Nickel foam	6 M KOH	0.5 A·g ⁻¹	196	–	–	[72]
4	ZIF-8/PAN derived NPCF	314.7	Glassy carbon electrode	1 M H ₂ SO ₄	1 A·g ⁻¹	332	98.9	5000	[73]
5	ZIF-8/PAN derived HPCNFs-N	417.9	–	2 M H ₂ SO ₄	1 A·g ⁻¹	307.2	98.2	10 000	[74]
6	ZIF-11 derived N-PCMPs	2188	Glassy carbon electrode	1 M H ₂ SO ₄	1 A·g ⁻¹	307	90	4000	[75]
7	Ni/Co-MOF derived NPC	1135	Nickel foam	2 M KOH	1 A·g ⁻¹	1214	98.8	6000	[210]
8	MOF-5 derived NPC	1515	–	6 M KOH	0.05 A·g ⁻¹	212	95.9	1000	[211]
9	ZIF-69 derived NPC	2263	Glassy carbon electrode	0.5 M H ₂ SO ₄	5 mV·s ⁻¹	168	–	–	[212]
10	N-doped ZIF-8 derived NPC	1630	–	6 M KOH	0.1 A·g ⁻¹	285.8	72.8	1000	[213]

remarkable electrochemical properties. In addition, MOFs and their derived structures (e.g., Cu-MOF, Ni-doped ZIF-67, Ni-Co-MOF, SnO₂ quantum dots@ZIF-8, and SnO_x quantum dots@Zr-MOFs) seem to be interlinked with graphene oxide

Table 3. Summary of MOF composites as electrode materials for SC applications.

Sr. No.	Electrode material	Electrolyte	Substrate used	Scan rate/ Current density	Specific capacitance	Energy density	Cyclic stability [%]	Number of cycles	References
MOF@metal oxides/hydroxides									
1	Ni-MOF/NiO	3 M KOH	Nickel foam	1 mA·cm ⁻²	1853 C·cm ⁻²	39.2 Wh·kg ⁻¹	94	3000	[94]
2	Co-MOF/Co ₃ O ₄	3 M KOH	Nickel foam	0.5 A·g ⁻¹	1020 F·g ⁻¹	21.6 mWh·cm ⁻³	96.7	5000	[95]
3	MHCF/ MnOx	1 M Na ₂ SO ₄	Pt-coated polyethylene terephthalate	0.5 mA·cm ⁻²	175 mF·cm ⁻²	210 Wh kg ⁻¹	94.5	10 000	[96]
4	NiC ₂ O ₄ /ZIF-67	6 M KOH	Nickel foam	5 mV·s ⁻¹	1019.7 F·g ⁻¹	–	73	2000	[214]
5	Cu-MOF/ δ -MnO ₂	1 M Na ₂ SO ₄		1 A·g ⁻¹	667 F·g ⁻¹	–	95	6000	[215]
MOF@CPs									
1	PPy/UIO-66/CT	1 M H ₂ SO ₄	Cotton fiber	0.8 mA·cm ⁻²	565 F·g ⁻¹	38.2 Wh kg ⁻¹	90	500	[100]
2	CFs/UIO-66/PPY	3 M KCl	Cotton fiber	5 mV·s ⁻¹	206 mF·cm ⁻²	12.8 μ Wh·cm ⁻²	96	1200	[101]
3	ZIF-67/PANI	3 M KCl	Carbon cloth	10 mV·s ⁻¹	2146 mF·cm ⁻²	0.0161 mWh·cm ⁻³	80	2000	[102]
4	Cu-bipy-BTC/POAP	0.1 M HClO ₄	–	1 mA·cm ⁻²	422 F·g ⁻¹	–	93	1000	[103]
5	Co-MOF/PANI	1 M KOH	Nickel foil	1 A·g ⁻¹	504 F·g ⁻¹	–	90	5000	[104]
6	Zn-MOF/PANI	1 M H ₂ SO ₄	Titanium mesh	1 A·g ⁻¹	477 F·g ⁻¹	–	≈ 90	100	[216]
MOF@MOF									
1	Ni-MOF-24/Cu-MOF	1 M KOH	carbon fiber paper	2 A·cm ⁻²	1424 F·g ⁻¹	57 Wh·kg ⁻¹	94.3	7000	[112]
2	ZIF-67/ZIF	6 M KOH	Nickel foam	1 A·g ⁻¹	1176.8 F·g ⁻¹	23.4 Wh·kg ⁻¹	98	1000	[113]
3	ZIF-L(Zn)/ZIF-67	2 M KOH	Graphite	2 A·g ⁻¹	2,52.1 F·g ⁻¹	–	91.2	10 000	[114]
4	ZIF-8@ZIF-67	1 M H ₂ SO ₄	Cosmetic cotton	1 A·g ⁻¹	386.6	30 Wh·kg ⁻¹	89.5	5000	[217]
MOF@CNT nanocomposites									
1	ZIF-8/MWCNTs	1 M H ₂ SO ₄	Carbon cloth	0.5 A·g ⁻¹	259.2 F·g ⁻¹	–	92	5000	[121]
2	NiCo-MOF/MWCNT	2 M KOH	Nickel foam	0.5 A·g ⁻¹	1010 F·g ⁻¹	19.7 Wh·kg ⁻¹	100	3000	[122]
3	Ni-MOF/CNTs	6 M KOH	Nickel foam	0.5 A·g ⁻¹	1765 F·g ⁻¹	36.6 Wh·kg ⁻¹	95	5000	[123]
4	Ni(TA)/MWCNTs	2 M KOH	Nickel foam	2 A·g ⁻¹	115 mA h g ⁻¹	–	81.56	5000	[124]
5	Cu-MOF@CNT	1 M Na ₂ SO ₄	Glassy carbon electrode	1.6 A·g ⁻¹	380 F·g ⁻¹	–	63.63	4000	[218]
MOF@GO nanocomposites									
1	Cu-MOF/grapheme	6 M KOH	Nickel foam	10 mV·s ⁻¹	482 F·g ⁻¹	34.5 Wh·kg ⁻¹	93.8	1000	[127]
2	Ni-doped ZIF-67/rGO	1 M H ₂ SO ₄	Carbon paper	1 A·g ⁻¹	304 F·g ⁻¹	21.5 Wh·kg ⁻¹	99	1000	[128]
3	Ni-Co-MOF/GO	6 M KOH	Nickel foam	1 A·g ⁻¹	447.2 F·g ⁻¹	–	99.6	300	[129]
4	ZIF-67/rGO	0.2 M K ₃ [Fe(CN) ₆] in 1 M Na ₂ SO ₄	Graphite	4.5 A·g ⁻¹	1453 F·g ⁻¹	25.5 Wh·kg ⁻¹	90.5	1000	[130]
5	Ni/Co-MOF/rGO	6 M KOH	Nickel foam	1 A·g ⁻¹	860 F·g ⁻¹	72.8 Wh·kg ⁻¹	91.6	6000	[219]
MOF@metal									
1	Mo-doped Ni-MOF	3 M KOH	Nickel foam	1 A·g ⁻¹	802 C·g ⁻¹	59 Wh·kg ⁻¹	92.9	20 000	[131]
2	Zn-doped Ni-MOF	6 M KOH	Stainless steel mesh	0.25 A·g ⁻¹	1620 F·g ⁻¹	27.56 Wh·kg ⁻¹	91	3000	[79]
3	Mn-doped Ni-MOF	6 M KOH	Nickel foam	2 mA·cm ⁻²	1178 C·g ⁻¹	39.6 Wh·kg ⁻¹	80.6	5000	[132]
4	Ni@Cu-MOF	6 M KOH	Nickel foam	1 A·g ⁻¹	48.7 F·g ⁻¹	17.3 Wh·kg ⁻¹	80	1200	[133]
5	Co-doped Ni-based MOF	6 M KOH	Nickel foam	1 A·g ⁻¹	1300 F·g ⁻¹	25.92 Wh·kg ⁻¹	71	3000	[220]
MOF@QD									
1	SnO ₂ quantum dots@ZIF-8	6 M KOH	Nickel foam	5 mV·s ⁻¹	931 F·g ⁻¹	–	–	500	[135]
2	SnOx quantum dots @Zr-MOFs (UIO-66)	1 M LiPF ₆	Copper foil	50 mA·g ⁻¹	2196 mAh·g ⁻¹	–	–	100	[136]
3	ZIF-8 derived Carbon/GQDs	6 M KOH	Nickel foam	2 A·g ⁻¹	130 F·g ⁻¹	493 mAh·g ⁻¹	96.9	10 000	[137]

sheets to accomplish high specific capacitances in the range of 300–1400 F g⁻¹ (Table 3). In addition to carrying high-level specific capacitances, MOF@GO and MOF@QD composites also ensure better cyclic stability and upgraded energy density values (e.g., ZIF-8-derived Carbon/GQDs = 493 mAhg⁻¹), compared to other classes of MOF composites.

6. Conclusion and Future Outlook

In summary, the pristine MOFs, including their derivatives and composites, have been significantly explored as SC electrodes because of their structural diversity, tunable pore features, and high electronic properties. This minioverview presents recent progress in designing and synthesizing the pristine MOFs and their derivatives and MOF-based composites for SC applications. In particular, MOF-derived metal oxides, NPC materials, and MOF-based composites with metal oxide/hydroxides, CPs, CNTs, quantum dots, and graphene have been highlighted. In addition, we have discussed essential aspects related to the electrolytes, such as aqueous, organic, and RAE, and their selection with MOF-based materials.

Despite advances in the research into SCs using MOF-based electrode materials, their practical application remains a challenge. We have outlined several challenges and perspectives, as follows.

The present MOFs are largely concerned with 2D structures. Nonetheless, the electrochemical performances of MOFs including energy density and power density are limited by their limited theoretical surface area and 1D-like channel for ion swapping. This constraint can be solved by creating 3D MOFs with large surface area and plentiful channels that allow ion transport in both directions, resulting in efficient cation–anion swapping. As a result, greater research into the structural design of MOFs with 3D frameworks is required.

The pristine MOFs' low electrical conductivity, poor crystallinity, lack of structural flaws and crystalline boundaries, and mediocre specific surface area remain significant hurdles. Combining MOFs with other conductive and dependable electrochemical materials helps overcome these hurdles. Mixed metal or bimetal MOFs are an excellent choice for improving the aforementioned properties. Combining larger surface area with more conductive and synergistic effects from selected chemicals yields more desired SC outcomes.

More research into new MOF materials with novel structures, compositions, and electrical conductivities is required. Pre-/postmodification techniques to MOFs and structural optimization are critical for developing micro-/nanoscale materials with controllable structures. As a result, future avenues that must be pursued include upgrading existing synthetic processes to create improved synthetic strategies for manufacturing diverse MOF derivatives.

In several research reports, MOFs have been used as a cathode for SC applications; however, the search for an anode based on MOFs has mostly been restricted to NPC materials. Therefore, researchers might focus their efforts in this field to fabricate innovative negative electrodes for SCs based on 3D MOFs that have improved electrochemical performance over those made of conventional carbon materials.

Future energy storage devices must optimize and improve the electrochemical charge storage efficiencies of MOF-based materials for practical applications. Prior to investigating the optimized link between structure, element composition, coordination environment of metals, and electrochemical performance, it is important to identify the significant aspects that contribute to performance decline. Therefore, it is possible to investigate the energy storage mechanism and structural development during electrochemical testing using in situ/operando methods, DFT calculations, and MD simulations. Second, the development of effective strategies that could provide oxygen vacancy, surface functionalization, crystal phase variation, stress engineering, heterostructured interconnected morphologies, and high electrochemical activity are crucial factors to boost the electronic properties and surface properties of the electrodes. Finally, to improve the total charge storage capabilities of SCs, optimum electrode preparation, electrochemical experiments, testing settings, and electrolyte selection are all essential elements.

The use of MOF-based materials and the development of improved SC technologies are crucial. Despite the numerous challenges, the achievements to date are encouraging, and the contents of this minireview are only a small indication of the research required to properly comprehend and fully exploit the pristine MOFs, MOF-derived functional materials, and MOF-based composites. With consistent research contributions and technical innovation, we should have a good possibility of witnessing the revolution of new EESC technologies in the near future, as well as realising further applications of MOF-based materials in the sectors of renewable energy and environmental science.

Acknowledgements

The authors are thankful to UGC-SAP, DST-FIST, and DST-PURSE programmes for support to instrument facilities at the Department of Chemistry, Shivaji University, Kolhapur. One of the authors R.B. is thankful to SARTHI, Government of Maharashtra, India for the 'Chhatrapati Shahu Maharaj National Research Fellowship-2021'. This work was partially supported by the National Research Foundation of Korea (NRF) grant funded by the Korea government (MSIT, grant No. 2020H1D3A1A04081472).

Conflict of Interest

The authors declare no conflict of interest.

Keywords

composites, electrolytes, metal–organic frameworks, nanomaterials, supercapacitors

Received: February 14, 2023

Revised: May 3, 2023

Published online: July 8, 2023

[1] K. B. Wang, Q. Xun, Q. Zhang, *EnergyChem* **2020**, *2*, 100025.

[2] C. Zhu, Y. He, Y. Liu, N. Kazantseva, P. Saha, Q. Cheng, *J. Energy Chem.* **2019**, *35*, 124.

- [3] Y. N. Liu, L. N. Jin, H. T. Wang, X. H. Kang, S. W. Bian, *J. Colloid Interface Sci.* **2018**, *530*, 29.
- [4] P. E. Lokhande, S. Kulkarni, S. Chakrabarti, H. M. Pathan, M. Sindhu, D. Kumar, J. Singh, A. Kumar, Y. Kumar Mishra, D. C. Toncu, M. Syväjärvi, A. Sharma, A. Tiwari, *Coord. Chem. Rev.* **2022**, *473*, 214771.
- [5] M. Pumera, *Energy Environ. Sci.* **2011**, *4*, 668.
- [6] I. Hussain, C. Lamiel, M. Sufyan Javed, M. Ahmad, X. Chen, S. Sahoo, X. Ma, M. A. Bajaber, M. Zahid Ansari, K. Zhang, *Chem. Eng. J.* **2023**, *454*, 140313.
- [7] D. Larcher, J. M. Tarascon, *Nat. Chem.* **2015**, *7*, 19.
- [8] P. He, Q. Chen, M. Yan, X. Xu, L. Zhou, L. Mai, C. W. Nan, *EnergyChem* **2019**, *1*, 1000222.
- [9] J. Xie, P. Gu, Q. Zhang, *ACS Energy Lett.* **2017**, *2*, 1985.
- [10] Y. Zhai, Y. Dou, D. Zhao, P. F. Fulvio, R. T. Mayes, S. Dai, *Adv. Mater.* **2011**, *23*, 4828.
- [11] G. Liu, Y. Sheng, J. W. Ager, M. Kraft, R. Xu, *EnergyChem* **2019**, *1*, 100014.
- [12] M. S. Javed, A. Mateen, I. Hussain, S. Ali, S. Asim, A. Ahmad, E. tag Eldin, M. A. Bajaber, T. Najam, W. Han, *Chem. Eng. J.* **2023**, *452*, 139455.
- [13] G. A. Tafete, M. K. Abera, G. Thothadri, *J. Energy Storage* **2022**, *48*, 103938.
- [14] Y. Wang, Y. Song, Y. Xia, *Chem. Soc. Rev.* **2016**, *45*, 5925.
- [15] Q. Abbas, A. Mateen, S. H. Siyal, N. U. Hassan, A. A. Alothman, M. Ouladmane, S. M. Eldin, M. Z. Ansari, M. S. Javed, *Chemosphere* **2023**, *313*, 137421.
- [16] Z. Y. Sui, P. Y. Zhang, M. Y. Xu, Y. W. Liu, Z. X. Wei, B. H. Han, *ACS Appl. Mater. Interfaces* **2017**, *9*, 43171.
- [17] W. Raza, F. Ali, N. Raza, Y. Luo, K. H. Kim, J. Yang, S. Kumar, A. Mehmood, E. E. Kwon, *Nano Energy* **2018**, *52*, 441.
- [18] A. Mateen, M. S. Javed, S. Khan, A. Saleem, M. K. Majeed, A. J. Khan, M. F. Tahir, M. A. Ahmad, M. A. Assiri, K. Q. Peng, *J. Energy Storage* **2022**, *49*, 104150.
- [19] R. R. Salunkhe, Y. V. Kaneti, J. Kim, J. H. Kim, Y. Yamauchi, *Acc. Chem. Res.* **2016**, *49*, 2796.
- [20] M. Zheng, X. Xiao, L. Li, P. Gu, X. Dai, H. Tang, Q. Hu, H. Xue, H. Pang, *Sci. China Mater.* **2018**, *61*, 185.
- [21] T. Wang, S. Zhang, H. Wang, *Sci. China Mater.* **2018**, *61*, 296.
- [22] G. Yu, X. Xie, L. Pan, Z. Bao, Y. Cui, *Nano Energy* **2013**, *2*, 213.
- [23] R. S. Kate, S. A. Khalate, R. J. Deokate, *J. Alloys Compd.* **2018**, *734*, 89.
- [24] Y. Zhang, H. Feng, X. Wu, L. Wang, A. Zhang, T. Xia, H. Dong, X. Li, L. Zhang, *Int. J. Hydrogen Energy* **2009**, *34*, 4889.
- [25] Y. Wang, F. Xu, L. Sun, S. Fang, J. Lao, C. Zhang, S. Wei, L. Liao, Y. Guan, Y. Xia, Y. Luo, Y. Sun, Y. Zou, Z. Yu, Q. Shao, Y. Zhu, Y. Luo, *J. Energy Storage* **2023**, *58*, 106395.
- [26] M. Li, X. Jiang, J. Liu, Q. Liu, N. Lv, N. Qi, Z. Chen, *J. Alloys Compd.* **2023**, *930*, 167354.
- [27] H. B. Wu, X. W. Lou, *Sci. Adv.* **2017**, *3*, 9252.
- [28] X. F. Lu, Y. Fang, D. Luan, X. W. D. Lou, *Nano Lett.* **2021**, *21*, 1555.
- [29] H. C. J. Zhou, S. Kitagawa, *Chem. Soc. Rev.* **2014**, *43*, 5415.
- [30] P. Y. Liu, J. J. Zhao, Z. P. Dong, Z. L. Liu, Y. Q. Wang, *J. Alloys Compd.* **2021**, *854*, 157181.
- [31] F. Zhan, H. Wang, Q. He, W. Xu, J. Chen, X. Ren, H. Wang, S. Liu, M. Han, Y. Yamauchi, L. Chen, *Chem. Sci.* **2022**, *13*, 11981.
- [32] G. G. Amatucci, F. Badway, A. Du Pasquier, T. Zheng, *J. Electrochem. Soc.* **2001**, *148*, A930.
- [33] Z. Chen, V. Augustyn, X. Jia, Q. Xiao, B. Dunn, Y. Lu, *ACS Nano* **2012**, *6*, 4319.
- [34] S. Komaba, T. Hasegawa, M. Dahbi, K. Kubota, *Electrochem. Commun.* **2015**, *60*, 172.
- [35] H. Wang, M. Wang, Y. Tang, *Energy Storage Mater.* **2018**, *13*, 1.
- [36] J. Liang, D. W. Wang, *Adv. Energy Mater.* **2022**, *12*, 2200920.
- [37] H. Zhang, J. Nai, L. Yu, X. W. (David) Lou, *Joule* **2017**, *1*, 77.
- [38] H. Wang, Q. L. Zhu, R. Zou, Q. Xu, *Chem* **2017**, *2*, 52.
- [39] Z. Liang, C. Qu, D. Xia, R. Zou, Q. Xu, *Angew. Chem. Int. Ed.* **2018**, *57*, 9604.
- [40] J. Yu, X. Gao, Z. Cui, Y. Jiao, Q. Zhang, H. Ding, L. Yu, L. Dong, *Energy Technol.* **2019**, *7*, 1900018.
- [41] T. Qiu, Z. Liang, W. Guo, H. Tabassum, S. Gao, R. Zou, *ACS Energy Lett.* **2020**, *5*, 520.
- [42] D. Sheberla, J. C. Bachman, J. S. Elias, C. J. Sun, Y. Shao-Horn, M. Dincă, *Nat. Mater.* **2017**, *16*, 220.
- [43] N. Sahiner, S. Demirci, M. Yildiz, *J. Electron. Mater.* **2017**, *46*, 790.
- [44] F. Wang, S. Xiao, Y. Hou, C. Hu, L. Liu, Y. Wu, *RSC Adv.* **2013**, *3*, 13059.
- [45] Y. Tan, W. Zhang, Y. Gao, J. Wu, B. Tang, *RSC Adv.* **2015**, *5*, 17601.
- [46] R. Bhosale, S. Bhosale, P. Kumbhar, D. Narale, R. Ghaware, C. Jambhale, S. Kolekar, *New J. Chem.* **2023**, *47*, 6749.
- [47] C. Yang, X. Li, L. Yu, X. Liu, J. Yang, M. Wei, *Chem. Commun.* **2020**, *56*, 1803.
- [48] Y. Yan, P. Gu, S. Zheng, M. Zheng, H. Pang, H. Xue, *J. Mater. Chem. A* **2016**, *4*, 19078.
- [49] G. Krishnamurthy, B. M. Omkaramurthy, *Indian J. Adv. Chem. Sci.* **2019**, *7*, 12.
- [50] G. Zhu, H. Wen, M. Ma, W. Wang, L. Yang, L. Wang, X. Shi, X. Cheng, X. Sun, Y. Yao, *Chem. Commun.* **2018**, *54*, 10499.
- [51] Y. Wang, Y. Liu, H. Wang, W. Liu, Y. Li, J. Zhang, H. Hou, J. Yang, *ACS Appl. Energy Mater.* **2019**, *2*, 2063.
- [52] F. Bigdeli, C. T. Lollar, A. Morsali, H. C. Zhou, *Angew. Chem. Int. Ed.* **2020**, *59*, 4652.
- [53] Y. Li, Y. Xu, W. Yang, W. Shen, H. Xue, H. Pang, *Small* **2018**, *14*, 1.
- [54] J. Li, D. Yan, S. Hou, T. Lu, Y. Yao, D. H. C. Chua, L. Pan, *Chem. Eng. J.* **2018**, *335*, 579.
- [55] Z. Zhang, Y. Huang, S. Bai, *Mater. Sci. Forum* **2017**, *890*, 68.
- [56] M. Lan, X. Wang, R. Zhao, M. Dong, L. Fang, L. Wang, *J. Alloys Compd.* **2020**, *821*, 153546.
- [57] Z. Xiao, L. Fan, B. Xu, S. Zhang, W. Kang, Z. Kang, H. Lin, X. Liu, S. Zhang, D. Sun, *ACS Appl. Mater. Interfaces* **2017**, *9*, 41827.
- [58] M. K. Wu, C. Chen, J. J. Zhou, F. Y. Yi, K. Tao, L. Han, *J. Alloys Compd.* **2018**, *734*, 1.
- [59] G. C. Li, P. F. Liu, R. Liu, M. Liu, K. Tao, S. R. Zhu, M. K. Wu, F. Y. Yi, L. Han, *Dalt. Trans.* **2016**, *45*, 13311.
- [60] J. Xu, S. Liu, Y. Liu, *RSC Adv.* **2016**, *6*, 52137.
- [61] G. Liuting, X. U. Miao, M. A. Renping, H. A. N. Yingping, X. U. Hongbo, S. H. I. Gang, *Sci. China Technol. Sci.* **2020**.
- [62] M. Zhong, E. K. Kim, J. P. McGann, S. E. Chun, J. F. Whitacre, M. Jaroniec, K. Matyjaszewski, T. Kowalewski, *J. Am. Chem. Soc.* **2012**, *134*, 14846.
- [63] Z. Lei, D. Bai, X. S. Zhao, *Microporous Mesoporous Mater.* **2012**, *147*, 86.
- [64] H. Zhu, J. Yin, X. Wang, H. Wang, X. Yang, *Adv. Funct. Mater.* **2013**, *23*, 1305.
- [65] R. R. Salunkhe, Y. Kamachi, N. L. Torad, S. M. Hwang, Z. Sun, S. X. Dou, J. H. Kim, Y. Yamauchi, *J. Mater. Chem. A* **2014**, *2*, 19848.
- [66] T. Wang, J. Tang, X. Fan, J. Zhou, H. Xue, H. Guo, J. He, *Nanoscale* **2014**, *6*, 5359.
- [67] M. Sevilla, A. B. Fuertes, *Carbon NY* **2006**, *44*, 468.
- [68] Z. Chen, Y. Qin, D. Weng, Q. Xiao, Y. Peng, X. Wang, H. Li, F. Wei, Y. Lu, *Adv. Funct. Mater.* **2009**, *19*, 3420.
- [69] J. Ren, Y. Huang, H. Zhu, B. Zhang, H. Zhu, S. Shen, G. Tan, F. Wu, H. He, S. Lan, X. Xia, Q. Liu, *Carbon Energy* **2020**, *2*, 176.
- [70] J. Tang, R. R. Salunkhe, J. Liu, N. L. Torad, M. Imura, S. F. Furukawa, Y. Yamauchi, *J. Am. Chem. Soc.* **2015**, *137*, 1572.
- [71] Y. Liu, G. Li, Y. Guo, Y. Ying, X. Peng, *ACS Appl. Mater. Interfaces* **2017**, *9*, 14043.
- [72] H. H. Duan, C. H. Bai, J. Y. Li, Y. Yang, B. L. Yang, X. F. Gou, M. L. Yue, Z. X. Li, *Inorg. Chem.* **2019**, *58*, 2856.

- [73] C. Wang, C. Liu, J. Li, X. Sun, J. Shen, W. Han, L. Wang, *Chem. Commun.* **2017**, 53, 1751.
- [74] L. F. Chen, Y. Lu, L. Yu, X. W. Lou, *Energy Environ. Sci.* **2017**, 10, 1777.
- [75] F. Hao, L. Li, X. Zhang, J. Chen, *Mater. Res. Bull.* **2015**, 66, 88.
- [76] S. H. Kazemi, B. Hosseinzadeh, H. Kazemi, M. A. Kiani, S. Hajati, *ACS Appl. Mater. Interfaces* **2018**, 10, 23063.
- [77] X. Xu, J. Tang, H. Qian, S. Hou, Y. Bando, M. S. A. Hossain, L. Pan, Y. Yamauchi, *ACS Appl. Mater. Interfaces* **2017**, 9, 38737.
- [78] A. Mahmood, R. Zou, Q. Wang, W. Xia, H. Tabassum, B. Qiu, R. Zhao, *ACS Appl. Mater. Interfaces* **2016**, 8, 2148.
- [79] J. Yang, C. Zheng, P. Xiong, Y. Li, M. Wei, *J. Mater. Chem. A* **2014**, 2, 19005.
- [80] N. Campagnol, R. Romero-Vara, W. Deleu, L. Stappers, K. Binnemans, D. E. De Vos, J. Fransaer, *ChemElectroChem* **2014**, 1, 1182.
- [81] D. Y. Lee, D. V. Shinde, E. K. Kim, W. Lee, I. W. Oh, N. K. Shrestha, J. K. Lee, S. H. Han, *Microporous Mesoporous Mater.* **2013**, 171, 53.
- [82] H. Wang, N. Zhang, S. Li, Q. Ke, Z. Li, M. Zhou, *J. Semicond.* **2020**, 41, 091707.
- [83] F. Boorboor Ajdari, E. Kowsari, M. Niknam Shahrak, A. Ehsani, Z. Kiaei, H. Torkzaban, M. Ershadi, S. Kholghi Eshkalak, V. Haddadi-Asl, A. Chinnappan, S. Ramakrishna, *Coord. Chem. Rev.* **2020**, 422, 213441.
- [84] S. Li, H. Chai, L. Zhang, Y. Xu, Y. Jiao, J. Chen, *J. Colloid Interface Sci.* **2023**, 642, 235.
- [85] S. Sundriyal, H. Kaur, S. K. Bhardwaj, S. Mishra, K. H. Kim, A. Deep, *Coord. Chem. Rev.* **2018**, 369, 15.
- [86] J. Jiang, Y. Li, J. Liu, X. Huang, C. Yuan, X. W. Lou, *Adv. Mater.* **2012**, 24, 5166.
- [87] L. F. Chen, Z. Y. Yu, J. J. Wang, Q. X. Li, Z. Q. Tan, Y. W. Zhu, S. H. Yu, *Nano Energy* **2015**, 11, 119.
- [88] T. Zhai, L. Wan, S. Sun, Q. Chen, J. Sun, Q. Xia, H. Xia, *Adv. Mater.* **2017**, 29, 1604167.
- [89] B. Li, P. Gu, Y. Feng, G. Zhang, K. Huang, H. Xue, H. Pang, *Adv. Funct. Mater.* **2017**, 27, 1605784.
- [90] F. Grote, Z. Y. Yu, J. L. Wang, S. H. Yu, Y. Lei, *Small* **2015**, 11, 4666.
- [91] Q. Liao, N. Li, S. Jin, G. Yang, C. Wang, *ACS Nano* **2015**, 9, 5310.
- [92] W. Zhan, Q. Kuang, J. Zhou, X. Kong, Z. Xie, L. Zheng, *J. Am. Chem. Soc.* **2013**, 135, 1926.
- [93] Q. L. Zhu, Q. Xu, *Chem. Soc. Rev.* **2014**, 43, 5468.
- [94] S. Xiong, S. Jiang, J. Wang, H. Lin, M. Lin, S. Weng, S. Liu, Y. Jiao, Y. Xu, J. Chen, *Electrochim. Acta* **2020**, 340, 135956.
- [95] S. Zheng, Q. Li, H. Xue, H. Pang, Q. Xu, *Natl. Sci. Rev.* **2020**, 7, 305.
- [96] Y. Z. Zhang, T. Cheng, Y. Wang, W. Y. Lai, H. Pang, W. Huang, *Adv. Mater.* **2016**, 28, 5242.
- [97] D. Fu, H. Zhou, X. M. Zhang, G. Han, Y. Chang, H. Li, *ChemistrySelect* **2016**, 1, 285.
- [98] Q. Meng, K. Cai, Y. Chen, L. Chen, *Nano Energy* **2017**, 36, 268.
- [99] L. Pan, H. Qiu, C. Dou, Y. Li, L. Pu, J. Xu, Y. Shi, *Int. J. Mol. Sci.* **2010**, 11, 2636.
- [100] C. Zhang, J. Tian, W. Rao, B. Guo, L. Fan, W. Xu, J. Xu, *Cellulose* **2019**, 26, 3387.
- [101] K. Qi, R. Hou, S. Zaman, Y. Qiu, B. Y. Xia, H. Duan, *ACS Appl. Mater. Interfaces* **2018**, 10, 18021.
- [102] L. Wang, X. Feng, L. Ren, Q. Piao, J. Zhong, Y. Wang, H. Li, Y. Chen, B. Wang, *J. Am. Chem. Soc.* **2015**, 137, 4920.
- [103] A. Ehsani, J. Khodayari, M. Hadi, H. M. Shiiri, H. Mostaanzadeh, *Ionic* **2017**, 23, 131.
- [104] R. Srinivasan, E. Elaiyappillai, E. J. Nixon, I. Sharmila Lydia, P. M. Johnson, *Inorganica Chim. Acta* **2020**, 502, 119393.
- [105] C. Liu, J. Wang, J. Wan, C. Yu, *Coord. Chem. Rev.* **2021**, 432, 213743.
- [106] A. Q. Wu, W. Q. Wang, H. Bin Zhan, L. A. Cao, X. L. Ye, J. J. Zheng, P. N. Kumar, K. Chiranjeevulu, W. H. Deng, G. E. Wang, M. S. Yao, G. Xu, *Nano Res.* **2021**, 14, 438.
- [107] Y. Gu, Y. N. Wu, L. Li, W. Chen, F. Li, S. Kitagawa, *Angew. Chem. Int. Ed.* **2017**, 56, 15658.
- [108] H. Ji, S. Lee, J. Park, T. Kim, S. Choi, M. Oh, *Inorg. Chem.* **2018**, 57, 9048.
- [109] X. Yang, S. Yuan, L. Zou, H. Drake, Y. Zhang, J. Qin, A. Alsalme, H. C. Zhou, *Angew. Chemie - Int. Ed.* **2018**, 57, 3927.
- [110] L. Zhang, J. Wang, X. Ren, W. Zhang, T. Zhang, X. Liu, T. Du, T. Li, J. Wang, *J. Mater. Chem. A* **2018**, 6, 21029.
- [111] P. Falcaro, K. Okada, T. Hara, K. Ikgaki, Y. Tokudome, A. W. Thornton, A. J. Hill, T. Williams, C. Doonan, M. Takahashi, *Nat. Mater.* **2017**, 16, 342.
- [112] T. Deng, X. Shi, W. Zhang, Z. Wang, W. Zheng, *iScience* **2020**, 23, 101220.
- [113] C. Hu, J. Xu, Y. Wang, M. Wei, Z. Lu, C. Cao, *J. Mater. Sci.* **2020**, 55, 16360.
- [114] J. Zhang, Y. Wang, K. Xiao, S. Cheng, T. Zhang, G. Qian, Q. Zhang, Y. Feng, *New J. Chem.* **2018**, 42, 6719.
- [115] C. H. Shen, C. H. Chuang, Y. J. Gu, W. H. Ho, Y. Da Song, Y. C. Chen, Y. C. Wang, C. W. Kung, *ACS Appl. Mater. Interfaces* **2021**, 13, 16418.
- [116] F. Cao, M. Gan, L. Ma, X. Li, F. Yan, M. Ye, Y. Zhai, Y. Zhou, *Synth. Met.* **2017**, 234, 154.
- [117] J. M. Schnorr, T. M. Swager, *Chem. Mater.* **2011**, 23, 646.
- [118] K. E. Gregorczyk, A. C. Kozen, X. Chen, M. A. Schroeder, M. Noked, A. Cao, L. Hu, G. W. Rubloff, *ACS Nano* **2015**, 9, 464.
- [119] Y. Zhang, B. Lin, Y. Sun, X. Zhang, H. Yang, J. Wang, *RSC Adv.* **2015**, 5, 58100.
- [120] S. Sun, Y. Wang, L. Chen, M. Chu, Y. Dong, D. Liu, P. Liu, D. Qu, J. Duan, X. Li, *Colloids Surf. A Physicochem. Eng. Asp.* **2022**, 643, 128727.
- [121] D. Zhang, J. Zhang, M. Pan, Y. Wang, T. Sun, *J. Alloys Compd.* **2021**, 853, 157368.
- [122] X. Wang, N. Yang, Q. Li, F. He, Y. Yang, B. Wu, J. Chu, A. Zhou, S. Xiong, *J. Solid State Chem.* **2019**, 277, 575.
- [123] P. Wen, P. Gong, J. Sun, J. Wang, S. Yang, *J. Mater. Chem. A* **2015**, 3, 13874.
- [124] Q. Wang, Q. Wang, B. Xu, F. Gao, F. Gao, C. Zhao, *Electrochim. Acta* **2018**, 281, 69.
- [125] M. Saraf, R. Rajak, S. M. Mobin, *J. Mater. Chem. A* **2016**, 4, 16432.
- [126] P. Srimuk, S. Luanwuthi, A. Krittayavathananon, M. Sawangphruk, *Electrochim. Acta* **2015**, 157, 69.
- [127] M. Azadfalah, A. Sedghi, H. Hosseini, *J. Electron. Mater.* **2019**, 48, 7011.
- [128] S. Sundriyal, V. Shrivastav, S. Mishra, A. Deep, *Int. J. Hydrogen Energy* **2020**, 45, 30859.
- [129] J. Hong, S. J. Park, S. Kim, *Electrochim. Acta* **2019**, 311, 62.
- [130] S. Sundriyal, V. Shrivastav, H. Kaur, S. Mishra, A. Deep, *ACS Omega* **2018**, 3, 17348.
- [131] Q. Li, H. Guo, R. Xue, M. Wang, M. Xu, W. Yang, J. Zhang, W. Yang, *Int. J. Hydrogen Energy* **2020**, 45, 20820.
- [132] D. Zheng, H. Wen, X. Sun, X. Guan, J. Zhang, W. Tian, H. Feng, H. Wang, Y. Yao, *Chem.* **2020**, 26, 17149.
- [133] Y. Wang, S. Nie, Y. Liu, W. Yan, S. Lin, G. Cheng, H. Yang, J. Luo, *Polymers* **2019**, 11, 821.
- [134] Y. Xue, S. Zheng, H. Xue, H. Pang, *J. Mater. Chem. A* **2019**, 7, 7301.
- [135] Y. Gao, J. Wu, W. Zhang, Y. Tan, J. Zhao, B. Tang, *Mater. Lett.* **2014**, 128, 208.
- [136] W. Li, Z. Li, F. Yang, X. Fang, B. Tang, *ACS Appl. Mater. Interfaces* **2017**, 9, 35030.
- [137] H. Yu, W. Zhu, H. Zhou, J. Liu, Z. Yang, X. Hu, A. Yuan, *RSC Adv.* **2019**, 9, 9577.

- [138] L. Xia, L. Yu, D. Hu, G. Z. Chen, *Mater. Chem. Front.* **2017**, *1*, 584.
- [139] D. Aurbach, Y. Talyosef, B. Markovsky, E. Markevich, E. Zinigrad, L. Asraf, J. S. Gnanaaraj, H. J. Kim, *Electrochim. Acta* **2004**, *50*, 247.
- [140] B. H. Wee, J. D. Hong, *Langmuir* **2014**, *30*, 5267.
- [141] S. Paul, K. S. Choi, D. J. Lee, P. Sudhagar, Y. S. Kang, *Electrochim. Acta* **2012**, *78*, 649.
- [142] K. Tönurist, T. Thomborg, A. Jänes, I. Kink, E. Lust, *Electrochem. Commun.* **2012**, *22*, 77.
- [143] B. Pal, S. Yang, S. Ramesh, V. Thangadurai, R. Jose, *Nanoscale Adv.* **2019**, *1*, 3807.
- [144] T. Xiong, T. L. Tan, L. Lu, W. S. V. Lee, J. Xue, *Adv. Energy Mater.* **2018**, *8*, 1702630.
- [145] G. Wang, H. Wang, X. Lu, Y. Ling, M. Yu, T. Zhai, Y. Tong, Y. Li, *Adv. Mater.* **2014**, *26*, 2676.
- [146] L. Zhang, X. S. Zhao, *Chem. Soc. Rev.* **2009**, *38*, 2520.
- [147] C. Zhong, Y. Deng, W. Hu, J. Qiao, L. Zhang, J. Zhang, *Chem. Soc. Rev.* **2015**, *44*, 7484.
- [148] B. Pal, S. G. Krishnan, B. L. Vijayan, M. Harilal, C. C. Yang, F. I. Ezema, M. M. Yusoff, R. Jose, *J. Electroanal. Chem.* **2018**, *817*, 217.
- [149] L. Kong, M. Cheng, H. Huang, J. Pang, S. Liu, Y. Xu, X. H. Bu, *Energy Chem* **2022**, *4*, 100090.
- [150] K. Fic, G. Lota, M. Meller, E. Frackowiak, *Energy Environ. Sci.* **2012**, *5*, 5842.
- [151] S. Sundriyal, V. Shrivastav, A. Kaur, Mansi, A. Deep, S. R. Dhakate, *J. Energy Storage* **2021**, *41*, 103000.
- [152] M. Z. Iqbal, S. Zakar, S. S. Haider, *J. Electroanal. Chem.* **2020**, *858*, 113793.
- [153] Q. B. Le, T. H. Nguyen, H. Fei, I. Sapurina, F. A. Ngwabebhoh, C. Bubulinca, L. Munster, E. D. Bergerová, A. Lengalova, H. Jiang, T. D. Tran, N. Bugarova, M. Ormastova, N. E. Kazantseva, P. Saha, *Electrochim. Acta* **2021**, *367*, 137563.
- [154] Q. Zhang, J. Rong, D. Ma, B. Wei, *Energy Environ. Sci.* **2011**, *4*, 2152.
- [155] P. Kurzweil, M. Chwistek, *J. Power Sources* **2008**, *176*, 555.
- [156] R. R. Salunkhe, C. Young, J. Tang, T. Takei, Y. Ide, N. Kobayashi, Y. Yamauchi, *Chem. Commun.* **2016**, *52*, 4764.
- [157] S. Ghosh, A. De Adhikari, J. Nath, G. C. Nayak, H. P. Nayek, *ChemistrySelect* **2019**, *4*, 10624.
- [158] K. M. Choi, H. M. Jeong, J. H. Park, Y. B. Zhang, J. K. Kang, O. M. Yaghi, *ACS Nano* **2014**, *8*, 7451.
- [159] A. A. Łatoszyńska, G. Z. Zukowska, I. A. Rutkowska, P. L. Taberna, P. Simon, P. J. Kulesza, W. Wieczorek, *J. Power Sources* **2015**, *274*, 1147.
- [160] L. Q. Fan, J. Zhong, J. H. Wu, J. M. Lin, Y. F. Huang, *J. Mater. Chem. A* **2014**, *2*, 9011.
- [161] H. Du, Z. Wu, Y. Xu, S. Liu, H. Yang, *Polymers* **2020**, *12*, 297.
- [162] M. L. Verma, M. Minakshi, N. K. Singh, *Electrochim. Acta* **2014**, *137*, 497.
- [163] B. Pal, A. Yasin, R. Kunwar, S. Yang, M. M. Yusoff, R. Jose, *Ind. Eng. Chem. Res.* **2019**, *58*, 654.
- [164] S. Hong, H. Kim, S. Gao, R. L. Lavall, H. Y. Jung, Y. J. Jung, *J. Power Sources* **2019**, *432*, 16.
- [165] S. T. Senthilkumar, R. K. Selvan, J. S. Melo, *J. Mater. Chem. A* **2013**, *1*, 12386.
- [166] X. M. Cao, Z. J. Sun, S. Y. Zhao, B. Wang, Z. B. Han, *Mater. Chem. Front.* **2018**, *2*, 1692.
- [167] R. Zhao, Y. Wu, Z. Liang, L. Gao, W. Xia, Y. Zhao, R. Zou, *Energy Environ. Sci.* **2020**, *13*, 2386.
- [168] M. Wang, Y. Ma, J. Ye, *J. Power Sources* **2020**, *474*, 228681.
- [169] L. Shao, Q. Wang, Z. Ma, Z. Ji, X. Wang, D. Song, Y. Liu, N. Wang, *J. Power Sources* **2018**, *379*, 350.
- [170] A. B. Kanj, R. Verma, M. Liu, J. Helfferich, W. Wenzel, L. Heinke, *Nano Lett.* **2019**, *19*, 2114.
- [171] L. Yu, G. Z. Chen, *Front. Chem.* **2019**, *7*, 272.
- [172] S. Shahzad, A. Shah, E. Kowsari, F. J. Iftikhar, A. Nawab, B. Piro, M. S. Akhter, U. A. Rana, Y. Zou, *Glob. Challenges* **2019**, *3*, 1800023.
- [173] S. Pan, M. Yao, J. Zhang, B. Li, C. Xing, X. Song, P. Su, H. Zhang, *Front. Chem.* **2020**, *8*, 261.
- [174] X. Sang, J. Zhang, J. Xiang, J. Cui, L. Zheng, J. Zhang, Z. Wu, Z. Li, G. Mo, Y. Xu, J. Song, C. Liu, X. Tan, T. Luo, B. Zhang, B. Han, *Nat. Commun.* **2017**, *8*, 175.
- [175] M. Zhang, A. M. Zhang, X. X. Wang, Q. Huang, X. Zhu, X. L. Wang, L. Z. Dong, S. L. Li, Y. Q. Lan, *J. Mater. Chem. A* **2018**, *6*, 8735.
- [176] K. Fujie, R. Ikeda, K. Otsubo, T. Yamada, H. Kitagawa, *Chem. Mater.* **2015**, *27*, 7355.
- [177] L. Zhang, S. Yang, J. Chang, D. Zhao, J. Wang, C. Yang, B. Cao, *Front. Chem.* **2020**, *8*, 1.
- [178] B. Akinwolemiwa, C. Peng, G. Z. Chen, *J. Electrochem. Soc.* **2015**, *162*, A5054.
- [179] S. Sundriyal, V. Shrivastav, M. Sharma, S. Mishra, A. Deep, *ChemSelect* **2019**, *4*, 2585.
- [180] W. Ye, H. Wang, J. Ning, Y. Zhong, Y. Hu, *J. Energy Chem.* **2021**, *57*, 219.
- [181] S. Balasubramaniam, A. Mohanty, S. K. Balasingam, S. J. Kim, *Nano Micro Lett.* **2020**, *12*, 85.
- [182] S. Zhang, D. Li, S. Chen, X. Yang, X. Zhao, Q. Zhao, S. Komarneni, D. Yang, *J. Mater. Chem. A* **2017**, *5*, 12453.
- [183] X. Xiong, L. Zhou, W. Cao, J. Liang, Y. Wang, S. Hu, F. Yu, B. Li, *CrystEngComm* **2017**, *19*, 7177.
- [184] L. Wang, Y. Han, X. Feng, J. Zhou, P. Qi, B. Wang, *Coord. Chem. Rev.* **2016**, *307*, 361.
- [185] M. Kaempgen, C. K. Chan, J. Ma, Y. Cui, G. Gruner, *Nano Lett.* **2009**, *9*, 1872.
- [186] P. Simon, Y. Gogotsi, *Nat. Mater.* **2008**, *7*, 845.
- [187] A. Deep, S. K. Bhardwaj, A. K. Paul, K. H. Kim, P. Kumar, *Biosens. Bioelectron.* **2015**, *65*, 226.
- [188] H. Nishihara, H. Itoi, T. Kogure, P. X. Hou, H. Touhara, F. Okino, T. Kyotani, *Chem.* **2009**, *15*, 5355.
- [189] G. Wang, L. Zhang, J. Zhang, *Chem. Soc. Rev.* **2012**, *41*, 797.
- [190] D. Giliopoulos, A. Zamboulis, D. Giannakoudakis, D. Bikiaris, K. Triantafyllidis, *Molecules* **2020**, *25*, 1.
- [191] Z. Xie, W. Xu, X. Cui, Y. Wang, *ChemSusChem* **2017**, *10*, 1645.
- [192] Y. Zheng, S. Zheng, H. Xue, H. Pang, *Adv. Funct. Mater.* **2018**, *28*, 1.
- [193] K. D. Fong, T. Wang, S. K. Smoukov, *Sustain. Energy Fuels* **2017**, *1*, 1857.
- [194] Y. Pan, K. Xu, C. Wu, *Nanotechnol. Rev.* **2019**, *8*, 299.
- [195] W. Yan, J. Su, Z. M. Yang, S. Lv, Z. Jin, J. L. Zuo, *Small* **2021**, *17*, 2005209.
- [196] J. Sun, L. Guo, X. Sun, J. Zhang, Y. Liu, L. Hou, C. Yuan, *J. Mater. Chem. A* **2019**, *7*, 24788.
- [197] W. Feng, J. Zhang, A. Yusuf, X. Ao, D. Shi, V. Etacheri, D. Y. Wang, *Chem. Eng. J.* **2022**, *427*, 130919.
- [198] Y. Zhang, Y. Li, X. Wang, X. Teng, L. Guan, H. Yang, Z. He, Y. Wan, S. Guo, H. Hu, M. Wu, *J. Mater. Chem. A* **2022**, *10*, 19852.
- [199] L. Shen, H. Lv, S. Chen, P. Kopold, P. A. van Aken, X. Wu, J. Maier, Y. Yu, *Adv. Mater.* **2017**, *29*, 1700142.
- [200] C. Leng, Z. Zhao, J. Guo, R. Li, X. Wang, J. Xiao, Y. V. Fedoseeva, L. G. Bulusheva, J. Qiu, *Chem. Commun.* **2021**, *57*, 8778.
- [201] Y. Wang, F. Yuan, Z. Li, D. Zhang, Q. Yu, B. Wang, *APL Mater.* **2022**, *10*, 030902.
- [202] D. Y. Lee, S. J. Yoon, N. K. Shrestha, S. H. Lee, H. Ahn, S. H. Han, *Microporous Mesoporous Mater.* **2012**, *153*, 163.
- [203] S. C. Wechsler, F. Z. Amir, *ChemSusChem* **2020**, *13*, 1491.
- [204] P. A. Shinde, Y. Seo, S. Lee, H. Kim, Q. N. Pham, Y. Won, S. Chan Jun, *Chem. Eng. J.* **2020**, *387*, 122982.
- [205] P. Du, Y. Dong, C. Liu, W. Wei, D. Liu, P. Liu, *J. Colloid Interface Sci.* **2018**, *518*, 57.

- [206] Z. Sun, L. Hui, W. Ran, Y. Lu, D. Jia, *New J. Chem.* **2016**, *40*, 1100.
 [207] H. Mei, Y. Mei, S. Zhang, Z. Xiao, B. Xu, H. Zhang, L. Fan, Z. Huang, W. Kang, D. Sun, *Inorg. Chem.* **2018**, *57*, 10953.
 [208] S. Maiti, A. Pramanik, S. Mahanty, *Chem. Commun.* **2014**, *50*, 11717.
 [209] Y. Z. Zhang, Y. Wang, Y. L. Xie, T. Cheng, W. Y. Lai, H. Pang, W. Huang, *Nanoscale* **2014**, *6*, 14354.
 [210] P. Zhou, J. Wan, X. Wang, K. Xu, Y. Gong, L. Chen, *J. Colloid Interface Sci.* **2020**, *575*, 96.
 [211] M. Yu, L. Zhang, X. He, H. Yu, J. Han, M. Wu, *Mater. Lett.* **2016**, *172*, 81.
 [212] Q. Wang, W. Xia, W. Guo, L. An, D. Xia, R. Zou, *Chem.* **2013**, *8*, 1879.
 [213] S. Zhong, C. Zhan, D. Cao, *Carbon* **2015**, *85*, 51.
 [214] Y. Gao, J. Wu, W. Zhang, Y. Tan, J. Gao, J. Zhao, B. Tang, *New J. Chem.* **2015**, *39*, 94.
 [215] J. Xu, Y. Wang, S. Cao, J. Zhang, G. Zhang, H. Xue, Q. Xu, H. Pang, *J. Mater. Chem. A* **2018**, *6*, 17329.
 [216] S. N. Guo, Y. Zhu, Y. Y. Yan, Y. L. Min, J. C. Fan, Q. J. Xu, H. Yun, *J. Power Sources* **2016**, *316*, 176.
 [217] G. Zhao, X. Xu, G. Zhu, J. Shi, Y. Li, S. Zhang, M. S. A. Hossain, K. C. W. Wu, J. Tang, Y. Yamauchi, *Microporous Mesoporous Mater.* **2020**, *303*, 110257.
 [218] S. N. Ansari, M. Saraf, A. K. Gupta, S. M. Mobin, *Chem.* **2019**, *14*, 3566.
 [219] M. S. Rahmanifar, H. Hesari, A. Noori, M. Y. Masoomi, A. Morsali, M. F. Mousavi, *Electrochim. Acta* **2018**, *275*, 76.
 [220] J. Wang, Q. Zhong, Y. Xiong, D. Cheng, Y. Zeng, Y. Bu, *Appl. Surf. Sci.* **2019**, *483*, 1158.



Rakhee Bhosale obtained her Master's degree (2016) in chemistry from the Department of Chemistry, Shivaji University, Kolhapur, India, and is currently a doctoral student in same department, with an emphasis on material science. Her research interests are focused on the synthesis, characterization, and application of self-assembled nanoparticles and nanocomposites, aiming at the improvement of their performances in energy storage, production, and conversion by synergistic effects.



Sneha Bhosale obtained her Master's degree (2019) in chemistry and is pursuing her doctoral studies at the Department of Chemistry, Shivaji University, Kolhapur, India. She has expertise in the synthesis of nanomaterials for exotics applications including biomedical, gas sensor, energy storage, etc. Her doctoral research area is in mesoporous carbon, the synthesis of metal oxide nanostructures, and its composites for biomedical applications.



Madagonda Vadiyar is currently working as brain pool postdoctoral fellow at the Department of Energy and Materials Engineering, Dongguk University, Seoul, South Korea. He received his Ph.D. (2017) in chemistry from Shivaji University, Kolhapur, India. In 2017, he joined as a postdoctoral researcher at Laurentian University, Sudbury, and later at Concordia University, Montreal, Canada. His current research interests are synthesizing metal/covalent organic frameworks, covalent triazine frameworks, and their derived materials for energy storage devices, particularly for the development of high-performance supercapacitors and batteries.



Chitra Jambhale obtained her Master's degree in 1992 and doctoral degree in 2018 from Shivaji University, India. She is a visiting researcher at the Department of Physics, The Ohio State University, Columbus, Ohio, USA (2018), where she carried out postdoctoral research in condensed matter physics. She is currently an assistant professor of physics at Sangola College, Sangola. Her current research interest is in the area of development of materials for supercapacitors.



Kyung-Wan Nam is a professor in the Department of Energy and Materials Engineering, at Dongguk University, Seoul, South Korea. He received his B.S. (1998), M.S. (2000), and Ph.D. (2005) in metallurgical engineering from Yonsei University, South Korea. In 2006, he joined the Chemistry Department of Brookhaven National Laboratory as a research associate and then became a staff scientist in 2009. His research is focused on energy storage materials (e.g., lithium- and sodium-ion batteries and supercapacitors) and revealing structure–property correlations of battery materials using various synchrotron X-Ray techniques, including in situ/ex situ X-Ray diffraction, X-Ray absorption spectroscopy (XAS), and pair distribution function (PDF) analysis.



Sanjay Kolekar is a senior professor of chemistry at Shivaji University, Kolhapur, India. He received his doctoral degree (2003) in chemistry from Shivaji University, India. He is invited scientist at Chonnam National University as brain pool Fellow, National Research Foundation, South Korea, and is visiting professor at Hanyang University, South Korea. He has been invited as Member on European Research Council and is Scientific Expert, Ministry of Education, Universities and Research, Rome, Italy. For his research in specialized area, he has been awarded National Level “Mid-Career Award” by University Grants Commission, India. His research group interests include the synthesis of ferrite materials and metal–organic framework (MOF) nanostructures for their applications in supercapacitors and battery; synthesis of nanocrystals and colloidal quantum dots; and their applications in water splitting.

Construction of Well-Defined Two-Dimensional Architectures of Trimetallic Metal–Organic Frameworks for High-Performance Symmetric Supercapacitors

Rakhee Bhosale, Sneha Bhosale, Dattatray Narale, Chitra Jambhale, and Sanjay Kolekar*



Cite This: *Langmuir* 2023, 39, 12075–12089



Read Online

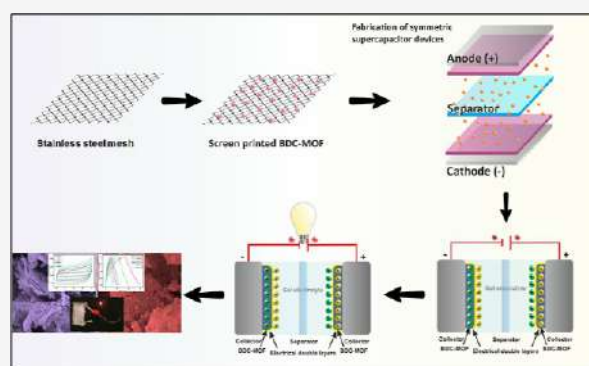
ACCESS |

Metrics & More

Article Recommendations

Supporting Information

ABSTRACT: The high surface-to-volume ratio and extraordinarily large-surface area of two-dimensional (2D) metal–organic framework (MOF) architectures have drawn particular interest for use in supercapacitors. To achieve an excellent electrode material for supercapacitors, well-defined 2D nanostructures of novel trimetallic MOFs were developed for supercapacitor applications. Multivariate MOFs (terephthalate and trimesate MOF) with distinctive nanobrick and nanoplate-like structures were successfully synthesized using a straightforward one-step reflux condensation method by combining Ni, Co, and Zn metal species in equimolar ratios with two different ligands. Furthermore, the effects of the tricarboxylic and dicarboxylic ligands on cyclic voltammetry, charge–discharge cycling, and electrochemical impedance spectroscopy were studied. The derived terephthalate and trimesate MOFs are supported with stainless-steel mesh and provide a suitable electrolyte environment for rapid faradaic reactions with an elevated specific capacity, excellent rate capability, and exceptional cycling stability. It shows a specific capacitance of 582.8 F g^{-1} , a good energy density of $40.47 \text{ W h kg}^{-1}$, and a power density of 687.5 W kg^{-1} at 5 mA cm^{-2} with an excellent cyclic stability of 92.44% for 3000 charge–discharge cycles. A symmetric BDC–MOF//BDC–MOF supercapacitor device shows a specific capacitance of 95.22 F g^{-1} with low capacitance decay, high energy, and power densities which is used for electronic applications. These brand-new trimetallic MOFs display outstanding electrochemical performance and provide a novel strategy for systematically developing high-efficiency energy storage systems.



INTRODUCTION

Over the past few decades, the need to develop clean and sustainable energy has become extremely urgent due to the increasing requirement for clean energy and solving serious environmental problems.¹ Nowadays, much research is focused on current renewable energy storage devices in order to minimize pollution and raise worries about future energy problems.^{2,3} Under some environmental circumstances, it is challenging to produce power from sustainable energy sources (biomass, hydro, solar, wind, etc.), which causes an imbalance between the supply and demand of energy. In order to balance and equalize energy needs, energy storage devices must be integrated with energy production, which is crucial for a renewable energy supply.^{4,5} Because of their excellent energy capability and clean electrical systems, electrochemical energy storage equipment have gained widespread interest. One energy storage device that stands out above most of the others is the supercapacitor, which shows the utmost characteristics like high energy density, fast charging/discharging process, and excellent cycle stability, and also they are feasibly used in many fields.^{6–8} The energy storage mechanism is non-identical for every class because of the different materials used within the

components.⁹ It is broadly confessed that the features of electrode materials like structure, morphology, electronic conductivity, electrochemical activity, and chemical and mechanical stability all put up to their electrochemical performance.^{10,11} Transition metals have fascinated ample interest for many energy storage devices due to their good physical and chemical characteristics, high conductivity, improved redox activity, and long cycle stability.¹² The supercapacitor's performance is also affected by the electrolyte utilized. Electrolytes are important and necessary components of supercapacitors. Due to their physical and chemical characteristics, they have a significant impact on the electrochemical performances of specific capacity, energy density, power density, rate capability, cycle stability, and safety. In comparison to aqueous electrolytes, the solid-state electrolyte

Received: May 18, 2023

Revised: July 31, 2023

Published: August 14, 2023



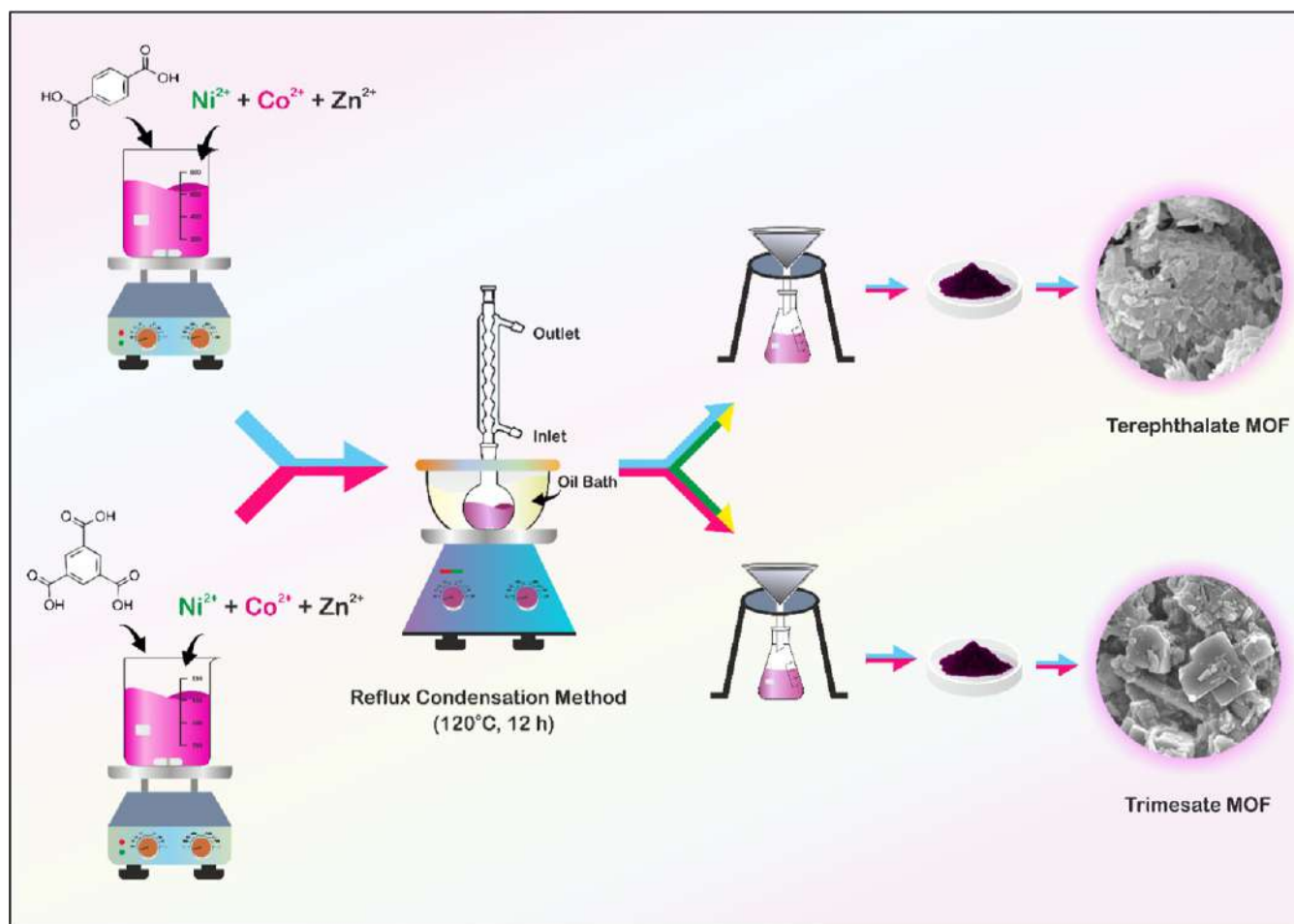


Figure 1. Schematic illustrations of the synthesis of trimetallic MOFs.

is a crucial element that might significantly affect the capacitance retention and stability of supercapacitors. Liquid electrolytes possess some limitations like leakage problems, and it shows low electrochemical performance. Gel polymer electrolytes (GPEs) are the most commonly used solid-state electrolytes in solid-state supercapacitors due to their relatively high ionic conductivity, improved interfacial contacts between electrodes and GPE, broad operating potential range, higher ion transfer number, and improved stability.^{13,14}

Metal–organic frameworks (MOFs) have emerged as attractive prospects in a variety of sectors in recent years due to structural and electrical properties such as high porosity, excellent specific surface area (SSA), high stability, and adjustable arrangement of active sites. Owing to the structural and electronic features of MOFs, they are employed in supercapacitors. MOFs show pseudocapacitive nature because of the oxidative–reductive behavior of positively charged metal ions inside MOFs which create channels for electrons as well as show electric double layer capacitor (EDLC) behavior due to the organic linker structure which promotes charge transfer inside the framework which leads to the EDLC behavior.^{15,16} MOFs are formed at the micro/nanosize using central metal nodes and organic linkers, resulting in one-dimensional (1D), two-dimensional (2D) structures, and three-dimensional superstructures.^{17,18} In the exploration of advanced materials with enhanced characteristics over standard MOFs, the tendency is to encourage synergistic effects succeeding from the existence of two or more metals in multimetallic MOFs.¹⁹

In comparison to monometallic MOFs, the multimetallic MOFs have many advantages including strong chemical reactivity, improved electronic charge transfer, a variety of morphologies, high selectivity and sensitivity, virtue, strain in the lattice, different geometric impacts, and chemical change.^{20–24} Due to the excellent properties of MOFs, the electrochemical performance of supercapacitors is enhanced by their ability to store a huge quantity of charge and by encouraging the dissemination of electrolyte ions. As a result, MOFs have received a lot of interest when it comes to the use of supercapacitor electrode materials.²⁵ The limitations of the monometallic MOFs have been overcome by multimetallic MOFs which have advantages like the synergic effect which enhance the redox reactions and electrical conductivity. Also, the presence of various metal centers enhances the electroactive sites for ion transfer and helps the interaction with electrolyte in the course of the electrochemical reactions. The advancement of an perfect and beneficial electrode material composed of non-noble metals with remarkable steadiness and nature depicts the key challenge in these areas.^{26–28} As an outcome, a considerable study has been performed to reduce the obstacles caused by MOF's low conductivity and structural configuration. The direct application of MOF-based materials for effective supercapacitors remains difficult, despite the significant advances made in manufacturing MOF-based materials for energy storage applications.²⁹ Nagaraju et al. put together binder-free Ni–Co–Mn-based MOFs via a polarity-induced solution-phased technique. Dual-layered

Ni–Co–Mn-based MOFs with versatile features demonstrated the highest capacity of 1311.4 A h cm⁻² at a 5 mA cm⁻² current density with high capacitance retention of about 86.1% after applying 4000 cycles in the aqueous alkaline electrolyte. Additionally, they have created a pouch-type supercapattery with a bilayered Ni–Co–Mn-based MOF/Ni foam as an anode and nitrogen-oxygen-enriched activated carbon/Ni foam as a cathode. This device exhibits good cycling durability due to the high capacity of the supercapattery retained at 90.1% and the good Faradaic efficiency of 98.6%. Furthermore, they created a pouch-type supercapattery using bilayered Ni–Co–Mn-based MOF/Ni foam as an anode and nitrogen-oxygen-enriched activated carbon/Ni foam as a cathode, resulting in a supercapattery with a high capacity retention of 90.1% and an exceptional Faradaic efficiency of 98.6%, illustrating the device's great cycling longevity.³⁰ Andikaey et al. prepared a new nanocomposite mesoporous ordered silica SBA-15/MWCNTs embellished with a trimetallic organic framework (NiCoCu-BTC) using a facile, cost-effective one-step solvothermal technique. The synthesized nanocomposite exhibited outstanding electrochemical performance having a remarkable 868 C g⁻¹ (2067 F g⁻¹) specific capacity at a 1 A g⁻¹ current density with great cycling durability. Additionally, they have fabricated an asymmetric supercapacitor device with a high energy density 52.4 W h kg⁻¹ at a power density of 1124 W kg⁻¹ with high capacitance retention of about 87.2% after applying 5000 cycles.³¹

In view of this, we present the synthesis of trimetallic MOFs for high-performance symmetric supercapacitors by applying two different organic linkers, i.e., trimesic acid and terephthalic acid. To the finest of our information, this is the primary report in which a comparative study of two MOFs is carried out only by changing the organic linker, and they are used as dynamic anode materials for supercapacitors. The physico-chemical properties of both the trimetallic MOFs were thoroughly investigated by using different characterization techniques. In addition, a symmetric supercapacitor shows a high energy density and great chemical steadiness in a 2 M KOH electrolyte.

■ EXPERIMENTAL SECTION

Synthesis of MOFs. All chemicals used to synthesize trimetallic MOFs were obtained from Loba Chemie (India) and were used without further purification. The trimetallic Ni–Co–Zn–BDC MOFs (BDC–MOF) were prepared using a single-step reflux condensation method. In a typical synthesis, 0.415 g of terephthalic acid (BDC), 0.363 g of nickel nitrate hexahydrate, 0.363 g of cobalt nitrate hexahydrate, and 0.371 g zinc nitrate hexahydrate were dissolved step by step in 30 mL of *N,N*-dimethylformamide with continuous stirring at ambient temperature.

After which, the reaction mixture was transferred to a 50 mL round-bottom flask. The reaction mixture was kept at 120 °C for 12 h to produce the BDC–MOF sample and then cooled at ambient temperature. The final precipitate was carefully washed a few times with alcohol. Finally, the purple-colored product was air-dried for 12 h at 80 °C. A similar procedure was adopted for the synthesis of trimetallic Ni–Co–Zn–BTC MOF (BTC–MOF), except that terephthalic acid was replaced with trimesic acid. A schematic illustration for the synthesis of trimetallic MOFs by the reflux condensation method is shown in Figure 1.

Structural and Elemental Characterization. The crystal structure and phase purity of the synthesized trimetallic MOFs were confirmed by the X-ray diffraction (XRD) technique [Bruker D8 Phaser X-ray diffractometer with Cu K α radiation ($\lambda = 1.541 \text{ \AA}$)]. The types of bonding and functional groups were analyzed by Fourier

transform infrared (FT-IR) spectroscopy (PerkinElmer 1760X spectrophotometer). The Raman spectrometer (LabRAM HR Evolution Confocal Raman Microscope, France) was used for point group analysis. The morphology of the as-prepared materials was investigated by scanning electron microscopy (SEM) (JEOL-JSM 6360, Japan). The elemental composition of the trimetallic MOFs was examined using an energy-dispersive X-ray analysis (EDAX) spectrometer [Oxford Instrumentations inbuilt with field emission (FE-SEM)]. The elemental oxidation state and chemical composition of the as-prepared materials were investigated by X-ray photoelectron spectroscopy (XPS) with a K-alpha (Thermo VG, UK) spectrometer and a monochromatic Al X-ray source (AlK α line: 1486.6 eV, 3 mA, and 12 kV). The surface area and pore size were determined by Brunauer–Emmett–Teller (BET) (NOVA1000e Quantachrome, USA).

Electrochemical Measurements with a Three-Electrode Assembly. Electrochemical measurements were performed on a CHI608 electrochemical analyzer (CH Instruments Inc, Austin, USA). A standard three-electrode assembly in a 2 M KOH electrolyte was used to explore the electrochemical characteristics of a constructed electrode. A saturated Ag/AgCl was used as a reference electrode, graphite as the counter electrode, and trimetallic MOF-loaded stainless-steel mesh as the working electrode. The working electrode was fabricated by making a paste of 80 wt % of active materials (BDC–MOF and BTC–MOF), 10 wt % of carbon black (Super P) as a conducting material, and 10 wt % of polyvinylidene fluoride (PVDF) as a binder in the *N*-methyl-2-pyrrolidone (NMP) solvent. This paste was applied to a stainless-steel mesh measuring with size about 1 cm² and then air-dried for 12 h at 80 °C. With the help of electrochemical workstation, cyclic voltammetry (CV), galvanostatic charge–discharge (GCD), and electrochemical impedance spectroscopy (EIS) studies were carried out. In the frequency range of 1 Hz to 100 kHz, the EIS test was conducted. According to eq 1, specific capacitance of the prepared samples was determined.

$$C = \frac{I \times \Delta t}{\Delta V \times m} \quad (1)$$

where “*C*” stands for the specific capacitance measured in F g⁻¹, “*I*” stands for the current measured in mA, “ Δt ” stands for the discharging time measured in seconds, “ ΔV ” stands for the potential window measured in volt, and “*m*” stands for the mass of the active electrode material measured in mg.

Electrochemical Measurements of the Symmetric Supercapacitor. A solid-state symmetric supercapacitor (SSC) device was constructed by stainless-steel mesh substrates with size about 2 cm coated with the BDC–MOF, and a thick layer of polyvinyl alcohol (PVA)–KOH was sandwiched in between them. The device was allowed to naturally dry out overnight at ambient temperature. As per literature report, the PVA–KOH gel electrolyte was prepared.³² Using a conventional method, 1 g of PVA was dissolved in 20 mL of distilled water while the bath solution temperature was held at 80 °C for 30 min. To create the viscous gel electrolyte, the PVA solution was combined with the aqueous KOH solution dropwise and heated once more at 80 °C for 30 min.

Using 2, the specific capacitance, energy density, and power density of the symmetric supercapacitor were computed, respectively.^{33,34}

$$C_s = \frac{I \times \Delta t}{\Delta V \times M} \quad (2)$$

$$E = \frac{0.5 \times C \times \Delta V^2}{3.6} \quad (3)$$

$$P = \frac{E \times 3600}{\Delta t} \quad (4)$$

where “*C_s*” stands for the specific capacitance measured in F g⁻¹, “*E*” stands for the specific energy measured in W h kg⁻¹, “*P*” stands for the specific power measured in W kg⁻¹, and “*M*” stands for the total mass of the two electrodes measured in mg.

RESULTS AND DISCUSSION

The crystallographic structure and crystallite size of the trimetallic BDC–MOF and BTC–MOF were found by using the XRD pattern, and the results are presented in Figure 2. For the BDC–MOF, the peak located at an angle 10.0° is

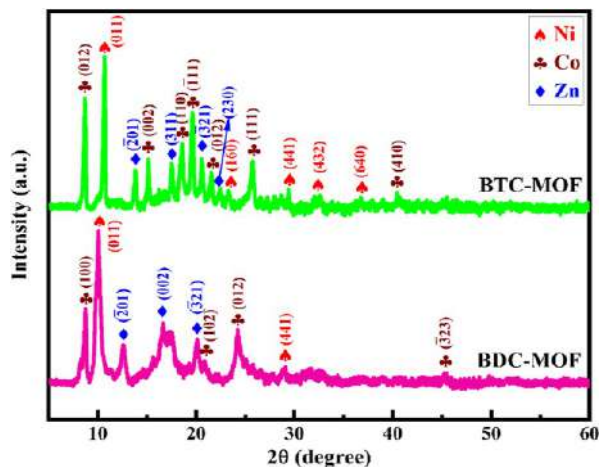


Figure 2. XRD patterns of BDC–MOF and BTC–MOF.

indexed to the (011) plane of Ni (PDF no. 10-0735), the diffraction peak at 8.7° is attributed to the (100) plane of Co (PDF no. 19-1523), and the diffraction peak at 16.6° is attributed to the (002) plane of Zn (PDF no. 01-0037). While for the BTC–MOF, the peak located at 10.6° is indexed to the (011) plane of Ni (PDF no. 10-0735), the diffraction peak at 8.7° is attributed to the (100) plane of Co (PDF no. 13-0733), and the diffraction peak at 17.5° is attributed to the (311) plane of Zn (PDF no. 01-0037), respectively, indicating that these MOFs have the similar structure.^{35,36} Furthermore, the crystallite size was determined using Debye–Scherrer’s formula, as shown in eq 5.³⁷

$$D = \frac{0.9\lambda}{\beta \cos \theta} \quad (5)$$

where “ D ” stands for the average crystallite size, “ λ ” stands for the wavelength of the X-rays, “ β ” stands for the full-width half-maxima (fwhm), and “ θ ” stands for Bragg’s diffraction angle. According to the XRD spectra, the trimetallic BDC–MOF and BTC–MOF derived from the (011) plane have average crystallite sizes of 3.55 and 5.97 nm, respectively.

The identification of the functional group of the BDC–MOF and BTC–MOF was obtained by using the FT-IR spectra. Trimetallic MOF FT-IR spectra are shown in Figure 3. The bands at 3351 and 3310 cm^{-1} were caused by moisture-induced O–H stretching vibrations in BDC–MOF and BTC–MOF, respectively. Aromatic C=C in plane vibrations are assigned to the bands at 1647 and 1609 cm^{-1} . The asymmetric stretching vibration of the coordinated (–COO–) group displays the peak at 1436 cm^{-1} , while the symmetric stretching vibrations show the peak at 1361 cm^{-1} . In BDC–MOF, the sp^2 carbon stretching vibration peaks of C=O due to the carboxylic group are displayed at 1677 cm^{-1} , and the peak at 1575 cm^{-1} represents the aromatic C=C in-plane vibrations. The C–H bending vibrations of CH_3 and CH_2 are represented by the prominent adsorption peaks at 1373 and 1287 cm^{-1} , respectively. The in-plane and out-of-plane C–H bending modes are allocated to several bands in the ranges of 1200 –

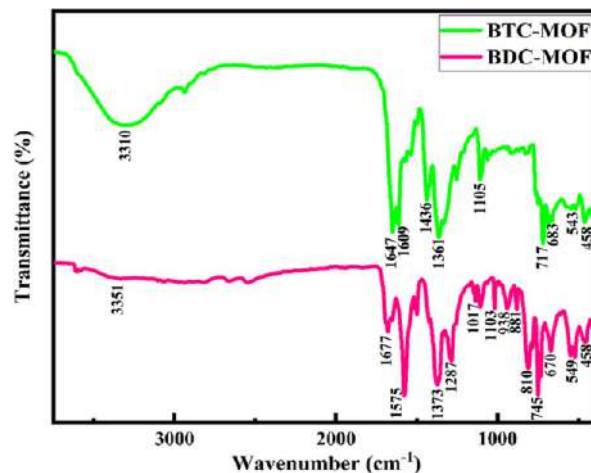


Figure 3. FT-IR spectra of BDC–MOF and BTC–MOF.

1000 and 1000 – 700 cm^{-1} , respectively. Multiple bands in the range of 700 – 400 cm^{-1} are assigned to the metal–oxygen bands.^{38,39}

The bond vibration of trimetallic MOFs was confirmed by Raman spectroscopy, as seen in Figure 4. The peaks of

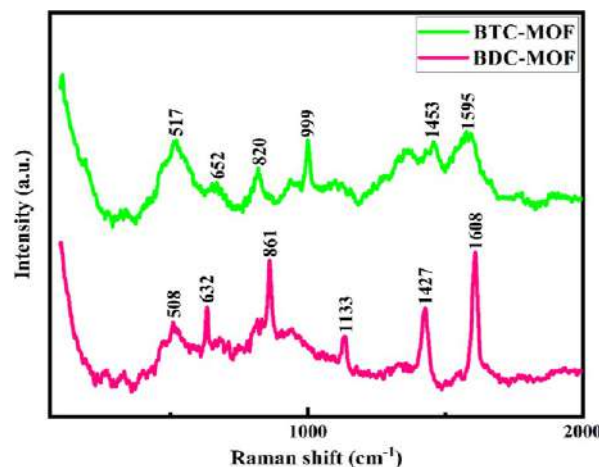


Figure 4. Raman spectra of BDC–MOF and BTC–MOF.

trimetallic MOFs correlate to different bands, confirming the existence of the BDC and BTC moieties in the material. The Raman spectra of BDC–MOF and BTC–MOF displayed a $\nu(\text{C}=\text{C})$ modes of the benzene ring observed at 1133 and 999 cm^{-1} , respectively, and the observed peaks at the low-frequency region of 500 – 850 cm^{-1} correspond to benzene ring C–H bending modes and the presence of metal–oxygen bond vibration, respectively.^{40,41} In BDC–MOF, the vibrational modes of $\nu_{\text{as}}(\text{COO}^-)$ and $\nu_{\text{s}}(\text{COO}^-)$ were noticed as doublets at 1608 and 1427 cm^{-1} in BDC–MOF, and the vibrational modes of $\nu_{\text{as}}(\text{COO}^-)$ and $\nu_{\text{s}}(\text{COO}^-)$ were noticed as doublets at 1595 and 1453 cm^{-1} in BTC–MOF, respectively, and these findings point to the synthesis of trimetallic MOFs, which was previously supported by FT-IR data.^{42,43}

SEM was used to study the surface morphology of BTC–MOF and BDC–MOF. The influence of the trimesic and terephthalic ligands on the formation of surface morphology for MOF was examined. Figure 5 reveals the surface morphological images of BTC–MOF and BDC–MOF with

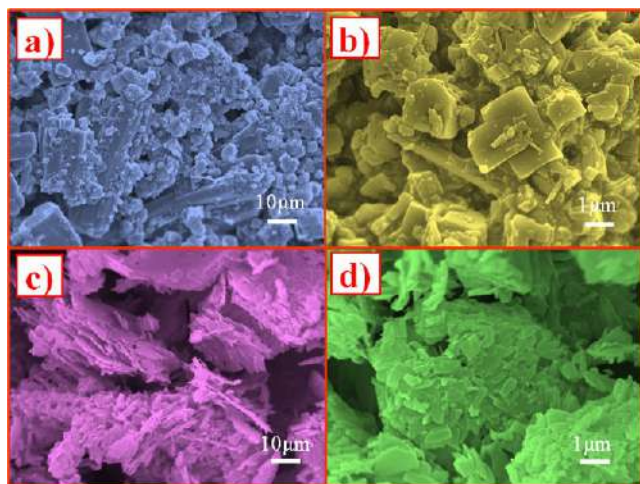


Figure 5. SEM images of BTC-MOF (a,b) and BDC-MOF (c,d) at different magnifications.

different magnifications. From Figure 5a,b, it has been observed that the small nanoparticles start to construct the nanobrick-like morphology of BTC-MOF, and nanobricks were observed all over area of the sample which are randomly distributed in the sample. The width of the nanobricks was observed from 200 to 300 nm in size. It was noticed that nanobricks are interconnected to each other, and also the edges of the nanobricks are mingling with one another; hence, the nanobricks are found to be cut in small pieces, which are responsible for the irregular shapes of nanobricks formed in the BTC-MOF sample. Additionally, some of the spacing between two nanobricks is seen in the BTC-MOF sample, which is helpful for adsorbing the electrolyte and boosts the material-specific capacitance. It is seen that the variation of ligands in MOF samples has a great impact on the characteristic morphology of MOF samples. Here, it is observed that with change in the ligands, there was a change in the surface morphology of MOF samples.

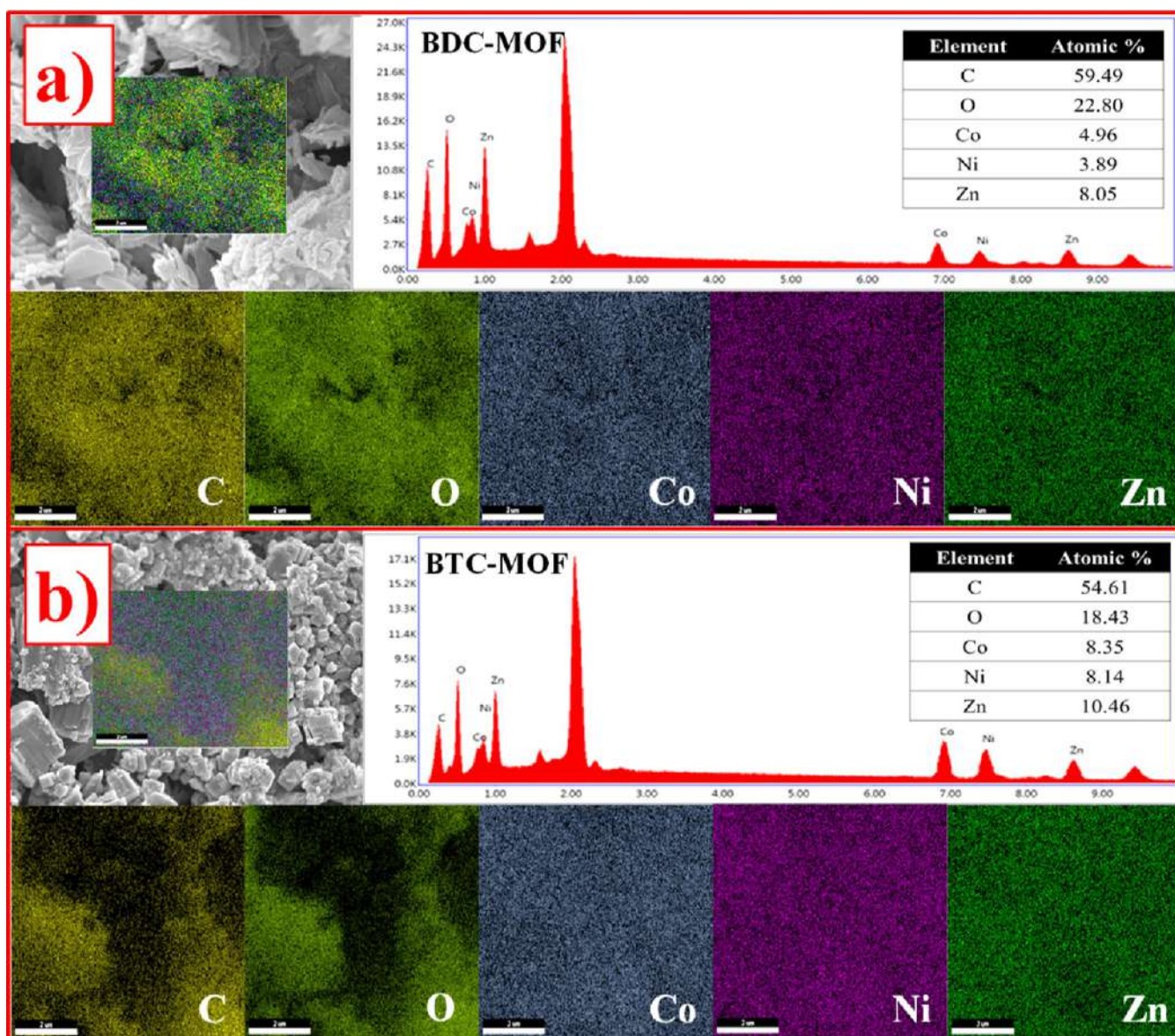


Figure 6. EDX spectra and elemental mapping of C, O, Co, Ni, and Zn elements for (a) BDC-MOF and (b) BTC-MOF.

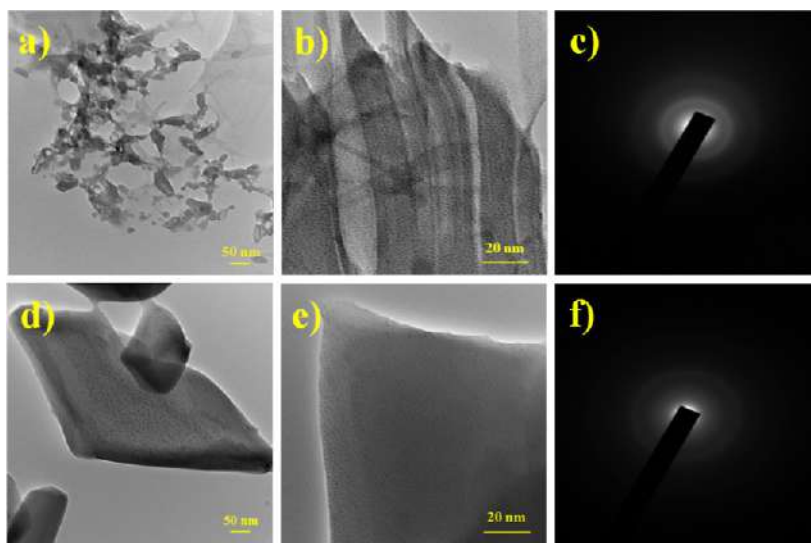


Figure 7. TEM, HR-TEM, and SAED pattern of (a) BDC-MOF and (b) BTC-MOF.

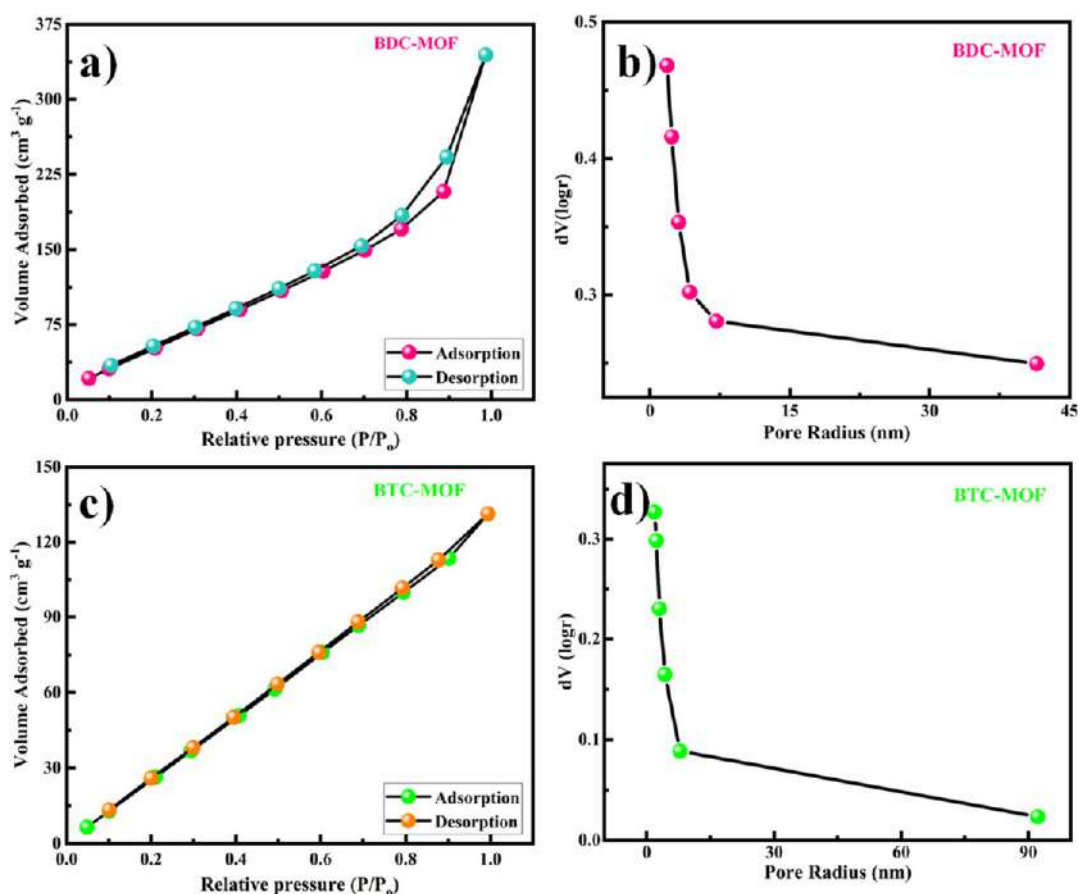


Figure 8. (a,b) N₂ adsorption–desorption isotherm and BJH pore size distribution curve of BDC-MOF. (c,d) N₂ adsorption–desorption isotherm and BJH pore size distribution curve of BTC-MOF.

The sample BDC-MOF demonstrated the nanoplatform-like morphology with irregular arrangement of the nanoplatforms occurring throughout the sample. Some of the nanoplatforms were formed together, leading to big porous bricks which are shown in Figure 5c,d. The thickness of the nanoplatforms was observed in the nanometer range, and a bunch of the nanoplatforms formed the brick-like morphology, hence increasing the surface area of the sample. The bunch of nanoplatforms provides a larger SSA for

the adsorption of the electrolyte increasing the specific capacitance of the sample. The surface area of BDC-MOF is the greatest of the two samples examined in the BET investigation. Also, SEM outcomes are in good agreement with BET analysis. Hence, among these two samples, BDC-MOF executes a good electrochemical performance.

The EDAX of both the trimetallic MOFs is presented in Figure 6. Figure 6 demonstrates that the elements Ni, Co, Zn,

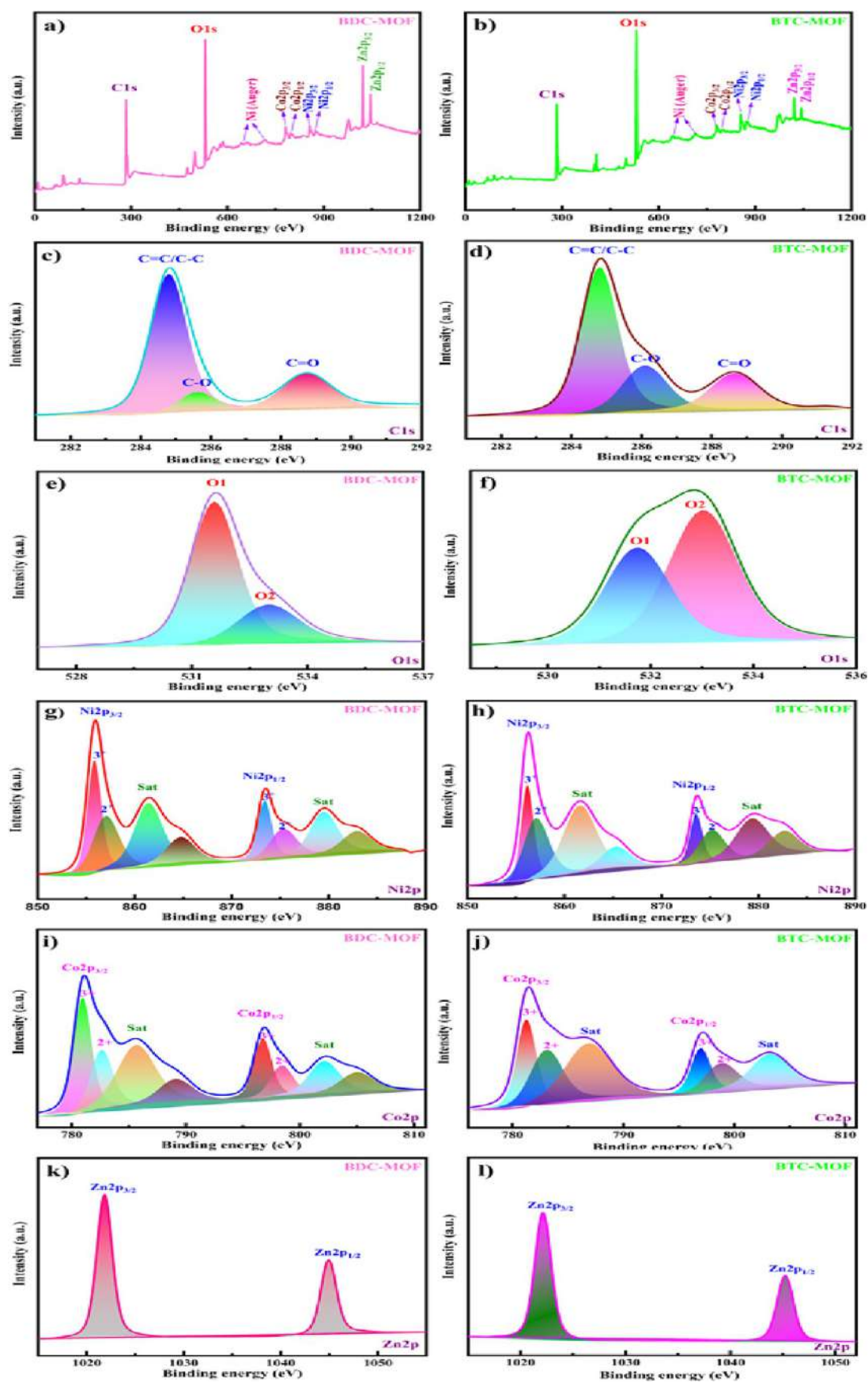


Figure 9. XPS survey spectra of BDC–MOF (a) and BTC–MOF (b), high-resolution spectra of C 1s (c,d), O 1s (e,f), Ni 2p (g,h), Co 2p (i,j), and Zn 2p (k,l) of BDC–MOF and BTC–MOF, respectively.

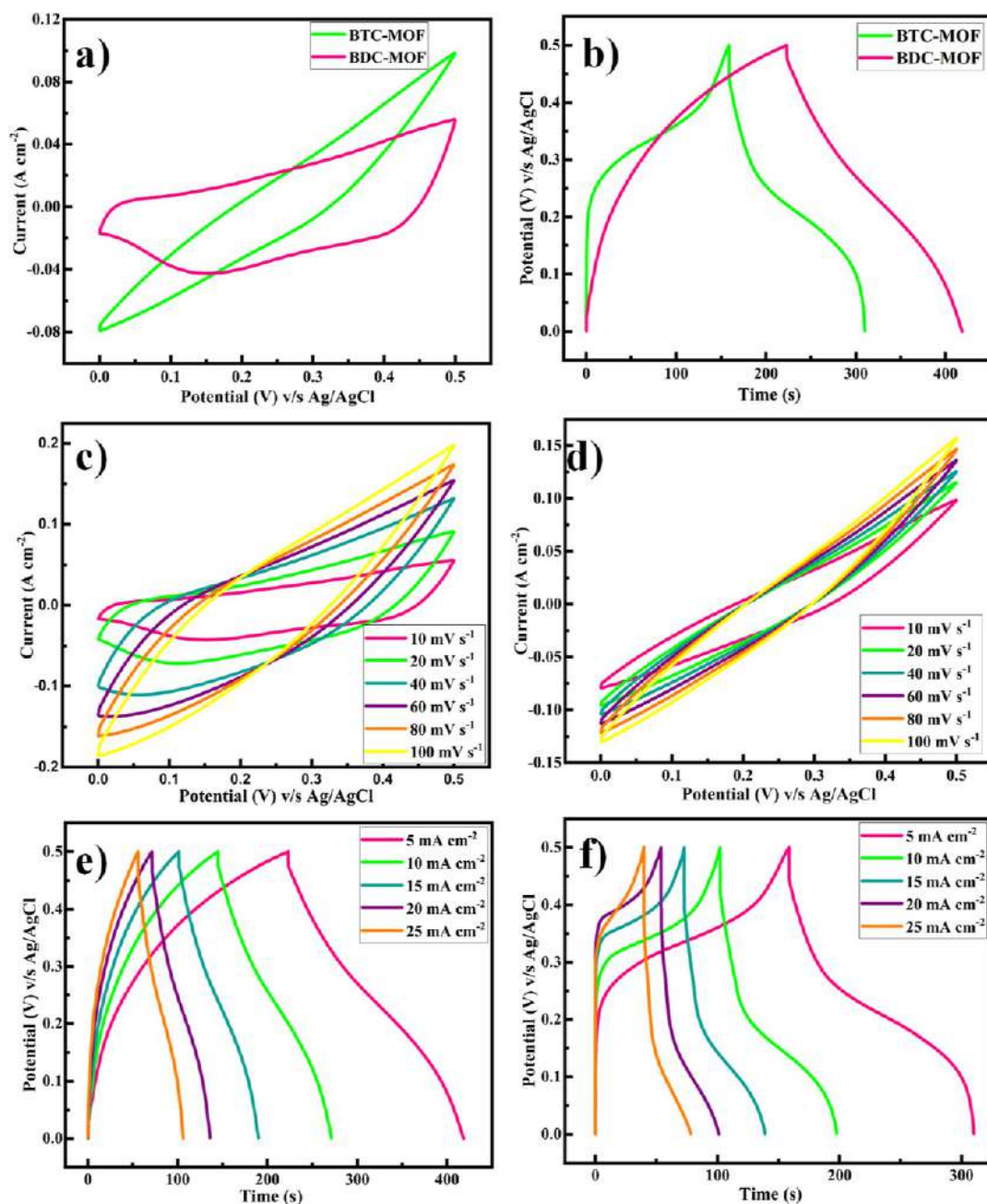


Figure 10. (a) Comparative CV curves at 10 mV s^{-1} scan rate, (b) comparative GCD curves at 5 mA cm^{-2} current density, (c) CV curves of BDC-MOF at different scan rates, (d) CV curves of BTC-MOF at different scan rates, (e) GCD curves of BDC-MOF at different current densities, and (f) GCD curves of BTC-MOF at different densities.

C, and O are distributed evenly throughout the sample, which confirms the presence of three metal ions in the MOFs as well as maintained the stoichiometry of the samples; hence, it proved that the trimetallic MOFs were obtained. The SSA and pore diameter of the MOF samples were obtained by using BET analysis.

Transmission electron microscopy (TEM) examination was performed to have a better understanding of the structure of the as-prepared nanomaterials. Figure 7a depicts a typical TEM image of BDC-MOF with a 2D nanoplate-like shape with many voids. Furthermore, the high-resolution TEM (HRTEM) image of BDC-MOF (Figure 7b) confirms an amorphous nature due to the lack of apparent lattice fringes and no indication of crystallinity, representing that the particles

were amorphous. The selected area electron diffraction (SAED) pattern (Figure 7c) consistently exposed only diffuse rings, confirming the amorphous nature of the as-synthesized BDC-MOF particles. Figure 7d shows a typical TEM image of a 2D nanobrick-like morphology of BTC-MOF. The HRTEM image of BTC-MOF (Figure 7e) disseminated that the particles were amorphous due to the lack of visible lattice fringes and no evidence of crystallinity, suggesting that the particles were amorphous. The SAED pattern (Figure 7f) consistently displayed only diffuse rings, confirming the amorphous nature of the BTC-MOF particles as synthesized.

N_2 adsorption/desorption measurements confirmed the porous structure of the obtained MOFs, and the corresponding isotherms are shown in Figure 8. Before adsorption measure-

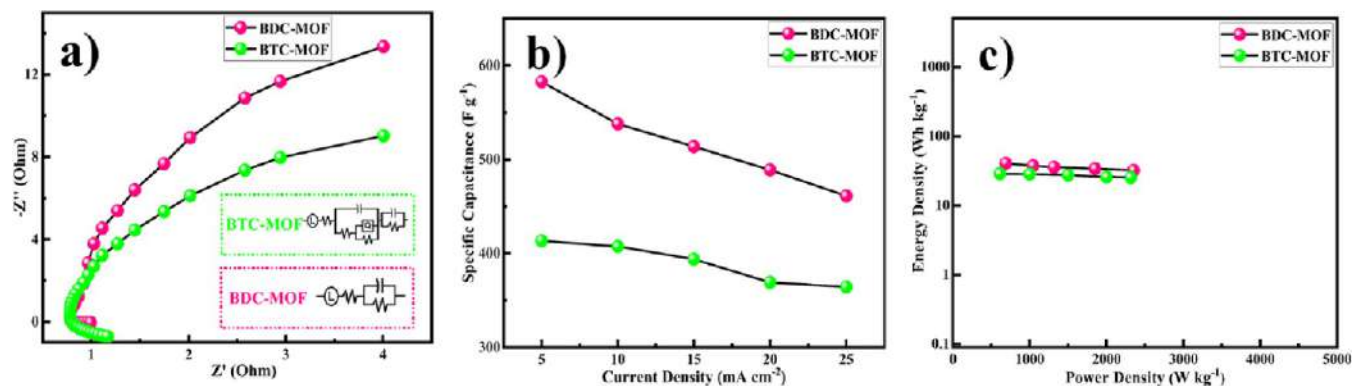


Figure 11. (a) Nyquist plots (inset electrical equivalent circuit), (b) variation of specific capacitance as a function of current density, and (c) Ragone plot showing the energy density versus power density.

ments, MOF samples were outgassed at 100 °C for 4 h. BDC–MOF and BTC–MOF had SSA of 267.85 and 216.93 $\text{m}^2 \text{g}^{-1}$, respectively. The average pore size of BDC–MOF and BTC–MOF was found to be 16 and 31 nm simultaneously, which is obtained from the BJH curve. According to the IUPAC classifications, the BDC–MOF and BTC–MOF isotherms are types IV and II, respectively,⁴⁴ clearly indicating that the BDC–MOF have a larger SSA than the BTC–MOF. The SSA and average pore radius values agree well with the crystallite size determined by XRD and the specific capacitance determined by electrochemical performance study.

The chemical composition and oxidation states of trimetallic MOFs were obtained by using XPS and explored the charge-transfer mechanisms in the valence state of the Ni, Zn, and Co ions of trimetallic MOFs along with the synergetic effect of its species. Figure 9a,b shows the survey spectra of both trimetallic MOFs. The core level spectra of C 1s, Ni 2p, Co 2p, O 1s, and Zn 2p of both the trimetallic MOFs are depicted in Figure 9c–i. As seen in Figure 9a,b, the existence of trimetallic MOFs was attributed by the XPS full survey scan spectrum, which contained the signals of the elements Ni, Co, O, C, and Zn. Figure 9c,d reveals the C 1s spectra of both the MOFs. It consists of distinct peaks caused by benzene rings from the BDC and BTC ligands with binding energy 284.7 and 284.8 eV, respectively. Then, carboxylate rings from the (–C=O) groups of the organic ligand with binding energy 288.7 and 288.6 eV, respectively, of both the MOFs and the species –C–O with a binding energy of 285.5 and 286.0 eV are shown. Furthermore, the O 1s spectra of BDC and BTC MOF are presented in Figure 9e,f, which includes two oxygen peaks denoted as O1 and O2. The first fitted peak at a 531.5 and 531.6 eV binding energy is related to the presence of metal–oxygen bond, i.e., oxygen atoms on the Ni, Co, and Zn–O bonds of both the MOFs, and the second fitted peak at 532.9 eV binding energy is associated with the carboxylate moiety of the organic ligand of MOF samples.⁴⁵ The Ni 2p emission spectrum shows two distinct nickel species, Ni^{2+} and Ni^{3+} . The Ni 2p spectra were deconvoluted into two spin–orbit doublets (Ni 2p_{1/2} and Ni 2p_{3/2}) and two satellite peaks using the Gaussian fitting method, as shown in Figure 9g,h. The peak fitted at binding energies of 855.9 and 873.4 eV are ascribed to Ni 2p_{3/2} and Ni 2p_{1/2} for BDC–MOF. Similarly, the binding energies of Ni 2p_{3/2} and Ni 2p_{1/2} for BTC–MOF are 856.2 and 873.6 eV, respectively, as illustrated in Figure 9h. The spin–orbital energy of the Ni peaks in two MOF slightly differs. First, the binding energy difference between these two

peaks is determined to be 17.5 eV for BDC–MOF, and the binding energy peak of the “Ni” element was shifted at lower binding energy, i.e., 17.4 eV may be due to the acidic behavior for BTC MOF.

The satellite peaks, as shown in Figure 9i,j, indicate two types of Co species, comprising Co^{2+} and Co^{3+} for two spin–orbit doublets (Co 2p_{1/2} and Co 2p_{3/2}), which were observed as a result of fitting the Co 2p emission spectra of both the MOFs. The fitted peaks with binding energy of 781.0 and 796.8 eV indicate the Co 2p_{3/2} and Co 2p_{1/2}, respectively, for the BDC–MOF sample. The Co peak spin–orbital energies in two MOFs varied slightly from one another. For BDC–MOF, the binding energy difference between these two peaks spin–orbital coupling is found to be 15.8 eV, and the “Co” element’s binding energy peak was relocated to a lower binding energy for BTC MOF, i.e., 15.7 eV. Again the peaks at 781.4 and 797.1 eV are associated to the Co 2p_{3/2} and Co 2p_{1/2} for the BTC–MOF sample. The other satellite peaks of Co elements for both the MOFs samples are also observed in Figure 9i,j.^{46–48} The peaks at binding energy 1021.8 and 1022.0 eV are assigned to the energy level Zn 2p_{3/2} in BDC–MOF and BTC–MOF, respectively. Similarly, the peaks at 1044.8 and 1045.1 eV are observed for Zn 2p_{1/2} for BDC–MOF and BTC–MOF, respectively. The detailed deconvolution peaks of Zn 2p_{3/2} and Zn 2p_{1/2} are observed in Figure 9k,l. The differences between the spin–orbital energy of both the MOF samples are nearly equal, confirming that prepared samples are well matched with the literature value of XPS.^{49–51} The calculated binding energy difference among these two peaks spin–orbital coupling is 23 eV, which is in good accordance with the literature value. Moreover, the difference between the spin–orbital energy of the BTC–MOF sample is slightly changed which may be due to the more acidic nature of the BTC–MOF sample.

The electrochemical characteristics of the MOF samples were assessed to determine their suitability for usage as active materials in supercapacitors. CV measurements of the as-synthesized MOF hybrid structures with various organic ligands (trimesic acid and terephthalic acid) were performed in a 2 M KOH electrolyte in a potential sweep window of 0–0.5 V, as shown in Figure 10. The CV curves of trimetallic MOFs reveal that the integral areas change throughout the operating potential range at 0–0.5 V, indicating that the charge storage mechanism is both pseudocapacitive and electric double layer type. The capacitance is mostly due to the charge stored at the electrode–electrolyte interface. The region

beneath the CV curve of BDC–MOF is larger than that of BTC–MOF, as shown in Figure 10a.

In the potential range of 0–0.5 V, the GCD profiles (Figure 10b) were examined at a current density of 5 mA cm⁻². As predicted, compared to the BTC–MOF electrode, the BDC–MOF electrode displayed a significantly longer charge/discharge time and increased specific capacitance. A comparison of the CV curves of both trimetallic MOFs, i.e., BDC–MOF and BTC–MOF (Figure 10c,d) at a different scan rate was performed in the potential range of 0–0.5 V. As the scan rate decreases, the area under the CV curve decreases; hence, specific capacitance increases. This occurs due to the complete diffusion of electrolyte ions into the electrode material at slower scan rates. Hence, a charge on the whole active surface of the electrode material may be stored. Only the superficial active surface is used for charge storage at a higher scan rate because diffusion limits the passage of electrolyte ions.⁵² The area under the curve grows from 0 to 0.5 V with a broad range of scan rates from 10 to 100 mV s⁻¹, indicating rapid rates of ionic and electronic transport at the electrode/electrolyte interfaces. The GCD characteristics of BDC–MOF and BTC–MOF electrodes were investigated at current densities ranging from 5 to 25 mA cm⁻² in 2 M KOH electrolyte across a potential range of 0–0.5 V (Figure 10e,f).

EIS measurements were performed to determine the internal resistive characteristics as well as the capacitive behavior of the MOF electrode. The Nyquist plots of MOFs in 2 M KOH electrolyte are shown in Figure 11a. A straight line detected in the lower-frequency portion of the Nyquist plot was due to the migration of electrolyte ions from the bulk solution to the electrode surface. The charge-transfer activity at the electrode/electrolyte interface is responsible for the presence of a semicircle in the high-frequency zone, and the semicircle diameter shows the charge-transfer resistance (R_{ct}). The charge-transfer resistance of BDC–MOF and BTC–MOF is 0.19 and 0.46 Ω , respectively. BDC–MOF (0.19 Ω) has a lower charge-transfer resistance than BTC–MOF (0.46 Ω). These R_{ct} values show that both electrodes have high electrical conductivities, which are connected to the presence of carbon in their composition, which increases the conductivity of the manufactured electrode. In practice, the carbon in the electrode structure reduces the resistance to charge transfer and improves the connectivity between the active sites for electron transfer.⁵³ Figure 11b depicts the change of specific capacitance as a function of current density, and Figure 11c depicts the Ragone plot of energy density vs power density for both trimetallic MOFs. The specific capacitance of the BDC–MOF electrode is 582.8 F g⁻¹ at 5 mA cm⁻² current density, which is more than the specific capacitance of the BTC–MOF electrode, which has 413.4 F g⁻¹ at 5 mA cm⁻² current density, according to the GCD curves. The examined BDC–MOF and BTC–MOF electrodes exhibit a longer charge and discharge time with lowering currents, resulting in greater specific capacitance values, implying that as current increases, the specific capacitance falls in typical behavior. Trimesic acid and terephthalic acid have pK_a values of 3.14 and 4.82, respectively. Trimesic acid has a low pK_a value, which makes it act as a strong acid since it has a high acidity.⁵⁴ Due to the high acidity, the BTC–MOF electrode gets etched, which degrades the deposition of the film that clogs the pores and prevents the electrolyte from entering the electrode material, increasing resistance and lowering specific capacitance. The cluster of nanoplates that comprise the porous brick-like morphology of

BDC–MOF operate as an “ion-buffering reservoir”, enhancing charge–discharge and shortening the diffusion length for ions to enter the electrode. The charging/discharging curves are also affected by the trimesic and terephthalic ligands; the nature of the curves differs for BDC–MOF and BTC–MOF.

To examine the cycling stability of the MOF electrodes, the specific capacitance as a function of cycle number was measured at a prolonged current density of 25 mA cm⁻². The BDC–MOF electrode demonstrated good cycling stability after 3000 continuous cycles, with about 92.44% retention of the original capacitance (Figure 12). This

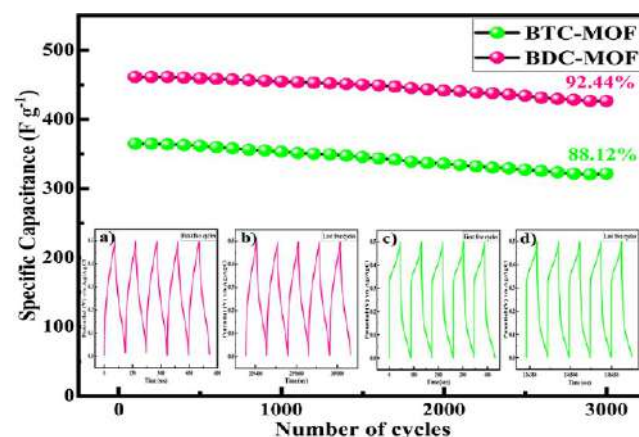


Figure 12. Cycling performance at 25 mA cm⁻², and the inset shows the first and last five cycles of BDC–MOF and BTC–MOF.

exceptional long-cycle lifespan was greater than that of the BTC–MOF, which has 88.12% retention even after 3000 GDC cycles at a current density of 25 mA cm⁻², as shown in Figure 12. On 1D stainless-steel mesh substrate with substantially poorer electrical conductivity, BDC–MOF demonstrated a remarkable specific capacity of 528.8 F g⁻¹. At all the current densities, the specific capacity of BDC–MOF was relatively high, and a reversible capacity of 461.2 F g⁻¹ can be sustained at an extremely high current density of 25 mA cm⁻², with 86.14% capacity retention compared to the capacity at 5 mA cm⁻², showing a high rate capability. The increase in the cycle number causes a drop in specific capacitance due to the partial leaching of the active electrode material during faradic operations.⁵⁵ The remarkable energy storage efficiency can be attributed to the combined impact of a group of nanoplates forming the porous bricks, such as morphology, and the huge SSA of the extremely porous material. The electrochemical performance of a few different MOFs that have been previously characterized is compared to that of the synthesized trimetallic MOF in Table 1.

A SSC device was assembled with BDC–MOF for both electrodes and PVA/KOH gel both as the separator and electrolyte to further evaluate the practical application of the BDC–MOF. The slurry coating method was used to prepare both electrodes. In short, the slurry was made by combining 80 mg of active material (BDC–MOF), 10 mg of PVDF, and 10 mg of carbon black in 0.5 mL of the NMP solvent. The appropriate volume of slurry was then dispersed onto a 2 × 2 cm flexible stainless-steel mesh and air-dried overnight at 60 °C. To avoid electrical contact, the electrode borders were first made non-conducting using a band. The PVA–KOH gel was applied to one side of the electrode, resulting in one point of electrical contact. Both electrodes were eventually patched

Table 1. Comparison of the Specific Capacitances of Trimetallic MOFs with Previously Reported Materials

sr. no.	material	electrolyte	substrate	specific capacitance	current density	stability (%)	refs
1	NiCoMn-MOF	3 M KOH	nickel foam	907.4 C g ⁻¹	1 A g ⁻¹	64.7	56
2	ZnNi-MOF	3 M KOH	nickel foam	466.5 F g ⁻¹	0.5 A g ⁻¹	44.0	57
3	NiCo-MOF	1 M KOH	nickel foam	1107.3 F g ⁻¹	1 A g ⁻¹	70.1	58
4	Ni/Co-MOF	6 M KOH	nickel foam	982.5 F g ⁻¹	0.5 A g ⁻¹	84.0	59
5	NiCoZn-MOF	2 M KOH	stainless-steel mesh	582.8 F g ⁻¹	5 mA cm ⁻²	92.44	this work

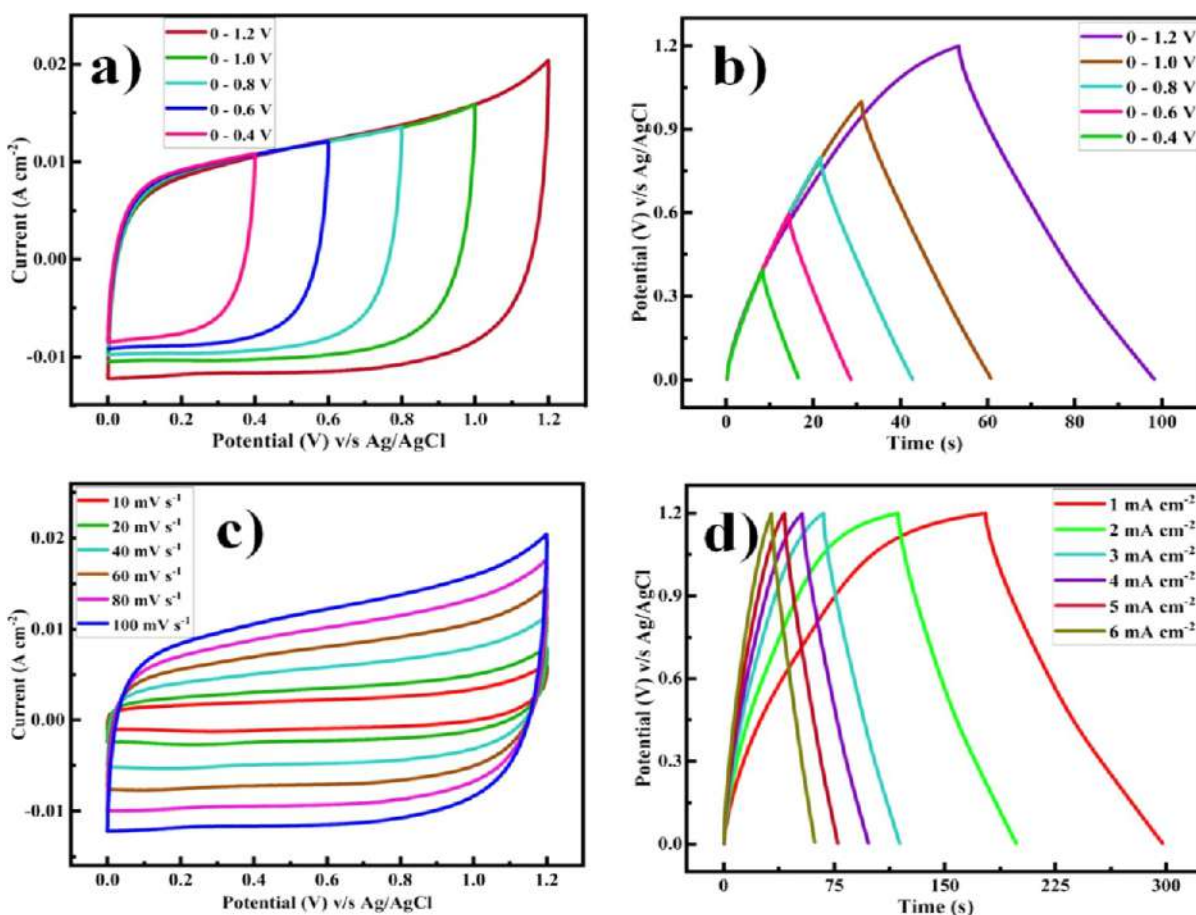


Figure 13. (a) CV, (b) GCD curves of the symmetric device within the various potential windows (0.4, 0.6, 0.8, 1.0, and 1.2 V), (c) CV curves of the symmetric device at different scan rates, and (d) GCD curves of the symmetric device at different current densities.

together in the shape of a sandwich, with gel-pasted sides facing each other. For 12 h, the device was subjected to 1-ton pressure to establish a strong connection between the electrodes and gel electrolyte and to eliminate the air gap. Following that, the device was utilized to evaluate electrochemical performance. CV, GCD, and EIS measurements were performed to examine the performance of the assembled SSC device. The assembled SSC device CV curves displayed ideal rectangular shapes within an operating voltage window 0.4–1.2 V, demonstrating excellent capacitive behavior. Figure 13a,b displays CV and GCD profiles of the SSC device within various potential windows and exhibits excellent linear slopes and triangular shapes, which suggest ideal capacitive behavior in line with the CV curves.

In practice, the SSC device's potential window can reach 1.2 V without causing significant changes in the CV and GCD curves, signifying outstanding electrochemical stability. Figure 13c depicts the SSC device's CV curves at various scan rates. The CV curves remained consistent when the scan rate was

raised from 10 mV s⁻¹ to 100 mV s⁻¹; however, the closed regions grew, confirming the symmetric device's high rate capacity. Furthermore, the GCD curves of the SSC device at various current densities are shown in Figure 13d, and the nearly symmetric charge/discharge curves indicate excellent rate capability.

The EIS studies show that the fabricated SSC device has good electrical conductivity with low ionic resistance and a charge-transfer resistance of 0.4 Ω, as depicted in Figure 14a. As a result, the small semicircle diameter reveals low charge-transfer resistance and excellent conductivity. The specific capacities calculated from the discharge curves at current densities of 1, 2, 3, 4, 5, and 6 mA cm⁻² were 94.92, 93.56, 91.83, 90.67, 89.44, and 87.74 F g⁻¹, respectively (Figure 14b). Figure 14c depicts the Ragone plot of the SSC device, and also the SSC device delivers a high energy density of 47.59 W h kg⁻¹ at a power density of 1367.42 W kg⁻¹. Additionally, at a current density of 6 mA cm⁻², the SSC device exhibits outstanding cycling performance, with 99.26% capacitance

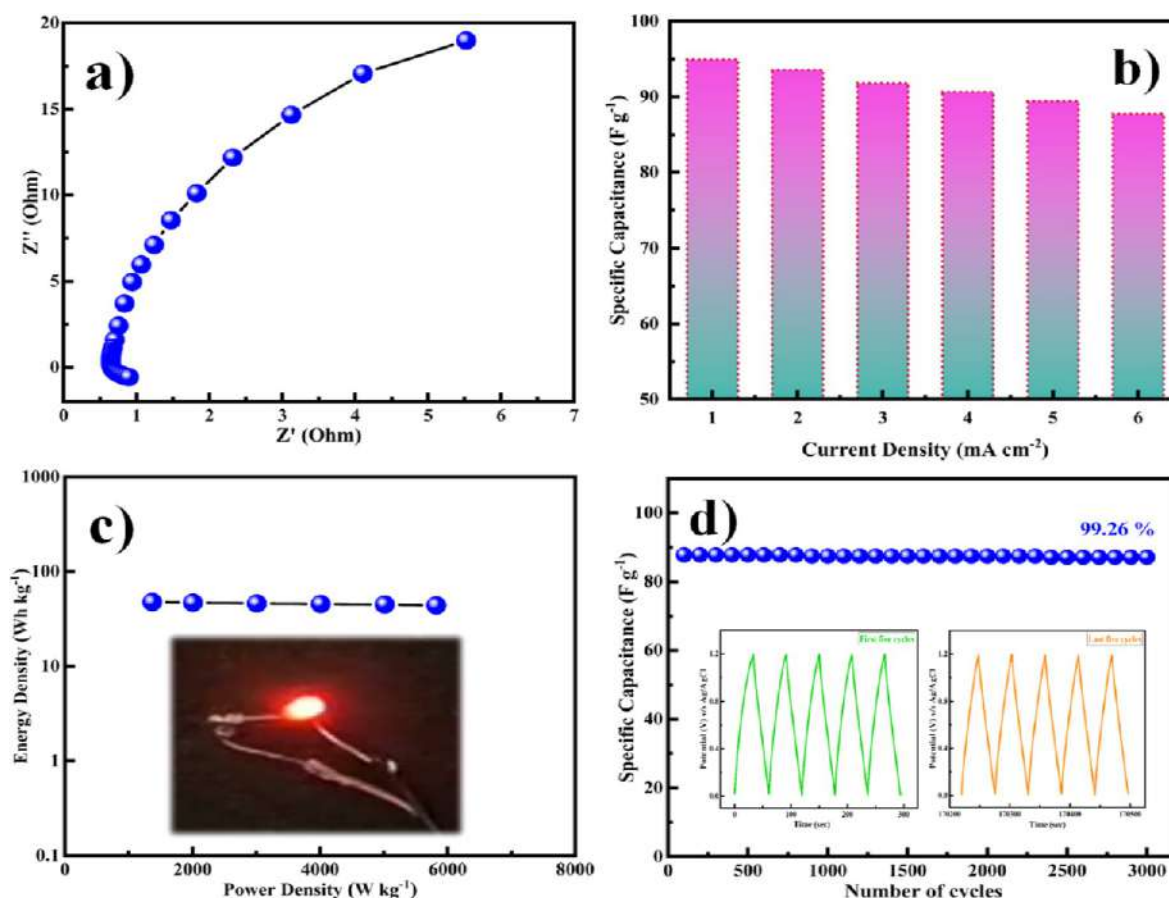


Figure 14. (a) Nyquist plot, (b) variation of specific capacitance as a function of current density, (c) Ragone plot showing the energy density versus power density, and (d) cycling performance at 6 mA cm^{-2} , and the inset shows the first and last five cycles of the symmetric device.

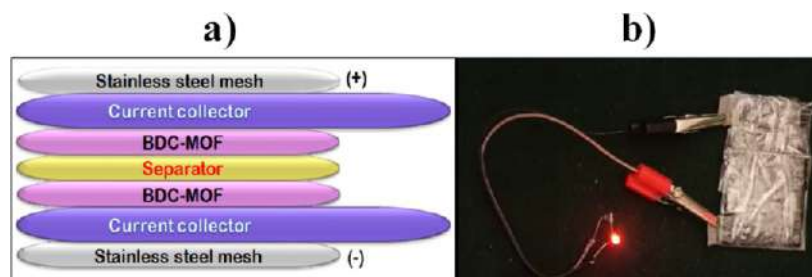


Figure 15. (a) Fabrication schematic of the BDC-MOF//2 M KOH//BDC-MOF SSC device. (b) Two handmade SSC devices which glow a red LED.

retention even after 3000 cycles (Figure 14d). Power density and energy density are critical parameters for assessing the supercapacitor electrochemical performance. The BDC-MOF architecture exceptional electrochemical performance is due to its distinct hierarchical structure. Good electrochemical activity is ensured by the uniform distribution of the brick-like morphology of the nanoplates, and the electrolyte's hierarchical structure offers a high SSA that can make sufficient contact with the electrolyte and enhance ion transport. Finally, the distinct hierarchical structure of the BDC-MOF architecture reduces volume expansion during the cycle process, improving structural integrity and enhancing cycle stability.

The lighting red light-emitting diode (LED) shows that how our SSC device can be used in real applications by connecting two of them in series (where each device is of size $2 \times 2 \text{ cm}$). Figure 15a shows the schematic presentation of the SSC

device, and Figure 15b displays the device's digital image. The LED was glowing brilliantly for about a minute after the device had been charged for just 2 s, demonstrating the astonishing application of our solid-state SSC devices (Supporting Information). The developed capacitor is suitable for use in real-world energy storage and transfer applications because the discharge time is longer than the charging time.

The electrochemical behavior of chemically produced trimetallic MOFs was compared using a radar graph, as shown in Figure 16. Each vertex indicates the properties of the different trimetallic MOFs, such as crystallite size, specific capacitance, energy density, power density, stability, charge-transfer resistance, SSA, and average pore radius. The electrochemical performance of trimetallic MOFs is represented by the integral area under the curve. According to Figure 16, the integral area of BDC-MOF is greater than that

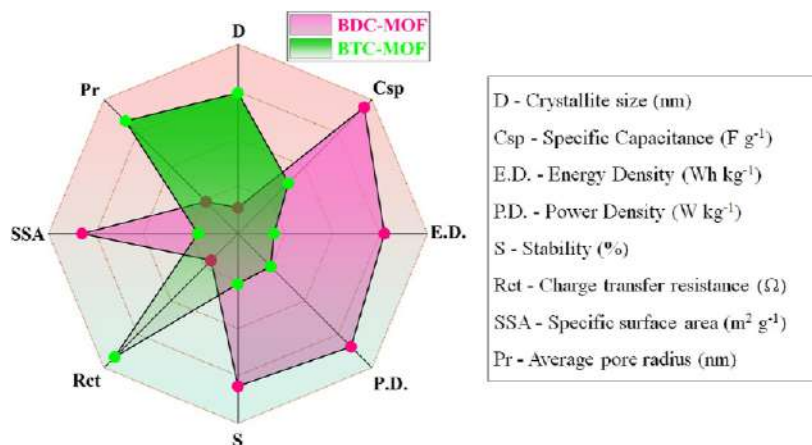


Figure 16. Radar graph for the comparative study of BDC–MOF and BTC–MOF based on supercapacitive properties.

of BTC–MOF. It has been established that the BDC–MOF small crystallite size, large SSA, and low charge-transfer resistance come up with increased specific capacitance, energy density, power density, and cycle stability.

CONCLUSIONS

In outline, a novel 2D architecture of trimetallic MOFs (BDC–MOF and BTC–MOF) as supercapacitor electrode materials was successfully prepared by the reflux condensation method which is simple, low cost, and environmentally friendly. The effects of different ligands of MOFs on the structural, surface, and electrochemical performance of MOF samples have been studied systematically. Due to their nanoplate-like structures with good mechanical and electrical contact, rich redox reactions, low crystallinity, good tuneability, high conductivity and transport rate for both electrolyte ions and electrons, and lower acidity, BDC–MOFs exhibit improved electrochemical performance. The BDC–MOFs show higher capacitance due to the synergistic effect, also they exhibit pseudocapacitive behavior due to the redox activity of metal cations inside MOFs, which offers a channel for electrons, as well as EDLC behavior due to the organic linker structure, which facilitates charge transfer within the framework. The BDC–MOF electrode material achieves a good SSA of $265.87 \text{ m}^2 \text{ g}^{-1}$, specific capacity of 582.8 F g^{-1} at a current density of 5 mA cm^{-2} , and exceptional cycling stability with 92.44% retention after 3000 cycles at 25 mA cm^{-2} due to its porous nature and adequate SSA. The SSC device BDC–MOF//BDC–MOF was built with the BDC–MOF as both electrodes have a high energy density of $47.59 \text{ W h kg}^{-1}$ at a power density of $1367.42 \text{ W kg}^{-1}$ and exceptional cycling stability with 99.26% capacitance retention over 3000 cycles. This novel 2D trimetallic MOF electrode synthesis technique throws light on prospective high-performance MOF-based electrode materials, with the generated BDC–MOF serving as a promising electrode material for better energy storage devices. It is necessary to further enhance the MOF thermal, mechanical, and chemical stability. Since most MOFs decompose and have their skeletons collapse in water, acid, or base, their widespread use in energy storage applications has been severely hampered. Sensible selection of organic ligands and metal secondary building blocks can overcome this issue. The inherent fragility and finite processability of MOFs may also be overcome by using novel methods, such as pressing and

phase change treatment operations, without changing their original properties.

ASSOCIATED CONTENT

Supporting Information

The Supporting Information is available free of charge at <https://pubs.acs.org/doi/10.1021/acs.langmuir.3c01337>.

LED glow using fabricated solid-state SSC devices (MP4)

AUTHOR INFORMATION

Corresponding Author

Sanjay Kolekar – Analytical Chemistry and Material Science Research Laboratory, Department of Chemistry, Shivaji University, Kolhapur 416 004, India; orcid.org/0000-0002-4367-6014; Email: sskolekar@gmail.com

Authors

Rakhee Bhosale – Analytical Chemistry and Material Science Research Laboratory, Department of Chemistry, Shivaji University, Kolhapur 416 004, India

Sneha Bhosale – Analytical Chemistry and Material Science Research Laboratory, Department of Chemistry, Shivaji University, Kolhapur 416 004, India

Dattatray Narale – Analytical Chemistry and Material Science Research Laboratory, Department of Chemistry, Shivaji University, Kolhapur 416 004, India

Chitra Jambhale – Analytical Chemistry and Material Science Research Laboratory, Department of Chemistry, Shivaji University, Kolhapur 416 004, India

Complete contact information is available at: <https://pubs.acs.org/10.1021/acs.langmuir.3c01337>

Author Contributions

R.B.: Formal analysis, investigation, methodology, and writing—original draft; S.B.: data curation; D.N.: discussion and review; C.J.: editing of the draft; and S.K.: conceptualization, supervision, and funding acquisition.

Notes

The authors declare no competing financial interest.

ACKNOWLEDGMENTS

The authors are thankful to UGC-SAP, DST-FIST, and DST-PURSE for the financial support and instrument facilities at the

Department of Chemistry, Shivaji University, Kolhapur. One of the author (R.B.) is thankful to SARTHI, Government of Maharashtra, India, for the "Chhatrapati Shahu Maharaj National Research Fellowship-2021".

REFERENCES

- (1) Wei, C.; Tan, L.; Zhang, Y.; Wang, Z.; Xi, B.; Xiong, S.; Feng, J. Interfacial Engineering on Metal Anodes in Rechargeable Batteries. *EnergyChem* **2022**, *4*, 100089–100120.
- (2) Ray, A.; Roy, A.; Saha, S.; Ghosh, M.; Roy Chowdhury, S.; Maiyalagan, T.; Bhattacharya, S. K.; Das, S. Electrochemical Energy Storage Properties of Ni-Mn-Oxide Electrodes for Advance Asymmetric Supercapacitor Application. *Langmuir* **2019**, *35*, 8257–8267.
- (3) Swain, N.; Saravanakumar, B.; Kundu, M.; Schmidt-Mende, L.; Ramadoss, A. Recent Trends in Template Assisted 3D Porous Materials for Electrochemical Supercapacitors. *J. Mater. Chem. A* **2021**, *9*, 25286–25324.
- (4) Katkar, P. K.; Marje, S. J.; Parale, V. G.; Lokhande, C. D.; Gunjekar, J. L.; Park, H. H.; Patil, U. M. Fabrication of a High-Performance Hybrid Supercapacitor Based on Hydrothermally Synthesized Highly Stable Cobalt Manganese Phosphate Thin Films. *Langmuir* **2021**, *37*, 5260–5274.
- (5) Mehek, R.; Iqbal, N.; Noor, T.; Amjad, M. Z. B.; Ali, G.; Vignarooban, K.; Khan, M. A. Metal-Organic Framework Based Electrode Materials for Lithium-Ion Batteries: A Review. *RSC Adv.* **2021**, *11*, 29247–29266.
- (6) Zhao, X.; Bi, Q.; Yang, C.; Tao, K.; Han, L. Design of Trimetallic Sulfide Hollow Nanocages from Metal-Organic Frameworks as Electrode Materials for Supercapacitors. *Dalton Trans.* **2021**, *50*, 15260–15266.
- (7) Chatterjee, D. P.; Nandi, A. K. A Review on the Recent Advances in Hybrid Supercapacitors. *J. Mater. Chem. A* **2021**, *9*, 15880–15918.
- (8) Sun, Y. A.; Chen, L. T.; Hsu, S. Y.; Hu, C. C.; Tsai, D. H. Silver Nanoparticles-Decorating Manganese Oxide Hybrid Nanostructures for Supercapacitor Applications. *Langmuir* **2019**, *35*, 14203–14212.
- (9) Tafete, G. A.; Abera, M. K.; Thothadri, G. Review on Nanocellulose-Based Materials for Supercapacitors Applications. *J. Energy Storage* **2022**, *48*, 103938–103953.
- (10) Song, W.; Teng, X.; Liu, Y.; Wang, J.; Niu, Y.; He, X.; Zhang, C.; Chen, Z. Rational Construction of Self-Supported Triangle-like MOF-Derived Hollow (Ni,Co)Se₂ Arrays for Electrocatalysis and Supercapacitors. *Nanoscale* **2019**, *11*, 6401–6409.
- (11) Bai, Y.; Liu, C.; Chen, T.; Li, W.; Zheng, S.; Pi, Y.; Luo, Y.; Pang, H. MXene-Copper/Cobalt Hybrids via Lewis Acidic Molten Salts Etching for High Performance Symmetric Supercapacitors. *Angew. Chem., Int. Ed.* **2021**, *60*, 25318–25322.
- (12) Acharya, J.; Ojha, G. P.; Pant, B.; Park, M. Construction of Self-Supported Bimetallic MOF-Mediated Hollow and Porous Trimetallic Selenide Nanosheet Arrays as Battery-Type Electrodes for High-Performance Asymmetric Supercapacitors. *J. Mater. Chem. A* **2021**, *9*, 23977–23993.
- (13) Cheng, X.; Pan, J.; Zhao, Y.; Liao, M.; Peng, H. Gel Polymer Electrolytes for Electrochemical Energy Storage. *Adv. Energy Mater.* **2018**, *8*, 1702184–2170220.
- (14) Lu, X.; Yu, M.; Wang, G.; Tong, Y.; Li, Y. Flexible Solid-State Supercapacitors: Design, Fabrication and Applications. *Energy Environ. Sci.* **2014**, *7*, 2160–2181.
- (15) Yin, X.; Li, H.; Yuan, R.; Lu, J. Hierarchical Self-Supporting Sugar Gourd-Shape MOF-Derived NiCo₂O₄ Hollow Nanocages@SiC Nanowires for High-Performance Flexible Hybrid Supercapacitors. *J. Colloid Interface Sci.* **2021**, *586*, 219–232.
- (16) Tahir, M. U.; Arshad, H.; Zhang, H.; Hou, Z.; Wang, J.; Yang, C.; Su, X. Room Temperature and Aqueous Synthesis of Bimetallic ZIF Derived CoNi Layered Double Hydroxides and Their Applications in Asymmetric Supercapacitors. *J. Colloid Interface Sci.* **2020**, *579*, 195–204.
- (17) Li, W.; Guo, X.; Geng, P.; Du, M.; Jing, Q.; Chen, X.; Zhang, G.; Li, H.; Xu, Q.; Braunstein, P.; Pang, H. Rational Design and General Synthesis of Multimetallic Metal–Organic Framework Nano-Octahedra for Enhanced Li–S Battery. *Adv. Mater.* **2021**, *33*, 2105163–2105169.
- (18) Zheng, S.; Li, Q.; Xue, H.; Pang, H.; Xu, Q. A Highly Alkaline-Stable Metal Oxide@metal-Organic Framework Composite for High-Performance Electrochemical Energy Storage. *Natl. Sci. Rev.* **2020**, *7*, 305–314.
- (19) Jiao, Y.; Pei, J.; Chen, D.; Yan, C.; Hu, Y.; Zhang, Q.; Chen, G. Mixed-Metallic MOF Based Electrode Materials for High Performance Hybrid Supercapacitors. *J. Mater. Chem. A* **2017**, *5*, 1094–1102.
- (20) Akhter, S.; Mohd Zain, N. K.; Shalauddin, M.; Singh, V. K.; Misnon, I. I.; Sharma, R. K.; Das, S.; Basirun, W. J.; Johan, M. R.; Jose, R. Tri-Metallic Co-Ni-Cu Based Metal Organic Framework Nanostructures for the Detection of an Anticancer Drug Nilutamide. *Sens. Actuators, A* **2021**, *325*, 112711–112722.
- (21) Makgopa, K. ScienceDirect Electrochemistry Intrinsic Properties of Metal – Organic Frameworks (MOFs) in Supercapacitor Applications. *Curr. Opin. Electrochem.* **2022**, *36*, 101112–101121.
- (22) Kang, C.; Ma, L.; Chen, Y.; Fu, L.; Hu, Q.; Zhou, C.; Liu, Q. Metal-Organic Framework Derived Hollow Rod-like NiCoMn Ternary Metal Sulfide for High-Performance Asymmetric Supercapacitors. *Chem. Eng. J.* **2022**, *427*, 131003–131013.
- (23) Taherinia, D.; Hatami, H.; Valadi, F. M. Trimetallic Co-Ni-Mn Metal-Organic Framework as an Efficient Electrocatalyst for Alkaline Oxygen Evolution Reaction. *J. Electroanal. Chem.* **2022**, *922*, 116720–116729.
- (24) Han, X. G.; Wang, P. F.; Zhang, Y. H.; Liu, H. Y.; Tang, J. J.; Yang, G.; Shi, F. N. Addition of Dissimilar Metal Nodes to Improve the Electrochemical Performance of MOF as a Supercapacitor. *Inorg. Chim. Acta.* **2022**, *536*, 120916–120927.
- (25) Zhang, B.; Song, S.; Li, W.; Zheng, L.; Ma, X. Asymmetric Supercapacitors with High Energy Density and High Specific Capacitance Based on Ni-Co-Mn Multiphase Metal Structure MOF. *Ionics* **2021**, *27*, 3553–3566.
- (26) Luo, X.; Abazari, R.; Tahir, M.; Fan, W. K.; Kumar, A.; Kalthorizadeh, T.; Kirillov, A. M.; Amani-Ghadim, A. R.; Chen, J.; Zhou, Y. Trimetallic Metal–Organic Frameworks and Derived Materials for Environmental Remediation and Electrochemical Energy Storage and Conversion. *Coord. Chem. Rev.* **2022**, *461*, 214505–214529.
- (27) Wang, H.; Li, J.; Li, K.; Lin, Y.; Chen, J.; Gao, L.; Nicolosi, V.; Xiao, X.; Lee, J. M. Transition Metal Nitrides for Electrochemical Energy Applications. *Chem. Soc. Rev.* **2021**, *50*, 1354–1390.
- (28) Rajak, R.; Kumar, R.; Ansari, S. N.; Saraf, M.; Mobin, S. M. Recent Highlights and Future Prospects on Mixed-Metal MOFs as Emerging Supercapacitor Candidates. *Dalton Trans.* **2020**, *49*, 11792–11818.
- (29) Seo, Y.; Shinde, P. A.; Park, S.; Chan Jun, S. Self-Assembled Bimetallic Cobalt–Manganese Metal–Organic Framework as a Highly Efficient, Robust Electrode for Asymmetric Supercapacitors. *Electrochim. Acta* **2020**, *335*, 135327–135336.
- (30) Nagaraju, G.; Sekhar, S. C.; Ramulu, B.; Hussain, S. K.; Narsimulu, D.; Yu, J. S. Ternary MOF-Based Redox Active Sites Enabled 3D-on-2D Nanoarchitected Battery-Type Electrodes for High-Energy-Density Supercapacitors. *Nano-Micro Lett.* **2021**, *13*, 17–18.
- (31) Andikaey, Z.; Ensafi, A. A.; Rezaei, B.; Malek, S. S.; Hu, J. S. MWCNT-Mesoporous Silica Nanocomposites Inserted in a Polyhedral Metal-Organic Framework as an Advanced Hybrid Material for Energy Storage Device. *New J. Chem.* **2021**, *45*, 18090–18101.
- (32) Bhosale, R.; Bhosale, S.; Kumbhar, P.; Narale, D.; Ghaware, R.; Jambhale, C.; Kolekar, S. Design and Development of a Porous Nanorod-Based Nickel-Metal–Organic Framework (Ni-MOF) for High-Performance Supercapacitor Application. *New J. Chem.* **2023**, *47*, 6749–6758.
- (33) Liu, S.; Lee, S. C.; Patil, U.; Shackery, I.; Kang, S.; Zhang, K.; Park, J. H.; Chung, K. Y.; Jun, S. C. Hierarchical MnCo-Layered

Double Hydroxides@Ni(OH)₂ Core-Shell Heterostructures as Advanced Electrodes for Supercapacitors. *J. Mater. Chem. A* **2017**, *5*, 1043–1049.

(34) Vijeth, H.; Ashokkumar, S. P.; Yesappa, L.; Niranjana, M.; Vandana, M.; Devendrappa, H. Flexible and High Energy Density Solid-State Asymmetric Supercapacitor Based on Polythiophene Nanocomposites and Charcoal. *RSC Adv.* **2018**, *8*, 31414–31426.

(35) Gopi, S.; Perumal, S.; Al Olayan, E. M.; AlAmri, O. D.; Aloufi, A. S.; Kathiresan, M.; Yun, K. 2D Trimetal-Organic Framework Derived Metal Carbon Hybrid Catalyst for Urea Electro-Oxidation and 4-Nitrophenol Reduction. *Chemosphere* **2021**, *267*, 129243–129254.

(36) Li, Y.; Lu, M.; Wu, Y.; Xu, H.; Gao, J.; Yao, J. Trimetallic Metal–Organic Framework Derived Carbon-Based Nanoflower Electrocatalysts for Efficient Overall Water Splitting. *Adv. Mater. Interfaces* **2019**, *6*, 1900290–1900298.

(37) Vadiyar, M. M.; Kolekar, S. S.; Deshpande, N. G.; Chang, J. Y.; Kashale, A. A.; Ghule, A. V. Binder-Free Chemical Synthesis of ZnFe₂O₄ Thin Films for Asymmetric Supercapacitor with Improved Performance. *Ionics* **2017**, *23*, 741–749.

(38) Gupta, N. K.; Kim, S.; Bae, J.; Kim, K. S. Chemisorption of Hydrogen Sulfide over Copper-Based Metal-Organic Frameworks: Methanol and UV-Assisted Regeneration. *RSC Adv.* **2021**, *11*, 4890–4900.

(39) You, S.-M.; El Roubi, W. M. A.; Assaud, L.; Doong, R.-A.; Millet, P. Water Photo-Electrooxidation Using Mats of TiO₂ Nanorods, Surface Sensitized by a Metal–Organic Framework of Nickel and 1,2-Benzene Dicarboxylic Acid. *Hydrogen* **2021**, *2*, 58–75.

(40) Li, H.; Qin, J.; Zhang, Y.; Xu, S.; Du, J.; Tang, J. The Efficiency and Mechanism of Dibutyl Phthalate Removal by Copper-Based Metal Organic Frameworks Coupled with Persulfate. *RSC Adv.* **2018**, *8*, 39352–39361.

(41) Zha, Q.; Li, M.; Liu, Z.; Ni, Y. Hierarchical Co,Fe-MOF-74/Co/Carbon Cloth Hybrid Electrode: Simple Construction and Enhanced Catalytic Performance in Full Water Splitting. *ACS Sustain. Chem. Eng.* **2020**, *8*, 12025–12035.

(42) Nguyen, V. H.; Nguyen, T. D.; Van Nguyen, T. Microwave-Assisted Solvothermal Synthesis and Photocatalytic Activity of Bismuth(III) Based Metal–Organic Framework. *Top. Catal.* **2020**, *63*, 1109–1120.

(43) Kaur, R.; Chhibber, M.; Mahata, P.; Mittal, S. K. Induction of Catalytic Activity in ZnO Loaded Cobalt Based MOF for the Reduction of Nitroarenes. *ChemistrySelect* **2018**, *3*, 3417–3425.

(44) Sing, K. S. W.; Everett, D. H.; Haul, R. A. W.; Moscou, L.; Pierotti, R. A.; Rouquerol, J.; Siemieniowska, T. Reporting physisorption data for gas/solid systems with special reference to the determination of surface area and porosity (Recommendations 1984). *Pure Appl. Chem.* **1985**, *57*, 603–619.

(45) Zain, N. K. M.; Karuppiyah, C.; Misnon, I. I.; Das, S.; Ozoemena, K. I.; Yang, C. C.; Jose, R. High Capacity and Rate Capability Binder-Less Ternary Transition Metal-Organic Framework as Anode Material for Lithium-Ion Battery. *Electroanalysis* **2020**, *32*, 3180–3188.

(46) Beka, L. G.; Bu, X.; Li, X.; Wang, X.; Han, C.; Liu, W. A 2D Metal-Organic Framework/Reduced Graphene Oxide Heterostructure for Supercapacitor Application. *RSC Adv.* **2019**, *9*, 36123–36135.

(47) Shu, H.; Lai, T.; Ren, J.; Cui, X.; Tian, X.; Yang, Z.; Xiao, X.; Wang, Y. Trimetallic Metal-Organic Frameworks (Fe, Co, Ni-MOF) Derived as Efficient Electrochemical Determination for Ultra-Micro Imidacloprid in Vegetables. *Nanotechnology* **2022**, *33*, 135502–135517.

(48) Thangasamy, P.; Shanmuganathan, S.; Subramanian, V. A NiCo-MOF Nanosheet Array Based Electrocatalyst for the Oxygen Evolution Reaction. *Nanoscale Adv.* **2020**, *2*, 2073–2079.

(49) Wu, Y.; Song, X.; Xu, S.; Chen, Y.; Oderinde, O.; Gao, L.; Wei, R.; Xiao, G. Chemical Fixation of CO₂ into Cyclic Carbonates Catalyzed by Bimetal Mixed MOFs: The Role of the Interaction between Co and Zn. *Dalton Trans.* **2020**, *49*, 312–321.

(50) Lin, J.; Zeng, C.; Lin, X.; Reddy, R. C. K.; Niu, J.; Liu, J.; Cai, Y. Trimetallic MOF-Derived Cu_{0.39}Zn_{0.14}Co_{2.47}O₄-CuO Interwoven with Carbon Nanotubes on Copper Foam for Superior Lithium Storage with Boosted Kinetics. *ACS Sustain. Chem. Eng.* **2019**, *7*, 15684–15695.

(51) Wei, Y.; Zhang, Y.; Chen, J. S.; Mao, C.; Jin, B. K. An Electrochemiluminescence Biosensor for P53 Antibody Based on Zn-MOF/GO Nanocomposite and Ag+DNA Amplification. *Microchim. Acta* **2020**, *187*, 455–459.

(52) Manikandan, M. R.; Cai, K. P.; Hu, Y. D.; Li, C. L.; Zhang, J. T.; Zheng, Y. P.; Liang, Y. F.; Song, H. R.; Shang, M. Y.; Shi, X. N.; Zhang, J. X.; Yin, S. Q.; Shang, S. Y.; Wang, X. W. Influence of Hydrothermal Reaction Time on the Supercapacitor Performance of Ni-MOF Nanostructures. *Appl. Phys. Mater. Sci. Process* **2021**, *127*, 421–431.

(53) Song, W. W.; Wang, B.; Li, C. N.; Wang, S. M.; Han, Z. B. 3D Hierarchical Core-Shell Spiny Globe Shaped Co₂P@Ni₂P/NiCo₂O₄@CoO for Asymmetric Supercapacitors. *J. Mater. Chem. A* **2022**, *10*, 3710–3721.

(54) Mouchaham, G.; Wang, S.; Serre, C. The Stability of Metal–Organic Frameworks. *Metal-Org. Frameworks: Applications in Separations and Catalysis* **2018**, 1–28.

(55) Suksomboon, M.; Srimuk, P.; Krittayavathananon, A.; Luanwuthi, S.; Sawangphruk, M. Effect of Alkaline Electrolytes on the Charge Storage Capacity and Morphology of Porous Layered Double Cobalt Hydroxide-Coated Graphene Supercapacitor Electrodes. *RSC Adv.* **2014**, *4*, 56876–56882.

(56) Ashourdan, M.; Semnani, A.; Hasanpour, F.; Moosavifard, S. E. Synthesis of Nickel Cobalt Manganese Metal Organic Framework@high Quality Graphene Composites as Novel Electrode Materials for High Performance Supercapacitors. *J. Electroanal. Chem.* **2021**, *895*, 115452.

(57) Zhu, Y.; Tao, Z.; Cai, C.; Tan, Y.; Wang, A.; Yang, Y. Facile Synthesis Zn-Ni Bimetallic MOF with Enhanced Crystallinity for High Power Density Supercapacitor Applications. *Inorg. Chem. Commun.* **2022**, *139*, 109391.

(58) Zhang, X.; Wang, J.; Ji, X.; Sui, Y.; Wei, F.; Qi, J.; Meng, Q.; Ren, Y.; He, Y.; Zhuang, D. Flake-like Nickel/Cobalt Metal-Organic Framework as High-Performance Electrodes for Supercapacitors. *J. Mater. Sci. Mater. Electron.* **2020**, *31*, 16260–16268.

(59) Kang, X.; Wang, J.; Ma, Y.; Shi, X.; Chen, X.; Tian, H.; Ran, F. 3D Juniperus Sabina-like Ni/Co Metal-Organic Framework as an Enhanced Electrode Material for Supercapacitors. *J. Solid State Chem.* **2022**, *310*, 123056.

PART II

1. University Name : Shivaji University Kolhapur
2. Department of : Chemistry
3. Name of Researcher : Miss. Rakhee Raghunath Bhosale
4. Name of Guide : Prof. (Dr.) S. S. Kolekar
5. Type of Degree : Ph.D.
6. Registration Date : 01/01/2020
7. Completed Date : 16/09/2023
8. Thesis Title : “Exploring Metal–Organic Frameworks
Derived Nanomaterials for Advanced
Supercapacitors Impact of Quality”
9. Size of thesis : 250 pages
31.1 MB

**EXPLORING METAL-ORGANIC FRAMEWORKS
DERIVED NANOMATERIALS FOR ADVANCED
SUPERCAPACITORS**

A THESIS SUBMITTED TO

SHIVAJI UNIVERSITY, KOLHAPUR

FOR THE DEGREE OF

DOCTOR OF PHILOSOPHY

IN

CHEMISTRY

UNDER THE FACULTY OF

SCIENCE AND TECHNOLOGY

BY

Miss. RAKHEE RAGHUNATH BHOSALE

M. Sc.

UNDER THE GUIDANCE OF

PROF. (Dr.) SANJAY S. KOLEKAR

M. Sc., Ph. D.

**ANALYTICAL CHEMISTRY AND MATERIALS SCIENCE LABORATORY,
DEPARTMENT OF CHEMISTRY,
SHIVAJI UNIVERSITY,
KOLHAPUR – 416 004 M.S., INDIA**

JUNE - 2023

DECLARATION

I hereby declare that the thesis entitled, “*EXPLORING METAL-ORGANIC FRAMEWORKS DERIVED NANOMATERIALS FOR ADVANCED SUPERCAPACITORS*”, completed and written by me has not formed earlier on the basis for the award of any degree or similar title of this or any other university or examining body. Further, I declare that I have not violated any of the provisions under the acts of Copyright/Piracy/Cyber/IPR, etc. amended from time to time.

In view of University Grants Commission (Promotion of Academic Integrity and Prevention of Plagiarism in Higher Educational Institutions) Regulations, 2018 dated 31st July 2018, I hereby submit an undertaking that this thesis is my original work and it is free of any plagiarism. Further, this thesis has been duly checked through a Plagiarism detection tool approved by Shivaji University, Kolhapur.

Place: Kolhapur
Date:

Miss. Rakhee Raghunath Bhosale
Research Student
Department of Chemistry,
Shivaji University, Kolhapur

CERTIFICATE

This is to certify that the thesis entitled, “*EXPLORING METAL-ORGANIC FRAMEWORKS DERIVED NANOMATERIALS FOR ADVANCED SUPERCAPACITORS*”, being submitted herewith for the award of **Doctor of Philosophy in Chemistry** under the Faculty of Science and Technology of Shivaji University, Kolhapur is the result of the original research work completed by **Miss. Rakhee Raghunath Bhosale** under my supervision and guidance and to the best of my knowledge and belief, the work embodied in this thesis has not formed earlier on the basis for the award of any degree or similar title of this or any other University or examining body.

In view of university Grants Commission (Promotion of Academic Integrity and Prevention of plagiarism in Higher Educational Institutions) Regulations, 2018 dated 31st July 2018, this is to certify that the work done by the Miss. Rakhee Raghunath Bhosale is plagiarism free.

Place: Kolhapur
Date:

Prof. (Dr.) S. S. Kolekar
Research Guide
Department of Chemistry,
Shivaji University, Kolhapur

Professor and Head
Department of Chemistry,
Shivaji University, Kolhapur

ACKNOWLEDGMENT

First and foremost, I am profoundly indebted to my supervisor, Prof. (Dr.) S. S. Kolekar, Department of Chemistry, Shivaji University, Kolhapur, who gave me an opportunity to join his research group. This thesis could not have been accomplished without his inspiring, enthusiastic guidance, constructive criticism and continuous motivation throughout the course of my research work.

It is a great privilege for me to express my gratitude to Hon'ble, Prof. (Dr.) D. T. Shirke, Vice-Chancellor, Shivaji University, Kolhapur, Hon'ble, Prof. (Dr.) P. S. Patil, Pro Vice-Chancellor, Shivaji University, Kolhapur, Prof. (Dr.) K. D. Sonawane, Head, Department of Chemistry and Prof. (Dr.) G. S. Gokavi, Former Head, Department of Chemistry, Shivaji University, Kolhapur, for the encouragement to achieve excellence at the Department.

It would be great contentment to say thanks to my teachers from the Department of Chemistry for their keen interest and support in my research work. I am also thankful to all the non-teaching staff of the Chemistry Department for their kind help. As well as I would like to thank the technical staff from CFC and staff from USIC, Shivaji University, Kolhapur for their time to time helps.

I am always grateful to my research colleagues and friends Dr. Suryakant Patil, Dr. Pramod Kumbhar, Dattatray Narale, Rachana Ghaware, Omkar Kulkarni, Rohini Sankannavar, Tabbu Shaikh, and Sandip Pise for their kind cooperation, fruitful discussions, affable support and encouragement all through my research efforts. It's my immense pleasure to utter my humble gratitude to Dr. Vithoba Patil, Mr. Vijay Chavan and Prof. Deok-kee Kim.

I would like to extend my thanks to my family especially my brother Ruthivik, my husband Vinod, my sisters Tejaswini and Sneha for their heartfelt support. It's always the happiest feeling to get optimistic support from my family group including in-laws, brother-in-law Vijay, my little niece Swara and every family member, wouldn't be possible to conclude this thesis without the intense support, blessings, unconditional love and affection received from my entire family. I am immensely obliged for the sacrifices put in by my mother Supriya and father Raghunath throughout my life who always stood beside me in all the circumstances.

I am thankful to the Chhatrapati Shahu Maharaj National Research Fellowship, Government of India for their financial support. Finally, I would like to thank all the persons who directly or indirectly gave me support and encouragement throughout my research tenure.

Rakhee



List of Figures

Figure No.	Figure Caption	Page No.
1.1	Different type's energy storage devices	4
1.2	The Ragone plot depicts the energy and power densities of several energy storage devices	5
1.3	Classification of supercapacitors	10
1.4	Charge storage mechanism of supercapacitors, (a) EDLCs, (b) Pseudocapacitors and (c) Hybrid supercapacitors. ³⁶ Reproduced with permission. Copyright © 2021, Royal Society of Chemistry	11
1.5	Properties of MOFs	18
1.6	MOFs as an electrode material for supercapacitor	19
1.7	Schematic of the pristine MOFs for supercapacitor application	20
1.8	Development of the use of various MOFs in the field of supercapacitor application	25
1.9	Diagrammatic representation of plan of thesis	31
2.1	Schematic depiction of reflux condensation assembly	40
2.2	Various sophisticated techniques for the characterization of MOFs and its derived materials	43
2.3	Schematic diagram of X-Ray diffraction techniques	44
2.4	Schematic diagram of FTIR spectrometer	45
2.5	Energy level diagrams showing the states involved in Raman signal	47
2.6	Schematic diagram of Raman spectrometer	48
2.7	Schematic representation of XPS spectrometer	49
2.8	Schematic representation of scanning electron microscope	51
2.9	Schematic diagram showing the possible transition ¹⁴	52
2.10	BET instrument	54
2.11	Schematic representation of transmission electron microscope	55
2.12	Digital photograph of vibrating sample magnetometer	57
2.13	A typical cyclic voltammogram curves of (a) Supercapacitor and (b) Battery. Reproduced with permission. ²⁷ Copyright © 2018, American Chemical Society	59

2.14	A typical galvanostatic charge-discharge curves of (a) Supercapacitor and (b) Battery. Reproduced with permission. ²⁷ Copyright © 2018, American Chemical Society	60
2.15	A Nyquist plot featuring labeled significant regions. Reproduced with permission. ³⁰ Copyright © 2021, Royal Society of Chemistry	61
3.1	Schematic of synthesis of Ni-MOF nanorods via a wet chemical route	70
3.2	XRD pattern of Ni-MOF	72
3.3	FT-IR pattern of Ni-MOF	73
3.4	Raman Spectroscopy of Ni-MOF	73
3.5	SEM images of Ni-MOF	74
3.6	(a) N ₂ adsorption-desorption isotherms, (b) Pore size distribution of Ni-MOF	75
3.7	(a) XPS survey spectrum of Ni-MOF. High-resolution XPS spectra of Ni 2p, (b) C 1s, (c) and O 1s (d) regions	76
3.8	(a) CV profile of Ni-MOF at different scan rates operated from 0 to 0.3 V, (b) GCD profile for Ni-MOF at different current rates (5 to 35 mA cm ⁻²), (c) Nyquist plot of the Ni-MOF, (d) Plot of specific capacitance vs. current densities, (e) Cyclic durability test at a high current of 35 mA cm ⁻² over 3000 GCD cycles with inset of first and last five cycles, (f) Coulombic efficiency as a function of current density	79
3.9	(a) Schematic illustration of hybrid supercapacitor with Ni-MOF as a positive electrode and activated carbon as a negative electrode in KOH aqueous electrolyte, (b) Digital photograph of Ni-MOF//AC HSC device	81
3.10	(a) CV profile of HSC cell at different scan rates operated from 0 to 0.9 V, (b) GCD profile for HSC cell at different current rates (2 to 6 mA cm ⁻²), (c) Nyquist plot of the HSC device, (d) Plot of specific capacitance vs. current densities, (e) Ragone plot of HSC cell, (f) Cyclic durability test at a high current of 6 mA cm ⁻² over 3000 GCD cycles with inset of first and last five cycles	83
3.11	The handmade asymmetric supercapacitor device charged for 15 seconds and glow a red LED for almost 105 seconds (i.e. charging time 15 second discharging time 105 sec)	84

3.12	Radar plot for Ni-MOF based on supercapacitive properties	85
4.1	Schematic illustrations of the synthesis of trimetallic MOFs	94
4.2	XRD patterns of BDC-MOF and BTC-MOF	97
4.3	FTIR spectra of BDC-MOF and BTC-MOF	98
4.4	Raman spectra of BDC-MOF and BTC-MOF	99
4.5	SEM images of (a, b) BTC-MOF and (c, d) BDC-MOF at different magnifications	100
4.6	EDX spectra and elemental mapping of C, O, Co, Ni and Zn elements for (a) BDC-MOF and (b) BTC-MOF	101
4.7	TEM, HR-TEM and SAED pattern of (a) BDC-MOF and (b) BTC-MOF	102
4.8	(a, b) N ₂ adsorption-desorption isotherm and pore size distribution curve BDC-MOF, (c, d) N ₂ adsorption-desorption isotherm and pore size distribution curve BTC-MOF	103
4.9	XPS survey spectra of (a) BDC-MOF and (b) BTC-MOF, high-resolution spectra of C 1s (c, d), O 1s (e, f), Ni 2p (g, h), Co 2p (i, j) and Zn 2p (k, l) of BDC-MOF and BTC-MOF, respectively	104
4.10	(a) Comparative CV curves at 10 mV s ⁻¹ scan rate, (b) Comparative GCD curves at 5 mA cm ⁻² current density, (c) CV curves of BDC-MOF at different scan rates, (d) CV curves of BTC-MOF at different scan rates, (e) GCD curves of BDC-MOF at different current densities, (f) GCD curves of BTC-MOF at different densities	107
4.11	(a) Nyquist plots, (b) Variation of specific capacitance as a function of current density, (c) Ragone plot showing the energy density versus power density	108
4.12	Cycling performance at 25 mA cm ⁻² , and the inset shows the first and last five cycles of BDC-MOF and BTC-MOF	109
4.13	(a) CV, (b) GCD curves of the symmetric device within the various potential windows (0.4 V, 0.6 V, 0.8 V, 1.0 V and 1.2 V), (c) CV curves of the symmetric device at different scan rates, (d) GCD curves of the symmetric device at different current densities	111
4.14	(a) Nyquist plot, (b) Variation of specific capacitance as a function of current density, (c) Ragone plot showing the energy density versus	112

	power density, (d) Cycling performance at 6 mA cm^{-2} , and the inset shows the first and last five cycles of the symmetric device	
4.15	(a) Fabrication schematic of BDC-MOF//2M KOH//BDC-MOF symmetric supercapacitor device, (b) The two handmade symmetric supercapacitor device which glows a red LED	113
4.16	Radar graph for comparative study of BDC-MOF and BTC-MOF based on supercapacitive properties	114
5.1	Schematic diagram of $\text{MnFe}_2\text{-MOF}$ derived manganese ferrite (MnFe_2O_4)	123
5.2	X-ray diffraction patterns of $\text{MnFe}_2\text{-MOF}$ and its derived MnFe_2O_4	126
5.3	FT-IR spectra of $\text{MnFe}_2\text{-MOF}$ and its derived MnFe_2O_4	127
5.4	Raman spectra of $\text{MnFe}_2\text{-MOF}$ and its derived MnFe_2O_4	128
5.5	SEM images at different magnifications of (a, b) $\text{MnFe}_2\text{-MOF}$ and (c, d) its derived MnFe_2O_4	129
5.6	Elemental mapping images of (a) $\text{MnFe}_2\text{-MOF}$ and (b) its derived MnFe_2O_4	130
5.7	TEM, HR-TEM and SAED patterns of (a-d) $\text{MnFe}_2\text{-MOF}$ and (e-h) its derived MnFe_2O_4	131
5.8	Nitrogen adsorption/desorption isotherms of (a) $\text{MnFe}_2\text{-MOF}$ and (b) derived MnFe_2O_4 (the insets show pore size distribution)	132
5.9	Hysteresis curves of $\text{MnFe}_2\text{-MOF}$ and its derived MnFe_2O_4	132
5.10	High-resolution XPS spectra of (a-d) $\text{MnFe}_2\text{-MOF}$ (e-g) its derived MnFe_2O_4	134
5.11	(a) Comparison of cyclic voltammograms of $\text{MnFe}_2\text{-MOF}$ and its derived MnFe_2O_4 electrodes at a potential sweep rate of 100 mV s^{-1} , (b) Comparison of GCD curves of $\text{MnFe}_2\text{-MOF}$ and its derived MnFe_2O_4 electrodes at a current density of 1 mA cm^{-2} , (c) CV curves of $\text{MnFe}_2\text{-MOF}$ in $1 \text{ M Na}_2\text{SO}_4$ at various scan rates, (d) CV curves of derived MnFe_2O_4 in $1 \text{ M Na}_2\text{SO}_4$ at various scan rates, (e) GCD curves of $\text{MnFe}_2\text{-MOF}$ at various current densities, (f) GCD curves of MnFe_2O_4 at various current densities	135
5.12	(a) Comparative rate capability of the $\text{MnFe}_2\text{-MOF}$ and derived MnFe_2O_4 electrodes at 1 to 10 mA cm^{-2} , (b) Ragone plots of the $\text{MnFe}_2\text{-}$	136

	MOF and derived MnFe ₂ O ₄ (c) Nyquist plots of the MnFe ₂ -MOF and derived MnFe ₂ O ₄	
5.13	Cyclic stability (left versus bottom) and Coulombic efficiency (right versus bottom) of (a) MnFe ₂ -MOF and (b) Derived MnFe ₂ O ₄ electrodes for 3000 cycles measured at a current density of 10 mA cm ⁻² , the inset shows the charge-discharge curves of the first and last five cycles	137
5.14	(a) Comparison of cyclic voltammograms of ASC device at a potential sweep rate of 100 mV s ⁻¹ , (b) Comparison of GCD curves of ASC device at a current density of 1 mA cm ⁻² , (c) CV curves of ASC device in 1 M Na ₂ SO ₄ at various scan rates; (d) GCD curves of ASC device at various current densities	138
5.15	(a) Comparative rate capability of the ASC device at 1 to 8 mA cm ⁻² , (b) Ragone plots of the ASC device, (c) Nyquist plots of the ASC device	140
5.16	Cyclic stability (left versus bottom) and Coulombic efficiency (right versus bottom) of ASC device for 3000 cycles measured at a current density of 8 mA cm ⁻² , the inset shows the charge-discharge curves of the first and last five cycles	140
5.17	(a) Schematic illustration of fabricated asymmetric supercapacitor device, (b) Digital photograph of fabricated two handmade asymmetric supercapacitor device connected in series to glow the LEDs	141
5.18	Radar plot for comparative study of MnFe ₂ -MOF and derived MnFe ₂ O ₄ electrodes based on electrochemical properties	142
6.1	Schematic illustration of the synthesis of CoFe ₂ -MOF, its derived CoFe ₂ O ₄ and nanoporous carbon (NPC)	152
6.2	XRD patterns of CoFe ₂ -MOF, CoFe ₂ O ₄ and nanoporous carbon (NPC)	153
6.3	FTIR spectra of CoFe ₂ -MOF, CoFe ₂ O ₄ and nanoporous carbon (NPC)	154
6.4	Raman spectra of CoFe ₂ -MOF, CoFe ₂ O ₄ and nanoporous carbon (NPC)	155
6.5	SEM images at different magnifications of (a, b) CoFe ₂ -MOF (c, d) CoFe ₂ O ₄ (e, f) NPC	157
6.6	Elemental mapping images of (a) CoFe ₂ -MOF and its derived (b) CoFe ₂ O ₄ (c) NPC	158
6.7	TEM, HR-TEM and SAED pattern of the as-prepared CoFe ₂ -MOF (a-d), derived CoFe ₂ O ₄ (e-h) and Nanoporous carbon (i-l)	159

6.8	Nitrogen adsorption-desorption isotherm and BJH pore size distribution plots of (a, d) CoFe ₂ -MOF, (b, e) CoFe ₂ O ₄ and (c, f) NPC	160
6.9	Hysteresis curves of CoFe ₂ -MOF, its derived MnFe ₂ O ₄ and nanoporous carbon	161
6.10	High-resolution XPS spectra of (a-d) CoFe ₂ -MOF (e-g) CoFe ₂ O ₄ (h-j) NPC	162
6.11	CV curves of CoFe ₂ -MOF, CoFe ₂ O ₄ , and NPC within different operating potential windows at a constant scan rate of 100 mV s ⁻¹	163
6.12	The three-electrode electrochemical performances of CoFe ₂ -MOF-derived CoFe ₂ O ₄ and NPC: CV curves at various scan rates of (a) CoFe ₂ -MOF (b) CoFe ₂ O ₄ and (c) NPC, GCD curves at various current densities of (d) CoFe ₂ -MOF (e) CoFe ₂ O ₄ and (f) NPC	164
6.13	(a) Specific capacitance at the different current densities of CoFe ₂ -MOF, CoFe ₂ O ₄ and NPC, (b) Ragone plot of CoFe ₂ -MOF, CoFe ₂ O ₄ and NPC, (c) EIS curves of CoFe ₂ -MOF, CoFe ₂ O ₄ and NPC	165
6.14	Cycle lives measured from galvanostatic charge-discharge of the CoFe ₂ -MOF (at 10 mA cm ⁻² current density), CoFe ₂ O ₄ (at 10 mA cm ⁻² current density) and NPC (at 12 mA cm ⁻² current density) electrodes	166
6.15	Schematic illustration of fabrication of all-in-one hybrid supercapacitor device	168
6.16	Electrochemical tests of the CoFe ₂ O ₄ //NPC hybrid supercapacitor device (HSC). (a) CV curves of the CoFe ₂ O ₄ //NPC HSC device at a scan rate of 100 mV s ⁻¹ within different potential windows, (b) CV curves of CoFe ₂ O ₄ //NPC HSC device at different scan rates, (c) GCD curves of the CoFe ₂ O ₄ //NPC HSC device at 1 mA cm ⁻² with varied potential windows, (d) GCD curves of CoFe ₂ O ₄ //NPC HSC device at various current densities	169
6.17	(a) Rate capability of the CoFe ₂ O ₄ //NPC HSC device according to the GCD curves from 1 to 5 mA cm ⁻² , (b) Ragone plot of the CoFe ₂ O ₄ //NPC HSC device, (c) Nyquist plot of the CoFe ₂ O ₄ //NPC HSC device	170
6.18	Cyclic stability and Coulombic efficiency of CoFe ₂ O ₄ //NPC HSC device for 5000 cycles at the current density of 5 mA cm ⁻² (inset show first and last five GCD cycles of the stability test)	171

6.19	Radar plot for comparative study of CoFe ₂ -MOF, derived CoFe ₂ O ₄ and NPC electrodes based on supercapacitive properties	172
7.1	Schematic illustration of work carried out for thesis	181

List of Tables

Table No.	Table Caption	Page No.
1.1	Relationship between supercapacitors and other energy storage technologies	8
1.2	Properties of transition first series elements	27
2.1	X-ray diffraction methods	45
3.1	Comparison of the specific capacitances of Ni-MOF	77
4.1	Comparison of the specific capacitances of trimetallic MOF with previously reported materials	110
6.1	Textural properties of CoFe ₂ -MOF, its derived CoFe ₂ O ₄ and NPC	160

List of Abbreviations

Abbreviations	Long forms
MOF	Metal-organic framework
EDLC	Electric double-layer capacitor
W kg ⁻¹	Watt per kilogram
Wh kg ⁻¹	Watt hours per kilogram
Q	Charge
V	Voltage
SC	Supercapacitor
PC	Pseudocapacitor
AC	Activated carbon
CNTs	Carbon nanotubes
ESR	Equivalent series resistance
EES	Energy storage systems
1D	One dimensional
2D	Two dimensional
3D	Three dimensional
Csp	Specific capacitance
Es	Energy density
Ps	Power density
F g ⁻¹	Farad per gram
A g ⁻¹	Ampere per gram
mA cm ⁻²	Milliampere per centimeter square
m ² g ⁻¹	Meter square per gram
°C	Degree centigrade
mV s ⁻¹	Millivolt per second
nm	Nanometer
NPC	Nanoporous carbon
BET	Brunauer–Emmett–Teller
ASC	Asymmetric supercapacitor
CV	Cyclic voltammetry
GCD	Galvanostatic charge-discharge
EIS	Electrochemical impedance spectroscopy
LED	Light emitting diode

XRD	X-ray diffraction
FTIR	Fourier transform infrared spectroscopy
XPS	X-ray photoelectron spectroscopy
SEM	Scanning electron microscope
TEM	Transmission electron microscope
GPEs	Gel-polymer electrolytes
EDS	Energy dispersive X-ray spectroscopy
VSM	Vibrating sample magnetometer
Ni-MOF	Nickel-metal organic framework
DMF	N, N-dimethylformamide
PVA	Polyvinyl alcohol
JCPDS	Joint committee on powder diffraction standard
R_s	Series resistance
R_{ct}	Charge transfer resistance
HSC	Hybrid supercapacitor
PVDF	Polyvinylidene fluoride
NMP	N-methyl-2-pyrrolidone
η	Coulombic efficiency
BDC	Terephthalic acid
BTC	Trimesic acid
FWHM	Full-width half maxima
SSC	Symmetric supercapacitor
IUPAC	International union of pure and applied chemistry
SSA	Specific surface area
BJH	Barrett-Joyner-Halenda
MnFe ₂ -MOF	Mn/Fe metal-organic framework
MnFe ₂ O ₄	Manganese ferrite
CoFe ₂ -MOF	Cobalt-iron metal-organic framework
CoFe ₂ O ₄	Cobalt ferrite
PTA	Terephthalic acid

INDEX

Sr. No.	Content	Page No.
1.0	Introduction and Theoretical Background	1 – 37
1.1	Outline	1
1.2	Introduction	2
	1.2.1 The need of supercapacitor	2
	1.2.2 Brief history and current developments in supercapacitor	3
	1.2.3 Types of electrochemical energy storage devices	4
	1.2.3.1 Capacitor	5
	1.2.3.2 Battery	6
	1.2.3.3 Fuel cell	7
	1.2.3.4 Supercapacitor	7
	1.2.4 Types of supercapacitors	9
	1.2.4.1 Electrical double-layer capacitor (EDLC)	10
	1.2.4.2 Pseudocapacitor (PC)	10
	1.2.4.3 Hybrid capacitor	10
	1.2.5 Supercapacitor materials	11
	1.2.5.1 Carbon-based supercapacitor	11
	1.2.5.2 Conducting polymers-based supercapacitor	13
	1.2.5.3 Metal oxides-based supercapacitor	13
	1.2.5.4 MOF-based supercapacitor	14
	1.2.6 Electrical characteristics of the supercapacitor	15
	1.2.6.1 Specific capacitance	15
	1.2.6.2 Specific energy and specific power	15
	1.2.6.3 Operating potential voltage	16
	1.2.6.4 Cyclic stability	16
	1.2.7.5 Electrolyte	16
1.3	General introduction and literature survey of the materials	17
	1.3.1 Introduction to the MOF	17
	1.3.2 Literature survey of MOFs for supercapacitors	18
	1.3.2.1 Pristine MOFs for supercapacitors	19
	1.3.2.2 MOF-derived metal oxides for supercapacitors	21
	1.3.2.3 MOF-derived carbon for supercapacitors	22
	1.3.3 MOFs derived from the first transition series elements serve as electrodes for supercapacitors	25
	1.3.3.1 The properties of transition elements	26
1.4	Purpose of the dissertation	27
1.5	Plan of the work	28
1.6	References	32

2.0	Experimental Details and Characterization Techniques		38-64
2.1	Outline		38
2.2	Introduction		39
2.3	Experimental details		40
	2.3.1	Aqueous chemical method/reflux condensation method	40
	2.3.2	Substrate cleaning	41
	2.3.3	Procedure of the seed slurry and fabrication of working electrodes	42
2.4	Characterization techniques		42
	2.4.1	X-ray diffraction (XRD)	43
	2.4.2	Fourier transform infrared (FTIR) spectroscopy	45
	2.4.3	Fourier transform raman (FT-Raman) spectroscopy	46
	2.4.4	X-ray photoelectron spectroscopy (XPS)	49
	2.4.5	Scanning electron microscope (SEM)	50
	2.4.6	Energy dispersive X-ray (EDS) spectroscopy	52
	2.4.7	Specific surface area analyzer using Brunauer– Emmett– Teller (BET)	53
	2.4.8	Transmission electron microscope (TEM)	55
	2.4.9	Vibrating sample magnetometer (VSM)	56
	2.4.10	Electrochemical studies	57
	2.4.10.1	Cyclic voltammetry (CV)	58
	2.4.10.2	Galvanostatic charge-discharge (GCD)	59
	2.4.10.3	Electrochemical impedance spectroscopy (EIS)	60
	2.4.11	Supercapacitor device fabrication	61
	2.4.11.1	Electrode materials	62
	2.4.11.2	Separator	62
	2.4.11.3	Gel-polymer electrolyte (GPE)	62
2.5	References		63
3.0	Design and Development of Porous Nanorods-Based Nickel-Metal Organic Framework (Ni-MOF) for High-Performance Supercapacitor Application		65-89
3.1	Outline		65
3.2	Introduction		66
3.3	Experimental section		69
	3.3.1	Reagents	69
	3.3.2	Preparation of nickel-based metal-organic framework (Ni-MOF)	68
	3.3.3	Characterization techniques details	70
	3.3.4	Evaluation of electrode materials and electrochemical studies	70
3.4	Results and discussion		71
	3.4.1	X-ray diffraction of Ni-MOF	71
	3.4.2	Fourier transform infrared spectroscopy of Ni-MOF	72

	3.4.3	Raman spectroscopy of Ni-MOF	73
	3.4.4	Scanning electron microscopy of Ni-MOF	74
	3.4.5	Brunauer– Emmett– Teller analysis of Ni-MOF	75
	3.4.6	X-ray photoelectron spectroscopy of Ni-MOF	76
	3.4.7	Electrochemical measurements of Ni-MOF electrode	77
	3.4.8	Electrochemical measurements of hybrid supercapacitor device	81
3.5	Conclusion		85
3.6	References		86
4.0	Construction of Well-Defined Two-Dimensional Architectures of Trimetallic Metal-Organic Frameworks for High-Performance Symmetric Supercapacitors		90-119
4.1	Outline		90
4.2	Introduction		91
4.3	Experimental section		93
	4.3.1	Synthesis of MOFs	93
	4.3.2	Structural and elemental characterization	94
	4.3.3	Electrochemical measurements with a three-electrode assembly	95
	4.3.4	Electrochemical measurements of the symmetric supercapacitor	96
4.4	Results and discussion		96
	4.4.1	X-ray diffraction of trimetallic MOFs	96
	4.4.2	FT-IR spectroscopy of trimetallic MOFs	97
	4.4.3	Raman spectroscopy of trimetallic MOFs	98
	4.4.4	Scanning electron microscopy of trimetallic MOFs	99
	4.4.5	Energy dispersive X-ray analysis of trimetallic MOFs	101
	4.4.6	Transmission electron microscopy of trimetallic MOFs	101
	4.4.7	Brunauer-Emmett-Teller analysis of trimetallic MOFs	102
	4.4.8	X-ray photoelectron spectroscopy of trimetallic MOFs	103
	4.4.9	Electrochemical measurements of trimetallic MOFs	106
	4.4.10	Electrochemical measurements of symmetric supercapacitors device	110
4.5	Conclusion		114
4.6	References		116
5.0	Bimetallic MnFe₂-MOF and Its Derived MnFe₂O₄ Nanostructures for Supercapacitive Applications		120-146
5.1	Outline		120
5.2	Introduction		121
5.3	Experimental Section		123
	5.3.1	Materials	123
	5.3.2	Synthesis of MnFe ₂ -MOF and MnFe ₂ O ₄	124
	5.3.3	Structural and elemental characterization	124

	5.3.4	Electrochemical properties evaluation and preparation of working electrodes	126
5.4	Results and discussion		126
	5.4.1	X-ray diffraction of MnFe ₂ -MOF and MnFe ₂ O ₄	126
	5.4.2	FT-IR spectroscopy of MnFe ₂ -MOF and MnFe ₂ O ₄	127
	5.4.3	Raman spectroscopy of MnFe ₂ -MOF and MnFe ₂ O ₄	127
	5.4.4	Scanning electron microscopy of MnFe ₂ -MOF and MnFe ₂ O ₄	128
	5.4.5	Energy dispersive X-ray analysis of MnFe ₂ -MOF and MnFe ₂ O ₄	129
	5.4.6	Transmission electron microscopy of MnFe ₂ -MOF and MnFe ₂ O ₄	130
	5.4.7	Brunauer-Emmett-Teller analysis of MnFe ₂ -MOF and MnFe ₂ O ₄	131
	5.4.8	Vibrating-sample magnetometer of MnFe ₂ -MOF and MnFe ₂ O ₄	132
	5.4.9	X-ray photoelectron spectroscopy of MnFe ₂ -MOF and MnFe ₂ O ₄	133
	5.4.10	Capacitance characterization of electrode	134
	5.4.11	Capacitance characterization of solid-state asymmetric supercapacitor (ASC) device (MnFe ₂ -MOF//AC)	137
5.5	Conclusion		142
5.6	References		144
6.0	Hybrid Supercapacitor Based on Nanoporous Carbon and CoFe₂O₄ Derived From a Single Bimetallic-Organic Framework: One-for-All Approach		147-175
6.1	Outline		147
6.2	Introduction		148
6.3	Experimental section		149
	6.3.1	Chemicals	149
	6.3.2	Synthesis of CoFe ₂ -MOF and its derived cobalt ferrite and nanoporous carbon	150
	6.3.3	Material characterization	150
	6.3.4	Preparation of working electrodes	151
	6.3.5	Preparation of an all-in-one solid-state hybrid supercapacitor device	151
	6.3.6	Electrochemical measurements	151
6.4	Results and discussion		152
	6.4.1	X-ray diffraction of CoFe ₂ -MOF, CoFe ₂ O ₄ and NPC	153
	6.4.2	FT-IR spectroscopy of CoFe ₂ -MOF, CoFe ₂ O ₄ and NPC	154
	6.4.3	Raman spectroscopy of CoFe ₂ -MOF, CoFe ₂ O ₄ and NPC	155
	6.4.4	Scanning electron microscopy of CoFe ₂ -MOF, CoFe ₂ O ₄ and NPC	156

	6.4.5	Energy dispersive X-ray analysis of CoFe ₂ -MOF, CoFe ₂ O ₄ and NPC	158
	6.4.6	Transmission electron microscopy of CoFe ₂ -MOF, CoFe ₂ O ₄ and NPC	158
	6.4.7	Brunauer-Emmett-Teller analysis of CoFe ₂ -MOF, CoFe ₂ O ₄ and NPC	160
	6.4.8	Vibrating-sample magnetometer of CoFe ₂ -MOF, CoFe ₂ O ₄ and NPC	161
	6.4.9	X-ray photoelectron spectroscopy of CoFe ₂ -MOF, CoFe ₂ O ₄ and NPC	162
	6.4.10	Electrochemical measurements of CoFe ₂ -MOF, CoFe ₂ O ₄ and NPC electrodes	163
	6.4.11	Electrochemical characterization of CoFe ₂ O ₄ //NPC all-in-one hybrid supercapacitor device (CoFe ₂ O ₄ //NPC HSC device)	167
6.5	Conclusion		172
6.6	References		173
7.0	80-Recommendation		176-182
7.1	Outline		176
7.2	Introduction		177
7.3	Conclusion		177
7.4	Summary		180
7.5	Future findings		182

CHAPTER ONE

Introduction and Theoretical Background

1.1 Outline

This chapter provides an overview of energy storage technologies such as supercapacitors and MOF-based supercapacitors, as well as theoretical background of these devices, electrochemical properties and variables affecting their performance. It is also addressed, how metal-organic frameworks are now used in supercapacitor applications. A comprehensive review of the literature has been offered together with suggestions on how to enhance the electrochemical performance of supercapacitors. The numerous methods and procedures for improving the electrochemical characteristics of MOF as a supercapacitor material that are described in the literature are also illustrated. This chapter aims to encourage ongoing innovation to enhance MOF-derived functional materials for supercapacitor application. It also offers some perspectives on current key obstacles and their potential solutions. Finally, a detailed survey of the top five groups on MOF and its derived materials used in supercapacitor applications is provided using the Scopus database.

1.2 Introduction

In the twenty-first century, the quickly growing modern world of technology, transportation, and industrialisation needs massive energy. Due to the limited availability of fossil fuels and their limited global deposition, clean energy sources that include energy storage and conversion are crucial for the sustainable development of human society. A crucial foundation for economic growth is the entry of energy. Industrialization, which is supported by non-renewable resources such as coal, crude oil, and petrol, is the cause of contemporary economic progress. The world is currently dealing with an irreversible environmental problem called global warming, caused by overconsumption of non-renewable resources, which leads to exhaustion. Efforts are being made to produce clean, inexpensive, efficient, and dependable energy sources since they are crucial for socio-economic development in order to address this issue. Renewable energy sources are the only way to meet the need for clean and secure energy sources. But these resources' biggest flaw is that they are sporadic, which makes them unreliable. We need strong and trustworthy energy storage devices to get over this limitation of renewable fuels. In other words, we need to transition from "scanty, sparse and unreliable energy collectors" to "reliable, speedy, superior and sustainable energy storage benefits".¹⁻³

1.2.1 The need of supercapacitor

The growth of technology and human civilization has resulted in increased energy consumption, necessitating expensive energy conversion and storage equipment. Additionally, to lessen the crisis of running out of fossil fuels, combat global warming, and to reduce pollution brought on by the population boom, sustainable and clean energy conversion and storage technologies are needed.⁴ Batteries, capacitors, supercapacitors, and fuel cells are just a few of the energy storage technologies developed to store electrical energy. The benefits and drawbacks of each of these technologies vary. Fuel cells and electrochemical supercapacitors are the two most significant energy storage and conversion innovations. The terms electrochemical double layer capacitor and electrochemical supercapacitor are also used. Initially, the idea of an electrochemical supercapacitor was based on an electrical double layer that was present at the boundary of two plates of an electrolytic capacitor, a condenser that contained an electrolyte solution. First and second generation capacitors are electrostatic and electrolytic capacitors, respectively. The

third generation, known as supercapacitor, has been created as a result of fast material development.^{5,6}

1.2.2 Brief history and current developments in supercapacitor

Supercapacitors have been widely researched during the last few decades. They could offer distinct characteristics such as elevated energy density, high reversibility, quick charge-discharge cycles, and long cycle life stability, all of which are critical parameters for energy storage and conversion. Helmholtz first outlined the notion of a two layer capacitor in 1853. Becker received the construction of a two layer capacitor and its first patent in 1957 from General Electric Corporation Limited (GECL). In that invention, porous carbon material was employed to manufacture electrode material for supercapacitor applications.^{7,8} Standard Oil Company, Cleveland, Ohio (SOHIO) issued a patent on an energy generating and storage system having a porous carbon electrode in 1962. In that instance, the EDLC interface functions like an electrochemical capacitor and has the highest specific capacitance.⁹ Additionally, SOHIO received a patent for a disc-type capacitor in 1970 that used carbon paste solution as its electrolyte.¹⁰ In 1971, NEC obtained a licence from SOHIO on double layer capacitance, and it produced the first double layer capacitor on a commercial scale under the moniker 'supercapacitor'.¹¹ Since then, the supercapacitor has begun to undergo industrialisation, modernization, and the creation of new technologies. This important invention enhanced the process used to make supercapacitors in general. The Panasonic Company, founded in 1978, has since been utilised as a backup source for memory applications. As a result, the supercapacitor is sometimes known as a gold capacitor. The Pinnacle Research Institute (PRI), under the name PRI Ultracapacitors, created the first metal oxide-based material for high power density EDLC in 1982. Later, Conway et al. created a RuO₂ electrode material for supercapacitors that had reduced internal resistance and a maximum specific capacitance and that demonstrated the substantial advances made in the 1970s and 1980s.^{12,13} Hybrid cars were first mentioned by the US Energy Department in 1992, with a major contribution coming from Maxwell's use of ultracapacitors.

Many industries around the world have reported supercapacitor production. Industries including Panasonic, AVX, NEC, Epcos, Cooper, and ELNA, among others, have created several versions of EDLC and its components in America and Japan. Additionally, using integrated circuits, Maxwell and Evans created and produced voltage balanced circuits. By offering several types of electric double layer

capacitors, ESMA created hybrid electric vehicles in Russia and improved power quality applications. Due to supercapacitors' special characteristics and numerous applications listed below, their commercialization and use have dramatically increased in recent years. In the sphere of transportation, supercapacitors are utilised as an electric backup source in autos, electric vehicles, hybrid electric vehicles, regenerative braking systems, startup applications, and energy conversion systems. Supercapacitors are also used as a power backup source in consumer devices including microcomputers, keyboards, clocks, telecoms, toys, digital cameras, and uninterruptible power supply. Supercapacitors are employed in robotics and factory automation in industrial applications. Additionally, supercapacitors have applications in the production of energy from renewable sources, including wind and solar energy systems.¹⁴⁻¹⁹

1.2.3 Types of electrochemical energy storage devices

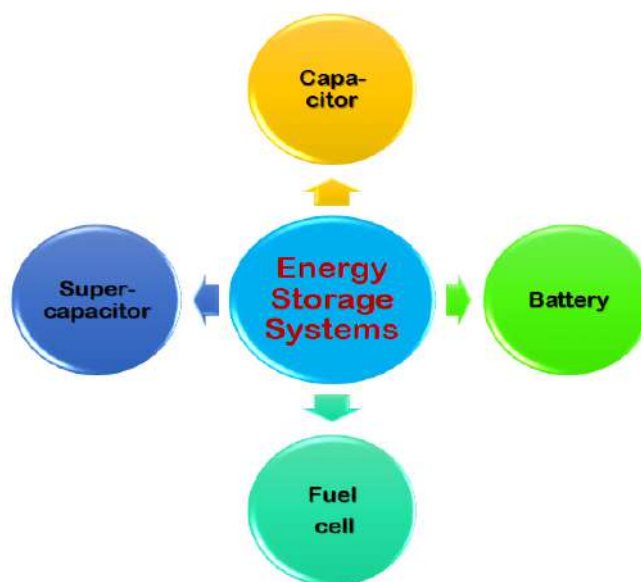


Figure 1.1: Different type's energy storage devices

Energy storage alternatives come in a variety of forms, and new ones are appearing as the technology becomes increasingly important to the development of the global energy systems of the future. The figure 1.1 represents the different types of energy storage devices. The development of future wearable and bio-integrated electronics depends on a programmable electrochemical energy storage system. Electrochemical energy storage systems convert electrical energy into chemical energy or vice versa, allowing heterogeneous chemical processes to occur using charge transfer to or from electrodes (i.e. cathodic or anodic). Reversible electrochemical processes are used in electrochemical energy storage systems to

convert and store electrical energy through the simultaneous movement of electrons and ions. The electrochemical thermodynamics and kinetics are the most crucial aspects that should be considered in order to sustain adequate electrochemical performance under severe circumstances.^{20,21}

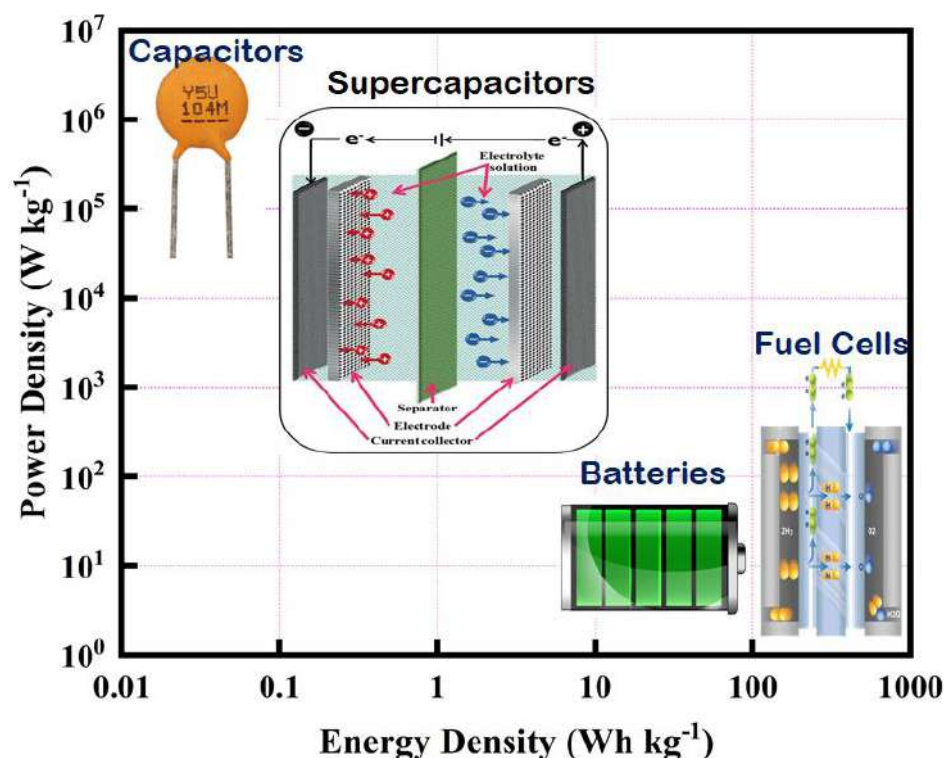


Figure 1.2: The Ragone plot depicts the energy and power densities of several energy storage devices

As illustrated in figure 1.2, the Ragone plot is the diagram that explains the comparative research of the performance of various energy storage systems. The power density is shown in this graph along the Y axis, measured in Watt per kilogram ($W\ kg^{-1}$), while the energy density is shown along the X axis, measured in Watt hours per kilogram ($Wh\ kg^{-1}$). In order to show how much energy is available in the devices as well as how rapidly the energy can be provided or stored, a Ragone plot is frequently employed. The four most significant electrochemical energy storage devices are capacitors, battery, fuel cell and supercapacitors, as seen in a Ragone plot.²²

1.2.3.1 Capacitor

A capacitor is a device that holds electrical charge. As illustrated in Figure 1.2, a capacitor consists of two conducting plates that are spaced apart by a modest distance and have a dielectric substance filled in the space between them. Different

types of dielectric materials exist, including titanate, mica, air, oiled papers, glass, and porcelain. The capacitor charges when a potential difference between outside sources is placed across its two plates. Positive charge gradually accrue on one plate while charging, while negative charges gradually build up on the other plate. When the external voltage difference is eliminated, the positive and negative charges both moved in the direction of the corresponding electrodes.²³

As a result, capacitors are used to separate the electrical charges. The following is a definition of capacitance:

$$C = \frac{Q}{V} \dots\dots\dots (1.1)$$

The following equation is used to calculate how much charge is present in the capacitor.

$$C = \epsilon \frac{A}{d} \dots\dots\dots (1.2)$$

Where C, ϵ , A and d denotes the capacitance, dielectric constant of medium, area and thickness of the dielectric media, respectively.

1.2.3.2 Battery

A battery is a device made up of different electrochemical cells that use chemical reduction-oxidation processes to transform stored chemical energy to electrical energy. Because of its small weight, high energy density, and capacity to be recharged, batteries are frequently utilised as a power source for a variety of gadgets in modern life, including laptops, hybrids, and electric automobiles. Two current collectors, an anode, a separator, an electrolyte, and a cathode make up a battery. When a battery is discharging, a flow of electrons from one side to the other is created when the anode discharges lithium ions to the cathode. In contrast, as the battery is being charged, the cathode releases lithium ions, which the anode then collects.²⁴

Batteries are divided into two categories based on the charging process:

(i) **Primary Battery:** Primary batteries are also called as non-rechargeable disposable batteries. When primary cells are completely depleted, they cannot be recharged, and the battery is said to be a single-cycle battery. They have a chemical within that is consumed through time and use, and after it is completely emptied, it must be disposed-off. Alkaline batteries, Aluminum-Air batteries, dry cells are types of primary batteries.

(ii) **Secondary Battery:** Multicycle batteries are the ones used in these batteries. These batteries have a long lifespan and may be recharged several times.

These batteries are typically used in electric vehicles (EVs), phones, cars, portable electronics, and a variety of other applications. Li-ion battery, Li-polymer battery, and Lead acid battery are types of secondary batteries.²⁵

1.2.3.3 Fuel cell

In 1838, the first fuel cell was invented by William Grove. NASA's space programmes saw the first commercial application of fuel cells. Fuel cell is electrochemical machinery that extracts electricity from fuel without accumulating it first. Similar to other electrochemical devices, fuel cells use reactants that are supplied from outside sources as they are consumed. Through a chemical process with oxygen or another oxidising agent, the fuel cells turn the chemical energy of the fuel into electrical energy. One of the fuels most frequently utilised in fuel cells is hydrogen. The process through which fuel is converted into energy is electrochemical. This energy production method uses electrochemistry, which is a simple, efficient, and clean process. The primary classification of these fuel cells is depending on the fuel utilised. Fuel cells are still in the research and development stage and are looking for a useful application that can break into the energy industry while remaining competitive with batteries and supercapacitors.^{26,27}

1.2.3.4 Supercapacitor

A supercapacitor (SC), also known as an ultracapacitor, is an electrochemical capacitor with a large capacity and capacitance values that are significantly greater than those of conventional capacitors. Supercapacitors operate similar to traditional capacitors. The increased charge can be held by the many pores inside the electrodes' high surface area, but supercapacitors are able to store more energy since the charge separation happens over a relatively short distance, i.e. among the electrolyte and an electrode. An electrolyte, a separator, and two electrodes are the basic components of a supercapacitor. Electrodes possess high surface area. Water-based combination of positive and negative ions is known as an electrolyte. The membrane, or separator, that separates these two electrodes permits the movement of charged ions. A cylindrical container is formed by rolling or folding the separator. It might be aqueous, organic, or solid state. Ion adsorption or quick surface redox reactions are two ways that supercapacitors store energy. Owing to this power features, supercapacitors are employed in hybrid electric cars to improve the power distribution and storage capabilities of batteries and fuel cells, supplying the necessary power for quick acceleration. This is because of their distinctive qualities, which include

environmental friendliness, short charging times, increased power densities, and increased durability.^{28,29} In summary, supercapacitors are gaining popularity because they include ion motions to and from electrode surfaces, resulting in fast storage. Furthermore, supercapacitors are low-maintenance materials with a long life cycle.

The following list includes several supercapacitor characteristics:

- ❖ Supercapacitors are known for their extended cycling times and high cycle efficiencies, which are regarded as some of their most crucial characteristics.
- ❖ Supercapacitors have a lower potential for contamination because no heavy metals are employed in their production.
- ❖ Supercapacitors have the ability to have a longer service life of roughly 10 to 15 years.
- ❖ Capacitance in supercapacitors can range from 1mF to more than 10 kF.
- ❖ Supercapacitors may charge or discharge between a few seconds to a few milliseconds.
- ❖ The energy density of supercapacitors can reach 10 Wh kg⁻¹.
- ❖ Supercapacitors are chosen over batteries and traditional capacitors because they have larger capacitance with small voltage restrictions.

Table 1.1: Relationship between supercapacitors and other energy storage technologies

Variables	Capacitors	Battery	Fuel cell	Supercapacitor
Electrode materials	Tantalum, Aluminum, Silver plates i.e. Conductive plates	Metal oxide materials, carbon materials	Gold coated carbon / Platinum / metal base	Conducting polymer, metal oxides, carbon materials, sulphides, nitrides
Storage mechanism	Electrode polarization caused by an applied electric field	Chemical energy is converted into electrical energy	Chemical energy is converted into electrical energy	An applied electric field causes the formation of an electric-double layer and a redox reaction

Principle	Polarization	Faradaic reactions in the bulk of the electrode	Oxidation and reduction	Faradaic/ Non-Faradaic
Electrolyte	Dielectric materials is used in place of electrolytes.	Acids, salt (NaCl, ClO ⁴⁻ , PF ⁶⁻ , BF ⁴⁻) + solvent (water, PLC, EC)	Sulphonated polymers, KOH, H ₃ PO ₄	Aqueous, organic, polymer electrolytes and Ionic liquids
Potential window	6 to 800	1.25 to 4.2	0.6	1 to 4
Energy density	<0.1	8 to 600	300 to 3000	1 to 10
Power density	0.25 to 10000	0.005 to 0.4	0.001 to 0.1	10 to 120
Life span	>100000 cycles	150 to 1500 cycles	1500 to 1000 h	50000 + h, unlimited cycles
Efficiency	>95%	70 to 85%	Up to 60%	90 to 95%

1.2.4 Types of supercapacitors

Supercapacitors are also known as ultracapacitors, power capacitors, gold capacitors, and super condensers. These are divided into three groups based on their charge storage mechanism as shown in figure 1.3 and 1.4.

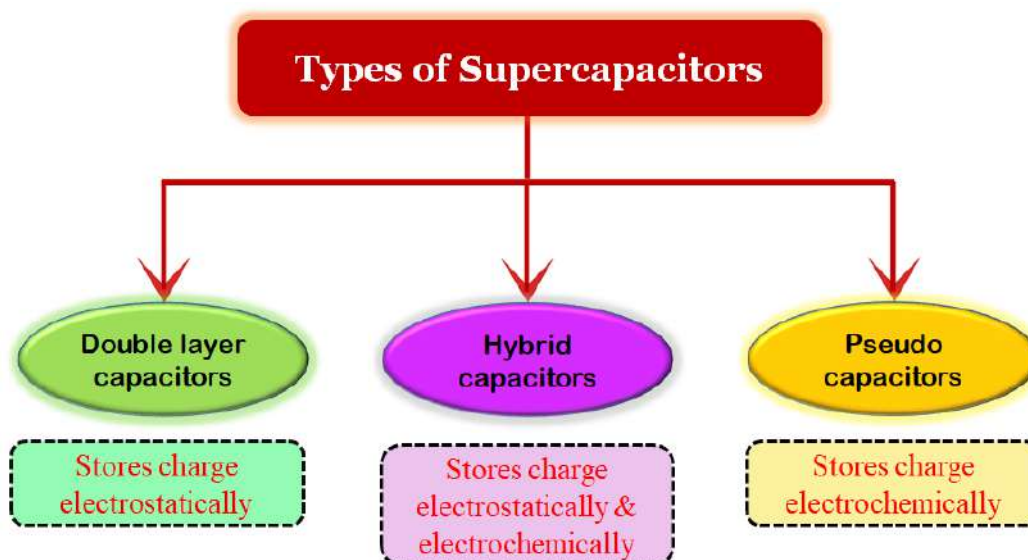


Figure 1.3: Classification of supercapacitors

1.2.4.1 Electrical double-layer capacitor (EDLC)

This type of capacitor operates on the charge storage mechanism, whereby a charge is really held on the electrode surface without resulting in any irreversible chemical processes by forming an electrical double layer. Carbon-based electrodes are often employed in supercapacitors that are detached by a dielectric material that functions as an insulator and has electrical characteristics that impact the supercapacitor's performance. In EDLC, charges are held electrostatically. As soon as a voltage is employed across the terminals, an electric field is produced at each electrolyte and that causes the electrolyte to become polarized. Ions then diffuse to the porous electrodes with opposing charges via the dielectric as a consequence. At every electrode, an electric double layer is created in this fashion. As a result, the space between the electrodes is compressed and each electrode's surface area increases.^{30,31}

1.2.4.2 Pseudocapacitor (PC)

Pseudo-capacitors are also referred to as faradaic supercapacitors. Pseudo-capacitors employ electrodes constructed of redox-active substances like metal oxides and conducting polymers. These electrodes use reversible faradaic reaction processes to store charge close to the electrode or at the electrode surface, where charges are transported across the metal-electrolyte junction. Capacitance or charge storage in pseudo-capacitors arises from charge transfer among the electrode and electrolyte.^{32,33}

1.2.4.3 Hybrid capacitors

Hybrid capacitors are created by combining techniques from pseudo-capacitors and double layer capacitors. The mechanics of both EDLCs and

pseudocapacitors have been included into these capacitors. Electrodes with varied properties depending on chemical as well as electrical principles make up hybrid capacitors. Because of this, one electrode displays electrostatic capacitance, while the other offers electrochemical capacitance. Hybrid supercapacitors are made up of two electrodes with distinct properties, and those are further classified as composite, symmetric, asymmetric, and battery type capacitors. Comparing the hybrid capacitors to individual EDLC and pseudocapacitors reveals improved power and energy densities. This promotes the use of them as energy storage devices rather than alternative storage technologies.^{34,35}

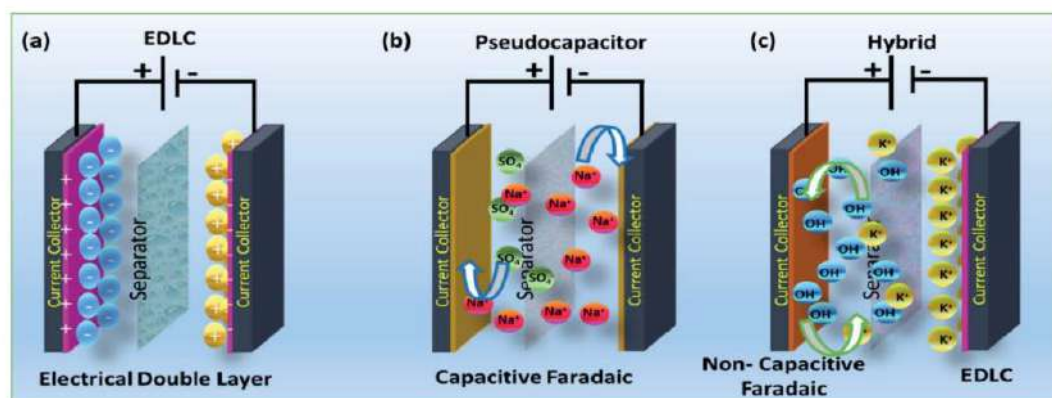


Figure 1.4: Charge storage mechanism of supercapacitors, (a) EDLCs, (b) pseudocapacitors and (c) hybrid supercapacitors.³⁶ Reproduced with permission. Copyright © 2021, Royal Society of Chemistry

1.2.5 Supercapacitor materials

A crucial factor that can affect a supercapacitor's electrochemical performance is the electrode material. They need to be very conductive, superbly temperature stable, chemically stable, possess a high specific surface area, be reasonably priced, and be environmentally benign. To create a high-performance supercapacitor, selecting an efficient and effective electrode material is crucial. The next sections highlight a few of the materials that have been used for energy storage devices, such as carbon based materials, conducting polymers, metal oxides, and metal-organic frameworks.³⁷

1.2.5.1 Carbon-based supercapacitor

Carbon materials have been discovered to be relevant materials for supercapacitor electrodes on account of they are ample in nature, inexpensive, environmental safe, high electrical conductivity, simple scalable processing,

adjustable pore size, good chemical stability, large specific surface area, and stable performance over a broad temperature range. The physical characteristic of carbon-based substances appears akin to that of a semiconductor, possessing a lower charge density of charge carriers (either electrons or holes), which renders them valuable electrode materials. In EDLC, electrode materials used are mostly carbon-based materials, and the storage mechanism they provide is an electrochemical double layer created at the electrode/electrolyte interface. As a result, capacitance is mostly determined by the surface area available to electrolyte ions. Specific surface area, pore size distribution, pore shape and structure, electrical conductivity and surface functionality are all important aspects that determine electrochemical performance.³⁸

Depending on the output need, a variety of carbon materials, including activated carbon, graphene, carbon nanotubes, and carbon aerogel, are employed as supercapacitor electrodes. Activated carbon is a common choice for electrode materials as it possesses a large surface area, porous structure, and excellent conductivity. Historically, AC was derived from fossil fuels such as petroleum coke and coal, however, due to the limited availability of these resources, scientists have been compelled to explore alternative, eco-friendly sources of carbon. Currently, numerous investigators are concentrating on producing supercapacitor electrodes using economical and environmentally friendly sources of carbon such as biomass residue. The carbon that is obtained from the precursor of biomass has exceptional qualities such as large surface area, customizable structure, diverse range of pore sizes, and great conductivity. Despite having limited surface area, CNTs have a network of mesopores that facilitate even charge distribution and enhance the utilization of surface area to a greater extent than activated carbon electrodes. Carbon aerogels are highly porous carbon materials that possess a three-dimensional hierarchical structure and are commonly utilized in various sustainable energy-based applications. It consists of a consistent mesh of carbon nanoparticles possessing a mesoporous configuration. Its chemical bonding ability with the existing collector eliminates the need for any external adhesive. The carbon aerogel's impressive power density and low ESR make it an appealing choice as a lightweight electrode material for supercapacitors. Graphene is a different variation of carbon that consists of a singular layer of graphite wherein the atoms are arranged in a sp^2 hybridized form. This displays remarkable characteristics such as significant flexibility in structure, a favorable relationship between surface area and volume, a broad range of potential

operating conditions, and excellent electrical conductivity. The utilization of graphene as an electrode encounters certain drawbacks, such as a decrease in specific capacitance caused by the restacking of graphene sheets through van der Waals interaction.³⁹⁻⁴³

1.2.5.2 Conducting polymers-based supercapacitor

A group of scientists consisting of Alan G. Heeger, Aann G. MacDiarmid, and Hideki Shirakawa developed conducting polymers in the 19th century. These polymers are made up of a chain of linked monomers and possess exceptional electrical conductivity. In the year 2000, those three researchers achieved the honor of receiving the Nobel Prize in Chemistry.⁴⁴ The significance of conducting polymers lies in their ability to serve as a replacement for metallic substrates and semiconductors, as well as their advantageous properties such as supreme flexibility, excellent conductivity, and highly-redox behavior, allowing them to be utilized as functional materials. The most notable conductive polymers include polypyrrole, polyaniline, polythiophene and poly(3,4-ethylenedioxythiophene). These polymers exhibit significant electrical conductivity under typical conditions. The capacity for these polymers to alternate smoothly between redox states and exhibit strong ion-exchange characteristics is made possible through their synthesis using both aqueous and organic media.⁴⁵⁻⁴⁷ The electrochemical capability of a supercapacitor is negatively impacted by the swelling and shrinking of conducting polymer electrodes that occurs during the charge-discharge process, leading to mechanical breakage. In order to reduce this problem, conducting polymers are utilized to create composites with carbon or metal oxide based substances to enhance the cyclic stability and general electrochemical functioning.

1.2.5.3 Metal oxides-based supercapacitor

In the past few years, there has been an increasing focus on the advancement of supercapacitors based on metal oxides due to their superior energy density compared to carbon materials and greater stability compared to electrode materials made from polymers. The metal oxide electrode materials facilitate energy storage through rapid and reversible faradic reactions occurring at the interface between the electrolyte and electrode. A range of transition metal oxides including NiO, MnO₂, RuO₂, Co₂O₃, IrO₂, SnO₂, and Fe₂O₃ have been investigated as potential supercapacitor electrodes. Out of all the options available, RuO₂ stands out with various benefits including an extensive potential range, exceptional specific

capacitance, conductive metallic characteristics, and an incredibly efficient reversible oxidation-reduction process. RuO₂ is prohibitively costly to manufacture and poses a hazard to human health. Researchers are currently investigating the possible use of MnO₂ in supercapacitors as a substitute for RuO₂. This is due to the fact that MnO₂ is significantly more affordable to produce, widely accessible, and lacks toxic properties.⁴⁸ Transition metal oxide-derived electroactive materials are highly intriguing for their unique blend of electrical, mechanical, structural, and electrochemical characteristics. Their abundance, environment-friendly nature, and rich redox chemistry enable them to possess prominent specific capacitance and energy density. Additionally, their rapid and reversible charge-discharge processes at a relatively low-cost make them the most favorable materials for the development of next-generation supercapacitors.⁴⁹

1.2.5.4 MOF-based supercapacitor

Over the last few decades, there has been an impressive discovery and development of Metal-organic frameworks (MOFs), which was initially conceptualized by Yaghi and Li in 1995.⁵⁰ MOFs are a recently developed class of porous materials that consist of crystalline structures constructed from metal ions or clusters, combined with organic linkers. Transition metals, alkaline earth metals, and lanthanides are commonly employed as metal equivalents. On the other hand, organic linkers commonly consist of molecules that possess donor atoms such as oxygen (O-) or nitrogen (N-) like polyamines, pyridyl, carboxylates, etc. Introducing side chain ligands can enhance the material's capabilities, enabling the potential for a highly customizable molecular system. By carefully selecting the metal ions and organic linkers used in synthesizing MOFs, researchers are able to achieve the desired level of tunability in terms of network dimensionality (1D, 2D, or 3D) and unique topologically diverse open network structures. MOFs possess several benefits over traditional porous materials including a varied scaffold structure, modifiable pore size, notable surface area, and a profusion of active sites. Due to their exceptional characteristics, MOFs are widely utilized in the realm of energy storage systems (EES).⁵¹⁻⁵³ MOFs can be utilized in two primary ways for supercapacitor electrodes. The first approach involves using MOFs as a framework to create various porous materials, such as metal oxide, metal sulfides, and metal phosphides, and their composites, through pyrolytic processing or ion exchange.⁵⁴⁻⁵⁶ The second approach involves directly using MOFs as supercapacitor electrode materials.^{57,58}

1.2.6 Electrical characteristics of the supercapacitor

1.2.6.1 Specific capacitance

Specific capacitance is important property of a supercapacitor. Capacitance is the term used to describe a circuit's capacity for holding and maintaining electrical energy in the form of a charge. The specific capacitance refers to the measure of capacitance in relation to the active material's mass. The nature of the electrode materials utilized plays a critical role in determining the specific capacitance of a supercapacitor. Employing a porous material for constructing supercapacitors amplifies the specific capacitance owing to the considerable increase in surface area. The supercapacitor's high mass causes a reduction in specific capacitance. As a result, the inverse relationship between specific capacitance and mass is observed. At higher current densities, the primary reason for reduced capacitance values is the notable impact of the Ohmic drop, along with slow electrochemical kinetics.

The specific capacitance of the supercapacitor is calculated by using formula,

$$C_{sp} = \frac{I \times t}{m \times V} \dots\dots\dots (1.3)$$

Where C_{sp} , I , t , m and V denotes specific capacitance, current density, discharge time, mass of the supercapacitor and working potential window of the device, respectively.

1.2.6.2 Specific energy and specific power

The specific energy of supercapacitors is the maximum amount of energy that may be held in a given mass. The measurement is determined gravimetrically and expressed as watt-hours per kilogram. Even though supercapacitors have lower energy density compared to batteries, they possess a superior specific power density than batteries. The capability of a device to rapidly provide the energy it has stored to the load is referred to as specific power. Supercapacitors exhibit a considerably higher specific power than batteries, approximately tenfold. This kind of technology is utilized in situations that require the rapid release of energy stored in a device.

Equation 1.4 and 1.5 represents the formula used to determine the specific energy and specific power by analyzing the charge-discharge curve.

$$E_s = \frac{0.5 \times C_{sp} \times \Delta V^2}{3.6} \dots\dots\dots (1.4)$$

$$P_s = \frac{E_s \times 3600}{\Delta t} \dots\dots\dots (1.5)$$

Where E_s and P_s denotes specific energy in Wh kg^{-1} and specific power in W kg^{-1} , respectively.

1.2.6.3 Operating potential voltage

Super capacitors are devices that operate at comparatively lower voltages. To ensure safe usage of the device, it is necessary to maintain the voltage within the designated range. The rated voltage is commonly referred to as the level of safety. The rated voltage incorporates a safety buffer range as well as the voltage point at which the electrolyte breaks down. When the voltage applied surpasses its rated level, the solvent molecules fail to uphold a proper distance between the electrical charges, leading to their breakdown into hydrogen gas or the initiation of a short circuit. The operating voltage is significantly influenced by the type of electrolyte utilized. When working with aqueous electrolytes, it is necessary to apply a rated voltage within the 2.0 - 2.2 V range. However, when utilizing organic solvents, the required voltage range is between 2.5 to 2.7 V. On the other hand, employing ionic electrolytes can result in an operating voltage surpassing 3.5 V. By maintaining a voltage level lower than the rated voltage of the supercapacitor, it is possible to prolong the cycles of charging and discharging. Nevertheless, in situations where elevated voltages are necessary, an arrangement of electrochemical cells must be linked in a series configuration.

1.2.6.4 Cyclic stability

The endurance of supercapacitors depends on the cyclic stability of its electrodes, which is a significant indicator of performance. The ability of supercapacitors to maintain their capacitance under standardized testing conditions after a specific working period or number of charging-discharging cycles is referred to as cyclic stability of electrode materials or devices. Supercapacitors possess an infinite lifespan in terms of cycles, whereas batteries are limited to a cycle range of 500-1200. Supercapacitors are highly valuable in situations that demand repeated storage and conversion of energy owing to their exceptional cyclic stability. Parameters like operating potential window, type of electrode material, current density/ scan rate and electrolyte used strongly influence the cyclic stability of supercapacitor.⁵⁹

1.2.6.5 Electrolyte

Electrolytes are essential and significant components in supercapacitors. Due to their physical and chemical properties, they play a vital role in electrochemical

performances, such as specific capacity, energy density, power density, rate performance, cycling stability, and safety.^{60,61} The necessities for an ideal electrolyte are broad potential window, high ionic conductivity, extended operating temperature range, high chemical and electrochemical stability, large chemical and electrochemical inertness to supercapacitor constituents (e.g., electrodes, current collectors, and packaging), convenience with electrode materials, low volatility and flammability, eco-friendliness, and inexpensiveness. In all honesty, it is challenging for an electrolyte to fulfill all of these necessities; also, each possesses its advantages and limitations. The selection of electrolytes is vital to safe and high-performance supercapacitors. Concerning electrochemical supercapacitor electrolytes, various electrolytes used in the supercapacitors that have been studied are aqueous electrolytes, organic electrolytes, ionic liquid electrolytes, redox-active electrolytes, and solid-state or quasi solid-state electrolytes.⁶²⁻⁶⁵

1.3 General introduction and literature survey of the materials

1.3.1 Introduction to the MOF

In 1995, a new category of porous materials with remarkable properties known as metal-organic frameworks (MOFs) was introduced by Yaghi. These materials are notable for their enduring porosity and extensive surface area, thanks to the robust bonds formed between metallic ions and electrically charged organic ligands.⁶⁶ MOFs offer several advantages over conventional porous materials, such as the ability to achieve crystal engineering and create crystal structures that are deliberately designed and considered highly desirable. Additionally, the synthetic potential of MOFs coupled with their ability to integrate various chemical functionalities enables the creation of MOFs featuring lightweight organic linkages, which exhibit high specific surface area and exceptional porosity that are beyond the realm of conventional materials like zeolites and porous carbon. Because of their enormous surface area and redox-active metal ions (Figure 1.5), MOFs have recently received a lot of attention as electrode materials for SCs.^{67,68}



Figure 1.5: Properties of MOFs

1.3.2 Literature survey of MOFs for supercapacitors

MOFs can be employed in supercapacitors in three different ways:

- 1) Pristine MOFs can be utilized to house electrolyte ions on their internal surfaces for the purpose of accumulating electric charges through physical adsorption, in order to leverage the reversible redox reactions of the metal centers.
- 2) MOFs are utilized to produce metal oxides and maintain the movement of electrons through charge transfer from the electrode to the electrolyte.
- 3) One method for enhancing capacitance involves using MOFs to create porous carbon materials with improved electrical conductivity.

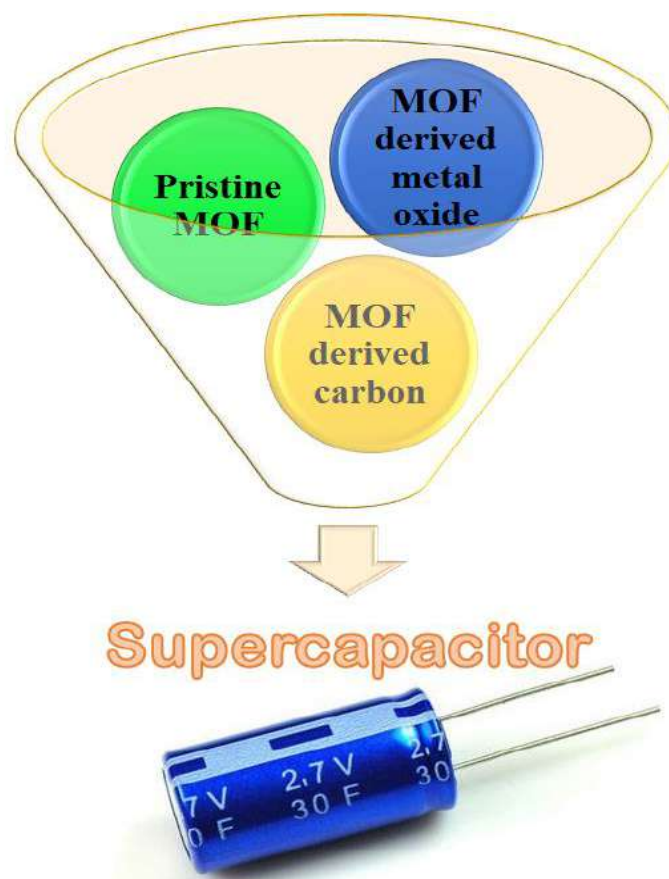


Figure 1.6: MOFs as an electrode material for supercapacitor

1.3.2.1 Pristine MOFs for supercapacitors

Building block patterns of the pristine MOFs can be realized by wise choice and transformation of metal ions and organic linkers. The pristine MOF has physical and chemical properties, such as versatile compositions, high surface area, tunable pores, uniform dispersion, and defined active centres.^{69,70} Pure MOFs store energy through the physisorption of electrolyte ions on their internal surfaces at the metal centres.⁷¹ The important parameters that influence the electrochemical performance are the structure of MOF, which includes chemical structure, and the geometries of the organic ligands.⁷² Due to their longer charge/discharge cyclabilities, larger specific capacitances, and faster ion diffusion, pristine MOFs are used for electrode preparation. To date, more than 40 types of pristine MOFs have been fabricated using many different metals, such as Cu, Cr, Co, Ni, Fe, Mn, Zr, Zn, In, Al, Cd, and Mg in mixture with organic ligands like BTC, BDC, and imidazole.^{73,74}

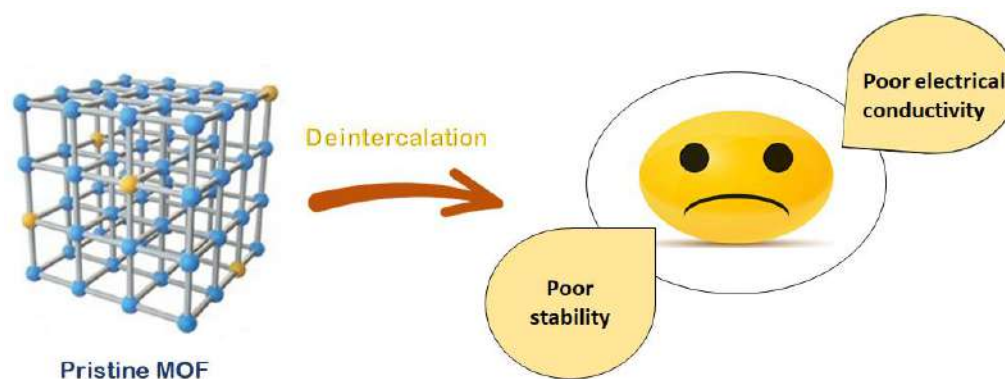


Figure 1.7: Schematic of the pristine MOFs for supercapacitor application

Yang et al. synthesized a layered gear-like Ni–TDA $[(\text{Ni}_3(\text{OH})_2(\text{C}_2\text{H}_6\text{O}_4\text{S})_2, \text{Ni-MOF}]$ material that was found to be a promising electrode material for the flexible all-solid-state asymmetric supercapacitor, and with high specific capacitance of 1518.8 F g^{-1} at a current density of 1 A g^{-1} . The capacitance retention of over 95.5 % can be maintained even after 10000 cycles at current density of 20 A g^{-1} , which shows excellent cycling stability at higher current densities.⁷⁵ Yan et al. prepared a novel accordion-like Ni–MOF superstructure $[(\text{Ni}_3(\text{OH})_2(\text{C}_8\text{H}_4\text{O}_4)_2(\text{H}_2\text{O})_4)] \cdot 2\text{H}_2\text{O}$ to fabricate a flexible supercapacitor. It shows specific capacitances of 988 and 823 F g^{-1} at a current densities of 1.4 and 7.0 A g^{-1} respectively, while sustaining excellent cycling stability (capacitance retention of 96.5 % after 5000 cycles at current density of 1.4 A g^{-1}). Additionally, by using Ni–MOF and activated carbon, a high performance flexible solid-state asymmetric supercapacitor was constructed with a specific capacitance of 230 mF cm^{-2} at current densities of 1.0 mA cm^{-2} , which shows little capacitance change after more than 5000 charge–discharge cycles, with only 7.2 % decay at a current density of 5.0 mA cm^{-2} .⁷⁶ Krishnamurthy et al. used a solvothermal method to report Mn–MOF $(\text{Mn}[\text{Tpa}][\text{Mi}][\text{DMF}])$ employing terephthalic acid and methyl imidazole ligands. It shows specific capacitance up to 4000 F g^{-1} . Also, it has an energy density and power density of 500 Wh kg^{-1} and 0.125 W kg^{-1} , respectively. The surface area of this material is outstanding, i.e. $2352 \text{ m}^2 \text{ g}^{-1}$ and pore volume of $0.00569 \text{ cc g}^{-1}$; Mn-MOF electrode possesses a high charge–discharge Coulombic efficiency, low polarization, and high specific capacitance, along with good cycling stability.⁷⁷ Zhu et al. synthesized a 3D hierarchically structured Co-MOF supported on nickel foam (Co-MOF/NF), which shows better capacitive properties with good rate performance in 2 M KOH. Further, they constructed an asymmetric supercapacitor device by using Co-MOF/NF as a

positive electrode and activated carbon as a negative electrode; it shows a high energy density of 1.7 mWh cm^{-2} at a power density of 4.0 mW cm^{-2} , with capacitance retention of almost 69.70 % after 2000 cycles.⁷⁸

1.3.2.2 MOF-derived metal oxides for supercapacitors

The poor structural stability and electrical conductivity of the pristine MOFs have hampered their practical utilization as electrodes in supercapacitor applications. Transforming the pristine MOFs into metal oxides is a significant way of enhancing their structural and electrochemical stability, including electrical conductivity. The MOF-derived metal oxide show unique structural features, such as porous morphology, robust structure, high electrical conductivity, and high redox behaviour. Therefore, metal oxides derived from MOFs are preferred for the construction of electrode materials. MOF-derived metal oxides electrode materials store energy through charge transfer between electrolyte-ions and the electrodes. Metal oxides are mostly made via the general procedure of calcination. MOFs are heated to a temperature of a few hundred degrees in an inert furnace.⁷⁹ Throughout the annealing procedure, metal sites are oxidized to the isonomous metal oxides, and organic ligands are transmuted into carbon dioxide and water vapour, which frame ample pores. MOF-derived metal oxides sustain their primitive morphology, showing huge pores and associated gaps.^{80,81}

Lan et al. prepared a porous flower-like MnNi_2O_4 using bimetallic Mn/Ni–MOF as a precursor that exhibits astounding electrochemical behaviour with the most significant specific capacitance of 2848 F g^{-1} at 1 A g^{-1} with good stability of 93.25 % capacitance retention after 5000 cycles at 10 A g^{-1} . Further, they constructed an asymmetric supercapacitor using MnNi_2O_4 positive electrode and active carbon as the negative electrode, which shows a large energy density of 142.8 Wh kg^{-1} at a high-power density of 800 W kg^{-1} .⁸² Xiao et al. synthesized an ultrathin Co_3O_4 nanosheet using Co-based MOF by hydrolysis followed by calcination procedure, which exhibits outstanding supercapacitor performance due to the abundant meso- and macro-pores. In addition, they fabricated an asymmetric supercapacitor using Co_3O_4 nanosheets as a positive electrode and activated carbon as a negative electrode, which shows a high energy density of 32.8 Wh kg^{-1} at the power density of 752 W kg^{-1} and retains 98.1 % of its initial capacitance after 6000 charge/discharge cycles at the current density of 2 A g^{-1} with long-term cycling stability.⁸³ Wu and co-workers synthesized hollow core in double-shell NiO nanospheres by the calcination of Ni-based MOF; as they are

calcined at different temperatures, they show distinct surface areas and electrical conductivities, which play an important role in the redox reaction that takes place at the surface of the active materials. Material calcined at 400 °C shows a specific capacitance of 473 F g⁻¹ at the current density of 0.5 A g⁻¹, which shows good cycling stability, even after 3000 cycles. Additionally, they constructed an asymmetric supercapacitor with high energy storage capacity and outstanding cycling performance.⁸⁴ Li et al. fabricated hierarchical double-shelled NiO/ZnO hollow spheres by annealing a bimetallic organic framework in air and used it as an electrode material for high-performance supercapacitor applications. It shows a specific capacitance of 497 F g⁻¹ at a current density of 1.3 A g⁻¹ with outstanding cycling stability, even after 2000 cycles.⁸⁵ Xu et al. investigated a scheme to set up unique Co₃O₄/ZnO nano heterostructures through the thermal conversion of center-shell ZIF-eight@ZIF-67, displaying superior pseudocapacitive behaviour. It shows a high specific capacitance of 415 F g⁻¹ at 0.5 A g⁻¹ with enhanced rate capability (93.2 % retention at 10 A g⁻¹), compared to Co₃O₄ and ZnO derived from single MOFs precursor. Further, they fabricated an asymmetric supercapacitor by using Co₃O₄/ZnO heterostructure as a positive electrode, and active carbon as a negative electrode. The electrochemical performance determined in an aqueous electrolyte, i.e., 6 M KOH in expanded 1.4 V working voltage, shows an energy density of 43.2 Wh kg⁻¹ at a power density of 1401 W kg⁻¹.⁸⁶ The nanoporous NiO, NiCo₂O₄, and Co₃O₄ were prepared using the hydrothermal method and an annealing process that exhibits a large surface area and porous nature. As compared with monometallic oxides, the mixed metal oxides, i.e., NiCo₂O₄, shows high specific capacitance of 684 F g⁻¹ at 0.5 A g⁻¹ current density, and outstanding cycling stability with the specific capacitance retention of 86 % after 3000 cycles at the current density of 10 A g⁻¹, performance of which makes it a promising material for energy storage and conversion devices.⁸⁷

1.3.2.3 MOF-derived carbon for supercapacitors

MOF-derived nanoporous carbon (NPC) material is obtained by the calcination of MOF at high temperatures or the pyrolysis of MOF followed by acid treatment or base activation. NPCs maintain the structure and morphology of MOF, which enables the conducting properties of carbon. Many nanoporous carbon (NPC) materials have been widely examined for supercapacitor applications, due to their outstanding chemical and mechanical stability, large specific surface area, good electrical conductivity, and adjustable pore structure.⁸⁸⁻⁹⁰ To increase the capacitance

of carbon material, heteroatom doping (e.g., B, S, N, P) is a new strategy to elevate the surface wettability and contribute reversible pseudo-capacitor behaviour to a material. The addition of metals can supply extra benefits in the carbon array, which encourages the applications of carbon materials as electrode materials. Incorporating specific metals like Co, Ni, and Fe can amazingly ameliorate the crystallinity and electrical conductivity of carbon, owing to their catalytic graphitization of the amorphous carbon. Hence, heteroatom doping or metal-modified carbons are promising materials for supercapacitor application and have attracted much interest.^{91–94} Nowadays, the performance of supercapacitors is mainly influenced by electrode materials. Among different electrode materials, carbon is the most broadly used material for supercapacitors due to its multiple advantages: wide source, large specific surface area, environmental warmth, and good electrical conductivity. Large specific surface area and suitable pore size are the chief techniques to achieve high capacitance of carbon materials; carbon materials mainly store energy by constructing an electric double-layer across the separated charges of electrolyte ions on the surface.⁹⁵

Due to its easy synthesis, controllable morphology, and high nitrogen content, ZIF-8 is a common precursor for synthesizing many porous carbon materials for supercapacitors. Tang et al. put nanoporous hybrid carbon materials containing nitrogen-doped carbon (NC) as the cores and highly graphitic carbon (GC) as the shells using core-shell structured ZIF-8@ZIF-67 crystals. This novel NC@GC material holds a high surface area (up to $1276 \text{ m}^2 \text{ g}^{-1}$) and high N content (10.6 wt. %) derived from core ZIF-8, and a better graphitic structure derived from shell ZIF-67. It shows an eminent specific capacitance of 270 F g^{-1} at a current density of 2 A g^{-1} .⁹⁶ Liu et al. investigated a new strategy to design a flexible hierarchical porous carbon film (HPCF) for binder-free and high-performance energy storage devices consisting of MOF-derived porous carbon polyhedra and carbon nanotubes (CNTs). They prepared HPCF (1, 2, 3, 4, and 5) by the calcination at different temperatures of 400, 500, 600, 800, and 900°C respectively, from which HPCF₄ gives the largest BET ($620.1 \text{ m}^2 \text{ g}^{-1}$), and shows the highly porous structure, excellent flexibility, with highest electrical conductivity (1320 S m^{-1}). HPCF₄ offers excellent rate capability larger than 60 % retention from (2 to 100) A g^{-1} with high electrical conductivity and successful ion transport networks, compared with the other flexible carbon electrodes. In addition, they fabricated an aqueous symmetrical supercapacitor that shows an

energy density of 9.1 Wh kg^{-1} with a power density of 3500 W kg^{-1} .⁹⁷ Duan and his co-workers discovered three types of activated porous carbon (APC) by the annealing and thermolysis of Cu-MOF with different morphologies, varying its reaction temperatures at 0, 25, and 60°C . APC-25 reveals cabbage-like morphology out of those APCs with the largest specific surface area, i.e. $1880.4 \text{ m}^2 \text{ g}^{-1}$ and $0.81 \text{ cm}^3 \text{ g}^{-1}$ pore volume; it also exhibits the highest specific capacitance of 196 F g^{-1} at 0.5 A g^{-1} current density. Additionally, they fabricated an asymmetric supercapacitor (ASC) device using APC-25, giving an incredible 11.8 Wh kg^{-1} energy density at a power density of 350 W kg^{-1} with outstanding cycling stability. Noticeably, using six ASCs, five light-emitting diodes are lighted, which confirms that APC-25 might be used in energy storage devices.⁹⁸ Wang et al. demonstrated a fruitful route to increase the conductivity performance of N-doped MOFs-based hierarchical carbon (NPC) to defeat the insulating problems of MOFs by electrochemically twisting together MOF crystals with a conductive polymer. They prepared a new N-doped MOFs-based hierarchical carbon (NPC) by electrospinning method, followed by pyrolysis to get nanofibers; it shows superior energy storage capacity to that of the earlier recorded MOF-derived carbon materials with innovative 1D hollow structures. NPCF exhibits 332 F g^{-1} specific capacitance at 1 A g^{-1} current density and excellent cycling stability with a specific capacitance retention of 98.9 % after 5000 cycles at 1 A g^{-1} current density.⁹⁹

Chen and colleagues investigated a fruitful method for manufacturing hollow particle-based nitrogen-doped carbon nanofibers (HPCNFs-N) by an easy carbonization treatment of an electrospun ZIF-8/PAN composite precursor. HPCNFs-N material significantly increases the electrochemical property as an electrode material for supercapacitors with incredible specific capacitance at different current densities, high energy/power density, and long cycling stability of over 10000 cycles.¹⁰⁰ Hao et al. synthesized nitrogen-doped porous carbon polyhedra (N-PCMPs) by directly carbonizing ZIF-11 polyhedra stimulated by fused KOH to enhance the surface area and pore volume. Activated N-PCMPs (N-PCMPs-A) show 307 F g^{-1} specific capacitance at 1.0 A g^{-1} current density, which is incredibly higher than that of N-PCMPs, i.e. 165 F g^{-1} ; even further, the specific capacitance of N-PCMPs-A retains 198 F g^{-1} at a regular high amount of current density, i.e. 10 A g^{-1} , which compared to N-PCMPs, is significant. N-PCMPs show incredible cycling stability

with a specific capacitance retention of 90 %, even after 4000 cycles at the current density of 10 A g^{-1} .¹⁰¹

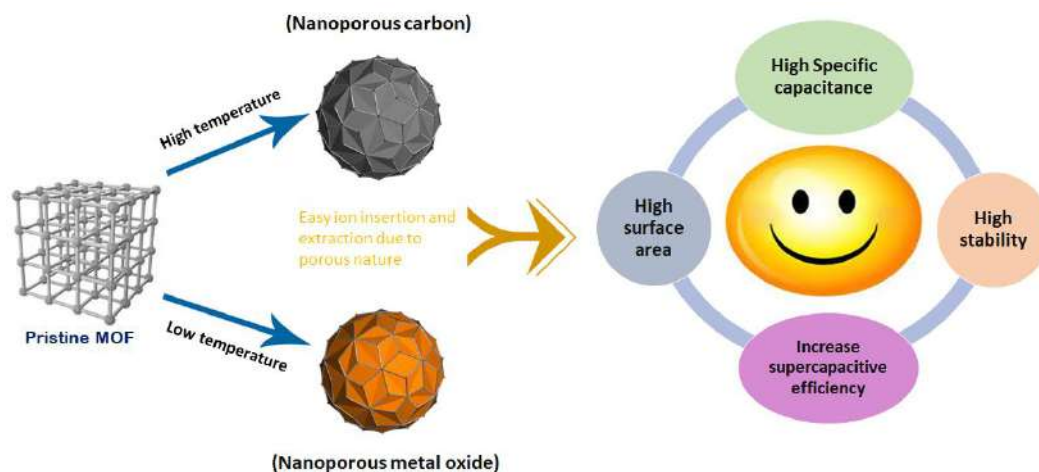


Figure 1.8: Development of the use of various MOFs in the field of supercapacitor application

1.3.3 MOFs derived from the first transition series elements serve as electrodes for supercapacitors

Metal-organic compounds derived from the first transition elements have emerged as prime contenders for top-notch active materials in supercapacitor, thanks to their advantageous characteristics, as outlined below.¹⁰²

- ❖ Metal-organic compounds belonging to the first transition metal series come with several benefits, including simplified synthesis, affordable pricing, regulated structure, and a vast range of structural variations. Additionally, the metals that belong to the initial series of transition metals are abundant on the earth, economical, and non-harmful.
- ❖ The high valence states of transition elements facilitate redox reactions and effective electron transfer, which enable the pseudocapacitive mechanism to operate efficiently.
- ❖ Transition metals can create porous structures by coordinating tetrahedrally or octahedrally and by using multidentate ligands. This process is often utilized in the creation of porous structures within metal coordination polymers, particularly in metal-organic frameworks (MOFs). The EDLC mechanism gains an advantage from this as it allows for an increased number of channels that facilitate the transportation of ions during the procedures of charging and discharging.

- ❖ In contrast to the other transition elements, the first transition elements exhibit lower molecular weights, leading to increased values of specific gravimetric capacitance.

1.3.3.1 The properties of transition elements

Transition elements, or sometimes referred to as transition metals, are a group of elements possessing d orbitals that are only partially occupied. According to the International Union of Pure and Applied Chemistry, transition elements can be classified as elements with a partially filled d subshell of electrons or elements that possess the capacity to generate stable cations using an incompletely filled d orbital.

The general characteristics of the transition elements are as described below:

- ❖ The presence of these components results in the creation of coloured compounds and ions. The color of this can be attributed to the d-d electron transition.
- ❖ These elements have the capability to bind with a vast range of ligands. As a result, transition elements can generate a diverse range of stable compound structures.
- ❖ The elevated boiling and melting points of transition elements can be attributed to the involvement of delocalized d electrons within metallic bonding.
- ❖ The possible oxidation states of transition elements have a relatively small energy difference. Hence, the elements in the transition group demonstrate various states of oxidation.
- ❖ These elements have the ability to form several paramagnetic compounds owing to the unpaired electrons present in the d orbital.
- ❖ These elements exhibit a high charge-to-radius ratio.
- ❖ The ability of transition elements to conduct electricity proficiently is attributed to their metallic bonding, which involves the delocalized d electrons.
- ❖ Transition elements possess a hard nature and display greater densities in contrast to other elements.

The five elements from transition first series elements namely Manganese (Mn), Iron (Fe), Cobalt (Co), Nickel (Ni) and Zinc (Zn) are more potential. The table below outlines the distinct characteristics of these elements.

Table 1.2: Properties of transition first series elements

Property	Manganese	Iron	Cobalt	Nickel	Zinc
Electron configuration	[Ar]3d ⁵ 4s ²	[Ar]3d ⁶ 4s ²	[Ar]3d ⁷ 4s ²	[Ar]3d ⁸ 4s ²	[Ar]3d ¹⁰ 4s ²
Melting point (°C)	1246	1538	1495	1455	419.5
Boiling point (°C)	2061	2862	2927	2730	907
Density (g/cm ³)	7.21–7.44	7.87	8.9	8.9	7.133
Electro negativity	1.55	1.83	1.88	1.91	1.65
Covalent radius (Å)	1.39	1.32	1.26	1.24	1.22
Ionic radius (Å)	0.80	0.69	0.70	0.72	0.74

1.4 Purpose of the dissertation

Energy holds significant significance in several facets of human existence. As long as the population continues to grow and people aspire to live a better lifestyle, the demand for energy will persistently increase. To satisfy the rising global energy needs, it is imperative that the energy sources of the future are not only efficient and reliable but also cleaner and adaptable. Energy is found in diverse forms that are not readily accessible, thus various energy storage devices are designed to transform the difficult-to-use energy into more convenient forms. Batteries and capacitors are the typical energy storage mechanisms that are commonly accessible. The usage of batteries is limited due to their low energy delivery rate, making them unsuitable for applications that require fast energy delivery. Capacitors are capable of delivering power rapidly, but their ability to store energy is significantly restricted. The gadget exhibiting dual features is known as the supercapacitor. Supercapacitors possess the prospective advantages of elevated energy and power density, prolonged lifespan, and accelerated charge and discharge rates, contributing to their enhanced efficiency. The electrode material is a crucial factor in the charge storing process of a supercapacitor device. Extensive research has been conducted on numerous electrode materials for supercapacitors, however, there are still certain obstacles that need to be overcome.

To conquer these obstacles, the metal-organic frameworks are used as an electrode materials in supercapacitors due to its exceptional chemical and structural characteristics. MOFs can serve as both a precursor and a template to create a diverse range of functional materials for supercapacitor.

The objective of the current research is to create a supercapacitor device that is sustainable, economical, and effective. This supercapacitor device should have a high specific capacitance and energy and power density, as well as an exceptional cycle life. With this aim, the MOFs are used as electrode materials due to their customizable pore structures, vast surface areas, and versatile structures. After a thorough investigation of prior research, it is discovered that MOF exhibits favorable electrochemical characteristics, its potential for commercialization is hindered by limited charge rate ability and low stability. Various approaches have been put in place up until now to address these downsides, which have been specifically discussed earlier. Upon thorough analysis of the methods employed thus far, we have observed that scientists have utilized combinations of MOF with various functional components to overcome its limitations. Despite their excellent electrochemical charge storage capacity, they exhibit low electrical conductivity and cyclic stability. Consequently, in order to enhance both the rate capability and durability, it is necessary to alter the substance through thermal processing so that it displays favorable features such as effective electrical conductivity, efficient capacity for holding electrochemical charge, and consistent long-term performance. With regards to all of these factors, the objective of this dissertation is to enhance the MOF's ability to store charges, its rate of capability, and its stability by constructing a highly conductive derived material by heat treatment of MOF that demonstrate pseudocapacitive charge storage capability. The synergic effect of high surface area of MOF and its derived materials will greatly enhance the specific capacitance and energy density of supercapacitor electrode. This electrode further used for fabrication of symmetric, asymmetric and hybrid supercapacitors devices.

1.5 Plan of the work

The following strategies are employed in this thesis to address the issues highlighted in the preceding section.

Chapter 1 covers the topic of energy storage mechanisms, including battery, capacitors, and the advancement of supercapacitor technology. The operations and

categories of supercapacitor gadgets have also been deliberated. Following this, issues related to the earlier literature are outlined, along with the rationale for conducting the current research and the significance of the findings.

In Chapter 2, the methods employed for producing MOFs are detailed alongside the techniques utilized to analyze their structural attributes. Additionally, it encompasses the process of crafting working electrodes and supercapacitor gadgets. In conclusion, the electrochemical properties of the working electrodes and devices produced through fabrication are thoroughly examined using an electrochemical workstation.

In the Chapter 3, a straightforward and inexpensive reflux method is employed to synthesize and characterize pure Ni-MOF. In order to provide a detailed analysis of the structural components, characterization methods were utilized. The electrochemical features of Ni-MOF were investigated by means of various methods such as CV, GCD, and EIS in an aqueous electrolyte of 2 M KOH. Additionally, a hybrid supercapacitor device was constructed to evaluate the capacity of Ni-MOF.

Chapter 4 focuses on creating new trimetallic MOFs with the intention of developing superb electrode materials for supercapacitors. To thoroughly examine the structural elements, an array of characterization techniques were employed. Research was conducted to investigate how the structural and electrochemical characteristics of MOF are impacted by tricarboxylic and dicarboxylic ligands. We have successfully manufactured a symmetrical device with a solid-state symmetric supercapacitor which glows a red LED light. This remarkable achievement showcases the vast potential of our device.

Chapter 5 outlines the procedure for creating a new bimetallic MOF and its resulting oxide through a straightforward heat treatment method. Sophisticated techniques were employed to comprehensively examine the structural components. The electrochemical properties of bimetallic MOF and its corresponding oxides are explored through multiple techniques including CV, GCD, and EIS in a 1 M neutral Na₂SO₄ electrolyte. We have effectively produced a solid-state asymmetrical supercapacitor device that illuminates a cluster of red LED lights. The immense capabilities of our device are clearly demonstrated by this impressive accomplishment.

Chapter 6 explores the synthesis and characterization of a bimetallic MOF, its oxide derivative, and nanoporous carbon. The purpose of this investigation is to create

exceptional electrode materials for supercapacitors. Advanced methods were utilized to thoroughly analyze the structural constituents. Several techniques including CV, GCD, and EIS were utilized to investigate the electrochemical characteristics of bimetallic MOF, its corresponding oxide, and nanoporous carbon in a 2 M KOH electrolyte. A single all-in one device called the solid-state asymmetrical supercapacitor has been successfully constructed, that utilizes the electrodes made from derived materials i.e. nanoporous carbon and oxide which shows remarkable electrochemical performance.

In Chapter 7, the key findings from this thesis are summarized and suggestions are provided for potential future endeavors that could build upon the outcomes of this research.

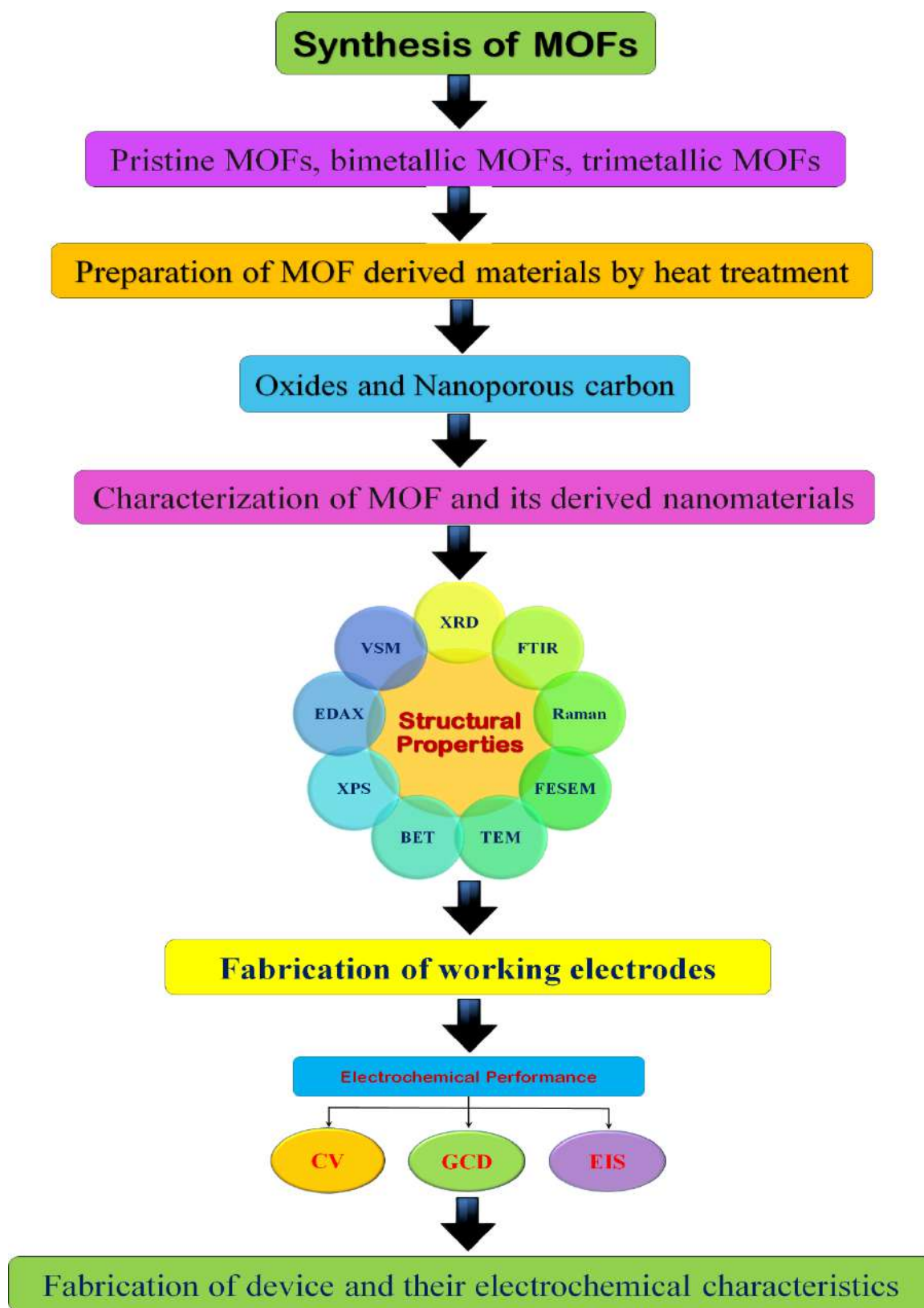


Figure 1.9: Diagrammatic representation of plan of thesis

1.6 References

- 1 L. Zhang and X. S. Zhao, *Chem. Soc. Rev.*, 2009, **38**, 2520–2531.
- 2 P. J. Hall and E. J. Bain, *Energy Policy*, 2008, **36**, 4352–4355.
- 3 J. Murray and D. King, *Nature*, 2012, **481**, 433–435.
- 4 M. Winter and R. J. Brodd, *Chem. Rev.*, 2004, **104**, 4245–4269.
- 5 J. R. Miller and P. Simon, *Science*, 2008, **321**, 651–652.
- 6 A. Burk, *J. Power Sources*, 2000, **91**, 37–50.
- 7 H. Kelly-Holmes, *Advert. as Multiling. Commun.*, 2016, **45**, 1–206.
- 8 H. I. Becker, *US Pat.*, 1957, 2800616-2800624.
- 9 R. A. Rightmire, *US Pat.*, 1966, 3288641-3288650.
- 10 D. L. Boos and G. Heights, *US Pat.*, 1970, 3536963-3536969.
- 11 M. Endo, T. Takeda, Y. J. Kim, K. Koshiba and K. Ishii, *Carbon Sci.*, 2001, **1**, 117–128.
- 12 B. E. Conway, *Proc. Int. Power Sources Symp.*, 1991, 319–327.
- 13 B. E. Conway, *Electrochem. Encycl.*, 2003, 1–8.
- 14 A. Schneuwly and R. Gallay, *Pcim*, 2000, 1–10.
- 15 G. Wang, L. Zhang and J. Zhang, *Chem. Soc. Rev.*, 2012, **41**, 797–828.
- 16 P. Sharma and T. S. Bhatti, *Energy Convers. Manag.*, 2010, **51**, 2901–2912.
- 17 J. P. Zheng, *J. Electrochem. Soc.*, 2005, **152**, A1864-A1869.
- 18 C. Z. Yuan, B. Gao and X. G. Zhang, *J. Power Sources*, 2007, **173**, 606–612.
- 19 J. R. Miller, *Electrochim. Acta*, 2006, **52**, 1703–1708.
- 20 S. P. S. Badwal, S. S. Giddey, C. Munnings, A. I. Bhatt and A. F. Hollenkamp, *Front. Chem.*, 2014, **2**, 1–28.
- 21 J. Maier, *Angew. Chemie - Int. Ed.*, 2013, **52**, 4998–5026.
- 22 T. Brousse, D. Bélanger, K. Chiba, M. Egashira, F. Favier, J. Long, J. R. Miller, M. Morita, K. Naoi, P. Simon and W. Sugimoto, *Springer Handbooks*, 2017, 495–561.
- 23 A. Nishino, *J. Power Sources*, 1996, **60**, 137–147.
- 24 T. Jin, G. Singer, K. Liang and Y. Yang, *Mater. Today*, 2022, **62**, 151–167.
- 25 D. Linden and T. B. Reddy, *Handbook of batteries*, 1995, **3**, 1-50.
- 26 S. S. Siwal, Q. Zhang, N. Devi and V. K. Thakur, *Polymers*, 2020, **12**, 1–31.
- 27 I. Staffell, D. Scamman, A. Velazquez Abad, P. Balcombe, P. E. Dodds, P. Ekins, N. Shah and K. R. Ward, *Energy Environ. Sci.*, 2019, **12**, 463–491.

- 28 P. S. Joshi and D. S. Sutrave, *J. Inf. Comput. Sci.*, 2019, **9**, 609-625.
- 29 S. I. Kim, S. W. Kim, K. Jung, J. B. Kim and J. H. Jang, *Nano Energy*, 2016, **24**, 17–24.
- 30 H. Ji, X. Zhao, Z. Qiao, J. Jung, Y. Zhu, Y. Lu, L. L. Zhang, A. H. MacDonald and R. S. Ruoff, *Nat. Commun.*, 2014, **5**, 1–7.
- 31 X. You, M. Misra, S. Gregori and A. K. Mohanty, *ACS Sustain. Chem. Eng.*, 2018, **6**, 318–324.
- 32 S. Fleischmann, J. B. Mitchell, R. Wang, C. Zhan, D. E. Jiang, V. Presser and V. Augustyn, *Chem. Rev.*, 2020, **120**, 6738–6782.
- 33 N. R. Chodankar, H. D. Pham, A. K. Nanjundan, J. F. S. Fernando, K. Jayaramulu, D. Golberg, Y. K. Han and D. P. Dubal, *Small*, 2020, **16**, 1–35.
- 34 A. Borenstein, O. Hanna, R. Attias, S. Luski, T. Brousse and D. Aurbach, *J. Mater. Chem. A*, 2017, **5**, 12653–12672.
- 35 A. Vlad, N. Singh, J. Rolland, S. Melinte, P. M. Ajayan and J. F. Gohy, *Sci. Rep.*, 2014, **4**, 1–7.
- 36 N. Swain, B. Saravanakumar, M. Kundu, L. Schmidt-Mende and A. Ramadoss, *J. Mater. Chem. A*, 2021, **9**, 25286–25324.
- 37 Z. S. Iro, C. Subramani and S. S. Dash, *Int. J. Electrochem. Sci.*, 2016, **11**, 10628–10643.
- 38 H. Jiang, P. S. Lee and C. Li, *Energy Environ. Sci.*, 2013, **6**, 41–53.
- 39 R. Singh, S. Sansare and S. Shidhaye, *Biomed. Appl. Nanoparticles*, 2019, 319–339.
- 40 Y. Zhai, Y. Dou, D. Zhao, P. F. Fulvio, R. T. Mayes and S. Dai, *Adv. Mater.*, 2011, **23**, 4828–4850.
- 41 L. Deng, R. J. Young, I. A. Kinloch, A. M. Abdelkader, S. M. Holmes, D. A. De Haro-Del Rio and S. J. Eichhorn, *ACS Appl. Mater. Interfaces*, 2013, **5**, 9983–9990.
- 42 S. Sundriyal, V. Shrivastav, H. D. Pham, S. Mishra, A. Deep and D. P. Dubal, *Resour. Conserv. Recycl.*, 2021, **169**, 105548-105555.
- 43 P. Forouzandeh, V. Kumaravel and S. C. Pillai, *Catalysts*, 2020, **10**, 1–73.
- 44 H. Shirakawa, E. J. Louis, A. G. MacDiarmid, C. K. Chiang and A. J. Heeger, *J. Chem. Soc. Chem. Commun.*, 1977, 578–580.
- 45 Q. Meng, K. Cai, Y. Chen and L. Chen, *Nano Energy*, 2017, **36**, 268–285.
- 46 I. Shown, A. Ganguly, L. C. Chen and K. H. Chen, *Energy Sci. Eng.*, 2015, **3**,

- 2–26.
- 47 G. A. Snook, P. Kao and A. S. Best, *J. Power Sources*, 2011, **196**, 1–12.
- 48 J. Liu, J. Bao, X. Zhang, Y. Gao, Y. Zhang, L. Liu and Z. Cao, *RSC Adv.*, 2022, **12**, 35556–35578.
- 49 A. Kumar, H. K. Rathore, D. Sarkar and A. Shukla, *Electrochem. Sci. Adv.*, 2021, **2**, e2100187-e2100229.
- 50 O. M. Yaghi and H. Li, *J. Am. Chem. Soc.*, 1995, **117**, 10401–10402.
- 51 H. Gao, H. Shen, H. Wu, H. Jing, Y. Sun, B. Liu, Z. Chen, J. Song, L. Lu, Z. Wu and Q. Hao, *Energy and Fuels*, 2021, **35**, 12884–12901.
- 52 F. Boorboor Ajdari, E. Kowsari, M. Niknam Shahrak, A. Ehsani, Z. Kiaei, H. Torkzaban, M. Ershadi, S. Kholghi Eshkalak, V. Haddadi-Asl, A. Chinnappan and S. Ramakrishna, *Coord. Chem. Rev.*, 2022, **422**, 213441-213448.
- 53 Y. Zhao, J. Liu, M. Horn, N. Motta, M. Hu and Y. Li, *Sci. China Mater.*, 2018, **61**, 159–184.
- 54 J. Y. Long, Z. S. Yan, Y. Gong and J. H. Lin, *Appl. Surf. Sci.*, 2018, **448**, 50–63.
- 55 R. R. Salunkhe, Y. V. Kaneti and Y. Yamauchi, *ACS Nano*, 2017, **11**, 5293–5308.
- 56 Z. Lv, Q. Zhong and Y. Bu, *Appl. Surf. Sci.*, 2018, **439**, 413–419.
- 57 Y. Wang, Y. Liu, H. Wang, W. Liu, Y. Li, J. Zhang, H. Hou and J. Yang, *ACS Appl. Energy Mater.*, 2019, **2**, 2063–2071.
- 58 F. Bigdeli, C. T. Lollar, A. Morsali and H. C. Zhou, *Angew. Chemie - Int. Ed.*, 2020, **59**, 4652–4669.
- 59 Q. Wu, T. He, Y. Zhang, J. Zhang, Z. Wang, Y. Liu, L. Zhao, Y. Wu and F. Ran, *J. Mater. Chem. A*, 2021, **9**, 24094–24147.
- 60 L. Xia, L. Yu, D. Hu and G. Z. Chen, *Mater. Chem. Front.*, 2017, **1**, 584–618.
- 61 D. Aurbach, Y. Talyosef, B. Markovsky, E. Markevich, E. Zinigrad, L. Asraf, J. S. Gnanaraj and H. J. Kim, *Electrochim. Acta*, 2004, **50**, 247–254.
- 62 K. Tönurist, T. Thomberg, A. Jänes, I. Kink and E. Lust, *Electrochem. commun.*, 2012, **22**, 77–80.
- 63 S. Paul, K. S. Choi, D. J. Lee, P. Sudhagar and Y. S. Kang, *Electrochim. Acta*, 2012, **78**, 649–655.
- 64 B. H. Wee and J. D. Hong, *Langmuir*, 2014, **30**, 5267–5275.
- 65 B. Pal, S. Yang, S. Ramesh, V. Thangadurai and R. Jose, *Nanoscale Adv.*,

- 2019, **1**, 3807–3835.
- 66 X. Zhang, Z. Chen, X. Liu, S. L. Hanna, X. Wang, R. Taheri-Ledari, A. Maleki, P. Li and O. K. Farha, *Chem. Soc. Rev.*, 2020, **49**, 7406–7427.
- 67 W. Li, X. Zhao, Q. Bi, Q. Ma, L. Han and K. Tao, *Dalt. Trans.*, 2021, **50**, 11701–11710.
- 68 R. Vinodh, R. S. Babu, R. Atchudan, H. J. Kim, M. Yi, L. M. Samyn and A. L. F. de Barros, *Catalysts*, 2022, **12**, 375–391.
- 69 J. Yu, X. Gao, Z. Cui, Y. Jiao, Q. Zhang, H. Dong, L. Yu and L. Dong, *Energy Technol.*, 2019, **7**, 1900018–1900039.
- 70 T. Qiu, Z. Liang, W. Guo, H. Tabassum, S. Gao and R. Zou, *ACS Energy Lett.*, 2020, **5**, 520–532.
- 71 D. Sheberla, J. C. Bachman, J. S. Elias, C. J. Sun, Y. Shao-Horn and M. Dincă, *Nat. Mater.*, 2017, **16**, 220–224.
- 72 N. Sahiner, S. Demirci and M. Yildiz, *J. Electron. Mater.*, 2017, **46**, 790–801.
- 73 F. Wang, S. Xiao, Y. Hou, C. Hu, L. Liu and Y. Wu, *RSC Adv.*, 2013, **3**, 13059–13084.
- 74 Y. Tan, W. Zhang, Y. Gao, J. Wu and B. Tang, *RSC Adv.*, 2015, **5**, 17601–17605.
- 75 C. Yang, X. Li, L. Yu, X. Liu, J. Yang and M. Wei, *Chem. Commun.*, 2020, **56**, 1803–1806.
- 76 Y. Yan, P. Gu, S. Zheng, M. Zheng, H. Pang and H. Xue, *J. Mater. Chem. A*, 2016, **4**, 19078–19085.
- 77 B. M. Omkaramurthy, G. Krishnamurthy and S. Foro, *Mater. Res. Express*, 2019, **6**, 125544–125557.
- 78 G. Zhu, H. Wen, M. Ma, W. Wang, L. Yang, L. Wang, X. Shi, X. Cheng, X. Sun and Y. Yao, *Chem. Commun.*, 2018, **54**, 10499–10502.
- 79 Y. Li, Y. Xu, W. Yang, W. Shen, H. Xue and H. Pang, *Small*, 2018, **14**, 1–24.
- 80 J. Li, D. Yan, S. Hou, T. Lu, Y. Yao and L. Pan, *Chem. Eng. J.*, 2018, **354**, 172–181.
- 81 Z. Zhang, Y. Huang and S. Bai, *Mater. Sci. Forum*, 2017, **890**, 68–73.
- 82 M. Lan, X. Wang, R. Zhao, M. Dong, L. Fang and L. Wang, *J. Alloys Compd.*, 2020, **821**, 153546–153554.
- 83 Z. Xiao, L. Fan, B. Xu, S. Zhang, W. Kang, Z. Kang, H. Lin, X. Liu, S. Zhang and D. Sun, *ACS Appl. Mater. Interfaces*, 2017, **9**, 41827–41836.

- 84 M. K. Wu, C. Chen, J. J. Zhou, F. Y. Yi, K. Tao and L. Han, *J. Alloys Compd.*, 2018, **734**, 1–8.
- 85 G. C. Li, P. F. Liu, R. Liu, M. Liu, K. Tao, S. R. Zhu, M. K. Wu, F. Y. Yi and L. Han, *Dalt. Trans.*, 2016, **45**, 13311–13316.
- 86 J. Xu, S. Liu and Y. Liu, *RSC Adv.*, 2016, **6**, 52137–52142.
- 87 L. T. Gong, M. Xu, R. P. Ma, Y. P. Han, H. B. Xu and G. Shi, *Sci. China Technol. Sci.*, 2020, **63**, 1470–1477.
- 88 Z. Lei, D. Bai and X. S. Zhao, *Microporous Mesoporous Mater.*, 2012, **147**, 86–93.
- 89 M. Zhong, E. K. Kim, J. P. McGann, S. E. Chun, J. F. Whitacre, M. Jaroniec, K. Matyjaszewski and T. Kowalewski, *J. Am. Chem. Soc.*, 2012, **134**, 14846–14857.
- 90 H. Zhu, J. Yin, X. Wang, H. Wang and X. Yang, *Adv. Funct. Mater.*, 2013, **23**, 1305–1312.
- 91 T. A. Centeno, A. B. Fuertes and F. Stoeckli, *Electrochim. Acta*, 2009, **52**, 3207–3215.
- 92 T. Wang, J. Tang, X. Fan, J. Zhou, H. Xue, H. Guo and J. He, *Nanoscale*, 2014, **6**, 5359–5371.
- 93 R. R. Salunkhe, Y. Kamachi, N. L. Torad, S. M. Hwang, Z. Sun, S. X. Dou, J. H. Kim and Y. Yamauchi, *J. Mater. Chem. A*, 2014, 19848–19854.
- 94 Z. Chen, Y. Qin, D. Weng, Q. Xiao, Y. Peng, X. Wang, H. Li, F. Wei and Y. Lu, *Adv. Funct. Mater.*, 2009, **19**, 3420–3426.
- 95 J. Ren, Y. Huang, H. Zhu, B. Zhang, H. Zhu, S. Shen, G. Tan, F. Wu, H. He, S. Lan, X. Xia and Q. Liu, *Carbon Energy*, 2020, **2**, 176–202.
- 96 J. Tang, R. R. Salunkhe, J. Liu, N. L. Torad, M. Imura, S. Furukawa and Y. Yamauchi, *J. Am. Chem. Soc.*, 2015, **137**, 1572–1580.
- 97 Y. Liu, G. Li, Y. Guo, Y. Ying and X. Peng, *ACS Appl. Mater. Interfaces*, 2017, **9**, 14043–14050.
- 98 H. H. Duan, C. H. Bai, J. Y. Li, Y. Yang, B. L. Yang, X. F. Gou, M. L. Yue and Z. X. Li, *Inorg. Chem.*, 2019, **58**, 2856–2864.
- 99 C. Wang, C. Liu, J. Li, X. Sun, J. Shen and W. Han, *ChemComm*, 2017, **1**, 1751–1754.
- 100 L. F. Chen, Y. Lu, L. Yu and X. W. Lou, *Energy Environ. Sci.*, 2017, **10**, 1777–1783.

- 101 F. Hao, L. Li, X. Zhang and J. Chen, *Mater. Res. Bull.*, 2015, **66**, 88–95.
102 B. Chen, L. Xu, Z. Xie and W. Y. Wong, *EcoMat*, 2021, **3**, e12106-e12160.

CHAPTER TWO

Experimental Details and Characterization Techniques

2.1 Outline

This chapter provides a thorough explanation of the experimental and characterization techniques. The theoretical background, along with characterization techniques and the synthesis method, has been briefly discussed. The article thoroughly examines various physicochemical analyses that can be employed to verify the properties of materials utilized in the testing and production of supercapacitors. An explanation of the electrode's fabrication and the experimental setup of this technique is provided. This chapter provides an in-depth account of the various physical characterization techniques used to analyze the pristine MOFs, MOF-derived metal oxides and nanoporous carbon samples that have been developed as part of this study. These techniques include X-ray diffraction, Fourier transform infrared spectroscopy, Raman spectroscopy, X-ray photoelectron spectroscopy, Field emission scanning electron microscopy, Energy dispersive X-ray analysis, Brunauer–Emmett–Teller analysis, Transmission electron microscopy and Vibrating sample magnetometer. This chapter provides a comprehensive discussion of the electrochemical performance of the materials, which was evaluated using an electrochemical workstation.

2.2 Introduction

This thesis aims to enhance the efficiency of supercapacitors by proposing novel approaches. The introductory chapter provides a description of the background. The current study involves the synthesis of MOF materials to serve as electrodes and electrolytes in order to assemble a supercapacitor. This chapter outlines the experimental method employed for the synthesis of the MOF and its derived materials. Afterwards, the characterization methods implemented are explained in detail. First, the electrode and electrolyte materials are prepared and characterized and then, supercapacitors are fabricated and characterized. The electrode materials that were taken into consideration were pristine MOF, bimetallic MOFs, trimetallic MOFs, ferrites and nanoporous carbon. Pristine MOF, bimetallic and trimetallic MOFs were synthesized using a wet chemical method i.e. Reflux condensation method. Also, the ferrites and nanoporous carbon are prepared by using MOFs as a precursors via simple pyrolysis process. The methods of preparation are elaborated in details.

The physical properties of the synthesized materials are investigated through a variety of techniques such as X-ray diffraction (XRD), Fourier transform infrared spectroscopy (FTIR), Raman spectroscopy, X-Ray Photoelectron Spectroscopy (XPS) Technique, Scanning electron microscope (SEM), Energy dispersive X-ray (EDAX) spectroscopy, Specific surface area analyzer using Brunauer– Emmett– Teller (BET) Technique and Transmission electron microscope (TEM). This chapter includes a comprehensive explanation of these methods. Adequate electrolyte solutions were created through the dispersion of the corresponding salt in an appropriate solvent. Appropriate aqueous electrolytes were prepared by dissolving the relevant salt in water. To prepare gel-polymer electrolytes (GPEs), the polyvinyl alcohol polymer was utilized to encapsulate the aqueous electrolyte. The efficiency of constructed supercapacitor cells were assessed using a two-electrode assembly. The characterization techniques employed for the evaluation of electrochemical performance are cyclic voltammetry (CV), galvanostatic charge-discharge (GCD) and electrochemical impedance spectroscopy (EIS). The succeeding section also covers the discussion of these methods of characterization.

2.3 Experimental details

2.3.1 Aqueous chemical method/reflux condensation method

The reflux technique is a cost-effective and facile wet chemical method to produce nanomaterials. The reflux technique involves gradually growing crystals by controlling precipitation through the hydrolysis and condensation reactions of metal ions or their complexes in a solution. Reflux is a process by which the vapors are condensed and the resulting condensate is reintroduced back into the system it came from. It has applications both in industrial settings and laboratory setups for the purpose of distillation. In chemistry, it is employed to provide sustained energy to reactions. The reflux setup, as depicted in figure 2.1, comprises various components that include a round bottom flask (reaction bath), a condenser (cooling mode), and a temperature controller unit with an integrated stirring and heating mechanism. The precursor solution was stirred with a magnetic bar in a round-bottomed flask to produce a uniform solution. By utilizing a temperature controller, a stable and uninterrupted amount of thermal energy was supplied to the flask to carry out the reaction. The reaction can proceed for any desired duration because the reactant solvent cannot evaporate from the system, thanks to the process of condensation.¹



Figure 2.1: Schematic depiction of reflux condensation assembly

The reflux technique offers numerous benefits when compared to other synthesis methods. Following are several benefits that are highlighted:

- ❖ The reaction may be sustained over a prolonged duration without the need for further solvent addition or concern regarding the drying of the reaction vessel owing to the fact that the condenser readily captures the vapors.
- ❖ The primary benefit of utilizing this method is the upsurge in output, as all the reactants are fully employed in the reaction.
- ❖ By adjusting reaction time, temperature, pH of solution, and other reaction parameters, the characteristics of nanomaterial can be readily optimized.
- ❖ This approach can be readily implemented for industrial purposes as it does not necessitate a vacuum or top-notch targets at any point.

2.3.2 Substrate cleaning

To evaluate the electrochemical performance of the material, it should be deposited on the conductive substrate to form an electrode. The fabrication of an electrode involves the use of a substrate, and achieving high-quality and consistent results is heavily dependent on thoroughly cleaning the substrate. This process is crucial for ensuring that the electrode displays strong adhesion and a uniform, smooth surface. The approach utilized for cleaning will vary based on the type of surface, the level of cleanliness desired, and the type of pollutants that need to be eliminated. Some of the usual impurities that can be found are oil droplets, dust particles that are carried in the air, absorbed water, as well as grease. The act of cleansing involves the detachment of impurities from the base materials while keeping the materials unharmed. Numerous techniques exist for providing energy to break those bonds, including ion bombardment, thermal means, and scraping. The prescribed technique employed to clean the stainless steel mesh substrates was as follows.

- ❖ In the initial stage of substrate cleaning, the stainless steel mesh was first thoroughly rinsed with regular water.
- ❖ Then, the stainless steel mesh was subjected to treat with laboratory-grade cleaning agent for 15 minutes and subsequently rinsed with ordinary water.
- ❖ An ample amount of distilled water was poured into the beaker to facilitate the immersion of the stainless steel mesh, which were subsequently sonicate it in the distilled water for 15 minutes.
- ❖ Lastly, the stainless steel mesh substrates were rinsed with acetone to remove the impurities.

- ❖ The cleaned stainless steel mesh were dried at 70°C and further used as a substrate for fabrication of electrode.

2.3.3 Procedure of the seed slurry and fabrication of working electrodes

To fabricate the electrode, a seed slurry was prepared by mixing the active material, binder, and acetylene black in an appropriate proportion. To prepare seed slurry, 80 wt% of MOFs and its derived materials were used as active materials, 10 wt% of polyvinylidene pyrrolidone as a binder, and 10 wt% of acetylene black as a conducting material were grinded in N-Methyl-2-Pyrrolidone as a solvent. Then it was grinded to prepare a smooth and homogeneous seed slurry. Finally, it is ready to be used for the construction of the working electrode.

For the construction of working electrodes, stainless steel mesh was used as a substrate. The earlier prepared seed slurry was pasted on a stainless steel mesh of area 1 cm² to prepare the working electrode. Finally, the pasted stainless steel mesh was dried in an oven at 70°C for few hours, and it is now ready to be used as a working electrode to evaluate the electrochemical performance.

2.4 Characterization techniques

In present time, nanoscience and nanotechnology have emerged as the most effective answers to various technological challenges owing to their collaboration with materials science. It is imperative to utilize diverse conventional methods of characterization in order to examine the physical and chemical attributes of these materials. The newly created materials possess a set of distinctive characteristics, which include their structural, morphological, optical, electrical, and surface properties. As a consequence, the materials science field has witnessed the development of numerous innovative methods.² This section encompasses various physical and chemical methods along with their operating principles (Figure 2.2).

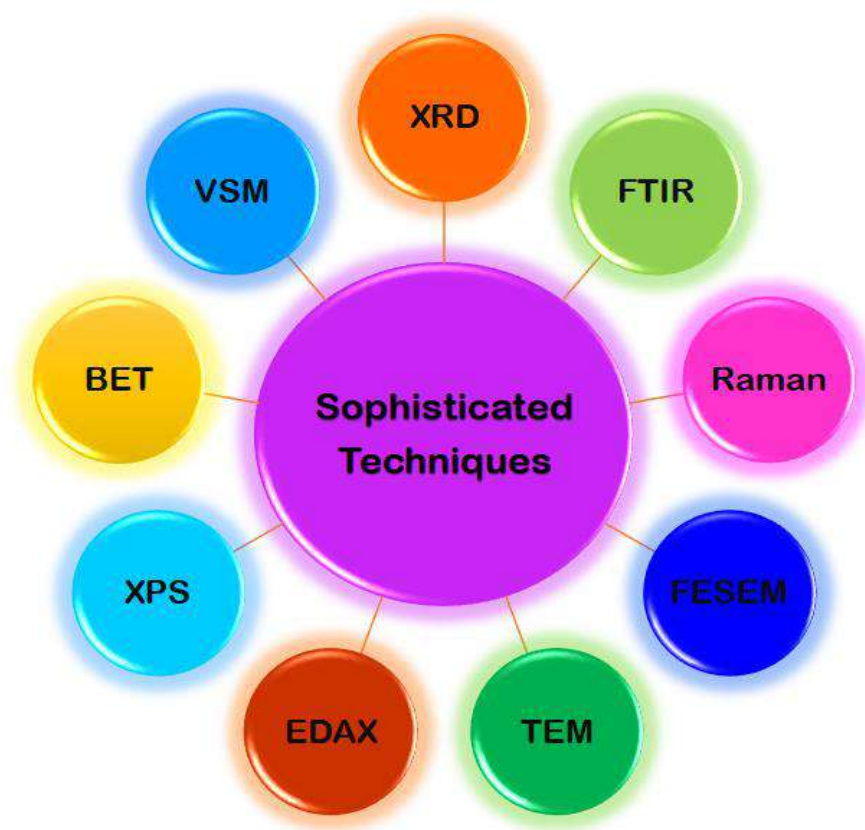


Figure 2.2: Various sophisticated techniques for the characterization of MOFs and its derived materials

2.4.1 X-ray diffraction (XRD)

Principle

Using a monochromatic X-ray beam to irradiate the target material, the non-invasive XRD technique measures the scattering angles and intensities of the diffracted beam. At angles when Bragg's law ($2d\sin\theta = n\lambda$) is satisfied, the maximum intensity of the diffracted beam is observed.^{3,4}

Construction and working of XRD

The XRD is made up of three parts

1. X-ray tube
2. Sample holder
3. X-ray detector

Figure 2.3 displays the schematic of XRD machines. A monochromatic X-ray beam is produced by the X-ray tube, which is essentially a Cathode Ray Tube (CRT). The CRT tube is constructed up of

- ❖ Evacuated glass tube: makes it possible for the molecules to hit the target without touching.

- ❖ Heated filament (Cathode): This substance typically has low ionization energy.
- ❖ Target (Anode): Usually, this is a substance having a high melting point, like Mo or W.
- ❖ Cooling system: In order to stop the anode from melting.
- ❖ High voltage source: The thermionic electrons are accelerated using a high voltage of 20–60 kV.

The produced monochromatic X-ray beam is collimated and directed at the target substance. Typically, a monochromatic beam of 1.54 \AA is produced using a Cu filter with a Ni filter. Diffraction occurs when the monochromatic beam comes into contact with the sample. The sample serves as a scattering center for the incident X-rays, while the detector collects the diffracted photons. For the angles that comply with Bragg's law, an intensity peak is created. The sample is scanned from 10 to 90° s, and the diffraction pattern is obtained. By comparing the data with the databases of the Joint Committee on Powder Diffraction or the American Standard for Testing of Materials (ASTM), one can identify the material from the sample by looking at this pattern.

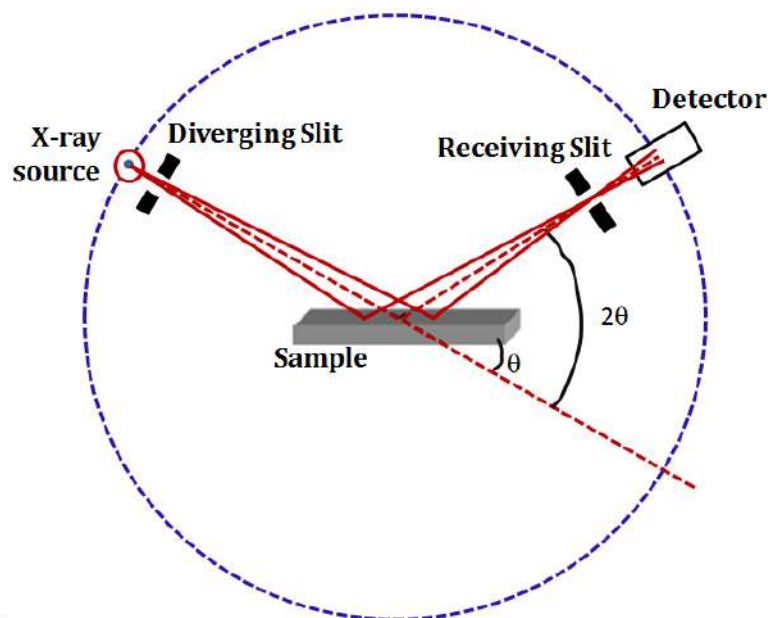


Figure 2.3: Schematic diagram of X-Ray diffraction techniques

[<http://pd.chem.ucl.ac.uk/pdnn/inst1/optics1.htm>]

We can identify the phase, ascertain the crystal structure, assess the quality of the thin film, and calculate a number of parameters, including residual stress/strain, crystal size, crystallographic roughness, flaws, etc. from the XRD pattern.

Bragg's condition in crystals can be fulfilled in one of two ways: continually changing or all over the experiment. Three distinct diffraction methods are produced by varying these parameters. These are listed in table 2.1, which is provided below.

Table 2.1: X-ray diffraction methods

Sr. No.	Method	λ	θ
1	Rotating crystal Method	Fixed	Variable (in part)
2	Powder Method	Fixed	Variable
3	Laue Method	Variable	Fixed

According to the Bragg's law, for certain d values, constructive interference of diffracted X-rays should occur at specific θ (i.e., Bragg's angle), and for other angles, destructive interference should occur, resulting in the least intensity of the diffracted beam. Subsequently, if the diffracting crystal's size is tiny, there won't be any more completely destructive interference at $\theta \pm d\theta$, which causes the peak to broaden in proportion to crystallite size and is used to determine crystallite size.

2.4.2 Fourier transform infrared (FTIR) spectroscopy

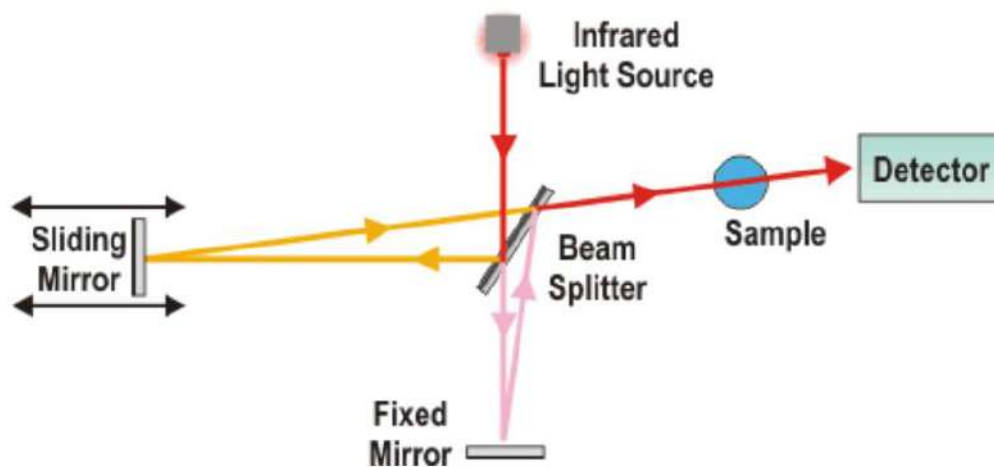


Figure 2.4: Schematic diagram of FTIR spectrometer

(<https://www.tribonet.org/wiki/fourier-transform-infrared-spectroscopy/>)

The FTIR technique plays a significant role in revealing details about the molecular structure or chemical bonds present in materials. The FTIR generates results based on frequency. The illustration depicted in figure 2.4 displays the schematic layout of the FTIR spectrometer. When a sample is exposed to IR radiation, a portion of the radiation is absorbed by the sample while the rest passes through it. When the sample is detected, a signal is obtained that essentially serves as its unique identifier, reflecting its particular fingerprint or structure.

The unique spectral signatures vary among various chemicals. The absorption is directly related to the specific bonds within the molecule. The wave numbers that are usually measured in the FTIR spectrum are within the frequency range of 400-6000 cm^{-1} . Initially, the IR source is evaluated for its emission spectrum, after which the emission spectrum of the IR source is measured along with the sample. The absorption spectrum of samples can be accurately determined by observing the ratio between the sample spectrum and the background spectrum. The absorption spectrum that arises from the natural vibration of the bond is produced as a result. The frequencies detected imply the existence of diverse functional groups and chemical bonds within the specimen. Due to the distinctive vibrational frequencies in the infrared range, FTIR is highly beneficial in determining organic molecular groups and compounds, which encompass a variety of functional groups, cross-links, and side chains.^{5,6}

The process of identifying functional groups occurs in the following manner.

- (1) Source: A black-body source generates and emits infrared radiation. The level of energy delivered to the specimen is regulated by the aperture, which enables the beam to pass through.
- (2) Interferometer: The phenomenon known as "Spectral encoding" takes place at the moment the beam goes into the interferometer. Afterwards, the signal from the interferogram is released through the interferometer.
- (3) Sample: The sample compartment serves as the entry point for the beam, which interacts with the sample's surface based on the specific analysis being conducted, either by passing through or bouncing off it. The sample absorbs distinct frequencies of energy that are indicative of its unique characteristics.
- (4) Detector: After navigating through the system, the beam ultimately arrives at the detector for its ultimate evaluation. The utilized sensors are uniquely engineered to gauge the distinctive interferogram signal generated.
- (5) Computer: By using computer hardware and software, the digitized signal is processed. The ultimate infrared spectrum is displayed to the user for analysis and additional alterations.

2.4.3 Fourier transform Raman (FT-Raman) spectroscopy

Raman spectroscopy is one of the spectroscopic methods used to examine rotational, vibrational, and specific additional modes in a system among the various spectroscopic techniques. Sir C. V. Raman discovered in 1928 that some of the light

that is deflected by a transparent medium changes in wavelength. This phenomenon is known as Raman scattering and this results from the Raman Effect. It depends on Raman scattering, also known as inelastic scattering of monochromatic light, which typically comes from a laser and may be in the visible, near-infrared, or near-ultraviolet spectrum. In Raman spectroscopy, laser radiations engage with the system's molecular vibrations generating phonons or other excitations. It causes the energy of the laser photons to change, either upward or downward. It provides details on the system's vibrational modes. There are possibilities with rotational and vibrational spectroscopes. With the aid of stimulating radiations energy, the type of transition that takes place will be identified.⁷

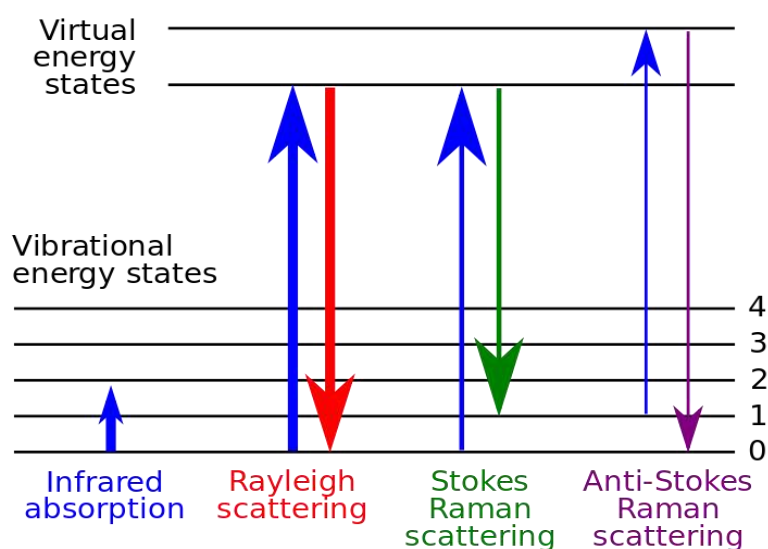


Figure 2.5: Energy level diagrams showing the states involved in Raman signal

[https://en.wikipedia.org/wiki/Raman_spectroscopy]

In Raman spectroscopy, a sample is lit with a laser beam, and the light that is scattered from that area is then captured with a lens spectrometer and provided through a monochromator. Due to elastic Rayleigh scattering, wavelengths that are nearer the laser line are filtered out, and the remaining collected light is scattered onto a detector. Separating weakly elastically scattered light from slightly more intense Rayleigh scattered laser light is the main challenge in Raman spectroscopy. The reason for this is because spontaneous Raman scattering is usually relatively feeble. To obtain a high level of laser rejection, spectroscopic Raman spectrometers used holographic gratings and numerous dispersion stages. The preferred detector for dispersive Raman setups in the past was a photomultiplier.

Principle

A molecule experiences the Raman Effect when light strikes it and interacts with its electron cloud and bonds. A photon excites the molecule in the case of the spontaneous Raman Effect, moving it from its ground state to a simulated energy level. The molecule, which is in an excited state, relaxes during which it produces a photon and returns to a rotational or vibrational state. The frequency of the emitted photon shifts away from the excitation wavelength due to the energy difference between the original state and the new state. The Raman Effect is a phenomena of light scattering as opposed to absorption, which occurs when a molecule is excited to a distinct energy level, as in fluorescence. The states involved in the Raman signal are depicted in figure 2.5 energy level diagram.

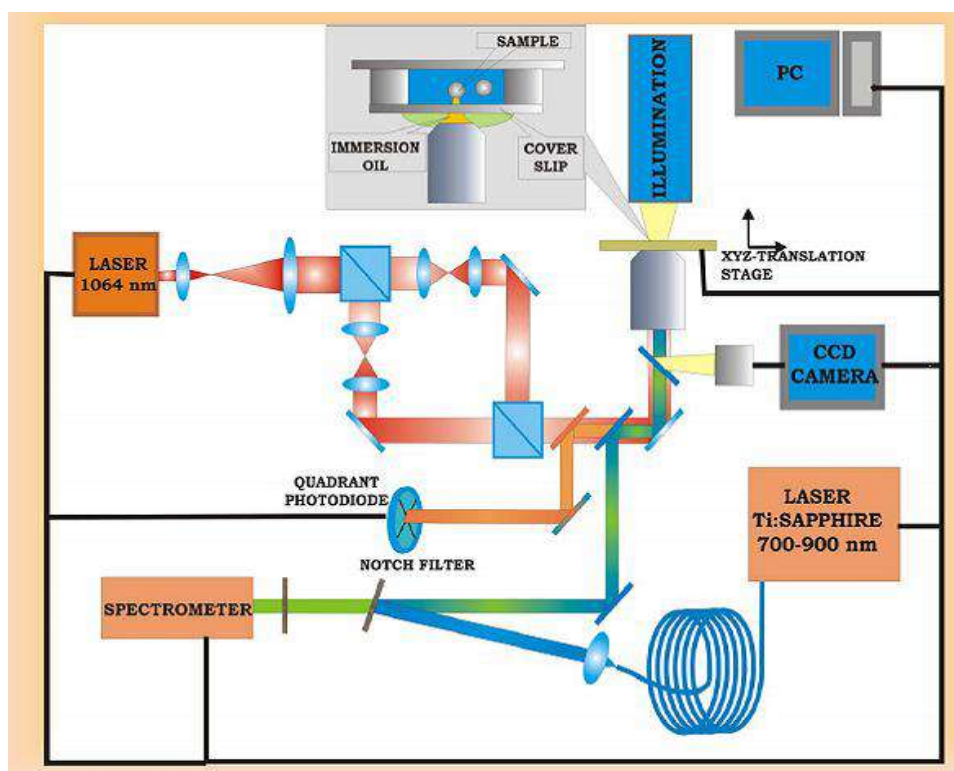


Figure 2.6: Schematic diagram of Raman spectrometer

If a molecule's long-term vibrational state is more energetic than its original condition, then the transmitted photon's frequency shifts towards a lower frequency, and the ideal state of the systems overall energy of molecules is maintained. Stokes shift describes this change in frequency. The same is true when a molecule's ultimate vibrational state is less energetic than its beginning state, the emitted photon's frequency shifts in favour of higher frequency. Anti-Stokes shift is the term used to

describe this change in frequency. Raman scattering is a manifestation of inelastic scattering due to the energy transfer that occurs when molecules and photons interact.

A schematic diagram of a Raman spectrometer is shown in figure 2.6. There are typically five main parts within the Raman system:

1. Excitation source (Laser)
2. Sample illumination system and light collection optics
3. Wavelength selector (Filter or Spectrophotometer)
4. Detector (Photodiode array, CCD or PMT)
5. Computer Interfacing software

2.4.4 X-ray photoelectron spectroscopy (XPS)

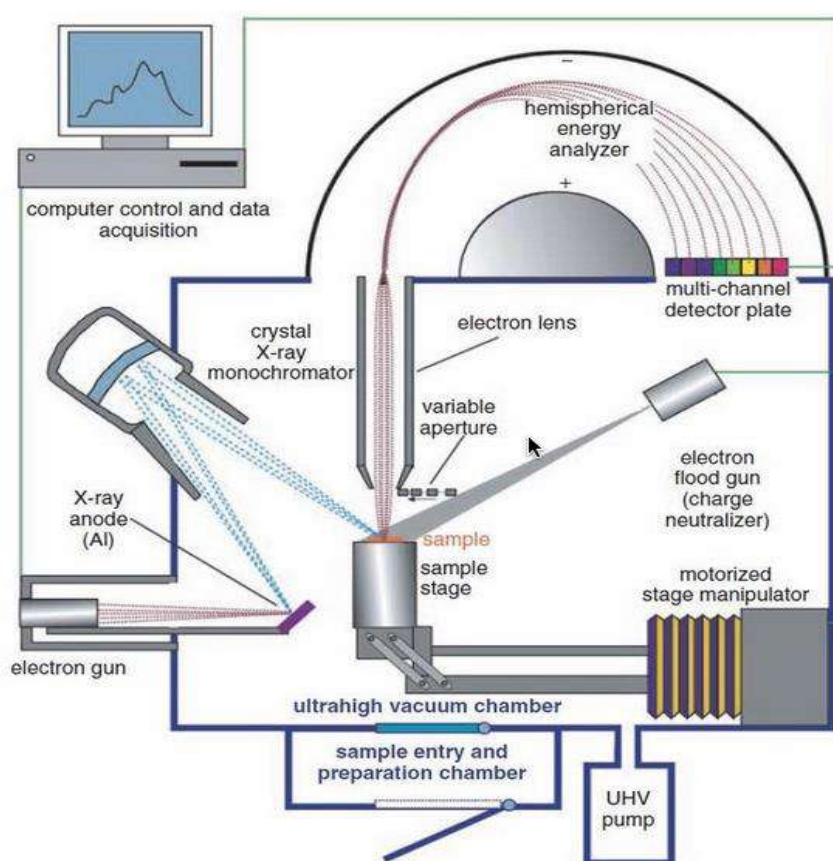


Figure 2.7: Schematic representation of XPS spectrometer

[https://serc.carleton.edu/msu_nanotech/methods/xps.html]

One of the most accurate methods for determining the chemical environment and composition of the specimen surface is X-ray photoelectron spectroscopy (XPS). It is based on the fundamental idea of the photoelectron effect, according to which an incident photon with enough energy ($E = h\nu$) causes the emission of an electron from an atom on the surface of the specimen (10–15 nm away).^{8,9}

Principle:

Monochromatic low energy (1.5 keV) X-rays incident on the surface of the specimen cause photoelectrons to be produced. These photoelectrons have energy that is specific to a given atomic state and can reveal important details about the chemical environment of specimen's.

The following are the components of typical XPS equipment:

1. A source of monochromatic low energy X-rays
2. Ultra-high vacuum chamber
3. An electron energy analyzer (concentric hemispherical analyzer)

In XPS, a monochromatic X-rays photons of sufficient (~ 1.5 keV) known energy are produced from X-ray source, are impinged on the specimen surface placed on a specimen stage. In order to allow an interference-free study of photo emitted electrons, the specimen stage is enclosed in an ultra-high vacuum chamber. As seen in figure 2.7, these X-ray photons interact with the specimen's atoms and cause their core level electrons to emit. The photoelectrons that are released will definitely have kinetic energies lower than these energies, leading to an extremely short electronic mean-free path. The signal is only created from the core level electrons expelled from the atoms present in the few atomic layers at the surface since the electron produced much deeper in the specimen's bulk will be absorbed in the specimen itself.

2.4.5 Scanning electron microscope (SEM)

An image that shows the morphological and topological details of the specimen in a scanning electron microscope is produced by the collection and non-destructive processing of secondary and backscattered electrons that are produced during the scattering of a high mono-energetic and focused electron beam accelerated (30kV) onto the surface of the specimen under vacuum.

In SEM, the specimen surface is incident with a mono-energetic beam that has been well targeted. When this mono-energetic electron beam interacts with the specimen, secondary electrons and backscattered electrons form, and these electrons are primarily utilised for generating the specimen image. The atomic number of the host atoms impacts the amount of backscattered electrons. The valence electrons of the constituent atoms emit secondary electrons, which are then developed. Only secondary electrons generated and released from specimen surfaces are detected because their energy is quite low, whereas secondary electrons generated in the bulk of the specimen are destroyed. In spite of their high sensitivity to the specimen's

surface, these secondary electrons generate the brightness and contrast needed for images. The electrons that are elastically dispersed backward from their host atoms are known as backscattered electrons. These electrons are more energetic than secondary electrons and are affected by the specimen's composition.^{10,11}

Construction in brief

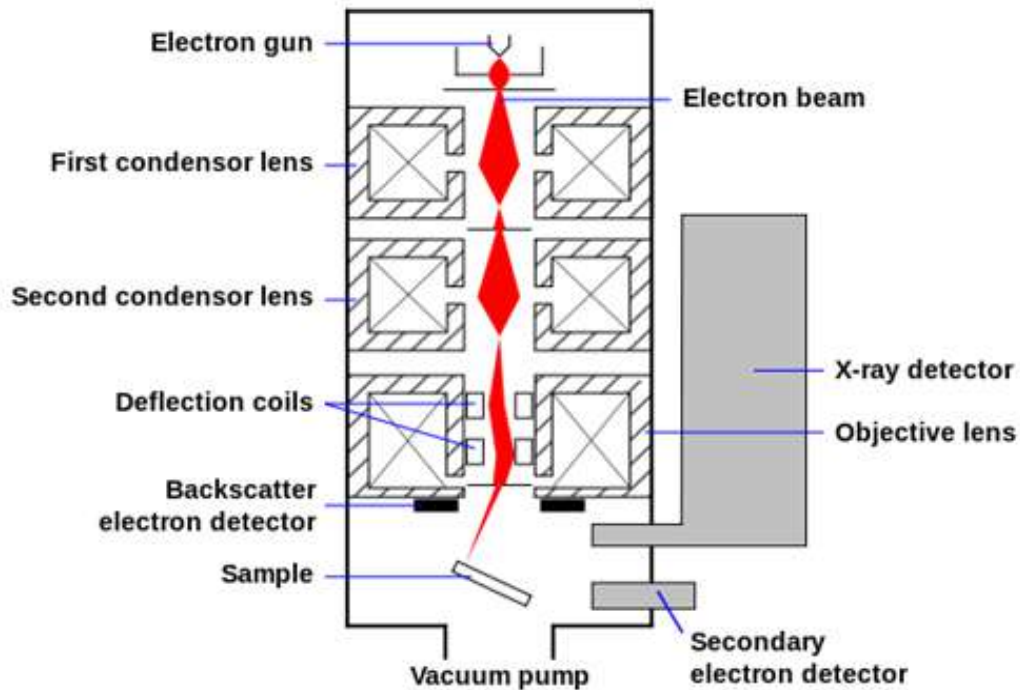


Figure 2.8: Schematic representation of scanning electron microscope

[http://en.wikipedia.org/wiki/Scanning_electron_microscope]

In a typical SEM, an electron gun is largely needed to provide an electron probe beam that gives light in an optical microscope. A series of magnetic electron lenses and deflection coils combine to form an electron beam that scans the surface of a specimen put on a specimen stage in an electron optical system. High vacuum is required to maintain an undistorted electron beam, in the path of which is positioned a specimen stage that allows the research specimen to be readily oriented in the proper direction for a detailed analysis. The specimen surface is hit by an electron beam, which generates a variety of signals, including secondary and backscattered electrons, which must be collected out. In order to collect the appropriate electrons and other signals, such as X-rays, for energy dispersive analysis of the X-rays from the specimen, a group of detectors is used.

An image display unit that offers the necessary view of specimen morphology further processes and displays the signal generated by this set of detectors. The figure

2.8 depicts the schematic representation of SEM and its key elements. So an electron gun, electron lenses, a sample stage, a vacuum chamber, detectors for the appropriate signals, a data output device, cooling system, and power supply make up a typical SEM machine.

2.4.6 Energy dispersive X-ray (EDS) spectroscopy

The elements present in the material are quantitatively examined using energy dispersive X-ray analysis (EDS). With the help of the EDS technique, the elements with atomic numbers 4 (Be) to 92 (U) can be identified; this is one of the best benefits over other techniques to detect a wide range of elements.^{12,13}

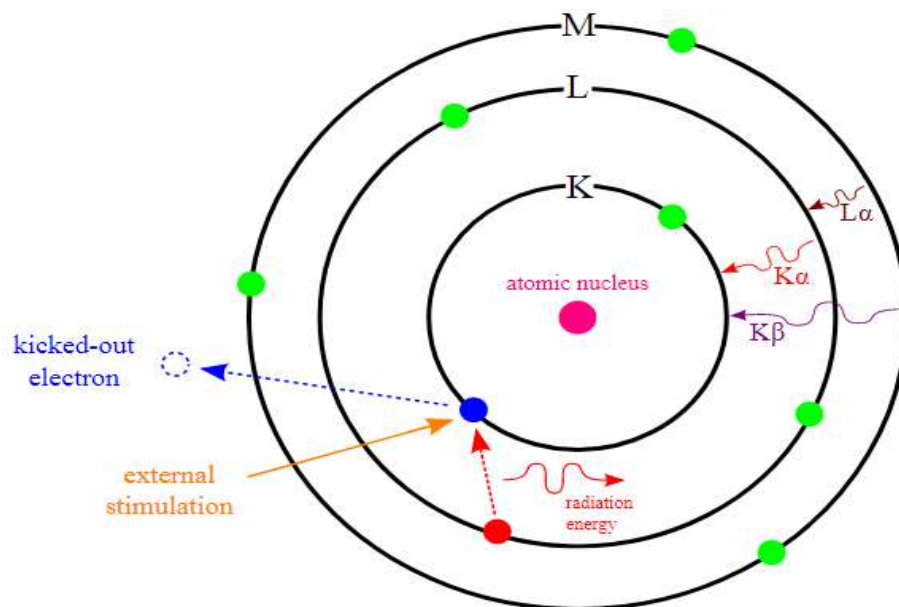


Figure 2.9: Schematic diagram showing the possible transition¹⁴

Principle of EDS

Using the EDS analytical method, the chemical characterization of materials and quantitative evaluation of components are explored. In EDS, an electron ray with enough energy can hit the samples top layer, causing inner shell electrons to change and eject from an atomic orbit. Then, with the same amount of time, an electron from the top energy shell falls to take its place. As upper energy shell electrons continuously go down, they give up some of their energy to get into the low energy shell. The transition shown in figure 2.9 is one that is likely to occur and release energy on the order of an X-ray wavelength. This energy is then counted, gathered, and converted to atomic or weight percentages. With only a few spectral peaks, the various elements often generate characteristic X-rays at different energies that overlap.

Working of EDS

In EDS, precise electron beam energy that is focused on the sample is employed for material analysis. Energy is lost when an electron beam interacts with a material in a number of ways (e.g. X-ray emission). In particular, inelastic collisions in the incident electron beam can cause the electron to be ejected from the material. As a result, an atom produces an electron vacancy that creates a hole. It follows that this causes the atom to lose energy and to automatically rearrange its electron shells. The atom's distinctive property is the generation of free X-rays. Using the X-ray detector, EDS calculates the big amount of released X-ray energy. A solid-state lithium-drifted silicon detector is typically utilized. When the emitted X-ray hits the detector, it produces a pulse with that energy. This pulse alters a voltage pulse within the charge-sensitive amplifier. Then, a different channel analyzer has created a range of voltage-related pulses. The measurement of voltage to all incident X-rays is determined by energy and sent to the computer for data analysis. The X-ray energy against counts was used to determine the percentage of the elements in the sample. The precision of the EDS is based on the several variables that are connected to the sample. Less than 5 atomic number elements (such as Be, H, and He) cannot be detected by an EDS detector. Another is that high voltage in the EDS can alter the position of the peak in the spectrum. Additionally, the peaks of certain elements, such as Mn K_{β} and Fe K_{α} have not yet split as well. Furthermore, the sample's inherent characteristics affect how precisely the EDS spectrum is generated. As a result, the EDS is the most effective method to determine the proportion of elements in the sample with atomic numbers greater than 6.

2.4.7 Specific surface area analyzer using Brunauer– Emmett– Teller (BET)

Principle

A low-temperature nitrogen gas adsorption on a solid surface of a material is used in Brunauer-Teller-Emmett (BET) surface area study. It is a crucial technique since it provides details about the materials' surface area and porosity. The BET theory is an important analytical tool for determining a material's specific surface area, pore size, and pore volume. It also explains the physical adsorption of gas molecules on solid surfaces.^{15–17}

With the following hypotheses, Stephen Brunauer, Paul Hugh Emmett, and Edward Teller expanded Langmuir theory, a theory for monolayer molecule adsorption, to multilayer adsorption.

- i) Physically, gas molecules adhere to a solid in an unlimited number of layers.
- ii) Every adsorption layer is independent of one another.
- iii) Each layer can be analysed using the Langmuir theory.

Working

As impurities like water and oil may impact the actual surface area of a given material, sample preparation is crucial before analysis in BET surface area measurement. As a result, solid surfaces must be free of these contaminants before conducting gas sorption tests. Most frequently, a sample is placed in a glass cell and heated under vacuum or a flowing gas to remove such impurities this process is known as surface cleaning (degassing).

By using an external bath, the prepared sample is heated to an accurate temperature. Then, tiny volumes of gas (a Nobel gas like N_2) are gradually allowed into the sample zone that has been evacuated. A thin layer that covers the whole surface of the solid (adsorbent) is stated to be formed when N_2 gas molecules adhere to the solid's surface and are considered to have been adsorbed. The volume of gas adsorbed onto the surface of a powdered or porous substance can be calculated as its surface area. The entire surface that the gas can reach, whether it is exterior or internal, is included in the surface area analysed.



Figure 2.10: BET instrument

In general, only Van der Waals forces cause solids to absorb weakly bonded gases. The solid must be properly frozen to the gas's boiling point in order for enough gas to be absorbed for surface area measurement. Most frequently, liquid nitrogen (77.35 K) is used to cool down the solid while nitrogen gas serves as the adsorbate.

Adsorption doesn't stop until the concentration of N₂ in the gas phase and the amount of N₂ adsorbed are in equilibrium.

2.4.8 Transmission electron microscope (TEM)

When an ultrathin specimen (less than 200 nm) is exposed to a high-energetic beam of accelerated electrons at a voltage of about 300 kV, a variety of interactions result obtained; that causes the transmission of direct or distributed electrons through the specimen. Depending on the mode of operation, these transmitted electrons are focused through a set of electromagnetic lenses to create an image, a diffraction pattern, or another nano-analytical spectrum.^{18,19}

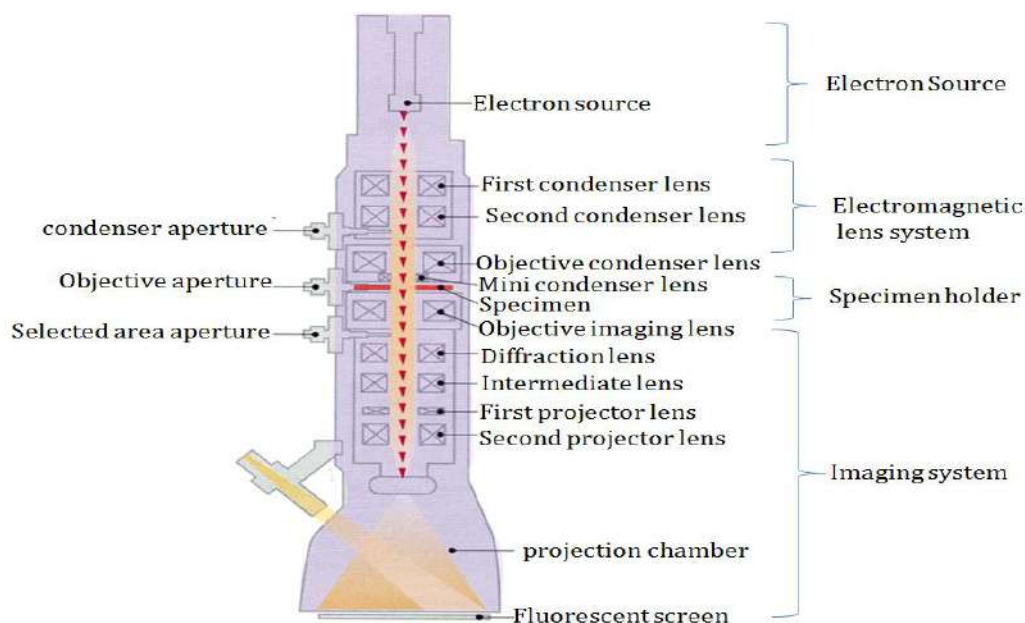


Figure 2.11: Schematic representation of transmission electron microscope

[<http://micron.ucr.edu/public/manuals/Tem-intro.pdf>]

The fundamental structure of a TEM is similar to that of an optical microscope, however with a TEM, an electron beam with high energy is employed in place of light, and electromagnetic lenses are used in place of glass lenses. Figure 2.11 depicts a common TEM setup design. We can see from the picture that a TEM can be easily broken down into four primary components. The specimen holder, imaging system, electromagnetic lens system, and electron source or gun.

Electron Gun: It offers a potent, powerful, and highly energetic electron beam. Depending on the phenomenon employed for electron ejection, there are three primary categories of electron guns.

Thermionic emission (TE) electron gun: When the cathode filament is heated to a high temperature and propelled towards the anode with a certain acceleration voltage (up to 30 kV), electrons are released.

Field emission (FE) electron gun: When high resolution imaging is necessary, this electron gun is utilized. The field emission happens when a strong field is applied to a metal tip that is very small (less than 100 nm) and electrons are released as a result of the tunneling phenomena. In contrast to the thermionic electron gun's 10–20 mm diameter, the electron beam created here functions as an electron source with a diameter of 5–10 nm.

Shottkey-emission (SE) electron gun: With an additional applied electric field on the heated metal surface, it is comparable to the TE gun. Compared to a FE gun, this electron gun creates a beam with a bit less stability but a higher current. It can be viewed as combining more of the benefits and less of the drawbacks of both TE and FE guns.

Electromagnet lens system: An essential element of an electron microscope is the magnetic lens system. It is used to channel post-interaction electrons for picture generation as well as to focus an electron beam on the subject. Condenser lenses, objective lenses, and projector lenses are the three basic types of electromagnet lens systems. A group of lenses known as condenser lenses is in charge of controlling the spot size of the primary electron beam convergence. An image is created by the objective lens, which gathers transmitted electrons from the specimen, and is then magnified and projected by a group of intermediate and projector lenses.

Specimen holder: The specimen is held by the sample holder, which is a platform with a mechanical arm and a feature for regulating the specimen's position.

Imaging system: A set of electromagnetic lenses and the display device are also included in it. Here, the electromagnetic lenses serve two purposes specifically. The image is magnified and projected on a phosphorescent screen or a detector that shows the image on a monitor by one method of focusing the electrons sent through the specimen, while the image is shown on the monitor by another method.

2.4.9 Vibrating sample magnetometer (VSM)

The materials magnetic characteristics are measured using a vibrating sample magnetometer (VSM). The material was magnetized after being placed in a constant magnetic field, using a piezoelectric material, physical sinusoidal vibration of the sample was applied. In a typical setup, a lock-in amplifier that uses the piezoelectric

signal as the reference signal calculates the induced voltage. It is possible to obtain the materials hysteresis curve by estimating the field of an outside electromagnet. The foundation of VSM is Faraday's law of induction, which states that an electric field is produced when a magnetic field changes. This measured electric field can reveal information about the formation of the magnetic field. If the sample is magnetized, the alignment of the magnetic domains in the field leads the sample to become magnetized. The magnetization increases as the constant field size increases.²⁰⁻²³ The digital photograph of vibrating sample magnetometer as shown in figure 2.12.



Figure 2.12: Digital photograph of vibrating sample magnetometer
(<https://qdusa.com/products/ppms.html>)

2.4.10 Electrochemical studies

Sophisticated electrochemical analysis methods are employed in order to methodically investigate how the working electrode stores charges and their kinetics. This thesis employs both two-electrode and three-electrode configurations for electrochemical experimentation. The three-electrode step-up was used to investigate the electrochemical responses and capacity for storing charges in an electrode system. Additionally, the two-electrode setup is employed to assess the practical potential of a constructed supercapacitor device.

In order to gain insights into how an electrode behaves electrochemically, a variety of characterization tests are performed, including cyclic voltammetry, galvanostatic charge-discharge, and electrochemical impedance spectroscopy.

2.4.10.1 Cyclic voltammetry (CV)

Cyclic voltammetry refers to a variety of potentiodynamic electrochemical techniques. Cyclic voltammetry is a well-regarded electrochemical method that is employed to investigate the oxidation and reduction mechanism of manufactured materials. To scrutinize the capacitive characteristics of the electrodes, CV assessments are carried out with variable scan rates, while keeping the voltage range steady. Three electrode assembly was used to study the single electrode system. The CV graph is depicted by placing voltage along the x-axis and current along the y-axis, as shown in figure 2.13. The CV would appear as a rectangle in the case of an ideal capacitor. The CV curves of EDLC based materials show a rectangular in shape. Simultaneously, the electrode with a battery-type or pseudocapacitor material displays peaks indicative of redox processes in cyclic voltammetry graphs. In CV measurements, the applied voltage is studied in relation to the cell current. During a CV experiment, the electrode's potential is swept linearly from the beginning to the end and then back to the starting point. The peak current is observed at the voltage of maximum potential after the electrochemical species present on the electrodes surface have been exhausted. The amount of Faradic current reflects the speed of electron transfer between the electrode and redox molecule.²⁴⁻²⁶

The conclusions derived from CV curves:

- ❖ The use of a CV curves can effectively examine redox reactions and various chemical reactions that involve the transfer of electrons.
- ❖ The working electrodes charge storage capacity can be determined using CV curves.
- ❖ It is possible to distinguish between supercapacitor and battery electrodes based on the configuration of their CV curves. In the case of a supercapacitor electrode, a rectangular curve is observed in the CV, whereas batteries typically exhibit strong redox peaks that are reflective of the material being used.
- ❖ The charge storage kinetics of electrodes can be comprehensively analyzed by thoroughly examining the CV curves.

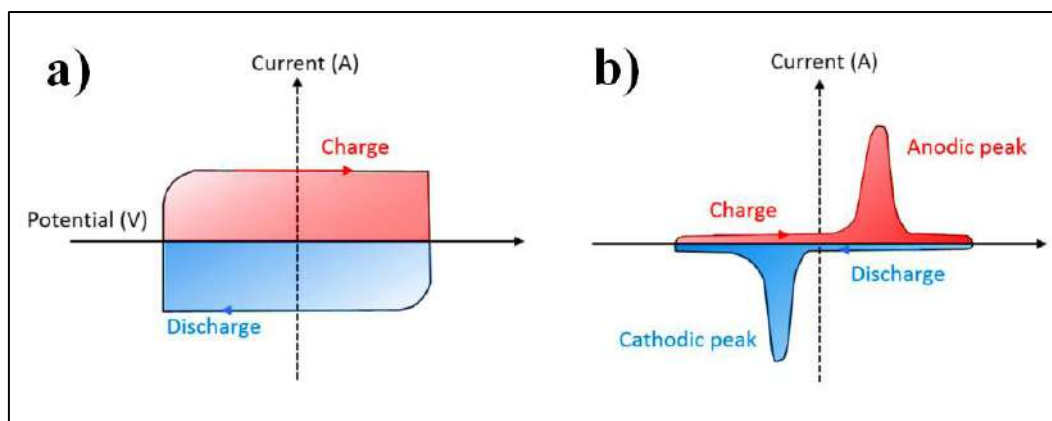


Figure 2.13: A typical cyclic voltammogram curves of a) supercapacitor and b) battery. Reproduced with permission.²⁷ Copyright © 2018, American Chemical Society

2.4.10.2 Galvanostatic charge-discharge (GCD)

Galvanostatic charge-discharge evaluation are utilised to assess a materials ability to store charge. The process involves charging and discharging the supercapacitor at a constant applied current within a defined range of two voltages, as depicted in figure 2.14. Ideally, the GCD curve would exhibit a linear pattern, characterized by alternating positive and negative gradients. Non-linearities may arise as a result of the swift decline in voltage during the transition from charging to discharging. Furthermore, it can be observed that authentic supercapacitors tend to discharge themselves when they are fully charged and left without any external load being connected.

The electrodes specific capacitance (computed in $F g^{-1}$) can be obtained from the GCD curve using the equation:

$$C_{sp} = \frac{I \times \Delta t}{m \times \Delta V} \dots\dots\dots (2.1)$$

Where C is the specific capacity ($F g^{-1}$), I is the current density (A), Δt is the discharging time (s), m is the mass (g) of the active electrode materials, and ΔV is the potential window of the discharge process (V). The GCD tests hold significant value in assessing capacitance. The potential range for pseudocapacitors remains in a fixed state. However, in the scenario of EDLC, the scope of plausible windows is not limited since the capacity for storing charge is not reliant on potential.

The GCD curve was used to calculate the specific energy and specific power for a two-electrode cell setup, using the given formulas.²⁸

$$E = \frac{0.5 \times C_{sp} \times \Delta V^2}{3.6} \dots\dots\dots (2.2)$$

$$P = \frac{E \times 3600}{\Delta t} \dots\dots\dots (2.3)$$

Where E and P are the specific energy (Wh kg⁻¹) and specific power (W kg⁻¹), respectively, ΔV is the discharging voltage (V), and Δt is the discharging time in seconds.

The effective use of the supercapacitor in practical applications is dependent on its ability to maintain capacitance over a long period, known as cyclic stability. This capability is achieved through the deployment of GCD. The cell consistently performs charging and discharging cycles without interruption. The assessment of performance differences or similarities is conducted by measuring the difference in capacitance before and after cycling. Typically, EDLCs exhibit greater durability compared to pseudocapacitors, which have a limited cycle life due to factors like redox reactions, electrode material swelling and shrinking caused by charge/discharge cycle.²⁹

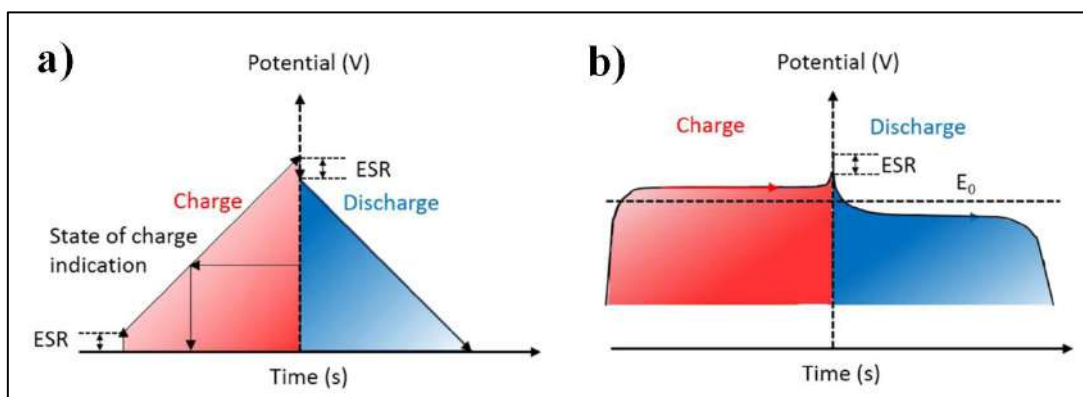


Figure 2.14: A typical galvanostatic charge–discharge curves of a) supercapacitor and b) battery. Reproduced with permission.²⁷ Copyright © 2018, American Chemical Society

2.4.10.3 Electrochemical impedance spectroscopy (EIS)

The EIS examinations assess the electrodes resistance at a constant voltage throughout different frequencies. In this evaluation, a consistent voltage is overlaid with a low-amplitude sinusoidal voltage. The Nyquist plot is a useful tool for analyzing the signal produced by the EIS technique. The Nyquist plot depicts the relationship between the real impedance (Z') and imaginary impedance (Z'') in graphical form. The Nyquist plot is divided into three distinct parts as shown in figure 2.15.

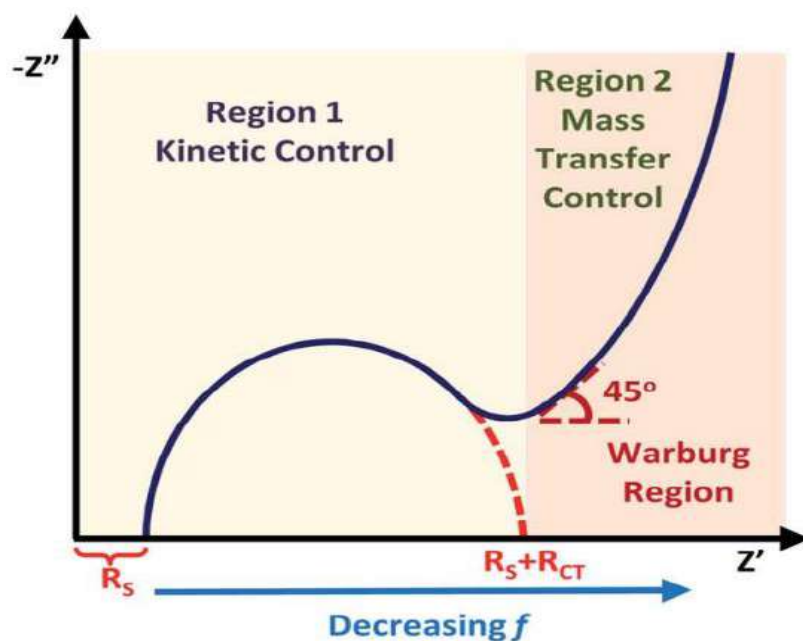


Figure 2.15: A Nyquist plot featuring labeled significant regions. Reproduced with permission.³⁰ Copyright © 2021, Royal Society of Chemistry

- (1) The high-frequency interceptions imply the resistance of the solution.
- (2) In the range of high to medium frequencies, a semicircle can be observed that signifies the presence of charge transfer resistance at the interface of the electrode and electrolyte.
- (3) In the low-frequency region, the presence of a Warburg resistance is signaled by vertical line or a straight line angled around 45° degrees to the real axis.

2.4.11 Supercapacitor device fabrication

The supercapacitor device is constructed to understand the real practical ability of the electrode materials. Supercapacitor device generally consist of electrodes, electrolyte and a separator. Depending on the electrode material used to fabricate supercapacitor device, the supercapacitors are again divided into subtypes are symmetric, asymmetric and hybrid supercapacitor device.

Based on the electrolyte used, the supercapacitor device is of two types, i.e. aqueous or liquid state supercapacitor device and solid-state-supercapacitor device. The advantages of the solid-state supercapacitor device as compared to the liquid-based supercapacitors device are numerous, such as increased flexibility, hassle-free production, improved safety features and ability to operate in a broader temperature range. Solid-state supercapacitors possess distinctive electrochemical features such as exceptional stability, elevated power output, flexible structure, and moderate energy density, implying their immense potential for various prospective applications.

Flexibly constructed solid-state supercapacitors can serve as a source for powering electronic gadgets and various energy storage or conversion tools including lithium-ion batteries, fuel cells and so on.³¹

2.4.11.1 Electrode materials

Superior performance of supercapacitors can be attained by creating appropriate electrodes utilizing inexpensive and environmentally friendly techniques. Through these techniques, it becomes possible to produce materials that have a morphology and porosity that align with predetermined specifications. A thorough comprehension of the process of storing charges, routes for ion transportation, and locations of electrochemically responsive areas is necessary. A variety of electrode materials are utilized in the application of supercapacitors. These encompass electrode materials comprised of carbon based materials, polymers that conduct electricity, as well as oxides derived from transition metals and rare earth elements.

2.4.11.2 Separator

The separator plays a crucial role in the operation of a supercapacitor device. These materials have the ability to facilitate the transportation of charges while preventing the physical and electrical connection between two electrodes due to their ion-permeability. Typically, nonwoven fabric or polymer-coated paper is used as separators in SCs that employ aqueous electrolytes. Typically, these insulators are saturated in the electrolytic solution for a set amount of time prior to their utilization in the apparatus.

2.4.11.3 Gel-polymer electrolyte (GPE)

Gel-polymer electrolyte are a type of electrolyte that involves the confinement of liquid electrolytes in a polymer matrix. Gel-polymer electrolytes have a reduced amount of available water when compared to liquid electrolytes. This attribute results in lower levels of water oxidation processes. As a result, gel-polymer electrolytes can widen the range of voltages that can be used, which was previously a limitation in supercapacitors based on liquid electrolytes. As a result, polyvinyl alcohol served as a matrix for KOH/Na₂SO₄ as the liquid electrolyte. Polyvinyl alcohol ability to hold water and promote effective ion conduction pathways was due to its -OH/SO₄ groups.³²

2.5 References

- 1 S. K. Aditha, A. D. Kurdekar, L. A. A. Chunduri, S. Patnaik and V. Kamiseti, *MethodsX*, 2016, **3**, 35–42.
- 2 S. Mourdikoudis, R. M. Pallares and N. T. K. Thanh, *Nanoscale*, 2018, **10**, 12871–12934.
- 3 C. F. Holder and R. E. Schaak, *ACS Nano*, 2019, **13**, 7359–7365.
- 4 A. A. Bunaciu, E. gabriela Udriștioiu and H. Y. Aboul-Enein, *Crit. Rev. Anal. Chem.*, 2015, **45**, 289–299.
- 5 M. Dendisová, A. Jenišťová, A. Parchaňská-Kokaislová, P. Matějka, V. Prokopec and M. Švecová, *Anal. Chim. Acta*, 2018, **1031**, 1–14.
- 6 J. L. R. Arrondo, A. Muga, J. Castresana and F. M. Goñi, *Prog. Biophys. Mol. Biol.*, 1993, **59**, 23–56.
- 7 B. Chase, *Mikrochim. Acta*, 1987, **93**, 81–91.
- 8 F. A. Stevie and C. L. Donley, *J. Vac. Sci. Technol. A*, 2020, **38**, 063204-063225.
- 9 E. Korin, N. Froumin and S. Cohen, *ACS Biomater. Sci. Eng.*, 2017, **3**, 882–889.
- 10 M. Pluskal, L. Oskwarek, R. Rak and A. Czerwinski, *2007 IEEE Instrumentation & Measurement Technology Conference IMTC 2007*, 2007, 1-4.
- 11 A. Mohammed and A. Abdullah, *Proc. 2018 Int. Conf. Hydraul. Pneum. - HERVEX*, 2019, 77–85.
- 12 H. Schwenke, J. Knoth, *Nucl. Instrum. Methods Phys. Res.*, 1982, **193**, 239–243.
- 13 W. C. Campbell, *Analyst*, 1979, **104**, 177-195.
- 14 Z. M. Zhang, C. J. Fu and Q. Z. Zhu, *Advances in Heat Transfer*, 2003, **37**, 179–296.
- 15 F. Ambroz, T. J. Macdonald, V. Martis and I. P. Parkin, *Small*, 2018, **2**, 1800173-1800190.
- 16 R. Bardestani, G. S. Patience and S. Kaliaguine, *Can. J. Chem. Eng.*, 2019, **97**, 2781–2791.
- 17 D. N. P. R. Jayakantha, N. Gunawardhana, H. M. N. Bandara, E. Comini, N. M. Gunawardana and S. M. M. L. Karunarathne, *Instrum. Sci. Technol.*, 2021,

- 50**, 47–56.
- 18 M. Malatesta, *Int. J. Mol. Sci.*, 2021, **22**, 12789-12806.
- 19 L. E. Franken, K. Grünewald, E. J. Boekema and M. C. A. Stuart, *Small*, 2020, **16**, 1906198-1906213.
- 20 E. E. Bragg and M. S. Seehra, *J. Phys. E.*, 1977, **10**, 216-223.
- 21 B. R. Sankhi and E. Turgut, *J. Magn. Magn. Mater.*, 2020, **502**, 166560-166567.
- 22 J. P. Phillips, S. Yazdani, W. Highland and R. Cheng, *Magnetochemistry*, 2022, **8**, 1–7.
- 23 J. A. Gerber, W. L. Burmester and D. J. Sellmyer, *Rev. Sci. Instrum.*, 1982, **53**, 691–693.
- 24 G. A. Mabbott, *J. Chem. Educ.*, 1983, **60**, 697–702.
- 25 P. T. Kissinger and W. R. Heineman, *J. Chem. Educ.*, 1983, **60**, 702–706.
- 26 N. Elgrishi, K. J. Rountree, B. D. McCarthy, E. S. Rountree, T. T. Eisenhart and J. L. Dempsey, *J. Chem. Educ.*, 2018, **95**, 197–206.
- 27 Y. Shao, M. F. El-Kady, J. Sun, Y. Li, Q. Zhang, M. Zhu, H. Wang, B. Dunn and R. B. Kaner, *Chem. Rev.*, 2018, **118**, 9233–9280.
- 28 R. Bhosale, S. Bhosale, P. Kumbhar, D. Narale, R. Ghaware, C. Jambhale and S. Kolekar, *New J. Chem.*, 2023, **47**, 6749–6758.
- 29 Q. Wu, T. He, Y. Zhang, J. Zhang, Z. Wang, Y. Liu, L. Zhao, Y. Wu and F. Ran, *J. Mater. Chem. A*, 2021, **9**, 24094–24147.
- 30 N. O. Laschuk, E. B. Easton and O. V Zenkina, *RSC Adv.*, 2021, **11**, 27925–27936.
- 31 X. Lu, M. Yu, G. Wang, Y. Tong and Y. Li, *Energy Environ. Sci.*, 2014, **7**, 2160–2181.
- 32 A. Barua and A. Paul, *Energy Fuels*, 2021, **35**, 10262–10273.

CHAPTER THREE

Design and Development of Porous Nanorods-Based Nickel-Metal Organic Framework (Ni-MOF) for High-Performance Supercapacitor Application

3.1 Outline

Metal-organic frameworks have received increasing attention as promising electrode materials in supercapacitors. In this study, we synthesized a nickel-metal-organic framework (Ni-MOF) by a simple and low-cost reflux condensation technique using non-hazardous trimesic acid as an organic ligand. The structures and morphologies of the Ni-MOF material were characterized by X-ray diffraction, Fourier-transform infrared spectroscopy, and scanning electron microscopy techniques. The prepared Ni-MOF was found to have a rod-like morphology and these morphologies can provide beneficial paths for electrolyte ion penetration, obtaining an enlarged contact area between the active material and electrolyte. The Ni-MOF had a considerable specific surface area of $398.4 \text{ m}^2 \text{ g}^{-1}$. Further, its highly porous structure offered excellent supercapacitor performance. The charge-storage mechanism of the electrodes was investigated by cyclic voltammetry, charge-discharge cycling, and electrochemical impedance spectroscopy using 2 M KOH as an electrolyte in a three-electrode assembly. The specific capacitance of the Ni-MOF was found to be 1956.3 F g^{-1} at a current density of 5 mA cm^{-2} by GCD studies and it retained 81.13% of its initial capacitance even after 3000 GCD cycles at a 35 mA cm^{-2} current density. An as-fabricated Ni-MOF//activated carbon hybrid supercapacitor (HSC) exhibited a specific energy of 98.15 Wh kg^{-1} at a specific power of $1253.47 \text{ W kg}^{-1}$ and excellent capacity retention of 99.29% over 3000 cycles. The results of this study imply a great potential of the Ni-MOF for application in efficient and sustainable energy-storage devices.

3.2 Introduction

In the 21st century, the production of energy from different sources has tremendously increased, and its transformation is also increasing day by day in different ways with the ever-increasing demands from industry, buildings, utilities, and transportation.¹ The increasing demand for energy and fuel due to the ever-increasing world population has become one of the important worries for all the global prime economies. Today there is an urgent need for environmentally friendly renewable energy resources to solve the problems related to the dwindling reserves of fossil fuels.^{2,3} In this regard, energy-conversion and -storage technologies have acquired significant attention to support the future use of renewable energy sources. Many researchers from around the globe are devoted to developing sustainable energy sources, like wind, solar, hydropower, and tidal energy, to address the shortage of fossil fuels and to reduce carbon emissions and global warming. Hence, from various points of view, electrochemical energy-storage devices (EESDs), like rechargeable batteries, supercapacitors, fuel cells, and hybrid devices, have an important part to play in strategies to produce various amounts of energy and power density to meet the demands from different application scenarios.⁴⁻⁶

Supercapacitors (SCs), also known as electrochemical capacitors, offer the advantages of batteries as well as conventional capacitors, and have consequently become extraordinary energy-storage devices for large power output applications. Supercapacitors.^{7,8} SCs generally offer a fast charging-discharging process (1–10 s), large power density (500–10 000 W kg⁻¹), high cyclic stability (4500 000 h), and easy operation. However, current SCs have a low energy density (1–10 W h kg⁻¹), which remains a prime challenge in the development of SC technologies. To conquer the drawback of their low energy density, there is a need for the development of high-performance electrode materials for SCs.^{9,10} Due to their profitable features, such as high power density, excellent cyclic stability, exceptional rate capability, and eco-friendliness, SCs have become key components in many fields, such as aerospace, electronic communications, and electric transport, and thus have attracted increasing attention, but still, there is a need for further advancements in SCs to meet the excessive energy demand of modern society.¹¹ A supercapacitor is like a battery, which means it stores and releases electricity, but instead of storing energy in the form of chemicals, supercapacitors store electricity in a static state, making them

better at rapidly charging and discharging energy. Supercapacitors can be mainly divided into two types based on the charge-storage mechanism. The first type is electric double-layer supercapacitors (EDLCs). In EDLCs, the capacitance is obtained from the electrostatic charge assembled at the electrode/electrolyte interface; hence, it is completely dependent on the surface area of the electrode materials that is available to electrolyte ions. The other type is pseudocapacitors, in which the capacitance comes from the reversible redox reactions between the electrolyte and electroactive species on the surface of the electrodes under the applied potential.¹²⁻¹⁴ The electrochemical performance of a supercapacitor device depends on numerous parameters, like choosing its constituents, the synthesis route used for the electrode materials, the potential window of the electrodes, the choice of electrolytes, and the type of current collectors, binders, and separators.^{15,16}

Metal-organic frameworks (MOFs) are attractive materials to fulfil the requirement for next-generation energy-storage technologies because of their extraordinary properties, such as high porosity, many accessible active sites, high surface area, extraordinary stability, vast structural and chemical tunability, tailorable pore size, and pre-and post-synthesis structural modifiability. Also, MOFs are a unique type of nanoporous materials formed by coordinated metal nodes and organic linkers. MOF-based materials have been utilized in many applications, including energy storage and conversion, catalysis, gas separation, drug delivery, hydrogen storage, gas adsorption, and purification.¹⁷⁻²⁰ Concurrently, due to the strong coordination capability of transition metals (TMs), TMs are often used as the metal centres of MOFs, and they also offer the advantages of possessing variable valences and good electrochemical properties, which means they can work as pseudocapacitive redox centres.²¹ MOFs can be feasibly included in a supercapacitor by two strategies: by directly utilizing the MOF as an electrode material for supercapacitors or by utilizing MOF-derived materials, like nanoporous carbon, oxides, sulfides, ferrites, which can be evolved and then utilized as electrode materials, such as the Ni, Co, Zn, Cu, and Fe-based MOFs, which have been reported previously to possess good supercapacitive performance.²²⁻³¹ However, the current, MOFs show poor electrical conductivity; therefore, scientists have taken efforts to increase the electrical conductivity through different strategies, such as through developing composite MOFs with different conductive materials, like metal oxides,³² metals,³³ conductive polymers,³⁴ carbon nanotubes,³⁵ graphene.³⁶ Wang et al. proposed a surfactant-free

and solvent-assisted solvothermal method to synthesize microflower Ni-MOF, which exhibited a high specific capacitance of 1093 F g^{-1} at 1 A g^{-1} with good rate capability, which were attributed to the fast ion transport and low electrical resistance emerging from its microflower-like structure and the specific capacitance resulting from the incorporation of nickel hydroxide species.³⁷ Wu et al. investigated nanosheet-stacked flower-like Ni-MOF via a solvothermal method using anionic surfactants. The usage of the static sealing effect among the negatively charged anionic surfactant head groups and metal ions suppressed the growth of crystals on the crystal surface. Their study revealed that the electrochemical performance of Ni-MOF with the surfactant was superior to that of Ni-MOF without the surfactant, whereby it possessed a specific capacitance of 1030 F g^{-1} at a current density of 1 A g^{-1} with a capacitance retention of 50% after even 3000 cycles. Further, they assembled an asymmetric supercapacitor by using Ni-MOF as a positive electrode and activated carbon as a negative electrode.³⁸ Gao et al. reported the cuboid Ni-MOF by a simple one-step hydrothermal method, which showed a loosely stacked layer-cuboid structure with plentiful mesopores, which were useful for the charge transfer and ion transport for supercapacitors. It also exhibited an exceptional specific capacitance of 804 F g^{-1} at a current density of 1 A g^{-1} , with a retention of 302 F g^{-1} after 5000 cycles. Additionally, they fabricated an asymmetric supercapacitor using Ni-MOF and activated carbon as the positive and negative electrodes, respectively.³⁹ Zhang et al. prepared Ni-MOF using a mixed-ligand approach, using trimesic acid as a modulator to partially replace the terephthalic acid. Replacing the terephthalic acid with trimesic acid influenced the formation of an albizia flower-like spheres@nanosheets structure, which helped the adsorption of OH^- ions on the surface. Also, the electrochemical performance was increased due to the synergistic effect of the surface property and its unique structure. It exhibited an excellent specific capacitance of 920 F g^{-1} at a current density of 1 A g^{-1} . In addition, they constructed an asymmetric supercapacitor with the help of Ni-MOF as a positive electrode and activated carbon as a negative electrode, which showed a high energy density of 42.4 W h kg^{-1} at a power density of 0.8 kW kg^{-1} .⁴⁰

In the present work, we used an unprecedented simple and scalable method, i.e. a reflux condensation method, to prepare a nanorod-like nickel-based metal-organic framework (Ni-MOF), in a controlled high temperature. The as-synthesized Ni-MOF revealed a one-dimensional (1D) nanorod-like morphology with a high

specific surface area $398.4 \text{ m}^2 \text{ g}^{-1}$ and highly nanoporous structure, which could produce more electrochemical sites, which increased the consumption of the electroactive material. In addition, for the fabrication of the electrode we used a stainless steel mesh substrate, which has not been reported to date, which is easily available and low cost compared to other reported substrates. Because of the abundant active sites and extremely porous nature of the material, the penetration of electrolyte ions into the material was increased, resulting in an enhancement of the specific capacitance of the material. Also, we constructed a handmade asymmetric supercapacitor device, which could get a red LED to glow for almost 105 s after charging for only 15 s.

3.3 Experimental section

3.3.1 Reagents

Nickel nitrate hexahydrate, N, N-dimethylformamide (DMF), and potassium hydroxide (KOH) were purchased from Loba Chemie (India). Benzene-1, 3, 5-tricarboxylic acid (H3BTC), carbon black, polyvinylidene difluoride (PVDF), N-methyl-2-pyrrolidone (NMP) were purchased from Sigma Aldrich (USA). All the reagents were of analytical grade and used as received without any further purification.

3.3.2 Preparation of nickel-based metal-organic framework (Ni-MOF)

Ni-MOF was synthesized by the method reported elsewhere⁴¹ with slight modification. The reflux method was used for the synthesis of Ni-MOF, which also helped to lower the reaction time of Ni-MOF compared to that reported in the literature. First, 0.15 M of H3BTC was dissolved in 10 mL of DMF with continuous stirring at room temperature; this mixture was denoted as H3BTC solution. Then, the H3BTC solution was transferred to a 50 mL round-bottom flask and heated up to 100°C using an oil bath with constant stirring. Thereafter, 0.3 M aqueous nickel nitrate (20 mL) solution was added drop by drop into the H3BTC solution. The reaction mixture was stirred for 24 h at 100°C. After cooling, the resulting precipitate was washed with alcohol several times and finally, a pale-green coloured precipitate was obtained and then dried at 80°C for 12 h. Figure 3.1 shows a schematic of the preparation of the Ni-MOF.

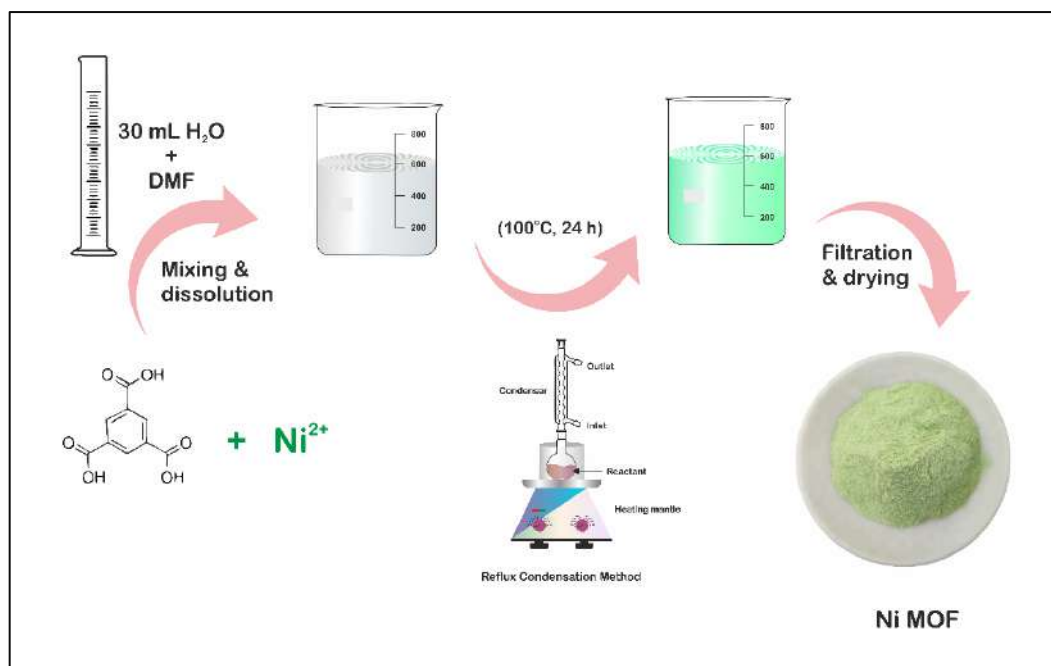


Figure 3.1: Schematic of synthesis of Ni-MOF nanorods via a wet chemical route

3.3.3 Characterization techniques details

The phase and crystallinity of the Ni-MOF sample was investigated by using an X-ray diffractometer (XRD) (Bruker D8 Phaser X-ray diffractometer with Cu K α radiation ($\lambda = 1.541 \text{ \AA}$)). The functional groups and types of bonding were confirmed by Fourier transform infrared (FT-IR) spectroscopy (Bruker Alpha-100508 spectrometer) and the microstructure and surface topography of the Ni-MOF sample was studied by using scanning electron microscopy (JEOL-JSM 6360, Japan). The Raman spectrometer (LabRAM HR Evolution Confocal Raman Microscope, France) was used for point group analysis. The chemical composition and elemental valence states of as-prepared Ni-MOF was evaluated by X-ray photoelectron spectroscopy (JPS 9030, JEOL ASIA PTE LTD.). In addition, N₂ isotherms and pore size distribution data were collected from a surface area and pore volume analyzer (NOVA1000e Quantachrome, USA).

3.3.4 Evaluation of electrode materials and electrochemical studies

All the electrochemical experiments were performed on a CHI608 electrochemical analyzer using a conventional three-electrode system in 2 M KOH electrolyte at room temperature, with graphite employed as the counter electrode, saturated Ag/AgCl as the reference electrode, and Ni-MOF loaded stainless steel mesh as the working electrode. The working electrode was prepared by making a slurry of 80 wt% Ni-MOF (active material), 10 wt% polyvinylidene fluoride (PVDF),

and 10 wt% carbon black (Super P) in NMP solvent. This slurry was coated on the stainless steel mesh (1 cm × 1 cm), followed by vacuum drying at 80°C for 12 h.

The electrochemical tests included cyclic voltammetry (CV), galvanostatic charging–discharging (GCD) profiles, and electrochemical impedance spectroscopy (EIS) measurements. A solid-state hybrid supercapacitor (Ni-MOF//AC) was fabricated using Ni-MOF as the positive electrode and activated carbon as the negative electrode. As a separator, cellulose filter paper was used as a sandwich between two electrodes, with the separator and PVA-KOH gel loaded between the two electrodes and assembled on opposite sides. The device was kept at room temperature overnight for natural drying. The PVA-KOH gel electrolyte was prepared according to a literature report.⁴² In a typical procedure, 1 g of polyvinyl alcohol (PVA) was dissolved in 20 mL distilled water keeping the temperature of the bath solution at 80°C for 30 min. The aqueous KOH solution was then added dropwise to the PVA solution and heated at 80°C for 30 min to give a viscous gel electrolyte.

The specific capacitance was calculated according to the equation (3.1),

$$C = \frac{I \Delta t}{m \Delta V} \dots\dots\dots (3.1)$$

where, C is the specific capacity (F g⁻¹), I is the current density (A), Δt is the discharging time (s), m is the mass (g) of the active electrode materials and ΔV is the potential window of the discharge process(V).

Using equations (3.2) and (3.3), the specific energy and specific power of the hybrid supercapacitor were calculated, respectively.⁴³

$$E = \frac{0.5 \times C \times \Delta V^2}{3.6} \dots\dots\dots (3.2)$$

$$P = \frac{E \times 3600}{\Delta t} \dots\dots\dots (3.3)$$

Where E and P are the specific energy (Wh kg⁻¹) and specific power (W kg⁻¹), respectively. ΔV is the discharging voltage (V) and Δt is the discharging time in seconds.

3.4 Results and discussion

3.4.1 X-ray diffraction of Ni-MOF

The phase purity and crystallinity of the Ni-MOF sample were investigated by the XRD technique. The obtained XRD pattern of prepared Ni-MOF together with the data of JCPDS card no. 00-028-1734 are shown in figure 3.2. The prepared Ni-MOF data were in close agreement with the given JCPDS card,⁴⁴⁻⁴⁶ revealing that the Ni-

MOF had a polycrystalline nature. Some of the major peaks obtained were in good agreement with the corresponding angles as reported earlier for Ni-MOF. Furthermore, using Debye–Scherrer’s formula [equation (3.4)], the crystallite size was calculated for the major characteristic peak of Ni-MOF,

$$D = \frac{0.9\lambda}{\beta \cos\theta} \dots\dots\dots (3.4)$$

Where D is the average crystallite size, λ is the wavelength of the X-rays, β is the full-width half maxima and θ is Bragg’s diffraction angle. The average crystallite size derived from the (110) plane is 6.89 nm.

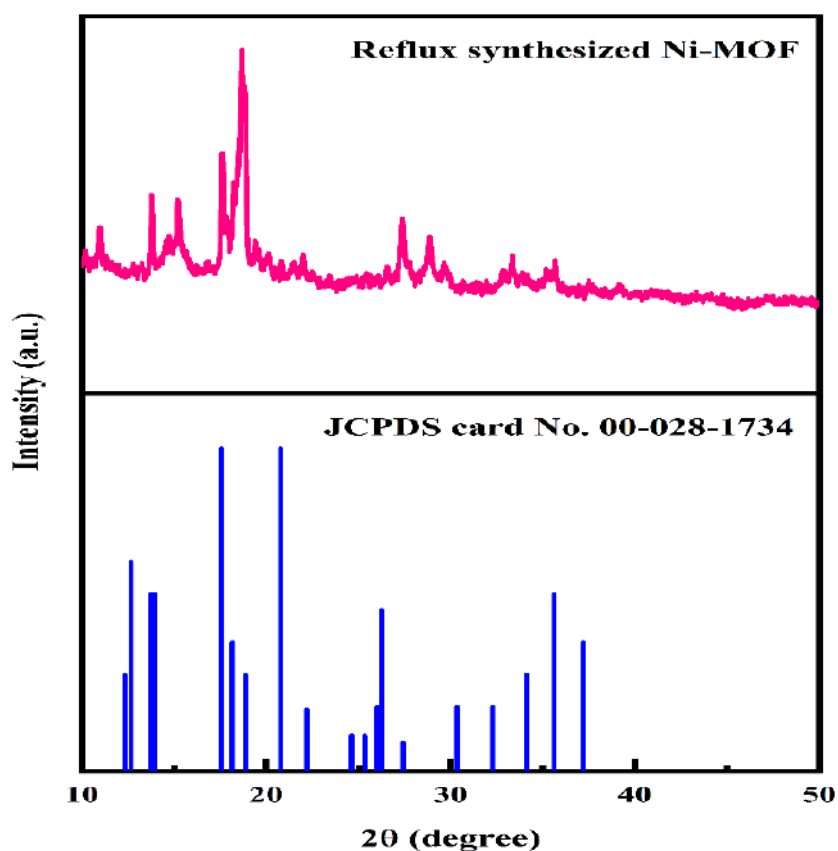


Figure 3.2: XRD pattern of Ni-MOF

3.4.2 FT-IR spectroscopy of Ni-MOF

Investigation of the chemical structure and functional groups of Ni-MOF was carried out by FT-IR. The FT-IR spectrum of the Ni-MOF sample is shown in figure 3.3. In the spectrum, the strong absorption peak at 1349 cm^{-1} was assigned to the C–H stretching vibrations, while the peaks at 3081 and 3399 cm^{-1} could be indexed to the O–H stretching vibrations of water molecules, showing that water molecules existed within the Ni-MOF structure. Additionally, the peaks observed at 1506 and 1608 cm^{-1} were attributed to the symmetric and asymmetric vibrations of carboxyl groups (–

COO⁻), related to the BTC linkers.^{47,48} Another intense peak was observed at 715 cm⁻¹, confirming the presence of the Ni-O bond.

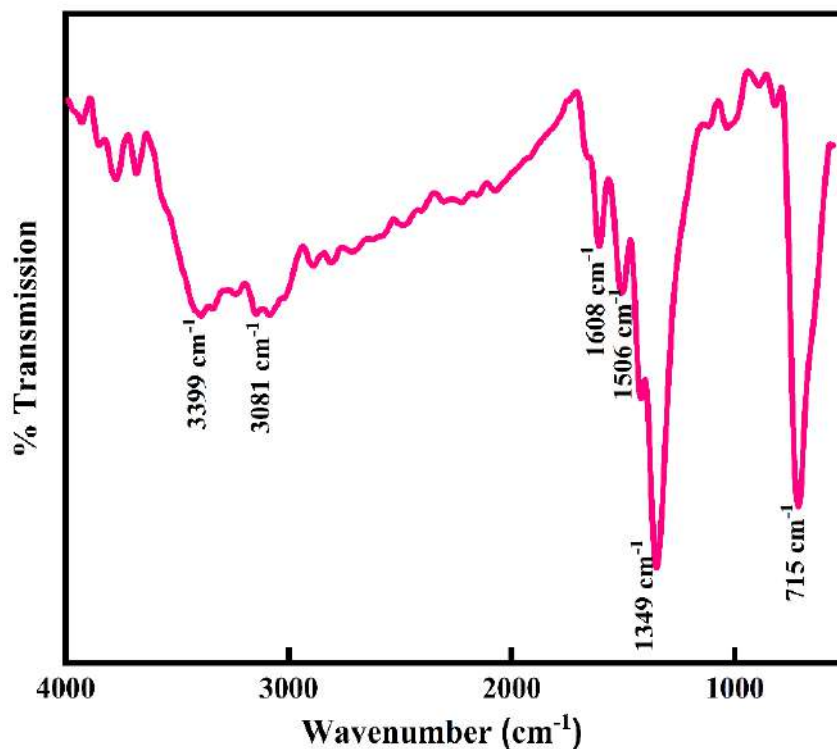


Figure 3.3: FT-IR pattern of Ni-MOF

3.4.3 Raman spectroscopy of Ni-MOF

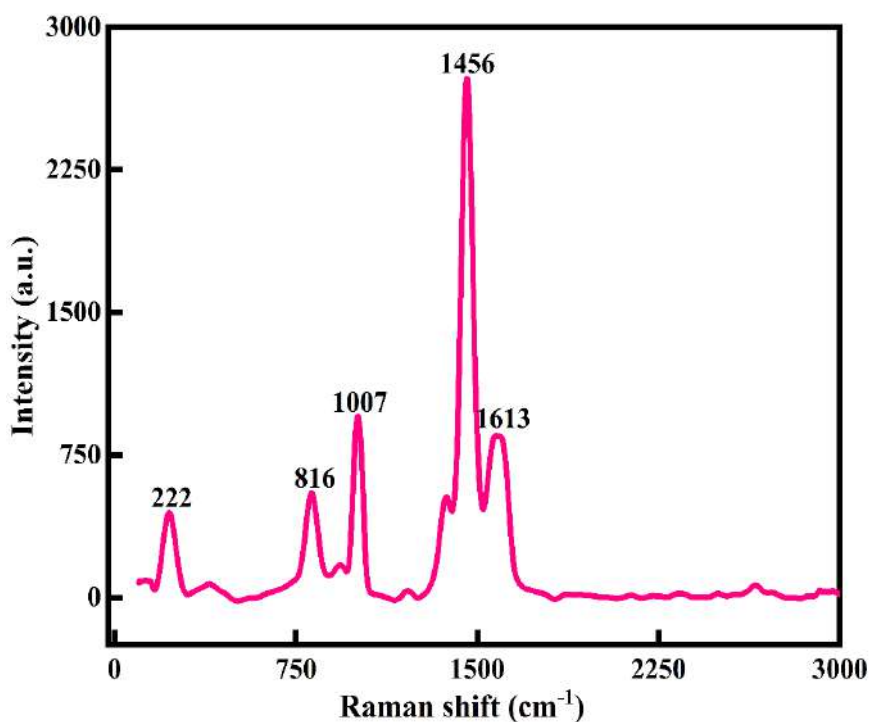


Figure 3.4: Raman Spectroscopy of Ni-MOF

Raman spectroscopy was used to confirm the crystallography of the prepared Ni-MOF samples. Also, the inelastic scattering of the Ni-MOF samples was confirmed by Raman spectroscopy. The Raman spectrum of the Ni-MOF and the specified peaks of the prepared sample are shown in figure 3.4. The peaks of Ni-MOF at 816 and 1007 cm^{-1} could be associated to the plane deformation of the C-H in the aromatic ring and C-O stretching of the trimesic ligand, respectively. Also, D and G bands were observed at 1456 and 1613 cm^{-1} due to the in-plane vibration mode of the benzene ring.⁴⁹ The peak at 222 cm^{-1} could be attributed to H-O-H. All these peaks revealed the crystallography and structure of the Ni-MOF sample.

3.4.4 Scanning electron microscopy of Ni-MOF

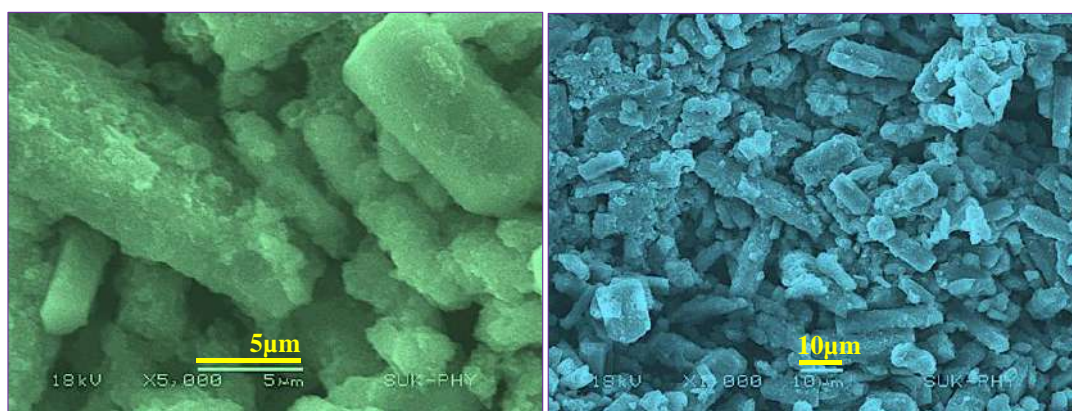


Figure 3.5: SEM images of Ni-MOF

The surface morphology of the Ni-MOF was investigated by SEM, and the SEM images of Ni-MOF with different magnifications are shown in figure 3.5. The SEM images showed a nanorod-like morphology and porous nature of the Ni-MOF, which was responsible for the increased surface area of the Ni-MOF and also for the increase in the specific capacitance. The average length of the nanorods was about 19.09 nm. The different lengths and diameters of the nanorods indicated an increase in the aspect ratio of the nanorods. Also, the porous nanorods were interconnected to each other, which provides more active sites for the transportation of the charging kinetics and decreases the diffusion length of the electrolyte, which is helpful for improvement of the energy storage and high rate capability. Again, a birds-eye view of the SEM images showed that the small and large sized nanorods overlapped with each other and between these two nanorods there were some voids, which in turn would support the enhanced adsorption of electrolyte ions, which would help to increase the specific capacitance of the Ni-MOF. The porous and 1D morphology was

favourable for ion diffusion and hence contributed to an increase in the specific capacitance of the Ni-MOF.

3.4.5 Brunauer-Emmett-Teller analysis of Ni-MOF

The surface area and porosity of the Ni-MOF were obtained by using the BET technique and measuring nitrogen adsorption-desorption isotherm of the samples at 77 K. Here, the prepared sample was degassed at 150°C under a nitrogen atmosphere for 4 h before the measurements. The surface area and pore-size distribution of the sample were calculated by the Brunauer-Emmett-Teller (BET) equation and NLDFT method. The BET measurement results are presented in figure 3.6(a). The calculated surface area of the Ni-MOF sample was found to be 398.4 m² g⁻¹. Based on the literature, it has been observed that the larger the pore radius, then the higher porosity a sample will show in nature. Also, the pore-size distribution for Ni-MOF was estimated using the NLDFT method to establish the correct distribution of pores in the material, as shown in figure 3.6 (b).^{50,51} The half pore width measured by DFT was 1.585 nm, with a micropore volume of 0.831 cc g⁻¹, confirming the extremely mesoporous nature and hierarchical pore-size distribution. According to the literature, Ni-MOF shows a type II isotherm with plenty of mesopores in the material.⁵² This massive amount of mesopores in the structure boosts the permeation of electrolyte ions into the electrode, hence increasing the specific capacitance of the material. Such a high specific surface area and mesoporous structure could produce more electrochemical reaction sites, which increases the consumption of the electroactive material.

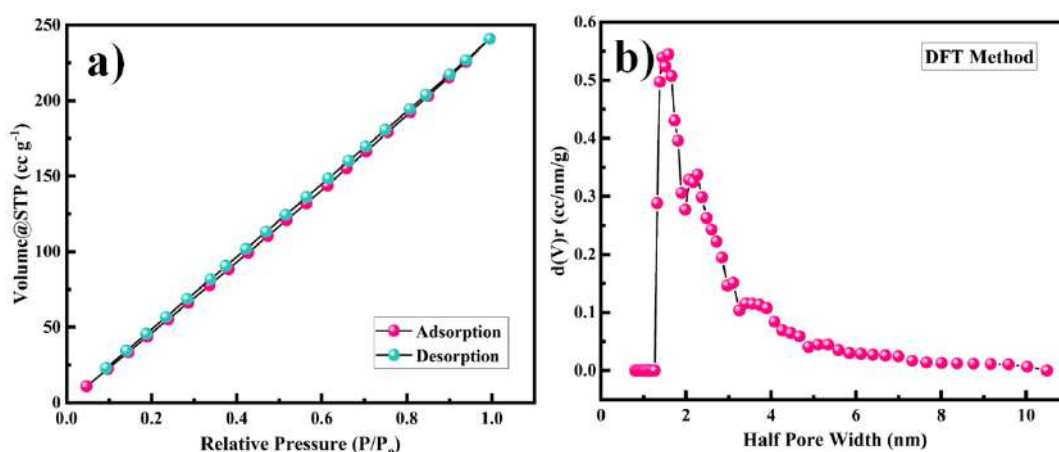


Figure 3.6: (a) N₂ adsorption–desorption isotherms, (b) Pore size distribution of Ni-MOF

3.4.6 X-ray photoelectron spectroscopy of Ni-MOF

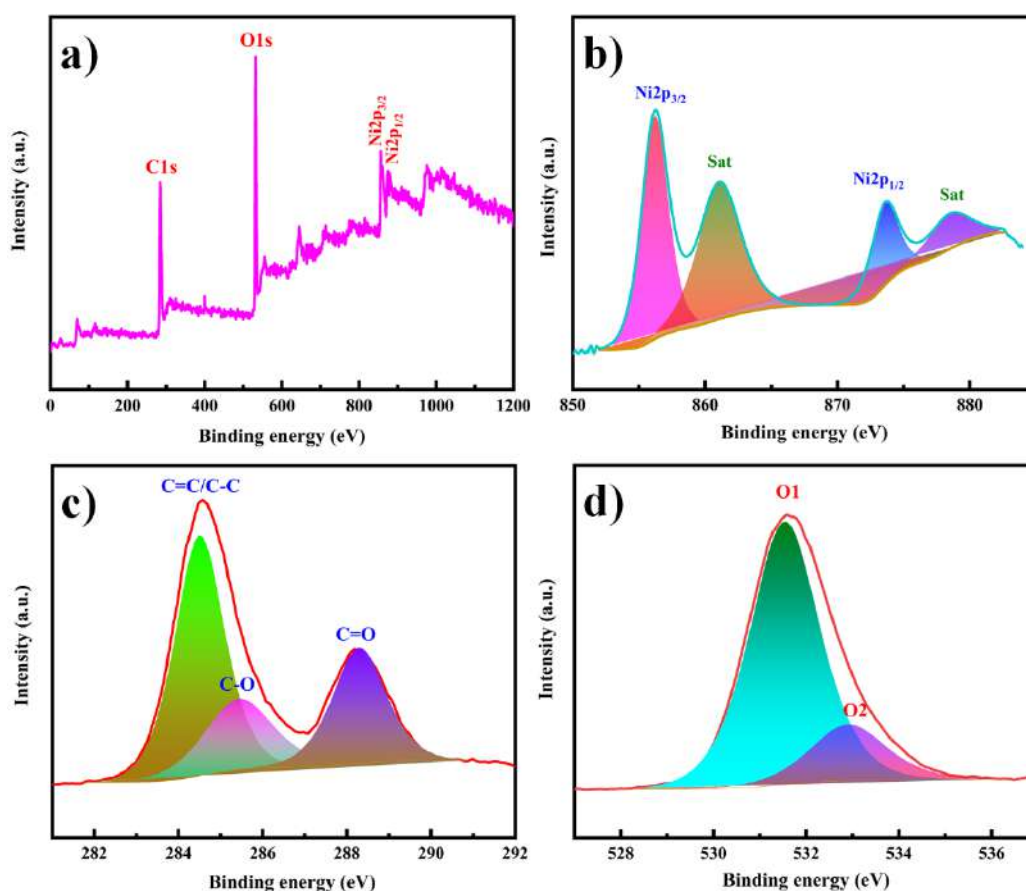


Figure 3.7: (a) XPS survey spectrum of Ni-MOF. High-resolution XPS spectra of Ni 2p, (b) C 1s, (c) and O 1s (d) regions

XPS was used to examine the surface elemental composition and valence states of Ni-MOF. The presence of Ni, C, and O elements was confirmed by the survey spectrum in figure 3.7 (a). Ni 2p_{1/2} and 2p_{3/2} displayed two significant peaks at 873.6 and 856.2 eV, respectively, with two satellite peaks at 878.7 and 861.0 eV, implying the presence of Ni in a divalent state [Figure 3.7(b)]. The peak at 284.5 eV in the C 1s area [Figure 3.7(c)] is a typical outcome for specimens charging using C 1s as the reference. The peak at 288.2 eV was associated with the O=C–OH, whereas the peak at 285.4 eV was associated with the aryl carbon from the benzene ring. The spectrum of O 1s (Figure 3.7(d)) could be separated into two peaks. Carbonyl displayed a peak at 531.5 eV, and the –OH group from the adsorbed H₂O molecules had a peak at 532.8 eV.^{53,54}

3.4.7 Electrochemical measurements of Ni-MOF electrode

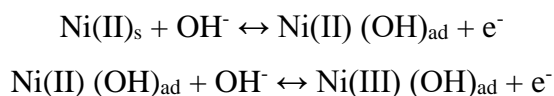
The electrochemical performance of the as-prepared Ni-MOF electrode was evaluated by using the three-electrode system in 2 M KOH electrolyte and the results are presented in figure 3.8. As shown in figure 3.8(a), cyclic voltammetry (CV) was carried out in the potential range from 0 to 0.3 V at scan rates from 10 to 100 mV s⁻¹. It could be observed that the area under the CV curve of the Ni-MOF electrode was higher and the redox current density also increased, leading to a greater capacitive behaviour compared to the literature (Table 3.1).

Table 3.1: Comparison of the specific capacitances of Ni-MOF

Electrode material	Substrate used	Electrolyte	Current density	Specific capacitance	Ref.
Ni-MOF	Nickel foam	3 M KOH	5 A g ⁻¹	1224.6 F g ⁻¹	58
Ni-MOF	Nickel foam	3 M KOH	5 A g ⁻¹	612.25 F g ⁻¹	59
Ni-MOF	Nickel foam	6 M KOH	5 A g ⁻¹	430 C g ⁻¹	60
Ni-MOF	Nickel foam	3 M KOH	5 A g ⁻¹	95 F g ⁻¹	61
Ni-MOF	Platinum plate	2 M KOH	5 mA cm ⁻²	47 F g ⁻¹	62
Ni-MOF	Stainless steel mesh	2 M KOH	5 mA cm⁻²	1956.3 F g⁻¹	This work

All the CV curves revealed well-defined redox pairs, which specified the change in the oxidation states of the Ni²⁺/Ni³⁺, redox reactions, and intercalation–deintercalation of the K⁺ ion in the porous structure during the electrochemical reactions, due to the pseudocapacitive behaviour of the prepared Ni-MOF.^{55,56} This could be due to a shift in the valence states of nickel ions, specifying that the pseudocapacitance was mostly driven by surface oxidation generated by the reduction reaction. Additionally, the diffusion of OH⁻ ions also contributed to the redox reaction, and the diffusion might be because of the impurity ions in the aqueous electrolyte. The redox peaks of Ni-MOF in aqueous electrolytes were caused by the

reversible redox between Ni²⁺/Ni³⁺, and the reaction can be explained by the possible charge-discharge mechanism of Ni-MOF as follows,



With increasing the scanning speed, the curve area and peak current rose, demonstrating a good capacitive behaviour and charge-storage capabilities. The equivalent and similar CV curves obtained at different scan rates showed a shift in the redox peaks and specified the pseudocapacitive behaviour of the material, as shown in figure 3.8(a). The area under the CV curve increased with the increase in the scan rate, whereas the specific capacitance decreased as the scan rate increased. This is due to the fact that at slower scan rates, electrolyte ions are completely diffused within the electrode material. As a result, the complete active surface of the electrode material can be used to store charge. At higher scan rates, however, diffusion restricts the movement of electrolyte ions, and only the outer active surface is employed for charge storage.⁵⁷ The outstanding performance of the Ni-MOF electrode could be assigned to the good crystallinity and porous nanorod-like structure, which could successfully boost the intercalation/deintercalation of OH⁻ ions within the Ni-MOF electrode. One of the important tools for assessing the electrochemical properties of an electrode is the charge-discharge measurement. Figure 3.8(b) presents the charge-discharge curves of the Ni-MOF electrode in aqueous 2 M KOH electrolyte. The charging and discharging times were directly in tune with the charge-storage capacity of the active material. The impact of different current densities (5-35 mA cm⁻²) on the charge-discharge curve was also studied. The natures of the curves were identical to each other, which supported the pseudocapacitive properties of the Ni-MOF nanorods. The specific capacitance of the Ni-MOF was calculated using the discharging curve and equation (3.1). The maximum specific capacitance of 1956.3 F g⁻¹ at the 5 mA cm⁻² current density was obtained. This specific capacitance value is higher than those reported earlier (Table 3.1). Due to the plentiful active sites and highly porous nature, the penetration of electrolyte ions into the material increased, which supported the enhancement of the specific capacitance of the material.

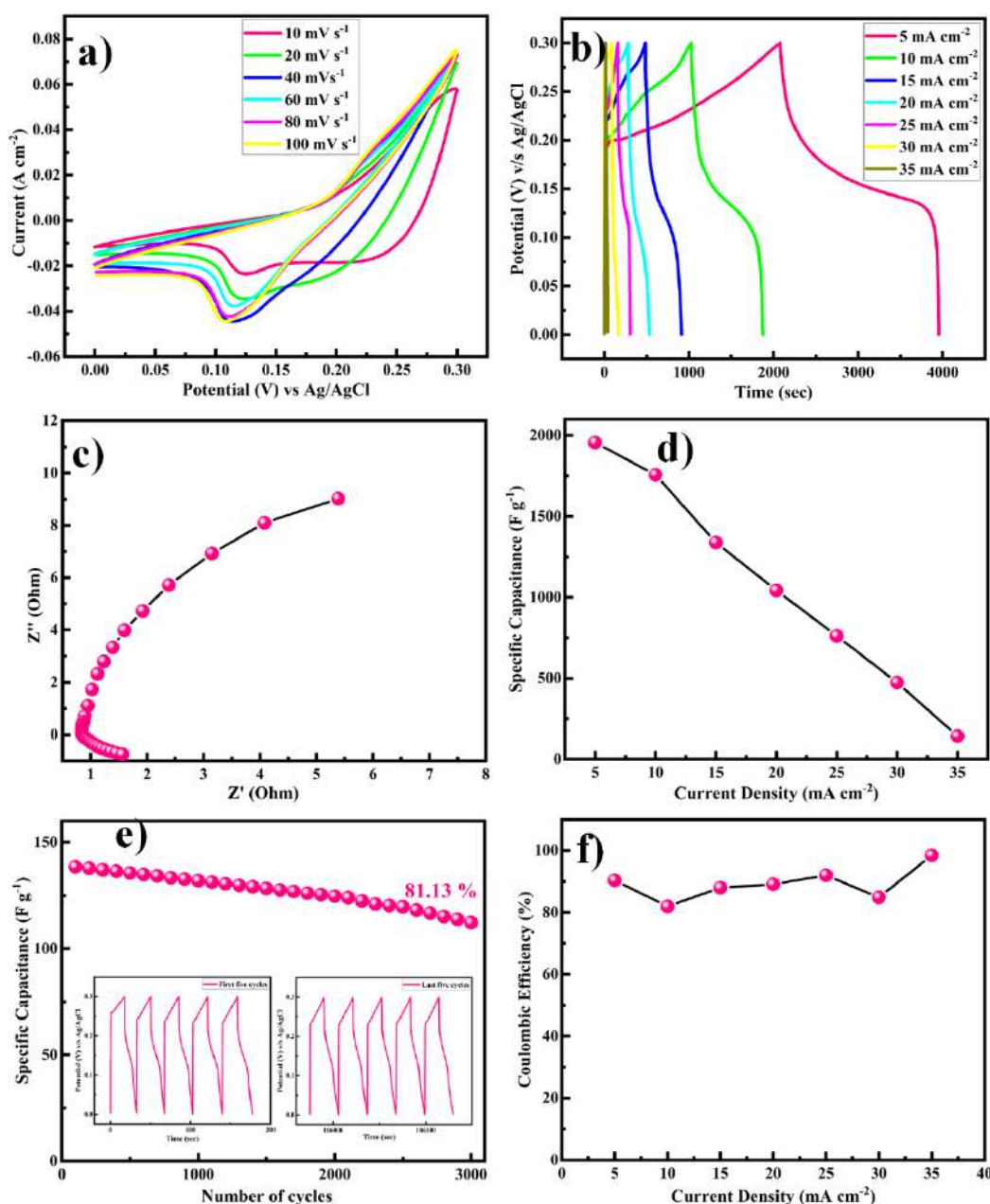


Figure 3.8: (a) CV profile of Ni-MOF at different scan rates operated from 0 to 0.3 V, (b) GCD profile for Ni-MOF at different current rates (5 to 35 mA cm⁻²), (c) Nyquist plot of the Ni-MOF, (d) Plot of specific capacitance vs. current densities, (e) Cyclic durability test at a high current of 35 mA cm⁻² over 3000 GCD cycles with inset of first and last five cycles, (f) Coulombic efficiency as a function of current density

One of the important factors for supercapacitor electrodes is the electrical resistance, which can be determined from electrochemical impedance spectroscopy (EIS) measurements. EIS tests were thus carried out to investigate the electroconductibility and reaction kinetics of the Ni-MOF electrode, as shown in

figure 3.8(c). The electrode's charge-transfer resistance (R_{ct}) could be obtained from the diameter of a semicircle in the high-frequency area. It was demonstrated that the Ni-MOF had a small diameter and thus a smaller charge-transfer resistance, while the slope of the lines in the low-frequency area represents the ion-diffusion resistance. The Nyquist plot had a high slope, which showed that the as-prepared Ni-MOF was beneficial to ion transport and electrolyte diffusion because of its typical structure, which meant it possessed a high specific surface area and could support rich ion transportation. The straight line in the low-frequency region was due to Warburg resistance. Based on the preceding results, it can be concluded that the Ni-MOF had a higher conductivity. Hence, the smaller charge-transfer resistance (0.5Ω) confirmed that the prepared Ni-MOF porous nanorods had highly pseudocapacitive properties. The specific capacitance decreased from 1756.3, 1338.4, 1043.8, 761.5, 473.8, and 142.2 F g^{-1} with the increase in the current density to 10, 15, 20, 25, 30, and 35 mA cm^{-2} , respectively, as shown in figure 3.8(d). The specific capacitance decreased as the current density increased because at higher current density the electrolyte ions participate in the bulk surface for the electrochemical reaction, and due to this there is a restriction in the ion transport, so the value of the specific capacitance decreases, and considering the low current density, the electrolyte ions have enough time to move across the inner pores of the electrode material, resulting in a higher specific capacitance value. The Ni-MOF showed a longer discharging time, which clearly indicated that the porous nanorods structure of the Ni-MOF possessed more surface active sites for the efficient charge-discharge process and increased the energy-storage ability of the Ni-MOF electrode. The cyclic stability of the electrode was explored by galvanostatic charge-discharge (GCD) persistence tests at 35 mA cm^{-2} current density for 3000 cycles, as shown in figure 3.8(e). It could be seen that the specific capacitance was retained at over 81.13% after 3000 cycles for the Ni-MOF electrode, which suggested its good electrochemical reversibility during the charge-discharge process.

The Coulombic efficiency ($\eta\%$), another important parameter to examine the interfacial stability of Ni-MOF electrode as a function of charge-discharge cycles, is shown in figure 3.8(f). Equation (3.5) was used to calculate the Coulombic efficiency for the Ni-MOF electrode at different current densities.⁶³

$$\eta (\%) = \frac{t_d}{t_c} \times 100 \dots \dots \dots (3.5)$$

where t_d and t_c are the discharging and charging times in seconds, respectively.

The Coulombic efficiencies of the Ni-MOF electrode were 90.37%, 81.92%, 87.98%, 89.11%, 92.00%, 84.88%, and 98.45% at different current densities of 5, 10, 15, 20, 25, 30, and 35 mA cm⁻², respectively. The Coulombic efficiency of the Ni-MOF electrode rose and the specific capacitance decreased with the increase in current density, which might be assigned to the electrodes inner active sites, which were not capable of supporting the redox reactions at high current density. A promising electrochemical stability and excellent reversibility of Ni-MOF electrodes were observed for up to the 3000 GCD cycles. The Ni-MOF samples showed that the orchestrating effects of the 1D morphology, surface area, and porosity led to their excellent application potential in terms of specific capacitance, energy density, power density, and cyclic stability.

3.4.8 Electrochemical measurements of hybrid supercapacitor device

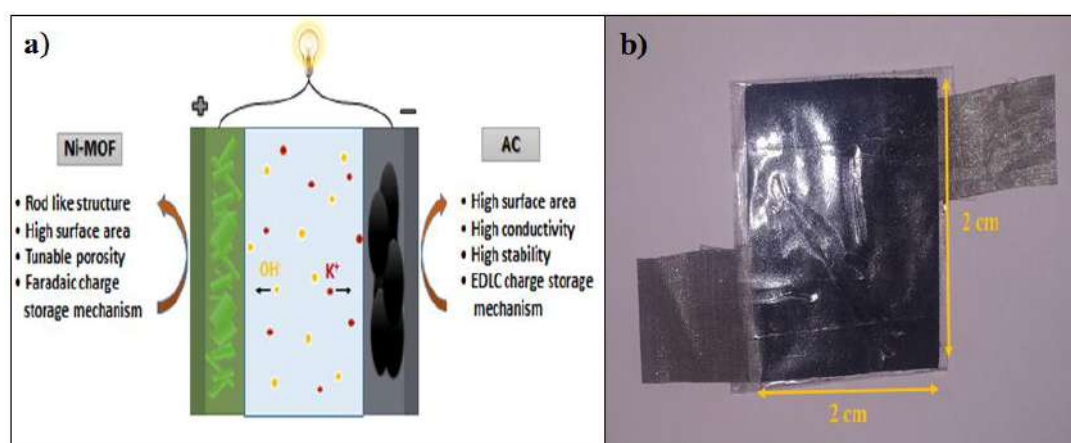


Figure 3.9: (a) Schematic illustration of hybrid supercapacitor with Ni-MOF as a positive electrode and activated carbon as a negative electrode in KOH aqueous electrolyte, (b) Digital photograph of Ni-MOF//AC HSC device

To understand the practical ability of the Ni-MOF electrode in functional devices, a hybrid supercapacitor device was assembled using the as-prepared Ni-MOF as a positive electrode and activated carbon as the negative electrode, as shown in figure 3.9. Both electrodes were prepared by the slurry coating method. In short, the slurry was prepared by mixing the active material (Ni-MOF or AC) (80 mg), polyvinylidene fluoride (10 mg), and carbon black (10 mg) in 0.5 mL of methyl-2-pyrrolidone (NMP) solvent. Then, the required volume of the slurry was dispersed onto a stainless steel mesh with an area of 2 cm × 2 cm and dried at 60°C overnight. Primarily, the side borders of the electrodes were formed as non-conducting through

insertion of a band to avoid electrical contact. The PVA-KOH gel was pasted on one side of the electrodes and created one side of the electrical contact. Later, both electrodes were patched together like a sandwich, with the gel-pasted sides facing each other. The fabricated device was kept under 1 ton pressure for 12 h, to acquire a good connection within the electrodes and gel electrolyte and also to remove the air gap. Afterwards, the device was used for assessment of the electrochemical performance. Hybrid supercapacitor devices have advantages, like high energy density, high specific capacitance, long cycle stability, and large potential window, over symmetric supercapacitors. The performance of the assembled hybrid device was studied using CV, GCD, and EIS measurements.

Primarily, CV tests were performed to understand the electrochemical performance of the Ni-MOF//AC hybrid supercapacitor (HSC) at different scan rates, as shown in figure 3.10(a). The Ni-MOF//AC hybrid SC exhibited a symmetric rectangular CV curve and a large area enclosed under the CV curve at up to 0-0.9 V. With the increase in scan rate from 10 to 100 mV s^{-1} , the increase in area under the CV curves revealed the excellent reversibility of the Ni-MOF. Additionally, GCD curves were obtained at different current densities from the hybrid device, indicating the ideal capacitive behaviour of the device, as shown in figure 3.10(b). The Nyquist plots of the Ni-MOF//AC HSC device are shown in figure 3.10(c), indicating that the fabricated device had an R_{ct} value of 0.36 Ω . According to the EIS studies, the fabricated Ni-MOF//AC HSC device had good electrical conductivity with a low ionic resistance. However, the specific capacitance decreased from 195.76, 94.79, 60.0, 42.70, and 31.67 F g^{-1} with the increase in the current density from 2, 3, 4, 5, and 6 mA cm^{-2} , respectively, as shown in figure 3.10(d). The Ragone plot of the as-constructed HSC, expressing the relationship between the energy density (E) and power density (P), was obtained based on the galvanostatic charge-discharge curves [Figure 3.10(e)].

The cyclic stability of the assembled hybrid supercapacitor device was investigated systematically. The device showed 99.29% capacitance retention over 3000 cycles, indicating its excellent cyclic stability. The specific capacitance was constant over 2500 cycles and later it slightly decreased. The insets of figure 3.10(f) show the first and last five charge-discharge cycles of the device in 2 M KOH electrolyte. The Coulombic efficiencies of the asymmetric supercapacitor device were 84.15%, 65.00%, 68.57%, 74.54%, and 80.00% at various current densities of 2, 3, 4,

5, and 6 mA cm⁻², respectively [equation (3.5)]. The device's energy density and power density were calculated using equation (3.2) and (3.3). The HSC device exhibited a maximum energy density of 79.5 Wh kg⁻¹ at a higher power density of 1015.3 W kg⁻¹, which was comparable to or even higher than recent literature values (Table 3.1) for hybrid supercapacitors.

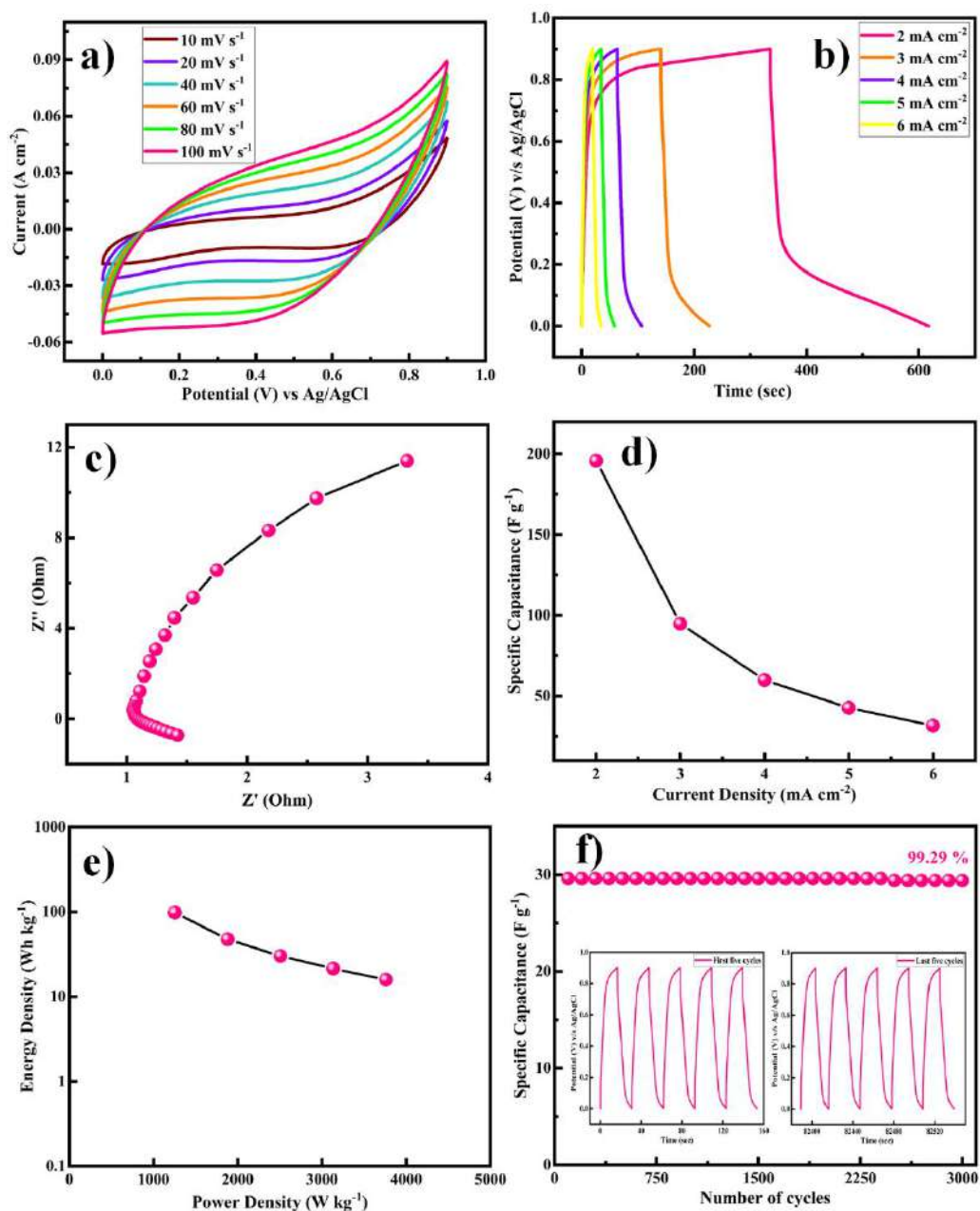


Figure 3.10: (a) CV profile of HSC cell at different scan rates operated from 0 to 0.9 V, (b) GCD profile for HSC cell at different current rates (2 to 6 mA cm⁻²), (c) Nyquist plot of the HSC device, (d) Plot of specific capacitance vs. current densities, (e) Ragone plot of HSC cell, (f) Cyclic durability test at a high current of 6 mA cm⁻² over 3000 GCD cycles with inset of first and last five cycles

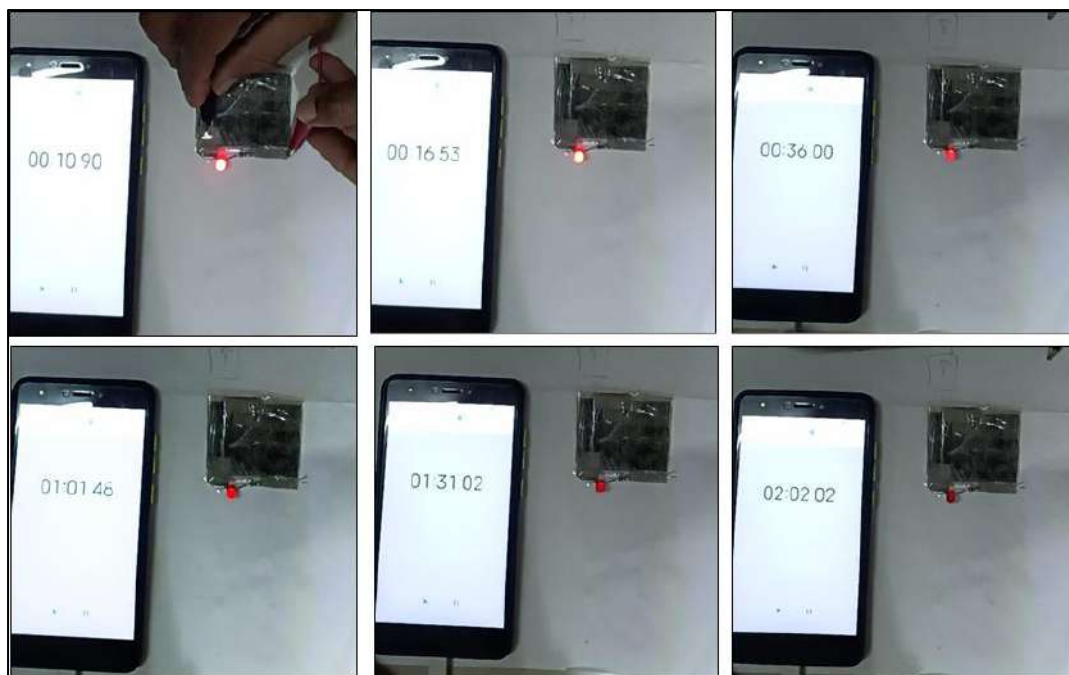


Figure 3.11: The handmade asymmetric supercapacitor device charged for 15 seconds and glow a red LED for almost 105 seconds (i.e. charging time 15 second discharging time 105 sec)

The fabricated device could light a red-light-emitting diode (LED) for over 105 s when charged for 15 s due to the device's high energy density and maximum operational potential of 0.9 V, as shown in figure 3.11. It can be seen that the dazzling light was obvious at first, and then the brightness change is shown over time. After 105 s, we can see that the red light was still faintly glowing, confirming that the Ni-MOF//AC HSC device had an amazing ability to store charge. The good performance could be attributed to Ni-MOF's rod-like structure and pore-size distribution. The study discovered that the encouraging results may pave the way for the development of new electrode materials for supercapacitors and other energy-storage devices.

The study of the electrochemical parameters at different current densities of the chemically synthesized Ni-MOF is concluded in the radar graph shown in figure 3.12. The different apexes reveal the various parameters, such as specific capacitance, energy density, power density, and Coulombic efficiency, of the Ni-MOF. As seen in figure 3.12, this report contains the script for the Ni-MOF-based supercapacitor. These results indicate that the Ni-MOF has much better electrochemical performance than that of other reported MOFs due to its high specific capacitance, high energy density, large power density, and good Coulombic efficiency.

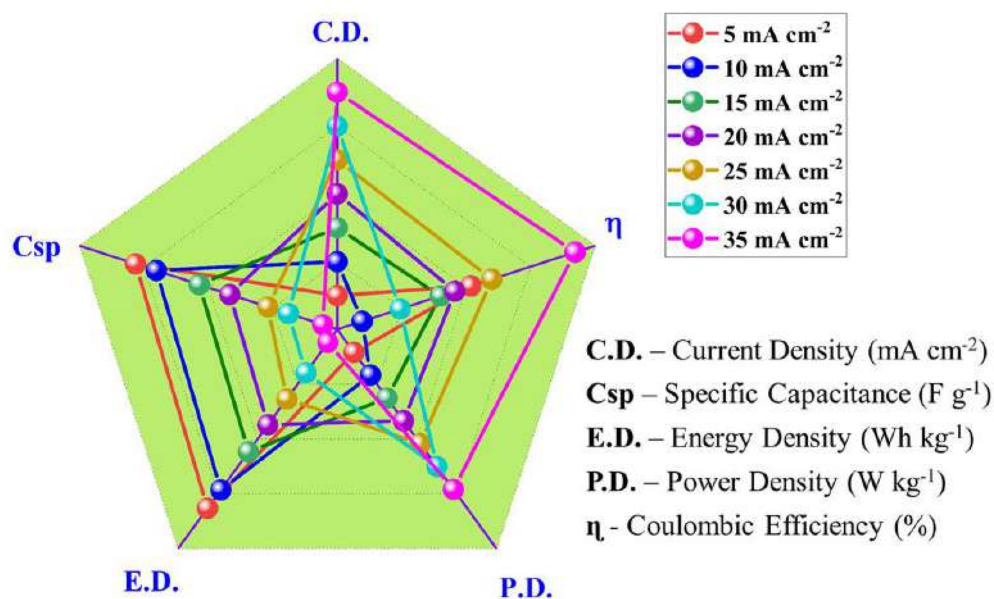


Figure 3.12: Radar plot for Ni-MOF based on supercapacitive properties

3.5 Conclusion

In summary, we successfully prepared Ni-MOF by using the reflux condensation technique. The structural properties and electrochemical performance of the Ni-MOF were studied systematically using various advanced tools. The porous and nanorod-like morphology, as confirmed by SEM analysis, provided both faster and more electroactive sites. An as-prepared Ni-MOF sample exhibited a high surface area of $398.4 \text{ m}^2 \text{ g}^{-1}$. Furthermore, In a three-electrode system with 2 M KOH aqueous electrolyte, the synthesized Ni-MOF porous nanorods showed a high specific capacitance of 1956.3 F g^{-1} at a current density of 5 mA cm^{-2} , and more stability for 3000 cycles with 81.13% retention. When assessed as a positive electrode for a flexible hybrid supercapacitor (HSC) device in combination with activated carbon as a negative electrode, the HSC cell exhibited a superhigh electrochemical behaviour. The device also exhibited a high charge-storage capacity of 195.76 F g^{-1} at a current density of 2 mA cm^{-2} , super-specific energy (98.15 Wh kg^{-1}), and excellent power density ($1253.47 \text{ W kg}^{-1}$), including long-term stability of 3000 cycles with 99.29% capacity retention. The extraordinary energy-storage properties of the Ni-MOF electrode are attributed to its nanorod-like structure and higher surface area. This study provides a new platform for supercapacitors and other energy-storage devices.

3.6 References

- 1 S. Koochi-Fayegh and M. A. Rosen, *J. Energy Storage*, 2020, **27**, 101047-101070.
- 2 M. B. Askari, P. Salarizadeh, M. Seifi, M. H. Ramezan zadeh and A. Di Bartolomeo, *J. Alloys Compd.*, 2021, **860**, 158497-158508.
- 3 X. Zhao, K. Tao and L. Han, *Nanoscale*, 2022, **14**, 2155–2166.
- 4 Y. Tang, W. Guo and R. Zou, *Coord. Chem. Rev.*, 2022, **451**, 214242-214268.
- 5 Poonam, K. Sharma, A. Arora and S. K. Tripathi, *J. Energy Storage*, 2019, **21**, 801–825.
- 6 S. Sanati, Z. Rezvani and B. Habibi, *New J. Chem.*, 2018, **42**, 18426–18436.
- 7 S. De, C. K. Maity, S. Sahoo and G. C. Nayak, *ACS Appl. Energy Mater.*, 2021, **4**, 3712–3723.
- 8 H. M. Nguyet, L. T. T. Tam, D. T. Tung, N. T. Yen, H. T. Dung, N. T. Dung, H. Phan N, L. A. Tuan, P. N. Minh and L. T. Lu, *New J. Chem.*, 2022, **46**, 13996–14003.
- 9 Y. Shao, M. F. El-Kady, J. Sun, Y. Li, Q. Zhang, M. Zhu, H. Wang, B. Dunn and R. B. Kaner, *Chem. Rev.*, 2018, **118**, 9233–9280.
- 10 R. Liu, A. Zhou, X. Zhang, J. Mu, H. Che, Y. Wang, T. T. Wang, Z. Zhang and Z. Kou, *Chem. Eng. J.*, 2021, **412**, 128611-128633.
- 11 A. Mohanty, D. P. Jaihindh, Y. P. Fu, S. P. Senanayak, L. S. Mende and A. Ramadoss, *J. Power Sources*, 2021, **488**, 229444-229467.
- 12 S. Kumar, G. Saeed, L. Zhu, K. N. Hui, N. H. Kim and J. H. Lee, *Chem. Eng. J.*, 2021, **403**, 126352-126370.
- 13 L. Li, J. Meng, M. Zhang, T. Liu and C. Zhang, *Chem. Commun.*, 2022, **58**, 185–207.
- 14 X. Chu, F. Meng, T. Deng and W. Zhang, *Nanoscale*, 2021, **13**, 5570–5593.
- 15 P. Forouzandeh, P. Ganguly, R. Dahiya and S. C. Pillai, *J. Power Sources*, 2022, **519**, 230744-230771.
- 16 C. V. V. Muralee Gopi, R. Vinodh, S. Sambasivam, I. M. Obaidat and H. J. Kim, *J. Energy Storage*, 2020, **27**, 101035-101060.
- 17 S. Sanati, R. Abazari, A. Morsali, A. M. Kirillov, P. C. Junk and J. Wang, *Inorg. Chem.*, 2019, **58**, 16100–16111.
- 18 A. E. Baumann, D. A. Burns, B. Liu and V. S. Thoi, *Commun. Chem.*, 2019, **2**,

- 1–14.
- 19 W. Li, X. Zhao, Q. Bi, Q. Ma, L. Han and K. Tao, *Dalt. Trans.*, 2021, **50**, 11701–11710.
- 20 H. M. Ma, J. W. Yi, S. Li, C. Jiang, J. H. Wei, Y. P. Wu, J. Zhao and D. S. Li, *Inorg. Chem.*, 2019, **58**, 9543–9547.
- 21 Y. Liang, W. Yao, J. Duan, M. Chu, S. Sun and X. Li, *J. Energy Storage*, 2021, **33**, 1–11.
- 22 L. Zheng, J. Song, X. Ye, Y. Wang, X. Shi and H. Zheng, *Nanoscale*, 2020, **12**, 13811–13821.
- 23 S. Zhou, S. Wang, S. Zhou, H. Xu, J. Zhao, J. Wang and Y. Li, *Nanoscale*, 2020, **12**, 8934–8941.
- 24 P. Du, Y. Dong, C. Liu, W. Wei, D. Liu and P. Liu, *J. Colloid Interface Sci.*, 2018, **518**, 57–68.
- 25 C. Yang, X. Li, L. Yu, X. Liu, J. Yang and M. Wei, *Chem. Commun.*, 2020, **56**, 1803–1806.
- 26 U. A. Khan, N. Iqbal, T. Noor, R. Ahmad, A. Ahmad, J. Gao, Z. Amjad and A. Wahab, *J. Energy Storage*, 2021, **41**, 102999-103009.
- 27 S. Wang, S. Wang, X. Guo, Z. Wang, F. Mao, L. Su, H. Wu, K. Wang and Q. Zhang, *Inorg. Chem. Front.*, 2021, **8**, 4878–4886.
- 28 N. Wu, H. Wu, J. Zhang, Y. Zhang, D. Cao, L. Bai and T. Hu, *J. Alloys Compd.*, 2021, **856**, 157466-157506.
- 29 N. Liu, X. Liu and J. Pan, *J. Colloid Interface Sci.*, 2022, **606**, 1364–1373.
- 30 D. Y. Lee, S. J. Yoon, N. K. Shrestha, S. H. Lee, H. Ahn and S. H. Han, *Microporous Mesoporous Mater.*, 2012, **153**, 163–165.
- 31 G. Zhu, H. Wen, M. Ma, W. Wang, L. Yang, L. Wang, X. Shi, X. Cheng, X. Sun and Y. Yao, *Chem. Commun.*, 2018, **54**, 10499–10502.
- 32 S. Xiong, S. Jiang, J. Wang, H. Lin, M. Lin, S. Weng, S. Liu, Y. Jiao, Y. Xu and J. Chen, *Electrochim. Acta*, 2020, **340**, 135956-135967.
- 33 Q. Li, H. Guo, R. Xue, M. Wang, M. Xu, W. Yang, J. Zhang and W. Yang, *Int. J. Hydrogen Energy*, 2020, **45**, 20820–20831.
- 34 L. Wang, X. Feng, L. Ren, Q. Piao, J. Zhong, Y. Wang, H. Li, Y. Chen and B. Wang, *J. Am. Chem. Soc.*, 2015, **137**, 4920–4923.
- 35 X. Wang, N. Yang, Q. Li, F. He, Y. Yang, B. Wu, J. Chu, A. Zhou and S. Xiong, *J. Solid State Chem.*, 2019, **277**, 575–586.

- 36 M. Azadfalsh, A. Sedghi and H. Hosseini, *J. Electron. Mater.*, 2019, **48**, 7011–7024.
- 37 C. H. Wang, D. W. Zhang, S. Liu, Y. Yamauchi, F. B. Zhang and Y. V. Kaneti, *Chem. Commun.*, 2022, **58**, 1009–1012.
- 38 Y. Wu, X. Ding, Y. Luo, F. Xu, L. Sun, J. H. Lao, X. Qin, C. Dan, Y. Wang, Q. Yin, T. Wang, K. Zhang, B. Li, H. Zhang and Y. Zou, *Int. J. Electrochem. Sci.*, 2021, **16**, 1–11.
- 39 S. Gao, Y. Sui, F. Wei, J. Qi, Q. Meng and Y. He, *J. Mater. Sci.*, 2018, **53**, 6807–6818.
- 40 X. Zhang, N. Qu, S. Yang, Q. Fan, D. Lei, A. Liu and X. Chen, *J. Colloid Interface Sci.*, 2020, **575**, 347–355.
- 41 V. Veeramani, B. M. Matsagar, Y. Yamauchi, A. Y. Badjah, M. Naushad, M. Habila, S. Wabaidur, Z. A. Alothman, Z. L. Wang and K. C. W. Wu, *J. Taiwan Inst. Chem. Eng.*, 2019, **96**, 634–638.
- 42 R. Velmurugan, J. Premkumar, R. Pitchai, M. Ulaganathan and B. Subramanian, *ACS Sustain. Chem. Eng.*, 2019, **7**, 13115–13126.
- 43 S. B. Bandgar, M. M. Vadiyar, Y. C. Ling, J. Y. Chang, S. H. Han, A. V. Ghule and S. S. Kolekar, *ACS Appl. Energy Mater.*, 2018, **1**, 638–648.
- 44 S. Gao, Y. Sui, F. Wei, J. Qi, Q. Meng and Y. He, *J. Mater. Sci. Mater. Electron.*, 2018, **29**, 2477–2483.
- 45 F. Israr, D. Chun, Y. Kim and D. K. Kim, *Ultrason. Sonochem.*, 2016, **31**, 93–101.
- 46 F. Israr, D. K. Kim, Y. Kim and W. Chun, *Quim. Nova*, 2016, **39**, 669–675
- 47 X. Zhang, N. Qu, S. Yang, D. Lei, A. Liu and Q. Zhou, *Mater. Chem. Front.*, 2021, **5**, 482–491.
- 48 X. Liu, D. Xu, Q. Wang and L. Zhang, *Small*, 2018, **14**, 1–12.
- 49 Q. Liu, L. Xie, X. Shi, G. Du, A. M. Asiri, Y. Luo and X. Sun, *Inorg. Chem. Front.*, 2018, **5**, 1570–1574.
- 50 M. Thommes, K. Kaneko, A. V. Neimark, J. P. Olivier, F. Rodriguez-Reinoso, J. Rouquerol and K. S. W. Sing, *Pure Appl. Chem.*, 2015, **87**, 1051–1069.
- 51 R. Bardestani, G. S. Patience and S. Kaliaguine, *Can. J. Chem. Eng.*, 2019, **97**, 2781–2791.
- 52 M. Khalifaoui, S. Knani, M. A. Hachicha and A. Ben Lamine, *J. Colloid Interface Sci.*, 2003, **263**, 350–356.

- 53 G. Li, Y. Qi, H. Lin, N. Lu, J. Chen, J. Wang, Q. Han and F. Liu, *J. Memb. Sci.*, 2021, **635**, 1–9.
- 54 Q. Bi, Q. Ma, K. Tao and L. Han, *Dalt. Trans.*, 2021, **50**, 8179–8188.
- 55 J. Yang, P. Xiong, C. Zheng, H. Qiu and M. Wei, *J. Mater. Chem. A*, 2014, **2**, 16640–16644.
- 56 X. G. Han, P. F. Wang, Y. H. Zhang, H. Y. Liu, J. J. Tang, G. Yang and F. N. Shi, *Inorganica Chim. Acta*, 2022, **536**, 120916-120927.
- 57 S. S. Shah, E. Cevik, M. A. Aziz, T. F. Qahtan, A. Bozkurt and Z. H. Yamani, *Synth. Met.*, 2021, **277**, 116765-116780.
- 58 C. Zhang, Q. Zhang, K. Zhang, Z. Xiao, Y. Yang and L. Wang, *RSC Adv.*, 2018, **8**, 17747–17753.
- 59 Y. Li, Y. Xu, Y. Liu and H. Pang, *Small*, 2019, **15**, 1–8.
- 60 J. W. Wang, Y. X. Ma, X. Y. Kang, H. J. Yang, B. L. Liu, S. S. Li, X. D. Zhang and F. Ran, *J. Solid State Chem.*, 2022, **309**, 122994-123012.
- 61 S. Wang, J. Wang, M. Zeng, J. Yang, N. Hu, Y. Su, Z. Zhou, H. Pang and Z. Yang, *J. Energy Storage*, 2021, **38**, 102528-102537.
- 62 C. Feng, C. P. Lv, Z. Q. Li, H. Zhao and H. H. Huang, *J. Solid State Chem.*, 2018, **265**, 244–247.
- 63 K. T. Kubra, A. Javaid, R. Sharif, G. Ali, F. Iqbal, A. Salman, F. Shaheen, A. Butt and F. J. Iftikhar, *J. Mater. Sci. Mater. Electron.*, 2020, **31**, 12455–12466.

CHAPTER FOUR

Construction of Well-Defined Two-Dimensional Architectures of Trimetallic Metal-Organic Frameworks for High-Performance Symmetric Supercapacitors

4.1 Outline

The high surface-to-volume ratio and extraordinarily large-surface area of two-dimensional (2D) metal-organic framework (MOF) architectures have drawn particular interest for use in supercapacitors. To achieve an excellent electrode material for supercapacitors, well-defined 2D nanostructures of novel trimetallic MOFs were developed for supercapacitor applications. Multivariate MOFs (terephthalate and trimesate MOF) with distinctive nanobrick and nanoplate-like structures were successfully synthesized using a straightforward one-step reflux condensation method by combining Ni, Co, and Zn metal species in equimolar ratios with two different ligands. Furthermore, the effects of the tricarboxylic and dicarboxylic ligands on cyclic voltammetry, charge-discharge cycling, and electrochemical impedance spectroscopy were studied. The derived terephthalate and trimesate MOFs are supported with stainless-steel mesh and provide a suitable electrolyte environment for rapid faradaic reactions with an elevated specific capacity, excellent rate capability, and exceptional cycling stability. It shows a specific capacitance of 582.8 F g^{-1} , a good energy density of $40.47 \text{ W h kg}^{-1}$, and a power density of 687.5 W kg^{-1} at 5 mA cm^{-2} with an excellent cyclic stability of 92.44% for 3000 charge-discharge cycles. A symmetric BDC-MOF//BDC-MOF supercapacitor device shows a specific capacitance of 95.22 F g^{-1} with low capacitance decay, high energy, and power densities which is used for electronic applications. These brand-new trimetallic MOFs display outstanding electrochemical performance and provide a novel strategy for systematically developing high-efficiency energy storage systems.

4.2 Introduction

Over the past few decades, the need to develop clean and sustainable energy has become extremely urgent due to the increasing requirement for clean energy and solving serious environmental problems.¹ Nowadays, much research is focused on current renewable energy storage devices in order to minimize pollution and raise worries about future energy problems.^{2,3} Under some environmental circumstances, it is challenging to produce power from sustainable energy sources (biomass, hydro, solar, wind, etc.), which causes an imbalance between the supply and demand of energy. In order to balance and equalize energy needs, energy storage devices must be integrated with energy production, which is crucial for a renewable energy supply.^{4,5} Because of their excellent energy capability and clean electrical systems, electrochemical energy storage equipment have gained widespread interest. One energy storage device that stands out above most of the others is the supercapacitor, which shows the utmost characteristics like high energy density, fast charging/discharging process, and excellent cycle stability, and also they are feasibly used in many fields.⁶⁻⁸ The energy storage mechanism is non-identical for every class because of the different materials used within the components.⁹ It is broadly confessed that the features of electrode materials like structure, morphology, electronic conductivity, electrochemical activity, and chemical and mechanical stability all put up to their electrochemical performance.^{10,11} Transition metals have fascinated ample interest for many energy storage devices due to their good physical and chemical characteristics, high conductivity, improved redox activity, and long cycle stability.¹² The supercapacitor's performance is also affected by the electrolyte utilized. Electrolytes are important and necessary components of supercapacitors. Due to their physical and chemical characteristics, they have a significant impact on the electrochemical performances of specific capacity, energy density, power density, rate capability, cycle stability, and safety. In comparison to aqueous electrolytes, the solid-state electrolyte is a crucial element that might significantly affect the capacitance retention and stability of supercapacitors. Liquid electrolytes possess some limitations like leakage problems, and it shows low electrochemical performance. Gel polymer electrolytes (GPEs) are the most commonly used solid-state electrolytes in solid-state supercapacitors due to their relatively high ionic conductivity, improved interfacial contacts between electrodes and GPE, broad operating potential range, higher ion

transfer number, and improved stability.^{13,14} Metal-organic frameworks (MOFs) have emerged as attractive prospects in a variety of sectors in recent years due to structural and electrical properties such as high porosity, excellent specific surface area (SSA), high stability, and adjustable arrangement of active sites. Owing to the structural and electronic features of MOFs, they are employed in supercapacitors. MOFs show pseudocapacitive nature because of the oxidative-reductive behavior of positively charged metal ions inside MOFs which create channels for electrons as well as show electric double layer capacitor (EDLC) behavior due to the organic linker structure which promotes charge transfer inside the framework which leads to the EDLC behavior.^{15,16} MOFs are formed at the micro/nanosize using central metal nodes and organic linkers, resulting in one-dimensional (1D), two-dimensional (2D) structures, and three-dimensional superstructures.^{17,18} In the exploration of advanced materials with enhanced characteristics over standard MOFs, the tendency is to encourage synergistic effects succeeding from the existence of two or more metals in multimetallic MOFs.¹⁹ In comparison to monometallic MOFs, the multimetallic MOFs have many advantages including strong chemical reactivity, improved electronic charge transfer, a variety of morphologies, high selectivity and sensitivity, virtue, strain in the lattice, different geometric impacts, and chemical change.²⁰⁻²⁴ Due to the excellent properties of MOFs, the electrochemical performance of supercapacitors is enhanced by their ability to store a huge quantity of charge and by encouraging the dissemination of electrolyte ions. As a result, MOFs have received a lot of interest when it comes to the use of supercapacitor electrode materials.²⁵ The limitations of the monometallic MOFs have been overcome by multimetallic MOFs which have advantages like the synergic effect which enhance the redox reactions and electrical conductivity. Also, the presence of various metal centers enhances the electroactive sites for ion transfer and helps the interaction with electrolyte in the course of the electrochemical reactions. The advancement of an perfect and beneficial electrode material composed of non-noble metals with remarkable steadiness and nature depicts the key challenge in these areas.²⁶⁻²⁸ As an outcome, a considerable study has been performed to reduce the obstacles caused by MOF's low conductivity and structural configuration. The direct application of MOF-based materials for effective supercapacitors remains difficult, despite the significant advances made in manufacturing MOF-based materials for energy storage applications.²⁹ Nagaraju et al. put together binder-free Ni-Co-Mn-based MOFs via a polarity-induced solution-

phased technique. Dual-layered Ni-Co-Mn-based MOFs with versatile features demonstrated the highest capacity of $1311.4 \text{ Ah cm}^{-2}$ at a 5 mA cm^{-2} current density with high capacitance retention of about 86.1% after applying 4000 cycles in the aqueous alkaline electrolyte. Additionally, they have created a pouch-type supercapattery with a bilayered Ni-Co-Mn-based MOF/Ni foam as an anode and nitrogen-oxygen-enriched activated carbon/Ni foam as a cathode. This device exhibits good cycling durability due to the high capacity of the supercapattery retained at 90.1% and the good Faradaic efficiency of 98.6%. Furthermore, they created a pouch-type supercapattery using bilayered Ni-Co-Mn-based MOF/Ni foam as an anode and nitrogen-oxygen enriched activated carbon/Ni foam as a cathode, resulting in a supercapattery with a high capacity retention of 90.1% and an exceptional Faradaic efficiency of 98.6%, illustrating the device's great cycling longevity.³⁰ Andikaey et al. prepared a new nanocomposite mesoporous ordered silica SBA-15/ MWCNTs embellished with a trimetallic organic framework (NiCoCu-BTC) using a facile, cost-effective one-step solvothermal technique. The synthesized nanocomposite exhibited outstanding electrochemical performance having a remarkable 868 C g^{-1} (2067 F g^{-1}) specific capacity at a 1 A g^{-1} current density with great cycling durability. Additionally, they have fabricated an asymmetric supercapacitor device with a high energy density 52.4 W h kg^{-1} at a power density of 1124 W kg^{-1} with high capacitance retention of about 87.2% after applying 5000 cycles.³¹

In view of this, we present the synthesis of trimetallic MOFs for high-performance symmetric supercapacitors by applying two different organic linkers, i.e., trimesic acid and terephthalic acid. To the finest of our information, this is the primary report in which a comparative study of two MOFs is carried out only by changing the organic linker, and they are used as dynamic anode materials for supercapacitors. The physico-chemical properties of both the trimetallic MOFs were thoroughly investigated by using different characterization techniques. In addition, a symmetric supercapacitor shows a high energy density and great chemical steadiness in a 2 M KOH electrolyte.

4.3 Experimental section

4.3.1 Synthesis of MOFs

All chemicals used to synthesize trimetallic MOFs were obtained from Loba Chemie (India) and were used without further purification. The trimetallic Ni-Co-Zn-

BDC MOFs (BDC-MOF) were prepared using a single-step reflux condensation method. In a typical synthesis, 0.415 g of terephthalic acid (BDC), 0.363 g of nickel nitrate hexahydrate, 0.363 g of cobalt nitrate hexahydrate, and 0.371 g zinc nitrate hexahydrate were dissolved step by step in 30 mL of N, N-dimethylformamide with continuous stirring at ambient temperature.

After which, the reaction mixture was transferred to a 50 mL round-bottom flask. The reaction mixture was kept at 120 °C for 12 h to produce the BDC-MOF sample and then cooled at ambient temperature. The final precipitate was carefully washed a few times with alcohol. Finally, the purple-colored product was air-dried for 12 h at 80 °C. A similar procedure was adopted for the synthesis of trimetallic Ni-Co-Zn-BTC MOF (BTC-MOF), except that terephthalic acid was replaced with trimesic acid. A schematic illustration for the synthesis of trimetallic MOFs by the reflux condensation method is shown in Figure 4.1.

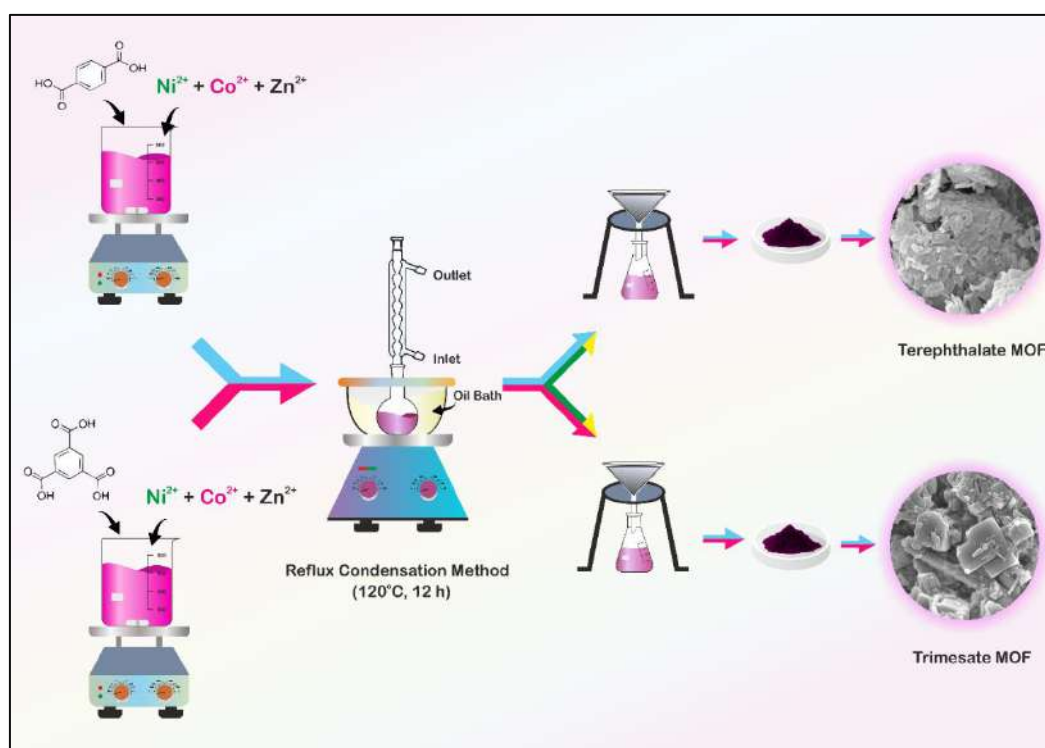


Figure 4.1: Schematic illustrations of the synthesis of trimetallic MOFs

4.3.2 Structural and elemental characterization

The crystal structure and phase purity of the synthesized trimetallic MOFs were confirmed by the X-ray diffraction (XRD) technique [Bruker D8 Phaser X-ray diffractometer with Cu K α radiation ($\lambda = 1.541 \text{ \AA}$)]. The types of bonding and functional groups were analyzed by Fourier transform infrared (FT-IR) spectroscopy (PerkinElmer 1760X spectrophotometer). The Raman spectrometer (LabRAM HR

Evolution Confocal Raman Microscope, France) was used for point group analysis. The morphology of the as-prepared materials was investigated by scanning electron microscopy (SEM) (JEOL-JSM 6360, Japan). The elemental composition of the trimetallic MOFs was examined using an energy-dispersive X-ray analysis (EDAX) spectrometer [Oxford Instrumentations inbuilt with field emission (FE-SEM)]. The elemental oxidation state and chemical composition of the as-prepared materials were investigated by X-ray photoelectron spectroscopy (XPS) with a K-alpha (Thermo VG, UK) spectrometer and a monochromatic Al X-ray source (AlK α line: 1486.6 eV, 3 mA, and 12 kV). The surface area and pore size were determined by Brunauer-Emmett-Teller (BET) (NOVA1000e Quantachrome, USA).

4.3.3 Electrochemical measurements with a three-electrode assembly

Electrochemical measurements were performed on a CHI608 electrochemical analyzer (CH Instruments Inc, Austin, USA). A standard three-electrode assembly in a 2 M KOH electrolyte was used to explore the electrochemical characteristics of a constructed electrode. A saturated Ag/AgCl was used as a reference electrode, graphite as the counter electrode, and trimetallic MOF-loaded stainless-steel mesh as the working electrode. The working electrode was fabricated by making a paste of 80 wt % of active materials (BDC-MOF and BTC-MOF), 10 wt % of carbon black (Super P) as a conducting material, and 10 wt % of polyvinylidene fluoride (PVDF) as a binder in the N-methyl-2-pyrrolidone (NMP) solvent. This paste was applied to a stainless-steel mesh measuring with size about 1 cm² and then air-dried for 12 h at 80 °C. With the help of electrochemical workstation, cyclic voltammetry (CV), galvanostatic charge-discharge (GCD), and electrochemical impedance spectroscopy (EIS) studies were carried out. In the frequency range of 1 Hz to 100 kHz, the EIS test was conducted. According to equation (4.1), specific capacitance of the prepared samples was determined.

$$C = \frac{I \times \Delta t}{\Delta V \times m} \dots\dots\dots (4.1)$$

Where “C” stands for the specific capacitance measured in F g⁻¹, “I” stands for the current measured in mA, “ Δt ” stands for the discharging time measured in seconds, “ ΔV ” stands for the potential window measured in volt, and “m” stands for the mass of the active electrode material measured in mg.

4.3.4 Electrochemical measurements of the symmetric supercapacitor

A solid-state symmetric supercapacitor (SSC) device was constructed by stainless-steel mesh substrates with size about 2 cm coated with the BDC-MOF, and a thick layer of polyvinyl alcohol (PVA)-KOH was sandwiched in between them. The device was allowed to naturally dry out overnight at ambient temperature. As per literature report, the PVA-KOH gel electrolyte was prepared.³² Using a conventional method, 1 g of PVA was dissolved in 20 mL of distilled water while the bath solution temperature was held at 80 °C for 30 min. To create the viscous gel electrolyte, the PVA solution was combined with the aqueous KOH solution dropwise and heated once more at 80 °C for 30 min.

Using equation (4.2-4.4), the specific capacitance, energy density, and power density of the symmetric supercapacitor were computed, respectively.^{33,34}

$$C_s = \frac{I \times \Delta t}{\Delta V \times M} \dots\dots\dots (4.2)$$

$$E = \frac{0.5 \times C \times \Delta V^2}{3.6} \dots\dots\dots (4.3)$$

$$P = \frac{E \times 3600}{\Delta t} \dots\dots\dots (4.4)$$

where “Cs” stands for the specific capacitance measured in F g⁻¹, “E” stands for the specific energy measured in Wh kg⁻¹, “P” stands for the specific power measured in W kg⁻¹, and “M” stands for the total mass of the two electrodes measured in mg.

4.4 Results and discussion

4.4.1 X-ray diffraction of trimetallic MOFs

The crystallographic structure and crystallite size of the trimetallic BDC-MOF and BTC-MOF were found by using the XRD pattern, and the results are presented in Figure 4.2. For the BDC-MOF, the peak located at an angle 10.0° is indexed to the (011) plane of Ni (PDF no. 10-0735), the diffraction peak at 8.7° is attributed to the (100) plane of Co (PDF no. 19-1523), and the diffraction peak at 16.6° is attributed to the (002) plane of Zn (PDF no. 01-0037). While for the BTC-MOF, the peak located at 10.6° is indexed to the (011) plane of Ni (PDF no. 10-0735), the diffraction peak at 8.7° is attributed to the (100) plane of Co (PDF no. 13-0733), and the diffraction peak at 17.5° is attributed to the (311) plane of Zn (PDF no. 01-0037), respectively, indicating that these MOFs have the similar structure.^{35,36} Furthermore, the crystallite size was determined using Debye-Scherrer’s formula, as shown in equation (4.5).³⁷

$$D = \frac{0.9\lambda}{\beta \cos\theta} \dots\dots\dots (4.5)$$

Where “D” stands for the average crystallite size, “λ” stands for the wavelength of the X-rays, “β” stands for the full-width half-maxima (fwhm), and “θ” stands for Bragg’s diffraction angle. According to the XRD spectra, the trimetallic BDC-MOF and BTC-MOF derived from the (011) plane have average crystallite sizes of 3.55 and 5.97 nm, respectively.

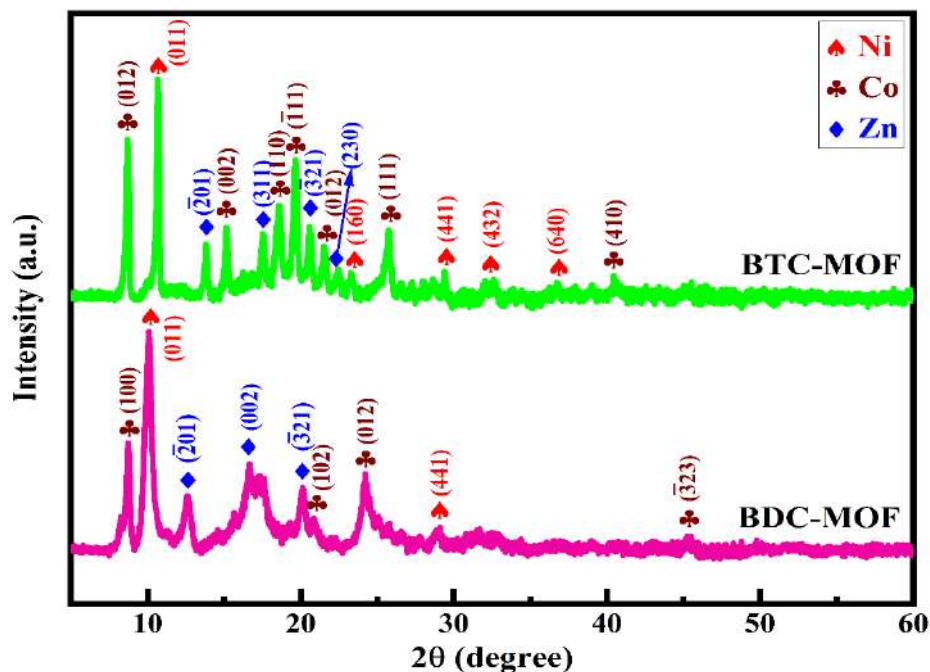


Figure 4.2: XRD patterns of BDC-MOF and BTC-MOF

4.4.2 FT-IR spectroscopy of trimetallic MOFs

The identification of the functional group of the BDC-MOF and BTC-MOF was obtained by using the FT-IR spectra. Trimetallic MOF FT-IR spectra are shown in Figure 4.3. The bands at 3351 and 3310 cm^{-1} were caused by moisture induced O-H stretching vibrations in BDC-MOF and BTC-MOF, respectively. Aromatic C=C in plane vibrations are assigned to the bands at 1647 and 1609 cm^{-1} . The asymmetric stretching vibration of the coordinated (-COO-) group displays the peak at 1436 cm^{-1} , while the symmetric stretching vibrations show the peak at 1361 cm^{-1} . In BDC-MOF, the sp^2 carbon stretching vibration peaks of C=O due to the carboxylic group are displayed at 1677 cm^{-1} , and the peak at 1575 cm^{-1} represents the aromatic C=C in-plane vibrations. The C-H bending vibrations of CH_3 and CH_2 are represented by the prominent adsorption peaks at 1373 and 1287 cm^{-1} , respectively. The in-plane and out-of-plane C-H bending modes are allocated to several bands in the ranges of 1200-

1000 and 1000-700 cm^{-1} , respectively. Multiple bands in the range of 700-400 cm^{-1} are assigned to the metal-oxygen bands.^{38,39}

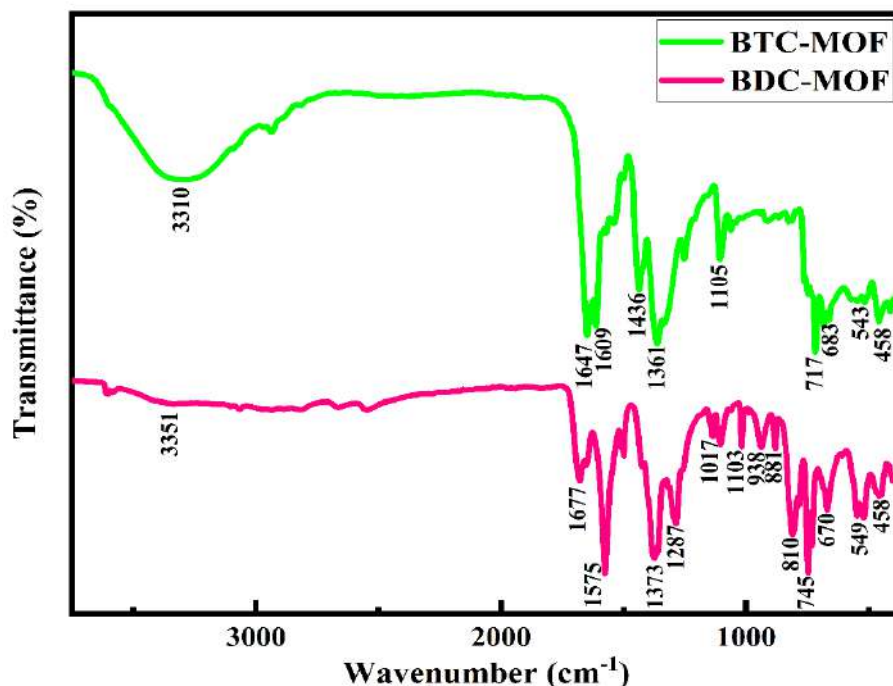


Figure 4.3: FTIR spectra of BDC-MOF and BTC-MOF

The bond vibration of trimetallic MOFs was confirmed by Raman spectroscopy, as seen in Figure 4.4. The peaks of trimetallic MOFs correlate to different bands, confirming the existence of the BDC and BTC moieties in the material. The Raman spectra of BDC-MOF and BTC-MOF displayed a $\nu(\text{C}=\text{C})$ modes of the benzene ring observed at 1133 and 999 cm^{-1} , respectively, and the observed peaks at the low-frequency region of 500-850 cm^{-1} correspond to benzene ring C-H bending modes and the presence of metal-oxygen bond vibration, respectively.^{40,41} In BDC-MOF, the vibrational modes of $\nu_{\text{as}}(\text{COO}^-)$ and $\nu_{\text{s}}(\text{COO}^-)$ were noticed as doublets at 1608 and 1427 cm^{-1} in BDC-MOF, and the vibrational modes of $\nu_{\text{as}}(\text{COO}^-)$ and $\nu_{\text{s}}(\text{COO}^-)$ were noticed as doublets at 1595 and 1453 cm^{-1} in BTC-MOF, respectively, and these findings point to the synthesis of trimetallic MOFs, which was previously supported by FT-IR data.^{42,43}

4.4.3 Raman spectroscopy of trimetallic MOFs

Raman spectroscopy was used to confirm the bond vibration of trimetallic MOFs, which is given in Figure 4.4. The trimetallic MOFs peaks corresponds to various bands which confirms the presence of the BDC and BTC moiety in the material. The Raman spectra of BDC-MOF and BTC-MOF exhibited a $\nu(\text{C}=\text{C})$ modes

of the benzene ring was observed at 1133 cm^{-1} and 999 cm^{-1} , respectively and the observed peaks at the low-frequency region of 500 to 850 cm^{-1} were assigned to benzene ring C-H bending modes and the presence of metal-oxygen bond vibration.^{35,36} In BDC-MOF, the vibrational modes of $\nu_{\text{as}}(\text{COO}^-)$ and $\nu_{\text{s}}(\text{COO}^-)$ were observed as doublets at 1608 and 1427 cm^{-1} in BDC-MOF and the vibrational modes of $\nu_{\text{as}}(\text{COO}^-)$ and $\nu_{\text{s}}(\text{COO}^-)$ were observed as doublets at 1595 and 1453 cm^{-1} in BTC-MOF, respectively and these results indicate the formation of BDC and BTC based trimetallic MOF which was earlier boosted by FT-IR results.^{37,38}

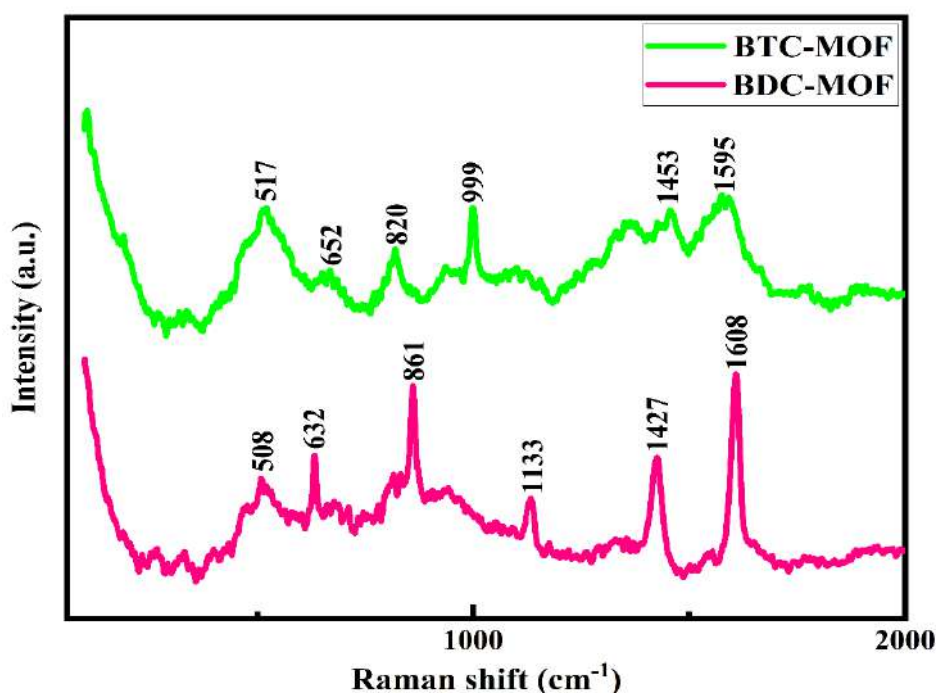


Figure 4.4: Raman spectra of BDC-MOF and BTC-MOF

4.4.4 Scanning electron microscopy of trimetallic MOFs

SEM was used to study the surface morphology of BTC-MOF and BDC-MOF. The influence of the trimesic and terephthalic ligands on the formation of surface morphology for MOF was examined. Figure 4.5 reveals the surface morphological images of BTC-MOF and BDC-MOF with different magnifications. From Figure 4.5(a, b), it has been observed that the small nanoparticles start to construct the nanobrick-like morphology of BTC-MOF, and nanobricks were observed all over area of the sample which are randomly distributed in the sample. The width of the nanobricks was observed from 200 to 300 nm in size. It was noticed that nanobricks are interconnected to each other, and also the edges of the nanobricks are mingling with one another; hence, the nanobricks are found to be cut in small

pieces, which are responsible for the irregular shapes of nanobricks formed in the BTC-MOF sample. Additionally, some of the spacing between two nanobricks is seen in the BTC-MOF sample, which is helpful for adsorbing the electrolyte and boosts the material-specific capacitance. It is seen that the variation of ligands in MOF samples has a great impact on the characteristic morphology of MOF samples. Here, it is observed that with change in the ligands, there was a change in the surface morphology of MOF samples.

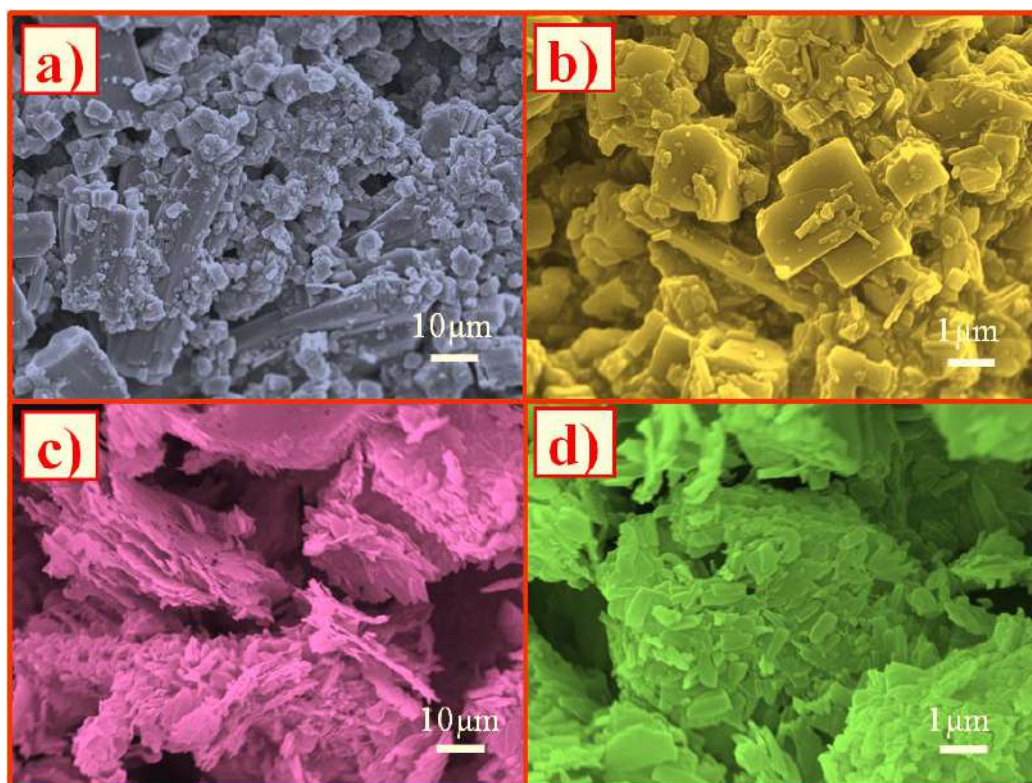


Figure 4.5: SEM images of (a, b) BTC-MOF and (c, d) BDC-MOF at different magnifications

The sample BDC-MOF demonstrated the nanoplate-like morphology with irregular arrangement of the nanoplates occurring throughout the sample. Some of the nanoplates were formed together, leading to big porous bricks which are shown in Figure 4.5(c, d). The thickness of the nanoplates was observed in the nanometer range, and a bunch of the nanoplates formed the brick-like morphology, hence increasing the surface area of the sample. The bunch of nanoplates provides a larger SSA for the adsorption of the electrolyte increasing the specific capacitance of the sample. The surface area of BDC-MOF is the greater of the two samples examined in the BET investigation. Also, SEM outcomes are in good agreement with BET

analysis. Hence, among these two samples, BDC-MOF executes a good electrochemical performance.

4.4.5 Energy dispersive X-ray analysis of trimetallic MOFs

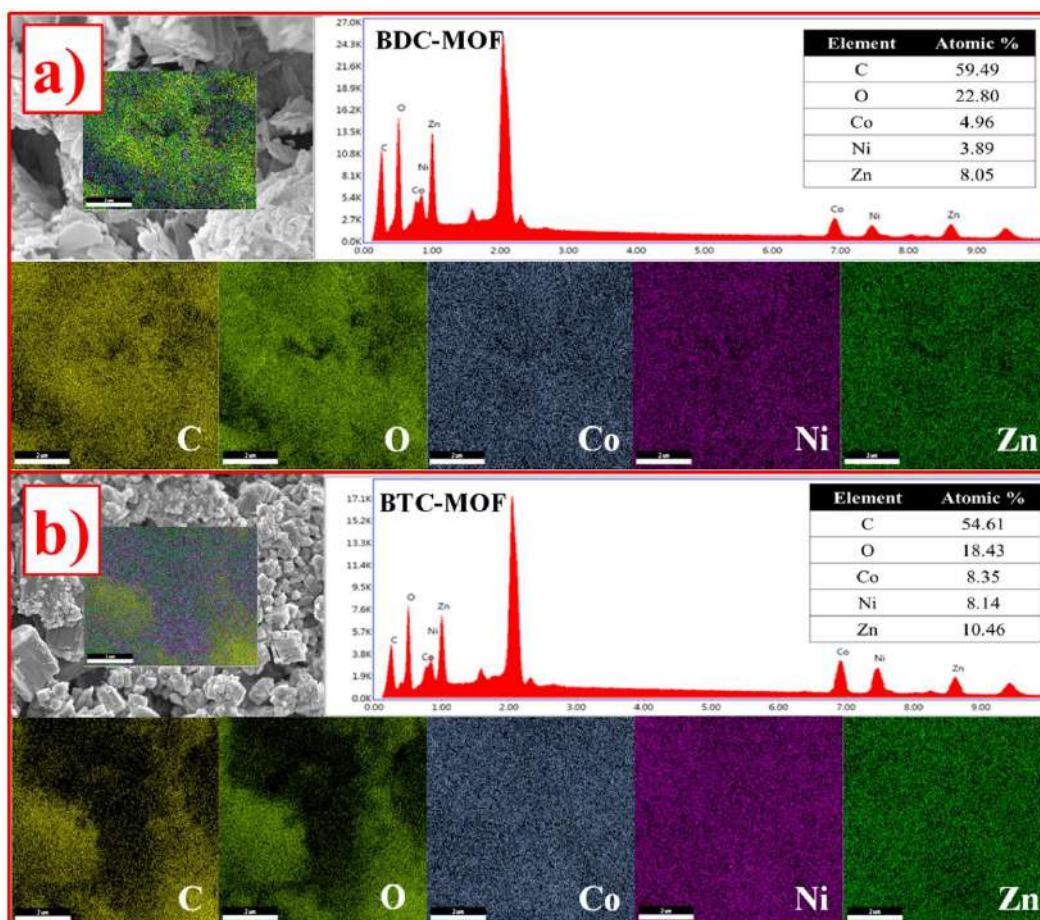


Figure 4.6: EDX spectra and elemental mapping of C, O, Co, Ni and Zn elements for (a) BDC-MOF and (b) BTC-MOF

The EDAX of both the trimetallic MOFs is presented in Figure 4.6. Figure 4.6 demonstrates that the elements Ni, Co, Zn, C, and O are distributed evenly throughout the sample, which confirms the presence of three metal ions in the MOFs as well as maintained the stoichiometry of the samples; hence, it proved that the trimetallic MOFs were obtained. The SSA and pore diameter of the MOF samples were obtained by using BET analysis.

4.4.6 Transmission electron microscopy analysis of trimetallic MOFs

Transmission electron microscopy (TEM) examination was performed to have a better understanding of the structure of the as-prepared nanomaterials. Figure 4.7(a) depicts a typical TEM image of BDC-MOF with a 2D nanoplate-like shape with many voids. Furthermore, the high-resolution TEM (HRTEM) image of BDC-MOF (Figure 4.7b) confirms an amorphous nature due to the lack of apparent lattice fringes

and no indication of crystallinity, representing that the particles were amorphous. The selected area electron diffraction (SAED) pattern (Figure 4.7c) consistently exposed only diffuse rings, confirming the amorphous nature of the as-synthesized BDC-MOF particles. Figure 4.7(d) shows a typical TEM image of a 2D nanobrick-like morphology of BTC-MOF. The HRTEM image of BTC-MOF (Figure 4.7e) disseminated that the particles were amorphous due to the lack of visible lattice fringes and no evidence of crystallinity, suggesting that the particles were amorphous. The SAED pattern (Figure 4.7f) consistently displayed only diffuse rings, confirming the amorphous nature of the BTC-MOF particles as synthesized.

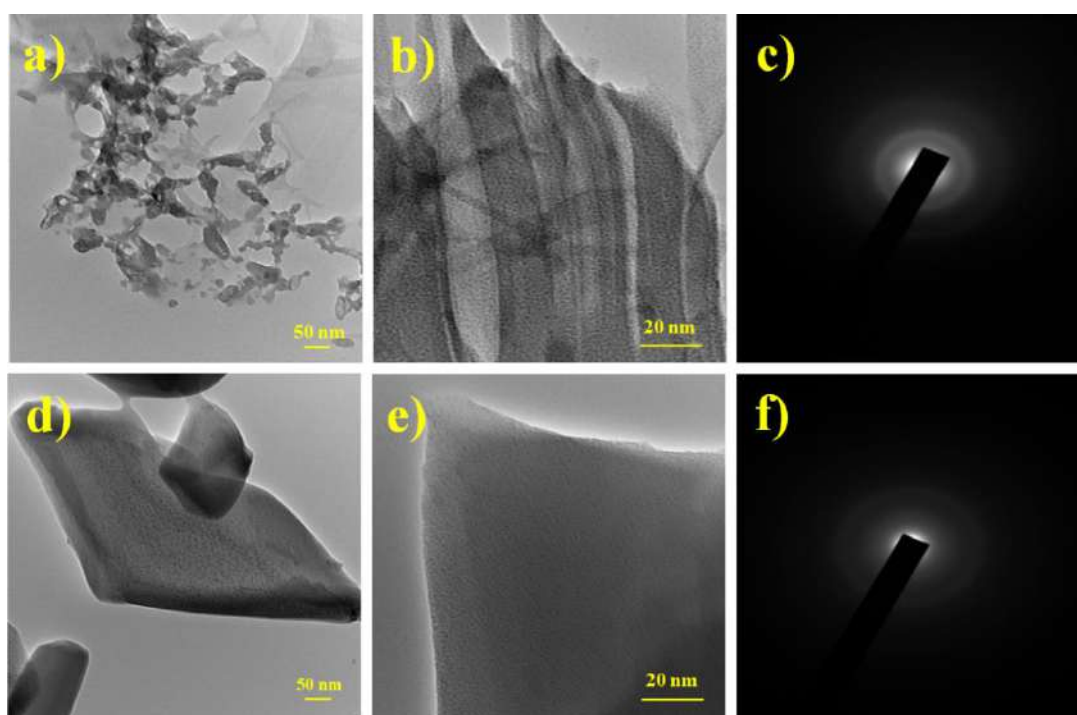


Figure 4.7: TEM, HR-TEM and SAED pattern of (a-c) BDC-MOF and (d-f) BTC-MOF

4.4.7 Brunauer-Emmett-Teller analysis of trimetallic MOFs

N₂ adsorption/desorption measurements confirmed the porous structure of the obtained MOFs, and the corresponding isotherms are shown in Figure 4.8. Before adsorption measurements, MOF samples were outgassed at 100 °C for 4 h. BDC-MOF and BTC-MOF had SSA of 267.85 and 216.93 m² g⁻¹, respectively. The average pore size of BDC-MOF and BTC-MOF was found to be 16 and 31 nm simultaneously, which is obtained from the BJH curve. According to the IUPAC classifications, the BDC-MOF and BTC-MOF isotherms are types IV and II, respectively,⁴⁴ clearly indicating that the BDC-MOF have a larger SSA than the

BTC-MOF. The SSA and average pore radius values agree well with the crystallite size determined by XRD and the specific capacitance determined by electrochemical performance study.

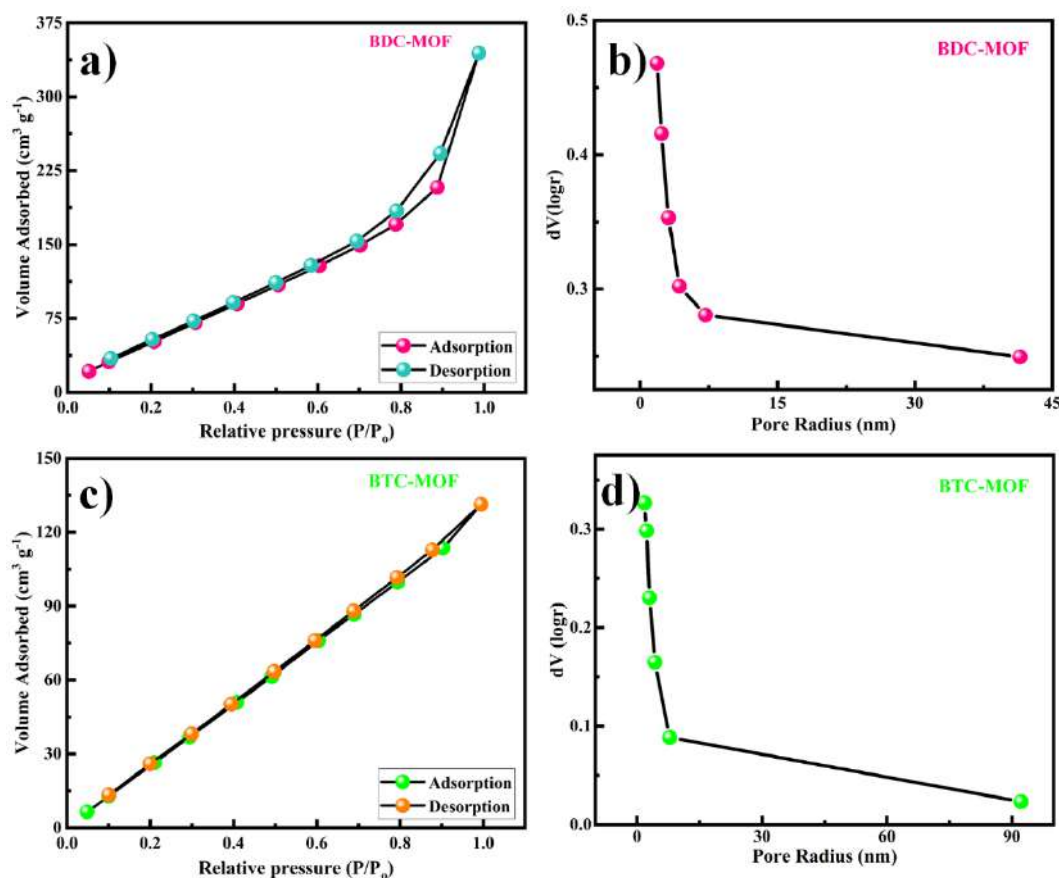


Figure 4.8: (a, b) N₂ adsorption-desorption isotherm and pore size distribution curve BDC-MOF, (c, d) N₂ adsorption-desorption isotherm and pore size distribution curve BTC-MOF

4.4.8 X-ray photoelectron spectroscopy of trimetallic MOFs

The chemical composition and oxidation states of trimetallic MOFs were obtained by using XPS and explored the charge-transfer mechanisms in the valence state of the Ni, Zn, and Co ions of trimetallic MOFs along with the synergetic effect of its species. Figure 4.9(a, b) shows the survey spectra of both trimetallic MOFs. The core level spectra of C 1s, Ni 2p, Co 2p, O 1s, and Zn 2p of both the trimetallic MOFs are depicted in Figure 4.9(c-i). As seen in Figure 4.9(a, b), the existence of trimetallic MOFs was attributed by the XPS full survey scan spectrum, which contained the signals of the elements Ni, Co, O, C, and Zn. Figure 4.9(c, d) reveals the C 1s spectra of both the MOFs. It consists of distinct peaks caused by benzene rings from the BDC and BTC ligands with binding energy 284.7 and 284.8 eV, respectively.

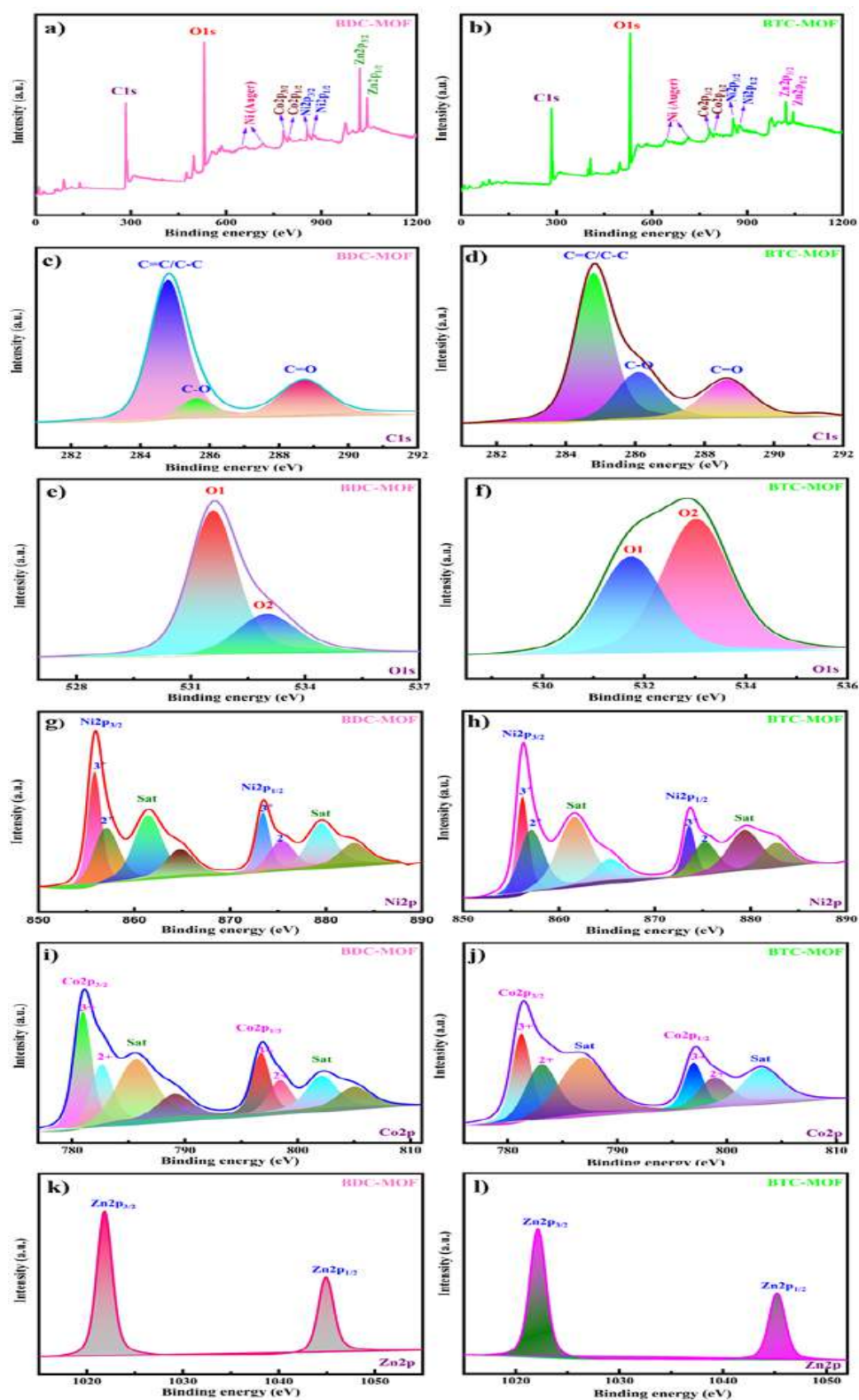


Figure 4.9: XPS survey spectra of BDC-MOF (a) and BTC-MOF (b), high-resolution spectra of C 1s (c, d), O 1s (e, f), Ni 2p (g, h), Co 2p (i, j), and Zn 2p (k, l) of BDC-MOF and BTC-MOF, respectively

Then, carboxylate rings from the (-C=O) groups of the organic ligand with binding energy 288.7 and 288.6 eV, respectively, of both the MOFs and the species -C-O with a binding energy of 285.5 and 286.0 eV are shown.

Furthermore, the O 1s spectra of BDC and BTC MOF are presented in Figure 4.9(e, f), which includes two oxygen peaks denoted as O1 and O2. The first fitted peak at a 531.5 and 531.6 eV binding energy is related to the presence of metal-oxygen bond, i.e., oxygen atoms on the Ni, Co, and Zn-O bonds of both the MOFs, and the second fitted peak at 532.9 eV binding energy is associated with the carboxylate moiety of the organic ligand of MOF samples.⁴⁵ The Ni 2p emission spectrum shows two distinct nickel species, Ni²⁺ and Ni³⁺. The Ni 2p spectra were deconvoluted into two spin-orbit doublets (Ni 2p_{1/2} and Ni 2p_{3/2}) and two satellite peaks using the Gaussian fitting method, as shown in Figure 4.9(g, h). The peak fitted at binding energies of 855.9 and 873.4 eV are ascribed to Ni 2p_{3/2} and Ni 2p_{1/2} for BDC-MOF. Similarly, the binding energies of Ni 2p_{3/2} and Ni 2p_{1/2} for BTC-MOF are 856.2 and 873.6 eV, respectively, as illustrated in Figure 4.9(h). The spin-orbital energy of the Ni peaks in two MOF slightly differs. First, the binding energy difference between these two peaks is determined to be 17.5 eV for BDC-MOF, and the binding energy peak of the “Ni” element was shifted at lower binding energy, i.e., 17.4 eV may be due to the acidic behavior for BTC MOF.

The satellite peaks, as shown in Figure 4.9(i, j), indicate two types of Co species, comprising Co²⁺ and Co³⁺ for two spin-orbit doublets (Co 2p_{1/2} and Co 2p_{3/2}), which were observed as a result of fitting the Co 2p emission spectra of both the MOFs. The fitted peaks with binding energy of 781.0 and 796.8 eV indicate the Co 2p_{3/2} and Co 2p_{1/2}, respectively, for the BDC-MOF sample. The Co peak spin-orbital energies in two MOFs varied slightly from one another. For BDC-MOF, the binding energy difference between these two peaks spin-orbital coupling is found to be 15.8 eV, and the “Co” element’s binding energy peak was relocated to a lower binding energy for BTC MOF, i.e., 15.7 eV. Again the peaks at 781.4 and 797.1 eV are associated to the Co 2p_{3/2} and Co 2p_{1/2} for the BTC-MOF sample. The other satellite peaks of Co elements for both the MOFs samples are also observed in Figure 4.9(i, j).⁴⁶⁻⁴⁸ The peaks at binding energy 1021.8 and 1022.0 eV are assigned to the energy level Zn 2p_{3/2} in BDC-MOF and BTC-MOF, respectively. Similarly, the peaks at 1044.8 and 1045.1 eV are observed for Zn 2p_{1/2} for BDC-MOF and BTC-MOF,

respectively. The detailed deconvolution peaks of Zn 2p_{3/2} and Zn 2p_{1/2} are observed in Figure 4.9(k, l). The differences between the spin-orbital energy of both the MOF samples are nearly equal, confirming that prepared samples are well matched with the literature value of XPS.⁴⁹⁻⁵¹ The calculated binding energy difference among these two peaks spin-orbital coupling is 23 eV, which is in good accordance with the literature value. Moreover, the difference between the spin-orbital energy of the BTC-MOF sample is slightly changed which may be due to the more acidic nature of the BTC-MOF sample.

4.4.9 Electrochemical measurements of trimetallic MOFs

The electrochemical characteristics of the MOF samples were assessed to determine their suitability for usage as active materials in supercapacitors. CV measurements of the as-synthesized MOF hybrid structures with various organic ligands (trimesic acid and terephthalic acid) were performed in a 2 M KOH electrolyte in a potential sweep window of 0-0.5 V, as shown in Figure 4.10. The CV curves of trimetallic MOFs reveal that the integral areas change throughout the operating potential range at 0-0.5 V, indicating that the charge storage mechanism is both pseudocapacitive and electric double layer type. The capacitance is mostly due to the charge stored at the electrode-electrolyte interface. The region beneath the CV curve of BDC-MOF is larger than that of BTC-MOF, as shown in Figure 4.10(a).

In the potential range of 0-0.5 V, the GCD profiles (Figure 4.10b) were examined at a current density of 5 mA cm⁻². As predicted, compared to the BTC-MOF electrode, the BDC-MOF electrode displayed a significantly longer charge/ discharge time and increased specific capacitance. A comparison of the CV curves of both trimetallic MOFs, i.e., BDC-MOF and BTC-MOF (Figure 4.10c, d) at a different scan rate was performed in the potential range of 0-0.5 V. As the scan rate decreases, the area under the CV curve decreases; hence, specific capacitance increases. This occurs due to the complete diffusion of electrolyte ions into the electrode material at slower scan rates. Hence, a charge on the whole active surface of the electrode material may be stored. Only the superficial active surface is used for charge storage at a higher scan rate because diffusion limits the passage of electrolyte ions.⁵² The area under the curve grows from 0 to 0.5 V with a broad range of scan rates from 10 to 100 mV s⁻¹, indicating rapid rates of ionic and electronic transport at the electrode/electrolyte interfaces. The GCD characteristics of BDC-MOF and BTC-MOF electrodes were

investigated at current densities ranging from 5 to 25 mA cm⁻² in 2 M KOH electrolyte across a potential range of 0-0.5 V (Figure 4.10e, f).

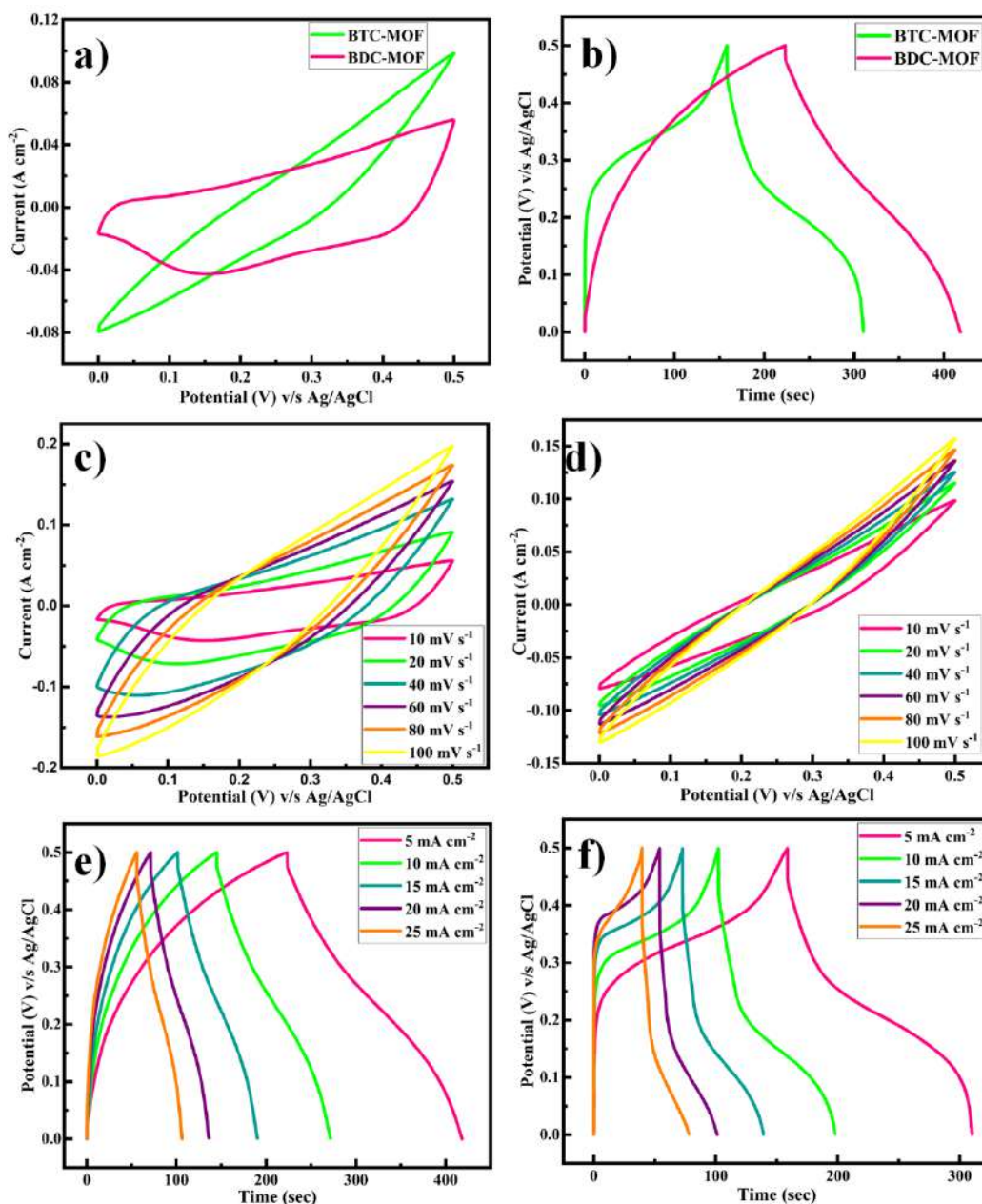


Figure 4.10: (a) Comparative CV curves at 10 mV s⁻¹ scan rate, (b) Comparative GCD curves at 5 mA cm⁻² current density, (c) CV curves of BDC-MOF at different scan rates, (d) CV curves of BTC-MOF at different scan rates, (e) GCD curves of BDC-MOF at different current densities, (f) GCD curves of BTC-MOF at different densities

EIS measurements were performed to determine the internal resistive characteristics as well as the capacitive behavior of the MOF electrode. The Nyquist plots of MOFs in 2 M KOH electrolyte are shown in Figure 4.11(a). A straight line

detected in the lower-frequency portion of the Nyquist plot was due to the migration of electrolyte ions from the bulk solution to the electrode surface. The charge-transfer activity at the electrode/ electrolyte interface is responsible for the presence of a semicircle in the high-frequency zone, and the semicircle diameter shows the charge-transfer resistance (Rct). The charge-transfer resistance of BDC-MOF and BTC-MOF is 0.19 and 0.46 Ω , respectively. BDC-MOF (0.19 Ω) has a lower charge-transfer resistance than BTC-MOF (0.46 Ω). These Rct values show that both electrodes have high electrical conductivities, which are connected to the presence of carbon in their composition, which increases the conductivity of the manufactured electrode. In practice, the carbon in the electrode structure reduces the resistance to charge transfer and improves the connectivity between the active sites for electron transfer.⁵³

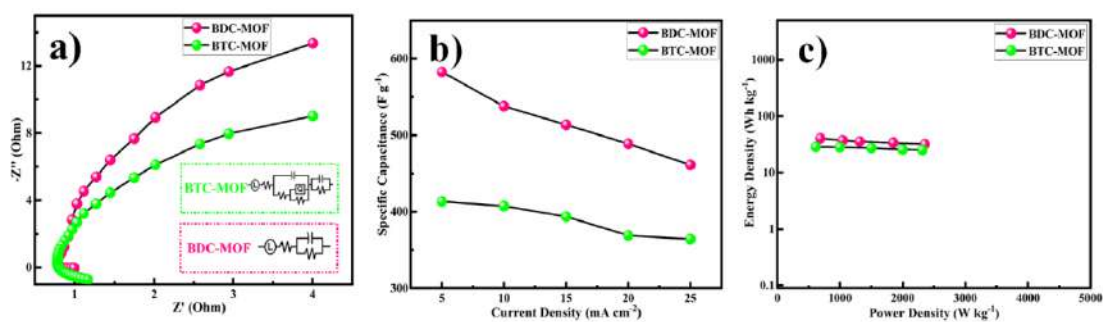


Figure 4.11: (a) Nyquist plots, (b) Variation of specific capacitance as a function of current density, (c) Ragone plot showing the energy density versus power density

Figure 4.11(b) depicts the change of specific capacitance as a function of current density, and Figure 4.11(c) depicts the Ragone plot of energy density vs power density for both trimetallic MOFs. The specific capacitance of the BDC-MOF electrode is 582.8 F g⁻¹ at 5 mA cm⁻² current density, which is more than the specific capacitance of the BTC-MOF electrode, which has 413.4 F g⁻¹ at 5 mA cm⁻² current density, according to the GCD curves. The examined BDC-MOF and BTC-MOF electrodes exhibit a longer charge and discharge time with lowering currents, resulting in greater specific capacitance values, implying that as current increases, the specific capacitance falls in typical behavior. Trimesic acid and terephthalic acid have pKa values of 3.14 and 4.82, respectively. Trimesic acid has a low pKa value, which makes it act as a strong acid since it has a high acidity.⁵⁴ Due to the high acidity, the BTC-MOF electrode gets etched, which degrades the deposition of the film that clogs the pores and prevents the electrolyte from entering the electrode material, increasing resistance and lowering specific capacitance. The cluster of nanoplates that comprise

the porous brick-like morphology of BDC-MOF operate as an “ion-buffering reservoir”, enhancing charge-discharge and shortening the diffusion length for ions to enter the electrode. The charging/discharging curves are also affected by the trimesic and terephthalic ligands; the nature of the curves differs for BDC-MOF and BTC-MOF.

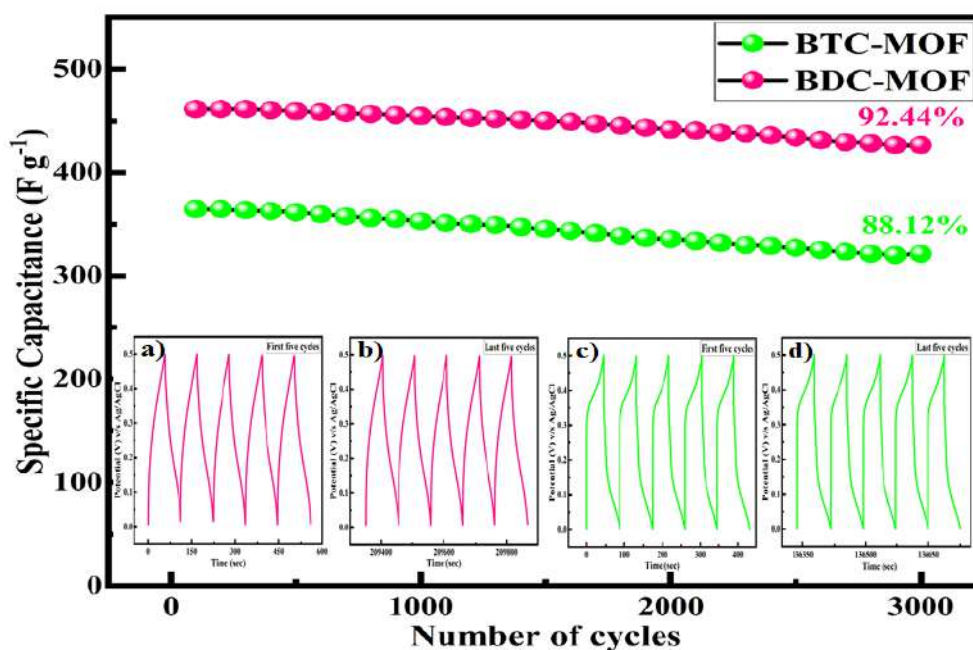


Figure 4.12: Cycling performance at 25 mA cm^{-2} , and the inset shows the first and last five cycles of BDC-MOF and BTC-MOF

To examine the cyclic stability of the MOF electrodes, the specific capacitance as a function of cycle number was measured at a prolonged current density of 25 mA cm^{-2} . The BDC-MOF electrode demonstrated good cycling stability after 3000 continuous cycles, with about 92.44% retention of the original capacitance (Figure 4.12). This exceptional long-cycle lifespan was greater than that of the BTC-MOF, which has 88.12% retention even after 3000 GDC cycles at a current density of 25 mA cm^{-2} , as shown in Figure 4.12. On 1D stainless-steel mesh substrate with substantially poorer electrical conductivity, BDC-MOF demonstrated a remarkable specific capacity of 528.8 F g^{-1} . At all the current densities, the specific capacity of BDC-MOF was relatively high, and a reversible capacity of 461.2 F g^{-1} can be sustained at an extremely high current density of 25 mA cm^{-2} , with 86.14% capacity retention compared to the capacity at 5 mA cm^{-2} , showing a high rate capability. The increase in the cycle number causes a drop in specific capacitance due to the partial leaching of the active electrode material during faradic operations.⁵⁵ The remarkable

energy storage efficiency can be attributed to the combined impact of a group of nanoplates forming the porous bricks, such as morphology, and the huge SSA of the extremely porous material. The electrochemical performance of a few different MOFs that have been previously characterized is compared to that of the synthesized trimetallic MOF in Table 4.1.

Table 4.1: Comparison of the specific capacitances of trimetallic MOFs with previously reported materials

Sr. No.	Material	Electrolyte	Substrate	Specific Capacitance	Current Density	Stability	Ref.
1	NiCoMn-MOF	3M KOH	Nickel foam	907.4 C g ⁻¹	1 A g ⁻¹	64.7%	⁵⁶
2	ZnNi-MOF	3M KOH	Nickel foam	466.5 F g ⁻¹	0.5 A g ⁻¹	44.0%	⁵⁷
3	NiCo-MOF	1M KOH	Nickel foam	1107.3 F g ⁻¹	1 A g ⁻¹	70.1%	⁵⁸
4	Ni/Co-MOF	6M KOH	Nickel foam	982.5 F g ⁻¹	0.5 A g ⁻¹	84.0%	⁵⁹
5	NiCoZn-MOF	2M KOH	Stainless steel mesh	582.8 F g ⁻¹	5 mA cm ⁻²	92.44%	This work

4.4.10 Electrochemical measurements of symmetric supercapacitors device

A SSC device was assembled with BDC-MOF for both electrodes and PVA/KOH gel both as the separator and electrolyte to further evaluate the practical application of the BDC-MOF. The slurry coating method was used to prepare both electrodes. In short, the slurry was made by combining 80 mg of active material (BDC-MOF), 10 mg of PVDF, and 10 mg of carbon black in 0.5 mL of the NMP solvent. The appropriate volume of slurry was then dispersed onto a 2 × 2 cm flexible stainless-steel mesh and air-dried overnight at 60 °C. To avoid electrical contact, the electrode borders were first made non-conducting using a band. The PVA-KOH gel was applied to one side of the electrode, resulting in one point of electrical contact. Both electrodes were eventually patched together in the shape of a sandwich, with gel-pasted sides facing each other. For 12 h, the device was subjected to 1-ton pressure to establish a strong connection between the electrodes and gel electrolyte and to eliminate the air gap. Following that, the device was utilized to evaluate electrochemical performance. CV, GCD, and EIS measurements were performed to

examine the performance of the assembled SSC device. The assembled SSC device CV curves displayed ideal rectangular shapes within an operating voltage window 0.4-1.2 V, demonstrating excellent capacitive behavior. Figure 4.13(a, b) displays CV and GCD profiles of the SSC device within various potential windows and exhibits excellent linear slopes and triangular shapes, which suggest ideal capacitive behavior in line with the CV curves.

In practice, the SSC device's potential window can reach 1.2 V without causing significant changes in the CV and GCD curves, signifying outstanding electrochemical stability. Figure 4.13(c) depicts the SSC device's CV curves at various scan rates. The CV curves remained consistent when the scan rate was raised from 10 mV s^{-1} to 100 mV s^{-1} ; however, the closed regions grew, confirming the symmetric device's high rate capacity. Furthermore, the GCD curves of the SSC device at various current densities are shown in Figure 4.13(d), and the nearly symmetric charge/discharge curves indicate excellent rate capability.

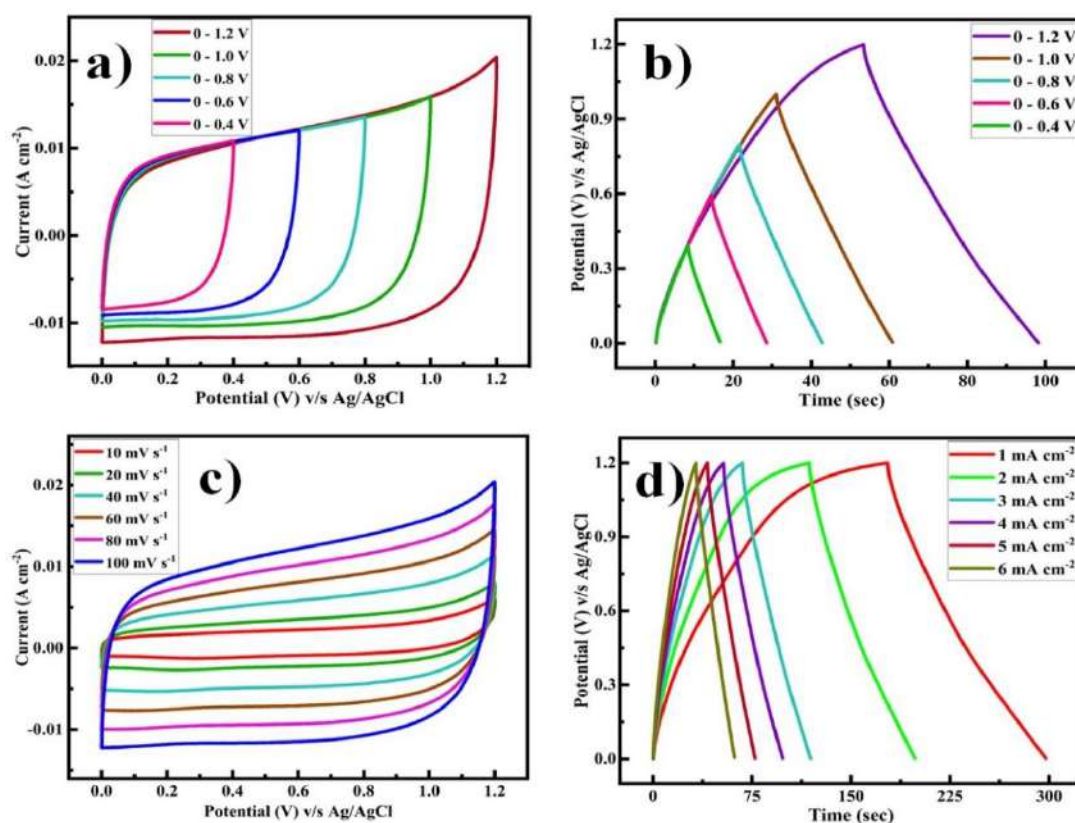


Figure 4.13: (a) CV, (b) GCD curves of the symmetric device within the various potential windows (0.4, 0.6, 0.8, 1.0, and 1.2 V), (c) CV curves of the symmetric device at different scan rates, (d) GCD curves of the symmetric device at different current densities

The EIS studies show that the fabricated SSC device has good electrical conductivity with low ionic resistance and a charge-transfer resistance of 0.4Ω , as depicted in Figure 4.14(a). As a result, the small semicircle diameter reveals low charge-transfer resistance and excellent conductivity. The specific capacities calculated from the discharge curves at current densities of 1, 2, 3, 4, 5, and 6 mA cm^{-2} were 94.92, 93.56, 91.83, 90.67, 89.44, and 87.74 F g^{-1} , respectively (Figure 4.14b). Figure 4.14(c) depicts the Ragone plot of the SSC device, and also the SSC device delivers a high energy density of $47.59 \text{ W h kg}^{-1}$ at a power density of $1367.42 \text{ W kg}^{-1}$. Additionally, at a current density of 6 mA cm^{-2} , the SSC device exhibits outstanding cycling performance, with 99.26% capacitance retention even after 3000 cycles (Figure 4.14d).

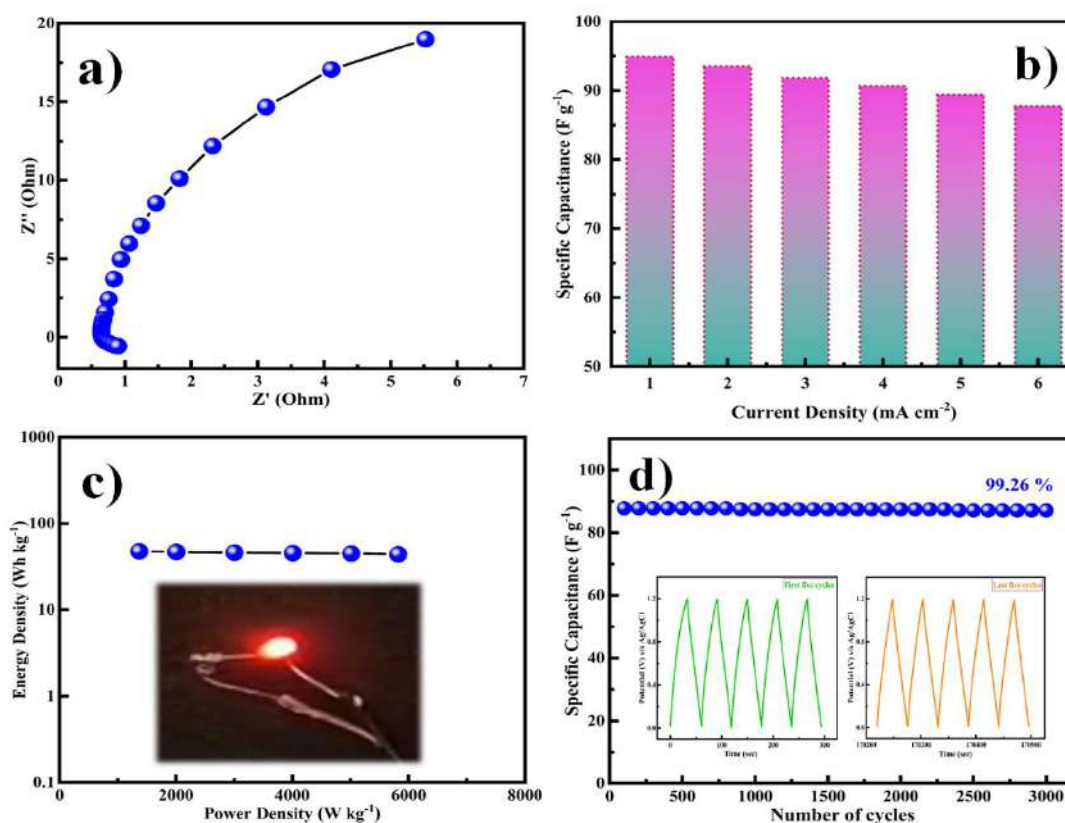


Figure 4.14: (a) Nyquist plot, (b) Variation of specific capacitance as a function of current density, (c) Ragone plot showing the energy density versus power density, (d) Cycling performance at 6 mA cm^{-2} , and the inset shows the first and last five cycles of the symmetric device

Power density and energy density are critical parameters for assessing the supercapacitor electrochemical performance. The BDC-MOF architecture exceptional electrochemical performance is due to its distinct hierarchical structure. Good

electrochemical activity is ensured by the uniform distribution of the brick-like morphology of the nanoplates, and the electrolyte's hierarchical structure offers a high SSA that can make sufficient contact with the electrolyte and enhance ion transport. Finally, the distinct hierarchical structure of the BDC-MOF architecture reduces volume expansion during the cycle process, improving structural integrity and enhancing cycle stability.

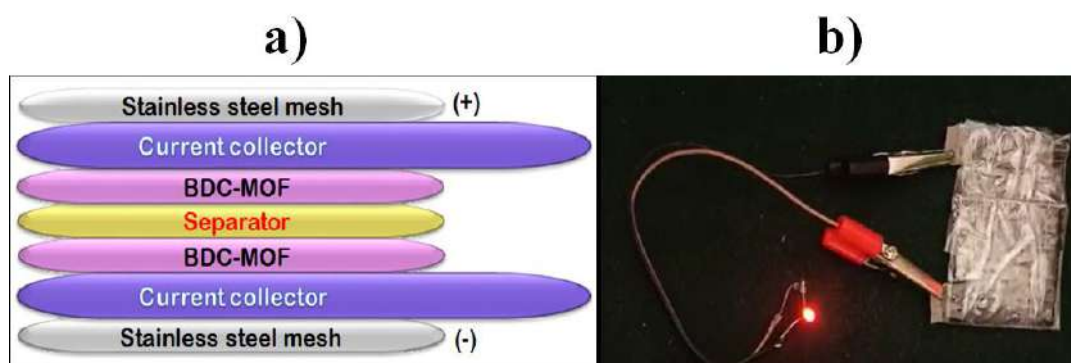


Figure 4.15: (a) Fabrication schematic of BDC-MOF//2M KOH//BDC-MOF symmetric supercapacitor device, (b) Two handmade symmetric supercapacitor device which glows a red LED

The lighting red light-emitting diode (LED) shows that how our SSC device can be used in real applications by connecting two of them in series (where each device is of size 2×2 cm). Figure 15a shows the schematic presentation of the SSC device, and Figure 4.15(b) displays the device's digital image. The LED was glowing brilliantly for about a minute after the device had been charged for just 2 s, demonstrating the astonishing application of our solid-state SSC devices (Supporting Information). The developed capacitor is suitable for use in real-world energy storage and transfer applications because the discharge time is longer than the charging time.

The electrochemical behavior of chemically produced trimetallic MOFs was compared using a radar graph, as shown in Figure 4.16. Each vertex indicates the properties of the different trimetallic MOFs, such as crystallite size, specific capacitance, energy density, power density, stability, charge-transfer resistance, SSA, and average pore radius. The electrochemical performance of trimetallic MOFs is represented by the integral area under the curve. According to Figure 4.16, the integral area of BDC-MOF is greater than that of BTC-MOF. It has been established that the BDC-MOF small crystallite size, large SSA, and low charge-transfer

resistance come up with increased specific capacitance, energy density, power density, and cycle stability.

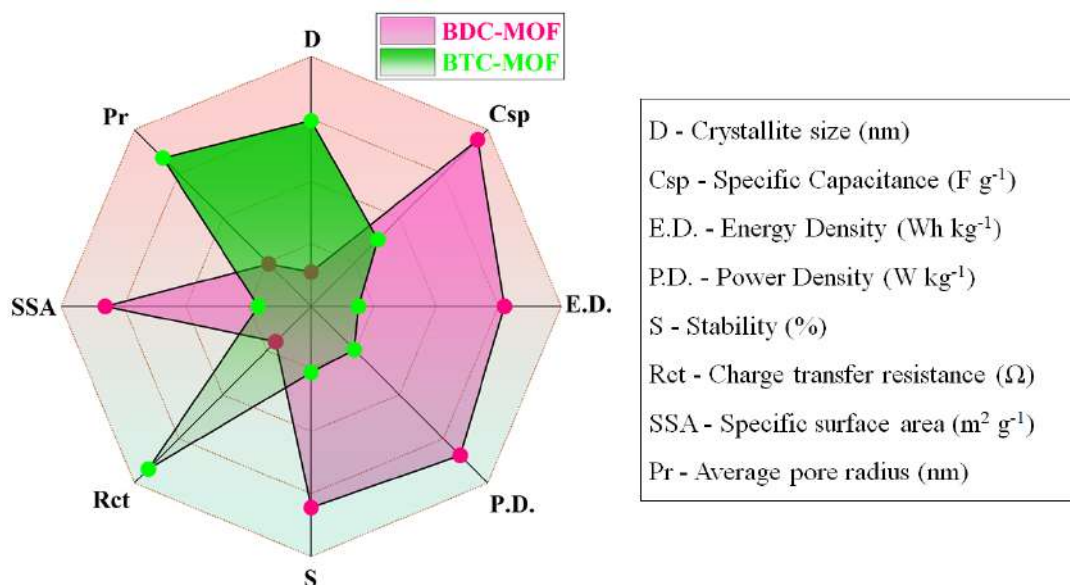


Figure 4.16: Radar graph for comparative study of BDC-MOF and BTC-MOF based on supercapacitive properties

4.5 Conclusion

In outline, a novel 2D architecture of trimetallic MOFs (BDC-MOF and BTC-MOF) as supercapacitor electrode materials was successfully prepared by the reflux condensation method which is simple, low cost, and environmentally friendly. The effects of different ligands of MOFs on the structural, surface, and electrochemical performance of MOF samples have been studied systematically. Due to their nanoplate-like structures with good mechanical and electrical contact, rich redox reactions, low crystallinity, good tuneability, high conductivity and transport rate for both electrolyte ions and electrons, and lower acidity, BDC-MOFs exhibit improved electrochemical performance. The BDC-MOFs show higher capacitance due to the synergistic effect, also they exhibit pseudocapacitive behavior due to the redox activity of metal cations inside MOFs, which offers a channel for electrons, as well as EDLC behavior due to the organic linker structure, which facilitates charge transfer within the framework. The BDC-MOF electrode material achieves a good SSA of 265.87 m² g⁻¹, specific capacity of 582.8 F g⁻¹ at a current density of 5 mA cm⁻², and exceptional cycling stability with 92.44% retention after 3000 cycles at 25 mA cm⁻² due to its porous nature and adequate SSA. The SSC device BDC-MOF//BDC-MOF was built with the BDC-MOF as both electrodes have a high energy density of 47.59

W h kg⁻¹ at a power density of 1367.42 W kg⁻¹ and exceptional cycling stability with 99.26% capacitance retention over 3000 cycles. This novel 2D trimetallic MOF electrode synthesis technique throws light on prospective high-performance MOF-based electrode materials, with the generated BDC-MOF serving as a promising electrode material for better energy storage devices. It is necessary to further enhance the MOF thermal, mechanical, and chemical stability. Since most MOFs decompose and have their skeletons collapse in water, acid, or base, their widespread use in energy storage applications has been severely hampered. Sensible selection of organic ligands and metal secondary building blocks can overcome this issue. The inherent fragility and finite processability of MOFs may also be overcome by using novel methods, such as pressing and phase change treatment operations, without changing their original properties.

4.6 References

- 1 C. Wei, L. Tan, Y. Zhang, Z. Wang, B. Xi, S. Xiong and J. Feng, *EnergyChem.*, 2022, **4**, 100089-100120.
- 2 A. Ray, A. Roy, S. Saha, M. Ghosh, S. Roy Chowdhury, T. Maiyalagan, S. K. Bhattacharya and S. Das, *Langmuir*, 2019, **35**, 8257–8267.
- 3 N. Swain, B. Saravanakumar, M. Kundu, L. Schmidt-Mende and A. Ramadoss, *J. Mater. Chem. A*, 2021, **9**, 25286-25324.
- 4 P. K. Katkar, S. J. Marje, V. G. Parale, C. D. Lokhande, J. L. Gunjekar, H. H. Park and U. M. Patil, *Langmuir*, 2021, **37**, 5260–5274.
- 5 R. Mehek, N. Iqbal, T. Noor, M. Z. B. Amjad, G. Ali, K. Vignarooban and M. A. Khan, *RSC Adv.*, 2021, **11**, 29247–29266.
- 6 X. Zhao, Q. Bi, C. Yang, K. Tao and L. Han, *Dalt. Trans.*, 2021, **50**, 15260–15266.
- 7 D. P. Chatterjee and A. K. Nandi, *J. Mater. Chem. A*, 2021, **9**, 15880–15918.
- 8 Y. A. Sun, L. T. Chen, S. Y. Hsu, C. C. Hu and D. H. Tsai, *Langmuir*, 2019, **35**, 14203–14212.
- 9 G. A. Tafete, M. K. Abera and G. Thothadri, *J. Energy Storage*, 2022, **48**, 103938-103953.
- 10 W. Song, X. Teng, Y. Liu, J. Wang, Y. Niu, X. He, C. Zhang and Z. Chen, *Nanoscale*, 2019, **11**, 6401–6409.
- 11 Y. Bai, C. Liu, T. Chen, W. Li, S. Zheng, Y. Pi, Y. Luo and H. Pang, *Angew. Chemie - Int. Ed.*, 2021, **60**, 25318–25322.
- 12 J. Acharya, G. P. Ojha, B. Pant and M. Park, *J. Mater. Chem. A*, 2021, **9**, 23977–23993.
- 13 X. Cheng, J. Pan, Y. Zhao, M. Liao and H. Peng, *Adv. Energy Mater.*, 2018, **8**, 1702184–2170220.
- 14 X. Lu, M. Yu, G. Wang, Y. Tong and Y. Li, *Energy Environ. Sci.*, 2014, **7**, 2160–2181.
- 15 X. Yin, H. Li, R. Yuan and J. Lu, *J. Colloid Interface Sci.*, 2021, **586**, 219–232.
- 16 M. U. Tahir, H. Arshad, H. Zhang, Z. Hou, J. Wang, C. Yang and X. Su, *J. Colloid Interface Sci.*, 2020, **579**, 195–204.
- 17 W. Li, X. Guo, P. Geng, M. Du, Q. Jing, X. Chen, G. Zhang, H. Li, Q. Xu, P. Braunstein and H. Pang, *Adv. Mater.*, 2021, **33**, 1–9.

- 18 S. Zheng, Q. Li, H. Xue, H. Pang and Q. Xu, *Natl. Sci. Rev.*, 2020, **7**, 305–314.
- 19 Y. Jiao, J. Pei, D. Chen, C. Yan, Y. Hu, Q. Zhang and G. Chen, *J. Mater. Chem. A*, 2017, **5**, 1094–1102.
- 20 S. Akhter, N. K. Mohd Zain, M. Shalauddin, V. K. Singh, I. I. Misnon, R. K. Sharma, S. Das, W. J. Basirun, M. R. Johan and R. Jose, *Sensors Actuators, A Phys.*, 2021, **325**, 112711-112722.
- 21 K. D. Modibane, *Curr. Opin. Electrochem.*, 2022, **36**, 101112–101121.
- 22 C. Kang, L. Ma, Y. Chen, L. Fu, Q. Hu, C. Zhou and Q. Liu, *Chem. Eng. J.*, 2022, **427**, 131003-131103.
- 23 D. Taherinia, H. Hatami and F. Mirzaee Valadi, *J. Electroanal. Chem.*, 2022, **922**, 116720-116729.
- 24 X. G. Han, P. F. Wang, Y. H. Zhang, H. Y. Liu, J. J. Tang, G. Yang and F. N. Shi, *Inorganica Chim. Acta*, 2022, **536**, 120916-120927.
- 25 B. Zhang, S. Song, W. Li, L. Zheng and X. Ma, *Ionics*, 2021, **27**, 3553–3566.
- 26 X. Luo, R. Abazari, M. Tahir, W. K. Fan, A. Kumar, T. Kalhorizadeh, A. M. Kirillov, A. R. Amani-Ghadim, J. Chen and Y. Zhou, *Coord. Chem. Rev.*, 2022, **461**, 214505-214529
- 27 H. Wang, J. Li, K. Li, Y. Lin, J. Chen, L. Gao, V. Nicolosi, X. Xiao and J. M. Lee, *Chem. Soc. Rev.*, 2021, **50**, 1354–1390.
- 28 R. Rajak, R. Kumar, S. N. Ansari, M. Saraf and S. M. Mobin, *Dalt. Trans.*, 2020, **49**, 11792–11818.
- 29 Y. Seo, P. A. Shinde, S. Park and S. Chan Jun, *Electrochim. Acta*, 2020, **335**, 135327–135336.
- 30 G. Nagaraju, S. C. Sekhar, B. Ramulu, S. K. Hussain, D. Narsimulu and J. S. Yu, *Nano-Micro Lett.*, 2021, **13**, 1–18.
- 31 Z. Andikaey, A. A. Ensafi, B. Rezaei, S. S. Malek and J. S. Hu, *New J. Chem.*, 2021, **45**, 18090–18101.
- 32 R. Bhosale, S. Bhosale, P. Kumbhar, D. Narale, R. Ghaware, C. Jambhale and S. Kolekar, *New J. Chem.*, 2023, **47**, 6749–6758.
- 33 S. Liu, S. C. Lee, U. Patil, I. Shackery, S. Kang, K. Zhang, J. H. Park, K. Y. Chung and S. Chan Jun, *J. Mater. Chem. A*, 2017, **5**, 1043–1049.
- 34 H. Vijeth, S. P. Ashokkumar, L. Yesappa, M. Niranjana, M. Vandana and H. Devendrappa, *RSC Adv.*, 2018, **8**, 31414–31426.
- 35 S. Gopi, S. Perumal, E. M. Al Olayan, O. D. AlAmri, A. S. Aloufi, M.

- Kathiresan and K. Yun, *Chemosphere*, 2021, **267**, 129243–129254.
- 36 Y. Li, M. Lu, Y. Wu, H. Xu, J. Gao and J. Yao, *Adv. Mater. Interfaces*, 2019, **6**, 1900290–1900298.
- 37 M. M. Vadiyar, S. S. Kolekar, N. G. Deshpande, J. Y. Chang, A. A. Kashale and A. V. Ghule, *Ionics*, 2017, **23**, 741–749.
- 38 N. K. Gupta, S. Kim, J. Bae and K. S. Kim, *RSC Adv.*, 2021, **11**, 4890–4900.
- 39 S.-M. You, W. M. A. El Rouby, L. Assaud, R.-A. Doong and P. Millet, *Hydrogen*, 2021, **2**, 58–75.
- 40 H. Li, J. Qin, Y. Zhang, S. Xu, J. Du and J. Tang, *RSC Adv.*, 2018, **8**, 39352–39361.
- 41 Q. Zha, M. Li, Z. Liu and Y. Ni, *ACS Sustain. Chem. Eng.*, 2020, **8**, 12025–12035.
- 42 V. H. Nguyen, T. D. Nguyen and T. Van Nguyen, *Top. Catal.*, 2020, **63**, 1109–1120.
- 43 R. Kaur, M. Chhibber, P. Mahata and S. K. Mittal, *ChemistrySelect*, 2018, **3**, 3417–3425.
- 44 K. S. W. Sing, D. H. Everett, R. A. W. Haul, L. Moscou, R. A. Pierotti, J. Rouquerol, T. Siemieniewska, (Recommendations 1984). *Pure Appl. Chem.* 1985, **57**, 603–619.
- 45 N. K. Mohd Zain, C. Karupiah, I. I. Misnon, S. Das, K. Ikechukwu Ozoemena, C. C. Yang and R. Jose, *Electroanalysis*, 2020, **32**, 3180–3188.
- 46 L. G. Beka, X. Bu, X. Li, X. Wang, C. Han and W. Liu, *RSC Adv.*, 2019, **9**, 36123–36135.
- 47 H. Shu, T. Lai, J. Ren, X. Cui, X. Tian, Z. Yang, X. Xiao and Y. Wang, *Nanotechnology*, 2022, **33**, 135502–135517.
- 48 P. Thangasamy, S. Shanmuganathan and V. Subramanian, *Nanoscale Adv.*, 2020, **2**, 2073–2079.
- 49 Y. Wu, X. Song, S. Xu, Y. Chen, O. Oderinde, L. Gao, R. Wei and G. Xiao, *Dalt. Trans.*, 2020, **49**, 312–321.
- 50 J. Lin, C. Zeng, X. Lin, R. C. K. Reddy, J. Niu, J. Liu and Y. Cai, *ACS Sustain. Chem. Eng.*, 2019, **7**, 15660–15670.
- 51 Y. ping Wei, Y. wen Zhang, J. S. Chen, C. jie Mao and B. K. Jin, *Microchim. Acta*, 2020, **187**, 1–9.
- 52 M. R. Manikandan, K. P. Cai, Y. D. Hu, C. L. Li, J. T. Zhang, Y. P. Zheng, Y.

- F. Liang, H. R. Song, M. Y. Shang, X. N. Shi, J. X. Zhang, S. Q. Yin, S. Y. Shang and X. W. Wang, *Appl. Phys. A Mater. Sci. Process.*, 2021, **127**, 421–431.
- 53 W. W. Song, B. Wang, C. N. Li, S. M. Wang and Z. B. Han, *J. Mater. Chem. A*, 2022, **10**, 3710–3721.
- 54 G. Mouchaham, S. Wang and C. Serre, *Metal-Org. Frameworks: Applications in Separations and Catalysis*, 2018, 1–28.
- 55 M. Suksomboon, P. Srimuk, A. Krittayavathananon, S. Luanwuthi and M. Sawangphruk, *RSC Adv.*, 2014, **4**, 56876–56882.
- 56 M. Ashourdan, A. Semnani, F. Hasanpour, S. E. Moosavifard, *J. Electroanal. Chem.* 2021, **895**, 115452-115463.
- 57 Y. Zhu, Z. Tao, C. Cai, Y. Tan, A. Wang, Y. Yang, *Inorg. Chem. Commun.* 2022, **139**, 109391-109400.
- 58 X. Zhang, J. Wang, X. Ji, Y. Sui, F. Wei, J. Qi, Q. Meng, Y. Ren, Y. He, D. Zhuang, *J. Mater. Sci. Mater. Electron.* 2020, **31**, 16260–16268.
- 59 X. Kang, J. Wang, Y. Ma, X. Shi, X. Chen, H. Tian, F. Ran, *J. Solid State Chem.* 2022, **310**, 123056-123067.

CHAPTER FIVE

Bimetallic MnFe₂-MOF and Its Derived MnFe₂O₄ Nanostructures for Supercapacitive Applications

5.1 Outline

At present, supercapacitor (SC) based on metal-organic frameworks (MOFs) has gained a lot of attention in energy storage and conversion application because of their fascinating properties such as low densities, variable chemical functions, high surface area, and porosity. The chapter covers the synthesis of bimetallic MOF and MOF-derived ferrites via chemically wet route and heat treatment process respectively. This prepared electrode material was utilised to construct the asymmetric supercapacitor devices. The MnFe₂-MOF electrode exhibits outstanding electrochemical properties over the derived MnFe₂O₄ along with high reversibility, fast kinetics, low charge transfer resistance (2.9 Ω), the excellent specific capacitance of 1226 F g⁻¹ at a current density of 1 A g⁻¹ with a superb cyclic stability of approximately 95.68 % of the initial capacitance even after 3000 subsequent charge-discharge cycles. Additionally, to confirm the practical viability of MnFe₂-MOF as an anode and activated carbon as a cathode, an asymmetric device was fabricated. The fabricated asymmetric device demonstrates an excellent specific capacitance of 91.87 F g⁻¹ at a 1 mA cm⁻² current density with a specific energy of 32.67 Wh kg⁻¹ and a high specific power of 1000 W kg⁻¹. Simultaneously, the fabricated ASC device unveil exceptional cyclic stability (98.52 %) and coulombic efficiency (96.75 %) of at a higher current density of 8 mA cm⁻² even after 3000 charge-discharge cycles. These perceptible results based on MOF-derived ferrite nanostructure can make it significant electrode material for supercapacitor application in today's technological applications.

5.2 Introduction

Energy storage technologies are being developed rapidly to fulfil global demand owing to the exhaustion of fossil fuels and associated environmental problems. To meet the long-term development demands of our civilization, the use of inexhaustible energies like solar, tidal, and wind in energy infrastructure has increased dramatically. Nevertheless, because sustainable energies are intermittent, the electricity produced from them cannot be straight away connected to the power system.¹⁻³ Hence, the construction of reliable and effective electrical energy storage (EES) systems is urgently required. Innovative energy storage systems and next-generation energy storage and conversion technologies have successfully been developed through study and exploration. The SC (electrochemical capacitor), a new kind of energy storage component in the middle of rechargeable batteries and conventional capacitors. It is utilized extensively in the fields of electronic appliances, defence, automobiles, communication technologies etc. due to its benefits of quick charge and discharge, enduring lifespan, high power potential, strong rate performance, energy savings, and environmental protection.⁴⁻⁷ Supercapacitors are still limited in their utility in many real-world scenarios because of their poor energy density. By utilizing porous materials in supercapacitors, it has been attempted to boost energy density by enhancing specific capacitance and extending the operating potential window of electrode materials.^{8,9}

Metal-organic frameworks are crystalline porous materials with attractive features like enormous surface area, well-defined crystalline structure, low density and effortlessly tunable structure and highly organized pores/channels. Metal-ligand coordination, metal cluster copolymerization, and interactions between hydrogen bonds have all been used as a scheme for assembling these frameworks. Several similar frameworks have been discovered to display favourable zeolitic characteristics like stability and microporosity.^{10,11} MOFs have been regarded as useful predecessors or sacrificial templates to produce unique porous nanomaterials with attractive features because of their varied topologies.^{12,13} Ferrites are appealing materials owing to their remarkable magnetic, electrical, and optical characteristics, also their capacity to show many redox states and electrochemical stability.

Throughout transition metal oxide derived from MOFs, iron-based MOF-derived transition metal oxides have superior electrical conductivity and much lower

charge activation energies. It has mixed valencies Fe²⁺ and Fe³⁺ which contribute to enhancing electrical conductivity.¹⁴⁻¹⁷ Patil et al. synthesized NiFe₂O₄ derived from NiFe₂ MOF using a solvothermal method followed by a heating process i.e. annealing. They have observed different morphologies like grains, mesh-like structures and threads at 550 °C (NFO550), 500 °C (NFO 500) and 460 °C (NFO460), respectively; hence morphology has been greatly influenced by the annealing temperatures. The NiFe₂O₄ electrode annealed at 500 °C (NFO500) temperature shows sharp-edged rhombus nanoplates with an interwoven mesh-like structure with mesoporous nature of the surface area of 38.17 m² g⁻¹. The NFO500 electrode derived from MOF shows the highest specific capacitance as compared to NFO460 and NFO550 electrodes. The NFO500 electrode reveals 833 F g⁻¹ specific capacitance at 0.25 A g⁻¹ current density with an outstanding capacitance retention of 74 % even after 3000 charge-discharge cycles at 3 A g⁻¹ current density. The mesh-like architecture that allows the migration of OH⁻ ions within the electrode and the small recombination resistance among the electrode and electrolyte contact are responsible for the good electrochemical performance of MOF-derived NFO500 in comparison to NFO460 and NFO550 electrodes. This research has the doors to modifying the morphologies of nanostructures produced from MOF for supercapacitor applications.¹⁸ Safari et al. synthesized Fe₂Co-MOF derived cobalt ferrite (CoFe₂O₄) nanostructured using a simple ultrasonic-assisted solvothermal method followed by calcination. During thermal treatment at 450 °C in air, the spindle shape of Fe₂Co-MOF converts into the yolk-shell morphology of CoFe₂O₄. The specific capacitance of Fe₂Co-MOF and CoFe₂O₄ electrodes are 489.9 and 192.6 F g⁻¹ at 1 A g⁻¹ current density, respectively, owing to a decrease in active sites on the CoFe₂O₄ electrode and low metal oxide conductivity. The cyclic stability of Fe₂Co-MOF and CoFe₂O₄ electrodes was investigated at 10 A g⁻¹ current density for 3000 cycles. The retention rates for Fe₂Co-MOF and CoFe₂O₄ electrodes were 92 % and 90 %, respectively. Further, they have fabricated an asymmetric supercapacitor device using Fe₂Co-MOF and activated carbon electrodes as anode and cathode respectively, which demonstrated that constructed electrodes are well-suited for energy storage applications.¹⁹

There are numerous reports for the synthesis of iron based bimetallic MOFs by using simple one-pot solvothermal reaction for exotics applications. However, to the best of our knowledge the synthesis of MnFe₂-MOF via reflux condensation method for energy storage application has not been reported so far. Inspired of this, the porous

magnetic MnFe₂O₄ has been successfully synthesized using a MnFe₂-MOF as a self-sacrificing template as well as predecessor. The synthesis comprises merely a simple reflux condensation to form MnFe₂-MOF, subsequent thermal annealing in air. Furthermore, the synthesized MnFe₂-MOF was employed as an electrode material for electrochemical experiments. MnFe₂-MOF showed a greater specific capacitance value than the rest of the sample. Furthermore, the fabricated asymmetric device shows an excellent specific capacitance of 91.87 F g⁻¹ at a 1 mA cm⁻² current density with a maximum specific energy of 32.67 Wh kg⁻¹ and a high specific power of 1000 W kg⁻¹.

5.3 Experimental section

5.3.1 Materials

Ferrous chloride tetrahydrate (FeCl₂·4H₂O) was purchased from Merck, USA. Terephthalic acid, N-Methyl-2-pyrrolidone (NMP) and polyvinylidene fluoride (PVDF) were purchased from Sigma-Aldrich, USA. Manganese chloride tetrahydrate (MnCl₂·4H₂O) and Acetylene black were obtained from, Loba Chemie, India and Alfa Aesar, USA respectively. All reagents were used without any further purification.

5.3.2 Synthesis of MnFe₂-MOF and MnFe₂O₄

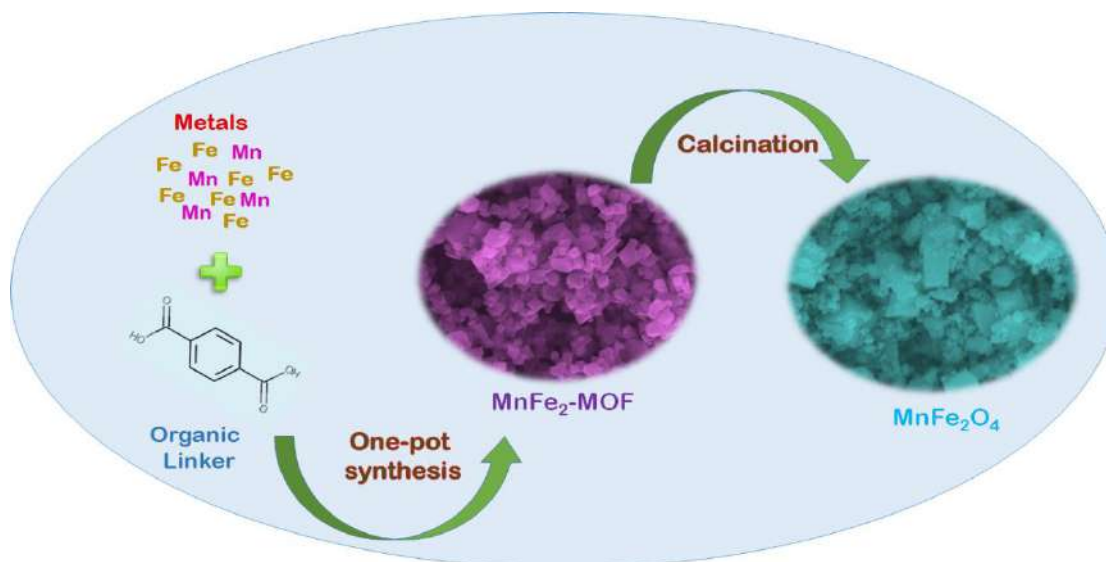


Figure 5.1: Schematic diagram of MnFe₂-MOF derived manganese ferrite (MnFe₂O₄)

The Mn/Fe metal-organic framework (MnFe₂-MOF) was synthesized by using a typical procedure. 0.1 M manganese chloride tetrahydrate and 0.2 M ferrous chloride tetrahydrate were dissolved in 25 ml N, N-dimethylformamide (DMF), and stirred well. 0.2 M terephthalic acid was then dissolved in 25 ml N, N-dimethylformamide (DMF) and add to it above metal salt solution. Then, after stirring

the solution for 10 min it was transferred to a round bottom flask maintained at 120 °C for 12 h. The subsequent brown-colored precipitate was collected by a DMF washing and drying process at 70 °C overnight and was referred as MnFe₂-MOF. The MOF-derived manganese ferrite (MnFe₂O₄) was prepared by thermal heating i.e. annealing of MnFe₂-MOF at 500 °C for 2 h in air and cooled at ambient temperature. Figure 5.1 shows the schematic presentation of synthesis of MnFe₂-MOF and its derived MnFe₂O₄.

5.3.3 Structural and elemental characterization

Crystal structure and phase purity of MnFe₂-MOF and derived MnFe₂O₄ were investigated by Bruker D8 Phaser X-ray diffractometer with Cu K α radiation ($\lambda=0.1541$ nm). The Perkin Elmer 1760X spectrophotometer was used to record Fourier Transform Infrared spectra between 400 and 4000 cm⁻¹. Raman spectra of MnFe₂-MOF and derived MnFe₂O₄ samples were studied by Renishaw in via Raman spectrometer by using a He-Ne (633 nm) laser excitation source. The surface morphology and elemental confirmation of the prepared samples were obtained from scanning electron microscopy and Energy dispersive X-ray Analysis spectrometer (EDAX, Oxford Instrumentations inbuilt with FE-SEM). Also, the surface morphology with d-spacing of the MnFe₂-MOF and derived MnFe₂O₄ samples were found by using transmission electron microscopy (TEM) analysis from Hitachi/HF-3300 TEM (300 kV). The oxidation states of the metals in the MnFe₂-MOF and derived MnFe₂O₄ was investigated using X-ray photoelectron spectroscopy (XPS) with a Thermo Fisher Scientific SIGMA PROBE. The porosity of the materials was investigated on NOVA1000e Quantachrome (BET), USA. The magnetic behavior of the MnFe₂-MOF and derived MnFe₂O₄ samples were investigated by using Vibrating-sample magnetometer (VSM) from superconducting quantum interference device (SQUID) vibrating sample magnetometry (VSM) (Quantum Design, USA).

5.3.4 Electrochemical properties evaluation and preparation of working electrodes

All electrochemical measurements were carried out on an electrochemical workstation (CHI 608E, CH instrument co., LTD, USA) for parameters like cyclic voltammograms (CV), galvanostatic charge-discharge (GCD), and electrochemical impedance spectra (EIS) at ambient temperature in 1 M Na₂SO₄ as a neutral electrolyte. The working electrodes were made by using a composition of 80:10:10 weight % of active material (MnFe₂-MOF and MnFe₂O₄), acetylene black and

polyvinylidene fluoride in N-Methyl-2-pyrrolidone as a solvent respectively to prepare a homogeneous paste. The obtained homogenous paste was coated on an unprecedented substrate stainless steel mesh area of 1 x 1 cm² and dried in an oven at 70 °C for 10 hours and used as the current collector. A three-electrode setup was employed to evaluate the electrochemical properties of the prepared electrodes by using an active material loaded stainless steel mesh, graphite, and a saturated Ag/AgCl as the working electrode, counter electrode, and reference electrode, respectively. CV curves were measured at different scan rates ranging from 10 to 100 mV s⁻¹ and GCD curves were measured at various current densities ranging from 1 to 10 mA cm⁻² in the operating potential window of 0 to 0.5 V.^{20,21}

For solid-state supercapacitor device fabrication, a solid gel electrolyte was prepared, 20 ml of distilled water was used to dissolve 1 g of polyvinyl alcohol (PVA) while maintaining bath solution at 80°C for 30 minutes. The sticky gel electrolyte was prepared by adding the aqueous Na₂SO₄ solution dropwise to the above PVA solution and heated it at 80 °C for 30 minutes.²² A solid-state asymmetric supercapacitor device (MnFe₂-MOF//AC) was constructed by using MnFe₂-MOF and AC electrode as anode and cathode respectively, a filter paper and PVA-Na₂SO₄ gel was employed as a separator and it was assembled between the two electrodes. The electrodes effective area for the devices were 2 x 2 cm². CV was measured at different scan rates and GCD was measured at different current densities of asymmetric supercapacitor device in potential range of 0 - 1.6 V. Cyclic stability measurement was performed in the 0 - 1.6 V range for the asymmetric supercapacitor device.

The specific capacity, specific energy density and specific power density were determined from charge-discharge cycles of the fabricated asymmetric supercapacitor devices using equations 5.1 to 5.3,²³⁻²⁵

$$C_s = \frac{I \times \Delta t}{m \times \Delta V} \dots\dots\dots (5.1)$$

$$E = \frac{C_s \times (\Delta V)^2}{7.2} \dots\dots\dots (5.2)$$

$$P = \frac{E \times 3600}{\Delta t} \dots\dots\dots (5.3)$$

Where, ‘C_s’ is the specific capacity measured in F g⁻¹, ‘E’ is the specific energy density measured in Wh kg⁻¹, ‘P’ is the specific power density measured in W kg⁻¹, ‘I’ is the discharge current measured in ampere, ‘Δt’ is the discharge time

measured in seconds, ‘m’ is the mass of the electrode material measured in grams, ‘ΔV’ is the potential window measured in volt in the process.

5.4 Results and discussion

5.4.1 X-ray diffraction of MnFe₂-MOF and MnFe₂O₄

X-ray diffraction was used to investigate the structural analysis and crystallite size of the MnFe₂-MOF and its derived manganese ferrite, as depicted in figure 5.2. The peaks were observed at 9.32°, 9.86°, 17.8°, 25.46° and 33.42° for MnFe₂-MOF are in good agreement with the earlier reported MnFe₂-MOF.²⁶ MnFe₂O₄ pattern observed peaks at 30.34°, 35.5°, 42.88°, 53.98° and 62.32° are assigned to the crystal planes of (220), (311), (400) and (440) respectively. The XRD pattern of derived MnFe₂O₄ shows cubic phase which is well matched with the literature value (JCPDS card No. 10-0319).²⁷ There are no additional peaks that suggests the purity of the prepared samples. According to the Debye-Scherrer’s equation, the average crystallite size were 7.8 and 15.6 nm of MnFe₂-MOF and its derived MnFe₂O₄, respectively.²⁸

$$D = \frac{0.9\lambda}{\beta \cos \theta} \dots\dots\dots (5.4)$$

Where, D stands for crystalline size, λ stands for the wavelength of X-rays emitted from the target, θ stands for the Bragg diffraction angle of the diffraction peaks, and β stands for the full width at half maximum (FWHM) of the diffraction peak. The smallest crystallite size was observed for MnFe₂-MOF sample as compared to the derived sample, which is helpful for the charge transportation in application part.

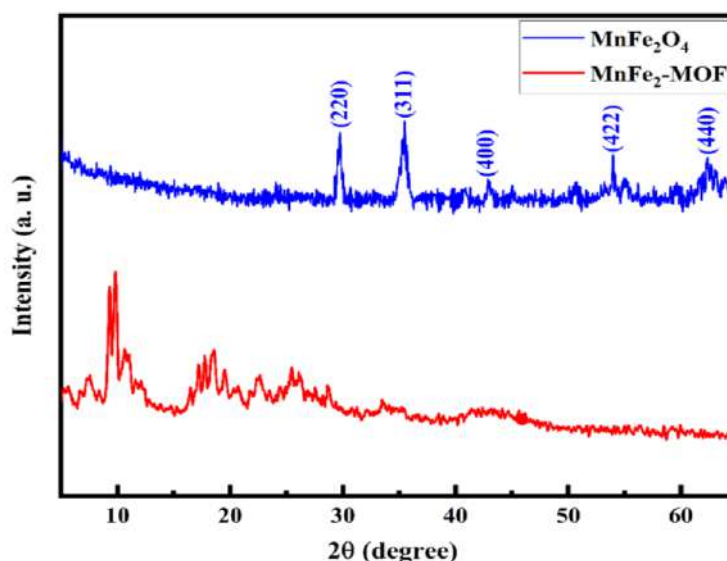


Figure 5.2: X-ray diffraction patterns of MnFe₂-MOF and its derived MnFe₂O₄

5.4.2 FT-IR spectroscopy of MnFe₂-MOF and MnFe₂O₄

To investigate the functional groups and molecular structure of the MnFe₂-MOF and its derivate MnFe₂O₄, Fourier transform infrared spectroscopy (FT-IR) was used. The FT-IR spectra of MnFe₂-MOF and its derived MnFe₂O₄ as shown in figure 5.3. In FT-IR spectra the absorption peaks at 1599 and 1379 cm⁻¹ in MnFe₂-MOF is attributed to the symmetric and asymmetric vibrations of the carboxylate group of ligand and the absorption band at 748 cm⁻¹ is assigned for C-H vibration of the benzene ring. Furthermore, the absorption peak appear at 534 cm⁻¹ in the MnFe₂-MOF spectrum indicate the oscillation of the metal-oxygen bonds.²⁹ In MnFe₂O₄ spectra, the peaks in the range of 400-600 cm⁻¹ are due to the Mn-O and Fe-O bonds of spinel form oxide.³⁰

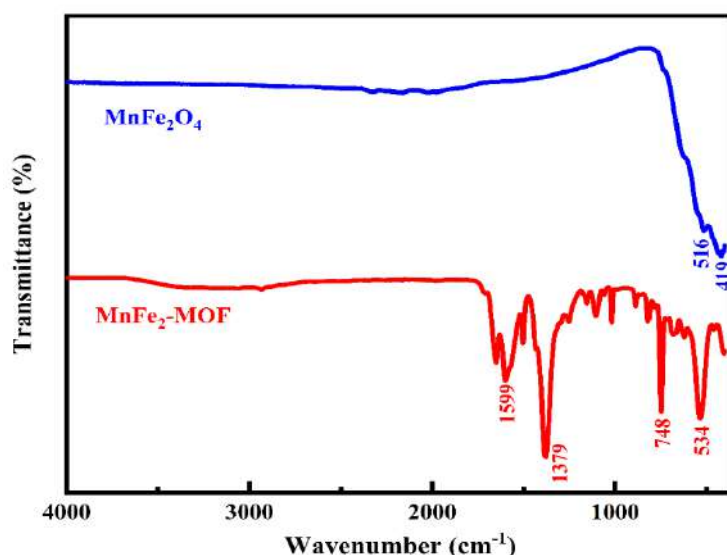


Figure 5.3: FT-IR spectra of MnFe₂-MOF and its derived MnFe₂O₄

5.4.3 Raman spectroscopy of MnFe₂-MOF and MnFe₂O₄

Raman spectroscopy study was used to explore the structural irregularities of MnFe₂-MOF and its derived MnFe₂O₄ at ambient temperature which is shown in figure 5.4. Raman spectra of MnFe₂-MOF shows a measurable peak at 1609 cm⁻¹ is assigned to the C=O stretching of carboxylate group, considering that the peaks at 1430 and 1140 cm⁻¹ are assigned to in-plane vibration modes of benzene ring and a small peak at 862 cm⁻¹ corresponds to the out-of-plane deformation of C-H bond.^{31,32} Raman spectra of MnFe₂O₄ shows four distinct peaks at 200-700 cm⁻¹ range as shown in figure 5.4. The noticeable four peaks in the spectrum at 217, 280, 391 and 595 cm⁻¹ are assigned to the stretching vibrational modes of MnFe₂O₄. And the peaks at 391 and 595 cm⁻¹ appear from E_g and T_{2g} vibrational modes, respectively.^{33,34}

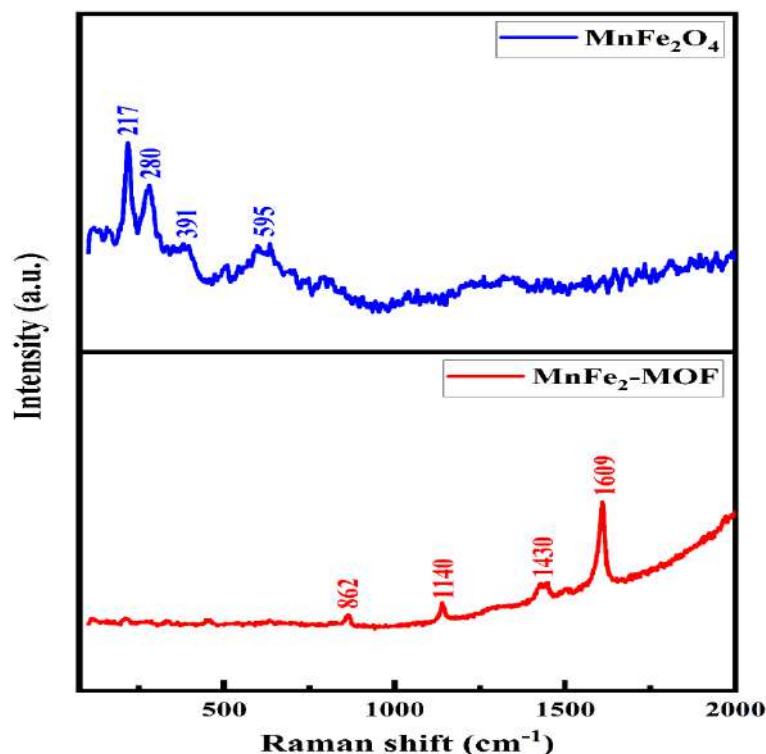


Figure 5.4: Raman spectra of MnFe₂-MOF and its derived MnFe₂O₄

5.4.4 Scanning electron microscopy of MnFe₂-MOF and MnFe₂O₄

The surface morphologies of the MnFe₂-MOF and its derived MnFe₂O₄ were characterized by SEM techniques and depicted in figure 5.5. It is observed that the cubic and bricks like morphology were obtained from MnFe₂-MOF and MnFe₂O₄, respectively as shown in figure 5.5(a-d). The lower and higher magnification of MnFe₂-MOF reveals that the size of the cube was irregular in shape but uniformity of the cubes was observed throughout the sample. Moreover, the surface of the cube became rougher and more porous in nature as shown in figure 5.5(a-b). The average length of the cube was measured to be approximately 200-300 nm in size. Also, more interestingly the voids are formed between the big cubes and small cubes. This voids and cube like morphology support in ion transfer and store more ions which were helpful for improving the electrochemical performance. Similarly, the SEM images of MnFe₂-MOF derived MnFe₂O₄ are as shown in figure 5.5(c-d) wherein, it was observed that the there is a bricks like morphology with some nanoparticles. Also, it was observed that bricks were irregular in shape as well as the cracks of the bricks converted into small pieces have adverse effect on the redox reaction. These bricks were compacted to each other and some of the space was covered by nanoparticles hence there were no voids for adsorption of electrolyte, resulting in the decrease in the

active surface area for redox reaction. Overall, it could be concluded that the MnFe₂-MOF is most favourable for improving the electrochemical performance of MnFe₂-MOF based supercapacitor electrode than MOF derived MnFe₂O₄ electrode.

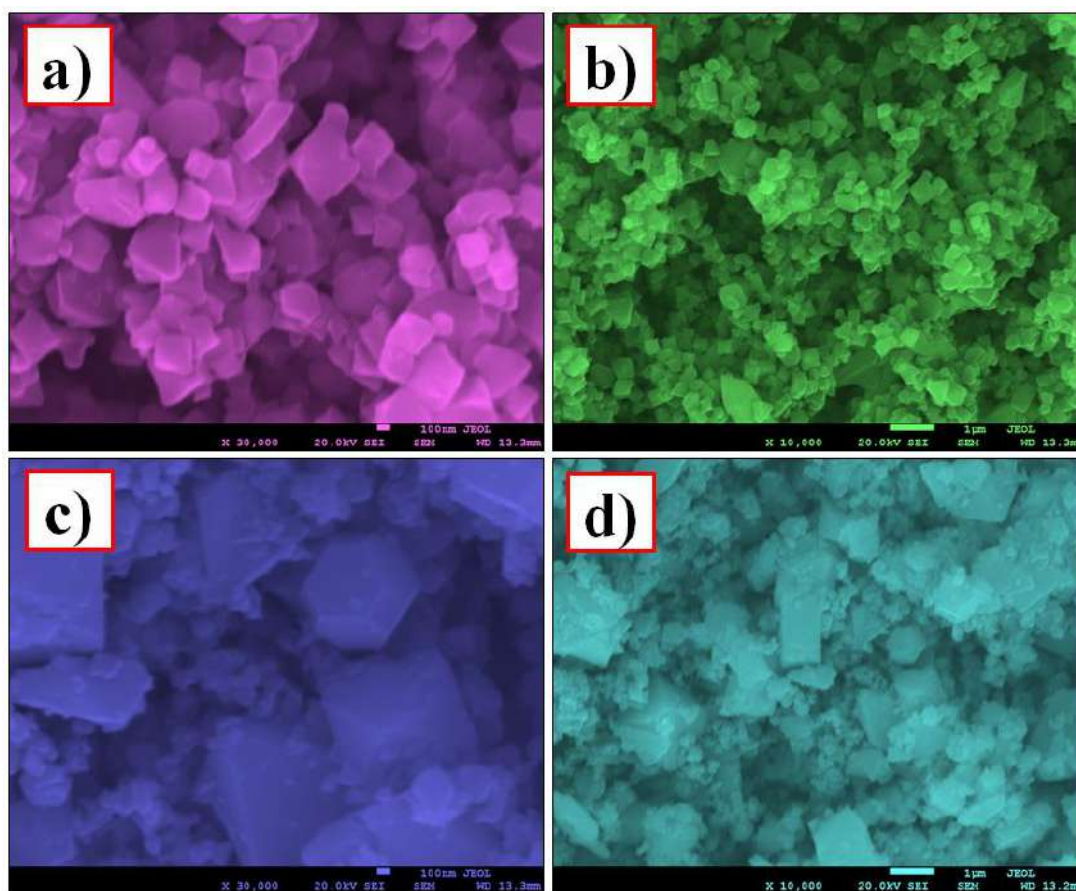


Figure 5.5: SEM images at different magnifications of (a, b) MnFe₂-MOF and (c, d) its derived MnFe₂O₄

5.4.5 Energy dispersive X-ray analysis of MnFe₂-MOF and MnFe₂O₄

The chemical composition and color mapping of MnFe₂-MOF and its derived MnFe₂O₄ were employed by using the EDX spectroscopy. The EDX spectrum and color mapping of both the samples are depicted in figure 5.6(a, b). From this spectrum, the elements like Mn, Fe, C, O and Mn, Fe, O were detected in the MnFe₂-MOF and its derived MnFe₂O₄ respectively. The atomic percentage of the corresponding elements is well distributed in resulting material. Hence, it was confirmed that our prepared samples were in the pure form and would be beneficial for energy storage applications.

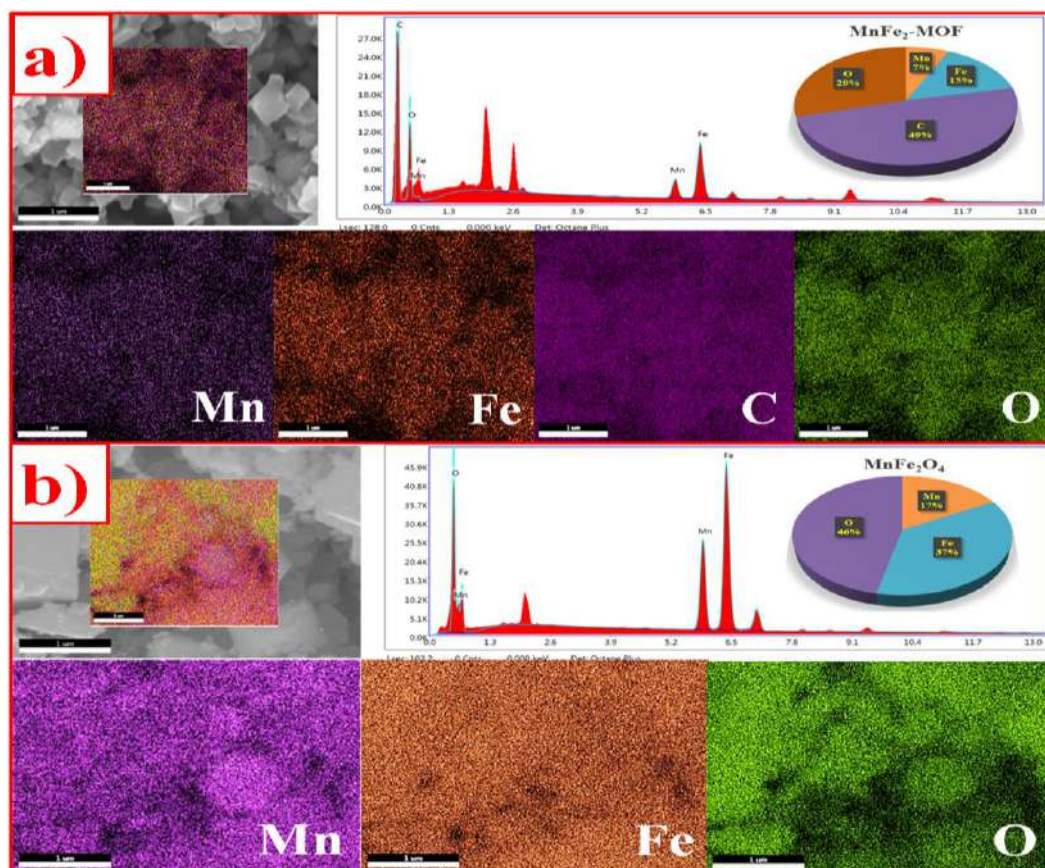


Figure 5.6: Elemental mapping images of (a) $MnFe_2-MOF$ and (b) its derived $MnFe_2O_4$

5.4.6 Transmission electron microscopy of $MnFe_2-MOF$ and $MnFe_2O_4$

The morphological and structural characteristics of $MnFe_2-MOF$ and its derived $MnFe_2O_4$ were investigated using TEM, HRTEM, and selected area electron diffraction (SAED). The TEM image in figure 5.7(a) indicates that the amorphous $MnFe_2-MOF$ s have a cubical shape with varying sizes, and the HRTEM images (Figure 5.7b, c) likewise demonstrates an amorphous nature due to the absence of apparent lattice fringes. Furthermore, a high-resolution TEM image revealed no indication of crystallinity, indicating that the particles were amorphous. The SAED pattern, as shown in figure 5.7(d), revealed only diffuse rings, implying that the as-synthesized $MnFe_2-MOF$ material is amorphous.³⁵ The TEM images of derived $MnFe_2O_4$ reveals the bricks like morphology with plenty of nanoparticles in it as shown in figure 5.7(e and f). The lattice fringe spacing in the accompanying HRTEM image as depicted in figure 5.7(g) is about 0.226 nm, which is consistent with the (311) plane of cubic $MnFe_2O_4$. The spinel cubic structure of $MnFe_2O_4$ is visible in the SAED pattern (Figure 5.7h), which is compatible with the XRD analysis and the

emergence of (220), (311), (400), (422) and (440) planes of material, indicating the formation of MnFe₂O₄.³⁶

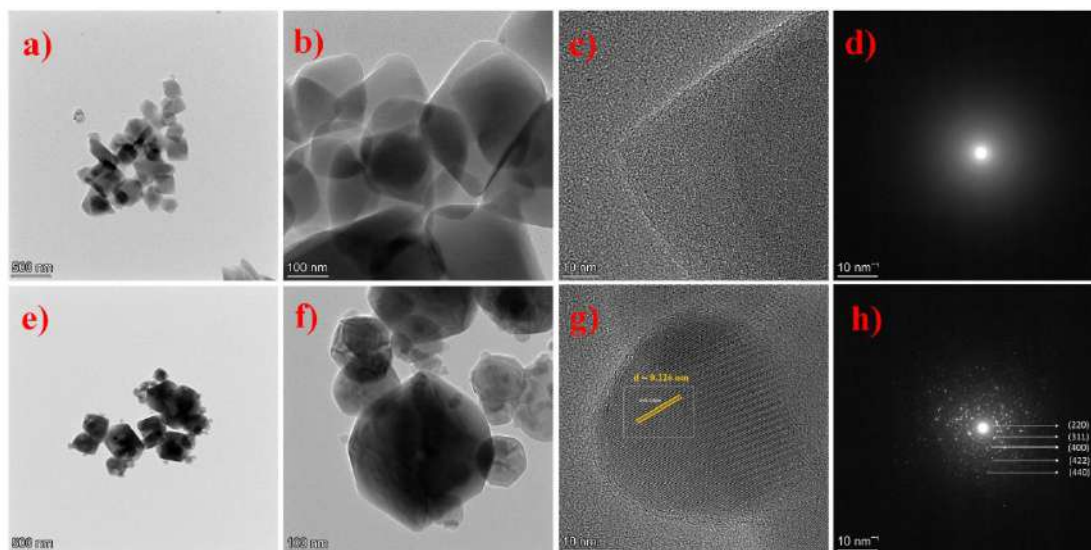


Figure 5.7: TEM, HR-TEM and SAED patterns of (a-d) MnFe₂-MOF and (e-h) its derived MnFe₂O₄

5.4.7 Brunauer-Emmett-Teller analysis of MnFe₂-MOF and MnFe₂O₄

The surface area is a crucial factor for effecting the storage capabilities of electrode materials because of its direct impact on the accessibility of reaction sites. Brunauer-Emmett-Teller analysis was used to study the surface area and porosity of the MnFe₂-MOF and its derived MnFe₂O₄. The N₂ adsorption/desorption isotherms and BJH pore size distribution curves of MnFe₂-MOF and its derived MnFe₂O₄ are depicted in figure 5.8. Figure 5.8(a, b) shows a typical type IV isotherm with hysteresis loop in a relative pressure (P/P₀) between 0.5 to 0.9 confirming the mesopores in the materials. The specific surface area of MnFe₂-MOF and its derived MnFe₂O₄ was determined to be 303 m² g⁻¹ and 263 m² g⁻¹, respectively. The results of the Barrett-Joyner-Halenda study showed a pore size distribution of MnFe₂-MOF and its derived MnFe₂O₄ at 16 nm and 24 nm, respectively. The MnFe₂-MOF with cubic morphology has the largest specific surface area compared to MnFe₂O₄, resulting in adsorption of electrolytes in the sites of the sample hence improved electrochemical properties. The average pore widths of MnFe₂-MOF and its derived MnFe₂O₄ were of mesopores nature that improves ion diffusion of materials and leads to better electrochemical performance.^{37,38}

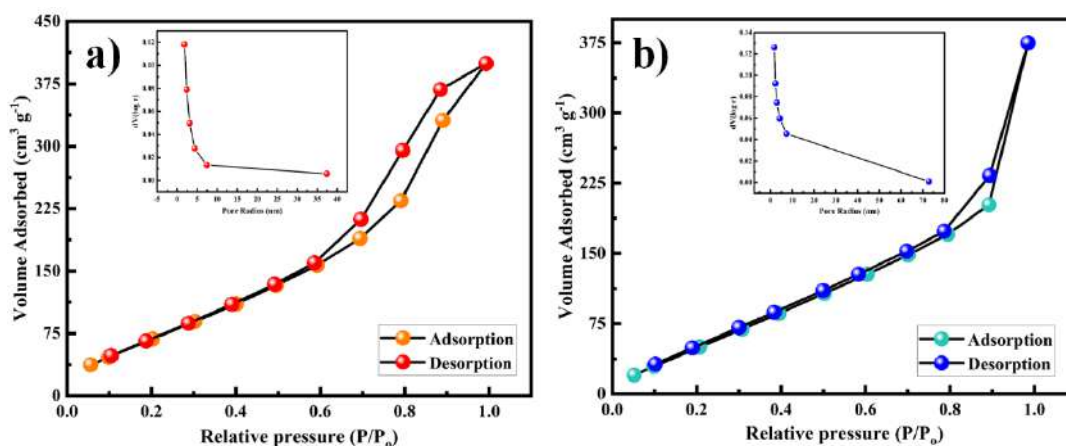


Figure 5.8: Nitrogen adsorption/desorption isotherms of (a) MnFe₂-MOF, (b) derived MnFe₂O₄ (the insets show pore size distribution)

5.4.8 Vibrating-sample magnetometer of MnFe₂-MOF and MnFe₂O₄

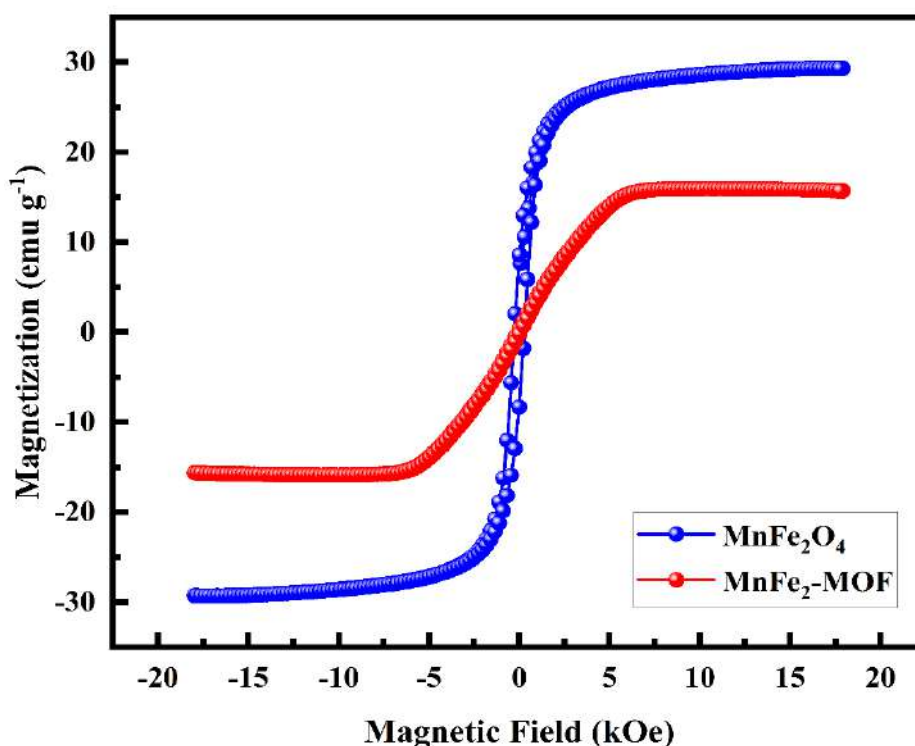


Figure 5.9: Hysteresis curves of MnFe₂-MOF and its derived MnFe₂O₄

The magnetization of the developed materials was measured using vibrating sample magnetometer (VSM) as a function of magnetic field. The samples MnFe₂O₄ and MnFe₂-MOF were subjected to extensive magnetic studies to examine the effect of functionalization on magnetic nanoparticles behaviour. Figure 5.9 displays the magnetization curves of the MnFe₂O₄ and MnFe₂-MOF at RT. Due to the non-saturating magnetization even at higher fields, the saturation magnetization (M_s) value was determined by fitting the M against 1/H curves. MnFe₂O₄ and MnFe₂-MOF

have Ms values of 29.324 and 15.917 emu g⁻¹, respectively. Thus, the Ms values plays vital role in supercapacitor application. The power density, energy density, and cyclic stability can be increased by the magnetic behavior of the nanomaterials. The charge/discharge behaviour of the materials is influenced by the magnetic field effect on electric diffusion and the shape of the EDLC charge transfer resistance.³⁹ The specific surface area, porosity, and the magnetic behavior of the MnFe₂-MOF sample would be beneficial for supercapacitor application.

5.4.9 X-ray photoelectron spectroscopy of MnFe₂-MOF and MnFe₂O₄

X-ray photoelectron spectroscopy investigate the chemical compositions of both the MnFe₂-MOF and its derived MnFe₂O₄, as shown in figure 5.10. The extensive XPS spectrum of the MnFe₂-MOF and its derived MnFe₂O₄ material suggests the presence of Mn, Fe, C, and O elements, which supports the results obtained through the elemental mapping. Figure 5.10(a) depicts the deconvoluted Mn 2p peaks of MnFe₂-MOF. The orbital separation energy between the peaks is significant 12 eV, which is consistent with the energies of Mn 2p_{3/2} and Mn 2p_{1/2}. The notable Mn 2p_{3/2} peaks found at 641.4 eV and the Mn 2p_{1/2} peaks at 653.1 eV are attributed to the Mn 2p binding state. Figure 5.10(b) depicts the deconvoluted XPS spectrum of Fe 2p of MnFe₂-MOF, which is ascribed to Fe³⁺ (711.6 and 725.2 eV) and accompanying shakeup satellites (715.3 and 728.6 eV). As shown in figure 5.10(c), the C 1s spectra of MnFe₂-MOF has three peaks at 284.5, 285.3, and 288.3 eV, which were assigned to C=C, C-C, and C=O bonds, respectively. The high-resolution spectra of MnFe₂-MOF O1s was deconvoluted into two peaks at 531.5 and 533.4 eV, which were ascribed to metal-oxygen and carboxylate bonding, respectively, in figure 5.10(d).^{40,41}

In figure 5.10(e), which depicts the high-resolution Mn 2p spectra of MnFe₂O₄, the peaks with centres at 641.4 and 653.2 are identified as Mn 2p_{3/2} and Mn 2p_{1/2} of Mn(II), respectively. The presence of the Mn²⁺ oxidation state in the MnFe₂O₄ is further supported by the two satellite peaks at 643.9 and 655.7 eV. The Fe 2p spectrum of MnFe₂O₄ is shown in figure 5.10(f), and it has two characteristic peaks of Fe 2p_{3/2} and Fe 2p_{1/2} at 710.4 and 724.7 eV, respectively. This indicates that the chemical state of Fe in the MnFe₂O₄ is +3. The O1s high-resolution spectra of MnFe₂O₄, as shown in figure 5.10(g) revealed three oxygen peaks at 529.5, 531.9, and 533.5 eV, respectively. The first peak, at 529.5 eV, was identified as a normal M-O bond, but the second peak, at 531.9 eV, may be attributed to various defect sites such

as hydroxyls or carboxyls. The third peak, centered at 533.5 eV, might be due to the physically either chemically absorbed water.^{42,43}

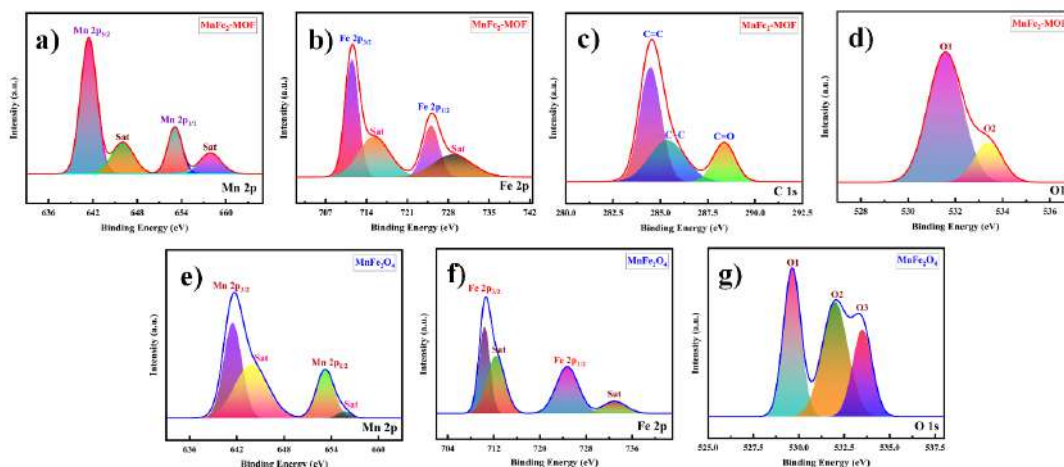


Figure 5.10: High-resolution XPS spectra of (a-d) MnFe₂-MOF, (e-g) its derived MnFe₂O₄

5.4.10 Capacitance characterization of electrode

The electrochemical measurements of prepared electrode materials were performed in a 1 M Na₂SO₄ neutral electrolyte in three-electrode assembly using standard Ag/AgCl as a reference electrode, graphite as a counter electrode and fabricated MnFe₂-MOF / MnFe₂O₄ as a working electrode. Figure 5.11(a) illustrates the comparative CV curves at a scan rate of 100 mV s⁻¹ and figure 5.11(b) depicts the comparative GCD curves at a 1 mA cm⁻² current density of the MnFe₂-MOF and MnFe₂O₄, in a potential window of 0 - 0.5 V. The cyclic voltammograms of MnFe₂-MOF and MnFe₂O₄ have an approximately semi-rectangular shape, indicating that the main electric double layer capacitance behaviour is present, as well as some pseudocapacitive character. Figure 5.11(c, d) show CV curves of MnFe₂-MOF and MnFe₂O₄ at different scan rates, i.e. 10 - 100 mV s⁻¹, which are almost symmetric, demonstrating the electrochemical reaction's excellent reversibility. Also, the semi-rectangular shape has demonstrated great kinetic capabilities because it has not distorted at higher scan rates. The area under the CV curves increases with scan rate, while specific capacitance falls because electrolyte ions completely penetrate the electrode materials at decreasing scan rates. As a result, charge storage may be used across the whole electrode material's surface. At higher scan speeds, however, only the outer active surface is used for charge storage because diffusion restricts the flow of electrolyte ions.⁴⁴ And it is clear from the CV curves that MnFe₂-MOF has a higher current than MnFe₂O₄.

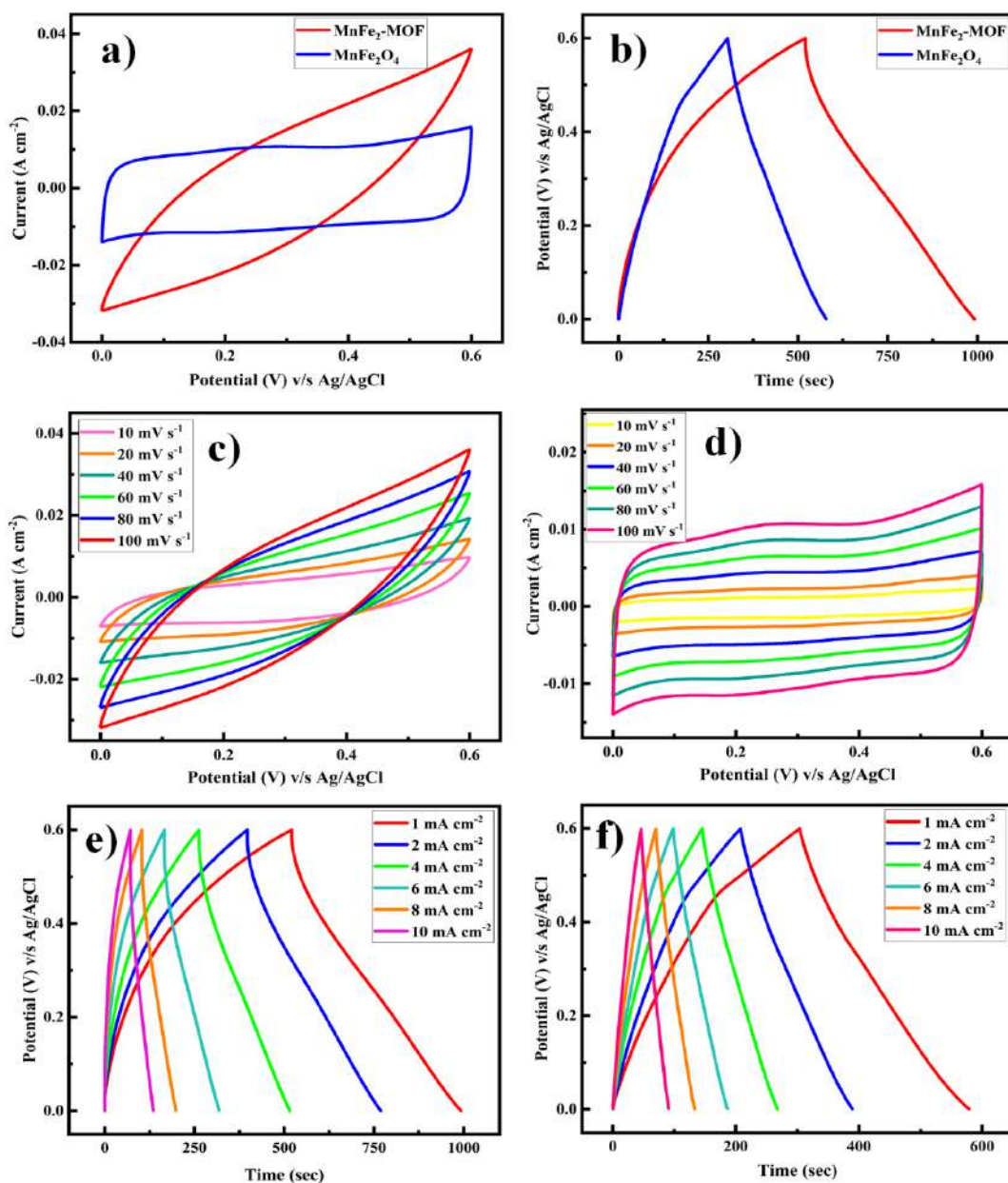


Figure 5.11: (a) Comparison of cyclic voltammograms of MnFe₂-MOF and its derived MnFe₂O₄ electrodes at a potential sweep rate of 100 mV s⁻¹, (b) Comparison of GCD curves of MnFe₂-MOF and its derived MnFe₂O₄ electrodes at a current density of 1 mA cm⁻², (c) CV curves of MnFe₂-MOF in 1 M Na₂SO₄ at various scan rates, (d) CV curves of derived MnFe₂O₄ in 1 M Na₂SO₄ at various scan rates, (e) GCD curves of MnFe₂-MOF at various current densities, (f) GCD curves of MnFe₂O₄ at various current densities

To examine the charge/discharge behaviour of various electrodes, galvanostatic charge/discharge (GCD) tests were performed at different current densities, as shown in figure 5.11(e, f). For MnFe₂-MOF and MnFe₂O₄, the GCD curves have triangular shapes, which are consistent with CV data indicating the

creation of an electric double layer. Equation (5.1) was used to determine the electrode materials specific capacitance using galvanostatic charge-discharge (GCD) curves. The specific capacitances determined from GCD curves (Figure 5.11 e) for MnFe₂-MOF is 1226, 1191, 1158, 1097, 1004 and 876 F g⁻¹ at 1, 2, 4, 6, 8 and 10 mA cm⁻², respectively. And also the specific capacitances evaluated from GCD curves (Figure 5.11f) for derived MnFe₂O₄ is 865, 802, 763, 710, 649 and 590 F g⁻¹ at 1, 2, 4, 6, 8 and 10 mA cm⁻², respectively. Rate capability MnFe₂-MOF and derived MnFe₂O₄ electrodes at 1 to 10 mA cm⁻² were shown in figure 5.12(a). For all determined current densities, the MnFe₂-MOF has the higher specific capacitance than the MnFe₂O₄. The Ragone plot are received from charge-discharge curves of the MnFe₂-MOF and derived MnFe₂O₄ at different power densities were depicted in figure 5.12(b). The energy and power densities of MnFe₂-MOF and its derived MnFe₂O₄ were calculated using equations (5.2 and 5.3). The Ragone plot indicates that as power density increases, energy density decreases.

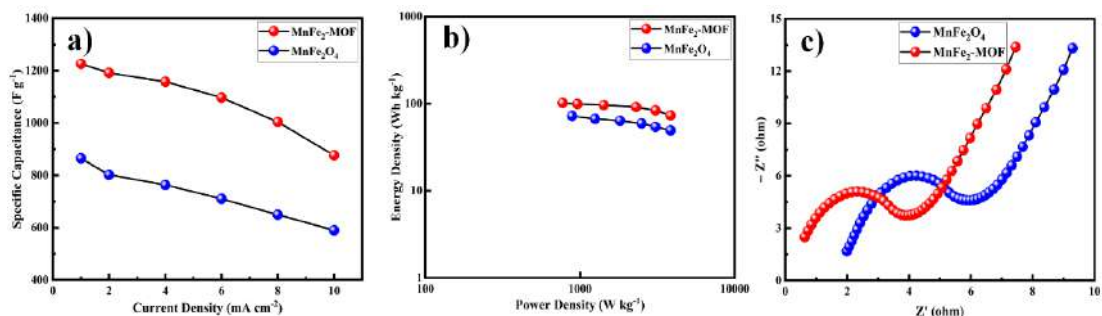


Figure 5.12: (a) Comparative rate capability of the MnFe₂-MOF and derived MnFe₂O₄ electrodes at 1 to 10 mA cm⁻², (b) Ragone plots of the MnFe₂-MOF and derived MnFe₂O₄, (c) Nyquist plots of the MnFe₂-MOF and derived MnFe₂O₄

Electrochemical impedance spectroscopy (EIS) were used to assess the charge-transfer behaviour of electrodes in order to better understand capacitive characteristics. The EIS spectrum is divided into two parts: the semicircle part in the high-frequency region, which is related to the charge transfer resistance (R_{ct}) at the electrode surface/electrolyte interface, and the sloped line part in the low-frequency region, which is associated to the ion diffusion behaviour of the electrolyte inside the electrode material. The Nyquist plots of MnFe₂-MOF and derived MnFe₂O₄ were shown in figure 5.12(c). Significantly, the MnFe₂-MOF electrode (2.9 ohm) show a

lower charge transfer resistance (R_{ct}) than the derived MnFe₂O₄ electrode (3.75 ohm), confirming the fast electron transport kinetics and high conductivity.

Cyclic stability is crucial factor for the virtual application of supercapacitors and Coulombic efficiency is important factor to inspect the interfacial stability of MnFe₂-MOF and derived MnFe₂O₄ electrodes as a function of GCD cycles, as depicted in figure 5.13(a and b). The cyclic stability of MnFe₂-MOF and derived MnFe₂O₄ electrodes were performed using charge-discharge cycles at 10 mA cm⁻² for 3000 cycles within a potential window of 0 to 0.6 V. After 3000 successive GCD cycles, the MnFe₂-MOF and MnFe₂O₄ electrodes still retained 95.68 % and 94.50 % of their original capacitance, respectively. The inset shows first five and last five charge-discharge cycles. Coulombic efficiency of MnFe₂-MOF and derived MnFe₂O₄ electrodes were determined using equation (5.5) at several GCD cycles. The MnFe₂-MOF and derived MnFe₂O₄ electrodes shows excellent Coulombic efficiency of 99.10 % and 97.93 %, respectively.⁴⁵

$$\eta = \frac{t_d}{t_c} \times 100 \dots \dots \dots (5.5)$$

Where, η stands for the Coulombic efficiency measured in %, t_d stands for the discharging time and t_c stands for the charging time measured in seconds.

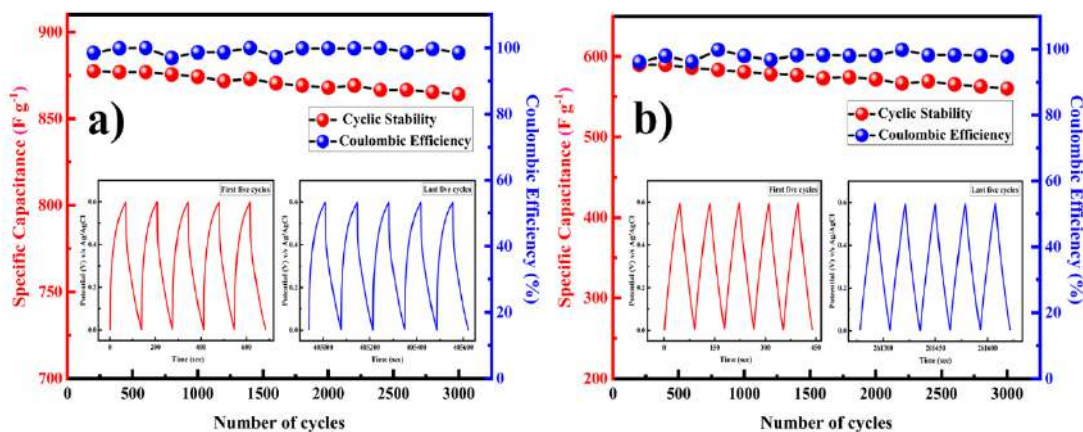


Figure 5.13: Cyclic stability (left versus bottom) and Coulombic efficiency (right versus bottom) of (a) MnFe₂-MOF and (b) derived MnFe₂O₄ electrodes for 3000 cycles measured at a current density of 10 mA cm⁻², the inset shows the charge-discharge curves of the first and last five cycles

5.4.11 Capacitance characterization of solid-state asymmetric supercapacitor (ASC) device (MnFe₂-MOF//AC)

It is familiar that one of the elements affecting the rise in supercapacitor energy density is the wide potential window. The potential window for an asymmetric

cell with an aqueous electrolyte is restricted to the range between 0 - 1 V due to water electrolysis. Using ionic liquids or organic electrolytes can result in a voltage window 3 - 4 times wider than using aqueous electrolytes, but several factors such as cost, toxicity, and flammability make their use less desirable. Therefore, the construction of asymmetric supercapacitor is proposed to overcome the challenges of water splitting in aqueous electrolytes. This arrangement ordinarily comprised of a positive electrode served as the energy source and a negative electrode served as the power source. As a result, boosting the cell's operating voltage improves energy density and specific capacitance in asymmetric supercapacitor devices.

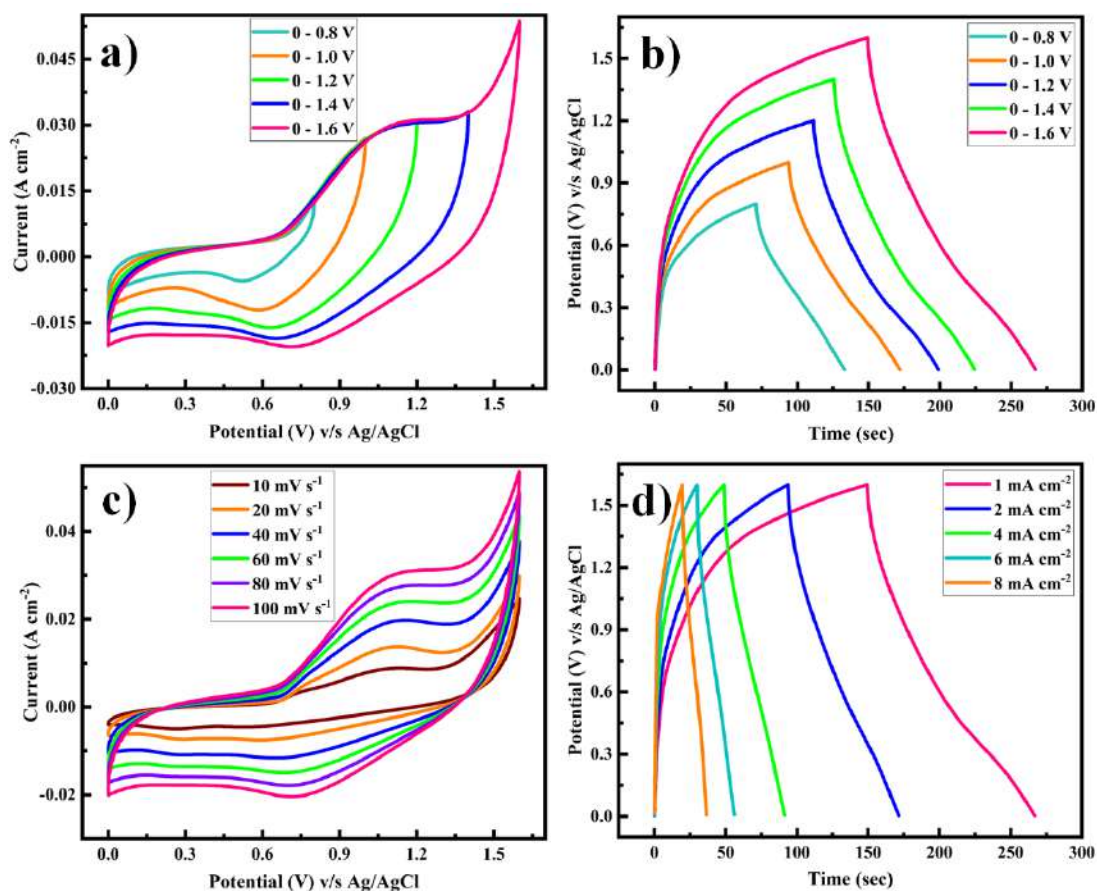


Figure 5.14: (a) Comparison of cyclic voltammograms of ASC device at a potential sweep rate of 100 mV s⁻¹, (b) Comparison of GCD curves of ASC device at a current density of 1 mA cm⁻², (c) CV curves of ASC device in 1 M Na₂SO₄ at various scan rates, (d) GCD curves of ASC device at various current densities

In this study, a solid-state asymmetric supercapacitor is put together utilizing MnFe₂-MOF and activated carbon (AC) electrodes as the anode and cathode in order to further evaluate the capacitive performance of the electrodes as obtained in a whole cell setup. This study utilized a gel electrolyte comprising a polyvinyl alcohol (PVA)-

Na₂SO₄ combination. This solid-state device provides a number of benefits over liquid-based supercapacitors, including flexibility, ease of production, a wide operating temperature range, and better safety. MnFe₂-MOF and AC were used as electrodes (2 x 2 cm²) in a solid-state asymmetric supercapacitor device sandwiched by a PVA-Na₂SO₄ gel electrolyte. Figure 5.14(a and b) depicts the comparative CV and GCD curves of the MnFe₂-MOF//AC device, which varied from 0 to 1.6 V due to the restrictions imposed by oxygen evolution at voltages greater than 1.6 V. As a result, the potential range of 1.6 V in the 1 M Na₂SO₄ electrolyte was chosen for all electrochemical measurements of the fabricated device. The CV curves of the MnFe₂-MOF//AC device are shown in figure 5.14(c) at various scan rates varying from 10 to 100 mV s⁻¹. Both electric double-layer capacitance from AC and pseudocapacitance from MnFe₂-MOF for charge storage validate this. As the scan rate increases, so does the area under the CV curves, and therefore the current. The GCD curves for the MnFe₂-MOF//AC device at various current densities, varying from 1 to 8 mA cm⁻², are shown in figure 5.14(d). The CV curves agree with the unconventional triangular shapes found using GCD curves. The specific capacitances of the MnFe₂-MOF//AC device evaluated from the charge-discharge cycles are depicted in figure 5.15(a). The as-constructed MnFe₂-MOF//AC device delivers specific capacitance from 91.87, 84.16, 76.25, 73.12 and 68.75 F g⁻¹ at 1, 2, 4, 6 and 8 mA cm⁻² current density, respectively. As current density increases the carbon-based electrode's ion exchange rate exceeds that of a pseudo capacitive electrode, resulting in unbalanced charges between the two electrodes of a MnFe₂-MOF//AC device and also the Faradaic process will be constrained at the electrodes' outer surfaces due to the restriction of the diffusion effect. As a result, as current density increases, the specific capacitances of the MnFe₂-MOF//AC device steadily decrease.

The Ragone plot of the assembled MnFe₂-MOF//AC device are exhibited in figure 5.15(b). As the results showed, the MnFe₂-MOF//AC device delivers a maximum energy density of 32.67 Wh kg⁻¹ with a power density of 1000 W kg⁻¹. The internal resistance and charge transfer resistance of the MnFe₂-MOF//AC device was examined using the EIS technique. Figure 5.15(c) shows the Nyquist plot of the MnFe₂-MOF//AC device which reveals low charge transfer resistance of 0.5 Ω with a 0.9 Ω internal resistance which demonstrates the best capacitor performance of the MnFe₂-MOF//AC device, small contact resistance, small diffusion resistance, and

quick electron transfer kinetics. A tiny semicircle denotes increased electrolyte ion buildup and redox reactions on the electrode surface.

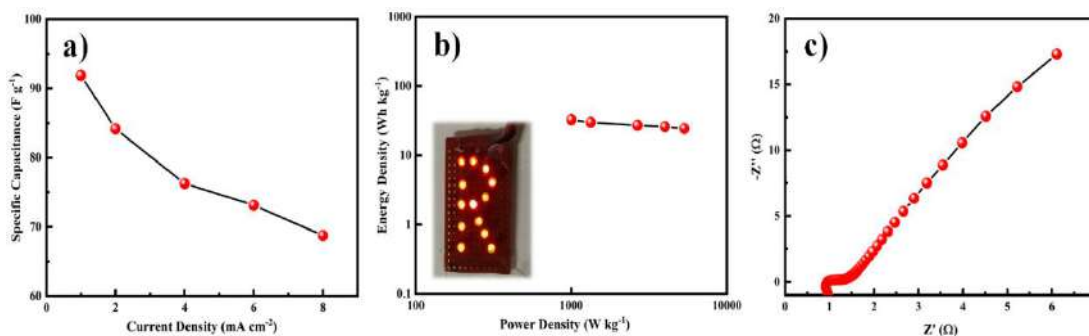


Figure 5.15: (a) Comparative rate capability of the ASC device at 1 to 8 mA cm⁻², (b) Ragone plots of the ASC device, (c) Nyquist plots of the ASC device

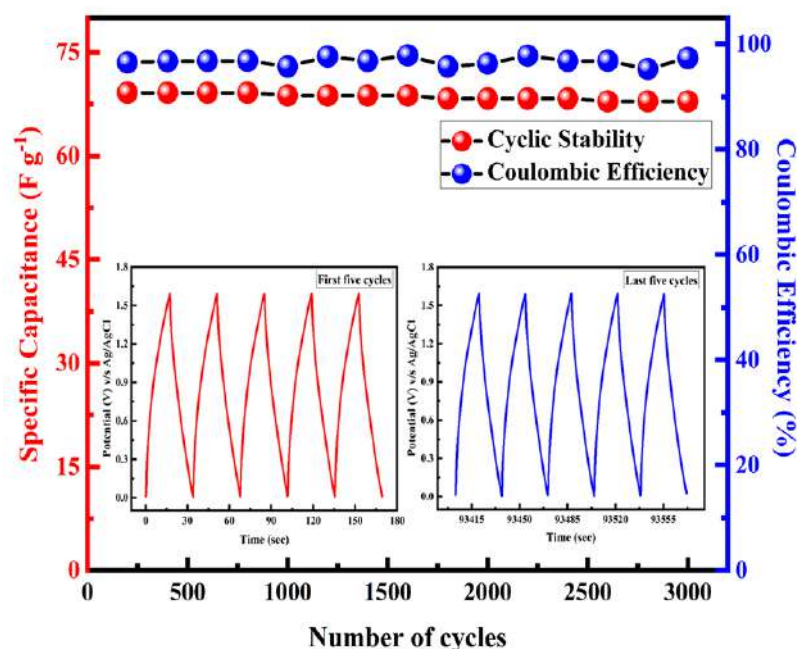


Figure 5.16: Cyclic stability (left versus bottom) and Coulombic efficiency (right versus bottom) of ASC device for 3000 cycles measured at a current density of 8 mA cm⁻², the inset shows the charge-discharge curves of the first and last five cycles

Figure 5.16 shows the cyclic stability and Coulombic efficiency which was investigated at a prolonged current density of 8 mA cm⁻² for 3000 GCD cycles. After repeating the 3000 charge-discharge cycles, the device shows high Coulombic efficiency of 96.75 % and the capacitance retention of the MnFe₂-MOF//AC fabricated asymmetric supercapacitor device achieved nearly 98.52 %, and no discernible degradation is seen, indicating that the MnFe₂-MOF exhibits outstanding stability as an electrode material for supercapacitor application. Its exceptional cycle stability is related to PVA as a binder and the polymer electrolyte's capacity to

safeguard the structure of MOF-based electrodes. Additionally, this type of all-solid-state supercapacitor device has a straightforward assembly procedure and eliminates the possibility of electrolyte leakage that is in liquid electrolyte capacitors.

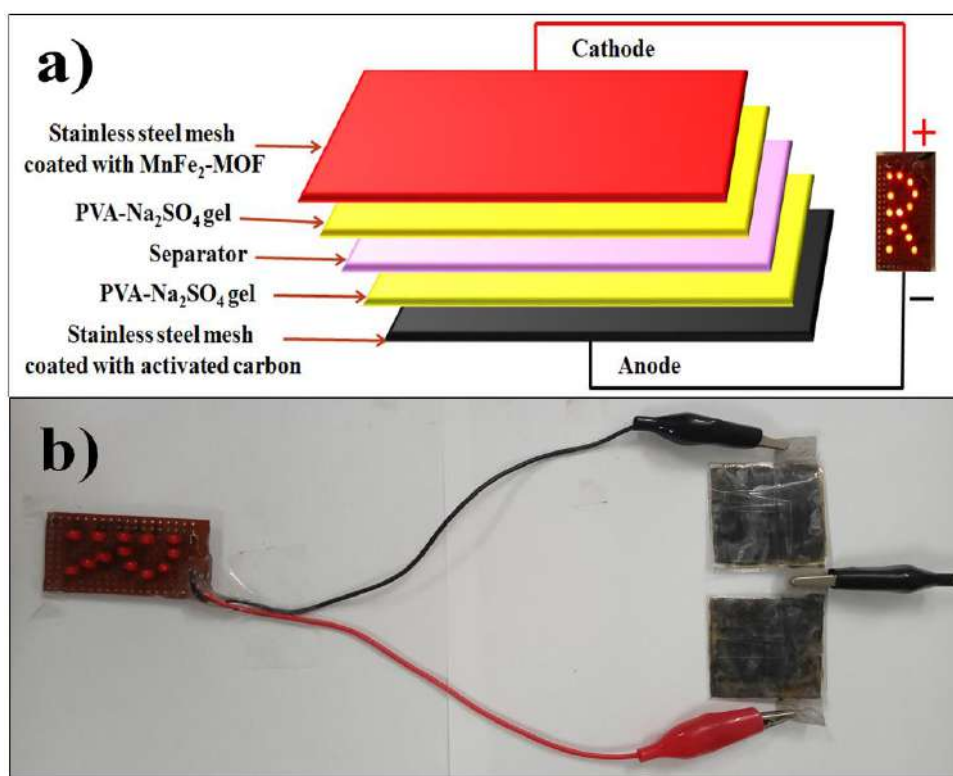


Figure 5.17: (a) Schematic illustration of fabricated asymmetric supercapacitor device, (b) Digital photograph of fabricated two handmade asymmetric supercapacitor device connected in series to glow the LEDs

The lighting red LEDs demonstrate how we may utilize our asymmetric supercapacitor device in real applications by connecting two such devices in series (each device is 2 cm X 2 cm in size). Figure 5.17(a) shows the schematic illustration of a fabricated asymmetric supercapacitor device and figure 5.17(b) displays the digital photograph of fabricated devices arranged in series to glow the red LEDs. After only fifteen seconds of charging, the LED shone brightly for almost seven minutes, illustrating the incredible utility of our solid-state asymmetric supercapacitor devices (see Supporting Information video). Our designed supercapacitor's longer discharge time than charging time makes it appropriate for use in practical energy storage and conversion applications.

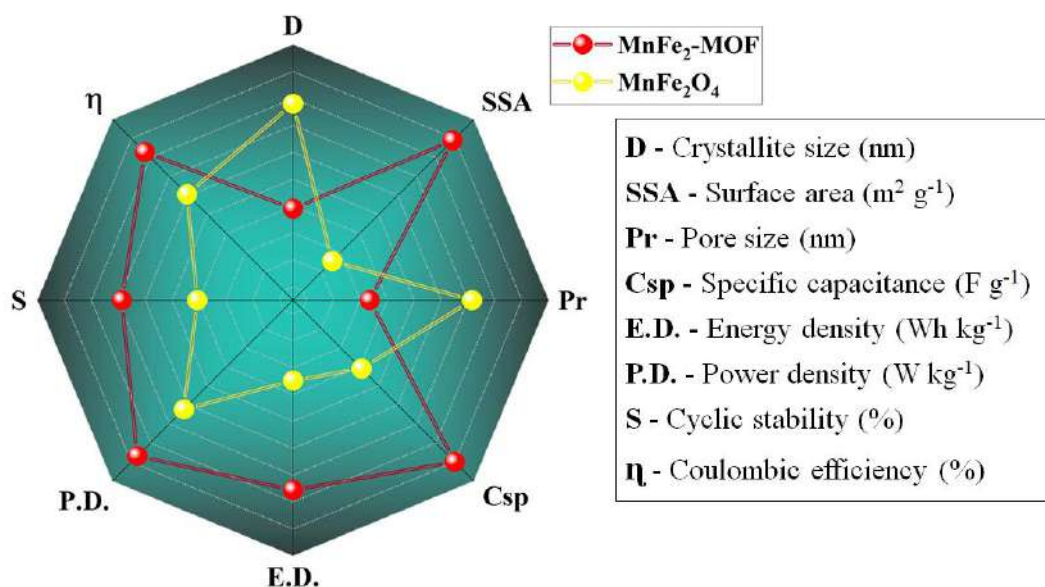


Figure 5.18: Radar plot for comparative study of MnFe₂-MOF and derived MnFe₂O₄ electrodes based on electrochemical properties

As shown in figure 5.18, a radar graph was used for the comparative investigation of the electrochemical properties of chemically synthesized MnFe₂-MOF and derived MnFe₂O₄. Each apex displays parameters such as crystallite size, specific surface area, pore size, specific capacitance, energy density, power density, cyclic stability and coulombic efficiency of the MnFe₂-MOF and derived MnFe₂O₄. The solid area under the curve indicates the electrochemical properties of the electrodes. Figure 5.18 shows that the integral area of MOF is significantly greater than that of ferrite. It has been observed that small crystallite size and large specific surface area contributed to excellent specific capacitance, energy density, power density, and cyclic stability.

5.5 Conclusion

A novel MnFe₂-MOF and its derived MnFe₂O₄ was synthesized for the first time using a simple reflux condensation technique followed by annealing process. XRD, FT-IR, Raman, SEM, EDX, TEM, VSM, BET, and XPS measurements were used to characterize the as-prepared. MnFe₂-MOF and its derived MnFe₂O₄. The electrochemical tests of MnFe₂-MOF and its derived MnFe₂O₄ in 1 M Na₂SO₄ neutral electrolyte exhibit a high specific capacitance of 1226 and 865 F g⁻¹ at 1 mA cm⁻² current density with excellent capacitance retention of 95.68 % and 94.50 % over 3000 cycles, respectively. The practical application of the prepared electrode was examined by fabricating a solid-state asymmetric supercapacitor device working at

1.6 V operating potential window using the electrodes as MnFe₂-MOF as anode and activated carbon as the cathode, and PVA-Na₂SO₄ gel as the gel-polymer electrolyte. The assembled asymmetric supercapacitor device illustrates a remarkable energy density of 32.67 Wh kg⁻¹ at a power density of 1000 W kg⁻¹ with an outstanding cyclic stability of 98.52 % even after 3000 GCD cycles. In conclusion, the electrochemical supercapacitor performance of MnFe₂-MOF//AC asymmetric cell can be utilized as potential application towards the electrochemical energy storage prospect effectively.

5.6 References

- 1 J. Zhou, S. Zhang, Y. N. Zhou, W. Tang, J. Yang, C. Peng and Z. Guo, *Electrochem. Energy Rev.*, 2021, **4**, 219-248.
- 2 Y. Jiang and J. Liu, *Energy Environ. Mater.*, 2019, **2**, 30-37.
- 3 J. Hao, H. Liu, S. Han and J. Lian, *ACS Appl. Nano Mater.*, 2021, **4**, 1330–1339.
- 4 X. Zhang, A. Chen, M. Zhong, Z. Zhang, X. Zhang, Z. Zhou and X. H. Bu, *Electrochem. Energy Rev.*, 2019, **2**, 29-104.
- 5 W. Li, X. Zhao, Q. Bi, Q. Ma, L. Han and K. Tao, *Dalt. Trans.*, 2021, **50**, 11701–11710.
- 6 H. Gao, H. Shen, H. Wu, H. Jing, Y. Sun, B. Liu, Z. Chen, J. Song, L. Lu, Z. Wu and Q. Hao, *Energy and Fuels*, 2021, **35**, 12884–12901.
- 7 S. Zallouz, B. Réty, L. Vidal, J. M. Le Meins and C. Matei Ghimbeu, *ACS Appl. Nano Mater.*, 2021, **4**, 5022–5037.
- 8 Y. Li, X. Han, T. Yi, Y. He and X. Li, *J. Energy Chem.*, 2019, 54–78.
- 9 D. P. Chatterjee and A. K. Nandi, *J. Mater. Chem. A*, 2021, **9**, 15880–15918.
- 10 X. Gao, Y. Dong, S. Li, J. Zhou, L. Wang and B. Wang, *Electrochem. Energy Rev.*, **2020**, **3**, 81-126.
- 11 O. M. Yaghi, H. Li, *J. Am. Chem. Soc.*, 1995, **117**, 10401–10402.
- 12 F. Zou, X. Hu, Z. Li, L. Qie, C. Hu, R. Zeng, Y. Jiang and Y. Huang, *Adv. Mater.*, 2014, **26**, 6622–6628.
- 13 G. Wang, Z. Yan, N. Wang, M. Xiang and Z. Xu, *ACS Appl. Nano Mater.*, 2021, **4**, 9034–9043.
- 14 and G. L. Shouheng Sun, Hao Zeng, David B. Robinson, Simone Raoux, Philip M. Rice, Shan X. Wang, *J. Am. Chem. Soc.*, 2004, **126**, 273–279.
- 15 B. Bhujun, M. T. T. Tan and A. S. Shanmugam, *Results Phys.*, 2017, **7**, 345–353.
- 16 C. D. Lokhande, D. P. Dubal and O. S. Joo, *Curr. Appl. Phys.*, 2011, **11**, 255–270.
- 17 L. Sun, C. H. Hendon, S. S. Park, Y. Tulchinsky, R. Wan, F. Wang, A. Walsh and M. Dincă, *Chem. Sci.*, 2017, **8**, 4450–4457.
- 18 P. D. Patil, S. R. Shingte, V. C. Karade, J. H. Kim, T. D. Dongale, S. H. Mujawar, A. M. Patil and P. B. Patil, *J. Energy Storage*, 2021, **40**, 102821-

- 102832.
- 19 M. Safari and J. Mazloom, *J. Solid State Electrochem.*, 2021, **25**, 2189–2200.
- 20 Y. Liu, G. Li, Y. Guo, Y. Ying and X. Peng, *ACS Appl. Mater. Interfaces*, 2017, **9**, 14043–14050.
- 21 P. Tang, L. Han and L. Zhang, *ACS Appl. Mater. Interfaces*, 2014, **6**, 10506–10515.
- 22 R. Velmurugan, J. Premkumar, R. Pitchai, M. Ulaganathan and B. Subramanian, *ACS Sustain. Chem. Eng.*, 2019, **7**, 13115–13126.
- 23 R. Barik, A. Raulo, S. Jha, B. Nandan and P. P. Ingole, *ACS Appl. Energy Mater.*, 2020, **3**, 11002–11014.
- 24 C. Yu, Y. Wang, J. Cui, D. Yu, X. Zhang, X. Shu, J. Zhang, Y. Zhang, R. Vajtai, P. M. Ajayan and Y. Wu, *J. Mater. Chem. A*, 2018, **6**, 8396–8404.
- 25 J. Yuan, D. Yao, L. Jiang, Y. Tao, J. Che, G. He and H. Chen, *ACS Appl. Energy Mater.*, 2020, **3**, 1794–1803.
- 26 P. Janjani, U. Bhardwaj, R. Gupta and H. Singh Kushwaha, *Anal. Chim. Acta*, 2022, **1202**, 339676-339687.
- 27 H. Qin, Y. Yang, W. Shi and Y. She, *Environ. Sci. Pollut. Res.*, 2021, **28**, 26558–26570.
- 28 S. J. S. Qazi, A. R. Rennie, J. K. Cockcroft and M. Vickers, *J. Colloid Interface Sci.*, 2009, **338**, 105–110.
- 29 T. T. K. Ngan, T. B. Thuy, L. van Tan and T. T. Nguyen, *Bull. Chem. React. Eng. Catal.*, 2021, **16**, 916–924.
- 30 F. Siadatnasab, S. Farhadi, A. A. Hoseini and M. Sillanpää, *New J. Chem.*, 2020, **44**, 16234–16245.
- 31 M. Fiaz, M. Kashif, M. Fatima, S. R. Batool, M. A. Asghar, M. Shakeel and M. Athar, *Catal. Letters*, 2020, **150**, 2648–2659.
- 32 R. A. Rather and Z. N. Siddiqui, *Appl. Organomet. Chem.*, 2019, **33**, 1–14.
- 33 A. Manohar, C. Krishnamoorthi, C. Pavithra and N. Thota, *J. Supercond. Nov. Magn.*, 2021, **34**, 251–259.
- 34 B. Bashir, W. Shaheen, M. Asghar, M. F. Warsi, M. A. Khan, S. Haider, I. Shakir and M. Shahid, *J. Alloys Compd.*, 2017, **695**, 881–887.
- 35 N. Saha, A. Sarkar, A. B. Ghosh, A. K. Dutta, G. R. Bhadu, P. Paul and B. Adhikary, *RSC Adv.*, 2015, **5**, 88848–88856.
- 36 M. Hazarika, P. Chinnamuthu and J. P. Borah, *J. Mater. Sci. Mater. Electron.*,

- 2018, **29**, 12231–12240.
- 37 B. Ameri, S. S. H. Davarani, R. Roshani, H. R. Moazami and A. Tadjarodi, *J. Alloys Compd.*, 2017, **695**, 114–123.
- 38 R. Roshani and A. Tadjarodi, *J. Mater. Sci. Mater. Electron.*, 2020, **31**, 23025–23036.
- 39 R. Sikkema and I. Zhitomirsky, *Appl. Phys. Rev.*, *Appl. Phys. Rev.*, 2023, **10**, 021307-021324.
- 40 K. Yuan, T. Song, D. Wang, Y. Zou, J. Li, X. Zhang, Z. Tang and W. Hu, *Nanoscale*, 2018, **10**, 1591–1597.
- 41 J. Zhou, Z. Han, X. Wang, H. Gai, Z. Chen, T. Guo, X. Hou, L. Xu, X. Hu, M. Huang, S. V. Levchenko and H. Jiang, *Adv. Funct. Mater.*, 2021, **31**, 1–13.
- 42 M. Hua, L. Xu, F. Cui, J. Lian, Y. Huang, J. Bao, J. Qiu, Y. Xu, H. Xu, Y. Zhao and H. Li, *J. Mater. Sci.*, 2018, **53**, 7621–7636.
- 43 R. Gupta, R. Tomar, S. Chakraverty and D. Sharma, *RSC Adv.*, 2021, **11**, 16942–16954.
- 44 S. S. Shah, E. Cevik, M. A. Aziz, T. F. Qahtan, A. Bozkurt and Z. H. Yamani, *Synth. Met.*, 2021, **277**, 116765-116780.
- 45 R. Bhosale, S. Bhosale, P. Kumbhar, D. Narale, R. Ghaware, C. Jambhale, S. Kolekar, *New J. Chem.*, 2023, **47**, 6749–6758.

CHAPTER SIX

Hybrid Supercapacitor Based on Nanoporous Carbon and CoFe₂O₄ Derived From a Single Bimetallic-Organic Framework: One-for-All Approach

6.1 Outline

The rational design of nanomaterials derived from metal-organic framework has received a lot of interest due to their high potential for energy storage and conversion applications because of their high conductivity, strong redox activity and large specific surface area. In this study, a “One-for-All” approach was used to synthesize positive and negative electrodes from a single bimetallic CoFe₂-MOF to fabricate a hybrid supercapacitor device. Hierarchical bimetallic CoFe₂-MOF architectures were synthesized by a straightforward scalable solution method. The Cobalt ferrite was prepared by annealing the bimetallic CoFe₂-MOF in air and the nanoporous carbon was achieved by heating the CoFe₂-MOF in an inert atmosphere. The CoFe₂-MOF derived nanoporous carbon exhibits a high specific capacitance of 1271 F g⁻¹ at 2 mA cm⁻² current density with an excellent cycle stability of 96.87 % even after 5000 cycles owing to its huge surface area of 614 m² g⁻¹ and plenty of mesopores in it. The as-prepared cobalt ferrite and nanoporous carbon derived from CoFe₂-MOF were employed to construct the All-in-One hybrid supercapacitor (HSC) device using PVA-KOH as a gel-polymer electrolyte. At 1 mA cm⁻² current density, the manufactured All-in-One HSC device shows a high specific capacitance of 112.1 F g⁻¹, an energy density of 56.2 Wh kg⁻¹, and a power density of 1091.5 W kg⁻¹. It demonstrated high cyclic stability of 97.91 % of its original capacitance over 5000 subsequent GCD cycles with a coulombic efficiency of 98.54 %. This discovery might significantly progress research towards the creation of MOF-derived electrode materials for a bright future in energy storage and conversion.

6.2 Introduction

The global demand for clean energy storage and delivery is pushing technological developments to their limits, as pollution and the energy crisis become more and more serious.^{1,2} Owing to the widespread concern over the rapidly increasing need for energy in the future, energy storage technologies are now in demand.³ Due to the intermittent nature of these emerging energy sources, it is critical to priorities fulfilling the rapid growth demands of energy storage and conversion devices.⁴ At present, supercapacitors, fuel cells and batteries are being considered as energy storage and conversion technologies. Supercapacitors have gained attention as renewable energy storage systems due to their comparatively good efficiency in storing the energy produced by these sources; however, the high demand for devices with smaller size, lighter weight, higher level of flexibility, energy density, and power density, excellent life cycle, and lower cost presents a challenge for these energy storage systems.⁵⁻⁷ Electrochemical double-layer capacitors (EDLCs), hybrid capacitors, and pseudocapacitors are the different types of supercapacitors that can be categorized based on their electrode configurations. Supercapacitor's ability to perform better is largely dependent on the materials they are made of, including the electrodes and electrolytes.^{8,9} Researchers worldwide have shown great interest in studying advanced materials with good textural and electrochemical properties, such as high porosity, excellent conductivity, and an abundance of redox-active sites, to further improve the performance of these electrodes.¹⁰ The advantages of batteries and supercapacitors might be combined in a hybrid device called an asymmetric supercapacitor (ASC), which could be used to power electric vehicles and other future multifunctional electrics. Therefore, recent advances in supercapacitor research have focused on the creation of such asymmetric supercapacitors.¹¹⁻¹³

Metal-organic frameworks (MOFs), often referred to as porous coordination polymers (PCPs), are created when metal ions and organic linkers self-assemble. MOFs have drawn a lot of attention in the fields of energy storage due to their distinctive advantages, including their highly devisable structures, well-dispersed metal components, super-large surface area and governable porosity.^{14,15} MOF-based materials have been broadly investigated within the field of electrochemical energy storage and conversion in recent years. However, many classic MOFs have restricted uses because of their poor electrical conductivity and stability. Thermal treatment is a

useful way to improve conductivity by partially carbonising the skeleton, but it can cause channel collapse and structural changes in MOFs. MOF-derived nanomaterials with exceptional stability not only serve as a vital supporting structure for a variety of electrode materials, but also increase specific surface area, enrich the active centers, and promote electrochemical reactions.¹⁶⁻¹⁹ A more fascinating advantage of utilizing MOFs as predecessor for the electrode materials in supercapacitors is the ability to create both the cathode (NPC) and anode (metal oxides) from a sole MOF by using the "One-for-All" approach.²⁰ Kang et al. have synthesized metal-organic frameworks (MOFs) derived from hollow rod-like NiCoMn ternary metal sulfides via the etching/ion-exchange reaction and additional sulfurization technique. The material has a rich redox reaction, great synergy, and exceptional electrical conductivity because of the multi-metal and sulphide composition. The as-prepared NiCoMn-S electrode shows an excellent specific capacitance of 2098.2 F g⁻¹ at 1 A g⁻¹ current density. Further, they have fabricated a NiCoMn-S//AC asymmetric supercapacitor device which exhibits an outstanding specific capacitance of 124.5 F g⁻¹ at 1 A g⁻¹ current density with a cycling stability of 73.6 % over 6000 cycles.²¹ Tang et al. successfully synthesized Ni/ZnO nano-sponges from bimetallic Ni/Zn-MOF via optimal heat treatment at 600°C. Ni/ZnO electrode exhibits a high specific capacitance of 807 F g⁻¹ at 1 A g⁻¹ current density and retains 86 % of its initial capacitance after 5000 charge/discharge cycles at the 10 A g⁻¹ current density with long-term cycling stability. Furthermore, they have manufactured an asymmetric supercapacitor (Ni/ZnO-600//AC) that exhibits remarkable cycling stability of 89 % over subsequent 5000 GCD cycles at a high current density of 5 A g⁻¹.²²

In this chapter, we have used the "One-for-all" approach to synthesize nanoporous carbon (NPC) and cobalt ferrite (CoFe₂O₄) from a single bimetallic cobalt-iron metal-organic framework (CoFe₂-MOF). As-prepared NPC and ferrite derived from bimetallic MOF were employed as cathode and anode in the construction of a hybrid supercapacitor (HSC) with 2 M KOH as the aqueous alkaline electrolyte. Capacitive performance was investigated using a three-electrode setup.

6.3 Experimental section

6.3.1 Chemicals

Cobalt nitrate hexahydrate (Co(NO₃)₂.6H₂O; 98%) and N, N-dimethylformamide (DMF; 99.8 %) were purchased from Loba Chemie India.

Terephthalic acid (PTA, 98 %), ferric chloride hexahydrate ($\text{FeCl}_3 \cdot 6\text{H}_2\text{O}$) and N-methyl-2-pyrrolidone (NMP) were purchased from Sigma Aldrich (USA). All chemicals were of analytical grade and were utilized without further purification.

6.3.2 Synthesis of $\text{CoFe}_2\text{-MOF}$ and its derived cobalt ferrite and nanoporous carbon

For the synthesis of $\text{CoFe}_2\text{-MOF}$, reflux condensation method was used in which terephthalic acid (0.15 M) was dissolved in DMF (20 ml). Cobalt nitrate hexahydrate (0.05 M) and ferric chloride hexahydrate (0.1 M) were dissolved in DMF (20 ml) to form a solution. Then, both these solutions were mixed and stirred for 10 min to obtain a homogeneous solution and NaOH solution was added dropwise to the above solution till precipitation. Finally, the precipitate was transferred to a round bottom flask and kept at 100 °C for 12 h. Next, the brown-colored suspension was filtered and the final powder was dried at 60 °C for 12 h to obtain $\text{CoFe}_2\text{-MOF}$.

Cobalt ferrite and nanoporous carbon both were prepared from the as-prepared $\text{CoFe}_2\text{-MOF}$. To get MOF-derived cobalt ferrite, the $\text{CoFe}_2\text{-MOF}$ was annealed at 500°C for 3 h at a heating rate of 5 °C min^{-1} in air; the resulting sample was designated as cobalt ferrite (CoFe_2O_4). For the synthesis of nanoporous carbon, the $\text{CoFe}_2\text{-MOF}$ was heated at 800 °C for 3 hrs at a ramping rate of 5 °C min^{-1} in a nitrogen environment, then cooled to room temperature.

6.3.3 Material characterization

Crystal structure and phase purity of $\text{CoFe}_2\text{-MOF}$ and derived nanoporous carbon were analysed on a Bruker D8 Phaser X-ray diffractometer with Cu $K\alpha$ radiation ($\lambda = 0.1541$ nm). The Perkin Elmer 1760X spectrophotometer was used to record Fourier Transform Infrared spectra between 400 and 4000 cm^{-1} . Raman spectra of $\text{CoFe}_2\text{-MOF}$ and derived nanoporous carbon samples were analyzed by Renishaw in via Raman spectrometer by using a He-Ne (633 nm) laser excitation source. The surface morphology and elemental confirmation of the prepared samples were obtained from scanning electron microscopy and Energy dispersive X-ray Analysis spectrometer (EDAX, Oxford Instrumentations inbuilt with FE-SEM). Also, the surface morphology with d-spacing of the $\text{CoFe}_2\text{-MOF}$ and derived nanoporous carbon samples were found by using transmission electron microscopy (TEM) analysis from Hitachi/HF-3300 TEM (300 kV). The elemental content of the $\text{CoFe}_2\text{-MOF}$ and derived nanoporous carbon samples was investigated using X-ray photoelectron spectroscopy (XPS) with a Thermo Fisher Scientific SIGMA PROBE.

The porosity of the material was investigated on NOVA1000e Quantachrome (BET), USA. The magnetic behavior of the CoFe₂-MOF and derived nanoporous carbon samples were investigated by using Vibrating-sample magnetometer (VSM) from superconducting quantum interference device (SQUID) vibrating sample magnetometry (VSM) (Quantum Design).

6.3.4 Preparation of working electrodes

Stainless steel mesh was employed as a current collector to fabricate working electrodes. Prior to the fabrication of the electrodes, the substrate, stainless steel mesh, was cleaned using an ultrasonic cleaning process with soap solution, deionized water, and acetone for 20 minutes each. To fabricate the working electrodes, stainless steel mesh was then coated with a homogenous slurry and dried at 70°C. The slurry contained CoFe₂-MOF/ CoFe₂O₄/ nanoporous carbon, polyvinylidene fluoride, and acetylene black in an 80:10:10 weight ratio in N, N-dimethyl formamide. Each electrode had a surface area of 1 cm × 1 cm.

6.3.5 Preparation of an all-in-one solid-state hybrid supercapacitor device

Gel electrolyte was prepared prior to the device's construction by combining 1 g of polyvinyl alcohol (PVA, 99 %, M. W. = 1700-1800, Loba Chemie Pvt. Ltd., India) powder with 20 ml of deionized water at 80 °C for 20 min. The aforementioned solution was then mixed with 10 ml of 2 M potassium hydroxide (KOH), dropwise, and agitated for an additional 2 hours at room temperature to produce a translucent gel electrolyte (PVA-KOH).²³ The constructed all-in-one hybrid supercapacitor device was then built in a sandwich type with two distinct working electrodes (CoFe₂O₄ and nanoporous carbon as a anode and cathode, respectively) coated with PVA-KOH gel electrolyte, joined together with gel sided face to each other, and left at room temperature overnight for natural drying.

6.3.6 Electrochemical measurements

Electrochemical performance of the CoFe₂-MOF, CoFe₂O₄ and NPC electrodes were tested on a CHI608 electrochemical analyzer at room temperature in an aqueous 2 M KOH electrolyte. The electrochemical properties of electrodes were assessed using cyclic voltammetry (CV), galvanostatic charge–discharge (GCD), and electrochemical impedance spectroscopy (EIS) using three electrode assembly in an aqueous 2 M KOH electrolyte. The fabricated CoFe₂-MOF, CoFe₂O₄ and NPC electrodes were employed as a working electrodes, saturated Ag/AgCl was employed as reference electrode and graphite is employed as a counter electrode. The frequency

range used for the electrochemical impedance spectroscopy (EIS) experiments was 1 Hz to 100 kHz.

Using the equation (6.1), the specific capacitance of the CoFe₂-MOF, CoFe₂O₄ and NPC electrode was estimated using a charge-discharge cycle.

$$C_{sp} = \frac{I\Delta t}{m\Delta V} \dots\dots\dots (6.1)$$

Where C_{sp} denotes specific capacitance measured in F g⁻¹, I denotes the specified current measured in ampere, Δt denotes the discharge time measured in seconds, m denotes the mass of the materials measured in grams, and ΔV denotes the potential window of the discharging process measured in volt.

The specific energy and power of the all-in-one hybrid supercapacitor device was determined by using equations (6.2-6.3),²⁴

$$E_s = \frac{0.5 \times C_{sp} \times \Delta V^2}{3.6} \dots\dots\dots (6.2)$$

$$P_s = \frac{E_s \times 3600}{\Delta t} \dots\dots\dots (6.3)$$

Where E_s denotes the specific energy measured in Wh kg⁻¹ and P_s denotes the specific power measured in W kg⁻¹.

6.4 Results and discussion

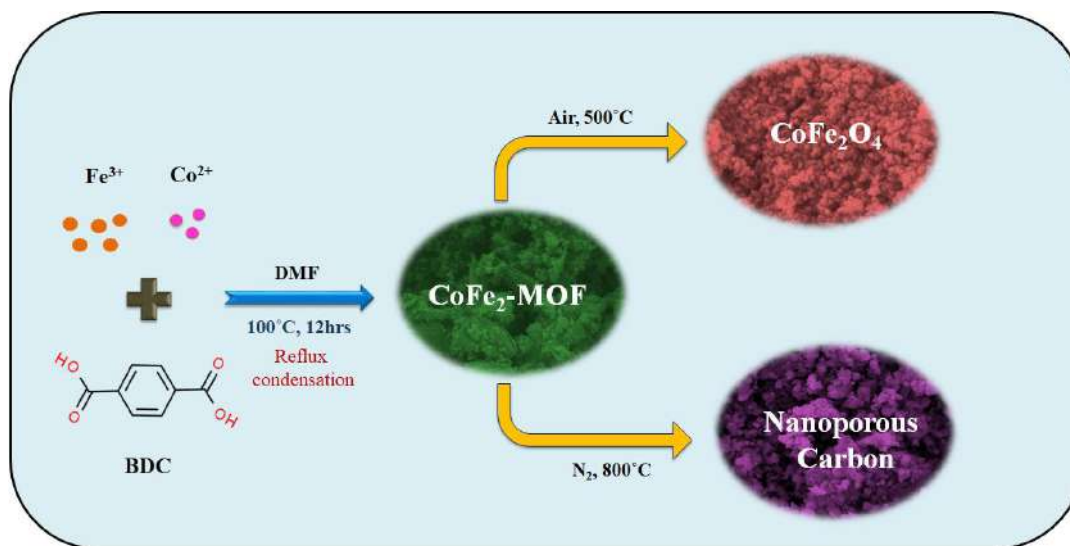


Figure 6.1: Schematic illustration of the synthesis of CoFe₂-MOF, its derived CoFe₂O₄ and nanoporous carbon (NPC)

Figure 6.1 depicts a schematic overview of the experimental procedures employed in this investigation to the synthesis of CoFe₂-MOF derived CoFe₂O₄ and nanoporous carbon using the "One-for-All" approach. Two basic steps were involved in the synthesis process. In the first step, the bimetallic CoFe₂-MOF array precursor

was initially prepared through the complexation reaction of Co^{2+} , Fe^{3+} , and terephthalic acid. Second, following the first step, the synthesized bimetallic $\text{CoFe}_2\text{-MOF}$ were used as a precursor to synthesize both CoFe_2O_4 and NPC by directly pyrolyzing them at 500°C in air atmosphere and 800°C in nitrogen atmosphere, respectively.

6.4.1 X-ray diffraction of $\text{CoFe}_2\text{-MOF}$, CoFe_2O_4 and NPC

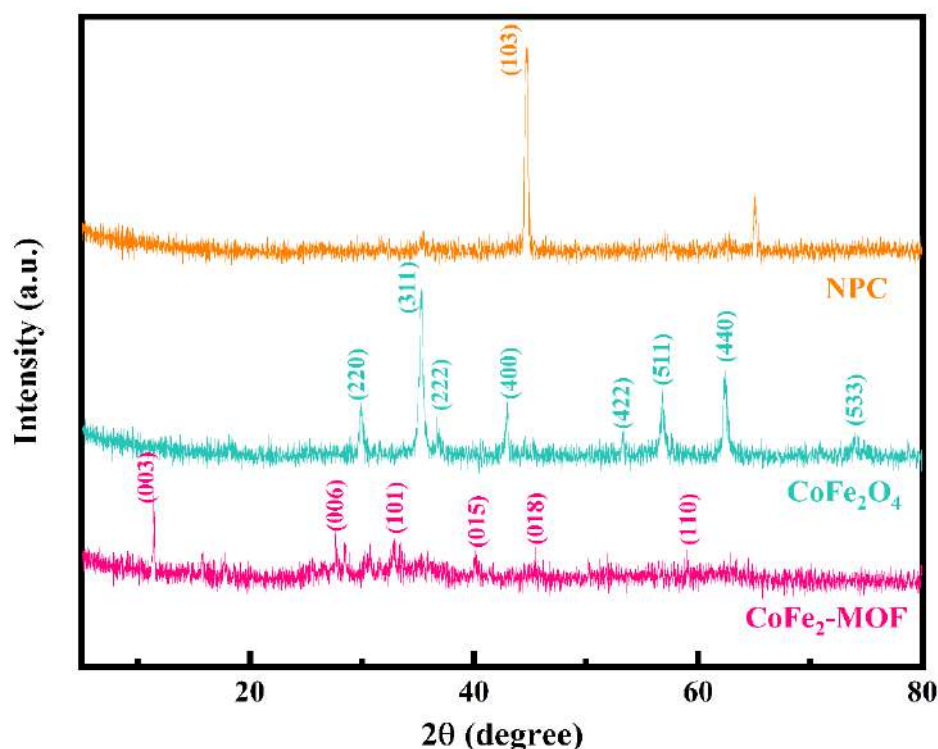


Figure 6.2: XRD patterns of $\text{CoFe}_2\text{-MOF}$, CoFe_2O_4 and NPC

The structural, morphological and compositional features of the as-synthesized hierarchical MOF and their derived materials were identified using a various characterization techniques. The $\text{CoFe}_2\text{-MOF}$ has been successfully synthesized, as indicated by the fact that the diffraction peaks closely match with those of the earlier reports.^{25,26} The XRD pattern of $\text{CoFe}_2\text{-MOF}$ exhibits major diffraction peaks at 2θ values of 11° , 26° , 33° , 39° , 46° , and 59° corresponding to (003), (006), (101), (015), (018) and (110) planes with a rhombohedral phase (JCPDS card No. 00-050-0235). To confirm the crystalline structure and phase of the $\text{CoFe}_2\text{-MOF}$ annealed at 500°C under air atmosphere was also examined by XRD technique. In the XRD pattern of CoFe_2O_4 , the diffraction peaks are located at 30° , 35° , 37° , 43° , 53° , 56° , 62° and 73° and can be ascribed to the (220), (311), (222), (400), (422), (511), (440) and (533) planes of the CoFe_2O_4 with a cubic phase (JCPDS card No. 01-077-0426). When the

bimetallic MOF was carbonized at 800°C it produces nanoporous carbon, the XRD pattern of NPC shows the presence of one intense peak rooting from the (103) plane at 2θ of 44° with a cubic phase which is well matched with the JCPDS card no. 01-075-0410.

6.4.2 FT-IR spectroscopy of CoFe₂-MOF, CoFe₂O₄ and NPC

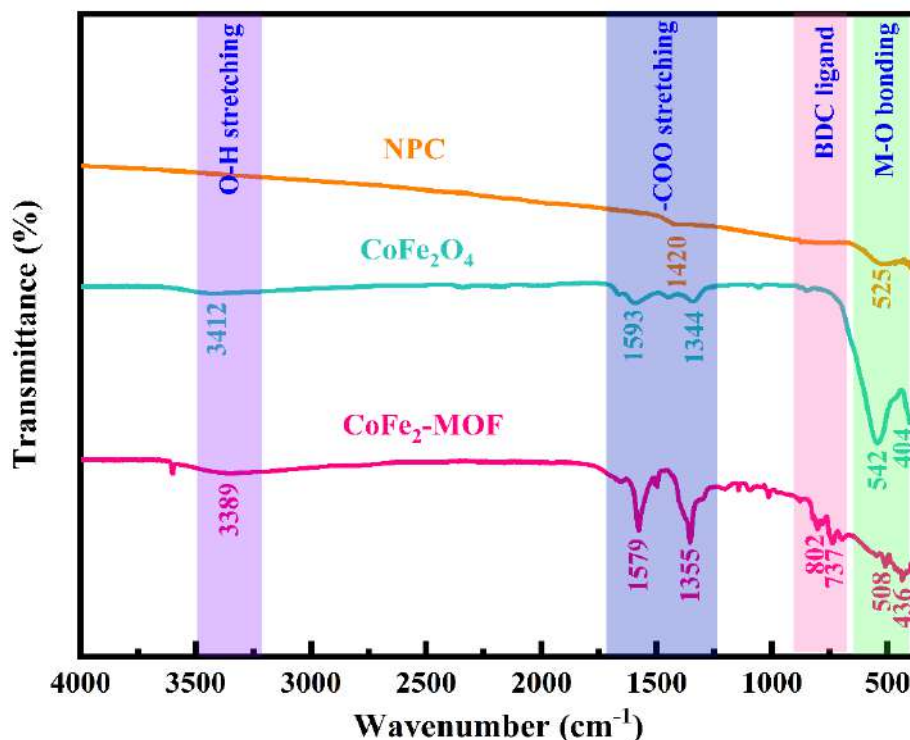


Figure 6.3: FTIR spectra of CoFe₂-MOF, CoFe₂O₄ and NPC

To investigate the presence of functional groups, the FTIR analysis of the CoFe₂-MOF and its MOF-derived CoFe₂O₄ and NPC was performed, depicted in figure 6.3. The absorption band at 3389 and 3412 cm⁻¹ in CoFe₂-MOF and CoFe₂O₄ spectra is responsible to stretching vibrations of the water molecules adsorbed from solvent. In the CoFe₂-MOF spectra, the absorption bands at 1355 and 1579 cm⁻¹ are assigned to the symmetric and asymmetric stretching modes of -COO groups, respectively.²⁷ The division of these symmetric and asymmetric modes suggests that carboxylate group of terephthalic acid (bidentate ligand) is coordinated to nickel with a formation of polymer structure. Additionally, the absorption bands at 737 and 802 cm⁻¹ in the CoFe₂-MOF spectra are attributed to the terephthalic ligand.²⁸ In the CoFe₂-MOF derived CoFe₂O₄ spectra, the weak absorption bands at 1593 and 1344 cm⁻¹, also in derived NPC spectra a weak band at 1420 cm⁻¹ are attributed to the asymmetric and symmetric stretching modes of -COO groups, respectively.^{29,30} The

bands ascribed to terephthalic acid are disappearing in CoFe_2O_4 and NPC due to the decomposition of organic ligand with increasing annealing temperature. The bands observed in the range $400\text{-}600\text{ cm}^{-1}$ in all the spectra are assigned to the metal-oxygen bonding.³¹

6.4.3 Raman spectroscopy of $\text{CoFe}_2\text{-MOF}$, CoFe_2O_4 and NPC

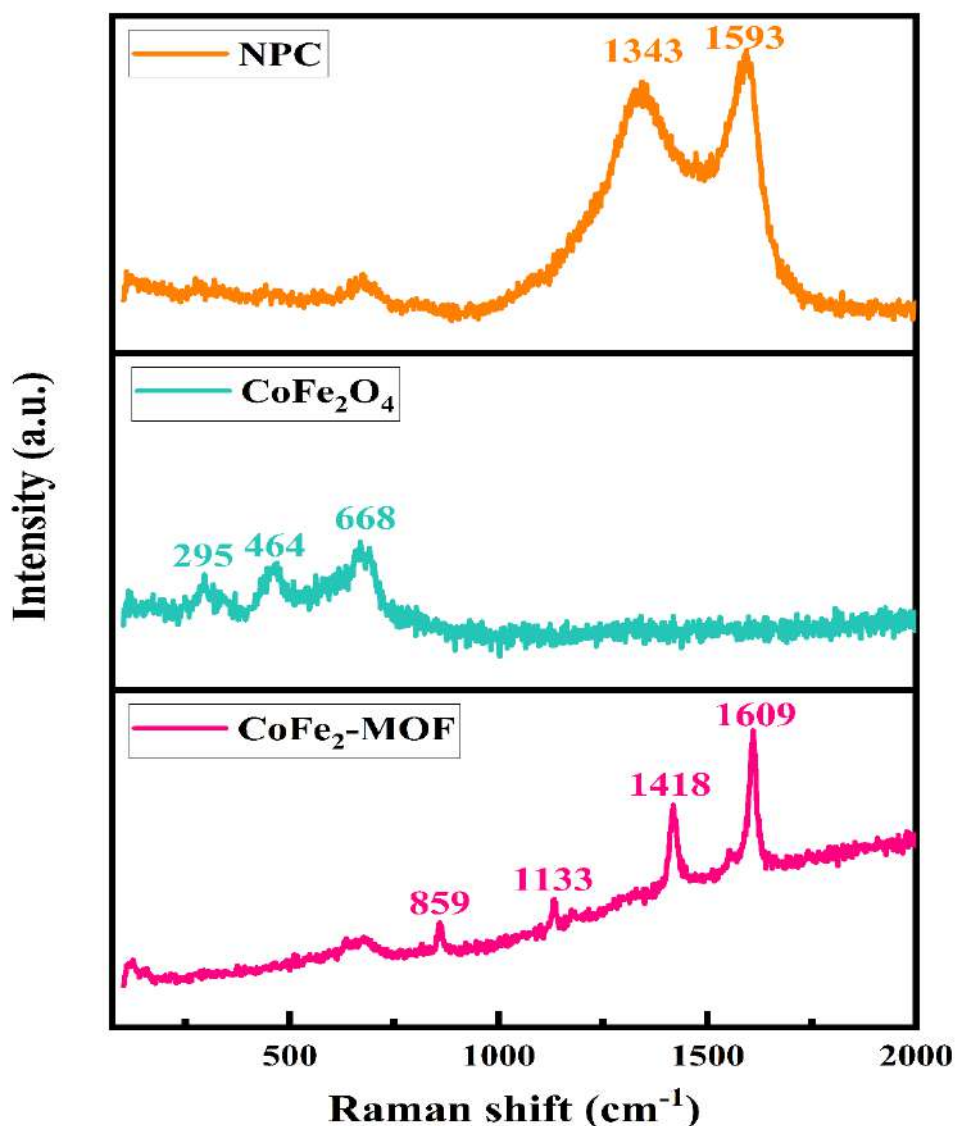


Figure 6.4: Raman spectra of $\text{CoFe}_2\text{-MOF}$, CoFe_2O_4 and NPC

Raman spectroscopy was utilized to explore the structure of $\text{CoFe}_2\text{-MOF}$ and changes in crystal structure as a result of heat treatment of $\text{CoFe}_2\text{-MOF}$. Raman spectra of $\text{CoFe}_2\text{-MOF}$ and $\text{CoFe}_2\text{-MOF}$ derived CoFe_2O_4 and NPC are presented in figure 6.4. In Raman spectra of $\text{CoFe}_2\text{-MOF}$, the bands observed at 1609 and 1418 cm^{-1} are due to the carboxylate group and they are assigned to the asymmetric and symmetric vibration modes. The band at 1133 cm^{-1} was attributed to the vibration of

C-C bond between the benzene ring and the carboxylate group, also the plane of C-H bonding deformation is ascribed to the band at 859 cm^{-1} . As shown in Raman spectra of CoFe₂-MOF, which included a BDC linker, and no Raman signals corresponding to cobalt oxides, iron oxides, or other contaminants were detected.³² According to figure 6.4, the Raman spectra of CoFe₂O₄ exhibit three different peaks in the $200\text{--}700\text{ cm}^{-1}$ region. The stretching vibrational modes of CoFe₂O₄ were attributed to the three spectral peaks at 295, 464, and 668 cm^{-1} .³³ Furthermore, the E_g and T_{2g} vibrational modes are responsible for the peaks at 464 and 668 cm^{-1} , respectively. Furthermore, the Raman spectra of NPC shows the peaks at 1343 and 1593 cm^{-1} , which reflect the D and G bands from the A_{1g} and E_{2g} symmetries for nano-structures graphitic carbon, also indicate that the nanoporous carbon calcined under nitrogen atmosphere contains graphitic carbon. Moreover, the D band presence can be linked to the disorder predominantly brought on by the presence of metals, as seen in the XRD and XPS results.^{34,35}

6.4.4 Scanning electron microscopy of CoFe₂-MOF, CoFe₂O₄ and NPC

Surface morphological study of bimetallic CoFe₂-MOF derived CoFe₂O₄ and NPC with lower and higher magnifications is as presented in Figure 5. The uniformly distributed rock shaped morphology of CoFe₂-MOF has been observed and presented in the figure 6.5 (a, b). Additionally, as meticulous observation it is seen that, the tiny granules with few nanometer in size are anchored all over side of the rock hence, the interconnected rocks are noticed in the material it will help to charge transportation in supercapacitor application. In between these two rocks some gaps also present, which is connected to tiny granules therefore has no any chance to interfere of electrolyte and working electrode. This gap increases the surface area of the sample which is useful at application level. The sizes of the rocks are in few micrometers but interconnected tiny granules are few nanometers in size throughout the sample. After modifying the experimental condition, the bimetallic CoFe₂-MOF gets converted into cobalt ferrite and nanoporous carbon at calcination temperature of $500\text{ }^{\circ}\text{C}$ in air atmosphere and $800\text{ }^{\circ}\text{C}$ temperature in nitrogen atmosphere respectively for 3 hr. The intersected layer structure with smooth surface of nanograin like morphology of CoFe₂O₄ has been seen in the figure 6.5 (c, d). The CoFe₂O₄ exhibited the interconnected grain like morphology with average size in few nanometers.

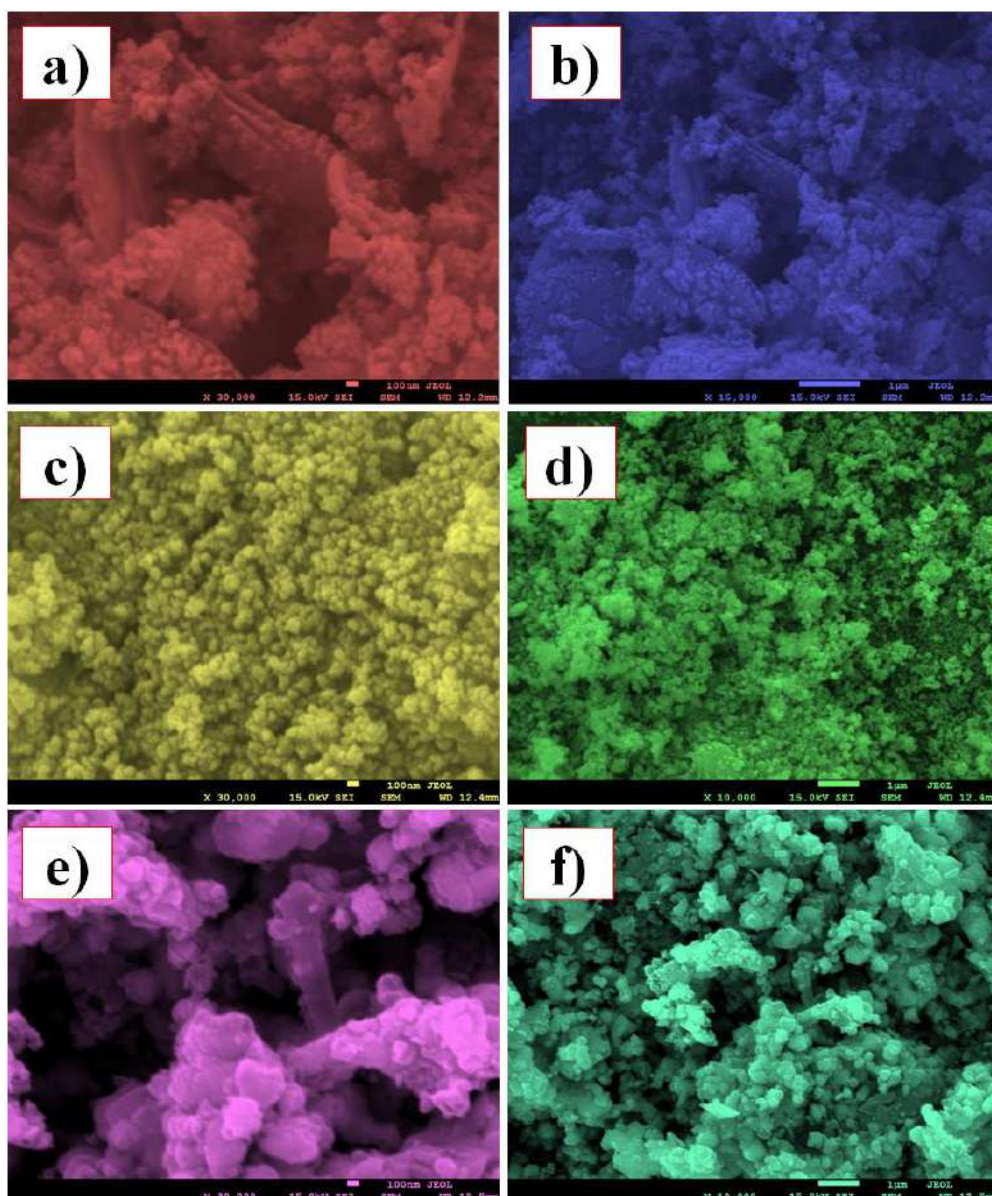


Figure 6.5: SEM images at different magnifications of (a, b) CoFe₂-MOF (c, d) CoFe₂O₄ (e, f) NPC

The CoFe₂O₄ morphology is totally different than bimetallic CoFe₂-MOF may be due to the calcination temperature plays major role in the morphological formation. After calcination in air, rock converted into the grain with porous nature of the sample and creates some pores on the surface of the grain which is discussed under the BET analysis. Then, moving towards calcination at 800 °C in nitrogen atmosphere, the bimetallic CoFe₂-MOF sample gets converted into nanoporous carbon. The small nanobricks like morphology with plenty of pores and the irregular arrangement with different shape and size of the nanobricks are observed (Figure 6.5 (e, f)). More interestingly, the numerous porous bricks are cross connected to each other creating the space in between these nanobricks, which could enhance the surface area of the

sample and it will be more beneficial for the ion-electrolyte transport hence improving electrochemical performance. Out of these three samples, NPC is most favorable sample for enhancing the electrochemical performance of supercapacitor electrode.

6.4.5 Energy dispersive X-ray analysis of CoFe₂-MOF, CoFe₂O₄ and NPC

Figure 6.6 (a-c) depicts the typical EDX spectrum and color mapping of bimetallic CoFe₂-MOF derived CoFe₂O₄ and NPC samples. In reality of Co, Fe, O, C and N peaks in EDX specify the samples contain the cobalt, iron, oxygen, carbon and nitrogen, as anticipated. The atomic percentage of all the samples are uniformly distributed all over the samples and it is in well agreement with the stoichiometry of all the samples. The inset of the figure reveals the pie diagram of all the elements in the corresponding samples. More interestingly, after calcination of the bimetallic CoFe₂-MOF in air, the percentage of the oxygen is rich in consent sample. Similarly, bimetallic CoFe₂-MOF calcination in nitrogen atmosphere shows increase in the percentage of the carbon in the corresponding sample. Also, the figure 6.6 (a-c) shows colour mapping of different elements like Co, Fe, O, C and N in all samples. Hence, it is confirmed that our prepared samples are in the pure form and will be beneficial for energy storage application.

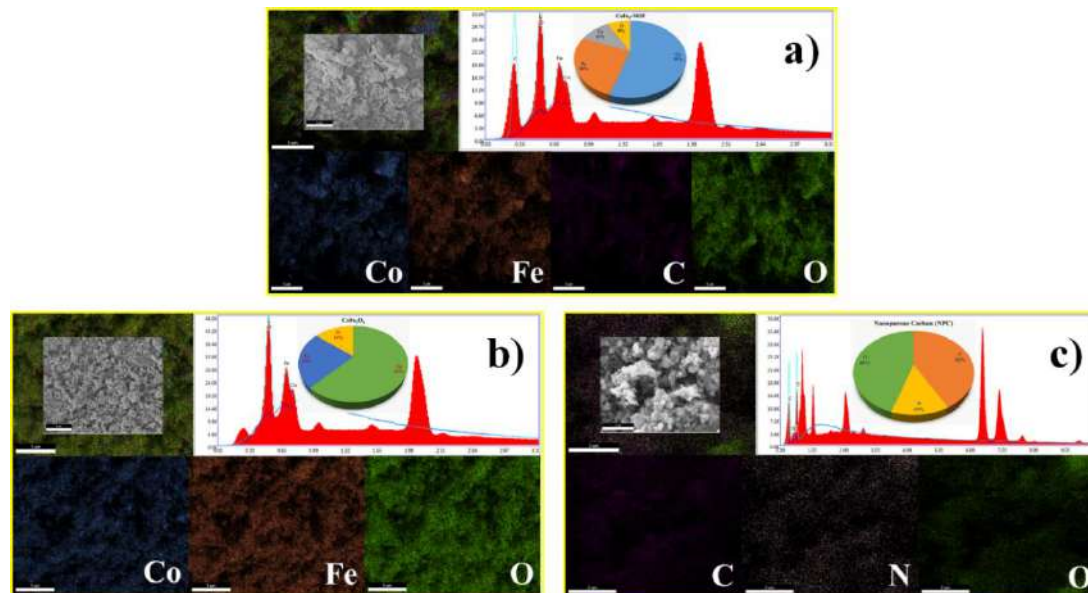


Figure 6.6: Elemental mapping images of (a) CoFe₂-MOF (b) CoFe₂O₄ (c) NPC

6.4.6 Transmission electron microscopy of CoFe₂-MOF, CoFe₂O₄ and NPC

TEM, HRTEM, and SAED analysis were carried out to gain a thorough understanding of the structure of CoFe₂-MOF and its generated CoFe₂O₄ and NPC. Figure 6.7(a and b) shows TEM images of CoFe₂-MOF with a rock-like shape, which

corresponds to the FESEM findings. The lattice fringe spacing in the following HRTEM image as shown in figure 6.7(c) is about 0.205 nm, which is compatible with the (003) plane of CoFe₂-MOF. The SAED pattern indicates the polycrystalline nature of CoFe₂-MOF as shown in figure 6.7(d) and that is consistent with the XRD findings, suggesting the development of CoFe₂-MOF.^{36,37} The TEM images of CoFe₂O₄ exhibit grain-like microstructures, as seen in figure 6.7(e and f), which are compatible with the FESEM pictures. The lattice spacing of 0.307 nm from the HRTEM image in figure 6.7(g) corresponds to the (311) plane of CoFe₂O₄. Furthermore, the SAED picture in figure 6.7(h) shows that CoFe₂O₄ is polycrystalline.^{38,39} The TEM images of NPC indicate nanobricks-like structures, as seen in figures 6.7(i and j) that are compatible with the FESEM images. The lattice spacing of 0.225 nm from the HRTEM image in figure 6.7(k) corresponds to the (103) plane of NPC. The SAED pattern, as shown in figure 6.7(l), reveals the polycrystalline nature of NPC and is compatible with the XRD findings, implying the creation of NPC.⁴⁰

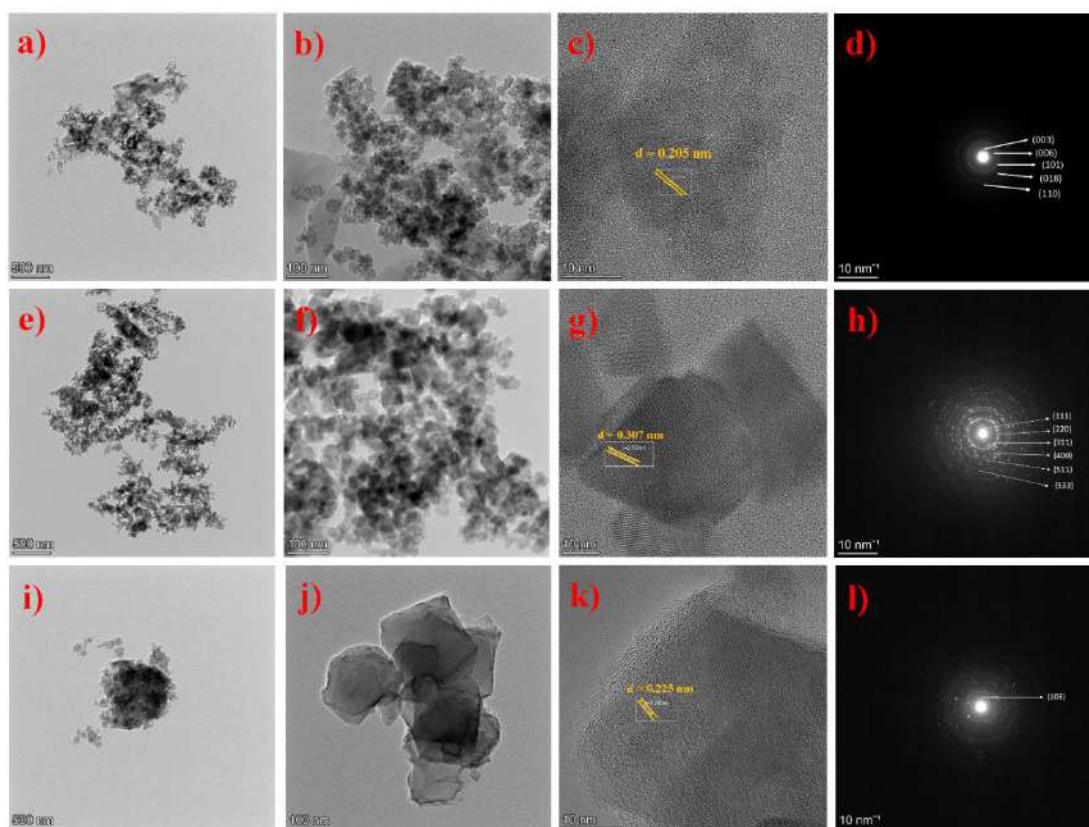


Figure 6.7: TEM, HR-TEM and SAED pattern of the as-prepared CoFe₂-MOF (a-d), CoFe₂O₄ (e-h) and NPC (i-l)

6.4.7 Brunauer-Emmett-Teller analysis of CoFe₂-MOF, CoFe₂O₄ and NPC

The specific surface area and porosity of NPC and CoFe₂O₄ derived from CoFe₂-MOF were characterised using nitrogen adsorption/desorption studies at 77 K and BJH pore size distributions analyses, as shown in figure 6.8(a-c). The fact that all of the samples exhibit a type-IV hysteresis loop at relative pressures between 0.4 and 0.9 indicates that the samples are mesoporous in nature. While CoFe₂-MOF (406 m² g⁻¹) and CoFe₂O₄ (289 m² g⁻¹) have lower specific surface areas than the NPC (614 m² g⁻¹), which is depicted in table 6.1. Furthermore, BJH pore size analysis of NPC reveals a 1.78 nm pore size with a maximal number of mesopores. CoFe₂-MOF and CoFe₂O₄ have pore radius of 1.80 and 1.84 nm, respectively, as illustrated in figure 6.8(d-f). NPC has a higher surface area than CoFe₂-MOF and CoFe₂O₄ according to BET surface area measurement.

Table 6.1: Textural properties of CoFe₂-MOF, its derived CoFe₂O₄ and NPC.

Samples	Surface area (m ² g ⁻¹)	Pore radius (nm)
CoFe ₂ -MOF	406	1.80
CoFe ₂ O ₄	289	1.84
NPC	614	1.78

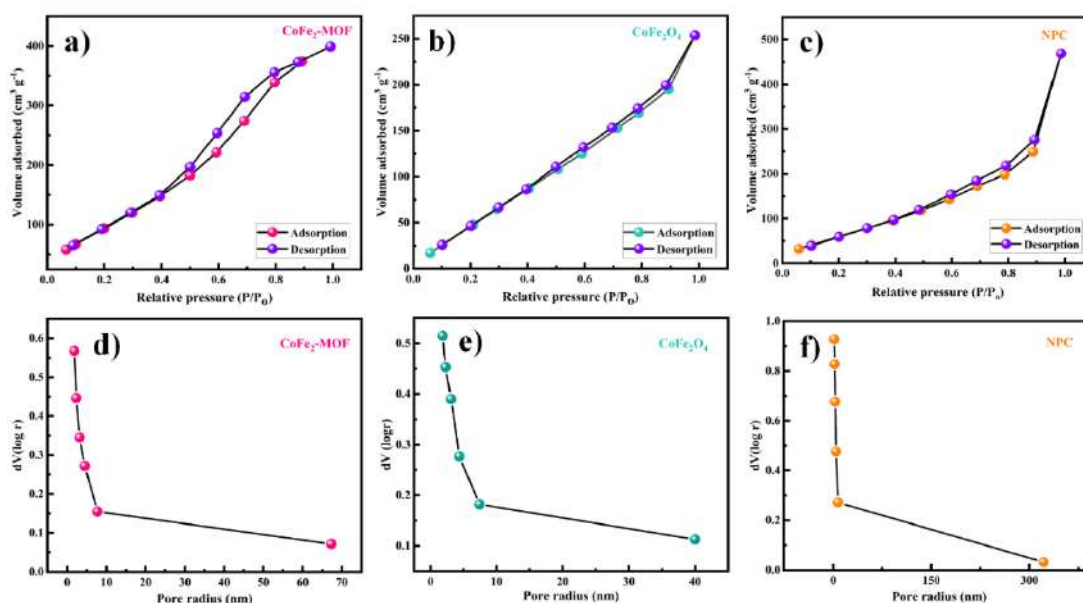


Figure 6.8: Nitrogen adsorption-desorption isotherm and BJH pore size distribution plots of (a, d) CoFe₂-MOF, (b, e) CoFe₂O₄ and (c, f) NPC

6.4.8 Vibrating sample magnetometer of CoFe₂-MOF, CoFe₂O₄ and NPC

The VSM measurements were performed to measure the magnetization of the prepared materials as a function of magnetic field. In-depth magnetic measurements were made on CoFe₂O₄, CoFe₂-MOF and CoFe-MOF derived nanoporous carbon in order to analyze the impact of functionalization on MNPs magnetic behavior. Figure 6.9 displays the magnetization curves of the NPC and CoFe₂O₄ derived from CoFe₂-MOF at ambient temperature. The saturation magnetization (M_s) value, calculated by fitting the M vs. $1/H$ curves due to the non-saturating magnetization even at higher fields. The M_s values of CoFe₂-MOF, CoFe₂O₄, and CoFe-MOF derived NPC are 2.12, 51.07, and 110.95 emu g⁻¹, respectively. Thus, the M_s value of NPC is much higher than the CoFe₂-MOF, CoFe₂O₄, samples.

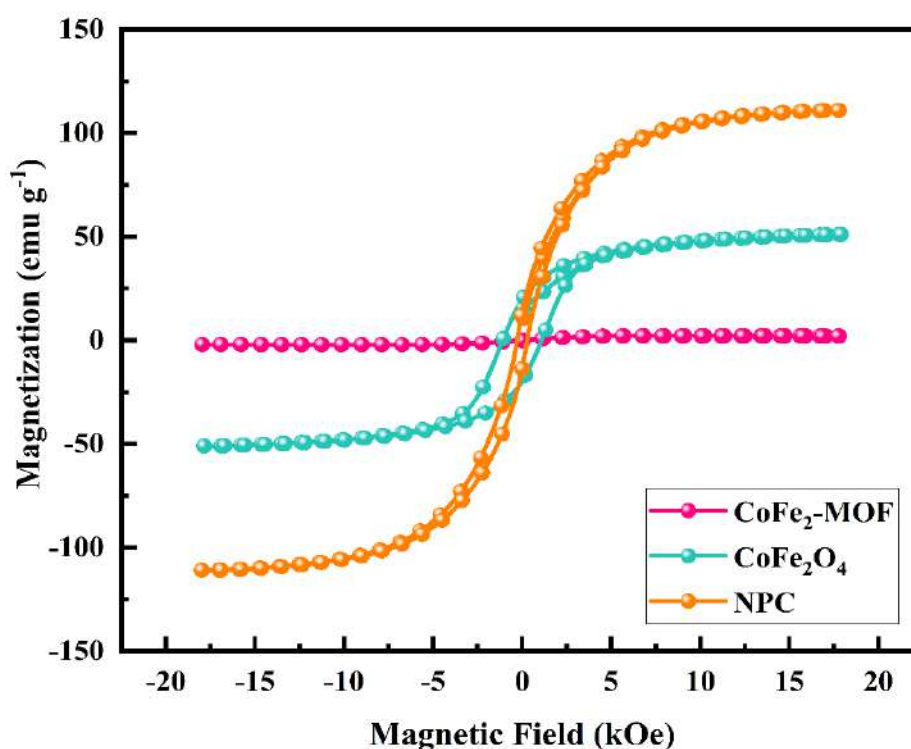


Figure 6.9: Hysteresis curves of CoFe₂-MOF, CoFe₂O₄ and NPC

Still, the relation between M_s and SC is not yet highly explored. The magnetic and electric coupling of the materials provides a new insightful way for magnetoelectric phenomenon. However, the magnetic field can enhance the power density, energy density, and improves cyclic stability. Further, Rebecca Sikkema et al. stated that higher the magneto capacitance and magnetoelectric phenomenon, the effect of magnetic field on electric diffusion, structure of EDLC charge transfer resistance influences the charge/discharge behavior of the materials.⁴¹ Hence, NPC

will be more beneficial for many technological applications especially for supercapacitor because of its surface area, pore size and higher M_s value. We believe that the obtained high M_s values and high capacitance value of the material will pave the way for the novel physio-chemical phenomena in the field of magnetoelectric supercapacitor.

6.4.9 X-ray photoelectron spectroscopy of CoFe₂-MOF, CoFe₂O₄ and NPC

The X-ray photoelectron spectroscopy analysis was utilized to examine the chemical makeup and electronic configuration of CoFe₂-MOF, CoFe₂O₄, and nanoporous carbon. The figure 6.10 shows the XPS spectrums of CoFe₂-MOF, CoFe₂O₄, and nanoporous carbon revealing the presence of Co, Fe, C, N and O components in the materials.

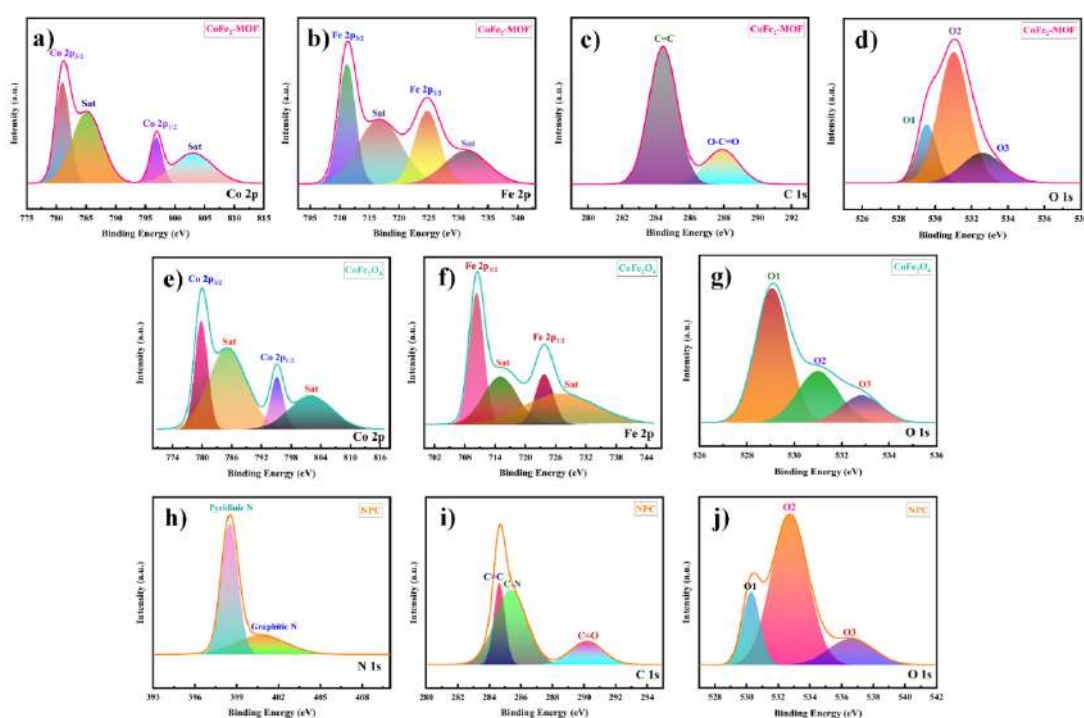


Figure 6.10: High-resolution XPS spectra of (a-d) CoFe₂-MOF (e-g) CoFe₂O₄ (h-j) NPC

The high-resolution XPS spectrum of Co 2p show peaks at 781.0 and 796.8 eV in CoFe₂-MOF, also the peaks at 779.8 and 795.1 eV in CoFe₂O₄ are assigned to Co 2p_{3/2} and Co 2p_{1/2} of Co(II) as depicted in figure 6.10(a, e). Moreover, the existence of two satellite peaks situated at 785.1 and 802.8 eV in CoFe₂-MOF and peaks at 785.0 and 801.7 eV in CoFe₂O₄ substantiates the occurrence of Co²⁺ oxidation state in the materials. In CoFe₂-MOF, the Fe2p spectrum exhibits peaks at 711.2 and 724.7 eV, while in CoFe₂O₄, the peaks are at 710.3 and 723.8 eV, indicates

the +3 oxidation state of Fe in both samples as shown in figure 6.10(b, f). At high magnification, the figure 6.10(c) shows the spectra of C1s reveal a dual peak structure with binding energies of 284.4 and 287.9 eV, which correspond to the C=C and O-C=O bonds found in CoFe₂-MOF. Additionally, three peaks can be observed at binding energies of 284.6, 285.3, and 290.1 eV, which provide confirmation of the existence of C=C, C-N, and C=O bonds in nanoporous carbon as shown in figure 6.10(i). Figure 6.10(d, g, j) displays the deconvoluted O1s spectra for CoFe₂-MOF, CoFe₂O₄, and nanoporous carbon. The presence of three peaks for each material indicates the existence of M-O, C-O, and C=O bonds in them.^{42,43} The N1s spectra of nanoporous carbon material were analyzed and two separate peaks were identified. These peaks corresponded to the binding energies of pyridinic-N at 398.4 eV and graphitic-N at 400.7 eV, as shown in the figure 6.10(h).⁴⁴

6.4.10 Electrochemical measurements of CoFe₂-MOF, CoFe₂O₄ and NPC electrodes

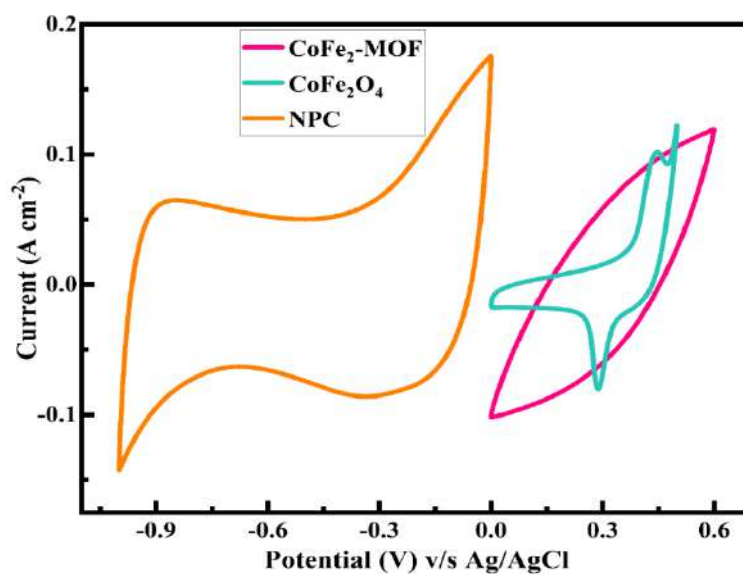


Figure 6.11: CV curves of CoFe₂-MOF, CoFe₂O₄, and NPC within different operating potential windows at a constant scan rate of 100 mV s⁻¹

The intriguing structural and morphological characteristics of CoFe₂-MOF, CoFe₂O₄ and NPC materials compel us to investigate their electrochemical properties. Electrochemical performance of the fabricated CoFe₂-MOF, CoFe₂O₄ and NPC electrodes were investigated using a 2 M KOH as aqueous electrolyte in a three-electrode system utilizing saturated Ag/AgCl employed as a reference electrode, graphite employed as a counter electrode and fabricated electrodes employed as a working electrode. The CV curves for CoFe₂-MOF, CoFe₂O₄ and NPC electrodes at a

scan rate of 100 mV s^{-1} are shown in figure 6.11. It is revealed that $\text{CoFe}_2\text{-MOF}$, CoFe_2O_4 and NPC electrodes operate in various potential range. Figure 6.12(a-c) represents the CV profiles of $\text{CoFe}_2\text{-MOF}$, CoFe_2O_4 and NPC electrodes at scan rates from 10 to 100 mV s^{-1} . The CV curves of $\text{CoFe}_2\text{-MOF}$ electrodes are semirectangular in form and may be characterised by the presence of double-layer capacitance as well as pseudocapacitive behaviour, as illustrated in figure 6.12(a). The CV curves of the CoFe_2O_4 electrode show distinct redox peaks, indicating that the unique capacitance properties are mostly caused by faradic redox reactions, as illustrated in figure 6.12(b). Furthermore, the CV profiles of NPC are rectangular in shape, indicating EDLC behaviour with good capacitive performance and quick current responses, as shown in figure 6.12(c). From the aforementioned CV results, it can be deduced that as scan rate decreases, the area under the CV curve also decreases, which leads to a decrease in current. This is because electric charges may find it challenging to occupy all of the available sites at the electrode-electrolyte interface assignable to their slow rate of migration and erratic orientation in the electrolyte.^{45,46} This behaviour also demonstrates that the NPC electrode facilitates fast ion diffusion via the pores at high rates, as compared to $\text{CoFe}_2\text{-MOF}$ and CoFe_2O_4 . The area under the CV curve of the NPC is bigger than that of the $\text{CoFe}_2\text{-MOF}$ and CoFe_2O_4 , showing improved EDLC behaviour.

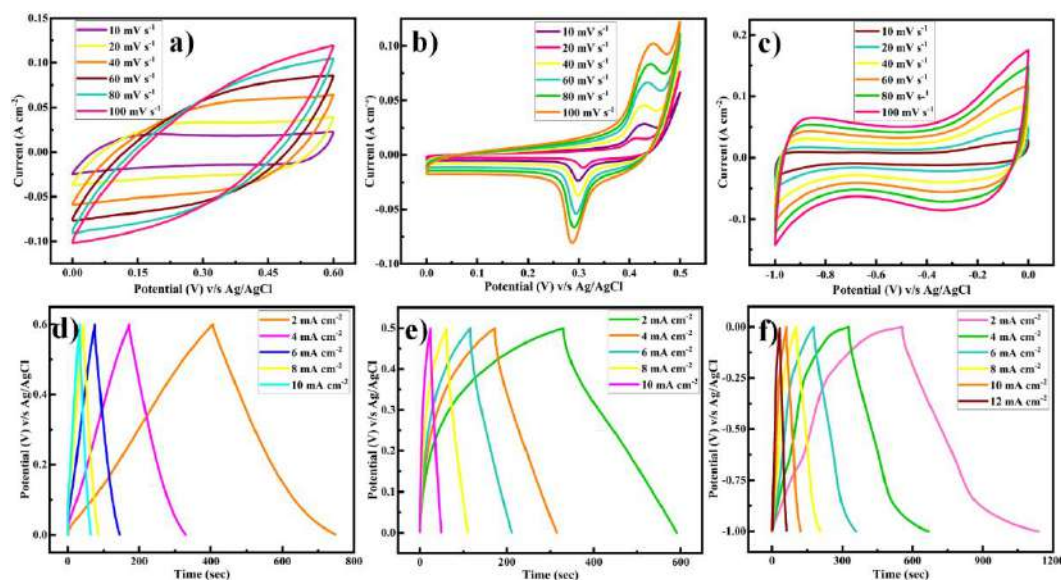


Figure 6.12: The three-electrode electrochemical performances of $\text{CoFe}_2\text{-MOF}$ -derived CoFe_2O_4 and NPC: CV curves at various scan rates of (a) $\text{CoFe}_2\text{-MOF}$, (b) CoFe_2O_4 , (c) NPC, GCD curves at various current densities of (d) $\text{CoFe}_2\text{-MOF}$, (e) CoFe_2O_4 , (f) NPC

Galvanostatic charge-discharge (GCD) testing with varied current densities is used to further examine the capacity and rate capabilities of CoFe₂-MOF, CoFe₂O₄, and NPC electrodes as shown in figure 6.12(d-f). Every GCD curve has a pair of charge-discharge plateaus. The charge-discharge curve shows remarkable symmetry, signifying excellent reversibility. The specific capacitance of the CoFe₂-MOF, CoFe₂O₄, and NPC electrodes is determined depending on GCD curves and equation (6.1), and outcomes are depicted in figure 6.13(a). The GCD outcomes strongly imply that the NPC electrode provided the maximum specific capacitance at different current densities and excellent electrochemical performance. The NPC electrode had a greater specific capacitance of 1271 F g⁻¹ at 2 mA cm⁻² than the CoFe₂-MOF (1038 F g⁻¹ at 2 mA cm⁻²) and CoFe₂O₄ (973 F g⁻¹ at 2 mA cm⁻²) electrodes. The specific capacitances of NPC were 1271, 1170, 992, 749, 553, and 331 F g⁻¹, corresponding to 2, 4, 6, 8, 10, and 12 mA cm⁻² current density, demonstrating the superior rate capability, which is significantly greater than that of CoFe₂-MOF (1038, 961, 670, 567 and 469 F g⁻¹, corresponding to 2, 4, 6, 8 and 10 mA cm⁻² current density) and CoFe₂O₄ (973, 906, 776, 628 and 437 F g⁻¹ corresponding to 2, 4, 6, 8 and 10 mA cm⁻² current density) electrodes. Figure 6.13(a) indicates the rate capability of CoFe₂-MOF, CoFe₂O₄ and NPC electrode, illustrating that when the current density increases, specific capacitance falls slightly. According to the preceding data, specific capacitance reduces as current density increases and vice versa. This is due to the fact that at higher current densities, the electrolyte ions participate in the bulk surface for the electrochemical reaction due to ion transport restrictions, so capacitance values decrease, whereas at low current densities, the electrolyte ions have enough time to move across the interior pores of the electrode material, so capacitance values increase.

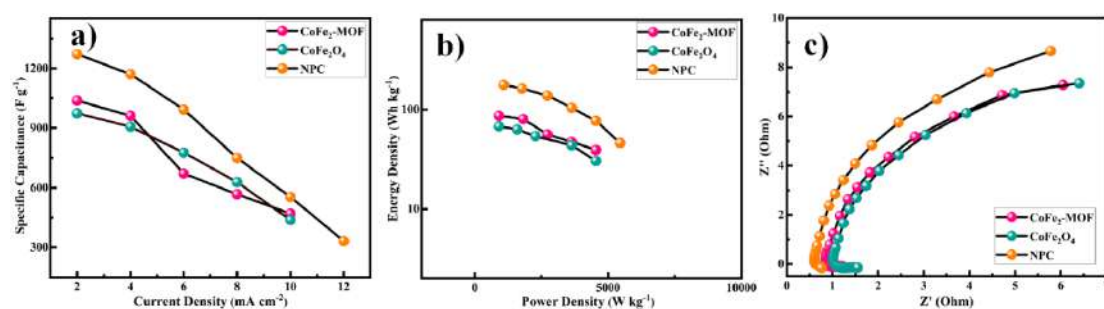


Figure 6.13: (a) Specific capacitance at the different current densities of CoFe₂-MOF, CoFe₂O₄ and NPC, (b) Ragone plot of CoFe₂-MOF, CoFe₂O₄ and NPC, (c) EIS curves of CoFe₂-MOF, CoFe₂O₄ and NPC

The two most important metrics for evaluating the performance of supercapacitor devices are energy density and power density, which were computed and depicted in the Ragone plot as shown in figure 6.13(b). The NPC reaches a maximum energy density of 176 Wh kg^{-1} at a power density of 1090 W kg^{-1} as compared to the $\text{CoFe}_2\text{-MOF}$ (86 Wh kg^{-1} at 909 W kg^{-1}) and CoFe_2O_4 (67 Wh kg^{-1} at 900 W kg^{-1}), respectively. EIS was used to examine the internal resistance of electrodes and the ion/electron transport kinetics at the electrode-electrolyte connection.⁴⁷ The EIS spectra for $\text{CoFe}_2\text{-MOF}$, CoFe_2O_4 and NPC electrodes were measured in the frequency range 1 Hz to 100 kHz and are displayed as Nyquist plots in figure 6.13(c). From EIS spectra, the semicircle in the high-frequency region was utilized to calculate the charge transfer resistance (R_{ct}) at the electrode-electrolyte contact. It is obvious that the semicircle of the NPC electrode was smaller than of the $\text{CoFe}_2\text{-MOF}$ and CoFe_2O_4 electrodes, indicating a quicker charge transfer that permitted the quick redox reactions. The charge transfer resistance of the $\text{CoFe}_2\text{-MOF}$, CoFe_2O_4 , and NPC electrodes were evaluated to be 0.34, 0.46 and 0.15Ω , respectively. Therefore, the improved electrochemical characteristics of the NPC electrode may be effectively explained by the combined benefits of ion diffusion kinetics and rapid electron transport.

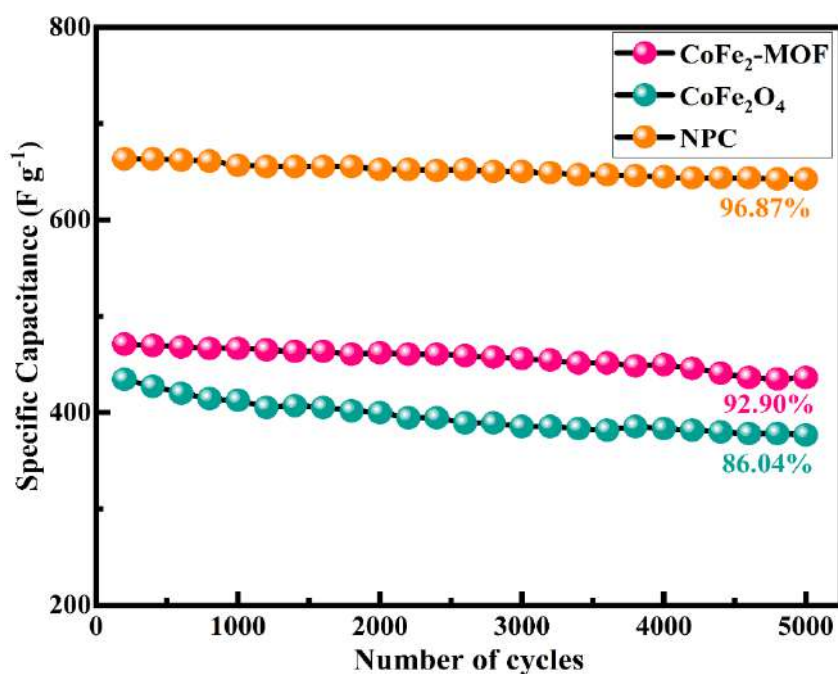


Figure 6.14: Cycle lives measured from galvanostatic charge-discharge of the $\text{CoFe}_2\text{-MOF}$ (at 10 mA cm^{-2} current density), CoFe_2O_4 (at 10 mA cm^{-2} current density) and NPC (at 12 mA cm^{-2} current density) electrodes

The cyclic stability of energy storage devices is crucial for their practical use. Figure 6.14 depicts the long-term cyclic stability evaluations of CoFe₂-MOF, CoFe₂O₄ and NPC electrodes performed at 10, 10, and 12 mA cm⁻² current density for 5000 charge-discharge cycles. Compared to CoFe₂-MOF and CoFe₂O₄ electrodes, the NPC electrode retained an ultrahigh cycling life with 96.87 % of the original capacitance as the current density grew six-fold up to 12 mA cm⁻² even after 5000 cycles. The MOF and ferrite electrode shows 92.90 and 86.04 % cyclic stability at five-fold increased current density of 10 mA cm⁻², respectively. The enormous surface area of NPCs, which can offer more active sites inside the pores for quick electrochemical reactions and enhance the transport of ions or electrons at the electrolyte/electrode contact, is a contributing factor in their superior electrochemical performance. The existence of mesopores in the NPC material can provide a rapid diffusion channel for electrolyte infusion as well as ion or electron transport.

6.4.11 Electrochemical characterization of CoFe₂O₄/NPC all-in-one hybrid supercapacitor device (CoFe₂O₄/NPC HSC device)

To further examine the feasibility of the CoFe₂-MOF, CoFe₂O₄, and NPC electrode materials for practical use, ‘all-in-one’ a hybrid supercapacitor device was built utilizing the synthesized CoFe₂O₄ electrode as an anode, NPC electrode as a cathode and PVA-KOH as a gel -polymer electrolyte (denoted as CoFe₂O₄/NPC). Liquid electrolytes used in supercapacitors poses a concern due to its susceptible to evaporation and leakage problem, which restricts their long-term usage. Gel-polymer electrolyte are made of liquid electrolytes that have been numbed in a polymer matrix, which solves the leakage issue. Gel-polymer electrolyte contain significantly less free water than liquid electrolytes, they can decrease water oxidation processes, therefore expands the operating voltage window, which have long been a barrier in liquid electrolyte-based supercapacitors. As a result, the KOH liquid electrolyte was embedded in a matrix of poly vinyl alcohol, on account of its OH⁻ groups, can retain water and provide excellent ion-conducting routes.^{48,49} Motivated by the electrode's excellent capacitive performance, its possibilities in real-world applications were built by fabricating a solid-state hybrid supercapacitor device, as illustrated in figure 6.15. CV, GCD, and EIS measurements were used to evaluate the capacitive performance of the fabricated all-in-one hybrid supercapacitor device. In the charge-discharge process, K⁺ and OH⁻ ions move in opposite directions, towards the negative and positive electrodes. On the negative electrode, EDLC behaviour is caused by the

adsorption and desorption of K^+ ions, whereas on the positive electrode, pseudocapacitive behaviour is caused by reversible fast surface redox processes involving OH^- ions. The operating potential range of the cathode and anode in a three-electrode assembly allows for adjustment of the hybrid supercapacitor's cell voltage. The $CoFe_2O_4//NPC$ HSC device displays strong rectangular-shaped CV curves with redox peaks at the cell voltage of 1.4 V, demonstrating the synergistic effect of EDLC and pseudocapacitance.

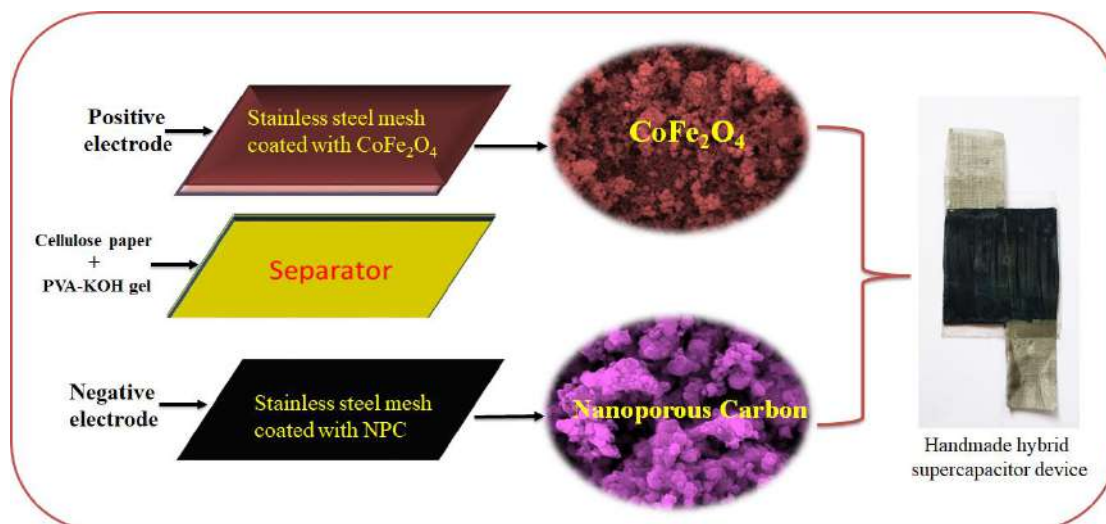


Figure 6.15: Schematic illustration of fabrication of all-in-one hybrid supercapacitor device

Figure 6.16(a) depicts the CV curves of a hybrid supercapacitor with a potential voltage of 0.6 - 1.4 V; moreover, there was no substantial change in the CV curves, suggesting that the voltage to be reached was achievable. Figure 6.16(b) displays the CV curves of the $CoFe_2O_4//NPC$ HSC device at different scan rate ranging from 10 to 100 $mV s^{-1}$. This is supported by both the pseudocapacitance from the $CoFe_2O_4$ and the electric double-layer capacitance from the NPC for the charge storage process. Similarly, GCD curves of $CoFe_2O_4//NPC$ HSC device at a fixed current density of 1 $mA cm^{-2}$ from potential range of 0.8 to 1.4 V demonstrated that there is no evident hydrogen or oxygen evolution behaviour and that the cell has excellent electrochemical reversibility, as shown in figure 6.16(c). As a result, a complete analysis of the $CoFe_2O_4//NPC$ HSC device is carried out in the voltage range of 0 - 1.4 V. The GCD curves of the $CoFe_2O_4//NPC$ HSC device at various current densities ranging from 1 to 5 $mA cm^{-2}$ are shown in figure 6.16(d). The triangular forms produced by GCD curves are consistent with CV curves. Figure 6.17(a) depicts the specific capacitances of the $CoFe_2O_4//NPC$ HSC device calculated

from the GCD curves using equation (6.1). The assembled $\text{CoFe}_2\text{O}_4/\text{NPC}$ HSC device achieved high specific capacitance from 112.1 F g^{-1} at 1 mA cm^{-2} to 85.1 F g^{-1} at 5 mA cm^{-2} current density. Additionally, even after raising the current density by five times, the initial specific capacitance retains, as is seen in figure 6.17(a). This outcome attests to its excellent electrochemical performance. Energy density and power density are used to assess the efficiency of supercapacitors.

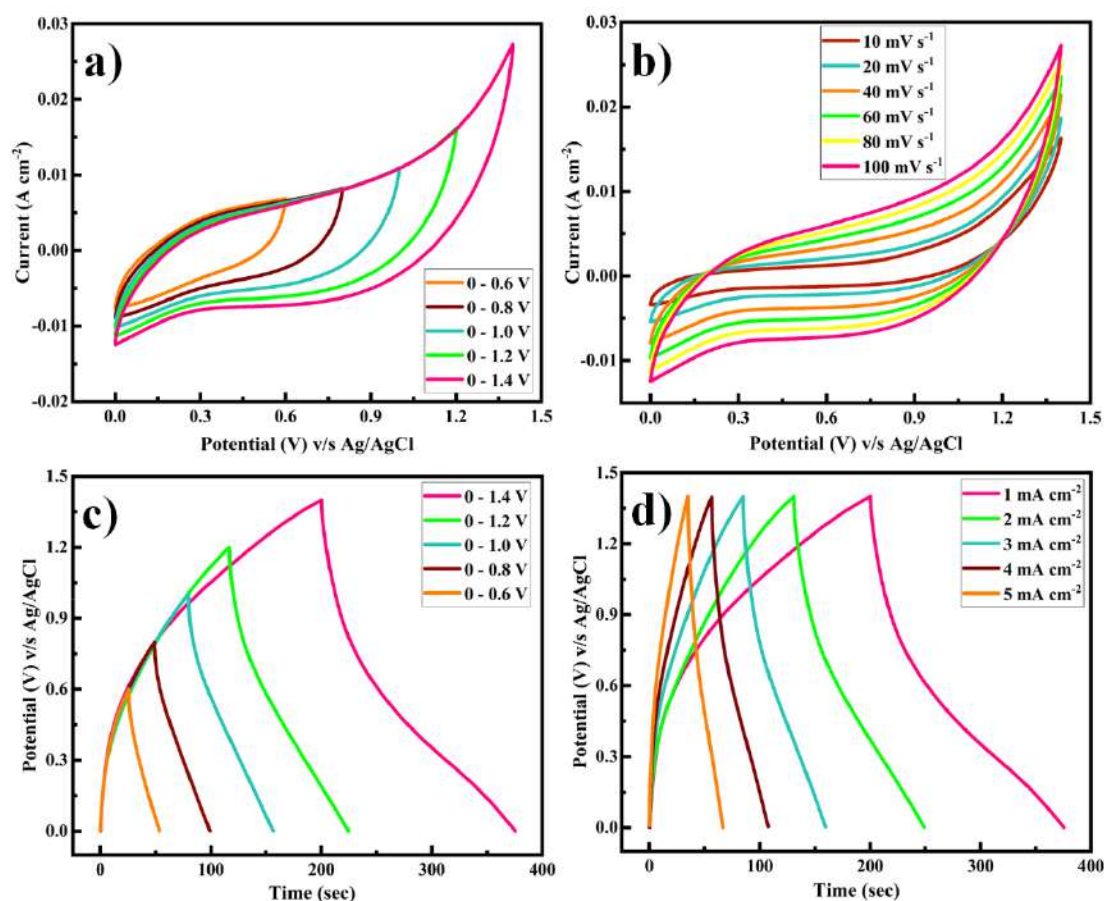


Figure 6.16: Electrochemical tests of the $\text{CoFe}_2\text{O}_4/\text{NPC}$ hybrid supercapacitor device (HSC), (a) CV curves of the $\text{CoFe}_2\text{O}_4/\text{NPC}$ HSC device at a scan rate of 100 mV s^{-1} within different potential windows, (b) CV curves of $\text{CoFe}_2\text{O}_4/\text{NPC}$ HSC device at different scan rates, (c) GCD curves of the $\text{CoFe}_2\text{O}_4/\text{NPC}$ HSC device at 1 mA cm^{-2} with varied potential windows, (d) GCD curves of $\text{CoFe}_2\text{O}_4/\text{NPC}$ HSC device at various current densities

The Ragone plot of the constructed $\text{CoFe}_2\text{O}_4/\text{NPC}$ HSC device at 1.4 V clearly shows that the device has extended energy and power densities. The figure 6.17(b) clearly shows that the manufactured $\text{CoFe}_2\text{O}_4/\text{NPC}$ HSC may deliver a high energy density without compromising much power density. The constructed $\text{CoFe}_2\text{O}_4/\text{NPC}$ HSC device showed an outstanding energy density of 56.2 Wh kg^{-1}

and a power density of 1091.5 W kg^{-1} at 1 mA cm^{-2} current density. Even at a high current density of 5 mA cm^{-2} , the fabricated $\text{CoFe}_2\text{O}_4/\text{NPC}$ HSC device provided an energy density of 42.6 Wh kg^{-1} and a power density of 4297.6 W kg^{-1} . To determine the charge transfer kinetics of the $\text{CoFe}_2\text{O}_4/\text{NPC}$ HSC device, EIS measurements were performed within the frequency range of 1 Hz to 100 kHz as shown in figure 6.17(c). The real axis intercept of the EIS Nyquist plot could be used to calculate the series resistance of the electrode (R_s), which included the inherent resistance of the constructed device. The charge transfer resistance (R_{ct}) at the interface between electrode and electrolyte was estimated using a semicircle in the high-frequency region. The R_s and R_{ct} of the $\text{CoFe}_2\text{O}_4/\text{NPC}$ HSC device were found to be 1.25 and 5.14Ω , respectively.

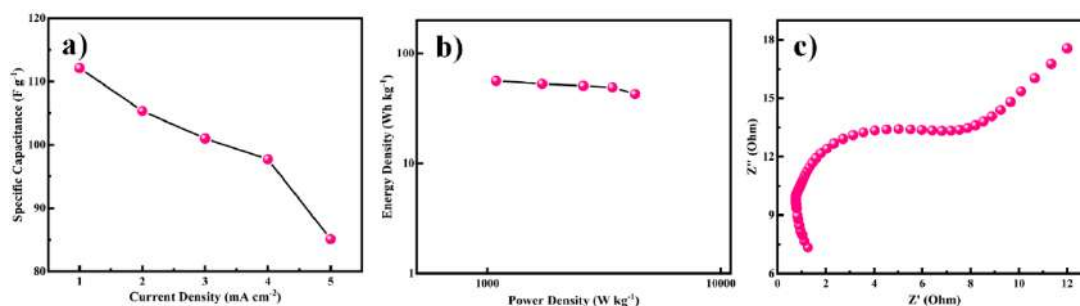


Figure 6.17: (a) Rate capability of the $\text{CoFe}_2\text{O}_4/\text{NPC}$ HSC device according to the GCD curves from 1 to 5 mA cm^{-2} , (b) Ragone plot of the $\text{CoFe}_2\text{O}_4/\text{NPC}$ HSC device, (c) Nyquist plot of the $\text{CoFe}_2\text{O}_4/\text{NPC}$ HSC device

Furthermore, the cycle life and Coulombic efficiency of the $\text{CoFe}_2\text{O}_4/\text{NPC}$ HSC device at 6 mA cm^{-2} current density for 5000 cycles are investigated and depicted in figure 6.18. During cycling, the coulombic efficiency stays about 98.54%, indicating good reversibility. After 5000 cycles, the specific capacitance as a function of cycle number exhibits outstanding electrochemical stability of 97.91%. Additionally, inset of figure 6.18 displays the first five and last five cycles. Even after 5000 GCD cycles, the nature of GCD curve remained almost unchanged, further demonstrating the exceptional cyclic stability. The $\text{CoFe}_2\text{O}_4/\text{NPC}$ HSC device's extended cycle life is due to its high specific area and hierarchical structure, which promotes OH^- diffusion and provides ample room for buffering stresses throughout the charge and discharge process. These findings revealed that the HSCs device constructed with the CoFe_2O_4 and NPC produced from the single $\text{CoFe}_2\text{-MOF}$ predecessor had intriguing potentials in the realm of applicable energy storage devices.

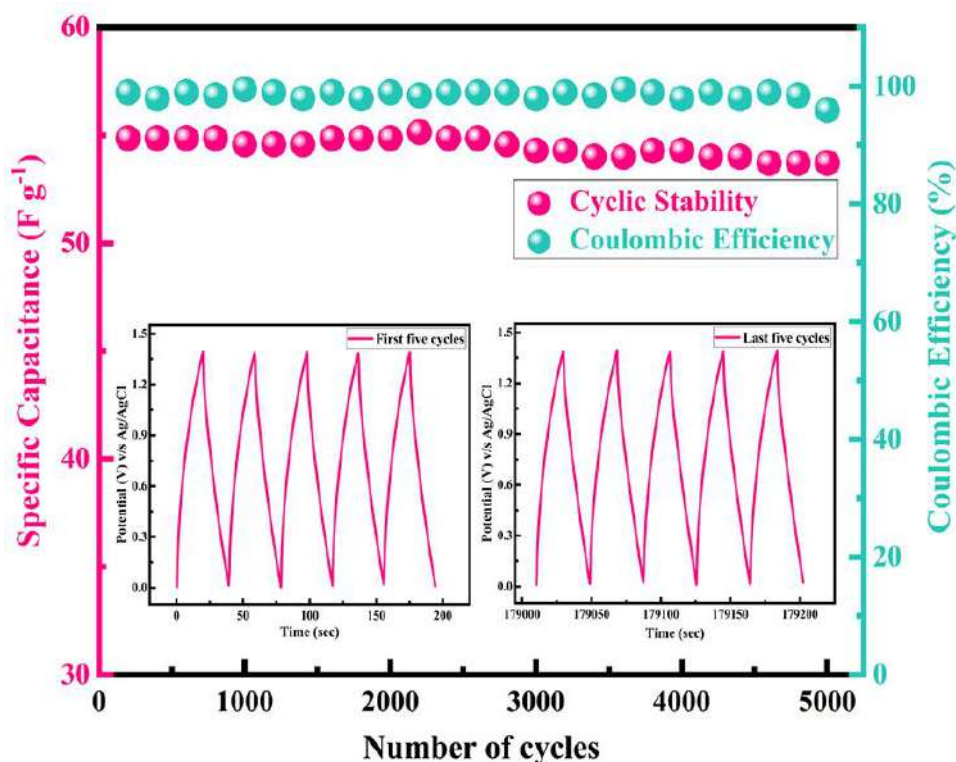


Figure 6.18: Cyclic stability and Coulombic efficiency of CoFe₂O₄//NPC HSC device for 5000 cycles at the current density of 5 mA cm⁻² (inset show first and last five GCD cycles of the stability test)

From above fabricated devices, two were linked in series to investigate their potential uses based on the constructed HSC device's exceptional electrochemical performance. The LED glowed brilliantly for approximately eight minutes after only fifteen seconds of charging, demonstrating the extraordinary usefulness of our all-in-one gadgets (Supporting Information video). A LED powered by the tandem devices, implies the promising application perspective of the constructed all-in-one CoFe₂O₄//NPC HSC device as a developing energy storage and conversion systems.

As illustrated in figure 6.19, a radar graph was plotted to compare the electrochemical characteristics of chemically synthesized bimetallic CoFe₂-MOF, its derived CoFe₂O₄ and NPC. Each vertex exhibits characteristics such as specific surface area, pore radius, specific capacitance, energy density, power density, charge transfer resistance and cyclic stability of the CoFe₂-MOF, its derived CoFe₂O₄ and NPC. The electrodes' electrochemical characteristics are indicated by the filled region beneath the curve. The integral area of NPC is much bigger than that of CoFe₂-MOF and CoFe₂O₄, as seen in figure 6.19. It has been noted that minute crystallite size and

great specific surface area contributed to outstanding specific capacitance, energy density, power density, and cyclic stability.

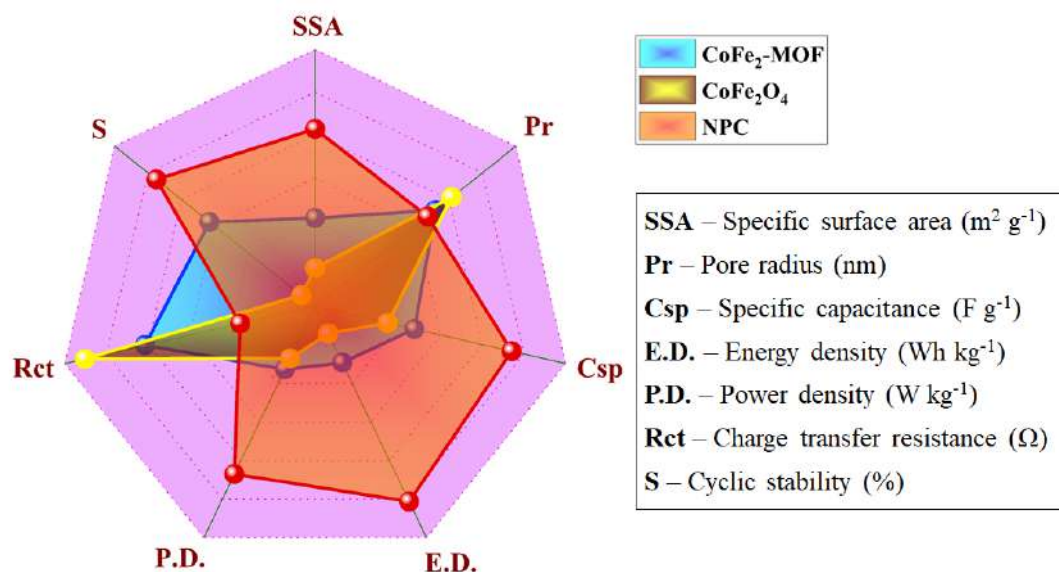


Figure 6.19: Radar plot for comparative study of CoFe₂-MOF, CoFe₂O₄ and NPC electrodes based on supercapacitive properties

6.5 Conclusion

In conclusion, a straightforward "One-for-All" approach is used to produce both anode and cathode for HSC device from a single bimetallic MOF, with CoFe₂O₄ and NPC deriving from CoFe₂-MOF as the sole precursor. To prepare CoFe₂O₄ and NPC, the conversion procedure was improved. By annealing CoFe₂-MOF at 500 °C in air and 800 °C in an inert environment, CoFe₂O₄ and NPC materials with greater phase purity are produced. The derived nanoporous carbon has good electrochemical characteristics, a large specific surface area, and very hierarchically porous structures because of its special structure. The constructed all-in-one CoFe₂O₄//NPC HSC device exhibits an excellent specific capacitance with energy density of 56.2 Wh kg⁻¹ and power density of 1091.5 W kg⁻¹ at 2 mA cm⁻² current density. Additionally, it shows outstanding cyclic stability of 97.91 % over 5000 GCD cycles. This research presents a revolutionary 'One-for-All' concept, which opens up a new potential for next-generation supercapacitors with excellent safety, cheap cost, a wide voltage window, and prolonged cycle stability.

6.6 References

- 1 A. E. Baumann, D. A. Burns, B. Liu and V. S. Thoi, *Commun. Chem.*, 2019, **2**, 1–14.
- 2 S. Lai, J. Zhu, W. Zhang, J. Jiang and X. Li, *Energy and Fuels*, 2021, **35**, 3407–3416.
- 3 N. Swain, B. Saravanakumar, M. Kundu, L. Schmidt-Mende and A. Ramadoss, *J. Mater. Chem. A*, 2021, **9**, 25286–25324.
- 4 C. Y. Zhu, Y. W. Ye, X. Guo and F. Cheng, *New Carbon Mater.*, 2022, **37**, 59–92.
- 5 T. M. Gür, *Energy Environ. Sci.*, 2018, **11**, 2696–2767.
- 6 L. Li, Z. Wu, S. Yuan, X. B. Zhang, *Energy Environ. Sci.*, 2014, **7**, 2101–2122.
- 7 K. Allado, M. Liu, A. Jayapalan, D. Arvapalli, K. Nowlin, J. Wei, *Energy and Fuels*, 2021, **35**, 8396–8405.
- 8 S. Verma, S. Arya, V. Gupta, S. Mahajan, H. Furukawa, A. Khosla, *J. Mater. Res. Technol.*, 2022, **11**, 564–599.
- 9 B. Pal, S. Yang, S. Ramesh, V. Thangadurai, R. Jose, *Nanoscale Adv.*, 2019, **1**, 3807–3835.
- 10 K. O. Otun, M. S. Xaba, S. Zong, X. Liu, D. Hildebrandt, S. M. El-Bahy, Z. M. El-Bahy, *Colloids Surfaces A Physicochem. Eng. Asp.*, 2022, **634**, 128019–128030.
- 11 M. J. Deng, T. H. Chou, L. H. Yeh, J. M. Chen, K. T. Lu, *J. Mater. Chem. A*, 2018, **6**, 20686–20694.
- 12 C. Guo, Y. Zhang, T. Zeng, D. Huang, Q. Wan, N. Yang, *Carbon*, 2020, **157**, 298–307.
- 13 W. Ma, H. Nan, Z. Gu, B. Geng, X. Zhang, *J. Mater. Chem. A*, 2015, **3**, 5442–5448.
- 14 Q. Jing, W. Li, J. Wang, X. Chen, H. Pang, *Inorg. Chem. Front.*, 2021, **8**, 4222–4229.
- 15 D. Chen, L. Wei, J. Li, Q. Wu, *J. Energy Storage*, 2020, **30**, 101525–101537.
- 16 W. Hu, M. Zheng, B. Xu, Y. Wei, W. Zhu, Q. Li, H. Pang, *J. Mater. Chem. A*, 2021, **9**, 3880–3917.
- 17 H. Duan, Z. Zhao, J. Lu, W. Hu, Y. Zhang, S. Li, M. Zhang, R. Zhu, H. Pang, *ACS Appl. Mater. Interfaces*, 2021, **13**, 33083–33090.

- 18 W. Liu, F. Zhu, B. Ge, L. Sun, Y. Liu, W. Shi, *Chem. Eng. J.*, 2022, **427**, 130788-130797.
- 19 R. Zhu, J. Ding, J. Yang, H. Pang, Q. Xu, Q. Xu, D. Zhang, P. Braunstein, *ACS Appl. Mater. Interfaces*, 2020, **12**, 25037–25041.
- 20 C. Qu, Z. Liang, Y. Jiao, B. Zhao, B. Zhu, D. Dang, S. Dai, Y. Chen, R. Zou, M. Liu, *Small*, 2018, **14**, 1–8.
- 21 C. Kang, L. Ma, Y. Chen, L. Fu, Q. Hu, C. Zhou, Q. Liu, *Chem. Eng. J.*, 2022, **427**, 131003-131013.
- 22 A. Tang, C. Wan, X. Hu, X. Ju, *Nano Res.*, 2021, **14**, 4063–4072.
- 23 R. Velmurugan, J. Premkumar, R. Pitchai, M. Ulaganathan, B. Subramanian, *ACS Sustain. Chem. Eng.*, 2019, **7**, 13115–13126.
- 24 R. Bhosale, S. Bhosale, P. Kumbhar, D. Narale, R. Ghaware, C. Jambhale, S. Kolekar, *New J. Chem.*, 2023, **47**, 6749–6758.
- 25 M. Safari, J. Mazloom, *J. Solid State Electrochem.*, 2021, **25**, 2189–2200.
- 26 T. Zhang, J. Du, P. Xi, C. Xu, *ACS Appl. Mater. Interfaces*, 2017, **9**, 362–370.
- 27 T. K. N. Tran, C. P. K. Phan, T. C. Q. Ngo, N. B. Hoang, L. D. Truong, T. K. O. Nguyen, *Processes*, 2022, **10**, 1–14.
- 28 P. D. Patil, S. R. Shingte, V. C. Karade, J. H. Kim, T. D. Dongale, S. H. Mujawar, A. M. Patil, P. B. Patil, *J. Energy Storage*, 2021, **40**, 102821-102832.
- 29 T. Prabhakaran, R. V. Mangalaraja, J. C. Denardin, K. Varaprasad, *J. Mater. Sci. Mater. Electron.*, 2018, **29**, 11774–11782.
- 30 G. R. Patta, V. R. Kumar, B. V. Ragavaiah, N. A. Veeraiah, *Appl. Phys. A Mater. Sci. Process.*, 2020, **126**, 1–11.
- 31 E. K. Nyutu, W. C. Conner, S. M. Auerbach, C. H. Chen, S. L. Suib, *J. Phys. Chem. C*, 2008, **112**, 1407–1414.
- 32 V. H. Nguyen, T. D. Nguyen, L. G. Bach, T. Hoang, Q. T. P. Bui, L. D. Tran, C. V. Nguyen, D. V. N. Vo, S. T. Do, *Catalysts*, 2018, **8**, 487-507.
- 33 P. B. Kharat, S. B. Somvanshi, J. S. Kounsalye, S. S. Deshmukh, P. P. Khirade, K. M. Jadhav, *AIP Conf. Proc.*, 2018, 1–5.
- 34 A. K. Ipadeola, R. Barik, S. C. Ray, K. I. Ozoemena, *Electrocatalysis*, 2019, **10**, 366–380.
- 35 K. Kim, K. J. Lopez, H. J. Sun, J. C. An, G. Park, J. Shim, *J. Appl. Electrochem.*, 2018, **48**, 1231–1241.
- 36 M. G. Radhika, B. Gopalakrishna, K. Chaitra, L. K. G. Bhatta, K. Venkatesh,

- M. K. Sudha Kamath, N. Kathyayini, *Mater. Res. Express*, 2020, **7**, 054003-054017.
- 37 R. Jia, C. Zhao, Z. Huang, X. Liu, D. Wang, Z. Hui, X. Xu, *Ionics*, 2020, **26**, 6309–6318.
- 38 P. Sivagurunathan, S. R. Gibin, *J. Mater. Sci. Mater. Electron.*, 2016, **27**, 8891–8898.
- 39 G. P. Ratkovski, K. T. O. Do Nascimento, G. C. Pedro, D. R. Ratkovski, F. D. S. Gorza, R. J. Da Silva, B. G. Maciel, L. C. Mojica-Sánchez, C. P. De Melo, *Langmuir*, 2020, **36**, 2920–2929.
- 40 M. Sevilla, C. Salinas Martínez-De Lecea, T. Valdés-Solís, E. Morallón, A. B. Fuertes, *Phys. Chem. Chem. Phys.*, 2008, **10**, 1433–1442.
- 41 R. Sikkema, I. Zhitomirsky, *Appl. Phys. Rev.*, 2023, **10**, 021307-021324.
- 42 K. Liu, Y. Chen, X. Dong, Y. Hu, H. Huang, *Electrochim. Acta*, 2023, **456**, 142441-142450.
- 43 P. Sayadi, S. Zeinali, S. Momeni, S. F. NamiAna, M. Tohidi, *J. Electron. Mater.*, 2023, **52**, 3877–3891.
- 44 R. R. Salunkhe, J. Tang, Y. Kamachi, T. Nakato, J. H. Kim, Y. A. Yamauchi, *ACS Nano*, 2015, **9**, 6288-6296.
- 45 D. P. Dubal, R. Holze, *Energy*, 2013, **51**, 407–412.
- 46 S. S. Shah, E. Cevik, M. A. Aziz, T. F. Qahtan, A. Bozkurt, Z. H. Yamani, *Synth. Met.*, 2021, **277**, 116765-116780.
- 47 P. L. Taberna, P. Simon, J. F. Fauvarque, *J. Electrochem. Soc.*, 2003, **150**, A292-A300.
- 48 A. Barua, A. Paul, *Energy Fuels*, 2021, **35**, 10262–10273.
- 49 S. Alipoori, S. Mazinani, S. H. Aboutalebi, F. Sharif, *J. Energy Storage*, 2020, **27**, 101072-101095.

List of Publications

1	R. Bhosale , S. Bhosale, P. Kumbhar, D. Narale, R. Ghaware, C. Jambhale and S. Kolekar, Design and development of a porous nanorod-based nickel-metal-organic framework (Ni-MOF) for high-performance supercapacitor application, <i>New Journal of Chemistry</i> , 2023, 47, 6749.
2	R. Bhosale , S. Bhosale, M. Vadiyar, C. Jambhale, K. -W. Nam, S. Kolekar, Recent Progress on Functional Metal-organic Framework for Supercapacitive Energy Storage Systems, <i>Energy Technology</i> , 2023, 2300147.
3	R. Bhosale , S. Bhosale, D. Narale, C. Jambhale, S. Kolekar, Construction of well-defined two-dimensional architectures of trimetallic metal-organic frameworks for high-performance symmetric supercapacitors, <i>Langmuir</i> , 2023, 39, 34, 12075.
4	R. Bhosale , S. Bhosale, R. Sankannavar, V. Chavan, C. Jambhale, H. Kim, S. Kolekar, Bimetallic MnFe ₂ -MOF and Its Derived MnFe ₂ O ₄ Nanostructures for Supercapacitive Applications, <i>ACS Applied Nano Materials (Revision submitted)</i> .
5	R. Bhosale , S. Bhosale, V. Chavan, C. Jambhale, D. -k Kim, S. Kolekar, Hybrid supercapacitor based on nanoporous carbon and CoFe ₂ O ₄ derived from a single bimetallic-organic framework: One-for-All Approach, <i>ACS Applied Nano Materials (Revision submitted)</i> .
6	P. Kumbhar, D. Narale, R. Bhosale , C. Jambhale, J. -H. Kim, S. Kolekar, Synthesis of tea waste/Fe ₃ O ₄ magnetic composite (TWMC) for efficient adsorption of crystal violet dye: Isotherm, kinetic and thermodynamic studies, <i>Journal of Environmental Chemical Engineering</i> , 2022, 10, 107893.
7	D. Narale, P. Kumbhar, R. Bhosale , R. Ghaware, K. Patil, J. H. Kim, S. Kolekar, Rational design of binder free NiFe ₂ O ₄ @CoFe ₂ O ₄ core-shell nanoflake arrays synthesized by chemical bath deposition for supercapacitor application, <i>Journal of Energy Storage</i> , 2023, 66, 107477.
8	S. Bhosale, R. Bhosale , K. Jagadhane, A. Gore, G. Kolekar, S. Kolekar, P. Anbhule, J. Recent trends in synthetic Top-down approach for Mesoporous Carbon: A seminal review, <i>Journal of Materials Nanoscience</i> , 2023, 10, 601.
9	S. Bhosale, R. Bhosale , S. Shinde, A. Moyo, R. Dhavale, S. Kolekar, P. Anbhule, Biomass nanoarchitectonics with Annona reticulate flowers for mesoporous

carbon impregnated on CeO₂ nanogranular electrode for energy storage application, *Inorganic Chemistry Communications*, 2023, 154, 110949.

- 10 R. Ghaware, P. Sanadi, D. Narale, **R. Bhosale**, K. Patil, J. Kim, S. Kolekar, Effect of Small Change in Reaction Conditions on the Size of Monoclinic BiVO₄ Nanoparticles and their Photocatalytic Abilities, *ChemistrySelect*, 2023, 8, e202301320.

International/National Conferences Presentation

1	Got 3 rd prize for Poster Presentation at the International Conference on “Sustainable Development in Chemistry and Scientific Application” organized by the Department of Chemistry, Sadguru Gadage Maharaj College, Karad on 16 th -17 th December 2021.
2	National Conference on ‘Impact of Chemistry and Biology to the Society and Industry’ organized by the Department of Industrial Chemistry, Kuvempu University, Shivamogga, Karnataka, 20 th - 21 st May 2022.
3	National Seminar on ‘Advances in Chemistry and Material Science’ organized by Prof. Dr. N. D. Patil Mahavidyalaya, Malkapur, 28 th May 2022.
4	Two-day “International Conference on Functional Material and Nanotechnology (ICFMN-2K22)” organized by the Department of Physics, Nehru Institute of Technology, Coimbatore in collaboration with Indian Association for Crystal Growth on 20 & 21 July 2022.
5	9 th Interdisciplinary Symposium on Materials Chemistry, ISMC–2022 organized by Society for Materials Chemistry, Mumbai & Chemistry Division, BARC on 7 to 10 th December 2022.
6	Two-day National Conference on “Advances in Analytical Techniques for Materials and Biomedical Applications” organized by the Rani Channamma University, Belagavi, Karnataka, India on 15 -16 December 2022.
7	International Conference on "Emerging Trends in Basic and Applied Sciences (ETBAS-2023)" organized by Karmaveer Hire Arts, Science, Commerce and Education College, Gargoti, on 17 January 2023.
8	International Conference on Frontier Areas of Science and Technology (ICFAST-2023) organized jointly by Shivaji University, Kolhapur (SUK) & Indian JSPS Alumni Association (IJAA) on 8 & 9 September 2023.

Participated in Workshop

1	Two Day Workshop & hands-on training on Vector Network Analyzer (VNA) organized by SAIF (CFC), Shivaji University, Kolhapur under the STRIDE (Scheme for Trans-disciplinary Research for India's Developing Economy) program on 22-23 Feb 2021.
2	One Day National Level Workshop on "How To Write Review Article?" organized by the Department of Chemistry, Balwant College, Vita on Thursday, 1st July 2021.
3	Workshop and hands-on training on BIO-ATOMIC FORCE MICROSCOPY (BIO-AFM) organized by SAIF (CFC) Shivaji University Kolhapur, 4-5 th January 2022.
4	Workshop 'IP Awareness/Training program under National Intellectual Property Awareness Mission' organized by Intellectual Property Office India, 04 March 2022.

PAPER



Cite this: *New J. Chem.*, 2023, 47, 6749

Design and development of a porous nanorod-based nickel-metal–organic framework (Ni-MOF) for high-performance supercapacitor application

Rakhee Bhosale,  Sneha Bhosale, Pramod Kumbhar, Dattatray Narale, Rachana Ghaware, Chitra Jambhale  and Sanjay Kolekar *

Metal–organic frameworks have received increasing attention as promising electrode materials in supercapacitors. In this study, we synthesized a nickel-metal–organic framework (Ni-MOF) by a simple and low-cost reflux condensation technique using non-hazardous trimesic acid as an organic ligand. The structures and morphologies of the Ni-MOF material were characterized by X-ray diffraction, Fourier-transform infrared spectroscopy, and scanning electron microscopy techniques. The prepared Ni-MOF was found to have a rod-like morphology and these morphologies can provide beneficial paths for electrolyte ion penetration, obtaining an enlarged contact area between the active material and electrolyte. The Ni-MOF had a considerable specific surface area of $398.4 \text{ m}^2 \text{ g}^{-1}$. Further, its highly porous structure offered excellent supercapacitor performance. The charge-storage mechanism of the electrodes was investigated by cyclic voltammetry, charge–discharge cycling, and electrochemical impedance spectroscopy using 2 M KOH as an electrolyte in a three-electrode assembly. The specific capacitance of the Ni-MOF was found to be 1956.3 F g^{-1} at a current density of 5 mA cm^{-2} by GCD studies and it retained 81.13% of its initial capacitance even after 3000 GCD cycles at a 35 mA cm^{-2} current density. An as-fabricated Ni-MOF//activated carbon hybrid supercapacitor (HSC) exhibited a specific energy of $98.15 \text{ W h kg}^{-1}$ at a specific power of $1253.47 \text{ W kg}^{-1}$ and excellent capacity retention of 99.29% over 3000 cycles. The results of this study imply a great potential of the Ni-MOF for application in efficient and sustainable energy-storage devices.

Received 30th January 2023,
Accepted 5th March 2023

DOI: 10.1039/d3nj00456b

rsc.li/njc

Introduction

In the 21st century, the production of energy from different sources has tremendously increased, and its transformation is also increasing day by day in different ways with the ever-increasing demands from industry, buildings, utilities, and transportation.¹ The increasing demand for energy and fuel due to the ever-increasing world population has become one of the important worries for all the global prime economies. Today there is an urgent need for environmentally friendly renewable energy resources to solve the problems related to the dwindling reserves of fossil fuels.^{2,3} In this regard, energy-conversion and -storage technologies have acquired significant attention to support the future use of renewable energy sources. Many researchers from around the globe are devoted to developing sustainable energy sources, like wind, solar, hydropower, and tidal energy, to address the shortage of fossil fuels and to

reduce carbon emissions and global warming. Hence, from various points of view, electrochemical energy-storage devices (EESDs), like rechargeable batteries, supercapacitors, fuel cells, and hybrid devices, have an important part to play in strategies to produce various amounts of energy and power density to meet the demands from different application scenarios.^{4–6}

Supercapacitors (SCs), also known as electrochemical capacitors, offer the advantages of batteries as well as conventional capacitors, and have consequently become extraordinary energy-storage devices for large power output applications.^{7,8} SCs generally offer a fast charging–discharging process (1–10 s), large power density ($500\text{--}10\,000 \text{ W kg}^{-1}$), high cycling stability ($> 500\,000 \text{ h}$), and easy operation. However, current SCs have a low energy density ($1\text{--}10 \text{ W h kg}^{-1}$), which remains a prime challenge in the development of SC technologies. To conquer the drawback of their low energy density, there is a need for the development of high-performance electrode materials for SCs.^{9,10} Due to their profitable features, such as high power density, excellent cycling stability, exceptional rate capability, and eco-friendliness, SCs have become key components in many fields, such as aerospace, electronic communications, and electric

Analytical Chemistry and Materials Science Research Laboratory, Department of Chemistry, Shivaji University, Kolhapur 416 004, India.
E-mail: sskolekar@gmail.com

transport, and thus have attracted increasing attention, but still, there is a need for further advancements in SCs to meet the excessive energy demand of modern society.¹¹ A supercapacitor is like a battery, which means it stores and releases electricity, but instead of storing energy in the form of chemicals, supercapacitors store electricity in a static state, making them better at rapidly charging and discharging energy. Supercapacitors can be mainly divided into two types based on the charge-storage mechanism. The first type is electric double-layer supercapacitors (EDLCs). In EDLCs, the capacitance is obtained from the electrostatic charge assembled at the electrode/electrolyte interface; hence, it is completely dependent on the surface area of the electrode materials that is available to electrolyte ions. The other type is pseudocapacitors, in which the capacitance comes from the reversible redox reactions between the electrolyte and electroactive species on the surface of the electrodes under the applied potential.^{12–14} The electrochemical performance of a supercapacitor device depends on numerous parameters, like choosing its constituents, the synthesis route used for the electrode materials, the potential window of the electrodes, the choice of electrolytes, and the type of current collectors, binders, and separators.^{15,16}

Metal–organic frameworks (MOFs) are attractive materials to fulfil the requirement for next-generation energy-storage technologies because of their extraordinary properties, such as high porosity, many accessible active sites, high surface area, extraordinary stability, vast structural and chemical tunability, tailorable pore size, and pre- and post-synthesis structural modifiability. Also, MOFs are a unique type of nanoporous materials formed by coordinated metal nodes and organic linkers. MOF-based materials have been utilized in many applications, including energy storage and conversion, catalysis, gas separation, drug delivery, hydrogen storage, gas adsorption, and purification.^{17–20} Concurrently, due to the strong coordination capability of transition metals (TMs), TMs are often used as the metal centres of MOFs, and they also offer the advantages of possessing variable valences and good electrochemical properties, which means they can work as pseudocapacitive redox centres.²¹ MOFs can be feasibly included in a supercapacitor by two strategies: by directly utilizing the MOF as an electrode material for supercapacitors or by utilizing MOF-derived materials, like nanoporous carbon, oxides, sulfides, ferrites, which can be evolved and then utilized as electrode materials, such as the Ni, Co, Zn, Cu, and Fe-based MOFs, which have been reported previously to possess good supercapacitive performance.^{22–31} However, the current, MOFs show poor electrical conductivity; therefore, scientists have taken efforts to increase the electrical conductivity through different strategies, such as through developing composite MOFs with different conductive materials, like metal oxides,³² metals,³³ conductive polymers,³⁴ carbon nanotubes,³⁵ and graphene.³⁶ Wang *et al.* proposed a surfactant-free and solvent-assisted solvothermal method to synthesize microflower Ni-MOF, which exhibited a high specific capacitance of 1093 F g⁻¹ at 1 A g⁻¹ with good rate capability, which were attributed to the fast ion transport and low electrical resistance emerging from its microflower-like structure and the specific capacitance resulting from the incorporation of nickel hydroxide species.³⁷ Wu *et al.* investigated nanosheet-

stacked flower-like Ni-MOF *via* a solvothermal method using anionic surfactants. The usage of the static sealing effect among the negatively charged anionic surfactant head groups and metal ions suppressed the growth of crystals on the crystal surface. Their study revealed that the electrochemical performance of Ni-MOF with the surfactant was superior to that of Ni-MOF without the surfactant, whereby it possessed a specific capacitance of 1030 F g⁻¹ at a current density of 1 A g⁻¹ with a capacitance retention of 50% after even 3000 cycles. Further, they assembled an asymmetric supercapacitor by using Ni-MOF as a positive electrode and activated carbon as a negative electrode.³⁸ Gao *et al.* reported the cuboid Ni-MOF by a simple one-step hydrothermal method, which showed a loosely stacked layer-cuboid structure with plentiful mesopores, which were useful for the charge transfer and ion transport for supercapacitors. It also exhibited an exceptional specific capacitance of 804 F g⁻¹ at a current density of 1 A g⁻¹, with a retention of 302 F g⁻¹ after 5000 cycles. Additionally, they fabricated an asymmetric supercapacitor using Ni-MOF and activated carbon as the positive and negative electrodes, respectively.³⁹ Zhang *et al.* prepared Ni-MOF using a mixed-ligand approach, using trimesic acid as a modulator to partially replace the terephthalic acid. Replacing the terephthalic acid with trimesic acid influenced the formation of an albizia flower-like spheres@nanosheets structure, which helped the adsorption of OH⁻ ions on the surface. Also, the electrochemical performance was increased due to the synergistic effect of the surface property and its unique structure. It exhibited an excellent specific capacitance of 920 F g⁻¹ at a current density of 1 A g⁻¹. In addition, they constructed an asymmetric supercapacitor with the help of Ni-MOF as a positive electrode and activated carbon as a negative electrode, which showed a high energy density of 42.4 W h kg⁻¹ at a power density of 0.8 kW kg⁻¹.⁴⁰

In the present work, we used an unprecedented simple and scalable method, *i.e.* a reflux condensation method, to prepare a nanorod-like nickel-based metal–organic framework (Ni-MOF), in a controlled high temperature. The as-synthesized Ni-MOF revealed a one-dimensional (1D) nanorod-like morphology with a high specific surface area 398.4 m² g⁻¹ and highly nanoporous structure, which could produce more electrochemical sites, which increased the consumption of the electroactive material. In addition, for the fabrication of the electrode we used a stainless steel mesh substrate, which has not been reported to date, which is easily available and low cost compared to other reported substrates. Because of the abundant active sites and extremely porous nature of the material, the penetration of electrolyte ions into the material was increased, resulting in an enhancement of the specific capacitance of the material. Also, we constructed a hand-made asymmetric supercapacitor device, which could get a red LED to glow for almost 105 s after charging for only 15 s.

Experimental section

Reagents

Nickel nitrate hexahydrate, *N,N*-dimethylformamide (DMF), and potassium hydroxide (KOH) were purchased from Loba

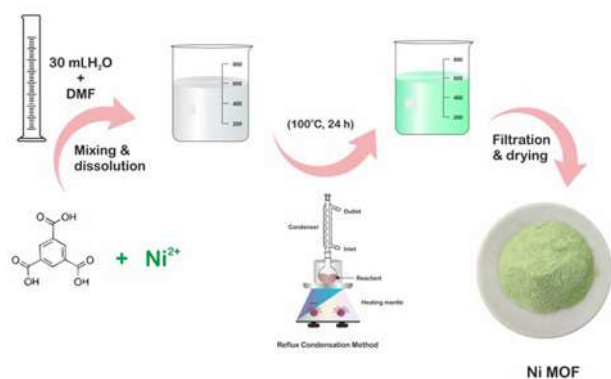


Fig. 1 Schematic of the synthesis of Ni-MOF nanorods via a wet chemical route.

Chemie (India). Benzene-1,3,5-tricarboxylic acid (H3BTC), carbon black, polyvinylidene difluoride (PVDF), and *N*-methyl-2-pyrrolidone (NMP) were purchased from Sigma Aldrich (USA). All the reagents were of analytical grade and used as received without any further purification.

Preparation of nickel-based metal–organic framework (Ni-MOF)

Ni-MOF was synthesized by a method reported elsewhere⁴¹ with slight modification. The reflux method was used for the synthesis of Ni-MOF, which also helped to lower the reaction time of Ni-MOF compared to that reported in the literature. First, 0.15 M of H3BTC was dissolved in 10 mL of DMF with continuous stirring at room temperature; this mixture was denoted as H3BTC solution. Then, the H3BTC solution was transferred to a 50 mL round-bottom flask and heated up to 100 °C using an oil bath with constant stirring. Thereafter, 0.3 M aqueous nickel nitrate (20 mL) solution was added drop by drop into the H3BTC solution. The reaction mixture was stirred for 24 h at 100 °C. After cooling, the resulting precipitate was washed with alcohol several times and finally, a pale-green coloured precipitate was obtained and then dried at 80 °C for 12 h. Fig. 1 shows a schematic of the preparation of the Ni-MOF.

Material characterization

The phase and crystallinity of the Ni-MOF sample were investigated by X-ray diffractometry (XRD) (Bruker D8 Phaser X-ray diffractometer) with Cu K α radiation ($\lambda = 1.541 \text{ \AA}$). The functional groups and types of bonding were confirmed by Fourier-transform infrared (FT-IR) spectroscopy (Bruker Alpha-100508 spectrometer) and the microstructure and surface topography of the Ni-MOF sample were studied by scanning electron microscopy (SEM, JEOL-JSM 6360, Japan). Raman spectroscopy (Lab RAM HR Evolution Confocal Raman Microscope, France) was used for the point group analysis. The chemical composition and elemental valence states of the as-prepared Ni-MOF were evaluated by X-ray photoelectron spectroscopy (XPS, JPS 9030, JEOL ASIA PTE LTD.). In addition, N₂ isotherms and

pore-size distribution data were collected using a surface area and pore volume analyzer (NOVA1000e Quantachrome, USA).

Evaluation of the electrode materials and electrochemical studies

All the electrochemical experiments were performed on a CHI608 electrochemical analyzer using a conventional three-electrode system in 2 M KOH electrolyte at room temperature, with graphite employed as the counter electrode, saturated Ag/AgCl as the reference electrode, and Ni-MOF loaded stainless steel mesh as the working electrode. The working electrode was prepared by making a slurry of 80 wt% Ni-MOF (active material), 10 wt% polyvinylidene fluoride (PVDF), and 10 wt% carbon black (Super P) in NMP solvent. This slurry was coated on the stainless steel mesh (1 cm \times 1 cm), followed by vacuum drying at 80 °C for 12 h.

The electrochemical tests included cyclic voltammetry (CV), galvanostatic charging–discharging (GCD) profiles, and electrochemical impedance spectroscopy (EIS) measurements. A solid-state hybrid supercapacitor (Ni-MOF//AC) was fabricated using Ni-MOF as the positive electrode and activated carbon as the negative electrode. As a separator, cellulose filter paper was used as a sandwich between two electrodes, with the separator and PVA-KOH gel loaded between the two electrodes and assembled on opposite sides. The device was kept at room temperature overnight for natural drying. The PVA-KOH gel electrolyte was prepared according to a literature report.⁴² In a typical procedure, 1 g of polyvinyl alcohol (PVA) was dissolved in 20 mL distilled water keeping the temperature of the bath solution at 80 °C for 30 min. The aqueous KOH solution was then added dropwise to the PVA solution and heated at 80 °C for 30 min to give a viscous gel electrolyte.

The specific capacitance was calculated according to eqn (1),

$$C = \frac{I\Delta t}{m\Delta V} \quad (1)$$

where C is the specific capacity (F g^{-1}), I is the current density (A), Δt is the discharging time (s), m is the mass (g) of the active electrode materials, and ΔV is the potential window of the discharge process (V).

Using eqn (2) and (3), the specific energy and specific power of the hybrid supercapacitor were calculated, respectively,⁴³

$$E = \frac{0.5 \times C \times \Delta V^2}{3.6} \quad (2)$$

$$P = \frac{E \times 3600}{\Delta t} \quad (3)$$

where E and P are the specific energy (W h kg^{-1}) and specific power (W kg^{-1}), respectively, ΔV is the discharging voltage (V), and Δt is the discharging time in seconds.

Results and discussion

The phase purity and crystallinity of the Ni-MOF sample were investigated by XRD. The obtained XRD pattern of the prepared

Ni-MOF together with the data of JCPDS card no. 00-028-1734 are shown in Fig. 2(a). The prepared Ni-MOF data were in close agreement with the given JCPDS card,^{44–46} revealing that the Ni-MOF had a polycrystalline nature. Some of the major peaks obtained were in good agreement with the corresponding angles as reported earlier for Ni-MOF. Furthermore, using Debye-Scherrer's formula (eqn (4)), the crystallite size was calculated for the major characteristic peak of Ni-MOF,

$$D = \frac{0.9\lambda}{\beta \cos \theta} \quad (4)$$

where D is the average crystallite size, λ is the wavelength of the X-rays, β is the full-width at half maxima, and θ is Bragg's diffraction angle. The average crystallite size derived from the (110) plane was 6.89 nm.

Investigation of the chemical structure and functional groups of Ni-MOF was carried out by FT-IR. The FT-IR spectrum of the Ni-MOF sample is shown in Fig. 2(b). In the spectrum, the strong absorption peak at 1349 cm^{-1} was assigned to the C-H stretching vibrations, while the peaks at 3081 and 3399 cm^{-1} could be indexed to the O-H stretching vibrations of water molecules, showing that water molecules existed within the Ni-MOF structure. Additionally, the peaks observed at 1506 and 1608 cm^{-1} were attributed to the symmetric and asymmetric vibrations of carboxyl groups ($-\text{COO}^-$), related to the BTC linkers.^{47,48} Another intense peak was observed at 715 cm^{-1} , confirming the presence of the Ni-O bond.

Raman spectroscopy was used to confirm the crystallography of the prepared Ni-MOF samples. Also, the inelastic scattering of the Ni-MOF samples was confirmed by Raman spectroscopy. The Raman spectrum of the Ni-MOF and the specified peaks of the prepared sample are shown in Fig. 3. The peaks of Ni-MOF at 816 and 1007 cm^{-1} could be associated to the plane deformation of the C-H in the aromatic ring and C-O stretching of the trimesic ligand, respectively. Also, D and G bands were observed at 1456 and 1613 cm^{-1} due to the in-plane vibration mode of the benzene ring.⁴⁹ The peak at 222 cm^{-1} could be attributed to H-O-H. All these peaks revealed the crystallography and structure of the Ni-MOF sample.

The surface morphology of the Ni-MOF was investigated by SEM, and the SEM images of Ni-MOF with different magnifications are shown in Fig. 4. The SEM images showed a

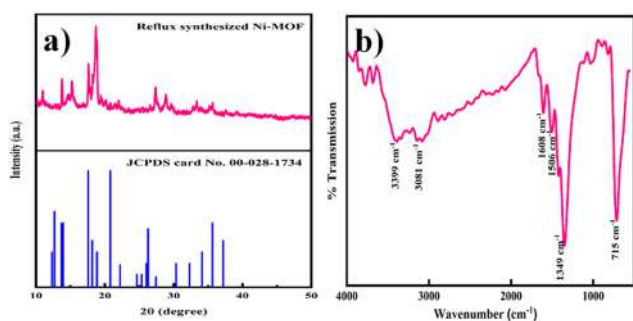


Fig. 2 (a) XRD pattern of Ni-MOF and JCPDS card. (b) FTIR spectra of Ni-MOF.

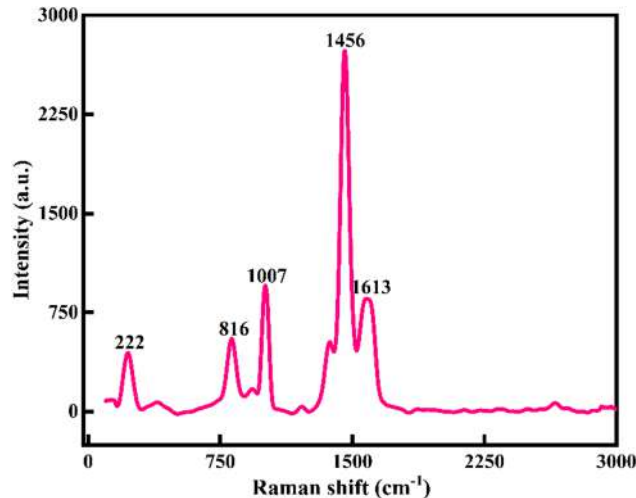


Fig. 3 Raman spectrum of Ni-MOF.

nanorod-like morphology and porous nature of the Ni-MOF, which was responsible for the increased surface area of the Ni-MOF and also for the increase in the specific capacitance. The average length of the nanorods was about 19.09 nm.

The different lengths and diameters of the nanorods indicated an increase in the aspect ratio of the nanorods. Also, the porous nanorods were interconnected to each other, which provides more active sites for the transportation of the charging kinetics and decreases the diffusion length of the electrolyte, which is helpful for improvement of the energy storage and high rate capability. Again, a birds-eye view of the SEM images showed that the small and large sized nanorods overlapped with each other and between these two nanorods there were some voids, which in turn would support the enhanced adsorption of electrolyte ions, which would help to increase the specific capacitance of the Ni-MOF. The porous and 1D morphology was favourable for ion diffusion and hence contributed to an increase in the specific capacitance of the Ni-MOF.

The surface area and porosity of the Ni-MOF were obtained by using the BET technique and measuring nitrogen adsorption-desorption isotherm of the samples at 77 K. Here, the prepared sample was degassed at $150 \text{ }^\circ\text{C}$ under a nitrogen atmosphere for 4 h before the measurements. The surface area and pore-size distribution of the sample were calculated by the Brunauer-Emmett-Teller (BET) equation and NLDFT method. The BET measurement results are presented in Fig. 5. The

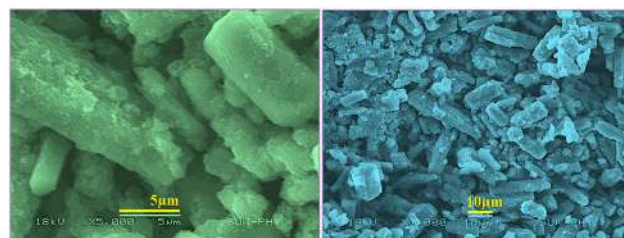


Fig. 4 SEM images of Ni-MOF.

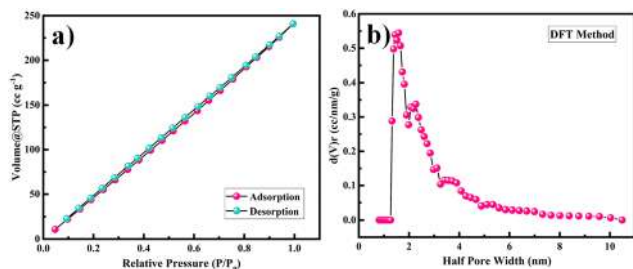


Fig. 5 (a) N_2 adsorption–desorption isotherms and (b) pore-size distribution of Ni-MOF.

calculated surface area of the Ni-MOF sample was found to be $398.4 \text{ m}^2 \text{ g}^{-1}$. Based on the literature, it has been observed that the larger the pore radius, then the higher porosity a sample will show in nature. Also, the pore-size distribution for Ni-MOF was estimated using the NLDFT method to establish the correct distribution of pores in the material, as shown in Fig. 5(c).^{50,51} The half pore width measured by DFT was 1.585 nm, with a micropore volume of 0.831 cc g^{-1} , confirming the extremely mesoporous nature and hierarchical pore-size distribution. According to the literature, Ni-MOF shows a type II isotherm with plenty of mesopores in the material.⁵² This massive amount of mesopores in the structure boosts the permeation of electrolyte ions into the electrode, hence increasing the specific capacitance of the material. Such a high specific surface area and mesoporous structure could produce more electrochemical reaction sites, which increases the consumption of the electroactive material.

XPS was used to examine the surface elemental composition and valence states of Ni-MOF. The presence of Ni, C, and O elements was confirmed by the survey spectrum in Fig. 6(a). Ni $2p_{1/2}$ and $2p_{3/2}$ displayed two significant peaks at 873.6 and 856.2 eV, respectively, with two satellite peaks at 878.7 and 861.0 eV, implying the presence of Ni in a divalent state (Fig. 6(b)). The peak at 284.5 eV in the C 1s area (Fig. 6(c)) is a typical outcome for specimens charging using C 1s as the reference. The peak at 288.2 eV was associated with the O=C–OH, whereas the peak at 285.4 eV was associated with the aryl carbon from the benzene ring. The spectrum of O 1s (Fig. 6(d)) could be separated into two peaks. Carbonyl displayed a peak at 531.5 eV, and the –OH group from the adsorbed H_2O molecules had a peak at 532.8 eV.^{53,54}

The electrochemical performance of the as-prepared Ni-MOF electrode was evaluated by using the three-electrode system in 2 M KOH electrolyte and the results are presented in Fig. 7. As shown in Fig. 7(a), cyclic voltammetry (CV) was carried out in the potential range from 0 to 0.3 V at scan rates from 10 to 100 mV s^{-1} . It could be observed that the area under the CV curve of the Ni-MOF electrode was higher and the redox current density also increased, leading to a greater capacitive behaviour compared to the literature (Table 1). All the CV curves revealed well-defined redox pairs, which specified the change in the oxidation states of the Ni^{2+}/Ni^{3+} , redox reactions, and intercalation–deintercalation of the K^+ ion in the porous

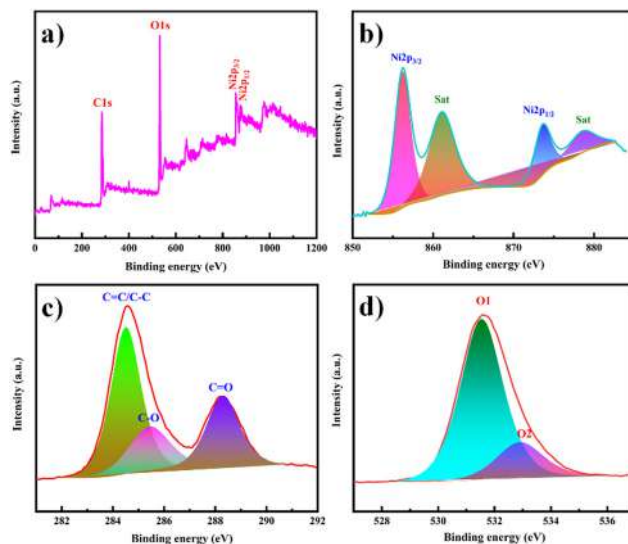


Fig. 6 (a) XPS survey spectrum of Ni-MOF. High-resolution XPS spectra in the (b) Ni 2p, (c) C 1s and (d) O 1s regions.

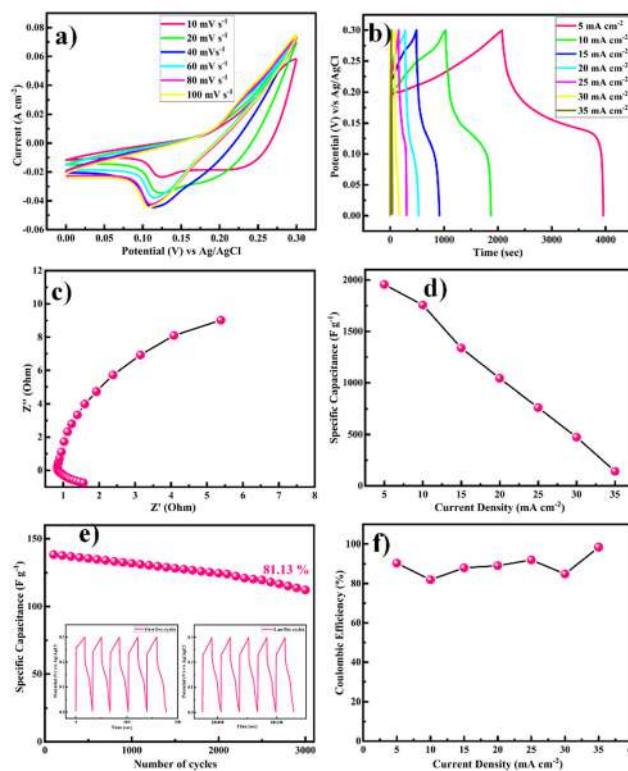


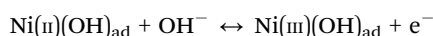
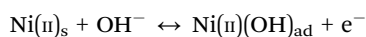
Fig. 7 (a) CV profile of Ni-MOF at different scan rates operated from 0 to 0.3 V. (b) GCD profiles for Ni-MOF at different current rates (5–35 mA cm^{-2}). (c) Nyquist plot of the Ni-MOF. (d) Plot of the specific capacitance vs. current density. (e) Cyclic durability test at a high current of 35 mA cm^{-2} over 3000 GCD cycles; insets show the first and last five cycles. (f) Coulombic efficiency as a function of the current density.

structure during the electrochemical reactions, due to the pseudocapacitive behaviour of the prepared Ni-MOF.^{55,56} This

Table 1 Comparison of the specific capacitances of Ni-MOF in different studies

Electrode material	Substrate used	Electrolyte	Current density	Specific capacitance	Ref.
Ni-MOF	Nickel foam	3 M KOH	5 A g ⁻¹	1224.6 F g ⁻¹	58
Ni-MOF	Nickel foam	3 M KOH	5 A g ⁻¹	612.25 F g ⁻¹	59
Ni-MOF	Nickel foam	6 M KOH	5 A g ⁻¹	430 C g ⁻¹	60
Ni-MOF	Nickel foam	3 M KOH	5 A g ⁻¹	95 F g ⁻¹	61
Ni-MOF	Platinum plate	2 M KOH	5 mA cm ⁻²	47 F g ⁻¹	62
Ni-MOF	Stainless steel mesh	2 M KOH	5 mA cm ⁻²	1956.3 F g ⁻¹	This work

could be due to a shift in the valence states of nickel ions, specifying that the pseudocapacitance was mostly driven by surface oxidation generated by the reduction reaction. Additionally, the diffusion of OH⁻ ions also contributed to the redox reaction, and the diffusion might be because of the impurity ions in the aqueous electrolyte. The redox peaks of Ni-MOF in aqueous electrolytes were caused by the reversible redox between Ni²⁺/Ni³⁺, and the reaction can be explained by the possible charge-discharge mechanism of Ni-MOF as follows,



With increasing the scanning speed, the curve area and peak current rose, demonstrating a good capacitive behaviour and charge-storage capabilities.

The equivalent and similar CV curves obtained at different scan rates showed a shift in the redox peaks and specified the pseudocapacitive behaviour of the material, as shown in Fig. 7(a). The area under the CV curve increased with the increase in the scan rate, whereas the specific capacitance decreased as the scan rate increased. This is due to the fact that at slower scan rates, electrolyte ions are completely diffused within the electrode material. As a result, the complete active surface of the electrode material can be used to store charge. At higher scan rates, however, diffusion restricts the movement of electrolyte ions, and only the outer active surface is employed for charge storage.⁵⁷ The outstanding performance of the Ni-MOF electrode could be assigned to the good crystallinity and porous nanorod-like structure, which could successfully boost the intercalation/deintercalation of OH⁻ ions within the Ni-MOF electrode. One of the important tools for assessing the electrochemical properties of an electrode is the charge-discharge measurement. Fig. 7(b) presents the charge-discharge curves of the Ni-MOF electrode in aqueous 2 M KOH electrolyte. The charging and discharging times were directly in tune with the charge-storage capacity of the active material. The impact of different current densities (5–35 mA cm⁻²) on the charge-discharge curve was also studied. The natures of the curves were identical to each other, which supported the pseudocapacitive properties of the Ni-MOF nanorods. The specific capacitance of the Ni-MOF was calculated using the discharging curve and eqn (1).

A maximum specific capacitance of 1956.3 F g⁻¹ at a 5 mA cm⁻² current density was obtained. This specific

capacitance value is higher than those reported earlier (Table 1). Due to the plentiful active sites and highly porous nature, the penetration of electrolyte ions into the material increased, which supported the enhancement of the specific capacitance of the material. One of the important factors for supercapacitor electrodes is the electrical resistance, which can be determined from electrochemical impedance spectroscopy (EIS) measurements. EIS tests were thus carried out to investigate the electroconductibility and reaction kinetics of the Ni-MOF electrode, as shown in Fig. 7(c). The electrode's charge-transfer resistance (R_{ct}) could be obtained from the diameter of a semicircle in the high-frequency area. It was demonstrated that the Ni-MOF had a small diameter and thus a smaller charge-transfer resistance, while the slope of the lines in the low-frequency area represents the ion-diffusion resistance. The Nyquist plot had a high slope, which showed that the as-prepared Ni-MOF was beneficial to ion transport and electrolyte diffusion because of its typical structure, which meant it possessed a high specific surface area and could support rich ion transportation. The straight line in the low-frequency region was due to Warburg resistance. Based on the preceding results, it can be concluded that the Ni-MOF had a higher conductivity. Hence, the smaller charge-transfer resistance (0.5 Ω) confirmed that the prepared Ni-MOF porous nanorods had highly pseudocapacitive properties. The specific capacitance decreased from 1756.3, 1338.4, 1043.8, 761.5, 473.8, and 142.2 F g⁻¹ with the increase in the current density to 10, 15, 20, 25, 30, and 35 mA cm⁻², respectively, as shown in Fig. 7(d). The specific capacitance decreased as the current density increased because at higher current density the electrolyte ions participate in the bulk surface for the electrochemical reaction, and due to this there is a restriction in the ion transport, so the value of the specific capacitance decreases, and considering the low current density, the electrolyte ions have enough time to move across the inner pores of the electrode material, resulting in a higher specific capacitance value. The Ni-MOF showed a longer discharging time, which clearly indicated that the porous nanorods structure of the Ni-MOF possessed more surface active sites for the efficient charge-discharge process and increased the energy-storage ability of the Ni-MOF electrode. The cyclic stability of the electrode was explored by galvanostatic charge-discharge (GCD) persistence tests at 35 mA cm⁻² current density for 3000 cycles, as shown in Fig. 7(e). It could be seen that the specific capacitance was retained at over 81.13% after 3000 cycles for the Ni-MOF electrode, which suggested its good electrochemical reversibility during the charge-discharge process.

The Coulombic efficiency (η %), another important parameter to examine the interfacial stability of Ni-MOF electrode as a function of charge–discharge cycles, is shown in Fig. 7(f). Eqn (5) was used to calculate the Coulombic efficiency for the Ni-MOF electrode at different current densities,⁶³

$$\eta(\%) = \frac{t_d}{t_c} \times 100 \quad (5)$$

where t_d and t_c are the discharging and charging times in seconds, respectively.

The Coulombic efficiencies of the Ni-MOF electrode were 90.37%, 81.92%, 87.98%, 89.11%, 92.00%, 84.88%, and 98.45% at different current densities of 5, 10, 15, 20, 25, 30, and 35 mA cm⁻², respectively. The Coulombic efficiency of the Ni-MOF electrode rose and the specific capacitance decreased with the increase in current density, which might be assigned to the electrodes inner active sites, which were not capable of supporting the redox reactions at high current density.

A promising electrochemical stability and excellent reversibility of Ni-MOF electrodes were observed for up to the 3000 GCD cycles. The Ni-MOF samples showed that the orchestrating effects of the 1D morphology, surface area, and porosity led to their excellent application potential in terms of specific capacitance, energy density, power density, and cyclic stability.

To understand the practical ability of the Ni-MOF electrode in functional devices, a hybrid supercapacitor device was assembled using the as-prepared Ni-MOF as a positive electrode and activated carbon as the negative electrode, as shown in Fig. 8. Both electrodes were prepared by the slurry coating method. In short, the slurry was prepared by mixing the active material (Ni-MOF or AC) (80 mg), polyvinylidene fluoride (10 mg), and carbon black (10 mg) in 0.5 mL of methyl-2-pyrrolidone (NMP) solvent. Then, the required volume of the slurry was dispersed onto a stainless steel mesh with an area of 2 cm × 2 cm and dried at 60 °C overnight. Primarily, the side borders of the electrodes were formed as non-conducting through insertion of a band to avoid electrical contact. The PVA-KOH gel was pasted on one side of the electrodes and created one side of the electrical contact. Later, both electrodes were patched together like a sandwich, with the gel-pasted sides facing each other. The fabricated device was kept under 1 ton pressure for 12 h, to acquire a good connection within the

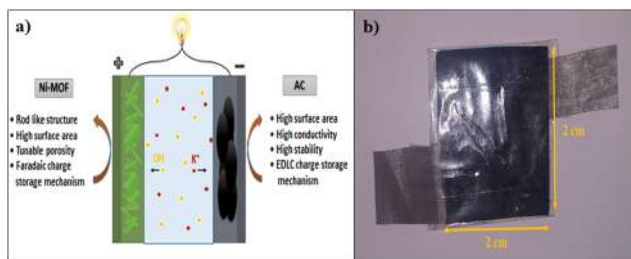


Fig. 8 (a) Schematic illustration of a hybrid supercapacitor with Ni-MOF as a positive electrode and activated carbon as a negative electrode in KOH aqueous electrolyte. (b) Digital photograph of the Ni-MOF//AC HSC device.

electrodes and gel electrolyte and also to remove the air gap. Afterwards, the device was used for assessment of the electrochemical performance. Hybrid supercapacitor devices have advantages, like high energy density, high specific capacitance, long cycle stability, and large potential window, over symmetric supercapacitors. The performance of the assembled hybrid device was studied using CV, GCD, and EIS measurements.

Primarily, CV tests were performed to understand the electrochemical performance of the Ni-MOF//AC hybrid supercapacitor (HSC) at different scan rates, as shown in Fig. 9(a). The Ni-MOF//AC hybrid SC exhibited a symmetric rectangular CV curve and a large area enclosed under the CV curve at up to 0–0.9 V. With the increase in scan rate from 10 to 100 mV s⁻¹, the increase in area under the CV curves revealed the excellent reversibility of the Ni-MOF. Additionally, GCD curves were obtained at different current densities from the hybrid device, indicating the ideal capacitive behaviour of the device, as shown in Fig. 8(b). The Nyquist plots of the Ni-MOF//AC HSC device are shown in Fig. 9(c), indicating that the fabricated device had an R_{ct} value of 0.36 Ω. According to the EIS studies, the fabricated Ni-MOF//AC HSC device had good electrical conductivity with a low ionic resistance. However, the specific capacitance decreased from 195.76, 94.79, 60.0, 42.70, and 31.67 F g⁻¹ with the increase in the current density from 2, 3,

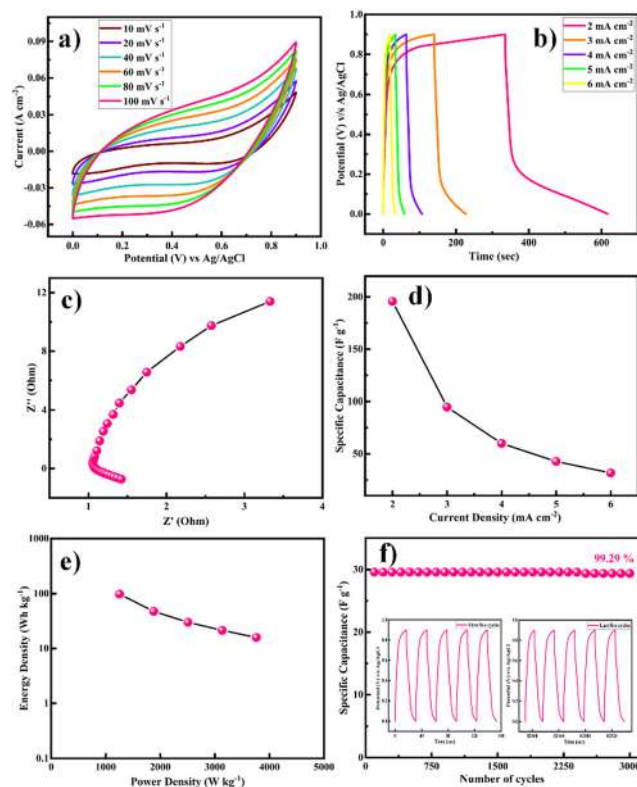


Fig. 9 (a) CV profile of HSC cell at different scan rates operated from 0 to 0.9 V. (b) GCD profiles for the HSC cell at different current rates (2–6 mA cm⁻²). (c) Nyquist plot of the HSC device. (d) Plot of the specific capacitance vs. current density. (e) Ragone plot for the HSC cell. (f) Cyclic durability test at a high current of 6 mA cm⁻² over 3000 GCD cycles; insets show the first and last five cycles.

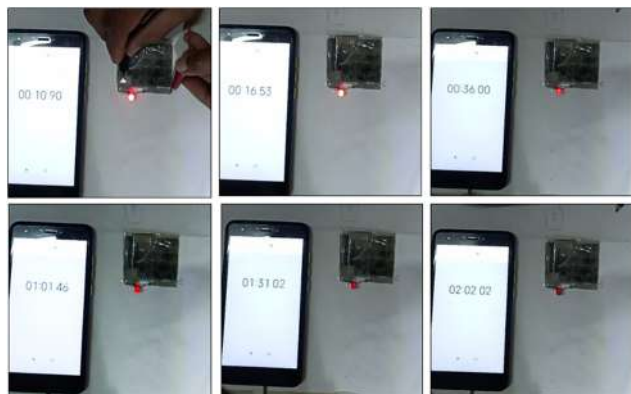


Fig. 10 The handmade asymmetric supercapacitor device was charged for 15 s and caused a red LED to glow for almost 105 s (i.e. charging time 15 s and discharging time 105 s).

4, 5, and 6 mA cm⁻², respectively, as shown in Fig. 9(d). The Ragone plot of the as-constructed HSC, expressing the relationship between the energy density (E) and power density (P), was obtained based on the galvanostatic charge–discharge curves (Fig. 9(e)). The cycling stability of the assembled hybrid supercapacitor device was investigated systematically. The device showed 99.29% capacitance retention over 3000 cycles, indicating its excellent cycle stability. The specific capacitance was constant over 2500 cycles and later it slightly decreased. The insets of Fig. 9(f) show the first and last five charge–discharge cycles of the device in 2 M KOH electrolyte. The Coulombic efficiencies of the asymmetric supercapacitor device were 84.15%, 65.00%, 68.57%, 74.54%, and 80.00% at various current densities of 2, 3, 4, 5, and 6 mA cm⁻², respectively (eqn (5)).

The device's energy density and power density were calculated using eqn (2) and (3). The HSC device exhibited a maximum energy density of 79.5 W h kg⁻¹ at a higher power density of 1015.3 W kg⁻¹, which was comparable to or even higher than recent literature values (Table 1) for hybrid supercapacitors.

The fabricated device could light a red-light-emitting diode (LED) for over 105 s when charged for 15 s due to the device's high energy density and maximum operational potential of 0.9 V, as shown in Fig. 10. It can be seen that the dazzling light was obvious at first, and then the brightness change is shown over time. After 105 s, we can see that the red light was still faintly glowing, confirming that the Ni-MOF//AC HSC device had an amazing ability to store charge. The good performance could be attributed to Ni-MOF's rod-like structure and pore-size distribution. The study discovered that the encouraging results may pave the way for the development of new electrode materials for supercapacitors and other energy-storage devices.

The study of the electrochemical parameters at different current densities of the chemically synthesized Ni-MOF is concluded in the radar graph shown in Fig. 11. The different apexes reveal the various parameters, such as specific capacitance, energy density, power density, and Coulombic efficiency, of the Ni-MOF. As seen in Fig. 11, this report contains the script

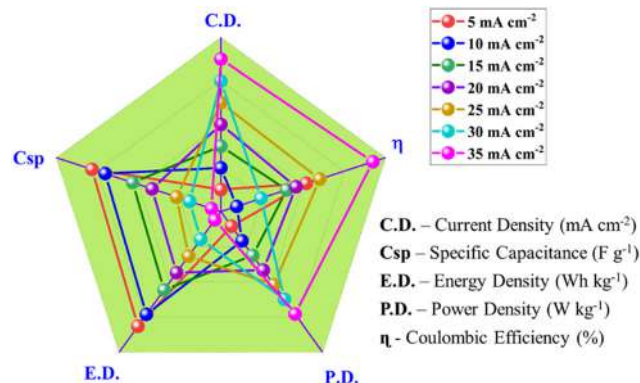


Fig. 11 Radar plot for Ni-MOF based on its supercapacitive properties.

for the Ni-MOF-based supercapacitor. These results indicate that the Ni-MOF has much better electrochemical performance than that of other reported MOFs due to its high specific capacitance, high energy density, large power density, and good Coulombic efficiency.

Conclusions

In summary, we successfully prepared Ni-MOF by using the reflux condensation technique. The structural properties and electrochemical performance of the Ni-MOF were studied systematically using various advanced tools. The porous and nanorod-like morphology, as confirmed by SEM analysis, provided both faster and more electroactive sites. An as-prepared Ni-MOF sample exhibited a high surface area of 398.4 m² g⁻¹. Furthermore, in a three-electrode system with 2 M KOH aqueous electrolyte, the synthesized Ni-MOF porous nanorods showed a high specific capacitance of 1956.3 F g⁻¹ at a current density of 5 mA cm⁻², and more stability for 3000 cycles with 81.13% retention. When assessed as a positive electrode for a flexible hybrid supercapacitor (HSC) device in combination with activated carbon as a negative electrode, the HSC cell exhibited a superhigh electrochemical behaviour. The device also exhibited a high charge-storage capacity of 195.76 F g⁻¹ at a current density of 2 mA cm⁻², super-specific energy (98.15 W h kg⁻¹), and excellent power density (1253.47 W kg⁻¹), including long-term stability of 3000 cycles with 99.29% capacity retention. The extraordinary energy-storage properties of the Ni-MOF electrode are attributed to its nanorod-like structure and higher surface area. This study provides a new platform for supercapacitors and other energy-storage devices.

Author contributions

Rakhee Bhosale: formal analysis, investigation, methodology and writing original draft; Sneha Bhosale: data curation; Pramod Kumbhar: visualisation; dattatray Narale: validation and methodology; Rachana Ghaware: discussions and review; Chitra Jambhale: editing of the draft; Sanjay Kolekar: conceptualization, supervision and funding acquisition.

Conflicts of interest

There are no conflicts to declare.

Acknowledgements

The authors are thankful to UGC-SAP, DST-FIST and DST-PURSE for the financial support and instrument facilities at the Department of Chemistry, Shivaji University, Kolhapur. Author Rakhee Bhosale is thankful to SARTHI, Government of Maharashtra, India for the 'Chhatrapati Shahu Maharaj National Research Fellowship-2021'.

References

- 1 S. Koohi-Fayegh and M. A. Rosen, *J. Energy Storage*, 2020, **27**, 101047.
- 2 M. B. Askari, P. Salarizadeh, M. Seifi, M. H. Ramezan zadeh and A. Di Bartolomeoss, *J. Alloys Compd.*, 2021, **860**, 158497.
- 3 X. Zhao, K. Tao and L. Han, *Nanoscale*, 2022, **14**, 2155–2166.
- 4 Y. Tang, W. Guo and R. Zou, *Coord. Chem. Rev.*, 2022, **451**, 214242.
- 5 Poonam, K. Sharma, A. Arora and S. K. Tripathi, *J. Energy Storage*, 2019, **21**, 801–825.
- 6 S. Sanati, Z. Rezvani and B. Habibi, *New J. Chem.*, 2018, **42**, 18426–18436.
- 7 S. De, C. K. Maity, S. Sahoo and G. C. Nayak, *ACS Appl. Energy Mater.*, 2021, **4**, 3712–3723.
- 8 H. M. Nguyet, L. T. T. Tam, D. T. Tung, N. T. Yen, H. T. Dung, N. T. Dung, H. Phan N, L. A. Tuan, P. N. Minh and L. T. Lu, *New J. Chem.*, 2022, **46**, 13996–14003.
- 9 Y. Shao, M. F. El-Kady, J. Sun, Y. Li, Q. Zhang, M. Zhu, H. Wang, B. Dunn and R. B. Kaner, *Chem. Rev.*, 2018, **118**, 9233–9280.
- 10 R. Liu, A. Zhou, X. Zhang, J. Mu, H. Che, Y. Wang, T. T. Wang, Z. Zhang and Z. Kou, *Chem. Eng. J.*, 2021, **412**, 128611.
- 11 A. Mohanty, D. P. Jaihindh, Y. P. Fu, S. P. Senanayak, L. S. Mende and A. Ramadoss, *J. Power Sources*, 2021, **488**, 229444.
- 12 S. Kumar, G. Saeed, L. Zhu, K. N. Hui, N. H. Kim and J. H. Lee, *Chem. Eng. J.*, 2021, **403**, 126352.
- 13 L. Li, J. Meng, M. Zhang, T. Liu and C. Zhang, *Chem. Commun.*, 2022, **58**, 185–207.
- 14 X. Chu, F. Meng, T. Deng and W. Zhang, *Nanoscale*, 2021, **13**, 5570–5593.
- 15 P. Forouzandeh, P. Ganguly, R. Dahiya and S. C. Pillai, *J. Power Sources*, 2022, **519**, 230744.
- 16 C. V. V. Muralee Gopi, R. Vinodh, S. Sambasivam, I. M. Obaidat and H. J. Kim, *J. Energy Storage*, 2020, **27**, 101035.
- 17 S. Sanati, R. Abazari, A. Morsali, A. M. Kirillov, P. C. Junk and J. Wang, *Inorg. Chem.*, 2019, **58**, 16100–16111.
- 18 A. E. Baumann, D. A. Burns, B. Liu and V. S. Thoi, *Commun. Chem.*, 2019, **2**, 1–14.
- 19 W. Li, X. Zhao, Q. Bi, Q. Ma, L. Han and K. Tao, *Dalton Trans.*, 2021, **50**, 11701–11710.
- 20 H. M. Ma, J. W. Yi, S. Li, C. Jiang, J. H. Wei, Y. P. Wu, J. Zhao and D. S. Li, *Inorg. Chem.*, 2019, **58**, 9543–9547.
- 21 Y. Liang, W. Yao, J. Duan, M. Chu, S. Sun and X. Li, *J. Energy Storage*, 2021, **33**, 1–11.
- 22 L. Zheng, J. Song, X. Ye, Y. Wang, X. Shi and H. Zheng, *Nanoscale*, 2020, **12**, 13811–13821.
- 23 S. Zhou, S. Wang, S. Zhou, H. Xu, J. Zhao, J. Wang and Y. Li, *Nanoscale*, 2020, **12**, 8934–8941.
- 24 P. Du, Y. Dong, C. Liu, W. Wei, D. Liu and P. Liu, *J. Colloid Interface Sci.*, 2018, **518**, 57–68.
- 25 C. Yang, X. Li, L. Yu, X. Liu, J. Yang and M. Wei, *Chem. Commun.*, 2020, **56**, 1803–1806.
- 26 U. A. Khan, N. Iqbal, T. Noor, R. Ahmad, A. Ahmad, J. Gao, Z. Amjad and A. Wahab, *J. Energy Storage*, 2021, **41**, 102999.
- 27 S. Wang, S. Wang, X. Guo, Z. Wang, F. Mao, L. Su, H. Wu, K. Wang and Q. Zhang, *Inorg. Chem. Front.*, 2021, **8**, 4878–4886.
- 28 N. Wu, H. Wu, J. Zhang, Y. Zhang, D. Cao, L. Bai and T. Hu, *J. Alloys Compd.*, 2021, **856**, 157466.
- 29 N. Liu, X. Liu and J. Pan, *J. Colloid Interface Sci.*, 2022, **606**, 1364–1373.
- 30 D. Y. Lee, S. J. Yoon, N. K. Shrestha, S. H. Lee, H. Ahn and S. H. Han, *Microporous Mesoporous Mater.*, 2012, **153**, 163–165.
- 31 G. Zhu, H. Wen, M. Ma, W. Wang, L. Yang, L. Wang, X. Shi, X. Cheng, X. Sun and Y. Yao, *Chem. Commun.*, 2018, **54**, 10499–10502.
- 32 S. Xiong, S. Jiang, J. Wang, H. Lin, M. Lin, S. Weng, S. Liu, Y. Jiao, Y. Xu and J. Chen, *Electrochim. Acta*, 2020, **340**, 135956.
- 33 Q. Li, H. Guo, R. Xue, M. Wang, M. Xu, W. Yang, J. Zhang and W. Yang, *Int. J. Hydrogen Energy*, 2020, **45**, 20820–20831.
- 34 L. Wang, X. Feng, L. Ren, Q. Piao, J. Zhong, Y. Wang, H. Li, Y. Chen and B. Wang, *J. Am. Chem. Soc.*, 2015, **137**, 4920–4923.
- 35 X. Wang, N. Yang, Q. Li, F. He, Y. Yang, B. Wu, J. Chu, A. Zhou and S. Xiong, *J. Solid State Chem.*, 2019, **277**, 575–586.
- 36 M. Azadfalsh, A. Sedghi and H. Hosseini, *J. Electron. Mater.*, 2019, **48**, 7011–7024.
- 37 C. H. Wang, D. W. Zhang, S. Liu, Y. Yamauchi, F. B. Zhang and Y. V. Kaneti, *Chem. Commun.*, 2022, **58**, 1009–1012.
- 38 Y. Wu, X. Ding, Y. Luo, F. Xu, L. Sun, J. H. Lao, X. Qin, C. Dan, Y. Wang, Q. Yin, T. Wang, K. Zhang, B. Li, H. Zhang and Y. Zou, *Int. J. Electrochem. Sci.*, 2021, **16**, 1–11.
- 39 S. Gao, Y. Sui, F. Wei, J. Qi, Q. Meng and Y. He, *J. Mater. Sci.*, 2018, **53**, 6807–6818.
- 40 X. Zhang, N. Qu, S. Yang, Q. Fan, D. Lei, A. Liu and X. Chen, *J. Colloid Interface Sci.*, 2020, **575**, 347–355.
- 41 V. Veeramani, B. M. Matsagar, Y. Yamauchi, A. Y. Badjah, M. Naushad, M. Habila, S. Wabaidur, Z. A. Allothman, Z. L. Wang and K. C. W. Wu, *J. Taiwan Inst. Chem. Eng.*, 2019, **96**, 634–638.
- 42 R. Velmurugan, J. Premkumar, R. Pitchai, M. Ulaganathan and B. Subramanian, *ACS Sustainable Chem. Eng.*, 2019, **7**, 13115–13126.
- 43 S. B. Bandgar, M. M. Vadiyar, Y. C. Ling, J. Y. Chang, S. H. Han, A. V. Ghule and S. S. Kolekar, *ACS Appl. Energy Mater.*, 2018, **1**, 638–648.

- 44 S. Gao, Y. Sui, F. Wei, J. Qi, Q. Meng and Y. He, *J. Mater. Sci.: Mater. Electron.*, 2018, **29**, 2477–2483.
- 45 F. Israr, D. Chun, Y. Kim and D. K. Kim, *Ultrason. Sonochem.*, 2016, **31**, 93–101.
- 46 F. Israr, D. K. Kim, Y. Kim and W. Chun, *Quim. Nova*, 2016, **39**, 669–675.
- 47 X. Zhang, N. Qu, S. Yang, D. Lei, A. Liu and Q. Zhou, *Mater. Chem. Front.*, 2021, **5**, 482–491.
- 48 X. Liu, D. Xu, Q. Wang and L. Zhang, *Small*, 2018, **14**, 1–12.
- 49 Q. Liu, L. Xie, X. Shi, G. Du, A. M. Asiri, Y. Luo and X. Sun, *Inorg. Chem. Front.*, 2018, **5**, 1570–1574.
- 50 M. Thommes, K. Kaneko, A. V. Neimark, J. P. Olivier, F. Rodriguez-Reinoso, J. Rouquerol and K. S. W. Sing, *Pure Appl. Chem.*, 2015, **87**, 1051–1069.
- 51 R. Bardestani, G. S. Patience and S. Kaliaguine, *Can. J. Chem. Eng.*, 2019, **97**, 2781–2791.
- 52 M. Khalfaoui, S. Knani, M. A. Hachicha and A. Ben Lamine, *J. Colloid Interface Sci.*, 2003, **263**, 350–356.
- 53 G. Li, Y. Qi, H. Lin, N. Lu, J. Chen, J. Wang, Q. Han and F. Liu, *J. Membr. Sci.*, 2021, **635**, 1–9.
- 54 Q. Bi, Q. Ma, K. Tao and L. Han, *Dalton Trans.*, 2021, **50**, 8179–8188.
- 55 J. Yang, P. Xiong, C. Zheng, H. Qiu and M. Wei, *J. Mater. Chem. A*, 2014, **2**, 16640–16644.
- 56 X. G. Han, P. F. Wang, Y. H. Zhang, H. Y. Liu, J. J. Tang, G. Yang and F. N. Shi, *Inorg. Chim. Acta*, 2022, **536**, 120916.
- 57 S. S. Shah, E. Cevik, M. A. Aziz, T. F. Qahtan, A. Bozkurt and Z. H. Yamani, *Synth. Met.*, 2021, **277**, 116765.
- 58 C. Zhang, Q. Zhang, K. Zhang, Z. Xiao, Y. Yang and L. Wang, *RSC Adv.*, 2018, **8**, 17747–17753.
- 59 Y. Li, Y. Xu, Y. Liu and H. Pang, *Small*, 2019, **15**, 1–8.
- 60 J. W. Wang, Y. X. Ma, X. Y. Kang, H. J. Yang, B. L. Liu, S. S. Li, X. D. Zhang and F. Ran, *J. Solid State Chem.*, 2022, **309**, 122994.
- 61 S. Wang, J. Wang, M. Zeng, J. Yang, N. Hu, Y. Su, Z. Zhou, H. Pang and Z. Yang, *J. Energy Storage*, 2021, **38**, 102528.
- 62 C. Feng, C. P. Lv, Z. Q. Li, H. Zhao and H. H. Huang, *J. Solid State Chem.*, 2018, **265**, 244–247.
- 63 K. T. Kubra, A. Javaid, R. Sharif, G. Ali, F. Iqbal, A. Salman, F. Shaheen, A. Butt and F. J. Iftikhar, *J. Mater. Sci.: Mater. Electron.*, 2020, **31**, 12455–12466.

Recent Progress on Functional Metal–Organic Frameworks for Supercapacitive Energy Storage Systems

Rakhee Bhosale, Sneha Bhosale, Madagonda Vadiyar, Chitra Jambhale, Kyung-Wan Nam,* and Sanjay Kolekar*

As porous coordination organic polymers, both metal–organic frameworks (MOFs) and their derived materials and MOF-based composites offer unique organic or inorganic chemistries that display superior features of high specific surface area, accessible active sites, robust structural and chemical diversity, tailorable pore size, exceptional porosity, and pre- and postsynthesis structural tunability. Therefore, MOF-based materials are attractive for energy storage applications, specifically for supercapacitor devices. This review presents recent progress in designing and utilizing pristine MOFs, MOF-derived nanomaterials, and MOF-based composite materials for supercapacitors. Most importantly, herein, recent highlights and classifications of electrolytes and their vital role in the structure–property correlation between the structures of MOF-based materials and suitable electrolyte choices for ideal supercapacitor devices are discussed. Finally, together with a discussion of the progress and outcomes of MOF electrodes, the obstacles and prospects for future MOF-related research and applications are discussed. To help this intriguing topic continue to advance, this review offers useful insights into the logical design of MOF-based electrode materials.

to the isolated large-scale power plant facilities that presently supply most electrical energy.^[4,5] Likewise, we need better energy storage systems to efficiently use these energy sources, for example, transportation systems and pulsed electronic devices.^[6] Unfortunately, we can currently store only about 1% of the energy produced worldwide, primarily based on hydroelectric energy (98%) storage.^[7] To address these issues, there is a great demand for clean, environment-friendly, sustainable, and high-efficiency energy storage technologies.^[8–11]

The Ragone plot is a tool for comparing the performance of various energy storage technologies. In this plot, the values of the energy densities (Wh kg^{-1}) are plotted against the power densities (W kg^{-1}) of the energy storage devices. Energy storage devices like batteries, conventional capacitors, and supercapacitors (SCs) are located in the Ragone plot, as shown in **Figure 1**.

SCs offer a workable middle ground between capacitors and batteries.^[12,13] Among various electrochemical energy storage devices, batteries and SCs are the most favorable due to their high energy and power density, fast charging/discharging, and long cycle life.^[14,15] Of particular interest, SCs are the best-suited energy storage devices that can be coupled with intermittent renewable systems due to their unmaintainable long lifespan, fast charging and discharging times, and high power density.^[16–18] Based on the charge storage mechanism, the SC is classified as a non-Faradaic electric double-layer capacitor (EDLC), a pseudocapacitor, and hybrid capacitor. EDLC involves physical adsorption and desorption of ions at the electrolyte/electrode interface, while a pseudocapacitor stores charge via facile reversible surface redox reactions.^[19,20] The electrode materials for SCs must possess beneficial characteristics, like high electrochemical activity, large specific surface area, adjustable pore size distribution, and good electrical conductivity and hybrid capacitors depending on both types of mechanisms.^[21]


EDLCs exhibit a high power density and strong cycle stability but a low specific capacitance. Although pseudocapacitors show large specific capacitance, they possess low power density and cyclic stability. Thus, both faradaic and non-Faradaic methods may be used to store charge in order to achieve high power densities and alleviate the disadvantages of low cyclability in both pseudocapacitors and EDLCs, where the right electrode pairings can boost cell voltage and specific capacitance. Because of this,

1. Introduction

With the ever-increasing global energy requirements, the unsustainable burning of fossil fuels, and the limitations of renewable energy resources, securing energy sources for the future is one of the most critical tasks.^[1–3] Undoubtedly, a favorite choice is utilizing renewable clean energies, such as solar, wind, biomass, and tidal energy. Recently, different types of solar cells, such as silicon, biohybrid, dye-sensitized, perovskites, and thin-film cells, have been developed to efficiently convert this renewable energy into electricity. However, these renewable resources are all inherently intermittent and mostly dispersed compared

R. Bhosale, S. Bhosale, C. Jambhale, S. Kolekar
Analytical Chemistry and Materials Science Research Laboratory
Department of Chemistry
Shivaji University
Kolhapur 416004, Maharashtra, India
E-mail: ssk_chem@unishivaji.ac.in

M. Vadiyar, K.-W. Nam
Department of Energy and Materials Engineering
Dongguk University
Seoul 04620, Republic of Korea
E-mail: knam@dongguk.edu

 The ORCID identification number(s) for the author(s) of this article can be found under <https://doi.org/10.1002/ente.202300147>.

DOI: 10.1002/ente.202300147

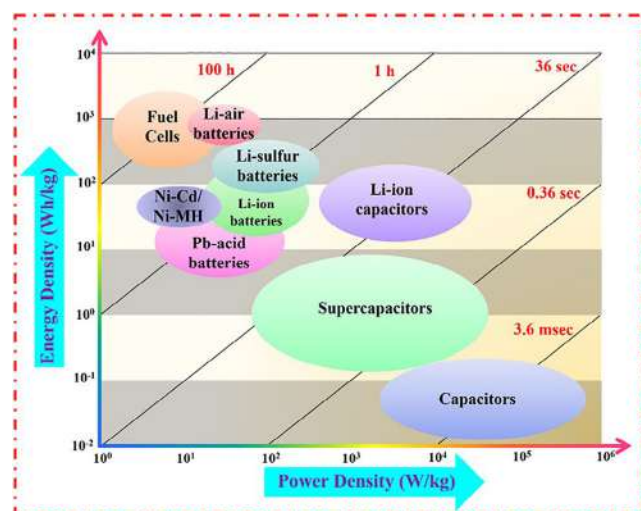


Figure 1. Ragone plot showing the specific power versus specific energy of different EES devices. Reproduced with permission.^[12] Copyright 2023, Elsevier.

these hybrid SCs can retain stability, have longer cycle life, and have greater energy and power densities.^[22–24]

Owing to their definite structure and the large specific surface area, metal–organic frameworks (MOFs) materials have attracted significant attention in multifunctional applications. MOFs are porous materials prepared using metal ions or clusters (secondary building units, or SBUs) and organic ligands.^[25,26] The pristine MOFs, MOF composites, and MOF derivatives have attracted increasing interest in electrochemical energy storage and conversion (EESC) applications thanks to their outstanding chemical stability and electrochemical performance.^[27,28] The field of MOFs has become one of the most rapidly growing areas in chemistry due to their structural and functional tunability. Their high porosity and systematic porous structure have resulted in MOFs being considered as good electrode materials for SCs.^[29,30] With the high-speed development of pristine MOFs, MOF composites, MOF-derived materials, and many EESC technologies, a small but all-inclusive review that “summarizes” the most recent growth and discovery may prove to be useful for their future developments in several high-efficiency EESC systems.

Due to their remarkable features, MOFs offer a lot of advantages over both inorganic and organic materials, and they have a lot of promise for use in metal-ion hybrid capacitors (MIHCs).

MIHCs are seen to be a viable option for bridging the gap between metal-ion batteries and SCs. MIHCs use distinct mechanisms for the cathode and anode to produce high power and energy densities at the same time. The benefits of MIBs and SCs are combined in MIHCs, which provide high energy and extended cycle life without compromising high power.^[31] Several MIHCs have been produced, including lithium-ion hybrid capacitors (LIHCs),^[32] sodium-ion hybrid capacitors (SIHCs),^[33] potassium-ion hybrid capacitors (PIHCs),^[34] zinc-ion hybrid capacitors (ZIHCs),^[35] and other forms of multivalent MIHCs. MIHCs have a battery-type anode and a capacitor-type cathode, which have two different charge storage processes, resulting in a mismatch in the capacity and kinetics of the anode and cathode, making it challenging to attain MIHCs’ overall high performance.^[36] Some of the MOFs as electrode materials for MIHCs are summarized in **Table 1**.

In this minireview, we provide a current study survey of the electrochemical performance of pristine MOFs, MOF composites, and MOF derivatives. We first briefly introduce the synthetic strategies for MOF composites and MOF-derived materials based on their composition, structure, and performance growth. Then, we focus on the recent advances in engineering MOF-derived functional materials as advanced electrodes for SC applications. Specifically, we discuss the following: 1) MOFs and their derived materials; 2) MOF composites with different materials; 3) different electrolytes for the electrochemical performance of a derived electrode for SC application; and 4) MOF application in an energy storage device, that is, a SC. Finally, this minireview concludes with some of our perceptions of the recent significant hurdles and their prospective solutions, hoping to stimulate continuous innovation to advance MOF-derived functional materials for SC application.

2. MOFs and Their Derived Materials

MOFs and their derived materials are influenced by the porous types of MOFs and their interesting elements, together with different kinds of organic linkers and metal-containing units. MOFs have been significantly investigated as attractive precursors to synthesize various nanomaterials, varying from carbon-based materials to metal-based materials (e.g., oxides, hydroxides, carbides, chalcogenides, and phosphides) with well-ordered porous structures.^[37] MOFs and their derived materials have also been broadly provided for energy storage applications, due to their

Table 1. MOFs as electrode materials for MIHCs.

Sr. No.	MOF materials	Composition	Applications	Current density [A g ⁻¹]	Energy density [Wh kg ⁻¹]	Power density [W kg ⁻¹]	Cyclic stability [Cycles]	References
1	Zr-MOF	Zr-MOF//AC	LIHC	2	122.5	12 500	1000	[195]
2	Co ₃ (HHTP) ₂	Co ₃ (HHTP) ₂ //AC spheres	LIHC	1	64	10 000	1000	[196]
3	UiO-66@PVDF-HFP	TiO ₂ //AC	SIHC	1	182	5280	10 000	[197]
4	Glass fiber@ZIF-7	Li ₂ TiSiO ₅ //AC	LIHC	2	238.56	14 295	4000	[198]
5	Ni-HAB	Ni-HAB//Na ₃ V ₂ O ₂ (PO ₄) ₂ F//AC	SIHC	1	127	17 309	5000	[199]
6	Carbon cloth@ZIF-8	Zn/carbon cloth@ZIF-8//carbon	ZIHC	1	107.4	16 200	10 000	[200]
7	Black phosphorus@ZIF-8	Black phosphorus@ZIF-8//AC	PIHC	1	93	9380	6500	[201]

unique organic–inorganic hybrid nature, well-defined porosity, high surface area, tunable chemical composition, and facile adjustability. Modifying MOFs into several MOF-derived nanostructures by thermal or chemical treatment can also lead to unique properties over the pristine MOFs.^[38,39]

2.1. The Pristine MOFs

Building block patterns of the pristine MOFs can be realized by wise choice and transformation of metal ions and organic linkers. The pristine MOF has physical and chemical properties, such as versatile compositions, high surface area, tunable pores, uniform dispersion, and defined active centers.^[40,41] Pure MOFs store energy through the physisorption of electrolyte ions on their internal surfaces at the metal centers.^[42] The important parameters that influence the electrochemical performance are the structure of MOF, which includes chemical structure and the geometries of the organic ligands.^[43] Due to their longer charge/discharge cyclabilities, larger specific capacitances, and faster ion diffusion, pristine MOFs are used for electrode preparation. To date, more than 40 types of pristine MOFs have been fabricated using different metals, such as Cu, Cr, Co, Ni, Fe, Mn, Zr, Zn, In, Al, Cd, and Mg in mixture with organic ligands like BTC, BDC, and imidazole.^[44–46]

Yang et al. synthesized a layered gear-like Ni–TDA [(Ni₃(OH)₂(C₂H₆O₄S)₂, Ni–MOF] material that was found to be a promising electrode material for the flexible all-solid-state asymmetric SC (ASC), with high specific capacitance of 1518.8 F g⁻¹ at a current density of 1 A g⁻¹. The capacitance retention of over 95.5% can be maintained even after 10 000 cycles at current density of 20 A g⁻¹, which shows excellent cycling stability at higher current densities.^[47] Yan et al. prepared a novel accordion-like Ni–MOF superstructure [(Ni₃(OH)₂(C₈H₄O₄)₂(H₂O)₄·2H₂O) to fabricate a flexible SC. It shows specific capacitances of 988 and 823 F g⁻¹ at a current density of 1.4 and 7.0 A g⁻¹ respectively, while sustaining excellent cycling stability (capacitance retention of 96.5% after 5000 cycles at current density of 1.4 A g⁻¹). Additionally, using Ni–MOF and activated carbon (AC), a high-performance flexible solid-state ASC was constructed with a specific capacitance of 230 mF cm⁻² at current density of 1.0 mA cm⁻², which shows little capacitance change after more than 5000 charge–discharge cycles, with only 7.2% decay at a current density of 5.0 mA cm⁻².^[48] Krishnamurthy et al. used a solvothermal method to report Mn–MOF (Mn[Tpa][Mi][DMF]) using terephthalic acid and methyl imidazole ligands. It shows specific capacitance up to 4000 F g⁻¹. Also, it has an energy density and power density of 500 Wh kg⁻¹ and 0.125 W kg⁻¹, respectively. The surface area of this material is outstanding, that is, 2352 m² g⁻¹ and pore volume of 0.00569 cc g⁻¹; Mn–MOF electrode possesses high-charge–discharge Coulombic efficiency, low polarization, and high specific capacitance, along with good cycling stability.^[49] Zhu et al. synthesized a 3D hierarchically structured Co–MOF supported on nickel foam (Co–MOF/NF), which shows better capacitive properties with good rate performance in 2 M KOH. Further, they constructed an ASC device using Co–MOF/NF as a positive electrode and AC as a negative electrode; it shows a high energy density of 1.7 mWh·cm⁻² at a

power density of 4.0 mW·cm⁻², with capacitance retention of almost 69.70% after 2000 cycles (Figure 2).^[50]

Wang and co-workers successfully synthesized an ultrathin NiCo–MOF nanosheet via facile ultrasonication at room temperature (RT), which is used as a promising electrode material for SC applications. It shows a high specific capacitance of 1202.1 F g⁻¹ at 1 A g⁻¹; furthermore, an ASC was fabricated using NiCo–MOF and AC, which shows a high energy density of 49.4 Wh kg⁻¹ at a power density of 562.5 W kg⁻¹ and 76.3% capacitance retention after 5000 cycles (Figure 3).^[51]

In short, the MOFs have metal ions and ligands, which give them a lot of redox sites for electrochemical processes. Therefore, the electrochemical performance of MOFs and the materials generated from them is greatly influenced by the pores, architectures, and crystal shapes. Using pristine MOFs as electrode materials is directly fraught with difficulties, which limits their usefulness. Even though most MOFs have weak conductivity, it can be improved by creating conjugate systems and 3D network topologies, allowing for the direct use of well-designed pristine MOFs as electrode materials for SCs.

2.2. MOF-Derived Metal Oxides

The poor structural stability and electrical conductivity of the pristine MOFs have hampered their practical utilization as electrodes in SC applications. Transforming the pristine MOFs into metal oxides is a significant way of enhancing their structural and electrochemical stability, including electrical conductivity. The MOF-derived metal oxide shows unique structural features, such as porous morphology, robust structure, high electrical conductivity, and high redox behavior. Therefore, metal oxides derived from MOFs are preferred for the construction of electrode materials. MOF-derived metal oxide electrode materials store energy through charge transfer between electrolyte–ions and the electrodes. Metal oxides are mostly made via the general procedure of calcination. MOFs are heated to a temperature of a few hundred degrees in an inert atmosphere furnace.^[52,53] Throughout the annealing procedure, metal sites are oxidized to the isonomous metal oxides, and organic ligands are transmuted into carbon dioxide and water vapor, which frame ample pores. MOF-derived metal oxides sustain their primitive morphology, showing huge pores and associated gaps.^[54,55]

Lan et al. prepared a porous flower-like MnNi₂O₄ using bimetallic Mn/Ni–MOF as a precursor that exhibits astounding electrochemical behavior with the most significant specific capacitance of 2848 F g⁻¹ at 1 A g⁻¹ with good stability of 93.25% capacitance retention after 5000 cycles at 10 A g⁻¹ (Figure 4). Further, they constructed an ASC using MnNi₂O₄ positive electrode and active carbon as the negative electrode, which shows a large energy density of 142.8 Wh kg⁻¹ at a high power density of 800 W kg⁻¹.^[56]

Xiao et al. synthesized an ultrathin Co₃O₄ nanosheet using Co-based MOF by hydrolysis followed by calcination procedure, which exhibits outstanding SC performance due to the abundant meso- and macropores. In addition, they fabricated an ASC using Co₃O₄ nanosheets as a positive electrode and AC as a negative electrode, which shows a high energy density of 32.8 Wh kg⁻¹ at the power density of 752 W kg⁻¹ and retains 98.1% of its initial

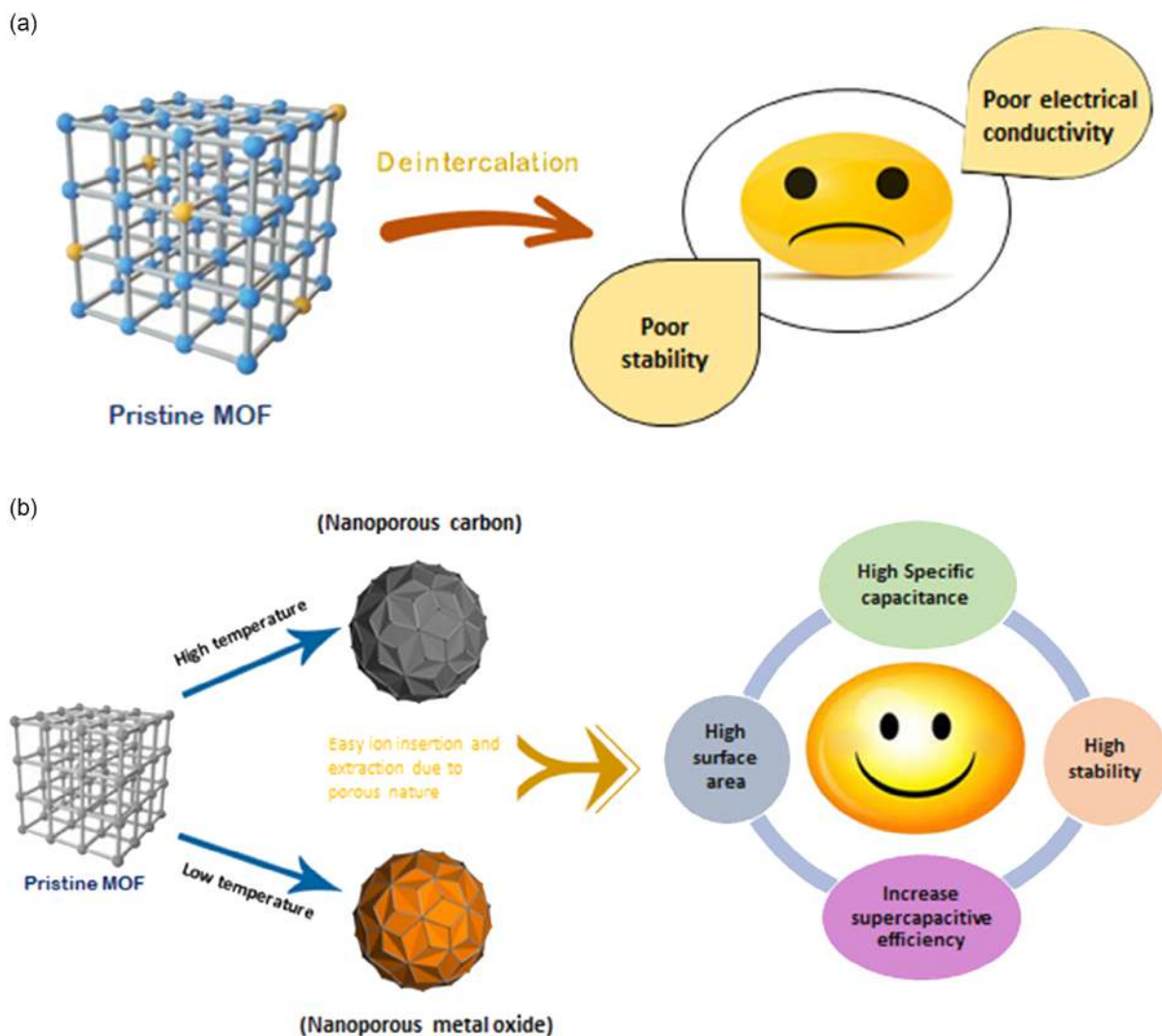


Figure 2. a) Schematic of the pristine MOFs for SC application. b) Development of the use of various MOFs in the field of SC application.

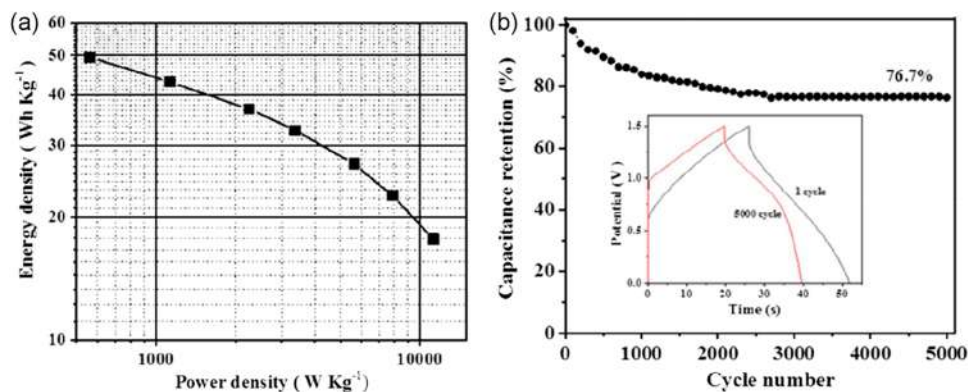


Figure 3. a) Ragone plot of the ASC device and b) the cycling stability at 5 A g⁻¹ over 5000 cycles. Reproduced with permission.^[51] Copyright 2019, American Chemical Society.

capacitance after 6000 charge/discharge cycles at the current density of 2 A g⁻¹ with long-term cycling stability.^[57] Wu and co-workers synthesized hollow core in double-shell NiO

nanospheres by the calcination of Ni-based MOF; as they are calcined at different temperatures, they show distinct surface areas and electrical conductivities, which play an important role in the

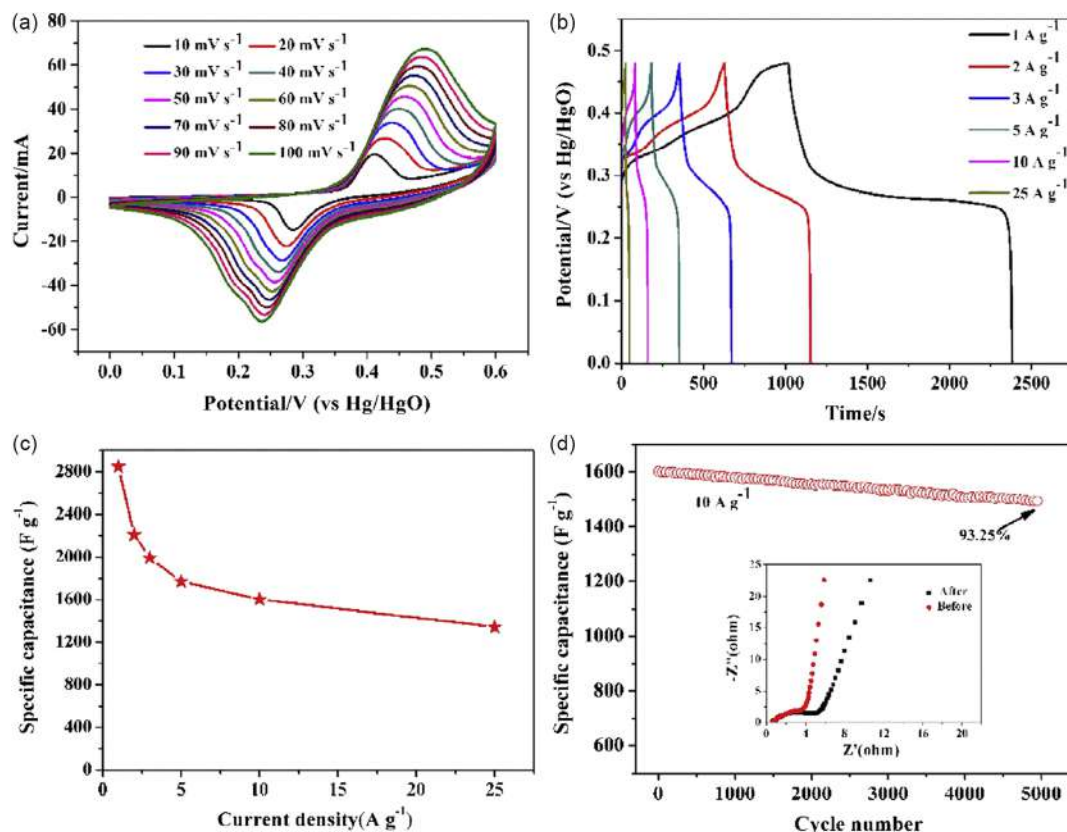


Figure 4. a) Cyclic voltammetry (CV) curves at different scan rates from 10 to 100 mV s^{-1} , and b) charge/discharge curves of the MnNi_2O_4 electrode at various current densities from 1 to 25 A g^{-1} . c) Specific capacitance of the MnNi_2O_4 electrode. d) Cycling stability of the MnNi_2O_4 electrode at a current density of 10 A g^{-1} ; the inset presents Nyquist plots of the MnNi_2O_4 electrode before and after cycling. Reproduced with permission.^[56] Copyright 2019, Elsevier.

redox reaction that takes place at the surface of the active materials. Material calcined at 400 °C shows a specific capacitance of 473 F g^{-1} at the current density of 0.5 A g^{-1} , which shows good cycling stability, even after 3000 cycles. Additionally, they constructed an ASC with high-energy storage capacity and outstanding cycling performance.^[58] Li et al. fabricated hierarchical double-shelled NiO/ZnO hollow spheres by annealing a bimetallic organic framework in air and used it as an electrode material for high-performance SC applications. It shows a specific capacitance of 497 F g^{-1} at a current density of 1.3 A g^{-1} with outstanding cycling stability, even after 2000 cycles.^[59] Xu et al. investigated a scheme to set up unique $\text{Co}_3\text{O}_4/\text{ZnO}$ nano heterostructures through the thermal conversion of center-shell $\text{ZIF-8}@/\text{ZIF-67}$, displaying superior pseudocapacitive behavior. It shows a high specific capacitance of 415 F g^{-1} at 0.5 A g^{-1} with enhanced rate capability (93.2% retention at 10 A g^{-1}), compared to Co_3O_4 and ZnO derived from single MOF precursor.

Further, they fabricated an ASC using $\text{Co}_3\text{O}_4/\text{ZnO}$ heterostructure as a positive electrode and active carbon as a negative electrode. The electrochemical performance determined in an aqueous electrolyte (AE), that is, 6 M KOH in expanded 1.4 V working voltage, shows an energy density of 43.2 Wh kg^{-1} at a power density of 1401 W kg^{-1} .^[60] The nanoporous NiO , NiCo_2O_4 , and Co_3O_4 were prepared using the hydrothermal

method and an annealing process that exhibits a large surface area and porous nature. As compared with monometallic oxides, the mixed metal oxides, that is, NiCo_2O_4 , show high specific capacitance of 684 F g^{-1} at 0.5 A g^{-1} current density and outstanding cycling stability with the specific capacitance retention of 86% after 3000 cycles at the current density of 10 A g^{-1} , whose performance makes it a promising material for energy storage and conversion devices.^[61]

2.3. MOF-Derived Nanoporous Carbon Materials

MOF-derived nanoporous carbons (NPC) material is obtained by the calcination of MOF at high temperatures or the pyrolysis of MOF followed by acid treatment or base activation. NPCs maintain the structure and morphology of MOF, which enables the conducting properties of carbon. Many NPCs materials have been widely examined for SC applications, due to their outstanding chemical and mechanical stability, large specific surface area, good electrical conductivity, and adjustable pore structure.^[62–64] To increase the capacitance of carbon material, heteroatom doping (e.g., B, S, N, P) is a new strategy to elevate the surface wettability and contribute reversible pseudocapacitor behavior to a material. The addition of metals can supply extra benefits in the carbon array, which encourages the applications of carbon

materials as electrode materials. Incorporating specific metals like Co, Ni, and Fe can amazingly ameliorate the crystallinity and electrical conductivity of carbon, owing to their catalytic graphitization of the amorphous carbon. Hence, heteroatom doping or metal-modified carbons are promising materials for SC applications and has attracted much interest.^[65–68] Nowadays, the performance of SCs is mainly influenced by electrode materials. Among different electrode materials, carbon is the most broadly used material for SCs due to its multiple advantages: wide source, large specific surface area, environmental warmth, and good electrical conductivity. Large specific surface area and suitable pore size are the chief techniques to achieve high capacitance of carbon materials; carbon materials mainly store energy by constructing an electric double layer across the separated charges of electrolyte ions on the surface.^[69]

Due to its easy synthesis, controllable morphology, and high nitrogen content, ZIF-8 is a common precursor for synthesizing many porous carbon materials for SCs. Tang et al. put nanoporous hybrid carbon materials containing nitrogen-doped carbon (NC) as the cores and highly graphitic carbon (GC) as the shell using core-shell-structured ZIF-8@ZIF-67 crystals. This novel NC@GC material holds a high surface area (up to $1276 \text{ m}^2 \text{ g}^{-1}$) and high N content (10.6 wt%) derived from core ZIF-8 and a better graphitic structure derived from shell ZIF-67. It shows an eminent specific capacitance of 270 F g^{-1} at a current density

of 2 A g^{-1} (Figure 5).^[70] Liu et al. investigated a new strategy to design a flexible hierarchical porous carbon film (HPCF) for binder-free and high-performance energy storage devices consisting of MOF-derived porous carbon polyhedra and carbon nanotubes (CNTs). They prepared HPCF (1, 2, -3, -4, and -5) by the calcination at different temperatures of 400, 500, 600, 800, and $900 \text{ }^\circ\text{C}$ respectively, from which HPCF₄ gives the largest Brunauer–Emmett–Teller ($620.1 \text{ m}^2 \text{ g}^{-1}$) and shows the highly porous structure, excellent flexibility, with highest electrical conductivity (1320 S m^{-1}). HPCF₄ offers excellent rate capability larger than 60% retention from 2 to 100 A g^{-1} with high electrical conductivity and successful ion transport networks, compared with the other flexible carbon electrodes. In addition, they fabricated an aqueous symmetrical SC that shows an energy density of 9.1 Wh kg^{-1} with a power density of 3500 W kg^{-1} .^[71] Duan and co-workers discovered three types of activated porous carbon (APC) by the annealing and thermolysis of Cu–MOF with different morphologies, varying the reaction temperatures at 0, 25, and $60 \text{ }^\circ\text{C}$. APC-25 reveals cabbage-like morphology, out of those APCs with the largest specific surface area, that is, $1880.4 \text{ m}^2 \text{ g}^{-1}$ and $0.81 \text{ cm}^3 \text{ g}^{-1}$ pore volume; it also exhibits the highest specific capacitance of 196 F g^{-1} at 0.5 A g^{-1} current density. Additionally, they fabricated an ASC device using APC-25, giving an incredible 11.8 Wh kg^{-1} energy density at a power density of 350 W kg^{-1} with outstanding cycling stability.

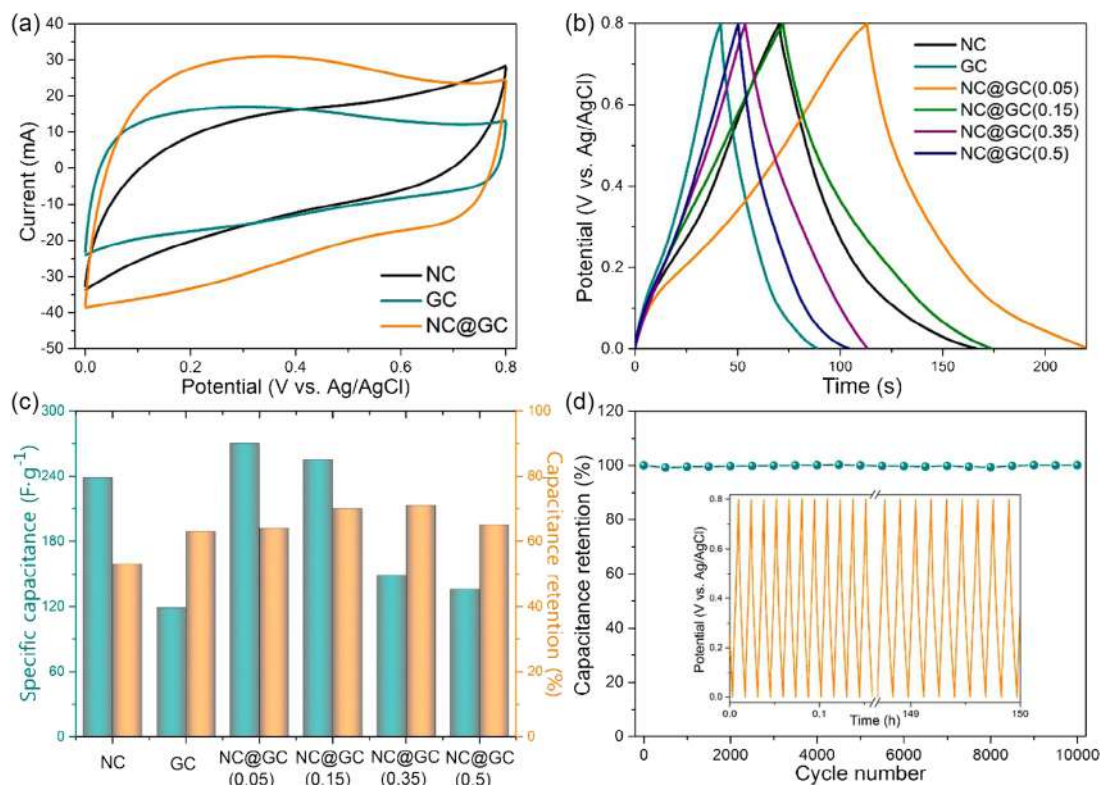


Figure 5. a) CV at a potential scan rate of 200 mV s^{-1} for NC, GC, and NC@GC (0.15). b) Charge–discharge curves of NC, GC, NC@GC (0.05), NC@GC (0.15), NC@GC (0.35), and NC@GC (0.5) electrodes at a current density of 2 A g^{-1} . c) The specific capacitance values obtained at a current density of 2 A g^{-1} and the capacitance retention ratios at a higher current density of 10 A g^{-1} for NC, GC, NC@GC (0.05), NC@GC (0.15), NC@GC (0.35), and NC@GC (0.5) electrodes, respectively. d) Cyclic stability of NC@GC (0.15) at a charge–discharge current density of 5 A g^{-1} for 10 000 cycles. Inset shows the galvanostatic charge–discharge curves. All measurements were conducted in $1.0 \text{ M H}_2\text{SO}_4$ using a three-electrode system. Reproduced with permission.^[70] Copyright 2015, American Chemical Society.

Noticeably, using six ASCs, five light-emitting diodes (LED) were lighted, which confirms that APC-25 might be used in energy storage devices.^[72] Wang et al. demonstrated a fruitful route to increase the conductivity performance of N-doped MOFs-based hierarchical carbon (NPC) to defeat the insulating problems of MOFs by electrochemically twisting together MOF crystals with a conductive polymer. They prepared a new N-doped MOFs-based hierarchical carbon (NPC) by electrospinning method, followed by pyrolysis to get nanofibers; it shows superior energy storage capacity to that of the earlier recorded MOF-derived carbon materials with innovative 1D hollow structures. NPCF exhibits 332 F g^{-1} specific capacitance at 1 A g^{-1} current density and excellent cycling stability with a specific capacitance retention of 98.9% after 5000 cycles at 1 A g^{-1} current density.^[73]

Chen and colleagues investigated a fruitful method for manufacturing hollow particle-based nitrogen-doped carbon nanofibers (HPCNFs-N) by an easy carbonization treatment of an electrospun ZIF-8/PAN composite precursor. HPCNFs-N material significantly increases the electrochemical property as an electrode material for SCs with incredible specific capacitance at different current densities, high energy/power density, and long cycling stability of over 10 000 cycles.^[74] Hao et al. synthesized nitrogen-doped porous carbon polyhedra (N-PCMPs) by directly carbonizing ZIF-11 polyhedra stimulated by fused KOH to enhance the surface area and pore volume. Activated N-PCMPs (N-PCMPs-A) show 307 F g^{-1} specific capacitance at 1.0 A g^{-1} current density, which is incredibly higher than that of N-PCMPs, that is, 165 F g^{-1} ; even further, the specific capacitance of N-PCMPs-A retains 198 F g^{-1} at a regular high amount of current density, that is, 10 A g^{-1} , which compared to N-PCMPs, is significant. N-PCMPs show incredible cycling stability with a specific capacitance retention of 90%, even after 4000 cycles at the current density of 10 A g^{-1} .^[75]

In this part, we provided a brief summary of material design techniques to illustrate the wide range of potential applications from the chemical makeup and physical characteristics of MOF-derived materials. The development of a variety of fascinating functional materials with desirable composition, tuning morphologies, structures, and characteristics can be facilitated by the use of MOFs as potential precursors or sacrificial templates. As a result of numerous benefits, such as high surface area, ordered porosity, adaptable topological morphology, and various chemical composition of MOFs, as well as improvements in material synthesis and characterization techniques, functional materials derived from MOFs have demonstrated great potential for creating advanced electrodes for clean, secure, and long-lasting energy storage systems.

3. MOF Composites with Different Materials

MOFs are novel spongy coordination polymers that exhibit remarkable properties, like organized porous structure, a large surface area, an adjustable structure, a high electrochemical response, and chemical tunability and hence have been broadly studied for energy conversion and storage applications. These nanostructures are profitably used as electrode materials in energy storage devices like SCs, due to their enhancement of charge transfer within the MOF structure and the redox nature

of their metal ions.^[76–78] While the research of MOF as an electrode material for SC applications is still in the primary phase, the field is becoming larger at a rapid rate. Some works have been published for energy storage devices, such as Ni-MOF, Fe-MOF, Co-MOF, and Co-Zn MOF as electrode materials for SCs. However, from an overall point of view, most MOFs still suffer from poor stability, narrow micropores, poor electrical conductivity, low use of active sites, and hindered ion entrance, which mostly limit the practical applications of many of the MOFs for SC applications.^[79–83] One strategy to overcome these problems is to upgrade MOFs by designing composites. MOF composites are prepared using MOFs and different functional materials, like metal oxides/hydroxides, quantum dots, reduced graphene oxide, metal sulfides, conducting polymers (CP), etc., to minimize the disadvantages of an individual building block.

To construct MOF composites, the direct reaction of MOFs with functional materials is a logical strategy and makes them candidates for energy storage applications.^[84] The composites can be synthesized in two ways: first, in a one-step procedure, where the different functional materials participate in the reaction during MOFs preparation. The second way is the composite of MOFs with different functional materials that can be executed after the preparation of MOFs. Single materials tend to run across certain obstacles and limitations; hence, materials with various advantageous features are incorporated. A synergistic effect within two compounded materials can be applied to boost the advantages of single materials or orderly reduce their limitations. Due to this, the composite formation logical strategy permits the construction of hybrid electrodes for SC applications. Hybrid electrodes can sustain the EDLC and pseudocapacitive feature compared to single materials. This hybrid plan helps develop a high value of specific capacitance, long cycle life, high energy density, and power density. We have reviewed the research work to explore MOF composites with proper materials given later in subgroups. Those hybrid materials have been certified to be beneficial to fabricate unique electrodes for highly advanced SCs.^[85] The production of a hybrid MOF with different functional materials to engender MOF composites exhibits immense advantages, due to their synergistic effect.

3.1. MOF@metal Oxides/Hydroxides

Owing to their size, crystallinity, controllable shape, and functionality, metal oxide nanomaterials are extensively used in energy storage applications.^[86–88] Metal oxide nanomaterials are measured as perfect pseudocapacitive electrode materials due to their high theoretical specific capacitance, inexpensiveness, and significant reversibility. However, they have increased surface energies and are prone to aggregation, moving toward pseudocapacitive performance.^[89,90] Furthermore, metal oxides as an electrode material for energy storage devices are widely limited, due to low surface area.^[91] Hence, a low-cost procedure is needed to enhance the specific surface areas of metal oxides, which is essential to obtain significant pseudocapacitive activity.

One of the plans of action is to combine the merits of both metal oxides and MOFs by mixing metal oxides with MOFs possessing large surface area, in which a single building block preserves its character while contributing remarkable features to

the entire process.^[92,93] Xiong and co-workers reported a new reverse thinking strategy to prepare a well-arranged porous metal oxide@MOF composite, that is, NiO@Ni-MOF/NF, by a two-step hydrothermal method. The hydrothermal method was selected due to the rapidity of its synthesis technique and also its effortlessness. To begin with, nickel foam (NF) was used as a unique self-sacrificing template and precursor for the preparation of nickel oxides (NiO), followed by the addition of the organic ligand (H₃BTC) to transform into Ni-MOF. Finally, the metal oxide@MOF composite was fruitfully prepared under the fine-tuned conditions, exhibiting 1853 C cm⁻² specific capacitance at 1 mA cm⁻² current density (**Figure 6**).

Furthermore, they assembled ASC devices using NiO@Ni-MOF/NF as a positive electrode and CNT as a negative electrode. This HSC device exhibits 144 F g⁻¹ specific capacitance at 1 A g⁻¹ current density with a high energy density of 39.2 Wh kg⁻¹ at a power density of 700 W kg⁻¹ and 94% capacitance retention after 3000 cycles (**Figure 7**). This synthetic technique takes a significant direction and provides a well-organized approach to obtaining other well-arranged metal oxide@MOFs composite materials.^[94]

Zheng et al. designed and reported highly alkaline stable cobalt oxide nanocubes on Co-MOF sheet composite (Co₃O₄@Co-MOF) by a facile and controllable one-pot hydrothermal method. The Co₃O₄@Co-MOF composite exhibits 1020 F g⁻¹ specific capacitance at 0.5 A g⁻¹ current density and enormous cycling stability with only 3.3% decay after 5000 cycles at 5 A g⁻¹ current density. Furthermore, they fabricated the Co₃O₄@Co-MOF//AC solid-state flexible device with maximum

energy density, revealing that solid-state flexible devices can be used in movable, portable, and lightweight electronic applications.^[95] Zhang et al. established that an effortless one-step chemical method gives rise to the self-transformation process to form the composite by combining metal oxides into the MOF systems using MOF-manganese hexacyanoferrate hydrate (MHCF) nanocubes as a starting material. The composite MnO_x-MHCF exhibits a remarkable threefold increase in capacitance compared to the pristine MOFs, revealing that MnO_x-MHCF composite material shows excellent promise for flexible energy storage. Furthermore, a flexible solid state-hybrid-SC (SSHHC) device was constructed using MnO_x-MHCF and AC as two electrodes, which exhibited an areal capacitance of 175 mF cm⁻² at 0.5 mA cm⁻² current density. Also, the device exhibits capacitance retention of 94.5% after 10 000 cycles at 5.0 mA·cm⁻² current density, with excellent long-term cycling stability.^[96]

3.2. MOF@CPs

While metal-organic frameworks are used as promising electrode materials in SCs due to their remarkable features, such as high surface area, tunable pore size, highly porous framework, open metal sites, and controllable functional linkers, some MOFs possess low conductivity.^[97] Unfortunately, due to low conductivity, the MOFs have limitations in utilization in SCs. An efficient strategy to enhance the conductivity of MOFs is the mixing of conductive polymers (CPs), like polyethylene dioxythiophene (PEDOT), polyaniline (PANI), and polypyrrole (PPy),

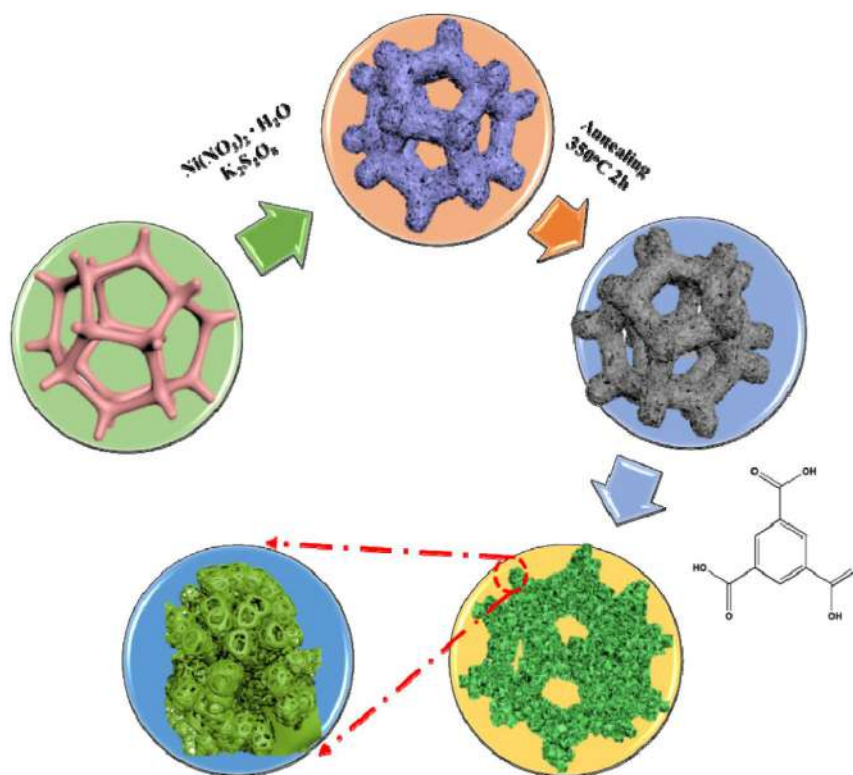


Figure 6. Schematic of the fabrication of NiO@Ni-MOF on Ni foam. Reproduced with permission.^[94] Copyright 2020, Elsevier.

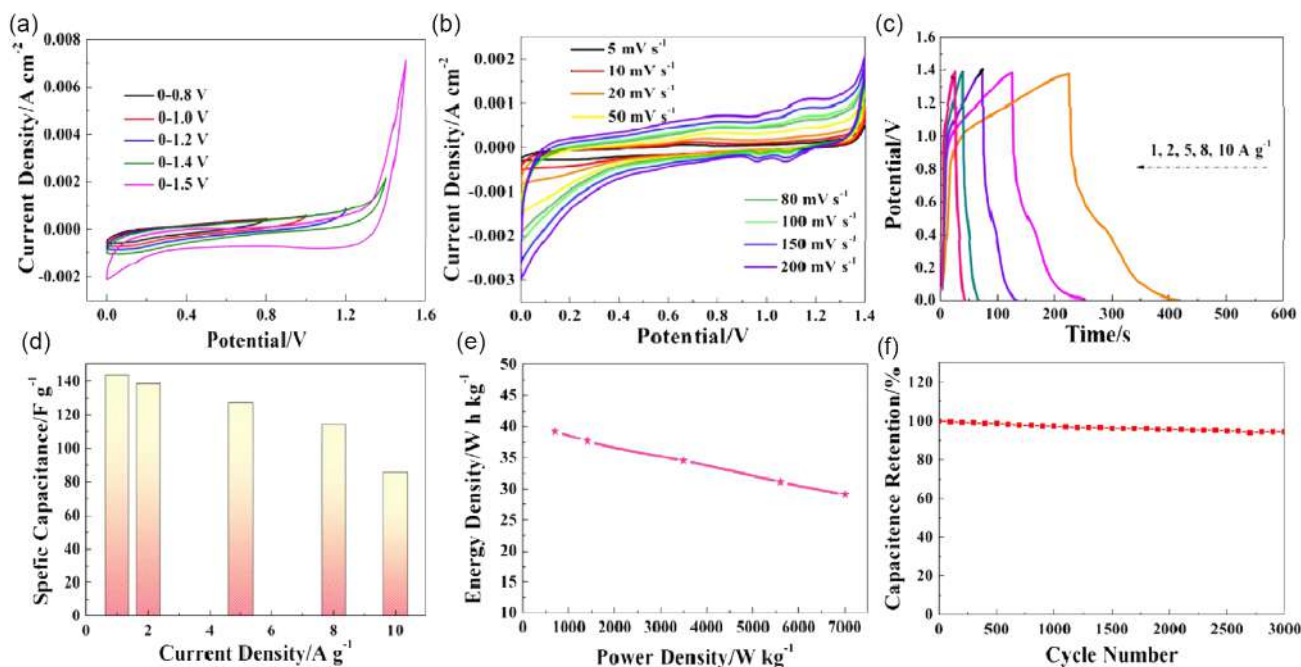


Figure 7. The electrochemical performance of NiO@Ni-MOF-12//CNT hybrid SC: a) CV curves at various voltage windows at the scan rate of 50 mV s^{-1} ; b) CV curves at various scan rates ranging from 5 to 200 mV s^{-1} in the voltage window of 0 – 1.4 V ; c) Galvanostatic charge/discharge (GCD) curves at different current densities ranging from 1 to 10 A g^{-1} in the voltage window 0 – 1.4 V . d) Histogram of the specific capacitance at different current densities. e) Ragone plot (energy density vs power density). f) Cycling performance up to 3000 cycles at the current density of 10 A g^{-1} . Reproduced with permission.^[94] Copyright 2020, Elsevier.

which adds up to a conducting route for MOFs. Owing to their low cost, effortless preparation, large theoretical specific capacitance, and excellent conductivity, CPs-based electrode materials are widely used in SCs.^[98–100]

Zhang et al. constructed PPy@UIO-66@CT fabric electrodes for flexible SCs by depositing polypyrrole (PPy) nanotubes and Zr-based MOF (UiO-66) particles on cotton fabrics. Primarily, UIO-66 was developed in situ on the surface of cotton fabric via a facile solvothermal method; later, PPy nanotubes were placed on the surface of UIO-66@CT, utilizing a reactive template, that is, FeCl_3 -MO complex. Due to its outstanding aqueous, acid, and thermal stability, UIO-66 was used along with PPy nanotubes to provide conductive connectors for UIO-66 particles because of its better conductivity. PPy@UIO-66@CT fabric electrodes possess high conductivity with better specific capacitance of 565 F g^{-1} at 0.8 mA cm^{-2} current density in a two-electrode system. Also, fabric electrodes exhibit admirable stability with capacitance retention of 90% after 500 charge/discharge cycles and upstanding rate capability.^[100] Qi et al. reported a strategy to design and construct a MOF/CP hybrid, that is, UiO-66/polypyrrole hybrid, for a high-performance all-solid-state fabric fiber SC via a one-pot electrodeposition method in the presence of dopamine. The manufactured UiO-66/PPY hybrid fabric fiber has high-performance capacitive properties, broad working temperatures, good mechanical flexibility, and long-term cycling stability; these properties show great potential for the fibrous energy storage device. It exhibits a specific capacitance of 10 mF cm^{-1} (206 mF cm^{-2}), a power density of $132 \mu\text{W cm}^{-1}$ ($2102 \mu\text{W cm}^{-2}$), and an energy density of $0.8 \mu\text{Wh cm}^{-1}$

($12.8 \mu\text{Wh cm}^{-2}$) with outstanding mechanical flexibility over a broad range of working temperatures.

Moreover, the fabricated fiber device was applied under a straight variety of bending angles and frizzy conditions to estimate its practical, flexible property.^[101] Wang et al. summarized a novel approach to attain high-performance SCs to overcome the insulating difficulty of MOFs by the electrochemically blending of MOF crystals with a conductive polymer. They fabricated the PANI-ZIF-67-CC electrode by depositing ZIF-67 on carbon cloth and then electrochemically blended PANI with it (Figure 8). PANI-ZIF-67-CC electrodes possess a high areal capacitance of 2146 mF cm^{-2} at 10 mV s^{-1} , compared to other reported SCs based on carbon nanoparticles (CNPs), CNTs, reduced graphene oxide, conductive polymers, and metal oxides. In addition, they fabricated a flexible solid-state SC device with an outstanding areal capacitance of 35 mF cm^{-2} and power density of 0.833 W cm^{-3} at 0.05 mA cm^{-2} current density; also, it exhibits capacitance retention of 80% after 2000 cycles at 0.05 mA cm^{-2} current density with excellent cycling stability.^[102] Ehsani et al. reported an RT electrochemically synthesized novel nanocomposite material, that is, poly ortho aminophenol/Cu-bipy-BTC composite for electrochemical redox capacitors possessing remarkable benefits, like simple method, high surface area, and stability in AE. Here, poly ortho aminophenol (POAP) is used as a polymer to enhance the more active sites for the Faradaic reaction and increase the specific capacitance of Cu-bipy-BTC.^[103] Srinivasan and co-workers prepared Co-MOF/PANI composite from cobalt nitrate, 1,3,5-benzene tricarboxylic acid, and aniline by the in situ chemical oxidative polymerization process. Here, PANI

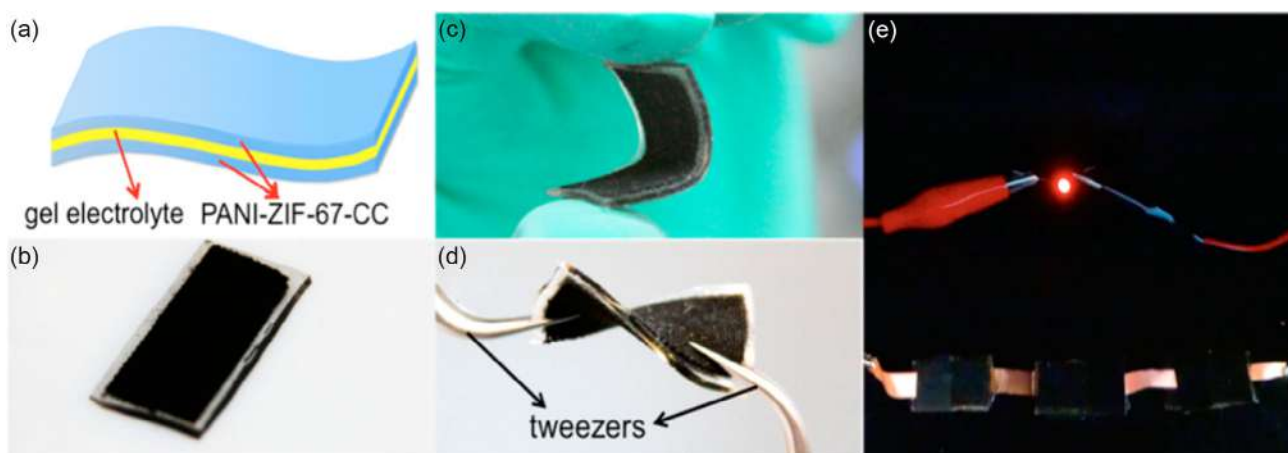


Figure 8. a) Schematic of the PANI-ZIF-67-CC flexible solid-state SC device. b–d) Optical photographs of the fabricated flexible solid-state SC device under b) normal, c) bent, and d) twisted state. e) Photograph of a red LED powered by the three SCs connected in series. Reproduced with permission.^[102] Copyright 2015, American Chemical Society.

is used as a polymer, because it is the cheapest and the most thermally stable intrinsic conductive polymer; it supplies high specific capacitance owing to its unique proton/dedoping technique. Co-MOF/PANI composite shows 504 F g^{-1} specific capacitance at 1 A g^{-1} current density and good cycling stability with the specific capacitance retention of 90% after 5000 cycles at 2 A g^{-1} current density, which reveals that Co-MOF/PANI composite can be utilized as electrode material in energy storage devices.^[104]

3.3. MOF@MOF

Like single MOF, the MOF-on-MOF hybrid is a promising material for energy storage devices. MOF-on-MOF scheme can enhance the composition, like organic linkers and metal ions, and the structural varieties of MOF, like pore, surface properties, and roles.^[105] Many MOF-on-MOF hybrids are established by different strategies, like surfactant-assisted growth, ligand exchange, nucleation kinetic-guided growth, epitaxial growth, and heteroepitaxial growth, with several building designs containing core-satellite, hollow multishell, core-shell, yolk-shell, asymmetric structure, and film on film.^[106,107] The combination of more than two MOFs possessing diverse structures and building blocks by the MOF-on-MOF development method is an exciting strategy for manufacturing hybrid MOFs bearing complex, novel features and ably designed from their composite components and structures. Some MOF-on-MOF composites show excellent features, enhanced conductivity, and better electrochemical performance due to the dual MOFs, while the limitations of single MOFs can be neutralized by making hybrid MOFs.^[108–111]

Deng et al. introduced a new MOF-on-MOF strategy to increase 2D MOFs conductivity and electrochemical performance. They prepared integrated two-layered MOFs, that is, Ni-MOF-24// $\text{Cu}_3(\text{HITP})_2$ (Ni//Cu MOF) array by Ni-MOF-24 as an active unit and $\text{Cu}_3(\text{HITP})_2$ (HITP = 2,3,6,7,10,11-hexamino-triphenylene) used as a conducting MOF to activate near-Ni-MOF-24, which exhibits

a triple high capacitance of 1424 F g^{-1} at a current density 2 A cm^{-2} and outstanding rate capability, in comparison with the pristine Ni-MOF. In addition, they fabricated a hybrid SC that shows a high energy density of 57 Wh kg^{-1} and an extreme power density of $48\,000 \text{ W kg}^{-1}$. The conductive $\text{Cu}_3(\text{HITP})_2$ MOF both extends the intrinsic conductivity for electron transfer and is uniformly scattered in the structure to motivate near Ni^{2+} species in a redox reaction, which increases the specific capacitance, energy density, power density, and rate capability of the hybrid MOF (Figure 9).^[112]

Hu et al. successfully synthesized core-shell ZIF-67@amorphous ZIF material via a facile solvothermal method, which shows a high specific capacitance of 1176.8 F g^{-1} at low current density of 1 A g^{-1} with excellent capacitance retention of 98% after 1000 cycles. Synthesized core-shell ZIF-67@amorphous-based electrodes are promising materials for energy storage devices, revealing a larger specific capacitance and outstanding cycling stability, compared to the individual ZIF-67 and amorphous ZIF. Furthermore, they fabricated an ASC device using ZIF-67@amorphous ZIF as a positive electrode, and AC as a negative electrode. The ASC device exhibits 65.9 F g^{-1} specific capacitance at 0.5 A g^{-1} current density with energy density of 23.4 Wh kg^{-1} at power density of 0.48 W kg^{-1} and 100% capacitance retention after 2000 cycles at 10 A g^{-1} .^[113] Zhang and colleagues prepared core-shell ZIF-L(Zn)@ZIF-67 nanoleaves in an aqueous medium at RT, used as anion templates for hierarchically meso/microporous hybrid carbon materials having graphitic carbon as the shells and amorphous carbon as the cores with nitrogen doping. Their strategy was to synthesize various core-shell designs of ZIFs, and further, they provided a new approach to the preparation of unique core-shell N-C@GC/CNTs with higher capacitance and outstanding stability. The achieved N-C@GC/CNTs materials are used to fabricate SCs from the optimized N-C@GC/CNTs to show the eminent capacitance of 252.1 F g^{-1} with 91.2% capacitance retention after 10 000 cycles, owing to their high nitrogen content, hierarchical pore structure, and better electrical conductivity, arising from the graphitic structure and CNTs.^[114]

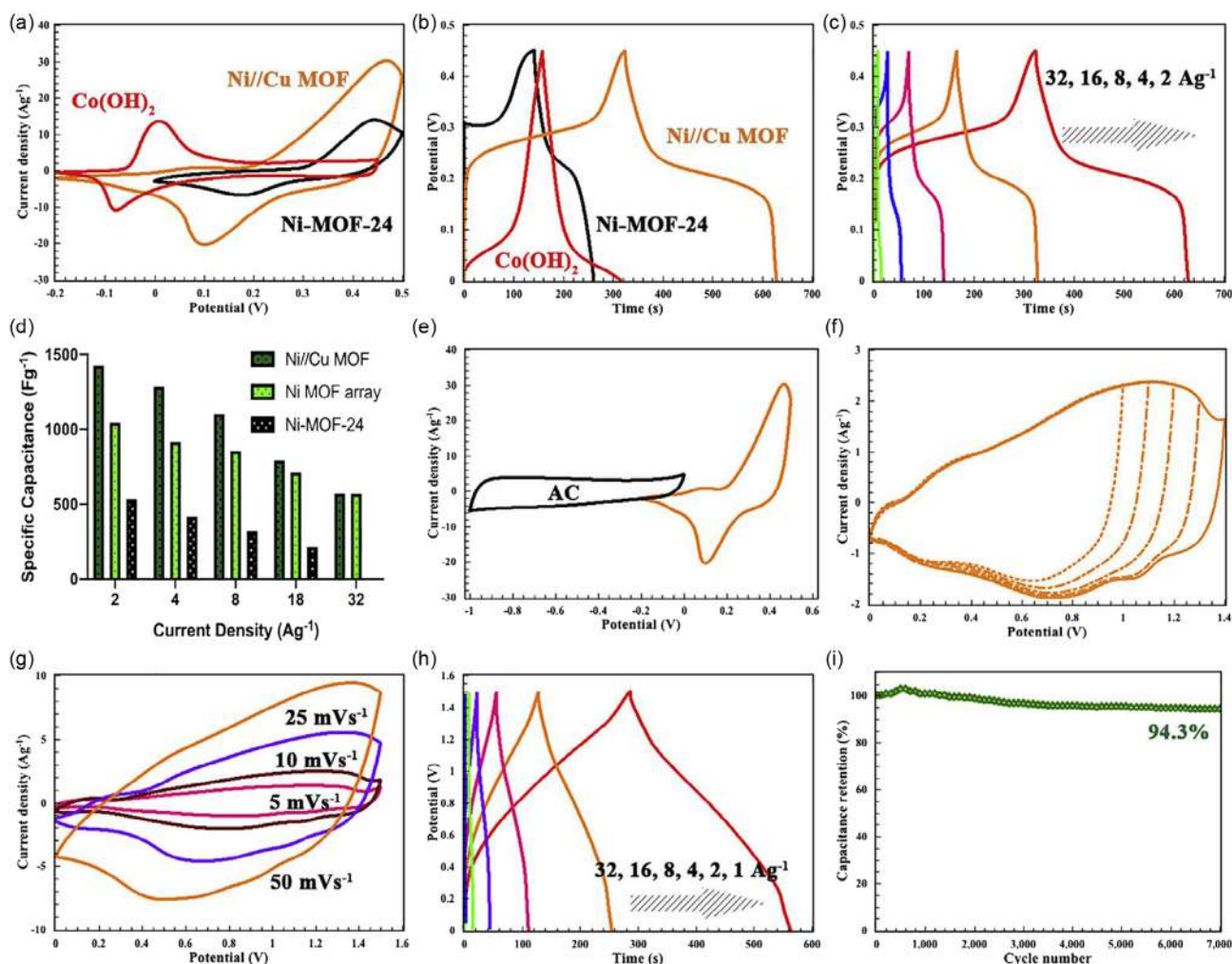


Figure 9. Electrochemical evaluation of Ni//Cu MOF and the corresponding hybrid SC. a) The CV curve of Ni//Cu MOF, Ni-MOF-24, and Co(OH)₂ was collected at 10 mV s⁻¹. b) Galvanostatic profiles of Ni//Cu MOF, Ni-MOF-24, and Co(OH)₂ at the current density of 2 A g⁻¹, and the capacitance can reach 1472, 533, and 688 F g⁻¹, respectively. c) Galvanostatic profiles of Ni//Cu MOF at various current densities. d) The capacitance comparison of Ni//Cu MOF, Ni MOF array, and powder Ni-MOF-24 at all current densities. e) CV curves of Ni//Cu MOF and AC at the scan rate of 10 mV s⁻¹. f) CV curves of hybrid SC with different potential windows. g) CV curves at different scan rates, ranging from 5 to 50 mV s⁻¹. h) Galvanostatic profiles were collected at various current densities. i) The stability test of the capacitor. After 7000 cycles, the capacitance holds 94.3% retention of its initial capacitance. Reproduced with permission.^[112] Copyright 2020, Elsevier.

3.4. MOF@CNT Nanocomposites

Owing to their low conductivity and minor stability, MOFs have limitations in electrochemical energy storage applications. Thus, it is a feasible scheme to incorporate conductive and stable materials with MOFs to design composites.^[115,116] CNT are a superb functional material for MOF composites and are 1D carbon materials with graphene layer structure. CNTs show electrical conductivity, unique pore structure, good thermal/mechanical stabilities, and excellent flexibility.^[117,118] On that account, the MOF@CNTs composites can fulfil the needs of an efficient electrode material for SC applications. However, MOFs@CNT hybrid composites possess large specific area and excellent pore size distribution because of MOFs and better electrical conductivity through highly conducting CNTs.^[119,120]

Zhang et al. introduced a unique necklace-like zeolitic imidazole framework@multiwalled CNTs (ZIF-8@MWCNTs) via a rapid and low-cost electrodeposition method; in addition to carbonization and acid treatment, it gives porous carbon material (C-ZIF-8@MWCNTs) that sustains the necklace-like design with a large surface area of 1063.2 m² g⁻¹. It exhibits large specific capacitance of 259.2 F g⁻¹ at 0.5 A g⁻¹ current density with capacitance retention of 92%, even after 5000 cycles at 15 A g⁻¹ current density. (Figure 10).^[121]

Wang and co-workers constructed flower-string-like NiCo-MOF/MWCNT composites material by a facile solvothermal process where MWCNT is enfolded with 2D NiCo-MOF nanosheets. The optimized NiCo-MOF/MWCNT composite exhibited specific capacitance of 1010 F g⁻¹ at current density of 0.5 A g⁻¹ with good rate capability and excellent cycling stability.

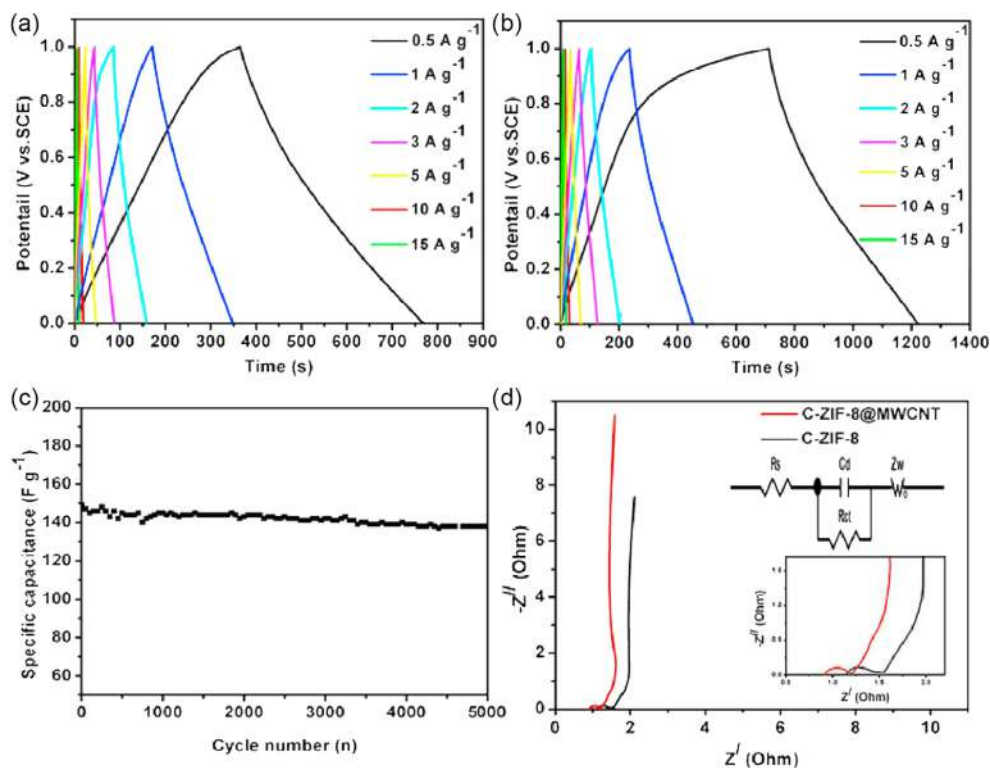


Figure 10. GCD curves at various current densities for a) C-ZIF-8, b) C-ZIF-8@MWCNTs, c) cyclic stability at 15 A g^{-1} for C-ZIF-8@MWCNTs, and d) EIS results for C-ZIF-8 and C-ZIF-8@MWCNTs (magnified Nyquist plots of C-ZIF-8 and C-ZIF-8@MWCNTs). Reproduced with permission.^[121] Copyright 2020, Elsevier.

Using NiCo-MOF/MWCNT composite as an electrode material, they assembled an ASC that reveals large energy density at high power density, outstanding rate capability, great cycling stability, and reversibility.^[122] Wen et al. prepared nickel metal-organic frameworks/CNTs (Ni-MOF/CNTs) composites via a simple solvothermal method, which exhibits outstanding electrochemical performance (i.e., 1765 F g^{-1} specific capacitance at 0.5 A g^{-1} current density) because of the synergistic effects of the Ni-MOF specific design and high conductivity from CNTs. Further, they assembled an ASC utilizing Ni-MOF/CNTs as a positive electrode and reduced graphene oxides/graphitic carbon nitride (rGO/g- C_3N_4) as a negative electrode, which reveals excellent energy density of 36.6 Wh kg^{-1} at power density of 480 W kg^{-1} with capacitance retention of 95%, even after 5000 cycles. Hence, it is a most promising material for future high-energy storage devices.^[123] Wang et al. proposed a simple one-step solvothermal approach to construct core-shell-structured flower-like composite MWCNTs@Ni(TA) by incorporating MWCNTs into Ni(TA), by which the surface area and the electroactivity of the composite were immensely enhanced. This reveals a specific capacitance of 115 mAh g^{-1} at 2 A g^{-1} current density and excellent cycling stability with capacitance retention of 81.6%, even after 5000 cycles at 10 A g^{-1} current density.^[124]

3.5. MOF@Graphene Nanocomposites

Individual MOFs exhibit restricted performance owing to their intrinsic weaker features, like electrical conductivity, electroactivity, and stability. Hence, multielement systems combine

MOFs with different materials, such as graphene, carbon black, and CNT. From these, graphene or reduced graphene oxide has emerged as a unique conducting additive for energy storage applications, due to its large electrical conductivity and exceptional mechanical strength arising from its 2D carbon structure.^[125,126]

Azadfalsh et al. prepared novel hierarchical flower-like copper metal-organic frameworks/graphene composite by a facile and low-cost one-step solvothermal method. The composite shows excellent electrochemical performance due to the synergistic effects of Cu-MOF design and the large conductivity of graphene. It shows a high specific capacitance of 482 F g^{-1} at a scan rate of 10 mV s^{-1} and exhibits outstanding cycling stability with specific capacitance retention of 93.8%, even after 1000 cycles at 0.3 A g^{-1} current density in 6 M KOH . Additionally, they demonstrated an ASC that reveals a high energy density of 34.5 Wh kg^{-1} and power density of 1350 W kg^{-1} at 0.5 A g^{-1} current density. Electrochemical investigation revealed that the Cu-MOF/G nanocomposite is a promising electrode for high-performance energy storage materials.^[127] Sundriyal et al. prepared Ni-doped ZIF-67/rGO composite by an easy one-pot stirring procedure, which possesses high porosity, high surface area, and enhanced electrical conductivity. To achieve beneficial redox activity and electrical conductivity, the doping percentage of Ni is 33%, and the 20% of reduced graphene oxide (wt%) in the composite material is optimized, which delivers high specific capacitance of 304 F g^{-1} at a current density of 1 A g^{-1} in $1 \text{ M H}_2\text{SO}_4$.

Furthermore, they prepared a solid-state symmetric SC that exhibits high energy density of 21.5 Wh kg^{-1} at 1 kW kg^{-1} power density with capacitance retention of 87%, even after 4500 cycles.^[128] Hong et al. synthesized Ni-Co-MOF/GO composite by directly developing dual metal centers metal-organic framework on graphene oxide sheets using a one-pot solvothermal method, by optimizing the quantity of graphene oxide 3D chestnut-shaped nanostructures that were obtained. Ni-Co-MOF/GO-2 (quantity of graphene oxide, 0.2 g) yields a maximum specific capacitance of 447.2 F g^{-1} at 1 A g^{-1} current density with excellent cycling stability of 99.6%, even after 300 cycles. The synthesized Ni-Co-MOF/GO composite is a beneficial material for high-performance SC electrode materials due to its novel mechanical strength, large surface area, controllable porous structure, good charge transfer route, and a stable interface between the electrolyte and electrodes.^[129] Sundriyal et al. prepared a highly porous ZIF-67/rGO composite by an easy stirring, acid-free, and environment-friendly process, which shows a large specific surface area (e.g., $947 \text{ m}^2 \text{ g}^{-1}$) and excellent electrochemical performance in the presence of redox additive electrolytes (RAEs). ZIF-67/rGO composite delivers a high specific capacitance of 1453 F g^{-1} at the current density of 4.5 A g^{-1} with outstanding cycling stability of 90.5%, even after 1000 cycles; the use of RAE is to increase the electrochemical performance. In addition, they fabricated a symmetric SC that possesses an energy density of 25.5 Wh kg^{-1} at a power density of 2.7 kW kg^{-1} with a capacitance retention of 88.8%, even after 1000 cycles.^[130]

3.6. MOF@Metal

Metal-doped MOFs are a unique strategy to increase the electrochemical performance of the individual MOFs, as they can supply the benefits of the doping metal material, such as better conductivity, good redox centers, and structural stability. Utilizing this concept, Li et al. constructed Mo-doped Ni-MOF nanosheets (M-NMN) via a one-pot hydrothermal method, from which M-NMN-1 composite (Ni: Mo = 1:1) shows excellent performance, compared to the different quantity of materials. M-NMN-1 electrode yields high specific capacity of 802 C g^{-1} at current density of 1 A g^{-1} with capacitance retention of 96%, even after 20 000 cycles. The metal Mo doping enlarged the potential window and enhanced the conductivity and stability of materials. Also, they constructed a battery-SC hybrid device (M-NMN-1//AC) that reveals outstanding energy density of 59 Wh kg^{-1} at power density of 802 W kg^{-1} with excellent capacitance retention of 93%, even after 20 000 cycles.^[131] For the first time, Yang et al. designed Zn-doped Ni-MOFs composite material with a flower-like microsphere; it exhibits charge transfer resistances that express a faster electron transfer rate. It shows high specific capacitances of 1620 and 854 F g^{-1} at current density of 0.25 and 10 A g^{-1} , respectively, with capacitance retention of 91%, even after 3000 cycles. Zn-doped Ni-MOFs composite material is used as electrode material for SCs due to its layered design with extended interlayer gap, high specific capacitance, high rate capability, outstanding cycling stability, and flower-like microsphere morphology.^[79] Zheng and colleagues constructed an Mn-doped ultrathin Ni-MOF nanosheet array on nickel foam (Mn_{0.1}-Ni-MOF/NF) from manganese nickel layered double

hydroxide (MnNi-LDH/NF) by a solvothermal method. The Mn_{0.1}-Ni-MOF/NF reveals ultrahigh areal capacity of 6.48 and 4.72 C cm^{-2} (C: (1178 and 858) C g^{-1}) at current densities of 2 and 20 mA cm^{-2} , respectively, with capacitance retention of 80.6%, even after 5000 cycles in 6 M KOH. Furthermore, they assembled an ASC device (Mn_{0.1}-Ni-MOF/NF//AC) that delivers high energy density of 39.6 Wh kg^{-1} at a power density of 143.8 W kg^{-1} with capacitance retention of 83.6%, even after 5000 cycles. Hence, Mn_{0.1}-Ni-MOF/NF contributes to a highly stable and capacitive SC positive electrode.^[132] Wang et al. designed a nickel-functionalized copper MOF (Ni@Cu-MOF) via a facile volatilization process, followed by a post-modification synthesis method at RT. This shows higher specific capacitance of 526 F g^{-1} at current density of 1 A g^{-1} , compared to the monometallic Cu-MOF, that is, 126 F g^{-1} , and also exhibits good cycling stability with specific capacitance retention of 80% after 1200 cycles. Also, they fabricated an ASC device (Ni@Cu-MOF //AC) that yielded a specific capacitance value of 48.7 F g^{-1} at current density of 1 A g^{-1} with high energy density of 17.3 Wh kg^{-1} at power density of 798.5 W kg^{-1} . Therefore, the outcomes reveal that bimetallic MOFs are favorable candidates for SCs.^[133]

3.7. MOF@QD

Quantum dots are 0D semiconductor nanocrystals of (2–10) nm in size. Due to their novel tunable and size-dependent electronic features, quantum dots have been utilized in many applications. Xue et al. extended their implementation by using them with MOF as a functional material to form MOF@QD composite.^[134] MOF@QD composite can be prepared by one-pot synthesis, the double solvent method, and the solvothermal method by directly incorporating presynthesized QDs in MOFs.

Gao and co-workers prepared SnO₂ quantum dots@ZIF-8 using a facile in situ epoxide precipitation approach; this shows good pseudocapacitive performance due to its synergistic effect of ZIF-8 and SnO₂ quantum dots. Due to the porous structure of ZIF-8, it easily incorporates SnO₂ quantum dots to accelerate the usage of active material, leading to high specific capacitance. It exhibits the highest specific capacitance of 931 F g^{-1} at scan rate of 5 mV s^{-1} , which is much higher than that of SnO₂ quantum dots and ZIF-8, with outstanding cycling stability over 500 cycles. The synthesized SnO₂ quantum dots@ZIF-8 composite material shows good electrochemical performance in 6 M KOH; hence, it is used as electrode material in SC devices (Figure 11).^[135]

Li et al. synthesized SnO_x quantum dots@Zr-MOFs (UIO-66) composites by a unique technique that blends the dehydration of inorganic group in metal-organic frameworks with water-free sol-gel chemistry, followed by a pyrolysis method to yield SnO_x quantum dots@Zr-MOFs (UIO-66) composites with remarkable properties, like high thermal stability (upto 773 K), a highly porous structure, and excellent electrochemical stability of UIO-66. After 100 cycles, it still shows a specific capacity of 994 mAh g^{-1} at current density of 50 mA g^{-1} . This approach is appropriate, low cost, and time-saving, with increased specific capacity, outstanding rate capability, and excellent cycling stability, leading to a promising anode material in LIBs.^[136] Yu et al. manufactured C@GQD composite via a successful in situ self-assembly method by blending MOF (ZIF-8) and graphene

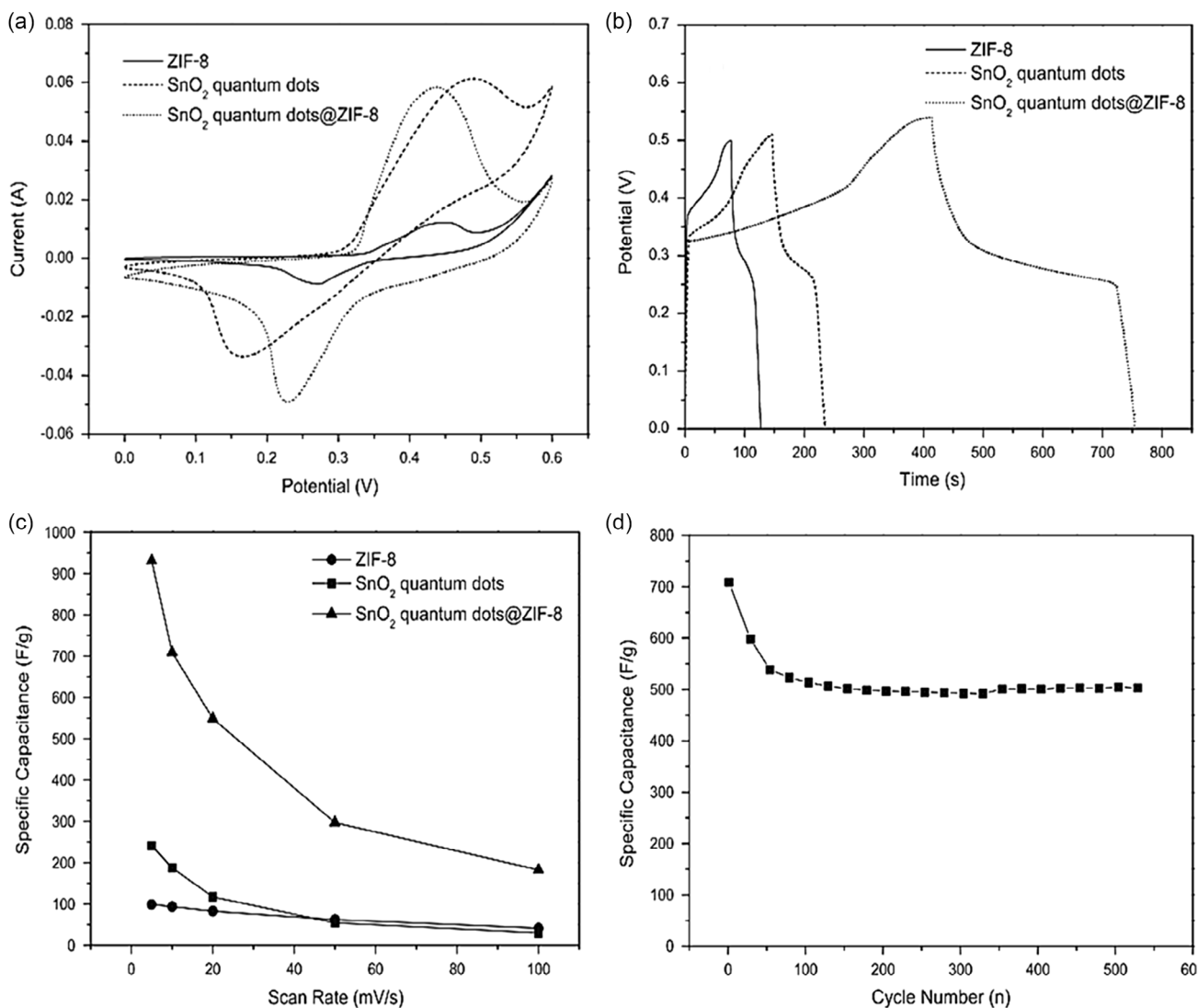


Figure 11. a) CV curves of different samples at a scan rate of 5 mVs⁻¹. b) CP curves of different samples at a current density of 5 mA cm⁻². c) The specific capacitance as a function of the scan rate of different samples. d) Cycling performance of SnO₂ quantum dots@ZIF-8 at scan rate of 10 mVs⁻¹. Reproduced with permission.^[135] Copyright 2014, Elsevier.

quantum dots, followed by high-temperature calcination and etching to obtain a novel class of porous carbonaceous material. The C@GQD composite possesses many micro- and mesopores with high specific surface area of 668 m² g⁻¹. In addition, it is used as a SC electrode material to show outstanding double-layer capacitance and specific capacitance retention of 130 F g⁻¹ at current density of 2 A g⁻¹ with long-term cycling stability, even after 10 000 cycles.^[137]

Concisely, pristine MOFs have been restricted by their weak electrical conductivity and small micropores. As a result, there are synergistic effects and unique potentialities that cannot be realized by separate pieces. The advantages of MOFs and other kinds of functional materials may be successfully integrated in MOF composites, and the production of MOF-based composites will become easy. In order to counteract the drawbacks of individual components, MOF composites, in which MOFs are mixed

with a range of functional materials, have been developed. MOF composite materials may be employed directly as outstanding materials for development of energy storage devices.

4. Designing Electrolyte Selection by Metal–Organic Frameworks and Their Composites for SC Application

An electrolyte is an ionic conductor, although an electronic insulator; it is either a solid or, more frequently, a liquid that generally works with a sponge-like layer or gel in electrochemical energy storage devices. Electrolytes are essential and significant components in SCs. Due to their physical and chemical properties, they play a vital role in electrochemical performances, such as specific capacity, energy density, power density, rate performance,

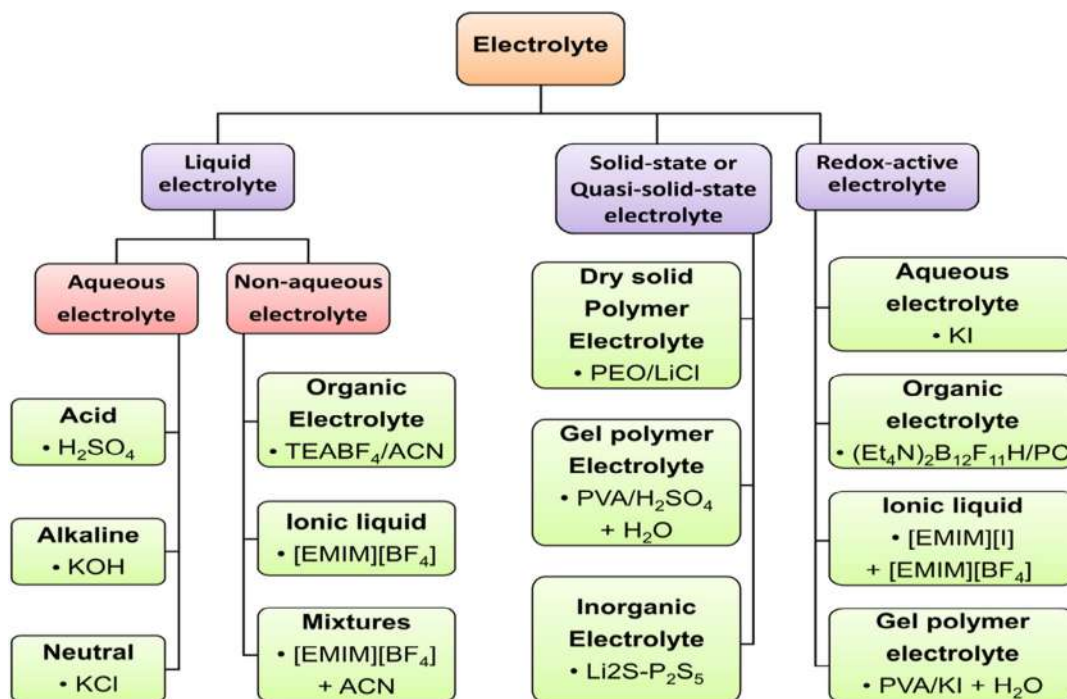


Figure 12. Classification of electrolytes used in SCs.

cycling stability, and safety.^[138,139] The necessities for an ideal electrolyte are broad potential window, high ionic conductivity, extended operating temperature range, high chemical and electrochemical stability, large chemical and electrochemical inertness to SC constituents (e.g., electrodes, current collectors, and packaging), convenience with electrode materials, low volatility and flammability, ecofriendliness, and inexpensiveness. In all honesty, it is challenging for an electrolyte to fulfill all of these necessities; also, each possesses its advantages and limitations.^[140–143]

The selection of electrolytes is vital to safe and high-performance SCs.^[144] Concerning electrochemical SC electrolytes, various electrolytes used in the SCs that have been studied are AEs, organic electrolytes (OEs), ionic liquid electrolytes (ILEs), redox-active electrolytes (RAEs), and solid-state or quasi-solid-state electrolytes.^[145,146] Ionic conductivity and mobility, dielectric constant, thermal stability, electrochemical stability, and dispersion interaction are the principal components to estimate the performance of electrolytes. The thermal stability of SCs is based on the electrolyte's interaction with an electrode and the thermal stability of the electrolyte itself. Hence, the thermal stability of an electrolyte is resolved mainly by its proportions, like salt, solvent, and additive.^[143] The safety and lifecycle of SCs depend on electrochemical stability, and electrochemical stability is based on the elements of the electrolyte and the affinity of the electrolyte to the electrode material. Equivalent series resistance (ESR) is the sum of different resistances containing intrinsic resistance of the electrode material and electrolyte, mass transfer resistance of the particle, and junction resistance between the electrode material and the current collector. ESR is a vital variable for calculating the power density of SCs; as

the ESR value increases, the power density decreases (**Figure 12**).^[147,148]

4.1. AEs

Because of their low cost, and simple handling in the laboratory compared to other electrolytes, AEs have been broadly applied in research and development. AEs acquire higher ionic concentrations, low resistance, smaller ionic radius, higher capacitance, and higher conductivity than ionic and OEs, which are advantageous for lowering the same series resistance and producing greater power density SCs.^[126] Altogether, AEs can be subdivided into acid, alkaline, and neutral AEs, in which H₂SO₄, KOH, and Na₂SO₄ are examples, they are the most used electrolytes.^[147,149]

The choosing criteria for AEs mainly consider the particle size of material, hydrated cations and anions, and the mobility of ions, which influence ionic conductivity and specific capacity. Survey shows that those neutral electrolytes have a wider range of potential windows than acid and alkaline electrolytes.^[150,151] Regarding MOFs and their composite materials, AEs are widely used, such as H₂SO₄, KCl, KOH, LiOH, NaOH, and Na₂SO₄. Some examples of analogous SCs were earlier reviewed in the previous parts. Below we go over a few selected examples.^[152] Metal oxide@MOF composite (Co₃O₄@Co-MOF)-based electrode was investigated in the presence of 3 M KOH. Synthesized composite material exhibits extraordinary alkaline stability, which sustains its original structure in 3 M KOH for a minimum of 15 days; it shows high cycling stability after 5000 cycles, with only 3.3% decay at 5 A g⁻¹ current density.^[95] Neutral AEs, such as KCl, Na₂SO₄, and LiCl, are primarily used in different concentrations. Due to the broad potential window with less

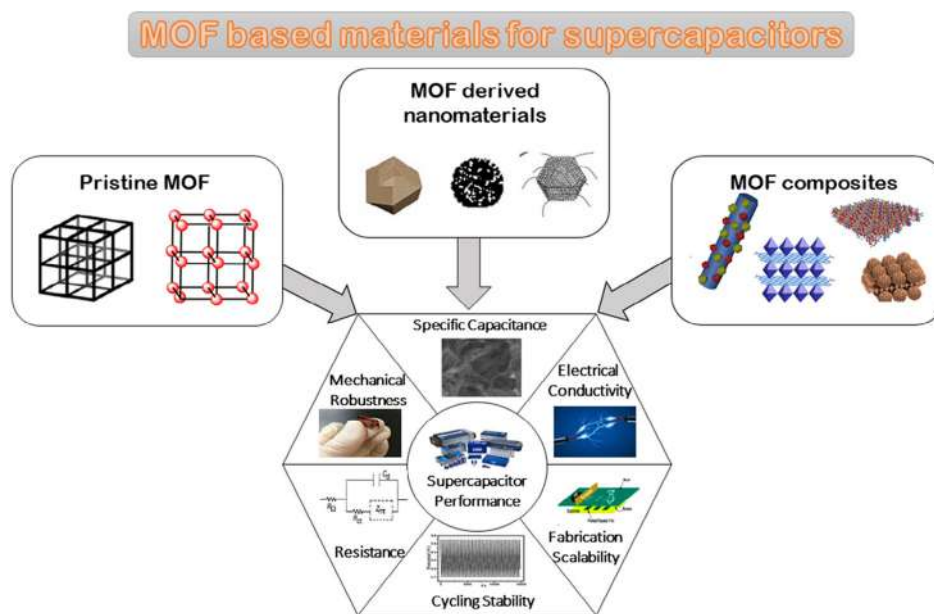


Figure 13. Schematic of MOF-based materials as electrode materials for SCs. Pristine MOF icon reproduced with permission.^[190] Copyright 2020, MDPI. MOF-derived nanomaterials icon reproduced with permission.^[191] Copyright 2017, Wiley. MOF composites icon reproduced with permission.^[191] Copyright 2017, Wiley and reproduced with permission.^[192] Copyright 2018, Wiley. Supercapacitor performance icon reproduced with permission.^[193] Copyright 2017, Royal Society of Chemistry and reproduced with permission.^[194] Copyright 2019, De Gruyter.

corrosive character, neutral AEs are safely used. Wang et al. proposed the application of 3 M KCl during their investigations of an electrode made of a ZIF-67/PANI composite that exhibits a specific capacitance of 371 F g^{-1} at a scan rate of 10 mV s^{-1} .^[102] H_2SO_4 is the most frequently used acid electrolyte for aqueous-based electrochemical SCs in MOF-based electrodes out of several acidic electrolytes, mainly because of its outstanding ionic conductivity.^[79,127] H_2SO_4 electrolytes show lower ESR value than neutral electrolytes, giving high specific capacitance and high conductivity. Bao et al. proposed the application of 1 M H_2SO_4 through their investigations of an rGO/Zn-MOF@PANI electrode, which reveals specific capacitance of 371.91 F g^{-1} at current density of 0.1 A g^{-1} .^[153]

To summarize, several factors of AEs significantly affect the electrochemical performance of SCs, like salt concentration, types of cationic and anionic species, hydrated ion size, specific conductance, and conductivity. Among AEs, neutral AEs are widely used because of their low cost, low corrosive action, and ecofriendliness, leading to a wide potential window, high specific capacity, and energy density. However, more development in the electrochemical performance of SCs with AEs is still required to enhance the energy density and cycling stability of SCs.

4.2. Organic Electrolytes (OEs)

OEs of acetonitrile, propylene carbonate (PC), diethylene carbonate, quaternary ammonium salts like tetraethyl ammonium tetrafluoroborate (TEABF_4), tetrahydrofuran (THF), and lithium hexafluoro phosphate (LiPF_6) are used in SCs to overcome the limitation of the confined potential window examined of AEs. OEs generally include conducting salts dissolved in organic

solvents for SC devices. Tetraethyl ammonium tetrafluoroborate (TEABF_4) is the most frequently used conducting salt for electrolytes in SCs.^[154] In addition to TEABF_4 , different salts have been evolved to enhance many properties of electrolytes, like solubility, conductivity, stability, and temperature performance. Several types of OEs have extraordinary applications in economic SCs, and also, they can supply a wide potential window with enhanced energy and power densities.

The potential window is an important property of the OE, which determines the electrochemical performance of SCs, like cell voltage, energy, and power densities. The potential window of the OEs depends on many aspects, like solvent, conducting salts like cation and anion, and impurities, such as a trace amount of water.^[155] Salunkhe et al. synthesized a high-performance SC made up of NPC material derived from ZIF-8; they investigated the electrochemical performance in OEs, that is, 2 M $\text{NEt}_4\text{BF}_4/\text{PC}$. The system shows a broad operating potential window of 2.4 V, revealing a specific capacitance of 20.6 F g^{-1} with very high surface area of $1873 \text{ m}^2 \text{ g}^{-1}$.^[156] Ghoshs group reported new materials, that is, lanthanide MOFs (MOF-Ce, MOF-Pr, and MOF-Nd), and investigated their electrochemical behavior in 1 M TEABF_4 in acetonitrile as an electrolyte within a potential window of 0.0–0.8 V for SC application. Among the three MOFs, MOF-Ce shows a maximum specific capacitance of 572 F g^{-1} at current density of 1 A g^{-1} with capacitance retention of 81%, even after 5000 cycles.^[157] Choi et al. reported a series of graphene-doped nMOFs and investigated the electrochemical performance in an OE, that is, 1 M $(\text{C}_2\text{H}_5)_4\text{NBF}_4$ in acetonitrile. This delivers high capacitance of 726 F g^{-1} at current density of 6.95 mA g^{-1} .^[158]

OEs have low conductivity, which leads to a higher ESR value that restricts the power density. Another limitation of OEs is the

higher resistivity than AEs, because of their large molecules, which need a large pore size in the electrodes. Compared to AEs, OEs are costly, and precautions should be taken because of their flammability, volatility, and toxicity, showing smaller specific capacity and lower ionic conductivity. In addition, OEs need intricate purification, and manufacturing procedures are restricted to controlled conditions to remove unused impurities (e.g., water), which show high-performance degradation and self-discharge problems.^[147]

4.3. Solid-State Electrolytes (SEs)

SEs offer more benefits than other electrolytes, such as simple packaging and fabrication processes, good ionic conducting media, and freedom from liquid leakage. The SEs are used as the ionic conducting media and a separator between electrodes. SEs progressed for energy storage devices like SCs depending on polymer electrolytes. The polymer-based SEs are further divided into three subtypes: the solid polymer electrolyte (SPEs, also named dry polymer electrolytes), the gel polymer electrolyte (GPE, due to the presence of liquid media, it is also called quasi-SE), and the polyelectrolyte.^[159,160]

Due to their advantages, like simple packaging and manufacturing process, good electrochemical stability, freedom from liquid leakage, and corrosion problem, SPEs and GPEs have mainly been used in electrolytes other than liquid electrolytes. However, SPEs have limitations in flexible devices, due to their low conductivity and poor elastic or flexible properties.^[161] SPEs are made up of dissolving the salt of alkali metals of type MX (M = Na, Li, Ag, Cu, etc. and X = F, Cl, I, and Br) in polymers like polyethylene oxide and polypropylene oxide.^[162] GPEs include conducting salt dissolved in solvent or composed of polymer (e.g., PEO, PEG, PVA, etc.) with AE (e.g., KOH, H₂SO₄, or K₂SO₄).^[163] Due to its properties, like higher ionic conductivity, high porosity, and outstanding mechanical properties through the freeze-thawing process, PVA has been widely used for hydrogel polymer electrolytes.^[164] In practical applications of energy storage devices, such as EDLCs, GPEs have received immense attention compared to other liquid electrolytes, due to disadvantages, like poor safety, liquid leakage, and strict geometry. However, compared to other liquid electrolytes, EDLCs investigated using GPEs possess lower specific capacity, low ionic mobility, and a poor electrode/electrolyte interface contact.^[165,166]

Currently, MOFs have revealed potential for the construction of high-performance SEs due to their porous crystalline inorganic-organic materials, which have grown into an exciting research area. MOFs provide great scope for manipulating the physicochemical and electrochemical features of SEs and supply perfect platforms to investigate the underlying mechanisms of ion conduction and the structure-property techniques.^[167] Wang et al. constructed flexible solid-state micro-SCs (MSCs) using induced graphene as flexible electrode materials and the multilayer film of ZIF-67 and PANI as substrates. The performance of a multilayer-modified LIG-PANI-ZIF-67 electrode in combination with PVA/H₂SO₄, which functioned as a polymer gel electrolyte, was investigated. The fabricated device shows specific capacitance of 719.2 mF cm⁻² at current density of 0.5 mA cm⁻² with capacitance retention of 87.6%, even after 6000 cycles.^[168] Similarly, Shao et al. used PVA/H₂SO₄ gel electrolyte in a SC

whose electrode was fabricated from a PANI/UiO-66 composite material. The device yielded specific capacitance of 647 F g⁻¹ at current density of 1 A g⁻¹ with capacitance retention of 91% after 5000 cycles.^[169]

Overall, among all these three types, GPEs have the highest ionic conductivity, due to the liquid phase. Because of their high ionic conductivity, GPEs are recently commanding SE-based SC devices, and due to this, the use of SPEs is restricted. However, owing to the presence of water and comparatively low mechanical strength, GPEs suffer from a narrow operative temperature range.

4.4. Ionic Liquid Electrolytes (ILEs)

Ionic liquids are unique new types of solvents and materials with special properties and have attracted immense attention in energy storage devices like SCs.^[170] They comprise bulky organic cations and inorganic or charged localized anions with beneficial properties like negligible volatility, low flammability, wide liquid temperature range, high ionized condition, and broad potential windows, compared to aqueous and OEs.^[171,172] Due to their advantageous properties, ionic liquids are safe alternatives to recent OEs. Hence, ionic liquids are an excellent substitute for conventional electrolytes for SCs and have attracted significant attention.^[173] Aprotic pyrrolidinium and imidazolium-based quaternary ammonium salts are commonly used ionic liquids as potential electrolytes for SC application.^[172]

Recently, ionic liquids have been used as solvents for MOF synthesis (ionothermal synthesis), providing multiple reaction conditions, due to their designable and tunable features. As compared to solvothermal synthesis, ionothermal synthesis for MOFs has many advantages. The ionic liquid both acts as a solvent and acts as a structure-directing agent. Additionally, an ionic liquid used as a solvent for MOF synthesis has attractive properties, like simultaneously dissolving organic and inorganic starting materials, greatly low volatility, and high thermal and chemical stability.^[174]

The design of MOF-based SCs using ILEs has not been sufficiently studied to date. Zhang et al. skilfully encapsulated ILs into polyoxometalate-based MOFs (POMOFs), to fabricate a series of conductivity-improved POMs-ILs@MOFs. Exclusively, the PMo₁₀V₂-ILs@MIL-100 achieved a noticeable capacity of 1248 mAh g⁻¹, even after 100 cycles. In addition, the charge capacity of PMo₁₀V₂-ILs@MIL-100 reduces slightly at 1032.8, 929.2, 774.7, 633.6, 503.8, and 347.5 mAh g⁻¹ with increased current density at 0.1, 0.2, 0.5, 1, 2, and 3 A g⁻¹ respectively.^[175] Similarly, Fujie et al. developed ionic liquid-based lithium electrolytes that are infused in the micropores of ZIF-8, a Zn-based MOF, to produce ionic conductors.^[176] Nowadays, high-performance energy storage devices are in need; SCs using ionic liquid-based electrolytes are slowly competing with other energy storage devices.

4.5. Redox-Active Electrolytes (RAEs)

A novel strategy has been developed to enhance the capacitance of SCs by influencing the pseudo capacitive supplement from the RAEs. RAEs are special electrolytes to which redox-active

materials have been added. This can significantly enhance the electrochemical performance of SCs for two reasons: first, the electrolyte additive is a vital part of the redox reactions of the SCs, and second, the electron transfer that occurs between the electrode material and the redox material in the electrolyte is due to the redox reactions in the electrolyte, which are conductive.^[177] The RAEs are made up of the addition of concentration of redox-active materials, like hydroquinone and halide ions, and $K_3[Fe(CN)_6]$ in commonly used AEs, like H_2SO_4 , Na_2SO_4 , and KOH. The RAEs encourage faster kinetics of redox reactions at the electrode surface, due to the presence of the redox-active materials.^[165,178]

Akinwolemiwa et al. reported the use of a redox additive (1 M Na_2SO_4 and 0.2 M $K_3[Fe(CN)_6]$) in conjunction with two of the same electrodes made up of a composite of ZIF-67/rGO.^[178] Ultrahigh specific capacitance of $326 F g^{-1}$ at current density of $3 A g^{-1}$ was achieved, and high energy density of $25.5 Wh kg^{-1}$ at power density of $2.7 kW kg^{-1}$.^[130] Similarly, Sundriyal et al. used 0.2 M $K_3[Fe(CN)_6]$ in 1 M Na_2SO_4 as a redox-active additive electrolyte in an SC whose electrode was assembled from an Mn-MOF. The device revealed high specific capacitance of $1590 F g^{-1}$ at current density of $3 A g^{-1}$ with capacitance retention of 82%, even after 3000 cycles.^[179] A RAE provides a wider potential window in SC applications than does AE. Likewise, several redox-active species or materials have still not been used as redox additives in electrolytes for SC applications.

As the data presented in this section shows, different electrolytes are being utilized to improve SCs; choosing a suitable electrolyte depends upon the needed performance and practical applications of electrochemical SCs by controlling the factors, like the ionic conductivity, ion mobility, operating voltage window, operating temperature range, and electrochemical and thermal stabilities of the electrolytes.^[180]

5. Performance Appraisal of MOF-Derived Electrodes in SCs

With increasing global and environmental concerns, plentiful work has been done to advance alternative energy technologies. In recent years, a widening interest in affordable, efficient, renewable, sustainable, and environment-friendly energy storage devices has been highly recognized. A SC is a renewable electrochemical energy storage device with high energy and power density, fast charge and recharge capability, and rate efficiency, due to its exceptional reaction mechanism.^[181,182] The evolution of MOF-based materials used as SCs in new, leading energy storage devices has attracted rapidly evolving importance, due to their adjustable pore size, controllable microporous structure, and large surface area. MOF materials are used for supercapacitive applications in three different ways, as the prepared MOFs material are used directly as an energetic electrode material for SCs.^[47–51] MOFs are used as a template to synthesize metal oxides.^[56–61] and porous carbon compounds^[70–75] for SCs. Finally, MOFs are hybridized using different functional materials to form MOF composites for SCs (Figure 13).^[183]

Table 2 summarizes several parameters of MOFs and their derived nanostructured electrodes, such as electrical density, energy density, specific capacitance, and life cycle, to compare

their electrochemical performance. However, the direct application of pristine MOFs as electrodes may not provide good electrical conductivity. The migration of electrons and ions is easy with high specific surface area and uniform pore size distribution of MOFs. If such MOFs are combined with AEs (e.g., H_2SO_4 and KOH), they could attain high specific capacitance of about (200–2800) $F g^{-1}$. Unlike the pristine MOFs, their derived structures (metal oxides and NPC) show remarkable electrical conductivity, while high specific surfaces can also be maintained.^[184] MOFs like Mn/Ni-MOFs, UPC-9, MOF-74, ZIF-8, and ZIF-67 are successfully converted into functional metal oxides, while NPC electrodes of AEs looks to be a more preferable choice than other kinds of electrolytes.

Similarly, Table 3 shows that MOFs may be conjugated with CPs, metal oxides/hydroxides, CNTs, graphene oxide (GO), and quantum dots (QD) for SC applications.^[185] In such a way, the resultant composites provide large surface areas, high chemical and thermal stabilities, notable specific capacitance, energy densities, and cyclic stability.^[186,187] MOFs (e.g., UIO-66, ZIF-67, Co-MOF, and Zn-MOF) have been interlinked with CPs (e.g., CT, PPy, PANI, and POAP), to integrate their discrete pseudocapacitive properties. As a result, MOF@CPs composite provides rapid kinetics between oxidation and reduction to give specific capacitances of about 200–550 $F g^{-1}$. Nevertheless, cyclic stability was sometimes inadequate, due to their participation in the Faradaic reactions.^[188] Hence, further research is required to optimize the specific capacitance and cyclic stability of the MOF@CP-based SCs. Likewise, MOFs and their derivatives (e.g., Ni-MOF, Co-MOF, and MHCF, ZIF-67) are also used to fabricate metal MOF@metal oxide/hydroxides, MOF@MOF, and MOF@metal electrodes, working on the principle of Faradaic reactions.^[119] Since these composites possess different porous morphologies in contrast with CPs and exhibit larger specific surface areas, they show pseudocapacitive charge transport and deliver specific capacitances of as high as 1500 $F g^{-1}$ with adequate cyclic stability. The SC electrode made from MOF@CP, MOFs@metal oxide/hydroxide, MOF@MOF, and MOF@metal governs the pseudocapacitive behavior. However, these composites suffer from issues, such as low energy and power densities with relatively short cycle lives. MOFs have been interlinked with various nanomaterials that permit the enlargement of electrode materials of the EDLC.^[189] In particular, MOFs can be nanocomposites with CNTs (SWCNTs and MWCNTs), graphene oxide, and quantum dots to achieve high specific capacitance and good energy density. Nanocomposites of MOFs containing CNT, graphene oxide, or quantum dots are usually determined by non-Faradaic reaction mechanisms; hence, they equally improve the whole stability and cycle life of the respective SC, compared to the composite of MOF with CP or metal oxide/hydroxides. So, when MOFs were combined with CNTs, most MOFs (e.g., ZIF-8, NiCo-MOF, and Ni(TA)) showed pseudocapacitive and EDLC properties; as a result, it was used to make electrodes with upgraded specific capacitances (e.g., of 200–2000 $F g^{-1}$). Generally, H_2SO_4 or KOH was preferably used as electrolyte.

Furthermore, MOF@GO and MOF@QD composites are superior materials in the research field of SCs. MOF@graphene and MOF@QD with large specific surface areas, uniform pore size distribution, and high electrical conductivities can drive

Table 2. MOF and their modified nanostructures as electrodes for SC.

Sr. No.	Electrode material	Specific surface area [$\text{m}^2 \text{g}^{-1}$]	Substrate used	Electrolyte	Scan rate/ Current density	Specific capacitance [F g^{-1}]	Cyclic stability [%]	Number of cycles	References
The Pristine MOFs									
1	Ni-MOF	–	–	2 M KOH	1 A·g ⁻¹	1518.8	95.5	10 000	[47]
2	Ni-MOF	117.42	Nickel foam	3 M KOH	1.4 A·g ⁻¹	988.0	96.5	5000	[48]
3	Mn-MOF	1.2352	Nickel mesh	3 M KOH	10 mV·s ⁻¹	270.0	–	–	[49]
4	Co-MOF	–	Nickel foam	2 M KOH	2 A·g ⁻¹	13.6	79.4	1000	[50]
5	NiCo-MOF	54.6	Nickel foam	2 M KOH	1 A·g ⁻¹	1202.1	89.5	5000	[51]
6	Co-MOF	2900	ITO coated glass	1 M LiOH	0.6 A·g ⁻¹	206.76	98.5	1000	[202]
7	Ni ₃ (HITP) ₂ MOF	–	Nickel foam	0.5 M Na ₂ SO ₄	0.1 mA·cm ⁻²	279.1	97	6500	[203]
8	Mn-BDC	202	Nickel foam	2 M KOH	1 A·g ⁻¹	567.5 mAh·g ⁻¹	92.3	5000	[204]
9	Ni-MOF	40.36	Carbon cloth	3 M KOH	1 A·g ⁻¹	1057	70	2500	[205]
MOF derived metal oxides									
1	Mn/Ni-MOFs derived porous MnNi ₂ O ₄	50.80	Nickel foam	6 M KOH	1 A·g ⁻¹	2848	93.25	5000	[56]
2	UPC-9 derived Co ₃ O ₄ nanosheets	101.7	Nickel foam	6 M KOH	1 A·g ⁻¹	1121	98.2	6.000	[57]
3	Ni-MOF derived NiO nanospheres	66.8	Nickel foam	3 M KOH	0.5 A·g ⁻¹	473	94	3000	[58]
4	Ni-Zn MOF derived NiO/ZnO hollow spheres	36.4	Nickel foam	3 M KOH	1.3 A·g ⁻¹	497	117.1	2000	[59]
5	ZIF8@ZIF-67 derived Co ₃ O ₄ /ZnO	–	Nickel foam	6 M KOH	0.5 A·g ⁻¹	415	93.2	1000	[60]
6	MOF-74 derived NiO, NiCo ₂ O ₄ , Co ₃ O ₄	59.6	Nickel foam	1 M KOH	0.5 A·g ⁻¹	684	89.0	3000	[61]
7	Ni-MOF derived NiO nanosheets	118.2	–	–	1 A·g ⁻¹	527.1	80.2	500	[206]
8	Co/Ni-MOF derived NiCo ₂ O ₄ nanoparticles	178.3	Nickel foam	6 M KOH	5 A·g ⁻¹	1315	90.7	10 000	[207]
9	Ce-BTC derived CeO ₂	77	Nickel foam	3 M KOH + 0.1 M K ₄ Fe(CN) ₆	0.2 A·g ⁻¹	502	–	5000	[208]
10	ZIF-67 derived hollow Co ₃ O ₄	128	Nickel foam	3 M KOH	1.25 A·g ⁻¹	1100	95.1	6000	[209]
MOF derived NPC									
1	ZIF-8@ZIF-67 derived NPC	1276	Graphite	1 M H ₂ SO ₄	2 A·g ⁻¹	270	64	10 000	[70]
2	HKUST-1 derived HPCF	620.1	–	6 M KOH	2 A·g ⁻¹	194.8	95	10 000	[71]
3	Cu-MOF derived APCs	1880.4	Nickel foam	6 M KOH	0.5 A·g ⁻¹	196	–	–	[72]
4	ZIF-8/PAN derived NPCF	314.7	Glassy carbon electrode	1 M H ₂ SO ₄	1 A·g ⁻¹	332	98.9	5000	[73]
5	ZIF-8/PAN derived HPCNFs-N	417.9	–	2 M H ₂ SO ₄	1 A·g ⁻¹	307.2	98.2	10 000	[74]
6	ZIF-11 derived N-PCMPs	2188	Glassy carbon electrode	1 M H ₂ SO ₄	1 A·g ⁻¹	307	90	4000	[75]
7	Ni/Co-MOF derived NPC	1135	Nickel foam	2 M KOH	1 A·g ⁻¹	1214	98.8	6000	[210]
8	MOF-5 derived NPC	1515	–	6 M KOH	0.05 A·g ⁻¹	212	95.9	1000	[211]
9	ZIF-69 derived NPC	2263	Glassy carbon electrode	0.5 M H ₂ SO ₄	5 mV·s ⁻¹	168	–	–	[212]
10	N-doped ZIF-8 derived NPC	1630	–	6 M KOH	0.1 A·g ⁻¹	285.8	72.8	1000	[213]

remarkable electrochemical properties. In addition, MOFs and their derived structures (e.g., Cu-MOF, Ni-doped ZIF-67,

Ni-Co-MOF, SnO₂ quantum dots@ZIF-8, and SnO_x quantum dots@Zr-MOFs) seem to be interlinked with graphene oxide

Table 3. Summary of MOF composites as electrode materials for SC applications.

Sr. No.	Electrode material	Electrolyte	Substrate used	Scan rate/ Current density	Specific capacitance	Energy density	Cyclic stability [%]	Number of cycles	References
MOF@metal oxides/hydroxides									
1	Ni-MOF/NiO	3 M KOH	Nickel foam	1 mA·cm ⁻²	1853 C·cm ⁻²	39.2 Wh·kg ⁻¹	94	3000	[94]
2	Co-MOF/Co ₃ O ₄	3 M KOH	Nickel foam	0.5 A·g ⁻¹	1020 F·g ⁻¹	21.6 mWh·cm ⁻³	96.7	5000	[95]
3	MHCF/ MnOx	1 M Na ₂ SO ₄	Pt-coated polyethylene terephthalate	0.5 mA·cm ⁻²	175 mF·cm ⁻²	210 Wh kg ⁻¹	94.5	10 000	[96]
4	NiC ₂ O ₄ /ZIF-67	6 M KOH	Nickel foam	5 mV·s ⁻¹	1019.7 F·g ⁻¹	–	73	2000	[214]
5	Cu-MOF/ δ -MnO ₂	1 M Na ₂ SO ₄		1 A·g ⁻¹	667 F·g ⁻¹	–	95	6000	[215]
MOF@CPs									
1	PPy/UIO-66/CT	1 M H ₂ SO ₄	Cotton fiber	0.8 mA·cm ⁻²	565 F·g ⁻¹	38.2 Wh kg ⁻¹	90	500	[100]
2	CFs/UIO-66/PPY	3 M KCl	Cotton fiber	5 mV·s ⁻¹	206 mF·cm ⁻²	12.8 μ Wh·cm ⁻²	96	1200	[101]
3	ZIF-67/PANI	3 M KCl	Carbon cloth	10 mV·s ⁻¹	2146 mF·cm ⁻²	0.0161 mWh·cm ⁻³	80	2000	[102]
4	Cu-bipy-BTC/POAP	0.1 M HClO ₄	–	1 mA·cm ⁻²	422 F·g ⁻¹	–	93	1000	[103]
5	Co-MOF/PANI	1 M KOH	Nickel foil	1 A·g ⁻¹	504 F·g ⁻¹	–	90	5000	[104]
6	Zn-MOF/PANI	1 M H ₂ SO ₄	Titanium mesh	1 A·g ⁻¹	477 F·g ⁻¹	–	≈ 90	100	[216]
MOF@MOF									
1	Ni-MOF-24/Cu-MOF	1 M KOH	carbon fiber paper	2 A·cm ⁻²	1424 F·g ⁻¹	57 Wh·kg ⁻¹	94.3	7000	[112]
2	ZIF-67/ZIF	6 M KOH	Nickel foam	1 A·g ⁻¹	1176.8 F·g ⁻¹	23.4 Wh·kg ⁻¹	98	1000	[113]
3	ZIF-L(Zn)/ZIF-67	2 M KOH	Graphite	2 A·g ⁻¹	2,52.1 F·g ⁻¹	–	91.2	10 000	[114]
4	ZIF-8@ZIF-67	1 M H ₂ SO ₄	Cosmetic cotton	1 A·g ⁻¹	386.6	30 Wh·kg ⁻¹	89.5	5000	[217]
MOF@CNT nanocomposites									
1	ZIF-8/MWCNTs	1 M H ₂ SO ₄	Carbon cloth	0.5 A·g ⁻¹	259.2 F·g ⁻¹	–	92	5000	[121]
2	NiCo-MOF/MWCNT	2 M KOH	Nickel foam	0.5 A·g ⁻¹	1010 F·g ⁻¹	19.7 Wh·kg ⁻¹	100	3000	[122]
3	Ni-MOF/CNTs	6 M KOH	Nickel foam	0.5 A·g ⁻¹	1765 F·g ⁻¹	36.6 Wh·kg ⁻¹	95	5000	[123]
4	Ni(TA)/MWCNTs	2 M KOH	Nickel foam	2 A·g ⁻¹	115 mA h g ⁻¹	–	81.56	5000	[124]
5	Cu-MOF@CNT	1 M Na ₂ SO ₄	Glassy carbon electrode	1.6 A·g ⁻¹	380 F·g ⁻¹	–	63.63	4000	[218]
MOF@GO nanocomposites									
1	Cu-MOF/grapheme	6 M KOH	Nickel foam	10 mV·s ⁻¹	482 F·g ⁻¹	34.5 Wh·kg ⁻¹	93.8	1000	[127]
2	Ni-doped ZIF-67/rGO	1 M H ₂ SO ₄	Carbon paper	1 A·g ⁻¹	304 F·g ⁻¹	21.5 Wh·kg ⁻¹	99	1000	[128]
3	Ni-Co-MOF/GO	6 M KOH	Nickel foam	1 A·g ⁻¹	447.2 F·g ⁻¹	–	99.6	300	[129]
4	ZIF-67/rGO	0.2 M K ₃ [Fe(CN) ₆] in 1 M Na ₂ SO ₄	Graphite	4.5 A·g ⁻¹	1453 F·g ⁻¹	25.5 Wh·kg ⁻¹	90.5	1000	[130]
5	Ni/Co-MOF/rGO	6 M KOH	Nickel foam	1 A·g ⁻¹	860 F·g ⁻¹	72.8 Wh·kg ⁻¹	91.6	6000	[219]
MOF@metal									
1	Mo-doped Ni-MOF	3 M KOH	Nickel foam	1 A·g ⁻¹	802 C·g ⁻¹	59 Wh·kg ⁻¹	92.9	20 000	[131]
2	Zn-doped Ni-MOF	6 M KOH	Stainless steel mesh	0.25 A·g ⁻¹	1620 F·g ⁻¹	27.56 Wh·kg ⁻¹	91	3000	[79]
3	Mn-doped Ni-MOF	6 M KOH	Nickel foam	2 mA·cm ⁻²	1178 C·g ⁻¹	39.6 Wh·kg ⁻¹	80.6	5000	[132]
4	Ni@Cu-MOF	6 M KOH	Nickel foam	1 A·g ⁻¹	48.7 F·g ⁻¹	17.3 Wh·kg ⁻¹	80	1200	[133]
5	Co-doped Ni-based MOF	6 M KOH	Nickel foam	1 A·g ⁻¹	1300 F·g ⁻¹	25.92 Wh·kg ⁻¹	71	3000	[220]
MOF@QD									
1	SnO ₂ quantum dots@ZIF-8	6 M KOH	Nickel foam	5 mV·s ⁻¹	931 F·g ⁻¹	–	–	500	[135]
2	SnOx quantum dots @Zr-MOFs (UIO-66)	1 M LiPF ₆	Copper foil	50 mA·g ⁻¹	2196 mAh·g ⁻¹	–	–	100	[136]
3	ZIF-8 derived Carbon/GQDs	6 M KOH	Nickel foam	2 A·g ⁻¹	130 F·g ⁻¹	493 mAh·g ⁻¹	96.9	10 000	[137]

sheets to accomplish high specific capacitances in the range of 300–1400 F g⁻¹ (Table 3). In addition to carrying high-level specific capacitances, MOF@GO and MOF@QD composites also ensure better cyclic stability and upgraded energy density values (e.g., ZIF-8-derived Carbon/GQDs = 493 mAhg⁻¹), compared to other classes of MOF composites.

6. Conclusion and Future Outlook

In summary, the pristine MOFs, including their derivatives and composites, have been significantly explored as SC electrodes because of their structural diversity, tunable pore features, and high electronic properties. This minioverview presents recent progress in designing and synthesizing the pristine MOFs and their derivatives and MOF-based composites for SC applications. In particular, MOF-derived metal oxides, NPC materials, and MOF-based composites with metal oxide/hydroxides, CPs, CNTs, quantum dots, and graphene have been highlighted. In addition, we have discussed essential aspects related to the electrolytes, such as aqueous, organic, and RAE, and their selection with MOF-based materials.

Despite advances in the research into SCs using MOF-based electrode materials, their practical application remains a challenge. We have outlined several challenges and perspectives, as follows.

The present MOFs are largely concerned with 2D structures. Nonetheless, the electrochemical performances of MOFs including energy density and power density are limited by their limited theoretical surface area and 1D-like channel for ion swapping. This constraint can be solved by creating 3D MOFs with large surface area and plentiful channels that allow ion transport in both directions, resulting in efficient cation–anion swapping. As a result, greater research into the structural design of MOFs with 3D frameworks is required.

The pristine MOFs' low electrical conductivity, poor crystallinity, lack of structural flaws and crystalline boundaries, and mediocre specific surface area remain significant hurdles. Combining MOFs with other conductive and dependable electrochemical materials helps overcome these hurdles. Mixed metal or bimetal MOFs are an excellent choice for improving the aforementioned properties. Combining larger surface area with more conductive and synergistic effects from selected chemicals yields more desired SC outcomes.

More research into new MOF materials with novel structures, compositions, and electrical conductivities is required. Pre-/postmodification techniques to MOFs and structural optimization are critical for developing micro-/nanoscale materials with controllable structures. As a result, future avenues that must be pursued include upgrading existing synthetic processes to create improved synthetic strategies for manufacturing diverse MOF derivatives.

In several research reports, MOFs have been used as a cathode for SC applications; however, the search for an anode based on MOFs has mostly been restricted to NPC materials. Therefore, researchers might focus their efforts in this field to fabricate innovative negative electrodes for SCs based on 3D MOFs that have improved electrochemical performance over those made of conventional carbon materials.

Future energy storage devices must optimize and improve the electrochemical charge storage efficiencies of MOF-based materials for practical applications. Prior to investigating the optimized link between structure, element composition, coordination environment of metals, and electrochemical performance, it is important to identify the significant aspects that contribute to performance decline. Therefore, it is possible to investigate the energy storage mechanism and structural development during electrochemical testing using in situ/operando methods, DFT calculations, and MD simulations. Second, the development of effective strategies that could provide oxygen vacancy, surface functionalization, crystal phase variation, stress engineering, heterostructured interconnected morphologies, and high electrochemical activity are crucial factors to boost the electronic properties and surface properties of the electrodes. Finally, to improve the total charge storage capabilities of SCs, optimum electrode preparation, electrochemical experiments, testing settings, and electrolyte selection are all essential elements.

The use of MOF-based materials and the development of improved SC technologies are crucial. Despite the numerous challenges, the achievements to date are encouraging, and the contents of this minireview are only a small indication of the research required to properly comprehend and fully exploit the pristine MOFs, MOF-derived functional materials, and MOF-based composites. With consistent research contributions and technical innovation, we should have a good possibility of witnessing the revolution of new EESC technologies in the near future, as well as realising further applications of MOF-based materials in the sectors of renewable energy and environmental science.

Acknowledgements

The authors are thankful to UGC-SAP, DST-FIST, and DST-PURSE programmes for support to instrument facilities at the Department of Chemistry, Shivaji University, Kolhapur. One of the authors R.B. is thankful to SARTHI, Government of Maharashtra, India for the 'Chhatrapati Shahu Maharaj National Research Fellowship-2021'. This work was partially supported by the National Research Foundation of Korea (NRF) grant funded by the Korea government (MSIT, grant No. 2020H1D3A1A04081472).

Conflict of Interest

The authors declare no conflict of interest.

Keywords

composites, electrolytes, metal–organic frameworks, nanomaterials, supercapacitors

Received: February 14, 2023

Revised: May 3, 2023

Published online: July 8, 2023

[1] K. B. Wang, Q. Xun, Q. Zhang, *EnergyChem* **2020**, *2*, 100025.

[2] C. Zhu, Y. He, Y. Liu, N. Kazantseva, P. Saha, Q. Cheng, *J. Energy Chem.* **2019**, *35*, 124.

- [3] Y. N. Liu, L. N. Jin, H. T. Wang, X. H. Kang, S. W. Bian, *J. Colloid Interface Sci.* **2018**, *530*, 29.
- [4] P. E. Lokhande, S. Kulkarni, S. Chakrabarti, H. M. Pathan, M. Sindhu, D. Kumar, J. Singh, A. Kumar, Y. Kumar Mishra, D. C. Toncu, M. Syväjärvi, A. Sharma, A. Tiwari, *Coord. Chem. Rev.* **2022**, *473*, 214771.
- [5] M. Pumera, *Energy Environ. Sci.* **2011**, *4*, 668.
- [6] I. Hussain, C. Lamiel, M. Sufyan Javed, M. Ahmad, X. Chen, S. Sahoo, X. Ma, M. A. Bajaber, M. Zahid Ansari, K. Zhang, *Chem. Eng. J.* **2023**, *454*, 140313.
- [7] D. Larcher, J. M. Tarascon, *Nat. Chem.* **2015**, *7*, 19.
- [8] P. He, Q. Chen, M. Yan, X. Xu, L. Zhou, L. Mai, C. W. Nan, *EnergyChem* **2019**, *1*, 1000222.
- [9] J. Xie, P. Gu, Q. Zhang, *ACS Energy Lett.* **2017**, *2*, 1985.
- [10] Y. Zhai, Y. Dou, D. Zhao, P. F. Fulvio, R. T. Mayes, S. Dai, *Adv. Mater.* **2011**, *23*, 4828.
- [11] G. Liu, Y. Sheng, J. W. Ager, M. Kraft, R. Xu, *EnergyChem* **2019**, *1*, 100014.
- [12] M. S. Javed, A. Mateen, I. Hussain, S. Ali, S. Asim, A. Ahmad, E. tag Eldin, M. A. Bajaber, T. Najam, W. Han, *Chem. Eng. J.* **2023**, *452*, 139455.
- [13] G. A. Tafete, M. K. Abera, G. Thothadri, *J. Energy Storage* **2022**, *48*, 103938.
- [14] Y. Wang, Y. Song, Y. Xia, *Chem. Soc. Rev.* **2016**, *45*, 5925.
- [15] Q. Abbas, A. Mateen, S. H. Siyal, N. U. Hassan, A. A. Alothman, M. Ouladmane, S. M. Eldin, M. Z. Ansari, M. S. Javed, *Chemosphere* **2023**, *313*, 137421.
- [16] Z. Y. Sui, P. Y. Zhang, M. Y. Xu, Y. W. Liu, Z. X. Wei, B. H. Han, *ACS Appl. Mater. Interfaces* **2017**, *9*, 43171.
- [17] W. Raza, F. Ali, N. Raza, Y. Luo, K. H. Kim, J. Yang, S. Kumar, A. Mehmood, E. E. Kwon, *Nano Energy* **2018**, *52*, 441.
- [18] A. Mateen, M. S. Javed, S. Khan, A. Saleem, M. K. Majeed, A. J. Khan, M. F. Tahir, M. A. Ahmad, M. A. Assiri, K. Q. Peng, *J. Energy Storage* **2022**, *49*, 104150.
- [19] R. R. Salunkhe, Y. V. Kaneti, J. Kim, J. H. Kim, Y. Yamauchi, *Acc. Chem. Res.* **2016**, *49*, 2796.
- [20] M. Zheng, X. Xiao, L. Li, P. Gu, X. Dai, H. Tang, Q. Hu, H. Xue, H. Pang, *Sci. China Mater.* **2018**, *61*, 185.
- [21] T. Wang, S. Zhang, H. Wang, *Sci. China Mater.* **2018**, *61*, 296.
- [22] G. Yu, X. Xie, L. Pan, Z. Bao, Y. Cui, *Nano Energy* **2013**, *2*, 213.
- [23] R. S. Kate, S. A. Khalate, R. J. Deokate, *J. Alloys Compd.* **2018**, *734*, 89.
- [24] Y. Zhang, H. Feng, X. Wu, L. Wang, A. Zhang, T. Xia, H. Dong, X. Li, L. Zhang, *Int. J. Hydrogen Energy* **2009**, *34*, 4889.
- [25] Y. Wang, F. Xu, L. Sun, S. Fang, J. Lao, C. Zhang, S. Wei, L. Liao, Y. Guan, Y. Xia, Y. Luo, Y. Sun, Y. Zou, Z. Yu, Q. Shao, Y. Zhu, Y. Luo, *J. Energy Storage* **2023**, *58*, 106395.
- [26] M. Li, X. Jiang, J. Liu, Q. Liu, N. Lv, N. Qi, Z. Chen, *J. Alloys Compd.* **2023**, *930*, 167354.
- [27] H. B. Wu, X. W. Lou, *Sci. Adv.* **2017**, *3*, 9252.
- [28] X. F. Lu, Y. Fang, D. Luan, X. W. D. Lou, *Nano Lett.* **2021**, *21*, 1555.
- [29] H. C. J. Zhou, S. Kitagawa, *Chem. Soc. Rev.* **2014**, *43*, 5415.
- [30] P. Y. Liu, J. J. Zhao, Z. P. Dong, Z. L. Liu, Y. Q. Wang, *J. Alloys Compd.* **2021**, *854*, 157181.
- [31] F. Zhan, H. Wang, Q. He, W. Xu, J. Chen, X. Ren, H. Wang, S. Liu, M. Han, Y. Yamauchi, L. Chen, *Chem. Sci.* **2022**, *13*, 11981.
- [32] G. G. Amatucci, F. Badway, A. Du Pasquier, T. Zheng, *J. Electrochem. Soc.* **2001**, *148*, A930.
- [33] Z. Chen, V. Augustyn, X. Jia, Q. Xiao, B. Dunn, Y. Lu, *ACS Nano* **2012**, *6*, 4319.
- [34] S. Komaba, T. Hasegawa, M. Dahbi, K. Kubota, *Electrochem. Commun.* **2015**, *60*, 172.
- [35] H. Wang, M. Wang, Y. Tang, *Energy Storage Mater.* **2018**, *13*, 1.
- [36] J. Liang, D. W. Wang, *Adv. Energy Mater.* **2022**, *12*, 2200920.
- [37] H. Zhang, J. Nai, L. Yu, X. W. (David) Lou, *Joule* **2017**, *1*, 77.
- [38] H. Wang, Q. L. Zhu, R. Zou, Q. Xu, *Chem* **2017**, *2*, 52.
- [39] Z. Liang, C. Qu, D. Xia, R. Zou, Q. Xu, *Angew. Chem. Int. Ed.* **2018**, *57*, 9604.
- [40] J. Yu, X. Gao, Z. Cui, Y. Jiao, Q. Zhang, H. Ding, L. Yu, L. Dong, *Energy Technol.* **2019**, *7*, 1900018.
- [41] T. Qiu, Z. Liang, W. Guo, H. Tabassum, S. Gao, R. Zou, *ACS Energy Lett.* **2020**, *5*, 520.
- [42] D. Sheberla, J. C. Bachman, J. S. Elias, C. J. Sun, Y. Shao-Horn, M. Dincă, *Nat. Mater.* **2017**, *16*, 220.
- [43] N. Sahiner, S. Demirci, M. Yildiz, *J. Electron. Mater.* **2017**, *46*, 790.
- [44] F. Wang, S. Xiao, Y. Hou, C. Hu, L. Liu, Y. Wu, *RSC Adv.* **2013**, *3*, 13059.
- [45] Y. Tan, W. Zhang, Y. Gao, J. Wu, B. Tang, *RSC Adv.* **2015**, *5*, 17601.
- [46] R. Bhosale, S. Bhosale, P. Kumbhar, D. Narale, R. Ghaware, C. Jambhale, S. Kolekar, *New J. Chem.* **2023**, *47*, 6749.
- [47] C. Yang, X. Li, L. Yu, X. Liu, J. Yang, M. Wei, *Chem. Commun.* **2020**, *56*, 1803.
- [48] Y. Yan, P. Gu, S. Zheng, M. Zheng, H. Pang, H. Xue, *J. Mater. Chem. A* **2016**, *4*, 19078.
- [49] G. Krishnamurthy, B. M. Omkaramurthy, *Indian J. Adv. Chem. Sci.* **2019**, *7*, 12.
- [50] G. Zhu, H. Wen, M. Ma, W. Wang, L. Yang, L. Wang, X. Shi, X. Cheng, X. Sun, Y. Yao, *Chem. Commun.* **2018**, *54*, 10499.
- [51] Y. Wang, Y. Liu, H. Wang, W. Liu, Y. Li, J. Zhang, H. Hou, J. Yang, *ACS Appl. Energy Mater.* **2019**, *2*, 2063.
- [52] F. Bigdeli, C. T. Lollar, A. Morsali, H. C. Zhou, *Angew. Chem. Int. Ed.* **2020**, *59*, 4652.
- [53] Y. Li, Y. Xu, W. Yang, W. Shen, H. Xue, H. Pang, *Small* **2018**, *14*, 1.
- [54] J. Li, D. Yan, S. Hou, T. Lu, Y. Yao, D. H. C. Chua, L. Pan, *Chem. Eng. J.* **2018**, *335*, 579.
- [55] Z. Zhang, Y. Huang, S. Bai, *Mater. Sci. Forum* **2017**, *890*, 68.
- [56] M. Lan, X. Wang, R. Zhao, M. Dong, L. Fang, L. Wang, *J. Alloys Compd.* **2020**, *821*, 153546.
- [57] Z. Xiao, L. Fan, B. Xu, S. Zhang, W. Kang, Z. Kang, H. Lin, X. Liu, S. Zhang, D. Sun, *ACS Appl. Mater. Interfaces* **2017**, *9*, 41827.
- [58] M. K. Wu, C. Chen, J. J. Zhou, F. Y. Yi, K. Tao, L. Han, *J. Alloys Compd.* **2018**, *734*, 1.
- [59] G. C. Li, P. F. Liu, R. Liu, M. Liu, K. Tao, S. R. Zhu, M. K. Wu, F. Y. Yi, L. Han, *Dalt. Trans.* **2016**, *45*, 13311.
- [60] J. Xu, S. Liu, Y. Liu, *RSC Adv.* **2016**, *6*, 52137.
- [61] G. Liuting, X. U. Miao, M. A. Renping, H. A. N. Yingping, X. U. Hongbo, S. H. I. Gang, *Sci. China Technol. Sci.* **2020**.
- [62] M. Zhong, E. K. Kim, J. P. McGann, S. E. Chun, J. F. Whitacre, M. Jaroniec, K. Matyjaszewski, T. Kowalewski, *J. Am. Chem. Soc.* **2012**, *134*, 14846.
- [63] Z. Lei, D. Bai, X. S. Zhao, *Microporous Mesoporous Mater.* **2012**, *147*, 86.
- [64] H. Zhu, J. Yin, X. Wang, H. Wang, X. Yang, *Adv. Funct. Mater.* **2013**, *23*, 1305.
- [65] R. R. Salunkhe, Y. Kamachi, N. L. Torad, S. M. Hwang, Z. Sun, S. X. Dou, J. H. Kim, Y. Yamauchi, *J. Mater. Chem. A* **2014**, *2*, 19848.
- [66] T. Wang, J. Tang, X. Fan, J. Zhou, H. Xue, H. Guo, J. He, *Nanoscale* **2014**, *6*, 5359.
- [67] M. Sevilla, A. B. Fuertes, *Carbon NY* **2006**, *44*, 468.
- [68] Z. Chen, Y. Qin, D. Weng, Q. Xiao, Y. Peng, X. Wang, H. Li, F. Wei, Y. Lu, *Adv. Funct. Mater.* **2009**, *19*, 3420.
- [69] J. Ren, Y. Huang, H. Zhu, B. Zhang, H. Zhu, S. Shen, G. Tan, F. Wu, H. He, S. Lan, X. Xia, Q. Liu, *Carbon Energy* **2020**, *2*, 176.
- [70] J. Tang, R. R. Salunkhe, J. Liu, N. L. Torad, M. Imura, S. F. Furukawa, Y. Yamauchi, *J. Am. Chem. Soc.* **2015**, *137*, 1572.
- [71] Y. Liu, G. Li, Y. Guo, Y. Ying, X. Peng, *ACS Appl. Mater. Interfaces* **2017**, *9*, 14043.
- [72] H. H. Duan, C. H. Bai, J. Y. Li, Y. Yang, B. L. Yang, X. F. Gou, M. L. Yue, Z. X. Li, *Inorg. Chem.* **2019**, *58*, 2856.

- [73] C. Wang, C. Liu, J. Li, X. Sun, J. Shen, W. Han, L. Wang, *Chem. Commun.* **2017**, 53, 1751.
- [74] L. F. Chen, Y. Lu, L. Yu, X. W. Lou, *Energy Environ. Sci.* **2017**, 10, 1777.
- [75] F. Hao, L. Li, X. Zhang, J. Chen, *Mater. Res. Bull.* **2015**, 66, 88.
- [76] S. H. Kazemi, B. Hosseinzadeh, H. Kazemi, M. A. Kiani, S. Hajati, *ACS Appl. Mater. Interfaces* **2018**, 10, 23063.
- [77] X. Xu, J. Tang, H. Qian, S. Hou, Y. Bando, M. S. A. Hossain, L. Pan, Y. Yamauchi, *ACS Appl. Mater. Interfaces* **2017**, 9, 38737.
- [78] A. Mahmood, R. Zou, Q. Wang, W. Xia, H. Tabassum, B. Qiu, R. Zhao, *ACS Appl. Mater. Interfaces* **2016**, 8, 2148.
- [79] J. Yang, C. Zheng, P. Xiong, Y. Li, M. Wei, *J. Mater. Chem. A* **2014**, 2, 19005.
- [80] N. Campagnol, R. Romero-Vara, W. Deleu, L. Stappers, K. Binnemans, D. E. De Vos, J. Fransaer, *ChemElectroChem* **2014**, 1, 1182.
- [81] D. Y. Lee, D. V. Shinde, E. K. Kim, W. Lee, I. W. Oh, N. K. Shrestha, J. K. Lee, S. H. Han, *Microporous Mesoporous Mater.* **2013**, 171, 53.
- [82] H. Wang, N. Zhang, S. Li, Q. Ke, Z. Li, M. Zhou, *J. Semicond.* **2020**, 41, 091707.
- [83] F. Boorboor Ajdari, E. Kowsari, M. Niknam Shahrak, A. Ehsani, Z. Kiaei, H. Torkzaban, M. Ershadi, S. Kholghi Eshkalak, V. Haddadi-Asl, A. Chinnappan, S. Ramakrishna, *Coord. Chem. Rev.* **2020**, 422, 213441.
- [84] S. Li, H. Chai, L. Zhang, Y. Xu, Y. Jiao, J. Chen, *J. Colloid Interface Sci.* **2023**, 642, 235.
- [85] S. Sundriyal, H. Kaur, S. K. Bhardwaj, S. Mishra, K. H. Kim, A. Deep, *Coord. Chem. Rev.* **2018**, 369, 15.
- [86] J. Jiang, Y. Li, J. Liu, X. Huang, C. Yuan, X. W. Lou, *Adv. Mater.* **2012**, 24, 5166.
- [87] L. F. Chen, Z. Y. Yu, J. J. Wang, Q. X. Li, Z. Q. Tan, Y. W. Zhu, S. H. Yu, *Nano Energy* **2015**, 11, 119.
- [88] T. Zhai, L. Wan, S. Sun, Q. Chen, J. Sun, Q. Xia, H. Xia, *Adv. Mater.* **2017**, 29, 1604167.
- [89] B. Li, P. Gu, Y. Feng, G. Zhang, K. Huang, H. Xue, H. Pang, *Adv. Funct. Mater.* **2017**, 27, 1605784.
- [90] F. Grote, Z. Y. Yu, J. L. Wang, S. H. Yu, Y. Lei, *Small* **2015**, 11, 4666.
- [91] Q. Liao, N. Li, S. Jin, G. Yang, C. Wang, *ACS Nano* **2015**, 9, 5310.
- [92] W. Zhan, Q. Kuang, J. Zhou, X. Kong, Z. Xie, L. Zheng, *J. Am. Chem. Soc.* **2013**, 135, 1926.
- [93] Q. L. Zhu, Q. Xu, *Chem. Soc. Rev.* **2014**, 43, 5468.
- [94] S. Xiong, S. Jiang, J. Wang, H. Lin, M. Lin, S. Weng, S. Liu, Y. Jiao, Y. Xu, J. Chen, *Electrochim. Acta* **2020**, 340, 135956.
- [95] S. Zheng, Q. Li, H. Xue, H. Pang, Q. Xu, *Natl. Sci. Rev.* **2020**, 7, 305.
- [96] Y. Z. Zhang, T. Cheng, Y. Wang, W. Y. Lai, H. Pang, W. Huang, *Adv. Mater.* **2016**, 28, 5242.
- [97] D. Fu, H. Zhou, X. M. Zhang, G. Han, Y. Chang, H. Li, *ChemistrySelect* **2016**, 1, 285.
- [98] Q. Meng, K. Cai, Y. Chen, L. Chen, *Nano Energy* **2017**, 36, 268.
- [99] L. Pan, H. Qiu, C. Dou, Y. Li, L. Pu, J. Xu, Y. Shi, *Int. J. Mol. Sci.* **2010**, 11, 2636.
- [100] C. Zhang, J. Tian, W. Rao, B. Guo, L. Fan, W. Xu, J. Xu, *Cellulose* **2019**, 26, 3387.
- [101] K. Qi, R. Hou, S. Zaman, Y. Qiu, B. Y. Xia, H. Duan, *ACS Appl. Mater. Interfaces* **2018**, 10, 18021.
- [102] L. Wang, X. Feng, L. Ren, Q. Piao, J. Zhong, Y. Wang, H. Li, Y. Chen, B. Wang, *J. Am. Chem. Soc.* **2015**, 137, 4920.
- [103] A. Ehsani, J. Khodayari, M. Hadi, H. M. Shiri, H. Mostaanzadeh, *Ionic* **2017**, 23, 131.
- [104] R. Srinivasan, E. Elaiyappillai, E. J. Nixon, I. Sharmila Lydia, P. M. Johnson, *Inorganica Chim. Acta* **2020**, 502, 119393.
- [105] C. Liu, J. Wang, J. Wan, C. Yu, *Coord. Chem. Rev.* **2021**, 432, 213743.
- [106] A. Q. Wu, W. Q. Wang, H. Bin Zhan, L. A. Cao, X. L. Ye, J. J. Zheng, P. N. Kumar, K. Chiranjeevulu, W. H. Deng, G. E. Wang, M. S. Yao, G. Xu, *Nano Res.* **2021**, 14, 438.
- [107] Y. Gu, Y. N. Wu, L. Li, W. Chen, F. Li, S. Kitagawa, *Angew. Chem. Int. Ed.* **2017**, 56, 15658.
- [108] H. Ji, S. Lee, J. Park, T. Kim, S. Choi, M. Oh, *Inorg. Chem.* **2018**, 57, 9048.
- [109] X. Yang, S. Yuan, L. Zou, H. Drake, Y. Zhang, J. Qin, A. Alsalme, H. C. Zhou, *Angew. Chemie - Int. Ed.* **2018**, 57, 3927.
- [110] L. Zhang, J. Wang, X. Ren, W. Zhang, T. Zhang, X. Liu, T. Du, T. Li, J. Wang, *J. Mater. Chem. A* **2018**, 6, 21029.
- [111] P. Falcaro, K. Okada, T. Hara, K. Ikgaki, Y. Tokudome, A. W. Thornton, A. J. Hill, T. Williams, C. Doonan, M. Takahashi, *Nat. Mater.* **2017**, 16, 342.
- [112] T. Deng, X. Shi, W. Zhang, Z. Wang, W. Zheng, *iScience* **2020**, 23, 101220.
- [113] C. Hu, J. Xu, Y. Wang, M. Wei, Z. Lu, C. Cao, *J. Mater. Sci.* **2020**, 55, 16360.
- [114] J. Zhang, Y. Wang, K. Xiao, S. Cheng, T. Zhang, G. Qian, Q. Zhang, Y. Feng, *New J. Chem.* **2018**, 42, 6719.
- [115] C. H. Shen, C. H. Chuang, Y. J. Gu, W. H. Ho, Y. Da Song, Y. C. Chen, Y. C. Wang, C. W. Kung, *ACS Appl. Mater. Interfaces* **2021**, 13, 16418.
- [116] F. Cao, M. Gan, L. Ma, X. Li, F. Yan, M. Ye, Y. Zhai, Y. Zhou, *Synth. Met.* **2017**, 234, 154.
- [117] J. M. Schnorr, T. M. Swager, *Chem. Mater.* **2011**, 23, 646.
- [118] K. E. Gregorczyk, A. C. Kozen, X. Chen, M. A. Schroeder, M. Noked, A. Cao, L. Hu, G. W. Rubloff, *ACS Nano* **2015**, 9, 464.
- [119] Y. Zhang, B. Lin, Y. Sun, X. Zhang, H. Yang, J. Wang, *RSC Adv.* **2015**, 5, 58100.
- [120] S. Sun, Y. Wang, L. Chen, M. Chu, Y. Dong, D. Liu, P. Liu, D. Qu, J. Duan, X. Li, *Colloids Surf. A Physicochem. Eng. Asp.* **2022**, 643, 128727.
- [121] D. Zhang, J. Zhang, M. Pan, Y. Wang, T. Sun, *J. Alloys Compd.* **2021**, 853, 157368.
- [122] X. Wang, N. Yang, Q. Li, F. He, Y. Yang, B. Wu, J. Chu, A. Zhou, S. Xiong, *J. Solid State Chem.* **2019**, 277, 575.
- [123] P. Wen, P. Gong, J. Sun, J. Wang, S. Yang, *J. Mater. Chem. A* **2015**, 3, 13874.
- [124] Q. Wang, Q. Wang, B. Xu, F. Gao, F. Gao, C. Zhao, *Electrochim. Acta* **2018**, 281, 69.
- [125] M. Saraf, R. Rajak, S. M. Mobin, *J. Mater. Chem. A* **2016**, 4, 16432.
- [126] P. Srimuk, S. Luanwuthi, A. Krittayavathananon, M. Sawangphruk, *Electrochim. Acta* **2015**, 157, 69.
- [127] M. Azadfalah, A. Sedghi, H. Hosseini, *J. Electron. Mater.* **2019**, 48, 7011.
- [128] S. Sundriyal, V. Shrivastav, S. Mishra, A. Deep, *Int. J. Hydrogen Energy* **2020**, 45, 30859.
- [129] J. Hong, S. J. Park, S. Kim, *Electrochim. Acta* **2019**, 311, 62.
- [130] S. Sundriyal, V. Shrivastav, H. Kaur, S. Mishra, A. Deep, *ACS Omega* **2018**, 3, 17348.
- [131] Q. Li, H. Guo, R. Xue, M. Wang, M. Xu, W. Yang, J. Zhang, W. Yang, *Int. J. Hydrogen Energy* **2020**, 45, 20820.
- [132] D. Zheng, H. Wen, X. Sun, X. Guan, J. Zhang, W. Tian, H. Feng, H. Wang, Y. Yao, *Chem.* **2020**, 26, 17149.
- [133] Y. Wang, S. Nie, Y. Liu, W. Yan, S. Lin, G. Cheng, H. Yang, J. Luo, *Polymers* **2019**, 11, 821.
- [134] Y. Xue, S. Zheng, H. Xue, H. Pang, *J. Mater. Chem. A* **2019**, 7, 7301.
- [135] Y. Gao, J. Wu, W. Zhang, Y. Tan, J. Zhao, B. Tang, *Mater. Lett.* **2014**, 128, 208.
- [136] W. Li, Z. Li, F. Yang, X. Fang, B. Tang, *ACS Appl. Mater. Interfaces* **2017**, 9, 35030.
- [137] H. Yu, W. Zhu, H. Zhou, J. Liu, Z. Yang, X. Hu, A. Yuan, *RSC Adv.* **2019**, 9, 9577.

- [138] L. Xia, L. Yu, D. Hu, G. Z. Chen, *Mater. Chem. Front.* **2017**, *1*, 584.
- [139] D. Aurbach, Y. Talyosef, B. Markovsky, E. Markevich, E. Zinigrad, L. Asraf, J. S. Gnanaaraj, H. J. Kim, *Electrochim. Acta* **2004**, *50*, 247.
- [140] B. H. Wee, J. D. Hong, *Langmuir* **2014**, *30*, 5267.
- [141] S. Paul, K. S. Choi, D. J. Lee, P. Sudhagar, Y. S. Kang, *Electrochim. Acta* **2012**, *78*, 649.
- [142] K. Tönurist, T. Thomborg, A. Jänes, I. Kink, E. Lust, *Electrochem. Commun.* **2012**, *22*, 77.
- [143] B. Pal, S. Yang, S. Ramesh, V. Thangadurai, R. Jose, *Nanoscale Adv.* **2019**, *1*, 3807.
- [144] T. Xiong, T. L. Tan, L. Lu, W. S. V. Lee, J. Xue, *Adv. Energy Mater.* **2018**, *8*, 1702630.
- [145] G. Wang, H. Wang, X. Lu, Y. Ling, M. Yu, T. Zhai, Y. Tong, Y. Li, *Adv. Mater.* **2014**, *26*, 2676.
- [146] L. Zhang, X. S. Zhao, *Chem. Soc. Rev.* **2009**, *38*, 2520.
- [147] C. Zhong, Y. Deng, W. Hu, J. Qiao, L. Zhang, J. Zhang, *Chem. Soc. Rev.* **2015**, *44*, 7484.
- [148] B. Pal, S. G. Krishnan, B. L. Vijayan, M. Harilal, C. C. Yang, F. I. Ezema, M. M. Yusoff, R. Jose, *J. Electroanal. Chem.* **2018**, *817*, 217.
- [149] L. Kong, M. Cheng, H. Huang, J. Pang, S. Liu, Y. Xu, X. H. Bu, *Energy Chem* **2022**, *4*, 100090.
- [150] K. Fic, G. Lota, M. Meller, E. Frackowiak, *Energy Environ. Sci.* **2012**, *5*, 5842.
- [151] S. Sundriyal, V. Shrivastav, A. Kaur, Mansi, A. Deep, S. R. Dhakate, *J. Energy Storage* **2021**, *41*, 103000.
- [152] M. Z. Iqbal, S. Zakar, S. S. Haider, *J. Electroanal. Chem.* **2020**, *858*, 113793.
- [153] Q. B. Le, T. H. Nguyen, H. Fei, I. Sapurina, F. A. Ngwabebhoh, C. Bubulinca, L. Munster, E. D. Bergerová, A. Lengalova, H. Jiang, T. D. Tran, N. Bugarova, M. Ormastova, N. E. Kazantseva, P. Saha, *Electrochim. Acta* **2021**, *367*, 137563.
- [154] Q. Zhang, J. Rong, D. Ma, B. Wei, *Energy Environ. Sci.* **2011**, *4*, 2152.
- [155] P. Kurzweil, M. Chwistek, *J. Power Sources* **2008**, *176*, 555.
- [156] R. R. Salunkhe, C. Young, J. Tang, T. Takei, Y. Ide, N. Kobayashi, Y. Yamauchi, *Chem. Commun.* **2016**, *52*, 4764.
- [157] S. Ghosh, A. De Adhikari, J. Nath, G. C. Nayak, H. P. Nayek, *ChemistrySelect* **2019**, *4*, 10624.
- [158] K. M. Choi, H. M. Jeong, J. H. Park, Y. B. Zhang, J. K. Kang, O. M. Yaghi, *ACS Nano* **2014**, *8*, 7451.
- [159] A. A. Łatoszyńska, G. Z. Zukowska, I. A. Rutkowska, P. L. Taberna, P. Simon, P. J. Kulesza, W. Wieczorek, *J. Power Sources* **2015**, *274*, 1147.
- [160] L. Q. Fan, J. Zhong, J. H. Wu, J. M. Lin, Y. F. Huang, *J. Mater. Chem. A* **2014**, *2*, 9011.
- [161] H. Du, Z. Wu, Y. Xu, S. Liu, H. Yang, *Polymers* **2020**, *12*, 297.
- [162] M. L. Verma, M. Minakshi, N. K. Singh, *Electrochim. Acta* **2014**, *137*, 497.
- [163] B. Pal, A. Yasin, R. Kunwar, S. Yang, M. M. Yusoff, R. Jose, *Ind. Eng. Chem. Res.* **2019**, *58*, 654.
- [164] S. Hong, H. Kim, S. Gao, R. L. Lavall, H. Y. Jung, Y. J. Jung, *J. Power Sources* **2019**, *432*, 16.
- [165] S. T. Senthilkumar, R. K. Selvan, J. S. Melo, *J. Mater. Chem. A* **2013**, *1*, 12386.
- [166] X. M. Cao, Z. J. Sun, S. Y. Zhao, B. Wang, Z. B. Han, *Mater. Chem. Front.* **2018**, *2*, 1692.
- [167] R. Zhao, Y. Wu, Z. Liang, L. Gao, W. Xia, Y. Zhao, R. Zou, *Energy Environ. Sci.* **2020**, *13*, 2386.
- [168] M. Wang, Y. Ma, J. Ye, *J. Power Sources* **2020**, *474*, 228681.
- [169] L. Shao, Q. Wang, Z. Ma, Z. Ji, X. Wang, D. Song, Y. Liu, N. Wang, *J. Power Sources* **2018**, *379*, 350.
- [170] A. B. Kanj, R. Verma, M. Liu, J. Helfferich, W. Wenzel, L. Heinke, *Nano Lett.* **2019**, *19*, 2114.
- [171] L. Yu, G. Z. Chen, *Front. Chem.* **2019**, *7*, 272.
- [172] S. Shahzad, A. Shah, E. Kowsari, F. J. Iftikhar, A. Nawab, B. Piro, M. S. Akhter, U. A. Rana, Y. Zou, *Glob. Challenges* **2019**, *3*, 1800023.
- [173] S. Pan, M. Yao, J. Zhang, B. Li, C. Xing, X. Song, P. Su, H. Zhang, *Front. Chem.* **2020**, *8*, 261.
- [174] X. Sang, J. Zhang, J. Xiang, J. Cui, L. Zheng, J. Zhang, Z. Wu, Z. Li, G. Mo, Y. Xu, J. Song, C. Liu, X. Tan, T. Luo, B. Zhang, B. Han, *Nat. Commun.* **2017**, *8*, 175.
- [175] M. Zhang, A. M. Zhang, X. X. Wang, Q. Huang, X. Zhu, X. L. Wang, L. Z. Dong, S. L. Li, Y. Q. Lan, *J. Mater. Chem. A* **2018**, *6*, 8735.
- [176] K. Fujie, R. Ikeda, K. Otsubo, T. Yamada, H. Kitagawa, *Chem. Mater.* **2015**, *27*, 7355.
- [177] L. Zhang, S. Yang, J. Chang, D. Zhao, J. Wang, C. Yang, B. Cao, *Front. Chem.* **2020**, *8*, 1.
- [178] B. Akinwolemiwa, C. Peng, G. Z. Chen, *J. Electrochem. Soc.* **2015**, *162*, A5054.
- [179] S. Sundriyal, V. Shrivastav, M. Sharma, S. Mishra, A. Deep, *ChemSelect* **2019**, *4*, 2585.
- [180] W. Ye, H. Wang, J. Ning, Y. Zhong, Y. Hu, *J. Energy Chem.* **2021**, *57*, 219.
- [181] S. Balasubramaniam, A. Mohanty, S. K. Balasingam, S. J. Kim, *Nano Micro Lett.* **2020**, *12*, 85.
- [182] S. Zhang, D. Li, S. Chen, X. Yang, X. Zhao, Q. Zhao, S. Komarneni, D. Yang, *J. Mater. Chem. A* **2017**, *5*, 12453.
- [183] X. Xiong, L. Zhou, W. Cao, J. Liang, Y. Wang, S. Hu, F. Yu, B. Li, *CrystEngComm* **2017**, *19*, 7177.
- [184] L. Wang, Y. Han, X. Feng, J. Zhou, P. Qi, B. Wang, *Coord. Chem. Rev.* **2016**, *307*, 361.
- [185] M. Kaempgen, C. K. Chan, J. Ma, Y. Cui, G. Gruner, *Nano Lett.* **2009**, *9*, 1872.
- [186] P. Simon, Y. Gogotsi, *Nat. Mater.* **2008**, *7*, 845.
- [187] A. Deep, S. K. Bhardwaj, A. K. Paul, K. H. Kim, P. Kumar, *Biosens. Bioelectron.* **2015**, *65*, 226.
- [188] H. Nishihara, H. Itoi, T. Kogure, P. X. Hou, H. Touhara, F. Okino, T. Kyotani, *Chem.* **2009**, *15*, 5355.
- [189] G. Wang, L. Zhang, J. Zhang, *Chem. Soc. Rev.* **2012**, *41*, 797.
- [190] D. Giliopoulos, A. Zamboulis, D. Giannakoudakis, D. Bikiaris, K. Triantafyllidis, *Molecules* **2020**, *25*, 1.
- [191] Z. Xie, W. Xu, X. Cui, Y. Wang, *ChemSusChem* **2017**, *10*, 1645.
- [192] Y. Zheng, S. Zheng, H. Xue, H. Pang, *Adv. Funct. Mater.* **2018**, *28*, 1.
- [193] K. D. Fong, T. Wang, S. K. Smoukov, *Sustain. Energy Fuels* **2017**, *1*, 1857.
- [194] Y. Pan, K. Xu, C. Wu, *Nanotechnol. Rev.* **2019**, *8*, 299.
- [195] W. Yan, J. Su, Z. M. Yang, S. Lv, Z. Jin, J. L. Zuo, *Small* **2021**, *17*, 2005209.
- [196] J. Sun, L. Guo, X. Sun, J. Zhang, Y. Liu, L. Hou, C. Yuan, *J. Mater. Chem. A* **2019**, *7*, 24788.
- [197] W. Feng, J. Zhang, A. Yusuf, X. Ao, D. Shi, V. Etacheri, D. Y. Wang, *Chem. Eng. J.* **2022**, *427*, 130919.
- [198] Y. Zhang, Y. Li, X. Wang, X. Teng, L. Guan, H. Yang, Z. He, Y. Wan, S. Guo, H. Hu, M. Wu, *J. Mater. Chem. A* **2022**, *10*, 19852.
- [199] L. Shen, H. Lv, S. Chen, P. Kopold, P. A. van Aken, X. Wu, J. Maier, Y. Yu, *Adv. Mater.* **2017**, *29*, 1700142.
- [200] C. Leng, Z. Zhao, J. Guo, R. Li, X. Wang, J. Xiao, Y. V. Fedoseeva, L. G. Bulusheva, J. Qiu, *Chem. Commun.* **2021**, *57*, 8778.
- [201] Y. Wang, F. Yuan, Z. Li, D. Zhang, Q. Yu, B. Wang, *APL Mater.* **2022**, *10*, 030902.
- [202] D. Y. Lee, S. J. Yoon, N. K. Shrestha, S. H. Lee, H. Ahn, S. H. Han, *Microporous Mesoporous Mater.* **2012**, *153*, 163.
- [203] S. C. Wechsler, F. Z. Amir, *ChemSusChem* **2020**, *13*, 1491.
- [204] P. A. Shinde, Y. Seo, S. Lee, H. Kim, Q. N. Pham, Y. Won, S. Chan Jun, *Chem. Eng. J.* **2020**, *387*, 122982.
- [205] P. Du, Y. Dong, C. Liu, W. Wei, D. Liu, P. Liu, *J. Colloid Interface Sci.* **2018**, *518*, 57.

- [206] Z. Sun, L. Hui, W. Ran, Y. Lu, D. Jia, *New J. Chem.* **2016**, *40*, 1100.
 [207] H. Mei, Y. Mei, S. Zhang, Z. Xiao, B. Xu, H. Zhang, L. Fan, Z. Huang, W. Kang, D. Sun, *Inorg. Chem.* **2018**, *57*, 10953.
 [208] S. Maiti, A. Pramanik, S. Mahanty, *Chem. Commun.* **2014**, *50*, 11717.
 [209] Y. Z. Zhang, Y. Wang, Y. L. Xie, T. Cheng, W. Y. Lai, H. Pang, W. Huang, *Nanoscale* **2014**, *6*, 14354.
 [210] P. Zhou, J. Wan, X. Wang, K. Xu, Y. Gong, L. Chen, *J. Colloid Interface Sci.* **2020**, *575*, 96.
 [211] M. Yu, L. Zhang, X. He, H. Yu, J. Han, M. Wu, *Mater. Lett.* **2016**, *172*, 81.
 [212] Q. Wang, W. Xia, W. Guo, L. An, D. Xia, R. Zou, *Chem.* **2013**, *8*, 1879.
 [213] S. Zhong, C. Zhan, D. Cao, *Carbon* **2015**, *85*, 51.
 [214] Y. Gao, J. Wu, W. Zhang, Y. Tan, J. Gao, J. Zhao, B. Tang, *New J. Chem.* **2015**, *39*, 94.
 [215] J. Xu, Y. Wang, S. Cao, J. Zhang, G. Zhang, H. Xue, Q. Xu, H. Pang, *J. Mater. Chem. A* **2018**, *6*, 17329.
 [216] S. N. Guo, Y. Zhu, Y. Y. Yan, Y. L. Min, J. C. Fan, Q. J. Xu, H. Yun, *J. Power Sources* **2016**, *316*, 176.
 [217] G. Zhao, X. Xu, G. Zhu, J. Shi, Y. Li, S. Zhang, M. S. A. Hossain, K. C. W. Wu, J. Tang, Y. Yamauchi, *Microporous Mesoporous Mater.* **2020**, *303*, 110257.
 [218] S. N. Ansari, M. Saraf, A. K. Gupta, S. M. Mobin, *Chem.* **2019**, *14*, 3566.
 [219] M. S. Rahmanifar, H. Hesari, A. Noori, M. Y. Masoomi, A. Morsali, M. F. Mousavi, *Electrochim. Acta* **2018**, *275*, 76.
 [220] J. Wang, Q. Zhong, Y. Xiong, D. Cheng, Y. Zeng, Y. Bu, *Appl. Surf. Sci.* **2019**, *483*, 1158.



Rakhee Bhosale obtained her Master's degree (2016) in chemistry from the Department of Chemistry, Shivaji University, Kolhapur, India, and is currently a doctoral student in same department, with an emphasis on material science. Her research interests are focused on the synthesis, characterization, and application of self-assembled nanoparticles and nanocomposites, aiming at the improvement of their performances in energy storage, production, and conversion by synergistic effects.



Sneha Bhosale obtained her Master's degree (2019) in chemistry and is pursuing her doctoral studies at the Department of Chemistry, Shivaji University, Kolhapur, India. She has expertise in the synthesis of nanomaterials for exotics applications including biomedical, gas sensor, energy storage, etc. Her doctoral research area is in mesoporous carbon, the synthesis of metal oxide nanostructures, and its composites for biomedical applications.



Madagonda Vadiyar is currently working as brain pool postdoctoral fellow at the Department of Energy and Materials Engineering, Dongguk University, Seoul, South Korea. He received his Ph.D. (2017) in chemistry from Shivaji University, Kolhapur, India. In 2017, he joined as a postdoctoral researcher at Laurentian University, Sudbury, and later at Concordia University, Montreal, Canada. His current research interests are synthesizing metal/covalent organic frameworks, covalent triazine frameworks, and their derived materials for energy storage devices, particularly for the development of high-performance supercapacitors and batteries.



Chitra Jambhale obtained her Master's degree in 1992 and doctoral degree in 2018 from Shivaji University, India. She is a visiting researcher at the Department of Physics, The Ohio State University, Columbus, Ohio, USA (2018), where she carried out postdoctoral research in condensed matter physics. She is currently an assistant professor of physics at Sangola College, Sangola. Her current research interest is in the area of development of materials for supercapacitors.



Kyung-Wan Nam is a professor in the Department of Energy and Materials Engineering, at Dongguk University, Seoul, South Korea. He received his B.S. (1998), M.S. (2000), and Ph.D. (2005) in metallurgical engineering from Yonsei University, South Korea. In 2006, he joined the Chemistry Department of Brookhaven National Laboratory as a research associate and then became a staff scientist in 2009. His research is focused on energy storage materials (e.g., lithium- and sodium-ion batteries and supercapacitors) and revealing structure–property correlations of battery materials using various synchrotron X-Ray techniques, including in situ/ex situ X-Ray diffraction, X-Ray absorption spectroscopy (XAS), and pair distribution function (PDF) analysis.



Sanjay Kolekar is a senior professor of chemistry at Shivaji University, Kolhapur, India. He received his doctoral degree (2003) in chemistry from Shivaji University, India. He is invited scientist at Chonnam National University as brain pool Fellow, National Research Foundation, South Korea, and is visiting professor at Hanyang University, South Korea. He has been invited as Member on European Research Council and is Scientific Expert, Ministry of Education, Universities and Research, Rome, Italy. For his research in specialized area, he has been awarded National Level “Mid-Career Award” by University Grants Commission, India. His research group interests include the synthesis of ferrite materials and metal–organic framework (MOF) nanostructures for their applications in supercapacitors and battery; synthesis of nanocrystals and colloidal quantum dots; and their applications in water splitting.

Construction of Well-Defined Two-Dimensional Architectures of Trimetallic Metal–Organic Frameworks for High-Performance Symmetric Supercapacitors

Rakhee Bhosale, Sneha Bhosale, Dattatray Narale, Chitra Jambhale, and Sanjay Kolekar*



Cite This: *Langmuir* 2023, 39, 12075–12089



Read Online

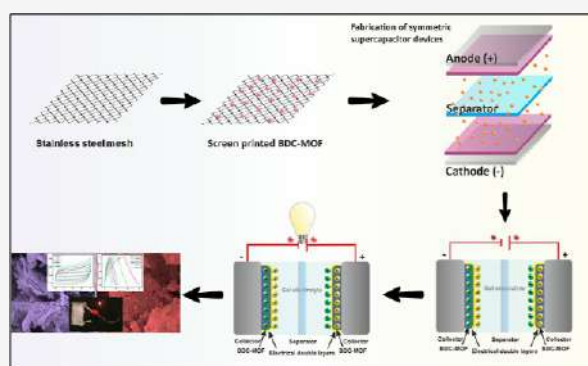
ACCESS |

Metrics & More

Article Recommendations

Supporting Information

ABSTRACT: The high surface-to-volume ratio and extraordinarily large-surface area of two-dimensional (2D) metal–organic framework (MOF) architectures have drawn particular interest for use in supercapacitors. To achieve an excellent electrode material for supercapacitors, well-defined 2D nanostructures of novel trimetallic MOFs were developed for supercapacitor applications. Multivariate MOFs (terephthalate and trimesate MOF) with distinctive nanobrick and nanoplate-like structures were successfully synthesized using a straightforward one-step reflux condensation method by combining Ni, Co, and Zn metal species in equimolar ratios with two different ligands. Furthermore, the effects of the tricarboxylic and dicarboxylic ligands on cyclic voltammetry, charge–discharge cycling, and electrochemical impedance spectroscopy were studied. The derived terephthalate and trimesate MOFs are supported with stainless-steel mesh and provide a suitable electrolyte environment for rapid faradaic reactions with an elevated specific capacity, excellent rate capability, and exceptional cycling stability. It shows a specific capacitance of 582.8 F g^{-1} , a good energy density of $40.47 \text{ W h kg}^{-1}$, and a power density of 687.5 W kg^{-1} at 5 mA cm^{-2} with an excellent cyclic stability of 92.44% for 3000 charge–discharge cycles. A symmetric BDC–MOF//BDC–MOF supercapacitor device shows a specific capacitance of 95.22 F g^{-1} with low capacitance decay, high energy, and power densities which is used for electronic applications. These brand-new trimetallic MOFs display outstanding electrochemical performance and provide a novel strategy for systematically developing high-efficiency energy storage systems.



INTRODUCTION

Over the past few decades, the need to develop clean and sustainable energy has become extremely urgent due to the increasing requirement for clean energy and solving serious environmental problems.¹ Nowadays, much research is focused on current renewable energy storage devices in order to minimize pollution and raise worries about future energy problems.^{2,3} Under some environmental circumstances, it is challenging to produce power from sustainable energy sources (biomass, hydro, solar, wind, etc.), which causes an imbalance between the supply and demand of energy. In order to balance and equalize energy needs, energy storage devices must be integrated with energy production, which is crucial for a renewable energy supply.^{4,5} Because of their excellent energy capability and clean electrical systems, electrochemical energy storage equipment have gained widespread interest. One energy storage device that stands out above most of the others is the supercapacitor, which shows the utmost characteristics like high energy density, fast charging/discharging process, and excellent cycle stability, and also they are feasibly used in many fields.^{6–8} The energy storage mechanism is non-identical for every class because of the different materials used within the

components.⁹ It is broadly confessed that the features of electrode materials like structure, morphology, electronic conductivity, electrochemical activity, and chemical and mechanical stability all put up to their electrochemical performance.^{10,11} Transition metals have fascinated ample interest for many energy storage devices due to their good physical and chemical characteristics, high conductivity, improved redox activity, and long cycle stability.¹² The supercapacitor's performance is also affected by the electrolyte utilized. Electrolytes are important and necessary components of supercapacitors. Due to their physical and chemical characteristics, they have a significant impact on the electrochemical performances of specific capacity, energy density, power density, rate capability, cycle stability, and safety. In comparison to aqueous electrolytes, the solid-state electrolyte

Received: May 18, 2023

Revised: July 31, 2023

Published: August 14, 2023



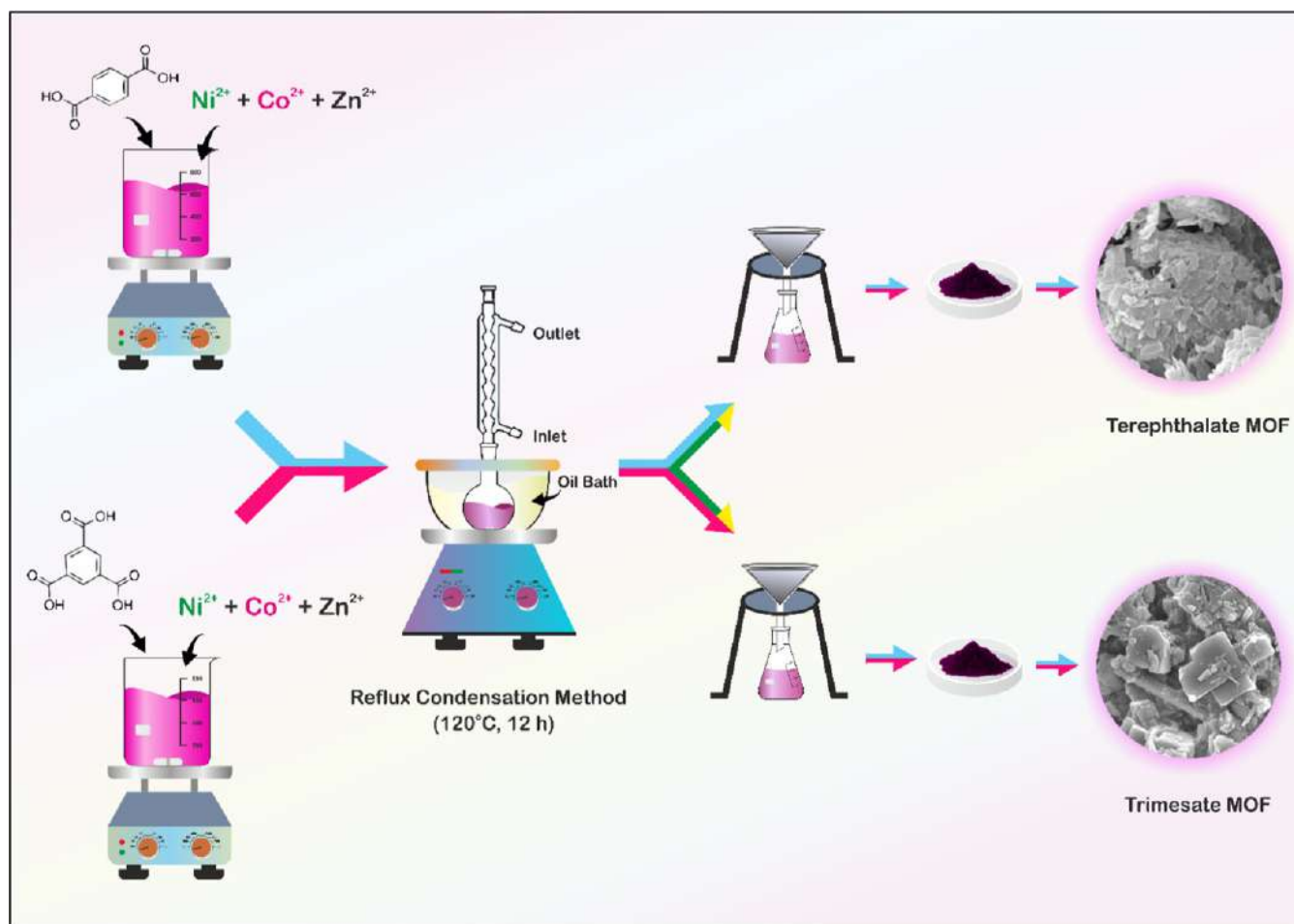


Figure 1. Schematic illustrations of the synthesis of trimetallic MOFs.

is a crucial element that might significantly affect the capacitance retention and stability of supercapacitors. Liquid electrolytes possess some limitations like leakage problems, and it shows low electrochemical performance. Gel polymer electrolytes (GPEs) are the most commonly used solid-state electrolytes in solid-state supercapacitors due to their relatively high ionic conductivity, improved interfacial contacts between electrodes and GPE, broad operating potential range, higher ion transfer number, and improved stability.^{13,14}

Metal–organic frameworks (MOFs) have emerged as attractive prospects in a variety of sectors in recent years due to structural and electrical properties such as high porosity, excellent specific surface area (SSA), high stability, and adjustable arrangement of active sites. Owing to the structural and electronic features of MOFs, they are employed in supercapacitors. MOFs show pseudocapacitive nature because of the oxidative–reductive behavior of positively charged metal ions inside MOFs which create channels for electrons as well as show electric double layer capacitor (EDLC) behavior due to the organic linker structure which promotes charge transfer inside the framework which leads to the EDLC behavior.^{15,16} MOFs are formed at the micro/nanosize using central metal nodes and organic linkers, resulting in one-dimensional (1D), two-dimensional (2D) structures, and three-dimensional superstructures.^{17,18} In the exploration of advanced materials with enhanced characteristics over standard MOFs, the tendency is to encourage synergistic effects succeeding from the existence of two or more metals in multimetallic MOFs.¹⁹

In comparison to monometallic MOFs, the multimetallic MOFs have many advantages including strong chemical reactivity, improved electronic charge transfer, a variety of morphologies, high selectivity and sensitivity, virtue, strain in the lattice, different geometric impacts, and chemical change.^{20–24} Due to the excellent properties of MOFs, the electrochemical performance of supercapacitors is enhanced by their ability to store a huge quantity of charge and by encouraging the dissemination of electrolyte ions. As a result, MOFs have received a lot of interest when it comes to the use of supercapacitor electrode materials.²⁵ The limitations of the monometallic MOFs have been overcome by multimetallic MOFs which have advantages like the synergic effect which enhance the redox reactions and electrical conductivity. Also, the presence of various metal centers enhances the electroactive sites for ion transfer and helps the interaction with electrolyte in the course of the electrochemical reactions. The advancement of an perfect and beneficial electrode material composed of non-noble metals with remarkable steadiness and nature depicts the key challenge in these areas.^{26–28} As an outcome, a considerable study has been performed to reduce the obstacles caused by MOF's low conductivity and structural configuration. The direct application of MOF-based materials for effective supercapacitors remains difficult, despite the significant advances made in manufacturing MOF-based materials for energy storage applications.²⁹ Nagaraju et al. put together binder-free Ni–Co–Mn-based MOFs via a polarity-induced solution-phased technique. Dual-layered

Ni–Co–Mn-based MOFs with versatile features demonstrated the highest capacity of 1311.4 A h cm⁻² at a 5 mA cm⁻² current density with high capacitance retention of about 86.1% after applying 4000 cycles in the aqueous alkaline electrolyte. Additionally, they have created a pouch-type supercapattery with a bilayered Ni–Co–Mn-based MOF/Ni foam as an anode and nitrogen-oxygen-enriched activated carbon/Ni foam as a cathode. This device exhibits good cycling durability due to the high capacity of the supercapattery retained at 90.1% and the good Faradaic efficiency of 98.6%. Furthermore, they created a pouch-type supercapattery using bilayered Ni–Co–Mn-based MOF/Ni foam as an anode and nitrogen-oxygen-enriched activated carbon/Ni foam as a cathode, resulting in a supercapattery with a high capacity retention of 90.1% and an exceptional Faradaic efficiency of 98.6%, illustrating the device's great cycling longevity.³⁰ Andikaey et al. prepared a new nanocomposite mesoporous ordered silica SBA-15/MWCNTs embellished with a trimetallic organic framework (NiCoCu-BTC) using a facile, cost-effective one-step solvothermal technique. The synthesized nanocomposite exhibited outstanding electrochemical performance having a remarkable 868 C g⁻¹ (2067 F g⁻¹) specific capacity at a 1 A g⁻¹ current density with great cycling durability. Additionally, they have fabricated an asymmetric supercapacitor device with a high energy density 52.4 W h kg⁻¹ at a power density of 1124 W kg⁻¹ with high capacitance retention of about 87.2% after applying 5000 cycles.³¹

In view of this, we present the synthesis of trimetallic MOFs for high-performance symmetric supercapacitors by applying two different organic linkers, i.e., trimesic acid and terephthalic acid. To the finest of our information, this is the primary report in which a comparative study of two MOFs is carried out only by changing the organic linker, and they are used as dynamic anode materials for supercapacitors. The physico-chemical properties of both the trimetallic MOFs were thoroughly investigated by using different characterization techniques. In addition, a symmetric supercapacitor shows a high energy density and great chemical steadiness in a 2 M KOH electrolyte.

EXPERIMENTAL SECTION

Synthesis of MOFs. All chemicals used to synthesize trimetallic MOFs were obtained from Loba Chemie (India) and were used without further purification. The trimetallic Ni–Co–Zn–BDC MOFs (BDC–MOF) were prepared using a single-step reflux condensation method. In a typical synthesis, 0.415 g of terephthalic acid (BDC), 0.363 g of nickel nitrate hexahydrate, 0.363 g of cobalt nitrate hexahydrate, and 0.371 g zinc nitrate hexahydrate were dissolved step by step in 30 mL of *N,N*-dimethylformamide with continuous stirring at ambient temperature.

After which, the reaction mixture was transferred to a 50 mL round-bottom flask. The reaction mixture was kept at 120 °C for 12 h to produce the BDC–MOF sample and then cooled at ambient temperature. The final precipitate was carefully washed a few times with alcohol. Finally, the purple-colored product was air-dried for 12 h at 80 °C. A similar procedure was adopted for the synthesis of trimetallic Ni–Co–Zn–BTC MOF (BTC–MOF), except that terephthalic acid was replaced with trimesic acid. A schematic illustration for the synthesis of trimetallic MOFs by the reflux condensation method is shown in Figure 1.

Structural and Elemental Characterization. The crystal structure and phase purity of the synthesized trimetallic MOFs were confirmed by the X-ray diffraction (XRD) technique [Bruker D8 Phaser X-ray diffractometer with Cu K α radiation ($\lambda = 1.541 \text{ \AA}$)]. The types of bonding and functional groups were analyzed by Fourier

transform infrared (FT-IR) spectroscopy (PerkinElmer 1760X spectrophotometer). The Raman spectrometer (LabRAM HR Evolution Confocal Raman Microscope, France) was used for point group analysis. The morphology of the as-prepared materials was investigated by scanning electron microscopy (SEM) (JEOL-JSM 6360, Japan). The elemental composition of the trimetallic MOFs was examined using an energy-dispersive X-ray analysis (EDAX) spectrometer [Oxford Instrumentations inbuilt with field emission (FE-SEM)]. The elemental oxidation state and chemical composition of the as-prepared materials were investigated by X-ray photoelectron spectroscopy (XPS) with a K-alpha (Thermo VG, UK) spectrometer and a monochromatic Al X-ray source (AlK α line: 1486.6 eV, 3 mA, and 12 kV). The surface area and pore size were determined by Brunauer–Emmett–Teller (BET) (NOVA1000e Quantachrome, USA).

Electrochemical Measurements with a Three-Electrode Assembly. Electrochemical measurements were performed on a CHI608 electrochemical analyzer (CH Instruments Inc, Austin, USA). A standard three-electrode assembly in a 2 M KOH electrolyte was used to explore the electrochemical characteristics of a constructed electrode. A saturated Ag/AgCl was used as a reference electrode, graphite as the counter electrode, and trimetallic MOF-loaded stainless-steel mesh as the working electrode. The working electrode was fabricated by making a paste of 80 wt % of active materials (BDC–MOF and BTC–MOF), 10 wt % of carbon black (Super P) as a conducting material, and 10 wt % of polyvinylidene fluoride (PVDF) as a binder in the *N*-methyl-2-pyrrolidone (NMP) solvent. This paste was applied to a stainless-steel mesh measuring with size about 1 cm² and then air-dried for 12 h at 80 °C. With the help of electrochemical workstation, cyclic voltammetry (CV), galvanostatic charge–discharge (GCD), and electrochemical impedance spectroscopy (EIS) studies were carried out. In the frequency range of 1 Hz to 100 kHz, the EIS test was conducted. According to eq 1, specific capacitance of the prepared samples was determined.

$$C = \frac{I \times \Delta t}{\Delta V \times m} \quad (1)$$

where “C” stands for the specific capacitance measured in F g⁻¹, “I” stands for the current measured in mA, “ Δt ” stands for the discharging time measured in seconds, “ ΔV ” stands for the potential window measured in volt, and “m” stands for the mass of the active electrode material measured in mg.

Electrochemical Measurements of the Symmetric Supercapacitor. A solid-state symmetric supercapacitor (SSC) device was constructed by stainless-steel mesh substrates with size about 2 cm coated with the BDC–MOF, and a thick layer of polyvinyl alcohol (PVA)–KOH was sandwiched in between them. The device was allowed to naturally dry out overnight at ambient temperature. As per literature report, the PVA–KOH gel electrolyte was prepared.³² Using a conventional method, 1 g of PVA was dissolved in 20 mL of distilled water while the bath solution temperature was held at 80 °C for 30 min. To create the viscous gel electrolyte, the PVA solution was combined with the aqueous KOH solution dropwise and heated once more at 80 °C for 30 min.

Using 2, the specific capacitance, energy density, and power density of the symmetric supercapacitor were computed, respectively.^{33,34}

$$C_s = \frac{I \times \Delta t}{\Delta V \times M} \quad (2)$$

$$E = \frac{0.5 \times C \times \Delta V^2}{3.6} \quad (3)$$

$$P = \frac{E \times 3600}{\Delta t} \quad (4)$$

where “C_s” stands for the specific capacitance measured in F g⁻¹, “E” stands for the specific energy measured in W h kg⁻¹, “P” stands for the specific power measured in W kg⁻¹, and “M” stands for the total mass of the two electrodes measured in mg.

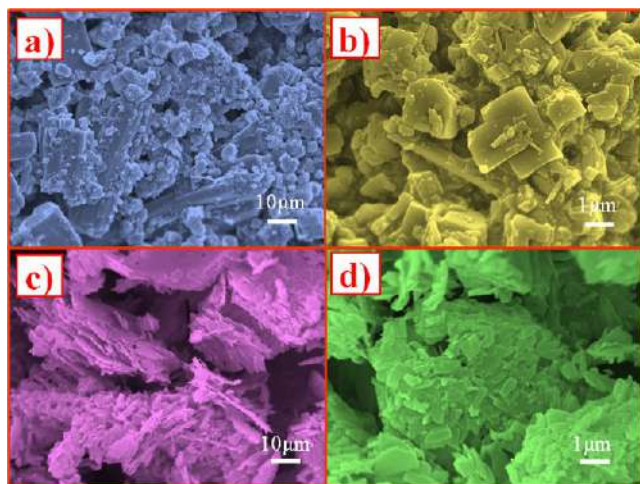


Figure 5. SEM images of BTC-MOF (a,b) and BDC-MOF (c,d) at different magnifications.

different magnifications. From Figure 5a,b, it has been observed that the small nanoparticles start to construct the nanobrick-like morphology of BTC-MOF, and nanobricks were observed all over area of the sample which are randomly distributed in the sample. The width of the nanobricks was observed from 200 to 300 nm in size. It was noticed that nanobricks are interconnected to each other, and also the edges of the nanobricks are mingling with one another; hence, the nanobricks are found to be cut in small pieces, which are responsible for the irregular shapes of nanobricks formed in the BTC-MOF sample. Additionally, some of the spacing between two nanobricks is seen in the BTC-MOF sample, which is helpful for adsorbing the electrolyte and boosts the material-specific capacitance. It is seen that the variation of ligands in MOF samples has a great impact on the characteristic morphology of MOF samples. Here, it is observed that with change in the ligands, there was a change in the surface morphology of MOF samples.

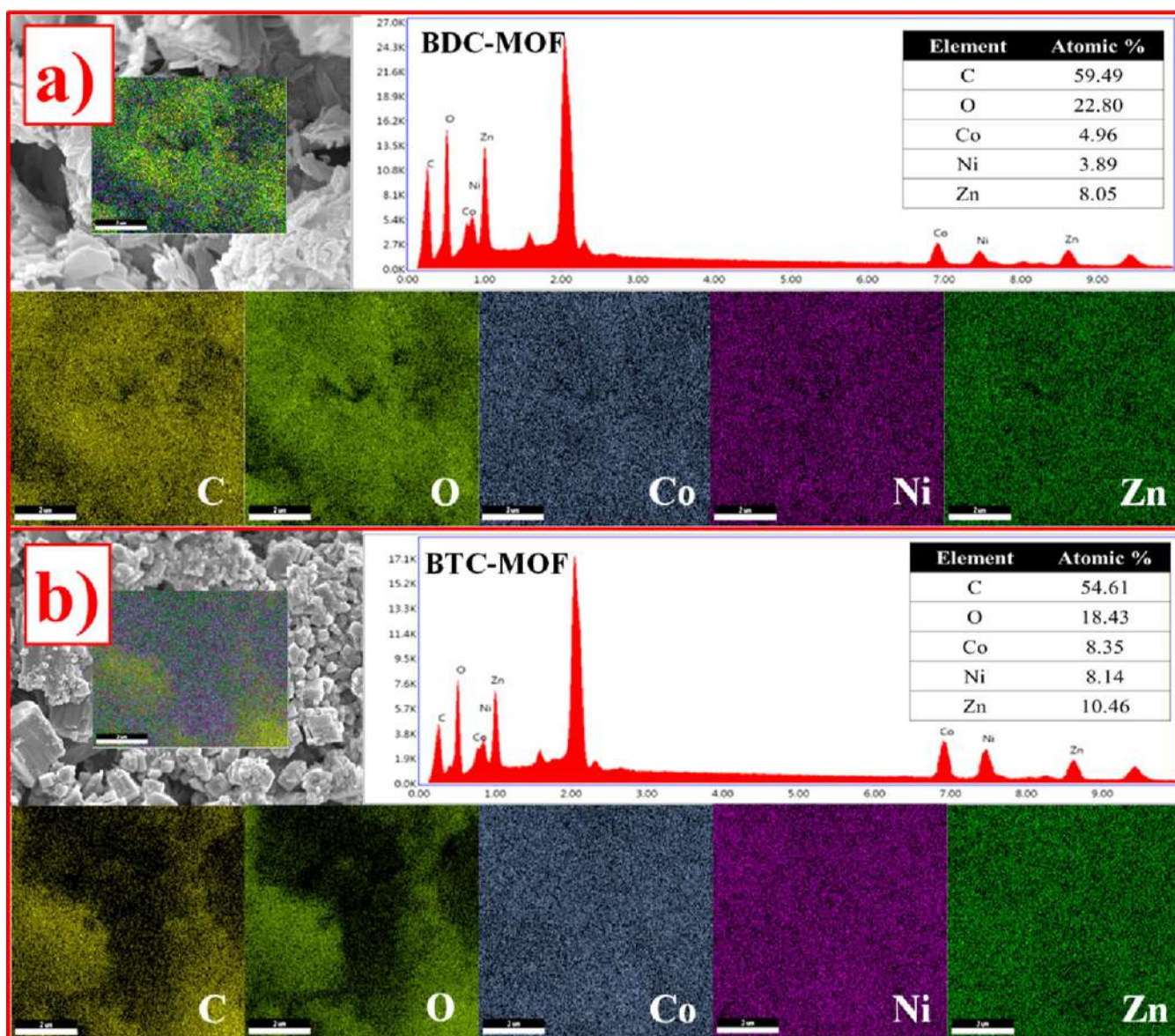


Figure 6. EDX spectra and elemental mapping of C, O, Co, Ni, and Zn elements for (a) BDC-MOF and (b) BTC-MOF.

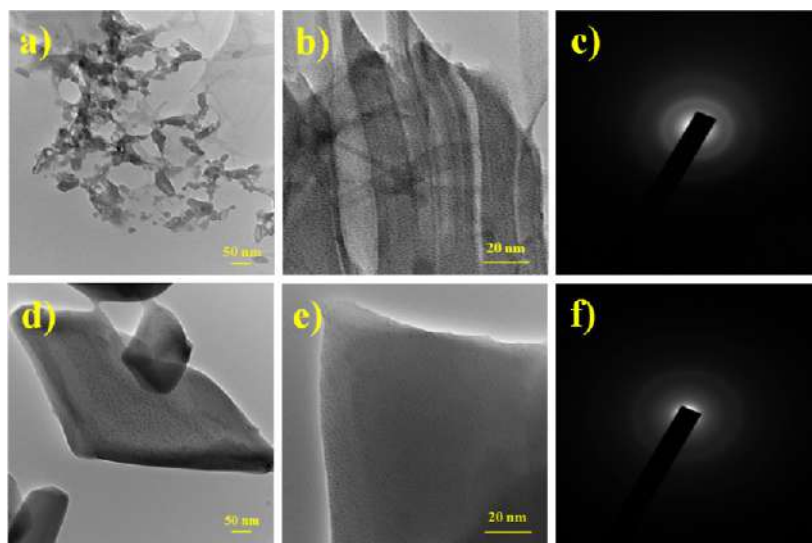


Figure 7. TEM, HR-TEM, and SAED pattern of (a) BDC-MOF and (b) BTC-MOF.

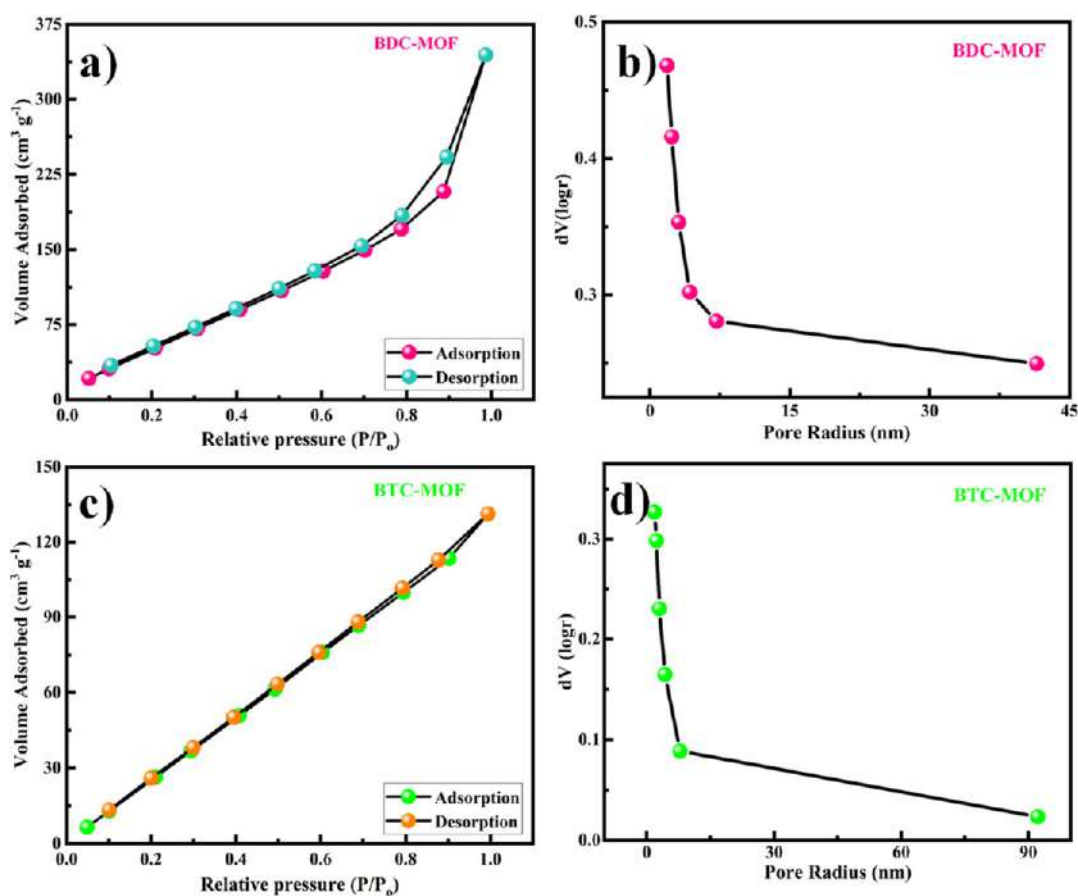


Figure 8. (a,b) N₂ adsorption–desorption isotherm and BJH pore size distribution curve of BDC-MOF. (c,d) N₂ adsorption–desorption isotherm and BJH pore size distribution curve of BTC-MOF.

The sample BDC-MOF demonstrated the nanoplatform-like morphology with irregular arrangement of the nanoplatforms occurring throughout the sample. Some of the nanoplatforms were formed together, leading to big porous bricks which are shown in Figure 5c,d. The thickness of the nanoplatforms was observed in the nanometer range, and a bunch of the nanoplatforms formed the brick-like morphology, hence increasing the surface area of the sample. The bunch of nanoplatforms provides a larger SSA for

the adsorption of the electrolyte increasing the specific capacitance of the sample. The surface area of BDC-MOF is the greatest of the two samples examined in the BET investigation. Also, SEM outcomes are in good agreement with BET analysis. Hence, among these two samples, BDC-MOF executes a good electrochemical performance.

The EDAX of both the trimetallic MOFs is presented in Figure 6. Figure 6 demonstrates that the elements Ni, Co, Zn,

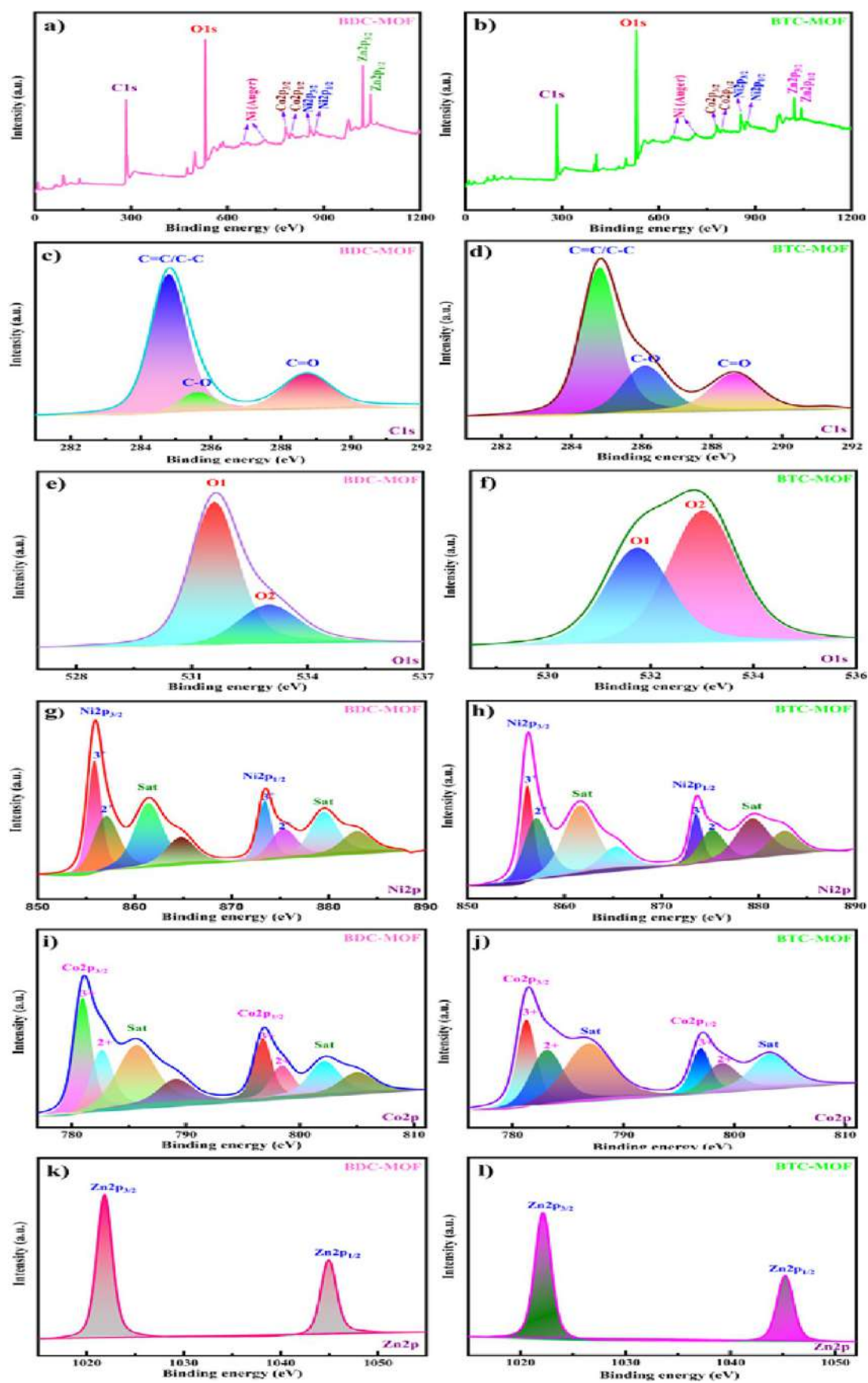


Figure 9. XPS survey spectra of BDC–MOF (a) and BTC–MOF (b), high-resolution spectra of C 1s (c,d), O 1s (e,f), Ni 2p (g,h), Co 2p (i,j), and Zn 2p (k,l) of BDC–MOF and BTC–MOF, respectively.

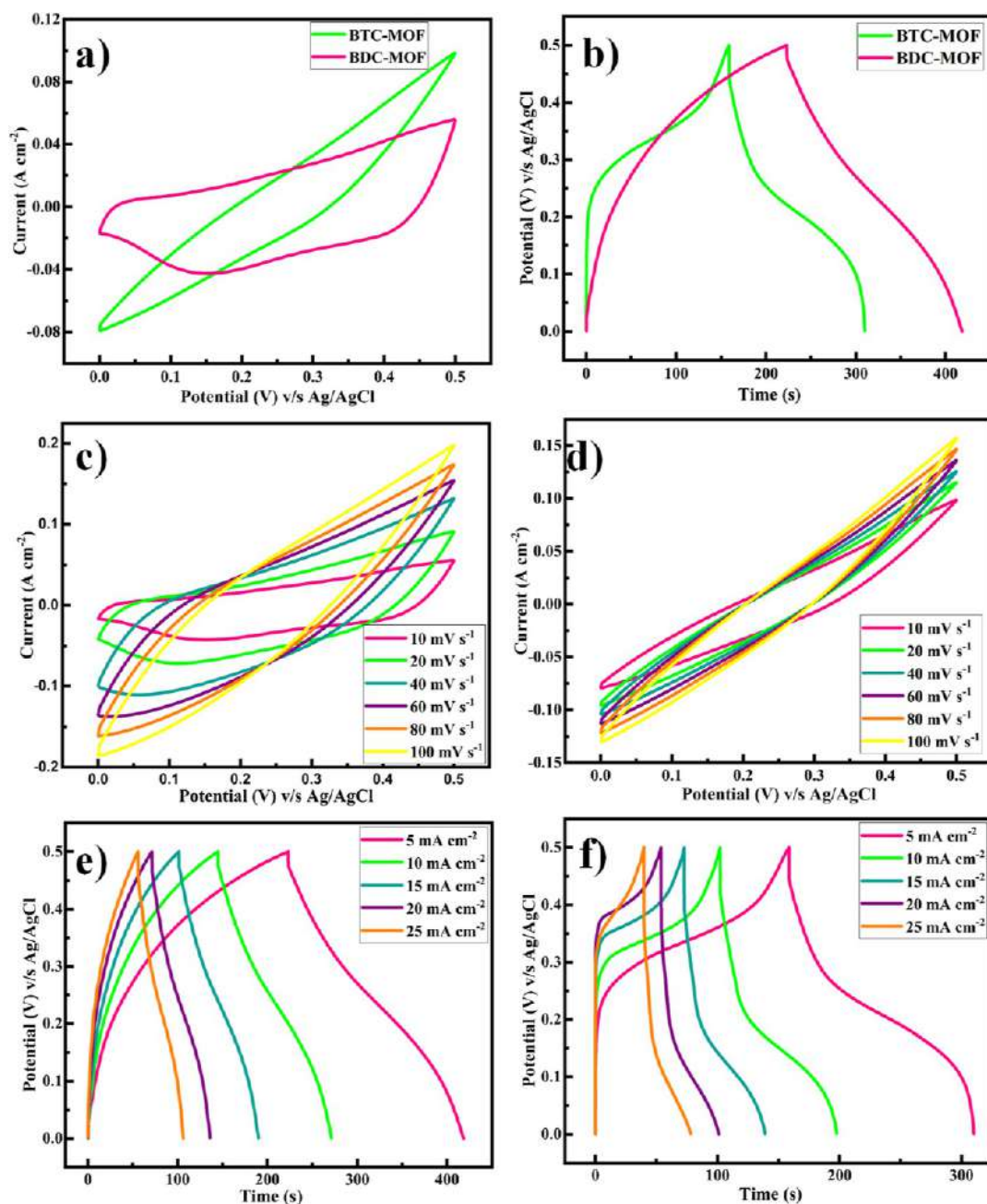


Figure 10. (a) Comparative CV curves at 10 mV s^{-1} scan rate, (b) comparative GCD curves at 5 mA cm^{-2} current density, (c) CV curves of BDC-MOF at different scan rates, (d) CV curves of BTC-MOF at different scan rates, (e) GCD curves of BDC-MOF at different current densities, and (f) GCD curves of BTC-MOF at different densities.

C, and O are distributed evenly throughout the sample, which confirms the presence of three metal ions in the MOFs as well as maintained the stoichiometry of the samples; hence, it proved that the trimetallic MOFs were obtained. The SSA and pore diameter of the MOF samples were obtained by using BET analysis.

Transmission electron microscopy (TEM) examination was performed to have a better understanding of the structure of the as-prepared nanomaterials. Figure 7a depicts a typical TEM image of BDC-MOF with a 2D nanoplate-like shape with many voids. Furthermore, the high-resolution TEM (HRTEM) image of BDC-MOF (Figure 7b) confirms an amorphous nature due to the lack of apparent lattice fringes and no indication of crystallinity, representing that the particles

were amorphous. The selected area electron diffraction (SAED) pattern (Figure 7c) consistently exposed only diffuse rings, confirming the amorphous nature of the as-synthesized BDC-MOF particles. Figure 7d shows a typical TEM image of a 2D nanobrick-like morphology of BTC-MOF. The HRTEM image of BTC-MOF (Figure 7e) disseminated that the particles were amorphous due to the lack of visible lattice fringes and no evidence of crystallinity, suggesting that the particles were amorphous. The SAED pattern (Figure 7f) consistently displayed only diffuse rings, confirming the amorphous nature of the BTC-MOF particles as synthesized.

N_2 adsorption/desorption measurements confirmed the porous structure of the obtained MOFs, and the corresponding isotherms are shown in Figure 8. Before adsorption measure-

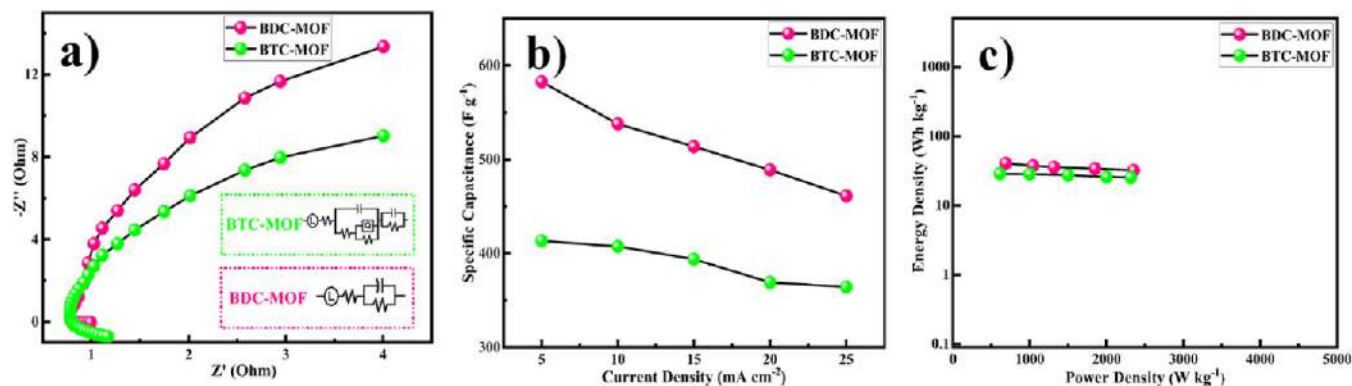


Figure 11. (a) Nyquist plots (inset electrical equivalent circuit), (b) variation of specific capacitance as a function of current density, and (c) Ragone plot showing the energy density versus power density.

ments, MOF samples were outgassed at 100 °C for 4 h. BDC–MOF and BTC–MOF had SSA of 267.85 and 216.93 $\text{m}^2 \text{g}^{-1}$, respectively. The average pore size of BDC–MOF and BTC–MOF was found to be 16 and 31 nm simultaneously, which is obtained from the BJH curve. According to the IUPAC classifications, the BDC–MOF and BTC–MOF isotherms are types IV and II, respectively,⁴⁴ clearly indicating that the BDC–MOF have a larger SSA than the BTC–MOF. The SSA and average pore radius values agree well with the crystallite size determined by XRD and the specific capacitance determined by electrochemical performance study.

The chemical composition and oxidation states of trimetallic MOFs were obtained by using XPS and explored the charge-transfer mechanisms in the valence state of the Ni, Zn, and Co ions of trimetallic MOFs along with the synergetic effect of its species. Figure 9a,b shows the survey spectra of both trimetallic MOFs. The core level spectra of C 1s, Ni 2p, Co 2p, O 1s, and Zn 2p of both the trimetallic MOFs are depicted in Figure 9c–i. As seen in Figure 9a,b, the existence of trimetallic MOFs was attributed by the XPS full survey scan spectrum, which contained the signals of the elements Ni, Co, O, C, and Zn. Figure 9c,d reveals the C 1s spectra of both the MOFs. It consists of distinct peaks caused by benzene rings from the BDC and BTC ligands with binding energy 284.7 and 284.8 eV, respectively. Then, carboxylate rings from the ($-\text{C}=\text{O}$) groups of the organic ligand with binding energy 288.7 and 288.6 eV, respectively, of both the MOFs and the species $-\text{C}-\text{O}$ with a binding energy of 285.5 and 286.0 eV are shown. Furthermore, the O 1s spectra of BDC and BTC MOF are presented in Figure 9e,f, which includes two oxygen peaks denoted as O1 and O2. The first fitted peak at a 531.5 and 531.6 eV binding energy is related to the presence of metal–oxygen bond, i.e., oxygen atoms on the Ni, Co, and Zn–O bonds of both the MOFs, and the second fitted peak at 532.9 eV binding energy is associated with the carboxylate moiety of the organic ligand of MOF samples.⁴⁵ The Ni 2p emission spectrum shows two distinct nickel species, Ni^{2+} and Ni^{3+} . The Ni 2p spectra were deconvoluted into two spin–orbit doublets ($\text{Ni } 2p_{1/2}$ and $\text{Ni } 2p_{3/2}$) and two satellite peaks using the Gaussian fitting method, as shown in Figure 9g,h. The peak fitted at binding energies of 855.9 and 873.4 eV are ascribed to $\text{Ni } 2p_{3/2}$ and $\text{Ni } 2p_{1/2}$ for BDC–MOF. Similarly, the binding energies of $\text{Ni } 2p_{3/2}$ and $\text{Ni } 2p_{1/2}$ for BTC–MOF are 856.2 and 873.6 eV, respectively, as illustrated in Figure 9h. The spin–orbital energy of the Ni peaks in two MOF slightly differs. First, the binding energy difference between these two

peaks is determined to be 17.5 eV for BDC–MOF, and the binding energy peak of the “Ni” element was shifted at lower binding energy, i.e., 17.4 eV may be due to the acidic behavior for BTC MOF.

The satellite peaks, as shown in Figure 9i,j, indicate two types of Co species, comprising Co^{2+} and Co^{3+} for two spin–orbit doublets ($\text{Co } 2p_{1/2}$ and $\text{Co } 2p_{3/2}$), which were observed as a result of fitting the Co 2p emission spectra of both the MOFs. The fitted peaks with binding energy of 781.0 and 796.8 eV indicate the $\text{Co } 2p_{3/2}$ and $\text{Co } 2p_{1/2}$, respectively, for the BDC–MOF sample. The Co peak spin–orbital energies in two MOFs varied slightly from one another. For BDC–MOF, the binding energy difference between these two peaks spin–orbital coupling is found to be 15.8 eV, and the “Co” element’s binding energy peak was relocated to a lower binding energy for BTC MOF, i.e., 15.7 eV. Again the peaks at 781.4 and 797.1 eV are associated to the $\text{Co } 2p_{3/2}$ and $\text{Co } 2p_{1/2}$ for the BTC–MOF sample. The other satellite peaks of Co elements for both the MOFs samples are also observed in Figure 9i,j.^{46–48} The peaks at binding energy 1021.8 and 1022.0 eV are assigned to the energy level $\text{Zn } 2p_{3/2}$ in BDC–MOF and BTC–MOF, respectively. Similarly, the peaks at 1044.8 and 1045.1 eV are observed for $\text{Zn } 2p_{1/2}$ for BDC–MOF and BTC–MOF, respectively. The detailed deconvolution peaks of $\text{Zn } 2p_{3/2}$ and $\text{Zn } 2p_{1/2}$ are observed in Figure 9k,l. The differences between the spin–orbital energy of both the MOF samples are nearly equal, confirming that prepared samples are well matched with the literature value of XPS.^{49–51} The calculated binding energy difference among these two peaks spin–orbital coupling is 23 eV, which is in good accordance with the literature value. Moreover, the difference between the spin–orbital energy of the BTC–MOF sample is slightly changed which may be due to the more acidic nature of the BTC–MOF sample.

The electrochemical characteristics of the MOF samples were assessed to determine their suitability for usage as active materials in supercapacitors. CV measurements of the as-synthesized MOF hybrid structures with various organic ligands (trimesic acid and terephthalic acid) were performed in a 2 M KOH electrolyte in a potential sweep window of 0–0.5 V, as shown in Figure 10. The CV curves of trimetallic MOFs reveal that the integral areas change throughout the operating potential range at 0–0.5 V, indicating that the charge storage mechanism is both pseudocapacitive and electric double layer type. The capacitance is mostly due to the charge stored at the electrode–electrolyte interface. The region

beneath the CV curve of BDC–MOF is larger than that of BTC–MOF, as shown in Figure 10a.

In the potential range of 0–0.5 V, the GCD profiles (Figure 10b) were examined at a current density of 5 mA cm⁻². As predicted, compared to the BTC–MOF electrode, the BDC–MOF electrode displayed a significantly longer charge/discharge time and increased specific capacitance. A comparison of the CV curves of both trimetallic MOFs, i.e., BDC–MOF and BTC–MOF (Figure 10c,d) at a different scan rate was performed in the potential range of 0–0.5 V. As the scan rate decreases, the area under the CV curve decreases; hence, specific capacitance increases. This occurs due to the complete diffusion of electrolyte ions into the electrode material at slower scan rates. Hence, a charge on the whole active surface of the electrode material may be stored. Only the superficial active surface is used for charge storage at a higher scan rate because diffusion limits the passage of electrolyte ions.⁵² The area under the curve grows from 0 to 0.5 V with a broad range of scan rates from 10 to 100 mV s⁻¹, indicating rapid rates of ionic and electronic transport at the electrode/electrolyte interfaces. The GCD characteristics of BDC–MOF and BTC–MOF electrodes were investigated at current densities ranging from 5 to 25 mA cm⁻² in 2 M KOH electrolyte across a potential range of 0–0.5 V (Figure 10e,f).

EIS measurements were performed to determine the internal resistive characteristics as well as the capacitive behavior of the MOF electrode. The Nyquist plots of MOFs in 2 M KOH electrolyte are shown in Figure 11a. A straight line detected in the lower-frequency portion of the Nyquist plot was due to the migration of electrolyte ions from the bulk solution to the electrode surface. The charge-transfer activity at the electrode/electrolyte interface is responsible for the presence of a semicircle in the high-frequency zone, and the semicircle diameter shows the charge-transfer resistance (R_{ct}). The charge-transfer resistance of BDC–MOF and BTC–MOF is 0.19 and 0.46 Ω , respectively. BDC–MOF (0.19 Ω) has a lower charge-transfer resistance than BTC–MOF (0.46 Ω). These R_{ct} values show that both electrodes have high electrical conductivities, which are connected to the presence of carbon in their composition, which increases the conductivity of the manufactured electrode. In practice, the carbon in the electrode structure reduces the resistance to charge transfer and improves the connectivity between the active sites for electron transfer.⁵³ Figure 11b depicts the change of specific capacitance as a function of current density, and Figure 11c depicts the Ragone plot of energy density vs power density for both trimetallic MOFs. The specific capacitance of the BDC–MOF electrode is 582.8 F g⁻¹ at 5 mA cm⁻² current density, which is more than the specific capacitance of the BTC–MOF electrode, which has 413.4 F g⁻¹ at 5 mA cm⁻² current density, according to the GCD curves. The examined BDC–MOF and BTC–MOF electrodes exhibit a longer charge and discharge time with lowering currents, resulting in greater specific capacitance values, implying that as current increases, the specific capacitance falls in typical behavior. Trimesic acid and terephthalic acid have pK_a values of 3.14 and 4.82, respectively. Trimesic acid has a low pK_a value, which makes it act as a strong acid since it has a high acidity.⁵⁴ Due to the high acidity, the BTC–MOF electrode gets etched, which degrades the deposition of the film that clogs the pores and prevents the electrolyte from entering the electrode material, increasing resistance and lowering specific capacitance. The cluster of nanoplates that comprise the porous brick-like morphology of

BDC–MOF operate as an “ion-buffering reservoir”, enhancing charge–discharge and shortening the diffusion length for ions to enter the electrode. The charging/discharging curves are also affected by the trimesic and terephthalic ligands; the nature of the curves differs for BDC–MOF and BTC–MOF.

To examine the cycling stability of the MOF electrodes, the specific capacitance as a function of cycle number was measured at a prolonged current density of 25 mA cm⁻². The BDC–MOF electrode demonstrated good cycling stability after 3000 continuous cycles, with about 92.44% retention of the original capacitance (Figure 12). This

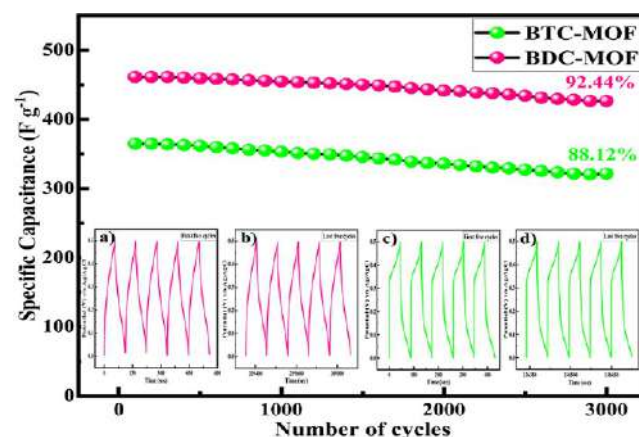


Figure 12. Cycling performance at 25 mA cm⁻², and the inset shows the first and last five cycles of BDC–MOF and BTC–MOF.

exceptional long-cycle lifespan was greater than that of the BTC–MOF, which has 88.12% retention even after 3000 GDC cycles at a current density of 25 mA cm⁻², as shown in Figure 12. On 1D stainless-steel mesh substrate with substantially poorer electrical conductivity, BDC–MOF demonstrated a remarkable specific capacity of 528.8 F g⁻¹. At all the current densities, the specific capacity of BDC–MOF was relatively high, and a reversible capacity of 461.2 F g⁻¹ can be sustained at an extremely high current density of 25 mA cm⁻², with 86.14% capacity retention compared to the capacity at 5 mA cm⁻², showing a high rate capability. The increase in the cycle number causes a drop in specific capacitance due to the partial leaching of the active electrode material during faradic operations.⁵⁵ The remarkable energy storage efficiency can be attributed to the combined impact of a group of nanoplates forming the porous bricks, such as morphology, and the huge SSA of the extremely porous material. The electrochemical performance of a few different MOFs that have been previously characterized is compared to that of the synthesized trimetallic MOF in Table 1.

A SSC device was assembled with BDC–MOF for both electrodes and PVA/KOH gel both as the separator and electrolyte to further evaluate the practical application of the BDC–MOF. The slurry coating method was used to prepare both electrodes. In short, the slurry was made by combining 80 mg of active material (BDC–MOF), 10 mg of PVDF, and 10 mg of carbon black in 0.5 mL of the NMP solvent. The appropriate volume of slurry was then dispersed onto a 2 × 2 cm flexible stainless-steel mesh and air-dried overnight at 60 °C. To avoid electrical contact, the electrode borders were first made non-conducting using a band. The PVA–KOH gel was applied to one side of the electrode, resulting in one point of electrical contact. Both electrodes were eventually patched

Table 1. Comparison of the Specific Capacitances of Trimetallic MOFs with Previously Reported Materials

sr. no.	material	electrolyte	substrate	specific capacitance	current density	stability (%)	refs
1	NiCoMn-MOF	3 M KOH	nickel foam	907.4 C g ⁻¹	1 A g ⁻¹	64.7	56
2	ZnNi-MOF	3 M KOH	nickel foam	466.5 F g ⁻¹	0.5 A g ⁻¹	44.0	57
3	NiCo-MOF	1 M KOH	nickel foam	1107.3 F g ⁻¹	1 A g ⁻¹	70.1	58
4	Ni/Co-MOF	6 M KOH	nickel foam	982.5 F g ⁻¹	0.5 A g ⁻¹	84.0	59
5	NiCoZn-MOF	2 M KOH	stainless-steel mesh	582.8 F g ⁻¹	5 mA cm ⁻²	92.44	this work

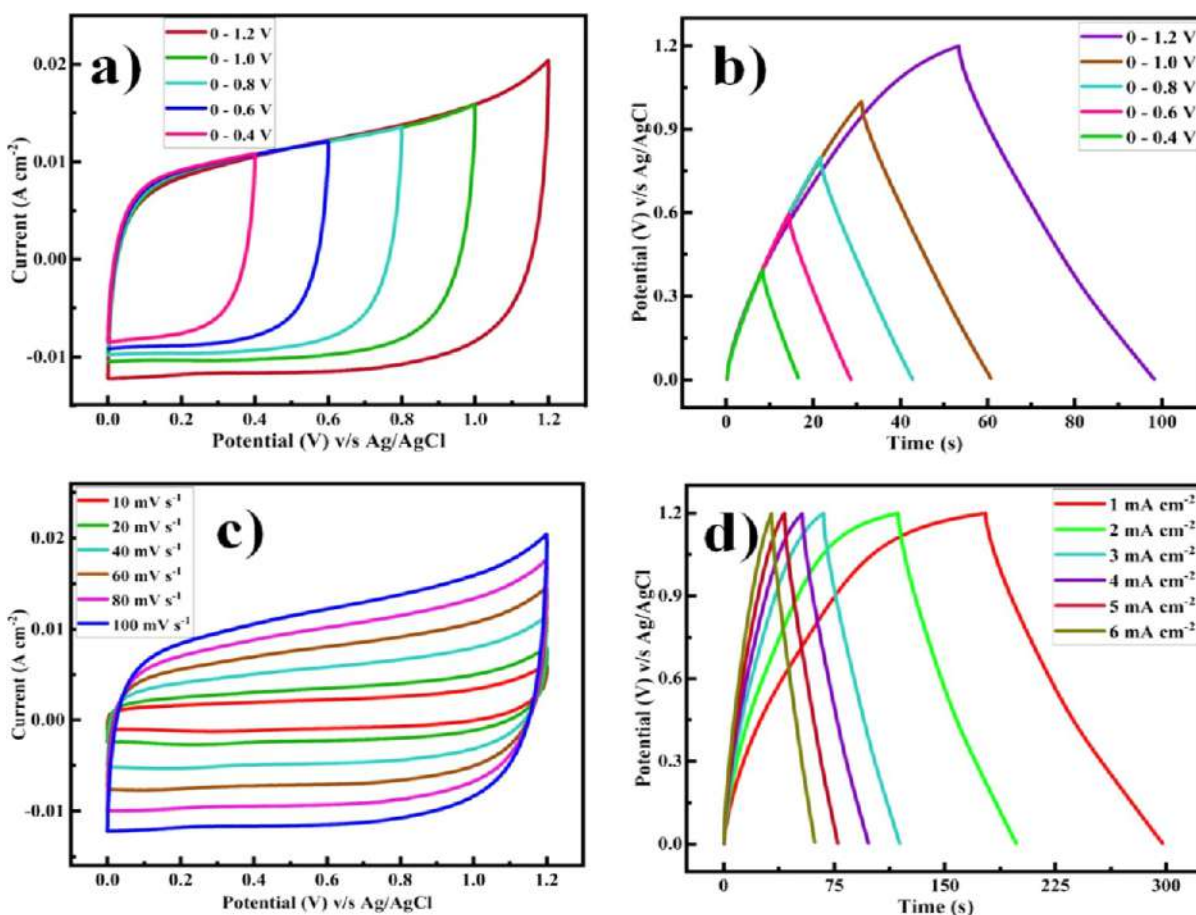


Figure 13. (a) CV, (b) GCD curves of the symmetric device within the various potential windows (0.4, 0.6, 0.8, 1.0, and 1.2 V), (c) CV curves of the symmetric device at different scan rates, and (d) GCD curves of the symmetric device at different current densities.

together in the shape of a sandwich, with gel-pasted sides facing each other. For 12 h, the device was subjected to 1-ton pressure to establish a strong connection between the electrodes and gel electrolyte and to eliminate the air gap. Following that, the device was utilized to evaluate electrochemical performance. CV, GCD, and EIS measurements were performed to examine the performance of the assembled SSC device. The assembled SSC device CV curves displayed ideal rectangular shapes within an operating voltage window 0.4–1.2 V, demonstrating excellent capacitive behavior. Figure 13a,b displays CV and GCD profiles of the SSC device within various potential windows and exhibits excellent linear slopes and triangular shapes, which suggest ideal capacitive behavior in line with the CV curves.

In practice, the SSC device's potential window can reach 1.2 V without causing significant changes in the CV and GCD curves, signifying outstanding electrochemical stability. Figure 13c depicts the SSC device's CV curves at various scan rates. The CV curves remained consistent when the scan rate was

raised from 10 mV s⁻¹ to 100 mV s⁻¹; however, the closed regions grew, confirming the symmetric device's high rate capacity. Furthermore, the GCD curves of the SSC device at various current densities are shown in Figure 13d, and the nearly symmetric charge/discharge curves indicate excellent rate capability.

The EIS studies show that the fabricated SSC device has good electrical conductivity with low ionic resistance and a charge-transfer resistance of 0.4 Ω, as depicted in Figure 14a. As a result, the small semicircle diameter reveals low charge-transfer resistance and excellent conductivity. The specific capacities calculated from the discharge curves at current densities of 1, 2, 3, 4, 5, and 6 mA cm⁻² were 94.92, 93.56, 91.83, 90.67, 89.44, and 87.74 F g⁻¹, respectively (Figure 14b). Figure 14c depicts the Ragone plot of the SSC device, and also the SSC device delivers a high energy density of 47.59 W h kg⁻¹ at a power density of 1367.42 W kg⁻¹. Additionally, at a current density of 6 mA cm⁻², the SSC device exhibits outstanding cycling performance, with 99.26% capacitance

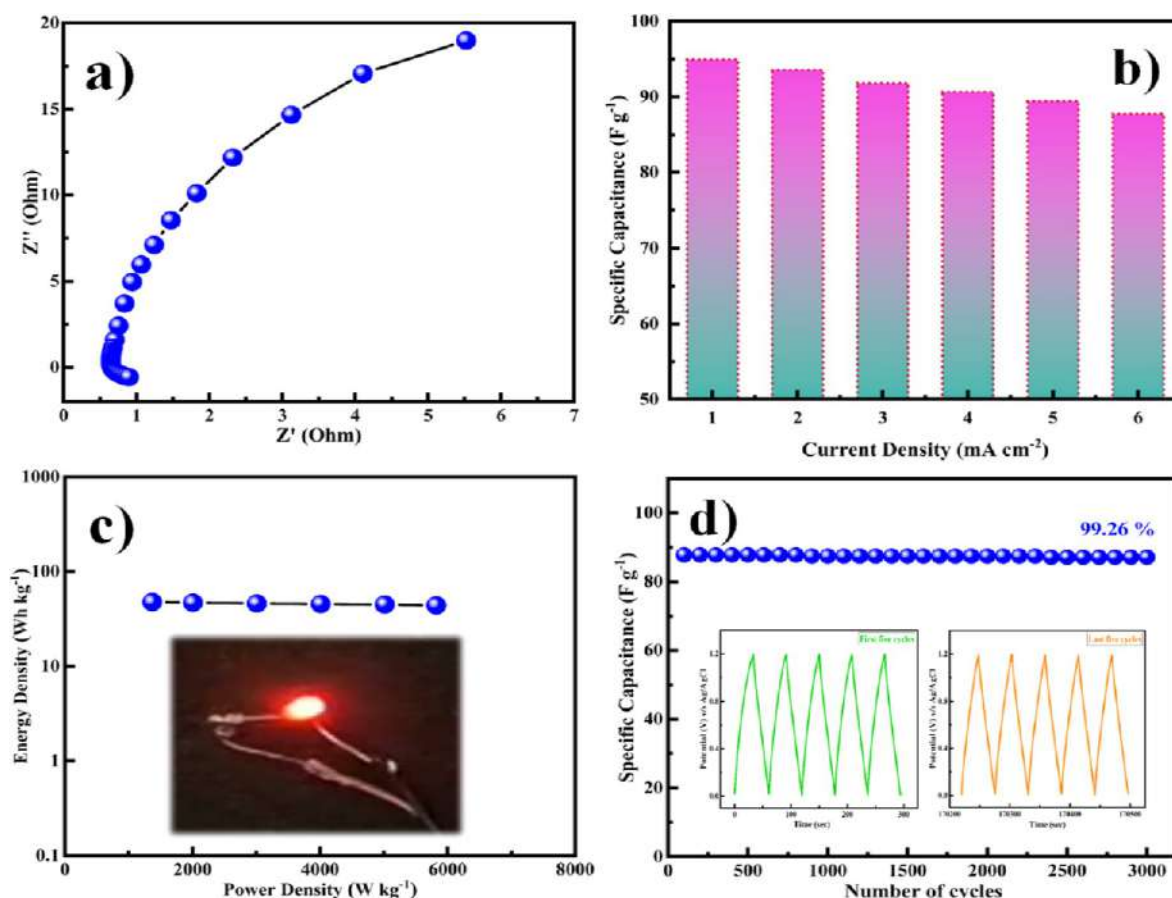


Figure 14. (a) Nyquist plot, (b) variation of specific capacitance as a function of current density, (c) Ragone plot showing the energy density versus power density, and (d) cycling performance at 6 mA cm^{-2} , and the inset shows the first and last five cycles of the symmetric device.

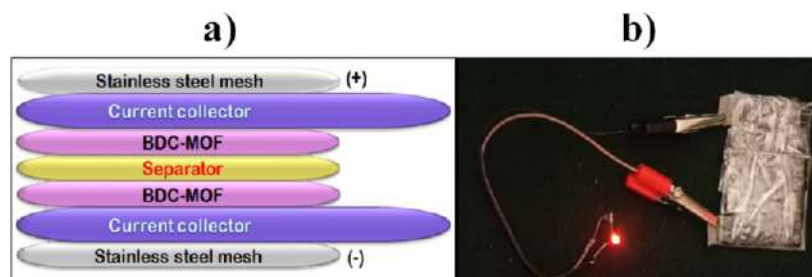


Figure 15. (a) Fabrication schematic of the BDC-MOF//2 M KOH//BDC-MOF SSC device. (b) Two handmade SSC devices which glow a red LED.

retention even after 3000 cycles (Figure 14d). Power density and energy density are critical parameters for assessing the supercapacitor electrochemical performance. The BDC-MOF architecture exceptional electrochemical performance is due to its distinct hierarchical structure. Good electrochemical activity is ensured by the uniform distribution of the brick-like morphology of the nanoplates, and the electrolyte's hierarchical structure offers a high SSA that can make sufficient contact with the electrolyte and enhance ion transport. Finally, the distinct hierarchical structure of the BDC-MOF architecture reduces volume expansion during the cycle process, improving structural integrity and enhancing cycle stability.

The lighting red light-emitting diode (LED) shows that how our SSC device can be used in real applications by connecting two of them in series (where each device is of size $2 \times 2 \text{ cm}$). Figure 15a shows the schematic presentation of the SSC

device, and Figure 15b displays the device's digital image. The LED was glowing brilliantly for about a minute after the device had been charged for just 2 s, demonstrating the astonishing application of our solid-state SSC devices (Supporting Information). The developed capacitor is suitable for use in real-world energy storage and transfer applications because the discharge time is longer than the charging time.

The electrochemical behavior of chemically produced trimetallic MOFs was compared using a radar graph, as shown in Figure 16. Each vertex indicates the properties of the different trimetallic MOFs, such as crystallite size, specific capacitance, energy density, power density, stability, charge-transfer resistance, SSA, and average pore radius. The electrochemical performance of trimetallic MOFs is represented by the integral area under the curve. According to Figure 16, the integral area of BDC-MOF is greater than that

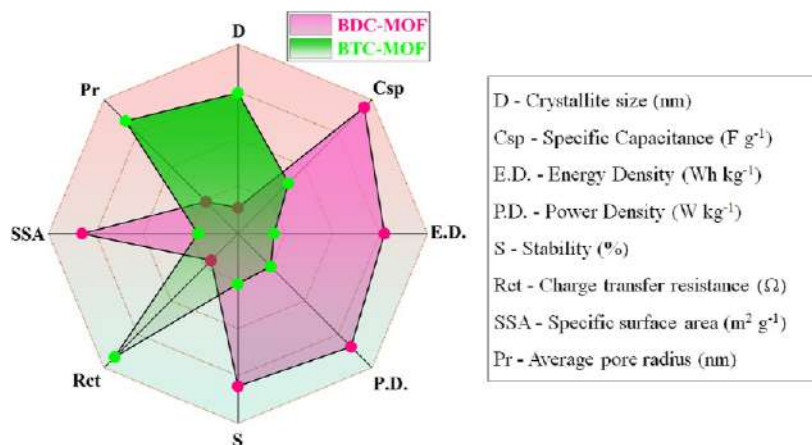


Figure 16. Radar graph for the comparative study of BDC–MOF and BTC–MOF based on supercapacitive properties.

of BTC–MOF. It has been established that the BDC–MOF small crystallite size, large SSA, and low charge-transfer resistance come up with increased specific capacitance, energy density, power density, and cycle stability.

CONCLUSIONS

In outline, a novel 2D architecture of trimetallic MOFs (BDC–MOF and BTC–MOF) as supercapacitor electrode materials was successfully prepared by the reflux condensation method which is simple, low cost, and environmentally friendly. The effects of different ligands of MOFs on the structural, surface, and electrochemical performance of MOF samples have been studied systematically. Due to their nanoplate-like structures with good mechanical and electrical contact, rich redox reactions, low crystallinity, good tuneability, high conductivity and transport rate for both electrolyte ions and electrons, and lower acidity, BDC–MOFs exhibit improved electrochemical performance. The BDC–MOFs show higher capacitance due to the synergistic effect, also they exhibit pseudocapacitive behavior due to the redox activity of metal cations inside MOFs, which offers a channel for electrons, as well as EDLC behavior due to the organic linker structure, which facilitates charge transfer within the framework. The BDC–MOF electrode material achieves a good SSA of $265.87 \text{ m}^2 \text{ g}^{-1}$, specific capacity of 582.8 F g^{-1} at a current density of 5 mA cm^{-2} , and exceptional cycling stability with 92.44% retention after 3000 cycles at 25 mA cm^{-2} due to its porous nature and adequate SSA. The SSC device BDC–MOF//BDC–MOF was built with the BDC–MOF as both electrodes have a high energy density of $47.59 \text{ W h kg}^{-1}$ at a power density of $1367.42 \text{ W kg}^{-1}$ and exceptional cycling stability with 99.26% capacitance retention over 3000 cycles. This novel 2D trimetallic MOF electrode synthesis technique throws light on prospective high-performance MOF-based electrode materials, with the generated BDC–MOF serving as a promising electrode material for better energy storage devices. It is necessary to further enhance the MOF thermal, mechanical, and chemical stability. Since most MOFs decompose and have their skeletons collapse in water, acid, or base, their widespread use in energy storage applications has been severely hampered. Sensible selection of organic ligands and metal secondary building blocks can overcome this issue. The inherent fragility and finite processability of MOFs may also be overcome by using novel methods, such as pressing and

phase change treatment operations, without changing their original properties.

ASSOCIATED CONTENT

Supporting Information

The Supporting Information is available free of charge at <https://pubs.acs.org/doi/10.1021/acs.langmuir.3c01337>.

LED glow using fabricated solid-state SSC devices (MP4)

AUTHOR INFORMATION

Corresponding Author

Sanjay Kolekar – Analytical Chemistry and Material Science Research Laboratory, Department of Chemistry, Shivaji University, Kolhapur 416 004, India; orcid.org/0000-0002-4367-6014; Email: sskolekar@gmail.com

Authors

Rakhee Bhosale – Analytical Chemistry and Material Science Research Laboratory, Department of Chemistry, Shivaji University, Kolhapur 416 004, India

Sneha Bhosale – Analytical Chemistry and Material Science Research Laboratory, Department of Chemistry, Shivaji University, Kolhapur 416 004, India

Dattatray Narale – Analytical Chemistry and Material Science Research Laboratory, Department of Chemistry, Shivaji University, Kolhapur 416 004, India

Chitra Jambhale – Analytical Chemistry and Material Science Research Laboratory, Department of Chemistry, Shivaji University, Kolhapur 416 004, India

Complete contact information is available at: <https://pubs.acs.org/10.1021/acs.langmuir.3c01337>

Author Contributions

R.B.: Formal analysis, investigation, methodology, and writing—original draft; S.B.: data curation; D.N.: discussion and review; C.J.: editing of the draft; and S.K.: conceptualization, supervision, and funding acquisition.

Notes

The authors declare no competing financial interest.

ACKNOWLEDGMENTS

The authors are thankful to UGC-SAP, DST-FIST, and DST-PURSE for the financial support and instrument facilities at the

Department of Chemistry, Shivaji University, Kolhapur. One of the author (R.B.) is thankful to SARTHI, Government of Maharashtra, India, for the “Chhatrapati Shahu Maharaj National Research Fellowship-2021”.

REFERENCES

- (1) Wei, C.; Tan, L.; Zhang, Y.; Wang, Z.; Xi, B.; Xiong, S.; Feng, J. Interfacial Engineering on Metal Anodes in Rechargeable Batteries. *EnergyChem* **2022**, *4*, 100089–100120.
- (2) Ray, A.; Roy, A.; Saha, S.; Ghosh, M.; Roy Chowdhury, S.; Maiyalagan, T.; Bhattacharya, S. K.; Das, S. Electrochemical Energy Storage Properties of Ni-Mn-Oxide Electrodes for Advance Asymmetric Supercapacitor Application. *Langmuir* **2019**, *35*, 8257–8267.
- (3) Swain, N.; Saravanakumar, B.; Kundu, M.; Schmidt-Mende, L.; Ramadoss, A. Recent Trends in Template Assisted 3D Porous Materials for Electrochemical Supercapacitors. *J. Mater. Chem. A* **2021**, *9*, 25286–25324.
- (4) Katkar, P. K.; Marje, S. J.; Parale, V. G.; Lokhande, C. D.; Gunjekar, J. L.; Park, H. H.; Patil, U. M. Fabrication of a High-Performance Hybrid Supercapacitor Based on Hydrothermally Synthesized Highly Stable Cobalt Manganese Phosphate Thin Films. *Langmuir* **2021**, *37*, 5260–5274.
- (5) Mehek, R.; Iqbal, N.; Noor, T.; Amjad, M. Z. B.; Ali, G.; Vignarooban, K.; Khan, M. A. Metal-Organic Framework Based Electrode Materials for Lithium-Ion Batteries: A Review. *RSC Adv.* **2021**, *11*, 29247–29266.
- (6) Zhao, X.; Bi, Q.; Yang, C.; Tao, K.; Han, L. Design of Trimetallic Sulfide Hollow Nanocages from Metal-Organic Frameworks as Electrode Materials for Supercapacitors. *Dalton Trans.* **2021**, *50*, 15260–15266.
- (7) Chatterjee, D. P.; Nandi, A. K. A Review on the Recent Advances in Hybrid Supercapacitors. *J. Mater. Chem. A* **2021**, *9*, 15880–15918.
- (8) Sun, Y. A.; Chen, L. T.; Hsu, S. Y.; Hu, C. C.; Tsai, D. H. Silver Nanoparticles-Decorating Manganese Oxide Hybrid Nanostructures for Supercapacitor Applications. *Langmuir* **2019**, *35*, 14203–14212.
- (9) Tafete, G. A.; Abera, M. K.; Thothadri, G. Review on Nanocellulose-Based Materials for Supercapacitors Applications. *J. Energy Storage* **2022**, *48*, 103938–103953.
- (10) Song, W.; Teng, X.; Liu, Y.; Wang, J.; Niu, Y.; He, X.; Zhang, C.; Chen, Z. Rational Construction of Self-Supported Triangle-like MOF-Derived Hollow (Ni,Co)Se₂ Arrays for Electrocatalysis and Supercapacitors. *Nanoscale* **2019**, *11*, 6401–6409.
- (11) Bai, Y.; Liu, C.; Chen, T.; Li, W.; Zheng, S.; Pi, Y.; Luo, Y.; Pang, H. MXene-Copper/Cobalt Hybrids via Lewis Acidic Molten Salts Etching for High Performance Symmetric Supercapacitors. *Angew. Chem., Int. Ed.* **2021**, *60*, 25318–25322.
- (12) Acharya, J.; Ojha, G. P.; Pant, B.; Park, M. Construction of Self-Supported Bimetallic MOF-Mediated Hollow and Porous Trimetallic Selenide Nanosheet Arrays as Battery-Type Electrodes for High-Performance Asymmetric Supercapacitors. *J. Mater. Chem. A* **2021**, *9*, 23977–23993.
- (13) Cheng, X.; Pan, J.; Zhao, Y.; Liao, M.; Peng, H. Gel Polymer Electrolytes for Electrochemical Energy Storage. *Adv. Energy Mater.* **2018**, *8*, 1702184–2170220.
- (14) Lu, X.; Yu, M.; Wang, G.; Tong, Y.; Li, Y. Flexible Solid-State Supercapacitors: Design, Fabrication and Applications. *Energy Environ. Sci.* **2014**, *7*, 2160–2181.
- (15) Yin, X.; Li, H.; Yuan, R.; Lu, J. Hierarchical Self-Supporting Sugar Gourd-Shape MOF-Derived NiCo₂O₄ Hollow Nanocages@SiC Nanowires for High-Performance Flexible Hybrid Supercapacitors. *J. Colloid Interface Sci.* **2021**, *586*, 219–232.
- (16) Tahir, M. U.; Arshad, H.; Zhang, H.; Hou, Z.; Wang, J.; Yang, C.; Su, X. Room Temperature and Aqueous Synthesis of Bimetallic ZIF Derived CoNi Layered Double Hydroxides and Their Applications in Asymmetric Supercapacitors. *J. Colloid Interface Sci.* **2020**, *579*, 195–204.
- (17) Li, W.; Guo, X.; Geng, P.; Du, M.; Jing, Q.; Chen, X.; Zhang, G.; Li, H.; Xu, Q.; Braunstein, P.; Pang, H. Rational Design and General Synthesis of Multimetallic Metal–Organic Framework Nano-Octahedra for Enhanced Li–S Battery. *Adv. Mater.* **2021**, *33*, 2105163–2105169.
- (18) Zheng, S.; Li, Q.; Xue, H.; Pang, H.; Xu, Q. A Highly Alkaline-Stable Metal Oxide@metal-Organic Framework Composite for High-Performance Electrochemical Energy Storage. *Natl. Sci. Rev.* **2020**, *7*, 305–314.
- (19) Jiao, Y.; Pei, J.; Chen, D.; Yan, C.; Hu, Y.; Zhang, Q.; Chen, G. Mixed-Metallic MOF Based Electrode Materials for High Performance Hybrid Supercapacitors. *J. Mater. Chem. A* **2017**, *5*, 1094–1102.
- (20) Akhter, S.; Mohd Zain, N. K.; Shalauddin, M.; Singh, V. K.; Misnon, I. I.; Sharma, R. K.; Das, S.; Basirun, W. J.; Johan, M. R.; Jose, R. Tri-Metallic Co-Ni-Cu Based Metal Organic Framework Nanostructures for the Detection of an Anticancer Drug Nilutamide. *Sens. Actuators, A* **2021**, *325*, 112711–112722.
- (21) Makgopa, K. ScienceDirect Electrochemistry Intrinsic Properties of Metal – Organic Frameworks (MOFs) in Supercapacitor Applications. *Curr. Opin. Electrochem.* **2022**, *36*, 101112–101121.
- (22) Kang, C.; Ma, L.; Chen, Y.; Fu, L.; Hu, Q.; Zhou, C.; Liu, Q. Metal-Organic Framework Derived Hollow Rod-like NiCoMn Ternary Metal Sulfide for High-Performance Asymmetric Supercapacitors. *Chem. Eng. J.* **2022**, *427*, 131003–131013.
- (23) Taherinia, D.; Hatami, H.; Valadi, F. M. Trimetallic Co-Ni-Mn Metal-Organic Framework as an Efficient Electrocatalyst for Alkaline Oxygen Evolution Reaction. *J. Electroanal. Chem.* **2022**, *922*, 116720–116729.
- (24) Han, X. G.; Wang, P. F.; Zhang, Y. H.; Liu, H. Y.; Tang, J. J.; Yang, G.; Shi, F. N. Addition of Dissimilar Metal Nodes to Improve the Electrochemical Performance of MOF as a Supercapacitor. *Inorg. Chim. Acta.* **2022**, *536*, 120916–120927.
- (25) Zhang, B.; Song, S.; Li, W.; Zheng, L.; Ma, X. Asymmetric Supercapacitors with High Energy Density and High Specific Capacitance Based on Ni-Co-Mn Multiphase Metal Structure MOF. *Ionics* **2021**, *27*, 3553–3566.
- (26) Luo, X.; Abazari, R.; Tahir, M.; Fan, W. K.; Kumar, A.; Kalthorizadeh, T.; Kirillov, A. M.; Amani-Ghadim, A. R.; Chen, J.; Zhou, Y. Trimetallic Metal–Organic Frameworks and Derived Materials for Environmental Remediation and Electrochemical Energy Storage and Conversion. *Coord. Chem. Rev.* **2022**, *461*, 214505–214529.
- (27) Wang, H.; Li, J.; Li, K.; Lin, Y.; Chen, J.; Gao, L.; Nicolosi, V.; Xiao, X.; Lee, J. M. Transition Metal Nitrides for Electrochemical Energy Applications. *Chem. Soc. Rev.* **2021**, *50*, 1354–1390.
- (28) Rajak, R.; Kumar, R.; Ansari, S. N.; Saraf, M.; Mobin, S. M. Recent Highlights and Future Prospects on Mixed-Metal MOFs as Emerging Supercapacitor Candidates. *Dalton Trans.* **2020**, *49*, 11792–11818.
- (29) Seo, Y.; Shinde, P. A.; Park, S.; Chan Jun, S. Self-Assembled Bimetallic Cobalt–Manganese Metal–Organic Framework as a Highly Efficient, Robust Electrode for Asymmetric Supercapacitors. *Electrochim. Acta* **2020**, *335*, 135327–135336.
- (30) Nagaraju, G.; Sekhar, S. C.; Ramulu, B.; Hussain, S. K.; Narsimulu, D.; Yu, J. S. Ternary MOF-Based Redox Active Sites Enabled 3D-on-2D Nanoarchitected Battery-Type Electrodes for High-Energy-Density Supercapacitors. *Nano-Micro Lett.* **2021**, *13*, 17–18.
- (31) Andikaey, Z.; Ensafi, A. A.; Rezaei, B.; Malek, S. S.; Hu, J. S. MWCNT-Mesoporous Silica Nanocomposites Inserted in a Polyhedral Metal-Organic Framework as an Advanced Hybrid Material for Energy Storage Device. *New J. Chem.* **2021**, *45*, 18090–18101.
- (32) Bhosale, R.; Bhosale, S.; Kumbhar, P.; Narale, D.; Ghaware, R.; Jambhale, C.; Kolekar, S. Design and Development of a Porous Nanorod-Based Nickel-Metal–Organic Framework (Ni-MOF) for High-Performance Supercapacitor Application. *New J. Chem.* **2023**, *47*, 6749–6758.
- (33) Liu, S.; Lee, S. C.; Patil, U.; Shackery, I.; Kang, S.; Zhang, K.; Park, J. H.; Chung, K. Y.; Jun, S. C. Hierarchical MnCo-Layered

Double Hydroxides@Ni(OH)₂ Core-Shell Heterostructures as Advanced Electrodes for Supercapacitors. *J. Mater. Chem. A* **2017**, *5*, 1043–1049.

(34) Vijeth, H.; Ashokkumar, S. P.; Yesappa, L.; Niranjana, M.; Vandana, M.; Devendrappa, H. Flexible and High Energy Density Solid-State Asymmetric Supercapacitor Based on Polythiophene Nanocomposites and Charcoal. *RSC Adv.* **2018**, *8*, 31414–31426.

(35) Gopi, S.; Perumal, S.; Al Olayan, E. M.; AlAmri, O. D.; Aloufi, A. S.; Kathiresan, M.; Yun, K. 2D Trimetal-Organic Framework Derived Metal Carbon Hybrid Catalyst for Urea Electro-Oxidation and 4-Nitrophenol Reduction. *Chemosphere* **2021**, *267*, 129243–129254.

(36) Li, Y.; Lu, M.; Wu, Y.; Xu, H.; Gao, J.; Yao, J. Trimetallic Metal–Organic Framework Derived Carbon-Based Nanoflower Electrocatalysts for Efficient Overall Water Splitting. *Adv. Mater. Interfaces* **2019**, *6*, 1900290–1900298.

(37) Vadiyar, M. M.; Kolekar, S. S.; Deshpande, N. G.; Chang, J. Y.; Kashale, A. A.; Ghule, A. V. Binder-Free Chemical Synthesis of ZnFe₂O₄ Thin Films for Asymmetric Supercapacitor with Improved Performance. *Ionics* **2017**, *23*, 741–749.

(38) Gupta, N. K.; Kim, S.; Bae, J.; Kim, K. S. Chemisorption of Hydrogen Sulfide over Copper-Based Metal-Organic Frameworks: Methanol and UV-Assisted Regeneration. *RSC Adv.* **2021**, *11*, 4890–4900.

(39) You, S.-M.; El Roubi, W. M. A.; Assaud, L.; Doong, R.-A.; Millet, P. Water Photo-Electrooxidation Using Mats of TiO₂ Nanorods, Surface Sensitized by a Metal–Organic Framework of Nickel and 1,2-Benzene Dicarboxylic Acid. *Hydrogen* **2021**, *2*, 58–75.

(40) Li, H.; Qin, J.; Zhang, Y.; Xu, S.; Du, J.; Tang, J. The Efficiency and Mechanism of Dibutyl Phthalate Removal by Copper-Based Metal Organic Frameworks Coupled with Persulfate. *RSC Adv.* **2018**, *8*, 39352–39361.

(41) Zha, Q.; Li, M.; Liu, Z.; Ni, Y. Hierarchical Co,Fe-MOF-74/Co/Carbon Cloth Hybrid Electrode: Simple Construction and Enhanced Catalytic Performance in Full Water Splitting. *ACS Sustain. Chem. Eng.* **2020**, *8*, 12025–12035.

(42) Nguyen, V. H.; Nguyen, T. D.; Van Nguyen, T. Microwave-Assisted Solvothermal Synthesis and Photocatalytic Activity of Bismuth(III) Based Metal–Organic Framework. *Top. Catal.* **2020**, *63*, 1109–1120.

(43) Kaur, R.; Chhibber, M.; Mahata, P.; Mittal, S. K. Induction of Catalytic Activity in ZnO Loaded Cobalt Based MOF for the Reduction of Nitroarenes. *ChemistrySelect* **2018**, *3*, 3417–3425.

(44) Sing, K. S. W.; Everett, D. H.; Haul, R. A. W.; Moscou, L.; Pierotti, R. A.; Rouquerol, J.; Siemieniowska, T. Reporting physisorption data for gas/solid systems with special reference to the determination of surface area and porosity (Recommendations 1984). *Pure Appl. Chem.* **1985**, *57*, 603–619.

(45) Zain, N. K. M.; Karuppiyah, C.; Misnon, I. I.; Das, S.; Ozoemena, K. I.; Yang, C. C.; Jose, R. High Capacity and Rate Capability Binder-Less Ternary Transition Metal-Organic Framework as Anode Material for Lithium-Ion Battery. *Electroanalysis* **2020**, *32*, 3180–3188.

(46) Beka, L. G.; Bu, X.; Li, X.; Wang, X.; Han, C.; Liu, W. A 2D Metal-Organic Framework/Reduced Graphene Oxide Heterostructure for Supercapacitor Application. *RSC Adv.* **2019**, *9*, 36123–36135.

(47) Shu, H.; Lai, T.; Ren, J.; Cui, X.; Tian, X.; Yang, Z.; Xiao, X.; Wang, Y. Trimetallic Metal-Organic Frameworks (Fe, Co, Ni-MOF) Derived as Efficient Electrochemical Determination for Ultra-Micro Imidacloprid in Vegetables. *Nanotechnology* **2022**, *33*, 135502–135517.

(48) Thangasamy, P.; Shanmuganathan, S.; Subramanian, V. A NiCo-MOF Nanosheet Array Based Electrocatalyst for the Oxygen Evolution Reaction. *Nanoscale Adv.* **2020**, *2*, 2073–2079.

(49) Wu, Y.; Song, X.; Xu, S.; Chen, Y.; Oderinde, O.; Gao, L.; Wei, R.; Xiao, G. Chemical Fixation of CO₂ into Cyclic Carbonates Catalyzed by Bimetal Mixed MOFs: The Role of the Interaction between Co and Zn. *Dalton Trans.* **2020**, *49*, 312–321.

(50) Lin, J.; Zeng, C.; Lin, X.; Reddy, R. C. K.; Niu, J.; Liu, J.; Cai, Y. Trimetallic MOF-Derived Cu_{0.39}Zn_{0.14}Co_{2.47}O₄-CuO Interwoven with Carbon Nanotubes on Copper Foam for Superior Lithium Storage with Boosted Kinetics. *ACS Sustain. Chem. Eng.* **2019**, *7*, 15684–15695.

(51) Wei, Y.; Zhang, Y.; Chen, J. S.; Mao, C.; Jin, B. K. An Electrochemiluminescence Biosensor for P53 Antibody Based on Zn-MOF/GO Nanocomposite and Ag+DNA Amplification. *Microchim. Acta* **2020**, *187*, 455–459.

(52) Manikandan, M. R.; Cai, K. P.; Hu, Y. D.; Li, C. L.; Zhang, J. T.; Zheng, Y. P.; Liang, Y. F.; Song, H. R.; Shang, M. Y.; Shi, X. N.; Zhang, J. X.; Yin, S. Q.; Shang, S. Y.; Wang, X. W. Influence of Hydrothermal Reaction Time on the Supercapacitor Performance of Ni-MOF Nanostructures. *Appl. Phys. Mater. Sci. Process* **2021**, *127*, 421–431.

(53) Song, W. W.; Wang, B.; Li, C. N.; Wang, S. M.; Han, Z. B. 3D Hierarchical Core-Shell Spiny Globe Shaped Co₂P@Ni₂P/NiCo₂O₄@CoO for Asymmetric Supercapacitors. *J. Mater. Chem. A* **2022**, *10*, 3710–3721.

(54) Mouchaham, G.; Wang, S.; Serre, C. The Stability of Metal–Organic Frameworks. *Metal-Org. Frameworks: Applications in Separations and Catalysis* **2018**, 1–28.

(55) Suksomboon, M.; Srimuk, P.; Krittayavathananon, A.; Luanwuthi, S.; Sawangphruk, M. Effect of Alkaline Electrolytes on the Charge Storage Capacity and Morphology of Porous Layered Double Cobalt Hydroxide-Coated Graphene Supercapacitor Electrodes. *RSC Adv.* **2014**, *4*, 56876–56882.

(56) Ashourdan, M.; Semnani, A.; Hasanpour, F.; Moosavifard, S. E. Synthesis of Nickel Cobalt Manganese Metal Organic Framework@high Quality Graphene Composites as Novel Electrode Materials for High Performance Supercapacitors. *J. Electroanal. Chem.* **2021**, *895*, 115452.

(57) Zhu, Y.; Tao, Z.; Cai, C.; Tan, Y.; Wang, A.; Yang, Y. Facile Synthesis Zn-Ni Bimetallic MOF with Enhanced Crystallinity for High Power Density Supercapacitor Applications. *Inorg. Chem. Commun.* **2022**, *139*, 109391.

(58) Zhang, X.; Wang, J.; Ji, X.; Sui, Y.; Wei, F.; Qi, J.; Meng, Q.; Ren, Y.; He, Y.; Zhuang, D. Flake-like Nickel/Cobalt Metal-Organic Framework as High-Performance Electrodes for Supercapacitors. *J. Mater. Sci. Mater. Electron.* **2020**, *31*, 16260–16268.

(59) Kang, X.; Wang, J.; Ma, Y.; Shi, X.; Chen, X.; Tian, H.; Ran, F. 3D Juniperus Sabina-like Ni/Co Metal-Organic Framework as an Enhanced Electrode Material for Supercapacitors. *J. Solid State Chem.* **2022**, *310*, 123056.

**EXPLORING METAL-ORGANIC FRAMEWORKS
DERIVED NANOMATERIALS FOR ADVANCED
SUPERCAPACITORS**

A THESIS SUBMITTED TO

SHIVAJI UNIVERSITY, KOLHAPUR

FOR THE DEGREE OF

DOCTOR OF PHILOSOPHY

IN

CHEMISTRY

UNDER THE FACULTY OF

SCIENCE AND TECHNOLOGY

BY

Miss. RAKHEE RAGHUNATH BHOSALE

M. Sc.

UNDER THE GUIDANCE OF

PROF. (Dr.) SANJAY S. KOLEKAR

M. Sc., Ph. D.

**ANALYTICAL CHEMISTRY AND MATERIALS SCIENCE LABORATORY,
DEPARTMENT OF CHEMISTRY,
SHIVAJI UNIVERSITY,
KOLHAPUR – 416 004 M.S., INDIA**

JUNE - 2023

80-RECOMMENDATION

1. Recommendation

As the global economy continues to grow at a rapid pace, there is an imminent need to create effective and dependable energy storage devices. In recent times, there has been a significant surge in popularity for a specific form of storage component known as a supercapacitor. This is mainly due to its exceptional features that effectively close the gap between a standard capacitor and a battery. During the forecast period, there is an expected rise in the demand for supercapacitors in energy harvesting applications such as trains, aircraft, electric vehicles, and low-power equipment like RAM, SRAM, PC cards, and micro-controllers. In order to take advantage of profitable prospects within the energy harvesting industry, the supercapacitor market must strive for ongoing innovations in its essential characteristics such as energy density, power density, ESR, as well as cyclic and mechanical stability.

In order to enhance the performance of supercapacitors, the main objective of this thesis is to concentrate on creating and studying MOFs and their derived materials to serve as electrode constituents for supercapacitors.

2. Conclusion

The current work has been planned with the above perspective. A focus has been placed on developing MOFs and their derived materials using simple chemical methods in order to create different nanostructure morphologies. The influence of the physicochemical outcome on the surface area, porosity, power density, specific capacitance and stability has been studied at length. The research work has been encompassed in seven chapters

Chapter – I

This chapter comprises the introduction and theoretical background of energy storage devices along with their characteristics and electrical parameters of devices in detail. Also, it includes the types of supercapacitors and the different electrode materials used in supercapacitors. The current status of the use of MOF material for supercapacitor application is discussed. The ways to improve the electrochemical performance and survey of literature have been systematically given. The various techniques and practices to prepare different materials using MOF as a template are also illustrated. Finally, the detailed literature survey based on the Scopus database on

MOF and its derived material used as electrode materials in supercapacitor application is given in detail.

Chapter – II

Chapter II provides thorough information on the experimental methodologies and characterization techniques. The section provides a detailed analysis of various physicochemical characterizations that are utilized to confirm the suitability of materials that have been evaluated for use in supercapacitors. The description of the experimental arrangement for these techniques and the construction process of the working electrode is elaborated. This chapter provides comprehensive information on various physical characterization methods employed in studying MOFs and the derived materials developed in this study. These techniques include X-ray diffraction, Fourier transform infrared spectroscopy, Raman spectroscopy, X-ray photoelectron spectroscopy, Field emission scanning electron microscopy, Energy dispersive X-ray analysis, Brunauer–Emmett–Teller analysis, Transmission electron microscopy and Vibrating sample magnetometer. This chapter extensively covers the electrochemical analysis of the materials using an electrochemical workstation, along with a detailed discussion of the relevant electrochemical parameters.

Chapter – III

Chapter – III deals with the synthesis and characterization of pristine Ni-MOF for supercapacitor application using a simple, low-cost reflux condensation method. The XRD patterns confirmed that the synthesized Ni-MOF were found to be polycrystalline in nature with an average crystallite size 6.89 nm. The SEM images revealed that the Ni-MOF possess nanorods like morphology with an average length of nanorod is 19.09 nm. The BET analysis reveals that synthesized Ni-MOF possess a large specific surface area with a plenty of mesopores in the materials. The synthesized Ni-MOF shows an excellent specific capacitance of 1956.3 F g⁻¹ at a current density of 5 mA cm⁻² and it retained 81.13% of its initial capacitance even after 3000 GCD cycles at a 35 mA cm⁻² current density. Additionally, a hybrid supercapacitor device was fabricated to examine the practical ability of the Ni-MOF. The extraordinary energy-storage properties of the Ni-MOF electrode are attributed to its nanorod-like structure and higher surface area. This study provides a new platform for supercapacitors and other energy-storage devices.

Chapter – IV

Chapter – IV focuses on the synthesis and characterization of novel trimetallic MOFs to study effect of tricarboxylic and dicarboxylic ligands on electrochemical properties of MOF. From this study it has been concluded that the MOF synthesized using dicarboxylic ligand i.e. terephthalate MOF (BDC-MOF) shows better electrochemical properties due to its less acidity of ligand than the tricarboxylic ligand. The terephthalate MOF shows nanobricks like morphology with high specific surface area of $267.85 \text{ m}^2 \text{ g}^{-1}$ and mesoporous in nature. The BDC-MOF electrode shows a specific capacitance of 582.8 F g^{-1} , a good energy density of 40.47 Wh kg^{-1} and a power density of 687.5 W kg^{-1} at 5 mA cm^{-2} with excellent cyclic stability of 92.44 % for 3000 charge-discharge cycles. Moreover, a symmetric supercapacitor device was constructed to evaluate the functional capacity of the BDC-MOF. A symmetric BDC-MOF//BDC-MOF supercapacitor device shows the specific capacitance of 95.22 F g^{-1} with low capacitance decay, high energy and power densities which is used for electronic applications.

Chapter – V

Chapter – V discusses the synthesis of novel bimetallic MOF ($\text{MnFe}_2\text{-MOF}$) by a simple reflux condensation method followed by simple heat treatment to get derived magnetic ferrite (MnFe_2O_4). The prepared MOF and its derived ferrite was characterised using various sophisticated techniques. The synthesized MOF and its derived ferrite possess nano cubes and bricks like morphology with voids in between them. Both the materials shows type IV isotherm with plenty of mesopores in the material. The $\text{MnFe}_2\text{-MOF}$ electrode has superior electrochemical characteristics compared to MnFe_2O_4 , including exceptional reversibility, fast kinetics, low internal resistance (measured at 0.2Ω), and impressive specific capacitance of 1226 F g^{-1} at 1 A g^{-1} current density. Additionally, this electrode exhibits excellent cyclic stability, retaining approximately 95.68% of its initial capacitance after 3000 charge-discharge cycles. Furthermore, in order to ensure the practical feasibility of $\text{MnFe}_2\text{-MOF}$ as a positive electrode, it was utilized in the production of an asymmetric device that displays remarkable electrochemical capabilities.

Chapter - VI

Chapter – VI comprises the synthesis of bimetallic MOF by a simple wet chemical method and followed by the pyrolysis technique a ferrite and nanoporous carbon were prepared. Among the derived materials, nanoporous shows better

magnetic properties than the ferrite material. Out of these materials the nanoporous carbon shows large specific surface area than other materials which helps to enhance the electrochemical performance. The nanoporous carbon electrode shows a specific capacitance of 1271 F g^{-1} at 2 mA cm^{-2} current density with excellent cyclic stability of 96.87 % for 5000 charge-discharge cycles. Additionally, a hybrid supercapacitor device was fabricated using derived ferrite as a positive electrode and derived nanoporous carbon as a negative electrode by an 'all-in-one strategy'. The study suggests that the application of ferrite and nanoporous carbon derived from bimetallic MOF precursor in hybrid supercapacitor device holds significant potential for practical energy storage.

Chapter - VII

Chapter - VII is about the research work's summary and conclusion.

3. Summary

To recapitulate, the major purpose of this research was to investigate MOF materials as electrode materials for supercapacitor applications using wet chemical procedures. The main results of the current thesis are described below.

The main focus was to synthesize the MOF and its derived materials as electrode materials for advanced supercapacitors. Firstly, a pristine Ni-MOF was prepared and used as an electrode material for asymmetric supercapacitor. Still, pristine MOFs have some limitations, to overcome those limitations we have studied trimetallic MOFs to study the appropriate use of ligands for MOF synthesis. From that study, we conclude that terephthalic acid is the most appropriate ligand for the synthesis of MOF for supercapacitor applications. Further, by using the terephthalic acid a bimetallic MOF was synthesized and through the heat treatment, a magnetic oxide was formed to overcome the thermal stability of MOF. Still, the oxides possess average electrochemical properties. To conquer all the above limitations, a bimetallic MOF was synthesized by a simple wet chemical route and also using a simple pyrolysis technique a magnetic oxide as well as nanoporous carbon was synthesized which shows excellent electrochemical properties. Moreover, cyclic stability is one of the key parameter in supercapacitor. Hence, we have focused to enhance the cyclic stability of the materials with different strategies. Among these strategies, bimetallic MOF derived oxides and nanoporous carbon exhibited outstanding specific capacitance as well as cyclic stability due to orchestrating effects including high

specific surface area, porosity, effective morphology, magnetic behavior and high thermal properties. Based on this approach we have designed a hybrid supercapacitor device using derived both magnetic oxide and nanoporous carbon employing an all-in-one approach. The script of the thesis related to cyclic stability is presented in graphical form as shown in figure 7.1 below.

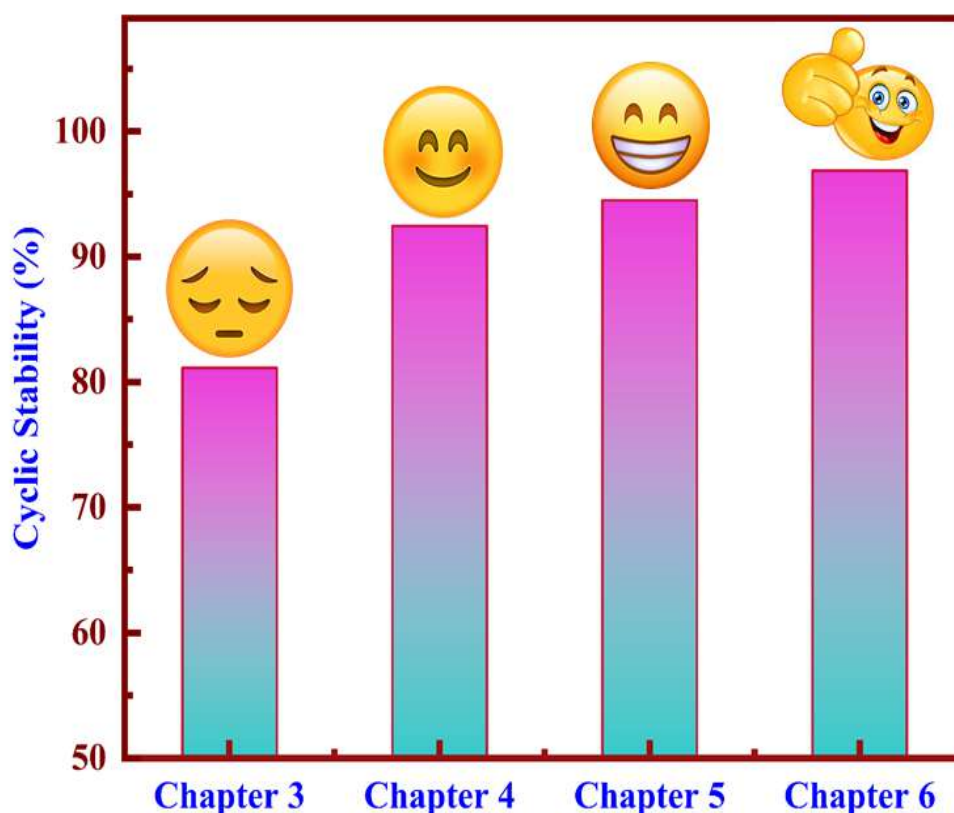


Figure 7.1: Schematic illustration of work carried out for thesis

4. Future findings

- ❖ The primary objective for the development of energy storage devices using supercapacitors is to achieve a substantial increase in energy density. A potential solution is modifying the gadget's components. One way to achieve this is to exchange one electrode in a supercapacitor for a Lithium-based substance, such as Lithium titanate ($\text{Li}_4\text{Ti}_5\text{O}_{12}$), which possesses battery qualities. This method combines the benefits of a supercapacitor and a battery, resulting in an extremely high energy density of over 100 Whkg^{-1} . These devices, similar to batteries, are commonly known as supercapacitors or supercapbatteries.

- ❖ The role of electrolytes is crucial in energy storage devices. Therefore, the creation of novel electrolytes such as ionic liquid and redox electrolytes that offer a wider potential window can lead to superior electrochemical capabilities.
- ❖ Our current research indicates that the behavior of the supercapacitor was analyzed utilizing stainless steel mesh as the current collector. Efforts will be made to create electrodes for supercapacitor devices that are both highly conductive and flexible by utilizing various substrates such as nickel foam, carbon cloths, ITO and FTO, with the ultimate goal of producing supremely efficient and portable supercapacitors.
- ❖ The utilization of molecular simulations holds significant potential in enhancing our comprehension of crucial factors like the function of mesopores and macropores in ion diffusion and electrode-electrolyte interaction. These findings can prove beneficial in the development of top-performing electrodes.